WILEY-VCH

Christian Iliadis

Nuclear Physics of Stars

Second, Revised and Enlarged Edition

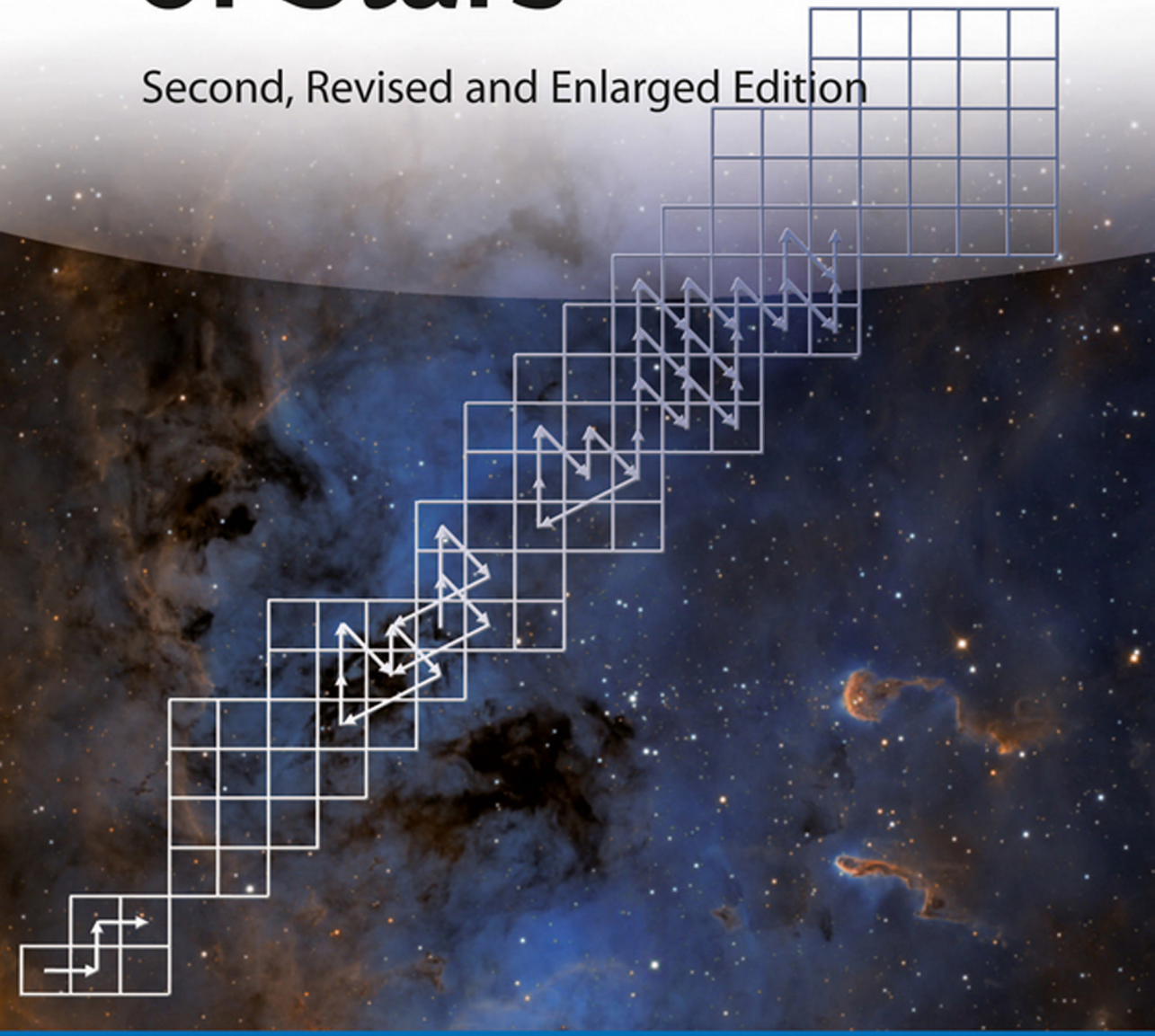

PHYSICS TEXTBOOK

Christian Iliadis

Nuclear Physics of Stars

Related Titles

Zelevinsky, V., Volya, A.

Physics of Atomic Nuclei

2016
Print ISBN: 978-3-527-41350-8
(Also available in a variety of electronic formats)

Bartelmann, M.

Theoretical Astrophysics

An Introduction

2013
Print ISBN: 978-3-527-41004-0
(Also available in a variety of electronic formats)

Nappi, E., Peskov, V.

Imaging Gaseous Detectors and their Applications

2012
Print ISBN: 978-3-527-40898-6
(Also available in a variety of electronic formats)

Christian Iliadis

Nuclear Physics of Stars

Second, Revised and Enlarged Edition

WILEY-VCH
Verlag GmbH & Co. KGaA

The Author

Prof. Dr. Christian Iliadis
The University of North Carolina at Chapel Hill
Department of Physics and Astronomy
232 Phillips Hall
Chapel Hill, NC 27599
United States

Library of Congress Card No.: applied for

British Library Cataloguing-in-Publication Data
A catalogue record for this book is available from the British Library.

Bibliographic information published by the Deutsche Nationalbibliothek
The Deutsche Nationalbibliothek lists this publication in the Deutsche Nationalbibliografie; detailed bibliographic data are available on the Internet at <http://dnb.d-nb.de>.

Print ISBN: 978-3-527-33648-7
ePDF ISBN: 978-3-527-33649-4
ePub ISBN: 978-3-527-33651-7
Mobi ISBN: 978-3-527-33650-0
oBook ISBN: 978-3-527-69266-8

Cover Design Adam Design, Weinheim, Germany
Typesetting Laserwords Private Limited, Chennai, India
Printing and Binding Markono Print Media Pte Ltd., Singapore

Printed on acid-free paper

Contents

Preface to the Second Edition

The publisher's suggestion of a second edition of "Nuclear Physics of Stars," only seven years after the first edition appeared, came as a surprise. However, I was easily convinced to undertake this endeavor because of the enthusiastic response to the first edition from students and colleagues at many universities and laboratories. This provided the opportunity to include several topics that were missing in the first edition. The following sections have been added:

1) explosive nucleosynthesis in core-collapse supernovae,
2) explosive nucleosynthesis in thermonuclear supernovae,
3) neutrino-induced nucleosynthesis,
4) big bang nucleosynthesis,
5) galactic cosmic ray nucleosynthesis.

Several sections have been revised, including the discussion of stellar enhancement factors and the extraction of cross sections from measured yields. All of the tables have been updated with the most recent information available. Many figures have been improved, some have been omitted, while others have been added. References have been updated and several new end-of-chapter problems have been included. Some of the material was rearranged for a more coherent discussion.

I would like to thank the following people for their suggestions and valuable comments: Art Champagne, Alessandro Chieffi, Alain Coc, Jack Dermigny, Lori Downen, Mounib El Eid, Peter Hoeflich, Sean Hunt, Jordi José, Keegan Kelly, Karl-Ludwig Kratz, Marco Limongi, Richard Longland, Maria Lugaro, Brad Meyer, Peter Mohr, Anuj Parikh, Nikos Prantzos, Ivo Seitenzahl, Frank Timmes, and John Wilkerson. This book is dedicated to my parents, for all that they have done.

Carrboro, August 2014 *Christian Iliadis*

Preface to the First Edition

Nuclear processes generate the energy that makes stars shine. The same nuclear processes in stars are responsible for the synthesis of the elements. When stars eject part of their matter through various means, they enrich the interstellar medium with the nuclear ashes and thereby provide the building blocks for the birth of new stars, of planets, and of life itself. The theory of this building of elements is called nucleosynthesis and it is remarkably successful in describing the nuclear processes in stars that are located so far away from us in space and time. It is equally remarkable how the theory predicts these processes based on the quantum mechanical properties of atomic nuclei. Nucleosynthesis, nuclear energy generation in stars, and other topics at the intersection of nuclear physics and astrophysics make up the science of nuclear astrophysics. Like most fields of physics, it involves both theoretical and experimental activities. The purpose of this book is to explain these concepts with special emphasis on nuclear processes and their interplay in stars.

Work on the manuscript for this book started when I was invited to teach a two-week long, graduate-level course on "Nuclear Physics of Stars" at the Universitat Politècnica de Catalunya in Barcelona, Spain, in June 2003. During the preparations for the course, it became quite obvious that it would be useful to have an up-to-date textbook available. The encouragement I received from many colleagues and students to write such a book was instrumental for my decision to begin work on a manuscript.

After a decade of teaching at the University of North Carolina at Chapel Hill I learned from my students to take no "well-established" fact for granted. They wanted to see derivations of equations when I attempted to state "the obvious." They insisted on more fundamental explanations when I just tried to "wave my hands." The style of the present book is certainly influenced by my teaching experience. Indeed, most equations are derived in the text and special emphasis has been placed on the art work. My main intention is to explain complicated concepts in the simplest and most intuitive manner. In some instances, more elegant formulations of concepts have been presented in the literature. For the manuscript these were considered only if I found it impossible to come up with a simpler explanation. Colleagues frequently wanted to know "which review paper" I used in the preparation of a specific section. My strategy was to consult review articles only

after I wrote a complete first draft of the section. That way I was forced to comprehend the subject myself from the beginning and to come up with a coherent presentation.

The present book is directed toward advanced undergraduate students, graduate students, and researchers in the fields of nuclear physics and astrophysics. Chapter 1 starts with the basic concepts in nuclear physics and stellar evolution. Chapter 2 develops the theory of nuclear reactions starting from basic quantum mechanical ideas. Nuclear processes in a stellar plasma are discussed in Chapter 3. Chapter 4 contains the most important experimental information needed in order to perform measurements in nuclear astrophysics. Chapter 5 provides a discussion of the theory of stellar nucleosynthesis. The appendices contain sections on basic solutions of the Schrödinger equation, angular momentum selection rules, kinematics, and the theory of angular correlations. At the end of the text, physical constants, mathematical symbols, and physical quantities are listed as an aid for the reader. As a prerequisite, the student should have taken an undergraduate course in modern physics with elementary coverage of wave functions. An undergraduate course in quantum mechanics or nuclear physics would also be helpful, but is not required.

The present book goes into considerable depth and, consequently, restrictions in time and space made it unavoidable for me to omit a number of important topics. The instructor who is using this book may wish to supplement the material presented here with information on primordial nucleosynthesis (J. Rich, *Fundamentals of Cosmology*, Berlin: Springer, 2001), cosmic-ray spallation reactions (E. Vangioni-Flam, M. Cassé and J. Audouze, *Phys. Rep.*, Vol. 333, p. 365, 2000), nucleochronology (J. J. Cowan, F.-K. Thielemann and J. W. Truran, *Ann. Rev. Astron. Astrophys.*, Vol. 29, p. 447, 1991), neutrino astrophysics (J. N. Bahcall, *Neutrino Astrophysics*, Cambridge: Cambridge University Press, 1989), ν-process (Woosley et al., *Astrophys. J.*, Vol. 356, p. 272, 1990), presolar grains (M. Lugaro, *Stardust from Meteorites*, Singapore: World Scientific, 2005) and indirect measurements of astrophysically important nuclear reactions. It is utterly impossible to recommend one, or even a few, references for the last topic, which represents a vast field in its own right.

I would certainly not have written this book without the influence of two of my colleagues. I am indebted to Jordi José, who invited me to Barcelona in 2003 and who organized my lectures and my wonderful stay there. I also wish to express my appreciation to Art Champagne, who supported me professionally through all stages during the preparation of the manuscript. A number of people have read through parts of the manuscript and have provided many valuable suggestions and comments. The book benefited substantially from their input. It is my pleasure to thank Carmen Angulo, Dick Azuma, Bruce Carney, Gerald Cecil, Art Champagne, Alan Chen, Alessandro Chieffi, Alain Coc, Pierre Descouvemont, Ryan Fitzgerald, Uwe Greife, Raph Hix, Jordi José, Franz Käppeler, Karl-Ludwig Kratz, Alison Laird, John Lattanzio, Marco Limongi, Richard Longland, Alex Murphy, Joe Newton, Anuj Parikh, Helmut Paul, Tommy Rauscher, Paddy Regan, Hendrik Schatz, Sumner Starrfield, and Claudio Ugalde. I would like to thank Daniel Aarhus for

typing the manuscript, and John Kelley for helping with the preparation of some figures. I would like to acknowledge support from a University Research Council publication grant from the University of North Carolina at Chapel Hill and I am also grateful for the support I received from the Triangle Universities Nuclear Laboratory. The book is dedicated to my daughter Alina, my son Kimon, and my wife Andrea, who certainly felt the significant investment of my private time in this project during the past four years.

Carrboro, September 2006 *Christian Iliadis*

1
Aspects of Nuclear Physics and Astrophysics

1.1
History

In 1920, Aston discovered that the mass of the helium atom is slightly less than four times the mass of the hydrogen atom. Immediately afterward, Eddington suggested in his 1920 presidential address to the British Association for the Advancement of Science that Aston's discovery would explain the energy generation of the Sun via the conversion of hydrogen to helium. However, Eddington could not explain why the stellar temperatures inferred from observation were well below those thought necessary to initiate fusion reactions. In 1928 Gamow, and independently Condon and Gourney, calculated the quantum mechanical probability for particles to tunnel through potential barriers and thereby explained the phenomenon of α-particle decay (Gamow, 1928; Condon and Gourney, 1929). Atkinson and Houtermans used Gamow's results to suggest that quantum mechanical tunneling may explain the energy generation of stars via nuclear fusion reactions (Atkinson and Houtermans, 1929).

Cockcroft and Walton (1932) initiated the first nuclear reaction using artificially accelerated particles by bombarding and disintegrating lithium nuclei with protons accelerated to several hundred kilo electron volts energy. Incidentally, the disintegration of lithium into two α-particles is one of the reactions of what would later be called the *pp chains*. Lauritsen and Crane produced in 1934 a 10-min radioactivity following the bombardment of carbon with protons. It was the first measurement of one of the reactions of what would later be called the *CNO cycle*.

Atkinson (1936) proposed the fusion of two hydrogen nuclei to deuterium as a source of stellar energy generation. A detailed treatment of this reaction was provided by Bethe and Critchfield who showed that the p + p reaction gives an energy generation of the correct order of magnitude for the Sun (Bethe and Critchfield, 1938). The energy production in stars via the CNO cycle was independently discovered by von Weizsäcker (1938) and Bethe (1939). The latter work, in particular, investigated for the first time the rate of energy production and the temperature dependence of the CNO cycle.

In the following years some of the pioneering ideas of nuclear astrophysics were established. In two papers, Hoyle first presented the theory of nucleosynthesis

Nuclear Physics of Stars, Second Edition. Christian Iliadis.

within the framework of stellar evolution using the nuclear data available at the time (Hoyle *et al.*, 1946; Hoyle, 1954). Nuclear experiments had firmly established that no stable nucleus of mass number 5 or 8 exists in nature. For this reason, it was a mystery how these mass gaps could be bypassed in the synthesis of heavier nuclei from lighter species. Salpeter suggested in 1951 that a small equilibrium concentration of unstable ^{8}Be could capture another α-particle to form stable ^{12}C and that this *triple-α reaction* could be the main energy source in red giant stars (Salpeter, 1952). Hoyle pointed out that the capture probability would be far too small unless an excited state existed in ^{12}C at about 7.7 MeV excitation energy. The level was experimentally verified (Dunbar *et al.*, 1953) and its properties determined (Cook *et al.*, 1957), thereby establishing the triple-α reaction as the mechanism to overcome the mass 5 and 8 gaps.

In an influential review, Suess and Urey demonstrated the existence of several double peaks in a greatly improved distribution of observed solar-system abundances (Suess and Urey, 1956). It became immediately clear that these abundance peaks were associated with the neutron shell fillings at the magic neutron numbers in the nuclear shell model that Jensen and Goeppert Mayer had developed in 1949. The nucleosynthesis processes for the heavy nuclides beyond iron via neutron captures became later known as the *s- and r-processes*.

Of great importance was the discovery of spectral lines from the element technetium in evolved red giant stars (Merrill, 1952). All of the technetium isotopes are unstable and the longest lived isotope has a half-life of $\approx 4.2 \times 10^6$ y. Such half-lives are very short on a cosmological time scale ($\approx 10^{10}$ y) and, consequently, the discovery showed beyond doubt that the technetium must have been produced *recently* within the stars and that the products of nucleosynthesis could reach the stellar surface with the help of mass loss and mixing.

The available knowledge at the time regarding the synthesis of elements was presented in a review article by Burbidge *et al.* (1957), and independently by Cameron (1957). These papers laid the ground work for the modern theory of nuclear astrophysics. The field has developed since into an exciting discipline with impressive achievements, linking the topics of astronomical observation, nuclear physics experiment, nuclear theory, stellar evolution, and hydrodynamics.

1.2 Nomenclature

Atomic nuclei consist of protons and neutrons. The symbol Z denotes the number of protons and is called *atomic number*. The number of neutrons is denoted by the symbol N. The *mass number* A is defined by the integer quantity $A = Z + N$. It is sometimes also referred to as *nucleon number*. Nuclei with the same number of protons and number of neutrons have the same nuclear properties. They can be represented by the symbol ${}^{A}_{Z}\mathrm{X}_{N}$, where X is the element symbol. Any individual nuclear species is called a *nuclide*. Nuclides with the same number of protons,

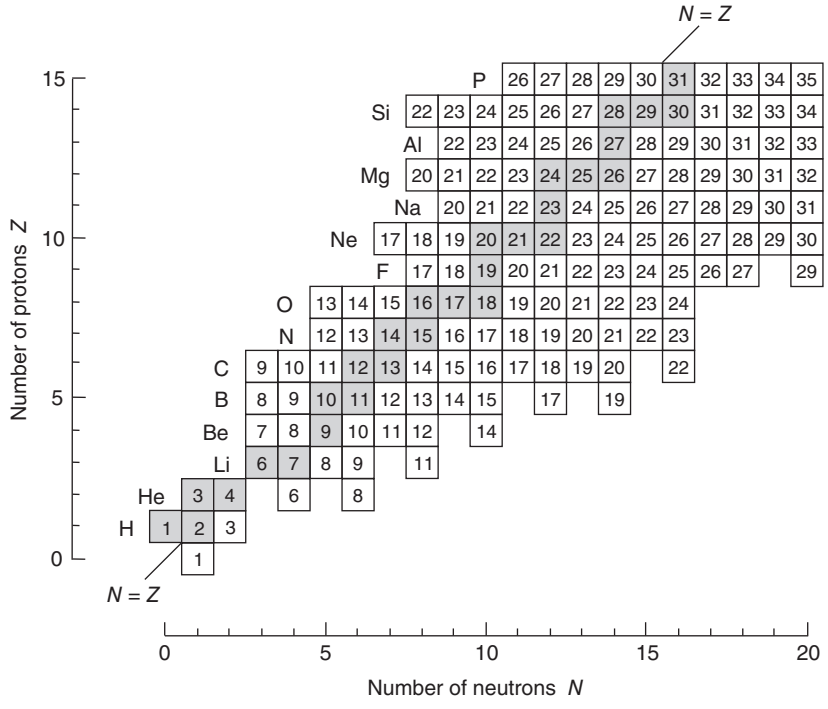

Figure 1.1 Section of the chart of the nuclides, showing the lightest species with $Z \leq 15$ and $N \leq 20$. The shaded squares represent stable nuclides, while the open squares correspond to unstable nuclides with half-lives in excess of 1 ms. The only exceptions are the nuclides ^{8}Be and ^{9}B, which have considerably shorter half-lives. No stable nuclides exist with a mass number of $A = 5$ or 8.

but different number of neutrons (and hence a different mass number A) are called *isotopes*. Nuclides of the same mass number, but with different numbers of protons and neutrons are called *isobars*. Nuclides with the same number of neutrons, but with different number of protons (and hence a different mass number A) are called *isotones*. Isotopes, isobars, and isotones have different numbers of protons or neutrons and, therefore, their nuclear physics properties are different.

Nuclides can be represented in a two-dimensional diagram, called *chart of the nuclides*. It displays the number of neutrons and protons on the horizontal and vertical axes, respectively. Each square in this diagram represents a different nuclide with unique nuclear physics properties. Figure 1.1 displays a section of the chart of the nuclides, showing the lightest species with $Z \leq 15$ and $N \leq 20$. The shaded squares represent stable nuclides, while the open squares correspond to unstable nuclides with half-lives in excess of 1 ms. Many more unstable than stable nuclides exist in nature. It is also striking that no stable nuclides exist with a mass number of $A = 5$ or 8. This circumstance has a profound influence on the nucleosynthesis in stars, as will be seen in Chapter 5.

Example 1.1

The nuclide of carbon ($Z = 6$) with 7 neutrons ($N = 7$) has a mass number of $A = Z + N = 13$ and is represented by the symbol ${}^{13}_{6}C_{7}$. Since the element symbol and the number of protons (atomic number) carry the same information, both $Z = 6$ and $N = A - Z = 7$ are frequently suppressed in the notation. The carbon species with mass number $A = 13$ is then unambiguously described by the symbol ${}^{13}C$.

The species ${}^{12}_{6}C_{6}$, ${}^{13}_{6}C_{7}$, and ${}^{14}_{6}C_{8}$ are isotopes of carbon ($Z = 6$); ${}^{20}_{10}Ne_{10}$, ${}^{20}_{11}Na_{9}$, and ${}^{20}_{12}Mg_{8}$ are isobars of $A = 20$; ${}^{28}_{14}Si_{14}$, ${}^{29}_{15}P_{14}$, and ${}^{30}_{16}S_{14}$ are isotones of $N = 14$.

1.3 Solar System Abundances

It is commonly accepted that the solar system formed from the collapse of a gaseous nebula that had an almost uniform chemical and isotopic abundance distribution. Abundances in the solar system are also similar to those found in many stars, in the interstellar medium of the Sun's neighborhood and in parts of other galaxies. Therefore, it was hoped for a long time that a careful study of solar system abundances would provide a "cosmic" or "universal" abundance distribution, that is, an average abundance distribution representative for all luminous matter in the universe. A closer comparison of abundances in the solar system and other parts of the universe shows, however, significant compositional differences. Furthermore, the discovery of presolar grains in primitive meteorites allowed for the first time a very precise chemical and isotopic analysis of interstellar matter. Measurements of isotopic abundances in these presolar grains revealed the existence of very large deviations compared to solar system values. Following common practice in the literature, we will avoid the term "universal" abundances and use instead the expression *solar system abundances* when referring to the abundance distribution in the solar system at the time of its formation. The latter distribution provides an important standard to which reference is frequently made.

There are two major, independent and sometimes complementary, sources of solar system elemental abundances: (i) observations of the solar photosphere, and (ii) analysis of a specific class of meterorites, called *CI carbonaceous chondrites*. The Sun contains most of the mass in the solar system and is, therefore, representative for the overall composition. On the other hand, planets contain considerably less mass but they underwent extensive chemical fractionation over the past 4.5 Gy since their formation (Cowley, 1995). Among the more than 20 000 recovered meteorites, there are only five known CI carbonaceous chondrites. Although they contain a minuscule amount of matter, they are believed to be among the most primitive objects in the solar system. They show the least evidence for chemical fractionation and remelting after condensation and thus they retained most of the elements (except for a few very volatile species) present in the original matter

of the solar nebula. Details on how these abundances are obtained will not be repeated here (see, e.g., Arnett, 1996; Grevesse and Sauval, 1998; Palme and Jones, 2003; Lodders, Palme, and Gail, 2009). It is sufficient to remark at this point that the abundances derived from the solar photosphere and from primitive meteorites are in remarkable overall agreement (better than ± 10% for most elements). Solar system *isotopic* abundances are then derived from the *elemental* abundances using mainly terrestrial isotopic ratios (Rosman and Taylor, 1998).

The solar system abundances of the nuclides are shown in Figure 1.2a versus mass number A. The abundances are normalized to the number of silicon atoms. In cases where two or more stable isobars exist for a specific mass number A, the sum of the individual abundances is shown. Figure 1.2b displays the abundances separately for even-A and odd-A nuclides. Almost all the mass is contained in ^{1}H (71.1%) and ^{4}He (27.4%). There is an abundance minimum in the $A = 5$–11 region, corresponding to the elements Li, Be, and B. More than half of the remaining mass (1.5%) is in the form of ^{12}C and ^{16}O. The abundances drop slowly with increasing mass number. Another minimum occurs in the $A = 41$–49 region, around the element Sc. The abundance curve exhibits a maximum in the $A =$ 50–65 region, near the element Fe. The nuclides in this region are referred to as the *iron peak*. Beyond the iron peak, the abundances in general decrease with increasing mass number, although pronounced maxima are visible in the $A = 110$–150 and $A = 180$–210 regions. Closer inspection of Figure 1.2b also reveals that even-A nuclides are generally more abundant than odd-A nuclides. Furthermore, the abundance curve for odd-A nuclides is considerably smoother than the one for even-A nuclides.

The outstanding gross features in Figure 1.2 are the abundance maxima and minima. Specifically, the abundances do not scatter randomly, but instead exhibit a certain regularity and systematics. It is reasonable to assume that the abundances within any group or subgroup of nuclides can be attributed primarily to a specific mechanism of nucleosynthesis. Starting with the work of Suess and Urey (1956), such tables of solar system abundances had an enormous influence on investigations of the origin of the elements and the development of nuclear astrophysics. Not only did it become possible to identify and study various processes of nucleosynthesis that left their distinctive signatures in the abundance distribution, but a connection could also be made to the environments in which these sources of nucleosynthesis operated. All nuclides, with few exceptions, are synthesized in stars. Therefore, the observed solar system abundances offer powerful clues to stellar history and evolution, and by extension, to the chemical evolution of the galaxy as a whole.

It is fascinating that the structures seen in Figure 1.2 reflect the nuclear physics properties of various processes occurring in nature. A few very general comments follow below. All of the hydrogen (^{1}H and ^{2}H) and most of the helium (^{3}He and ^{4}He) nuclei originated in the big bang. The most abundant of these, ^{1}H and ^{4}He, are the basic building blocks for the synthesis of heavier and more complex nuclei. A deep abundance minimum occurs in the Li–Be–B region. These nuclides are quickly destroyed in fusion reactions with protons since their cross sections are

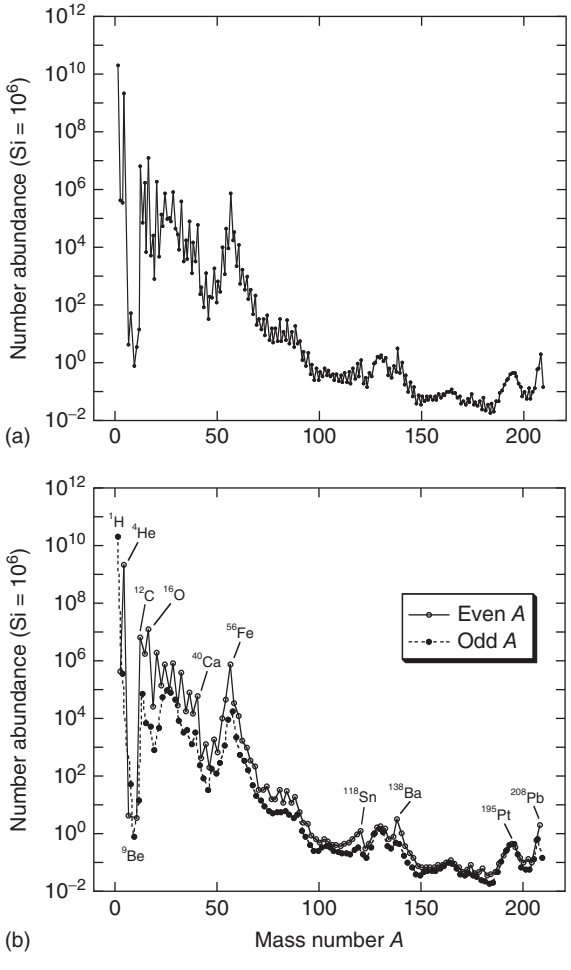

Figure 1.2 Abundances of the nuclides in the solar system at its birth. Number abundances are normalized to the number of silicon atoms (Si = 10^6). Data from Lodders (2003). (a) Sum of all nuclide abundances at a given value of A versus mass number. The maximum in the A = 50–65 region is referred to as the *iron peak*. (b) Separate abundance contributions from nuclides with an even or an odd value of A versus mass number. Even-A nuclides are in general more abundant than odd-A nuclides.

very large. Therefore, their observed solar system abundances must be explained by processes that occur in sites other than stellar interiors. They are thought to be produced via spallation reactions induced by Galactic cosmic rays. However, the big bang and certain stars did most likely contribute to the production of ^{7}Li. All of the heavier nuclides with $A \geq 12$ are produced in stars. The nuclides in the region between ^{12}C and ^{40}Ca are synthesized via charged-particle nuclear reactions in various stellar burning processes. Reactions between charged particles are subject to the Coulomb repulsion. The larger the charge of the reacting nuclei, the smaller

the nuclear reaction probability will become. This circumstance is reflected in the overall decline of the abundance curve from ^{12}C to ^{40}Ca. The abundance maximum of the iron peak occurs because these nuclides represent energetically the most stable species (Section 1.5.1). Because of the large Coulomb repulsion, the synthesis of nuclides beyond the iron peak via charged-particle reactions becomes very unlikely. These nuclei are instead produced by the capture of neutrons. The abundances of nuclides in the $A > 80$ region are on average a factor of 10^{10} smaller than the hydrogen abundance, as can be seen from Figure 1.2. The observed narrow and broad peaks in this mass region provide unambiguous evidence for the existence of two distinctive neutron capture processes. All of the above comments are very general and do not explain any details of the solar system abundance curve. An extensive discussion of the various nucleosynthetic processes will be given in Chapter 5. Information regarding the origin of the solar system nuclides is provided at the end of this book (Section 5.8).

1.4
Astrophysical Aspects

1.4.1
General Considerations

The study of stars is central to astronomy and astrophysics since stars are long-lived objects that are responsible for most of the visible light we observe from normal galaxies. The fusion of light nuclides into heavier species liberates kinetic energy at the expense of mass and serves as the interior source of the energy radiated from the surface. These very same reactions alter the composition of the stellar matter. As already pointed out, all nuclides with masses of $A \geq 12$ are produced in stars. When a star ejects part of its mass into space during certain evolutionary stages, the chemical composition of the interstellar medium will be altered by the thermonuclear debris. The interstellar medium, in turn, plays a key role in providing material out of which new generations of stars form. This cycling of matter between stars and the interstellar medium involves countless stars. By comparing the age of the Galaxy ($\approx$ 14 Gy) with the age of the Sun ($\approx$ 4.5 Gy) we can conclude that the cycling process that gave rise to the solar system abundance distribution operated for almost 10 billion years.

There is unambiguous *direct* evidence for the nucleosynthesis in stars. First, we already mentioned in Section 1.1 the observation of radioactive technetium in stellar spectra (Merrill, 1952). Second, γ-rays from radioactive ^{26}Al were discovered in the interstellar medium by spectrometers onboard satellites (Mahoney *et al.*, 1982; Diehl *et al.*, 1993). The half-life of this nuclide ($\approx 7.17 \times 10^5$ y) is even shorter than that for radioactive technetium, thus demonstrating again that nucleosynthesis is currently active in the Galaxy. Third, neutrinos are predicted to be the byproducts of nuclear processes in stars (Chapter 5). Since they interact very weakly with matter, they escape essentially unimpeded from stellar interiors.

Neutrinos from the Sun (Bahcall, 1989; Hirata *et al.*, 1990; Bellini *et al.*, 2014) and from the type II supernova 1987A (Hirata *et al.*, 1987; Bionta *et al.*, 1987) were detected on Earth, providing another direct test of stellar nucleosynthesis. Fourth, models of supernovae predict the ejection of radioactive ^{56}Ni (half-life of 6 days), which then decays to the radioactive daughter nucleus ^{56}Co (half-life of 77 days). The subsequent decay of this nuclide to stable ^{56}Fe is predicted to determine the decline of the light emission from these stellar explosions. The predictions agree well with the observed light curves of supernovae. Furthermore, the energetic γ-rays produced in the radioactive decays initially thermalize and deposit their energy via Compton scattering and photoelectric absorption. Because of the expansion, however, the column density decreases with time and the ejecta eventually become transparent. Photons from the radioactive decays of ^{56}Co and ^{44}Ti have been directly detected from supernova 1987A (Matz *et al.* 1988; Tueller *et al.* 1990; Grebenev *et al.* 2012).

The discovery of the existence of two distinct stellar populations by astronomers was also of paramount importance in this respect. The populations are referred to as *population I* and *population II* stars. They differ in their age and their content of metals, by which astronomers mean any element other than hydrogen and helium. Population I stars, including the Sun, are metal rich. They are young stars, having formed within the past few billion years, and can be found in the disk of the Galaxy. Extreme population I stars represent the youngest, most metal-rich stars and are found in the spiral arms of the Galaxy. Population II stars, on the other hand, are metal poor. They are relatively old and are found in the halo and the bulge of the Galaxy. Extreme population II stars represent the oldest, most metal poor stars and are found in the halo and in globular clusters. Their metal abundance, relative to hydrogen, is smaller by a factor of 100 or more compared to population I stars.

If one assumes that the initial composition of the Galaxy was uniform and if there exists no mechanism capable of concentrating the metals in the disk of the Galaxy, then the Galaxy must have synthesized an overwhelming fraction of its own metals. This argument provides strong support for the theory that nucleosynthesis is a natural process to occur during the evolution of stars. The metal content of the Galaxy increases with time since the matter out of which stars form is being cycled through an increasing number of stellar generations. Therefore, the differences in metallicity between the two stellar populations suggest that population I stars formed later during the history of the Galaxy when the interstellar medium became metal rich.

Nuclear reactions not only are required for explaining the bulk solar-system abundance distribution, but also are indispensable for explaining the observed chemical composition of individual stars. Such observations, even for trace elements, are crucial for constraining theoretical models of stars and for better understanding the complicated interplay of stellar hydrodynamics, convection, mixing, mass loss, and rotation. Stellar nucleosynthesis also plays a decisive role for explaining the chemical composition of the interstellar medium and is thus

intertwined with γ-ray astronomy, the study of primitive meteorites, and the nature of cosmic rays.

1.4.2 Hertzsprung–Russell Diagram

The total amount of radiation emitted per unit time, or the *luminosity*, varies strongly from star to star. The same holds for the effective stellar surface temperature. However, if we plot these two quantities for many individual stars in a diagram, then the result is not a random scatter of points, but most stars fall into several distinct groups. This correlation of stellar luminosity and effective surface temperature represents the single most important relationship of stellar properties. It is referred to as *Hertzsprung–Russell diagram* or color-magnitude diagram. The latter name implies that the surface temperature can be expressed in terms of the color of the star, while luminosity is related to the absolute magnitude. An explanation of these relationships can be found in any introductory astronomy textbook. The Hertzsprung–Russell diagram has a profound influence on the theory of stellar evolution and, by extension, on the history of the Galaxy as a whole.

Consider first Figure 1.3a, showing a Hertzsprung–Russell diagram for a sample of ≈ 5000 stars in the solar neighborhood. Each dot corresponds to a single star. The surface temperature increases from right to left in the figure. The vast majority of stars occupy the *main sequence* (MS), stretching diagonally from the upper left (hot and bright stars) to the lower right (cool and faint stars). The Sun, for example, belongs to the main sequence. In the low and right part (cool and faint stars) of the main sequence one finds the *red dwarfs* (RD). The *subgiant branch* (SGB) joins the main sequence and extends in a direction to cooler and brighter stars, where the populated region turns first into the *red clump* (RC), and then into the *red giant branch* (RGB). In a region corresponding to smaller luminosity and higher temperature (lower left), one finds a group of faint and hot stars known as *white dwarfs* (WD). A well-known example is Sirius B, the companion of Sirius. Some stars are located below the main sequence, but are considerably brighter than white dwarfs. These are known as *subdwarfs* (SD). A number of star categories do not appear in the figure. *Supergiants* (SG) are the brightest stars in the Galaxy and would occupy the upper end of the Hertzsprung–Russell diagram, but are very rare in the solar neighborhood. The cool and faint *brown dwarfs* would appear off scale way down in the lower-right, but are too faint to appear in the figure.

A Hertzsprung–Russell diagram for the globular cluster M 3 is shown in Figure 1.3b. There are about 200 globular clusters in the Galaxy. They are located in a spherical space surrounding the Galactic center, called the *halo of the Galaxy*. Each cluster consists of 10^4–10^6 gravitationally bound stars that are highly concentrated toward the cluster center. An image of the globular cluster M 10 is shown in color Figure 1 on page 613. Spectroscopic observations revealed that globular clusters are metal poor compared to the Sun, implying that they are very old and that they formed during the early stages of Galactic evolution. It is

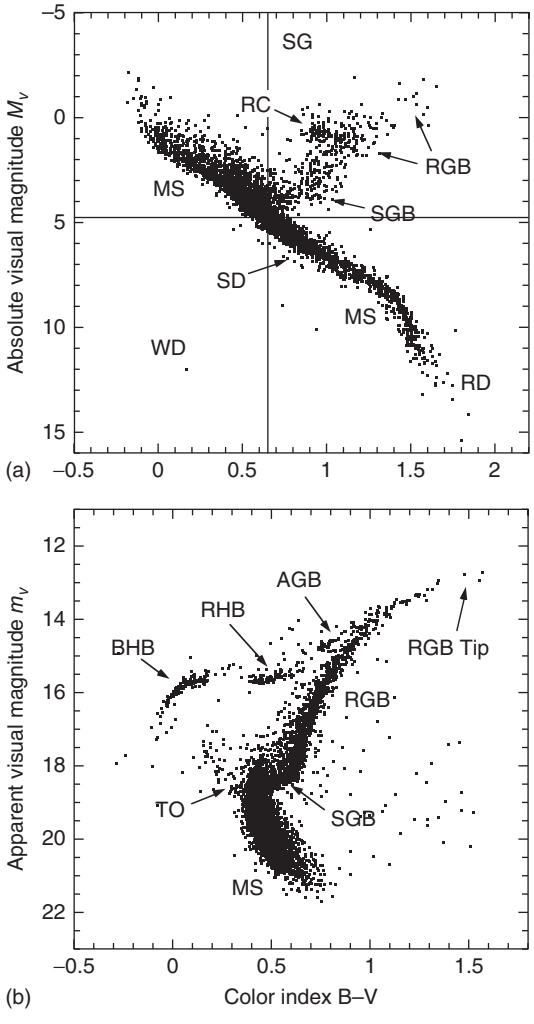

Figure 1.3 Observational Hertzsprung–Russell diagrams, showing visual magnitude versus color index B–V. Each dot corresponds to a star. See the text for an explanation of the labels. (a) Sample of ≈ 5000 stars in the solar neighborhood with precisely known distances. The data were acquired by the Hipparcos astrometry satellite. The vast majority of stars occupy the main sequence, stretching diagonally from the hot (blue) and luminous upper left to the cool (red) and faint lower right. The cross hair indicates the position of the Sun. Certain categories of stars do not appear in the figure, for example, supergiants, which are rare in the solar neighborhood, and brown dwarfs, which are too faint for detection by Hipparcos. (b) Data for the globular cluster M 3. Apparent rather than absolute magnitude is displayed on the vertical axis since the stars have the same distance from the Earth. The RR Lyrae variable stars, located between the red (RHB) and blue (BHB) horizontal branches, are omitted. Data from Corwin and Carney (2001).

commonly accepted that all stars in a typical globular cluster formed around the same time from material of very similar composition. The observation that the stars of a globular cluster occupy distinct regions in the Hertzsprung–Russell diagram must then be explained by differences in the only other major stellar property, that is, their initial mass. As will be shown below, the stellar mass is the most important property influencing the evolution of stars: the higher the mass, the faster a star will evolve.

Figure 1.3b shows some of the same stellar categories already mentioned in connection with Figure 1.3a. The densest region is occupied by main-sequence stars. The distinctive kink extending from the main sequence toward cooler and brighter stars is called the *turn-off point* (TO). The supergiant branch stars (SGB) are located on a horizontal part stretching toward the right, which turns upward into the red giant branch (RGB). Three more groups of stars can be distinguished on the left-hand side of the red giant branch: the asymptotic giant branch (AGB), the red horizontal branch (RHB), and the blue horizontal branch (BHB). As will be seen below, the different groups of stars seen in Figure 1.3a,b correspond to different stages of stellar evolution. Globular clusters in particular play an outstanding role in astrophysics since the distinct features in their Hertzsprung–Russell diagrams represent strong constraints for stellar models.

1.4.3 Stellar Evolution of Single Stars

One of the most important goals of the theory of stellar structure and evolution is to understand why certain stars appear only in specific regions of the Hertzsprung–Russell diagram and how they evolve from one region to another. Our aim in this section is to summarize without detailed justification the most important issues related to the nuclear physics of stars. An introduction to stellar evolution can be found in Binney and Merrifield (1998) or Iben (1985). A more comprehensive account is given, for example, in Kippenhahn and Weigert (1990). We will use in this section expressions such as hydrogen burning, helium burning, pp chain, CNO cycle, and so on, to obtain a general idea regarding nuclear processes in stars. These will be explained in depth in Chapter 5.

Theoretical models of stars in hydrostatic equilibrium are constructed in the simplest case by solving a set of four partial differential equations (for radius, luminosity, pressure, and temperature) that describe the structure of a star as a function of the distance from the center and as a function of time. A time sequence of such solutions, or stellar models, represents an *evolutionary track* in the Hertzsprung–Russell diagram. Stellar structure and evolution calculations rely heavily on large scale numerical computer codes. The time changes in the stellar properties are closely related to the energy budget. Energy is generated by the star via nuclear reactions and gravitational contraction, while energy is continuously lost from the stellar surface via emission of photons and neutrinos. As will become clear in the following discussion, a star spends most of its nuclear burning time fusing hydrogen to helium on the main sequence. Careful observations revealed a

direct correlation between the mass and the luminosity of a main-sequence star. The greater the total mass of the star, the greater the temperature and pressure in the core, the faster nuclear energy is generated, and the greater the energy output or the luminosity of the star. For example, a $10\,M_\odot$ main-sequence star has ≈ 3000 times the luminosity of the Sun. Furthermore, the main-sequence lifetime will also depend strongly on the stellar mass because a star burns the nuclear fuel at a rate that is determined by its luminosity. For example, solar-metallicity stars with masses of $1\,M_\odot$, $5\,M_\odot$, and $15\,M_\odot$ spend about 10 Gy, 100 My, and 12 My, respectively, on the main sequence. Once a star leaves the main sequence, the evolution speeds up significantly, as will be seen below.

Modern theories have been enormously successful in describing the properties of stars. Nevertheless, many open questions remain unsolved. Stellar evolution is an active research field and it is worthwhile to keep in mind the uncertainties in the model calculations. These reflect our incomplete knowledge of certain processes in stars, including the treatments of energy transport via convection, mass loss, atomic diffusion, turbulent mixing, rotation, and magnetic fields. For binary stars (Section 1.4.4), a host of additional problems is encountered because, first, the model assumption of spherical symmetry must be relaxed and, second, the interaction between the two stars becomes important. We will not discuss these effects in any detail other than to mention that most of them become increasingly important with ongoing stellar evolution. The effects of nuclear physics are deeply intertwined with these issues. When we discuss in later chapters the impact of nuclear physics uncertainties on the nuclear energy generation and the nucleosynthesis, it is very important to keep in mind that we are referring only to one piece in a complex puzzle. One of the main goals in nuclear astrophysics is to better understand the inner workings of stars. To this end, a reliable knowledge of nuclear physics is indispensable.

A chart showing the main evolutionary phases for single stars of various initial masses is shown in Figure 1.4 and will be helpful for the subsequent discussions. The stellar masses are shown on the left-hand side and time increases from left to right.

Premain-Sequence Stars

When an interstellar gas cloud consisting mainly of hydrogen and helium contracts, gravitational potential energy is transformed into thermal energy and into radiation. The gas is initially in gravitational free fall and most of the liberated energy is not retained but radiated away because the gas is relatively transparent. With increasing density, the opacity increases as well and some of the emitted radiation is retained in the cloud. As a result, the temperature and the pressure begin to rise and the contraction of the central, denser part of the cloud slows down. The increasing temperature causes first a dissociation of hydrogen molecules into atoms, and then an ionization of hydrogen and helium atoms. When a temperature of about 10^5 K is reached, the gas is essentially ionized. The electrons trap radiation efficiently and, as a result, the pressure and temperature increase and the collapse of the central part of the cloud halts. The premain-sequence star

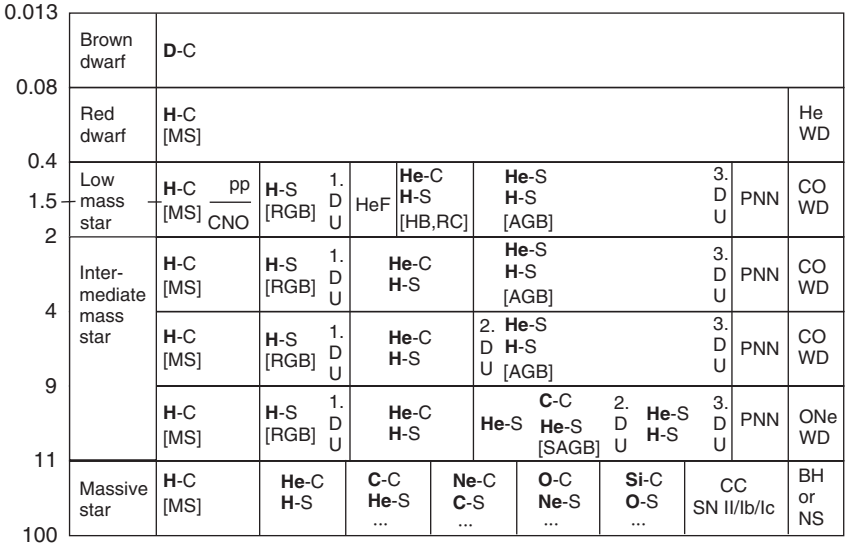

Figure 1.4 Major evolutionary stages for single stars in different mass ranges. The initial stellar mass is given on the left-hand side. Time increases from left to right. The nuclear fuel in each burning phase is shown in bold. For example, "**H**-C" refers to hydrogen burning in the core, "**He**-S" denotes helium burning in a shell, and so on. For lower-mass stars, the meaning of the labels in square brackets is described in the text (see also caption of Figure 1.5); "DU" denotes the different dredge-up events. For massive stars, the three dots indicate that there are additional overlying burning shells (Figure 1.7); the labels are: "CC" for core collapse, "SN" for supernova, "NS" for neutron star, and "BH" for black hole. The mass ranges are approximate estimates only and depend on the stellar metallicity. For the evolution of stars in the mass range of $M \geq 100\,M_{\odot}$, see Woosley, Heger, and Weaver (2002), and references therein.

eventually reaches a state of hydrostatic equilibrium, while still accreting matter from the outer parts of the cloud.

The source of energy is gravitational contraction, but the first nuclear reactions start to occur when the central temperature reaches a few million kelvin. Primordial deuterium fuses with hydrogen, a process that is called *deuterium burning* (Section 5.1.1), and primordial lithium may be destroyed via interactions with protons ($^7\mathrm{Li} + \mathrm{p} \rightarrow \alpha + \alpha$; the notation will be explained in Section 1.5.2). At this stage, energy is transported via convection and most of the star's matter, including surface material, is expected to be processed through the center. Although the nuclear energy release is very small, the reactions change the light element abundances and thus provide valuable information on the central temperatures.

When the temperature reaches several million kelvin, the fusion of hydrogen to helium starts to occur and contributes an increasing fraction to the total energy output. Ultimately, a point will be reached where hydrogen fusion in the core becomes the only source of energy. The star is now in hydrostatic and thermal equilibrium and has reached a location in the Hertzsprung–Russell diagram that

is referred to as the *zero age main sequence* (ZAMS). Stars with different initial masses reach the main sequence at different times. For example, the premain-sequence evolution of a $1\,M_\odot$ star lasts about 75 million years. Different stellar masses populate different locations on the zero age main sequence, which thus represents a line in the Hertzsprung–Russell diagram. Massive stars have higher temperatures, initiate nuclear reactions earlier, and are therefore located on the hotter and brighter part (upper left), while less massive stars will be found on the cooler and fainter part (lower right).

Newly born stars are difficult to observe because they are usually surrounded by a rotating disk of gas and dust. The solar system, for example, presumably formed from such a disk. Examples for premain-sequence objects are the *T Tauri stars*. Their lithium abundance is relatively high, indicating that the central temperature has not yet reached large enough values to destroy lithium via nuclear reactions involving protons.

The subsequent fate of stars depends strongly on their initial mass. We will consider the different mass ranges in turn. These main divisions are not sharp but depend somewhat on the chemical composition.

Initial Mass of $0.013\,M_\odot \lesssim M \lesssim 0.08\,M_\odot$

Theory predicts that objects in this mass range never reach the central temperatures required to sustain hydrogen fusion in their cores and are thus unable to generate sufficient nuclear energy to provide pressure support. The search for these very faint and cool stars provides important constraints for stellar evolution theory. Such objects have only been discovered in the mid-1990s and are referred to as *brown dwarfs*. They are predicted to be very abundant in the Galaxy and are, therefore, candidates for the elusive (baryonic) dark matter. Brown dwarfs are fully convective and their energy source in the early stages is provided by gravitational contraction.

Although brown dwarfs are not true stars, they do have enough mass to undergo deuterium burning, which sets them apart from massive planets such as Jupiter. This provides an additional, low-level, source of energy. They also have a relatively high lithium abundance since temperatures remain too low to destroy this element. The outer layers of a brown dwarf can be described by the ideal gas law. The core, however, becomes eventually electron degenerate. As a result, the contraction halts and the brown dwarf slowly cools, at approximately constant radius, by radiating its thermal energy into space. In the Hertzsprung–Russell diagram, a brown dwarf evolves almost vertically downward and straight past the main sequence (Figure 1.3).

A detailed description of the properties of degenerate matter is given in many modern physics textbooks and is not repeated here. We will summarize a few properties, however, that are also important for our discussion of other stars. Matter becomes degenerate at relatively high densities as a result of the Pauli exclusion principle which states that no more than two spin-1/2 particles (such as electrons) can occupy a given quantum state simultaneously. A degenerate gas strongly resists further compression because electrons cannot move into

lower energy levels that are already occupied. Unlike an ideal classical gas, whose pressure is proportional to its temperature, the pressure exerted by a completely degenerate gas does not depend on temperature. Or, in other words, increasing the temperature of a partially degenerate gas has only a small effect on the total pressure. It will be seen later that, when the temperature reaches a sufficiently high value, the degeneracy is lifted, by which we mean that the properties of such a gas revert to those of an ideal classical gas. Furthermore, there exists an upper limit to the pressure provided by a degenerate gas. If gravity exceeds this pressure, the star will collapse despite the presence of the degenerate particles. The maximum value for the mass of a star that can maintain an equilibrium between degeneracy pressure and gravity is called the *Chandrasekhar limit*. Its precise value depends on the composition. For an electron degenerate gas and matter characterized by two nucleons per electron (e.g., ^{4}He, ^{12}C, or ^{16}O), the limiting value is $\approx 1.44\,M_\odot$. Stars that enter a state of electron degeneracy toward the end of their evolution are called *white dwarfs*. White dwarfs with masses in excess of the Chandrasekhar limit are not observed in nature.

Initial Mass of $0.08\,M_\odot \lesssim M \lesssim 0.4\,M_\odot$

Stars in this mass range are sometimes referred to as *red dwarfs* (or M dwarfs). They are the most common type of star in the neighborhood of the Sun. For example, the nearest star to the Sun, Proxima Centauri, is a red dwarf. These stars have sufficient mass to fuse hydrogen to helium (*hydrogen burning*) in their cores via the pp chain. Starting from the zero age main sequence, the red dwarf evolves toward higher luminosity and increasing surface temperature (up and left). All stars that sustain hydrostatic equilibrium by burning hydrogen in their cores are called *main-sequence stars*. Theoretical models indicate that, for example, a $0.1\,M_\odot$ star of solar metallicity remains on the main sequence for about 6000 Gy. During this time the red dwarf is fully convective, which implies that its entire hydrogen content is available as nuclear fuel. Since the age of the universe is about 14 Gy, all red dwarfs that we observe must be main-sequence stars. Eventually, they will run out of nuclear fuel, that is, all their hydrogen will be converted to helium. Red dwarfs do not have enough mass to produce the higher temperatures required to fuse helium nuclei. Thus, they contract until electron degeneracy sets in. Their volume is constant from then on since the degeneracy pressure resists further compression. They become helium white dwarfs that cool slowly by radiating away their thermal energy.

Initial Mass of $0.4\,M_\odot \lesssim M \lesssim 2\,M_\odot$

The evolution of stars in this mass range is considerably more complicated compared to the previous cases. The life of the star starts on the zero age main sequence when hydrogen begins to fuse to helium in the core. In stars with masses below $M \approx 1.5\,M_\odot$, hydrogen fusion proceeds via the pp chains, while more massive stars burn hydrogen via the CNO cycles in their cores. It will be seen later that these different processes affect the stellar structure since they possess very different

temperature dependences (Section 5.1). In stars with $M \gtrsim 1.5\,M_\odot$, the strong temperature dependence of the CNO cycles concentrates the energy production in the center and, as a result, the core transports energy via convection. In stars with $M \lesssim 1.5\,M_\odot$, the energy generated in the core by the pp chains is transported via radiation.

As an example, we will discuss in the following the evolution of a special star, the Sun (see color Figure 2 on page 614). The evolutionary track is shown schematically in Figure 1.5a. The arguments given below follow the numerical results obtained by Sackmann, Boothroyd and Kraemer (1993). The Sun started central hydrogen burning via the pp chains on the zero age main sequence about 4.5 Gy ago. At present, the central temperature and density amount to $T \approx 15$ MK and $\rho \approx 150$ g/cm^3, respectively, and about one half of the original hydrogen in the core has been consumed so far. The Sun has a very small convective region at the surface, comprising only $\approx 2\%$ of its entire mass. About 4.8 Gy from now, the hydrogen in the core will be exhausted. The Sun will then be located at the bluest and hottest point on the main sequence, called the *turn-off point*. Note that in Figure 1.5a the track describing nuclear burning on the main sequence follows an arc. This partially explains why the main sequence in observational Hertzsprung–Russell diagrams represents a band rather than a narrow line.

Hydrogen fusion continues via the CNO cycles in a shell near the core where hydrogen is still left. The Sun slowly leaves the main sequence at this point. The Sun's center begins to contract to generate energy that is no longer provided by nuclear processes and the contraction causes further heating. As a result, the temperature in the hydrogen burning shell, and the associated nuclear energy generation rate, also increase. Initially, the Sun has not yet developed a fully convective envelope and it is called a *subgiant branch star* (SGB). Eventually, the envelope becomes fully convective. The extra energy output from the hydrogen burning shell results in a dramatic surface expansion and engulfs the planet Mercury. The Sun becomes a red giant star. While the Sun ascends the red giant branch, the luminosity increases continuously. Maximum luminosity is achieved on the tip of the red giant branch after about 0.6 Gy from the time when the Sun left the main sequence. During the red giant branch phase the Sun starts to experience significant mass loss. The contraction of the core during the red giant phase increases the central temperature and density by factors of 10 and 10^4, respectively, compared to the values at hydrogen ignition. The core achieves such high densities that the matter becomes electron degenerate. During the red giant branch phase, the convective envelope deepens significantly until it comprises about 75% of the Sun's mass. This deep convective envelope dredges up the products of hydrogen burning from the outer core. The process is referred to as the *first dredge-up*.

When the temperature reaches about $T \approx 0.1$ GK, the helium in the core starts to fuse to carbon and oxygen (*helium burning*). In a normal gas, the extra energy release would cause an expansion. As a result, the temperature would fall and the nuclear energy generation rate would decrease as well. This is the usual manner by which stars adjust to an energy increase in their interior, allowing them to stabilize.

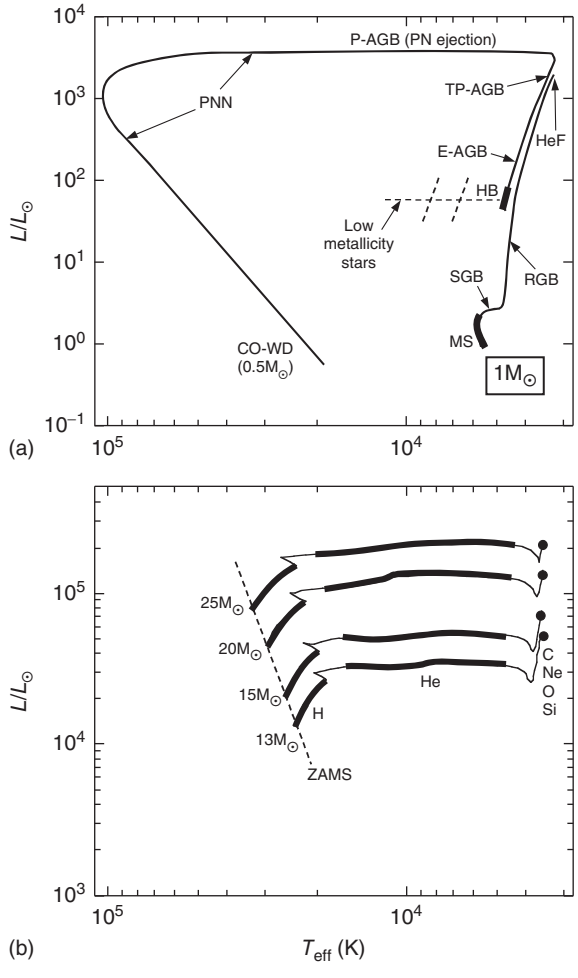

Figure 1.5 Schematic evolutionary tracks of (a) the Sun, and (b) massive stars of initial solar composition, in the Hertzsprung–Russell diagram; the luminosity on the vertical axis is given in units of the present solar luminosity. The heavy portions define the locations where major core nuclear burning phases occur. Details of tracks during transitions between major nuclear burning phases are omitted. The meaning of the labels are: main sequence (MS); zero age main sequence (ZAMS); subgiant branch (SGB); red giant branch (RGB); core helium flash (HeF); horizontal branch (HB); early asymptotic giant branch (E-AGB); thermally pulsing asymptotic giant branch (TP-AGB); post asymptotic giant branch (P-AGB); planetary nebula nucleus (PNN); carbon–oxygen white dwarf (CO-WD). Metal-poor stars in the initial mass range of $0.4\,M_\odot \lesssim M \lesssim 2\,M_\odot$ appear during core helium burning in a region marked by the horizontal dashed line in part (a), depending on the mass loss during the red giant branch phase. The two dashed diagonal lines indicate the instability strip. In part (b) the core burning phases are labeled by the nuclear fuel: hydrogen (H), helium (He), carbon (C), and so on. The onset of carbon burning is marked by the full circle. Note the vastly different luminosity scale in parts (a) and (b).

However, in a degenerate gas the temperature increase does not affect the pressure. No expansion occurs and, as a result, the temperature increases causing an even higher energy generation rate. As will be seen in Section 5.2, helium burning is highly temperature sensitive. The sequence of events repeats itself, giving rise to a *thermonuclear runaway*. It only terminates after a considerable energy is released that lifts the degeneracy. Thus, the ignition of helium in the core results in a violent *core helium flash* (HeF).

Notice that the helium flash does not represent a stellar explosion. The energy during the thermonuclear runaway goes into lifting the electron degeneracy and into the subsequent expansion of the core. The surface luminosity of the star does not increase, but the opposite happens. The surface luminosity declines by two orders of magnitude because the expansion of the core causes the surrounding hydrogen burning shell, which has been supplying all the surface luminosity, to cool and to generate less energy. Eventually, the Sun becomes a *horizontal branch* star, quietly burning helium in the core. The temperatures in the hydrogen shell just above the core are high enough for hydrogen to continue to burn via the CNO cycles. The nuclear energy release in helium fusion is considerably smaller compared to hydrogen fusion. Therefore, the duration of the core helium burning stage is considerably shorter than that of the core hydrogen burning stage. The Sun remains on the horizontal branch for about 0.1 Gy, which is typical for all stars in this mass range.

When the helium in the core is exhausted, the core contracts again, heats up, and ignites the helium in a surrounding shell. The Sun now burns nuclear fuel in two shells, helium in a shell surrounding the carbon–oxygen core, and hydrogen in a shell surrounding the helium burning region. The two shells are separated by an intershell region consisting mainly of helium. This stage is referred to as the *early asymptotic giant branch phase* (E-AGB), because the second ascent of the giant branch merges almost asymptotically with the first giant branch (at least for some stellar masses). While the Sun ascends the asymptotic giant branch, the helium burning shell becomes thermally unstable (Schwarzschild and Härm, 1965, see also Section 5.6.1). Energy is not generated at a steady rate, but the hydrogen and helium burning shells alternate as the major contributor to the overall luminosity. The details are rather complex, but an overview can be obtained from Figure 1.6, showing the time evolution of the stellar region at the interface of the hydrogen envelope and the carbon-oxygen core. The hydrogen and helium burning shell is depicted as thick and thin solid black line, respectively. For about 90% of the time, the hydrogen burning shell provides the Sun's nuclear energy, while the helium shell is only marginally active. Hydrogen burning adds continuously to the mass of the helium zone, however, so that the temperature and density near this zone rise until energy is generated by helium burning at a rate that is larger than the rate at which it can be carried outward by radiative diffusion. As a result, a thermonuclear runaway occurs. The sudden release of energy drives convection within the helium-rich intershell and extinguishes the hydrogen burning shell. The helium burning shell is now the only source of nuclear energy. Eventually, the expansion and associated cooling quenches the helium shell flash (or *thermal*

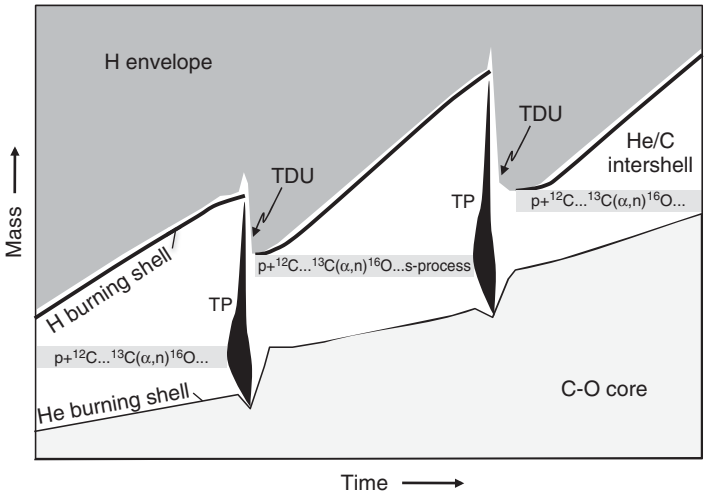

Figure 1.6 Schematic representation (mass versus time) of a low- or intermediate-mass ($M \lesssim 9\ M_{\odot}$), thermally pulsing AGB star. The figure is not to scale. Shown are: convective H envelope (dark gray); radiative ^{4}He-^{12}C intershell (white); degenerate C–O core (light gray). The thick and thin black line indicates the H-burning shell, which is active between thermal pulses, and the weakly active He-burning shell, respectively. For regular short periods of time, the barely active He shell ignites in a thermal pulse (TP), giving rise to a convective region (black) that extends over the entire intershell, extinguishing in the process the H-burning shell. When the thermal pulse comes to an end, the convective shell disappears and the quiescent He-burning resumes. Important mixing episodes occur at the end of each thermal pulse: (i) the convective envelope reaches into the intershell so that synthesized matter is transported to the stellar surface (third dredge-up; TDU); (ii) protons diffuse from the base of the envelope into the intershell, where they are captured by ^{12}C to produce (after β-decay) ^{13}C. Neutrons are then released by the ^{13}C(α,n)^{16}O reaction, producing *in situ* the main s-process component. During the subsequent thermal pulse, temperatures can be high enough to initiate the ^{22}Ne(α,n)^{25}Mg neutron source (Section 5.6.1).

pulse; solid black region labeled "TP" in Figure 1.6) and the Sun contracts again. The hydrogen burning shell reignites and ultimately takes over as the dominant nuclear energy source, until the next thermal pulse occurs about 10^5 y later. The cycle may repeat many times. This evolutionary stage is called the *thermally pulsing asymptotic giant branch (TP-AGB)*. The total amount of time the Sun spends on the AGB amounts only to about 20 My and is thus very short compared to the main-sequence lifetime. The thermal pulses cause the Sun's radius to vary periodically by a factor of 4, with the peak radius reaching close to the Earth.

The Sun suffers an episode of significant mass loss on the AGB via a strong stellar wind. Thermal pulses are ceasing at this point as the Sun becomes a post-asymptotic giant branch star (P-AGB), with only a fraction of its initial mass left and the other part returned to the interstellar medium. As more hydrogen of the envelope is ejected into space, hotter layers are uncovered and the Sun begins to move in the Hertzsprung–Russell diagram toward higher surface temperatures

(horizontally to the left). When the surface of the Sun becomes hot enough, the intense ultraviolet radiation ionizes the expanding ejecta, which begin to fluoresce brightly as a *planetary nebula* (PN). Two examples for planetary nebulae, the Dumbbell Nebula and the Cat's Eye Nebula, are shown in color Figures 3 and 4 on pages 615 and 616, respectively. The residual core is called a *planetary nebula nucleus* (PNN). Eventually, the hydrogen envelope disappears and the hydrogen burning shell extinguishes. The luminosity decreases rapidly causing the evolutionary track to turn downward and slightly to the right. The Sun will then end its existence as a white dwarf with a mass of $\approx 0.5\,M_{\odot}$, consisting mainly of carbon and oxygen. It is supported by electron degeneracy pressure and cools slowly by radiating away its thermal energy.

In the above discussion, the evolution beyond the red giant branch is rather uncertain because of our incomplete knowledge for predicting convection and mass loss. That these effects will occur has been demonstrated by stellar observations, but a deeper understanding is lacking at present. It is generally accepted that each thermal pulse during the TP-AGB phase provides favorable conditions for another dredge-up episode after the end of flash-burning in the helium shell. The convective envelope reaches deep into the intershell region, carrying the products of helium burning (mainly carbon, but also elements heavier than iron) to the stellar surface. This process is referred to as the *third dredge-up* (labeled "TDU" in Figure 1.6) and increases the carbon abundance in the envelope relative to other elements, for example, oxygen. Stars for which the number ratio of carbon to oxygen in their atmospheres exceeds unity are called *carbon stars*. Many of these have been observed and most are believed to correspond to stars in their TP-AGB phase. As will be seen later, AGB stars are also the source of many heavy nuclides with mass numbers beyond $A = 60$. Stellar models predict that these (s-process) nuclei are also dredged up to the surface where they can be observed in stellar atmospheres. The first direct evidence that nucleosynthesis takes place in stars and that the products could be mixed to the surface was the observation of radioactive technetium in certain (S-type) carbon stars (Section 1.1). For more information on AGB stars, see Habing and Olofsson (2004).

We are now in a position to understand some other details in the observational Hertzsprung–Russell diagrams shown in Figure 1.3. The precise location in luminosity and surface temperature of a star on the horizontal branch depends on the chemical composition of the envelope, the size of the helium core at the time of the helium flash, and the mass of the envelope which is influenced by the mass loss during the preceding red giant branch phase. In a globular cluster, all the stars start out with the same, low-metallicity, composition and their location on the horizontal branch is mainly influenced by mass loss. The more the mass lost from the hydrogen envelope, the hotter the layers in the star are uncovered. Stars with the smallest amount of mass in the hydrogen envelope populate the blue part (BHB), while stars with more hydrogen left in the envelope can be found on the red part (RHB). The horizontal branch intersects the instability strip (which is not related to nuclear burning). Stars located in this narrow and almost vertical band, indicated by the two vertical dashed lines in Figure 1.5a, are unstable to radial

pulsation and are called *RR Lyrae variables*. Their luminosity correlates with both their period (several hours to ≈ 1 day) and their metallicity. Therefore, they are important for determining the distances to globular clusters and for establishing a cosmic distance scale (Binney and Merrifield, 1998). Increasing the metallicity has the overall effect of making a star fainter and cooler. Therefore, stars in metal-rich clusters or in the solar neighborhood (Figure 1.3) accumulate at the red end (right) of the horizontal branch, fairly independent of their envelope mass. This region is called the *red clump* (RC).

The metallicity argument also applies to the subdwarfs. These are main-sequence stars of very low metallicity. They are hotter than solar-metallicity stars at a comparable evolutionary stage and are thus located to the left of the main sequence that is occupied by metal-rich stars.

It should also be clear now why the upper part of the main sequence in Figure 1.3b is missing. Globular clusters are metal-poor and old, and do not form new stars. The high-mass stars that were originally located on the upper part of the main sequence evolved a long time ago into red giants. Only the slowly evolving low-mass stars are left today on the main sequence. With increasing time lower mass stars will eventually become red giants and the main sequence will become shorter. It is interesting that the age of the cluster can be determined from the location of the turn-off point, located at the top of the surviving portion of the main sequence. If the distance to the cluster is known by independent means, the luminosity of the stars at the turn-off point can be related to their mass. Stellar evolution models can predict the main-sequence lifetime of stars with a given mass, which must then be nearly equal to the age of the cluster. Such investigations yield ages for the most metal-poor (and presumably oldest) globular clusters of about 12–13 Gy, indicating that these objects formed very early in the history of the Galaxy. This estimate also represents an important lower limit on the age of the universe (Krauss and Chaboyer, 2003).

Initial Mass of $2\,M_\odot \lesssim M \lesssim 11\,M_\odot$

We can divide this mass range into several subranges. Stars with initial masses of $2\,M_\odot \lesssim M \lesssim 4\,M_\odot$ evolve faster than less massive stars and their tracks will look quantitatively different from the results shown in Figure 1.5a. But otherwise they evolve through the same stages as a solar-like star. A major difference, however, arises for stars with $M \gtrsim 2\,M_\odot$ since their helium cores during the red giant branch phase do not become electron degenerate. Therefore, a helium flash does not occur but instead helium ignites quiescently in the center. Subsequently, these stars make excursions to the left (toward higher temperatures) in the Hertzsprung–Russell diagram and some of them are liable to pass into the instability strip. The observational counterparts of these variable stars are called *classical Cepheids*. They are important for establishing a cosmic distance scale since their observed pulsation period is correlated with their luminosity.

Stars with initial masses of $M \gtrsim 4\,M_\odot$ experience an additional episode of mixing. Following helium exhaustion in the core, the structural readjustment to helium shell burning results in a strong expansion, such that the hydrogen

burning shell is extinguished as the star begins to ascend the early asymptotic giant branch (E-AGB). At this time, the base of the convective envelope penetrates the dormant hydrogen shell, and the products of hydrogen burning are mixed to the surface. This process is referred to as the *second dredge-up*. Afterward, the hydrogen shell reignites and the star continues to evolve up the asymptotic giant branch (AGB). Subsequently, during the interpulse period of the TP-AGB phase, the base of the convective envelope reaches down to the top of the hydrogen burning shell, where the temperature exceeds 50 MK. The ensuing nucleosynthesis is referred to as *hot bottom burning*. Because the envelope is fully convective, it is completely cycled through this burning region and the products of hydrogen burning will be enriched at the stellar surface.

The evolution of stars in the initial mass range of $9\,M_\odot \lesssim M \lesssim 11\,M_\odot$ is more complicated and less established at present. Models predict a number of important differences compared to the evolution of lower mass stars. We will discuss the evolution of a $10\,M_\odot$ star with initial solar composition as an example (Ritossa, García-Berro, and Iben, 1996). The star starts out by burning hydrogen in the core via the CNO cycles for about 10 million years. Following the exhaustion of hydrogen in its center, the star evolves toward the red giant branch where eventually the first dredge-up event occurs. Helium burning starts in the core under nondegenerate conditions and lasts for about 270 000 years. After helium exhaustion, the core contracts and heats up, and the outer layers of the star expand. Thereafter, the hydrogen burning shell extinguishes, while helium continues to burn in a shell surrounding a partially electron degenerate carbon–oxygen core. Eventually, the core becomes sufficiently hot for the fusion of carbon nuclei (*carbon burning*). When carbon ignites, the star enters the super asymptotic giant branch (SAGB). Carbon burning starts with a thermonuclear runaway (*carbon flash*) and the energy generation rate from carbon fusion increases greatly. The energy release causes the overlying layers to expand, giving rise to a reduction in the helium shell burning energy generation rate. After a relaxation period, the helium burning shell returns to its prior energy output. Several of these flashes occur over the carbon burning lifetime, which lasts for about 20 000 years. When carbon is exhausted in the center, the electron degenerate core consists mainly of oxygen and neon. After carbon burning extinguishes, the second dredge-up event occurs. Subsequently, the dormant hydrogen shell on top of the helium burning shell is reactivated and a complicated interplay between these two burning shells gives rise to thermal pulses driven by helium shell flashes. During this time, the third dredge-up event occurs. Eventually, the hydrogen-rich surface is removed by a strong stellar wind and the star becomes the central object of a planetary nebula. It ends its existence as an oxygen–neon white dwarf with a mass of $\approx 1.2\,M_\odot$.

Initial Mass of $M \gtrsim 11\,M_\odot$

The evolution of stars in this mass range is in many ways fundamentally different compared to our earlier discussion. Schematic evolutionary tracks for $13\,M_\odot$, $15\,M_\odot$, $20\,M_\odot$, and $25\,M_\odot$ stars are shown in Figure 1.5b. The case of a $25\,M_\odot$ star with initial solar composition will be discussed in the following as an example

(Chieffi, Limongi, and Straniero, 1998; Limongi, Straniero, and Chieffi, 2000; Woosley, Heger, and Weaver, 2002). The total life of such a massive star is relatively short and amounts only to ≈ 7 My. The star spends 90% of this time on the main-sequence burning hydrogen to helium via the CNO cycles in the core. When the hydrogen in the center is exhausted, hydrogen burning continues in a shell. The core contracts and heats up until helium is ignited. This new source of nuclear energy heats the overlying hydrogen shell and the outer layers of the star expand greatly. The star becomes a supergiant. These stars show up in the Hertzsprung–Russell diagram at the highest observed luminosities. Examples are Rigel (blue supergiant) and Betelgeuse (red supergiant) in the constellation Orion.

Core helium burning lasts for about 800 000 years and some of the heavy nuclides with masses of $A > 60$ are synthesized during this stage via neutron captures (s-process; Section 5.6.1). When helium is exhausted in the center, helium burning continues in a shell located beneath the hydrogen burning shell. Eventually, carbon burning starts in the core. These burning stages have already been discussed above.

Stars with initial masses exceeding $\approx 11\,M_\odot$ are capable of igniting successive burning stages in their cores using the ashes of the previous core burning stage as fuel. Three distinct burning stages follow carbon burning. They are referred to as *neon burning*, *oxygen burning*, and *silicon burning*, and will be discussed in detail in Section 5.3. There is a fundamental difference between the initial and the advanced burning stages in the manner by which the nuclear energy generated in the stellar interior is transformed and radiated from the surface. For hydrogen and helium burning, nuclear energy is almost exclusively converted to light. During the advanced burning stages energy is almost entirely radiated as neutrino–antineutrino pairs and the light radiated from the star's surface represents only a very small fraction of the total energy release. Since the neutrino losses increase dramatically during the advanced burning stages and because the nuclear burning lifetime scales inversely with the total luminosity, the evolution of the star rapidly accelerates. For example, silicon burning will last for only about one day. Since the advanced burning stages transpire very quickly, the envelope has insufficient time to react to the structural changes in the stellar interior. Thus, from carbon burning onward, the star will no longer move in the Hertzsprung–Russell diagram, but remains at the position indicated by the solid circle in Figure 1.5b. Furthermore, since the star spends most of its life burning either hydrogen or helium in the core, these are typically the only phases that we can observe.

The approximate structure of the massive star after silicon has been exhausted in the core is shown in Figure 1.7 (left side). The star consists now of several layers of different composition that are separated by thin nuclear burning shells. The details of the nucleosynthesis are complicated and will be discussed in Chapter 5. It is sufficient to mention at this point that the heaviest and most stable nuclei (i.e., the iron peak nuclei; Section 1.3) are found in the core. Also, the luminosity during the red giant phase is so large that the star undergoes a significant mass loss. The effect is more pronounced for stars with $M \gtrsim 30$–$35\,M_\odot$ that lose eventually most of their hydrogen envelope. The observational counterparts of such stars are the

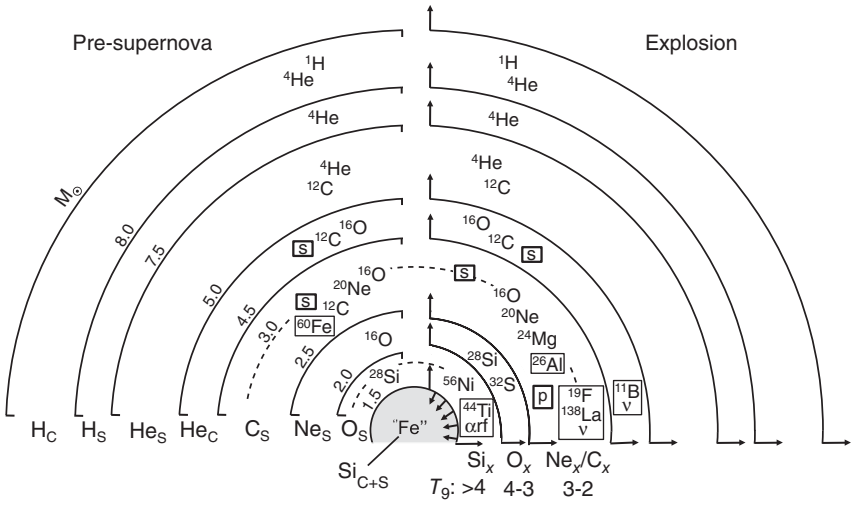

Figure 1.7 Structure and evolution of a $25M_{\odot}$ star of solar metallicity, as predicted by one-dimensional, spherically symmetric models (Limongi, Straniero, and Chieffi, 2000), shortly before and after core collapse (not to scale). Only the main constituents in each layer are shown. Minor constituents, among them important γ-ray emitters, are set in thin rectangles. Various processes are set in thick rectangles: weak s-process component (s); p-process (p); α-rich freeze-out (αrf); ν-process (ν). (Left) Snapshot of pre-supernova structure. Nuclear burning takes place in thin regions (burning shells) at the interface of different compositional layers, where each burning shell migrated outward to the position indicated by the black lines. The compositions result from burning stages indicated at the bottom (subscripts *C* and *S* stand for core and shell burning, respectively). The diagonally arranged numbers indicate the interior mass (in solar masses) for each burning shell. (Right) Explosive nucleosynthesis resulting from the passage of the shock wave through overlying layers, giving rise to explosive burning of silicon (Si_x), oxygen (O_x) and neon-carbon (Ne_x/C_x). Strictly speaking, this classification depends on the temperature range, not on the available fuel. Nevertheless, the names indicate approximately which compositional layers of the presupernova will usually be affected. Outside the outer dashed line, the composition is little altered by the shock. The inner dashed line indicates the approximate boundary of the part of the star that is ejected (mass cut). This model is sometimes referred to as the *onion shell structure* of a massive star.

hot and massive *Wolf–Rayet stars*, which have been observed to lose mass at a rate of $\approx 10^{-5}\,M_{\odot}$ per year at stellar wind speeds of ≈ 2000 km/s. An image of a Wolf–Rayet star is shown in color Figure 5 on page 617.

The electron degenerate stellar core has at this point no other sources of nuclear energy to its disposal and grows in mass as the overlying burning shells contribute more nuclear ashes. When the mass of the core reaches the Chandrasekhar limit ($\approx 1.4\,M_{\odot}$), the electron degeneracy pressure is unable to counteract gravity, and the core collapses freely at about a quarter of the speed of light. When the density reaches values on the order of the nuclear density ($\rho \approx 10^{14}$ g/cm^3), the nuclei and free nucleons begin to feel the short-range nuclear force, which is repulsive

at very short distances. The collapsing inner core reaches high inward velocities and overshoots the nuclear density. The nuclear potential acts as a stiff spring that stores energy in the compressive phase until it rebounds. The rebounding part of the core encounters infalling matter and thus gives rise to an outward moving prompt shock wave. The hot and dense inner core has become a proto-neutron star with a mass of $\approx 1.5\,M_\odot$. While the shock wave moves outward through the outer core region, it loses energy by photodisintegrating the iron peak nuclei. Furthermore, energy is removed from the shock wave by the emission of neutrinos. It takes about 1 s after core collapse, and about 10 ms after the core has bounced, for the shock wave to reach the outer edge of the core. At this time, the shock wave has lost all of its kinetic energy and it stalls. How exactly the shock is revived and how it will ultimately propagate through the stellar layers beyond the iron core and disrupt the star in a core-collapse supernova explosion is among the most elusive problems in nuclear astrophysics. We will discuss this issue in Section 5.4.

Once the shock wave is revived, it moves through the star and heats matter to high temperatures for a time period of seconds. Subsequently, the hot and dense matter expands nearly adiabatically. As a result, the star experiences several episodes of *explosive nuclear burning*. The silicon (^{28}Si) and oxygen (^{16}O) in the first layers the shock wave encounters are quickly converted to iron peak and intermediate-mass nuclei at high temperatures ($\approx$ 3–5 GK). As will be shown later, the nuclide $^{56}_{28}\mathrm{Ni}_{28}$ is among the most abundant products originating from these layers. Some other important nuclides are synthesized by the shock in other layers, among them the ^{26}Al observed in the interstellar medium (Section 1.7.5 and color Figure 12 on page 624). The character of the explosive nuclear burning depends, among other things, on the location of the shock and the expansion time scale. During the explosion nuclides that have been synthesized before and after the core collapse are ejected and are then mixed into the interstellar medium. Several nuclear processes that occur during the explosion are indicated in Figure 1.7 (right side) and will be discussed in more detail in Chapter 5.

Stellar model simulations support the idea that supernovae of type II and type Ib/Ic are the observational counterparts of the core collapse in massive stars. The different supernova types are classified observationally according to their optical spectra. Spectra of type II supernovae contain hydrogen lines, while those of type I supernovae do not. Type I supernovae whose spectra show absorption caused by the presence of silicon are referred to as *type Ia supernovae*; otherwise they are classified as type Ib or Ic supernovae (the latter distinction is based on a helium line feature in the spectrum). Type II supernovae tend to occur in the arms of spiral galaxies, but not in early-type galaxies (elliptical galaxies) that lack gas and show very low levels (if any) of star formation. Type Ib or Ic supernovae also seem to occur in spiral arms. On the other hand, type Ia supernovae show no such preference. Since the spiral arms contain many massive, and thus young, stars and elliptical galaxies only contain old stellar populations (with ages of $\approx 10^{10}$ y), the observations suggest that massive stars are the progenitors of type II and type Ib/Ic supernovae, but not of type Ia supernovae. Stars with initial masses of $M \lesssim 20$–$30\,M_\odot$ explode as a type II supernova and form a neutron star

as a remnant. Stars with masses above this range (Wolf-Rayet stars), or less massive stars in binaries, that have lost their hydrogen envelopes are thought to be the progenitors of type Ib and Ic supernovae. It is not clear at present if the latter explosions leave a neutron star or a black hole behind as a remnant, mainly because of our incomplete knowledge of post-main sequence mass loss and the details of fall-back of matter onto the central object. As will become clear in Chapter 5, core-collapse supernovae are of outstanding importance for three reasons: (i) they are predicted to be among the most prolific sources of element synthesis in the Galaxy; (ii) they are the sites where neutron stars are born; and (iii) they are a likely source of shock waves that are believed to accelerate Galactic cosmic rays (Section 5.7.2).

We still lack self-consistent models of core-collapse supernovae. Therefore, many current stellar models induce the shock wave artificially by depositing a given amount of energy somewhere near the iron core. The models are constrained by observation. In particular, observations of supernova 1987A, which exploded in the Large Magellanic Cloud in 1987, were of outstanding importance in this regard (see color Figure 6 on page 618). Since it was located so close to us, the event could be studied in greater detail than any other supernova. Observations of supernova 1987A and other type II supernova light curves estimate explosion energies of $\approx (1–2) \times 10^{44}$ J and, therefore, strongly constrain the magnitude of artificial energy deposition in the models. The location of artificial energy deposition is also constrained by observation: it can neither be located inside the iron core or otherwise neutron-rich iron group nuclides are overproduced, nor can it be located beyond the oxygen burning shell or the resulting neutron star mass, after fall-back of matter, will be too large. In most simulations, the *mass cut*, that is, the boundary between ejected and fall-back matter, is located in the silicon layer (inner dashed line on right side of Figure 1.7).

Current stellar models of core-collapse supernovae agree with observation in many respects. For example, a burst of neutrinos had long been predicted by theory and was detected for supernova 1987A (Section 1.4.1). Furthermore, current models reproduce the amount of the ejected radioactive ^{56}Ni that, after first decaying to ^{56}Co and then to stable ^{56}Fe, gives rise to the tail in the light curves of core-collapse supernovae. A famous type II supernova remnant, the Crab Nebula, is shown in color Figure 7 on page 619.

The supernova rate in our Galaxy amounts to ≈ 3 events per century, with an estimated systematic uncertainty of a factor of two (Li *et al.*, 2011b). For a volume-limited sample, within a radius of about 70 Mpc in the local universe, the observed fractions of supernovae of type II, Ia, and Ib/c are 57%, 24%, and 19%, respectively (Li *et al.*, 2011a). Type Ia supernovae will be discussed below.

1.4.4 Binary Stars

Perhaps as many as one half of all stars are members of binary star systems. If the stars are members of a close binary system, then they will significantly influence

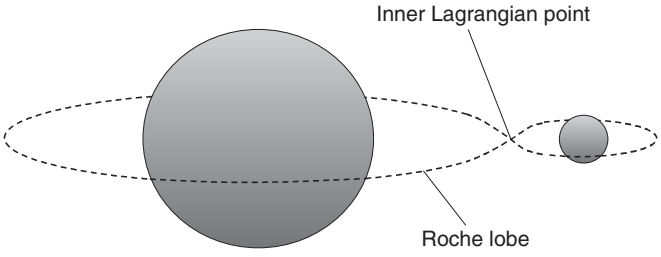

Figure 1.8 Binary star system. Each star is surrounded by a hypothetical surface, called the *Roche lobe*, that marks its gravitational domain. The intersection of the equatorial plane with the Roche lobes is shown as a dashed curve. The location where the two Roche lobes touch is called the *inner Lagrangian point*.

each other's evolution. In a close binary system, the separation may range from a few times the radii of the stars to a situation where both stars share a common envelope (*contact binaries*). Consider the binary star system shown in Figure 1.8. Each star is surrounded by a hypothetical surface marking its gravitational domain. This surface is referred to as the *Roche lobe* and its intersection with the equatorial plane is shown as a dashed figure-eight curve. The location where the two Roche lobes touch, that is, where the effects of gravity and rotation cancel each other, is called the *inner Lagrangian point*. When one of the stars evolves off the main sequence and becomes a red giant, it may fill its Roche lobe. Material is then free to flow from that star through the inner Lagrangian point onto its companion. Many different kinds of stars may be members of close binary systems and the transfer of mass from one star to another gives rise to very interesting phenomena (Iben, 1991). In the following we will focus on binary systems that contain a compact object, either a white dwarf or a neutron star.

Type Ia Supernovae

Type Ia supernovae are the brightest phenomena powered by nuclear energy release in the universe and they sometimes outshine their host galaxies. The observed mean velocities of the ejecta are of order 10 000 km/s, corresponding to kinetic energies of $\approx 10^{44}$ J. An image of the type Ia supernova 1994D is shown in color Figure 9 on page 621. Recall that type Ia supernovae occur in both early-type galaxies (elliptical galaxies) and spiral galaxies. The former show very low levels (if any) of star formation and all supernovae observed so far in elliptical galaxies are of type Ia. In spiral galaxies, the type Ia rate is positively correlated with the star formation rate. Therefore, type Ia supernovae are likely associated with older stellar populations and with stars of moderate mass. Their light curves are powered by the decay of radioactive ^{56}Ni to ^{56}Co, followed by the decay of ^{56}Co to stable ^{56}Fe. The inferred amount of ^{56}Ni synthesized in type Ia supernovae is $\approx 0.6\,M_{\odot}$ per event, significantly higher than the amount observed in type II supernovae (Section 5.4.4).

We already mentioned that type Ia supernovae are classified according to their spectra near maximum light: they lack hydrogen and helium lines, but contain an absorption feature caused by the presence of Si. During the peak phase, other intermediate-mass elements (O, Mg, S, Ca) are also observed in their spectra, together with contributions from Fe and Co. With progressing time, the relative contribution of the iron-peak elements increases. About two weeks after peak luminosity, the spectra are dominated by Fe, although Si and Ca lines are still present. The observations indicate that the thermonuclear explosion gave rise to the synthesis of intermediate-mass elements in the outer layers, which become visible early during the peak phase, and to the synthesis of iron-peak elements in the deeper layers, which become visible a few weeks later.

Type Ia supernovae are fascinating objects in their own right, but a deeper understanding of the explosion is crucial both for Galactic chemical evolution and for cosmology. About 70% of observed type Ia supernovae (Li *et al.*, 2011a) show a remarkably small spread in peak brightness. Supernova 1994D, for example, belongs to this class of *normal* type Ia supernovae. When the light curves of all type Ia supernovae are compared, including both normal and peculiar events, it is found that the peak luminosities correlate with the post-peak decline rate of the light curves (Phillips, 1993). This correlation can be used to compensate for the peak luminosity spread and, therefore, the intrinsic brightness can be determined to within a narrow range. By measuring their apparent luminosity it becomes hence possible to estimate their distance. Since type Ia supernovae are so bright, they can be observed across billions of light years. For these reasons, type Ia supernovae are used as *cosmological distance indicators*. By recording both their apparent luminosity and their redshifts, observations of very distant type Ia supernovae provide a measure for the expansion history of the universe. The surprising finding that the expansion is accelerating, driven by the elusive *dark energy* (Riess *et al.*, 1998; Perlmutter *et al.*, 1999), is an observation of paramount importance for cosmology.

The observed variation in peak luminosity among the majority of type Ia supernovae can be interpreted as a consequence of a single parameter, that is, the different amounts of ^{56}Ni synthesized during the thermonuclear explosion (Arnett, 1982). The more ^{56}Ni is produced, the larger the peak brightness. At the same time, expansion velocities are larger and the light curve becomes broader since the opacity increases with a higher concentration of iron-peak elements.

With an increasing number of type Ia supernovae discovered, it is now clear that they represent a class of some diversity and that their properties cannot be fully explained by a single parameter. For example, there is a spread in the expansion velocities at the photospheres even for similarly bright events. Furthermore, some peculiar type Ia supernovae of exceptionally high or extremely low luminosity do not obey the Phillips relation. These observations indicate that different type Ia supernovae may be caused by different progenitor systems. Furthermore, the Phillips relation is based on a sample of low redshift supernovae. It is concerning that systematic differences in the properties of local and high-redshift type Ia supernovae may exist, which could lead to erroneous cosmological distances.

The profound cosmological implications strongly motivate the identification and understanding of type Ia supernova progenitors.

Many different stellar models have been proposed to explain type Ia supernovae, but we are still lacking a satisfactory understanding. A common feature of all viable progenitor systems is a thermonuclear explosion of a carbon-oxygen white dwarf, which is initiated when the pressure and temperature become sufficient to fuse carbon (Hoyle and Fowler, 1960). As a result, a significant fraction of the initial carbon and oxygen is burned to ^{56}Ni, with a predicted nuclear energy release of $\approx 10^{44}$ J. About two thirds of this energy is invested in the kinetic energy of the expanding debris, in agreement with observation. The remaining fraction is responsible for disrupting the white dwarf at high velocity within a time scale of seconds (*thermonuclear supernovae*). An example is Tycho's supernova remnant (SN 1572), shown in color Figure 10 on page 622, where no compact remnant has been found, supporting the idea that the supernova was of type Ia. The conjecture of a primary white dwarf is also supported by observational constraints (Bloom *et al.*, 2012) obtained for the *normal* type Ia supernova SN 2011fe that was discovered in the Pinwheel galaxy (M 101).

All of these models include a companion (secondary) star that supplies mass to the (primary) white dwarf. When the Chandrasekhar limit ($\approx 1.4\,M_\odot$) is approached, carbon ignites under degenerate conditions. A thermonuclear runaway ensues because the temperature increase from the nuclear burning does not create an increase in pressure, and the temperature continues to increase until the degeneracy is lifted. At this point, the energy generation rate is so large that an explosion occurs. Stellar model simulations have also shown that the white dwarf must be composed mainly of ^{12}C and ^{16}O, instead of ^{16}O and ^{20}Ne (see Figure 1.4). In the latter case, the temperature during mass accretion toward the Chandrasekhar limit never becomes high enough to ignite oxygen or neon, and the result is most likely a core collapse instead of a thermonuclear supernova.

The nature of the secondary star is a matter of dispute. In the proposed single-degenerate scenario, the secondary is a main-sequence star, a red giant, or a helium star, whereas the double-degenerate scenario involves the merger of two white dwarfs as a result of angular momentum loss caused by gravitational wave emission. Both scenarios have difficulties in reproducing key observational features of type Ia supernovae. In the single-degenerate model, the companion star will survive the explosion. On the other hand, no remnant is left behind in the double-degenerate model. One way to distinguish between these models is to search for surviving companion stars near the centers of type Ia supernova remnants. However, the suggestion that Tycho G (a solar-like star) is the likely companion for SN 1572 (Ruiz-Lapuente *et al.*, 2004) is controversial at present.

Another important unresolved issue is related to the propagation of the thermonuclear burning front in the interior of the primary white dwarf. Two burning modes can be distinguished. One possibility is a detonation in which the nuclear flame propagates as a supersonic front. In this case, the flame compresses the

material and increases the temperature to the point of ignition. The energy release from the ignited material behind the flame supports its propagation. Another possibility is a deflagration in which the nuclear burning proceeds subsonically. Here, the heat released from nuclear burning is conducted by electrons and ignites the next layer, causing the white dwarf to expand. The observation of intermediate-mass elements in the spectra of type Ia supernovae rules out a pure detonation regime since it would prevent the expansion of the layers ahead of the burning front, giving most likely rise to the synthesis of iron-peak elements only. These two burning modes are not exclusive and a transition from one mode to another may occur. For example, a burning front could propagate via deflagration, causing the white dwarf to pre-expand, and may then transition by some, yet not understood, mechanism to a detonation (*delayed detonation*). The outcome depends on the density, temperature, chemical composition, and the velocity profiles at the time of ignition. Related to this issue is the question of where precisely, near or off center and at how many locations, the ignition occurs.

We will discuss the nucleosynthesis in type Ia supernovae in more detail in Section 5.5.1. More information on the progenitors of type Ia supernovae, including a discussion of sub-Chandrasekhar models and white dwarf collisions that may explain peculiar events, can be found in the reviews by Wang and Han (2012) and Höflich *et al.* (2013).

Classical Novae

Classical novae are stellar explosions that occur in close binary systems. In this case, hydrogen-rich matter is transferred via Roche lobe overflow from a low-mass main-sequence star to the surface of a compact white dwarf. The transferred matter does not fall directly onto the surface but is accumulated in an accretion disk surrounding the white dwarf. Typical accretion rates amount to $\approx 10^{-10}$–$10^{-9}\,M_\odot$ per year. A fraction of this matter spirals inward and accumulates on the white dwarf surface, where it is heated and compressed by the strong surface gravity. At some point, the bottom layer becomes electron degenerate. Hydrogen starts to fuse to helium (via the pp chains) during the accretion phase and the temperature increases gradually. The electron degeneracy prevents an expansion of the envelope and eventually a thermonuclear runaway occurs near the base of the accreted layers. At this stage, the nuclear burning is dominated by explosive hydrogen burning via the (hot) CNO cycles. Both the compressional heating and the energy release from the nuclear burning heat the accreted material until an explosion occurs.

The classical nova rate in the Galaxy is about ≈ 35 per year and thus they occur more frequently than supernovae (Section 1.4.3). Contrary to type Ia supernovae, which disrupt the white dwarf, all classical novae are expected to recur with periods of $\approx 10^4$–10^5 years. The luminosity increase during the outburst amounts to a factor of $\approx 10^4$. A classical nova typically ejects $\approx 10^{-5}$–$10^{-4}\,M_\odot$ of material, with mean ejection velocities of $\approx 10^3$ km/s. Also, there are other types of novae, such as dwarf novae or nova-like variables. However, these are not related to thermonuclear burning.

Optical, infrared, and ultraviolet spectra of classical novae reveal the presence of many elements in the expanding nova shells that are strongly overabundant compared to solar system values. For example, the observed overabundances of carbon and oxygen in all classical novae demonstrate that at some time during the evolution of the outburst the accreted material must have been mixed to a certain degree with matter from the white dwarf. This dredge-up of material gives rise to a more energetic explosion (by increasing the number of CNO catalyst nuclei; Section 5.5.2). The observation of an overabundance of neon in some classical novae showed that these outbursts do not involve a carbon–oxygen white dwarf, but a more massive white dwarf of oxygen–neon composition. The latter objects result from the evolution of intermediate mass stars with initial masses of $9\,M_\odot \lesssim M \lesssim 11\,M_\odot$ (Figure 1.4). The presence of large amounts of matter from the white dwarf core in the ejecta may imply that the white dwarf in a classical nova system is losing mass as a result of subsequent outbursts. Thus, these objects are unlikely to become progenitors of type Ia supernovae. Other observed overabundances, for example, of nitrogen, silicon, or sulfur, are the result of nuclear processing during the explosive burning of hydrogen. An image of Nova Cygni 1992 is shown in color Figure 11 on page 623.

Stellar model calculations indicate that the peak phase of explosive nuclear burning in classical novae lasts typically for several hundred seconds. The characteristics of the outburst depend on the white dwarf mass and luminosity, the mass accretion rate, and the chemical composition for both the accreted and the white dwarf material. For example, it has been demonstrated that the lower the mass accretion rate, the larger the amount of accreted mass before the thermonuclear runaway is initiated. A more massive accreted layer, in turn, gives rise to a higher pressure in the bottom layers and hence a more violent explosion. On the other hand, if a too large accretion rate is assumed, no thermonuclear runaway is initiated. Simulations also indicate that classical nova outbursts on the surface of the heavier oxygen–neon white dwarfs achieve higher peak temperatures than those exploding on carbon–oxygen cores. For more information on classical novae, see José, Hernanz, and Iliadis (2006) and Starrfield, Iliadis, and Hix (2006).

Type I X-Ray Bursts

A number of close binary star systems involve a neutron star as a compact object. A neutron star has a mass of $\approx 1.4\,M_\odot$, a radius of about 10–15 km, and a density of order 10^{14} g/cm^3. These binary star systems belong to a class of objects that are called *X-ray binaries*. The accretion of matter from the companion on the surface of the neutron star gives rise to a large gravitational energy release. As a result, the temperatures near the neutron star surface are high ($\approx 10^7$ K) and the persistent thermal emission occurs at X-ray energies.

In high-mass X-ray binaries, the companion is a massive ($\gtrsim 5\,M_\odot$) population I star, while the neutron star has a strong magnetic field. The matter is accreted at relatively high rates and is funneled along the magnetic field lines onto the

magnetic poles. This creates a hot spot of X-ray emission and, if the rotational axis of the neutron star is inclined with respect to the magnetic axis, this gives rise to an X-ray pulsar. Typical rotation periods range from 0.1 s to a fraction of an hour. The rotational periods for some X-ray pulsars have been observed to decrease, indicating that the neutron stars spin up as a result of accretion of matter.

In low-mass X-ray binaries, the companion is a low mass ($\lesssim 1.5\,M_\odot$) population II star and matter is transferred to a weakly magnetized neutron star via Roche lobe overflow. Many of these systems produce, apart from the persistent X-ray emission, bursts in the X-ray intensity (Lewin, van Paradijs, and Taam, 1993). For a rare variety, called *type II X-ray bursts*, the bursts occur in rapid succession and are separated by a few minutes. The profile of each burst rises and falls abruptly. They are most likely associated with a sudden increase in the mass transfer rate caused by instabilities in the accretion disk.

The large majority of bursts belong to the class of type I X-ray bursts. In this case, the X-ray luminosity typically increases by an order of magnitude. They are believed to be of thermonuclear origin, unlike the X-ray binary varieties discussed above. When hydrogen- and helium-rich matter from the low-mass companion is first accreted in a disk and then falls onto the surface of the neutron star, the temperatures and densities are high enough to fuse hydrogen continuously to helium via the (hot) CNO cycles. The accreted or synthesized helium, however, is not fusing yet but sinks deeper into the neutron star atmosphere. Eventually the helium is ignited via the triple-α reaction under electron degenerate conditions and a thermonuclear runaway occurs. The helium flash triggers the explosive burning of the outer region consisting of a mixture of hydrogen and helium. This is just one possible scenario. In other models the ignition occurs in pure helium or in mixed hydrogen–helium accreted material. The details of the nucleosynthesis depend on the temperatures and densities achieved in the various burning layers. Calculations show that in the innermost and hottest layers elements up to – and perhaps beyond – the iron peak are synthesized. After the termination of a burst, a new shell of matter is accreted and the cycle repeats.

The above model explains the basic features of type I X-ray bursts. A burst lasts typically for < 1 min and repeats after several hours to days. The luminosity profile shows a rapid rise within $\approx$ 1–10 s, caused by the sudden nuclear energy release, and a slower decline of order $\approx$ 5–100 s, reflecting the cooling of the neutron star surface. Some bursts show millisecond oscillations of the X-ray flux. These have been suggested to arise from a surface wave in the nuclear burning layer or perhaps from anisotropies in the nuclear burning caused by a spreading hot spot on the surface of a rapidly spinning neutron star.

Stellar models of type I X-ray bursts are sensitive to a number of parameters and assumptions, such as the mass accretion rate, rotation, the number of ignition points, the propagation of the burning front across the neutron star surface, and the composition of the accreted matter.

It is unlikely for any significant amount of accreted and processed matter to escape the large gravitational potential of the neutron star. Therefore, type I X-ray bursts are probably not important contributors to the chemical evolution of the Galaxy. They are important, however, for probing the properties of neutron stars, such as the mass, radius, and the composition. For more information, see Parikh *et al.* (2013a), and references therein.

1.5
Masses, Binding Energies, Nuclear Reactions, and Related Topics

1.5.1
Nuclear Mass and Binding Energy

The most fundamental property of the atomic nucleus is its mass. Early mass measurements showed that the total nuclear mass, $m_{\rm nuc}$, is less than the sum of masses of the constituent nucleons. We may write

$$m_{\rm nuc} = Zm_{\rm p} + Nm_{\rm n} - \Delta m \tag{1.1}$$

According to the Einstein relationship between mass and energy, the *mass defect* Δm is equivalent to an energy of $\Delta E = \Delta m \cdot c^2$. The quantity ΔE is referred to as *nuclear binding energy*. It is defined as the energy released in assembling a given nucleus from its constituent nucleons, or equivalently, the energy required to separate a given nucleus into its constituent nucleons. We may express the binding energy as

$$B(Z,N) = \left(Zm_{\rm p} + Nm_{\rm n} - m_{\rm nuc}\right) c^2 \tag{1.2}$$

A plot of experimental binding energies per nucleon, $B(Z,N)/A$, for the most tightly bound nuclide at each mass number A is shown in Figure 1.9a. An expanded region is displayed in part (b), where the round symbols have the same meaning as in the part (a). Most of these nuclides, which are stable in the laboratory, have binding energies between 7 and 9 MeV per nucleon. Nuclides with mass numbers in the range of $A = 50$–65 have the largest binding energies per nucleon. They are the iron peak species, which we already encountered in Section 1.3. It appears that nature favors the synthesis of the most tightly bound and most stable nuclides, as will be explained in detail in later chapters. The most tightly bound nuclides of all are ^{62}Ni, ^{58}Fe, and ^{56}Fe with binding energies per nucleon of $B(Z,N)/A = 8794.546 \pm 0.008$ keV, 8792.239 ± 0.008 keV, and 8790.342 ± 0.008 keV, respectively (Wang *et al.*, 2012). Lighter or heavier nuclei are less tightly bound. The square symbols in the bottom part refer to $N = Z$ nuclides above $A = 40$, which are all radioactive. The most tightly bound $N = Z$ species is ^{56}Ni, with a binding energy per nucleon of $B(Z,N)/A = 8642.767 \pm 0.010$ keV. It follows that nuclear processes liberate energy as long as the binding energy per nucleon of the final products exceeds

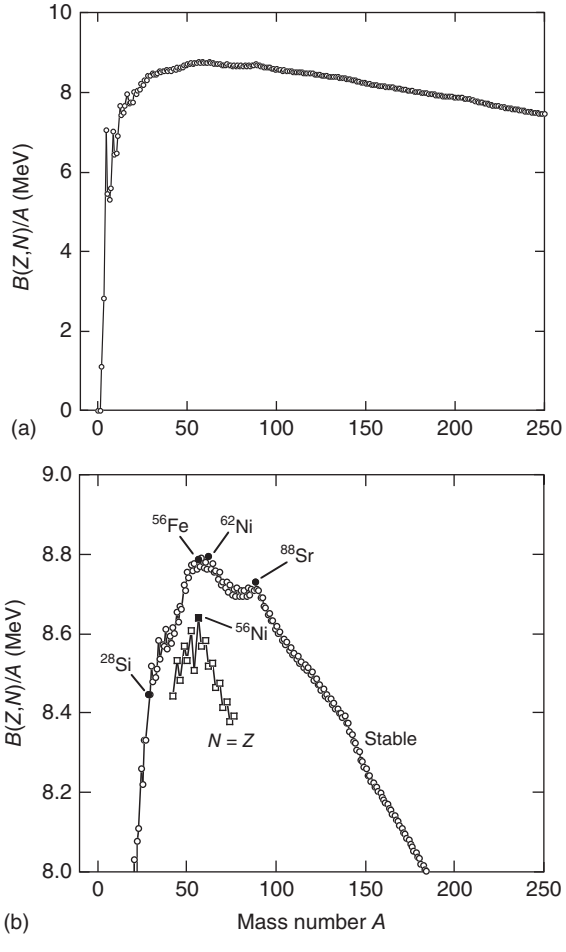

Figure 1.9 Experimental binding energy per nucleon, $B(Z,N)/A$, versus mass number, A. (a) Value of $B(Z,N)/A$ for the most tightly bound nuclide at a given mass number A. (b) Expanded section; the round symbols have the same meaning as in part (a), that is, they correspond to the most tightly bound nuclide of a given mass number; the nuclide with the largest binding energy per nucleon is ^{62}Ni ($B/A = 8.795$ MeV); the square symbols show $B(Z,N)/A$ values for $N = Z$ nuclides above $A = 40$, which are all radioactive; the $N = Z$ species with the largest binding energy per nucleon is ^{56}Ni ($B/A = 8.643$ MeV). Data from Wang *et al.* (2012).

the binding energy per nucleon of the initial constituents. Consequently, nuclear energy can be liberated by the fusion of nuclei lighter than iron, or by the fission of nuclei heavier than iron. For example, if a star consists initially of pure hydrogen (^{1}H), an energy of ≈ 7 MeV per nucleon can be liberated by fusing hydrogen to helium (^{4}He), or almost 9 MeV per nucleon is liberated by fusing hydrogen to ^{56}Fe.

Example 1.2

The binding energies per nucleon of deuterium (^{2}H or d) and helium (^{4}He or α) are given by $B(\mathrm{d})/A = 1.112$ MeV and $B(\alpha)/A = 7.074$ MeV. Calculate the energy released when two deuterium nuclei are combined to form one ^{4}He nucleus.

First, we calculate the binding energies of deuterium and ^{4}He:

$$B(\mathrm{d}) = \frac{B(\mathrm{d})}{A}A = (1.112\,\mathrm{MeV}) \cdot 2 = 2.224\,\mathrm{MeV}$$
$$B(\alpha) = \frac{B(\alpha)}{A}A = (7.074\,\mathrm{MeV}) \cdot 4 = 28.296\,\mathrm{MeV}$$

By combining two deuterium nuclei to one ^{4}He nucleus, the total energy release amounts to

$$(28.296\,\mathrm{MeV}) - (2.224\,\mathrm{MeV}) - (2.224\,\mathrm{MeV}) = 23.85\,\mathrm{MeV}$$

corresponding to a value of 5.96 MeV per nucleon.

1.5.2 Energetics of Nuclear Reactions

A nuclear interaction may be written symbolically as

$$0 + 1 \rightarrow 2 + 3 \qquad \text{or} \qquad 0(1,2)3 \tag{1.3}$$

where 0 and 1 denote two colliding nuclei before the interaction, while 2 and 3 denote the interaction products. Most nuclear interactions of astrophysical interest involve just two species before and after the interaction. If species 0 and 1 are identical to species 2 and 3, then the interaction is called *elastic* or *inelastic* scattering. Otherwise, the above notation refers to a *nuclear reaction*. Photons may also be involved in the interaction. If species 2 is a photon, then the interaction is called *radiative capture reaction*. If species 1 is a photon, then we are considering a *photodisintegration reaction*. All of these interactions will be discussed in later chapters.

Figure 1.10 shows schematically the energetics of nuclear reactions and can be used to illustrate a number of relationships that will be employed frequently in the following chapters. The vertical direction represents energy. Consider Figure 1.10a, showing a reaction $0 + 1 \rightarrow 2 + 3$, where all species involved in the interaction are particles with rest mass. The rest masses of 0 and 1 (before the reaction) and of 2 and 3 (after the reaction) are indicated by horizontal solid lines. The total relativistic energy in a nuclear reaction must be conserved. Thus, one may write

$$m_0c^2 + m_1c^2 + E_0 + E_1 = m_2c^2 + m_3c^2 + E_2 + E_3 \qquad \text{or}$$
$$Q_{01\rightarrow 23} \equiv m_0c^2 + m_1c^2 - m_2c^2 - m_3c^2 = E_2 + E_3 - E_0 - E_1 \tag{1.4}$$

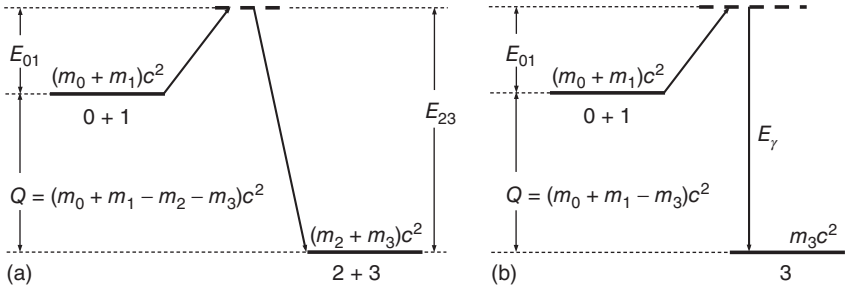

Figure 1.10 Energy level diagrams to illustrate the energetics of nuclear reactions. The vertical direction represents an energy scale. Part (a) corresponds to a situation where all species participating in the reaction are particles with rest mass. In part (b) one of the species is a photon.

where E_i are kinetic energies and m_i are rest masses. The difference in masses before and after the reaction, or the difference in kinetic energies after and before the reaction, is equal to the energy release and is referred to as the *reaction Q-value*. If Q is positive, the reaction releases energy and is called *exothermic*. Otherwise the reaction consumes energy and is called *endothermic*. Apart from a few exceptions, the most important nuclear reactions in stars are exothermic ($Q > 0$). Equation (1.4) is applicable in any reference frame. The difference between center-of-mass and laboratory reference frame is discussed in Appendix C. The quantities E_{01} and E_{23} in Figure 1.10a represent the total kinetic energies in the center-of-mass system before and after the reaction, respectively. It is apparent that the center-of-mass kinetic energies and the Q-value are related by

$$E_{23} = E_{01} + Q_{01\to 23} \tag{1.5}$$

Figure 1.10b shows a radiative capture reaction $0 + 1 \to \gamma + 3$. In this case we find accordingly

$$\begin{aligned} &m_0c^2 + m_1c^2 + E_0 + E_1 = m_3c^2 + E_3 + E_\gamma \qquad \text{or} \\ &Q_{01\to\gamma 3} \equiv m_0c^2 + m_1c^2 - m_3c^2 = E_3 + E_\gamma - E_0 - E_1 \end{aligned} \tag{1.6}$$

Center-of-mass kinetic energies and the Q-value are now related by

$$E_{\gamma 3} = E_{01} + Q_{01\to\gamma 3} \tag{1.7}$$

where $E_{\gamma 3}$ denotes the sum of the energy of the emitted photon (E_γ) and the center-of-mass kinetic energy of the recoil nucleus 3. The latter contribution is usually very small so that one can frequently set $E_{\gamma 3} \approx E_\gamma$ (see Appendix C).

The reaction Q-value for a radiative capture reaction is equal to the energy released when nuclei 0 and 1 combine to form a composite nucleus 3. If one would add this very same amount of energy to nucleus 3, then it becomes energetically possible for nucleus 3 to separate into the fragments 0 and 1. Thus,

the *particle separation energy* of nucleus 3 is equal to the Q-value of the reaction $0 + 1 \rightarrow \gamma + 3$, that is, $S_{3\rightarrow 01} = Q_{01\rightarrow\gamma 3}$. Separation energies will be used frequently in the following chapters. Their values depend on the nuclear properties of species 0, 1, and 3. For example, suppose we start out with a stable nucleus in Figure 1.1 and remove one neutron at a time. As a result, we move in the chart of the nuclides to the left toward increasingly proton-rich nuclei. The farther we move away from the group of stable nuclei, the larger the proton–neutron imbalance becomes, and the less energy is required to remove a proton from a given nucleus. In other words, the proton separation energy S_p decreases. After a certain number of neutrons have been removed, a nuclide is eventually reached for which S_p becomes negative. Such nuclides are called *proton unstable* since they decay via the emission of a proton. The line in the chart of the nuclides with $S_p = 0$ (on the proton-rich side) is referred to as *proton dripline*. Similarly, if we remove from a given stable nucleus protons instead of neutrons, then we would move in the chart of the nuclides downward. The neutron–proton imbalance increases while the neutron separation energy S_n decreases with each removal of a proton. The line with $S_n = 0$ (on the neutron-rich side) defines now the *neutron dripline*. Particle driplines play an important role in certain stellar explosions (Chapter 5).

1.5.3 Atomic Mass and Mass Excess

Direct measurements of nuclear masses are complicated by the presence of the atomic electrons. Atomic masses, on the other hand, can be measured with very high precision. For this reason, experimental mass evaluations tabulate atomic rather than nuclear masses. These quantities are related by

$$m_{\text{atom}}(A, Z) = m_{\text{nuc}}(A, Z) + Zm_e - B_e(Z) \tag{1.8}$$

where m_e and B_e denote the electron mass and the electron binding energy in the atom, respectively. Nuclear reactions conserve the total charge. Therefore, one may replace nuclear by atomic masses since the same number of electron rest masses is added on both sides of a reaction equation. An error is introduced by this approximation because of the difference in the electron binding energies in the atom. The electron binding energy can be approximated by (Lunney, Pearson, and Thibault, 2003)

$$B_e(Z) = 14.4381\, Z^{2.39} + 1.55468 \times 10^{-6}\, Z^{5.35} \quad \text{(eV)} \tag{1.9}$$

This contribution is smaller than the nuclear mass differences and is often neglected. In the following we will be using atomic rather than nuclear masses, unless noted otherwise.

Frequently, a quantity called *atomic mass excess* (in units of energy) is introduced, which is defined by

$$\text{M.E.} \equiv (m_{\text{atom}} - Am_u)c^2 \tag{1.10}$$

where the integer A is the mass number. The quantity m_u denotes the (unified) atomic mass unit, u, defined as one-twelfth of the mass of the neutral ^{12}C atom. Numerically, one finds $m_u c^2 = 931.494$ MeV (Appendix E). The Q-value for a reaction $0 + 1 \rightarrow 2 + 3$ can be expressed in terms of the mass excess as

$$\begin{aligned} Q &= m_0c^2 + m_1c^2 - m_2c^2 - m_3c^2 \\ &= (m_0c^2 + m_1c^2 - m_2c^2 - m_3c^2) + (A_2m_uc^2 + A_3m_uc^2 - A_0m_uc^2 - A_1m_uc^2) \\ &= (\text{M.E.})_0 + (\text{M.E.})_1 - (\text{M.E.})_2 - (\text{M.E.})_3 \end{aligned} \tag{1.11}$$

Using atomic masses or atomic mass excesses gives precisely the same result when calculating reaction Q-values. If positrons are involved in a reaction, then the Q-value obtained using atomic masses (or atomic mass excesses) includes the annihilation energy $2m_ec^2 = 1022$ keV of the positron with another electron from the environment, as will be shown below. In numerical expressions, we will frequently use the quantity

$$M_i = \frac{m_i}{m_u} \tag{1.12}$$

called *relative atomic mass* of species i, which is given in atomic mass units, u. The relative atomic mass for a given species is numerically close to its (integer) mass number, but for accurate work the former quantity should be used. An evaluation of atomic masses is presented in Wang *et al.* (2012). Mass measurement techniques and various theoretical mass models are reviewed in Lunney, Pearson, and Thibault (2003).

Experimental values for atomic mass excesses, binding energies, and relative atomic masses for the light nuclides are listed in Table 1.1. Note that $(\text{M.E.})_{^{12}C} \equiv 0$ by definition. The following example illustrates their use for calculating Q-values.

Example 1.3

Calculate the Q-values for the reactions (i) $^{17}\text{O} + \text{p} \rightarrow \alpha + {}^{14}\text{N}$ and (ii) $\text{p} + \text{p} \rightarrow \text{e}^+ + \nu + \text{d}$ using the information listed in Table 1.1. (The symbols e^+ and ν denote a positron and a neutrino, respectively.)

(i) For the $^{17}\text{O}(\text{p},\alpha)^{14}\text{N}$ Reaction, we find from Eq. (1.11)

$$\begin{aligned} Q &= (\text{M.E.})_{^{17}\text{O}} + (\text{M.E.})_{^1\text{H}} - (\text{M.E.})_{^{14}\text{N}} - (\text{M.E.})_{^4\text{He}} \\ &= [(-808.76) + (7288.97) - (2863.42) - (2424.92)]\,\text{keV} = 1191.87\,\text{keV} \end{aligned}$$

Exactly the same result is obtained if atomic masses are used. (ii) For the $\text{p}(\text{p},\text{e}^+\nu)\text{d}$ reaction one obtains

$$\begin{aligned} Q &= (m_{^1\text{H}} + m_{^1\text{H}} - m_{^2\text{H}})c^2 = (\text{M.E.})_{^1\text{H}} + (\text{M.E.})_{^1\text{H}} - (\text{M.E.})_{^2\text{H}} \\ &= 2 \times (7288.97\,\text{keV}) - (13135.72\,\text{keV}) = 1442.22\,\text{keV} \end{aligned}$$

Table 1.1 Experimental values of the atomic mass excess (M.E.), binding energy per nucleon (B/A), and relative atomic mass (M) for light nuclides in the $A \leq 20$ mass region.

A	Element	M.E. (keV)	B/A (keV)	M (u)
1	n	8071.3171	0.0	1.0086649158
	H	7288.97059	0.0	1.00782503223
2	H	13135.72174	1112.283	2.01410177812
3	H	14949.8061	2827.266	3.0160492779
	He	14931.2155	2572.681	3.0160293201
4	He	2424.91561	7073.915	4.00260325413
6	Li	14086.8789	5332.331	6.0151228874
7	Li	14907.105	5606.439	7.016003437
	Be	15769.00	5371.548	7.01692872
8	Li	20945.80	5159.712	8.02248625
	Be	4941.67	7062.435	8.00530510
	B	22921.6	4717.15	8.0246073
9	Li	24954.90	5037.768	9.02679019
	Be	11348.45	6462.668	9.01218307
10	Be	12607.49	6497.630	10.01353470
	B	12050.7	6475.07	10.0129369
11	Be	20177.17	5952.540	11.02166108
	B	8667.9	6927.72	11.0093054
	C	10650.3	6676.37	11.0114336
12	B	13369.4	6631.22	12.0143527
	C	0.0	7680.144	12.0000000
13	B	16562.1	6496.41	13.0177802
	C	3125.00875	7469.849	13.00335483507
	N	5345.48	7238.863	13.00573861
14	C	3019.893	7520.319	14.003241988
	N	2863.41669	7475.614	14.00307400443
	O	8007.46	7052.301	14.00859636
15	C	9873.1	7100.17	15.0105993
	N	101.4387	7699.460	15.0001088989
	O	2855.6	7463.69	15.0030656
16	N	5683.9	7373.80	16.0061019
	O	−4737.00137	7976.206	15.99491461957
17	N	7870.0	7286.2	17.008449
	O	−808.7636	7750.728	16.9991317565
	F	1951.70	7542.328	17.00209524
18	N	13113.0	7038.6	18.014078
	O	−782.8156	7767.097	17.9991596129
	F	873.1	7631.638	18.0009373
19	O	3332.9	7566.49	19.0035780
	F	−1487.4443	7779.018	18.9984031627
	Ne	1752.05	7567.342	19.00188091
20	F	−17.463	7720.134	19.99998125
	Ne	−7041.9306	8032.240	19.9924401762
	Na	6850.6	7298.50	20.0073544

Errors are not listed.
Source: Wang *et al.* (2012).

This value includes the annihilation energy $2m_e c^2 = 1022$ keV of the positron with another electron from the environment, as can be seen from

$$\begin{aligned} Q &= [m_{^1\mathrm{H}} + m_{^1\mathrm{H}} - m_{^2\mathrm{H}}]c^2 = [(m_\mathrm{p} + m_\mathrm{e}) + (m_\mathrm{p} + m_\mathrm{e}) - (m_\mathrm{d} + m_\mathrm{e})]c^2 \\ &= [m_\mathrm{p} + m_\mathrm{p} - m_\mathrm{d} + m_\mathrm{e}]c^2 = [(m_\mathrm{p} + m_\mathrm{p} - m_\mathrm{d} - m_\mathrm{e}) + 2m_\mathrm{e}]c^2 \end{aligned}$$

The symbols ^{1}H, ^{2}H and p, d in the above expression denote atomic and nuclear masses, respectively.

1.5.4 Number Abundance, Mass Fraction, and Mole Fraction

The number density of nuclei i in a stellar plasma, N_i, is equal to the total number of species i per unit volume. Avogadro's number N_A is defined as the number of atoms of species i that makes M_i gram, that is, $N_A = M_i/m_i = 6.022 \times 10^{23}$ mol^{-1}. The *mass density* is then given by $\rho = N_i m_i = N_i M_i / N_A$ if only species i is present, or by $\rho = (1/N_A)\sum_i N_i M_i$ for a mixture of species. We write

$$\begin{aligned} \frac{\sum_i N_i M_i}{\rho N_A} &= \frac{N_1 M_1}{\rho N_A} + \frac{N_2 M_2}{\rho N_A} + \frac{N_3 M_3}{\rho N_A} + \cdots \\ &= X_1 + X_2 + X_3 + \cdots = \sum_i X_i = 1 \end{aligned} \tag{1.13}$$

where the quantity

$$X_i \equiv \frac{N_i M_i}{\rho N_A} \tag{1.14}$$

represents the fraction of the mass that is bound in species i and, therefore, is called the *mass fraction*. A related quantity is the *mole fraction*, defined by

$$Y_i \equiv \frac{X_i}{M_i} = \frac{N_i}{\rho N_A} \tag{1.15}$$

In a stellar plasma, the number density N_i will change if nuclear transmutations take place. But it will also change as a result of variations in the mass density caused by compression or expansion of the stellar gas. In situations where the mass density of the stellar plasma varies, it is of advantage to express abundances in terms of the quantity Y_i instead of N_i. In a simple expansion of matter without nuclear reactions or mixing, the former quantity remains constant, whereas the latter quantity is proportional to the mass density ρ.

Strictly speaking, the mass density ρ is not a conserved quantity even if no compression or expansion of the stellar gas occurs. The reason is that nuclear transmutations transform a fraction of the nuclear mass into energy or leptons (e.g., electrons or positrons) and vice versa. To avoid this difficulty, the density is sometimes defined as $\rho_A = (1/N_A)\sum_i N_i A_i$ in terms of the number of nucleons (i.e., the mass number A_i) instead of the relative atomic mass M_i, since the number of nucleons is always conserved in a nuclear transmutation. The mass

fraction of Eq. (1.14) should in principle be replaced by the *nucleon fraction* $X_i = N_i A_i/(\rho_A N_A)$. However, the difference between mass density and nucleon density, or between mass fraction and nucleon fraction, is very small and the distinction is usually not important numerically. To avoid confusion, we will be using in this book mass densities and mass fractions. For more information on abundances see, e.g., Arnett (1996).

Example 1.4

The mass fractions of ^{1}H and ^{4}He at the time of the Sun's birth are equal to 0.71 and 0.27, respectively. Calculate the ratio of the corresponding number densities.

From Eq. (1.14) and Table 1.1, we find

$$\frac{N(^1\mathrm{H})}{N(^4\mathrm{He})} = \frac{\frac{\rho N_A \mathrm{X}(^1\mathrm{H})}{M(^1\mathrm{H})}}{\frac{\rho N_A \mathrm{X}(^4\mathrm{He})}{M(^4\mathrm{He})}} = \frac{M(^4\mathrm{He})}{M(^1\mathrm{H})}\frac{\mathrm{X}(^1\mathrm{H})}{\mathrm{X}(^4\mathrm{He})} = \frac{(4.0026\,\mathrm{u})}{(1.0078\,\mathrm{u})}\frac{0.71}{0.27} = 10.4$$

1.5.5 Decay Constant, Mean Lifetime, and Half-Life

The time evolution of the number density N (or of the absolute number of nuclei $\mathcal{N}$) of an unstable nuclide is given by the differential equation

$$\left(\frac{dN}{dt}\right) = -\lambda N \tag{1.16}$$

The quantity λ represents the probability of decay per nucleus per time. Since it is constant for a given nuclide under specific conditions (constant temperature and density), it is referred to as *decay constant*. Integration of the above expression immediately yields the radioactive decay law for the number density of undecayed nuclei remaining after a time t,

$$N = N_0 e^{-\lambda t} \tag{1.17}$$

where N_0 is the initial number density at $t = 0$. The time it takes for the number density N to fall to one-half of the initial abundance, $N_0/2 = N_0 e^{-\lambda T_{1/2}}$, is called the *half-life* $T_{1/2}$, with

$$T_{1/2} = \frac{\ln 2}{\lambda} = \frac{0.69315}{\lambda} \tag{1.18}$$

The time it takes for N to fall to $1/e = 0.36788$ of the initial abundance, $N_0/e = N_0 e^{-\lambda\tau}$, is called the *mean lifetime* τ, with

$$\tau = \frac{1}{\lambda} = 1.4427\, T_{1/2} \tag{1.19}$$

If a given nuclide can undergo different competing decays (e.g., γ- and β-decay, or different γ-ray transitions), then the total decay probability in Eqs. (1.16)–(1.19) is

given by the sum of the decay probabilities for the individual processes. Hence,

$$\lambda = \sum_i \lambda_i \qquad \text{or} \qquad \frac{1}{\tau} = \sum_i \frac{1}{\tau_i} \tag{1.20}$$

where the quantities λ_i and τ_i are called *partial* decay constant and *partial* lifetime, respectively. The product of the absolute number of nuclei, $\mathcal{N}$, and the decay constant determines the number of decays per unit time and is referred to as the *activity*, $A \equiv \lambda\mathcal{N} = -d\mathcal{N}/dt$. Common units of the activity are the curie (1 Ci $= 3.7 \times 10^{10}$ decays per second) and the becquerel (1 Bq = 1 decay per second). It must be emphasized that Eqs. (1.16)–(1.20) apply to any nuclear decay, such as β-decay, α-particle decay, γ-ray decay of excited levels, and the destruction of nuclei via nuclear reactions in a stellar plasma, as will be shown later.

1.6 Nuclear Shell Model

A detailed treatment of the nuclear shell model is beyond the scope of this book. Basic discussions are presented in many introductory nuclear physics texts (e.g., Krane, 1988). For a more detailed account, the reader is referred to DeShalit and Talmi (1963) or Brussaard and Glaudemans (1977). In the following we will summarize some of the important assumptions and predictions of the model. Our aim is to better understand how nuclear properties, such as binding energies, spins, and parities, can be explained from the underlying configurations of the nucleons. These considerations are also important because a number of nuclear structure properties that are mentioned in this text, for example, reduced γ-ray transition strengths, weak interaction matrix elements, and spectroscopic factors, are frequently computed using the shell model.

The *atomic* shell model has been enormously successful in describing the properties of atoms. In the case of an atom, the heavy nucleus represents a center for the Coulomb field in which the light electrons move independently in first-order approximation. The spherical Coulomb potential is given by $V_C = Ze^2/r$, with Z the atomic number, e the electron charge, and r the distance between nucleus and electron. Solving the Schrödinger equation for this system yields the electron orbits, or shells, that are characterized by various quantum numbers. In general, several of these (sub-)shells are almost degenerate in energy and together they form major shells. The rules for building up the atomic electron configuration follow immediately from the Pauli exclusion principle, stating that no more than two spin-1/2 particles can occupy a given quantum state simultaneously. The shells are then filled up with electrons in order of increasing energy. We thus obtain an inert core of filled shells and some number of valence electrons that primarily determine the atomic properties. Atoms with all states of the major shells occupied exhibit a high stability against removal or addition of an electron. These are the inert gases.

The application of a similar model to the atomic nucleus encounters a number of complications. First, the nuclear interaction is very different from the Coulomb

interaction and, moreover, the nature of the nucleon–nucleon interaction is not precisely known. Second, there are two kinds of elementary particles present in the nucleus (protons and neutrons) as opposed to the atomic case (electrons). Third, there is no heavy center of force for the nucleons. Despite these complications, the nuclear shell model has been highly successful in describing many properties of nuclei. Its basic assumption is that the interaction of each nucleon with all the other protons and neutrons in the nucleus is well approximated by some average potential $V(r)$. A single nucleon moves independently in this potential and can be described by a single-particle state of discrete energy and constant angular momentum.

The independent motion of the nucleons can be understood qualitatively in the following manner. According to the Pauli exclusion principle, no more than two protons or neutrons can exist in a given quantum state. The single-particle levels are filled with nucleons up to some level, depending on how many nucleons are present. Consider now a single nucleon, occupying some intermediate single-particle level, moving through the nucleus. The nuclear force has a short range and, therefore, we expect that the nuclear potential will strongly fluctuate. The nucleon may collide with other protons or neutrons, but it cannot gain or lose energy easily since the neighboring levels are already occupied and thus cannot accept an additional nucleon. It may gain a large amount of energy and hence move to a higher lying, unoccupied single-particle level. But such collisions with a significant energy transfer are less likely to occur. Consequently, the motion of the nucleon will often be fairly smooth.

1.6.1
Closed Shells and Magic Numbers

We will start from the assumption that the interaction between one nucleon and all the other nucleons in the nucleus can be approximated by a suitable single-particle potential. In the simplest case, it consists of a central potential (e.g., a harmonic oscillator potential or a Woods–Saxon potential) and a strong spin–orbit coupling term. The solutions of the Schrödinger equation for such a potential are bound single-particle states characterized by the values of the radial quantum number n, orbital angular momentum quantum number ℓ, and total angular momentum quantum number j (the latter is obtained from the coupling $\vec{j} = \vec{\ell} + \vec{s}$, where s denotes the intrinsic spin equal to 1/2 for protons or neutrons; see Appendix B). In particular, the energies of the single-particle states depend explicitly on the values of n, ℓ, and j. The single-particle states are energetically clustered in groups and thus reveal a shell structure. Each state of given j can be occupied by a maximum number of $(2j + 1)$ identical nucleons, corresponding to the number of magnetic substates $(m_j = -j, -j + 1, \ldots, j - 1, j)$, and thus represents a *subshell*. Several different subshells lying close in energy can be grouped together and form a *major shell*. Furthermore, each single-particle state possesses a definite parity (Appendix A), given by $\pi = (-1)^{\ell}$. The shells are filled up according to the Pauli exclusion principle.

The single-particle levels for either protons or neutrons are shown in Figure 1.11 where the horizontal direction represents an energy scale. The left-hand side, part (a), displays the single-particle energies of a harmonic oscillator potential as a function of the oscillator quantum number $N = 2(n-1) + \ell$, corresponding to the total number of oscillator quanta excited. Part (b) shows the single-particle energies of a Woods–Saxon potential. This potential is more realistic but mathematically less tractable. It is defined by $V(r) = V_0[1 + e^{(r-R_0)/a}]^{-1}$, where V_0, R_0, and a denote the potential depth, the potential radius, and the diffuseness, respectively. In part (a), each single-particle state of given N consists in general of states with different values of ℓ. These have the same energies and are thus called *degenerate*. The degeneracy does not occur for the more realistic Woods–Saxon potential, that is, states with different values of ℓ possess different energies. It is customary to use the spectroscopic notation s, p, d, f, g, … for states with orbital angular momenta of ℓ = 0, 1, 2, 3, 4, …, respectively. If an additional spin–orbit term is added to the potential, then each state of given ℓ value (except $\ell = 0$) can have a total angular momentum of either $j = \ell + 1/2$ or $j = \ell - 1/2$ (Appendix B). Since ℓ is an integer, j must be of odd half-integer value. Part (c) shows how the spin–orbit term splits each state with $\ell > 0$ into two levels. The number of identical particles (protons or neutrons) that can occupy a state of given j amounts to $(2j + 1)$ and is presented in part (d). Part (e) displays the single-particle states in spectroscopic notation as $n\ell_j$. The quantum number n corresponds to the order in which the various states of given ℓ and j appear in energy. Thus, $1s_{1/2}$ is the first $\ell = 0$, $j = 1/2$ state, $2s_{1/2}$ is the second, and so on. The parities of the single-particle levels are shown in part (f), and part (g) indicates the subtotal of the number of identical nucleons that can fill all the states up to a given level.

Notice that the spin–orbit coupling term is so strong that it changes the energies of the single-particle states significantly. For example, consider the $N = 3$ and 4 oscillator shells. The g-state ($\ell = 4$) in part (b) splits into two levels, $1g_{7/2}$ and $1g_{9/2}$. Since the spin–orbit coupling is strong the $1g_{9/2}$ state is depressed and appears to be close in energy to the $2p_{1/2}$, $1f_{5/2}$, and $2p_{3/2}$ states that originate from the $N = 3$ oscillator shell. There is now an energy gap at a subtotal nucleon (or occupation) number of 50 and, consequently, this group of states forms a major shell. Similar arguments apply to other groups of levels. It can be seen from Figure 1.11 that gaps (or major shell closures) in the single-particle energy spectrum appear at occupation numbers of 2, 8, 20, 28, 50, 82, and 126. These are referred to as *magic numbers*.

Nuclei with filled major shells of protons or neutrons exhibit an energetically favorable configuration, resulting in an extra stability compared to neighboring nuclei with only partly filled shells. The magic numbers manifest themselves in many observed nuclear properties, such as masses, particle separation energies, nuclear charge radii, electric quadrupole moments, and so on. For example, Figure 1.12 shows the difference of the measured ground-state atomic mass excess from its mean value that is calculated using a smooth semiempirical mass formula. At the locations of magic neutron numbers, the atomic mass excess is

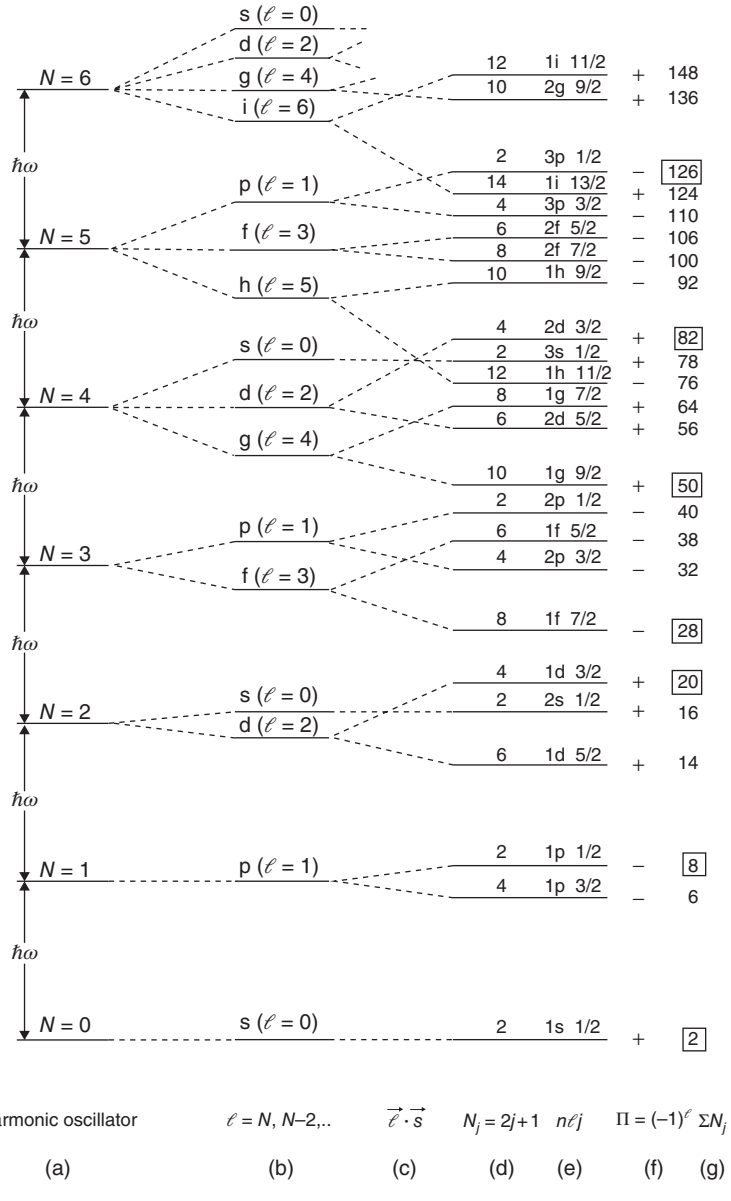

Figure 1.11 Approximate sequence of single-particle states for identical nucleons (protons or neutrons). The magic numbers (given in boxes on the right-hand side) appear at the energy gaps and correspond to the cumulative number of nucleons up to that state. The level pattern represents qualitative features only. This holds specifically for states with $N \geq 4$, where the level order differs for protons (which are subject to the Coulomb interaction) and neutrons. (Reprinted with permission from Brussaard and Glaudemans (1977). Copyright by P. J. Brussaard.)

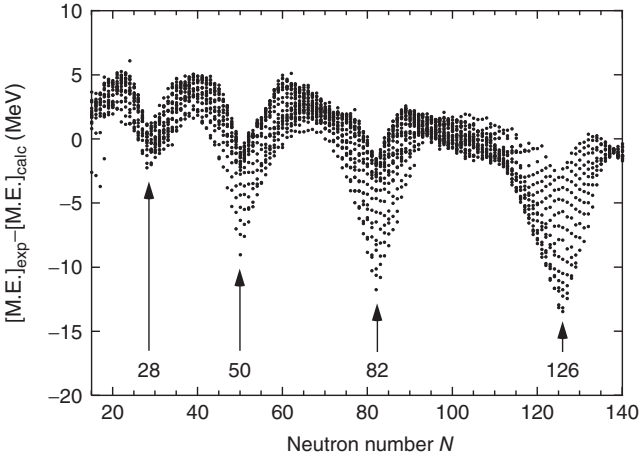

Figure 1.12 Difference between experimental ground-state atomic mass excess (Audi *et al.*, 2003) and the mass excess predicted by the spherical macroscopic part of the finite-range droplet (FRDM) mass formula (Möller *et al.*, 1995) versus neutron number.

smaller, resulting in a smaller atomic mass and a larger binding energy according to Eqs. (1.2) and (1.10). Another example will be given later in connection with neutron capture cross sections (Figure 5.67). Such observations provide unambiguous evidence for the shell structure of nuclei. As will become apparent in Section 5.6, the synthesis of the heavy elements is strongly influenced by the magic neutron numbers of $N = 50$, 82, and 126. It has to be emphasized again that the magic numbers as they are observed in nature can be reproduced only if a strong spin–orbit coupling term is introduced into the independent-particle potential.

1.6.2
Nuclear Structure and Nucleon Configuration

The shell model not only predicts the properties of closed shell nuclei, but also predicts the properties of nuclei with partly filled shells. The nuclear properties follow directly from the configuration of the nucleons: (i) the binding energy or mass of the nucleus is determined by the single-particle energies (caused by the independent motion of the nucleons in an average potential) and by the mutual interaction of the valence nucleons (i.e., those located outside a closed major shell); (ii) the total angular momentum of the nucleus (or the *nuclear spin*) is obtained by coupling the angular momenta of the independent single-particle states according to the quantum mechanical rules for vector addition (Appendix B); and (iii) the total parity of the nucleus is determined by the product of the parities for all nucleons.

Consider first a nucleus with completely filled subshells. In each subshell j all magnetic substates m_j are occupied and thus, the sum of j_z over all nucleons in the subshell must be zero. In other words, the nucleons in a completely filled subshell

must couple to an angular momentum of zero. Furthermore, since $(2j + 1)$ is an even number, the total parity of the nucleons amounts to $\pi = +1$. Indeed, the observed spin and parity of nuclei with closed subshells (or closed major shells) amount to $J^\pi = 0^+$ (e.g., ${}^{4}_{2}\mathrm{He}_{2}$, ${}^{12}_{6}\mathrm{C}_{6}$, ${}^{14}_{6}\mathrm{C}_{8}$, ${}^{14}_{8}\mathrm{O}_{6}$, ${}^{16}_{8}\mathrm{O}_{8}$, ${}^{28}_{14}\mathrm{Si}_{14}$, ${}^{32}_{16}\mathrm{S}_{16}$, or ${}^{40}_{20}\mathrm{Ca}_{20}$). A closed-shell nucleus can only be excited by promoting at least one nucleon to a higher lying, unoccupied, subshell. This is consistent with the observation that the first excited states of such nuclei are usually found at relatively high excitation energies. Nuclei with partly filled shells may have excited states that result from a recoupling of the angular momenta only. This explains why in such cases the observed excitation energies are significantly smaller.

By considering Figure 1.11, we can easily explain the quantum numbers for the ground states of nuclei when a single nucleon is located outside a closed subshell. In this case, the ground-state spin and parity is given by the lowest single-particle state available to the valence nucleon. For example, we find $J^\pi = 1/2^-$ for ${}^{13}_{6}\mathrm{C}_{7}$, $J^\pi = 5/2^+$ for ${}^{17}_{8}\mathrm{O}_{9}$, $J^\pi = 1/2^+$ for ${}^{29}_{14}\mathrm{Si}_{15}$, or $J^\pi = 3/2^+$ for ${}^{33}_{16}\mathrm{S}_{17}$. A single valence nucleon outside a closed subshell behaves in this respect the same as a single *hole* in an otherwise filled subshell. The ground-state spin and parity, for example, of ${}^{27}_{14}\mathrm{Si}_{13}$ amounts to $J^\pi = 5/2^+$ because it has a single neutron hole in the $1\mathrm{d}_{5/2}$ shell.

The situation is more complicated when the subshells are only partly filled. We observe experimentally that the ground states of all doubly even nuclei possess a spin and parity of $J^\pi = 0^+$. For example, this applies to ${}^{26}_{12}\mathrm{Mg}_{14}$ although neither the protons nor the neutrons completely fill the subshells. This means that it is energetically favorable for pairs of protons or neutrons to couple to a total spin and parity of $J^\pi_{\mathrm{pair}} = 0^+$. This *pairing effect* also influences the proton and neutron separation energies of neighboring nuclei, as will be seen in Section 5.6. The shell model can then be used to predict the ground-state spins and parities for odd-A nuclei. For example, consider ${}^{23}_{10}\mathrm{Ne}_{13}$. All the protons couple pairwise to quantum numbers of 0^+, as do 12 of the neutrons. The lowest available level for the odd neutron is the $1\mathrm{d}_{5/2}$ state (Figure 1.11) and thus the ground-state spin of ${}^{23}\mathrm{Ne}$ amounts to $J^\pi = 5/2^+$. These simplistic considerations reproduce many of the observed ground-state spins, but fail in some cases. According to the above arguments, one would expect a ground-state spin and parity of $J^\pi = 5/2^+$ for ${}^{23}_{11}\mathrm{Na}_{12}$, but instead we observe $J^\pi = 3/2^+$. The discrepancy is caused by the complicated interplay of many nucleons in an unfilled shell so that an even number of protons or neutrons does not always couple to a total angular momentum of $J = 0$ for the ground state. This is especially true for excited nuclear levels.

In all but the simplest situations, the nucleon configuration must be taken into account explicitly. Further complications arise since a given nuclear level may be described by a mixed configuration, that is, by different nucleon configurations that couple to the same value of J^π. In such cases, large-scale shell model calculations must be performed with numerical computer codes. The shell model has been enormously successful in explaining the structure of nuclei. It is frequently used in nuclear astrophysics to calculate nuclear quantities that have not yet been measured in the laboratory. Reduced γ-ray transition strengths (Section 1.7.2) or weak interaction transition strengths (Section 1.8.3), for instance, depend

on nuclear matrix elements that connect an initial (decaying) state with a final state. The matrix elements can be calculated numerically with the shell model in a straightforward manner once an appropriate form for the transition operator (for the electromagnetic or weak interaction) is assumed. Another important quantity in nuclear astrophysics is the spectroscopic factor. It will be explained in Section 2.5.7 how this property can be used for estimating an unknown cross section of a nuclear reaction $A + a \rightarrow B$. The spectroscopic factor is defined in terms of the overlap integral between the final state wave function of B and the initial state wave function of $A + a$. It does not depend on a transition operator, but only on a wave function overlap, and thus can be calculated rather reliably for many nuclei.

1.7 Nuclear Excited States and Electromagnetic Transitions

1.7.1 Energy, Angular Momentum, and Parity

Every nucleus exhibits excited states. They can be populated by many different means, for example, nuclear reactions, β-decays, thermal excitations (see below), inelastic electron or particle scattering, and Coulomb excitation. Each nuclear level is characterized by its excitation energy E_x, defined as the binding energy difference between the level in question and the ground state of the nucleus. For the ground state we have, as per definition, $E_x = 0$. In the laboratory, each excited level of energy E_i can make a transition to a lower lying state of energy E_f via three different processes that are all induced by the electromagnetic interaction: (i) γ-ray emission, (ii) internal conversion, and (iii) internal pair formation. *Internal conversion* refers to a process where an excited nucleus de-excites by transferring its energy directly, that is, in a single step, to an orbital electron. *Internal pair formation* denotes the de-excitation of a nucleus by creating an electron–positron pair, in which case the de-excitation energy must exceed twice the value of the electron rest energy ($2m_e c^2$). Although the three processes can in principle compete with each other, the emission of a γ-ray is by far the most important one for nuclear astrophysics and will be discussed in the following.

In a γ-ray transition between two nuclear levels, the energy of the emitted photon is given by

$$E_\gamma = E_i - E_f - \Delta E_{\mathrm{rec}} \tag{1.21}$$

where the origin of the *recoil shift* ΔE_{rec} is described in Appendix C.1 We are mainly concerned here with γ-ray energies in the range of 100 keV to 15 MeV. For such energies, the recoil shift is very small and can usually be neglected. Hence, we may use in most cases $E_\gamma \approx E_i - E_f$. This assumes that the excited nucleus decays from rest. If the decaying level is populated via a nuclear reaction, then another

correction (the Doppler shift) must also be taken into account (Appendix C.1). In any case, the emitted γ-rays will exhibit discrete energies. If E_f corresponds to the ground state, then no further emission of γ-rays is possible. Otherwise, de-excitation of the nucleus by emission of one or more photons before reaching the ground state is likely to occur.

The emitted (or absorbed) electromagnetic radiation can be classified according to the angular momentum $L\hbar$ carried by each photon, and according to its parity (Appendix B). The angular momentum carried away by the photon determines the multipolarity of the radiation. A value of L for the angular momentum corresponds to 2^L-pole radiation with its characteristic angular distribution for the emitted intensity. For example, $L = 1$ and $L = 2$ correspond to dipole (2^1) and quadrupole (2^2) radiation, respectively. Two identical radiation patterns for a given value of L may correspond to different waves, *electric* 2^L-pole radiation and *magnetic* 2^L-pole radiation, which differ through their parity. For example, E2 and M1 correspond to electric quadrupole radiation and magnetic dipole radiation, respectively. In a γ-ray transition between two nuclear levels the total angular momentum and parity of the system (nucleus plus electromagnetic field) are conserved. The conservation laws give rise to certain selection rules that must be fulfilled for an emission (or absorption) of radiation of given character to occur. The quantum mechanical rules are explained in Appendix B.

1.7.2 Transition Probabilities

A detailed discussion of the quantum theory for the interaction of nuclei with electromagnetic radiation is beyond the scope of this book. We will instead summarize the most important steps in the derivation of the transition probability. For more information, see Blatt and Weisskopf (1952).

The decay constant (i.e., the probability per unit time) for the emission of electromagnetic radiation of a given character (e.g., E1 or M2) in a transition connecting two given nuclear levels can be calculated using perturbation theory. The result is (Blatt and Weisskopf, 1952)

$$\lambda(\overline{\omega}L) = \frac{8\pi(L+1)}{\hbar L[(2L+1)!!]^2}\left(\frac{E_\gamma}{\hbar c}\right)^{2L+1} B(\overline{\omega}L) \tag{1.22}$$

with E_γ and L the energy and multipolarity of the radiation, respectively; $\overline{\omega}$ denotes either electric (E) or magnetic (M) radiation and the double factorial is defined as $(2L+1)!! \equiv 1 \cdot 3 \cdot 5 \cdot \ldots \cdot (2L+1)$. The quantity $B(\overline{\omega}L)$ is called the *reduced transition probability*. It contains the wave functions of the initial and final nuclear states, and the multipole operator, that is, the operator responsible for changing the initial to the final state while simultaneously creating a photon of proper energy, multipolarity, and character. Reduced transition probabilities can be calculated using nuclear structure models, for example, the shell model (Section 1.6). In the simplest case, one may assume that the nucleus consists of an inert core

plus a single nucleon, that the γ-ray transition is caused by this nucleon changing from one shell-model state to another, and that the radial wave functions of the initial and final states are constant over the nuclear interior and vanish outside the nucleus. With these assumptions, one obtains the *Weisskopf estimates* for the γ-ray transition probabilities, which are given below for the lowest – and as will be seen, most important – multipolarities:

$$\lambda_W(\mathrm{E1})\hbar = 6.8\times10^{-2}A^{2/3}E_\gamma^3, \qquad \lambda_W(\mathrm{M1})\hbar = 2.1\times10^{-2}E_\gamma^3 \tag{1.23}$$

$$\lambda_W(\mathrm{E2})\hbar = 4.9\times10^{-8}A^{4/3}E_\gamma^5, \qquad \lambda_W(\mathrm{M2})\hbar = 1.5\times10^{-8}A^{2/3}E_\gamma^5 \tag{1.24}$$

$$\lambda_W(\mathrm{E3})\hbar = 2.3\times10^{-14}A^{2}E_\gamma^7, \qquad \lambda_W(\mathrm{M3})\hbar = 6.8\times10^{-15}A^{4/3}E_\gamma^7 \tag{1.25}$$

In these numerical expressions, A denotes the mass number of the decaying nucleus, the photon energy E_γ is in units of mega electron volts, and the Weisskopf estimates are in units of electron volts. It will be shown later that the product $\lambda\hbar$ is equal to a γ-ray partial width.

The Weisskopf estimates for the γ-ray decay probability are shown in Figure 1.13 versus γ-ray energy for emitted radiations of different multipolarity and character. It is apparent that the quantity λ_W rises strongly with increasing γ-ray energy. We will be using in later chapters the relation $\Gamma = \lambda\hbar \sim E_\gamma^{2L+1}$, as predicted by the Weisskopf estimates, when describing the energy dependence of γ-ray partial widths. Also, the decay probability depends strongly on the multipolarity L and the character $\overline{\omega}$ of the radiation. Furthermore, according to the selection rules (Appendix B), electric and magnetic radiations of the same multipolarity cannot be emitted together in a transition between two given nuclear levels. For a

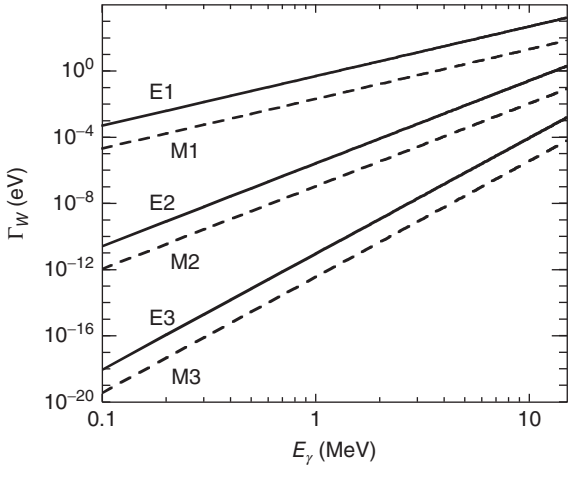

Figure 1.13 Weisskopf estimate of the γ-ray decay probability for pure electric (E) and magnetic (M) multipole radiations emitted in transitions between two nuclear levels of energy difference E_γ. The γ-ray partial width Γ_W is equal to the product $\lambda_W\hbar$. The curves are calculated for A = 20 and a nuclear radius of $R = 1.20A^{1/3}$ fm = 3.3 fm.

transition connecting two levels of opposite parities, we find from Figure 1.13 the inequalities

$$\lambda_W(\mathrm{E1}) \gg \lambda_W(\mathrm{M2}) \gg \lambda_W(\mathrm{E3}) \gg \cdots \tag{1.26}$$

In this case, the lowest multipole permitted by the selection rules usually dominates. In particular, if E1 radiation is allowed it will dominate the transition strength in the vast majority of astrophysical applications. For a transition connecting two levels of the same parity, one obtains

$$\lambda_W(\mathrm{M1}) \gg \lambda_W(\mathrm{E2}) \gg \lambda_W(\mathrm{M3}) \gg \cdots \tag{1.27}$$

However, experimentally measured γ-ray transition strengths do not support the conclusion that M1 transitions are always faster than E2 transitions if both radiations are allowed by the selection rules. The decay strengths may deviate strongly from the Weisskopf estimates since the latter are obtained using rather crude assumptions. It turns out that for many transitions the observed decay constants are several orders of magnitude smaller than the theoretically predicted value of λ_W, indicating a poor overlap in the wave functions of the initial and final nuclear levels. On the other hand, for E2 transitions it is found that the observed decay probability frequently exceeds the Weisskopf estimate by large factors. This indicates that more than one nucleon must be taking part in the transition and that the excitation energy of the decaying level is stored in the collective in-phase motion of several nucleons.

The Weisskopf estimates are very useful since they provide a standard against which to compare observed transition strengths. The latter are frequently quoted in *Weisskopf units*, defined as

$$M^2_W(\overline{\omega}L) \equiv \frac{\lambda(\overline{\omega}L)}{\lambda_W(\overline{\omega}L)} = \frac{\Gamma(\overline{\omega}L)}{\Gamma_W(\overline{\omega}L)} \qquad \text{or} \qquad \lambda(\overline{\omega}L) = M^2_W(\overline{\omega}L)\,\mathrm{W.u.} \tag{1.28}$$

This definition removes the strong energy dependence of the decay probability. Several thousand observed γ-ray transitions were analyzed in this manner and their transition strengths in Weisskopf units have been presented separately according to the multipolarity and character of the radiation (Endt, 1993, and references therein). The resulting distributions of transition strengths extend from some small value of $M^2_W(\overline{\omega}L)$, which is strongly influenced by the sensitivity of the detection apparatus, to the largest observed transition probability. The latter value defines for each combination of $\overline{\omega}L$ a *recommended upper limit* (RUL). For the mass region $A = 5$–44, the following values have been reported (Endt, 1993)

$$\begin{aligned} &\mathrm{RUL(E1)} = 0.5\,\mathrm{W.u.}, && \mathrm{RUL(M1)} = 10\,\mathrm{W.u.} \\ &\mathrm{RUL(E2)} = 100\,\mathrm{W.u.}, && \mathrm{RUL(M2)} = 5\,\mathrm{W.u.} \\ &\mathrm{RUL(E3)} = 50\,\mathrm{W.u.}, && \mathrm{RUL(M3)} = 10\,\mathrm{W.u.} \end{aligned}$$

These values are important for estimating the maximum expected γ-ray decay probability for an unobserved transition (Problem 1.5). It is tempting to estimate

average decay strengths based on the centroids of the observed transition strength distributions (see Figure 2 in Endt, 1993). However, one has to be very careful since the "averages" (as well as the "lower limits") depend on the γ-ray detection limit and thus may decrease with an improvement in the sensitivity of the detection equipment.

1.7.3 Branching Ratio and Mixing Ratio

So far we discussed γ-ray transitions of specific multipolarity L and character $\overline{\omega}$. In practice, however, a given initial state may decay to a number of different final states. Furthermore, each transition connecting two given states may proceed via a mixture of radiations according to the selection rules. These complications can be described by introducing two new quantities, the branching ratio and the mixing ratio. In the following we will express these quantities in terms of the γ-ray decay probability in units of energy, $\Gamma = \lambda\hbar$, also called the γ-ray partial width. Consider Figure 1.14 showing the γ-ray decay of an initial excited level i. The *total* γ-ray width of the initial state can be expressed in terms of *partial* γ-ray widths that each correspond to a transition to a specific final state j as

$$\Gamma_{\text{tot}} = \sum_j \Gamma_j \tag{1.29}$$

Assuming that the initial state decays only by γ-ray emission, the *γ-ray branching ratio* is defined by

$$B_j \equiv \frac{\Gamma_j}{\Gamma_{\text{tot}}} \times 100\% \tag{1.30}$$

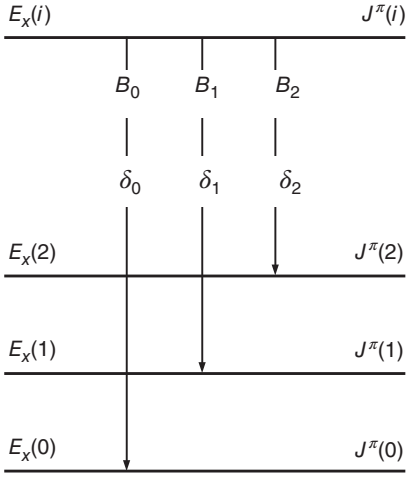

Figure 1.14 Energy level diagram showing the γ-ray decay of an initial state i to the ground state (0) and to two excited states (1, 2). The branching ratio B_j represents the relative intensity of a particular decay branch as a percentage of the total intensity and δ_j denotes the multipolarity mixing ratio.

and is usually given in percent. Each γ-ray branch may result from radiations of different multipolarities L and characters $\overline{\omega}$. Although the selection rules may allow for three or more possibilities (e.g., a $2^+ \rightarrow 1^+$ transition may proceed via M1, E2, or M3 radiations), in most practical cases not more than the lowest two values of $\overline{\omega}L$ need to be taken into account. If we assume that only radiations with $\overline{\omega}'L$ and $\overline{\omega}L + 1$ contribute to the transition (M1 and E2 in the above example), the partial γ-ray width is given by

$$\Gamma_j(\overline{\omega}L + 1; \overline{\omega}'L) = \Gamma_j(\overline{\omega}L + 1) + \Gamma_j(\overline{\omega}'L) \tag{1.31}$$

The *γ-ray multipolarity mixing ratio* is defined as

$$\delta_j^2 \equiv \frac{\Gamma_j(\overline{\omega}L + 1)}{\Gamma_j(\overline{\omega}'L)} \tag{1.32}$$

By combining Eqs. (1.29)–(1.32), we may express the individual widths in terms of the total width as

$$\Gamma_j(\overline{\omega}'L) = \frac{1}{1 + \delta_j^2} \frac{B_j}{100} \Gamma_{\text{tot}} \tag{1.33}$$

$$\Gamma_j(\overline{\omega}L + 1) = \frac{\delta_j^2}{1 + \delta_j^2} \frac{B_j}{100} \Gamma_{\text{tot}} \tag{1.34}$$

A highly excited nuclear state with many different decay probabilities to lower lying levels will preferably decay via those transitions that correspond to the largest decay strengths, that is, via emission of radiations with the smallest multipoles. If a given level is located, say, above at least 20 lower lying states, then the observed γ-ray decays from this level are in almost all instances either of dipole (E1 or M1, depending on the parity of the initial and final level) or of E2 character. This empirical finding is called the *dipole or E2 rule* (Endt, 1990) and is useful for estimating unknown spin and parities of nuclear levels.

1.7.4
γ-Ray Transitions in a Stellar Plasma

In a hot plasma, excited states in a given nucleus are thermally populated, for example, through absorption of photons (photoexcitation), Coulomb excitation by surrounding ions, inelastic particle scattering, and other means. The time scale for excitation and de-excitation (e.g., via emission and absorption of photons) in a hot stellar plasma is usually – with the important exception of isomeric states (see below) – considerably shorter than stellar hydrodynamical time scales, even under explosive conditions (Fowler, Caughlan, and Zimmerman, 1975). These excited levels will participate in nuclear reactions and β-decays, as will be explained later, and thus their population must in general be taken into account.

For a given nuclide in a nondegenerate plasma at thermodynamic equilibrium, the ratio of the number density of nuclei in excited state μ, denoted by N_μ, and the total number density of nuclei, N, is given by a Boltzmann distribution (Ward and Fowler, 1980)

$$P_\mu = \frac{N_\mu}{N} = \frac{g_\mu e^{-E_\mu/kT}}{\sum_\mu g_\mu e^{-E_\mu/kT}} = \frac{g_\mu e^{-E_\mu/kT}}{G} \tag{1.35}$$

with $g_\mu \equiv (2J_\mu + 1)$, J_μ and E_μ the statistical weight, spin and excitation energy, respectively, of state μ; the quantity k denotes the Boltzmann constant and T is the plasma temperature. The sum over μ in the denominator includes the ground state and is referred to as the *partition function, G*. Equation (1.35) follows directly from statistical thermodynamics and encompasses all the different processes for the excitation and de-excitation of levels (i.e., not only the emission and absorption of photons). The thermal population of excited nuclear levels becomes more important with increasing temperature and lower excitation energy. These properties of Eq. (1.35) are explored in Problem 1.6.

1.7.5
Isomeric States and the Case of ^{26}Al

In most cases, the nuclear levels decaying by γ-ray emission have very high transition probabilities, corresponding to half-lives that are generally $< 10^{-9}$ s. However, in some cases the half-lives are longer by many orders of magnitude, amounting to seconds, minutes or even days. Such long-lived excited nuclear levels are referred to as *isomeric states* (or isomers, or metastable states) and the corresponding γ-ray decays are called *isomeric transitions*. We will denote these levels with the superscript m (e.g., $^A\mathrm{X}^m$).

The two aspects that are mainly responsible for the long half-lives of isomeric states are (i) a large difference for the spins of the isomeric and the final nuclear level, and (ii) a relatively small energy difference between the two levels. The first aspect implies a large γ-ray multipolarity (e.g., M4 or E5). The second aspect implies a small γ-ray energy. According to Eq. (1.22), both of these effects have the tendency to reduce the decay probability substantially.

We will illustrate some of the complexities that arise from the presence of an isomer by discussing the important case of ^{26}Al. An energy level diagram is displayed in Figure 1.15. Focus first only on the left-hand part, showing the ground state ($E_x = 0$, $J^\pi = 5^+$) and three excited states ($E_x = 228$ keV, $J^\pi = 0^+$; $E_x = 417$ keV, $J^\pi = 3^+$; and $E_x = 1058$ keV, $J^\pi = 1^+$) in ^{26}Al. According to the selection rules, the direct γ-ray de-excitation of the first excited state at $E_x = 228$ keV would require the emission of M5 radiation. The γ-ray decay probability for such a high multipolarity is very small and thus the first excited state is an isomer ($^{26}\mathrm{Al}^m$). It decays via a β-transition (which is considerably more likely to occur than the M5 γ-ray transition) to the ground state of ^{26}Mg with a half-life of $T_{1/2}(^{26}\mathrm{Al}^m) = 6.34$ s. The ^{26}Al ground state is also β-unstable and decays with a half-life of

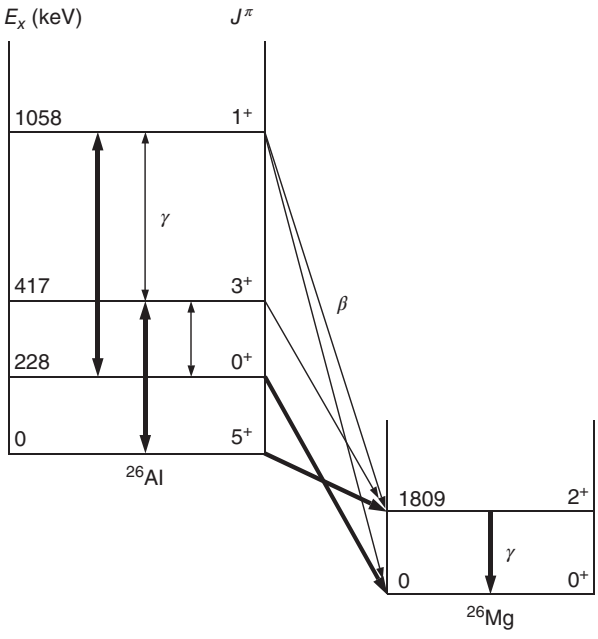

Figure 1.15 Energy level schemes of ^{26}Al and ^{26}Mg, showing the lowest lying states in each nuclide. The vertical arrows represent γ-ray decays, while the diagonal arrows indicate β-decay transitions. Only the transitions indicated by the thick arrows have been observed experimentally. The transitions shown as thin arrows play an important role in the equilibration of the ground state and the isomer at E_x = 228 keV in ^{26}Al. The direct γ-ray de-excitation of the isomer is strongly inhibited by the selection rules. The presence of ^{26}Al^g in the interstellar medium is inferred from the observed intensity of the 1809 keV γ-ray, originating from the de-excitation of the first excited state in ^{26}Mg. A small β-decay branch of the ^{26}Al ground state to the E_x = 2938 keV ($J^\pi = 2^+$) level in ^{26}Mg is omitted in the figure for clarity.

$T_{1/2}(^{26}\mathrm{Al}^g) = 7.17 \times 10^5$ y mainly to the first excited state at $E_x = 1809$ keV in ^{26}Mg. This level, in turn, de-excites quickly via γ-ray emission of E2 character.

Interestingly, photons with an energy of 1809 keV originating from the interstellar medium have been detected first by the HEAO-3 spacecraft (Mahoney *et al.*, 1982), and subsequently by other instruments. The E_x = 1809 keV level in ^{26}Mg decays so quickly (within a fraction of a second) that, if it is populated via nuclear reactions in the interiors of stars, the emitted 1809 keV photons would immediately be absorbed by the surrounding matter and would never be able to escape from the stellar production site. However, suppose instead that ^{26}Al^g is synthesized via nuclear reactions in the stellar interior. The long half-life of the ground state provides ample opportunity for this species to be expelled from a star into the interstellar medium, where it then decays so that the emitted photons can reach the Earth. Only the decay of the ground state, but not the decay of the isomer, in ^{26}Al gives rise to the emission of 1809 keV γ-rays.

An all-sky map of the 1809 keV γ-ray line, obtained by the Imaging Compton Telescope (COMPTEL) aboard the Compton Gamma Ray Observatory (CGRO), is shown in color Figure 12 on page 624. The discovery of $^{26}Al^g$ in the interstellar medium is of paramount importance, as already pointed out (Section 1.4.1). It demonstrates that nucleosynthesis is currently active since the $^{26}Al^g$ half-life is considerably shorter than the time scale of Galactic chemical evolution ($\approx 10^{10}$ y). From the observed γ-ray intensity, it is estimated that the production rate of $^{26}Al^g$ in the Galaxy amounts to $\approx 2M_\odot$ per 10^6 y. The origin of the Galactic $^{26}Al^g$ is controversial at present. However, the observational evidence favors massive stars as sources. For example, the all-sky map of the 1809 keV γ-ray line shows that $^{26}Al^g$ is confined along the Galactic disk and that the measured intensity is clumpy and asymmetric. Furthermore, the measurement of the Doppler shift of the 1809 keV line demonstrated that the $^{26}Al^g$ co-rotates with the Galaxy and hence supports a Galaxy-wide origin for this species (Diehl *et al.*, 2006). Stellar model calculations for massive stars suggest that $^{26}Al^g$ is mainly produced in type II supernovae during explosive neon–carbon burning (Section 5.4.3 and right side of Figure 1.7). A smaller fraction is possibly synthesized in Wolf–Rayet stars during core hydrogen burning and in the subsequent type Ib/Ic supernova explosion. For more information, see Limongi and Chieffi (2006).

We noted above that in a hot stellar plasma, most nuclear levels quickly achieve thermal equilibrium since the time scales for excitation and de-excitation are very short. However, this is not necessarily the case for isomeric states. For example, the γ-ray transition probabilities for the de-excitation of the ^{26}Al isomer at $E_x =$ 228 keV and for its population from the ground state via absorption of radiation depend on the same reduced transition strength. Since the emission or absorption of M5 radiation is unlikely, the ground and isomeric states in ^{26}Al cannot achieve thermal equilibrium directly (i.e., Eq. (1.35) is not generally valid in this case). Thermal equilibrium may nevertheless be achieved indirectly via transitions involving higher lying levels in ^{26}Al.

Consider again Figure 1.15. In this case, the ground state and the isomer can communicate via the $E_x = 417$ keV state ($0 \leftrightarrow 417 \leftrightarrow 228$) or via the $E_x =$ 1058 keV state ($0 \leftrightarrow 417 \leftrightarrow 1058 \leftrightarrow 228$). Higher lying ^{26}Al states also play a role as the temperature is increased, but have been omitted in the figure for clarity. The thermal equilibration of ^{26}Al can be calculated by solving numerically a set of linear differential equations that describe all possible γ-ray and β-decay transitions. For some of these (indicated by thick arrows), the experimental transition strengths are known, while for others (thin arrows) the transition strengths have to be calculated using the shell model (Section 1.6). The procedure is described in detail in Coc, Porquet, and Nowacki (1999) and Runkle, Champagne, and Engel (2001), and is not repeated here. The resulting effective lifetime of ^{26}Al versus temperature is displayed in Figure 1.16. The solid line is obtained numerically by taking explicitly the equilibration of the ground and isomeric states via thermal excitations involving higher lying levels into account. The dashed curve is calculated analytically by assuming that the ground and isomeric states are in thermal

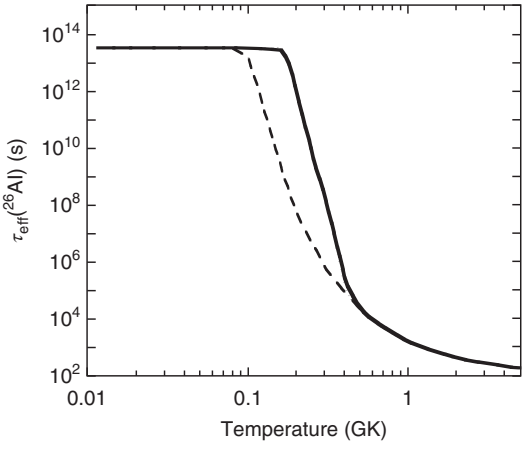

Figure 1.16 Effective lifetime of ^{26}Al as a function of temperature. The solid line is adopted from Coc, Porquet, and Nowacki (1999) and Runkle, Champagne, and Engel (2001). It was obtained numerically by taking explicitly the equilibration of the ground and isomeric states via thermal excitations involving higher lying levels into account. At each temperature, the calculation was started with a given amount of pure ^{26}Al^g. The value of $\tau_{eff}(^{26}Al)$ is then defined by the time necessary for the total (ground plus isomeric state) ^{26}Al abundance to decline by $1/e$. The dashed curve is calculated analytically by assuming that the ground and isomeric states are in thermal equilibrium (Example 1.5).

equilibrium (Example 1.5). Below $T = 0.1$ GK, the effective lifetime is given by the laboratory lifetime of ^{26}Al^g ($\tau = 1.4427\, T_{1/2} = 3.3 \times 10^{13}$ s). Above $T = 0.4$ GK, the ground and isomeric states are in thermal equilibrium. At intermediate temperatures, $T = 0.1$–0.4 GK, the equilibration of ^{26}Al via higher lying levels results in an effective lifetime that differs significantly from the thermal equilibrium value.

We focussed here on the case of ^{26}Al. Other important examples of isomers in nuclear astrophysics are ^{176}Lu^m (Zhao and Käppeler, 1991) and ^{180}Ta^m (Wisshak *et al.*, 2001). For a distinction between the kind of isomer discussed above (also called *spin-isomer*) and other types of isomers (*shape-* and *K-isomers*), see Walker and Dracoulis (1999).

1.8 Weak Interaction

The strong nuclear force and the electromagnetic force govern the nuclear reactions that are of outstanding importance for the energy generation and the nucleosynthesis in stars. However, weak interactions also play an important role in stars for several reasons. First, when a radioactive nuclide is produced during the nuclear burning, its decay via weak-interaction processes will compete with its

destruction via nuclear reactions, as will become apparent in Chapter 5. Second, weak interactions determine the *neutron excess parameter* during the nucleosynthesis, defined as

$$\eta \equiv \sum_i (N_i - Z_i) Y_i = \sum_i \frac{(N_i - Z_i)}{M_i} X_i \qquad \text{with} \qquad -1 \leq \eta \leq 1 \tag{1.36}$$

where N_i, Z_i, M_i, Y_i, and X_i denote the number of neutrons and protons, the relative atomic mass (in atomic mass units), the mole fraction, and the mass fraction, respectively. The sum runs over all nuclides i in the plasma. Note that $\eta = 0$ if only $N = Z$ nuclei (^{4}He, ^{12}C, ^{16}O, and so on) are present. The quantity η represents physically the number of *excess* neutrons per nucleon in the plasma and can only change as a result of weak interactions. A closely related quantity is the electron mole fraction, Y_e, which, according to Eqs. (1.13) and (1.15), is equal to the electron-to-baryon ratio, or the proton-to-baryon ratio,

$$Y_e = \frac{N_e}{\sum_i N_i M_i} \tag{1.37}$$

where the sum is again over all nuclides present and N_e denotes the electron number density. Thus, the electron mole fraction is related to the neutron excess parameter via

$$\eta = 1 - 2Y_e \tag{1.38}$$

The neutron excess must be monitored carefully in stellar model computations, since it is of crucial importance for the nucleosynthesis during the late burning stages in massive stars and during explosive burning (Section 5.3). Furthermore, we already mentioned that electron capture is very important for the dynamic behavior of the core collapse in massive stars before a type II supernova explosion because it reduces the number of electrons available for pressure support (Section 1.4.3). Third, neutrinos emitted in weak interactions affect the energy budget of stars and thus influence models of stellar evolution and explosion.

We will focus in this section on the process of nuclear β-decay, which involves the proton, neutron, electron, positron, neutrino, and antineutrino, and we will summarize some concepts that are important in the present context. Weak interaction processes in stars will be addressed in Chapter 5. A note regarding the nomenclature. Neutrinos come in three types, or *flavors*: electron neutrinos, muon neutrinos, and tau neutrinos. For weak interaction processes where this distinction matters, we will use appropriate subscripts for the different flavors (ν_e, ν_μ, ν_τ). If no subscript is used, the symbol ν refers explicitly to electron neutrinos.

1.8.1 Weak Interaction Processes

Consider first the free neutron. It decays into a proton under the influence of the weak interaction via

$$n \rightarrow p + e^- + \overline{\nu} \tag{1.39}$$

where e^- and $\overline{\nu}$ denote an electron and antineutrino, respectively. The half-life of the free neutron amounts to $T_{1/2} = 10.2$ min. This decay is slower by many orders of magnitude compared to typical nuclear reaction time scales or electromagnetic decay probabilities and demonstrates that the interaction causing β-decay is very weak. The most common weak interaction processes in nuclear β-decay are listed below:

$$ {}^{A}_{Z}X_N \rightarrow {}^{A}_{Z+1}X'_{N-1} + e^- + \overline{\nu} \qquad \beta^-\text{-decay (electron emission)} \qquad (1.40) $$

$$ {}^{A}_{Z}X_N \rightarrow {}^{A}_{Z-1}X'_{N+1} + e^+ + \nu \qquad \beta^+\text{-decay (positron emission)} \qquad (1.41) $$

$$ {}^{A}_{Z}X_N + e^- \rightarrow {}^{A}_{Z-1}X'_{N+1} + \nu \qquad \text{electron capture} \qquad (1.42) $$

$$ {}^{A}_{Z}X_N + \nu \rightarrow {}^{A}_{Z+1}X'_{N-1} + e^- \qquad \text{neutrino capture} \qquad (1.43) $$

$$ {}^{A}_{Z}X_N + \overline{\nu} \rightarrow {}^{A}_{Z-1}X'_{N+1} + e^+ \qquad (1.44) $$

Here e^+, ν, and $\overline{\nu}$ denote a positron, neutrino, and antineutrino, respectively. In each of these interactions, the decaying nuclide changes its chemical identity, but the mass number A remains the same. The light particles e^-, e^+, ν, and $\overline{\nu}$ are leptons, that is, they do not interact via the strong nuclear force.

The first three decays represent the most common weak interaction processes of radioactive nuclei in the laboratory. Consider an example, the β-decay of ${}^{64}_{29}Cu_{35}$. It may proceed via ${}^{64}_{29}Cu_{35} \rightarrow {}^{64}_{30}Zn_{34} + e^- + \overline{\nu}$ (β^--decay), ${}^{64}_{29}Cu_{35} \rightarrow {}^{64}_{28}Ni_{36} + e^+ + \nu$ (β^+-decay), or ${}^{64}_{29}Cu_{35} + e^- \rightarrow {}^{64}_{28}Ni_{35} + \nu$ (electron capture). When the electron is captured from the atomic K-shell, the process is called *K capture*. Neutrino capture is observed, for example, in the reaction ${}^{37}_{17}Cl_{20} + \nu \rightarrow {}^{37}_{18}Ar_{19} + e^-$, which has been used for the detection of solar neutrinos (Davis, Harmer, and Hoffman, 1968). Antineutrinos produced by nuclear power plants have been observed via the process $p + \overline{\nu} \rightarrow e^+ + n$ (Reines and Cowan, 1959).

Positron emission and electron capture populate the same daughter nuclide. In later chapters, both of these decays will sometimes be considered together, while at other times it will be important to distinguish between these processes. We will be using the following abbreviated notation. The β-decay of ^{64}Cu to ^{64}Ni, irrespective of the specific process, will be denoted by $^{64}\mathrm{Cu}(\beta^+\nu)^{64}\mathrm{Ni}$. When we would like to make specific reference to the positron emission or electron capture, we write $^{64}\mathrm{Cu}(e^+\nu)^{64}\mathrm{Ni}$ or $^{64}\mathrm{Cu}(e^-,\nu)^{64}\mathrm{Ni}$, respectively. The β^--decay of ^{64}Cu to ^{64}Zn will be denoted by $^{64}\mathrm{Cu}(\beta^-\nu)^{64}\mathrm{Zn}$, irrespective of the fact that an antineutrino rather than a neutrino is emitted in this decay.

1.8.2 Energetics

The total energy release in nuclear β-decay can be expressed by the difference of the *atomic* masses before and after the interaction. We find (Problem 1.7)

$$ Q_{\beta^-} = \left[m({}^{A}_{Z}X_N) - m({}^{A}_{Z+1}X'_{N-1})\right] c^2 \qquad \beta^-\text{-decay} \qquad (1.45) $$

$$ Q_{e^+} = \left[m({}^{A}_{Z}X_N) - m({}^{A}_{Z-1}X'_{N+1}) - 2m_e\right] c^2 \qquad \text{positron emission} \qquad (1.46) $$

$$ Q_{EC} = \left[m({}^{A}_{Z}X_N) - m({}^{A}_{Z-1}X'_{N+1})\right] c^2 - E_b \qquad \text{electron capture} \qquad (1.47) $$

where m_e and E_b denote the electron mass and the atomic binding energy of the captured electron, respectively. The released energy is almost entirely transferred to the emitted leptons. For example, in β^--decay we have $Q_{\beta^-} = K_e + E_\nu$, where K_e and E_ν denote the kinetic electron energy and the total neutrino energy, respectively. Since there are three particles after the interaction, the electron and neutrino energy distributions must be continuous, ranging from zero to Q_{β^-} for each lepton. In electron capture, only one lepton is emitted and thus the neutrino is monoenergetic, with $Q_{EC} = E_\nu$. Furthermore, this decay mode is accompanied by X-ray emission since the vacancy in the atomic shell caused by the captured electron is quickly filled by other atomic electrons. Electron capture competes in general with positron emission since both decay modes populate the same daughter nucleus. However, if the difference in *atomic* masses amounts to $[m(^A_Z X_N) - m(^A_{Z-1}X'_{N+1})]c^2 < 2m_e c^2 = 1022$ keV, then only electron capture is energetically allowed.

It must be emphasized that for positron emission in a stellar plasma, the energy release calculated from the mass difference of parent and daughter nucleus alone, $Q'_{e^+} = [m(^A_Z X_N) - m(^A_{Z-1}X'_{N+1})]c^2$, includes the annihilation energy $2m_e c^2 = 1022$ keV of the positron with another electron from the environment, as can be seen by comparison with Eq. (1.46). Therefore, the quantity Q'_{e^+} rather than Q_{e^+} is of primary interest when calculating the energy release of positron emission in a stellar plasma. Also, Q'_{e^+} must be properly corrected for neutrino losses (see below).

We considered so far only β-decay transitions involving nuclear ground states. If a transition proceeds to an excited state in the daughter nucleus, then we have to replace Q_i by $Q_i^{gs} - E_x$ in Eqs. (1.45)–(1.47), where Q_i^{gs} and E_x denote the ground-state energy release and the excitation energy, respectively. Sometimes a β-decay populates levels in the daughter nucleus that are unstable by emission of light particles (protons, neutrons, or α-particles). These transitions give rise to *β-delayed particle decays*. They compete with transitions to bound states in the daughter nucleus. Therefore, both of these processes have to be distinguished carefully when modeling the nucleosynthesis in certain scenarios. For example, consider the β-decay of ^{29}S which proceeds with about equal probability to bound states in ^{29}P and to excited ^{29}P levels that are unbound by proton emission. In the first case, ^{29}S decays to the final nucleus ^{29}P via $^{29}\mathrm{S} \rightarrow \mathrm{e}^+ + \nu + {}^{29}\mathrm{P}$, while in the second case ^{29}S decays to the final nucleus ^{28}Si via $^{29}\mathrm{S} \rightarrow \mathrm{e}^+ + \nu + {}^{29}\mathrm{P}^*$ and $^{29}\mathrm{P}^* \rightarrow {}^{28}\mathrm{Si} + \mathrm{p}$. These processes can be distinguished using the notations $^{29}\mathrm{S}(\mathrm{e}^+\nu)^{29}\mathrm{P}$ and $^{29}\mathrm{S}(\mathrm{e}^+\nu\mathrm{p})^{28}\mathrm{Si}$.

The neutrinos released in nuclear β-decay interact so weakly with matter that they are lost from the star unless the density is very large ($\rho \geq 10^{11}$ g/cm^3). Consequently, the average neutrino energy must usually be subtracted from the total nuclear energy liberated when considering the energy budget of a star. An approximate expression for the average neutrino energy loss in β^--decay or positron emission is given by (Fowler, Caughlan, and Zimmerman, 1967)

$$\overline{E}_\nu^\beta \approx \frac{m_e c^2}{2} w \left(1 - \frac{1}{w^2}\right)\left(1 - \frac{1}{4w} - \frac{1}{9w^2}\right) \tag{1.48}$$

where $w = (Q_\beta + m_e c^2)/m_e c^2$. The energy release of the β-decay, Q_β, is given by Eqs. (1.45) and (1.46), and may need to be corrected for the excitation energy if the transition proceeds to an excited state in the daughter nucleus. As already mentioned above, the neutrinos emitted in electron capture are monoenergetic.

Neutrino emission is also important for the transport of energy from the stellar interior to the surface, from which the energy can be radiated. During the early evolutionary stages of stars, internal energy is mainly transported by mechanisms such as radiative diffusion or convection. As a result, the rate of energy outflow is related to the temperature gradient of the star. At high temperature ($T > 10^9$ K), however, a relatively large number of photons have energies in excess of the threshold for pair production, $\gamma \rightarrow e^+ + e^-$ (Section 4.2.2). The positron and electron, in turn, may either annihilate via $e^+ + e^- \rightarrow 2\gamma$ or via $e^+ + e^- \rightarrow \nu + \overline{\nu}$. These neutrinos emerge directly from their point of origin and will escape from the star. During the late evolutionary stages of massive stars, this production of neutrino–antineutrino pairs represents the dominant energy loss mechanism. The energy outflow is in this case directly determined by the neutrino production rate. Neutrino energy losses rise strongly with temperature and have a profound influence on the stellar evolution of massive stars (Section 1.4.3 and Chapter 5).

1.8.3 β-Decay Probabilities

A detailed discussion of the theory of weak interactions in nuclei is beyond the scope of the present book. A modern account can be found, for example, in Holstein (1989). Here we will focus on the elementary Fermi theory of β-decay which explains satisfactorily lifetimes and the shapes of electron (or positron) energy distributions. Fermi's theory of β-decay is discussed in most introductory nuclear physics texts (see, e.g., Krane, 1988). We will initially assume that the β-decay occurs under laboratory conditions. Beta-decays in stellar plasmas will be addressed afterward. The rate of nuclear β-decay can be calculated from the golden rule of time-dependent, first-order perturbation theory (Messiah, 1999). To illustrate the most important results, we will first discuss β^--decay, although the derived expressions are equally valid for positron emission. The case of electron capture is subsequently discussed.

Electron or Positron Emission

The probability $N(p)\,dp$ per unit time that an electron (or positron) with linear momentum between p and $p + dp$ is emitted can be written as

$$d\lambda = N(p)\,dp = \frac{2\pi}{\hbar}\left|\int \Psi_f^* H \Psi_i\, dV\right|^2 \frac{dn}{dE_0} = \frac{2\pi}{\hbar}\left|H_{fi}\right|^2 \frac{dn}{dE_0} \tag{1.49}$$

where Ψ_i and Ψ_f are the total wave functions before and after the decay, respectively, H is the Hamiltonian associated with the weak interaction, and dV is a volume element. The factor dn/dE_0 denotes the number of final states per unit

energy. A given transition is more likely to proceed if the number of accessible final states is large. The experimental evidence shows that the shapes of many measured electron (or positron) energy distributions are dominated by the factor dn/dE_0. The integral H_{fi} (or matrix element), which depends only weakly on energy, determines the overall magnitude of the decay probability. It can be expressed in terms of the separate wave functions of the final nuclear state (ψ_f) and of the leptons (ϕ_e, ϕ_ν) after the decay as

$$H_{fi} = g \int \left[\psi_f^* \phi_e^* \phi_\nu^*\right] \Omega \Psi_i \, dV \tag{1.50}$$

where the constant g determines the strength of the interaction. For electron (or positron) decay, the total wave function before the transition is equal to the wave function of the parent nucleus, $\Psi_i = \psi_i$. The operator Ω describes the transition from nuclear level ψ_i to level ψ_f. The emitted neutrino (or antineutrino) can be treated as a free particle because it interacts only weakly. The emitted electron (or positron) can also be treated as a free particle because it has a relatively high velocity and is little affected by the nuclear Coulomb field. Thus, we may approximate the lepton wave functions by plane waves, normalized within the nuclear volume V, and expand the exponentials according to

$$\phi_e(\vec{r}) = \frac{1}{\sqrt{V}} e^{-i\vec{p}\cdot\vec{r}/\hbar} \approx \frac{1}{\sqrt{V}} \left(1 + \frac{i\vec{p}\cdot\vec{r}}{\hbar} + \cdots\right) \tag{1.51}$$

$$\phi_\nu(\vec{r}) = \frac{1}{\sqrt{V}} e^{-i\vec{q}\cdot\vec{r}/\hbar} \approx \frac{1}{\sqrt{V}} \left(1 + \frac{i\vec{q}\cdot\vec{r}}{\hbar} + \cdots\right) \tag{1.52}$$

where $\vec{p}$ and $\vec{q}$ are the linear momenta of the electron (or positron) and the neutrino (or antineutrino), respectively. Consider, for example, the emission of an electron in β^--decay with a typical kinetic energy of 1 MeV. The relativistic electron momentum amounts in this case to $p = 1.4$ MeV/c. For a nuclear radius of $r \approx 5$ fm, we find then a value of $pr/\hbar = 0.035$. Hence, the second term in the expansion of Eq. (1.51) is usually very small and, therefore, the electron wave function is approximately constant over the nuclear volume. Similar arguments apply to the neutrino wave function. In the simplest case, one may then retain just the first, leading, term in Eqs. (1.51) and (1.52). It follows

$$|H_{fi}|^2 = \frac{1}{V^2} \left| g \int \psi_f^* \Omega \psi_i \, dV \right|^2 = \frac{1}{V^2} g^2 M^2 \tag{1.53}$$

The nuclear matrix element M describes the transition probability between the initial and final nuclear levels. A proper relativistic treatment of β-decay results in two different matrix elements with different strengths that may contribute to the overall transition probability. Thus, we have to replace Eq. (1.53) by

$$|H_{fi}|^2 = \frac{1}{V^2} \left(G_V^2 M_F^2 + G_A^2 M_{GT}^2\right) \tag{1.54}$$

where G_V and G_A are the vector and axial-vector coupling constants, and M_F and M_{GT} are referred to as *Fermi* and *Gamow–Teller matrix element*, respectively.

It can be shown that no interference term between vector and axial-vector interaction occurs. The two matrix elements depend on the structure of the initial and final nuclear states and can be calculated by using the shell model (Section 1.6).

The above nonrelativistic treatment of the nucleons and the assumption of constant lepton wave functions over the nuclear volume results in nuclear matrix elements that are independent of the lepton energies and define the *allowed β-decay transitions*. In some decays, however, it turns out that angular momentum and parity selection rules prevent allowed transitions. In such cases, the next terms in the plane wave approximations of Eqs. (1.51) and (1.52) have to be taken into account and the nuclear matrix element is no longer independent of energy. These transitions are termed *forbidden* since they are considerably less likely to occur than allowed decays. The degree by which a transition is forbidden depends on how many terms in the plane wave approximation need to be taken into account until a nonvanishing nuclear matrix element is obtained. The second term gives rise to *first-forbidden* transitions, the third to *second-forbidden*, and so on. We will consider in the following only allowed β-decay transitions.

The density of final states, dn/dE_0, in Eq. (1.49) determines for allowed transitions the shape of the electron (or positron) energy distribution. It is given by (Problem 1.10)

$$\frac{dn}{dE_0} = \frac{dn_e dn_\nu}{dE_0} = \frac{(4\pi)^2 V^2}{h^6} p^2\, dp\, q^2\, dq \frac{1}{dE_0} \tag{1.55}$$

The final state (or total decay) energy is $E_0 = Q = K_e + E_\nu$, where Q is the energy release for the transition under consideration (see Eqs. (1.45) and (1.46); if the decay proceeds to an excited state, Q must account for the excitation energy). Since the neutrino mass is very small, we may use $m_\nu c^2 \approx 0$, so that $q = E_\nu/c = (E_0 - K_e)/c$ and $dq/dE_0 = 1/c$. A correction must be applied to Eq. (1.55) that takes into account the Coulomb interaction between the daughter nucleus and the emitted electron or positron. The electron in β^--decay feels an attractive Coulomb force, while the positron in β^+-decay experiences a repulsive force. Hence, the electron or positron plane wave in Eq. (1.51) has to be replaced by a distorted wave. The correction factor is referred to as *Fermi function*, $F(Z', p)$, and depends on the electron or positron momentum and the charge of the daughter nucleus. The function $F(Z', p)$ can be calculated numerically and is tabulated in Gove and Martin (1971).

It follows from Eqs. (1.49), (1.54), and (1.55) that

$$d\lambda = N(p)\, dp = \frac{1}{2\pi^3 \hbar^7 c^3} \left(G_V^2 M_F^2 + G_A^2 M_{GT}^2\right) F(Z', p) p^2 (E_0 - K_e)^2\, dp \tag{1.56}$$

This distribution vanishes for $p = 0$ and at the endpoint where the maximum electron or positron kinetic energy is equal to the total decay energy, $K_e^{max} = E_0 = Q$. Hence, a measurement of the momentum or energy distribution in a given decay yields a value for the total energy release in β-decay. Total relativistic energy, kinetic energy, and linear momentum of the electron or positron are related by

$$E_e = K_e + m_e c^2 = \sqrt{(m_e c^2)^2 + (pc)^2} \tag{1.57}$$

The total decay constant is then given by the integral

$$\lambda = \frac{\ln 2}{T_{1/2}} = \frac{\left(G_V^2 M_F^2 + G_A^2 M_{\mathrm{GT}}^2\right)}{2\pi^3 \hbar^7 c^3} \int_0^{p_{\max}} F(Z', p) p^2 (E_0 - K_{\mathrm{e}})^2 \, dp$$
$$= \frac{m_{\mathrm{e}}^5 c^4}{2\pi^3 \hbar^7} \left(G_V^2 M_F^2 + G_A^2 M_{\mathrm{GT}}^2\right) f(Z', E_{\mathrm{e}}^{\max}) \tag{1.58}$$

The dimensionless quantity

$$f(Z', E_{\mathrm{e}}^{\max}) = \frac{1}{m_{\mathrm{e}}^5 c^7} \int_0^{p_{\max}} F(Z', p) p^2 (E_{\mathrm{e}}^{\max} - E_{\mathrm{e}})^2 \, dp \tag{1.59}$$

is referred to as the *Fermi integral* and depends only on the charge Z' of the daughter nucleus and on the maximum total energy of the electron, $E_{\mathrm{e}}^{\max}$. Numerical values of $f(Z', E_{\mathrm{e}}^{\max})$ have also been tabulated. For the derivation of Eq. (1.58), we used the relationships $p_{\max} c = \sqrt{(E_{\mathrm{e}}^{\max})^2 - (m_e c^2)^2}$ and $E_0 - K_{\mathrm{e}} = K_{\mathrm{e}}^{\max} - K_{\mathrm{e}} = E_{\mathrm{e}}^{\max} - E_{\mathrm{e}}$ that are obtained from Eq. (1.57).

We can rewrite Eq. (1.58) as

$$f(Z', E_{\mathrm{e}}^{\max}) T_{1/2} = \frac{2\pi^3 \hbar^7}{m_{\mathrm{e}}^5 c^4} \frac{\ln 2}{\left(G_V^2 M_F^2 + G_A^2 M_{\mathrm{GT}}^2\right)} \tag{1.60}$$

The quantity $f(Z', E_{\mathrm{e}}^{\max}) T_{1/2}$ is called the *ft-value* and is experimentally obtained from measurements of the half-life and the maximum energy of the emitted electrons or positrons. The ft-value is a standard measure for the strength of a particular β-decay transition and yields information about the nuclear matrix elements and the coupling constants.

Electron Capture

The decay constant for allowed electron capture can be obtained in a similar manner. Recall that in this case the energy spectrum of the emitted neutrino is not continuous, but monoenergetic with $Q_{EC} = E_0 = E_\nu$. Instead of Eq. (1.49) we write

$$\lambda = \frac{2\pi}{\hbar} \left| \int \Psi_f^* H \Psi_i \, dV \right|^2 \frac{dn}{dE_0} = \frac{2\pi}{\hbar} |H_{fi}|^2 \frac{dn_\nu}{dE_0} \tag{1.61}$$

The density of final states in this case is given by (Problem 1.10)

$$\frac{dn_\nu}{dE_0} = \frac{Vq^2}{2\pi^2 \hbar^3} \frac{dq}{dE_0} = \frac{VE_\nu^2}{2\pi^2 \hbar^3 c^3} \tag{1.62}$$

where we used $E_\nu = qc$. The total wave functions before and after the decay are now given by $\Psi_i = \psi_i \phi_{\mathrm{e}}$ and $\Psi_f = \psi_f \phi_\nu$ (the subscripts have the same meaning as before). Usually an electron from the atomic K shell is captured because these have the largest probability of being near the nucleus. But the electron is now in a bound state and cannot be described by a free-particle plane wave. One can approximate ϕ_{e} by the electron wave function ϕ_K of the K orbit at the location of the nucleus,

$$\phi_e(\vec{r}) = \phi_K(\vec{r}) = \frac{1}{\sqrt{\pi}} \left(\frac{Z}{a_0}\right)^{3/2} e^{-Zr/a_0}$$
$$\approx \phi_K(0) = \frac{1}{\sqrt{\pi}} \left(\frac{Z}{a_0}\right)^{3/2} = \frac{1}{\sqrt{\pi}} \left(\frac{Z m_e e^2}{\hbar^2}\right)^{3/2} \tag{1.63}$$

with Z the atomic number of the parent nucleus. The constant a_0 denotes the Bohr radius, $a_0 = \hbar^2/(m_e e^2) = 0.0529$ nm. For the neutrino wave function ϕ_ν, we use again only the first (constant) term in the plane wave approximation.

From Eqs. (1.52), (1.61)–(1.63), one finds for the decay constant of allowed electron capture

$$\lambda_K = 2\frac{Z^3 m_e^3 e^6}{\pi^2 \hbar^{10} c^3} \left(G_V^2 M_F^2 + G_A^2 M_{GT}^2\right) E_\nu^2 \tag{1.64}$$

where the matrix elements are defined as before in terms of initial and final state nuclear wave functions. These are identical to the matrix elements that occur in Eq. (1.54) for positron emission, since they connect the very same nuclear states. The additional factor of two in Eq. (1.64) arises because either of the two electrons in the K shell can be captured. The transition probability for the weaker L-capture can be calculated in a similar manner. The electron capture probability increases strongly with the charge Z of the parent nucleus. This is the reason why electron capture is greatly favored over positron emission in heavy nuclei. The above expression must be corrected for relativistic effects and the influence of the shielding of the nuclear Coulomb field by the outer electrons. Such corrections have been calculated numerically and are tabulated, for example, in Gove and Martin (1971).

Fermi and Gamow–Teller Transitions

We already commented on the classification of β-decays into allowed and forbidden transitions. In the first case, the leptons do not remove any orbital angular momentum. In the latter case, the radiations are inhibited because angular momentum conservation requires the leptons to carry off orbital angular momentum or because the parities of the initial and final nuclear states are mismatched. The allowed radiations are further subdivided into *Fermi transitions* and *Gamow–Teller transitions*. They can only occur (i.e., the corresponding matrix elements M_F or M_{GT} are nonzero only) if certain selection rules are satisfied for the nuclear spins (J_i, J_f) and parities (π_i, π_f) of the initial and final nuclear states connected by the transition:

$$\Delta J \equiv |J_i - J_f| = 0, \qquad \pi_i = \pi_f \qquad \text{for Fermi transitions} \tag{1.65}$$
$$\Delta J \equiv |J_i - J_f| = 0 \text{ or } 1, \qquad \pi_i = \pi_f \qquad \text{for Gamow–Teller transitions (but not } J_i = 0 \to J_f = 0) \tag{1.66}$$

It follows that one can study these cases separately since decays with $0 \to 0$ ($\Delta J = 0$) and $\pi_i = \pi_f$ represent pure Fermi transitions ($M_{GT} = 0$), while decays with

$\Delta J = 1$ and $\pi_i = \pi_f$ are pure Gamow–Teller transitions ($M_F = 0$). Examples for pure Fermi and Gamow–Teller transitions are $^{14}\mathrm{O} \rightarrow {}^{14}\mathrm{N} + \mathrm{e}^+ + \nu$ ($J_i = 0^+ \rightarrow J_f = 0^+$) and $^6\mathrm{He} \rightarrow {}^6\mathrm{Li} + \mathrm{e}^- + \overline{\nu}$ ($J_i = 0^+ \rightarrow J_f = 1^+$). The decay of the free neutron in Eq. (1.39), on the other hand, represents a mixed transition. From studies of such decays, the values of the coupling constants G_V and G_A can be deduced (see, e.g., Wilkinson, 1994).

In the laboratory, where the parent nucleus is usually in its ground state, β-decay transitions proceed to all energetically accessible states in the daughter nucleus. The total decay constant is given by the sum of transition probabilities for all of these β-decay branches. Such laboratory β-decay constants or half-lives are independent of temperature and density. Experimental values of $T_{1/2}$ are tabulated in Audi *et al.* (2012) and this reference will be used as a source of terrestrial half-lives throughout this book, unless mentioned otherwise.

1.8.4
β-Decays in a Stellar Plasma

Consider now the weak interaction processes that take place when β-decays occur in a stellar plasma at elevated temperature T and density ρ. In a hot plasma, excited states in the parent nucleus are thermally populated and these excited levels may also undergo β-decay transitions to the ground state or to excited states in the daughter nucleus. The total β-decay rate in a stellar plasma, λ_β^*, is given by the weighted sum of the individual transition rates, λ_{ij}, according to

$$\lambda_\beta^* = \sum_i P_i \sum_j \lambda_{ij} \tag{1.67}$$

The sum on i and j is over parent and daughter states, respectively. The population probabilities, P_i, of excited states in a nondegenerate plasma at thermodynamic equilibrium are given by Eq. (1.35). Since the quantity P_i is temperature dependent, it follows immediately that λ_β^* will also depend on temperature. If the decay constants for excited state β-decays are larger than the one for ground-state β-decay, the total decay constant λ_β^* may become strongly temperature dependent. Even if the ground state of the parent nucleus is stable in the laboratory, it may nevertheless undergo β-decay in a hot stellar plasma. Similar considerations apply to the β-decay of the daughter nucleus. In the laboratory, it cannot decay back to the parent nucleus because the transition is energetically forbidden. In a hot plasma, however, β-decay transitions may occur from thermally populated excited states in the daughter nucleus to the ground state or to excited states in the parent nucleus. The situation is schematically shown in Figure 1.17. In practice, one finds that most of the transition probability for β^--decay or positron emission in a hot stellar plasma arises from the first few levels in a given parent nucleus. The β^--decay rate becomes also density dependent at sufficiently large values of ρ when the electron gas is degenerate. The decay rate decreases with increasing density since the number of final states available for the emitted electron to occupy is reduced (Langanke and Martinez-Pinedo, 2000).

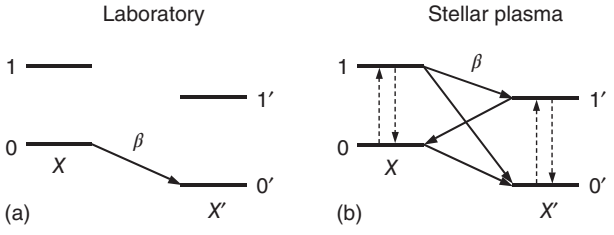

Figure 1.17 β-Decays (a) in the laboratory, and (b) in a hot stellar plasma. The vertical direction corresponds to an energy scale. For reasons of clarity, only two levels are shown in the parent nucleus X and the daughter nucleus X'. The ground and first excited state are labeled by 0 and 1, respectively. In the laboratory, the β-decay proceeds from the ground state of nucleus X to levels in nucleus X', while far more β-decay transitions are energetically accessible in a stellar plasma owing to the thermal excitation of levels (dashed vertical arrows).

Example 1.5

In the laboratory, β^+-decays of the nuclide ^{26}Al have been observed both from the ground state ($J^\pi = 5^+$) and from the first excited (isomeric) state ($J^\pi = 0^+$) located at an excitation energy of $E_x = 228$ keV (Figure 1.15). The ground state decays via positron emission to excited levels in the daughter nucleus ^{26}Mg (we will neglect a small electron capture branch) with a half-life of $T^{gs}_{1/2} = 7.17 \times 10^5$ y, while the first excited state decays to the ^{26}Mg ground state with a half-life of $T^{m}_{1/2} = 6.345$ s. Above a temperature of $T = 0.4$ GK, both of these ^{26}Al levels are in thermal equilibrium (Figure 1.16). Calculate the *stellar* half-life of ^{26}Al when the plasma temperature amounts to $T = 2$ GK.

According to Eq. (1.67), the decay constant of ^{26}Al in the stellar plasma is given by

$$\lambda^*_\beta = P_{gs}\lambda_{gs} + P_m\lambda_m = P_{gs}\frac{\ln 2}{T^{gs}_{1/2}} + P_m\frac{\ln 2}{T^{m}_{1/2}}$$

where the subscripts *gs* and *m* denote the ground state and the first excited state, respectively. The thermal population probability P_i (i.e., the fraction of ^{26}Al nuclei residing in either the ground or the first excited state) can be calculated from Eq. (1.35) (a numerical expression for the quantity kT is given in Section 3.1.1). Thus

$$\begin{aligned}
\lambda^*_\beta &= \frac{\ln 2}{g_{gs}e^{-E_{gs}/kT} + g_m e^{-E_m/kT}}\left[\frac{g_{gs}e^{-E_{gs}/kT}}{T^{gs}_{1/2}} + \frac{g_m e^{-E_m/kT}}{T^{m}_{1/2}}\right] \\
&= \frac{\ln 2}{(2\cdot 5+1) + (2\cdot 0+1)e^{-0.228/kT}}\left[\frac{(2\cdot 5+1)}{T^{gs}_{1/2}} + \frac{(2\cdot 0+1)e^{-0.228/kT}}{T^{m}_{1/2}}\right] \\
&= \frac{\ln 2}{11 + e^{-0.228/0.0862\,T_9}}\left[\frac{11}{T^{gs}_{1/2}} + \frac{e^{-0.228/0.0862\,T_9}}{T^{m}_{1/2}}\right] \\
&\approx \frac{\ln 2}{11}\left[\frac{e^{-0.228/0.0862\,T_9}}{6.345\,\mathrm{s}}\right] = 9.93\times 10^{-3}e^{-2.646/T_9} \quad (\mathrm{s}^{-1})
\end{aligned}$$

Hence, we find at $T = 2$ GK ($T_9 = 2$)

$$\lambda_\beta^* = 9.93 \times 10^{-3} e^{-2.646/2.0}\ \mathrm{s}^{-1} = 0.0026\ \mathrm{s}^{-1}$$

and the stellar half-life of ^{26}Al amounts to $T_{1/2}^* = \ln 2/\lambda_\beta^* = 270$ s. The result is valid only for densities of $\rho \leq 10^6$ g/cm^3, since at higher densities electron capture needs to be taken into account (see below). The results from the above method for calculating the stellar half-life of ^{26}Al are shown as the dashed line in Figure 1.16. The values are only correct for temperatures in the range of $T = 0.4$–5 GK. At lower temperatures, the ground and isomeric states are not in thermal equilibrium (Section 1.7.5), while at higher temperatures the thermal populations of other excited states in ^{26}Al have to be taken into account.

We will now discuss the interesting case of electron capture. It will be shown later (Section 3.1.1) that the average thermal energies at the temperatures typical for the interior of main-sequence stars and red giants amount to ≈ 1 keV and a few tens of kilo electron volts, respectively. For most atoms, however, the ionization energies are smaller than these values. Therefore, most nuclei in these environments possess few, if any, bound electrons. The decay constant for bound electron capture, given by Eq. (1.64), may thus be very small or even zero. In the hot interiors of stars, however, there is an appreciable density of free electrons. Hence, β-decays can proceed by capture of (free) electrons from the continuum. The probability of continuum electron capture is proportional to the free electron density at the location of the nucleus and is inversely proportional to the average electron velocity which depends on the plasma temperature. Consequently, the rate of continuum electron capture depends on the local electron temperature and the density. At lower stellar temperatures, a given parent nucleus may not be completely ionized. In that case, both bound and continuum electron capture contribute to the total decay constant.

At low densities, the kinetic energies of the free electrons are usually small. At very high densities, however, the (Fermi) energy of the degenerate electrons may become sufficiently large to cause nuclei to undergo continuum capture of energetic electrons, even if they are stable under laboratory conditions. Electron capture transitions involving thermally excited nuclear levels must also be taken into account according to Eq. (1.67).

Moreover, at high temperature ($T > 1$ GK) a large number of photons have energies in excess of the threshold energy for pair production (Section 4.2.2). Although a positron annihilates quickly in the stellar plasma with an electron, the pair production rate becomes eventually so large at high temperatures that the positron density is a significant fraction of the electron density. Thus, capture of continuum positrons by nuclei must be considered in addition to continuum electron capture.

The decay constant for continuum electron capture can be obtained for a given nuclide if its laboratory decay constant for bound electron capture is known. The ratio of stellar to laboratory decay constant is approximately equal to the ratio of

the electron densities at the nucleus for the stellar and laboratory environments, that is, the ratio of probabilities for finding an electron at the nucleus where it can be captured. An order of magnitude estimate for the ratio of electron capture probabilities is given by

$$\frac{\lambda_{\rm star}}{\lambda_{\rm lab}} \approx \frac{n_{\rm e^-}\langle F(Z,p)\rangle}{2N_A|\phi_{\rm e}(0)|^2} \tag{1.68}$$

where $n_{\rm e^-}/N_A = \rho(1-\eta)/2 = \rho Y_{\rm e}$ is the electron density (Fowler, Caughlan, and Zimmerman, 1967), η is the neutron excess parameter given by Eq. (1.36), $Y_{\rm e}$ is the electron mole fraction given by Eq. (1.37), and $|\phi_{\rm e}(0)|^2$ is given by Eq. (1.63). The Fermi function $F(Z,p)$ accounts for the distortion of the wave function of the captured electron by the nuclear Coulomb field. Since the electron velocities in the plasma are given by a distribution, the Fermi function must be averaged over the electron velocities. It can be seen from Eq. (1.68) that the ratio $\lambda_{\rm star}/\lambda_{\rm lab}$ depends on the density and composition (through $n_{\rm e^-}$), and on the temperature (through $\langle F(Z,p)\rangle$). The above expression is independent of nuclear matrix elements. For more information, including a discussion of induced continuum electron capture (i.e., when a nuclide is stable in the laboratory), see Bahcall (1964).

Many different transitions contribute to the stellar decay rate of a given nucleus. In the laboratory, the decay proceeds from the ground state of parent nucleus X to energetically accessible states in the daughter nucleus X'. In a stellar plasma, the labels "parent" and "daughter" can alternatively apply to both nuclei. For example, in the laboratory ^{56}Mn decays to the stable nuclide ^{56}Fe via $^{56}{\rm Mn}(\beta^-\nu)^{56}{\rm Fe}$. At high temperatures and densities, however, ^{56}Fe decays via continuum electron capture, $^{56}{\rm Fe}({\rm e}^-,\nu)^{56}{\rm Mn}$, and via positron emission through thermally populated ^{56}Fe states, $^{56}{\rm Fe}({\rm e}^+\nu)^{56}{\rm Mn}$.

The estimation of stellar β-decay rates essentially reduces to the calculation of (i) nuclear matrix elements using some model of nuclear structure (e.g., the shell model; Section 1.6), and (ii) the appropriate Fermi functions and integrals for all energetically accessible transitions from the parent to the daughter nucleus. The calculations can be constrained and tested by experimental measurements of half-lives and Gamow–Teller strength distributions. Stellar weak interaction rates and the associated neutrino energy losses for a range of temperatures and densities are tabulated in Fuller, Fowler, and Newman (1982) (for the proton, neutron, and nuclides with $A = 21$–60), Oda *et al.* (1994) (for $A = 17$–39), and Langanke and Martinez-Pinedo (2001) (for $A = 45$–65). Figure 1.18 shows as an example the stellar decay constants versus temperature for the electron capture (solid lines) and positron emission (dashed line) of ^{37}Ar. The three lines for electron capture correspond to different values of $\rho Y_{\rm e} = \rho(1-\eta)/2$. The strong density dependence of the electron capture rate is apparent. In the laboratory, ^{37}Ar decays to ^{37}Cl by bound electron capture with a half-life of $T_{1/2} = 35.0$ d (horizontal solid line).

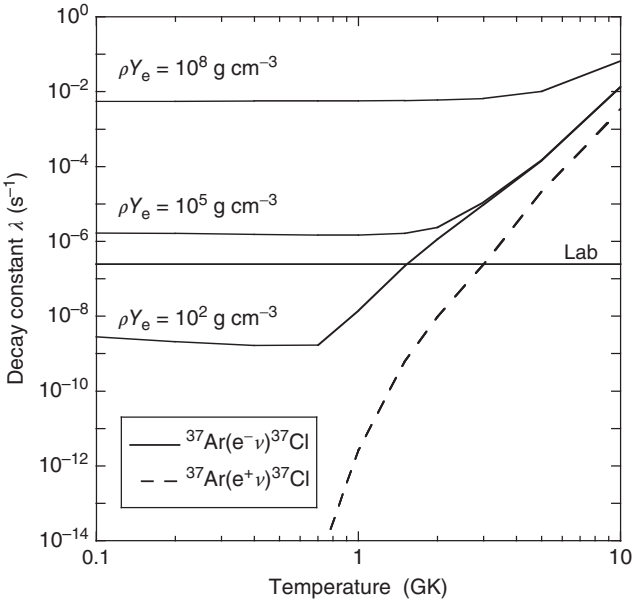

Figure 1.18 Stellar decay constants versus temperature for the electron capture (thin solid lines) and positron emission (dashed line) of ^{37}Ar. The three lines for electron capture correspond to different values of $\rho Y_e = \rho(1-\eta)/2$, whereas the decay rate for positron emission is independent of density. In the laboratory, ^{37}Ar decays to ^{37}Cl by bound electron capture with a decay constant of $\lambda_{lab} = 2.3{\times}10^{-7}$ s^{-1} ($T_{1/2} = \ln 2/\lambda_{lab}$ = 35.0 d), shown as the horizontal solid line labeled "Lab". Data from Oda *et al.* (1994).

Finally, we will briefly discuss a neutrino energy loss mechanism that becomes important at very high temperatures and densities. It is referred to as the *Urca process* (Gamow and Schoenberg, 1940) and consists of alternate electron captures and β^--decays involving the same pair of parent and daughter nuclei

$$ {}^{A}_{Z}\mathrm{X}_{N}(\mathrm{e}^-,\nu)_{Z-1}{}^{A}\mathrm{X}'_{N+1}(\beta^-\nu)^{A}_{Z}\mathrm{X}_{N}\ldots \tag{1.69}$$

The net result of two subsequent decays gives ${}^{A}_{Z}\mathrm{X}_{N} + \mathrm{e}^- \rightarrow {}^{A}_{Z}\mathrm{X}_{N} + \mathrm{e}^- + \nu + \overline{\nu}$. A neutrino–antineutrino pair is produced with no change in the composition, but energy in the form of neutrinos is lost from the star. It is obvious from energy arguments that both the electron capture and the β^--decay cannot occur spontaneously. The first step may be induced by continuum electron capture of energetic electrons when the density is high, while the second step may proceed from thermally populated excited states when the temperature is high. In the end, thermal energy is lost every time a pair of interactions goes to completion. The mechanism represents an efficient cooling process that will not only depend on temperature and density but also on the composition of the stellar plasma. The Urca process is thought to be vital for understanding the explosion mechanism in some models of type Ia supernovae (Section 1.4.4).

Problems

1.1 Determine the number of protons, Z, and the number of neutrons, N, for the nuclides ^{18}F, ^{56}Ni, ^{82}Rb, ^{120}In, ^{150}Gd, and ^{235}U.

1.2 How much energy is released in the following reactions: (i) ^{3}He(d,p)^{4}He; (ii) ^{17}O(p,γ)^{18}F; (iii) ^{12}C(α,γ)^{16}O; and (iv) ^{13}C(α,n)^{16}O? Assume that the reactions involve nuclei only in their ground states. Use the results presented in Table 1.1.

1.3 Consider the chain of radioactive decays, $1 \rightarrow 2 \rightarrow 3$, where 1, 2, and 3 denote a parent, daughter, and final nuclide respectively. Assume that initially only the parent nuclei are present, that is, $N_1(t = 0) = N_0$, $N_2(t = 0) = 0$, $N_3(t = 0) = 0$, and that species 3 is stable. (i) Set up the differential equation describing the abundance change of species 2 and find the time evolution of the daughter abundance, $N_2(t)$. (ii) Find the time evolution of the final nuclide abundance, $N_3(t)$. (iii) Examine the abundances N_1, N_2, and N_3 at small values of t. Keep only the linear terms in the expansion of the exponential function and interpret the results.

1.4 With the aid of Figure 1.11, predict the spins and parities of ^{19}O, ^{31}P, and ^{37}Cl for both the ground state and the first excited state. Compare your answer with the observed values. These can be found in Endt (1990) and Tilley *et al.* (1995).

1.5 Suppose that an excited state with spin and parity of 2^+ in a nucleus of mass $A = 20$ decays via emission of a γ-ray with a branching ratio of 100% to a lower lying level with spin and parity of 0^+. Assume that the γ-ray energy amounts to $E_\gamma = E_i - E_f = 6$ MeV. Estimate the maximum expected γ-ray transition probability $\Gamma = \lambda\hbar$.

1.6 Consider a nucleus in a plasma at thermal equilibrium. Calculate the population probabilities of the ground state ($E_0 = 0$) and of the first three excited states ($E_1 = 0.1$ MeV, $E_2 = 0.5$ MeV, $E_3 = 1.0$ MeV). Perform the computations for two temperatures, $T = 1.0 \times 10^9$ K and 3.0×10^9 K, and assume for simplicity that all states have the same spin value.

1.7 Derive the relationships of Eqs. (1.45)–(1.47) from the differences in *nuclear* masses before and after the decay.

1.8 How much energy is released in the following β-decays: (i) ^{7}Be(e$^-$,ν)^{7}Li; (ii) ^{14}C($\beta^-\nu$)^{14}N; and (iii) ^{18}F(e$^+\nu$)^{18}O? Assume that the decays involve nuclei in their ground states only. Use the results presented in Table 1.1.

1.9 Calculate the average neutrino energy losses in the decays ^{13}N(e$^+\nu$)^{13}C and ^{15}O(e$^+\nu$)^{15}N. Assume that the positron emissions involve the ground states of the parent and daughter nuclei only. Use the results presented in Table 1.1.

1.10 Derive Eq. (1.55) for the density of final states. Recall that the final state contains both an electron and a neutrino. You have to count the states in the six-dimensional *phase space* that is defined by three space and three linear momentum coordinates. The unit volume in phase space is h^3.

2
Nuclear Reactions

2.1
Cross Sections

The cross section, σ, is a quantitative measure of the probability that an interaction will occur. In the following, we define several quantities that are displayed in Figure 2.1. Suppose that a beam of $\mathcal{N}_b$ particles per unit time t, covering an area A, is incident on a target. The number of *nonoverlapping* target nuclei within the beam is $\mathcal{N}_t$. We assume that the total number of interactions that occur per unit time, $\mathcal{N}_R/t$, is equal to the total number of emitted (nonidentical) interaction products per unit time, $\mathcal{N}_e/t$. If the interaction products are scattered incident particles, then we are referring to elastic scattering. If the interaction products have an identity different from the incident particles, then we are referring to a reaction. The number of interaction products emitted at an angle θ with respect to the beam direction into the solid angle $d\Omega$ is $\mathcal{N}_e^{d\Omega}$. The area perpendicular to the direction θ covered by a radiation detector is given by $dF = r^2\, d\Omega$. The cross section is defined by

$$\sigma \equiv \frac{(\text{number of interactions per time})}{(\text{number of incident particles per area per time})(\text{number of target nuclei within the beam})} = \frac{(\mathcal{N}_R/t)}{\left[\mathcal{N}_b/(tA)\right]\mathcal{N}_t} \tag{2.1}$$

We will use this general definition to describe reaction probabilities in astrophysical plasmas and in laboratory measurements of nuclear reactions. In the latter case, two situations are frequently encountered: (i) if the beam area, A, is larger than the target area, A_t, then

$$\frac{\mathcal{N}_R}{t} = \frac{\mathcal{N}_b}{tA}\,\mathcal{N}_t\sigma \tag{2.2}$$

and the number of reactions per unit time is expressed in terms of the incident *particle flux*, $\mathcal{N}_b/(tA)$, the number of target nuclei, $\mathcal{N}_t$, and the cross section; (ii) if the target area, A_t, is larger than the beam area, A, then

$$\frac{\mathcal{N}_R}{t} = \frac{\mathcal{N}_b}{t}\frac{\mathcal{N}_t}{A}\,\sigma \tag{2.3}$$

Nuclear Physics of Stars, Second Edition. Christian Iliadis.

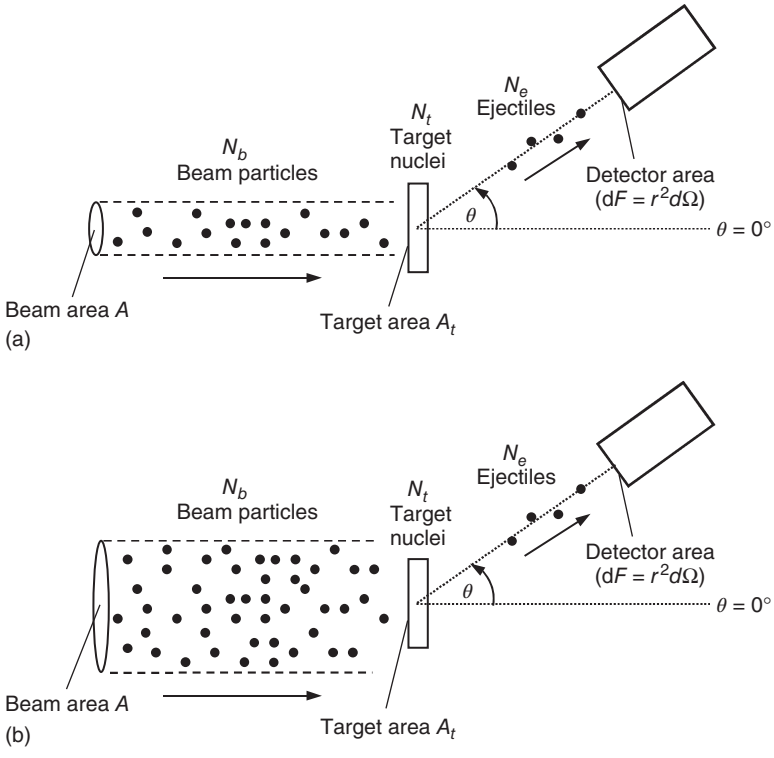

Figure 2.1 Typical nuclear physics counting experiment, showing a beam of $\mathcal{N}_b$ particles per unit time, $\mathcal{N}_t$ nonoverlapping target nuclei within the beam area A, $\mathcal{N}_e$ interaction products and a detector of area dF. The detector is located at an angle of θ with respect to the incident beam direction. The two situations are as follows: (a) the target area is larger than the beam area; and (b) the beam area is larger than the target area.

and the number of reactions per unit time is expressed in terms of the incident *particle current*, $\mathcal{N}_b/t$, the total number of target nuclei within the beam per area covered by the beam, $\mathcal{N}_t/A$, and the cross section. For a homogeneous target, $\mathcal{N}_t/A$ is equal to the *total* number of target nuclei divided by the *total* target area A_t. The latter quantity is easier to determine in practice. We can also express the total cross section, σ, and the differential cross section, $d\sigma/d\Omega$, in terms of the number of emitted interaction products

$$\frac{\mathcal{N}_e}{t} = \sigma \frac{(\mathcal{N}_b/t)}{A} \mathcal{N}_t \tag{2.4}$$

$$\frac{\mathcal{N}_e^{d\Omega}}{t} = \left(\frac{d\sigma}{d\Omega}\right) \frac{(\mathcal{N}_b/t)}{A} \mathcal{N}_t \, d\Omega \tag{2.5}$$

If we define $\mathcal{N}_{et} \equiv \mathcal{N}_e/\mathcal{N}_t$, that is, the number of emitted interaction products per target nucleus, then we obtain

$$\sigma = \frac{(\mathcal{N}_{et}/t)}{(\mathcal{N}_b/t)(1/A)} \qquad \text{and} \qquad \left(\frac{d\sigma}{d\Omega}\right) = \frac{(\mathcal{N}_{et}^{d\Omega}/t)}{(\mathcal{N}_b/t)(1/A)}\frac{1}{d\Omega} \tag{2.6}$$

With the definition of a flux or current density j as the number of particles per time per area, we can write for the beam and emitted interaction products

$$j_b = \frac{(\mathcal{N}_b/t)}{A} \tag{2.7}$$

$$j_{et} = \frac{(\mathcal{N}_{et}^{d\Omega}/t)}{dF} \tag{2.8}$$

For the total and differential cross section, one finds

$$\sigma = \frac{(\mathcal{N}_{et}/t)}{j_b} \tag{2.9}$$

$$\left(\frac{d\sigma}{d\Omega}\right) = \frac{j_{et}\,dF}{j_b\,d\Omega} = \frac{j_{et}r^2\,d\Omega}{j_b\,d\Omega} = \frac{j_{et}r^2}{j_b} \tag{2.10}$$

These quantities are related by

$$\sigma = \int \left(\frac{d\sigma}{d\Omega}\right) d\Omega \tag{2.11}$$

Common units of nuclear reaction and scattering cross sections are

$$1\,\text{b} \equiv 10^{-24}\,\text{cm}^2 = 10^{-28}\,\text{m}^2$$
$$1\,\text{fm}^2 = (10^{-15}\,\text{m})^2 = 10^{-30}\,\text{m}^2 = 10^{-2}\,\text{b}$$

In this chapter, all kinematic quantities are given in the center-of-mass system (Appendix C), unless noted otherwise.

2.2 Reciprocity Theorem

Consider the reaction $A + a \rightarrow B + b$, where A and a denote the target and projectile, respectively, and B and b are the reaction products. The cross section of this reaction is fundamentally related to that of the reverse reaction, $B + b \rightarrow A + a$, since these processes are invariant under time-reversal, that is, the direction of time does not enter explicitly in the equations describing these processes. At a given total energy, the corresponding cross sections $\sigma_{Aa\rightarrow Bb}$ and $\sigma_{Bb\rightarrow Aa}$ are not equal but are simply related by the phase space available in the exit channel or, equivalently, by the number of final states per unit energy interval in each case. The number of states available for momenta between p and $p + dp$ is proportional to p^2 (Messiah, 1999). Hence

$$\sigma_{Aa\rightarrow Bb} \sim p_{Bb}^2 \qquad \text{and} \qquad \sigma_{Bb\rightarrow Aa} \sim p_{Aa}^2 \tag{2.12}$$

The linear momentum and the de Broglie wavelength are related by $\lambda = h/p$. The wave number k of the free particle is defined in terms of the de Broglie wavelength by $\lambda \equiv 2\pi/k$. Hence, we have $p = mv = \hbar k$. It follows (Blatt and Weisskopf, 1952) that

$$\frac{k_{Aa}^2 \sigma_{Aa\to Bb}}{(1+\delta_{Aa})} = \frac{k_{Bb}^2 \sigma_{Bb\to Aa}}{(1+\delta_{Bb})} \tag{2.13}$$

This expression, called the *reciprocity theorem*, holds for differential as well as total cross sections. The factors $(1 + \delta_{ij})$ appears because the cross sections between identical particles in the entrance channel are twice those between different particles, other factors being equal.

When particles with spin are involved in the reactions, then the above equation must be modified by multiplying the density of final states by their statistical weights. Since there are $(2j_i + 1)$ states of orientation available for a particle with spin j_i, we can write for unpolarized particles

$$\frac{k_{Aa}^2 (2j_A+1)(2j_a+1)\sigma_{Aa\to Bb}}{(1+\delta_{Aa})} = \frac{k_{Bb}^2 (2j_B+1)(2j_b+1)\sigma_{Bb\to Aa}}{(1+\delta_{Bb})} \tag{2.14}$$

$$\frac{\sigma_{Bb\to Aa}}{\sigma_{Aa\to Bb}} = \frac{(2j_A+1)(2j_a+1)}{(2j_B+1)(2j_b+1)} \frac{k_{Aa}^2(1+\delta_{Bb})}{k_{Bb}^2(1+\delta_{Aa})} \tag{2.15}$$

It follows that the cross section $\sigma_{Bb\to Aa}$ can be easily calculated, independently from any assumptions regarding the reaction mechanism, if the quantity $\sigma_{Aa\to Bb}$ is known experimentally or theoretically. Equation (2.15) is applicable to particles with rest mass as well as to photons. In the former case, the wave number is given by $k = \sqrt{2mE}/\hbar$, and the linear momentum can be expressed as $p^2 = \hbar^2 k^2 = 2mE$, where E denotes the (nonrelativistic) center of mass energy and m is the reduced mass (see Appendix C). In the latter case, the wave number is defined as $k = E/(\hbar c)$, and the linear momentum can be expressed as $p^2 = \hbar^2 k^2 = E^2/c^2$, where E denotes the photon energy; furthermore, $(2j_\gamma + 1) = 2$ for photons. See also Eqs. (3.27) and (3.28). It must be emphasized that the symbols A, a, b, and B do not only refer to specific nuclei but, more precisely, to specific states. In other words, the reciprocity theorem connects the same nuclear levels in the forward and in the reverse reaction.

The reciprocity theorem has been tested in a number of experiments. An example is shown in Figure 2.2. Compared are differential cross sections for the reaction pair ^{24}Mg(α,p)^{27}Al (open circles) and ^{27}Al(p,α)^{24}Mg (crosses), connecting the ground states of ^{24}Mg and ^{27}Al. Both reactions were measured at the same center-of-mass total energy and angle. The differential cross sections exhibit a complicated structure, presumably caused by overlapping broad resonances. Despite the complicated structure, it can be seen that the agreement between forward and reverse differential cross section is excellent. Such results support the conclusion that nuclear reactions are invariant under time-reversal. See also Blanke *et al.* (1983).

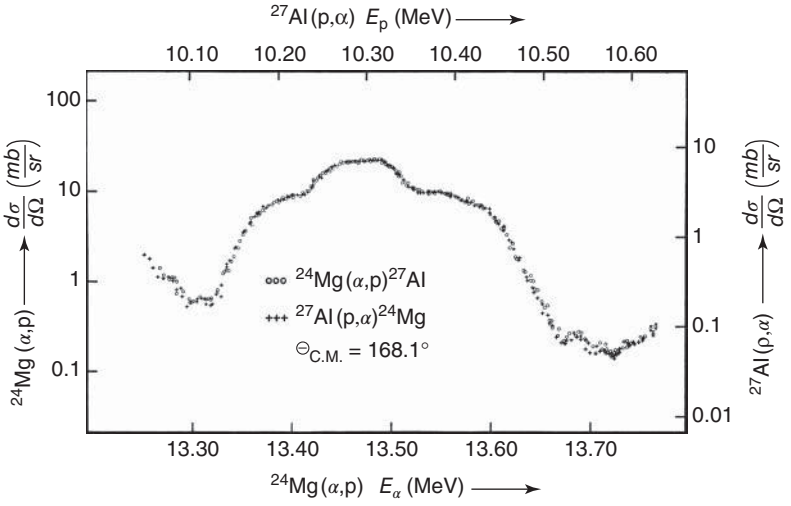

Figure 2.2 Experimental test of the reciprocity theorem for the reaction pair ^{24}Mg(α,p)^{27}Al (open circles) and ^{27}Al(p,α)^{24}Mg (crosses), connecting the ground states of ^{24}Mg and ^{27}Al. The differential cross sections of both reactions are shown for the same total energy and detection angle in the center-of-mass system. The cross sections have also been adjusted to compensate for differences in spins. (Reprinted with permission from W. von Witsch, A. Richter and P. von Brentano, Phys. Rev. Vol. 169, p. 923 (1968). Copyright (1968) by the American Physical Society.)

2.3
Elastic Scattering and Method of Partial Waves

2.3.1
General Aspects

The interactions between nucleons within a nucleus and between nucleons participating in nuclear reactions have to be described using quantum mechanics. The fundamental strong interaction is very complicated and not precisely known. We know from experiments that it is of short range. Furthermore, it exhibits a part that is attractive at distances comparable to the size of a nucleus and another part that is repulsive at very short distances. Because of the complexity of this nucleon–nucleon interaction it is necessary to employ approximations. Instead of calculating all the interactions between all nucleons exactly, one frequently resorts to using effective potentials. These describe the behavior of a nucleon, or a group of nucleons (such as an α-particle), in the effective (average) field of all the other nucleons. Because of the approximate nature of this approach, the resulting effective potentials are usually tailored to specific reactions and energies and thus lack generality. The most widely used approximate potentials are called *central potentials*. They depend on the magnitude of the radius vector, but not on its direction,

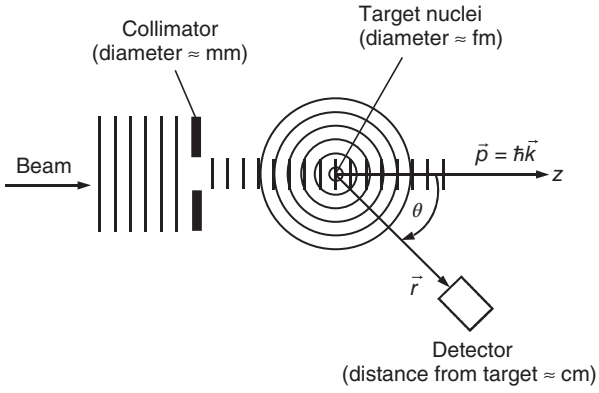

Figure 2.3 Schematic representation of the scattering process. A plane wave is incident along the z-direction on a scattering center (target) which gives rise to an outgoing spherical wave. Note the significant differences in the dimensions of the collimator (≈ mm), target nuclei (≈ fm), and detector distance (≈ cm), which are typical for nuclear physics experiments.

that is, $V(\vec{r}) = V(r)$. Since the nuclear potential is of short range, we will consider here only potentials that for large distances ($r \to \infty$) approach $V(r) \to 0$ faster than $1/r$.

In this section, we will initially focus on the problem of elastic scattering. The formalism is then extended to include nuclear reactions. A general treatment of nuclear scattering involves solutions of the time-dependent Schrödinger equation, that is, the scattering of wave packets. However, the most important physics aspects can be derived by considering the simpler stationary problem of solving the time-independent Schröodinger equation. No further assumptions about the nuclear potential are made here. We will derive the general formalism, which relates the observed scattering cross section to the wave function far away from the scattering center. The cross section will be expressed in terms of *phase shifts*. To determine the latter quantity, knowledge of the wave function in the nuclear region is necessary. These considerations will be discussed in subsequent sections.

The scattering process is schematically shown in Figure 2.3. Consider a beam of monoenergetic particles incident on a target along the z-direction. The value and the uncertainty of the z-component of the linear momentum are given by $p_z = \text{const}$ and $\Delta p_z = 0$, respectively. It follows immediately from the Heisenberg uncertainty principle ($\Delta p_z \Delta z \approx \hbar$) that $\Delta z \to \infty$. Hence, the incoming wave has a large extent in the z-direction, that is, the process is nearly stationary. Furthermore, we assume for the x- and y-components of the linear momentum $p_x = p_y = 0$. This implies, according to $\lambda_i = h/p_i$, that $\lambda_x = \lambda_y \to \infty$. In other words, the incoming particles are represented by a wave of very large wavelength in the x- and y-directions, that is, an incident plane wave.

The stationary scattering problem is described by the time-independent Schrödinger equation

$$\left[-\frac{\hbar^2}{2m}\nabla^2 + V(\vec{r})\right]\psi(\vec{r}) = E\psi(\vec{r}) \tag{2.16}$$

At the position of the target nucleus, we cannot specify the total wave function further without assuming an explicit nuclear potential. However, far away from the scattering center, at the position of our detector, we can express the total wave function as a sum of two stationary waves: an incoming plane wave and an outgoing spherical wave. Therefore, for the total wave function at large distances we start with the ansatz

$$\psi_T(\vec{r}) = N\left[e^{i\vec{k}\cdot\vec{r}} + f(\theta)\frac{e^{ikr}}{r}\right], \quad r \to \infty \tag{2.17}$$

The term $e^{i\vec{k}\cdot\vec{r}}$ represents a plane wave traveling in the z-direction (a free particle). The second term contains a spherical wave (e^{ikr}), a quantity $f(\theta)$ called *scattering amplitude*, and the factor $1/r$ since the scattered intensity must obey an inverse square law; N is an overall normalization factor.

2.3.2 Relationship Between Differential Cross Section and Scattering Amplitude

The particle density (in units of inverse volume) is given by $P = \psi^*\psi$ and the current density (or flux, in units of inverse area per time) of beam particles or scattered particles with velocity v can be written as $j = vP$. For the incoming plane wave, we can write

$$j_b = v_b(Ne^{-ikz})(Ne^{ikz}) = v_b N^2 \tag{2.18}$$

whereas we obtain for the scattered spherical wave

$$j_s = v_s\left[Nf^*(\theta)e^{-ikr}\frac{1}{r}\right]\left[Nf(\theta)e^{ikr}\frac{1}{r}\right] = v_s N^2|f(\theta)|^2\frac{1}{r^2} \tag{2.19}$$

Substitution of j_b and j_s into Eq. (2.10) yields

$$\left(\frac{d\sigma}{d\Omega}\right) = \frac{j_s r^2}{j_b} = |f(\theta)|^2 \tag{2.20}$$

since for elastic scattering we can assume that $v_b = v_s$. The important result here is that the differential cross section is equal to the square of the scattering amplitude.

2.3.3 The Free Particle

It is instructive to consider first the force-free particle. The plane wave $e^{i\vec{k}\cdot\vec{r}}$ represents a free particle of momentum $\vec{p} = \hbar\vec{k}$ and energy $E = \hbar^2k^2/(2m)$. The potential is $V(r) = 0$ and, therefore, we have $f(\theta) = 0$. If we choose the z axis along $\vec{k}$ (see Figure 2.4), the plane wave can be written as

$$e^{i\vec{k}\cdot\vec{r}} = e^{ikr\cos\theta} = e^{ikr(z/r)} = e^{ikz} \tag{2.21}$$

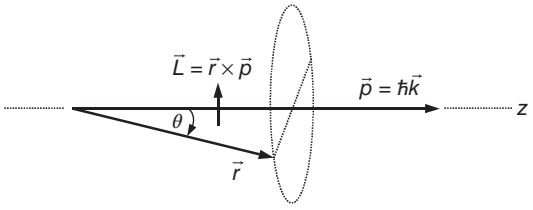

Figure 2.4 Linear and angular momenta of the free particle. The vector $\vec{p}$ points along the z axis, while the projection of $\vec{L}$ on the z axis is zero ($m = 0$).

which is independent of the angle ϕ. Since $\vec{L} = \vec{r} \times \vec{p}$, we only need to consider values of $m = 0$ for the magnetic quantum number. In this case, the spherical harmonics are given by (see Eq. (A.9))

$$Y_{\ell 0} = \sqrt{\frac{2\ell + 1}{4\pi}}\, P_\ell(\cos\theta) \tag{2.22}$$

where $P_\ell(\cos\theta)$ is a Legendre polynomial. With the substitutions $E = p^2/(2m) = \hbar^2 k^2/(2m)$ and $\rho \equiv kr$, the radial equation for the free particle can be written as (see Eq. (A.23))

$$\frac{d^2 u_\ell}{d\rho^2} + \left[1 - \frac{\ell(\ell+1)}{\rho^2}\right] u_\ell = 0 \tag{2.23}$$

The solutions, $j_\ell(kr)$, are called *spherical Bessel functions* (Appendix A.2) and we can write for the asymptotic values

$$u_\ell^{\text{f.p.}} = (kr) j_\ell(kr) = \sin(kr - \ell\pi/2), \quad r \to \infty \tag{2.24}$$

The eigenfunctions of the free particle, $j_\ell(kr)P_\ell(\cos\theta)$, form a complete orthonormal set. Therefore, we expand the plane wave according to

$$e^{ikz} = \sum_{\ell=0}^{\infty} c_\ell j_\ell(kr) P_\ell(\cos\theta) \tag{2.25}$$

The derivation of the expansion coefficients, which is not repeated here (see, e.g., Messiah, 1999), yields $c_\ell = (2\ell + 1)i^\ell$. Thus

$$e^{ikz} = \sum_{\ell=0}^{\infty} (2\ell + 1) i^\ell j_\ell(kr) P_\ell(\cos\theta) \tag{2.26}$$

It can be seen that the plane wave with linear momentum kr has been expanded into a set of *partial waves*, each having an orbital angular momentum of $\hbar\sqrt{\ell(\ell+1)}$, an amplitude of $(2\ell + 1)$, and a phase factor of i^ℓ. For very large distances appropriate for any experimental detector geometry, we find for the free particle

$$\psi_T^{\text{f.p.}} = e^{ikz} = \sum_{\ell=0}^{\infty} (2\ell + 1) i^\ell \frac{\sin(kr - \ell\pi/2)}{kr} P_\ell(\cos\theta), \quad r \to \infty \tag{2.27}$$

Using the relationship $\sin x = (i/2)(e^{-ix} - e^{ix})$ we write

$$\psi_T^{\text{f.p.}} = \frac{1}{2kr}\sum_{\ell=0}^{\infty}(2\ell+1)i^{\ell+1}\left[e^{-i(kr-\ell\pi/2)} - e^{i(kr-\ell\pi/2)}\right]P_\ell(\cos\theta), \quad r\to\infty \tag{2.28}$$

For the special case of s-waves ($\ell = 0$), we have $u_0^{\text{f.p.}} = \sin(kr)$ instead of Eq. (2.24) (see also Eq. (A.26)). Consequently, Eqs. (2.27) and (2.28) are not only valid for $r \to \infty$, but also apply in this case to all distances.

2.3.4 Turning the Potential On

For a central potential (Section 2.3.1) with $V(r) \neq 0$ and $f(\theta) \neq 0$, only the solution to the radial equation will change. Instead of $u_\ell^{\text{f.p.}}$ we have to write u_ℓ. The two functions $u_\ell^{\text{f.p.}}$ and u_ℓ essentially differ only for small r where $V(r) \neq 0$. For large distances r, we have $V(r) = 0$ and both functions must satisfy the same radial equation. We write

$$u_\ell = \sin(kr - \ell\pi/2 + \delta_\ell), \quad r\to\infty \tag{2.29}$$

This solution can differ at most from the radial wave function of the free particle (Eq. (2.24)) by a phase shift δ_ℓ, which arises from the different r dependence in the region where $V(r) \neq 0$. For s-waves ($\ell = 0$), Eq. (2.29) applies again to all distances outside the potential.

Similar to the case of the free particle (see Eq. (2.25)), we can expand the total wave function into partial waves

$$e^{ikz} + f(\theta)\frac{e^{ikr}}{r} = \sum_{\ell=0}^{\infty} b_\ell \frac{u_\ell(kr)}{kr}P_\ell(\cos\theta) \tag{2.30}$$

The expansion coefficients are given by $b_\ell = (2\ell+1)i^\ell e^{i\delta_\ell}$ (Problem 2.1). Thus

$$\begin{aligned}\psi_T &= e^{ikz} + f(\theta)\frac{e^{ikr}}{r} \\ &= \sum_{\ell=0}^{\infty}(2\ell+1)i^\ell e^{i\delta_\ell}\frac{\sin(kr-\ell\pi/2+\delta_\ell)}{kr}P_\ell(\cos\theta), \quad r\to\infty\end{aligned} \tag{2.31}$$

Using the relation $\sin x = (i/2)(e^{-ix} - e^{ix})$ we write

$$\psi_T = \frac{1}{2kr}\sum_{\ell=0}^{\infty}(2\ell+1)i^{\ell+1}\left[e^{-i(kr-\ell\pi/2)} - e^{2i\delta_\ell}e^{i(kr-\ell\pi/2)}\right]P_\ell(\cos\theta), \quad r\to\infty \tag{2.32}$$

Comparison to the total wave function of the free particle (Eq. (2.28)) shows that the potential modifies at large distances each outgoing spherical wave by a factor of $e^{2i\delta_\ell}$ and thereby shifts each outgoing spherical wave by a phase δ_ℓ.

2.3.5 Scattering Amplitude and Elastic Scattering Cross Section

We solve first for the scattering amplitude $f(\theta)$ by writing

$$f(\theta)\frac{e^{ikr}}{r} = \psi_T - \psi_T^{\text{f.p.}} = \frac{1}{2kr}\sum_{\ell=0}^{\infty}(2\ell+1)i^{\ell+1}\left[e^{i(kr-\ell\pi/2)}\left(1-e^{2i\delta_\ell}\right)\right]P_\ell(\cos\theta) \tag{2.33}$$

Using $e^{i\pi\ell/2} = \cos(\pi\ell/2) + i\sin(\pi\ell/2) = i^\ell$ and the identity $e^{i\delta}\sin\delta \equiv (i/2)(1 - e^{2i\delta})$ yields

$$f(\theta) = \frac{i}{2k}\sum_{\ell=0}^{\infty}(2\ell+1)\left(1-e^{2i\delta_\ell}\right)P_\ell(\cos\theta) = \frac{1}{k}\sum_{\ell=0}^{\infty}(2\ell+1)e^{i\delta_\ell}\sin\delta_\ell P_\ell(\cos\theta) \tag{2.34}$$

It is again apparent that the effect of the scattering potential is to shift the phase of each outgoing partial wave.

The differential elastic scattering cross section can be written as

$$\begin{aligned}\left(\frac{d\sigma}{d\Omega}\right)_{\text{el}} &= f^*(\theta)f(\theta) = \frac{1}{4k^2}\left|\sum_{\ell=0}^{\infty}(2\ell+1)\left(1-e^{2i\delta_\ell}\right)P_\ell(\cos\theta)\right|^2 \\ &= \frac{1}{k^2}\left|\sum_{\ell=0}^{\infty}(2\ell+1)\sin\delta_\ell P_\ell(\cos\theta)\right|^2\end{aligned} \tag{2.35}$$

The interference terms involving different functions $P_\ell(\cos\theta)$ generally give rise to nonisotropic angular distributions. Using the orthogonality relation for Legendre polynomials,

$$\int_{d\Omega} P_\ell(\cos\theta)P_{\ell'}(\cos\theta)d\Omega = \frac{4\pi}{2\ell+1}\delta_{\ell\ell'} \tag{2.36}$$

where $\delta_{\ell\ell'}$ denotes a Kronecker symbol, we obtain for the total elastic scattering cross section

$$\sigma_{\text{el}} = \int\left(\frac{d\sigma}{d\Omega}\right)_{\text{el}}d\Omega = \sum_{\ell=0}^{\infty}\sigma_{\text{el},\ell} \tag{2.37}$$

$$\sigma_{\text{el},\ell} = \frac{\pi}{k^2}(2\ell+1)\left|1-e^{2i\delta_\ell}\right|^2 = \frac{4\pi}{k^2}(2\ell+1)\sin^2\delta_\ell \tag{2.38}$$

For the special case of s-waves ($\ell = 0$), we find

$$\left(\frac{d\sigma}{d\Omega}\right)_{\text{el},0} = \frac{1}{k^2}\sin^2\delta_0 \tag{2.39}$$

$$\sigma_{\text{el},0} = \frac{4\pi}{k^2}\sin^2\delta_0 \tag{2.40}$$

and the angular distribution becomes isotropic (i.e., independent of θ). It follows that the cross section is entirely determined by the phase shifts δ_ℓ. It is also apparent that $\delta_\ell \to 0$ as $V(r) \to 0$ for all ℓ.

So far, we have assumed that at least one particle participating in the interaction is uncharged. If both nuclei are charged, then we have to replace the phase δ_ℓ for the short-range nuclear potential with $\delta_\ell + \sigma_\ell$, where σ_ℓ is the phase shift caused by the long-range Coulomb potential. The Coulomb phase shift can be calculated analytically (see Eq. (D.13)). We write

$$1 - e^{2i(\delta_\ell + \sigma_\ell)} = \left(1 - e^{2i\sigma_\ell}\right) + e^{2i\sigma_\ell}\left(1 - e^{2i\delta_\ell}\right) \tag{2.41}$$

and the scattering amplitude can be expressed as

$$\begin{aligned} f(\theta) &= \frac{i}{2k}\sum_{\ell=0}^{\infty}(2\ell+1)\left[1 - e^{2i(\delta_\ell+\sigma_\ell)}\right]P_\ell(\cos\theta) \\ &= \frac{i}{2k}\sum_{\ell=0}^{\infty}(2\ell+1)\left(1 - e^{2i\sigma_\ell}\right)P_\ell(\cos\theta) \\ &\quad + \frac{i}{2k}\sum_{\ell=0}^{\infty}(2\ell+1)e^{2i\sigma_\ell}\left(1 - e^{2i\delta_\ell}\right)P_\ell(\cos\theta) \end{aligned} \tag{2.42}$$

The first term describes the scattering from a pure Coulomb field (Rutherford scattering). The second term contains the phase shifts δ_ℓ and σ_ℓ. The cross section will exhibit interference terms corresponding to the scattering from both the nuclear and the Coulomb potential.

2.3.6 Reaction Cross Section

We can now consider the possibility that a nuclear reaction occurs, that is, any process that is different from elastic scattering (e.g., particle capture or inelastic scattering). A specific set of conditions (momentum, quantum numbers, and so on) for the outgoing particle is called a *channel*. A more precise definition of this concept will be given in later sections. Elastic scattering, inelastic scattering to a final excited state x, inelastic scattering to a different excited final state y, and so on, all correspond to different channels.

Suppose first that elastic scattering is the only possible process. In that case, as many particles enter as exit from an imaginary sphere surrounding the target nucleus (Figure 2.5a). As a result, the integral over the current density j_T, corresponding to the total wave function ψ_T for elastic scattering, is zero

$$\int_{d\Omega} j_T \, d\Omega = 0 \tag{2.43}$$

Suppose now that nonelastic processes occur as well. In that case, a fraction of the incoming particles will either change kinetic energies, for example, in inelastic scattering (n,n′), or change identity, for example, in particle capture (n,γ). A number of incoming particles will disappear and, consequently, there will be a net current of particles into the sphere (Figure 2.5b). The rate of disappearance from the

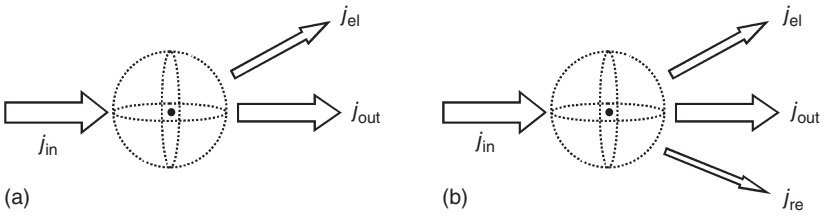

Figure 2.5 Representation of the current density if (a) scattering is the only possible process, and (b) both elastic and nonelastic processes occur. In part (a), the same number of particles enter and exit from an imaginary sphere surrounding the target nucleus and the integral over the total current density is zero. In part (b), a number of incoming particles disappear because of reactions and thus there is a net current of particles into the sphere.

elastic channel corresponds to the reaction cross section. Formally, we can write

$$\sigma_{\mathrm{re}} = \frac{r^2}{j_b} \int_{d\Omega} j_T \, d\Omega \tag{2.44}$$

Recall that the wave function ψ_T, corresponding to the current density j_T, represents the wave function for elastic scattering only. In the following, an expression is derived, which relates the reaction cross section to the phase shifts. We start from the quantum mechanical expression for the current density (Messiah, 1999),

$$j = \frac{\hbar}{2mi} \left(\psi^* \frac{\partial \psi}{\partial r} - \frac{\partial \psi^*}{\partial r} \psi \right) \tag{2.45}$$

From this expression, we find for the incoming plane wave e^{ikz}

$$j_b = \frac{\hbar}{2mi} \left[e^{-ikz} (e^{ikz} ik) - e^{-ikz} (-ik) e^{ikz} \right] = \frac{\hbar k}{m} \tag{2.46}$$

Substitution of the total elastic scattering wave function ψ_T (see Eq. (2.32)) into Eq. (2.45) yields, after some algebra,

$$j_T = \frac{\hbar}{4mkr^2} \left\{ \left| \sum_{\ell=0}^{\infty} (2\ell + 1) i^{\ell+1} e^{i\ell\pi/2} P_\ell(\cos\theta) \right|^2 - \left| \sum_{\ell=0}^{\infty} (2\ell + 1) i^{\ell+1} e^{2i\delta_\ell} e^{-i\ell\pi/2} P_\ell(\cos\theta) \right|^2 \right\} \tag{2.47}$$

With the orthogonality relation for Legendre polynomials (see Eq. (2.36)), one finds

$$\sigma_{\mathrm{re}} = \sum_{\ell=0}^{\infty} \sigma_{\mathrm{re},\ell} \tag{2.48}$$

$$\sigma_{\mathrm{re},\ell} = \frac{\pi}{k^2} (2\ell + 1) \left(1 - \left| e^{2i\delta_\ell} \right|^2 \right) \tag{2.49}$$

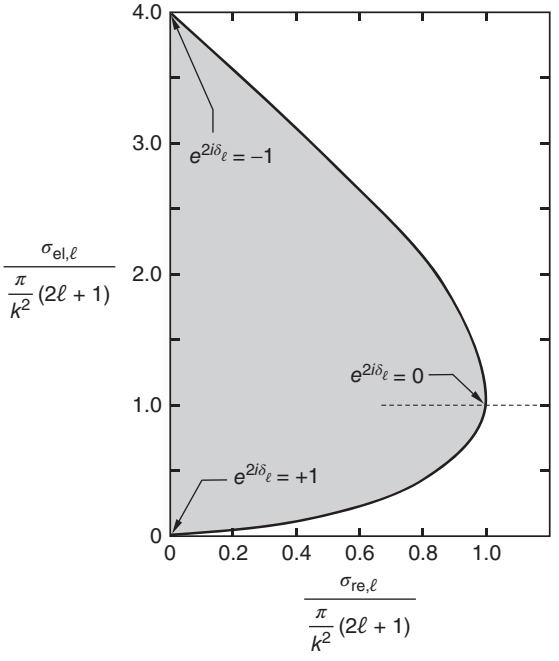

Figure 2.6 Upper and lower limit of elastic scattering cross section for a given reaction cross section. Values inside the shaded region are allowed, while those outside the shaded region are impossible. The quantity $e^{2i\delta_\ell}$ is real for all points located on the solid curve.

We require $|e^{2i\delta_\ell}|^2 \leq 1$ since otherwise σ_{re} becomes negative. In general, the phase shift δ_ℓ will be a complex number, that is, $\delta_\ell = \delta_{\ell_1} + i\delta_{\ell_2}$. For the special case that δ_ℓ is real, one finds $|e^{2i\delta_\ell}|^2 = 1$. In other words, reactions cannot occur and elastic scattering is the only possible process. The allowed range of values for $\sigma_{\text{re},\ell}$ and $\sigma_{\text{el},\ell}$ is represented by the shaded region in Figure 2.6. Recall that the expression for the elastic scattering cross section (see Eq. (2.38)) holds only for uncharged particles. The maximum elastic scattering cross section occurs at $e^{2i\delta_\ell} = -1$, yielding

$$\sigma_{\text{el},\ell}^{\max} = \frac{4\pi}{k^2}(2\ell + 1) \qquad \text{and} \qquad \sigma_{\text{re},\ell} = 0 \tag{2.50}$$

The maximum reaction cross section is obtained for $e^{2i\delta_\ell} = 0$, leading to

$$\sigma_{\text{re},\ell}^{\max} = \sigma_{\text{el},\ell} = \frac{\pi}{k^2}(2\ell + 1) \tag{2.51}$$

It follows that elastic scattering may occur without any reactions taking place, but reactions can never occur without elastic scattering being present. When the reaction cross section is at maximum, its value is equal to the elastic scattering cross section.

Traditionally, the theory of scattering has been applied to study the nature of the nuclear potential. Usually, the differential cross section $d\sigma/d\Omega$ is given by experiment and it is desired to find the corresponding potential $V(r)$. The experimental

phase shifts δ_ℓ are obtained by fitting the cross section formula to experimental angular distribution data, provided that a satisfactory fit is achieved by means of a small number of terms in the partial wave expansion. This procedure is repeated for several values of the incident energy. One then attempts to find a potential $V(r)$, which reproduces the observed phase shifts, by solving the Schrödinger equation numerically for each value of ℓ.

2.4 Scattering by Simple Potentials

The cross section is determined by the phase shifts. The latter can be obtained from the wave function in the nuclear region that is generated by an explicit nuclear potential. In this section, we will consider the case of s-wave ($\ell = 0$) scattering of neutral and spinless particles. Two simple potentials will be discussed explicitly: (i) an attractive square-well potential, and (ii) an attractive square-well plus square-barrier potential. Although very simple, these models contain qualitatively most of the physics that will be encountered later in the discussion of far more complex situations. We will specifically calculate the phase shifts δ_0 and the intensity of the wave function in the region of the potential by solving the radial Schrödinger equation. It will be seen how the properties of the potential determine the phase shift and the wave function intensity.

2.4.1 Square-Well Potential

The potential is displayed in Figure 2.7. For $\ell = 0$, the radial equation becomes (Appendix A.1)

$$\frac{d^2u}{dr^2} + \frac{2m}{\hbar^2}[E - V(r)]u = 0 \tag{2.52}$$

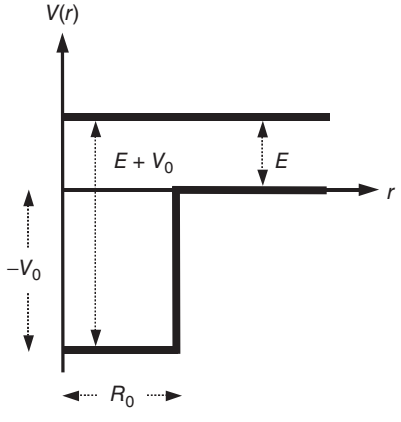

Figure 2.7 Three-dimensional square-well potential of radius R_0 and potential depth V_0. The upper horizontal line indicates the total particle energy E. For the calculation of the transmission coefficient, it is necessary to consider a one-dimensional potential step that extends from $-\infty$ to $+\infty$.

For a constant potential, $V(r) = \text{const}$, we obtain with $\hat{k}^2 = (2m/\hbar^2)(E - V)$ the radial equation

$$\frac{d^2u}{dr^2} + \hat{k}^2 u = 0 \tag{2.53}$$

The general solution in terms of complex exponentials is given by

$$u = \alpha e^{i\hat{k}r} + \beta e^{-i\hat{k}r} \tag{2.54}$$

We will consider the two regions $r < R_0$ and $r > R_0$ separately. For $r < R_0$, we have $E - V > 0$ and, therefore,

$$\begin{aligned} u_{\text{in}} &= A' e^{iKr} + B' e^{-iKr}, \quad K^2 = \frac{2m}{\hbar^2}(E + V_0) \\ &= A'[\cos(Kr) + i\sin(Kr)] + B'[\cos(Kr) - i\sin(Kr)] \end{aligned} \tag{2.55}$$

At the boundary, we require $u_{\text{in}}(0) = 0$, otherwise the radial wave function $u(r)/r$ will diverge at $r = 0$. It follows immediately that $u_{\text{in}}(0) = A' + B' = 0$ and the cosine terms in Eq. (2.55) disappear. Hence

$$u_{\text{in}} = A' i \sin(Kr) - A'[-i\sin(Kr)] = 2iA' \sin(Kr) = A\sin(Kr) \tag{2.56}$$

where we used the definition $A \equiv 2iA'$. In the region $r > R_0$, one finds again $E - V > 0$, and the general solution is given by

$$\begin{aligned} u_{\text{out}} &= C' e^{ikr} + D' e^{-ikr}, \quad k^2 = \frac{2m}{\hbar^2}E \\ &= C'[\cos(kr) + i\sin(kr)] + D'[\cos(kr) - i\sin(kr)] \\ &= i[C' - D']\sin(kr) + [C' + D']\cos(kr) = C''\sin(kr) + D''\cos(kr) \end{aligned} \tag{2.57}$$

It is convenient to rewrite this expression. The sum of $\sin x$ and $\cos x$ again gives a sine function, which is shifted along the x-axis. Using $C'' = C\cos\delta_0$ and $D'' = C\sin\delta_0$ we can formally write

$$u_{\text{out}} = C\left[\sin(kr)\cos\delta_0 + \cos(kr)\sin\delta_0\right] \tag{2.58}$$

With $\sin(x \pm y) = \sin x \cos y \pm \cos x \sin y$ one finds

$$u_{\text{out}} = C\sin(kr + \delta_0) \tag{2.59}$$

The solutions u_{in} (see Eq. (2.56)) and u_{out} (see Eq. (2.59)) will be used below.

Transmission Probability

We are interested in the probability of transmission from the outer to the inner region. It is convenient to start from the wave function solutions in terms of complex exponentials (see Eqs. (2.55) and (2.57)). It should be pointed out that for real potentials, the transmission probability is only defined for the one-dimensional

case (see, e.g., Messiah, 1999). Instead of considering the three-dimensional potential shown in Figure 2.7, we will assume that the particles are incident from the right-hand side, that a one-dimensional potential steps down at a distance of $x = R_0$ by an amount of V_0, and that the potential step extends to $-\infty$. We obtain for the one-dimensional radial wave functions

$$u_{\text{in}} = A' e^{iKx} + B' e^{-iKx} \tag{2.60}$$

$$u_{\text{out}} = C' e^{ikx} + D' e^{-ikx} \tag{2.61}$$

Although we do not have to consider the time-dependent Schrödinger equation here, it is instructive to investigate the full time-dependent solution obtained by multiplying the complex exponentials by the factor $e^{-i\omega t}$, where $\omega = E/\hbar$. It can easily be seen, for example, that the second term of u_{in} corresponds to a plane wave that propagates into the negative x direction. The first and second terms of u_{out} correspond to plane waves reflected from the boundary at R_0 and moving toward R_0, respectively. We are interested in the scattering process. The particle density of incident projectiles, for example, is given by $|D' e^{-ikx}|^2 = |D'|^2$. The current density (or flux) of incident particles is given by the product of particle density and velocity in the outer region, $j_{\text{inc}} = v_{\text{out}}|D'|^2$ (Section 2.3.2). Similarly, one finds for the transmitted and reflected particle flux $j_{\text{trans}} = v_{\text{in}}|B'|^2$ and $j_{\text{refl}} = v_{\text{out}}|C'|^2$, respectively. It follows for the probability that an individual particle will be transmitted from the outer to the inner region

$$\hat{T} = \frac{j_{\text{trans}}}{j_{\text{inc}}} = \frac{v_{\text{in}}|B'|^2}{v_{\text{out}}|D'|^2} = \frac{K|B'|^2}{k|D'|^2} \tag{2.62}$$

The quantity $\hat{T}$ is called the *transmission coefficient*.

The continuity condition requires that the wave functions and their derivatives are continuous at the boundary $x = R_0$,

$$\left(u_{\text{in}}\right)_{R_0} = \left(u_{\text{out}}\right)_{R_0} \tag{2.63}$$

$$\left(\frac{du_{\text{in}}}{dx}\right)_{R_0} = \left(\frac{du_{\text{out}}}{dx}\right)_{R_0} \tag{2.64}$$

We obtain

$$A' e^{iKR_0} + B' e^{-iKR_0} = C' e^{ikR_0} + D' e^{-ikR_0} \tag{2.65}$$

$$\frac{K}{k}\left(A' e^{iKR_0} - B' e^{-iKR_0}\right) = \left(C' e^{ikR_0} - D' e^{-ikR_0}\right) \tag{2.66}$$

Setting $A' = 0$, since there is no plane wave approaching the boundary R_0 from the left-hand side, and eliminating C' yields

$$\frac{K}{k}\left(-B' e^{-iKR_0}\right) = B' e^{-iKR_0} - 2D' e^{-ikR_0} \quad \text{or} \quad \frac{B'}{D'} = 2\frac{e^{-ikR_0}}{e^{-iKR_0}}\frac{k}{K+k} \tag{2.67}$$

For the transmission coefficient, we find with Eqs. (2.62) and (2.67)

$$\hat{T} = \frac{K}{k}\frac{|B'|^2}{|D'|^2} = 4\frac{kK}{(K+k)^2} = 4\frac{\frac{2m}{\hbar^2}\sqrt{(E+V_0)E}}{\left[\sqrt{\frac{2m}{\hbar^2}(E+V_0)} + \sqrt{\frac{2m}{\hbar^2}E}\right]^2} \tag{2.68}$$

We will use this result later in connection with the continuum theory of nuclear reactions (Section 2.6).

Phase Shift and Resonance Phenomenon

The quantity $\hat{T}$ describes the transmission probability from the right- to the left-hand side in Figure 2.7. We have considered so far only the amplitude ratio of two waves: one approaching the boundary R_0 from the right, the other one receding from R_0 to the left. We will now consider the full radial wave function solution for the three-dimensional case. We start from Eqs. (2.56) and (2.59),

$$u_{\text{in}} = A\sin(Kr) \tag{2.69}$$

$$u_{\text{out}} = C\sin(kr + \delta_0) \tag{2.70}$$

From the continuity condition (see Eqs. (2.63) and (2.64)), one finds

$$A\sin(KR_0) = C\sin(kR_0 + \delta_0) \tag{2.71}$$

$$AK\cos(KR_0) = Ck\cos(kR_0 + \delta_0) \tag{2.72}$$

First, we divide both equations to solve for the phase shift δ_0. The result is

$$\frac{1}{K}\tan(KR_0) = \frac{1}{k}\tan(kR_0 + \delta_0) \tag{2.73}$$

$$\delta_0 = -kR_0 + \arctan\left[\frac{k}{K}\tan(KR_0)\right] \tag{2.74}$$

This expression can be rewritten in terms of the total energy as

$$\delta_0 = -\frac{\sqrt{2mE}}{\hbar}R_0 + \arctan\left[\sqrt{\frac{E}{E+V_0}}\tan\left(\frac{\sqrt{2m(E+V_0)}}{\hbar}R_0\right)\right] \tag{2.75}$$

It can be seen that the phase shift is determined by the properties of the potential (R_0,V_0) and the properties of the particle (E,m). For $V_0 \to 0$, one finds $\delta_0 \to 0$, as already pointed out above. The cross section can be calculated simply from the phase shift (see Eq. (2.40)). Second, one can solve for $|A|^2/|C|^2$, that is, the ratio of wave function intensities in the interior ($r < R_0$) and exterior regions ($r > R_0$). By squaring and adding Eqs. (2.71) and (2.72) we obtain

$$\frac{|A|^2}{|C|^2} = \frac{k^2}{k^2 + [K^2 - k^2]\cos^2(KR_0)} = \frac{E}{E + V_0\cos^2\left(\frac{\sqrt{2m(E+V_0)}}{\hbar}R_0\right)} \tag{2.76}$$

where the identity $\sin^2(kr+\delta) + \cos^2(kr+\delta) = 1$ has been used.

Plots of $|A|^2/|C|^2$ and δ_0 versus E for the scattering of a neutron by a square-well potential are shown in Figure 2.8. A potential depth of $V_0 = 100$ MeV and a

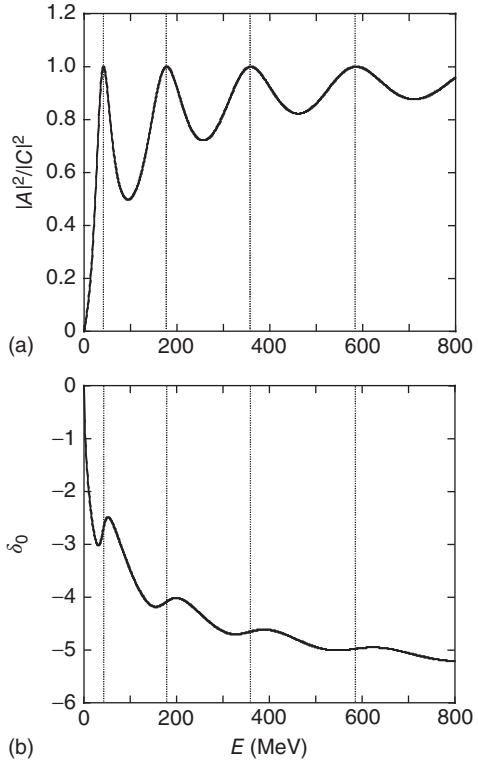

Figure 2.8 (a) Ratio of wave function intensities in the interior ($r < R_0$) and exterior ($r > R_0$) regions, $|A|^2/|C|^2$, and (b) phase shift δ_0 versus total energy E for the scattering of neutrons ($2m/\hbar^2 = 0.0484$ MeV^{-1} fm^{-2}) by a square-well potential (Figure 2.7). For the potential depth and the radius, the values of $V_0 = 100$ MeV and $R_0 = 3$ fm, respectively, are assumed. The curves show the resonance phenomenon.

potential radius of $R_0 = 3$ fm are assumed. The quantity $|A|^2/|C|^2$ measures the relative intensity of the wave function in the interior region $r < R_0$. It is apparent that $|A|^2/|C|^2$ oscillates between extreme values. This remarkable behavior is referred to as *resonance phenomenon*. At certain discrete energies E_i (resonance energies), the probability for finding the particle inside the boundary $r < R_0$ is at maximum. It can also be seen that each resonance shifts the phase δ_0 by some amount. The resonances occur at energies at which $\cos^2(KR_0) = 0$ in Eq. (2.76), that is, $KR_0 = (n + 1/2)\pi$. Hence

$$K = \frac{\left(n + \frac{1}{2}\right)\pi}{R_0} = \frac{2\pi}{\lambda_{\text{in}}} \tag{2.77}$$

$$\lambda_{\text{in}} = \frac{2R_0}{\left(n + \frac{1}{2}\right)} = \frac{R_0}{\left(\frac{n}{2} + \frac{1}{4}\right)} \tag{2.78}$$

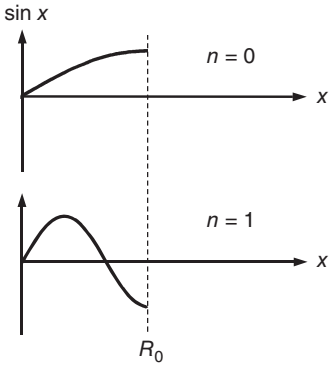

Figure 2.9 Two simplest solutions for the radial wave function inside the square-well potential. Both solutions give rise to a resonance since the derivative of the wave function at the potential radius R_0 is zero. The solutions are characterized by the number of wave function nodes n in the interior region ($r < R_0$). They are shown here for illustrative purposes. Neither of these functions represent physical solutions for the conditions adopted in Figure 2.8.

with λ_{in} the wavelength in the interior region. Since $(n/2 + 1/4) = \frac{1}{4}, \frac{3}{4}, \frac{5}{4}, \ldots$ it follows that resonances occur when precisely $(n/2 + 1/4)$ wavelengths fit into the interior region. At those wavelengths, the derivative of the interior wave function (a sine function; see Eq. (2.69)) at the radius R_0 is zero. As can be seen in Figure 2.9, n also corresponds to the number of wave function nodes in the region $r < R_0$. For the resonance energies, we obtain from Eq. (2.77)

$$E_n = \frac{\hbar^2}{2m}\frac{\pi^2}{R_0^2}\left(n + \frac{1}{2}\right)^2 - V_0 \tag{2.79}$$

In the above example of neutron scattering by a square-well potential of depth $V_0 = 100$ MeV and radius $R_0 = 3$ fm, one has $(\hbar\pi)^2/(2mR_0^2) = 22.648$ MeV. We obtain

$$E_2 = 41.5\,\text{MeV}, \quad E_3 = 177.4\,\text{MeV}, \quad E_4 = 358.6\,\text{MeV}, \ \ldots \tag{2.80}$$

No physical solution exists for $n = 0$ or 1, that is, for the potential depth chosen it is not possible to match the interior and exterior wave functions by fitting either 1/4 or 3/4 wavelengths into the region $r < R_0$. In other words, there are no solutions with either no node or only one node in the interior region.

The results obtained from the above formalism are illustrated qualitatively in Figure 2.10 showing radial wave functions for different depths of an attractive square-well potential. The bombarding energy is low (i.e., the wavelength is large compared to R_0) and held constant. In Figure 2.10a, the potential depth is zero (free particle) and the wave function is given by a sine function. In Figure 2.10b, the potential depth increases and, therefore, the wavelength in the interior decreases according to

$$\frac{\lambda_{\text{in}}}{2\pi} = \frac{1}{K} = \frac{1}{\sqrt{(2m/\hbar^2)(E + V_0)}}, \quad \lambda_{\text{in}} = \frac{h}{\sqrt{2m(E + V_0)}} \tag{2.81}$$

The values and derivatives of the inside and outside wave functions can only be matched by shifting the outside solution inward. This is the physical meaning of a phase shift. If the potential depth is increased further, the wavelength in the interior becomes smaller and the exterior wave must shift inward, until

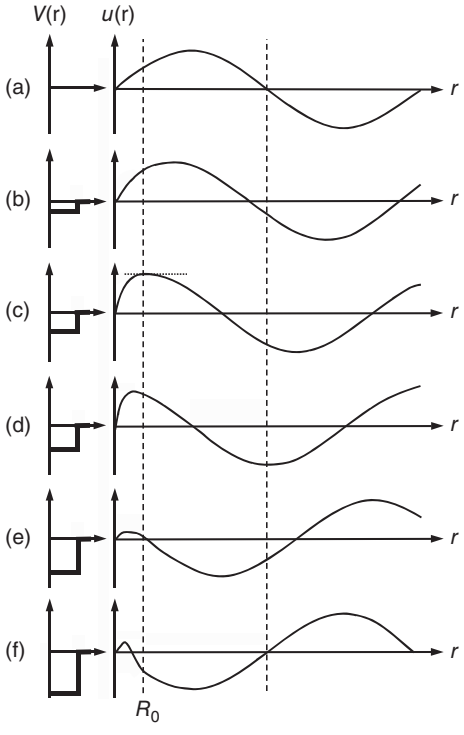

Figure 2.10 Square-well potential (a–f) and corresponding radial wave function solutions for different potential depths. For a given depth of the potential, the values and derivatives of the inside and outside wave functions must be matched by shifting the outside solution. The phase shift is a measure for this displacement. In part (c), the derivative of the wave function at R_0 is zero and the system is in resonance.

exactly 1/4 wavelength fit into the interior region. When this happens, the derivative of the wave function at R_0 becomes zero, corresponding to a maximum amplitude inside the potential region. The system is in resonance as shown in Figure 2.10c. A further increase in the potential depth results in: a decreasing amplitude in the interior (Figure 2.10d); a minimum interior amplitude because of poor wave function matching conditions (Figure 2.10e); and the appearance of the first node in the interior region (Figure 2.10f).

A plot of $|A|^2/|C|^2$ versus potential depth V_0 is shown in Figure 2.11. A total energy of $E = 1$ MeV and a potential radius of $R_0 = 3$ fm are assumed. Solving Eq. (2.79) for the potential depth V_0 yields

$$V_{0,n} = \frac{\hbar^2}{2m}\frac{\pi^2}{R_0^2}\left(n + \frac{1}{2}\right)^2 - E \tag{2.82}$$

Thus, we expect resonances to occur at $V_{0,0} = 4.7$ MeV, $V_{0,1} = 49.9$ MeV, $V_{0,2} = 140.5$ MeV, $V_{0,3} = 276.4$ MeV, $V_{0,4} = 457.6$ MeV, and so on (with $n = 0, 1, 2, 3, 4$

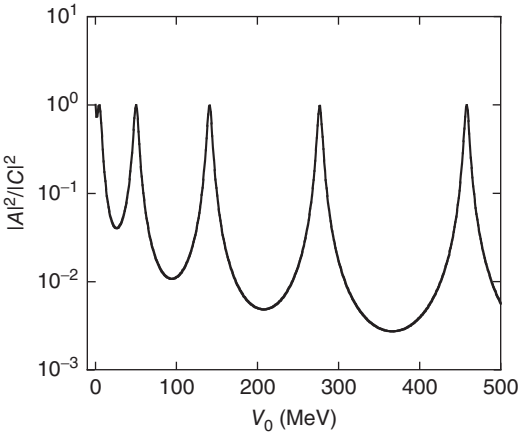

Figure 2.11 Plot of $|A|^2/|C|^2$ versus potential depth V_0 for the scattering of neutrons by a square-well potential. For the total energy and the potential radius, values of $E = 1$ MeV and $R_0 = 3$ fm are assumed. The maxima show resonances corresponding to $n = 0$, 1, 2, 3, and 4 radial wave function nodes in the interior region.

nodes in the interior region, respectively), in agreement with the results displayed in Figure 2.11.

2.4.2 Square-Barrier Potential

In the following, we will again consider the simple case of s-wave ($\ell = 0$) scattering. In addition to an attractive square well, the potential displays a repulsive square barrier. This is a simple model for a nuclear reaction if a barrier is present. For example, the Coulomb potential provides a barrier in reactions involving charged particles. By solving the Schrödinger equation explicitly, we will find the probability for transmission through the potential barrier and the intensity of the wave in the interior region. The potential is displayed in Figure 2.12. We will consider the three regions I, II, III separately. In each region, the potential is constant and, assuming $\ell = 0$, we again obtain with $\hat{k}^2 = (2m/\hbar^2)(E - V)$ the radial equation (Appendix A.1)

$$\frac{d^2u}{dr^2} + \hat{k}^2 u = 0 \tag{2.83}$$

For region I, we have $E - V > 0$ and, therefore,

$$\begin{aligned} u_{\mathrm{I}} &= Ae^{iKr} + Be^{-iKr}, \quad K^2 = \frac{2m}{\hbar^2}(E + V_0) \\ &= A' \sin(Kr) \end{aligned} \tag{2.84}$$

The solution is the same as the one obtained in the study of the square-well potential (see Eq. (2.56)). In region II, we have $E - V < 0$ and k_{II} becomes imaginary. The

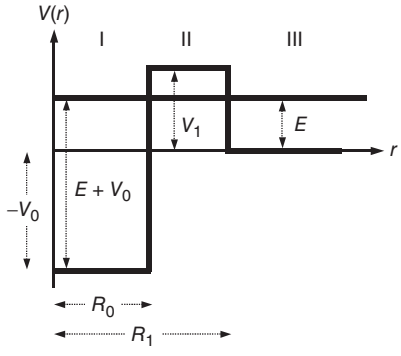

Figure 2.12 Three-dimensional square-well potential of radius R_0 and potential depth V_0 and a repulsive square-barrier potential of thickness $R_1 - R_0$ and height V_1. The total particle energy (horizontal line) is smaller than the barrier height, $E < V_1$. For the calculation of the transmission coefficient, it is necessary to consider a one-dimensional potential that extends from $-\infty$ to $+\infty$.

solution can be written in terms of real exponentials as

$$u_{II} = Ce^{ik_{II}r} + De^{-ik_{II}r}, \quad k_{II}^2 = \frac{2m}{\hbar^2}(E - V_1) = i^2\frac{2m}{\hbar^2}(V_1 - E) \equiv i^2\kappa^2$$
$$= Ce^{-\kappa r} + De^{\kappa r} \tag{2.85}$$

In region III, we have again $E - V > 0$, and the general solution is given by

$$u_{III} = Fe^{ikr} + Ge^{-ikr}, \quad k^2 = \frac{2m}{\hbar^2}E$$
$$= F' \sin(kr + \delta_0) \tag{2.86}$$

The solution is the same as the one obtained in the study of the square-well potential (see Eq. (2.59)).

Transmission Through the Barrier

First, we are interested in the probability of transmission through the potential barrier. It is convenient to start from the wave function solutions in terms of complex exponentials (see Eqs. (2.84)–(2.86)). We must again perform the calculation for the one-dimensional case. Instead of considering the three-dimensional potential shown in Figure 2.12, we will assume that the particles are incident from the right-hand side, that they encounter at a distance of $x = R_1$ a one-dimensional step barrier of height V_1, that at a distance of $x = R_0$ the potential steps down to $-V_0$, and that this potential continues to $-\infty$. We obtain for the one-dimensional radial wave functions

$$u_I = Ae^{iKx} + Be^{-iKx} \tag{2.87}$$
$$u_{II} = Ce^{-\kappa x} + De^{\kappa x} \tag{2.88}$$
$$u_{III} = Fe^{ikx} + Ge^{-ikx} \tag{2.89}$$

The second term of u_I corresponds to a plane wave that propagates into the negative x direction, whereas the first and second terms of u_{III} correspond to plane waves reflected from the barrier and moving toward the barrier, respectively. The transmission coefficient is then given by $\hat{T} = j_{trans}/j_{inc} = (K|B|^2)/(k|G|^2)$ (see Eq. (2.62)).

The continuity condition (see Eqs. (2.63) and (2.64)) requires that the wave functions and their derivatives are continuous at the boundaries $x = R_0$ and $x = R_1$

$$\left(u_{\mathrm{I}}\right)_{R_0} = \left(u_{\mathrm{II}}\right)_{R_0} \qquad \left(u_{\mathrm{II}}\right)_{R_1} = \left(u_{\mathrm{III}}\right)_{R_1} \tag{2.90}$$

$$\left(\frac{du_{\mathrm{I}}}{dx}\right)_{R_0} = \left(\frac{du_{\mathrm{II}}}{dx}\right)_{R_0} \qquad \left(\frac{du_{\mathrm{II}}}{dx}\right)_{R_1} = \left(\frac{du_{\mathrm{III}}}{dx}\right)_{R_1} \tag{2.91}$$

We obtain specifically

$$Ae^{iKR_0} + Be^{-iKR_0} = Ce^{-\kappa R_0} + De^{\kappa R_0} \tag{2.92}$$

$$i\frac{K}{\kappa}\left(Ae^{iKR_0} - Be^{-iKR_0}\right) = -Ce^{-\kappa R_0} + De^{\kappa R_0} \tag{2.93}$$

$$Ce^{-\kappa R_1} + De^{\kappa R_1} = Fe^{ikR_1} + Ge^{-ikR_1} \tag{2.94}$$

$$-Ce^{-\kappa R_1} + De^{\kappa R_1} = i\frac{k}{\kappa}\left(Fe^{ikR_1} - Ge^{-ikR_1}\right) \tag{2.95}$$

Adding and subtracting pairs of equations yields

$$A\left(1 + i\frac{K}{\kappa}\right)e^{iKR_0} + B\left(1 - i\frac{K}{\kappa}\right)e^{-iKR_0} = 2De^{\kappa R_0} \tag{2.96}$$

$$A\left(1 - i\frac{K}{\kappa}\right)e^{iKR_0} + B\left(1 + i\frac{K}{\kappa}\right)e^{-iKR_0} = 2Ce^{-\kappa R_0} \tag{2.97}$$

$$2De^{\kappa R_1} = F\left(1 + i\frac{k}{\kappa}\right)e^{ikR_1} + G\left(1 - i\frac{k}{\kappa}\right)e^{-ikR_1} \tag{2.98}$$

$$2Ce^{-\kappa R_1} = F\left(1 - i\frac{k}{\kappa}\right)e^{ikR_1} + G\left(1 + i\frac{k}{\kappa}\right)e^{-ikR_1} \tag{2.99}$$

Elimination of the coefficients C and D, and using the definitions $\alpha \equiv 1 + iK/\kappa$ and $\beta \equiv 1 + ik/\kappa$ gives

$$A\alpha e^{iKR_0} + B\alpha^* e^{-iKR_0} = e^{-\kappa(R_1 - R_0)}\left(F\beta e^{ikR_1} + G\beta^* e^{-ikR_1}\right) \tag{2.100}$$

$$A\alpha^* e^{iKR_0} + B\alpha e^{-iKR_0} = e^{\kappa(R_1 - R_0)}\left(F\beta^* e^{ikR_1} + G\beta e^{-ikR_1}\right) \tag{2.101}$$

Of interest is the transmission coefficient $\hat{T}$ of a wave incident from the right-hand side of the potential barrier. Since there is no wave approaching the barrier from the left-hand side, we set $A = 0$. We can also eliminate F and obtain

$$B\left[\alpha^*\beta^* e^{\kappa\Delta} - \alpha\beta e^{-\kappa\Delta}\right] = G\left[(\beta^*)^2 - \beta^2\right]e^{-i(kR_1 - KR_0)} = -2i\frac{k}{\kappa}Ge^{-i(kR_1 - KR_0)} \tag{2.102}$$

where we used $\Delta \equiv R_1 - R_0$. The transmission coefficient is then given by

$$\hat{T} = \frac{K}{k}\frac{|B|^2}{|G|^2} = \frac{4Kk/\kappa^2}{\left|\alpha^*\beta^* e^{\kappa\Delta} - \alpha\beta e^{-\kappa\Delta}\right|^2} \tag{2.103}$$

Using the relation $\sinh^2 z = (1/4)(e^{2z} + e^{-2z}) - 1/2$ yields after some algebra

$$\hat{T} = \frac{Kk}{[K + k]^2 + \left[\kappa^2 + K^2 + k^2 + K^2k^2/\kappa^2\right]\sinh^2(\kappa\Delta)} \tag{2.104}$$

In terms of energies, one finds explicitly

$$\frac{1}{\hat{T}} = \frac{1}{\sqrt{E(E+V_0)}} \left\{ \left[2E + V_0 + 2\sqrt{E(E+V_0)} \right] + \left[E + V_0 + V_1 + \frac{E(E+V_0)}{V_1 - E} \right] \sinh^2 \left[\sqrt{(2m/\hbar^2)(V_1 - E)}\, \Delta \right] \right\} \tag{2.105}$$

This result is remarkable since it shows that a particle approaching the potential barrier from the right-hand side can reach the left-hand side even if its total energy is less than the barrier height. This is referred to as the *tunnel effect* and is of central importance for charged-particle reactions in stars, as will be shown in Chapter 3.

Plots of $\hat{T}$ versus E for the scattering of neutrons are shown in Figure 2.13. The values used are (Figure 2.13a) $V_0 = 100$ MeV, $V_1 = 10$ MeV, $R_0 = 3$ fm, $R_1 = 8$ fm, and (Figure 2.13b) $V_0 = 50$ MeV, $V_1 = 10$ MeV, $R_0 = 3$ fm, $R_1 = 8$ fm. It can be seen that the transmission coefficient drops rapidly with a decreasing energy E. It is also apparent from the absolute magnitude of $\hat{T}$ that the intensity of the wave receding from the barrier to the left-hand side is considerably smaller than the intensity of the wave approaching the barrier from the right-hand side.

Frequently, the case of a low bombarding energy or a thick barrier is of interest,

$$\kappa\Delta = \frac{\sqrt{2m(V_1 - E)}}{\hbar}(R_1 - R_0) \gg 1 \tag{2.106}$$

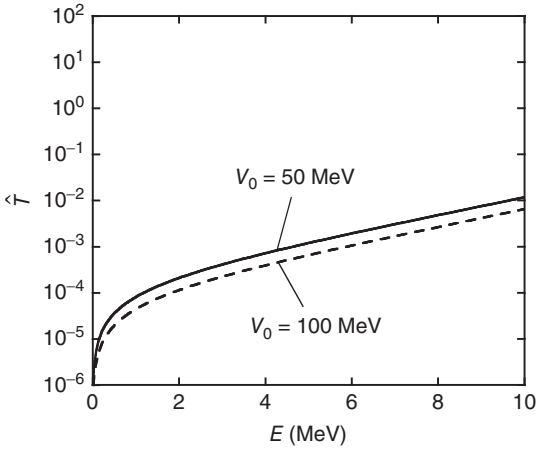

Figure 2.13 Transmission coefficient $\hat{T}$ versus energy E for the scattering of neutrons by the square-barrier potential shown in Figure 2.12. The potential properties are: (a) $V_0 = 100$ MeV, $V_1 = 10$ MeV, $R_0 = 3$ fm, $R_1 = 8$ fm, and (b) $V_0 = 50$ MeV, $V_1 = 10$ MeV, $R_0 = 3$ fm, $R_1 = 8$ fm. The drastic drop of the transmission coefficient at small energies is apparent.

In this case, we can approximate the denominator in Eq. (2.103) by

$$\left|\alpha^*\beta^* e^{\kappa\Delta} - \alpha\beta e^{-\kappa\Delta}\right|^2 \approx \left|\alpha^*\beta^* e^{\kappa\Delta}\right|^2 \tag{2.107}$$

After some algebra we obtain

$$\hat{T} \approx 4\frac{\sqrt{E(E+V_0)}(V_1-E)}{V_1(V_0+V_1)}\, e^{-2\kappa(R_1-R_0)} \tag{2.108}$$

The energy dependence of the transmission coefficient is entirely dominated by the exponential factor. For physically reasonable values of E, V_0, and V_1, the coefficient in front of the exponential is of order unity. Hence, we find

$$\hat{T} \approx e^{-(2/\hbar)\sqrt{2m(V_1-E)}(R_1-R_0)} \tag{2.109}$$

This important result, which strictly applies to the s-wave ($\ell = 0$) scattering of neutral particles, will be used later in connection with the transmission through the Coulomb barrier (Section 2.4.3).

Resonances

In the previous section, we derived the transmission probability for a one-dimensional square-barrier potential. The full radial wave function solution for the three-dimensional case will now be considered. It is interesting to have a closer look at the situation. For region I, we expect again a resonance phenomenon because of good wave function matching conditions. For region III, we expect again a phase shift to match the solutions smoothly at $r = R_1$. The barrier in region II provides an extra complication. Here, the wave function u_{II} is given by real exponentials and, depending on the relative magnitude of the coefficients C and D, may represent a decreasing, an increasing, or a more complicated function of the radius r.

As we did in the study of the square-well potential, we will calculate the energy dependence of the phase shift δ_0 and of $|A'|^2$, the intensity of the wave in the interior region $r < R_0$. We start from the wave function solutions (see Eqs. (2.84)–(2.86))

$$u_{\mathrm{I}} = A' \sin(Kr) \tag{2.110}$$

$$u_{\mathrm{II}} = Ce^{-\kappa r} + De^{\kappa r} \tag{2.111}$$

$$u_{\mathrm{III}} = F' \sin(kr + \delta_0) \tag{2.112}$$

and apply again the continuity condition (see Eqs. (2.63) and (2.64)) to the boundaries $r = R_0$ and $r = R_1$. It follows that

$$A' \sin(KR_0) = Ce^{-\kappa R_0} + De^{\kappa R_0} \tag{2.113}$$

$$A'\frac{K}{\kappa}\cos(KR_0) = -Ce^{-\kappa R_0} + De^{\kappa R_0} \tag{2.114}$$

$$Ce^{-\kappa R_1} + De^{\kappa R_1} = F' \sin(kR_1 + \delta_0) \tag{2.115}$$

$$-Ce^{-\kappa R_1} + De^{\kappa R_1} = F'\frac{k}{\kappa}\cos(kR_1 + \delta_0) \tag{2.116}$$

Solving for δ_0 by eliminating A', F', C, and D yields

$$\delta_0 = -kR_1 + \arctan\left[\frac{k}{\kappa}\frac{\sin(KR_0)\left(e^{-\kappa\Delta}+e^{\kappa\Delta}\right)+\frac{K}{\kappa}\cos(KR_0)\left(e^{\kappa\Delta}-e^{-\kappa\Delta}\right)}{\sin(KR_0)\left(e^{\kappa\Delta}-e^{-\kappa\Delta}\right)+\frac{K}{\kappa}\cos(KR_0)\left(e^{-\kappa\Delta}+e^{\kappa\Delta}\right)}\right] \tag{2.117}$$

For $k \to 0$ (or $E \to 0$), we obtain $\delta_0 \to 0$.

The wave intensity in the interior region, $|A'|^2$, is found by eliminating the constants C, D, and the phase shift δ_0. Furthermore, we use the expressions $e^{2x} + e^{-2x} = 4\sinh^2 x + 2$ and $e^x - e^{-x} = 2\sinh x$. The tedious algebra is not given here explicitly. The result is

$$\begin{aligned}\frac{|F'|^2}{|A'|^2} &= \sin^2(KR_0) + \left(\frac{K}{k}\right)^2\cos^2(KR_0) \\ &\quad + \sin^2(KR_0)\sinh^2(\kappa\Delta)\left[1+\left(\frac{\kappa}{k}\right)^2\right] \\ &\quad + \cos^2(KR_0)\sinh^2(\kappa\Delta)\left[\left(\frac{K}{\kappa}\right)^2+\left(\frac{K}{k}\right)^2\right] \\ &\quad + \sin(KR_0)\cos(KR_0)\sinh(2\kappa\Delta)\left[\left(\frac{K}{\kappa}\right)+\left(\frac{K}{\kappa}\right)\left(\frac{\kappa}{k}\right)^2\right]\end{aligned} \tag{2.118}$$

The energy dependence of the quantities $|A'|^2/|F'|^2$, $|A'|^2/(|F'|^2\hat{T})$ and δ_0 for neutron scattering by a square-barrier potential is shown in Figure 2.14, where the transmission coefficient $\hat{T}$ is obtained from the approximation of Eq. (2.109). We assume values of $V_0 = 100$ MeV, $V_1 = 10$ MeV, $R_0 = 3$ fm, $R_1 = 8$ fm (dashed lines) and $V_0 = 50$ MeV, $V_1 = 10$ MeV, $R_0 = 3$ fm, $R_1 = 8$ fm (solid lines). The figure reflects both the effects of the barrier transmission and the resonance phenomenon. For a potential depth of $V_0 = 100$ MeV, no resonance occurs over the energy range shown and the plot looks almost identical to the corresponding part in Figure 2.13. Consequently, the quantity $|A'|^2/(|F'|^2\hat{T})$ is almost constant with energy. Furthermore, the phase shift varies smoothly with energy. For a potential depth of $V_0 = 50$ MeV, on the other hand, the interior wave function solution has a large amplitude because of good matching conditions. The resulting resonance is seen in Figure 2.14a. The shape of the resonance is distorted by the barrier transmission coefficient. In Figure 2.14b, the effects of the barrier transmission are removed and, consequently, the shape of the resonance becomes symmetric. It is also evident that the resonance shifts the phase by a significant amount. This method of removing the transmission coefficient from the wave function intensity or the cross section is of crucial importance in nuclear astrophysics, as will be seen in Chapter 3.

A plot of $|A'|^2/|F'|^2$ versus potential depth V_0 in the region $r < R_0$ is shown in Figure 2.15. The graph is obtained for the potential parameters $V_1 = 10$ MeV, $R_0 = 3$ fm, $R_1 = 8$ fm, and $E = 5$ MeV. Several resonances that become broader with an increasing value of V_0 are apparent. By changing V_0 we change the

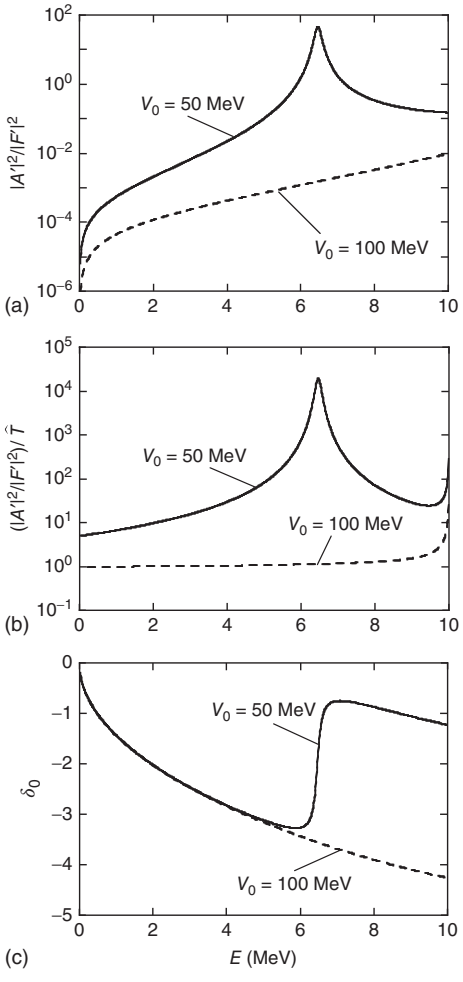

Figure 2.14 Energy dependence of the quantities (a) $|A'|^2/|F'|^2$, (b) $|A'|^2/(|F'|^2\hat{T})$ and (c) δ_0 for neutron scattering by a square-barrier potential (Figure 2.12). The properties of the potential are V_1 = 10 MeV, R_0 = 3 fm and R_1 = 8 fm. The dashed and solid lines are obtained for potential depths of V_0 = 100 MeV and V_0 = 50 MeV, respectively. The curves represent the effects of both the barrier transmission and the resonance phenomenon. In part (b), the effects of the barrier transmission are removed and the shape of the resonance becomes symmetric (solid line).

wavelength in the interior region (see Eq. (2.81)). As was the case for the simple square-well potential (Section 2.4.1), the resonances result from favorable wave function matching conditions at the boundaries. The first resonance corresponds to a wave function with no node in the region $r < R_0$. The second resonance corresponds to one node, the third resonance to two nodes, and so on. Comparison

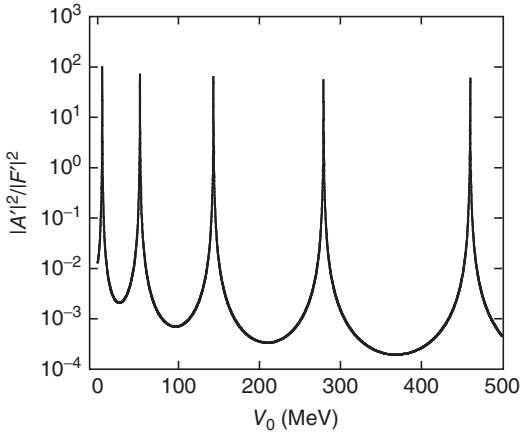

Figure 2.15 Plot of $|A'|^2/|F'|^2$ versus potential depth V_0 in the interior region for the scattering of neutrons by a square-barrier potential. The curve is calculated for the parameters $V_1 = 10$ MeV, $R_0 = 3$ fm, $R_1 = 8$ fm and $E = 5$ MeV. The maxima correspond to resonances that result from favorable wave function matching conditions at the boundaries.

to Figure 2.11 shows that the resonances are much narrower because of the repulsive square-barrier potential.

As a final example, Figure 2.16 shows schematically the radial wave functions for three cases. In Figure 2.16a, the potential depth is zero. The amplitude of the wave function in the interior is very small and reflects primarily the transmission through the barrier. In Figure 2.16b, the amplitude in the interior is at maximum because of favorable matching conditions. The system is in resonance with no wave function node in the interior. Figure 2.16c displays the wave function for the second resonance, showing one node in the interior region.

2.4.3
Transmission Through the Coulomb Barrier

The low-energy s-wave transmission coefficient for a square-barrier potential (see Eq. (2.109)) can be easily generalized since a potential barrier of arbitrary shape may be divided into thin slices of width dr. The total s-wave transmission coefficient is then given by the product of the transmission coefficients for each slice,

$$\hat{T} = \hat{T}_1 \cdot \hat{T}_2 \cdot \ldots \cdot \hat{T}_n \approx \exp\left[-\frac{2}{\hbar}\sum_i \sqrt{2m(V_i - E)}(R_{i+1} - R_i)\right]$$
$$\xrightarrow[n\,\text{large}]{} \exp\left[-\frac{2}{\hbar}\int_{R_0}^{R_c} \sqrt{2m[V(r) - E]}\,dr\right] \qquad (2.119)$$

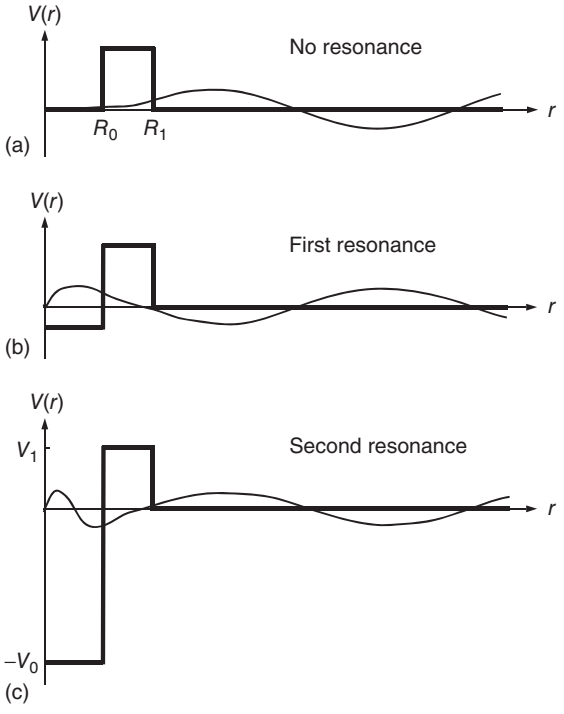

Figure 2.16 Schematic representation of radial wave functions (thin solid lines) for the scattering of neutral particles by a square-barrier potential (thick solid line) of different potential depths V_0. The wave functions are appropriate for (a) no resonance, (b) the first resonance with no wave function node in the interior region ($r < R_0$), and (c) the second resonance with one node in the interior.

For the important case of the Coulomb potential, displayed in Figure 2.17, we obtain

$$\hat{T} \approx \exp\left(-\frac{2}{\hbar}\sqrt{2m}\int_{R_0}^{R_c}\sqrt{\frac{Z_0Z_1e^2}{r}-E}\,dr\right) \tag{2.120}$$

with Z_0 and Z_1 the charge of the projectile and target, respectively. The quantity R_0 is the radius of the square-well potential and defines the height of the Coulomb barrier, $V_C = Z_0Z_1e^2/R_0$. Numerically, one finds $V_C = 1.44Z_0Z_1/R_0$ (MeV), with R_0 in units of femtometers; we can approximate this radius using the expression given in Section 2.5.5. The quantity R_c is the distance at which the incoming particle would be reflected classically. It is referred to as the *classical turning point* and is defined by $E = Z_0Z_1e^2/R_c$ or $E/V_C = R_0/R_c$. The integral in Eq. (2.120) can be solved analytically. Rewriting the above expression using the definition of the classical turning point yields

$$\hat{T} \approx \exp\left(-\frac{2}{\hbar}\sqrt{2mZ_0Z_1e^2}\int_{R_0}^{R_c}\sqrt{\frac{1}{r}-\frac{1}{R_c}}\,dr\right) \tag{2.121}$$

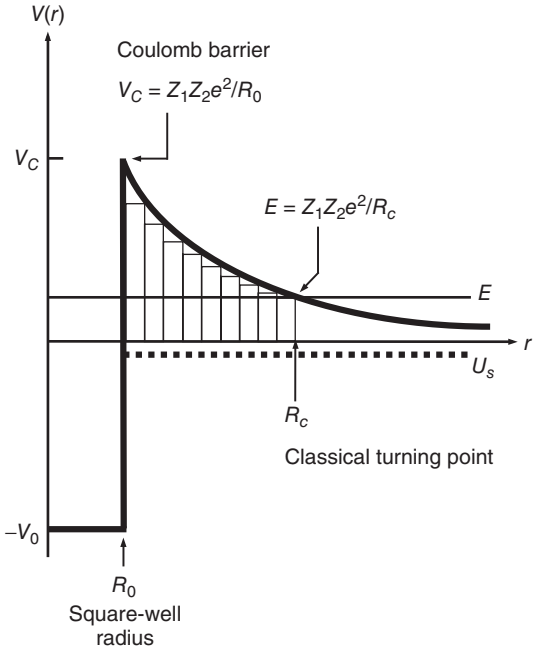

Figure 2.17 Attractive nuclear square-well potential ($r < R_0$) plus repulsive Coulomb potential ($r > R_0$), shown as thick solid line. The transmission coefficient can be calculated analytically by dividing the Coulomb barrier of height $V_C = Z_1Z_2e^2/R_0$ into infinitesimally thin square-barrier potentials. The radius R_c at which the total particle energy E (thin solid line) is equal to the Coulomb potential, $E = Z_1Z_2e^2/R_c$, is referred to as *the classical turning point*. The thick dashed line indicates a small negative (attractive) potential U_s that results from the polarization of the electron–ion plasma (electron screening), giving rise to a modification of both the Coulomb potential and the energetics of the reaction (Section 3.2.6).

Substitution of $z \equiv r/R_c$ gives

$$\begin{aligned}\hat{T} &\approx \exp\left(-\frac{2}{\hbar}\sqrt{2mZ_0Z_1e^2}\int_{R_0/R_c}^{1}\sqrt{\frac{1}{zR_c}-\frac{1}{R_c}}R_c\,dz\right)\\ &= \exp\left(-\frac{2}{\hbar}\sqrt{\frac{2m}{E}}Z_0Z_1e^2\int_{R_0/R_c}^{1}\sqrt{\frac{1}{z}-1}\,dz\right)\end{aligned} \tag{2.122}$$

The result is

$$\hat{T} \approx \exp\left(-\frac{2}{\hbar}\sqrt{\frac{2m}{E}}Z_0Z_1e^2\left[\arccos\sqrt{\frac{E}{V_C}}-\sqrt{\frac{E}{V_C}\left(1-\frac{E}{V_C}\right)}\right]\right) \tag{2.123}$$

For low energies compared to the Coulomb barrier height, $E/V_C \ll 1$, we use the expansion $\arccos\sqrt{x}-\sqrt{x(1-x)} \approx \pi/2 - 2\sqrt{x} + x^{3/2}/3$ and obtain

$$\hat{T} \approx \exp\left(-\frac{2}{\hbar}\sqrt{\frac{2m}{E}}Z_0Z_1e^2\left[\frac{\pi}{2}-2\sqrt{\frac{E}{V_C}}+\frac{1}{3}\left(\frac{E}{V_C}\right)^{3/2}\right]\right)$$
$$= \exp\left(-\frac{2\pi}{\hbar}\sqrt{\frac{m}{2E}}Z_0Z_1e^2\left[1+\frac{2}{3\pi}\left(\frac{E}{V_C}\right)^{3/2}\right]+\frac{4}{\hbar}\sqrt{2mZ_0Z_1e^2R_0}\right) \tag{2.124}$$

The first term in the exponential is larger than the third term by a factor of $(\pi/4)\sqrt{V_C/E}$ and therefore dominates the transmission coefficient. The third term vanishes in the limit $R_0 \to 0$ and represents a correction caused by a finite radius to which the projectile must penetrate. The larger the radius R_0, the smaller the penetration distance (Figure 2.17) and the larger the transmission coefficient will become. The second term represents a correction factor to the first term when the energy becomes a significant fraction of the Coulomb barrier height. The leading term of the s-wave Coulomb barrier transmission coefficient for small energies compared to the Coulomb barrier height,

$$\hat{T} \approx \exp\left(-\frac{2\pi}{\hbar}\sqrt{\frac{m}{2E}}Z_0Z_1e^2\right) \equiv e^{-2\pi\eta} \tag{2.125}$$

is called the *Gamow factor* and will play an important role in the discussion of thermonuclear reaction rates for charged particles (Section 3.2.1). The quantity η is the Sommerfeld parameter and its numerical value is given in Section 3.2.1.

2.5 Theory of Resonances

2.5.1 General Aspects

Up to now we have discussed wave function intensities, phase shifts, and transmission probabilities for simple nuclear potentials. In the following, the resulting cross sections will be considered. Initially, we will restrict ourselves again to the case of s-wave scattering of neutral particles, that is, the complications of the Coulomb and centripetal barriers are disregarded. The total elastic scattering and reaction cross sections are then given by Eqs. (2.40) and (2.49),

$$\sigma_{\mathrm{el},0} = \frac{\pi}{k^2}\left|1-e^{2i\delta_0}\right|^2 = \frac{4\pi}{k^2}\sin^2\delta_0 \tag{2.126}$$

$$\sigma_{\mathrm{re},0} = \frac{\pi}{k^2}\left(1-\left|e^{2i\delta_0}\right|^2\right) \tag{2.127}$$

The cross sections are entirely determined by the phase shift δ_0.

It is interesting to plot the total elastic scattering cross sections for the potential models considered in Sections 2.4.1 and 2.4.2. They are shown in Figure 2.18 for (a) a square-well potential with $R_0 = 3$ fm, $V_0 = 100$ MeV; (b) a square-barrier potential with $R_0 = 3$ fm, $R_1 = 8$ fm, $V_0 = 100$ MeV, $V_1 = 10$ MeV; and (c) a

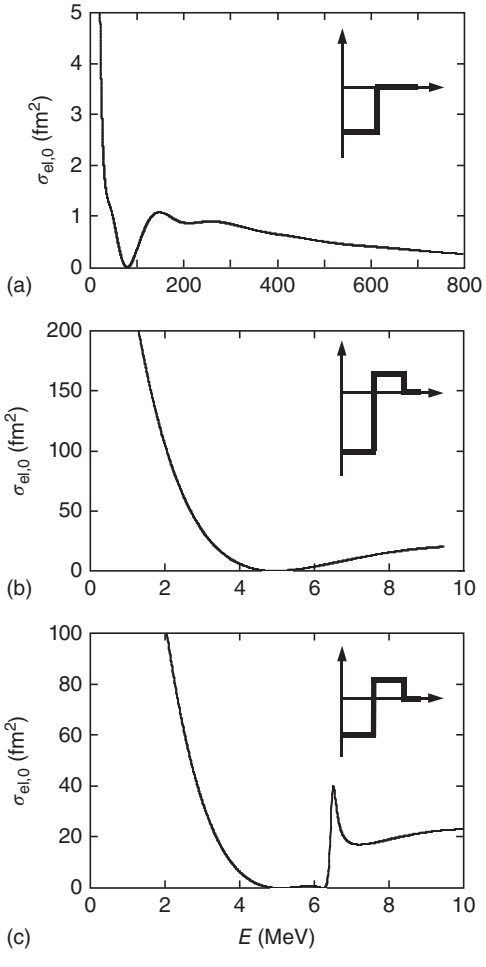

Figure 2.18 Elastic scattering cross sections for s-wave neutrons versus energy for the simple potentials discussed in Sections 2.4.1 and 2.4.2: (a) square-well potential with $R_0 = 3$ fm, $V_0 = 100$ MeV; (b) square-barrier potential with $R_0 = 3$ fm, $R_1 = 8$ fm, $V_0 = 100$ MeV, $V_1 = 10$ MeV; (c) square-barrier potential with $R_0 = 3$ fm, $R_1 = 8$ fm, $V_0 = 50$ MeV, $V_1 = 10$ MeV. A resonance is observed only in part (c).

square-barrier potential with $R_0 = 3$ fm, $R_1 = 8$ fm, $V_0 = 50$ MeV, $V_1 = 10$ MeV. We expect resonances in parts (a) and (c), as is apparent from Figures 2.8 and 2.14. However, a resonance is observed only in Figure 2.18c. And even in this case the resulting shape of the total elastic scattering cross section looks complicated.

Up to now we considered single-particle potentials. The spacing of resonances, referred to as *single-particle resonances*, calculated by these models amounts to many mega electron volts. However, experiments performed since the 1930s frequently showed closely spaced resonances (sometimes a few kilo electron volts or

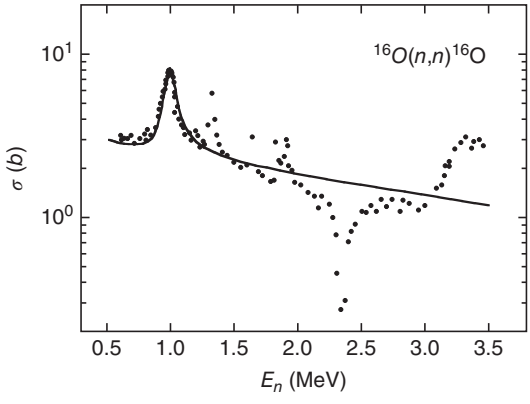

Figure 2.19 Experimental total cross section for the elastic scattering $^{16}O(n,n)^{16}O$ (data points) and calculated elastic scattering cross section using a (Woods–Saxon) single-particle potential (solid line). The potential reproduces only one of the observed resonances but cannot account for the entire observed structure. Data are from Westin and Adams (1972).

less apart) of very narrow widths. For example, Figure 2.19 shows the experimental elastic scattering cross section of neutrons on ^{16}O. In contrast to our theoretical results obtained so far, a very complicated structure consisting of several resonances with different widths is observed. The solid line in Figure 2.19 represents a calculation using a single-particle potential. It reproduces only one of the many resonances shown. Although some observed resonances can be described by single-particle potentials, in the vast majority of cases the single-particle picture is not appropriate for the explanation of the observed rapid cross section variations.

At this point, we suspect that the interactions of many nucleons inside the nucleus are complicated and cannot be expressed in terms of a single radial wave function generated by a single-particle potential. In the following, we will develop a different model to describe a nuclear resonance in general terms without using an explicit assumption for the nuclear potential. A specific assumption regarding the many-particle nuclear potential may even be undesirable since at this point neither the nuclear forces between the nucleons nor their motion in the nuclear interior are precisely known.

2.5.2
Logarithmic Derivative, Phase Shift, and Cross Section

Since we will not make reference to a specific nuclear potential, this model will not be able to predict the absolute magnitude of cross sections. Most resonance theories reformulate the cross sections in terms of known quantities of the nuclear exterior (penetration and shift factors) and unknown quantities of the nuclear interior (reduced widths). Our goal is to predict relative cross sections *near* a resonance. The only assumptions we make regarding the nuclear potential is the

existence of a relatively well-defined spherical nuclear surface at $r = R$ and that the projectile and target have no nuclear interaction outside of this radius.

At this boundary, the interior and exterior wave functions and their derivatives have to be matched,

$$u_\ell^{\text{in}}(R) = u_\ell^{\text{out}}(R) \qquad \text{and} \qquad \left(\frac{du_\ell^{\text{in}}(r)}{dr}\right)_{r=R} = \left(\frac{du_\ell^{\text{out}}(r)}{dr}\right)_{r=R} \tag{2.128}$$

By dividing both expressions and by introducing a dimensionless quantity, called the *logarithmic derivative at the boundary*,

$$f_\ell \equiv R\left(\frac{1}{u_\ell(r)}\frac{du_\ell(r)}{dr}\right)_{r=R} = R\left(\frac{d\ln u_\ell(r)}{dr}\right)_{r=R} \tag{2.129}$$

we can rewrite the conditions of Eq. (2.128) as

$$f_\ell(u_\ell^{\text{in}}) = f_\ell(u_\ell^{\text{out}}) \tag{2.130}$$

In other words, the calculation of f_ℓ with u_ℓ^{in} and u_ℓ^{out} must yield the same value. The quantity f is related to the slope of the wave function at the radius $r = R$.

We start from the expression for the total wave function in the exterior region $r > R$ (see Eq. (2.32)). For s-waves ($\ell = 0$) it reduces to

$$\begin{aligned}\psi_{T,\text{out}} &= Ae^{ikr} + Be^{-ikr}, \quad k^2 = \frac{2mE}{\hbar^2} \\ &= -\frac{i}{2kr}e^{2i\delta_0}e^{ikr} + \frac{i}{2kr}e^{-ikr} = \frac{i}{2kr}\left(e^{-ikr} - e^{2i\delta_0}e^{ikr}\right) \\ &= \frac{1}{2kr}e^{i\delta_0}\left[e^{-i(kr+\delta_0)} - e^{i(kr+\delta_0)}\right] = \frac{1}{kr}e^{i\delta_0}\sin(kr+\delta_0)\end{aligned} \tag{2.131}$$

where the first expression ($Ae^{ikr} + Be^{-ikr}$) generally holds in the force-free region (Eqs. (2.57) and (2.86); see also Appendix A.1). Recall the meaning of the above equation: the outgoing spherical wave e^{ikr} is multiplied by a factor $e^{2i\delta_0}$, which effectively shifts the wave by an amount of δ_0.

As already implied in Sections 2.3.3 and 2.3.4, for the special case of s-waves, Eq. (2.32) (and thus Eq. (2.131)) is not only valid at large distances but also applies to all distances $r > R$. Furthermore, the spherical harmonic for $\ell = 0$ is constant (see Eq. (A.9)) and, therefore, the total wave function is given by the radial wave function

$$\psi_{T,\text{out}} = \frac{i}{2kr}\left(e^{-ikr} - e^{2i\delta_0}e^{ikr}\right) = \frac{u_{\text{out}}(r)}{r} \tag{2.132}$$

The cross section is determined by the phase shift δ_0. We will first find a relationship between δ_0 and f_0 and will then express the cross section in terms of f_0. From Eqs. (2.129) and (2.132), one obtains

$$\frac{f_0}{R} = \left(\frac{1}{u_{\text{out}}(r)}\frac{du_{\text{out}}(r)}{dr}\right)_{r=R} = \frac{-ike^{-ikR} - ike^{2i\delta_0}e^{ikR}}{e^{-ikR} - e^{2i\delta_0}e^{ikR}} \tag{2.133}$$

Solving for $e^{2i\delta_0}$ gives

$$e^{2i\delta_0} = \frac{f_0 + ikR}{f_0 - ikR}e^{-2ikR} \tag{2.134}$$

For the elastic scattering cross section (see Eq. (2.126)), we find

$$\sigma_{\mathrm{el},0} = \frac{\pi}{k^2}\left|1 - \frac{f_0 + ikR}{f_0 - ikR}e^{-2ikR}\right|^2 = \frac{\pi}{k^2}\left|e^{2ikR} - \frac{f_0 + ikR}{f_0 - ikR}\right|^2$$
$$= \frac{\pi}{k^2}\left|-\frac{2ikR}{f_0 - ikR} + e^{2ikR} - 1\right|^2 = \frac{\pi}{k^2}\left|A_{\mathrm{res}} + A_{\mathrm{pot}}\right|^2 \tag{2.135}$$

with

$$A_{\mathrm{res}} = -\frac{2ikR}{f_0 - ikR} \qquad \text{and} \qquad A_{\mathrm{pot}} = e^{2ikR} - 1 \tag{2.136}$$

It can be seen that A_{res} has a maximum if $f_0 = 0$, consistent with our identification of resonances as a slope of zero for the radial wave function at the boundary $r = R$.

Similarly, using $f_0 = \mathrm{Re}\, f_0 + i\ \mathrm{Im}\, f_0 = g + ih$, one obtains for the reaction cross section (see Eq. (2.127))

$$\sigma_{\mathrm{re},0} = \frac{\pi}{k^2}\left(1 - \left|\frac{f_0 + ikR}{f_0 - ikR}e^{-2ikR}\right|^2\right)$$
$$= \frac{\pi}{k^2}\left[1 - \left(\frac{g + ih + ikR}{g + ih - ikR}\right)\left(\frac{g - ih - ikR}{g - ih + ikR}\right)\right]$$
$$= \frac{\pi}{k^2}\frac{-4hkR}{g^2 + h^2 - 2hkR + k^2R^2} = \frac{\pi}{k^2}\frac{-4kR\,\mathrm{Im}\, f_0}{(\mathrm{Re}\, f_0)^2 + (\mathrm{Im}\, f_0 - kR)^2} \tag{2.137}$$

Only A_{res} depends on the interior region $r < R$ through f_0. Consequently, only this term can give rise to resonances and A_{res} is called *resonance scattering amplitude*. The term A_{pot} can be interpreted as follows. Suppose that $f_0 \to \infty$. In that case, $A_{\mathrm{res}} = 0$. From the definition of f_0 (see Eq. (2.129)), this implies $u(R) = 0$ and, therefore, an infinitely high potential for $r < R$ (i.e., the sphere of radius R is impenetrable). Thus, the quantity A_{pot} is called *hardsphere potential scattering amplitude*. Note also that $\mathrm{Im}\, f_0 \leq 0$, otherwise $\sigma_{\mathrm{re},0}$ becomes negative. For the special case that f_0 is real ($\mathrm{Im}\, f_0 = 0$), the reaction cross section disappears, $\sigma_{\mathrm{re},0} = 0$. Therefore, f_0 must be complex for reactions to occur.

It is also interesting to consider the elastic scattering phase shift δ_0. From Eq. (2.134) one finds

$$2i\delta_0 = \ln(f_0 + ikR) - \ln(f_0 - ikR) - 2ikR \tag{2.138}$$

Assuming $\mathrm{Im}\, f_0 = 0$ (or $\sigma_{\mathrm{re},0} = 0$) we find using the identity $\ln(a + ib) = (1/2)\ln(a^2 + b^2) + i\arctan(b/a)$

$$\delta_0 = \frac{1}{2i}\left[\frac{1}{2}\ln\left(f_0^2 + k^2R^2\right) + i\arctan\left(\frac{kR}{f_0}\right)\right]$$
$$- \frac{1}{2i}\left[\frac{1}{2}\ln\left(f_0^2 + k^2R^2\right) + i\arctan\left(\frac{-kR}{f_0}\right)\right] - kR$$
$$= \arctan\left(\frac{kR}{f_0}\right) - kR = \beta_0 + \varphi_0 \tag{2.139}$$

with

$$\beta_0 = \arctan\left(\frac{kR}{f_0}\right) \qquad \text{and} \qquad \varphi_0 = -kR \tag{2.140}$$

The phase shift δ_0 is expressed as a sum of two terms. The first term, β_0, depends on the scattering potential through f_0 and can give rise to resonances. The second term, φ_0, is independent of the scattering potential. It corresponds to the phase shift for hardsphere scattering, since $\delta_0 = \varphi_0$ for $f_0 \to \infty$ (or $u(R) = 0$).

2.5.3 Breit–Wigner Formulas

The logarithmic derivative at the boundary, f_0, has to be known to calculate $\sigma_{\mathrm{el},0}$ and $\sigma_{\mathrm{re},0}$. For the derivation of f_0, we need to make some assumptions regarding the wave function in the nuclear interior ($r < R$). Remember that the general solution with constant wave number K in the interior (see Eqs. (2.55) and (2.84))

$$u_{\mathrm{in}} = Ae^{iKr} + Be^{-iKr} \tag{2.141}$$

only applies for the simple assumption of a constant potential $V(r) = \text{const}$ (Section 2.4). The nuclear potential will be rather complicated since for $r < R$ the wave function of the incident particle will depend on the variables of all the other nucleons involved. Nevertheless, we will approximate the interior wave function, in the closest vicinity of the nuclear boundary only, by the above expression.

The complex amplitudes A and B depend on the properties of the nuclear system. We have to allow for a phase difference ζ between incoming (e^{-iKr}) and outgoing (e^{iKr}) spherical waves. Furthermore, one has to account for the possibility that the particle is absorbed in the nuclear interior because of reaction processes, that is, the amplitude of the outgoing wave e^{iKr} will generally be smaller than the amplitude of the incoming wave e^{-iKr}. We start with the ansatz

$$A = Be^{2i\zeta}e^{-2q} \tag{2.142}$$

where both ζ and q are real numbers. We also require $q \geq 0$ since no more particles can return than entered the nucleus originally. From Eqs. (2.141) and (2.142), one finds

$$\begin{aligned} u_{\mathrm{in}} &= Be^{2i\zeta}e^{-2q}e^{iKr} + Be^{-iKr} = \frac{B}{2}\left[e^{-i(Kr+\zeta+iq)} + e^{i(Kr+\zeta+iq)}\right]2e^{(i\zeta-q)} \\ &= 2Be^{(i\zeta-q)}\cos(Kr+\zeta+iq) \end{aligned} \tag{2.143}$$

The logarithmic derivative of the radial wave function must be continuous at $r = R$. Substitution of Eq. (2.143) into Eq. (2.129) yields

$$\begin{aligned} f_0 &= R\left(\frac{1}{u_{\mathrm{in}}(r)}\frac{du_{\mathrm{in}}(r)}{dr}\right)_{r=R} = R\frac{-2Be^{(i\zeta-q)}K\sin(KR+\zeta+iq)}{2Be^{(i\zeta-q)}\cos(KR+\zeta+iq)} \\ &= -KR\tan(KR+\zeta+iq) \end{aligned} \tag{2.144}$$

Clearly, f_0 depends on the energy-dependent quantities K, ζ, and q. If one knew these variables, then one could calculate resonance energies and cross sections directly from the properties of the nuclear interior. Unfortunately, this is not the case. Thus, our strategy will be to express the cross sections σ_{el} and σ_{re} near a single resonance in terms of measurable quantities.

We will assume that the argument of the tangent, $KR + \zeta + iq$, is a smooth function of energy, E. Furthermore, if $q = 0$ then f_0 becomes real, and the reaction cross section disappears. Recall that a resonance corresponds to a large wave function amplitude in the nuclear interior, implying a slope of zero for the radial wave function at $r = R$ (Figure 2.10). One can define *formal resonance energies*, E_λ, by the condition

$$f_0(E_\lambda, q) = -KR \tan(KR + \zeta + iq) = 0 \tag{2.145}$$

There is a whole set of such energies. Let us consider any one of them and study the behavior of f_0 near E_λ.

In the following, it is assumed that the absorption in the nuclear interior is weaker than the elastic scattering process, that is, $|q| \ll 1$. Expansion of $f_0(E, q)$ near E_λ and $q = 0$ into a Taylor series in both q and E gives

$$f_0 \approx f_0(E_\lambda, q) + (E - E_\lambda)\left(\frac{\partial f_0}{\partial E}\right)_{E_\lambda, q=0} + q\left(\frac{\partial f_0}{\partial q}\right)_{E_\lambda, q=0} \tag{2.146}$$

For the last term, one finds with Eq. (2.144)

$$q\left(\frac{\partial f_0}{\partial q}\right)_{E_\lambda, q=0} = -qKR\left[\frac{\partial}{\partial q}\tan(KR + \zeta + iq)\right]_{E_\lambda, q=0} = -iqKR \tag{2.147}$$

since at the resonance energy, E_λ, one has $\tan x = 0$ (see Eq. (2.145)) and thus $d(\tan x)/dx = \cos^{-2} x = 1$. It follows

$$f_0 \approx (E - E_\lambda)\left(\frac{\partial f_0}{\partial E}\right)_{E_\lambda, q=0} - iqKR = \mathrm{Re}\, f_0 + i\,\mathrm{Im}\, f_0 \tag{2.148}$$

Recall that $(\partial f_0/\partial E)_{E_\lambda, q=0}$ is a real quantity since $q = 0$ implies a vanishing reaction cross section. Substitution of Eq. (2.148) into Eqs. (2.136) and (2.137) gives for the resonance scattering amplitude and the reaction cross section

$$A_{\mathrm{res}} = \frac{-\frac{2ikR}{(\partial f_0/\partial E)_{E_\lambda, q=0}}}{(E - E_\lambda) - \frac{i(kR + qKR)}{(\partial f_0/\partial E)_{E_\lambda, q=0}}} \tag{2.149}$$

$$\sigma_{\mathrm{re},0} = \frac{\pi}{k^2}\frac{\frac{(2kR)(2qKR)}{(\partial f_0/\partial E)^2_{E_\lambda, q=0}}}{(E - E_\lambda)^2 + \frac{(qKR + kR)^2}{(\partial f_0/\partial E)^2_{E_\lambda, q=0}}} \tag{2.150}$$

We introduce the following definitions (the subscripts e and r stand for *elastic* and *reaction*, respectively):

$$\Gamma_{\lambda e} \equiv -\frac{2kR}{\left(\partial f_0/\partial E\right)_{E_\lambda, q=0}} \qquad \text{(particle width)} \tag{2.151}$$

$$\Gamma_{\lambda r} \equiv -\frac{2qKR}{\left(\partial f_0/\partial E\right)_{E_\lambda, q=0}} \qquad \text{(reaction width)} \tag{2.152}$$

$$\Gamma_\lambda \equiv \Gamma_{\lambda e} + \Gamma_{\lambda r} \qquad \text{(total width)} \tag{2.153}$$

Only the quantity $\Gamma_{\lambda r}$ depends on the parameter q describing absorption in the nuclear interior. The new quantities $\Gamma_{\lambda e}$, $\Gamma_{\lambda r}$, and Γ_λ have units of energy since f_0, kR, and KR are dimensionless. All widths refer to the resonance λ of interest. Also, f_0 depends on the channel through which the reaction is initiated. Rewriting Eqs. (2.149) and (2.150) in terms of the newly defined quantities yields, after some algebra, for the elastic scattering and reaction cross sections (see Eqs. (2.135) and (2.137))

$$\begin{aligned}\sigma_{el,0} &= \frac{\pi}{k^2}\left|\frac{i\Gamma_{\lambda e}}{(E-E_\lambda)+i\Gamma_\lambda/2} + e^{2ikR} - 1\right|^2 \\ &= \frac{\pi}{k^2}\left[2 - 2\cos(2kR)\right. \\ &\quad \left. + \frac{\Gamma_{\lambda e}^2 - \Gamma_{\lambda e}\Gamma_\lambda + \Gamma_{\lambda e}\Gamma_\lambda\cos(2kR) + 2\Gamma_{\lambda e}(E-E_\lambda)\sin(2kR)}{(E-E_\lambda)^2 + \Gamma_\lambda^2/4}\right]\end{aligned} \tag{2.154}$$

$$\sigma_{re,0} = \frac{\pi}{k^2}\frac{\Gamma_{\lambda e}\Gamma_{\lambda r}}{(E-E_\lambda)^2 + \Gamma_\lambda^2/4} \tag{2.155}$$

The last two expressions are referred to as *Breit–Wigner formulas* for s-wave neutrons.

Plots of $\sigma_{el,0}$ and $\sigma_{re,0}$ for incident neutrons versus energy E near a resonance are shown in Figure 2.20. We use the values $R = 3$ fm and $E_\lambda = 1$ MeV and assume energy-independent partial widths of $\Gamma_\lambda = 10.1$ keV and $\Gamma_{\lambda e} = 10$ keV. Several interesting aspects can be noticed. First, the full width at half maximum (FWHM) of the $\sigma_{re,0}$ curve (FWHM = 10.1 keV) corresponds precisely to the value of Γ_λ. Therefore, we identify this parameter with the *total resonance width*. The quantities $\Gamma_{\lambda e}$ and $\Gamma_{\lambda r}$ correspond then to *partial widths* for the scattering and reaction channel, respectively. Second, far away from the resonance ($|E - E_\lambda| \gg \Gamma_\lambda$) only the hardsphere potential scattering amplitude A_{pot} will contribute to the cross section. We obtain from Eq. (2.154) a value of $\sigma_{el,0} \approx (2\pi/k^2)[1 - \cos(2kR)] \approx 100\ \text{fm}^2$, shown as dashed line in Figure 2.20. Third, the numerator in the expression for $\sigma_{el,0}$ (see Eq. (2.154)) contains an interference term $2\Gamma_{\lambda e}(E - E_\lambda)\sin(2kR)$, which will change sign below and above the resonance. The structure seen in Figure 2.20a is caused by destructive ($E < E_\lambda$) and constructive ($E > E_\lambda$) interference of A_{res} and A_{pot}. This interference also causes FWHM in the elastic scattering cross section at the resonance to be different from the value of Γ_λ. Fourth, remember that a resonance corresponds

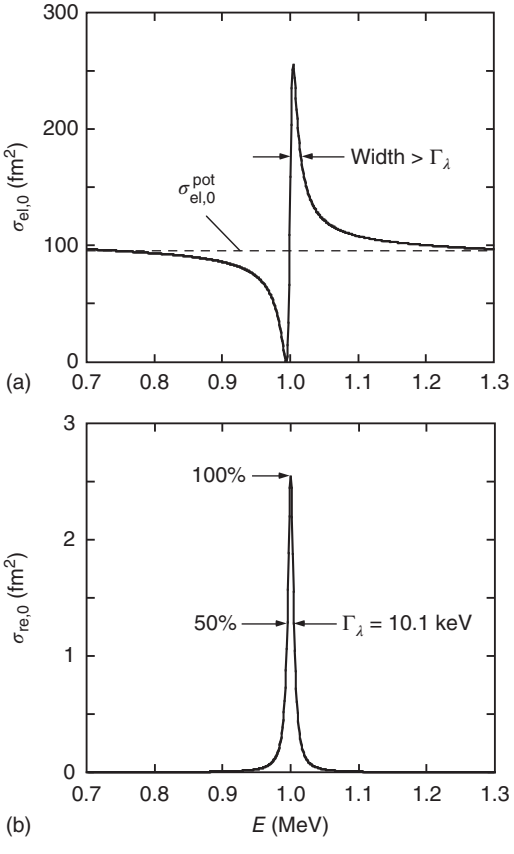

Figure 2.20 Plots of (a) $\sigma_{el,0}$ and (b) $\sigma_{re,0}$ versus energy E for incident neutrons near a resonance at $E_\lambda = 1$ MeV. A value of $R = 3$ fm is chosen for the radius. The widths are assumed to be energy independent with values of $\Gamma_\lambda = 10.1$ keV and $\Gamma_{\lambda e} = 10$ keV. See discussion in the text.

to a value of zero for the logarithmic derivative f_0 at the nuclear boundary. The implication is that in the scattering process the particle enters the nucleus with significant probability only near resonance. Off resonance the particle is almost entirely reflected at the boundary, and the wave function inside is weak. The resonance scattering is thus ascribed to the inside of the nucleus and the potential scattering to its surface.

The present results help us understand the complicated structures observed in the scattering cross sections for an explicit nuclear potential, as shown in Figure 2.18. The structures are caused, in part, by interference effects between the re-emission of the incident particle by the nucleus and the scattering near the nuclear surface. An additional complication is introduced because single-particle potential models predict several resonances that may interfere with each other.

We consider now the elastic scattering phase shift near a resonance, $\delta_0 = \beta_0 + \varphi_0 \approx \beta_0$. For Im $f_0 = 0$ ($q = 0$), we obtain from Eqs. (2.139), (2.148), and (2.151)

$$\beta_0 \approx \arctan\left[\frac{kR}{(E - E_\lambda)(\partial f_0/\partial E)_{E_\lambda, q=0}}\right] = \arctan\left[\frac{\Gamma_{\lambda e}}{2(E_\lambda - E)}\right] \tag{2.156}$$

At the resonance energy, $E = E_\lambda$, the argument of the arctan function becomes infinite and thus $\beta_0 = \pi/2$. Furthermore, since $d(\arctan x)/dx = (1 + x^2)^{-1}$, one finds for the energy derivative of the resonance elastic scattering phase shift at $E = E_\lambda$

$$\left(\frac{d\beta_0}{dE}\right)_{E_\lambda} = \frac{1}{2}\left[\frac{(d\Gamma_{\lambda e}/dE)(E_\lambda - E) + \Gamma_{\lambda e}}{(E_\lambda - E)^2 + (\Gamma_{\lambda e}/2)^2}\right]_{E_\lambda} = \frac{2}{(\Gamma_{\lambda e})_{E_\lambda}} \tag{2.157}$$

Hence, the resonance phase shift at $E = E_\lambda$ amounts to $\pi/2$, while its energy derivative determines the particle width. For the special case that $\Gamma_{\lambda e}$ is nearly constant with energy (e.g., for a narrow resonance), we find from Eq. (2.156) that $\beta_0 = \pi/4$ at $E = E_\lambda - \Gamma_{\lambda e}/2$ and $\beta_0 = 3\pi/4$ at $E = E_\lambda + \Gamma_{\lambda e}/2$. Thus, the particle width $\Gamma_{\lambda e}$ becomes equal to the energy interval over which β_0 increases from $\pi/4$ to $3\pi/4$. The above techniques involving the resonance phase shift are frequently employed for the calculation of particle partial widths.

Let us now consider the particle width $\Gamma_{\lambda e}$ in more detail. We define (see Eq. (2.151))

$$\Gamma_{\lambda e} = -\frac{2kR}{(\partial f_0/\partial E)_{E_\lambda, q=0}} \equiv 2P_0\gamma_{\lambda e}^2 \quad \text{with} \quad \gamma_{\lambda e}^2 \equiv -\left(\frac{\partial f_0}{\partial E}\right)^{-1}_{E_\lambda, q=0} \tag{2.158}$$

where the particle width has been split into two factors. The first factor, $P_0 = kR$, depends on the channel energy through the factor kR and on the conditions outside the nucleus. The second factor, $\gamma_{\lambda e}^2$, is called the *reduced width* and it incorporates all the unknown properties of the nuclear interior. The quantity $\gamma_{\lambda e}^2$ is characteristic of the resonance and the channel under consideration, and is independent of the channel energy E. The energy dependence of the partial widths $\Gamma_{\lambda e}$ and $\Gamma_{\lambda r}$ has to be taken into account when calculating the cross section for broad resonances, as will be explained in later sections.

2.5.4
Extension to Charged Particles and Arbitrary Values of Orbital Angular Momentum

The one-level Breit–Wigner formulas (see Eqs. (2.154) and (2.155)) have been obtained near a formal resonance energy E_λ assuming (i) neutrons as incident particles, (ii) an orbital angular momentum of $\ell = 0$, and (iii) interactions of spinless particles. The basic structure of the cross section expressions derived here is also applicable to the more general case. Although the general expressions are more complicated in appearance than the results for s-wave neutrons, no new physical ideas are involved. The properties of the nuclear interior enter into

the cross sections only through the logarithmic derivative f_ℓ of the wave function $u_\ell(r)$ at the nuclear boundary $r = R$.

In the following, the formulas will be generalized to arbitrary values of ℓ and to interacting charged particles. We will not derive the results in detail here (see, e.g., Blatt and Weisskopf, 1952) but will only sketch some results of the derivation. Of special interest to us is the modified reaction cross section $\sigma_{\mathrm{re},\ell}$.

The radial wave function solutions of the Schrödinger equation outside the nuclear surface are no longer given by incoming and outgoing spherical waves (e^{-ikr} and e^{ikr}), as in the case of $\ell = 0$ neutrons (see Eq. (2.131)), but are given in terms of the functions F_ℓ and G_ℓ. For neutrons, these represent spherical Bessel and Neumann functions, $F_\ell = (kr)j_\ell(kr)$ and $G_\ell = (kr)n_\ell(kr)$, respectively, while for charged particles they correspond to the regular and irregular Coulomb wave functions (Appendix A.3). The radial wave function outside the nuclear boundary is given in terms of F_ℓ and G_ℓ by

$$\begin{aligned} u_\ell(r) &= Au_\ell^+(r) + Bu_\ell^-(r), \quad r > R \\ &= Ae^{-i\sigma_\ell}[G_\ell(r) + iF_\ell(r)] + Be^{i\sigma_\ell}[G_\ell(r) - iF_\ell(r)] \end{aligned} \tag{2.159}$$

where u_ℓ^- and u_ℓ^+ correspond, for large distances, to incoming and outgoing spherical waves, respectively. The quantity σ_ℓ denotes the Coulomb phase shift and determines the purely Rutherford (electrostatic) scattering. For $\ell = 0$ neutrons, the above expression reduces to our previous result (Eq. (2.131); see Problem 2.4).

It is of advantage to introduce two real quantities, called *shift factor* S_ℓ and *penetration factor* P_ℓ, which are completely determined by the conditions outside the nucleus. We obtain with Eqs. (2.159) and (A.18)

$$\begin{aligned} &R\left(\frac{1}{u_\ell^+(r)}\frac{du_\ell^+(r)}{dr}\right)_{r=R} \\ &\quad = R\left[\frac{G_\ell(dG_\ell/dr) + F_\ell(dF_\ell/dr) + iG_\ell(dF_\ell/dr) - iF_\ell(dG_\ell/dr)}{F_\ell^2 + G_\ell^2}\right]_{r=R} \\ &\quad \equiv S_\ell + iP_\ell \end{aligned} \tag{2.160}$$

where

$$\begin{aligned} S_\ell &= R\left[\frac{F_\ell(dF_\ell/dr) + G_\ell(dG_\ell/dr)}{F_\ell^2 + G_\ell^2}\right]_{r=R} \quad \text{and} \\ P_\ell &= R\left(\frac{k}{F_\ell^2 + G_\ell^2}\right)_{r=R} \end{aligned} \tag{2.161}$$

The new quantities depend on the wave number k, the channel radius R, the orbital angular momentum ℓ, and on the charge parameter η (see Eq. (A.32)). For $\ell = 0$ neutrons, $F_\ell = (kr)j_0(kr) = \sin(kr)$ and $G_\ell = (kr)n_0(kr) = \cos(kr)$ (Appendix A.2), and we obtain from Eq. (2.160) $P_0 = kR$ and $S_0 = 0$. In other words, the shift factor vanishes without a barrier. With the quantities P_ℓ and S_ℓ,

the reaction cross section can be derived in a similar way as presented in the previous section. The calculation is not repeated here (see Blatt and Weisskopf, 1952). The result is the Breit–Wigner formula

$$\sigma_{\mathrm{re},\ell} = (2\ell + 1)\frac{\pi}{k^2}\frac{\Gamma_{\lambda\mathrm{e}}\Gamma_{\lambda\mathrm{r}}}{(E - E_r)^2 + \Gamma_\lambda^2/4} \tag{2.162}$$

with

$$\Gamma_{\lambda\mathrm{e}} \equiv -\frac{2P_\ell(E)}{(\partial f_\ell/\partial E)_{E_\lambda, q=0}} = 2P_\ell(E)\gamma_{\lambda\mathrm{e}}^2 \qquad \text{(particle width)} \tag{2.163}$$

$$\Gamma_{\lambda\mathrm{r}} \equiv -\frac{2qKR}{(\partial f_\ell/\partial E)_{E_\lambda, q=0}} \qquad \text{(reaction width)} \tag{2.164}$$

$$\Gamma_\lambda = \Gamma_{\lambda\mathrm{e}} + \Gamma_{\lambda\mathrm{r}} \qquad \text{(total width)} \tag{2.165}$$

$$E_r \equiv E_\lambda + \frac{S_\ell(E)}{(\partial f_\ell/\partial E)_{E_\lambda, q=0}} = E_\lambda - S_\ell(E)\gamma_{\lambda\mathrm{e}}^2 \qquad \text{(observed resonance energy)} \tag{2.166}$$

The similarity between Eq. (2.162) and the result obtained earlier for s-wave neutrons (see Eq. (2.155)) is apparent. The meaning of P_ℓ and S_ℓ becomes clear now. The penetration factor appears in the particle width expression since an incident particle must penetrate to the nuclear surface for a reaction to occur. The shift factor appears in the level shift expression and it causes the observed resonance energy E_r to be different from the formal resonance energy (or level energy) E_λ. Both the resonance energy shift and the particle width also depend on the properties of the nuclear interior through the reduced width $\gamma_{\lambda\mathrm{e}}^2$.

The penetration factor is closely related to the transmission coefficient. Both quantities describe the same physical concept, but are defined in slightly different ways. The former quantity is independent of the nuclear interior while the latter is defined in terms of the ratio of current densities in the interior and exterior regions (see Eqs. (2.62) and (2.103)). However, the energy dependences of both quantities should be very similar. The penetration factor can be calculated analytically for neutrons. The expressions are not repeated here (see Blatt and Weisskopf, 1952). It is sufficient to mention that for small neutron energies the neutron partial widths behave as $\Gamma_\ell(E) \sim P_\ell(E) \sim (kR)^{2\ell+1} \sim E^{\ell+1/2}$. For charged particles, on the other hand, the calculation of penetration factors is more involved. Various analytical approximations exist for estimating $P_\ell(E)$ (see, e.g., Clayton, 1983). The reader should be aware, however, that some of these approximations are not always accurate and that it is more reliable to compute penetration factors directly from numerical values of the Coulomb wave functions (Appendix A.3). The energy dependence of the s-wave penetration factor at low energies compared to the Coulomb barrier height ($E \ll V_C$) is given by Eqs. (2.124) and (2.125). For higher orbital angular momenta, the charged-particle penetration factors behave at low energies as $P_\ell(E) \sim \exp\left[-a/\sqrt{E} - b\ell(\ell+1)\right]$ (Problem 2.2), where the first exponential term represents the Gamow factor.

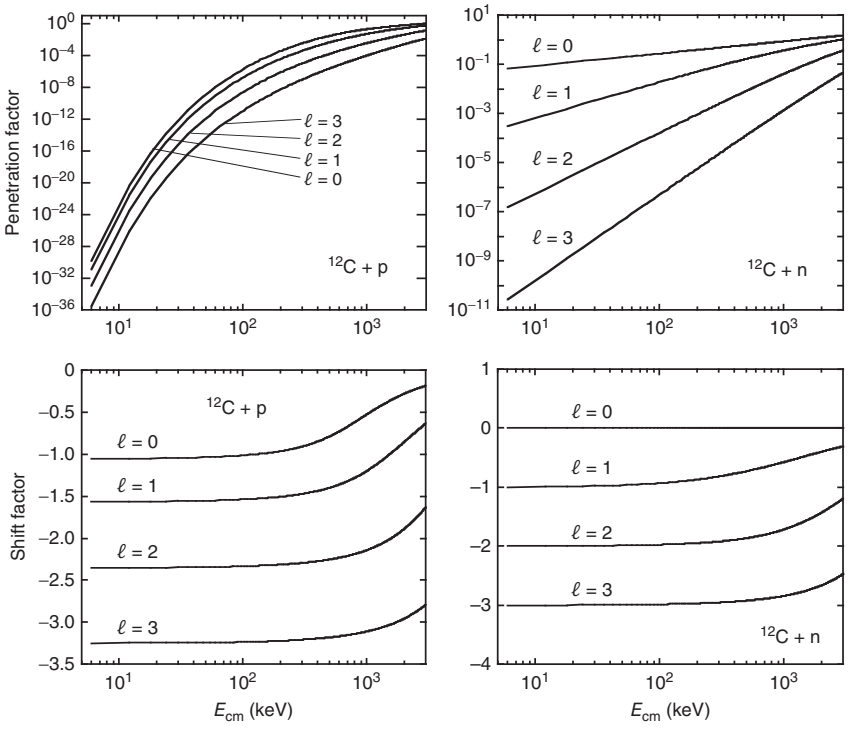

Figure 2.21 Penetration (top) and shift factors (bottom) for ^{12}C + p (left) and ^{12}C + n (right). In each panel, the curves show the results for orbital angular momenta of ℓ = 0, 1, 2, and 3. All curves are calculated for a radius of $R = 1.25(12^{1/3} + 1) = 4.1$ fm. The considerably stronger energy dependence of the penetration factor for protons compared to neutrons is apparent.

Numerical values for the factors P_ℓ and S_ℓ are displayed in Figure 2.21 for ^{12}C + p and ^{12}C + n to illustrate some important points. The curves are obtained using a radius of $R = 1.25(12^{1/3} + 1) = 4.1$ fm. The different energy dependences of P_ℓ for protons and neutrons is striking. The penetration factors for both protons and neutrons drop for decreasing energy, but the former values drop significantly faster since the Coulomb barrier has to be penetrated in addition to the centripetal barrier (for $\ell > 0$). The energy dependence of P_ℓ is similar for protons of all ℓ values, while for neutrons the energy dependence varies for different ℓ values. At higher energies ($E \approx 3$ MeV), we obtain $P_\ell \approx 1$ for protons and neutrons. The curve for the s-wave ($\ell = 0$) penetration factor of ^{12}C + n is simply given by $P_0 = kR$ (see earlier). The shift factors vary far less with energy than the penetration factors. For both neutrons and protons, S_ℓ is almost constant below an energy of a few hundred kilo electron volts. Also, one finds $S_0 = 0$ for neutrons, as already noted above.

The straight lines for $P_\ell(E)$ at low neutron energies in the log–log plot of Figure 2.21 are a consequence of the energy dependence $P_\ell(E) \sim E^{\ell+1/2}$.

The slopes of the curves are equal to $\ell + 1/2$ since $\log P_\ell(E) \sim \log E^{\ell+1/2} = (\ell + 1/2)\log E$. A similar procedure can be applied to charged particles. A graphic illustration of the energy dependence of the penetration factors for ^{12}C + p is given in Figure 2.22. Since we have $\log P_\ell(E) \sim -a/\sqrt{E} - b\ell(\ell+1)$, straight lines are obtained at low energies when $\log P_\ell(E)$ is plotted versus $-1/\sqrt{E}$. The slopes are similar at low energies where they are determined by the tunneling probability through the Coulomb barrier, while the intercepts depend on the value of ℓ. The straight lines shown in Figure 2.22 represent a useful tool when checking or interpolating values of $P_\ell(E)$ that are obtained numerically from computer codes.

Up to now we have not specified the reaction channel. Suppose that there are only two channels open for the resonance λ of interest, channel α and channel β. According to Eq. (2.162), the reaction cross sections near resonance in channels α and β are given by

$$\sigma_{\alpha,\mathrm{re},\ell} = (2\ell+1)\frac{\pi}{k_\alpha^2}\frac{\Gamma_{\lambda\alpha}\Gamma_{\lambda\mathrm{r}\alpha}}{(E_\alpha - E_{r\alpha})^2 + (\Gamma_{\lambda\alpha} + \Gamma_{\lambda\mathrm{r}\alpha})^2/4} = \sigma_{(\alpha,\beta)} \tag{2.167}$$

$$\sigma_{\beta,\mathrm{re},\ell} = (2\ell+1)\frac{\pi}{k_\beta^2}\frac{\Gamma_{\lambda\beta}\Gamma_{\lambda\mathrm{r}\beta}}{[(E_\alpha + Q) - (E_{r\alpha} + Q)]^2 + (\Gamma_{\lambda\beta} + \Gamma_{\lambda\mathrm{r}\beta})^2/4} = \sigma_{(\beta,\alpha)} \tag{2.168}$$

It follows directly from the reciprocity theorem, $k_\alpha^2\sigma_{(\alpha,\beta)} = k_\beta^2\sigma_{(\beta,\alpha)}$ (see Eq. (2.13)), that the reaction width of the (α,β) reaction is equal to the entrance channel width of the (β,α) reaction, and vice versa.

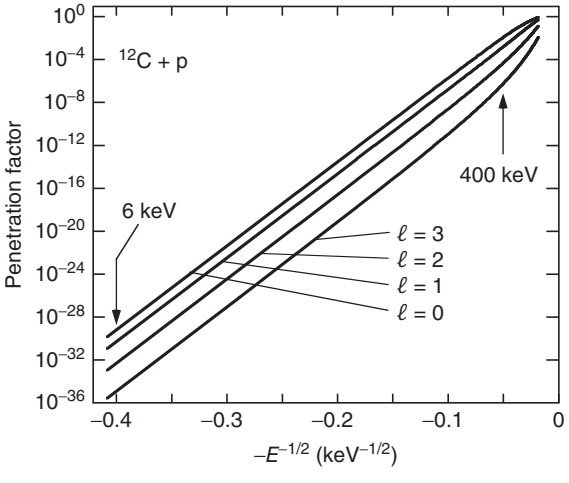

Figure 2.22 Penetration factor versus $-1/\sqrt{E}$ for the ^{12}C + p reaction. At low energies compared to the Coulomb barrier height ($E \ll V_C$), straight lines are obtained for each value of ℓ.

2.5.5 *R*-Matrix Theory

Let us summarize the assumptions we made in the derivation of the reaction cross section formula (see Eq. (2.162)): (i) the spins of the interacting nuclei are zero, (ii) the nucleus has a sharp radius, and (iii) a specific resonance corresponds to a logarithmic derivative of zero at the nuclear boundary. In the formal theory of resonance reactions (*R*-matrix theory), all of these assumptions are relaxed. We will not derive the formalism in any detail (see, e.g., Breit, 1959, or Lane and Thomas, 1958) but will instead present some of the main results. We are specifically interested in the application of the general theory to the case of a single and isolated resonance. As will be seen, the main physical ideas of the formalism developed so far will not change in the formal theory.

Consider again Eq. (2.148), but to describe the simplest possible case we will assume that elastic scattering is the only allowed process ($q = 0$). In that case,

$$f_0 = (E - E_\lambda)\left(\frac{\partial f_0}{\partial E}\right)_{E_\lambda, q=0} \tag{2.169}$$

By using the definitions of the logarithmic derivative f_0 (see Eq. (2.129)) and of the reduced width $\gamma^2_{\lambda e}$ (see Eq. (2.158)) we find near a particular level energy E_λ

$$\frac{1}{f_0} = \frac{1}{R}\left(\frac{u_{\text{in}}(r)}{du_{\text{in}}(r)/dr}\right)_{r=R} = \frac{(\partial f_0/\partial E)^{-1}_{E_\lambda, q=0}}{E - E_\lambda} = \frac{\gamma^2_{\lambda e}}{E_\lambda - E} \equiv \mathfrak{R} \tag{2.170}$$

The quantity $\mathfrak{R}$ is called *R-function*. When the energy E is not close to E_λ, the *R*-function is obtained by summing over all resonances λ. In general, elastic scattering will not be the only possible process, but other channels are present as well. To take these into account, the *R*-function becomes the *R-matrix*,

$$\mathfrak{R}_{c'c} = \sum_\lambda \frac{\gamma_{\lambda c'}\gamma_{\lambda c}}{E_\lambda - E} \tag{2.171}$$

Physically, the *R*-matrix relates the value of the wave function in the internal region to its derivative at each channel entrance. The above equation gives the energy dependence of the *R*-matrix explicitly in terms of the energy-independent parameters $\gamma_{\lambda c}$ and E_λ. The poles of the *R*-matrix, that is, the energies E_λ, are real and hence each of the elements $\mathfrak{R}_{c'c}$ represents a real number. Furthermore, the energies E_λ are independent of the channels c and c'. In other words, the poles of every matrix element $\mathfrak{R}_{c'c}$ occur at the same energies E_λ.

We need to be more precise when defining a *reaction channel c*. The quantity c denotes a set of quantum numbers $\{\alpha(I_1 I_2)s\ell, JM\}$ with

$\alpha(I_1 I_2)$	a specific pair of nuclei 1 and 2, with spins of I_1 and I_2, in a specific state of excitation (thus an excited state of 1 or 2 would correspond to a different α)

$\vec{s} = \vec{I}_1 + \vec{I}_2$	channel spin, with $\lvert I_1 - I_2 \rvert \leq s \leq I_1 + I_2$
ℓ	orbital angular momentum
$\vec{J}, M$	total spin and its component, with $\vec{J} = \vec{s} + \vec{\ell}$

For the entrance channel consisting of a projectile and a target nucleus, we set $\vec{I}_1 = \vec{j}_p$ and $\vec{I}_2 = \vec{j}_t$. Conservation of the total angular momentum restricts the possible J values of the resonance, which can be populated in the reaction to (Appendix B)

$$\vec{J} = \vec{\ell} + \vec{j}_p + \vec{j}_t \tag{2.172}$$

Each of these spins has $(2I + 1)$ orientations in space, which are determined by the magnetic quantum number $m_I = 0, 1, \ldots, \pm I$. Thus, there are $(2\ell + 1)(2j_p + 1)(2j_t + 1)$ different sets of spin orientations, corresponding to different quantum states of the system. For an unpolarized beam and target, each such state has the same probability, that is, $[(2\ell + 1)(2j_p + 1)(2j_t + 1)]^{-1}$. Therefore, the cross section has to be multiplied by the relative probability that the unpolarized projectiles and target nuclei will be found to have a total spin of J, given by

$$g(J) = \frac{2J + 1}{(2j_p + 1)(2j_t + 1)(2\ell + 1)} \tag{2.173}$$

From the R-matrix, the cross sections and phase shifts can be derived for any number of resonances and channels (Lane and Thomas, 1958). In the following, we will only focus on a particularly simple but useful case, that is, the reaction cross section near an isolated resonance λ of spin J. The one-level, many channel approximation of R-matrix theory (or generalized one-level Breit–Wigner formula) for the cross section of a reaction (α,α'), involving charged or neutral particles with projectile and target spins of j_p and j_t, is given by

$$\sigma_{\mathrm{re}}(\alpha, \alpha') = \frac{\pi}{k^2} \frac{2J + 1}{(2j_p + 1)(2j_t + 1)} \frac{\left(\sum_{\ell s} \Gamma_{\lambda c}\right)\left(\sum_{\ell' s'} \Gamma_{\lambda c'}\right)}{(E - E_\lambda - \Delta_\lambda)^2 + \Gamma_\lambda^2/4} \tag{2.174}$$

with

$$\Gamma_{\lambda c}(E) = 2P_c(E)\gamma_{\lambda c}^2 \qquad \text{(particle width)} \tag{2.175}$$

$$\Gamma_\lambda(E) = \sum_{c''} \Gamma_{\lambda c''}(E) \qquad \text{(total width)} \tag{2.176}$$

$$\Delta_\lambda(E) = \sum_{c''} \Delta_{\lambda c''}(E) \qquad \text{(total level shift)} \tag{2.177}$$

$$\Delta_{\lambda c}(E) = -[S_c(E) - B_c]\gamma_{\lambda c}^2 \qquad \text{(partial level shift)} \tag{2.178}$$

$$\beta(E) = \arctan \frac{\Gamma_\lambda(E)}{2[E_\lambda - E + \Delta_\lambda(E)]} \qquad \text{(resonance elastic scattering phase shift)} \tag{2.179}$$

The parameter B_c will be described later. The penetration and shift factors refer to the nuclear radius. In principle, one can chose an arbitrary radius beyond the range of the nuclear force so that the external wave functions reflect the solutions of the wave equation containing only the Coulomb interaction. However, it is also desirable to chose R as small as possible so that the characteristic quantities of the resonance theory contain primarily information concerning the nuclear interaction. Commonly, the interaction radius R is the smallest separation distance of the nuclear pair at which the nuclear potential is negligible. This radius is customarily chosen in R-matrix theory as $R = r_0(A_t^{1/3} + A_p^{1/3})$, with a radius parameter in the range of $r_0 = 1.0$–1.5 fm.

The above expression for the reaction cross section (see Eq. (2.174)) contains certain complications with respect to practical applications. This comes about because, in general, the energy dependence of the penetration and shift factor has to be taken into account. The quantity P_c is strongly energy dependent, but the energy dependence of S_c is weak (Figure 2.21). The usual approximation procedure, called the *Thomas approximation* (Thomas, 1951), is to expand the level shift linearly with respect to energy. We call the energy at which the cross section $\sigma_{\mathrm{re}}(\alpha, \alpha')$ has a maximum the *observed resonance energy* E_r. It is defined by the requirement

$$E_r - E_\lambda - \Delta_\lambda(E_r) = 0 \tag{2.180}$$

The boundary condition parameter B_c in Eq. (2.178), defined as the real and arbitrary value of the logarithmic derivative of the radial wave function in channel c at the radius R, determines the eigenvalues E_λ (in previous sections, we used implicitly the zero derivative condition, $B_c = 0$). It is customarily chosen as $B_c = S_c(E_r)$ so that the level shift Δ at the observed resonance energy E_r becomes zero,

$$\Delta_{\lambda c}(E_r) = -[S_c(E_r) - S_c(E_r)]\gamma_{\lambda c}^2 = 0 \qquad \text{and} \qquad E_r = E_\lambda \tag{2.181}$$

With the expansion

$$\Delta_\lambda(E) \approx \Delta_\lambda(E_r) + (E - E_r)\left(\frac{d\Delta_\lambda}{dE}\right)_{E_r} \tag{2.182}$$

we obtain using Eq. (2.180)

$$E_\lambda + \Delta_\lambda - E \approx E_r - E + (E - E_r)\left(\frac{d\Delta_\lambda}{dE}\right)_{E_r} = (E_r - E)\left[1 - \left(\frac{d\Delta_\lambda}{dE}\right)_{E_r}\right] \tag{2.183}$$

Substitution into Eq. (2.174) yields

$$\sigma_{\mathrm{re}}(\alpha, \alpha') = \frac{\pi}{k^2}\frac{2J+1}{(2j_p+1)(2j_t+1)}\frac{\left(\sum_{\ell s}\Gamma_{\lambda c}\right)\left(\sum_{\ell' s'}\Gamma_{\lambda c'}\right)}{(E_r - E)^2[1 - (d\Delta_\lambda/dE)_{E_r}]^2 + \Gamma_\lambda^2/4} \tag{2.184}$$

Dividing the numerator and denominator by $[1-(d\Delta_\lambda/dE)_{E_r}]^2$ gives

$$\sigma_{\rm re}(\alpha,\alpha') = \frac{\pi}{k^2}\frac{2J+1}{(2j_p+1)(2j_t+1)}\frac{\left(\sum_{\ell s}\Gamma^o_{\lambda c}\right)\left(\sum_{\ell' s'}\Gamma^o_{\lambda c'}\right)}{(E_r-E)^2+(\Gamma^o_\lambda)^2/4} \tag{2.185}$$

where the *observed* widths $\Gamma^o_{\lambda i}$ are given in terms of the previously defined *formal* widths $\Gamma_{\lambda i}$ (see Eq. (2.175)) by

$$\Gamma^o_{\lambda c} \equiv \frac{\Gamma_{\lambda c}}{1-(d\Delta_\lambda/dE)_{E_r}} = \frac{\Gamma_{\lambda c}}{1+\left(\sum_{c''}\gamma^2_{\lambda c''}\frac{dS_{c''}}{dE}\right)_{E_r}} \tag{2.186}$$

The main advantage of using Eq. (2.185) compared to Eq. (2.174) is that the complication of an energy-dependent shift factor in the denominator is absent. Since the former expression has a simpler (Lorentzian) structure, it is used in the vast majority of applications. However, we had to introduce a new quantity. The reader must be careful when applying Eq. (2.185) in the analysis of experimental data. It has to be understood that the partial widths thus obtained represent *observed* widths. As can be seen from Eq. (2.186), the difference between *observed* and *formal* partial width may be substantial for levels with a large reduced width. We can also introduce an *observed* reduced width by writing

$$\Gamma^o_{\lambda c} = \frac{2P_c(E)\gamma^2_{\lambda c}}{1+\left(\sum_{c''}\gamma^2_{\lambda c''}\frac{dS_{c''}}{dE}\right)_{E_r}} = 2P_c(E)(\gamma^o_{\lambda c})^2 \tag{2.187}$$

As a general guide, partial widths have to be interpreted as *observed* quantities whenever a Lorentzian structure is assumed for the cross section (e.g., in reaction rate calculations, mean lifetime measurements, or thick target yields).

Finally, we express the resonance phase shift and its energy derivative in terms of the *observed* total width. We obtain from Eqs. (2.179) and (2.183) immediately

$$\beta = \arctan\frac{\Gamma_\lambda/[1-(d\Delta_\lambda/dE)_{E_r}]}{2(E_r-E)} = \arctan\frac{\Gamma^o_\lambda}{2(E_r-E)} \tag{2.188}$$

and, similar to Eq. (2.157),

$$\left(\frac{d\beta}{dE}\right)_{E_r} = \frac{2}{(\Gamma^o_\lambda)_{E_r}} \tag{2.189}$$

This expression is frequently used in calculations of *observed* particle partial widths (see Section 2.5.7).

2.5.6
Experimental Tests of the One-Level Breit–Wigner Formula

The total cross section for neutrons incident on a target consisting of a natural isotopic mixture of cadmium is shown in Figure 2.23. The data are fitted by a one-level Breit–Wigner formula, superimposed on a $1/v$ background (Section 2.6).

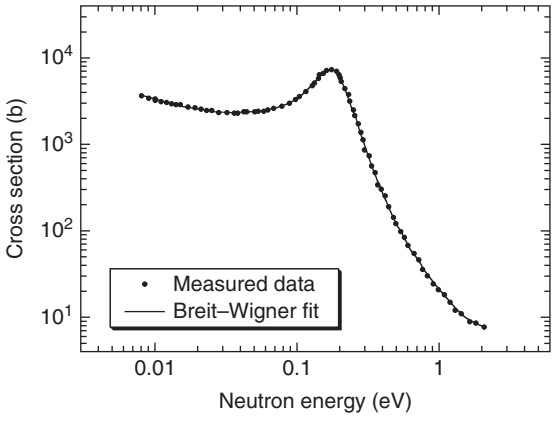

Figure 2.23 Total cross section for neutrons incident on a target consisting of a natural isotopic mixture of cadmium. The data are fitted by a one-level Breit–Wigner formula, superimposed on a $1/v$ background. The deduced resonance parameters are $E_\lambda = 0.176$ eV, $\Gamma = 0.115$ eV, and $\sigma_{max} = 7.2 \times 10^{-21}$ cm^2. The Breit–Wigner formula reproduces the shape of resonances accurately if their widths are small compared to their energy separation. Data from Goldsmith, Ibser, and Feld (1947).

The prediction agrees with the data. The Breit–Wigner formula describes reliably the shape of resonances if their widths are small compared to their energy separation.

The resonance reaction theory developed so far does not only apply to unbound states but also apply to bound states as well. In the latter case, the Breit–Wigner formula allows for the calculation of the cross section wing of a *subthreshold resonance* (Example 2.1). The Breit–Wigner formula has important applications in nuclear astrophysics, especially in cases where the cross section of interest cannot be measured directly and has to be estimated theoretically. For example, consider the following situation that is frequently encountered in practice. Data have been obtained in some higher lying bombarding energy range. The energy range of interest for stellar fusion, however, is located outside the range for which data have been measured. By fitting the existing data to a Breit–Wigner formula, one obtains the resonance energy and widths as phenomenological parameters, which can then be used to extrapolate the cross section to the energy region of interest.

Frequently, the widths of astrophysically important resonances are rather small (less than a few electron volts) and it is experimentally no longer feasible to measure the cross section directly at specific energies near the resonance. What is directly measured in such cases is the integral under the resonance cross section curve. The Breit–Wigner formula provides an accurate equation for integrating the resonance cross section, resulting in convenient analytical expressions for narrow-resonance reaction rates (Section 3.2.4) and thick-target yields (Section 4.8.1).

The total cross section for several overlapping resonances of different spins and parities can be described by an incoherent sum of one-level Breit–Wigner formulas. If two resonances have the same J^π value, however, they may interfere and the resulting expressions become more complicated. Also, the differential cross sections of two broad resonances may interfere even if their J^π values are different.

It must be emphasized again that the resonance theory described here is not capable of predicting resonance energies and widths. These quantities are treated as phenomenological parameters. Absolute cross sections can be obtained, for example, by fitting resonance data. Cross sections can also be obtained if the resonance energies and partial (or reduced) widths are independently known from other sources (Section 2.5.7). In the following numerical example, the one-level Breit–Wigner formula will be applied to a subthreshold resonance.

Example 2.1

The Q-value of the ^{20}Ne(p,γ)^{21}Na reaction amounts to $Q = 2431.3$ keV. The ^{21}Na level at $E_x = 2425$ keV ($J^\pi = 1/2^+$) is located just below the proton threshold and corresponds to a subthreshold s-wave ($\ell = 0$) resonance at a center-of-mass energy of $E_r = -6.4$ keV (Figure 2.24a). The (formal) reduced proton width for this level can be obtained from (d,n) proton transfer reaction measurements (Terakawa *et al.*, 1993). The value is $\gamma^2_{\mathrm{p},\ell=0} = 1.41 \times 10^6$ eV. The $E_x = 2425$ keV level decays to the ground state with a probability (branching ratio) of 1 (100%) via emission of M1/E2 radiation (Appendix B). The value of the (formal) γ-ray partial width at E_r, obtained from the measured mean lifetime of the state (Anttila, Keinonen, and Bister, 1977), amounts to $\Gamma_\gamma(E_r) = 0.30$ eV. Calculate the contribution of this level to the astrophysical S-factor (the S-factor is defined in Section 3.2.1) versus bombarding energy below 2 MeV.

In this case, only two channels are open. The level can decay via emission of either a proton or a γ-ray. We may write the Breit–Wigner formula (see Eq. (2.174)) as

$$\sigma_{^{20}\mathrm{Ne+p}}(\mathrm{p},\gamma) = \frac{\pi}{k^2}\frac{2J+1}{(2j_p+1)(2j_t+1)}\frac{\Gamma_{\mathrm{p},\ell=0}\Gamma_{\gamma,\mathrm{M1/E2}}}{(E-E_\lambda-\Delta_\lambda)^2+(\Gamma_{\mathrm{p},\ell=0}+\Gamma_{\gamma,\mathrm{M1/E2}})^2/4}$$

The cross section has a maximum at the observed resonance energy $E_r = E_\lambda + \Delta_\lambda(E_r) = E_\lambda$ (see Eqs. (2.180) and (2.181)) since we chose the boundary condition as $\Delta_\lambda(E_r) = 0$. Therefore, we set $E_\lambda = -6.4$ keV. We find the energy-dependent proton width from the expression $\Gamma_{\mathrm{p},\ell=0}(E) = 2P_{\ell=0}(E)\gamma^2_{\mathrm{p},\ell=0}$ (see Eq. (2.175)). The energy dependence of the γ-ray partial width is given by $\Gamma_{\gamma,L} \sim E_\gamma^{2L+1}$ (see Eq. (1.22)), with E_γ the γ-ray energy and L the γ-ray multipolarity. The M1/E2 multipolarity mixing ratio (see Eq. (1.32)) for this level is not known. It is sufficient to assume here that the transition to the ground state ($E_f = 0$) proceeds via pure M1 emission. Thus

$$\frac{\Gamma_{\gamma,\mathrm{M1}}(E)}{\Gamma_{\gamma,\mathrm{M1}}(E_r)} = \left[\frac{E_\gamma(E)}{E_\gamma(E_r)}\right]^{2L+1} = \left[\frac{E+Q-E_f}{E_r+Q-E_f}\right]^{2L+1} = \left[\frac{E+Q}{E_r+Q}\right]^3$$

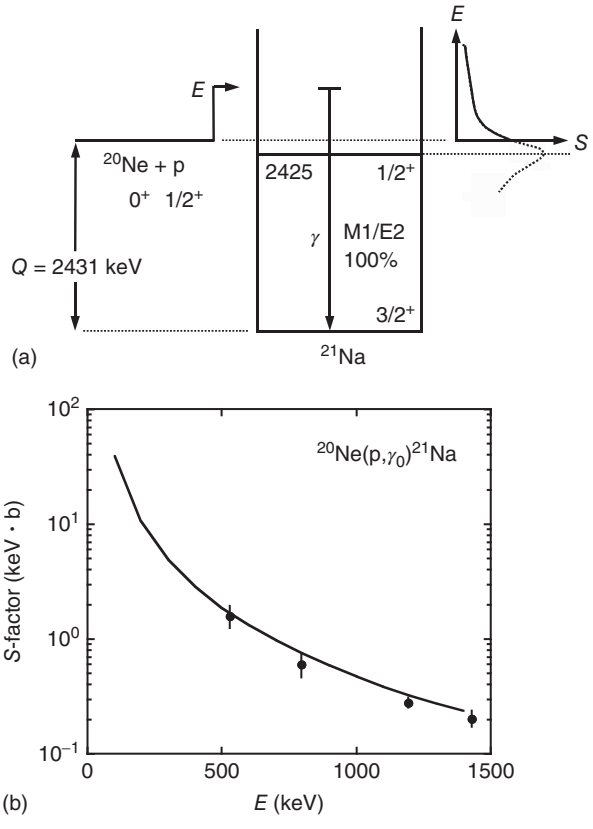

Figure 2.24 (a) Level scheme of ^{21}Na showing a subthreshold s-wave ($\ell = 0$) resonance in ^{20}Ne + p, corresponding to a level at E_x = 2425 keV ($J^\pi = 1/2^+$), which is located just below the proton threshold. (b) Astrophysical S-factor of the ^{20}Ne(p,γ)^{21}Na reaction versus center-of-mass proton energy for the γ-ray transition to the ground state of ^{21}Na. The data points display the measured S-factor (from Rolfs and Rodney, 1975), while the solid line shows the result of the calculation explained in the text. The solid line is not a fit to the data. The agreement between data and calculation is remarkable since the Breit–Wigner formula had to be extrapolated over more than 10^6 resonance widths.

The influence of the γ-ray channel on the level shift can be neglected. From Eqs. (2.177) and (2.178), one finds

$$\Delta_\lambda(E) \approx \Delta_{\mathrm{p},\ell=0}(E) = -[S_{\ell=0}(E) - S_{\ell=0}(E_r)]\gamma^2_{\mathrm{p},\ell=0}$$

We obtain from the definition of the astrophysical S-factor (see Eq. (3.71))

$$S_{^{20}\mathrm{Ne+p}}(\mathrm{p},\gamma) = E\, e^{2\pi\eta}\sigma_{^{20}\mathrm{Ne+p}}(p,\gamma)$$

$$= \frac{Ee^{2\pi\eta}\,\frac{\pi}{k^2}\,\frac{2J+1}{(2j_p+1)(2j_t+1)}\,2P_{\ell=0}(E)\gamma^2_{\mathrm{p},\ell=0}\Gamma_{\gamma,\mathrm{M1}}(E_r)\left(\frac{E+Q}{E_r+Q}\right)^3}{\left\{E - E_r + [S_{\ell=0}(E) - S_{\ell=0}(E_r)]\gamma^2_{\mathrm{p},\ell=0}\right\}^2 + [\Gamma(E)]^2/4}$$

with $\Gamma(E) = \Gamma_{\mathrm{p},\ell=0}(E) + \Gamma_{\gamma,\mathrm{M1}}(E)$. Numerically we find (with E in MeV and M_i in u)

$$2\pi\eta = 0.989510\, Z_p Z_t \sqrt{\frac{1}{E}\frac{M_t M_p}{M_t + M_p}}$$

$$E\frac{\pi}{k^2} = 6.56618216 \times 10^{-1}\frac{M_t + M_p}{M_t M_p} \qquad \text{(MeV b)}$$

$$\frac{2J+1}{(2j_p+1)(2j_t+1)} = \frac{2\cdot\frac{1}{2}+1}{\left(2\cdot\frac{1}{2}+1\right)(2\cdot 0+1)} = 1$$

$$S_{\ell=0}(E_r) = -1.537$$

The penetration and shift factors are directly computed from the Coulomb wave functions (see Eq. (2.161)). The resulting calculated S-factor for the ground-state transition in the ^{20}Ne(p,γ)^{21}Na reaction is shown as a solid line in Figure 2.24b. The data points display the experimental S-factor. These results represent one of the very few examples in nuclear physics where a tail of a subthreshold resonance is observed without interference from unbound states or direct radiative capture.

It must be emphasized that the solid line does not represent a fit to the data. It is calculated using the Breit–Wigner formula with parameters (resonance energy, proton and γ-ray partial widths) that are obtained from independent experiments (i.e., *not* from capture measurements). It should also be noted that the total width at the resonance energy amounts to $\Gamma(E_r) = \Gamma_\gamma(E_r) = 0.3$ eV. In other words, the S-factor is extrapolated over 1500 keV/0.3 eV $= 5 \times 10^6$ resonance widths. The agreement between experiment and calculation is remarkable and provides strong support for the applicability of the Breit–Wigner formula to isolated resonances.

2.5.7 Partial and Reduced Widths

We have seen how the resonance cross section can be expressed in terms of resonance energies and reduced widths. For some reactions, however, no cross section data are available. In such cases, it becomes important to estimate the cross section theoretically. The Breit–Wigner formula can only be used for this purpose if the resonance energies and reduced widths are known from independent sources (see Example 2.1).

Resonances that are generated by simple explicit potentials are discussed in Section 2.4. Such *single-particle resonances* are generally broad at higher bombarding energies and their energy separation is large. In contrast to these, many measured resonances are very narrow and their spacing is small (Figure 2.19). These resonances could not be explained by single-particle potentials and it was therefore necessary to develop a theory of resonances without reference to a

specific nuclear potential (Section 2.5.1). The reduced widths depend on, as yet unknown, properties of the nuclear interior and are treated as phenomenological parameters.

According to Bohr (1936), the observed resonances correspond to virtual states in the nucleus. These virtual states are not single-particle levels, but are the result of the interactions of many nucleons. This many-nucleon picture is also referred to as *compound nucleus description*. The close spacing of the observed resonances is then explained by the many different ways a large number of nucleons can be excited. The observed resonances are then caused by the rapid variation of the total nuclear wave function of the target-plus-projectile system with energy. In the following, we will develop this picture quantitatively. Our goal will be to relate the reduced widths to nuclear properties, which can be estimated using models of nuclear structure.

Consider the total wave function of the target-plus-projectile system, Ψ, with $H\Psi = E\Psi$. The total Hamiltonian H, although unknown, may be written as

$$\begin{aligned} H &= H_{\xi}^{t} + E_{K}^{p}(r) + \sum_{i=1}^{A} V_i(\xi_i, x) \\ &= \left[H_{\xi}^{t} + E_{K}^{p}(r) + \overline{V}(r)\right] + \left[-\overline{V}(r) + \sum_{i=1}^{A} V_i(\xi_i, x)\right] = H_0 + H' \end{aligned} \tag{2.190}$$

with H_{ξ}^{t} the Hamiltonian of the target nucleus consisting of A nucleons, $E_{K}^{p}(r)$ the kinetic energy of the projectile, $V_i(\xi_i, x)$ the interactions between each target nucleon with the projectile, and $\overline{V}(r)$ an average potential of the projectile in the field of the target nucleus. The quantity H_0 is the single-particle Hamiltonian, and H' describes the *residual interaction* (i.e., the deviation from an average potential). Without the residual interaction, the potential $\overline{V}(r)$ would give rise to single-particle resonances, corresponding to single-particle levels in the target-plus-projectile system. However, the quantity H' causes the single-particle levels to split into a large number of distinct levels. Each of these states corresponds to a complicated mixture of configurations and is described by a complicated sum of wave functions. Consequently, the logarithmic derivative of the radial wave function at the nuclear boundary, that is, the reduced width $\gamma_{\lambda c}^2$, will in general be different for each virtual state. Such levels are described by the configurations of many nucleons and are referred to as *compound-nucleus levels*.

The situation is shown schematically in Figure 2.25. The single-particle Hamiltonian H_0 gives rise to the single-particle levels p_1, p_2, p_3, and p_4. The levels p_1 and p_2 are bound states. The Hamiltonian H causes a splitting of each single-particle level into many states. These can be observed as resonances in the cross section (thin solid line). However, the single-particle character does not get entirely lost. If the measured cross section curve is averaged over the observed fine structure, then the single-particle resonances are approximately recovered (thick solid line). We may also say that, in this picture, each reduced width $\gamma_{\lambda c}^2$ of an actual level belongs to a definite single-particle level p_i. The entire set of reduced

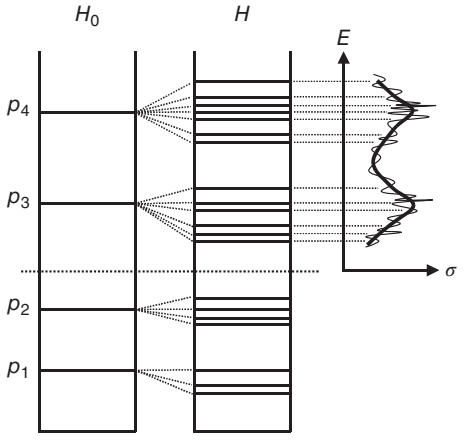

Figure 2.25 Level scheme and cross section versus energy. A single-particle Hamiltonian H_0 generates the single-particle levels p_1, p_2, p_3, p_4. The Hamiltonian H gives rise to a splitting of each single-particle level into many states. The latter show up as a fine structure in the cross section versus energy curve.

widths can then be split up into groups, each group corresponding to a definite value of p_i.

In the following, we will consider the simple case of only one open nucleon channel (elastic only) for compound nucleus formation or decay. It is useful at this point to express the particle width in a different way. We have seen that Γ_λ corresponds to the total width of a resonance λ, or the total width of a virtual level in the compound nucleus. A finite level width, in turn, implies a finite mean lifetime τ of the level, since $\Gamma_\lambda \tau_\lambda \approx \hbar$. Therefore, we can identify $1/\tau_\lambda \approx \Gamma_\lambda/\hbar$ with the decay (or formation) probability of the level per unit time. A partial width $\Gamma_{\lambda c}$ corresponds then to the decay (or formation) probability of level λ through a particular channel c. The decay of a compound nucleus state into two channels is shown schematically in Figure 2.26.

The partial width $\Gamma_{\lambda c}$ will now be determined from the flux of the particles through the only open channel c. The probability per unit time, $\Gamma_{\lambda c}/\hbar$, for the emission of a particle is given by the number of particles per second leaving the channel. This number can be calculated by integrating the current (see Eq. (2.45)) through a sphere of radius R over the full solid angle,

$$\frac{\Gamma_{\lambda c}}{\hbar} = \int_{d\Omega} R^2 j \, d\Omega = \int_{d\Omega} R^2 \frac{\hbar}{2mi} \left(\psi^* \frac{\partial \psi}{\partial r} - \frac{\partial \psi}{\partial r}^* \psi \right)_{r=R} d\Omega \tag{2.191}$$

With $\psi = Y(\theta, \phi) R_c(r) = Y(\theta, \phi) u_c(r)/r$ (Appendix A) we find

$$\begin{aligned} \frac{\Gamma_{\lambda c}}{\hbar} &= \frac{\hbar}{2mi} \int_{d\Omega} R^2 \left[\frac{u_c^*}{r} \frac{d}{dr} \left(\frac{u_c}{r} \right) - \frac{u_c}{r} \frac{d}{dr} \left(\frac{u_c^*}{r} \right) \right]_{r=R} |Y|^2 \, d\Omega \\ &= \frac{\hbar}{2mi} \int_{d\Omega} R^2 \frac{1}{R^2} \left(u_c^* \frac{du_c}{dr} - u_c \frac{du_c^*}{dr} \right)_{r=R} |Y|^2 \, d\Omega \end{aligned} \tag{2.192}$$

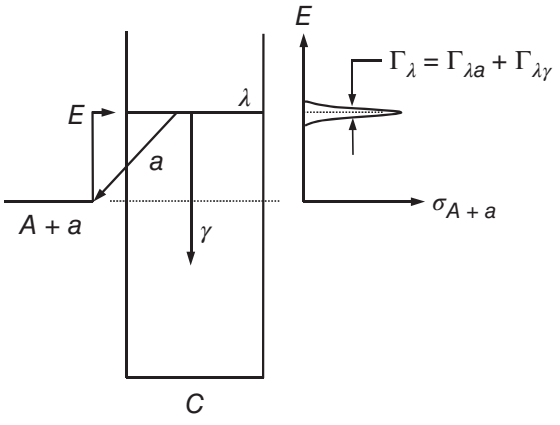

Figure 2.26 Level scheme of compound nucleus *C* showing a single unbound (or virtual) state λ that may decay by emission of particles (a) or photons (γ). The full width at half maximum (FWHM) of the resonance in the cross section versus energy curve corresponds to the total width Γ_λ, which is equal to the sum of all partial widths. The latter quantities are a measure for the decay (or formation) probability of level λ through a particular channel *c*.

The radial wave function u_c of the compound state can be expanded in terms of single-particle radial eigenfunctions u_{pc}, which form a complete set of orthonormal functions. The eigenfunctions u_{pc} describe a single nucleon moving in a single-particle potential. We may write

$$u_c(R) = \sum_p A_{\lambda pc} u_{pc}(R) \tag{2.193}$$

The above discussion of compound levels implies that, at a given energy, one particular single-particle state p contributes mainly to the width of level λ. This means that for a given level λ one of the terms in the sum of Eq. (2.193) is significantly larger than the others. Hence

$$u_c(R) \approx A_{\lambda pc} u_{pc}(R) \tag{2.194}$$

By using the normalization of the spherical harmonic Y and the definition of the logarithmic derivative, $f_{pc}(E) = R(u_{pc}^{-1}\, du_{pc}/dr)_{r=R}$ (see Eq. (2.129)), we obtain from Eqs. (2.192) and (2.194)

$$\begin{aligned}\Gamma_{\lambda c} &= \frac{\hbar^2}{2mi} A_{\lambda pc}^2 \left(u_{pc}^* \frac{du_{pc}}{dr} - u_{pc} \frac{du_{pc}^*}{dr} \right)_{r=R} \\ &= \frac{\hbar^2}{2miR} A_{\lambda pc}^2 \left(u_{pc}^* u_{pc} f_{pc} - u_{pc} u_{pc}^* f_{pc}^* \right)_{r=R} = \frac{\hbar^2 |u_{pc}(R)|^2}{2miR} A_{\lambda pc}^2 \left(f_{pc} - f_{pc}^* \right)\end{aligned} \tag{2.195}$$

Since we describe a decaying compound state, the radial wave function for $r > R$ is given by $u_{pc}(r) = A u_{pc}^+(r)$, that is, we have $B = 0$ for a purely outgoing wave (see Eq. (2.159)). This condition is equivalent to $f_{pc}(E) = S_c + iP_c$ (see Eq. (2.160)).

It follows that

$$\Gamma_{\lambda c} = \frac{\hbar^2 |u_{pc}(R)|^2}{2miR} A^2_{\lambda pc}[(S_c + iP_c) - (S_c - iP_c)] = 2\frac{\hbar^2}{mR^2} P_c A^2_{\lambda pc} \frac{R}{2} |u_{pc}(R)|^2 \quad (2.196)$$

This can be expressed as

$$\Gamma_{\lambda c} = 2\frac{\hbar^2}{mR^2} P_c \, C^2S \, \theta^2_{pc} \quad (2.197)$$

with

$$C^2S = A^2_{\lambda pc} \qquad \text{(spectroscopic factor)} \quad (2.198)$$

$$\theta^2_{pc} = \frac{R}{2} \left| u_{pc}(R) \right|^2 \qquad \text{(dimensionless single-particle reduced width)} \quad (2.199)$$

Comparison to Eq. (2.175) shows that the reduced width $\gamma^2_{\lambda c}$ has been reformulated in terms of a constant, $\hbar^2/(mR^2)$, and the quantities θ^2_{pc} and C^2S.

Strictly speaking, the quantities S and C^2 denote a spectroscopic factor (Section 1.6.2) and the square of an isospin Clebsch–Gordan coefficient, respectively. The former quantity is frequently calculated using the nuclear shell model (Section 1.6), while the latter depends on the nuclear reaction (see, e.g., Brussaard and Glaudemans, 1977). In the present context of partial widths, only the product C^2S is of interest. The spectroscopic factor depends on the many-nucleon structure of level λ and is a measure for the relative probability that a compound state λ can be described by the single-particle state p. The structure of Eq. (2.197) emphasizes that the partial width for nucleon emission from a compound level can be thought of as a product of three factors: (i) the probability that the nucleons will arrange themselves in a configuration corresponding to the final state, C^2S, (ii) the probability that the single nucleon will appear at the boundary, $|u_{pc}(R)|^2$, and (iii) the probability that the single nucleon will penetrate the Coulomb and angular momentum barriers, P_c. By introducing a single-particle partial width

$$\Gamma_{\lambda pc} = 2\frac{\hbar^2}{mR^2} P_c \theta^2_{pc} \quad (2.200)$$

we may also express Eq. (2.197) as

$$\Gamma_{\lambda c} = C^2S \, \Gamma_{\lambda pc} \quad (2.201)$$

In other words, the spectroscopic factor can be written as the ratio of the two quantities $\Gamma_{\lambda c}$ and $\Gamma_{\lambda pc}$. Since both of these partial widths are strongly energy dependent through the penetration factor P_c, they have to be calculated at the *same* incident energy E.

It is apparent that there are two different methods of estimating partial widths for nucleon channels once the spectroscopic factor C^2S has been obtained by independent means. If Eq. (2.197) is used, then the penetration factor P_c and the dimensionless single-particle reduced width θ^2_{pc} must be computed. On the other hand, if Eq. (2.201) is employed, then the single-particle partial width $\Gamma_{\lambda pc}$ has to be calculated. This can be achieved, for example, by solving the Schrödinger

equation numerically for the elastic scattering of nucleons by an appropriate single-particle potential (Schiffer, 1963; Iliadis, 1997). The single-particle partial width is then directly obtained from the slope of the resonance phase shift at the resonance energy (see Eq. (2.189)). The former method is computationally more convenient if values of θ_{pc}^2 are already available.

Numerical values of the dimensionless single-particle reduced width θ_{pc}^2 for protons are reported in Iliadis (1997) (Figure 2.27) and Barker (1998). The results were obtained by calculating u_{pc} for a Woods–Saxon single-particle potential (Section 1.6.1). The value of θ_{pc}^2 depends on the interaction radius, R, the orbital angular momentum, ℓ, and the number of nodes of the radial wave function in the nuclear interior. The numerical values shown in Figure 2.27 have been obtained with $R = 1.25(A_p^{1/3} + A_t^{1/3})$ fm. For estimates of $\Gamma_{\lambda c}$, the quantities θ_{pc}^2 and P_c have to be computed at the same radius R. The θ_{pc}^2 values from Iliadis (1997) represent *observed* quantities, while the results from Barker (1998) represent *formal* quantities. The dimensionless single-particle reduced width θ_{pc}^2 is frequently set equal to unity in the literature. In this case, a significant error is introduced in the estimation of partial widths.

Frequently, a resonance cannot be observed directly. This happens, for example, if the cross section is too small or if the target is radioactive. In such cases, the formalism discussed above can be used to estimate the absolute reaction cross

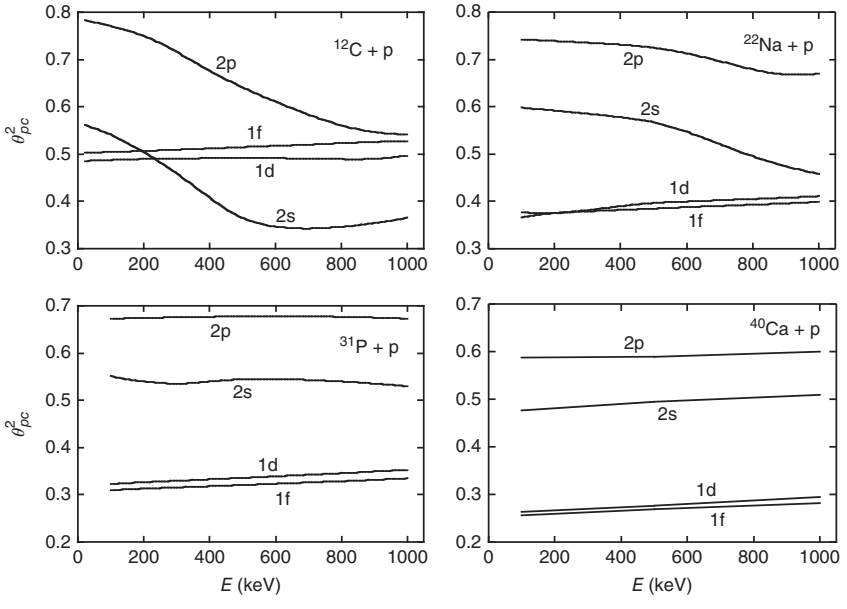

Figure 2.27 Observed dimensionless single-particle reduced width θ_{pc}^2 for ^{12}C + p, ^{22}Na + p, ^{31}P + p, and ^{40}Ca + p versus center-of-mass proton energy. In each panel, the curves correspond to different orbital angular momenta ($\ell = 0$, 1, 2, and 3) and have been computed for a radius of $R = 1.25(A_p^{1/3} + A_t^{1/3})$ fm.

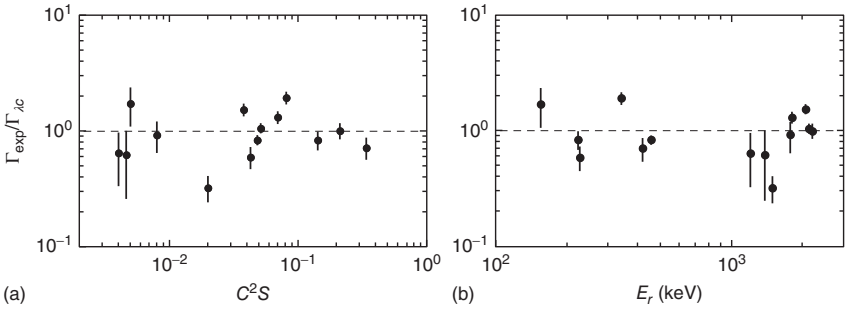

Figure 2.28 Ratio of measured and estimated proton partial widths, $\Gamma_{exp}/\Gamma_{\lambda c}$, for levels in ^{25}Al, ^{27}Al, and ^{31}P (a) versus the value of C^2S, and (b) versus the observed resonance energy E_r. The experimental proton widths Γ_{exp} were directly measured in resonance elastic proton scattering or proton capture reactions. The calculated values $\Gamma_{\lambda c}$ are obtained from Eq. (2.197) using spectroscopic factors measured in (^{3}He,d) transfer studies.

section. Once the spectroscopic factor is either calculated using the nuclear shell model (Section 1.6) or measured using transfer reactions, the particle partial width can be estimated in a straightforward way. The reaction cross section is then obtained by applying the Breit–Wigner formula.

It is interesting to investigate the reliability of Eq. (2.197) for the calculation of proton partial widths. Figure 2.28 shows a comparison of measured and estimated proton partial widths for compound levels in ^{25}Al, ^{27}Al, and ^{31}P. The ratio of partial widths, $\Gamma_{exp}/\Gamma_{\lambda c}$, is shown in Figure 2.28a versus the value of C^2S, and in Figure 2.28b versus the observed resonance energy E_r. The values of $\Gamma_{\lambda c}$ are estimated from Eq. (2.197) using proton spectroscopic factors measured in (^{3}He,d) transfer reactions and by computing θ_{pc}^2 and P_c numerically. The experimental proton widths Γ_{exp} were directly measured in resonance elastic proton scattering or proton capture reactions. The error bars of the displayed ratios consider only the uncertainties of the experimental proton widths. It can be seen that experimental and estimated proton partial widths agree on average within ≈50%. We expect that the parametrizations of $\Gamma_{\lambda c}$ (see Eqs. (2.197) and (2.201)) are more accurate than this since we have entirely neglected the errors in the measured transfer spectroscopic factors. Further systematic studies are needed.

Example 2.2

An important resonance in the ^{17}F(p,γ)^{18}Ne reaction occurs at a center-of-mass energy of $E_r = 600$ keV ($J^\pi = 3^+$). The spectroscopic factors for this resonance are known from independent measurements (i.e., neutron-stripping on the mirror target nucleus ^{17}O). Their values are $(C^2S)_{\ell=0} = 1.01$ and $(C^2S)_{\ell=2} \approx 0$. Estimate the *observed* proton partial width for this resonance.

We write with Eq. (2.197)

$$\Gamma^o_{\mathrm{p},\ell=0} = 2\frac{\hbar^2}{mR^2} P_{\ell=0}(C^2S)_{\ell=0}(\theta^o_{\mathrm{p},\ell=0})^2$$
$$= 2(2.22\times10^6\ \mathrm{eV})(8.10\times10^{-3})(1.01)(0.45) = 16.3\ \mathrm{keV}$$
$$\Gamma^o_{\mathrm{p},\ell=2} = 2\frac{\hbar^2}{mR^2} P_{\ell=2}(C^2S)_{\ell=2}(\theta^o_{\mathrm{p},\ell=2})^2$$
$$= 2(2.22\times10^6\ \mathrm{eV})(7.90\times10^{-5})(\approx 0)(0.45) \approx 0$$

The values of $(\theta^o_{\mathrm{p},\ell=0})^2$ and $(\theta^o_{\mathrm{p},\ell=2})^2$ are obtained by interpolating the results for ^{12}C + p and ^{22}Na + p shown in Figure 2.27. The estimated *observed* proton partial width is

$$\Gamma^o_{\mathrm{p}} = \Gamma^o_{\mathrm{p},\ell=0} + \Gamma^o_{\mathrm{p},\ell=2} = 16.3\ \mathrm{keV}$$

The calculated result is in excellent agreement with the experimental value of $\Gamma_{\mathrm{p}} = (18 \pm 2)$ keV that was directly measured in ^{17}F(p,p)^{17}F elastic scattering studies (Bardayan *et al.*, 2000).

Example 2.3

The *observed* proton partial width for the s-wave ($\ell = 0$) resonance at a center-of-mass energy of $E_r = 214$ keV ($J^\pi = 1/2^+$) in ^{24}Mg(p,γ)^{25}Al was directly measured. The result is $\Gamma^o_{\mathrm{p},\ell=0} = (1.40 \pm 0.12)\times10^{-2}$ eV (Powell *et al.*, 1999). Estimate the proton spectroscopic factor for the corresponding compound state.

First, we calculate the *observed* single-particle proton width from Eq. (2.200),

$$\Gamma^o_{\lambda pc} = 2\frac{\hbar^2}{mR^2} P_c(\theta^o_{pc})^2 = 2(1.84\times10^6\ \mathrm{eV})(4.56\times10^{-8})(0.59)$$
$$= 9.90\times10^{-2}\ \mathrm{eV}$$

We obtain from Eq. (2.201)

$$(C^2S)_{\ell=0} = \frac{\Gamma^o_{\mathrm{p},\ell=0}}{\Gamma^o_{\lambda pc}} = \frac{(1.40\pm0.12)\times10^{-2}\ \mathrm{eV}}{9.90\times10^{-2}\ \mathrm{eV}} = 0.14\pm0.01$$

The result is in excellent agreement with the value of $(C^2S)_{\ell=0} = 0.14$ measured independently in the proton transfer reaction ^{24}Mg(^{3}He,d)^{25}Al (Peterson and Ristinen, 1975).

2.6 Continuum Theory

It is interesting to discuss the extreme case where a projectile approaching the target in a particular channel α is very unlikely to reappear in the entrance

channel once it has penetrated into the nuclear interior. The condition is fulfilled, for example, if the number of open channels is very large. This is typically the case when the energy of the incident particle is considerably higher than the first few excitation energies of the target nucleus (say, $E > 3$ MeV for target masses of $A > 50$). The condition may also be fulfilled at low energies if the incident particle initiates a reaction with a large positive Q-value (say, $Q > 2$ MeV). In these cases we expect that, once the incident particle is inside the nucleus, it exchanges its energy rapidly with the other nucleons and the probability that it leaves by the same channel α is very small.

For simplicity, s-wave neutrons are considered again as incident particles. For the interior wave function, we find from Eq. (2.141)

$$u_{\text{in}} \sim e^{-iKr} \tag{2.202}$$

It has the form of an ingoing wave since it does not return. This is only a rough approximation since it is impossible to represent the motion of the incident particle inside the nucleus as a function of r only. However, it represents the main features of the dependence of the wave function on r. The logarithmic derivative of the radial wave function must be continuous at $r = R$. Hence, (see Eq. (2.129))

$$f_0 = R\left(\frac{1}{u_{\text{in}}(r)}\frac{du_{\text{in}}(r)}{dr}\right)_{r=R} = R\frac{\left[\frac{d}{dr}(Be^{-iKr})\right]_{r=R}}{Be^{-iKr}} = -iKR \tag{2.203}$$

Substitution into Eq. (2.137) yields immediately for the reaction cross section (since $\text{Re}\, f_0 = 0$ and $\text{Im}\, f_0 = -KR$)

$$\sigma_{\text{re},0} = \frac{\pi}{k^2}\left(1 - \left|e^{2i\delta_0}\right|^2\right) = \frac{\pi}{k^2}\frac{4kK}{(K+k)^2} \tag{2.204}$$

The wave number inside the nucleus, K, is the only information regarding the interior, which enters into this expression. Comparison to Eqs. (2.51) and (2.68) shows that the reaction cross section for s-wave neutrons can be interpreted as the product of the maximum cross section, π/k^2, and the s-wave transmission coefficient, $\hat{T}_0$,

$$\sigma_{\text{re},0} = \sigma_{\text{re},0}^{\max}\hat{T}_0 \tag{2.205}$$

where

$$\hat{T}_0 = 1 - \left|e^{2i\delta_0}\right|^2 \tag{2.206}$$

Since we assumed that the projectile is not re-emitted by the compound nucleus into the entrance channel α, the reaction cross section σ_{re} here is identical to the cross section $\sigma_{\alpha C}$ for the formation of the compound nucleus through channel α. Also, disregarding the possibility that the incident particle can return via the entrance channel means that Eq. (2.204) cannot give rise to resonances. For this reason, the above method for determining the cross section is referred to as *continuum theory*.

From Eq. (2.204), we can also estimate the s-wave reaction cross section for neutrons at low incident energies, E. For $k \ll K$, the wave number K in the interior does not change considerably with variations in k (see Figure 2.7) and one finds

$$\sigma_{\mathrm{re},0} = \frac{\pi}{k^2}\frac{4kK}{(K+k)^2} \approx \frac{4\pi}{Kk} \sim \frac{1}{k} \sim \frac{1}{v} \sim \frac{1}{\sqrt{E}} \tag{2.207}$$

where $p = \hbar k$ and v is the velocity of the incident neutron. The result is independent of the reaction mechanism and is referred to as $1/v$ *law* for reactions induced by s-wave neutrons. Reaction cross sections for ^{3}He(n,p)^{3}H, ^{6}Li(n,α)^{3}H and ^{10}B(n,α)^{7}Li are displayed in Figure 4.15a. Below a neutron energy of ≈ 1 keV, the cross sections follow the $1/v$ law.

Equations (2.204)–(2.206) are obtained under the assumption of s-wave neutrons as incident particles. They can be easily generalized for any projectile and orbital angular momentum (Blatt and Weisskopf, 1952). The cross section for the formation of the compound nucleus through channel α is then given by

$$\sigma_{\alpha C} = \frac{\pi}{k^2}\sum_{\ell}(2\ell+1)\hat{T}_{\ell}(\alpha) \tag{2.208}$$

where

$$\hat{T}_{\ell}(\alpha) = 1 - \left|e^{2i\delta_{\alpha\ell}}\right|^2 \tag{2.209}$$

is the transmission coefficient of channel α for orbital angular momentum ℓ and $\delta_{\alpha\ell}$ is the corresponding phase shift in channel α for elastic scattering by an appropriate potential. The potential must be complex for reactions to occur; otherwise the phase shift will be real and the transmission coefficient vanishes. This is consistent with our earlier discussion in Section 2.3.6. Transmission coefficients are usually calculated numerically from *optical model potentials*, which represent the average nuclear potential. For more information on optical model potentials, see Satchler (1990).

2.7 Hauser–Feshbach Theory

In Section 2.5, we considered the case where a reaction proceeds through an isolated narrow resonance. We will now discuss the other extreme situation. With increasing excitation energy in the compound nucleus, the resonances become broader and are located closer together. There is a continuous transition from sharp, isolated levels to the continuum, where levels overlap considerably such that little structure remains in the cross section. In other words, the cross section varies smoothly with energy. The reaction cross section, averaged over any resonance structure, is derived in the following.

The total angular momentum J and parity π of the compound nucleus will be conserved in a reaction (α,α'). The average cross section is then given by a sum of

contributions from separate J and π,

$$\langle \sigma_{\mathrm{re}}(\alpha, \alpha') \rangle = \sum_{J\pi} \langle \sigma_{\mathrm{re}}(\alpha, \alpha') \rangle^{J\pi} \tag{2.210}$$

Recall that α denotes a pair of particles (including their state of excitation) in a particular channel (Section 2.5.5). Unprimed and primed quantities refer to the incoming and outgoing channel of the reaction, respectively. Next, we factor each term $\langle \sigma_{\mathrm{re}}(\alpha, \alpha') \rangle^{J\pi}$ into a cross section for compound nucleus formation through channel α and a branching ratio for decay into channel α',

$$\langle \sigma_{\mathrm{re}}(\alpha, \alpha') \rangle^{J\pi} = \sigma_{\alpha C}^{J\pi} \frac{G_{\alpha'}^{J\pi}}{\sum_{\alpha''} G_{\alpha''}^{J\pi}} \tag{2.211}$$

The quantities $G_{\alpha}^{J\pi}$ represent probabilities for the decay into a specific outgoing channel, where the sum over α'' in the denominator is over all channels to which the compound nucleus can decay ($\sum_{\alpha''} G_{\alpha''}^{J\pi} = 1$). The factorization of the cross section in Eq. (2.211) reflects the independence of formation and decay of the compound nucleus while still fulfilling the requirement of total angular momentum and parity conservation. Substitution of the reciprocity theorem (see Eq. (2.14))

$$(2I_1 + 1)(2I_2 + 1)k_{\alpha}^2 \langle \sigma_{\mathrm{re}}(\alpha, \alpha') \rangle^{J\pi} = (2I_1' + 1)(2I_2' + 1)k_{\alpha'}^2 \langle \sigma_{\mathrm{re}}(\alpha', \alpha) \rangle^{J\pi} \tag{2.212}$$

into Eq. (2.211) gives

$$\frac{G_{\alpha'}^{J\pi}}{G_{\alpha}^{J\pi}} = \frac{(2I_1' + 1)(2I_2' + 1)k_{\alpha'}^2 \sigma_{\alpha' C}^{J\pi}}{(2I_1 + 1)(2I_2 + 1)k_{\alpha}^2 \sigma_{\alpha C}^{J\pi}} \tag{2.213}$$

where I_1 and I_2 are the spins of the particles in channel α. Summation over all channels α'' yields (since $\sum_{\alpha''} G_{\alpha''}^{J\pi} = 1$)

$$G_{\alpha'}^{J\pi} = \frac{(2I_1' + 1)(2I_2' + 1)k_{\alpha'}^2 \sigma_{\alpha' C}^{J\pi}}{\sum_{\alpha''} (2I_1'' + 1)(2I_2'' + 1)k_{\alpha''}^2 \sigma_{\alpha'' C}^{J\pi}} \tag{2.214}$$

For the formation of the compound nucleus, one can use Eq. (2.208),

$$\sigma_{\alpha C} = \sum_{J\pi} \sigma_{\alpha C}^{J\pi} = \frac{\pi}{k_{\alpha}^2} \sum_{\ell} (2\ell + 1) \hat{T}_{\ell}(\alpha) \tag{2.215}$$

Since the cross section is averaged over many overlapping resonances, we expect that the transmission coefficient does not depend on J. Therefore

$$\sigma_{\alpha C} = \frac{\pi}{k_{\alpha}^2} \sum_{\ell} (2\ell + 1) \sum_{J=|\ell - s|}^{\ell + s} \sum_{s=|I_1 - I_2|}^{I_1 + I_2} \frac{2J + 1}{(2I_1 + 1)(2I_2 + 1)(2\ell + 1)} \hat{T}_{\ell}(\alpha) \tag{2.216}$$

The quantities I, s, and ℓ have the same meanings as in Section 2.5.5 and refer to a specific channel α. The factor in front of the transmission coefficient takes the

number of different spin orientations into account (Section 2.5.5). Rearranging the order of summation yields

$$\sigma_{\alpha C} = \frac{\pi}{k_\alpha^2} \sum_{J\pi} \frac{2J+1}{(2I_1+1)(2I_2+1)} \sum_{s=|I_1-I_2|}^{I_1+I_2} \sum_{\ell=|J-s|}^{J+s} \hat{T}_\ell(\alpha) \tag{2.217}$$

Comparison of Eqs. (2.215) and (2.217) then gives

$$\sigma_{\alpha C}^{J\pi} = \frac{\pi}{k_\alpha^2} \frac{2J+1}{(2I_1+1)(2I_2+1)} \sum_{s\ell} \hat{T}_\ell(\alpha) \tag{2.218}$$

Combining Eqs. (2.210), (2.211), (2.214), and (2.218) results in

$$\begin{aligned} \langle \sigma_{\mathrm{re}}(\alpha,\alpha') \rangle &= \sum_{J\pi} (2I_1'+1)(2I_2'+1) k_{\alpha'}^2 \frac{\sigma_{\alpha C}^{J\pi} \sigma_{\alpha' C}^{J\pi}}{\sum_{\alpha''} (2I_1''+1)(2I_2''+1) k_{\alpha''}^2 \sigma_{\alpha'' C}^{J\pi}} \\ &= \frac{\pi}{k_\alpha^2} \sum_{J\pi} \frac{2J+1}{(2I_1+1)(2I_2+1)} \frac{\left[\sum_{s\ell} \hat{T}_\ell(\alpha)\right] \left[\sum_{s'\ell'} \hat{T}_{\ell'}(\alpha')\right]}{\sum_{\alpha''} \sum_{s''\ell''} \hat{T}_{\ell''}(\alpha'')} \end{aligned} \tag{2.219}$$

This is the *Hauser–Feshbach formula* for energy-averaged cross sections (Hauser and Feshbach, 1952; Vogt, 1968). The quantity α refers to the incoming channel of the reaction and thus I_1 and I_2 are the spins of the target and projectile, respectively. The sum over α'' is again over all channels that are energetically accessible for the decay of the compound nucleus at the total energy in the entrance channel. The sums over J^π, ℓ, and s run over all values allowed by the selection rules for angular momentum coupling (Appendix B): π is positive or negative; $J = 0, 1, 2, \ldots$ for A even, or $J = \frac{1}{2}, \frac{3}{2}, \frac{5}{2}, \ldots$ for A odd; s takes on all integer values between $|I_1 - I_2|$ and $I_1 + I_2$; ℓ takes on all even values between $|J - s|$ and $J + s$ if the pair α has the same parity as π, and all odd values otherwise. We assume here that the transmission coefficients are independent of the channel spin (i.e., the potential has no spin–orbit term) and, therefore, the sum over s in Eq. (2.219) becomes a simple multiplicative factor. See Problem 2.6.

The transmission coefficients $\hat{T}_\ell(\alpha)$ are determined by complex phase shifts $\delta_{\alpha\ell}$ (see Eq. (2.209)) that are usually calculated numerically from optical model potentials (Section 2.6). Recall that these represent the average nuclear potential only. Consequently, the transmission coefficients describe the formation probability of single-particle levels. In other words, the reaction cross section calculated from Eq. (2.219) cannot account for the fine structure shown in Figure 2.25, but corresponds to the average cross section shown as the thick solid line.

The Hauser–Feshbach theory is also applicable if a channel involves the emission or absorption of γ-rays (Cowan, Thielemann, and Truran, 1991). A correction must be applied to Eq. (2.219) because the processes of compound nucleus formation and decay are not completely independent of each other as can be shown by a more involved derivation of the Hauser–Feshbach formula using the resonance theory (Vogt, 1968). This *width-fluctuation correction* enhances the cross section for weak reaction channels at the cost of stronger ones and is most important

near thresholds, where additional channels become energetically accessible, and for reactions with few open channels (Moldauer, 1964).

Recall that α also specifies the state of excitation of a pair of particles in a particular channel. In practical applications, one is mostly interested in cross sections obtained by summing or averaging over specific sets of excited states. For example, what is usually measured in the laboratory is the quantity $\langle \sigma_{re}(\alpha, \alpha') \rangle$, with α representing the ground states of target and projectile, summed over excited states in the outgoing channel α'. Or, if the reaction takes place in a hot stellar plasma, $\langle \sigma_{re}(\alpha, \alpha') \rangle$ must be averaged over excited states in the entrance channel α (Section 3.1.5). In such cases, Eq. (2.219) is still valid if each of the transmission coefficients in the numerator is replaced by sums of transmission coefficients over the excited states in question. In exceptional cases, all the final states for compound nucleus decay and their quantum numbers are experimentally known. The Hauser–Feshbach formula can then be applied with essentially no adjustable parameters. In most cases of practical interest, however, the compound nucleus may decay to levels beyond the highest excited state for which energy, spin, and parity are explicitly known. The transmission coefficients in the numerator and denominator of Eq. (2.219) must then be modified to include terms that integrate a nuclear level density over the energy region beyond the known levels. This requires the development of expressions for the density of states as a function of excitation energy, spin, and parity. The evaluation of the overall cross section is then reduced to the problem of determining the required transmission coefficients and nuclear level densities. For a detailed discussion of

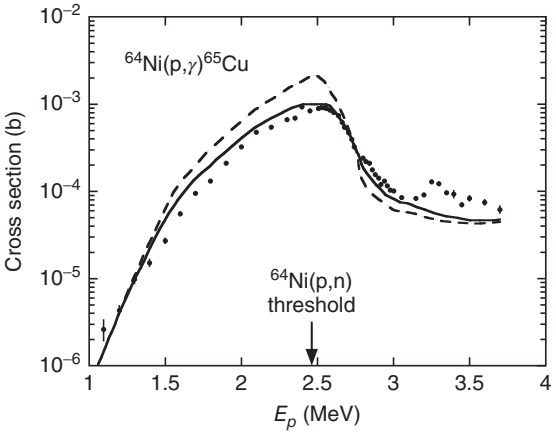

Figure 2.29 Cross section versus bombarding energy for the ^{64}Ni(p,γ)^{65}Cu reaction. Beyond an energy of $\approx$ 2.5 MeV the endothermic ^{64}Ni(p,n)^{64}Cu reaction is energetically allowed. The sharp drop in the cross section at the neutron threshold reflects the decrease of the flux in all other decay channels of the compound nucleus ^{65}Cu. The curves show the results of Hauser–Feshbach statistical model calculations with (solid line) and without (dashed line) width fluctuation corrections. Data adopted from Mann *et al.* (1975).

these quantities in connection with the Hauser–Feshbach model see, for example, Rauscher *et al.* (1997) or Arnould and Goriely (2003).

Figure 2.29 shows the cross section for the ^{64}Ni(p,γ)^{65}Cu reaction at bombarding energies between 1 MeV and 4 MeV. The ^{64}Ni(p,n)^{64}Cu reaction has a Q-value of ≈ -2.5 MeV, which means that at a bombarding energy close to 2.5 MeV the neutron channel opens and the (p,n) reaction will start to compete with the (p,γ) reaction. Since the total incoming flux must be constant, the opening of a new reaction channel corresponds to a reduction of flux into all other reaction channels. As a result, the cross section of the (p,γ) reaction drops substantially at the neutron threshold, giving rise to a *competition cusp*. The dashed curve in Figure 2.29 was obtained using Eq. (2.219) and is in qualitative agreement with the measurements. The theoretical description of the data is significantly improved if width fluctuation corrections are taken into account (solid line). A discussion of the Hauser–Feshbach model in the context of thermonuclear reaction rates is given in Section 3.2.7.

Problems

2.1 Show by substituting Eq. (2.27) into Eq. (2.30) that the expansion coefficients are given by $b_\ell = (2\ell + 1)i^\ell e^{i\delta_\ell}$. It is helpful for the derivation to write the sine functions as complex exponentials and to group separately the terms with e^{ikr} and e^{-ikr}.

2.2 The s-wave ($\ell = 0$) transmission coefficient at low energies compared to the Coulomb barrier height is given by Eq. (2.124). Derive the transmission coefficient at low energies for the Coulomb and centripetal potentials by substituting $V(r) = Z_0 Z_1 e^2/r + \ell(\ell + 1)\hbar^2/(2mr^2)$ into Eq. (2.119). The simplest procedure is to expand the square root in the integrand before integration.

2.3 Suppose that a hypothetical resonance occurs in the A(p,γ)B reaction. The *observed* proton and γ-ray partial widths amount to $\Gamma_p^o = 50$ meV and $\Gamma_\gamma^o = 50$ meV, respectively. Assume that no other reaction channels are open. Use the one-level Breit–Wigner formula to calculate the ratio of reaction cross sections at E_r and $E_r + \Gamma^o$ (Γ^o denotes the total resonance width). Disregard the small energy dependence of the wave number k and of the partial widths.

2.4 Show explicitly that the general solution of Eq. (2.159) reduces for $\ell = 0$ neutrons to $u_0(r) = Ae^{ikr} + Be^{-ikr}$ (see Eq. (2.131)).

2.5 The $E_r^{cm} = 518$ keV ($J^\pi = 1^-$) s-wave resonance (Figure 3.12) in the ^{13}C(p,γ)^{14}N reaction ($Q = 7550$ keV) has an *observed* proton and γ-ray partial width of $\Gamma_p^o = 37$ keV and $\Gamma_\gamma^o = 9.4$ eV, respectively, at the resonance energy. Both values are given here in the center-of-mass system. They are derived from the results reported in King *et al.* (1994). The latter value corresponds to the γ-ray partial width of the $E1$ transition to the ^{14}N ground state ($J^\pi = 1^+$). By using the energy dependences of the partial widths, find for this particular resonance the center-of-mass energy at which $\Gamma_p^o \approx \Gamma_\gamma^o$. Approximate the s-wave penetration factor by the Gamow factor and

disregard the small energy dependence of the dimensionless single-particle reduced width.

2.6 Consider the ^{23}Na(p,α)^{20}Ne reaction, leading to the ^{20}Ne ground state ($J^\pi = 0^+$), at a center-of-mass proton energy of $E_p \approx 0.4$ MeV [$J^\pi(^{23}\text{Na}) = 3/2^+$, $J_p^\pi = 1/2^+$]. The proton separation energy of ^{24}Mg (or the Q-value for the ^{23}Na(p,γ)^{24}Mg reaction) is $S_p = 11.693$ MeV (Wang *et al.*, 2012). Hence, the compound nucleus ^{24}Mg has an excitation energy near 11.7 MeV +0.4 MeV $\approx$ 12 MeV. At this energy, ^{24}Mg can decay by proton emission to the ^{23}Na ground state and by α-particle emission to the ^{20}Ne ground state or the ^{20}Ne first-excited state ($E_x = 1.63$ MeV, $J^\pi = 2^+$). Determine the energy-averaged cross section by writing down all terms of Eq. (2.219) up to and including $J = 2$.

3
Thermonuclear Reactions

3.1
Cross Sections and Reaction Rates

The Q-value represents the energy released in a particular nuclear reaction. Of importance in a stellar environment, however, is the total nuclear energy liberated in a stellar plasma per unit volume. The latter aspect depends on two additional quntities, the nuclear cross section and the velocity distribution of the particles in the plasma. The nuclear cross section is a measure for the probability per pair of interacting nuclei 0 and 1 that a nuclear reaction will occur. The total cross section (in units of area) is defined by Eq. (2.1). In general, nuclear cross sections depend on the relative velocity of the target-plus-projectile system, that is, $\sigma = \sigma(v)$.

Using Eq. (2.1), we may write the rate of a nuclear reaction (number of reactions per time t and unit volume V) as

$$\frac{\mathcal{N}_R}{V \cdot t} = (\sigma \mathcal{N}_t)\left(\frac{\mathcal{N}_b}{V \cdot A \cdot t}\right) = \sigma \frac{\mathcal{N}_t}{V}\frac{\mathcal{N}_b}{A \cdot t} = \sigma \frac{\mathcal{N}_t}{V} v \frac{\mathcal{N}_b}{V} \tag{3.1}$$

with the current density (number of particles per time and per area) given by $j_b = \mathcal{N}_b/(At) = v\mathcal{N}_b/V$.

3.1.1
Particle-Induced Reactions

Consider a reaction involving four species, $0 + 1 \rightarrow 2 + 3$, where both the projectile (0) and the target (1) are represented by particles with rest mass (i.e., neither 0 nor 1 represents a photon). With the definition $r_{01} \equiv \mathcal{N}_R/(Vt)$, we obtain for the reaction rate

$$r_{01} = N_0 N_1 v\sigma(v) \tag{3.2}$$

where $N_0 \equiv \mathcal{N}_t/V$ and $N_1 \equiv \mathcal{N}_b/V$ are the number densities of the interacting particles (in units of particles per volume). In a stellar plasma at thermodynamic equilibrium, the relative velocity of the interacting nuclei 0 and 1 is not constant, but there is a distribution of relative velocities, described by the probability function $P(v)$. In this case, $P(v)\,dv$ is the probability that the relative velocity of the

Nuclear Physics of Stars, Second Edition. Christian Iliadis.

interacting nuclei is in the range between v and $v + dv$, with

$$\int_0^\infty P(v)\,dv = 1 \tag{3.3}$$

We may generalize the reaction rate for a distribution of relative velocities by writing

$$r_{01} = N_0 N_1 \int_0^\infty v P(v)\sigma(v)\,dv \equiv N_0 N_1 \langle \sigma v \rangle_{01} \tag{3.4}$$

where $\langle \sigma v \rangle_{01}$ is the reaction rate per particle pair and $N_0 N_1$ is the total number density of pairs of nonidentical nuclei 0 and 1. For identical particles, the total number density of pairs is given by

$$\frac{N_0(N_0 - 1)}{2} \xrightarrow[N_0 \text{ large}]{} \frac{N_0^2}{2} \tag{3.5}$$

and we obtain for the reaction rate the general expression

$$r_{01} = \frac{N_0 N_1 \langle \sigma v \rangle_{01}}{(1 + \delta_{01})} \tag{3.6}$$

where δ_{01} is the Kronecker symbol. The number of reactions per unit volume and time is given by the product of the number of particle pairs and the reaction rate per particle pair. The latter quantity contains the nuclear physics information. In practice, it is the quantity $N_A \langle \sigma v \rangle_{01}$ (where N_A denotes the Avogadro constant) in units of $\mathrm{cm^3 mol^{-1} s^{-1}}$ rather than $\langle \sigma v \rangle_{01}$, which is tabulated and presented in the literature. For the case of three-particle reactions or decays, see Fowler, Caughlan, and Zimmerman (1967). In a stellar plasma, the kinetic energy available to nuclei is that of their thermal motion. Therefore, the reactions initiated by this motion are called *thermonuclear reactions*. With few exceptions, nuclei in a stellar plasma move nonrelativistically and are nondegenerate (see, e.g., Wolf, 1965). Thus, in most cases, the velocities of nuclei can be described by a Maxwell–Boltzmann distribution. The probability for the occurrence of a nuclear reaction depends on the *relative* velocities between the interacting nuclei. If the velocity distributions of the interacting nuclei at thermodynamic equilibrium are separately described by Maxwell–Boltzmann distributions, then it follows that the relative velocities between the two species of nuclei will also be Maxwellian (Clayton, 1983).

We may write for the Maxwell–Boltzmann distribution

$$P(v)\,dv = \left(\frac{m_{01}}{2\pi kT}\right)^{3/2} e^{-m_{01}v^2/(2kT)}\, 4\pi v^2\,dv \tag{3.7}$$

which gives the probability that the relative velocity has a value between v and $v + dv$. The Boltzmann constant is given by $k = 8.6173 \times 10^{-5}$ eV/K, T is the temperature, and m_{01} is the reduced mass $m_{01} = m_0 m_1/(m_0 + m_1)$ (Appendix C.2). With $E = m_{01}v^2/2$ and $dE/dv = m_{01}v$, we may write the velocity distribution as an energy distribution,

$$P(v)\,dv = P(E)\,dE = \left(\frac{m_{01}}{2\pi kT}\right)^{3/2} e^{-E/kT}\, 4\pi \frac{2E}{m_{01}} \frac{dE}{m_{01}} \sqrt{\frac{m_{01}}{2E}}$$
$$= \frac{2}{\sqrt{\pi}} \frac{1}{(kT)^{3/2}} \sqrt{E}\, e^{-E/kT}\, dE \tag{3.8}$$

The *velocity* distribution has a maximum at $v_T = \sqrt{2kT/m_{01}}$, corresponding to an energy of $E = kT$. The *energy* distribution has a maximum at $E = kT/2$. For the reaction rate per particle pair, we obtain

$$\langle \sigma v \rangle_{01} = \int_0^\infty v P(v) \sigma(v)\, dv = \int_0^\infty v \sigma(E) P(E)\, dE$$
$$= \left(\frac{8}{\pi m_{01}}\right)^{1/2} \frac{1}{(kT)^{3/2}} \int_0^\infty E\, \sigma(E)\, e^{-E/kT}\, dE \tag{3.9}$$

Numerically we obtain for the reaction rate at a given temperature T

$$N_A \langle \sigma v \rangle_{01} = \frac{3.7318 \times 10^{10}}{T_9^{3/2}} \sqrt{\frac{M_0 + M_1}{M_0 M_1}} \int_0^\infty E\, \sigma(E)\, e^{-11.605\, E/T_9}\, dE$$
$$(\mathrm{cm^3 mol^{-1} s^{-1}}) \tag{3.10}$$

where the center-of-mass energy E is in units of MeV, the temperature T_9 in GK ($T_9 \equiv T/10^9$ K), the relative atomic masses M_i in u, and the cross section σ in barn (1 b $\equiv 10^{-24}$ cm^2). The reaction rate depends critically on the cross section σ, which differs for each nuclear reaction.

Figure 3.1a shows the factor $(kT)^{-3/2} E\, e^{-E/kT}$, containing the Maxwell–Boltzmann distribution, versus energy E for three different scenarios: (i) the Sun's core ($T = 15$ MK), (ii) a classical nova ($T = 300$ MK), and (iii) a supernova

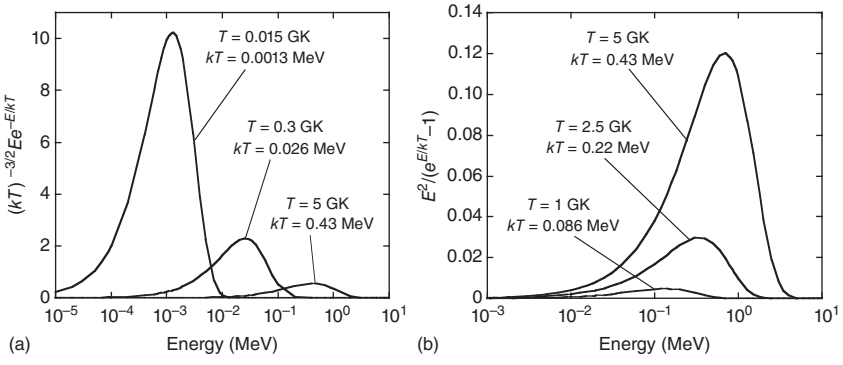

Figure 3.1 (a) The factor $(kT)^{-3/2} E\, e^{-E/kT}$ that occurs in the rate expression for reactions induced by particles with rest mass (see Eq. (3.10)) at three different temperatures, $T = 0.015$ GK, 0.3 GK, and 5 GK; these conditions are encountered in the Sun, in classical novae and in type II supernovae, respectively; (b) The factor $E_\gamma^2/(e^{E_\gamma/kT} - 1)$ that occurs in the expression of the decay constant for photodisintegration reactions (see Eq. (3.18)) at three different temperatures, $T = 1$ GK, 2.5 GK, and 5 GK.

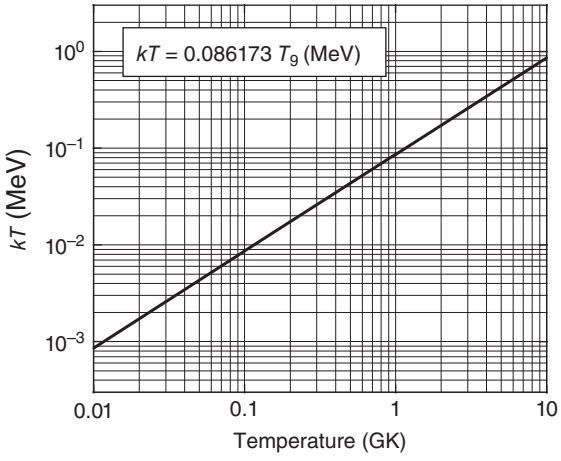

Figure 3.2 Energy maximum of the Maxwell–Boltzmann velocity distribution as a function of temperature.

($T = 5$ GK). Each displayed curve increases linearly at small energies, reaches a maximum at $E = kT$, and then decreases exponentially and approaches zero for large values of E. The term kT is numerically given by $kT = 86.173\ T_9$ (keV) $= 0.086173\ T_9$ (MeV), and is displayed in Figure 3.2. The maxima of the curves in Figure 3.1a occur at $E_{\max} = kT = 1.3$ keV, 26 keV, and 431 keV.

For neutron-induced reactions, such as (n,γ) or (n,α), the reaction rate is frequently expressed in terms of a Maxwellian-averaged cross section,

$$N_A\langle\sigma\rangle_T \equiv \frac{N_A\langle\sigma v\rangle}{v_T} = \frac{1}{v_T}N_A\int_0^\infty vP(v)\sigma_{\rm n}(v)\,dv$$
$$= \frac{4}{\sqrt{\pi}}\frac{N_A}{v_T^2}\int_0^\infty v\sigma_{\rm n}(v)\left(\frac{v}{v_T}\right)^2 e^{-(v/v_T)^2}\,dv \qquad (3.11)$$

with $v_T = \sqrt{2kT/m_{01}}$ the thermal velocity, that is, the maximum of the *velocity* distribution. The quantity $\langle\sigma\rangle_T$ rather than $\langle\sigma v\rangle$ is frequently presented in the literature. The usefulness of the above expression will become apparent in later sections.

3.1.2
Photon-Induced Reactions

When species 2 is a photon, the process $\gamma + 3 \rightarrow 0 + 1$ is called a *photodisintegration reaction*. The current density may be written as $j_b = \mathcal{N}_b/(At) = c\mathcal{N}_b/V$, with c the speed of light. With the definitions $r_{\gamma 3} \equiv \mathcal{N}_R/(Vt)$, $N_3 \equiv \mathcal{N}_t/V$, and $N_\gamma \equiv \mathcal{N}_b/V$, we obtain from Eq. (3.1)

$$r_{\gamma 3} = N_3 N_\gamma c\sigma(E_\gamma) \qquad (3.12)$$

The cross section depends on the γ-ray energy. Furthermore, in a stellar plasma at thermodynamic equilibrium, the number density of photons is not constant, but depends on the stellar temperature and on the γ-ray energy. We may generalize the reaction rate by writing

$$r_{\gamma 3} = N_3 \int_0^\infty c N_\gamma(E_\gamma)\sigma(E_\gamma)\, dE_\gamma \tag{3.13}$$

For the decay constant (probability of decay per nucleus per second), we find

$$\lambda_\gamma(3) = \frac{r_{\gamma 3}}{N_3} = \int_0^\infty c N_\gamma(E_\gamma)\sigma(E_\gamma)\, dE_\gamma \tag{3.14}$$

The energy density of electromagnetic waves with frequencies between ν and $\nu + d\nu$ at temperature T is given by the Planck radiation law

$$u(\nu)\, d\nu = \frac{8\pi h\nu^3}{c^3} \frac{1}{e^{h\nu/kT} - 1}\, d\nu \tag{3.15}$$

With the substitution $E_\gamma = h\nu$, we find for the energy density

$$u(E_\gamma)\, dE_\gamma = \frac{8\pi}{(hc)^3} \frac{E_\gamma^3}{e^{E_\gamma/kT} - 1}\, dE_\gamma \tag{3.16}$$

The number of photons with energies between E_γ and $E_\gamma + dE_\gamma$ per unit volume at a temperature T is then

$$N_\gamma(E_\gamma)\, dE_\gamma = \frac{u(E_\gamma)}{E_\gamma}\, dE_\gamma = \frac{8\pi}{(hc)^3} \frac{E_\gamma^2}{e^{E_\gamma/kT} - 1}\, dE_\gamma \tag{3.17}$$

With Eq. (3.14), we obtain for the photodisintegration decay constant at a given temperature

$$\lambda_\gamma(3) = \frac{8\pi}{h^3 c^2} \int_0^\infty \frac{E_\gamma^2}{e^{E_\gamma/kT} - 1} \sigma(E_\gamma)\, dE_\gamma \tag{3.18}$$

Since most photodisintegration reactions are endothermic ($Q_{\gamma 3 \to 01} < 0$), the lower integration limit is given by the threshold energy, $E_t = Q_{01 \to \gamma 3}$, of the reaction. Note that $\lambda_\gamma(3)$ does not depend on the stellar density.

Figure 3.1b shows the factor $E_\gamma^2/(e^{E_\gamma/kT} - 1)$ versus γ-ray energy for three different scenarios: (i) $T = 1$ GK ($kT = 86$ keV), (ii) $T = 2.5$ GK ($kT = 215$ keV), and (iii) $T = 5$ GK ($kT = 431$ keV). The maxima of the curves occur at $E_{\gamma,\max} \approx 1.6\, kT = 140$ keV, 349 keV, and 700 keV. The number of photons is not conserved, but is determined by the conditions of thermal equilibrium. For many important photodisintegration reactions, the threshold energies are considerably larger than the location of the maxima of the factor $E_\gamma^2/(e^{E_\gamma/kT} - 1)$, that is, $E_t \gg E_{\gamma,\max}$. Figure 3.3 compares the situation for two photodisintegration reactions of different threshold energies and with $E_t \gg E_{\gamma,\max}$. The integral $\lambda_\gamma(3) \sim \int_{E_t}^\infty E_\gamma^2 (e^{E_\gamma}/kT - 1)^{-1} \sigma(E_\gamma)\, dE_\gamma$ will be smaller for the reaction with the larger threshold energy if both reactions have similar photodisintegration cross sections.

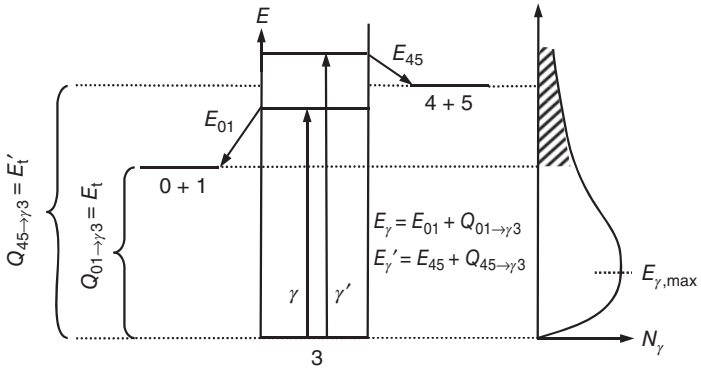

Figure 3.3 Energy level diagram comparing photodisintegration reactions of different threshold energies, E_t. The right-hand side shows schematically the factor $E_\gamma^2/(e^{E_\gamma/kT} - 1)$ (see Figure 3.1b). Only photons with energies above the threshold ($E_t = Q_{01\to\gamma 3}$ for photon γ; $E_t' = Q_{45\to\gamma 3}$ for photon γ') can initiate a photodisintegration reaction and contribute to the decay constant given by Eq. (3.18).

3.1.3 Abundance Evolution

Consider first a reaction between two nuclei 0 and 1, and disregard other processes. The reaction rate for $0 + 1$ is related to the mean lifetime τ of the nuclear species in the stellar plasma. The rate of change of the abundance (in terms of the number density) of nucleus 0 caused by reactions with nucleus 1 can be expressed as

$$\left(\frac{dN_0}{dt}\right)_1 = -\lambda_1(0)N_0 = -\frac{N_0}{\tau_1(0)} \tag{3.19}$$

where $\lambda \equiv 1/\tau$ is the decay constant. By using the reaction rate (see Eq. (3.6)), we may also write

$$\left(\frac{dN_0}{dt}\right)_1 = -(1+\delta_{01})r_{01} = -(1+\delta_{01})\frac{N_0 N_1\langle\sigma v\rangle_{01}}{(1+\delta_{01})} = -N_0 N_1\langle\sigma v\rangle_{01} \tag{3.20}$$

The Kronecker symbol appears since for identical nuclei each reaction destroys two particles. From Eqs. (3.19), (3.20), and (1.14), we obtain the relations

$$r_{01} = \frac{\lambda_1(0)N_0}{(1+\delta_{01})} = \frac{1}{(1+\delta_{01})}\frac{N_0}{\tau_1(0)} \tag{3.21}$$

$$\tau_1(0) = \frac{N_0}{(1+\delta_{01})r_{01}} = \frac{1}{N_1\langle\sigma v\rangle_{01}} = \left(\rho\frac{X_1}{M_1}N_A\langle\sigma v\rangle_{01}\right)^{-1} \tag{3.22}$$

$$\lambda_1(0) = \frac{1}{\tau_1(0)} = N_1\langle\sigma v\rangle_{01} = \rho\frac{X_1}{M_1}N_A\langle\sigma v\rangle_{01} \tag{3.23}$$

The decay constant of a nucleus for destruction via a particle-induced reaction depends explicitly on the stellar density and, as we shall see, implicitly on stellar

temperature through the reaction rate. If species 0 can be destroyed by several different reactions, its total lifetime is given by

$$\frac{1}{\tau(0)} = \sum_i \frac{1}{\tau_i(0)} \tag{3.24}$$

The above expressions are very useful and will be applied frequently in the discussion of nuclear burning stages (Chapter 5). The following example shows their use in determining the preferred process (reaction or β-decay) by which a particular nucleus is destroyed in a stellar plasma.

Example 3.1

In a stellar plasma, the nucleus ^{25}Al may be destroyed by the capture reaction ^{25}Al(p,γ)^{26}Si or by β^+-decay ($T_{1/2} = 7.18$ s). Neglecting other processes, determine the dominant destruction process at a stellar temperature of $T = 0.3$ GK assuming a reaction rate of $N_A\langle\sigma v\rangle = 1.8 \times 10^{-3}$ cm^{3}mol^{-1}s^{-1}. Assume a stellar density of $\rho = 10^4$ g/cm^3 and a hydrogen mass fraction of $X_\mathrm{H} = 0.7$.

Using Eqs. (1.19) and (3.22), we obtain for the mean lifetime of both processes

$$\beta^+\text{-decay: } \tau_{\beta^+}(^{25}\mathrm{Al}) = \frac{T_{1/2}}{\ln 2} = \frac{7.18\,\mathrm{s}}{0.693} = 10.36\,\mathrm{s}$$

$$\text{p capture: } \tau_p(^{25}\mathrm{Al}) = \left(\rho\frac{X_\mathrm{H}}{M_\mathrm{H}}N_A\langle\sigma v\rangle\right)^{-1}$$

$$= \left[(10^4\,\mathrm{g/cm^3}) \cdot \frac{0.7}{1.0078\,\mathrm{u}} \cdot (1.8 \times 10^{-3}\,\mathrm{cm^3 s^{-1} mol^{-1}})\right]^{-1} = 0.08\,\mathrm{s}$$

Thus, the proton capture reaction is the dominant destruction mechanism of ^{25}Al under these conditions.

Consider now the influence of several nuclear processes (reactions, photodisintegrations, and β-decays) together on the abundance evolution of a particular nucleus in a stellar plasma. As a specific example, we will choose again ^{25}Al (Figure 3.4). It may be produced by a number of processes that are represented by solid lines, including ^{24}Mg(p,γ)^{25}Al, ^{22}Mg(α,p)^{25}Al, ^{25}Si($\beta^+\nu$)^{25}Al, ^{26}Si(γ,p)^{25}Al, and so on. On the other hand, it is destroyed by the processes shown as dotted lines, such as ^{25}Al(p,γ)^{26}Si, ^{25}Al(α,p)^{28}Si, ^{25}Al($\beta^+\nu$)^{25}Mg, ^{25}Al(γ,p)^{24}Mg, and so forth. The time evolution of the ^{25}Al abundance is described by the expression

$$\begin{aligned}\frac{d(N_{^{25}\mathrm{Al}})}{dt} &= N_\mathrm{H}N_{^{24}\mathrm{Mg}}\langle\sigma v\rangle_{^{24}\mathrm{Mg(p,\gamma)}} + N_{^4\mathrm{He}}N_{^{22}\mathrm{Mg}}\langle\sigma v\rangle_{^{22}\mathrm{Mg}(\alpha,\mathrm{p})} \\ &\quad + N_{^{25}\mathrm{Si}}\lambda_{^{25}\mathrm{Si}(\beta^+\nu)} + N_{^{26}\mathrm{Si}}\lambda_{^{26}\mathrm{Si}(\gamma,\mathrm{p})} + \cdots \\ &\quad - N_\mathrm{H}N_{^{25}\mathrm{Al}}\langle\sigma v\rangle_{^{25}\mathrm{Al(p,\gamma)}} - N_{^4\mathrm{He}}N_{^{25}\mathrm{Al}}\langle\sigma v\rangle_{^{25}\mathrm{Al}(\alpha,\mathrm{p})} \\ &\quad - N_{^{25}\mathrm{Al}}\lambda_{^{25}\mathrm{Al}(\beta^+\nu)} - N_{^{25}\mathrm{Al}}\lambda_{^{25}\mathrm{Al}(\gamma,\mathrm{p})} - \cdots\end{aligned} \tag{3.25}$$

In general, if the only sources of abundance change are nuclear processes (i.e., there is no expansion or mixing of matter), then the abundance evolution of

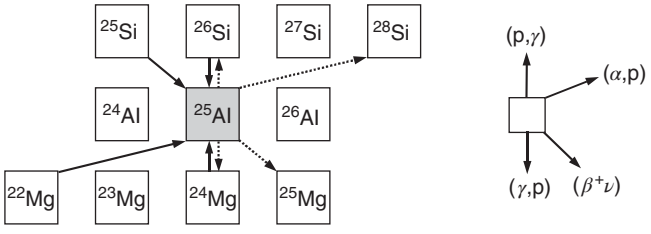

Figure 3.4 Relevant part of the chart of the nuclides showing processes that create (solid arrows) or destroy (dashed arrows) the species ^{25}Al.

nucleus i is given by the differential equation

$$\frac{dN_i}{dt} = \left[\sum_{j,k} N_j N_k \langle \sigma v \rangle_{jk\to i} + \sum_l \lambda_{\beta,l\to i} N_l + \sum_m \lambda_{\gamma,m\to i} N_m\right] - \left[\sum_n N_n N_i \langle \sigma v \rangle_{ni} + \sum_o \lambda_{\beta,i\to o} N_i + \sum_p \lambda_{\gamma,i\to p} N_i\right] \tag{3.26}$$

The terms in the first and second parenthesis represent all processes producing and destroying nucleus i, respectively. In the first parenthesis, the three terms stand for: the sum over all reactions producing nucleus i via reactions between j and k; the sum over all β-decays of nuclei l leading to i; and the sum over all photodisintegrations of nuclei m leading to i. Similar arguments apply to the terms in the second parenthesis. If a reaction between nonidentical particles ($j \neq k$) creates two nuclei i (e.g., ^{7}Li + p → α + α), then $N_j N_k \langle \sigma v \rangle_{jk\to i}$ has to be replaced by $2N_j N_k \langle \sigma v \rangle_{jk\to i}$. If a reaction between identical particles ($j = k$) produces only one particle i (e.g., p + p → d), then $N_j N_k \langle \sigma v \rangle_{jk\to i}$ must be replaced by $N_j^2 \langle \sigma v \rangle_{jj\to i}/2$. The above expression holds without modification for all other reactions involving identical particles. For the inclusion of three-particle reactions, see, for example, Chieffi, Limongi, and Straniero (1998). It is of advantage to express Eq. (3.26) in terms of mole fractions Y (Section 1.5.4) instead of number densities N if the mass density changes during the nucleosynthesis. In most discussions of nuclear burning stages and processes in Chapter 5, we will make the assumption of constant density ρ and thus the use of either N or Y is appropriate.

In any realistic situation, we have to consider the evolution of not just one nuclide, but of several (sometimes many) species simultaneously. For each nuclide, we can set up an expression of the form given by Eq. (3.26). Such a system of coupled, nonlinear ordinary differential equations is called a *nuclear reaction network*. In the simplest cases, we will solve the reaction network analytically. In more complex situations, however, the system of equations must be solved numerically. We do not concern ourselves with the numerical techniques of solving a reaction network here. These are described in detail by Arnett (1996), Timmes (1999), or Hix and Meyer (2006).

Sometimes, the solutions of nuclear reaction networks reveal certain fundamental properties, which simplify the interpretation of the results. The most

important of these properties are called *steady state* and *equilibrium*. A steady-state solution exists if for some part of the reaction network, the time derivatives of all abundances, dN_i/dt, are zero or nearly zero. This implies that in Eq. (3.26) the sum of all destruction terms is balanced by the sum of all creation terms. An equilibrium solution is more restrictive and applies to a situation where the abundances of a pair of nuclei (or of a group of nuclei) are locally balanced because of (almost) equally strong forward and reverse reaction rates (see Section 3.1.4). We will use both concepts in discussions of the nucleosynthesis.

3.1.4
Forward and Reverse Reactions

It was shown in Section 2.2 that the cross sections of a forward and a reverse reaction are fundamentally related by the reciprocity theorem. Here, we will derive a number of expressions for the corresponding reaction rates. For a reaction involving only particles with rest mass, $0 + 1 \rightarrow 2 + 3$, we obtain from Eq. (2.15) with $p^2 = 2mE$

$$\frac{\sigma_{23\rightarrow 01}}{\sigma_{01\rightarrow 23}} = \frac{(2j_0+1)(2j_1+1)}{(2j_2+1)(2j_3+1)} \frac{m_{01}E_{01}}{m_{23}E_{23}} \frac{(1+\delta_{23})}{(1+\delta_{01})} \tag{3.27}$$

where E_{01} and E_{23} denote the center-of-mass energies for the forward and reverse reaction, respectively. For a reaction involving photons, $0 + 1 \rightarrow \gamma + 3$, we obtain from Eq. (2.15) with $p^2 = E_\gamma^2/c^2$

$$\frac{\sigma_{\gamma 3\rightarrow 01}}{\sigma_{01\rightarrow \gamma 3}} = \frac{(2j_0+1)(2j_1+1)}{2(2j_3+1)} \frac{2m_{01}c^2E_{01}}{E_\gamma^2} \frac{1}{(1+\delta_{01})} \tag{3.28}$$

where $(2j_\gamma + 1) = 2$, since the photon has only two polarization directions (Messiah, 1999).

If the forward reaction, $0 + 1 \rightarrow 2 + 3$, and corresponding reverse reaction, $2 + 3 \rightarrow 0 + 1$, involve only particles with rest mass, we find for the reaction rates

$$N_A\langle\sigma v\rangle_{01\rightarrow 23} = \left(\frac{8}{\pi m_{01}}\right)^{1/2} \frac{N_A}{(kT)^{3/2}} \int_0^\infty E_{01}\,\sigma_{01\rightarrow 23}\,e^{-E_{01}/kT}\,dE_{01} \tag{3.29}$$

$$N_A\langle\sigma v\rangle_{23\rightarrow 01} = \left(\frac{8}{\pi m_{23}}\right)^{1/2} \frac{N_A}{(kT)^{3/2}} \int_0^\infty E_{23}\,\sigma_{23\rightarrow 01}\,e^{-E_{23}/kT}\,dE_{23} \tag{3.30}$$

The kinetic energies are related by $E_{23} = E_{01} + Q_{01\rightarrow 23}$ (see Eq. (1.5)). It follows (see also Fowler, Caughlan, and Zimmerman, 1967)

$$\begin{aligned}\frac{N_A\langle\sigma v\rangle_{23\rightarrow 01}}{N_A\langle\sigma v\rangle_{01\rightarrow 23}} &= \left(\frac{m_{01}}{m_{23}}\right)^{1/2} \frac{\int_0^\infty E_{23}\,\sigma_{23\rightarrow 01}\,e^{-E_{23}/kT}\,dE_{23}}{\int_0^\infty E_{01}\,\sigma_{01\rightarrow 23}\,e^{-E_{01}/kT}\,dE_{01}} \\ &= \frac{(2j_0+1)(2j_1+1)(1+\delta_{23})}{(2j_2+1)(2j_3+1)(1+\delta_{01})} \left(\frac{m_{01}}{m_{23}}\right)^{3/2} e^{-Q_{01\rightarrow 23}/kT}\end{aligned} \tag{3.31}$$

The rates $N_A\langle\sigma v\rangle_{01\rightarrow 23}$ and $N_A\langle\sigma v\rangle_{23\rightarrow 01}$ refer to the same stellar temperature T.

To find the relationship between forward and reverse reactions, if species 2 is a photon, we start from Eqs. (3.9) and (3.18)

$$\lambda_\gamma(3) = \frac{8\pi}{h^3c^2}\int_0^\infty \frac{E_\gamma^2}{e^{E_\gamma/kT}-1}\,\sigma_{\gamma 3\to 01}\,dE_\gamma \tag{3.32}$$

$$N_A\langle\sigma v\rangle_{01\to\gamma 3} = \left(\frac{8}{\pi m_{01}}\right)^{1/2}\frac{N_A}{(kT)^{3/2}}\int_0^\infty E_{01}\,\sigma_{01\to\gamma 3}\,e^{-E_{01}/kT}\,dE_{01} \tag{3.33}$$

From Eq. (3.28), we find

$$\frac{\lambda_\gamma(3)}{N_A\langle\sigma v\rangle_{01\to\gamma 3}} = \frac{\frac{8\pi}{h^3c^2}\int_0^\infty \frac{E_\gamma^2}{e^{E_\gamma/kT}-1}\frac{(2j_0+1)(2j_1+1)}{(2j_3+1)(1+\delta_{01})}\frac{m_{01}c^2E_{01}}{E_\gamma^2}\sigma_{01\to\gamma 3}\,dE_\gamma}{\left(\frac{8}{\pi m_{01}}\right)^{1/2}\frac{N_A}{(kT)^{3/2}}\int_0^\infty E_{01}\,\sigma_{01\to\gamma 3}\,e^{-E_{01}/kT}\,dE_{01}} \tag{3.34}$$

The energies are related by $E_{01} + Q_{01\to\gamma 3} = E_\gamma$, as shown in Figure 3.3. Most capture reactions have positive Q-values (i.e., $Q < 0$ for the corresponding reverse photodisintegration reactions), otherwise nucleus 3 would be unstable by particle emission. Furthermore, many capture reactions have large Q-values, on the order of several MeV. In this case, the integration over γ-ray energy E_γ will not start at zero but at a threshold energy of $E_t = Q_{01\to\gamma 3}$ as explained above (Figure 3.3). Since this implies $E_\gamma \gg kT$, we may use the approximation $e^{E_\gamma/kT} - 1 \approx e^{E_\gamma/kT}$. Figure 3.5 shows the factor $E_\gamma^2/(e^{E_\gamma/kT}-1)$ (solid line) and the approximation $E_\gamma^2/e^{E_\gamma/kT}$ (dashed line) versus γ-ray energy for a stellar temperature of $T = 5$ GK. If the threshold energy $E_t = Q_{01\to\gamma 3}$ is sufficiently large, the difference between the two expressions is negligible. The approximation also

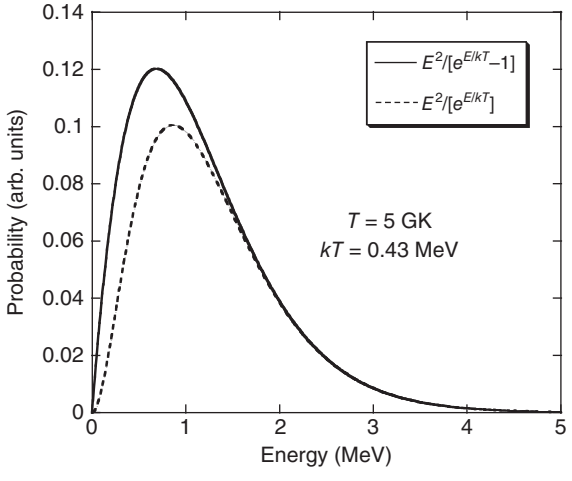

Figure 3.5 Comparison of the exact expression $E_\gamma^2/(e^{E_\gamma/kT}-1)$ (solid line) and the approximation $E_\gamma^2/e^{E_\gamma/kT}$ (dashed line) at a stellar temperature of $T = 5$ GK. For a sufficiently large threshold energy (in this case, for $E_t > 1.5$ MeV), the difference between the two expressions is negligible.

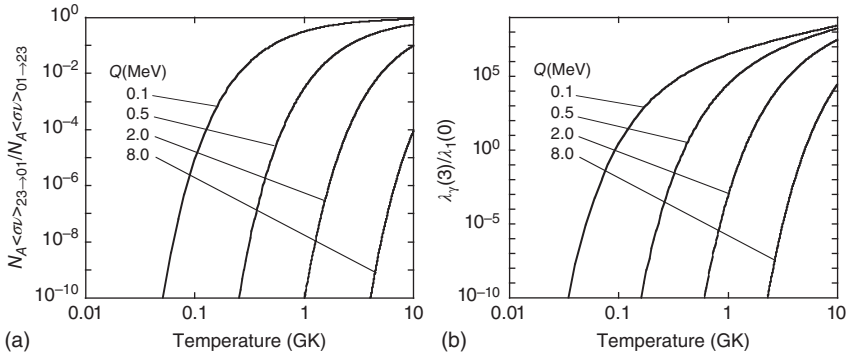

Figure 3.6 (a) Reaction rate ratio of forward and reverse reactions versus temperature. The curves correspond to different values of $Q_{01\to23}$. (b) Ratio of decay constants for photodisintegration reaction and corresponding capture reaction versus temperature for different values of $Q_{01\to\gamma3}$.

holds for smaller Q-values below 1 MeV if charged particles are involved in the process. The photodisintegration cross section is then suppressed at low energies (because of the tunnel effect) where the deviation between the solid and dashed lines in Figure 3.5 is largest. However, the approximation may not be valid for (n,γ) reactions with small Q-values.

With the approximation $e^{E_\gamma/kT} - 1 \approx e^{E_\gamma/kT}$, we obtain from Eq. (3.34) (see also Fowler, Caughlan, and Zimmerman, 1967)

$$\begin{aligned}\frac{\lambda_\gamma(3)}{N_A\langle\sigma v\rangle_{01\to\gamma3}} &= \frac{\frac{8\pi}{h^3c^2}(kT)^{3/2}m_{01}c^2}{\left(\frac{8}{\pi m_{01}}\right)^{1/2}N_A}\frac{(2j_0+1)(2j_1+1)}{(2j_3+1)(1+\delta_{01})} \\ &\quad\times\frac{\int_0^\infty E_{01}\,e^{-(E_{01}+Q_{01\to\gamma3})/kT}\sigma_{01\to\gamma3}\,dE_\gamma}{\int_0^\infty E_{01}\,e^{-E_{01}/kT}\sigma_{01\to\gamma3}\,dE_{01}} \\ &= \left(\frac{2\pi}{h^2}\right)^{3/2}\frac{(m_{01}kT)^{3/2}}{N_A}\frac{(2j_0+1)(2j_1+1)}{(2j_3+1)(1+\delta_{01})}\,e^{-Q_{01\to\gamma3}/kT} \qquad (3.35)\end{aligned}$$

Figure 3.6a shows the ratio of reaction rates, $N_A\langle\sigma v\rangle_{23\to01}/N_A\langle\sigma v\rangle_{01\to23} \approx e^{-Q_{01\to23}/kT}$, for reactions involving particles with rest mass, where the factor containing the spins and reduced masses in Eq. (3.31) is set equal to unity. The different curves correspond to different values of $Q_{01\to23}$. For a positive Q-value, the ratio $N_A\langle\sigma v\rangle_{23\to01}/N_A\langle\sigma v\rangle_{01\to23}$ is always less than unity. It is apparent that the reverse reaction becomes important at sufficiently large temperatures and at small Q-values. Figure 3.6b shows the ratio of decay constants, $\lambda_\gamma(3)/\lambda_1(0) = \lambda_\gamma(3)/[\rho(X_1/M_1)N_A\langle\sigma v\rangle_{01\to\gamma3}]$, for reactions involving photons, where the factor containing the spins in Eq. (3.35) and the term X_1/M_1 are set equal to unity. For the density, an arbitrary value of $\rho = 10^3$ g/cm^3 has been chosen. For all curves shown, the value of $Q_{01\to\gamma3}$ (i.e., for the capture reaction)

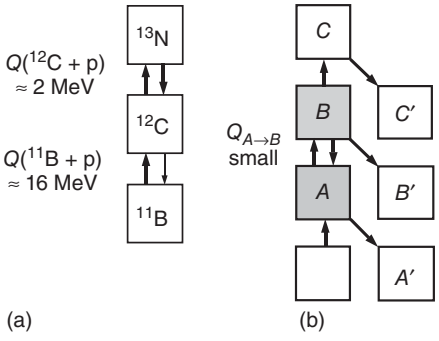

Figure 3.7 Sections of the nuclide chart indicating interactions between nuclei. Arrows that point vertically up show (p,γ) reactions; those pointing vertically down represent (γ,p) photodisintegrations; and those pointing diagonally down to the right correspond to β^+-decays. (a) The reaction chain ^{11}B+p↔^{12}C and ^{12}C+p↔^{13}N at elevated temperatures. (b) A situation depicting an equilibrium between the forward reaction $A+a \rightarrow \gamma+B$ and the reverse reaction $B+\gamma \rightarrow a+A$; see Section 3.1.6.

is positive. It can be seen that the ratio of photodisintegration and capture reaction decay constants can exceed unity and may become very large, depending on the values of temperature and reaction Q-value.

The strong Q-value dependence of the ratio $\lambda_\gamma(3)/\lambda_1(0)$ in Figure 3.6b has an important consequence. Capture reactions involving target nuclei with an even number of protons and neutrons usually have small Q-values, while the Q-values are larger for capture reactions involving an odd number of protons or neutrons. In other words, a relatively large amount of energy is released if an energetically favorable even–even structure can be achieved as a result of the capture process. For example, consider the reaction chain ^{11}B + p ↔ ^{12}C and ^{12}C + p ↔ ^{13}N shown in Figure 3.7a. The corresponding Q-values are $Q_{^{11}\mathrm{B+p}} = 16$ MeV and $Q_{^{12}\mathrm{C+p}} = 2$ MeV. At elevated temperatures, the photodisintegration of ^{12}C will be a relatively slow process, while the photodisintegration of ^{13}N will be considerably faster. As a consequence, the abundance of ^{12}C will be enhanced over that of the neighboring (and less stable) nuclei ^{11}B and ^{13}N. The net effect of photodisintegration processes in stellar plasmas at elevated temperatures is to convert nuclei to more stable species. These considerations will be especially important for the advanced burning stages of massive stars (Section 5.3) and for explosive burning (Sections 5.4.3 and 5.5.1).

3.1.5
Reaction Rates at Elevated Temperatures

Until now we considered only those reactions involving nuclei in their ground states. However, at elevated stellar temperatures, the nuclei will be thermally excited, for example, through photoexcitation, inelastic particle scattering, and other means. These excited states may also participate in nuclear reactions.

We already mentioned in Section 1.7.4 (see Eq. (1.35)) that for a nondegenerate plasma in thermodynamic equilibrium, the ratio of the number density $N_{i\mu}$ of nuclei i in excited state μ and the total number density N_i of nuclei i is given by a Boltzmann distribution

$$P_{i\mu} = \frac{N_{i\mu}}{N_i} = \frac{g_{i\mu} e^{-E_{i\mu}/kT}}{\sum_\mu g_{i\mu} e^{-E_{i\mu}/kT}} = \frac{g_{i\mu} e^{-E_{i\mu}/kT}}{G_i} \tag{3.36}$$

with $g_{i\mu} = (2J_{i\mu} + 1)$, $J_{i\mu}$ and $E_{i\mu}$ the statistical weight, spin, and excitation energy, respectively, of state μ in nucleus i. Recall that the sum over μ defining the partition function, G_i, of nucleus i includes the ground state. The related quantity

$$G_i^{\text{norm}} \equiv \frac{G_i}{g_{ig.s.}} = \frac{\sum_\mu g_{i\mu} e^{-E_{i\mu}/kT}}{g_{ig.s.}} \tag{3.37}$$

is referred to as the *normalized partition function*, where $g_{ig.s.}$ is the statistical weight of the ground state of nucleus i. Numerical values of G_i^{norm} versus temperature are given in Rauscher and Thielemann (2000) and Goriely, Hilaire, and Koning (2008).

Of primary astrophysical importance is the reaction rate involving thermally excited nuclei, $N_A\langle\sigma v\rangle^*$, rather than the rate involving nuclei in the ground state, $N_A\langle\sigma v\rangle$. For the reaction $0 + 1 \rightarrow 2 + 3$, the rate including thermally excited states is obtained by summing over all transitions to relevant excited states in nuclei 2 and 3, and by appropriately averaging over combinations of excited states in nuclei 0 and 1. The number densities N_i entering the reaction rate expression, $r_{01} = N_0 N_1 \langle\sigma v\rangle^*_{01\rightarrow 23}$, refer to the total number of nuclei i per unit volume. For the sake of simplicity, we will disregard in the following excited states of the light particles 1 and 2 in the entrance or exit channel (which is a valid assumption for the proton, neutron, and α-particle). We write for the *stellar* reaction rate

$$\begin{aligned} N_A\langle\sigma v\rangle^*_{01\rightarrow 23} &= \sum_\mu P_{0\mu} \sum_\nu N_A\langle\sigma v\rangle^{\mu\rightarrow\nu}_{01\rightarrow 23} \\ &= \frac{\sum_\mu g_{0\mu} e^{-E_{0\mu}/kT} \sum_\nu N_A\langle\sigma v\rangle^{\mu\rightarrow\nu}_{01\rightarrow 23}}{G_0} \end{aligned} \tag{3.38}$$

where μ and ν are labels for states in the target nucleus 0 and the residual nucleus 3, respectively, and G_0 denotes the partition function of target nucleus 0. It must be emphasized that experiments usually provide information only for the calculation of the *laboratory* reaction rate

$$N_A\langle\sigma v\rangle_{01\rightarrow 23} = \sum_\nu N_A\langle\sigma v\rangle^{\text{g.s.}\rightarrow\nu}_{01\rightarrow 23} \tag{3.39}$$

that is, the rate involving all transitions from the ground state of the target nucleus 0 to the ground state and to excited states of the residual nucleus 3. In most cases, cross sections involving excited target nuclei cannot be measured in the laboratory and have to be calculated using theoretical models.

We can derive a number of useful quantities from Eqs. (3.36)–(3.39). The ratio of stellar to laboratory reaction rates, called *stellar enhancement factor* (SEF), is defined by

$$\mathrm{SEF} \equiv \frac{N_A\langle\sigma v\rangle^{*}_{01\to 23}}{N_A\langle\sigma v\rangle_{01\to 23}} = \frac{\sum_\mu g_{0\mu} e^{-E_{0\mu}/kT} \sum_\nu N_A\langle\sigma v\rangle^{\mu\to\nu}_{01\to 23}}{G_0 \sum_\nu N_A\langle\sigma v\rangle^{\mathrm{g.s.}\to\nu}_{01\to 23}} \tag{3.40}$$

Numerical values, estimated by using the Hauser–Feshbach statistical model (Section 2.7), are given in Rauscher and Thielemann (2000) and Goriely, Hilaire, and Koning (2008). The above expressions are also valid if general thermodynamic equilibrium has not been attained, as long as the excited states are in equilibrium with the ground state (Fowler, Caughlan, and Zimmerman, 1967, 1975). Of primary astrophysical interest are the abundances of all levels that will decay to the ground state after final cooling in the stellar event. Therefore, the sums over μ and ν include all bound states up to an energy at which the levels become unbound and decay primarily via particle emission. Similar statements apply to the reverse reaction $2 + 3 \to 0 + 1$. An explicit expression for $N_A\langle\sigma v\rangle^{*}_{01\to 23}$ that is applicable to the special case of narrow resonances will be derived in Section 3.2.4.

It is frequently overlooked that the stellar "enhancement" factor can be smaller than unity. This may occur, for example, if a significant fraction of target nuclei, 0, reside in excited states and if, at the same time, the reaction rates involving these excited states for some reason (e.g., angular momentum, parity, or isospin selection rules) are much smaller than the ground state rate. For the same reason, a value of SEF ≈ 1 does not necessarily imply a negligible rate contribution from excited target states: the interplay of significant excited target state population, $P_{0\mu}$, and small reaction rates from excited target states, $N_A\langle\sigma v\rangle^{\mu\to\nu}_{01\to 23}$, can give rise to a stellar enhancement factor near unity.

To quantify the fractional contribution of the laboratory rate to the stellar rate, we introduce the *stellar rate ground state fraction* (GSF), defined by (Rauscher *et al.*, 2011)

$$\mathrm{GSF} \equiv \frac{P_{0g.s.} N_A\langle\sigma v\rangle_{01\to 23}}{N_A\langle\sigma v\rangle^{*}_{01\to 23}} = \frac{P_{0g.s.} \sum_\nu N_A\langle\sigma v\rangle^{g.s.\to\nu}_{01\to 23}}{\sum_\mu P_{0\mu} \sum_\nu N_A\langle\sigma v\rangle^{\mu\to\nu}_{01\to 23}} = \frac{1}{G_0^{\mathrm{norm}}\ \mathrm{SEF}} \tag{3.41}$$

The range of possible values amounts to $0 \le \mathrm{GSF} \le 1$. The limiting value of GSF $= 1$ is obtained for $P_{0g.s.} = 1$, and the stellar rate becomes equal to the laboratory rate, implying SEF $= 1$. It is apparent that the stellar rate ground state fraction contains more information than the stellar enhancement factor. It is also apparent that the interplay of population, $P_{0\mu}$, and reaction rates, $N_A\langle\sigma v\rangle^{\mu\to\nu}_{01\to 23}$, involving excited target states, μ, may give rise to a significant overall contribution of excited target states to the total rate (GSF < 1), although the stellar enhancement factor may not be affected (SEF $= 1$). Numerical values of the stellar enhancement factor and the stellar rate ground state fraction versus temperature for about 100 charged-particle-induced reactions involving stable and unstable target nuclei in the $A \le 40$ range are shown in Figure 3.8. With a

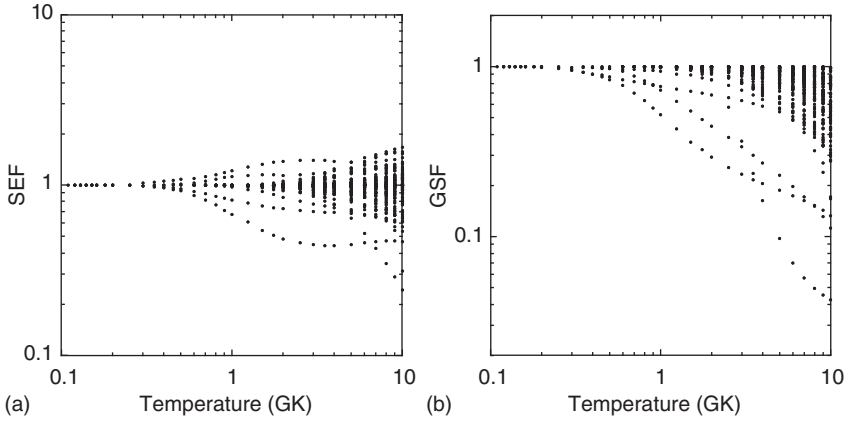

Figure 3.8 Values of (a) stellar enhancement factor (SEF) and (b) ground state fraction (GSF) versus stellar temperature for about 100 charged-particle-induced reactions on $A \leq 40$ target nuclei. Only those data points are shown for which either value deviates from unity; this applied to 20% of the cases. The data are adopted from Sallaska *et al.* (2013).

few exceptions, values of SEF range from 0.5 to 1.8, while GSF is typically larger than 0.3 in this target mass range. See also Problem 3.7.

It is interesting to point out that, at a given temperature, the SEFs for photodisintegration reactions, (γ,p), (γ,α), (γ,n), are usually considerably larger than those for particle-induced reactions. This can be explained as follows. The population of excited states decreases exponentially with increasing excitation energy, according to Eq. (3.36). At the same time, however, this effect is compensated by the larger number of photons available with a smaller energy sufficient to initiate the photodisintegration, according to Eq. (3.17). Thus, many thermally populated levels may have comparable contributions to the total stellar photodisintegration rate. In other words, the ground state (or laboratory) reaction rate may represent only a small fraction of the total stellar photodisintegration rate. Typically, at elevated temperatures in excess of ≈ 1 GK one finds stellar enhancement factors of ≈ 100–10000 for photon-induced reactions on heavy target nuclei (Mohr, Fülöp, and Utsunomiya, 2007). This cancellation effect is absent for either charged-particle or neutron-induced reactions since the astrophysically most important bombarding energy range is not altered by the energy of the excited state, as will be explained in Section 3.2. Thus, the impact of excited states on the total reaction rate generally decreases with increasing excitation energy and, as a result, the stellar enhancement factors are considerably smaller than for photodisintegration reactions.

The relationships between forward and reverse reaction rates derived in Section 3.1.4 assume that all interacting nuclei are in their ground states. They also need to be modified to take thermally excited states into account. As a simple example, consider the situation shown in Figure 3.9. A laboratory measurement

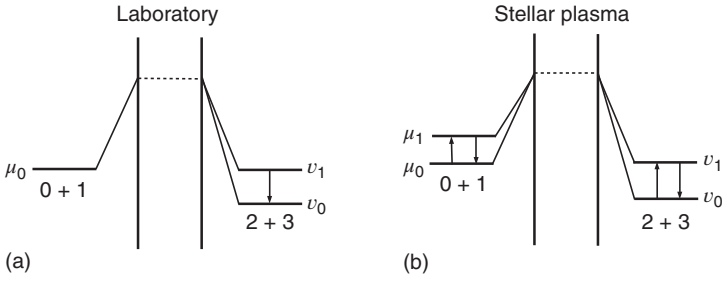

Figure 3.9 Reactions between the pairs of nuclei 0 + 1 and 2 + 3. (a) In the laboratory, the nuclei 0 and 1 are in their ground states and transitions may occur to excited levels of nuclei 2 and 3. (b) In the stellar plasma, excited levels participate in the reaction in both the entrance and the exit channel. Only a single excited state is shown in each channel for reasons of clarity.

of the cross section for the reaction $0 + 1 \rightarrow 2 + 3$ at a constant bombarding energy E considers only target nuclei 0 in their ground state and sums over all transitions to the ground state or to excited states in the final nucleus 3. In a stellar plasma, on the other hand, both the target and the residual nucleus may be thermally excited, and all possible transitions between excited states μ and ν in nuclei 0 and 3, respectively, have to be taken into account.

Suppose that there are a number of excited states in nucleus 0 and in nucleus 3 that are all in thermal equilibrium with their respective ground states. Furthermore, assume that the light particles 1 and 2 have no excited states. The *stellar* rates for forward and reverse reactions are then obtained by appropriately averaging over initial states and summing over final states. The expression for the forward stellar rate is given by Eq. (3.38), while for the reverse stellar rate one has

$$\begin{aligned} N_A\langle\sigma v\rangle^*_{23\rightarrow 01} &= \sum_\nu P_{3\nu} \sum_\mu N_A\langle\sigma v\rangle^{\nu\rightarrow\mu}_{23\rightarrow 01} \\ &= \frac{\sum_\nu g_{3\nu} e^{-E_{3\nu}/kT} \sum_\mu N_A\langle\sigma v\rangle^{\nu\rightarrow\mu}_{23\rightarrow 01}}{\sum_\nu g_{3\nu} e^{-E_{3\nu}/kT}} \end{aligned} \tag{3.42}$$

Into this expression, we substitute our earlier result (see Eq. (3.31))

$$\frac{N_A\langle\sigma v\rangle^{\nu\rightarrow\mu}_{23\rightarrow 01}}{N_A\langle\sigma v\rangle^{\mu\rightarrow\nu}_{01\rightarrow 23}} = \frac{g_{0\mu} g_1 (1+\delta_{23})}{g_{3\nu} g_2 (1+\delta_{01})} \left(\frac{m_{01}}{m_{23}}\right)^{3/2} e^{-Q^{\mu\rightarrow\nu}_{01\rightarrow 23}/kT} \tag{3.43}$$

We also make the nonrelativistic approximations $m_{01} = m^\mu_{01}$ and $m_{23} = m^\nu_{23}$. For the ground states, we have $e^{-E_0/kT} = e^{-E_3/kT} = 1$. By using $Q_{01\rightarrow 23} = Q^{\mu\rightarrow\nu}_{01\rightarrow 23} + E_{3\nu} - E_{0\mu}$ (Figure 3.9b), one obtains from Eqs. (3.38), (3.42), and (3.43)

$$\frac{N_A\langle\sigma v\rangle^*_{23\rightarrow 01}}{N_A\langle\sigma v\rangle^*_{01\rightarrow 23}} = \frac{(1+\delta_{23})}{(1+\delta_{01})} \left(\frac{m_{01}}{m_{23}}\right)^{3/2} \frac{g_0 g_1 G^{\text{norm}}_0}{g_2 g_3 G^{\text{norm}}_3} e^{-Q_{01\rightarrow 23}/kT} \tag{3.44}$$

where the quantity $Q_{01\rightarrow 23}$ denotes the Q-value connecting the ground states.

Equation (3.44) holds for any number of excited states in the target and residual nucleus. It is also independent of the reaction mechanism (e.g., nonresonant versus resonant process, number and properties of narrow resonances, and so on). We can easily generalize this result by allowing for excitations in the nuclei 1 and 2. Numerically, we find from Eq. (3.44) for reactions involving only particles with rest mass

$$\frac{N_A\langle\sigma v\rangle^*_{23\to 01}}{N_A\langle\sigma v\rangle^*_{01\to 23}} = \frac{(2j_0+1)(2j_1+1)(1+\delta_{23})}{(2j_2+1)(2j_3+1)(1+\delta_{01})} \times \left(\frac{G_0^{\rm norm}G_1^{\rm norm}}{G_2^{\rm norm}G_3^{\rm norm}}\right)\left(\frac{M_0M_1}{M_2M_3}\right)^{3/2} e^{-11.605\,Q/T_9} \tag{3.45}$$

and from Eq. (3.35) for reactions involving photons

$$\frac{\lambda^*_\gamma(3\to 01)}{N_A\langle\sigma v\rangle^*_{01\to\gamma 3}} = 9.8685\times 10^9\, T_9^{3/2}\frac{(2j_0+1)(2j_1+1)}{(2j_3+1)(1+\delta_{01})} \times \left(\frac{G_0^{\rm norm}G_1^{\rm norm}}{G_3^{\rm norm}}\right)\left(\frac{M_0M_1}{M_3}\right)^{3/2} e^{-11.605\,Q/T_9} \tag{3.46}$$

with j_i and M_i being the ground-state spins and masses (in u) of the nuclei, Q the ground-state Q-value of the forward reaction $0+1\to 2+3$ or $0+1\to\gamma+3$ (in MeV), and $T_9\equiv T/10^9$ K. In the following sections, we will mostly suppress the asterisk, with the understanding that rates or decay constants must take into account the effects of thermally excited states if appropriate.

Example 3.2

Evaluations of experimental thermonuclear reaction rates (Angulo *et al.*, 1999; Iliadis *et al.*, 2010; Sallaska *et al.*, 2013) list laboratory reaction rates and have to be modified for use in stellar model calculations. Consider the ^{32}S(p,γ)^{33}Cl reaction at a stellar temperature of $T = 10$ GK ($T_9 = 10$). For the laboratory reaction rate (assuming that the ^{32}S target nuclei are in the ground state), a value of $N_A\langle\sigma v\rangle_{^{32}\mathrm{S+p}} = 1.23\times 10^3$ cm^{3}mol^{-1}s^{-1} is reported in Iliadis *et al.* (2010). Calculate the stellar rate for the forward reaction and the stellar decay constant for the reverse reaction.

The stellar reaction rate (considering thermally excited ^{32}S nuclei) is given by

$$\begin{aligned} N_A\langle\sigma v\rangle^*_{^{32}\mathrm{S+p}} &= \mathrm{SEF}\cdot N_A\langle\sigma v\rangle_{^{32}\mathrm{S+p}} \\ &= 0.83\cdot 1.23\times 10^3\ \mathrm{cm^3mol^{-1}s^{-1}} = 1.02\times 10^3\ \mathrm{cm^3mol^{-1}s^{-1}} \end{aligned}$$

with a value of SEF = 0.83 adopted from Rauscher and Thielemann (2000). The corresponding stellar decay constant for the photodisintegration of ^{33}Cl is obtained from the spins $j_{^{32}\mathrm{S}} = 0$, $j_\mathrm{p} = 1/2$, $j_{^{33}\mathrm{Cl}} = 3/2$, the value $Q_{^{32}\mathrm{S+p}} = 2.2765$ MeV, and from the normalized partition functions $G^{\rm norm}_{^{32}\mathrm{S}} = 1.6$,

$G_{\mathrm{p}}^{\mathrm{norm}} = 1$, $G_{^{33}\mathrm{Cl}}^{\mathrm{norm}} = 1.9$ (Rauscher and Thielemann, 2000)

$$\begin{aligned}\lambda_\gamma^*(^{33}\mathrm{Cl} \to {}^{32}\mathrm{S} + \mathrm{p}) &= \frac{\lambda_\gamma^*(^{33}\mathrm{Cl} \to {}^{32}\mathrm{S} + \mathrm{p})}{N_A\langle\sigma v\rangle^*_{^{32}\mathrm{S+p}}} N_A\langle\sigma v\rangle^*_{^{32}\mathrm{S+p}} \\ &= 9.8685 \times 10^9 \cdot 10^{3/2} \frac{1\cdot 2}{4\cdot 1}\left(\frac{1.6\cdot 1}{1.9}\right)\left(\frac{32.0\cdot 1.0}{33.0}\right)^{3/2} \\ &\quad \times e^{-11.605\cdot 2.2765/10} \cdot 1.02 \times 10^3\,\mathrm{cm^3 mol^{-1} s^{-1}} \\ &= 9.11 \times 10^{12}\,\mathrm{s^{-1}}\end{aligned}$$

3.1.6 Reaction Rate Equilibria

Consider a forward and reverse reaction involving four particles with rest mass, $0 + 1 \to 2 + 3$ and $2 + 3 \to 0 + 1$. The overall reaction rate for $0 + 1 \leftrightarrow 2 + 3$ is then given by

$$r = r_{01\to 23} - r_{23\to 01} = \frac{N_0 N_1 \langle\sigma v\rangle_{01\to 23}}{(1+\delta_{01})} - \frac{N_2 N_3 \langle\sigma v\rangle_{23\to 01}}{(1+\delta_{23})} \tag{3.47}$$

For equilibrium conditions ($r = 0$), we find from Eqs. (3.45) and (3.47) for the ratio of nuclide abundances

$$\begin{aligned}\frac{N_2 N_3}{N_0 N_1} &= \frac{(1+\delta_{23})}{(1+\delta_{01})}\frac{\langle\sigma v\rangle_{01\to 23}}{\langle\sigma v\rangle_{23\to 01}} \\ &= \frac{(2j_2+1)(2j_3+1)}{(2j_0+1)(2j_1+1)}\frac{G_2^{\mathrm{norm}} G_3^{\mathrm{norm}}}{G_0^{\mathrm{norm}} G_1^{\mathrm{norm}}}\left(\frac{m_{23}}{m_{01}}\right)^{3/2} e^{Q_{01\to 23}/kT}\end{aligned} \tag{3.48}$$

Similarly, for reactions involving photons we find for the overall reaction rate $0 + 1 \leftrightarrow \gamma + 3$

$$r = r_{01\to\gamma 3} - r_{\gamma 3\to 01} = \frac{N_0 N_1 \langle\sigma v\rangle_{01\to\gamma 3}}{(1+\delta_{01})} - \lambda_\gamma(3) N_3 \tag{3.49}$$

and for equilibrium conditions ($r = 0$), we obtain from Eqs. (3.23), (3.46), and (3.49) the expression

$$\begin{aligned}\frac{N_3}{N_0 N_1} &= \frac{1}{(1+\delta_{01})}\frac{\langle\sigma v\rangle_{01\to\gamma 3}}{\lambda_\gamma(3)} = \frac{1}{(1+\delta_{01})}\frac{1}{N_1}\frac{\lambda_1(0)}{\lambda_\gamma(3)} \\ &= \left(\frac{\hbar^2}{2\pi}\right)^{3/2} \frac{1}{\left(m_{01}kT\right)^{3/2}} \frac{(2j_3+1)}{(2j_0+1)(2j_1+1)} \frac{G_3^{\mathrm{norm}}}{G_0^{\mathrm{norm}} G_1^{\mathrm{norm}}} e^{Q_{01\to\gamma 3}/kT}\end{aligned} \tag{3.50}$$

The last expression is referred to as the *Saha statistical equation*.

The equilibrium condition can also be expressed in terms of abundance evolutions. Suppose that 0 and 3 denote heavy nuclei and 1 and 2 represent light particles (protons, neutrons, or α-particles). The *partial* rates of change of isotopic

abundances N_0 and N_3 that are caused by the processes $0 + 1 \rightarrow 2 + 3$ and $2 + 3 \rightarrow 0 + 1$, respectively, are given by (see Eq. (3.20))

$$\left(\frac{dN_0}{dt}\right)_{01\rightarrow 23} = -r_{01\rightarrow 23} \tag{3.51}$$

$$\left(\frac{dN_3}{dt}\right)_{23\rightarrow 01} = -r_{23\rightarrow 01} \tag{3.52}$$

We may visualize these processes by flows of material from species 0 to 3 and vice versa. Therefore, the partial rates of change of abundances, $(dN_0/dt)_{01\rightarrow 23}$ and $(dN_3/dt)_{23\rightarrow 01}$, are referred to as *abundance flows*. The *net* abundance flow f between two species 0 and 3 is given by the difference between forward and reverse abundance flow

$$\begin{aligned} f_{03} &\equiv \left|\left(\frac{dN_0}{dt}\right)_{01\rightarrow 23} - \left(\frac{dN_3}{dt}\right)_{23\rightarrow 01}\right| = \left|r_{01\rightarrow 23} - r_{23\rightarrow 01}\right| \\ &= \left|N_0 N_1 \langle \sigma v\rangle_{01\rightarrow 23} - N_2 N_3 \langle \sigma v\rangle_{23\rightarrow 01}\right| \end{aligned} \tag{3.53}$$

The equilibrium condition can be expressed by either of the following relations:

$$\left(\frac{dN_0}{dt}\right)_{01\rightarrow 23} \approx \left(\frac{dN_3}{dt}\right)_{23\rightarrow 01} \gg f_{03} \approx 0 \tag{3.54}$$

$$\phi_{03} \equiv \frac{\left|r_{01\rightarrow 23} - r_{23\rightarrow 01}\right|}{\max(r_{01\rightarrow 23}, r_{23\rightarrow 01})} \approx 0 \tag{3.55}$$

In this case, the net abundance flow is considerably smaller in absolute magnitude than either the forward flow or the reverse flow. Contrary to the steady-state assumption (Section 3.1.3), the equilibrium condition does not imply constant abundances N_0 or N_3. Those may change if nuclei 0 and 3 are linked to other species by nuclear processes. The equilibrium condition refers to the (near) equality of forward and reverse abundance flows between a pair of nuclei. When a group of several pairs of nuclei comes into equilibrium, for example, via the processes (p,γ) $\leftrightarrow$ (γ,p), (n,γ) $\leftrightarrow$ (γ,n), and (α,γ) $\leftrightarrow$ (γ,α), the resulting solution of the reaction network is called a *quasi-equilibrium*. For more information on equilibria, see Arnett (1996).

In the following, we will discuss reactions involving photons in more detail. During the complex interplay involving several different nuclear reactions and β-decays, it happens frequently that a particular reaction converting nucleus A by particle capture to nucleus B ($A + a \rightarrow B$) exhibits a small Q-value. If the stellar plasma can attain sufficiently high temperatures, then the photodisintegration of nucleus B has to be taken into account and may significantly alter the nucleosynthesis.

Consider Figure 3.7b, showing a number of different nuclei involved in proton captures, photodisintegrations, and β^+-decays. Suppose now that the Q-value for the capture reaction $A(a,\gamma)B$ is relatively small (less than a few hundred kilo electron volt) and that the stellar temperature is high. An equilibrium between the

abundances of nuclei A and B is established for two necessary conditions,

$$\lambda_{A\to B} > \lambda_{A\to A'} \tag{3.56}$$

$$\lambda_{B\to A} > \lambda_{B\to C} + \lambda_{B\to B'} \tag{3.57}$$

If the first condition is not fulfilled, nucleus B is bypassed altogether. If the second condition is not fulfilled, there is no process that creates nucleus A after it has been destroyed. We will also assume that the photodisintegration of C is negligible (i.e., $\lambda_{C\to C'} > \lambda_{C\to B}$), so that C does not come into equilibrium with A and B. It is now of interest to determine which path the nucleosynthesis will follow, either bypassing the nucleus B via β^+-decay ($A \to A'$), or via the competing reaction sequence through nucleus B to either C or B' [$A \to B \to (C$ or $B')$]. The latter process, $A \to B \to C$, is referred to as *sequential two-particle capture*. For a distinction between sequential and direct two-particle capture, see Grigorenko and Zhukov (2005).

Suppose that an equilibrium between the abundances of nuclei A and B has been established. The reaction rate for conversion of nucleus A to either C (via capture of particle a) or B' (via β^+-decay) is then given by the expressions (see Eq. (3.21))

$$r_{A\to(C\text{ or }B')} = N_B^e \lambda_{B\to C} + N_B^e \lambda_{B\to B'} \tag{3.58}$$

$$r_{A\to(C\text{ or }B')} = N_A^e \lambda_{A\to B\to C} + N_A^e \lambda_{A\to B\to B'} = N_A^e \lambda_{A\to B\to(C\text{ or }B')} \tag{3.59}$$

where N_A^e and N_B^e denote the equilibrium abundances of A and B, respectively. From Eqs. (3.58) and (3.59), we obtain

$$\lambda_{A\to B\to(C\text{ or }B')} = \frac{N_B^e}{N_A^e}(\lambda_{B\to C} + \lambda_{B\to B'}) \tag{3.60}$$

For the equilibrium abundance ratio N_B^e/N_A^e, we use the Saha equation (see Eq. (3.50))

$$\begin{aligned}\frac{N_B}{N_A N_a} &= \frac{\langle\sigma v\rangle_{A\to B}}{\lambda_{B\to A}} = \frac{1}{N_a}\frac{\lambda_{A\to B}}{\lambda_{B\to A}} \\ &= \left(\frac{h^2}{2\pi}\right)^{3/2} \frac{1}{\left(m_{Aa}kT\right)^{3/2}} \frac{(2j_B+1)}{(2j_A+1)(2j_a+1)} \frac{G_B^{\text{norm}}}{G_A^{\text{norm}} G_a^{\text{norm}}}\, e^{Q_{A\to B}/kT}\end{aligned} \tag{3.61}$$

Thus,

$$\begin{aligned}\lambda_{A\to B\to(C\text{ or }B')} &= \frac{\lambda_{A\to B}}{\lambda_{B\to A}}\left(\lambda_{B\to C} + \lambda_{B\to B'}\right) \\ &= N_a \left(\frac{h^2}{2\pi}\right)^{3/2} \frac{1}{\left(m_{Aa}kT\right)^{3/2}} \frac{(2j_B+1)}{(2j_A+1)(2j_a+1)} \\ &\quad \times \frac{G_B^{\text{norm}}}{G_A^{\text{norm}} G_a^{\text{norm}}} e^{Q_{A\to B}/kT}\left(\lambda_{B\to C} + \lambda_{B\to B'}\right)\end{aligned} \tag{3.62}$$

Numerically, we find

$$\lambda_{A\to B\to(C\,\text{or}\,B')} = 1.0133\times10^{-10}\rho\frac{X_a}{M_a}\left(\frac{M_B}{M_A M_a}\right)^{3/2}\frac{g_B}{g_A g_a}\left(\frac{G_B^{\text{norm}}}{G_A^{\text{norm}}G_a^{\text{norm}}}\right) \times T_9^{-3/2}e^{11.605\,Q_{A\to B}/T_9}\left(\lambda_{B\to C}+\lambda_{B\to B'}\right) \tag{3.63}$$

where the normalized partition functions account for the influence of thermally excited levels and the Q-value is in mega electron volts. The quantity $\lambda_{A\to B\to(C\,\text{or}\,B')}$ introduced in Eq. (3.59) has a slightly different meaning from the usual decay constant of Eq. (3.19). The latter describes the decay probability of a particular nucleus per time, while the former represents the probability for the conversion of nucleus A along a specified path ($A \to B \to (C$ or B'), in this case). This distinction becomes important for identical particles. If the process $A \to B \to (C$ or $B')$ destroys two (or three) identical particles A, the right-hand sides of Eqs. (3.62) and (3.63) must be multiplied by a factor of 2 (or 3) to calculate the decay constant of nucleus A.

The path $A \to B \to (C$ or $B')$ becomes more important with increasing values of $\lambda_{A\to B}$, $\lambda_{B\to C}$, or $\lambda_{B\to B'}$, and decreasing values of $\lambda_{B\to A}$. It must be emphasized that the ratio $\lambda_{A\to B}/\lambda_{B\to A}$ is independent of the cross section, and depends mainly on the value of $Q_{A\to B}$. Also, we replaced the equilibrium abundance N_B^e/N_A^e by the ratio $\lambda_{A\to B}/\lambda_{B\to A}$, which in turn is determined by the reciprocity theorem (Section 3.1.4). Thus, we made no assumptions regarding the specific processes occurring between nuclei A and B. Those include, for example, particle capture and photodisintegration, or particle inelastic scattering and particle decay. Consequently, the above expression is also valid for negative values of $Q_{A\to B}$, that is, if nucleus B decays by direct particle emission. The factor $\rho\, e^{Q_{A\to B}/T}$ implies that $\lambda_{A\to B\to(C\,\text{or}\,B')}$ becomes smaller for a decreasing Q-value or an increasing temperature, but becomes larger for increasing density. It will be shown in Chapter 5 how the interplay of temperature, density, Q-values, half-lives, and reaction rates influences sensitively the most likely nucleosynthesis path. The decay constant for the case that three nuclei A, B, and C come into equilibrium will be addressed in Problem 3.1. See also Schatz *et al.* (1998).

Example 3.3

The following situation occurs in hydrogen burning environments at high temperatures (thermonuclear explosions). Consider the specific case shown in Figure 3.10a. The reaction $^{21}\text{Mg} + \text{p} \to \gamma + {}^{22}\text{Al}$ has a small estimated Q-value of $Q_{^{21}\text{Mg}+\text{p}} = 163$ keV. At $T = 0.6$ GK, $\rho = 10^4$ g/cm^3 and $X_\text{H}/M_\text{H} = 0.7$, the following decay constants are obtained from tabulated reaction rates and β-decay half-lives:

$$\lambda_{A\to B} = \lambda_{^{21}\text{Mg}\to{}^{22}\text{Al}} = 1.1\times10^3\ \text{s}^{-1}$$
$$\lambda_{A\to A'} = \lambda_{^{21}\text{Mg}\to{}^{21}\text{Na}} = 5.6\ \text{s}^{-1}$$

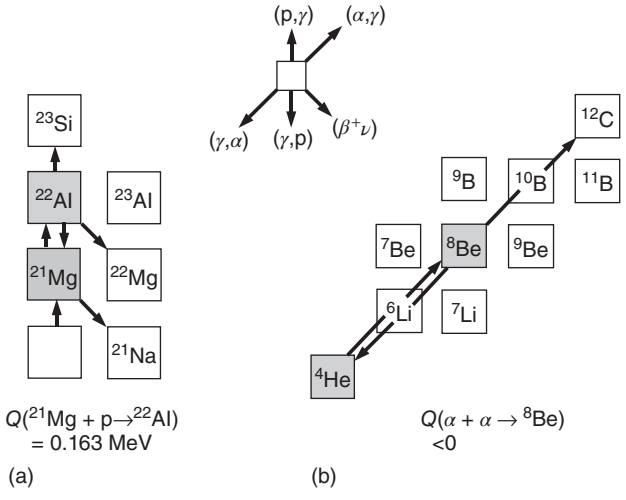

Figure 3.10 Sections of the nuclide chart depicting reaction rate equilibria involving (a) (p,γ)↔(γ,p) reactions and (b) the 3α reaction. In each case, equilibrium has been achieved between the two nuclei shown as gray squares.

$$\lambda_{B\to A} = \lambda_{^{22}\mathrm{Al}\to{}^{21}\mathrm{Mg}} = 3.4\times10^{7}\ \mathrm{s}^{-1}$$
$$\lambda_{B\to C} = \lambda_{^{22}\mathrm{Al}\to{}^{23}\mathrm{Si}} = 3.1\times10^{4}\ \mathrm{s}^{-1}$$
$$\lambda_{B\to B'} = \lambda_{^{22}\mathrm{Al}\to{}^{22}\mathrm{Mg}} = 26.2\,\mathrm{s}^{-1}$$

The above decay constants fulfill the conditions of Eqs. (3.56) and (3.57). Thus, an equilibrium between the abundances of ^{21}Mg and ^{22}Al is quickly established. We would like to determine if the nucleosynthesis proceeds via ^{21}Mg β^+-decay or via sequential two-proton capture to ^{23}Si. From Eq. (3.62), we obtain

$$\lambda_{^{21}\mathrm{Mg}\to{}^{22}\mathrm{Al}\to(^{23}\mathrm{Si}\ \mathrm{or}\ {}^{22}\mathrm{Mg})} = \frac{\lambda_{^{21}\mathrm{Mg}\to{}^{22}\mathrm{Al}}}{\lambda_{^{22}\mathrm{Al}\to{}^{21}\mathrm{Mg}}}\left(\lambda_{^{22}\mathrm{Al}\to{}^{23}\mathrm{Si}} + \lambda_{^{22}\mathrm{Al}\to{}^{22}\mathrm{Mg}}\right)$$
$$= \frac{1.1\times10^{3}\ \mathrm{s}^{-1}}{3.4\times10^{7}\ \mathrm{s}^{-1}}\left(3.1\times10^{4}\ \mathrm{s}^{-1} + 26.2\,\mathrm{s}^{-1}\right) = 1.0\,\mathrm{s}^{-1}$$

which has to be compared to

$$\lambda_{^{21}\mathrm{Mg}\to{}^{21}\mathrm{Na}} = 5.6\,\mathrm{s}^{-1}$$

Hence, the nucleosynthesis path via ^{21}Mg($\beta^+\nu$)^{21}Na is favored by a factor of $5.6/1.0 = 5.6$.

Example 3.4

One of the most important reactions involving α-particles is the *triple-α reaction* (3α). It proceeds in two steps: (i) $\alpha + \alpha \to {}^{8}$Be, and (ii) ^{8}Be + $\alpha \to {}^{12}$C. The Q-value for the first step is $Q_{\alpha+\alpha\to{}^{8}\mathrm{Be}} = -92.1$ keV and, therefore, ^{8}Be is particle unstable

(i.e., it decays by breaking up into two α-particles). This breakup is considerably faster than the fusion of two α-particles into ^{8}Be and, consequently, an equilibrium is established between the abundances of ^{4}He and ^{8}Be. The second step involves the capture of another α-particle on the small equilibrium abundance of ^{8}Be, as shown in Figure 3.10b. Estimate the decay constant, $\lambda_{\alpha+\alpha+\alpha\rightarrow{}^{12}\mathrm{C}}$, for the 3α reaction at a temperature of $T = 0.3$ GK and density of $\rho = 10^5$ g/cm^3, assuming a mass fraction of $X_\alpha = 1$ and $N_A\langle\sigma v\rangle_{\alpha+{}^8\mathrm{Be}\rightarrow{}^{12}\mathrm{C}} = 1.17\times10^{-2}$ cm^{3}mol^{-1}s^{-1} (Caughlan and Fowler, 1988).

From Eqs. (3.62) and (3.63), one finds

$$\begin{aligned}\lambda_{\alpha+\alpha+\alpha\rightarrow{}^{12}\mathrm{C}} &= 3N_\alpha\left(\frac{h^2}{2\pi}\right)^{3/2}\frac{1}{\left(m_{\alpha\alpha}kT\right)^{3/2}}\frac{g_{^8\mathrm{Be}}}{g_\alpha g_\alpha}\,e^{Q_{\alpha+\alpha\rightarrow{}^8\mathrm{Be}}/kT}\lambda_{^8\mathrm{Be}+\alpha\rightarrow{}^{12}\mathrm{C}}\\ &= 1.0133\times10^{-10}\rho\frac{X_\alpha}{M_\alpha}\,3\left(\frac{M_{^8\mathrm{Be}}}{M_\alpha M_\alpha}\right)^{3/2}\frac{g_{^8\mathrm{Be}}}{g_\alpha g_\alpha}\,T_9^{-3/2}\\ &\quad\times e^{11.605\,Q_{\alpha+\alpha\rightarrow{}^8\mathrm{Be}}/T_9}\lambda_{^8\mathrm{Be}+\alpha\rightarrow{}^{12}\mathrm{C}}\end{aligned}$$

Since three identical particles are destroyed by the 3α reaction, we have $3r_{\alpha\alpha\alpha} = N_\alpha\lambda_{\alpha\alpha\alpha}$ and a factor of three has been included in the above expression. At this temperature we adopt for all normalized partition functions a value of $G_i^{\mathrm{norm}} = 1$ (Rauscher and Thielemann, 2000). The spins of the α-particle and of ^{8}Be are $j_i = 0$, thus $g_i = 1$.

With the substitution $\lambda_{^8\mathrm{Be}+\alpha\rightarrow{}^{12}\mathrm{C}} = \rho(X_\alpha/M_\alpha)N_A\langle\sigma v\rangle_{^8\mathrm{Be}+\alpha\rightarrow{}^{12}\mathrm{C}}$ (see Eq. (3.23)), we find

$$\begin{aligned}\lambda_{\alpha+\alpha+\alpha\rightarrow{}^{12}\mathrm{C}} &= 1.0133\times10^{-10}(10^5)^2\left(\frac{1}{4.0}\right)^2\,3\left(\frac{8.0}{4.0\cdot4.0}\right)^{3/2}(0.3)^{-3/2}\\ &\quad\times e^{-11.605\cdot0.0921/0.3}\cdot1.17\times10^{-2} = 1.35\times10^{-4}\ \mathrm{s}^{-1}\end{aligned}$$

At very low ($T < 100$ MK) and very high ($T > 2$ GK) stellar temperatures, the decay constant for the 3α reaction cannot be calculated with the above expression and the formalism becomes more involved (Nomoto, Thielemann, and Miyaji, 1985; Angulo *et al.*, 1999).

3.1.7
Nuclear Energy Generation

Suppose that the forward reaction $0 + 1 \rightarrow 2 + 3$ is exothermic. The nuclear energy released per reaction is given by the Q-value. The energy production per unit time and unit mass is then given by

$$\varepsilon_{01\rightarrow23} = \frac{Q_{01\rightarrow23}r_{01\rightarrow23}}{\rho} = \frac{Q_{01\rightarrow23}}{\rho}\frac{N_0N_1\langle\sigma v\rangle_{01\rightarrow23}}{(1+\delta_{01})} \tag{3.64}$$

Similarly, for the endothermic reverse reaction, we obtain

$$\varepsilon_{23\to 01} = -\frac{Q_{01\to 23}}{\rho}\frac{N_2 N_3 \langle \sigma v\rangle_{23\to 01}}{(1+\delta_{23})} \tag{3.65}$$

$$\varepsilon_{\gamma 3\to 01} = -\frac{Q_{01\to 23}}{\rho} N_3 \lambda_\gamma(3) \tag{3.66}$$

At higher temperatures, the reverse reaction has to be taken into account and the overall energy generation for the process $0 + 1 \leftrightarrow 2 + 3$ is $\varepsilon_{01\to 23} + \varepsilon_{23\to 01}$ for reactions involving particles with rest mass and $\varepsilon_{01\to\gamma 3} + \varepsilon_{\gamma 3\to 01}$ if species 2 is a photon.

If reactions produce electrons, positrons, or γ-rays, then their energy is retained in the stellar plasma. Neutrinos, on the other hand, interact so weakly with the medium that they escape from the site of thermonuclear burning (except in special circumstances, such as the big bang or core collapse supernovae). Since the neutrino energy is usually not deposited in the star, it has to be subtracted from the Q-value when calculating the nuclear energy generation.

The energy generation rate can also be expressed using Eqs. (3.20), (3.21), and (3.64) as

$$\varepsilon_{01\to 23} = \frac{Q_{01\to 23}}{\rho}\frac{N_0\lambda_1(0)}{(1+\delta_{01})} = -\frac{Q_{01\to 23}}{\rho(1+\delta_{01})}\left(\frac{dN_0}{dt}\right)_1 \tag{3.67}$$

The total (time-integrated) released energy is obtained from

$$\int \varepsilon_{01\to 23}\, dt = -\int_{N_{0,\text{initial}}}^{N_{0,\text{final}}} \frac{Q_{01\to 23}}{\rho(1+\delta_{01})}(dN_0)_1 = \frac{Q_{01\to 23}}{\rho(1+\delta_{01})}(\Delta N_0)_1 \tag{3.68}$$

with $(\Delta N_0)_1 = N_{0,\text{initial}} - N_{0,\text{final}}$ the change in the abundance of nucleus 0 because of reactions with nucleus 1. Numerically we find from Eq. (1.14)

$$\int \varepsilon_{01\to 23}\, dt = \frac{N_A Q_{01\to 23}}{M_0(1+\delta_{01})}(\Delta X_0)_1 \qquad (\text{MeV/g}) \tag{3.69}$$

where $Q_{01\to 23}$ and M_0 are in units of MeV and u, respectively.

3.2 Nonresonant and Resonant Thermonuclear Reaction Rates

In the previous sections, we defined thermonuclear reaction rates, derived expressions for reaction rate ratios for forward and reverse reactions, and discussed reaction rate equilibria. In none of the expressions derived so far, have we made specific reference to the nuclear reaction cross section $\sigma(E)$. However, this quantity is essential for calculating the reaction rate. In the following, we will discuss

how to derive the thermonuclear reaction rate for particle- and photon-induced reactions.

The reaction rate for a particle-induced reaction is given by (see Eq. (3.10))

$$N_A\langle\sigma v\rangle = \left(\frac{8}{\pi m_{01}}\right)^{1/2} \frac{N_A}{(kT)^{3/2}} \int_0^\infty E\,\sigma(E)\,e^{-E/kT}\,dE \tag{3.70}$$

Once the cross section $\sigma(E)$ has either been measured or been estimated theoretically, the quantity $N_A\langle\sigma v\rangle$ can be found by solving the above integral numerically. If the cross section has a complicated energy dependence, there is usually no alternative to this procedure. On the other hand, if the energy dependence of the cross section is relatively simple, then the reaction rate can be calculated analytically. In this section, we will discuss such analytical expressions for several reasons. First, an analytical rather than numerical description provides additional insight into stellar fusion reactions. Second, in certain situations (e.g., for narrow resonances) the cross-section curve is not known explicitly, and hence the rate cannot be integrated numerically. Third, an analytical description also allows for improved estimates in cases where the reaction rate has to be extrapolated to the region of interest.

Two extreme cases will be discussed in detail, which apply to a large number of nuclear reactions. The first case refers to cross sections that vary smoothly with energy (*nonresonant cross sections*). The second case applies to cross sections that vary strongly in the vicinity of a particular energy (*resonant cross sections*).

3.2.1
Nonresonant Reaction Rates for Charged-Particle-Induced Reactions

The measured cross section for the $^{16}O(p,\gamma)^{17}F$ reaction is shown in Figure 3.11a. The cross section varies smoothly at higher energies, but drops at low energies by several orders of magnitude because of the decreasing transmission probability through the Coulomb barrier. The reaction rates may be obtained either using by numerical integration or by using analytical expressions that will be derived in this section. At this point, we introduce the *astrophysical S-factor*, $S(E)$, defined by

$$\sigma(E) \equiv \frac{1}{E}\,e^{-2\pi\eta}\,S(E) \tag{3.71}$$

This definition removes both the $1/E$ dependence of nuclear cross sections (see Eq. (2.49)) and the s-wave Coulomb barrier transmission probability (see Eq. (2.125)). Recall that the Gamow factor $e^{-2\pi\eta}$ is only an approximation for the s-wave transmission probability at energies well below the height of the Coulomb barrier. However, even if a particular fusion reaction proceeds via p- or d-partial waves, the removal of the strongly energy-dependent, s-wave

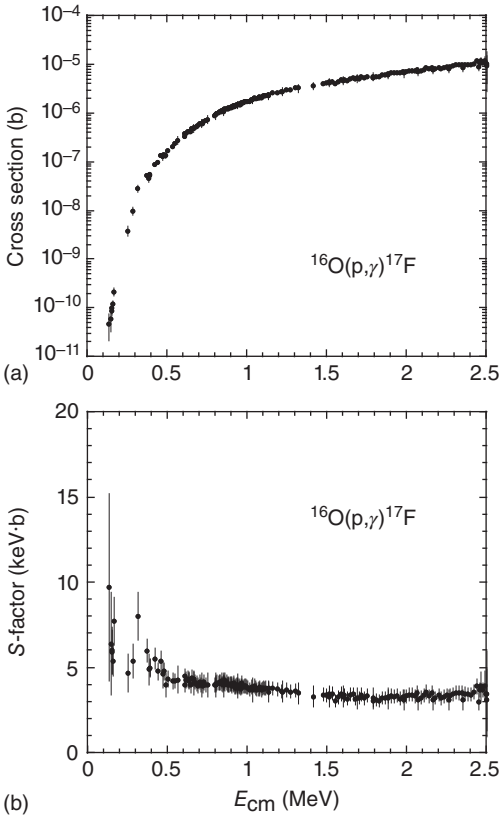

Figure 3.11 (a) Experimental cross section and (b) astrophysical *S*-factor of the ^{16}O(p,γ)^{17}F reaction. Note the strongly varying cross section on a logarithmic scale in part (a) and the smooth behavior of the *S*-factor on a linear scale in part (b). Data from Angulo *et al.* (1999).

transmission probability from the cross section will result in an *S*-factor with a greatly reduced energy dependence. This is demonstrated in Figure 3.11b, showing the *S*-factor for the ^{16}O(p,γ)^{17}F reaction. The *S*-factor varies far less with energy than the cross section. For reasons that will become clear later in this section, the *S*-factor is also a useful concept in the case of broad resonances. For example, Figure 3.12a shows the cross section for the ^{13}C(p,γ)^{14}N reaction, while the corresponding *S*-factor is displayed in Figure 3.12b. The much reduced energy dependence of the *S*-factor compared to the cross section is again evident. The above arguments are analogous to those we made in Section 2.4.2 in connection with the simple square-barrier potential and the removal of the transmission probability from the wave intensity in the nuclear interior (Figure 2.14).

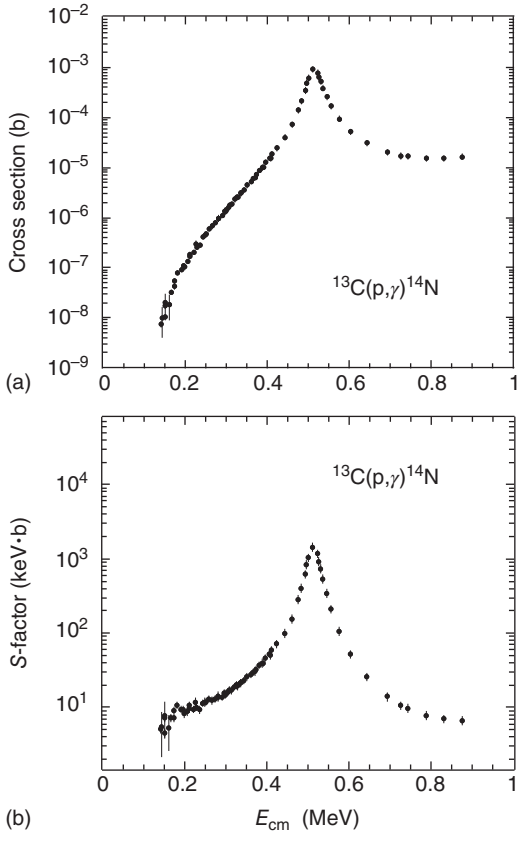

Figure 3.12 (a) Experimental cross section and (b) astrophysical *S*-factor of the ^{13}C(p,γ)^{14}N reaction. Note the considerably reduced energy dependence in part (b). The low-energy *S*-factor tail of the broad resonance at $E \approx 0.5$ MeV can also be described by the nonresonant reaction rate formalism, as shown in this section. A narrow resonance at $E = 0.45$ MeV has been omitted from the figure. Data from Angulo *et al.* (1999).

With the definition of the *S*-factor, we write for the nonresonant reaction rate (see Eqs. (2.125) and (3.70))

$$N_A\langle\sigma v\rangle = \left(\frac{8}{\pi m_{01}}\right)^{1/2} \frac{N_A}{(kT)^{3/2}} \int_0^\infty e^{-2\pi\eta}\, S(E)\, e^{-E/kT}\, dE$$
$$= \left(\frac{8}{\pi m_{01}}\right)^{1/2} \frac{N_A}{(kT)^{3/2}} \int_0^\infty \exp\left(-\frac{2\pi}{\hbar}\sqrt{\frac{m_{01}}{2E}}\, Z_0 Z_1\, e^2\right) S(E)\, e^{-E/kT}\, dE \tag{3.72}$$

with Z_i the charges of target and projectile. First, suppose that the astrophysical *S*-factor is constant, $S(E) = S_0$. We find

$$N_A\langle\sigma v\rangle = \left(\frac{8}{\pi m_{01}}\right)^{1/2} \frac{N_A}{(kT)^{3/2}} S_0 \int_0^\infty e^{-2\pi\eta}\, e^{-E/kT}\, dE \tag{3.73}$$

with

$$kT = 0.086173324\, T_9 \text{ (MeV)} \tag{3.74}$$

$$2\pi\eta = 0.98951013\, Z_0 Z_1 \sqrt{\frac{M_0 M_1}{M_0 + M_1}\frac{1}{E}} \tag{3.75}$$

where the relative atomic masses M_i and the energy E are in units of u and MeV, respectively. Atomic masses should be replaced by nuclear masses for precision work (Section 1.5.3). The integrand has an interesting energy dependence. The factor $e^{-E/kT}$, originating from the Maxwell–Boltzmann distribution, approaches zero for large energies, whereas the term $e^{-1/\sqrt{E}}$, reflecting the Gamow factor, approaches zero for small energies. The major contribution to the integral will come from energies where the product of both factors is near its maximum.

Figure 3.13a illustrates the situation for the reaction $^{12}C(\alpha,\gamma)^{16}O$ at $T = 0.2$ GK. The dashed and the dashed-dotted lines show the factor $e^{-E/kT}$ and $e^{-2\pi\eta}$, respectively. The solid line shows the integrand $e^{-E/kT}\, e^{-2\pi\eta}$. Note the logarithmic scale, indicating the small magnitude of the integrand compared to the Gamow and Maxwell–Boltzmann factors. The solid line in Figure 3.13b shows the integrand on a linear scale, displaying a relatively sharp peak. Part (b) also indicates the maximum of the Maxwell–Boltzmann distribution (arrow), which occurs at $kT =$ 17 keV. However, the integrand peaks at an energy of $E_0 = 315$ keV, which is considerably larger than kT, indicating that most of the reactions occur in the high-energy tail of the Maxwell–Boltzmann distribution. It appears that the Gamow factor effectively shifts the integrand to higher energies and, therefore, the integrand is commonly referred to as the *Gamow peak*. The Gamow peak represents the relatively narrow energy range over which most nuclear reactions occur in a stellar plasma.

The location E_0 of the maximum of the Gamow peak can be found from the first derivative of the integrand in Eq. (3.73) with respect to E,

$$\frac{d}{dE}\left(-\frac{2\pi}{\hbar}\sqrt{\frac{m_{01}}{2E}}\, Z_0 Z_1\, e^2 - \frac{E}{kT}\right)_{E=E_0} = \frac{\pi}{\hbar}\, Z_0 Z_1\, e^2 \sqrt{\frac{m_{01}}{2}}\frac{1}{E_0^{3/2}} - \frac{1}{kT} = 0 \tag{3.76}$$

Thus,

$$E_0 = \left[\left(\frac{\pi}{\hbar}\right)^2 \left(Z_0 Z_1\, e^2\right)^2 \left(\frac{m_{01}}{2}\right)(kT)^2\right]^{1/3} = 0.1220 \left(Z_0^2 Z_1^2 \frac{M_0 M_1}{M_0 + M_1}\, T_9^2\right)^{1/3} \quad \text{(MeV)} \tag{3.77}$$

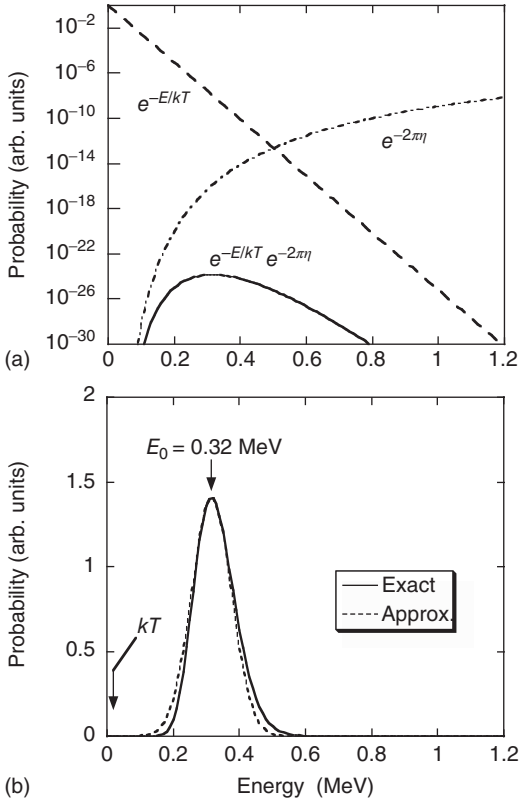

Figure 3.13 (a) Maxwell–Boltzmann factor ($e^{-E/kT}$; dashed line) and Gamow factor ($e^{-2\pi\eta}$; dashed-dotted line) versus energy for the $^{12}C(\alpha,\gamma)^{16}O$ reaction at a temperature of $T = 0.2$ GK. The product $e^{-E/kT}e^{-2\pi\eta}$, referred to as the *Gamow peak*, is shown as solid line. (b) The same Gamow peak shown on a linear scale (solid line). The maximum occurs at $E_0 = 0.32$ MeV while the maximum of the Maxwell–Boltzmann distribution is located at $kT = 0.017$ MeV (arrow). The dotted line shows the Gaussian approximation of the Gamow peak.

where in the numerical expression M_i are the relative atomic masses of projectile and target in units of u.

The energy E_0 is the most effective energy for nonresonant thermonuclear reactions. Figure 3.14 shows the Gamow peak energy E_0 versus temperature for a number of proton- and α-particle-induced reactions. The Gamow peak energy increases with increasing target–projectile charge. The open circles indicate the height V_C of the Coulomb barrier. Notice that, except for the highest temperatures near $T = 10$ GK, we find $E_0 \ll V_C$ and thus the interacting charged nuclei must always tunnel through the Coulomb barrier.

Figure 3.15 shows the Gamow peak at a temperature of $T = 30$ MK for three reactions: (i) p + p, (ii) ^{12}C + p, and (iii) $^{12}C + \alpha$. It demonstrates a crucial aspect

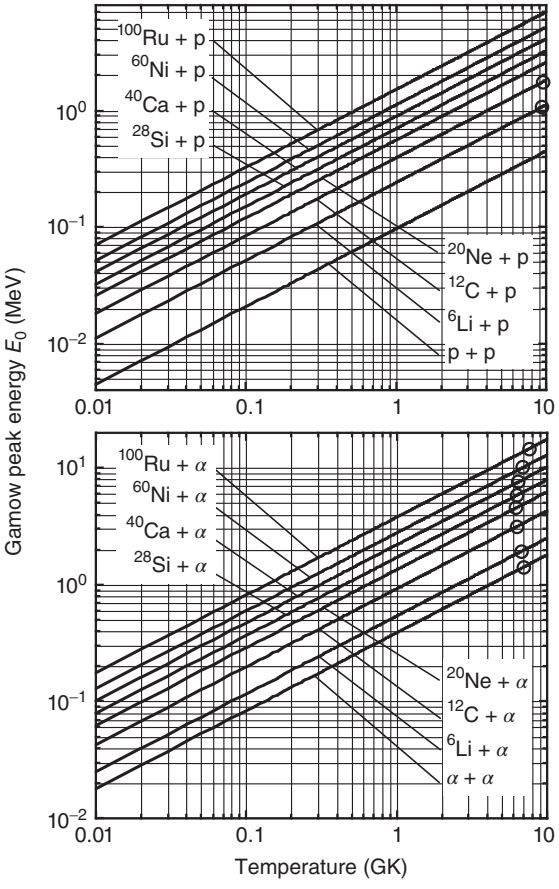

Figure 3.14 Location of the Gamow peak maximum versus temperature for a number of proton-induced (top) and α-particle-induced (bottom) reactions. The open circles on the right-hand side show the Coulomb barrier height, $V_C = 1.44\,Z_0Z_1/R_0$, with V_C and R_0 in units of MeV and fm, respectively (Section 2.4.3).

of thermonuclear burning in stars. Not only does the Gamow peak shift to higher energies for increasing target and projectile charges, but the area under the curves decreases rapidly as well. Suppose, for example, that a mixture of different nuclei is present in the stellar plasma at a particular time. Then those reactions with the smallest Coulomb barrier account frequently for most of the nuclear energy generation and will be consumed most rapidly, while reactions with larger Coulomb barriers usually do not contribute significantly to the energy production.

The Gamow peak may be approximated by a Gaussian function having a maximum of the same size and of the same curvature at $E = E_0$. From Eq. (3.77),

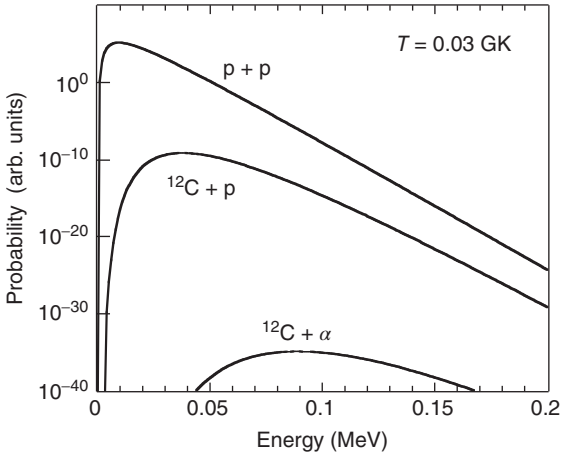

Figure 3.15 Gamow peaks for the p + p, ^{12}C + p, and ^{12}C + α reactions at a temperature of $T = 0.03$ GK.

we write

$$\exp\left(-\frac{2\pi}{\hbar}\sqrt{\frac{m_{01}}{2E}}\,Z_0Z_1e^2-\frac{E}{kT}\right)=\exp\left(-\frac{2E_0^{3/2}}{\sqrt{E}kT}-\frac{E}{kT}\right)$$
$$\approx\exp\left(-\frac{3E_0}{kT}\right)\exp\left[-\left(\frac{E-E_0}{\Delta/2}\right)^2\right] \tag{3.78}$$

where the $1/e$ width Δ of the Gaussian is obtained from the requirement that the second derivatives match at E_0. Thus,

$$\frac{d^2}{dE^2}\left(\frac{2E_0^{3/2}}{\sqrt{E}kT}+\frac{E}{kT}\right)_{E=E_0}=\frac{3}{2}\frac{1}{E_0kT} \tag{3.79}$$

$$\frac{d^2}{dE^2}\left(\frac{E-E_0}{\Delta/2}\right)^2_{E=E_0}=\frac{2}{(\Delta/2)^2} \tag{3.80}$$

Setting the right-hand sides of the last two expressions equal and solving for Δ gives

$$\Delta=\frac{4}{\sqrt{3}}\sqrt{E_0kT}=0.2368\left(Z_0^2Z_1^2\frac{M_0M_1}{M_0+M_1}\,T_9^5\right)^{1/6}\qquad\text{(MeV)} \tag{3.81}$$

Since usually $kT \ll E_0$, it is apparent that the width Δ of the Gamow peak is smaller than E_0. Figure 3.16 shows the Gamow peak width Δ versus temperature for a number of proton- and α-particle-induced reactions. It can be seen that the Gamow peak width increases with increasing Coulomb barrier. Thermonuclear reactions occur mainly over an energy window from $E_0 - \Delta/2$ to $E_0 + \Delta/2$, except in the case of narrow resonances (see below). For increasing charges of target or projectile, this window shifts to higher energies and becomes broader.

The nonresonant thermonuclear reaction rates can be calculated by replacing the Gamow peak with a Gaussian. From Eqs. (3.73) and (3.78), one finds

$$\begin{aligned} N_A\langle\sigma v\rangle &= \left(\frac{8}{\pi m_{01}}\right)^{1/2} \frac{N_A}{(kT)^{3/2}} S_0 \int_0^\infty e^{-2\pi\eta} e^{-E/kT}\, dE \\ &\approx \left(\frac{8}{\pi m_{01}}\right)^{1/2} \frac{N_A}{(kT)^{3/2}} S_0 e^{-3E_0/kT} \int_0^\infty \exp\left[-\left(\frac{E-E_0}{\Delta/2}\right)^2\right] dE \end{aligned} \tag{3.82}$$

The lower integration limit can be extended to minus infinity without introducing a significant error. The value of the integral over the Gaussian is then $\sqrt{\pi}\Delta/2$. For a constant S-factor, we obtain

$$N_A\langle\sigma v\rangle = N_A \sqrt{\frac{2}{m_{01}}} \frac{\Delta}{(kT)^{3/2}} S_0 e^{-3E_0/kT} \tag{3.83}$$

Alternatively, one finds with the substitution $\tau \equiv 3E_0/(kT)$ and Eqs. (3.77) and (3.81)

$$\begin{aligned} N_A\langle\sigma v\rangle &= N_A \sqrt{\frac{2}{m_{01}}} \frac{\Delta}{(kT)^{3/2}} S_0 e^{-\tau} \tau^2 \frac{(kT)^2}{9E_0^2} \\ &= \frac{1}{3}\left(\frac{4}{3}\right)^{3/2} \frac{\hbar}{\pi} \frac{N_A}{m_{01} Z_0 Z_1 e^2} S_0 \tau^2 e^{-\tau} \end{aligned} \tag{3.84}$$

One of the most striking features of thermonuclear reaction rates is their temperature dependence. The temperature dependence of $N_A\langle\sigma v\rangle$ and of the energy production rate ε near some energy $T = T_0$ can be derived by introducing a power law

$$N_A\langle\sigma v\rangle_T = N_A\langle\sigma v\rangle_{T_0} \left(\frac{T}{T_0}\right)^n \tag{3.85}$$

where

$$\ln N_A\langle\sigma v\rangle_T = \ln N_A\langle\sigma v\rangle_{T_0} + n(\ln T - \ln T_0) \tag{3.86}$$

$$\frac{\partial \ln N_A\langle\sigma v\rangle_T}{\partial \ln T} = n \tag{3.87}$$

With $\tau = 3E_0/(kT) = cT^{2/3}/T = cT^{-1/3}$ and $N_A\langle\sigma v\rangle_T = c' T^{-2/3} e^{-\tau}$, we may also write

$$\ln N_A\langle\sigma v\rangle_T = \ln c' - \frac{2}{3}\ln T - \tau \tag{3.88}$$

$$n = \frac{\partial \ln N_A\langle\sigma v\rangle_T}{\partial \ln T} = -\frac{2}{3} - \frac{\partial\tau}{\partial \ln T} = -\frac{2}{3} - \tau \frac{\partial \ln(cT^{-1/3})}{\partial \ln T} = -\frac{2}{3} + \frac{\tau}{3} \tag{3.89}$$

Hence,

$$N_A\langle\sigma v\rangle_T = N_A\langle\sigma v\rangle_{T_0} \left(\frac{T}{T_0}\right)^{(\tau-2)/3} \tag{3.90}$$

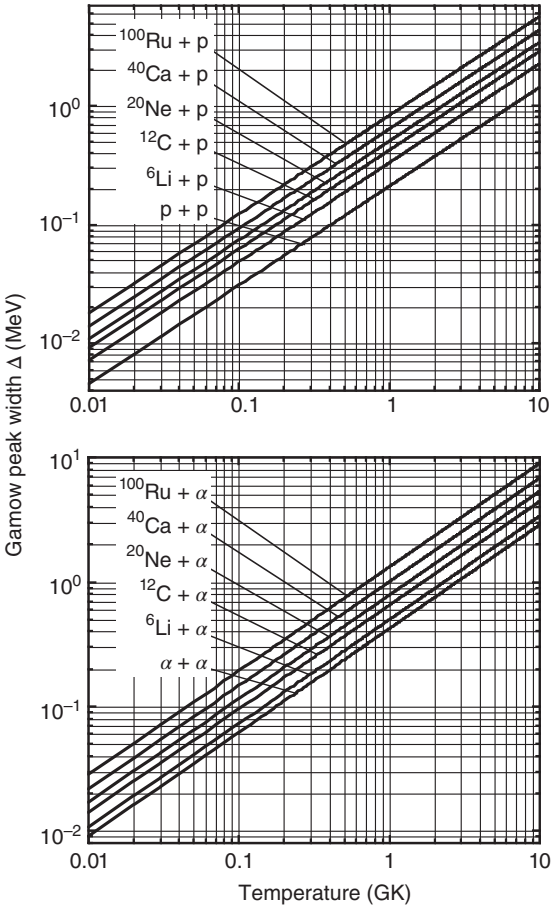

Figure 3.16 Width of the Gamow peak versus temperature for a number of proton-induced (top) and α-particle-induced (bottom) reactions.

The parameter $\tau = 3E_0/(kT)$ is numerically given by

$$\tau = 4.2487 \left(Z_0^2 Z_1^2 \frac{M_0 M_1}{M_0 + M_1} \frac{1}{T_9} \right)^{1/3} \tag{3.91}$$

Values of τ are shown in Figure 3.17 versus temperature for a number of reactions. For example, at $T = 15$ MK one obtains $\tau = 13.6$ for the p + p reaction, yielding for the exponent of T a value of $n \approx 3.9$. On the other hand, at $T = 200$ MK we obtain $\tau = 54.88$ for the ^{12}C + α reaction, resulting in $n \approx 17.6$. The striking temperature dependence of thermonuclear reaction rates has an important impact on stellar models. Small temperature fluctuations, which are likely to occur during stellar evolution, will cause dramatic changes in energy production. Therefore, an effective mechanism must exist to stabilize the star; otherwise,

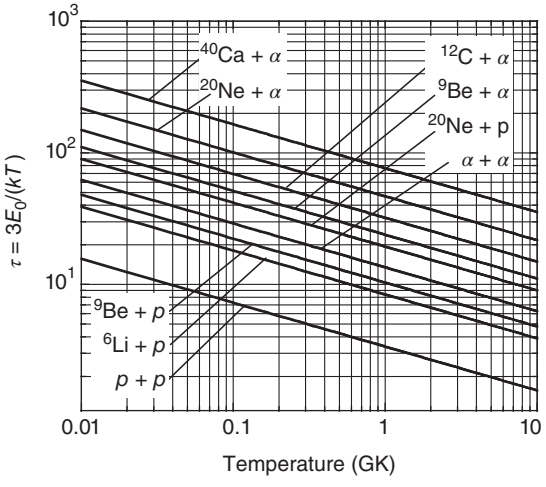

Figure 3.17 Numerical values of the parameter τ versus temperature for a number of proton- and α-particle-induced reactions. Note that τ is dimensionless.

in circumstances where this is not possible, a thermonuclear explosion is likely to occur.

Two corrections to the nonresonant reaction rate formalism derived so far will now be considered. The first correction is necessary since we have replaced the asymmetric Gamow peak by a symmetric Gaussian (see Eq. (3.78)) where the area under the latter function is given by $e^{-\tau}\sqrt{\pi}\Delta/2$ (see Eq. (3.83)). Figure 3.13b compares the two functions for the reaction $^{12}C(\alpha,\gamma)^{16}O$ at $T = 0.2$ GK. The solid line shows the Gamow peak while the dotted curve displays the Gaussian approximation. The reaction rate must be multiplied by a correction factor that represents the ratio of the areas under these two curves,

$$\begin{aligned} F(\tau) &= \frac{\int_0^\infty \exp\left(-\frac{2\pi}{\hbar}\sqrt{\frac{m_{01}}{2E}}Z_0Z_1e^2 - \frac{E}{kT}\right)dE}{e^{-\tau}\sqrt{\pi}\Delta/2} \\ &= \frac{2}{\sqrt{\pi}\sqrt{E_0kT}}\frac{\sqrt{3}}{4}e^{\tau}\int_0^\infty \exp\left(-\frac{2E_0^{3/2}}{kT}\frac{1}{\sqrt{E_0\epsilon}} - \frac{E_0\epsilon}{kT}\right)E_0\,d\epsilon \\ &= \sqrt{\frac{\tau}{\pi}}\frac{e^{\tau}}{2}\int_0^\infty \exp\left[-\frac{\tau}{3}\left(\epsilon + \frac{2}{\sqrt{\epsilon}}\right)\right]d\epsilon \end{aligned} \tag{3.92}$$

where we have introduced the dimensionless variable $\epsilon \equiv E/E_0$. It can be seen that the correction factor F is a function of τ only. It is also clear from Figure 3.17 that τ is usually a relatively large number. Therefore, it is of advantage to expand F in terms of a small parameter that varies inversely with τ. The result is (see Problem 3.2)

$$F(\tau) \approx 1 + \frac{5}{12\tau} \tag{3.93}$$

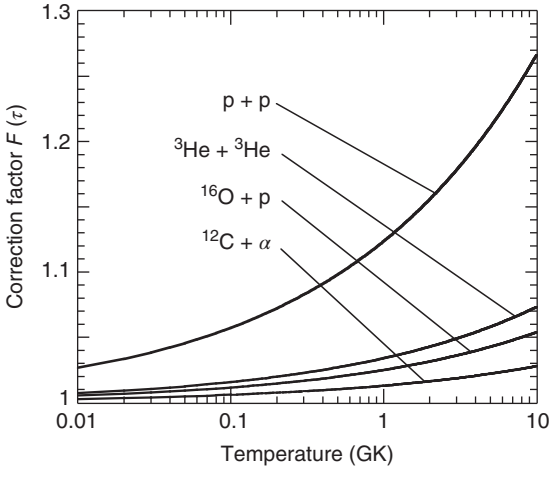

Figure 3.18 Correction factor $F(\tau)$ versus temperature for a number of reactions.

Figure 3.18 shows values of $F(\tau)$ versus temperature for a number of reactions. It can be seen that the correction factor is usually small (less than a few percent) at low temperatures. Its magnitude increases with rising temperature and lowering of the Coulomb barrier.

A second correction is necessary since for many nonresonant reactions the S-factor is not constant, but varies with energy. In most cases, it is sufficient to expand the experimental or theoretical S-factor into a Taylor series around $E = 0$,

$$S(E) \approx S(0) + S'(0)E + \tfrac{1}{2}S''(0)E^2 \tag{3.94}$$

where the primes indicate derivatives with respect to E. Substitution of this expansion into Eq. (3.72) yields a sum of integrals, where each integral can be expanded into powers of $1/\tau$. As a result of this procedure, which is not given here explicitly, one has to replace in Eq. (3.84) the constant S_0 by an effective S-factor. The result is (Fowler, Caughlan, and Zimmerman, 1967)

$$N_A\langle\sigma v\rangle = \frac{1}{3}\left(\frac{4}{3}\right)^{3/2}\frac{\hbar}{\pi}\frac{N_A}{m_{01}Z_0Z_1e^2}\,S_{\text{eff}}\tau^2e^{-\tau} \tag{3.95}$$

$$S_{\text{eff}}(E_0) = S(0)\left[1 + \frac{5}{12\tau} + \frac{S'(0)}{S(0)}\left(E_0 + \frac{35}{36}kT\right) + \frac{1}{2}\frac{S''(0)}{S(0)}\left(E_0^2 + \frac{89}{36}E_0kT\right)\right] \tag{3.96}$$

The first terms in the square bracket correspond to the factor $F(\tau)$ caused by the asymmetry of the Gamow peak, while the other terms arise from corrections caused by the S-factor variation with energy. Numerically, one finds (Lang, 1974)

$$N_A\langle\sigma v\rangle = \frac{C_1}{T_9^{2/3}}\,e^{-C_2/T_9^{1/3}}\left(1 + C_3T_9^{1/3} + C_4T_9^{2/3} + C_5T_9 + C_6T_9^{4/3} + C_7T_9^{5/3}\right) \qquad (\text{cm}^3\text{mol}^{-1}\text{s}^{-1}) \tag{3.97}$$

$$C_1 = 7.8324 \times 10^9 \left(Z_0^2 Z_1^2 \frac{M_0 M_1}{M_0 + M_1} \right)^{1/6} S(0) \sqrt{\frac{M_0 + M_1}{M_0 M_1}}$$

$$C_2 = 4.2475 \left(Z_0^2 Z_1^2 \frac{M_0 M_1}{M_0 + M_1} \right)^{1/3}$$

$$C_3 = 9.810 \times 10^{-2} \left(Z_0^2 Z_1^2 \frac{M_0 M_1}{M_0 + M_1} \right)^{-1/3}$$

$$C_4 = 0.1220 \frac{S'(0)}{S(0)} \left(Z_0^2 Z_1^2 \frac{M_0 M_1}{M_0 + M_1} \right)^{1/3}$$

$$C_5 = 8.377 \times 10^{-2} \frac{S'(0)}{S(0)}$$

$$C_6 = 7.442 \times 10^{-3} \frac{S''(0)}{S(0)} \left(Z_0^2 Z_1^2 \frac{M_0 M_1}{M_0 + M_1} \right)^{2/3}$$

$$C_7 = 1.299 \times 10^{-2} \frac{S''(0)}{S(0)} \left(Z_0^2 Z_1^2 \frac{M_0 M_1}{M_0 + M_1} \right)^{1/3}$$

where M_i is the relative atomic mass in u, and the quantities $S(0)$, $S'(0)$, and $S''(0)$ are in units of MeV·b, b, and b/MeV, respectively.

Figure 3.19 shows schematically three situations that are frequently encountered in practice. The data shown in Figure 3.9a display a very slowly varying S-factor. In this case, a linear Taylor expansion (solid line) seems appropriate for describing the data. If the Gamow peak is located, say, around $E = 0.7$ MeV, then the nonresonant reaction rates may be calculated from the fit coefficients $S(0)$ and $S'(0)$ to high accuracy. Depending on the hydrodynamical conditions at the astrophysical environment, however, the Gamow peak may be located at energies not directly accessible with present experimental techniques (say, below $E =$ 0.3 MeV in part (a) of the figure). In this case, the Taylor expansion may be used to extrapolate the S-factor to the energy range of the Gamow peak at low energies. This procedure represents the simplest way to estimate the reaction rates from cross section data obtained at higher energies if no data are available in the Gamow peak region. Although frequently applied in practice, one has to be careful with this method, and a more reliable S-factor extrapolation based on theoretical nuclear models (Chapter 2) is desirable in this case.

A different situation is shown in Figure 3.19b. Here, the data below $E = 0.65$ MeV may be best described by a quadratic Taylor expansion and the reaction rates are then evaluated using Eq. (3.97). However, at higher energies the Taylor expansion will diverge (in this case positively) and does no longer describe the data. Thus, the calculated reaction rates become inaccurate at temperatures where a substantial fraction of the Gamow peak is located beyond $E = 0.65$ MeV. For this reason, the nonresonant reaction rate expression (see Eq. (3.97)) is sometimes multiplied by a cutoff factor (Fowler, Caughlan, and Zimmerman, 1975)

$$f_{\text{cutoff}} \approx e^{-(T_9/T_{9,\text{cutoff}})^2} \tag{3.98}$$

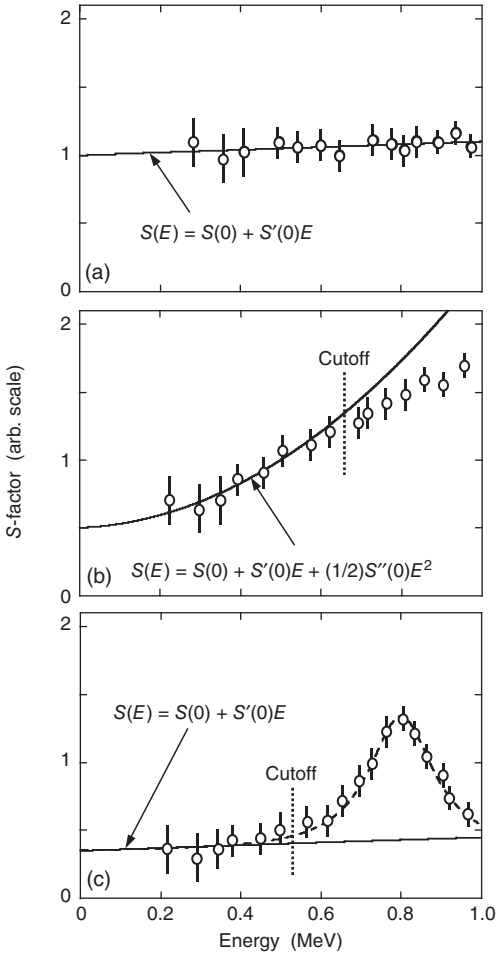

Figure 3.19 Schematic representation of the *S*-factor versus energy for (a) a very slowly varying *S*-factor curve; (b) an energy-dependent *S*-factor; and (c) a broad resonance. See discussion in the text.

with $T_{9,\mathrm{cutoff}}$ corresponding to the temperature where a substantial fraction of the Gamow peak lies in an energy region at which the *S*-factor parametrization starts to deviate from the data (the vertical dotted line in Figure 3.19b). Beyond this temperature, the reaction rates have to be evaluated by different means.

Consider now the situation shown in Figure 3.19c. In this case, the data display a resonance at $E = 0.8$ MeV corresponding to an *S*-factor, which varies strongly with energy. However, it can be seen that below $E \approx 0.55$ MeV the wing of the resonance varies rather slowly. Therefore, if one is mainly interested in stellar temperatures at which the Gamow peak is located below $E = 0.55$ MeV, then one can apply the nonresonant reaction rate formalism to the low-energy

tail of the broad resonance (see Eq. (3.97)). As was the case before, the calculated reaction rate has to be cut off at higher temperatures corresponding to energies where the S-factor expansion deviates from the data (dotted line in Figure 3.19c).

The S-factor for nonresonant reactions sometimes shows a strong energy dependence such that a Taylor series expansion is no longer applicable. Although analytical descriptions are reported in the literature for such cases (see, e.g., Fowler, Caughlan, and Zimmerman, 1975), it is usually more reliable to integrate the reaction rates numerically (see Eq. (3.70)).

Example 3.5

The measured S-factor for the reaction $^{12}C(p,\gamma)^{13}N$ below $E = 0.5$ MeV is shown in Figure 3.20. A broad resonance appears at $E \approx 0.4$ MeV. The S-factor below $E = 0.23$ MeV varies smoothly with energy and has been expanded around $E = 0$ into a quadratic Taylor series, with coefficients of $S(0) = 1.34 \times 10^{-3}$ MeV·b, $S'(0) = 2.6 \times 10^{-3}$ b, and $S''(0) = 8.3 \times 10^{-2}$ b/MeV (Adelberger *et al.*, 1998). (i) For a temperature of $T = 0.03$ GK, determine the location and width of the Gamow peak, and the temperature sensitivity of the reaction rates. (ii) Determine the maximum temperature at which the reaction rates can be calculated reliably with the S-factor parametrization given above.

From Eqs. (3.77), (3.81), (3.90), and (3.91), we find

$$E_0 = 0.1220 \left(1^2 6^2 \frac{1.0 \cdot 12.0}{1.0 + 12.0} 0.03^2\right)^{1/3} \text{MeV} = 0.038\,\text{MeV}$$

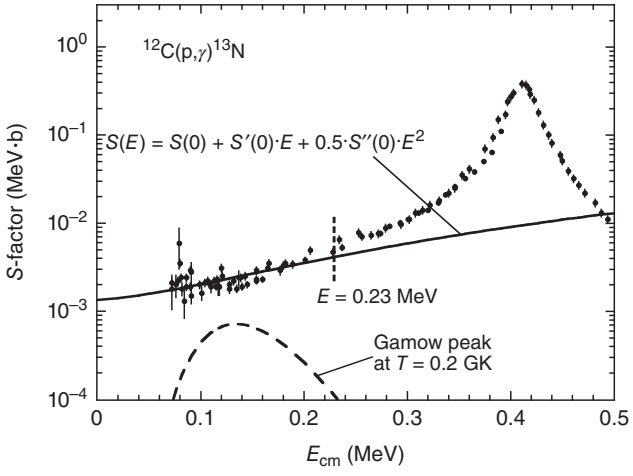

Figure 3.20 Experimental S-factor versus energy for the $^{12}C(p,\gamma)^{13}N$ reaction. The solid line represents an S-factor expansion that describes the data below $E = 0.23$ MeV. The dashed line shows the Gamow peak for a temperature of $T = 0.2$ GK. Data are from Angulo *et al.* (1999).

$$\Delta = 0.2368 \left(1^2 6^2 \frac{1.0 \cdot 12.0}{1.0 + 12.0} 0.03^5\right)^{1/6} \text{MeV} = 0.023\,\text{MeV}$$
$$\tau = 4.2487 \left(1^2 6^2 \frac{1.0 \cdot 12.0}{1.0 + 12.0} \frac{1}{0.03}\right)^{1/3} = 44.0$$

and thus $N_A\langle\sigma v\rangle_T \sim (T/T_0)^{(44.0-2)/3} = (T/T_0)^{14.0}$.

The quadratic S-factor expansion describes the data reliably only below $E = 0.23$ MeV. We seek the temperature range for which an insignificant fraction of the Gamow peak lies beyond $E = 0.23$ MeV, that is, $E_0(T) + \Delta(T) = 0.23$ MeV. From Figures 3.14 and 3.16, it can be seen that this condition is fulfilled only at $T \leq 0.2$ GK. Therefore, we expect that the reaction rates calculated with the given S-factor parameterization are reliable below this temperature. The situation is illustrated in Figure 3.20.

3.2.2 Nonresonant Reaction Rates for Neutron-Induced Reactions

Neutrons that are produced in a star quickly thermalize and their velocities are given by a Maxwell–Boltzmann distribution. For a smoothly varying neutron cross section, the reactions are most likely to occur near the maximum of the Maxwell–Boltzmann distribution, that is, at thermal energies of $E_T = kT$ or thermal velocities of $v_T = \sqrt{2kT/m_{01}}$ (see Section 3.1.1 and Figure 3.1a). For s-wave neutrons ($\ell = 0$) of low velocity, the reaction cross section is inversely proportional to the neutron velocity (see Eq. (2.207)),

$$\sigma \sim \frac{1}{v} \sim \frac{1}{\sqrt{E}} \tag{3.99}$$

Strictly speaking, if charged particles are released in neutron-induced processes, the cross section is modified by the transmission probability of the emitted particle through the Coulomb and centripetal barriers. However, since many neutron-induced reactions are exothermic with Q-values in excess of several mega electron volt, the transmission coefficient of the charged particle is approximately constant. Under these circumstances, the $1/v$ law applies not only to (n,γ) reactions but also to reactions such as (n,p) or (n,α) (Figure 4.15a). Furthermore, the $1/v$ law is also valid in certain cases where resonant contributions give rise to a smoothly varying reaction cross section for s-wave neutrons. For example, suppose that a neutron-induced reaction proceeds through the low-energy wing of a broad resonance. Setting $E \ll E_r$ in the Breit–Wigner formula (see Eq. (2.185)) and using the low-energy dependence of the neutron partial width, assuming that the partial width for the exit channel is approximately constant, yields $\sigma_{\ell=0} \sim (1/v^2)\Gamma_{\ell=0} \sim (1/v^2)v \sim 1/v$. Neutron capture by heavy nuclei with large $Q_{n\gamma}$ values is another important example. In this case, the reaction proceeds through many broad and overlapping resonances. These resonances are difficult to resolve experimentally so that a measurement yields an average cross section that varies smoothly with

energy. The cross section is then given by $\sigma_{\ell=0} = \sigma^{\max}_{\ell=0} \cdot \widehat{T} \sim 1/v$ (see Eq. (2.207)), where $\widehat{T}$ is the s-wave transmission coefficient.

For $\sigma \sim 1/v$, or $S \equiv \sigma v = \text{const}$, we obtain (see Eqs. (3.3) and (3.4))

$$N_A\langle\sigma v\rangle = N_A \int_0^\infty vP(v)\sigma(v)\,dv = N_A\sigma v = N_A S = \text{const} \tag{3.100}$$

The reaction rate is independent of temperature and, in principle, could be determined from σ measured at any velocity v. In practice, however, the nonresonant neutron cross section does not always follow the simple $1/v$ law for any of the following reasons: (i) the s-wave neutron energies are no longer small, (ii) a new reaction channel becomes energetically accessible, and (iii) higher partial waves may contribute to the neutron cross section.

In the latter case, the velocity or energy dependence can be found from the expression $\sigma_\ell \sim (1/v^2)\Gamma_\ell$. At low energies, we can use $\Gamma_\ell(E) \sim (vR)^{2\ell+1} \sim E^{\ell+1/2}$ (Section 2.5.4) and obtain $\sigma_\ell \sim v^{-1}, v, v^3$ (or $\sigma_\ell \sim E^{-1/2}, E^{1/2}, E^{3/2}$) for $\ell = 0, 1, 2$, respectively. Again, the above dependences on v (or E) do not apply in exceptional situations where the neutron binding energy (or $Q_{n\gamma}$) becomes comparable to the neutron kinetic energy since in such cases the influence of the exit channel must also be taken into account. With the above energy dependences of the different partial waves, the reaction rate is

$$N_A\langle\sigma v\rangle = \left(\frac{8}{\pi m_{01}}\right)^{1/2} \frac{N_A}{(kT)^{3/2}} \int_0^\infty E\sigma(E)\, e^{-E/kT}\, dE \sim \int_0^\infty E^{\ell+1/2} e^{-E/kT}\, dE \tag{3.101}$$

The integrand, $E^{\ell+1/2}e^{-E/kT}$, represents the stellar energy window in which most of the nonresonant neutron-induced reactions take place. It is plotted in Figure 3.21 for different ℓ-values (solid lines) and is compared to the Maxwell–Boltzmann factor, $E\,e^{-E/kT}$ (dashed line). All curves are plotted for $kT = 30$ keV and are normalized to the same maximum value. It can be seen that the centripetal barrier shifts the window of effective stellar energies. The maximum of the integrand occurs at $E_{\max} = (\ell + 1/2)kT$. The influence of the centripetal barrier on nonresonant neutron-induced reaction rates is far smaller than the influence of the Coulomb barrier on nonresonant charged-particle reactions. As an approximate rule, it can be assumed that the Maxwell–Boltzmann distribution provides a reliable estimate for the effective energy window in the case of nonresonant neutron-induced reactions.

If the product $S \equiv \sigma v$ is not constant but varies with velocity, it may be expanded into a Taylor series around $E = 0$ in terms of v or $\sqrt{E}$,

$$\sigma v = S(\sqrt{E}) \approx S(0) + \dot{S}(0)\sqrt{E} + \tfrac{1}{2}\ddot{S}(0)E \tag{3.102}$$

where the dots indicate derivatives with respect to $\sqrt{E} \sim v$, and $S(0)$, $\dot{S}(0)$, $\ddot{S}(0)$ are empirical constants. The energy dependence of the cross section is then given by

$$\sigma(E) \approx \sqrt{\frac{m_{01}}{2E}} \left(S(0) + \dot{S}(0)\sqrt{E} + \frac{1}{2}\ddot{S}(0)E\right) \tag{3.103}$$

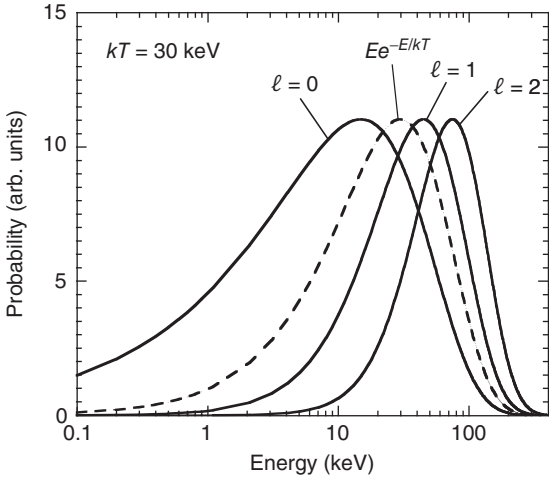

Figure 3.21 The factor $E^{\ell+1/2}e^{-E/kT}$ versus neutron energy, representing the stellar energy window in which most of the nonresonant neutron-induced reactions take place, for different values of the orbital angular momentum ℓ. The dashed curve shows the Maxwell–Boltzmann factor $Ee^{-E/kT}$ for comparison. All curves are calculated for kT = 30 keV.

Substitution into Eq. (3.10) yields for the reaction rate (Problem 3.3)

$$N_A\langle\sigma v\rangle = N_A\left(S(0) + \frac{2}{\sqrt{\pi}}\dot{S}(0)\sqrt{kT} + \frac{3}{4}\ddot{S}(0)kT\right) \tag{3.104}$$

Numerically, we find

$$N_A\langle\sigma v\rangle = 6.022\times10^{23}S(0) \times\left(1 + 0.3312\frac{\dot{S}(0)}{S(0)}\sqrt{T_9} + 0.06463\frac{\ddot{S}(0)}{S(0)}T_9\right)\ (\mathrm{cm^3mol^{-1}s^{-1}}) \tag{3.105}$$

with $\dot{S}(0)/S(0)$ and $\ddot{S}(0)/S(0)$ in units of $\mathrm{MeV}^{-1/2}$ and MeV^{-1}, respectively.

For many neutron-induced reactions, especially neutron captures, the reaction rate is expressed in terms of the Maxwellian-averaged cross section (Section 3.1.1),

$$N_A\langle\sigma v\rangle = N_A\langle\sigma\rangle_T v_T = N_A\frac{4}{v_T\sqrt{\pi}}\int_0^\infty v\sigma(v)\left(\frac{v}{v_T}\right)^2 e^{-(v/v_T)^2}\,dv \tag{3.106}$$

For s-wave neutrons at low energy, where $\sigma v = v_T\sigma(v_T) = v_T\sigma_T = \text{const}$, it follows

$$N_A\langle\sigma\rangle_T v_T = N_A\frac{4}{v_T\sqrt{\pi}}v_T\sigma(v_T)\int_0^\infty\left(\frac{v}{v_T}\right)^2 e^{-(v/v_T)^2}\,dv = N_A v_T\sigma(v_T) \tag{3.107}$$

and the Maxwellian-averaged cross section, $\langle\sigma\rangle_T$, is equal to the cross section measured at thermal velocity, σ_T. For different velocity dependences, for

example, $\sigma = \text{const}$ or $\sigma \sim 1/v^2$, direct substitution into the above equation yields $\langle\sigma\rangle_T = 1.13\sigma_T$, while for p-wave capture ($\sigma \sim v$) one obtains $\langle\sigma\rangle_T = 1.5\,\sigma_T$. Thus, for a smoothly changing cross section, a measurement of σ at a single velocity, v_T, provides a reaction rate that is not too far off from its true magnitude. However, to obtain precise values for the reaction rate, the cross section is measured in practice over a range of neutron energies in the effective stellar window that is given by the Maxwell–Boltzmann distribution. For more details, see Beer, Voss, and Winters (1992).

3.2.3 Nonresonant Reaction Rates for Photon-Induced Reactions

The majority of astrophysically important photodisintegration reactions, $\gamma + 3 \rightarrow 0 + 1$, have not been measured directly. Their reaction rates are most conveniently derived from the corresponding reverse particle-induced reaction rate by applying the reciprocity theorem (Section 3.1.4). Nevertheless, a number of photodisintegration reactions have been measured directly and it is interesting to investigate some general properties of their decay constants. From Eqs. (3.18) and (3.28), we find

$$\lambda_\gamma(3) = \frac{8\pi m_{01}}{h^3}\frac{(2j_0+1)(2j_1+1)}{(2j_3+1)}\int_0^\infty \frac{E_\gamma - Q_{01\rightarrow\gamma 3}}{e^{E_\gamma/kT}-1}\,\sigma_{01\rightarrow\gamma 3}\,dE_\gamma \tag{3.108}$$

with $E_{01} = E_\gamma - Q_{01\rightarrow\gamma 3}$. Recall that the above expression applies only to the forward and reverse reaction for a specific pair of initial and final states (Section 3.1.4). For simplicity, we will assume that the photodisintegration proceeds between the ground states of nuclei 3 and 0, while nucleus 1 denotes a light particle (p, n, or α). In this case, $Q_{01\rightarrow\gamma 3}$ is the ground-state Q-value of the forward reaction. With the approximation $e^{E_\gamma/kT} - 1 \approx e^{E_\gamma/kT}$ (Section 3.1.4) one obtains

$$\lambda_\gamma(3) = \frac{8\pi m_{01}}{h^3}\frac{(2j_0+1)(2j_1+1)}{(2j_3+1)}\int_0^\infty (E_\gamma - Q_{01\rightarrow\gamma 3})\,e^{-E_\gamma/kT}\sigma_{01\rightarrow\gamma 3}\,dE_\gamma \tag{3.109}$$

We must distinguish between the emission of charged particles, (γ,p) or (γ,α), and the emission of neutrons, (γ,n). For nonresonant charged-particle emission, the cross section is given by Eq. (3.71). For a nearly constant S-factor, the decay constant is

$$\begin{aligned}\lambda_\gamma(3) &\sim \int_0^\infty (E_\gamma - Q_{01\rightarrow\gamma 3})\,e^{-E_\gamma/kT}\frac{e^{-2\pi\eta}}{E_{01}}\,S(E_{01})\,dE_\gamma \\ &\sim S(E_0)\,e^{-Q_{01\rightarrow\gamma 3}/kT}\int_0^\infty e^{-2\pi\eta}e^{-E_{01}/kT}\,dE_{01}\end{aligned} \tag{3.110}$$

The integrand is equal to the Gamow peak (Section 3.2.1) for the forward reaction. The concept of a Gamow peak is also useful for photodisintegration reactions involving the emission of charged particles. Since the Gamow peak is located at E_0 and has a $1/e$ width of Δ (see Eqs. (3.77) and (3.81)), we expect that for the

photodisintegration reaction the γ-ray energy range of effective stellar burning is centered at

$$E_\gamma^{\text{eff}} = E_0 + Q_{01\to\gamma 3} \tag{3.111}$$

and has a width of Δ. For rising temperature, E_0 will increase and thus E_γ^{eff} will shift to a larger value. It is also apparent from Eq. (3.110) that, compared to the rate of the forward capture reaction (see Eq. (3.73)), the decay constant $\lambda_\gamma(3)$ has an additional temperature dependence through the term $e^{-Q/kT}$.

The situation is very different if a neutron is emitted in a nonresonant photodisintegration reaction. For small neutron energies, we found that the energy dependence of the (n,γ) cross section is given by $\sigma_\ell \sim E^{\ell-1/2}$ (Section 3.2.2). This cross-section behavior was derived under the assumption of relatively small neutron energies compared to the neutron binding energy. Most (n,γ) reactions have relatively large Q-values and, therefore, we can substitute this expression into Eq. (3.109). Thus,

$$\begin{aligned}\lambda_\gamma(3) &\sim \int_0^\infty (E_\gamma - Q_{01\to\gamma 3})\, e^{-E_\gamma/kT} E_{01}^{\ell-1/2}\, dE_\gamma \\ &\sim \int_0^\infty e^{-E_\gamma/kT} (E_\gamma - Q_{01\to\gamma 3})^{\ell+1/2}\, dE_\gamma \end{aligned} \tag{3.112}$$

It was already mentioned that for neutron-capture reactions the energy window of effective stellar burning is located at $E_n^{\text{eff}} = (\ell + 1/2)kT$ (Figure 3.21). Hence, we expect that the effective energy window for the reverse (γ,n) reaction is located at $E_\gamma^{\text{eff}} = (\ell + 1/2)kT + Q_{\text{n}\gamma}$ (Problem 3.4). For example, Figure 3.22 shows the integrand in Eq. (3.112) for the ^{148}Gd(γ,n)^{147}Gd reaction. The two curves correspond to temperatures of $T = 2$ and 3 GK and are calculated assuming emission of s-wave neutrons ($\ell = 0$). The Q-value for the ^{147}Gd(n,γ)^{148}Gd reaction amounts to $Q_{\text{n}\gamma} = 8.984$ MeV. Thus, the photodisintegration reaction can only proceed for γ-ray energies in excess of the threshold value $E_\gamma = Q_{\text{n}\gamma}$. Between $T = 2$ and 3 GK, the maximum of the integrand shifts by only ≈ 43 keV, a value barely noticeable in the figure. Therefore, the effective energy window for (γ,n) reactions of astrophysical interest is located closely to the reaction threshold, independent of the temperature. This behavior is in stark contrast compared to the considerably larger energy shift of the Gamow peak in (γ,p) or (γ,α) reactions. Also, the magnitude of the integrand increases by more than a factor of 10^7 between $T = 2$ and 3 GK, emphasizing the dramatic temperature dependence of decay constants for (γ,n) reactions.

3.2.4
Narrow-Resonance Reaction Rates

In the previous sections, reaction rates for smoothly varying S-factors were discussed. In this section, we will discuss the other extreme case, that is, strongly varying S-factors caused by resonances. We will consider here resonances

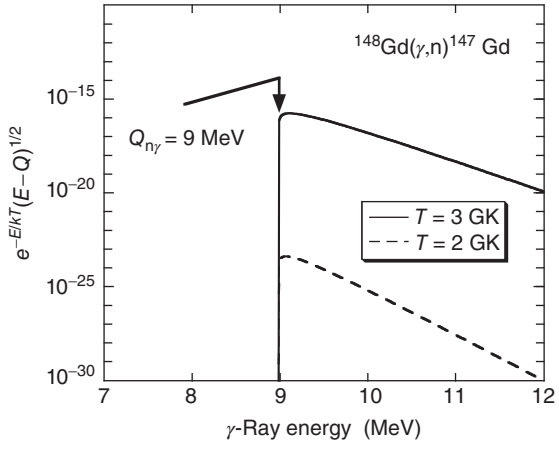

Figure 3.22 Integrand in Eq. (3.112) versus γ-ray energy at two temperatures ($T = 2$ and 3 GK) for the photodisintegration reaction ^{148}Gd(γ,n)^{147}Gd. The ground-state Q-value for the (forward) capture reaction is $Q_{n\gamma} = 8.984$ MeV (Wang *et al.*, 2012). This value is equal to the neutron separation energy of ^{148}Gd. Both curves are plotted for the emission of s-wave neutrons ($\ell = 0$). The integrand represents the γ-ray energy window of effective stellar burning.

that are isolated and narrow. The first condition implies that the level density in the compound nucleus is relatively small so that the resonances do not overlap significantly in amplitude. Several different definitions are used in the literature for a *narrow resonance*. Here, a resonance is called *narrow* if the corresponding partial widths are approximately constant over the total resonance width.

An isolated resonance is conveniently described by the one-level Breit–Wigner formula (see Eq. (2.185))

$$\sigma_{\mathrm{BW}}(E) = \frac{\lambda^2}{4\pi}\frac{(2J+1)(1+\delta_{01})}{(2j_0+1)(2j_1+1)}\frac{\Gamma_a\Gamma_b}{(E_r-E)^2+\Gamma^2/4} \tag{3.113}$$

where j_i are the spins of target and projectile, J and E_r are the spin and energy of the resonance, Γ_i are the resonance partial widths of entrance and exit channel, and Γ is the total resonance width. Each partial width has to be summed over all possible values of orbital angular momenta and channel spins. The wave number is substituted by the de Broglie wavelength $\lambda = 2\pi/k = 2\pi\hbar/\sqrt{2m_{01}E}$ to avoid confusion with the symbol for the Boltzmann constant. The factor $(1+\delta_{01})$ is included since the cross section for identical particles in the entrance channel increases by a factor of two. In the above expression the widths are expressed in terms of *observed* quantities (i.e., the Thomas approximation is used; see Section 2.5.5) since it will simplify the calculations substantially. For most narrow resonances, this approximation introduces a negligible error.

The reaction rates for a single narrow resonance can be calculated using Eqs. (3.10) and (3.113),

$$N_A\langle\sigma v\rangle = \left(\frac{8}{\pi m_{01}}\right)^{1/2} \frac{N_A}{(kT)^{3/2}} \int_0^\infty E\sigma_{\mathrm{BW}}(E) e^{-E/kT}\, dE$$
$$= N_A \frac{\sqrt{2\pi}\hbar^2}{(m_{01}kT)^{3/2}} \omega \int_0^\infty \frac{\Gamma_a\Gamma_b}{(E_r - E)^2 + \Gamma^2/4} e^{-E/kT} dE \tag{3.114}$$

where $\omega \equiv (2J+1)(1+\delta_{01})/[(2j_0+1)(2j_1+1)]$. For a sufficiently narrow resonance, the Maxwell–Boltzmann factor $e^{-E/kT}$ and the partial widths Γ_i are approximately constant over the total width of the resonance. They may be replaced by their value at E_r and the integral can be calculated analytically. Thus,

$$N_A\langle\sigma v\rangle = N_A \frac{\sqrt{2\pi}\hbar^2}{(m_{01}kT)^{3/2}} e^{-E_r/kT} \omega \frac{\Gamma_a\Gamma_b}{\Gamma} 2 \int_0^\infty \frac{\Gamma/2}{(E_r - E)^2 + \Gamma^2/4}\, dE$$
$$= N_A \frac{\sqrt{2\pi}\hbar^2}{(m_{01}kT)^{3/2}} e^{-E_r/kT} \omega \frac{\Gamma_a\Gamma_b}{\Gamma} 2\pi$$
$$= N_A \left(\frac{2\pi}{m_{01}kT}\right)^{3/2} \hbar^2 e^{-E_r/kT} \omega\gamma \tag{3.115}$$

where we used the definition $\omega\gamma \equiv \omega\Gamma_a\Gamma_b/\Gamma$. The quantity $\omega\gamma$ is proportional to the area under the resonance cross section, or equivalently, to the product of maximum cross section, $\sigma_{\mathrm{BW}}(E = E_r) = (\lambda_r^2/\pi)\omega\Gamma_a\Gamma_b/\Gamma^2$, and the total width Γ of the resonance,

$$\Gamma \cdot \sigma_{\mathrm{BW}}(E = E_r) = \Gamma \cdot \frac{\lambda_r^2}{\pi} \omega \frac{\Gamma_a\Gamma_b}{\Gamma^2} = \frac{\lambda_r^2}{\pi}\omega\gamma \tag{3.116}$$

Therefore, $\omega\gamma$ is referred to as the *resonance strength*. The reaction rates for narrow resonances depend only on the energy and the strength of the resonance, but not on the exact shape of the cross section curve. This is a fortunate circumstance since, as we shall see, for most narrow resonances the partial and total widths are experimentally not known.

If several narrow and isolated resonances contribute to the cross section, their contributions to the reaction rate add incoherently. Numerically, one finds

$$N_A\langle\sigma v\rangle = \frac{1.5399 \times 10^{11}}{\left(\frac{M_0 M_1}{M_0 + M_1} T_9\right)^{3/2}} \sum_i (\omega\gamma)_i e^{-11.605\, E_i/T_9} \qquad (\mathrm{cm^3 mol^{-1} s^{-1}}) \tag{3.117}$$

where i labels different resonances, $(\omega\gamma)_i$ and E_i are in units of MeV, and M_i are the relative atomic masses in u.

The temperature dependence of the reaction rate for a single narrow resonance can be found by performing a calculation similar to the one that was applied to the nonresonant case. Starting from Eqs. (3.85) and (3.87), we find with $N_A\langle\sigma v\rangle_T = cT^{-3/2}e^{-c'E_r/T}$

$$\ln N_A\langle\sigma v\rangle_T = \ln c - \frac{3}{2}\ln T - c'\frac{E_r}{T} \tag{3.118}$$
$$n = \frac{\partial \ln N_A\langle\sigma v\rangle_T}{\partial \ln T} = -\frac{3}{2} - c'E_r \frac{\partial(T^{-1})}{\partial \ln T} = \frac{c'E_r}{T} - \frac{3}{2} \tag{3.119}$$

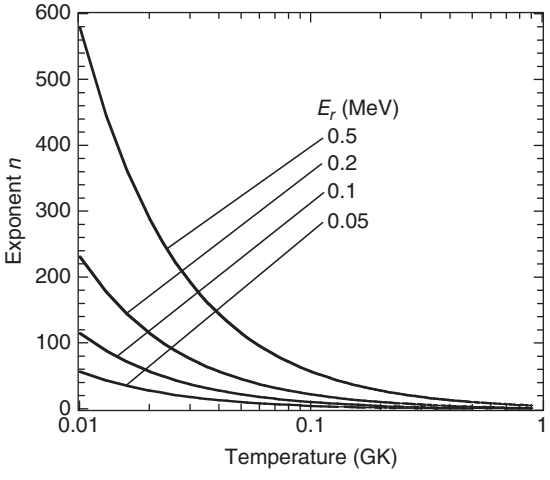

Figure 3.23 Temperature sensitivity of narrow-resonance reaction rates for various values of the resonance energy.

Hence,

$$N_A\langle\sigma v\rangle_T = N_A\langle\sigma v\rangle_{T_0}(T/T_0)^{c'E_r/T-3/2} = N_A\langle\sigma v\rangle_{T_0}(T/T_0)^{11.605\,E_r/T_9-3/2} \quad (3.120)$$

where E_r in the last term is given in units of mega electron volts. Figure 3.23 shows the exponent n versus temperature for several values of the resonance energy E_r. The temperature sensitivity of narrow-resonance reaction rates increases for decreasing temperatures and increasing resonance energies. Depending on the values of T and E_r, narrow-resonance reaction rates may even be more temperature sensitive than nonresonant reaction rates.

In the following, we will discuss the influence of the partial widths Γ_a and Γ_b on the reaction rates of a single narrow resonance using a capture reaction ($0 + 1 \rightarrow \gamma + 3$) as an example. Suppose further that only two channels are open, the particle channel (Γ_a) and the γ-ray channel (Γ_γ). The total width is $\Gamma = \Gamma_a + \Gamma_\gamma$. Experimental γ-ray partial widths typically amount to ≈ 1 meV–eV. Most neutron partial widths are in the range of ≈ 10 meV–keV. Neither of these partial widths are very sensitive to the value of E_r. Charged-particle partial widths, on the other hand, are governed by the transmission probability through the Coulomb barrier and are very sensitive to the resonance location, especially at low energies (Section 2.5.4).

Suppose first that the charged-particle width is smaller than the γ-ray partial width, a situation typical for low resonance energies (say, below $E_r \approx 0.5$ MeV). Since $\Gamma_a \ll \Gamma_\gamma$ we obtain from the definition of the resonance strength

$$\omega\gamma = \omega\frac{\Gamma_a\Gamma_\gamma}{\Gamma_a + \Gamma_\gamma} \approx \omega\frac{\Gamma_a\Gamma_\gamma}{\Gamma_\gamma} = \omega\Gamma_a \quad (3.121)$$

Thus, the resonance strength depends only on the charged-particle partial width. Depending on the precise value of the resonance energy, and to a lesser extent on the spectroscopic factor (see Eq. (2.197)), the resonance strength may become very small. Experimental studies of such low-energy resonances in charged-particle reactions represent a difficult challenge for the nuclear experimentalist (Chapter 4). For a very narrow resonance, only the small energy region near E_r contributes to the reaction rate. Nevertheless, the concept of a Gamow peak is also useful for narrow resonances if the resonance strength is determined by the charged-particle partial width. This can be seen by expressing the narrow-resonance reaction rates for $\Gamma_a \ll \Gamma_\gamma$ (and $\Gamma \approx \Gamma_\gamma$) as

$$\begin{aligned} N_A\langle\sigma v\rangle &\sim \int_0^\infty E\sigma_{\mathrm{BW}}(E)e^{-E/kT}\,dE \\ &\sim \int_0^\infty E\frac{1}{E}\frac{\Gamma_a\Gamma_\gamma}{(E_r-E)^2+\Gamma_\gamma^2/4}\,e^{-E/kT}\,dE \\ &\sim \int_0^\infty \frac{P_\ell(E)\Gamma_\gamma}{(E_r-E)^2+\Gamma_\gamma^2/4}\,e^{-E/kT}\,dE \\ &\sim \int_0^\infty \frac{\Gamma_\gamma}{(E_r-E)^2+\Gamma_\gamma^2/4}\,e^{-2\pi\eta}e^{-E/kT}\,dE \end{aligned} \tag{3.122}$$

where the energy *dependence* of the penetration factor $P_\ell(E)$ is approximated by the Gamow factor $e^{-2\pi\eta}$. Hence, the integrand can be written as a product of two factors: (i) the Gamow peak $e^{-2\pi\eta}e^{-E/kT}$, and (ii) a resonant S-factor curve of Lorentzian shape. The Lorentzian has a FWHM of Γ_γ and a maximum height of $4/\Gamma_\gamma$. Thus, for a narrow resonance, a change in Γ_γ has no influence on the area under the Lorentzian curve. It follows from Eq. (3.122) that, if a reaction cross section exhibits a number of narrow resonances, those resonances located in the region of the Gamow peak (at energies between $E_0 - \Delta/2$ and $E_0 + \Delta/2$) will be the major contributors to the total reaction rates. In other words, if there are resonances are located in the Gamow peak, other resonances located either below or above the Gamow peak are of minor importance. The situation is represented in Figure 3.24a. The dashed line shows the Maxwell–Boltzmann factor $e^{-E/kT}$, calculated for $T = 0.4$ GK, whereas the dashed-dotted line displays the Gamow factor. The solid lines show the Gamow peak and the narrow resonance S-factors. In this example, the narrow resonances at $E_r = 0.2$ MeV, 0.4 MeV, and 0.6 MeV will dominate the total reaction rates, while the resonances at $E_r = 0.05$ MeV and 0.8 MeV will be far less important.

Suppose now that the γ-ray partial width is smaller than the particle width, $\Gamma_a \gg \Gamma_\gamma$. This situation typically occurs for charged particles at higher resonance energies (say, above $E_r \approx 0.5$ MeV, where the particle partial width is frequently $\Gamma_a \gg 1$ eV), or for neutrons (except perhaps at very low energies). In this case, we obtain from the definition of the resonance strength

$$\omega\gamma = \omega\frac{\Gamma_a\Gamma_\gamma}{\Gamma_a+\Gamma_\gamma} \approx \omega\frac{\Gamma_a\Gamma_\gamma}{\Gamma_a} = \omega\Gamma_\gamma \tag{3.123}$$

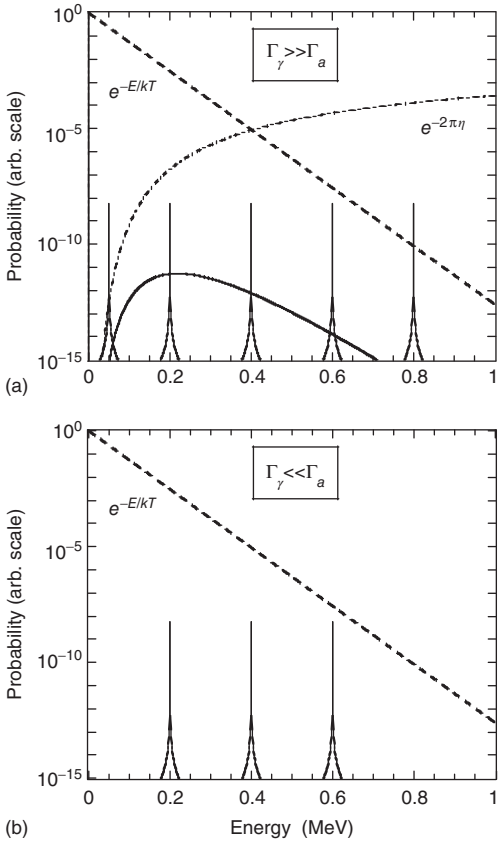

Figure 3.24 The influence of narrow resonances on reaction rates for the case (a) $\Gamma_\gamma \gg \Gamma_a$; (b) $\Gamma_\gamma \ll \Gamma_a$. The Maxwell–Boltzmann and Gamow factors are shown as dashed and dashed-dotted lines, respectively. The solid line in part (a) displays the Gamow peak. The sharp peaks indicate only the position of narrow resonances. In part (a), the displayed resonances have different strengths, while those in part (b) are assumed to have similar strengths.

The resonance strength depends only on the γ-ray partial width and will typically be on the order of 1 meV–eV. The precise value is determined by the complicated nuclear configurations involved in the reaction. Notice that "a most important energy window," such as the Gamow peak for charged particles or the Maxwell–Boltzmann distribution for neutrons, does not exist if $\Gamma_a \gg \Gamma_\gamma$. Figure 3.24b shows, for example, the factor $e^{-E/kT}$ at $T = 0.4$ GK (dashed line) together with three narrow resonances (solid lines) at locations of $E_r = 0.2$ MeV, 0.4 MeV, and 0.6 MeV. The resonances are assumed to have similar strengths, $\omega\gamma \approx \Gamma_\gamma$. For each resonance, only the region over the narrow resonance peak will contribute to the reaction rate. The reaction rate contribution of a narrow resonance increases rapidly for decreasing resonance energy, according to the

factor $e^{-E/kT}$. Hence, the resonance at $E_r = 0.2$ MeV will dominate the total reaction rate (note the vertical logarithmic scale in Figure 3.24b). The smaller the resonance energy, the larger the reaction rate contribution, as long as $\Gamma_a \gg \Gamma_\gamma$. Consequently, it becomes very important to locate all of the low-energy resonances.

It is often stated that in charged-particle reactions all resonances located within the Gamow peak ($E_0 \pm \Delta/2$) may contribute significantly to the total reaction rates. Based on the above discussion, it is clear that this assumption represents an oversimplification, since it applies only to those resonances for which the total width is dominated by the γ-ray partial width ($\Gamma_a \ll \Gamma_\gamma$). With increasing energy, a point will be reached in any capture reaction, where the particle partial width will dominate over the γ-ray partial width ($\Gamma_a \gg \Gamma_\gamma$), and for these resonances a Gamow peak does not exist. Therefore, one should not assume that all resonances located throughout the region $E_0 \pm \Delta/2$ contribute significantly to the total rates. The assumption is especially unjustified at higher stellar temperatures. This is demonstrated in Figure 3.25, showing the fractional contribution of each resonance to the total rate, $N_A\langle\sigma v\rangle_i / N_A\langle\sigma v\rangle_{\text{total}}$, versus resonance energy for: (i) ^{27}Al(p,γ)^{28}Si at $T = 3.5$ GK, and (ii) ^{24}Mg(α,γ)^{28}Si at $T = 2.5$ GK. All known resonances with center-of-mass energies in the range of $E_i = 0.2$–3.8 MeV in part (a) and $E_i = 1.1$–4.3 MeV in part (b) have been included. The dotted curves show the corresponding Gamow peaks. The main contribution to the total reaction rate derives from resonances located *below* the center of the Gamow peak, that is, $E_i < E_0$. The same applies to other (p,γ) and (α,γ) reactions on targets in the mass range $A = 20$–40 at temperatures of $T = 0.5$–10 GK. In the following chapters, we will still use the Gamow peak ($E_0 \pm \Delta/2$) as the conventional effective energy window, but the reader should keep in mind that this represents a crude estimate, especially at higher temperatures. For more information, see Newton *et al.* (2007).

Narrow resonances in the range of effective stellar energies have a dramatic effect on reaction rates. Therefore, it is important to locate all narrow resonances that could contribute to the total reaction rates. The situation is shown in Figure 3.26. As a first step, one typically measures the reaction of astrophysical interest, $0 + 1$, down to an energy of E_{min}, representing the smallest energy achievable in the laboratory (the dotted line in Figure 3.26). Charged-particle cross sections below an energy of E_{min} become so small because of Coulomb barrier considerations that present experimental techniques are not sensitive enough for direct measurements. In a second step, therefore, the energy range between $E = 0$ and E_{min} is investigated by means of indirect measurements. Such studies populate the astrophysically important levels in the compound nucleus C using reactions X+x other than the one of direct astrophysical interest (Section 4.1). From the measured nuclear properties (excitation energies, spins, parities, spectroscopic factors, and so on) of the compound levels close to the particle threshold, the resonance energies and strengths of astrophysically important resonances can be estimated.

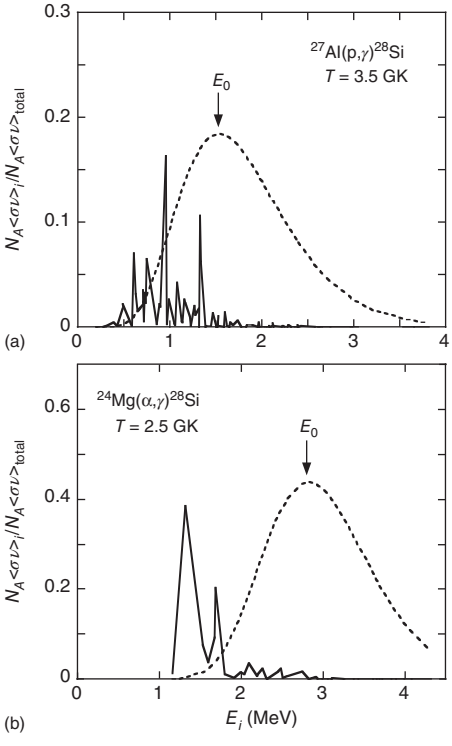

Figure 3.25 The fractional contribution of narrow resonances to the total reaction rate versus resonance energy for (a) ^{27}Al(p,γ)^{28}Si at $T = 3.5$ GK and (b) ^{24}Mg(α,γ)^{28}Si at $T = 2.5$ GK. The main contribution arises in both cases from resonances with energies of $E_i < E_0$. The Gamow peak is shown as a dotted line. The resonance energies and strengths are adopted from Endt (1990) and Iliadis *et al.* (2001). (Reprinted with permission from J. R. Newton *et al.*, Phys. Rev. C, Vol. 75, 045801 (2007). Copyright (2007) by the American Physical Society.)

For the influence of experimental uncertainties of E_r, $\omega\gamma$, and C^2S on the resulting narrow-resonance reaction rates, the reader is referred to Thompson and Iliadis (1999) and Iliadis *et al.* (2010).

Example 3.6

Suppose that four hypothetical narrow s-wave resonances occur at low energies in the ^{20}Ne(p,γ)^{21}Na reaction. The resonance energies are $E_r = 10$ keV, 30 keV, 50 keV, and 100 keV. The corresponding resonance strengths are $\omega\gamma = 7.24 \times 10^{-33}$ eV, 3.81×10^{-15} eV, 1.08×10^{-9} eV, and 3.27×10^{-4} eV. Each of these values has been obtained by assuming $\Gamma_p \ll \Gamma_\gamma$ and $C^2S = 1$. Which resonance do you expect to dominate the total reaction rates at $T = 0.02$ GK and 0.08 GK?

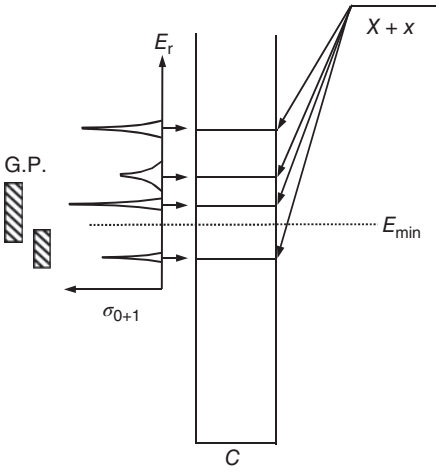

Figure 3.26 Energy level diagram, showing narrow resonances in the reaction 0 + 1 (left-hand side) and the corresponding levels in the compound nucleus *C*. The locations of two Gamow peaks (G.P.) at different temperatures are displayed as hatched bars. Below an energy of E_{min} (dotted line) charged-particle measurements are not feasible. In this case, one may estimate the reaction rates by measuring nuclear structure properties of levels in nucleus *C* via a reaction *X* + *x*.

At $T = 0.02$ GK, the Gamow peak location (see Eqs. (3.77) and (3.81)) is $E_0 \pm \Delta/2 = 40 \pm 10$ keV. Only the resonances at $E_r = 30$ keV and 50 keV are located in the Gamow peak and, therefore, these will dominate the reaction rates. At $T = 0.08$ GK, we obtain $E_0 \pm \Delta/2 = 100 \pm 30$ keV. Only the resonance at $E_r = 100$ keV is located in the Gamow peak and thus will dominate the total reactions rates. See also Problem 3.5.

We will now consider two issues that are important at elevated temperatures when a capture reaction, for example, (p,γ), (n,γ), or (α,γ), proceeds through narrow resonances. The first concerns the influence of excited target states on the reaction rates. From Eq. (3.38), we find for the *stellar* rate of the capture reaction $0 + 1 \rightarrow \gamma + 3$

$$N_A\langle\sigma v\rangle = \sum_\mu P_{0\mu} N_A\langle\sigma v\rangle^\mu = \frac{\sum_\mu g_{0\mu} e^{-E_{0\mu}/kT} N_A\langle\sigma v\rangle^\mu}{\sum_\mu g_{0\mu} e^{-E_{0\mu}/kT}} \tag{3.124}$$

where μ sums over the levels in the target nucleus 0 including the ground state, while excited states in the light particle 1 are neglected (a safe assumption for protons, neutrons or α-particles). The subscript "01 → 23" is suppressed for clarity and it is assumed that the reaction rate $N_A\langle\sigma v\rangle^\mu$ has already been properly summed over transitions to excited final states ν in nucleus 3. All other symbols have exactly the same meaning as in Section 3.1.5. Suppose now that the reaction rate $N_A\langle\sigma v\rangle^\mu$ for a specific target state μ is determined by a number of narrow

resonances that are labeled by ρ. From Eq. (3.115), we find

$$N_A\langle\sigma v\rangle^{\mu} = \sum_{\rho} N_A\langle\sigma v\rangle_{\rho}^{\mu} = \sum_{\rho} N_A \left(\frac{2\pi}{m_{01}kT}\right)^{3/2} \hbar^2 e^{-E_{\rho\mu}/kT}(\omega\gamma)_{\rho\mu}$$
$$= \sum_{\rho} N_A \left(\frac{2\pi}{m_{01}kT}\right)^{3/2} \hbar^2 e^{-E_{\rho\mu}/kT} \frac{g_\rho}{g_{0\mu}g_1} \frac{\Gamma_{\rho\mu}\Gamma_{\rho\gamma}}{\Gamma_\rho} \tag{3.125}$$

where g_ρ, $g_{0\mu}$, and g_1 are the statistical weights of the resonance, of the level in target nucleus 0 and of the light particle 1, respectively, with $\omega_{\rho\mu} \equiv g_\rho/(g_{0\mu}g_1)$; $\Gamma_{\rho\mu}$, $\Gamma_{\rho\gamma}$, and Γ_ρ are the particle partial width for resonance formation from target level μ, the (decay) γ-ray partial width, and the total width, respectively, of resonance ρ; $E_{\rho\mu}$ is the energy of resonance ρ for target level μ and $E_{\rho\mu_0} = E_{\rho\mu} + E_{0\mu}$ is the energy of resonance ρ for the target ground state μ_0. An energy level diagram is shown in Figure 3.27. From Eqs. (3.36), (3.37), (3.124), and (3.125), we obtain

$$N_A\langle\sigma v\rangle = \frac{\sum_\mu g_{0\mu} e^{-E_{0\mu}/kT} \sum_\rho N_A \left(\frac{2\pi}{m_{01}kT}\right)^{3/2} \hbar^2 e^{-E_{\rho\mu}/kT} \frac{g_\rho}{g_{0\mu}g_1} \frac{\Gamma_{\rho\mu}\Gamma_{\rho\gamma}}{\Gamma_\rho}}{\sum_\mu g_{0\mu} e^{-E_{0\mu}/kT}}$$
$$= \frac{1}{G_0^{\mathrm{norm}}} \sum_\rho N_A\langle\sigma v\rangle_\rho^{\mu_0} \sum_\mu \frac{\Gamma_{\rho\mu}}{\Gamma_{\rho\mu_0}} \tag{3.126}$$

Hence, the total stellar rate is given by a sum over narrow resonance ground-state rates, $N_A\langle\sigma v\rangle_\rho^{\mu_0}$, where each resonance term is modified by a factor of $(1 + \Gamma_{\rho\mu_1}/\Gamma_{\rho\mu_0} + \Gamma_{\rho\mu_2}/\Gamma_{\rho\mu_0} + \cdots)$, with $\Gamma_{\rho\mu}/\Gamma_{\rho\mu_0}$ denoting the ratio of particle partial widths for excited target level μ and the target ground state μ_0. The inclusion of excited target states in the total reaction rate introduces no additional temperature dependence other than a weak dependence through the quantity G_0^{norm}. For charged-particle reactions and low resonance energies, the penetration factor (and hence the particle partial width) varies strongly with energy (Section 2.5.4). Therefore, we expect in this case a negligible influence of excited target states on the total rate, that is, $\Gamma_{\rho\mu} \ll \Gamma_{\rho\mu_0}$, unless the target excitation energy $E_{0\mu}$ is very small, implying $E_{\rho\mu} \approx E_{\rho\mu_0}$ or $\Gamma_{\rho\mu} \approx \Gamma_{\rho\mu_0}$ (for similar values of the corresponding reduced widths; see Figure 3.27). It is also clear that in charged-particle reactions at higher resonance energies or in neutron-induced reactions, where the particle partial widths are less sensitive to energy variations, the ratio $\Gamma_{\rho\mu}/\Gamma_{\rho\mu_0}$ can be relatively large. Under such conditions, excited target states may dominate the total stellar reaction rates. See, for example, Vancraeynest *et al.* (1998) and Schatz *et al.* (2005).

The second issue concerns photodisintegration rates. Forward and reverse rates are related by Eqs. (3.35) or (3.46). Rewriting that expression by using the above notation yields

$$\frac{\lambda_\gamma(3)}{N_A\langle\sigma v\rangle} = \left(\frac{2\pi}{h^2}\right)^{3/2} \frac{(m_{01}kT)^{3/2}}{N_A} \frac{g_{0\mu_0}g_1}{g_{3\nu_0}} \left(\frac{G_0^{\mathrm{norm}}}{G_3^{\mathrm{norm}}}\right) e^{-Q_{01\to\gamma 3}/kT} \tag{3.127}$$

where for the sake of simplicity, we omitted the Kronecker delta (we assume nonidentical nuclei 0 and 1) and set $G_1^{\text{norm}} = 1$ (we disregard excited states in the light particle 1); $g_{0\mu_0}$, g_1, and $g_{3\nu_0}$ are the statistical weights of the target ground state, of light particle 1, and of the ground state of the residual nucleus, respectively; $Q_{01\to\gamma 3}$ denotes the Q-value for the ground states of nuclei 0, 1, and 3. If the forward reaction proceeds predominantly through isolated and narrow resonances, the rates for the (reverse) photodisintegration can be found by substitution of Eq. (3.126) into Eq. (3.127),

$$\begin{aligned}\lambda_\gamma(3) &= \left(\frac{2\pi}{h^2}\right)^{3/2} \frac{(m_{01}kT)^{3/2}}{N_A} \frac{g_{0\mu_0}g_1}{g_{3\nu_0}} \frac{1}{G_3^{\text{norm}}} e^{-Q_{01\to\gamma 3}/kT} \sum_\rho N_A\langle\sigma v\rangle_\rho^{\mu_0} \sum_\mu \frac{\Gamma_{\rho\mu}}{\Gamma_{\rho\mu_0}} \\ &= \frac{1}{\hbar} \frac{g_{0\mu_0}g_1}{g_{3\nu_0}} \frac{1}{G_3^{\text{norm}}} \sum_\rho e^{-E_{\rho x}/kT} \frac{g_\rho}{g_{0\mu_0}g_1} \frac{\Gamma_{\rho\mu_0}\Gamma_{\rho\gamma}}{\Gamma_\rho} \sum_\mu \frac{\Gamma_{\rho\mu}}{\Gamma_{\rho\mu_0}} \\ &= \frac{1.519\times 10^{21}}{G_3^{\text{norm}}} \frac{g_{0\mu_0}g_1}{g_{3\nu_0}} \sum_\rho e^{-11.605E_{\rho x}/T_9} (\omega\gamma)_{\rho\mu_0} \sum_\mu \frac{\Gamma_{\rho\mu}}{\Gamma_{\rho\mu_0}} \qquad (\text{cm}^3\text{mol}^{-1}\text{s}^{-1})\end{aligned} \tag{3.128}$$

where the excitation energy in the compound nucleus 3 (corresponding to resonance ρ) is equal to the sum of the resonance energy for the target ground state and the ground-state Q-value, $E_{\rho x} = E_{\rho\mu_0} + Q_{01\to\gamma 3}$ (see Figure 3.27). In the above numerical expression, the resonance energies and strengths are in units of mega electron volts. The photodisintegration rate depends exponentially on the excitation energies $E_{\rho x}$ of compound levels corresponding to resonances through which the forward reaction proceeds. The excitation energies also enter implicitly via the particle partial widths $\Gamma_{\rho\mu}$ and $\Gamma_{\rho\mu_0}$, and via the resonance strengths $(\omega\gamma)_{\rho\mu_0}$ for the target ground state. A numerical example is given in Problem 3.8.

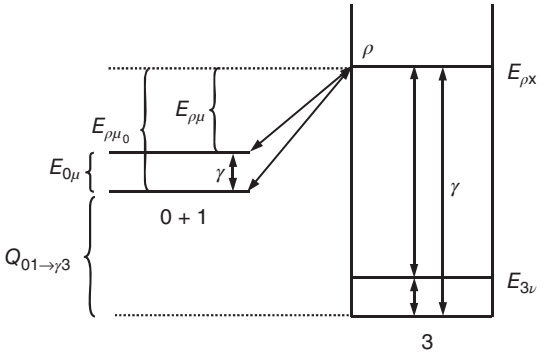

Figure 3.27 Energy level diagram for narrow resonances in the $0 + 1 \to \gamma + 3$ capture reaction, showing thermally excited states in the target and the final nucleus. For clarity, only a single narrow resonance (ρ) and one excited state is shown for the target 0 and the final nucleus 3. All vertical arrows represent γ-ray transitions. In the forward reaction $0 + 1 \to \gamma + 3$, the level ρ may be populated either from the target ground state or from the excited target state.

3.2.5
Broad-Resonance Reaction Rates

The results derived in the last section are independent of the precise shape of the resonance cross section. The formalism of narrow-resonance reaction rates is not applicable in cases for which the explicit energy dependence of the cross section is important. As an example, a charged-particle reaction will be discussed in the following. Three common situations are schematically displayed in Figure 3.28, showing in each case the Maxwell–Boltzmann factor (dashed line), the Gamow factor (dashed-dotted line), the Gamow peak (dotted line), and the cross section of a *broad* resonance (upper solid line). The reaction rates are proportional to the area under the lower solid line, that is, the product of the Maxwell–Boltzmann distribution and the cross section. The curves are obtained for the ^{24}Mg(p,γ)^{25}Al reaction at $T = 0.05$ GK. For simplicity, the resonant cross sections are calculated using an arbitrary constant γ-ray partial width; angular momenta are neglected and the penetration factor is approximated by the Gamow factor $e^{-2\pi\eta}$.

Part (a) shows a fictitious broad resonance at $E_r = 0.1$ MeV with a width of $\Gamma = 5$ keV, located inside the Gamow peak. It can no longer be assumed that the partial widths, the de Broglie wavelength, and the Maxwell–Boltzmann distribution are constant over the width of the resonance. The energy dependence of these quantities has to be taken into account. The product of Maxwell–Boltzmann distribution and cross section is now a complicated function of energy (lower solid line) and can no longer be integrated analytically. Instead, the reaction rates have to be calculated numerically by solving (see Eqs. (3.70) and (3.113))

$$N_A\langle\sigma v\rangle = \sqrt{2\pi}\,\frac{N_A\omega\hbar^2}{(m_{01}kT)^{3/2}}\int_0^\infty e^{-E/kT}\frac{\Gamma_a(E)\Gamma_b(E+Q-E_f)}{(E_r-E)^2+\Gamma(E)^2/4}\,dE \qquad (3.129)$$

where the partial width for the exit channel, Γ_b, has to be calculated at the energy $E_{23} = E_{01} + Q_{01\to 23} - E_f$ available to the pair 2 + 3. The above expression involves a transition from the resonance to a specific final state E_f. If the reaction involves transitions to several final states, the different contributions to the total cross section add incoherently. As a useful rule, if the resonance width is small compared to the width of the Gamow peak, $\Gamma \ll \Delta$, the reaction rates may be calculated using the narrow resonance formalism (Section 3.2.4). Otherwise, the reaction rates have to be obtained from a numerical integration of Eq. (3.129).

Figure 3.28b shows a fictitious resonance at $E_r = 0.25$ MeV with a width of $\Gamma = 0.6$ keV. It can be seen that the resonance is located outside the Gamow peak. We concluded in the last section that in such cases the contribution of this resonance to the total reaction rates is negligible compared to other narrow resonances that are located in the Gamow peak. But suppose that no other narrow resonances exist below $E = 0.25$ MeV. Notice that it would be incorrect in this case to calculate the reaction rates using the narrow resonance formalism (see Eq. (3.115)). The latter expressions were derived assuming a negligible energy dependence of the partial widths, de Broglie wavelength, and Maxwell–Boltzmann distribution over the total width of the resonance. The value of the Maxwell–Boltzmann distribution at the resonance energy, E_r, appears in

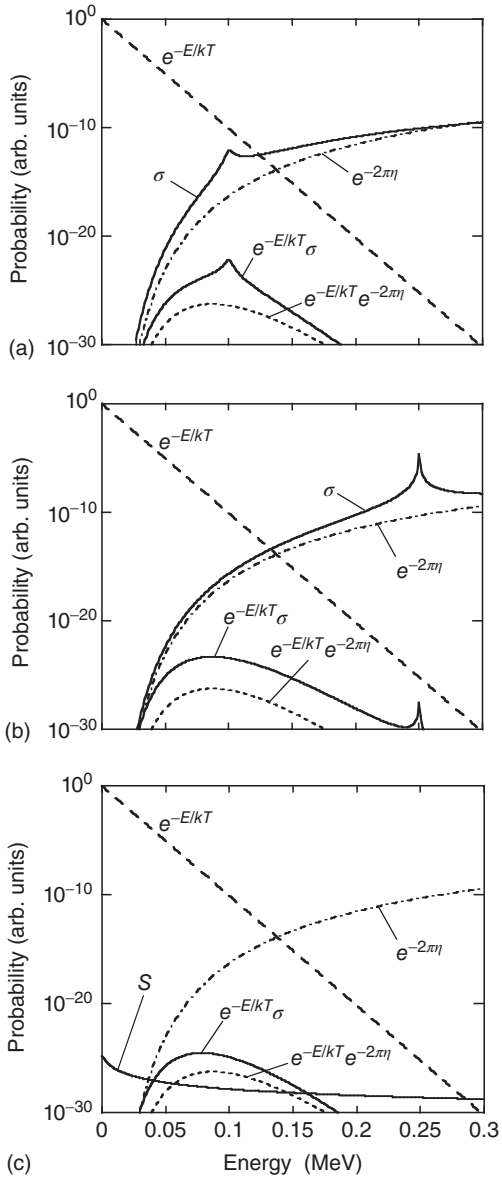

Figure 3.28 The influence of broad resonances on reaction rates for (a) a broad resonance located in the Gamow peak; (b) a broad resonance located outside the Gamow peak; and (c) a high-energy wing of a subthreshold resonance. In each panel, the Maxwell–Boltzmann factor, Gamow factor, and Gamow peak are shown as dashed, dashed-dotted, and dotted lines, respectively. The Breit–Wigner cross sections are displayed as upper solid lines and the product of cross section and Maxwell–Boltzmann factor as lower solid lines. The latter product determines the reaction rates (see Eqs. (3.70) and (3.129)). In part (c) the *S*-factor instead of the cross section is shown for clarity.

the narrow-resonance reaction rate expression, which takes only the reaction rate contribution at the resonance energy into account. However, the product of Maxwell–Boltzmann distribution and cross section (lower solid line) gives rise to another maximum at lower energies caused by the low-energy wing of the resonance. In this example, it is apparent that the first maximum gives a far larger contribution to the reaction rates than the second maximum at E_r. The reason is that the Maxwell–Boltzmann distribution has a stronger energy dependence than the cross section, as can be seen by comparing the magnitude of both functions at the positions of the two maxima of the lower solid line. As an approximate rule, if a resonance at E_r is located within the energy range between $E_0 - 2\Delta$ and $E_0 + 2\Delta$, the narrow resonance formalism is applicable (Section 3.2.4). Otherwise, the wing of the resonance has to be taken explicitly into account, even if the resonance is narrow in the sense that $\Gamma \ll \Delta$. In the latter case, the reaction rates can be calculated either by numerical integration or, if the S-factor of the resonance wing varies smoothly over the energy range of interest, by expanding the S-factor into a Taylor series and by applying the nonresonant reaction rate formalism.

Figure 3.28c shows a fictitious subthreshold resonance, corresponding to a compound nucleus level, located below the proton threshold. For reasons of clarity, the lower solid line displays the S-factor rather than the cross section. In this case the high-energy wing of the resonance has to be taken explicitly into account. The S-factor (or cross section) can be calculated using the one-level Breit–Wigner formula (see Eq. (2.185) and Example 2.1). Again, the reaction rates are then evaluated either by numerical integration or, if the S-factor varies smoothly over the energy range of interest, by using the nonresonant reaction formalism.

For the explicit calculation of broad-resonance reaction rates, it is of advantage to express the S-factor in terms of measured quantities. Using the one-level Breit–Wigner formula, the cross section can be written as

$$\sigma_{\mathrm{BW}}(E) = \frac{\pi\hbar^2\omega}{2m_{01}E}\,\frac{\Gamma_a(E)\Gamma_b(E+Q-E_f)}{(E_r-E)^2+\Gamma(E)^2/4} \tag{3.130}$$

Numerically, we find $\pi\hbar^2/(2m_{01}) = 0.6566\,(M_0+M_1)/(M_0M_1)$ MeV·b. Suppose first that the partial widths of the broad resonance at E_r, $\Gamma_a(E_r)$ and $\Gamma_b(E_r)$, are known experimentally. We may parametrize the particle partial width using $\Gamma_i(E) \sim P_i(E)$ (see Eq. (2.175)) and the γ-ray partial width by $\Gamma_\gamma(E_\gamma) \sim E_\gamma^{2L+1}$, where E_γ and L denote the energy and multipolarity, respectively, of the emitted γ-ray (see Eq. (1.22)). Although approximate expressions exist for the calculation of the penetration factors (see, e.g., Clayton, 1983), it is more reliable to obtain $P_i(E)$ directly from numerical computations of Coulomb wave functions (Section 2.5.4 and Appendix A.3). For reactions involving particles with rest mass, one finds from Eq. (3.130)

$$\sigma_{\mathrm{BW}}(E) = \frac{\pi\hbar^2\omega}{2m_{01}E}\,\frac{\frac{P_a(E)}{P_a(E_r)}\,\Gamma_a(E_r)\,\frac{P_b(E+Q-E_f)}{P_b(E_r+Q-E_f)}\,\Gamma_b(E_r+Q-E_f)}{(E_r-E)^2+\Gamma(E)^2/4} \tag{3.131}$$

and for reactions involving photon emission

$$\sigma_{\mathrm{BW}}(E) = \frac{\pi\hbar^2\omega}{2m_{01}E} \frac{\frac{P_a(E)}{P_a(E_r)}\,\Gamma_a(E_r)\left[\frac{E+Q-E_f}{E_r+Q-E_f}\right]^{2L+1}\Gamma_\gamma(E_r+Q-E_f)}{(E_r-E)^2+\Gamma(E)^2/4} \tag{3.132}$$

For many broad resonances, the partial widths Γ_i have not been measured, but only the resonance strength $\omega\gamma$ and the total width Γ, both measured at E_r, are known experimentally. With the definition of the resonance strength

$$\omega\gamma \equiv \omega\,\frac{\Gamma_a(E_r)\Gamma_b(E_r+Q-E_f)}{\Gamma(E_r)} \tag{3.133}$$

the cross section is given by

$$\sigma_{\mathrm{BW}}(E) = \frac{\pi\hbar^2}{2m_{01}E}\frac{P_a(E)}{P_a(E_r)}\frac{\Gamma_b(E+Q-E_f)}{\Gamma_b(E_r+Q-E_f)}\frac{\omega\gamma\Gamma(E_r)}{(E_r-E)^2+\Gamma(E)^2/4} \tag{3.134}$$

where the ratio of partial widths Γ_b is given as before: either by the ratio of penetration factors, $P_b(E+Q-E_f)/P_b(E_r+Q-E_f)$, for reactions involving particles with rest mass, or by the factor $[(E+Q-E_f)/(E_r+Q-E_f)]^{2L+1}$ for reactions emitting photons. The cross section for subthreshold resonances is calculated similarly (Example 2.1). It can be seen from the Breit–Wigner expression (see Eq. (3.130)) that broad resonances with an energy E_r close to E_0 and with large partial widths (i.e., a large value of C^2S and a small value of orbital angular momentum ℓ) will make the largest contributions to the total reaction rates.

Example 3.7

The s-wave resonance at $E_r = 214$ keV ($J^\pi = 1/2^+$) in ^{24}Mg(p,γ)^{25}Al has a measured strength of $\omega\gamma = 1.3\times10^{-2}$ eV, a proton width of $\Gamma_{\mathrm{p}} = 1.4\times10^{-2}$ eV, a γ-ray partial width of $\Gamma_\gamma = 1.4\times10^{-1}$ eV, and a total width of $\Gamma = 1.5\times10^{-1}$ eV (Powell *et al.*, 1999). All widths are *observed* quantities. No other channels are open, hence $\Gamma = \Gamma_{\mathrm{p}} + \Gamma_\gamma$. Suppose that the resonance decays via a dipole transition ($L = 1$) to the $E_f = 452$ keV state ($J^\pi = 1/2^+$) in ^{25}Al with a branching ratio of 100%. A level diagram is shown in Figure 3.29a. Calculate the reaction rate contribution of this resonance at temperatures between $T = 0.01$ GK and 1 GK using: (i) the narrow resonance formalism, and (ii) the broad resonance formalism (that is, by explicitly taking the energy dependence of the S-factor into account).

To calculate the narrow-resonance reaction rate, only the resonance energy E_r and strength $\omega\gamma$ is needed. The numerical results are shown as the dashed line in Figure 3.29b and have been obtained directly from Eq. (3.117). The resonant

S-factor is calculated from Eqs. (3.71) and (3.132),

$$S_{\mathrm{BW}}(E) = E\sigma_{\mathrm{BW}}(E)e^{2\pi\eta}$$
$$= \frac{\pi\hbar^2}{2m_{01}}\, e^{2\pi\eta}\omega \frac{\frac{P_a(E)}{P_a(E_r)}\Gamma_a(E_r)\left[\frac{E+Q-E_f}{E_r+Q-E_f}\right]^{2L+1}\Gamma_\gamma(E_r+Q-E_f)}{(E_r-E)^2+\Gamma(E)^2/4}$$

The penetration factors are obtained from numerically computed Coulomb wave functions for $\ell = 0$ (s-wave), using a radius parameter of $r_0 = 1.25$ fm. The broad-resonance reaction rates can then be calculated by numerical integration of Eq. (3.70). The results are shown as the solid line in Figure 3.29b.

It can be seen that above a temperature of $T = 0.05$ GK the narrow- and broad-resonance reaction rates are in agreement. The result is expected since for this temperature region the $E_r = 214$ keV resonance is located inside the Gamow peak.

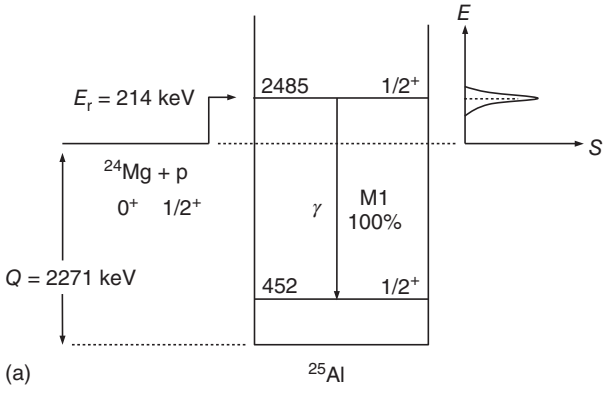

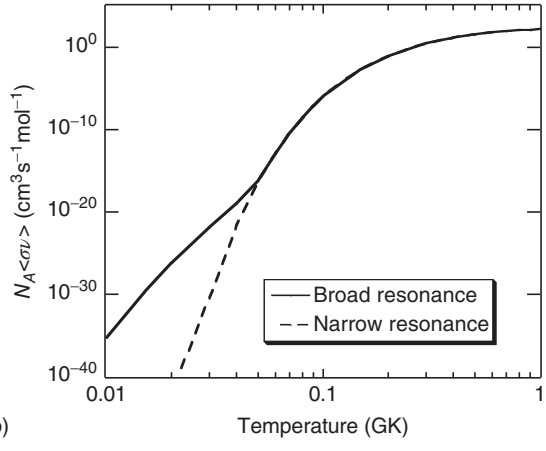

Figure 3.29 (a) Level diagram of ^{25}Al and (b) reaction rates for ^{24}Mg(p,γ)^{25}Al versus temperature. The solid and dashed curves in part (b) are calculated with the reaction rate formalism for broad resonances and narrow resonances, respectively.

Below $T = 0.05$ GK, the resonance is located outside the energy window $E_0 \pm 2\Delta$ and, therefore, the narrow resonance formalism underestimates the reaction rates considerably. The low-energy wing of the resonance provides a considerably larger reaction rate contribution than the contribution at E_r. Figure 3.29b displays at $T = 0.05$ GK a change in the slope of the reaction rates, reflecting the different temperature dependences of the narrow-resonance reaction rate expression (because of the contribution at the resonance energy E_r alone) and the broad-resonance reaction rate formalism (because of the additional contribution from the Gamow peak near E_0).

3.2.6 Electron Screening

The formalism discussed so far for calculating thermonuclear reaction rates involving two charged particles is based on the assumption that Coulomb interactions with electrons or with other nuclei are negligible. However, in a fully ionized stellar plasma electrons are attracted to a particular nucleus, while other nuclei are repelled. In other words, each nucleus will polarize its neighborhood. We may imagine that each nucleus is surrounded by an imaginary sphere containing an inhomogeneously charged cloud. Therefore, in a nuclear reaction, the potential seen by either one of the colliding nuclei is modified from the simple Coulomb form. The effective barrier for the nuclear fusion reaction becomes thinner and, therefore, both the tunneling probability and the reaction rate increase over their values obtained for the same reaction taking place in a vacuum. This effect is referred to as *electron screening*. The ratio of the reaction rate in the plasma to the vacuum rate is called the *screening factor* f_s and will be derived in the following.

Consider a nearly perfect gas at relatively low density for which the average Coulomb energy between two neighboring nuclei is considerably smaller than their thermal energy. In this case, the screened potential for two colliding nuclei 0 and 1 is given by (Salpeter, 1954)

$$V_s(r) = \frac{Z_0 Z_1 e^2}{r} e^{-r/R_D} \tag{3.135}$$

where R_D is the Debye–Hückel radius

$$R_D = \sqrt{\frac{kT}{4\pi e^2 \rho N_A \zeta^2}} = 2.812 \times 10^{-7} \rho^{-1/2} T_9^{1/2} \zeta^{-1} \text{ (cm)} \tag{3.136}$$

and

$$\zeta \equiv \sqrt{\sum_i \frac{(Z_i^2 + Z_i \theta_e) X_i}{A_i}} \tag{3.137}$$

with θ_e the electron degeneracy factor. The sum is over all types of positive ions present in the plasma and the density in the numerical expression is in units of grams per cubic centimeter.

The Debye–Hückel radius is a measure for the size of the charged cloud surrounding each nucleus. Beyond a distance of $r = R_D$ the screened potential vanishes quickly. The condition of a weak Coulomb energy compared to the thermal energy defines the *weak screening* regime. It is equivalent to the assumption that the Debye–Hückel radius is considerably larger than the average distance between neighboring nuclei. This condition, which holds for most thermonuclear reactions in stars, can be numerically expressed as (Clayton, 1983)

$$T \gg 10^5 \rho^{1/3} \zeta^2 \tag{3.138}$$

with T and ρ in units of kelvin and grams per cubic centimeter, respectively.

Consider now a nonresonant reaction for which the cross section is given by Eq. (3.71). The energy dependence of $\sigma(E)$ is mainly given by the Gamow factor, while the S-factor varies smoothly with energy. The s-wave transmission coefficient for the unscreened Coulomb potential can be found from

$$\begin{aligned} \widehat{T} &\approx \exp\left(-\frac{2}{\hbar}\sqrt{2m}\int_0^{R_c}\sqrt{\frac{Z_0 Z_1 e^2}{r} - E}\, dr\right) \\ &= \exp\left(-\frac{2}{\hbar}\sqrt{\frac{2m}{E}}\, Z_0 Z_1 e^2 \int_0^1 \sqrt{\frac{1}{z} - 1}\, dz\right) \\ &= \exp\left(-\frac{2\pi}{\hbar}\sqrt{\frac{m}{2E}}\, Z_0 Z_1 e^2\right) \equiv e^{-2\pi\eta} \end{aligned} \tag{3.139}$$

This derivation is simpler than that in Section 2.4.3 because we assume here that, for low bombarding energies compared to the Coulomb barrier height, the classical turning point is considerably larger than the radius of the square-well potential, $R_c \gg R_0$ (Figure 2.17). The lower integration limit for r is then $R_0 \to 0$, while that for z is $R_0/R_c \to 0$. Consequently, the Gamow factor is directly obtained without the correction of Eq. (2.124). For the screened Coulomb potential, the classical turning point is defined by

$$E = (Z_0 Z_1 e^2 / R_c) e^{-R_c/R_D} \tag{3.140}$$

Proceeding in exactly the same manner as in Section 2.4.3, we find for the modified transmission coefficient (Problem 3.9)

$$\widehat{T} \approx e^{x\pi\eta - 2\pi\eta} \tag{3.141}$$

where the variable $x = x(E) = R_c/R_D$ depends explicitly on energy through R_c. Equation (3.141) is derived assuming that x is a small number, $R_D \gg R_c$, which is frequently the case (see below). Substitution of the modified transmission coefficient into the expression for nonresonant reaction rates (see Eq. (3.72)) gives

$$N_A\langle\sigma v\rangle = \left(\frac{8}{\pi m_{01}}\right)^{1/2} \frac{N_A}{(kT)^{3/2}} \int_0^\infty S(E)\, e^{x\pi\eta} e^{-2\pi\eta} e^{-E/kT}\, dE \tag{3.142}$$

Both x and η depend on energy, but the above expression can be approximated by evaluating the factor $e^{x\pi\eta}$ at the most effective energy of the interaction in the

plasma, that is, the Gamow energy E_0. With $e^{x\pi\eta} \approx e^{(x\pi\eta)_{E_0}} \equiv f_s$ one obtains

$$N_A\langle\sigma v\rangle = \left(\frac{8}{\pi m_{01}}\right)^{1/2} \frac{N_A}{(kT)^{3/2}} f_s \int_0^\infty S(E)\, e^{-2\pi\eta} e^{-E/kT}\, dE \tag{3.143}$$

and, consequently, the screened reaction rate is simply obtained by multiplying the unscreened reaction rate by the screening factor $f_s = e^{(x\pi\eta)_{E_0}}$. The small corrections introduced by a more rigorous calculation, in which the integral in Eq. (3.142) is evaluated by taking the energy dependence of the factor $e^{x\pi\eta}$ into account, are discussed in Bahcall *et al.* (1998) and Liolios (2000). Numerically one finds

$$\begin{aligned} x(E_0) &= (R_c/R_D)_{E_0} = \frac{Z_0 Z_1 e^2}{E_0}\sqrt{\frac{4\pi e^2 \rho N_A}{kT}}\,\zeta \\ &= 4.197\times 10^{-6}(Z_0 Z_1)^{1/3}\left(\frac{M_0 M_1}{M_0+M_1}\right)^{-1/3}\sqrt{\rho}\, T_9^{-7/6}\zeta \qquad (3.144) \\ (x\pi\eta)_{E_0} &= (R_c/R_D)_{E_0}(\pi\eta)_{E_0} = \frac{Z_0 Z_1 e^2}{R_D}\frac{(\pi\eta)_{E_0}}{E_0} = \frac{Z_0 Z_1 e^2}{R_D kT} \\ &= 5.945\times 10^{-6}\sqrt{\rho}\, Z_0 Z_1 T_9^{-3/2}\zeta \qquad (3.145) \\ f_s &= e^{(x\pi\eta)_{E_0}} = e^{Z_0 Z_1 e^2/(R_D kT)} = e^{5.945\times 10^{-6}\sqrt{\rho} Z_0 Z_1 T_9^{-3/2}\zeta} \qquad (3.146) \end{aligned}$$

where it is assumed that the classical turning points for the screened and unscreened potentials are approximately equal. All nonresonant rate expressions for charged-particle reactions derived in this chapter have to be multiplied by f_s if the nuclear reaction takes place under the conditions of weak screening.

For increasing densities at a given temperature, a point is eventually reached where the average Coulomb energy of neighboring nuclei, $\langle E_c\rangle$, is no longer small compared to the thermal energy kT. The condition $\langle E_c\rangle \approx kT$ defines the intermediate screening regime, while strong screening refers to the regime $\langle E_c\rangle \gg kT$. Approximate expressions for the corresponding screening factors can be found, for example, in DeWitt, Graboske, and Cooper (1973) and Graboske *et al.* (1973).

Example 3.8

Calculate the electron screening correction for the nonresonant reaction p + p → $e^+ + \nu$ + d (Section 5.1.1) in the region where the Sun's nuclear energy production is at maximum. Assume for the temperature and density values of $T = 0.0135$ GK and $\rho = 93$ g/cm^3, respectively. The mass fractions of hydrogen, helium, and oxygen in this region amount to $X(^1\mathrm{H}) = 0.52$, $X(^4\mathrm{He}) = 0.46$, and $X(^{16}\mathrm{O}) = 0.01$. For the electron degeneracy factor, assume a value of $\theta_e = 0.92$.

First, the parameter ζ is computed

$$\begin{aligned}\zeta &\equiv \sqrt{\sum_i \frac{(Z_i^2 + Z_i\theta_e)\,X_i}{A_i}} \\ &= \sqrt{\frac{(1^2 + 1\cdot 0.92)0.52}{1} + \frac{(2^2 + 2\cdot 0.92)0.46}{4} + \frac{(8^2 + 8\cdot 0.92)0.01}{16}} \\ &= \sqrt{0.998 + 0.672 + 0.045} = 1.31\end{aligned}$$

Since $10^5\rho^{1/3}\zeta^2 = 8\times 10^{-4}$ GK $\ll 0.0135$ GK, the condition for the weak screening regime is fulfilled. For the Debye–Hückel radius, we find a value of

$$R_D = 2.812\times 10^{-7}(93)^{-1/2}(0.0135)^{1/2}(1.31)^{-1} = 2.58\times 10^{-9}\,\text{cm} = 25\,800\,\text{fm}$$

The parameter $x(E_0)$ amounts to

$$x(E_0) = 4.197\times 10^{-6}(1\cdot 1)^{1/3}\left(\frac{1\cdot 1}{1+1}\right)^{-1/3}\sqrt{93}(0.0135)^{-7/6}1.31 = 0.010$$

It is small compared to unity and thus the linear expansion of Eq. (3.141) is justified in this case. The screening factor is

$$f_s = \exp[5.945\times 10^{-6}\sqrt{93}\cdot 1\cdot 1(0.0135)^{-3/2}1.31] = e^{0.0479} = 1.049$$

Other examples are given in Liolios (2000).

We have discussed so far only nonresonant reactions. The electron screening correction for a narrow resonance depends on the relative magnitude of the incoming (Γ_a) and outgoing (Γ_b) partial widths. Consider for example a capture reaction $A(a,\gamma)B$. If $\Gamma_a \gg \Gamma_\gamma$, then exactly the same screening correction factor as in Eq. (3.146) is obtained, even though in this case the reaction rate is independent of the penetration factor for the incoming channel. This counterintuitive result can be explained by revisiting the derivation of the narrow-resonance reaction rate (Section 3.2.4). The screening potential (see Eq. (3.135)) can be approximated by

$$V_s(r) = \frac{Z_0Z_1e^2}{r}\,e^{-r/R_D} \approx \frac{Z_0Z_1e^2}{r} - \frac{Z_0Z_1e^2}{R_D} = \frac{Z_0Z_1e^2}{r} + U_s \tag{3.147}$$

The first term is the Coulomb potential, while the second term represents a perturbing potential caused by the shielding charge density. The latter potential is negative (attractive) and thus effectively increases the kinetic energy of the projectile by an amount $|U_s| = Z_0Z_1e^2/R_D$ (Figure 2.17). Without electron shielding, only those projectiles with energies near $E = E_r$ will be able to excite the resonance. But in a plasma it is the projectiles with *smaller* energies near $E' = E_r + U_s$ that give rise to the population of the resonance. Hence, for the condition $\Gamma_a \gg \Gamma_\gamma$, Eq. (3.115) must be replaced by

$$N_A\langle\sigma v\rangle = N_A\left(\frac{2\pi}{m_{01}kT}\right)^{3/2}\hbar^2 e^{-(E_r+U_s)/kT}\omega\Gamma_b \tag{3.148}$$

This expression differs from Eq. (3.115) only by a screening factor of $f_s = e^{-U_s/kT} = e^{Z_0 Z_1 e^2/(R_D kT)}$, that is, the same factor that appears in Eq. (3.143). An example for the applicability of this result is the 3α reaction, where the condition $\Gamma_a \gg \Gamma_b$ holds for each of the two successive interactions (Example 3.4 and Section 5.2.1). For the opposite case, $\Gamma_a \ll \Gamma_b$, the screening factor has a more complicated form. See Salpeter and Van Horn (1969) and Mitler (1977).

We end the discussion by noting that the electrons of target nuclei also introduce screening effects in laboratory measurements of nuclear reactions if the bombarding energy is sufficiently low. As was the case for a plasma, the screened laboratory cross section is larger than the unscreened one. In cases where such effects are found to be significant, the measured cross sections have to be divided by the appropriate screening factors, which differ from those derived for a stellar plasma, to calculate the laboratory cross section for bare nuclei (Assenbaum, Langanke, and Rolfs, 1987; Raiola *et al.*, 2002, and references therein). In a second step, the latter cross section may then be corrected for plasma screening effects when computing the screened reaction rates.

3.2.7
Total Reaction Rates

For the calculation of the total reaction rates, all processes contributing significantly to the reaction mechanism in the effective stellar energy range have to be taken into account. The effective energy range is given by the Gamow peak or the Maxwell–Boltzmann distribution for reactions induced by charged particles or neutrons, respectively. The details will be different for each nuclear reaction, but some general statements are useful at this point. We will use a capture reaction as an example.

Consider first low stellar temperatures corresponding to effective energies close to the particle threshold. For light target nuclei, the density of resonances in this energy region is relatively small and they can be resolved experimentally. For charged particles, the resonance strengths are usually determined by the small charged-particle partial width Γ_a (since $\omega\gamma \approx \omega\Gamma_a$). For neutrons, on the other hand, $\omega\gamma \approx \omega\Gamma_\gamma$. All contributions of narrow resonances have to be measured or estimated, since they may strongly influence the total reaction rates. If the resonances are too weak or if none are located at the effective stellar energies, then other processes, such as high-energy wings of subthreshold resonances, low-energy wings of broad resonances located at higher energies, and nonresonant reaction contributions, are likely to dominate the total rates. As already noted, charged-particle measurements are typically performed down to an energy of $E_{\min}$. Direct measurements at lower energies are difficult, if not impossible, with present experimental techniques. In this case, any expected narrow resonances have to be investigated indirectly by nuclear structure studies (Figure 3.26), while nonresonant cross sections or wings of broad resonances have to be extrapolated from measurements at higher energies. In neutron-induced reactions, on the other hand, an experimental cutoff energy $E_{\min}$ does not exist since the Coulomb

barrier is absent. Hence, the cross section can in principle be measured directly at the effective stellar energies.

For increasing stellar temperatures, the density of resonances in the effective energy range will become larger. These resonances are located at higher energies so that, for charged-particle reactions, the particle partial width may exceed the γ-ray partial width ($\Gamma_a \gg \Gamma_\gamma$), and hence $\omega\gamma \approx \omega\Gamma_\gamma$. The strengths or cross sections of narrow or broad resonances with energies of up to a few mega electron volts have been measured for many reactions.

At even higher energies, corresponding to effective energies in excess of a few MeV, the number of resonances and their total widths become so large that they strongly overlap. This situation pertains already at low energies in the case of neutron-induced reactions on heavy target nuclei when the $Q_{n\gamma}$ value is large. In some reactions, individual resonances are no longer resolved and the total cross section gives rise to a continuum that varies smoothly with energy. In other reactions, individual resonances may still be resolved, but their density in the effective stellar energy window is so large that only the energy-averaged cross section is of interest. Cross sections for some reactions have been measured directly in this energy regime.

As will be explained in Chapter 5, the nucleosynthesis in certain burning processes can involve a large number of reactions (from several hundred in the case of silicon burning to several thousands in the case of the p-process), many of which involve unstable target nuclei. Only a small fraction of these reactions has been measured and in the vast majority of cases the cross sections need to be estimated using theoretical models. The most widely used among these is the Hauser–Feshbach statistical model (Section 2.7). It assumes that near the incident energy there is a large number of levels for each J^π value in the compound nucleus through which the reaction can proceed. The Hauser–Feshbach formula (see Eq. (2.219)) predicts a cross section reliably if the input parameters, such as transmission coefficients and level densities, are fine-tuned for the reaction of interest. In reality, however, the number of unmeasured reactions is very large and thus it becomes important to compute the desired cross sections with *global* instead of *local* parameters. For proton- and neutron-induced reactions, such global Hauser–Feshbach calculations yield cross sections and reaction rates that are reliable within a factor of ≈ 2–3, provided that the level density in the compound nucleus is sufficiently large (say, at least 10 compound levels in the effective stellar energy window). For α-particle-induced reactions, however, the theoretical predictions are less reliable because of difficulties in constructing appropriate global optical model potentials. For comparisons of Hauser–Feshbach predictions with measured cross sections, see Rauscher *et al.* (1997), Sargood (1982), and Arnould and Goriely (2003). Another advantage of the Hauser–Feshbach model is that it can include the effects of thermally excited target states (Section 3.1.5).

The various contributions to the total reaction rates can be added incoherently if interferences are negligible, so that

$$N_A\langle\sigma v\rangle_{\text{total}} = \sum_i N_A\langle\sigma v\rangle^i_{\substack{\text{narrow}\\ \text{resonances}}} + \sum_k N_A\langle\sigma v\rangle^k_{\substack{\text{broad}\\ \text{resonances}}} + N_A\langle\sigma v\rangle_{\text{nonresonant}} + N_A\langle\sigma v\rangle_{\text{continuum}} \quad (3.149)$$

To a good approximation, interference effects are negligible for narrow resonances ($\Gamma < 1$ eV). No interference effects are expected between two broad resonances of different J^π values, or between a resonance and a nonresonant process of different incoming orbital angular momenta. In other situations, interference effects usually need to be taken into account in Eq. (3.149).

Examples for measured charged-particle-induced reaction cross sections have already been discussed in connection with the (p,γ) reactions on ^{13}C and ^{16}O (Figures 3.11 and 3.12). Both of these cross sections have relatively simple energy dependences. In many other charged-particle reactions, however, the total cross section has a complex structure. A schematic example for a typical *S*-factor is displayed in Figure 3.30, showing nonresonant contributions, narrow and broad resonances, and a continuum at higher energies caused by many overlapping contributions. The *S*-factor rather than the cross section is shown in Figure 3.30 since the latter quantity falls rapidly for decreasing energy. Total reaction rates $N_A\langle\sigma v\rangle$ of charged-particle-induced reactions depend strongly on temperature, as shown in Sections 3.2.1 and 3.2.4. The reaction rates fall rapidly for decreasing temperature in most reactions of astrophysical interest when the effective energies are below the height of the Coulomb barrier. Examples for reaction rates have already been discussed (Figure 3.29b).

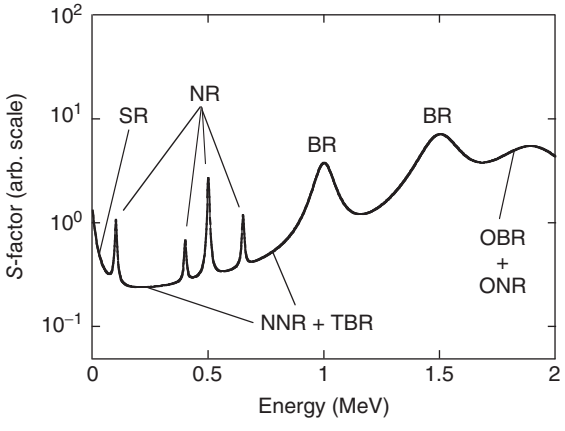

Figure 3.30 Schematic representation of an *S*-factor versus energy for a charged-particle-induced reaction. At low energies, narrow resonances (NR), wings of subthreshold resonances (SR), tails of broad resonances (TBR), and nonresonant processes (NNR) may typically contribute to the total *S*-factor. At higher energies, the *S*-factor is typically dominated by broad resonances (BR) and by overlapping narrow and broad resonances (OBR + ONR).

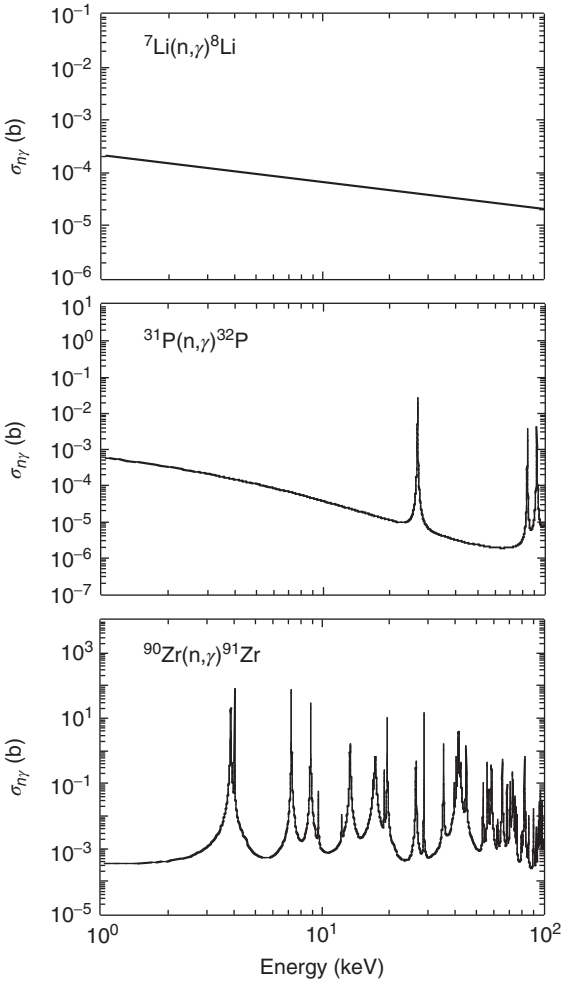

Figure 3.31 Cross sections for neutron capture on ^{7}Li, ^{31}P, and ^{90}Zr versus energy. The curve in the upper panel shows a $1/v$ behavior, while resonances are visible in the middle and lower panels.

Examples of cross sections for neutron capture on a light, medium, and heavy target nucleus are shown in Figure 3.31. The cross section for the ^{7}Li(n,γ)^{8}Li reaction ($Q_{n\gamma} = 2.0$ MeV) follows the $1/v$ law over the entire neutron energy range shown ($E_n = 1$–100 keV). For ^{31}P(n,γ)^{32}P ($Q_{n\gamma} = 7.9$ MeV), the cross section varies smoothly up to about $E = 20$ keV, where a few narrow isolated resonances start to appear. For ^{90}Zr(n,γ)^{91}Zr ($Q_{n\gamma} = 7.2$ MeV), many narrow and broad resonances are apparent. The density of resonances increases for larger neutron energies and they start to overlap strongly beyond an energy of ≈ 10 keV. The vastly different energy dependence of neutron reaction cross sections compared to charged-particle-induced reactions (Figures 3.11 and 3.12) is caused

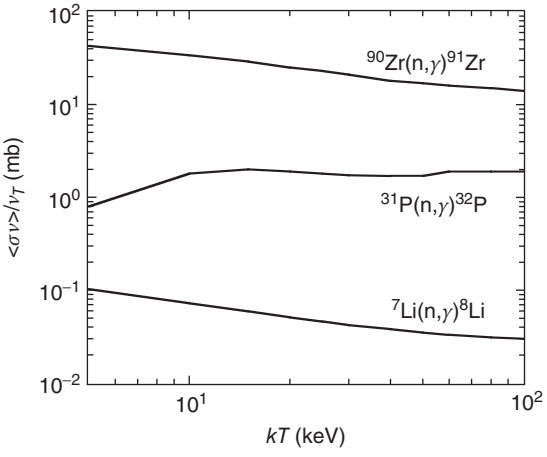

Figure 3.32 Maxwellian-averaged cross sections versus kT for ^{7}Li(n,γ)^{8}Li, ^{31}P(n,γ)^{32}P, and ^{90}Zr(n,γ)^{91}Zr. Data from Bao *et al.* (2000).

by the absence of the Coulomb barrier. The corresponding Maxwellian-averaged cross sections, $\langle \sigma v \rangle / v_T$, versus kT are displayed in Figure 3.32. It is apparent that neutron reaction rates are far less temperature sensitive than charged-particle reaction rates.

Problems

3.1 Consider a situation where the three species A, B, and C achieve equilibrium at elevated temperatures via the reactions $A + a \leftrightarrow B + \gamma$ and $B + b \leftrightarrow C + \gamma$ (Figure 3.7). In addition to Eqs. (3.56) and (3.57), the two conditions $\lambda_{C\to B} > \lambda_{C\to C'}$ and $\lambda_{B\to C} > \lambda_{B\to B'}$ must be fulfilled in order for such an equilibrium to be established. Derive an expression for $\lambda_{A\to B\to(C\to C' \text{ or } B')}$, that is, the decay constant of species A for consumption via the paths $A \to B \to C \to C'$ or $A \to B \to B'$.

3.2 Derive the correction factor $F(\tau)$ for nonresonant charged-particle-induced reaction rates (see Eq. (3.93)). Start by expressing F in terms of the new variables $y \equiv \sqrt{\epsilon} - 1$, $\beta \equiv \sqrt{3/\tau}$ and $\zeta \equiv y/\beta$. Then expand $F(\beta)$ into a quadratic Taylor series.

3.3 Derive the thermonuclear rate for nonresonant neutron-induced reactions when $S \equiv \sigma v$ depends on velocity (see Eq. (3.104)).

3.4 For an arbitrary value of ℓ, find the γ-ray energy at which the decay constant for nonresonant (γ, n) reactions (that is, the integrand in Eq. (3.112)) has a maximum.

3.5 Consider the narrow resonances described in Example 3.6. Calculate the reaction rates numerically for $T = 0.02$ GK and $T = 0.08$ GK and show that the arguments based on the Gamow peak concept are valid.

3.6 Find the temperature at which the reaction rate contribution of a single narrow resonance, located at an energy of E_i, is at maximum.

3.7 In a hypothetical reaction, only the target ground state and one excited state, at 50 keV excitation energy, can participate in the stellar burning. Assume for the ground state and the excited state reaction rate values of $40.0\,\mathrm{cm^3 s^{-1} mol^{-1}}$ and $30.0\,\mathrm{cm^3 s^{-1} mol^{-1}}$, respectively, at a stellar temperature of $T = 1$ GK. Set all statistical weights equal to unity. Calculate the population probability of the ground and excited state, the stellar reaction rate, and the stellar rate ground state fraction. Compare your answer to Sallaska *et al.* (2013).

3.8 Consider the ^{20}Ne(γ,α)^{16}O photodisintegration reaction at a temperature of $T = 1.5$ GK. The lowest lying narrow resonances in the forward ^{16}O(α,γ)^{20}Ne reaction ($Q = 4730$ keV) are located at $E_r^{\mathrm{cm}} = 891$ keV, 1058 keV, and 1995 keV, corresponding to ^{20}Ne levels at $E_x = 5621$ keV, 5788 keV, and 6725 keV, respectively (Figure 5.28). Their (ground-state) strengths amount to $\omega\gamma = 1.9 \times 10^{-3}$ eV, 2.3×10^{-2} eV, and 7.4×10^{-2} eV, respectively (Angulo *et al.*, 1999). Which level do you expect to dominate the stellar ^{20}Ne(γ,α)^{16}O reaction rates? Calculate and compare the individual level contributions to the total photodisintegration reaction rates. The spins of ^{4}He, ^{16}O, and ^{20}Ne are all $j_i = 0$; the normalized partition functions for these nuclei are equal to unity at $T = 1.5$ GK (see Rauscher and Thielemann, 2000). Also, the first excited state in ^{16}O is located at a relatively high energy ($E_x = 6049$ keV; Tilley, Weller, and Cheves, 1993) and, therefore, the (forward) capture reaction from excited target states is negligible at this temperature.

3.9 Derive the transmission coefficient (see Eq. (3.141)) for the screened Coulomb potential (see Eq. (3.135)). Assume that the variable $x = x(E) = R_c/R_D$ is a small number and use the expansions $e^x \approx 1 + x$ and $\sqrt{1-x} \approx 1 - x/2$. Retain only the terms that are linear in x.

3.10 Calculate the electron screening correction for the ^{12}C + ^{12}C reaction under typical hydrostatic carbon burning conditions ($T = 0.9$ GK and $\rho = 10^5\,\mathrm{g/cm^3}$; Section 5.3.1). The mass fractions of carbon, oxygen, and neon are given by $X(^{12}\mathrm{C}) = 0.25$, $X(^{16}\mathrm{O}) = 0.73$, $X(^{20}\mathrm{Ne}) = 0.01$, and $X(^{22}\mathrm{Ne}) = 0.01$. Assume that the reaction is nonresonant and disregard the electron degeneracy factor ($\theta_e = 1$).

4
Nuclear Physics Experiments

4.1
General Aspects

In this chapter, experimental techniques and procedures are discussed that are frequently applied in investigations of astrophysically important reactions. A vast number of different experimental procedures are used in the field of nuclear astrophysics. These can be divided into two groups, that is, direct and indirect measurements. A measurement of a cross section or a resonance strength in a given reaction of astrophysical interest is referred to as *direct measurement*. All other studies that are performed to improve the thermonuclear rates of this particular reaction, for example, elastic scattering, particle transfer, charge-exchange, and so on, represent indirect measurements (see also Section 3.2.4 and Figure 3.26). Here, we will focus our attention on *direct* measurements of nuclear reactions and a number of topics will be discussed in some depth. In most of this chapter, with the exception of Sections 4.8 and 4.9, all quantities are given in the laboratory system, unless mentioned otherwise. Expressions that relate kinematic quantities in the center-of-mass system and the laboratory system can be found in Appendix C.

Figure 4.1 shows schematically some major experimental components involved in nuclear reaction measurements. An accelerator provides collimated beams of well-defined energy. The beam is directed to a target containing the target nuclei involved in the nuclear reaction. The target has to be stable under beam bombardment. The nuclear reaction takes place in the target. Radiative capture reactions, $A(a,\gamma)B$, are among the most important types of reactions occurring in stars, but reactions involving only particles with rest mass, $A(a,b)B$, are of importance as well. The reaction products (e.g., γ-rays or light particles) emitted from the target are measured by a suitable detector of high efficiency. From the measured energies and intensities, the nuclear properties of interest (resonance and excitation energies, cross sections, spins and parities, lifetimes, branching ratios, angular correlations, and so on) are deduced. Frequently, unwanted background will contribute to the signal count rate of interest. This background must be reduced through various means to tolerable levels.

Nuclear Physics of Stars, Second Edition. Christian Iliadis.

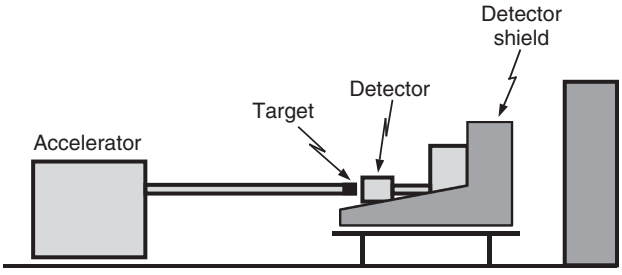

Figure 4.1 Basic components for the measurement of astrophysically important nuclear reactions. The shield must surround the detector as completely as possible.

A discussion of sources, accelerators and beam transport systems can be found in Rolfs and Rodney (1988). Here, we will briefly summarize some of the key requirements for beams in nuclear astrophysics measurements.

4.1.1 Charged-Particle Beams

The effective ion energies in a stellar plasma depend both on the temperature and the charges of the projectile and target nucleus involved in the reaction. It has been shown in Section 3.2 that thermonuclear reactions most likely proceed at energies below the Coulomb barrier height (Figures 3.13 and 3.14). Therefore, accelerators have to cover the energy range below a few mega electron volts for direct measurements of reactions. Indirect measurements, which investigate the structure of astrophysically important nuclei, are typically performed above the Coulomb barrier (i.e., in the tens of mega electron volts range). Most measurements of charged-particle reactions in nuclear astrophysics have been carried out using ion beams from electrostatic accelerators. Different types of electrostatic accelerators, such as Van de Graaff, Cockcroft–Walton, Dynamitron, and Pelletron, are widely used.

Cross sections of charged-particle reactions in general decrease rapidly with decreasing beam energy because of the Coulomb barrier (Figures 3.11 and 3.12). Therefore, measurements far below the Coulomb barrier require high ion beam currents up to and beyond the milliampere range to initiate a statistically significant number of nuclear reactions. For example, a 1 mA current of singly charged protons or α-particles corresponds to $\mathcal{N}_i/t = I/e = (1 \times 10^{-3}\ \mathrm{A})/(1.6 \times 10^{-19}\ \mathrm{C}) = 6.25 \times 10^{15}$ incident particles per second, where $e = 1.6 \times 10^{-19}$ C is the elementary charge. At higher energies (say, above 1 MeV) smaller currents in the 0.1–10 μA range are of advantage if detector count rates become limited by the intense radiation from contaminant reactions. Ion energy spreads of about 1 keV or better are usually necessary to resolve complex resonance structures.

The ion beam energy should be variable in steps of at least a few 100 eV to measure precise resonance energies. The beam should also be well collimated. Low-energy measurements far below the Coulomb barrier require a beam spot size

of a few square centimeters cross-sectional area (for solid targets) to reduce target heating and degradation to tolerable levels. Indirect measurements at higher energies usually require beam spots of considerably smaller size (a few square millimeters). The beam should also be as free of contaminants as possible.

The absolute energy calibration of the electrostatic accelerator is an important quantity for the determination of thermonuclear reaction rates. The precise energy of narrow resonances enters sensitively in the narrow resonance reaction rate formalism (see Eq. (3.117)). Furthermore, nonresonant cross sections are a steep function of energy below the Coulomb barrier and, thus, systematic shifts in absolute beam energy may cause large errors in the nonresonant reaction rates. We will illustrate this effect with two examples.

Consider first the $E_r = 151$ keV resonance in the ^{18}O(p,γ)^{19}F reaction corresponding to an energy of 143 keV in the center-of-mass system (see Eq. (C.24)). Suppose, that a measurement of E_r yields an erroneous value of 148 keV (or 140 keV in the center-of-mass system). At a temperature of $T = 0.06$ GK, the resulting narrow resonance reaction rates (see Eq. (3.117)) will then be too large by a factor of

$$\frac{N_A\langle\sigma v\rangle_{E_r-\Delta E}}{N_A\langle\sigma v\rangle_{E_r}} = \frac{e^{-11.605(0.143-0.003)/0.06}}{e^{-11.605\cdot 0.143/0.06}} \approx 1.80 \tag{4.1}$$

corresponding to a change of 80%. The variation will increase for lower temperatures.

As an example for a nonresonant reaction, consider ^{16}O(p,γ)^{17}F at 100 keV in the center-of-mass system. If the measurement is erroneously performed at a center-of-mass energy of 103 keV, then the cross section (see Eqs. (3.71) and (3.75)) will be too large by a factor of

$$\frac{\sigma(E+\Delta E)}{\sigma(E)} = \frac{\frac{1}{0.103}\,\exp\left(-0.9895\cdot 1\cdot 8\sqrt{\frac{16\cdot 1}{16+1}\frac{1}{0.103}}\right)}{\frac{1}{0.100}\,\exp\left(-0.9895\cdot 1\cdot 8\sqrt{\frac{16\cdot 1}{16+1}\frac{1}{0.100}}\right)} = 1.40 \tag{4.2}$$

corresponding to a variation of 40%. For this estimate, we assumed a negligible energy dependence of the S-factor (see Eq. (3.11)).

Frequently, a magnetic analyzer with input and output slits is used to define the beam energy. For an ideal system, the magnetic field strength B and the particle energy E are related by (Marion, 1966)

$$B = \frac{k}{q}\sqrt{2mc^2E + E^2} \tag{4.3}$$

where mc^2 and q are the rest energy and the charge state of the ion, respectively. The calibration constant k cannot be calculated precisely from the magnet geometry since B is not necessarily constant along the particle trajectory through the magnet and, furthermore, the magnetic field along the trajectory may not be proportional to the field measured at some reference point (e.g., using an NMR or a Hall probe). Therefore, k must be obtained through a calibration of the magnet

Table 4.1 Laboratory energies and widths of narrow resonances commonly used for ion beam calibrations.

Reaction	E_{lab} (keV)	Γ (eV)
$^{18}O(p,\alpha)^{15}N$	150.82(9)[c]	130(10)[c]
$^{19}F(p,\alpha\gamma)^{16}O$	223.99(7)[a]	985(20)[a]
	483.91(10)[a]	903(30)[a]
$^{23}Na(p,\gamma)^{24}Mg$	308.75(6)[a]	< 36[a]
$^{24}Mg(p,\gamma)^{25}Al$	222.89(8)[a]	< 32[a]
$^{26}Mg(p,\gamma)^{27}Al$	292.06(9)[a]	< 37[a]
$^{27}Al(p,\gamma)^{28}Si$	222.82(10)[a]	< 34[a]
	293.08(8)[a]	59(16)[a]
	326.97(5)[a]	< 38[a]
	405.44(10)[a]	< 42[a]
	991.756(17)[b]	70(14)[d]
	1316.87(3)[b]	35(4)[d]

The error is given in parenthesis and refers to the last significant digit(s). For example, 150.82(9) stands for 150.82 ± 0.09.
Sources: [a] Uhrmacher *et al.* (1985), [b] Bindhaban *et al.* (1994), [c] Becker *et al.* (1995), and [d] Endt (1998).

using energies of well-known nuclear reactions. For this purpose, narrow resonances are frequently used below $E \approx 2$ MeV, while (p,n) threshold energies are utilized at higher energies.

Absolute resonance energies of selected resonances below 1.5 MeV energy are listed in Table 4.1. It is interesting to point out that almost all published resonance energies are directly or indirectly related to the energy of the $E_r = 992$ keV resonance in $^{27}Al(p,\gamma)^{28}Si$. The table also lists total resonance widths, which should be small (< 1 keV) for energy calibration standards. The determination of precise resonance energies from measurements of the reaction yield versus energy will be discussed in Section 4.8.

4.1.2 Neutron Beams

For measurements of neutron-induced reactions on stable or long-lived target nuclei (Section 5.6.1), neutron beam energies between a fraction of a kilo electron volts and several hundred kilo electron volts are of primary interest. Neutrons can be produced using a variety of techniques, including linear electron or proton accelerators, and electrostatic accelerators.

At linear electron accelerators, neutrons are produced via (γ,n) reactions by bombarding heavy metal targets with pulsed electron beams of $\approx$ 50 MeV energy and repetition rates of $\approx$ 0.5 kHz. The neutrons are released with energies ranging from the subthermal region up to 50 MeV. They are slowed down by a moderator (Section 4.2.3) and are collimated before they impinge on the sample of

interest. The primary electron beam produces a very intense background caused by bremsstrahlung and thus the metal target area needs to be shielded well. The astrophysically important neutron energy range corresponds only to a small window of the entire neutron spectrum. Neutrons with a similar broad energy distribution are produced with high-energy proton beams at linear accelerators. In this case, the primary beam is incident on a suitable target and neutrons are produced via spallation reactions. Fluxes on the order of $\approx 10^6$ neutrons $s^{-1}cm^{-2}$, integrated over an energy range of 1–300 keV, are typically achieved at both kinds of facilities (Koehler, 2001). Reaction measurements with these moderated neutron sources are performed using time-of-flight techniques (Section 4.6.3).

Charged-particle beams from electrostatic accelerators can be utilized to produce neutrons via nuclear reactions (Hanson, Taschek, and Williams, 1949). For relatively low neutron energies of astrophysical interest, a frequently employed reaction is ^{7}Li(p,n)^{7}Be ($Q = -1.644$ MeV). It follows from the kinematics of this endothermic reaction that at the threshold ($E_p^{thresh} \approx -Q(m_n + m_{^7Be})/m_{^7Be} = 1.881$ MeV; Eq. (C.8)) neutrons are released with an energy of 30 keV and are emitted in the forward direction only. For proton bombarding energies up to $E_p = 1.92$ MeV, neutrons are emitted into a cone of limited angle in the forward direction. At each angle within this cone, two groups of neutrons with different energies are emitted. The cone widens with increasing proton energy until it includes the forward hemisphere. For $E_p > 1.92$ MeV, neutrons of only one discrete energy are emitted at each angle in the complete sphere about the target. A detailed discussion of the kinematics of endothermic reactions is given in Appendix C.1. The energy resolution of the released neutrons depends on the energy spread of the incident protons, the finite thickness of the ^{7}Li target, and the finite angle subtended by the sample to be irradiated.

An interesting technique has been applied in a number of neutron-induced reactions by bombarding a ≈ 10 μm thick metallic lithium target with protons of energy $E_p = 1912$ keV, only 31 keV above the reaction threshold. The released neutrons are emitted in the forward direction in a cone with an opening angle of 120°. In this case, the angle-integrated energy distribution of emitted neutrons closely resembles a Maxwell–Boltzmann distribution at $kT = 25$ keV, as shown in Figure 4.2. If the irradiation sample is mounted very close to the lithium target, then the energy distribution of neutrons incident on the sample is given by the same Maxwell–Boltzmann distribution. The measured average cross section gives then directly the Maxwellian-averaged cross section or the reaction rate (Section 3.2.2), as will be shown in Section 4.9.3. With typical proton beam currents of 50–100 μA, integrated yields of $\approx 10^8$–10^9 neutrons/s are achieved (Beer and Käppeler, 1980). This technique is useful because the energy of $kT = 25$ keV is close to the effective energy range of some s-process scenarios (Section 5.6.1). A similar procedure, but using the ^{3}H(p,n)^{3}He or ^{18}O(p,n)^{18}F reactions instead of ^{7}Li(p,n)^{7}Be, yields Maxwell–Boltzmann distributions of neutron energies at $kT = 52$ keV (Käppeler, Naqvi, and Al-Ohali, 1987) or 5 keV (Heil *et al.*, 2005), respectively. Direct measurements of Maxwellian-averaged cross sections are frequently performed using the activation method (Section 4.6.2).

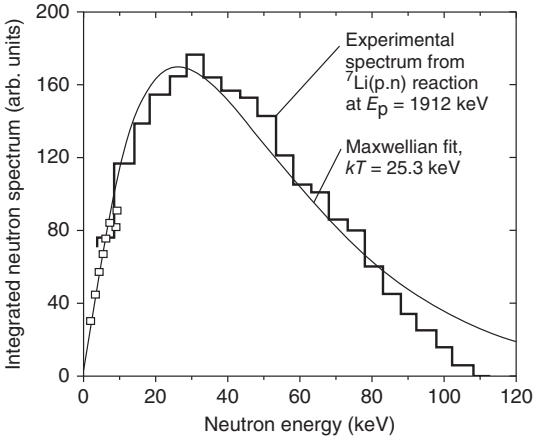

Figure 4.2 Angle-integrated neutron energy distribution resulting from the bombardment of a ≈ 10 μm thick metallic lithium target with E_p = 1912 keV protons. The neutrons are emitted in the forward direction in a cone with an opening angle of 120°. The angle-integrated energy distribution of emitted neutrons closely resembles a Maxwell–Boltzmann distribution at kT = 25 keV. (Reprinted with permission from Ratynski and Käppeler (1988). Copyright (1988) by the American Physical Society.)

Cross sections of neutron-induced reactions are usually larger than those of charged-particle-induced reactions (Figures 3.11, 3.12, and 3.31), thus compensating for the lower intensities available for neutron beams compared to charged particle beams.

4.2
Interaction of Radiation with Matter

Radiation interacts with matter and thereby loses part or all of its energy. This aspect is important for a number of experimental considerations. First, a particular incident particle may lose energy in the target prior to initiating a nuclear reaction. An exact knowledge of the energy loss is required to determine the effective energy and the probability with which the reaction takes place. Second, the energy or intensity of emitted reaction products may be influenced by interactions in the target or the surrounding material. Third, the reaction products have to be detected to determine the reaction cross section, that is, the probability with which the reaction occurs. Thus, knowledge of the processes by which radiation interacts with matter is of paramount importance for the design and performance of radiation detectors.

Figure 4.3 indicates schematically some experimental locations where radiation typically interacts with matter: (i) incident particle energy loss in the target, (ii) reaction product energy or intensity loss in the target, target holder, detector dead layer, and so on, and (iii) energy deposition of reaction products in the active

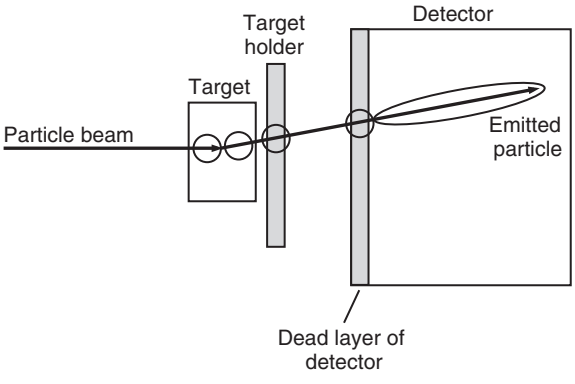

Figure 4.3 Schematic setup showing a beam incident on a target. The locations where the primary (beam) or secondary (emitted particle or photon) radiation typically interacts with matter are circled.

volume of the detector. The processes responsible for the interaction of radiation with matter depend on the type of radiation. In the following, interactions of heavy charged particles (e.g., protons and α-particles), photons, and neutrons are discussed in more detail. We will refer to the material in which the interactions occur as an *absorber*.

A frequently used quantity for the considerations of the present chapter is the number density N of atoms (in units of atoms per cubic centimeter). For a solid absorber with mass density ρ, consisting of atoms with relative atomic mass M (in units of u), there are N_A/M atoms per gram of absorber material. The number density of atoms is then given by

$$N = \rho \frac{N_A}{M} \tag{4.4}$$

For an absorber gas at pressure P and temperature T, the number density of atoms can be calculated from

$$N = \nu L \frac{P}{760\,\text{Torr}} \frac{273\,\text{K}}{T} \tag{4.5}$$

with the Loschmidt constant $L = 2.68678 \times 10^{19}\ \text{cm}^{-3}$ and ν the number of atoms per molecule.

4.2.1
Interactions of Heavy Charged Particles

Heavy charged particles, such as protons or α-particles, interact with matter primarily through: (i) inelastic collisions with atomic electrons of absorber atoms, and (ii) elastic scattering on absorber nuclei. These interactions cause an energy loss of the incident particle and a deflection of the particle from its incident direction. The former interaction occurs more frequently than the latter, except at very

low projectile energies where the contribution of elastic scattering on absorber nuclei has to be taken into account.

A heavy (positively) charged particle moving through matter interacts simultaneously with many electrons. Cross sections for these collisions are typically in the 10^{-17}–10^{-16} cm^2 range (corresponding to 10^7–10^8 b). In each encounter, an electron feels the attractive Coulomb force as the charged particle passes in close vicinity. Energy is transferred from the particle to an absorber atom, causing either excitation of an atomic electron to higher lying shells (soft collision) or complete removal of an electron, that is, ionization (hard collision). The maximum energy that can be transferred in each collision is a small fraction of the particle's total energy, but the number of collisions per path length is very large. At any given time, the particle interacts with many electrons, causing an almost continuous energy loss until the particle is stopped. The paths of heavy particles in matter are relatively straight because the particle is not strongly deflected by any one collision. After ionization, the electrons tend to recombine with positive ions. Most types of radiation detectors suppress the recombination process and utilize the number of created electron–ion pairs as a basis for the detector response (see Eq. (4.4)). In certain very close encounters, sufficient energy may be transferred to an electron that it can create electron–ion pairs in subsequent collisions. These high-energy electrons are referred to as δ (or knock-on) electrons.

4.2.1.1 Stopping Power

The collisions of heavy charged particles with absorber atoms are statistical in nature. Since the number of collisions per path length is very large, the fluctuations in the total energy loss are small. Thus, the slowing down process may be described in terms of an average energy loss per unit path length. The ratio of differential energy loss and differential path length is called *linear stopping power*, and is defined by

$$S_L(E) \equiv -\frac{dE}{dx} \tag{4.6}$$

in units, for example, of eV/cm. The linear stopping power depends on the number density of electrons in the absorber or, equivalently, the absorber mass density ρ. The related quantity

$$S_M(E) \equiv -\frac{1}{\rho}\frac{dE}{dx} \tag{4.7}$$

is called *mass stopping power* with units, for example, of eV cm^2/g. The stopping power may also be given per absorber atom. For an absorber of number density N (in units of atoms per cubic centimeter), we obtain

$$S_A(E) \equiv -\frac{1}{N}\frac{dE}{dx} \tag{4.8}$$

in units, for example, of eV cm^2/atom. The quantity $S_A(E)$ is called *stopping cross section*. For a given projectile of energy E, it is found that $S_M(E)$ and $S_A(E)$ vary relatively little over a wide range of absorber materials. In numerical calculations,

we will mainly be using the quantity $S_A(E)$ and simply refer to it as stopping power.

The theoretical calculation of stopping powers is complicated. For high projectile energies (> 0.6 MeV/u) the Bethe–Bloch formula, with a few empirically determined parameters, describes the energy loss accurately. For nonrelativistic projectile energies, the electronic stopping power (i.e., the contribution caused by inelastic collisions between projectile and atomic electrons) is given by (Knoll, 1989)

$$-\frac{dE}{dx} \approx \frac{4\pi e^4}{m_e}\frac{Z_p^2}{v^2}\left(N_A\rho\frac{Z_t}{M_t}\right)\ln\left(\frac{2m_e v^2}{I}\right) \tag{4.9}$$

where Z_p, v, Z_t, and M_t are the charge and velocity of the projectile, the atomic number and the relative atomic mass of the absorber, respectively; m_e is the electron rest mass, e the electron charge, and I represents an average excitation and ionization potential of the absorber, which is treated as an empirical parameter. The equation holds if the projectile velocity is large compared to the electron velocities in the absorber atoms. Over a wide energy range, excluding very high energies where the logarithmic term in Eq. (4.9) dominates, the magnitude of the stopping power decreases with increasing projectile energy as $1/v^2$ or $1/E$. This behavior can be explained by the projectile spending a greater time in the vicinity of a given electron if its velocity is small and, consequently, the energy transfer becomes large. The stopping power increases with Z_p^2. Hence, α-particles will experience a larger energy loss than protons in the same absorber medium. The stopping power also depends linearly on the absorber density ρ.

At very low projectile energies ($E < 30$ keV/u), where the projectile velocity is smaller than the electron velocities in the absorber atoms, the Bethe–Bloch formula is no longer applicable. This situation occurs in the slowing down process of recoil nuclei, for example, during implantation or in lifetime measurements. In this case, the projectile energy is too small to cause significant ionization of the absorber atoms. Also, the positively charged projectile tends to pick up electrons from the absorber. As a result, its effective charge and the stopping power are reduced. For this energy range, the electronic stopping power is usually calculated by the LSS theory (Lindhard, Scharff, and Schiott, 1963), which is not as accurate as the Bethe–Bloch formula. The electronic stopping power is given by

$$-\frac{dE}{dx} = k\sqrt{E} \tag{4.10}$$

where the constant k is a function of the masses and charges of projectile and absorber atoms. In addition, the contribution from elastic scattering of projectiles on absorber nuclei (nuclear stopping power) has to be taken into account at low energies. The intermediate energy range (30 keV/u < E < 0.6 MeV/u) is poorly covered by theory and a number of different formulas are in use.

The stopping power is shown schematically in Figure 4.4. At very low energies, it is influenced by the nuclear component (dotted line) and, with increasing energy,

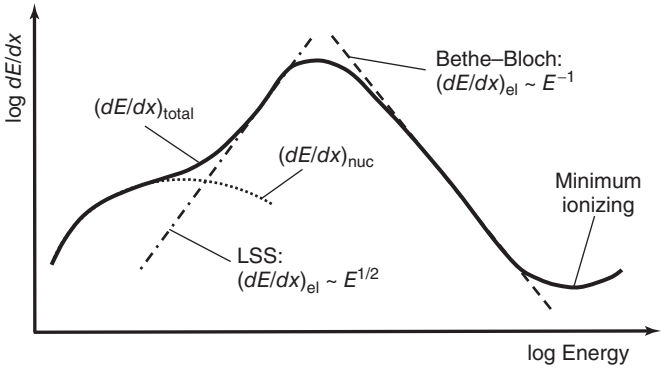

Figure 4.4 Schematic representation of total stopping power (solid line) and different components (dashed or dotted lines) versus particle energy.

follows the $\sqrt{E}$ behavior predicted by the LSS theory (dashed–dotted line). A maximum occurs where the velocities of the projectile and the atomic electrons of the absorber are comparable. For higher energies beyond the maximum, the stopping power is given by the Bethe–Bloch formula (dashed line). For nonrelativistic projectile energies, the stopping power is dominated by the $1/E$ dependence and decreases until $v \approx 0.96c$, where a minimum is reached. At this point, the projectiles are called *minimum ionizing*. This minimum value of dE/dx is approximately constant for all particles of the same charge Z_p. Beyond this point, the stopping power increases because of the logarithmic term in the Bethe–Bloch formula.

In practice, measured values of stopping powers are fit over a broad energy range by expressions containing the proper low- and high-energy behaviors. These fits may then be used for interpolations to obtain stopping powers for absorbers for which no experimental information exists. Tabulated stopping powers, including compilations of experimental values, can be found in Paul and Schinner (2002) or Ziegler (2003). For example, Figure 4.5 shows stopping powers in units of eV cm^2/atom for hydrogen and helium projectiles in various absorber elements versus energy.

It will become apparent later in this chapter that stopping power values enter in most experimental determinations of charged-particle cross sections and resonance strengths. Therefore, a reliable estimate of stopping power errors is very important. Errors of stopping powers calculated using the computer code SRIM (Ziegler, 2003) amount to a few percent at higher energies where the Bethe–Bloch formula is applicable. However, at lower energies important for direct nuclear astrophysics measurements, the errors are typically larger. The uncertainties of calculated stopping powers for a given projectile-absorber combination can be estimated from the average deviation between calculated and measured values and from the scatter in the measured data. Table 4.2 lists stopping power uncertainties for several projectiles and absorbers. The errors are estimated by considering tabulated stopping powers, obtained with the code SRIM, together with all measured data in a projectile energy range that is of primary importance for

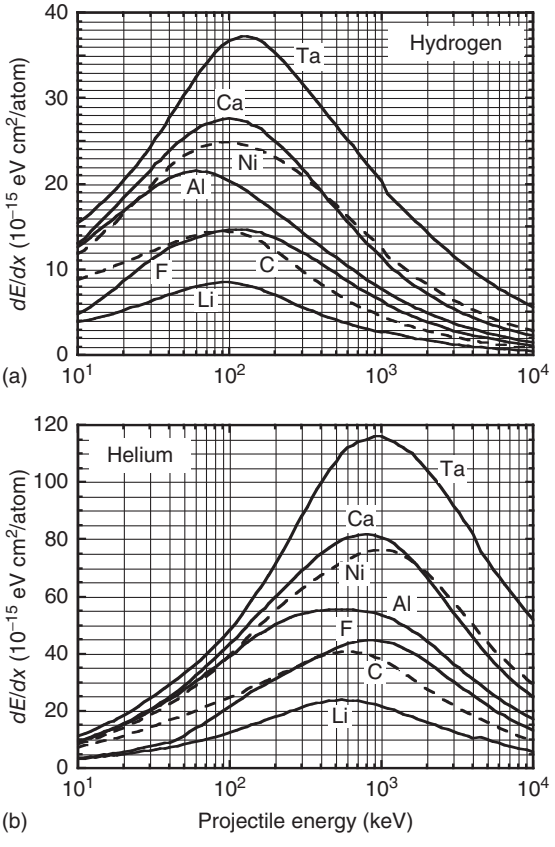

Figure 4.5 Stopping power (in units of 10^{-15} eV cm^2/atom) of (a) hydrogen and (b) helium projectiles versus particle energy in various absorber elements. Both the projectile energy and the stopping power are given in the laboratory system. The curves are calculated using the computer code SRIM (Ziegler, 2003).

direct measurements in nuclear astrophysics. The results are given in terms of the quantities Δ and σ (both given in percent), which are defined in Paul and Schinner (2005). In brief, Δ represents the *systematic* difference between tabulated and experimental stopping powers, while σ is the *random* error that provides information regarding the experimental scatter. It can be seen that in most cases Δ is close to zero and, therefore, the SRIM tabulation is reliable. Only in the case of heavy projectiles incident on H_2 gas is there a systematic deviation, amounting to $\Delta \approx -3\%$. The experimental scatter is seen to depend on the physical state of the absorber. For protons and α-particles incident on gaseous absorbers, one finds values of $\sigma \approx 3 - 4\%$, while for solid absorbers the experimental scatter amounts to $\sigma \approx 5 - 8\%$. Similar values are obtained for heavy projectiles incident on H_2 gas. The stopping power errors are expected to be larger for projectile-absorber combinations for which no data exist.

Table 4.2 Uncertainties of stopping powers.

Projectile	Energy (MeV/u)	Absorber	Number of points	Δ (%)	σ (%)
Protons	0.01–1.0	Al, B, Be, C, Ca, Co, Cr, Fe, Li, Mg, Mn, Ni, Se, Si, Ti, V	2518	0.7	8.0
Protons	0.01–1.0	Ar, Cl_2, N_2, Ne, O_2	504	0.1	3.9
α-particles	0.1–1.0	Al, B, Be, C, Ca, Co, Cr, Fe, Li, Mg, Mn, Ni, Si, Ti, V	975	0.7	4.7
α-particles	0.1–1.0	Ar, Cl_2, N_2, Ne, O_2	428	−0.1	3.2
Ar, B, C, Cl, Li, Mg, N, Na, Ne, S	0.2–20	H_2 gas	136	−3.0	8.4

The quantity Δ represents the systematic difference between tabulated and experimental values, while σ is the random error that provides information regarding the experimental scatter (Paul and Schinner, 2005). Tabulated and measured stopping power values are considered here only for the indicated projectile energy ranges appropriate for direct nuclear astrophysics measurements. Source: Courtesy of Helmut Paul.

Figure 4.6b shows schematically a beam of projectiles with energy E_0 incident on an infinitely thick absorber, meaning the projectiles are stopped in the medium. Figure 4.6a displays the stopping power versus energy. As the charged projectiles slow down in matter, their stopping power increases, that is, more energy is deposited per path length for an increasing length of the track. This may also be seen in a plot of dE/dx versus distance Figure 4.6c. Near the end of the track (at energy E_1) the charge of the projectile is reduced because of electron pickup and the curves fall off. The maximum, called the *Bragg peak*, indicates that projectiles lose the largest part of their energy toward the end of their path. Figure 4.6d shows the intensity of the projectiles in the absorber versus distance. For the largest distance over the projectile path, the intensity is constant. In other words, the projectiles slow down but their number does not change. Toward the end of the path, the intensity does not drop immediately to zero, but slopes down over a certain path length. This phenomenon is known as *range straggling*. It is caused by the statistical nature of the slowing down process, since two projectiles of the same mass and energy will, in general, not penetrate the absorber to exactly the same distance. The distance at which the projectile intensity falls by 50% is called the *mean range*.

The mean path length traveled by projectiles of incident energy E_0 can be calculated from

$$R = \int_0^{E_0} \frac{dE}{(dE/dx)} \tag{4.11}$$

The obtained value will differ from the straight-line penetration distance because each projectile is deflected slightly in each of the many collisions with absorber atoms. Figure 4.7 shows ranges versus incident energy for light ions in a silicon absorber. For example, if a silicon counter is used for measuring the total energy

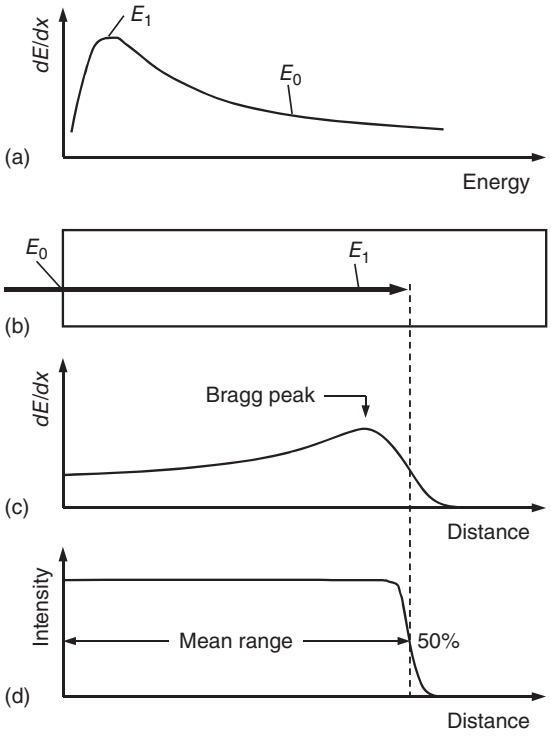

Figure 4.6 Schematic representation of a beam of projectiles with energy E_0 incident on an infinitely thick absorber (part b). (a) Stopping power versus projectile energy. (c) Stopping power versus distance. (d) Intensity of projectiles in absorber versus distance; the mean range corresponds to the distance where the projectile intensity falls to 50% of its initial value. The projectiles lose the largest part of their energy toward the end of the path. The maximum in parts (a) and (c), corresponding to an energy E_1, is called the *Bragg peak*. Note that the mean range is not equal to the straight-line penetration distance.

of incident charged particles (Sections 4.4.2 and 4.5.1), then its active thickness must be larger than the particle range.

The stopping power is also useful in cases where the projectiles lose only a fraction of their energy in an absorber. The thickness d of the absorber (in units of length) is related to the total energy loss of projectiles with incident energy E_0 by

$$d = \int_{E_0-\Delta E}^{E_0} \frac{dE}{(dE/dx)} \tag{4.12}$$

For a very thin absorber (target or detector), the energy lost by the projectile is relatively small and the stopping power is approximately constant over the absorber thickness. We obtain in this case

$$d = \frac{1}{(dE/dx)_{E_0}} \int_{E_0-\Delta E}^{E_0} dE = \frac{\Delta E}{(dE/dx)_{E_0}} \tag{4.13}$$

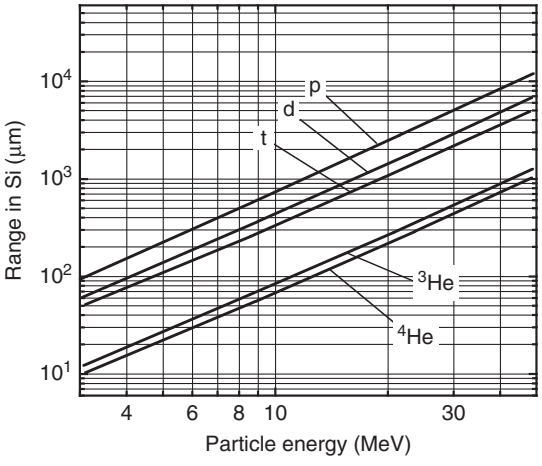

Figure 4.7 Range in silicon versus incident laboratory energy of light ions. Data from Skyrme *et al.* (1967).

or

$$\Delta E = \left(\frac{dE}{dx}\right)_{E_0} d = \left(\frac{1}{N}\frac{dE}{dx}\right)_{E_0} Nd = \left(\frac{1}{\rho}\frac{dE}{dx}\right)_{E_0} \rho d \tag{4.14}$$

where N denotes the number density of atoms and Nd is the number of atoms per square centimeter.

4.2.1.2 Compounds

We have discussed so far stopping powers for pure elements. For compounds, approximate stopping powers may be obtained by a weighted average over the individual stopping powers according to the fraction of electrons belonging to each element. This approximation is called *Bragg's rule*. For a compound $X_a Y_b$ consisting of two elements X and Y, where a and b are the number of atoms per molecule of element X and Y, respectively, one obtains for the stopping power per molecule

$$\frac{1}{N_c}\left(\frac{dE}{dx}\right)_c = a\frac{1}{N_X}\left(\frac{dE}{dx}\right)_X + b\frac{1}{N_Y}\left(\frac{dE}{dx}\right)_Y \tag{4.15}$$

where N_c is the number density of molecules and $(1/N_i)(dE/dx)_i$ is in units, for example, of eV cm^2 per atom (for pure elements) or per molecule (for the compound). Equivalently, we find with Eq. (4.4)

$$\frac{1}{\rho_c}\left(\frac{dE}{dx}\right)_c = \frac{aM_X}{M_c}\frac{1}{\rho_X}\left(\frac{dE}{dx}\right)_X + \frac{bM_Y}{M_c}\frac{1}{\rho_Y}\left(\frac{dE}{dx}\right)_Y \tag{4.16}$$

where $(1/\rho_i)(dE/dx)_i$ is in units, for example, of eV cm^2/g, with $M_c = aM_X + bM_Y$. Caution should be exercised when using Bragg's rule since for certain compounds experimental stopping powers differ by 10–20% from those calculated with Eqs. (4.15) and (4.16) (Knoll, 1989).

For projectiles of incident energy E_0, the energy loss in a thin absorber consisting of a compound X_aY_b is obtained from Eqs. (4.14) and (4.15) as

$$\begin{aligned}\Delta E_c &= \frac{1}{N_c}\left(\frac{dE}{dx}\right)_{c,E_0} N_c d = a\frac{1}{N_X}\left(\frac{dE}{dx}\right)_X N_c d + b\frac{1}{N_Y}\left(\frac{dE}{dx}\right)_Y N_c d \\ &= \frac{1}{N_X}\left(\frac{dE}{dx}\right)_X N_X d + \frac{1}{N_Y}\left(\frac{dE}{dx}\right)_Y N_Y d \end{aligned} \tag{4.17}$$

where $N_X = aN_c$ and $N_Y = bN_c$.

Example 4.1

Calculate the energy loss of a 500 keV proton beam moving through a 1 μm thick layer of ice. The stopping powers at $E_0 = 500$ keV, calculated with the computer code SRIM (Ziegler, 2003), amount to $(1/N_H)(dE/dx)_H = 1.8 \times 10^{-15}$ eV cm^2 and $(1/N_O)(dE/dx)_O = 8.1 \times 10^{-15}$ eV cm^2. Assume that the stopping powers are approximately constant over the thickness of the absorber. All of the above quantities are given in the laboratory system.

The density of ice (H_2O) is about 1 g/cm^3, corresponding to 3.3×10^{22} H_2O molecules/cm^3 (since 18 g contain 6.022×10^{23} H_2O molecules). Equation (4.17) gives

$$\begin{aligned}\Delta E &= a\frac{1}{N_H}\left(\frac{dE}{dx}\right)_H N_{H_2O} d + b\frac{1}{N_O}\left(\frac{dE}{dx}\right)_O N_{H_2O} d \\ &= 2(1.8 \times 10^{-15}\,\text{eV cm}^2)(3.3 \times 10^{22}\,\text{cm}^{-3})(10^{-4}\,\text{cm}) \\ &\quad + 1(8.1 \times 10^{-15}\,\text{eV cm}^2)(3.3 \times 10^{22}\,\text{cm}^{-3})(10^{-4}\,\text{cm}) = 39\,\text{keV}\end{aligned}$$

The same result is obtained from the number densities of H and O atoms, $N_H = 2 \cdot N_{H_2O} = 6.6 \times 10^{22}$ cm^{-3} and $N_O = 1 \cdot N_{H_2O} = 3.3 \times 10^{22}$ cm^{-3}. Hence

$$\begin{aligned}\Delta E &= \frac{1}{N_H}\left(\frac{dE}{dx}\right)_H N_H d + \frac{1}{N_O}\left(\frac{dE}{dx}\right)_O N_O d \\ &= (1.8 \times 10^{-15}\,\text{eV cm}^2)(6.6 \times 10^{22}\,\text{cm}^{-3})(10^{-4}\,\text{cm}) \\ &\quad + (8.1 \times 10^{-15}\,\text{eV cm}^2)(3.3 \times 10^{22}\,\text{cm}^{-3})(10^{-4}\,\text{cm}) = 39\,\text{keV}\end{aligned}$$

4.2.1.3 Energy Straggling

So far, we considered the mean energy loss of a projectile passing through an absorber. Suppose that the projectiles are represented by an initially monoenergetic beam. When a projectile penetrates into the absorber, it will undergo a large number of independent interactions, causing the projectile to slow down. Statistical fluctuations in the number of collisions and in the energy transferred per collision give rise to an energy distribution of the beam, centered around a value of $E_0 - \Delta E$, that is, the incident energy minus the mean energy loss.

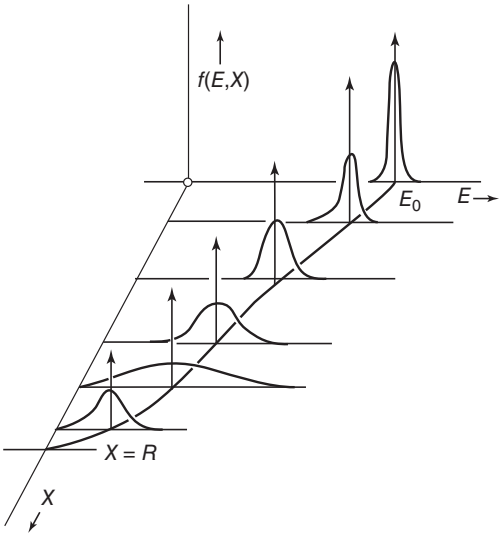

Figure 4.8 Schematic representation of energy distribution functions $f(E, x)$ for a beam of charged particles with a small initial energy spread as they move through an absorber along a path of length x; E is the particle energy. From Knoll (1989). (Reprinted with permission. Copyright ©1989 John Wiley & Sons, Inc.)

The maximum energy that a nonrelativistic heavy charged particle of mass m and kinetic energy E can transfer to a free atomic electron with mass m_e in a single collision is of the order (Problem 4.2)

$$4E[m_e m/(m_e + m)^2] \approx 4E(m_e/m) \approx 4E/(2000\,M) = 2 \times 10^{-3} E/M \quad (4.18)$$

with M in units of u. For example, a 10 MeV proton losing a total energy of 1 MeV in an absorber can transfer a maximum energy of 20 keV to a single electron and undergoes at least, and very likely many more than, $(1\,\text{MeV})/(20\,\text{keV}) = 50$ collisions. If the number of collisions is large, the energy distribution function will approach a Gaussian shape (Leo, 1987). If the number of collisions is not very large, the energy distribution function of projectiles passing through an absorber of a certain thickness will be skewed. A schematic representation of energy distribution functions $f(E, x)$ as the projectiles move through the absorber is shown in Figure 4.8, where x denotes the path length of the projectiles. A beam of projectiles with a small initial energy spread shows a broad and skewed distribution early on in the slowing down process. For increasing path length, corresponding to an increasing number of collisions between each projectile and the atomic electrons of the absorber, the energy spread increases, but the skewness weakens so that the energy distribution function resembles a Gaussian shape after a certain path length. Further energy loss close to the end of the projectile range results in a decreasing energy spread until all projectiles come eventually to rest in the absorber.

A useful approximation for the width of the Gaussian energy distribution function was derived by Bohr, assuming that the number of collisions between a non-relativistic projectile and the absorber electrons is very large and that, at the same time, the mean energy loss is small compared to the initial projectile energy (i.e., for relatively thin absorbers). The full width at half maximum (FWHM) of the energy distribution function is then given by (Bohr, 1915)

$$\text{FWHM} = 2\sqrt{2\ln 2}\sqrt{4\pi e^4 Z_p^2 Z_t N d} = 1.20 \times 10^{-12}\sqrt{Z_p^2 Z_t N d} \quad \text{(MeV)} \quad (4.19)$$

where in the numerical expression N and d are in units of atoms per cubic centimeter and centimeter, respectively.

4.2.2 Interactions of Photons

Photons interact with matter through processes that are fundamentally different from those involving charged particles. The main interactions of γ-rays in matter are: (i) the photoelectric effect, (ii) Compton scattering, and (iii) pair production. All of these processes may transfer either the entire energy or a substantial fraction of the photon energy to an electron of an absorber atom in a single interaction. Therefore, the photon either disappears or significantly deflects from its original direction of motion. These considerations have two important consequences. First, γ-rays are far more penetrating in matter than charged particles. Second, a beam of photons passing through matter is reduced in intensity depending on the absorber thickness. However, the photons that pass straight through the absorber did not undergo any interactions and hence possess their original energy.

The energetic electron, leaving the atom after the interaction, slows down in the absorber and thereby creates more charge carriers (electron–ion or electron–hole pairs). Gamma-ray detectors take advantage of these charge pairs to determine, for example, the total energy deposited by the incident photon in the absorber. Interaction processes involving photons are discussed in more detail below.

4.2.2.1 Photoelectric Effect

In the photoelectric effect, a photon transfers its entire energy to a single electron of an absorber atom and hence it disappears. The electron, called a *photoelectron*, is ejected from the atom with an energy of

$$E_e = E_\gamma - E_b \quad (4.20)$$

where E_γ and E_b are the incident photon energy and the binding energy of the photoelectron, respectively. A free electron cannot absorb a photon and at the same time conserve linear momentum. Hence, the photoelectric effect always involves bound electrons, with the whole atom absorbing the recoil momentum. For photon energies above 100 keV the photoelectron most likely originates from the K shell (the most tightly bound shell) of the atom.

The photoelectric effect transforms a neutral atom into an electron–ion pair. The vacancy in the ion is quickly filled through the capture of a free electron originating from other absorber atoms or by the rearrangement of electrons from other shells in the ion. During these secondary processes, characteristic X-ray photons or Auger electrons may be generated. In most cases, the X-rays undergo further photoelectric absorption near the primary photon–electron interaction site and thus their energy is retained in the absorber (Knoll, 1989).

The photoelectric effect is difficult to treat theoretically. A useful approximation for the probability per absorber atom of photoelectric absorption for photon energies above 100 keV is given by (Evans, 1955; Knoll, 1989)

$$p_{photo} \sim \frac{Z^n}{E_\gamma^{7/2}} \tag{4.21}$$

where Z is the atomic number of the absorber and n varies between 4 and 5 over the γ-ray energy region between 0.1 and 5 MeV. As will be seen later, the photoelectric effect is the predominant interaction process for photons of relatively low energy. The strong Z-dependence in Eq. (4.21) is the reason for using high-Z materials, such as lead, for shielding against background γ-rays. For the same reason, high-Z materials are preferred as the active volume of γ-ray detectors.

A graph of the photoelectric absorption probability (in units of centimeter square per gram; see later) for lead is shown in Figure 4.9. For decreasing photon energies, the probability increases, while the photon energy approaches the electron-binding energy of the most tightly bound shell (the K shell) in the absorber atom. For slightly smaller photon energies, the probability drops

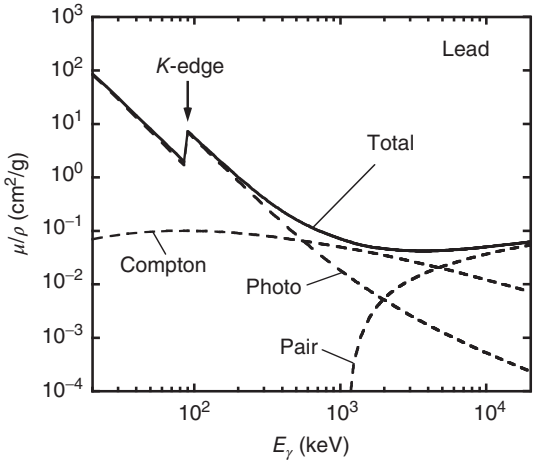

Figure 4.9 Mass attenuation coefficient of lead versus γ-ray energy. The solid line corresponds to the total mass attenuation coefficient, while the dashed lines show the individual components for Compton effect, photoelectric effect, and pair production. Data from Boone and Chavez (1996).

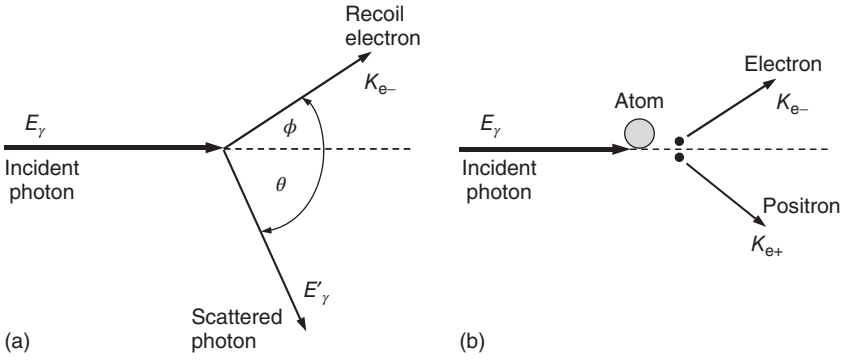

Figure 4.10 Representations of the (a) Compton effect, and (b) pair production. In part (b), neither the electron nor the positron existed before the interaction. The atom is only a spectator and facilitates the simultaneous conservation of energy and linear momentum.

drastically since the K electrons are no longer available for the photoelectric effect. This rapid decrease is called the *K absorption edge*. For even smaller photon energies, the probability increases again while the next shell (the L shell) is approached.

4.2.2.2 **Compton Effect**

The scattering of a photon by a free electron is referred to as the *Compton effect*. Although the absorber electrons are bound to atoms, they can be considered to be nearly free if the γ-ray energy is large compared to the electron binding energy. The process is shown schematically in Figure 4.10a. The electron is assumed to be initially at rest. A photon of incident energy E_γ transfers a fraction of its energy to the electron and is deflected by an angle θ with respect to its original direction, while the recoil electron emerges from the scattering center under an angle ϕ. All scattering angles are possible and, therefore, the transferred energy varies from zero to a large fraction of the incident photon energy.

The energies of the scattered photon and recoil electron can be obtained by solving simultaneously the equations for the conservation of energy and linear momentum. One finds (Leo, 1987)

$$E'_\gamma = \frac{E_\gamma}{1 + \frac{E_\gamma}{m_e c^2}(1 - \cos\theta)} \tag{4.22}$$

$$K_e = E_\gamma - E'_\gamma = E_\gamma \frac{\frac{E_\gamma}{m_e c^2}(1 - \cos\theta)}{1 + \frac{E_\gamma}{m_e c^2}(1 - \cos\theta)} \tag{4.23}$$

where $m_e c^2 = 511$ keV is the electron rest energy. For the special case of a photon-scattering angle of $\theta = 0°$ the recoil electron energy is zero and, therefore, the scattered photon loses no energy. The maximum energy transfer occurs at $\theta = 180°$,

where the energies of the recoil electron and scattered photon are given by

$$K_e^{\max} = E_\gamma \frac{2\frac{E_\gamma}{m_e c^2}}{1 + 2\frac{E_\gamma}{m_e c^2}} \tag{4.24}$$

$$(E'_\gamma)^{\min} = \frac{E_\gamma}{1 + 2\frac{E_\gamma}{m_e c^2}} \tag{4.25}$$

The cross section for Compton scattering is given by the Klein–Nishina formula (see, e.g., Leo, 1987). A polar plot of the angular distribution of scattered photons is shown in Figure 4.11a for different energies of incident photons that approach the scattering center from the bottom. It can be seen that the distribution is symmetric around $\theta = 90°$ for small photon energies ($E_\gamma < 1$ keV), whereas scattering into the forward direction is strongly preferred for large γ-ray energies. The Klein–Nishina formula also predicts the energy distribution of recoil electrons. The result is shown in Figure 4.11b for incident photons with energies of $E_\gamma = 0.5$ MeV, 1.0 MeV, and 1.5 MeV. Each curve displays a maximum recoil electron energy $K_e^{\max}$, called the *Compton edge*, corresponding to a photon-scattering angle of $\theta = 180°$. These recoil electrons are usually stopped in the absorber and,

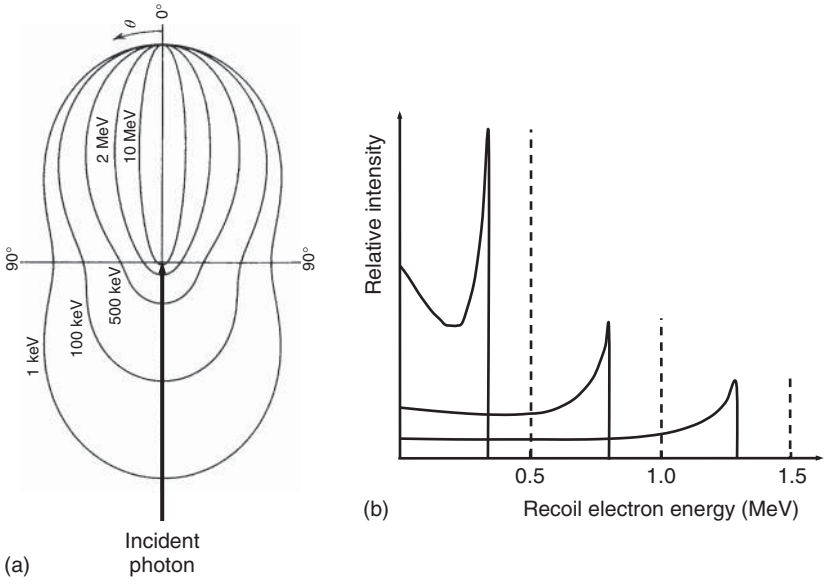

Figure 4.11 (a) Polar plot of the angular distribution of Compton-scattered photons for different incident energies. The incident photons approach the scattering center from the bottom. (b) Schematic graph of the energy distribution of recoil electrons after Compton scattering (solid lines). The dashed lines indicate the energies of the corresponding incident, monoenergetic photons ($E_\gamma = 0.5$ MeV, 1.0 MeV, and 1.5 MeV). The maxima of the distributions are referred to as *Compton edges*. They correspond to a photon-scattering angle of $\theta = 180°$.

therefore, the graphs also represent the distribution of energy deposited by the incident photons in the absorber (e.g., a γ-ray detector). For $E_\gamma \gg m_e c^2$, the energy difference between incident photon and maximum recoil electron energy is $E_\gamma - K_e^{\max} \approx m_e c^2/2 = 256$ keV. It has been assumed so far that the Compton scattering process involves an electron that is initially free. A proper consideration of the electron-binding energy prior to scattering results in a rounding-off of the sharp Compton edge displayed in Figure 4.11b.

The probability per absorber atom of Compton scattering increases with the number of electrons available as scattering targets and is approximately given by

$$p_{\text{Compton}} \sim \frac{Z}{E_\gamma} \tag{4.26}$$

This probability (in units of centimeter square per gram) is shown for lead in Figure 4.9. The Compton scattering probability varies moderately with incident photon energy. At an energy of $E_\gamma \approx 500$ keV (for lead) it becomes comparable to the photoelectric absorption probability and dominates over the latter at higher energies.

4.2.2.3 Pair Production

The process involving the transformation of a photon into an electron–positron pair is referred to as *pair production*, and is shown schematically in Figure 4.10b. The photon must have at least an energy of twice the electron rest energy (2×511 keV $= 1022$ keV) for this process to occur. Also, pair production must involve a third body, usually the nucleus of an absorber atom. Otherwise, total energy and linear momentum are not simultaneously conserved. The fraction $E_\gamma - 2m_e c^2$ of the incident photon energy is transferred to the kinetic energies of the electron and positron, that is,

$$E_\gamma = (K_{e^-} + m_e c^2) + (K_{e^+} + m_e c^2) \tag{4.27}$$

Both of these particles slow down in the absorber. The positron will subsequently annihilate with another electron. Thus, two annihilation photons of 511 keV energy, emitted into opposite directions, are produced as a byproduct of the interaction.

Theoretical expressions for the probability of the pair production process are rather complicated (Leo, 1987). The probability is approximately proportional to $Z(Z+1)$ and rises with increasing incident photon energy. The pair production probability (in units of centimeter square per gram) for lead is shown in Figure 4.9. It can be seen that pair production dominates over photoelectric absorption and Compton scattering above an energy of $E_\gamma \approx 5$ MeV.

4.2.2.4 Photon Attenuation

So far we considered individual photon interaction processes. We will now discuss the combined effect of multiple interactions for monoenergetic incident photons. Consider Figure 4.12 showing the interaction processes discussed in the previous sections for photons incident on an absorber. Cases (a), (b), and (d)

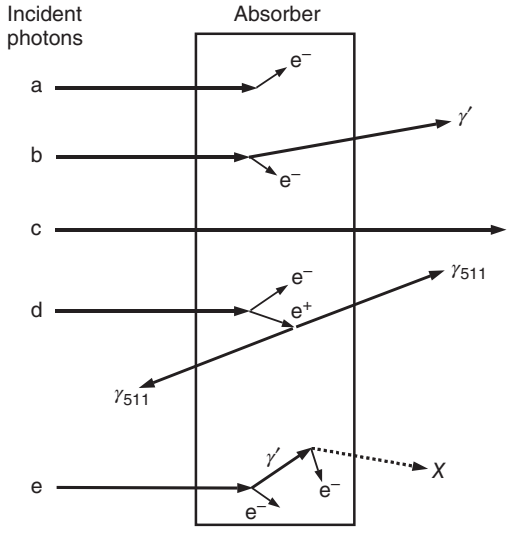

Figure 4.12 Possible interactions of monoenergetic photons incident on an absorber. See discussion in the text.

correspond to photons that undergo photoelectric absorption, Compton scattering, and pair production, respectively. More complicated interaction sequences are possible. For example, the Compton scattered photon in case (b) may in turn undergo photoelectric absorption, producing an X-ray photon, which leaves the absorber (case e). A complete description of all possible interactions involving the directions and energy distributions of scattered photons and electrons is rather complicated and can be achieved only by a Monte Carlo calculation. However, the most important information frequently of interest is the fraction of monoenergetic photons that traverse the absorber without any interaction (case c). As already pointed out, these photons possess their original energy and direction. The fraction of attenuated photons refers to those γ-rays that are either absorbed or scattered in the absorber.

Each process is characterized by the probability of the occurrence of the interaction, or equivalently, by the probability per unit path length in the absorber that a photon is removed from the incident beam by an interaction. This probability is called *linear absorption coefficient*. The total linear absorption coefficient μ is given by the sum of the partial absorption coefficients involving the different photon processes. Thus,

$$\mu = \mu_{\text{photo}} + \mu_{\text{Compton}} + \mu_{\text{pair}} \tag{4.28}$$

If a beam of monoenergetic photons is incident perpendicular to the surface of an absorber, the fractional intensity loss, dI/I, in traversing a thickness dx is

$$\frac{dI}{I} = -\mu\, dx \tag{4.29}$$

Hence, we obtain for the ratio of the number of transmitted and incident photons

$$\frac{I}{I_0} = e^{-\mu x} \tag{4.30}$$

where μ has dimensions of inverse length. The absorption coefficient is related to the mean free path λ, defined as the average distance traversed in the absorber before an interaction takes place, by

$$\lambda = \frac{\int_0^\infty x e^{-\mu x}\, dx}{\int_0^\infty e^{-\mu x}\, dx} = \frac{1}{\mu} \tag{4.31}$$

Values of λ typically amount to $\approx 10^{-3}$–10^{-1} m in solid absorbers for common γ-ray energies.

The probability for any photon interaction to occur depends on the absorber density, for example, whether the absorber is present in solid, liquid, or gaseous form. The density dependence is removed by introducing the quantity μ/ρ, called *mass attenuation coefficient*, which is widely used. Equation (4.30) can be written as

$$\frac{I}{I_0} = e^{-(\mu/\rho)\rho x} \tag{4.32}$$

where μ/ρ is in units, for example, of centimeter square per gram. The product ρx is called *mass thickness* and is in units of mass per area.

If the absorber consists of a compound $X_a Y_b$, the mass attenuation coefficient can be calculated from an expression similar to Bragg's rule (see Eq. (4.16)) by replacing the mass stopping power by the mass attenuation coefficient,

$$\left(\frac{\mu}{\rho}\right)_c = \frac{aM_X}{M_c}\left(\frac{\mu}{\rho}\right)_X + \frac{bM_Y}{M_c}\left(\frac{\mu}{\rho}\right)_Y \tag{4.33}$$

where $M_c = aM_X + bM_Y$. Total mass attenuation coefficients for two common γ-ray shielding materials (Fe and Ta) and two common γ-ray detector crystal materials (NaI and Ge) are displayed in Figure 4.13.

Certain geometrical considerations require careful consideration when using photon attenuation coefficients. Figure 4.14a shows γ-rays that are emitted from a point source and traverse an absorber. It can be seen that the γ-rays traverse the absorber at different angles. Therefore, the average path length through the absorber, rather than the absorber thickness, must be estimated and used in the calculation of the γ-ray attenuation. Figure 4.14b shows a typical detector arrangement. Gamma-rays from a point source are detected in the active volume of a detector. With the knowledge of the crystal size, the distance between source and crystal, and the number of photons emitted from the source, the total number of photons detected in the crystal can be calculated using the attenuation coefficient. However, massive absorbers such as lead are frequently used to shield the detector from unwanted γ-ray background. Consequently, the detector may respond not only to γ-rays coming directly from the source, but also to those reaching the detector after scattering in the shielding material, or to other types of secondary

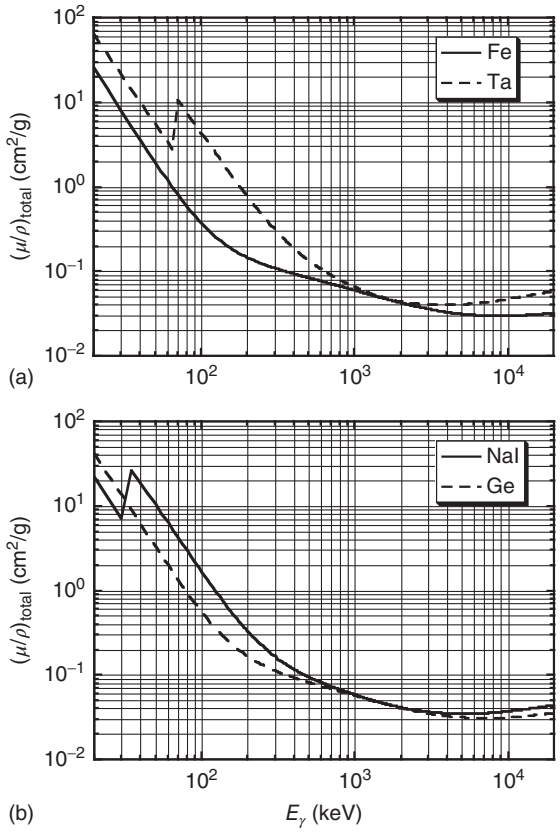

Figure 4.13 Total mass attenuation coefficients for the (a) common γ-ray shielding materials Fe and Ta, and (b) the common γ-ray detector crystal materials NaI and Ge. Data from Boone and Chavez (1996).

radiations induced by the source γ-rays in the shielding material. Thus, the number of photons counted in the detector will be larger compared to a setup without the shielding material. This effect has to be taken into account when estimating detector efficiencies (Section 4.5.2).

4.2.3 Interactions of Neutrons

Neutrons carry no charge and, therefore, cannot interact in matter via the Coulomb force. Instead, neutrons interact with absorber nuclei via the strong force. The range of this force is short and an interaction can occur only if the neutron comes within $\approx 10^{-15}$ m of a nucleus. As a result, neutron interactions are relatively rare and thus they can penetrate absorbers of many centimeter thickness without interaction. A neutron may interact with a nucleus via a

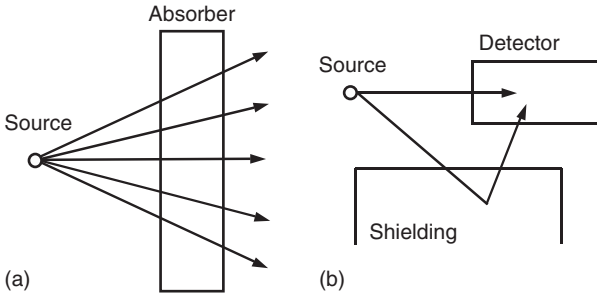

Figure 4.14 (a) Photons emitted by a point source traversing an absorber at different angles. (b) Photons reaching the detector after scattering in nearby shielding material.

number of different processes including: (i) elastic scattering (n,n), (ii) inelastic scattering (n,n′), (iii) radiative capture (n,γ), and (iv) reactions that produce charged particles such as (n,p) or (n,α). The relative importance of the various interaction types depends strongly on the neutron energy. In the following, neutrons with energies above and below ≈ 0.5 eV will be designated as *fast neutrons* and *slow neutrons*, respectively (Knoll, 1989).

Slow neutrons that are incident on an absorber may undergo elastic scattering. After many collisions have occurred, the neutrons are in thermal equilibrium with the absorber material before other types of interactions take place. These neutrons are referred to as *thermal neutrons*, corresponding to an average energy of $kT = 0.025$ eV at room temperature (Section 3.1.1). For many absorber materials, radiative capture is the most likely neutron-induced reaction that has important implications for neutron shielding considerations. The majority of slow neutron detectors, on the other hand, are based on the detection of secondary charged particles that are emitted in reactions of type (n,p), (n,α), and so on.

The cross section for the majority of neutron-induced reactions decreases rapidly with increasing neutron energy. Therefore, elastic scattering becomes the most likely process for fast neutrons. In this case, the neutron can transfer in each interaction a significant amount of energy to the recoil nucleus. As a result of many collisions, the incident neutron slows down. This process is referred to as *moderation*. Hydrogen is the most efficient moderator since, according to scattering kinematics (Appendix C), the neutron can lose all its energy in a single collision. Most fast neutron detectors rely on the detection of the (charged) recoil nuclei. For sufficiently high neutron energies, inelastic scattering may also occur. In this case, the recoil nucleus is left in an excited state and de-excites quickly via emission of secondary γ-rays. Inelastic scattering is an important process for the shielding of high-energy neutrons.

The total cross section for the interaction of neutrons with matter is given by the sum of the cross sections for the individual interactions,

$$\sigma_T = \sigma_{(\mathrm{n,n})} + \sigma_{(\mathrm{n,n'})} + \sigma_{(\mathrm{n},\gamma)} + \sigma_{(\mathrm{n,p})} + \sigma_{(\mathrm{n},\alpha)} + \cdots \tag{4.34}$$

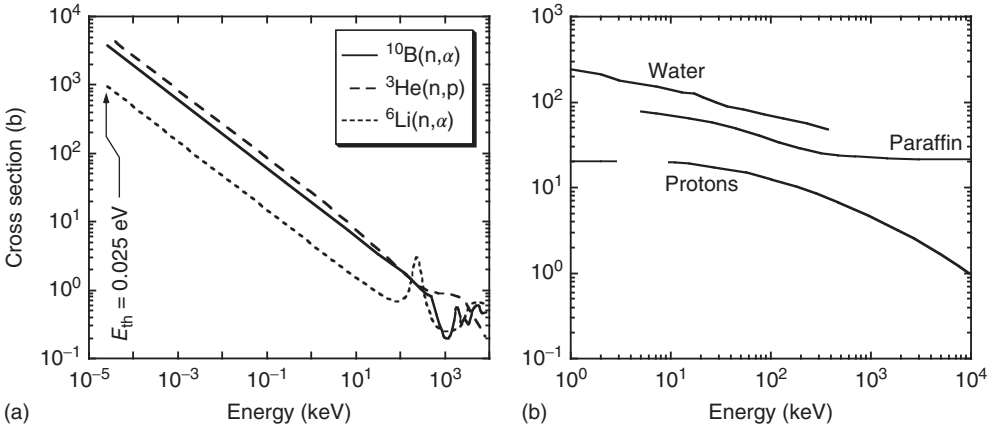

Figure 4.15 (a) Cross section versus neutron energy for reactions of interest to neutron detection. Below a neutron energy of $E_n \approx 1$ keV, the cross sections follow the $1/v$ law (Eq. 2.207). Data from Knoll (1989). (b) Total cross section versus neutron energy for common neutron shielding materials. Data from Leo (1987).

Cross sections versus neutron energy for some reactions of interest to neutron detection are shown in Figure 4.15a. Below a neutron energy of $E_n \approx 100$ keV, the cross sections follow the $1/v$ law (see Eq. (2.207)). Total cross sections for common neutron shielding materials are displayed in Figure 4.15b.

The product of the total cross section and the number density of atoms in the absorber, $N\sigma_T$, has dimensions of inverse length. This quantity represents the probability per path length in the absorber medium that any type of interaction will occur or, equivalently, that a neutron is removed by an interaction from the incident beam. It has the same physical meaning for neutrons as the linear absorption coefficient has for photons (Section 4.2.2). In analogy to photons, a beam of monoenergetic neutrons incident perpendicular to the surface of an absorber of thickness x will be attenuated exponentially. The transmission T (which is *not* related to the transmission coefficient $\hat{T}$ of Chapter 2) is given by

$$T = \frac{I}{I_0} = e^{-N\sigma_T x} \tag{4.35}$$

where I and I_0 are the measured intensities with and without absorber, respectively, between incident neutron beam and detector. The neutron mean free path is accordingly (see Eq. (4.31))

$$\lambda = \frac{1}{N\sigma_T} \tag{4.36}$$

Values of λ in solid absorbers typically amount to ≈ 1 cm and ≈ 10 cm for slow and fast neutrons, respectively. As was the case for γ-rays, the exponential attenuation (see Eq. (4.35)) applies only to a collimated beam of neutrons. For situations

in which neutrons can reach a detector after scattering in the material surrounding the active volume, corrections are necessary to predict the true number of transmitted neutrons.

If the incident neutrons are not monoenergetic, but are represented by a distribution where $f(E)$ is the fraction of incident neutrons having energies between E and $E + dE$ per unit energy interval with $\int f(E)\,dE = 1$, then the transmission is given by

$$T = \int_0^\infty f(E) e^{-n\sigma_T(E)}\,dE \tag{4.37}$$

where $n = Nx$ is the number of sample (or absorber) nuclei per unit area. If $\sigma_T(E) = \text{const}$ over the neutron distribution, then we obtain again Eq. (4.35). If, on the other hand, $\sigma_T(E) \neq \text{const}$ and the sample is very thin ($n\sigma_T \ll 1$), then one obtains from an expansion of the integrand in Eq. (4.37)

$$\begin{aligned} T &\approx \int_0^\infty f(E)[1 - n\sigma_T(E)]\,dE = 1 - n\int_0^\infty f(E)\sigma_T(E)\,dE \\ &\approx \exp\left(-n\int_0^\infty f(E)\,\sigma_T(E)\,dE\right) = e^{-n\overline{\sigma}_T} \end{aligned} \tag{4.38}$$

where we defined an average total cross section by $\overline{\sigma}_T \equiv \int f(E)\sigma_T(E)\,dE$.

If the absorber consists of a compound, the transmission is given by the product of the transmissions for hypothetical absorbers made of the individual elements alone, each containing the same number of nuclei per area as are present in the compound. The same procedure applies for pure elements containing more than one isotope.

Example 4.2

Calculate the attenuation of thermal neutrons ($E_n = 0.025$ eV) in a $^{10}BF_3$ gas region of 30 cm length. The gas pressure and temperature are $P = 600$ Torr and $T = 20°C$, respectively. Assume that the only process absorbing neutrons from the incident beam is the $^{10}B(n,\alpha)^7Li$ reaction, which has a cross section of 3840 b for thermal neutrons.

The number of ^{10}B atoms per cubic centimeter is calculated from Eq. (4.5),

$$N = 1 \cdot (2.68677 \times 10^{19}\,\text{cm}^{-3}) \cdot \left(\frac{600\,\text{Torr}}{760\,\text{Torr}}\right)\left(\frac{273\,\text{K}}{293\,\text{K}}\right) = 1.98 \times 10^{19}\,\text{cm}^{-3}$$

It follows

$$\frac{I}{I_0} = e^{-(1.98\times10^{19}\,\text{cm}^{-3})(3840\times10^{-24}\,\text{cm}^2)(30\,\text{cm})} = 0.10$$

Thus, about 90% of the incident neutrons are absorbed in the gas by the (n,α) reaction, while 10% traverse the absorber without undergoing an interaction.

4.3 Targets and Related Equipment

In the laboratory, a nuclear reaction is initiated by a beam bombarding a suitable target and the nuclear reaction takes place at the target position. Targets and associated equipment (target holders, chambers, and backings) have to be prepared and designed carefully for nuclear astrophysics experiments. Solid targets or backings can either be sufficiently thin for an ion beam to pass through, or can be relatively thick and stop the ion beam. These targets are referred to as *transmission* and beamstop targets, respectively. Targets in gaseous form are also being used. To avoid confusion, we will be using the term *sample* instead of target for neutron-induced reaction studies. The type of target or sample to be used in an experiment depends on the nuclear reaction and the observable to be measured. In the following, issues related to targets or samples for nuclear astrophysics experiments will be discussed in more detail.

4.3.1 Backings

The vast majority of targets that are used for charged-particle reaction studies are prepared by depositing the target material on some sort of backing. Exceptions are self-supporting targets and gas targets. There are several requirements for the backing material: (i) the target material should adhere uniformly to the backing, (ii) the backing should not cause unwanted background radiation if exposed to the ion beam, and (iii) for beamstop targets, the backing must provide efficient cooling to prevent target degradation.

Common materials used for beamstop target backings are tantalum, nickel, and copper. They have a high atomic number and thus do not initiate nuclear reactions at low bombarding energies. Their melting points are high and hence they are stable under intense ion bombardment. Before the deposition of the target material, the backing has to be cleaned to reduce surface contaminations. Common procedures are the etching of backings by a suitable mixture of acids to remove part of the surface (Vermilyea, 1953), and the subsequent resistive heating to temperatures above $\approx 1200^{\circ}$C to drive out remaining contaminants. Backings for beamstop targets are typically ≈ 0.5–2 mm thick. These are especially convenient for the study of capture reactions since they attenuate the capture γ-rays very little. For example, a 0.5 mm thick tantalum sheet has a 90% and 96% transmission for 0.5 MeV and 5 MeV γ-rays, respectively (Problem 4.3). This circumstance simplifies the setup considerably, since the γ-ray detector can be placed outside the vacuum chamber in very close geometry to the target, thus optimizing the counting efficiency.

Beamstop target backings produce a large number of Coulomb-scattered ions and, therefore, are not suitable for measurements of elastic scattering cross sections. Furthermore, at bombarding energies in excess of several mega electron volts, nuclear reactions induced by contaminants in the backing become

significant. In such instances, the use of transmission targets can be of advantage. However, these targets are difficult to cool and, therefore, they have to be sufficiently thin so that the heat deposited by the ion beam does not damage either the target or the backing. On the other hand, the backing has to be thick enough to allow for the deposition of the target material without damage. Frequently used backings for transmission targets are carbon foils of ≈ 5–$40\ \mu g/cm^2$ thickness, mounted on suitable metal frames.

In certain instances, the backing may be eliminated altogether. Examples are gas targets or self-supporting transmission targets. However, these can be prepared only for a restricted number of target elements. In the latter case, they are also easily destroyed in experiments at low energies involving high-intensity ion beams since they cannot be cooled efficiently.

For studies of neutron-induced reactions, requirements on sample backings are not as stringent since neutrons are far more penetrating than charged particles (Section 4.2.3) and the number of incident neutrons is considerably smaller than typical charged-particle beam currents. A variety of materials is used to support or contain the sample material, including carbon foils, thin-walled aluminum or stainless steel cans, adhesive tape, and pressurized stainless steel spheres for noble gas samples. The material of the backing or the containment vessel should not contribute significantly to the background and should be sufficiently thin to minimize neutron attenuation, scattering, and absorption of the reaction products. Also, self-supporting samples are more common in neutron work compared to charged-particle measurements.

4.3.2 Target Preparation

The yield of a nuclear reaction induced by charged particles is obtained by integrating the ratio of cross section and stopping power over the thickness of the target, as will be shown in Section 4.8. In most cases, the ion beam is not completely stopped, but loses only a fraction of its energy (typically $< 10\%$) moving through the target. Such targets are relatively thin and, as a consequence, the nuclear reaction of interest takes place in a localized region within the target with a rather well-defined interaction energy.

In neutron-induced reaction studies, on the other hand, each depth in a thin sample is exposed to the same neutron energy distribution. In general, samples can be made thicker (see below) to increase count rates. Requirements for the preparation of samples for neutron irradiation are less restrictive, resulting in a larger variety of sample materials in use, including metal foils, powders, compressed tablets and pellets, and implanted samples. If the sample reacts with air, it may be sealed in a tight thin-walled can.

4.3.2.1 Evaporated and Sputtered Targets

Solid targets are frequently prepared by evaporating or sputtering a thin layer of material containing the target nuclei in vacuum onto suitable backings (Holland,

1956; Maxman, 1967). Target preparation by evaporation or sputtering is an extensive subject and different researchers have different recipes. An ^{27}Al target, for example, is easily prepared by evaporating a thin layer of Al metal onto a backing. Aluminum targets are rather stable under ion bombardment and, furthermore, contain only a single isotope (^{27}Al). The preparation of suitable ^{23}Na targets, on the other hand, is more complicated. In this case, compounds, such as NaCl, NaBr, or Na_2WO_4, have to be used in the evaporation. All of these targets degrade to a certain degree at low bombarding energies with beam currents in excess of 100 μA. Also, the *inactive* atoms in these compounds (i.e., the atoms of elements other than the target element of interest) will also contribute to the slowing down process of the beam. Thus, for the same value of target thickness (in energy units) there will be fewer target atoms present in a chemical compound compared to a pure target. Consequently, the nuclear reaction yield will decrease. This undesirable effect becomes more pronounced with increasing number and charge of inactive atoms in the compound. On the other hand, the smaller the charge of the inactive atoms, the larger the probability that they contribute to unwanted beam-induced background radiation. Depending on the circumstance, a compromise has to be found.

Similar arguments hold for elements with more than one stable isotope. For example, the evaporation of natural magnesium will produce a target containing ^{24}Mg (79%), ^{25}Mg (10%), and ^{26}Mg (11%). Even if a pure Mg target is fabricated, the ion beam will very likely induce nuclear reactions involving the isotopes other than the one of interest. To avoid these unwanted contributions to the count rate, targets can be fabricated using isotropically enriched material that is commercially available. Such targets will also produce a higher reaction yield than a target made from a natural isotopic mixture. It should be emphasized that, when chemical compounds are evaporated, one should not assume that the composition of the target is the same as that of the original compound. A number of cross sections and resonance strengths reported in the literature are erroneous because of this unjustified assumption, as will be shown in Section 4.8.4.

4.3.2.2 **Implanted Targets**

Evaporated targets are in certain situations unsuitable for nuclear reaction studies. First, it may happen that none of the targets produced by evaporating chemical compounds are sufficiently stable under bombardment with a high-intensity ion beam. Second, even if the targets are stable and consist of a single element, isotopes other than that of interest may cause intolerable background radiation. Third, certain elements cannot be evaporated at all (e.g., noble gases). These problems are frequently solved using implanted targets. In this case, the target ions of interest are accelerated and mass separated using an electromagnetic isotope separator. Only ions of the isotope of interest are directed onto a suitable backing. These target nuclei are hence implanted into the backing. The accelerating voltage determines the range of the ions in the substrate and thus the effective target thickness for the subsequent nuclear

reaction study. Both implanted transmission targets and beamstop targets have been used extensively in nuclear reaction studies. In the latter case, the backings are usually directly water cooled if high-intensity ion beams are used during the implantation process. Implanted samples are also employed in studies of neutron-induced reactions.

Several factors limit the number of ions that can be implanted into a substrate. These include the sputtering yield, the range and mobility of the ions in the substrate, the number of incident ions per unit area, and the substrate temperature. Sputtering, which releases atoms from the substrate upon ion impact, is the dominant limiting mechanism at low substrate temperatures. Tantalum is frequently chosen as a substrate for beamstop targets since it has a relatively low sputtering yield (Almen and Bruce, 1961), and since diffusion velocities of various elements are small in tantalum. For transmission targets, carbon foils with thicknesses of $\approx$ 10–40 μg/cm^2 can be used as substrates. During the implantation process the beam power deposited in the carbon foil has to be limited ($<$ 25 mW/cm^2; see Smith *et al.*, 1992) to avoid rupture of the foil. Several procedures may be applied to extend the lifetime of thin carbon foils during implantation (Fifield and Orr, 1990; Smith *et al.*, 1992).

Table 4.3 provides information about some implanted targets and samples used in nuclear astrophysics studies. It lists incident ion energies and doses, as well as the measured number of implanted ions (either as stoichiometry for beamstop targets or in units of atoms per square centimeter for transmission targets or samples). The table also includes a few examples of implanted radioactive targets and samples. Many targets or samples become saturated during implantation. In other words, they reach a stage at which target atoms are lost because of sputtering and diffusion at the same rate as they are implanted into the substrate. On the other hand, for a number of ion species the sputtering ratio (the number of released atoms per incident ion) is small for collisions between ions and substrate atoms, and at the same time it is less than unity for ion–ion collisions (self-sputtering). In such cases, saturation is never reached and a pure layer of target material builds up on the substrate surface (e.g., for C, Si, and Ca implantation into tantalum; Almen and Bruce, 1961).

It has also been shown that for relatively small incident ion energies, the distribution of implanted atoms extends to the front surface of the backing (Selin, Arnell, and Almen, 1967). Hence, in the nuclear reaction study there is usually no substrate dead layer in which charged projectiles lose energy or neutrons are attenuated before reaching the target material. Implanted targets can also be stored for years without noticeable loss of target material (Selin, Arnell, and Almen, 1967; Geist *et al.*, 1996).

4.3.2.3 Gas Targets

In certain situations, it is desirable to use gaseous instead of solid targets. First, it can be seen from the Table 4.3, that the stoichiometries achieved for implanted noble gas targets are unfavorable since they contain more substrate atoms than target nuclei. Therefore, the reaction yield will be reduced compared

Table 4.3 Properties of implanted targets and samples.

Target	Backing[a]	Dose[b] (mC/cm^2)	Energy (keV)	Stoichiometry or ($ions/cm^2$)[c]	References
^{12}C	Ta	400	110	$^{12}C_3Ta_2$	Seuthe *et al.* (1987)
^{14}N	Ta	784	120	$^{14}N_3Ta_2$	Seuthe *et al.* (1987)
^{19}F	Fe	31	37	$^{19}F_1Fe_8$	Ugalde (2005)
^{20}Ne	C		15–40	2.2×10^{17}	Smith *et al.* (1992)
^{22}Ne	Ta	100	100	$^{22}Ne_2Ta_5$	Keegan Kelly, priv. comm.
^{22}Na	Ni	25–80 nA	60	5.7×10^{15}	Schmidt *et al.* (1995)
^{22}Na	C	25–80 nA	60	7.6×10^{16}	Schmidt *et al.* (1995)
^{23}Na	Ni	96	50	$^{23}Na_5Ni_1$	Seuthe *et al.* (1987)
^{24}Mg	Ta	426	100	$^{24}Mg_3Ta_1$	Powell *et al.* (1999)
^{28}Si	Ta	190	80	$^{28}Si_3Ta_1$	Iliadis (1996)
^{31}P	Ta	180	80	$^{31}P_3Ta_2$	Iliadis (1996)
^{32}S	Ta	108	80	$^{32}S_1Ta_1$	Iliadis (1996)
^{33}S	C	400 nA	300	1.6×10^{16}	Schatz *et al.* (1995)
^{36}S	C		50	2×10^{17}	Fifield and Orr (1990)
^{35}Cl	Ta	180	80	$^{35}Cl_1Ta_6$	Iliadis (1996)
	C	70	60	1×10^{17}	Iliadis (1996)
^{36}Ar	Ta	44	80	$^{36}Ar_1Ta_5$	Iliadis (1996)
^{135}Cs	C			1.8×10^{15}	Patronis *et al.* (2004)

[a] For beamstop targets, the range of backing thicknesses was 0.1–0.5 mm; for transmission targets, 30–75 μg/cm^2 carbon foils were used; the ^{33}S and ^{135}Cs ions were implanted into 0.7 mm and 0.1 mm thick C disks, respectively. [b] Incident dose of singly charged ions in mC/cm^2; for ^{22}Na and ^{33}S the incident beam current is quoted (in nA). [c] For beamstop targets the stoichiometry is given, while for transmission targets (and for ^{33}S) the total number of implanted target nuclei per square centimeter is listed.

to a pure target. Second, the backing may produce intolerable beam-induced background radiation. Third, in nuclear reaction studies that are performed in inverse kinematics (by directing a heavy ion beam onto hydrogen or helium target nuclei), it may prove impossible to prepare targets of sufficient purity other than gaseous targets.

Early gas target designs involved small cells containing a pure gas, with thin entrance and exit window foils for transmitting the ion beam. These foils have the undesirable effects of reducing the ion beam energy and of broadening the beam spread. Furthermore, they are sources of unwanted beam-induced background radiation. More sophisticated designs involve windowless gas targets. The ion beam is usually stopped sufficiently far away behind the target and detector region that the beam-induced background is kept small. Windowless gas targets involve several stages of high pumping speed to lower the gas pressure from typical target chamber pressures ($\approx 10^{-2}$ Torr to 10 Torr) down to 10^{-6} Torr in the beamline. Therefore, gas target designs are more complex compared to solid targets. High pumping speeds are achieved using large roots blowers and

turbo pumps (Rolfs and Rodney, 1988). Gas targets are either of the extended type (i.e., the gas is contained in a differentially pumped chamber) or are nearly point-like (e.g., a gas jet of small diameter streaming from a nozzle perpendicular to the beam direction). They have been used in several charged-particle reaction studies that would have been difficult to perform with solid targets (Rolfs and Rodney, 1988). Using gas jets, target thicknesses of $\approx 10^{19}$ atoms/cm^2 for H, N, and Ar have been achieved (Bittner, Kretschmer, and Schuster, 1979).

For neutron-capture studies, pressurized gas samples in stainless steel spheres of 2 cm diameter and 0.5 mm wall thickness have been employed, with sample masses of a few grams (Beer, 1991).

4.3.2.4 Target Thickness and Stability

The choice of target thickness depends on the type of experiment one wishes to perform. There is no apparent advantage to choosing a target thickness (in energy units) that is smaller than the ion beam resolution ($\approx$ 1 keV). If a charged-particle reaction is measured over an energy range containing previously observed resonances, the target thickness should be chosen to be smaller than the energy separation of the resonances. Below an ion energy of 1 MeV, typical target thicknesses are $\approx$ 5–20 keV, while at $E = 1$–2 MeV the density of resonances increases and target thicknesses are usually smaller ($\approx$ 1–5 keV). In searches for resonances at low bombarding ion energies, it is frequently of advantage to use thicker targets ($\approx$ 20–40 keV) to study the energy range of interest in a reasonable amount of time. Target thicknesses are conveniently determined by measuring yield curves of narrow, well-known resonances in charged-particle-induced reactions, as will be explained in Section 4.8.3. The target thickness should also be uniform if the ion beam spot has a smaller diameter than the target.

The stability of a particular target depends not only on the ion beam intensity, but also on the ion type. Targets that are stable under bombardment with high intensity (> 100 μA) proton beams will likely degrade to some degree if bombarded with a high intensity α-particle beam. Blistering is a particularly troublesome effect where the beam α-particles are implanted into the target and then move quickly to lattice defects. Eventually, high pressure gas blisters are formed, which rupture and thereby degrade the target locally (Cole and Grime, 1981). In some cases, there may be no alternative other than replacing the target after substantial degradation.

For neutron-induced reaction studies, the physical stability of the sample is usually of lesser concern. Samples must be thick enough to provide sufficiently high count rates, but have to be thin enough to minimize the attenuation and scattering of incident neutrons and the absorption of reaction products. Sample thicknesses for neutron work are typically in the range of $\approx$ mg/cm^2–g/cm^2, which significantly exceeds the target thicknesses used in charged-particle reaction studies.

4.3.3 Contaminants

Studies of nuclear reactions are frequently hampered by the presence of contaminants in either the target or the backing. Although the concentration of contaminants is usually very small, their cross section for reactions induced by the incident beam may be very large. Therefore, they may either contribute to, or obscure altogether, the count rate of interest. If both the reaction of interest and a given contaminant reaction proceed through narrow resonances of different energies, then it may be possible to adjust the beam energy so that the contaminant resonance is not excited. Alternatively, if the reaction of interest proceeds through a narrow resonance and the contaminant reaction proceeds either through a broad resonance or a nonresonant process, then it is often possible to measure the count rate just below, on top, and just above the resonance of interest. The difference between the on- and off-resonance spectra can then be used to estimate the contaminant contribution. This procedure is not applicable if both the reaction of interest and the contaminant reaction proceed through broad resonances or nonresonant processes. In such cases, it is useful to estimate the background contributions by comparing the count rates from different runs using the target plus backing and the backing alone (or gas in–gas out for gas targets).

For proton-induced reactions, one of the most troublesome contaminants is ^{19}F, which gives rise to γ-rays and α-particles through the ^{19}F(p,$\alpha\gamma$)^{16}O reaction. Another common contaminant is ^{11}B, which produces α-particles through the ^{11}B(p,α)2α reaction and γ-rays via ^{11}B(p,γ)^{12}C. Experience shows that the concentration of ^{19}F and ^{11}B, which remains in the backing after common cleaning procedures, varies greatly. Therefore, it is useful to test backing materials from different suppliers for minimum ^{19}F and ^{11}B concentrations. Proton captures on ^{12}C and ^{13}C also contribute to γ-ray background. Considerable care needs to be taken in preparing, storing, and handling targets to ensure that no additional contaminants are added to their surface.

An important contaminant for reactions induced by α-particles is ^{13}C, which produces neutrons via the ^{13}C(α,n)^{16}O reaction. The neutrons contribute either directly to the detector background count rate, or indirectly by producing secondary γ-rays in the surrounding material via neutron inelastic scattering or neutron capture.

Carbon contamination generally builds up on the target during ion bombardment. Hydrocarbons from organic components of the vacuum system (e.g., vacuum sealing O-rings) diffuse into the beam and are subsequently transported onto the target. This carbon layer not only contributes to beam-induced γ-ray background, but also causes a reduction of the incident beam energy before the projectiles strike the target. Carbon deposition can be reduced substantially by having the beam move through a liquid-nitrogen cooled metal tube that is placed close to the target (Section 4.3.4). Table 4.4 lists common contaminant reactions induced by low-energy ($E < 1$ MeV) proton and α-particle beams and, if applicable, the energies of their characteristic discrete γ-rays.

Table 4.4 Common contaminant reactions and their discrete characteristic γ-ray energies.

Contaminant	Reaction	E_γ (keV)
^{19}F	^{19}F(p,$\alpha\gamma$)^{16}O	6130
^{11}B	^{11}B(p,γ)^{12}C	4439
	^{11}B(p,α)2α	
^{15}N	^{15}N(p,$\alpha\gamma$)^{12}C	4439
^{12}C	^{12}C(p,γ)^{13}N	
^{13}C	^{13}C(p,γ)^{14}N	2313
	^{13}C(α,n)^{16}O	
^{16}O	^{16}O(p,γ)^{17}F	495
^{23}Na	^{23}Na(p,γ)^{24}Mg	1369
	^{23}Na(p,$\alpha\gamma$)^{20}Ne	1634
^{27}Al	^{27}Al(p,γ)^{28}Si	1779

In studies of neutron-induced reactions, accurate cross section and transmission measurements require precise knowledge of the sample composition. Oxidization is a potential problem when metal samples are used. The composition may also change as a result of hygroscopy, that is, the absorption of moisture from the air. Increases in sample weight by 16% because of hygroscopy have been observed for powdered samples (Mizumoto and Sugimoto, 1989). The water not only increases the weight of the sample but also gives rise to an additional energy loss for charged particles that are emitted in a neutron-induced reaction, causing an increased tailing in the pulse height spectrum. In neutron-capture studies, a fraction of the incident neutrons slows down via scattering on hydrogen. For the scattered neutrons, the reaction is induced at lower energies where either the capture cross section is higher, or the cross section fluctuates rapidly because of resonances. In both cases, the capture rate may increase drastically. In some instances, the moisture can be removed by heating in vacuum, as indicated by the weight loss of the sample.

4.3.4 Target Chamber and Holder

Targets are mounted in a target chamber which represents the location where the nuclear reactions take place. The specific design of the chamber depends on the type of target used (beamstop target, transmission target, or irradiation sample) and the type of detector employed (γ-ray detector, charged-particle detector, or neutron counter). For charged-particle-induced reaction studies, target chambers must provide an accurate measurement of the integrated ion beam charge and they also have to accommodate radiation detectors. The chamber has to hold a vacuum of $\approx 10^{-6}$ Torr or lower to minimize the interaction of the ion beam with residual gas molecules and to reduce the condensation

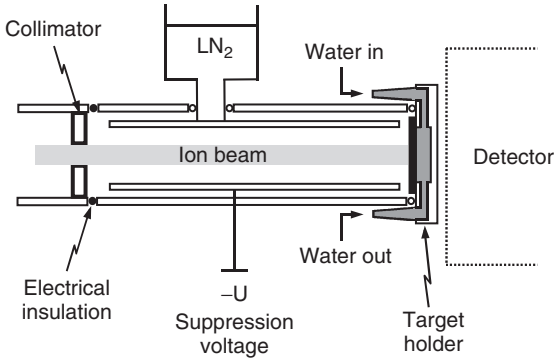

Figure 4.16 Typical target chamber design used in radiative capture reaction studies. The beam passes through a defining collimator and is incident on a directly water-cooled beamstop target. A copper tube, cooled to liquid-nitrogen (LN_2) temperature, reduces the buildup of contaminants (such as ^{12}C and ^{13}C) on the target. The chamber is electrically insulated from the rest of the beamline and thus acts as a Faraday cup for the integration of the total charge accumulated by the beam on the target. A negative voltage is applied to the copper tube to suppress the emission of secondary electrons. The small (full and open) circles show the location of vacuum O-ring seals.

of contaminants on the target surface. Figure 4.16 shows a target chamber designed for (p,γ) and (α,γ) reaction measurements at low energies ($E < 1$ MeV) with high intensity beams (currents of $I \approx 0.1$–1 A). The design will be discussed below because it takes several important considerations into account. Examples of experimental setups used for studies of other charged-particle-induced reactions or of neutron-induced reactions will be discussed in later sections.

The target shown in Figure 4.16 is a beamstop target. The beam loses its entire energy in the target and backing. The beam power (energy per time) deposited by the beam is given by the product of voltage and current, that is, $P = U \cdot I$. For example, for a singly charged ion beam of 100 keV energy and 1 mA current, the power amounts to $P = (0.1\ \text{MV})\ (1000\ \mu\text{A}) = 100$ W. If the beam spot on the target is too small, say, only a few square millimeters, then the locally produced heat will quickly destroy the target or backing. Therefore, it is important to defocus the beam sufficiently. Even with a defocused beam, the heat produced by the ion beam will degrade the target, unless efficient cooling is provided. Therefore, the backside of the target backing is directly water cooled. The water reservoir has to be large enough and the water flow strong enough to provide efficient cooling. On the other hand, the target holder thickness should be kept small so that the γ-ray detector can be placed as close as possible to the target to maximize counting efficiency. Furthermore, capture γ-rays are not attenuated substantially in a thin target holder before reaching the detector.

The chamber design shows several features that minimize beam-induced γ-ray background. A beam-defining aperture is mounted some distance away from the target and ensures that the beam hits only the target, but not other parts of the

target holder or chamber. The buildup of contaminants, such as ^{12}C and ^{13}C, on the target is reduced by having the beam move through a metal tube that is directly cooled by liquid nitrogen. Thus, troublesome hydrocarbons that are released by vacuum O-ring seals condense on the cold surface of the metal tube instead of the target. Since the target holder design involves several O-ring seals, the tube should extend as close as possible to the target without touching it.

The target chamber also represents a Faraday cup for integrating the ion beam current. If the charge state of the ion beam, q, is known, the total number of ions incident on the target, $\mathcal{N}_i$, can be easily calculated from $\mathcal{N}_i = Q/(qe)$, where Q is the total accumulated charge (or integrated beam current). The most important systematic error in the beam current integration arises from secondary electrons that are emitted from surfaces hit by the beam. For example, a singly charged positive ion hitting the target will deposit one elementary charge on the Faraday cup. At the same time, however, secondary electrons are emitted and these may move away from the target without being collected on the Faraday cup. Thus, the measured current will yield an overestimate for the number of positive ions hitting the target (since removing an electron from the Faraday cup has the same effect as adding a positive charge). For this reason, a reliable target chamber design must account for secondary electron suppression. In Figure 4.16, a negative voltage of several hundred volts (Rolfs and Rodney, 1988) is applied to the metal tube, thus repelling secondary electrons that are emitted from the target or the collimator. Also, possible current losses through the target cooling water need to be checked carefully.

4.4 Radiation Detectors

4.4.1 General Aspects

Nuclear reactions are studied by measuring the reaction products (e.g., protons, neutrons, α-particles, or γ-rays) with suitable detectors. Different types of radiation interact differently with matter and, therefore, the type of detector to be used will depend on the identity of the radiation of interest. Most detectors produce, directly or indirectly, a given amount of electric charge as a result of energy deposition by the radiation. The charge is collected by applying an electric field and, as a result, an electric signal is produced. The precise shape of this signal depends on, among other things, how and where the charge is produced in the active volume, how fast the charge is collected, and the characteristics of the electric circuit to which the detector is connected (e.g., preamplifier or photomultiplier tube). Although the signal shape varies strongly from one detector type to another, the amplitude of the signal pulse is usually directly proportional to the charge generated within the active volume or, equivalently, the energy deposited by the radiation in the detector. Furthermore, the rate at which such pulses occur depends

on the corresponding rate of radiation interactions within the active volume. This rate is directly proportional to the number of nuclear reactions occurring per time interval. If a large number of such pulses is examined, their amplitudes will not all be the same. Variations in pulse heights are caused by a number of effects: (i) the radiation incident on the detector may not be monoenergetic; (ii) even for incident monoenergetic radiation, different amounts of energy may be deposited in the detector; and (iii) fluctuations in the intrinsic detector response.

In practice, the output signal from a preamplifier or a photomultiplier tube is further amplified and shaped by additional electronic circuits (spectroscopy amplifiers) while still preserving the pulse height information. The data are then displayed as a differential pulse height distribution (or *pulse height spectrum*), showing the pulse height on the horizontal axis and the number of pulses observed within a pulse height interval, divided by the interval width, on the vertical axis. Physical interpretations almost always involve areas under the spectrum, or total counts, between two given pulse height values. Through careful energy and efficiency calibrations, the information displayed in a differential pulse height distribution can be related to the energies and intensities of the incident radiation. The latter information is then used to determine nuclear reaction cross sections.

A schematic pulse height spectrum (differential number of pulses per pulse height interval, dI/dH, versus pulse height, H) is shown in Figure 4.17a. The shape of the spectrum can be complicated and depends on the nature and energy of the incident radiation as well as the intrinsic detector response. The latter has to be well understood to relate the spectrum shape to properties of the incident radiation. Relatively narrow peaks in a spectrum frequently indicate that incident α-particles, protons, neutrons, or photons deposited their entire discrete energy in the active detector volume. Suppose that a sharp peak occurs at a pulse height of H_0, which is proportional to the energy of the incident radiation. The peak is superimposed on a background, representing a relatively flat part of the spectrum. The net intensity of the peak (shaded area labeled $\mathcal{N}$), which is proportional to the number of radiation quanta of specific incident energy, is calculated by subtracting the background (area labeled B) from the total number of counts in the region of interest between H_1 and H_2,

$$\mathcal{N} = T - B \tag{4.39}$$

The background B can be estimated from the number of counts in regions on the left- and right-hand side of the peak. Counts in nuclear physics experiments are distributed according to a Poisson probability density function, with the standard deviation given by the square root of the number of counts. Thus, we obtain for the error (one standard deviation) in the number of net counts

$$\Delta\mathcal{N} = \sqrt{(\Delta T)^2 + (\Delta B)^2} = \sqrt{T + B} \tag{4.40}$$

In more complicated cases, including overlapping peaks and nonlinear background structures, sophisticated fitting programs are usually employed. Elaborate discussions of statistical data analysis in nuclear counting experiments can be found in Leo (1987) and Knoll (1989).

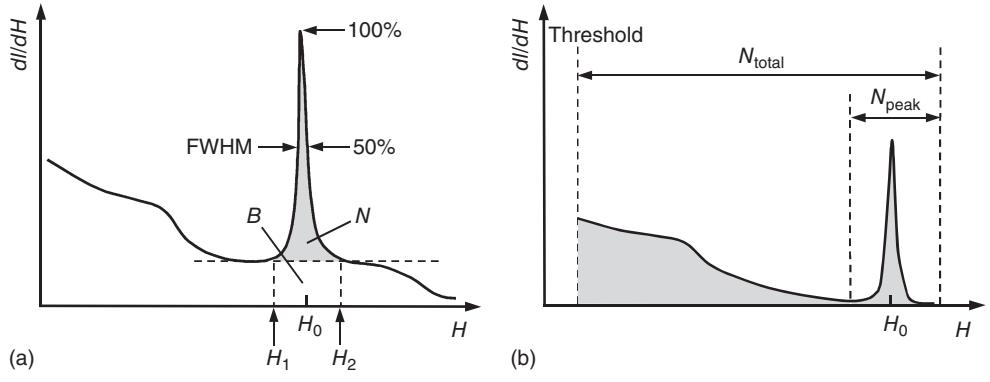

Figure 4.17 (a) Schematic pulse height spectrum. The net intensity of the peak centered around pulse height H_0 (area labeled $\mathcal{N}$) is obtained by subtracting the number of background counts (area labeled *B*) from the total number of counts between H_1 and H_2. The FWHM of the peak, as measured relative to the background level (dashed horizontal line) indicates the detector energy resolution. (b) Pulse height spectrum illustrating the difference between total and peak efficiencies. The former and latter quantities are calculated by dividing $\mathcal{N}_{\text{total}}$ and $\mathcal{N}_{\text{peak}}$, respectively, by the total number of quanta emitted by the source. Below the detection threshold (leftmost vertical dashed line) the spectrum is dominated by noise.

The full width at half maximum of the narrow peak (FWHM), as measured from the background level, is in general determined by the energy distribution of the incident radiation as well as the intrinsic response of the detector. Suppose that the spectrum shown in Figure 4.17a has been obtained by measuring monoenergetic incident radiation so that the observed FWHM of the peak is a measure for the intrinsic *energy resolution* of the detector. It is highly desirable that this peak width is as small as possible for two reasons. First, the detector will be able to better separate closely spaced peaks. Second, the detector will have a better sensitivity for observing weak peaks in the presence of a broad (background) continuum.

The energy resolution is quantitatively defined by the ratio of FWHM and the location of the peak centroid H_0,

$$R \equiv \frac{\text{FWHM}}{H_0} \tag{4.41}$$

and is frequently expressed in percent. The energy resolution is influenced by a number of factors that are present even if each incident radiation quantum deposits precisely the same amount of energy in the detector. These include pulse height drifts during the measurement, random noise from the detector and associated electronics, and statistical fluctuations in the number of created charge carriers. The last contribution sets an inherent limit on the detector performance (Knoll, 1989). For example, semiconductor detectors generate a very large number of charge carriers per event. Since this implies relatively small statistical fluctuations in the number of charge carriers, these types of detectors have excellent energy resolutions. In general, if several independent

factors contribute to the intrinsic detector energy resolution, then the overall detector response function will tend toward a Gaussian shape according to the central-limit theorem of statistics.

Another important detector property, called *detection efficiency*, is related to the probability of detecting a quantum of radiation emitted by a source (e.g., a radioisotope or a nuclear reaction). Efficiencies can be determined from the information presented in pulse height spectra. Suppose that the spectrum shown in Figure 4.17b is obtained by measuring a source that emits $\mathcal{N}_0$ monoenergetic radiation quanta. Some incident quanta deposit their entire energy in the spectrum, corresponding to the observed sharp peak, while others deposit only a fraction of their energy giving rise to a continuum below the full-energy peak. The leftmost vertical dashed line indicates a threshold below which electronic noise dominates the spectrum. The *total efficiency* is then defined by the ratio of total counts recorded in the spectrum above the threshold and the number of radiation quanta emitted by the source,

$$\eta_{\text{tot}} \equiv \frac{\mathcal{N}_{\text{total}}}{\mathcal{N}_0} \tag{4.42}$$

It is assumed that any background contributions unrelated to the source have been subtracted from $\mathcal{N}_{\text{total}}$. Furthermore, we can also define a (full-energy) *peak efficiency* as the ratio of counts recorded only in the full-energy peak and the number of quanta emitted by the source,

$$\eta_{\text{peak}} \equiv \frac{\mathcal{N}_{\text{peak}}}{\mathcal{N}_0} \tag{4.43}$$

It is again assumed that any background contributions have been subtracted from $\mathcal{N}_{\text{peak}}$. Sometimes, efficiencies are obtained by replacing the total number of emitted quanta in Eqs. (4.42) and (4.43) by the number of quanta that are incident on the detector. The resulting quantity is referred to as *intrinsic* (total or peak) detection efficiency. We write

$$\eta = \eta_{\text{int}} \frac{\Omega}{4\pi} \tag{4.44}$$

with Ω being the solid angle of the detector in steradian. Note that η_{tot} and η_{peak} include the effective solid angle subtended by the detector as an implicit factor and, therefore, are of primary interest for our considerations.

In the following, we will briefly address certain detector types that are frequently employed in nuclear astrophysics measurements. Extensive discussions of radiation detectors can be found in Leo (1987) and Knoll (1989).

4.4.2 Semiconductor Detectors

The operating principle of semiconductor detectors relies on the formation of a semiconductor junction. The junction is formed using doped semiconductors, with silicon and germanium being the most widely used materials. For example,

at the interface of a p-type and a n-type semiconductor, a region devoid of mobile charge carriers (electrons or holes) is created. If a reverse bias voltage is applied to the junction, for example, a negative voltage on the p-side, the depletion zone representing the active volume of a radiation detector is significantly enlarged. Incident ionizing radiation will deposit a certain amount of its energy in this zone and thereby create electron–hole pairs. These are swept out by the electric field and a current signal proportional to the amount of the deposited energy is produced.

A main advantage of semiconductors over other detector types is the very small average energy needed for the creation of an electron–hole pair. This energy amounts to only 3.8 eV and 3.0 eV for Si and Ge, respectively, at liquid-nitrogen temperature (77 K). These values are smaller by more than an order of magnitude compared to other types of radiation detectors, such as gas ionization chambers or scintillators. Therefore, for the same deposited radiation energy, the number of created charge carriers will be considerably larger in semiconductors and the energy resolution is significantly improved. Furthermore, the average energy needed for the creation of an electron–hole pair is independent of the radiation energy. Thus, the signal pulse height given by the total number of created electron–hole pairs is proportional to the amount of deposited energy and the response of a semiconductor detector is highly linear.

Silicon is the most common semiconductor material used for the detection of charged particles. The intrinsic efficiency amounts to about 100% since few incident particles will fail to produce some ionization in the active detector volume. For measurements of the incident particle energy, the depth of the depletion zone has to be larger than the particle range. For example, α-particles of 10 MeV energy have a range of ≈ 70 μm in silicon (Figure 4.7).

For the detection of photons, germanium is preferred over silicon because of its larger atomic number. However, the average energy for creating an electron–hole pair is smaller in germanium. As a result, the leakage current through the semiconductor junction is larger at room temperature, thus contributing to electronic noise at the detector output. Therefore, the germanium crystal must be cooled to liquid-nitrogen temperature.

The bias voltage determines the thickness of the depletion zone. Typical values for silicon charged-particle detectors amount to 50–300 V, while bias voltages of a few 1000 V are used for germanium photon detectors.

Semiconductor detectors are subject to radiation damage. Incident ionizing radiation causes lattice defects by knocking atoms out of their normal position. These defects can trap charge carriers, leading to incomplete charge collection. As a result, the leakage current increases and the energy resolution degrades. For example, significant deterioration in the performance of silicon charged-particle detectors has been observed for integrated incident fluxes of 10^{12}–10^{13} protons/cm^2 and 10^{11} α-particles/cm^2 (Knoll, 1989). For germanium photon detectors, significant degradation in energy resolution occurs for integrated fast neutron fluxes in excess of 10^7–10^9 cm^{-2}, depending on the detector specifications.

4.4.2.1 Silicon Charged-Particle Detectors

The most widely used silicon detectors for charged-particle measurements are silicon surface barrier detectors. In this case, a junction is formed between a doped semiconductor region and a metal, for example, n-type silicon and gold. Such junctions are called *Schottky barriers*. The situation is similar to the pn junction described above and a depletion zone extending over the entire semiconductor region is formed. The outer housing and the front surface of a silicon surface barrier detector are grounded, while the output signal is extracted from the back surface of the silicon wafer. Since usually n-type silicon is used for the production of surface barrier detectors, a positive voltage is required for the reverse bias voltage of the junction. Surface barrier detectors of various depletion zone thicknesses (between several micrometers and a few millimeters) and active areas (up to several tens of square centimeters) have been produced. They are of compact size and can be placed conveniently in scattering chambers.

Junctions are also produced by forming heavily doped n- or p-layers in semiconductor material via ion implantation. The depth profile and concentration of the impurity ions are controlled by adjusting the implantation energy and current. Ion-implanted detectors have improved properties for measuring charged particles compared to surface barrier detectors. The former have thinner entrance windows (several tens of nanometers), and the active area is less sensitive to surface contamination.

A typical pulse height spectrum of an implanted silicon detector, obtained with a ^{241}Am source, is shown in Figure 4.18. This source emits several discrete α-particle groups with energies around 5.5 MeV. The detector has an active surface area of 50 mm^2 and a resolution of 10 keV (for α-particles of 5.5 MeV). It resolves most of

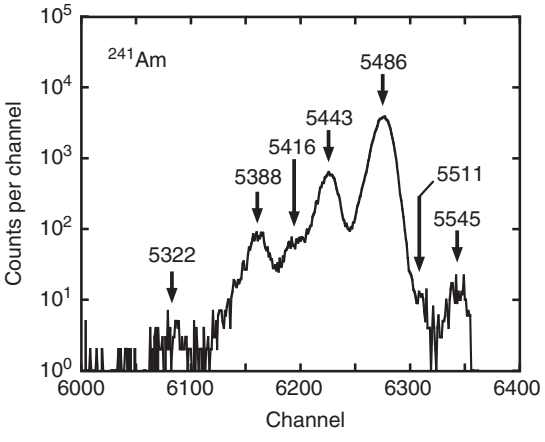

Figure 4.18 Pulse height spectrum of α-particles from an ^{241}Am source, measured using a high-resolution implanted silicon detector of 50 mm^2 active area and 10 keV resolution. The source emits several discrete α-particle groups. Their energies (in keV) are adopted from the National Nuclear Data Center, Brookhaven National Laboratory. Most of the known α-particle groups are resolved in the spectrum. (Courtesy of Joseph Newton.)

the α-particle groups. While energy resolutions of ≈ 10 keV (0.2%) are routinely achieved with such small silicon charged-particle detectors, resolutions for larger detectors typically amount to ≈ 15–20 keV.

4.4.2.2 Germanium Photon Detectors

The depletion depths of the semiconductor detectors discussed above are at most to a few millimeters and thus are too thin for the detection of more penetrating radiation, such as photons. In this case, larger active detector volumes are necessary. Gamma-ray detectors are produced from high-purity p- or n-type germanium (HPGe), with impurity concentrations below 10^{10} atoms/cm^3. In coaxial, closed-ended HPGe detectors, one of the electrical contacts is produced by forming a heavily doped n-type region of several 100 μm thickness (usually via lithium evaporation and diffusion), while the other contact represents a heavily doped p-type region of less than 1 μm thickness (formed, e.g., by ion implantation). The active volume is the entire region between the electrical contacts. The regions of the contacts do not produce charge carriers and, therefore, are called *dead layers*. The detector capsule includes the germanium crystal and the preamplifier. The germanium crystal is in thermal contact with liquid nitrogen contained in an insulated dewar, keeping the crystal at a temperature of 77 K.

The excellent energy resolution of semiconductor detectors compared to other types of γ-ray spectrometers is demonstrated in Figure 4.19. The spectra are obtained with a ^{152}Eu source using a HPGe detector Figure 4.19a and a NaI(Tl) scintillator Figure 4.19b. Scintillators will be discussed in Section 4.4.3. The superior energy resolution of the HPGe detector is striking. The ^{152}Eu source emits γ-rays of many discrete energies (Table 4.6). The excellent energy resolution in the HPGe detector spectrum allows the separation of many closely spaced γ-ray peaks that remain unresolved in the NaI(Tl) spectrum. For this reason, germanium detectors are used in the majority of γ-ray spectroscopy studies. The energy resolution varies with energy and, therefore, the values are specified at a fixed energy. For germanium photon detectors, energy resolutions are usually quoted for a γ-ray energy of 1333 keV (as provided by a ^{60}Co source). Measured values of the FWHM typically amount to ≈ 2–3 keV, corresponding to ≈ 0.2% (see Eq. (4.41)).

The output pulse shape of germanium detectors depends on a number of factors, including the charge collection process and the location in the crystal at which an incident radiation quantum deposits its energy. The latter effect is shown in Figure 4.20. The results are obtained from a Monte Carlo simulation and indicate, for a germanium detector, the fraction of the full-energy peak contributed by different interaction mechanisms. Above an energy of a few 100 keV, which is of main importance in nuclear astrophysics measurements, the photoelectric effect is less likely to occur than Compton scattering (Section 4.2.2). Thus, events contributing to the full-energy peak in this energy range arise mainly from multiple interactions, for example, one or more Compton scattering events followed by photoelectric absorption of the scattered γ-ray, rather than from a single photoelectric interaction. Such effects result in a large variation of the pulse rise time and

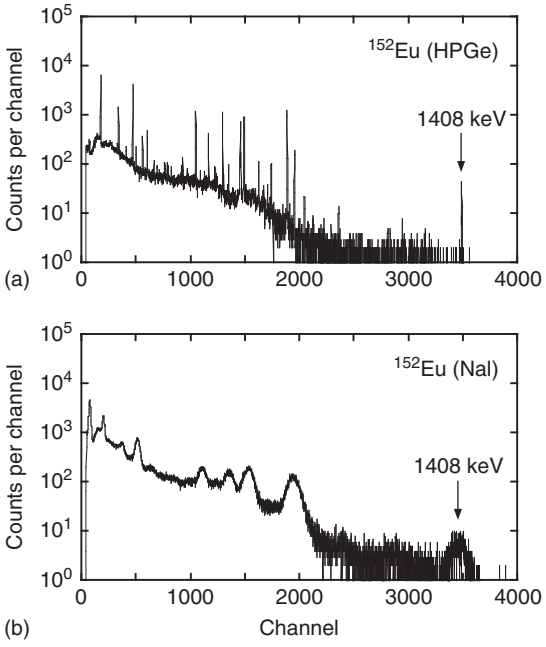

Figure 4.19 Pulse height spectra of γ-rays from a ^{152}Eu source, measured by using a (a) HPGe detector, and (b) NaI(Tl) detector. This particular γ-ray source emits photons of many discrete energies that are listed in Table 4.6. Far more peaks are visible in the top compared to the bottom spectrum, demonstrating the superior energy resolution of germanium detectors compared to scintillators. (Courtesy of Richard Longland.)

make germanium detectors sometimes less suitable for measurements in which the precise arrival time difference of two events is of interest.

4.4.3 Scintillation Detectors

Radiation incident on a scintillator deposits energy in the active volume and thereby excites atoms and molecules. The atoms de-excite mainly by prompt emission (within $\approx 10^{-8}$ s) of light, but delayed emission may also occur if some excited states are metastable. These processes are referred to as *fluorescence* and *phosphorescence*, respectively. The light strikes a photosensitive surface (photocathode), releasing at most one photoelectron per incident photon. These secondary electrons are accelerated and multiplied through a series of electrodes, called *dynodes*. They are finally collected on the anode and form the output pulse of the photomultiplier tube. These processes are shown in Figure 4.21. Scintillator detectors must have a high probability for converting absorbed energy into fluorescent light. They must be transparent to their own light, and the light emission spectrum has to be consistent with the response of the

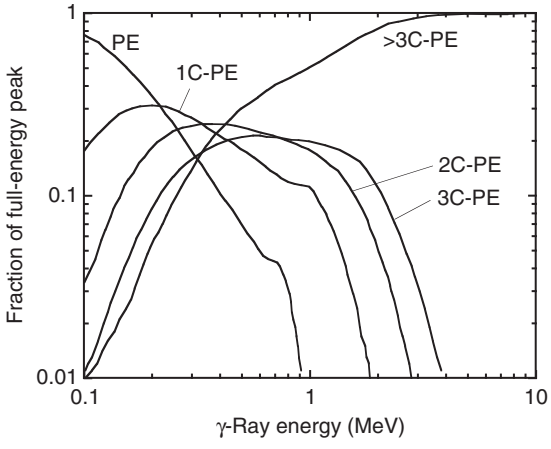

Figure 4.20 Fraction of full-energy peak contributed by different interaction mechanisms. The results are obtained from Monte Carlo simulations of photon interactions in a germanium detector with a crystal volume of 582 cm^3. The labels refer to: photoelectric event only (PE); single Compton scatter followed by photoelectric absorption (1C-PE); two successive Compton scatters followed by photoelectric absorption (2C-PR); three successive Compton scatters followed by photoelectric absorption (3C-PR); more than three successive Compton scatters followed by photoelectric absorption (>3C-PR). The latter contribution dominates for photon energies above 1 MeV. (Courtesy of Chris Howard.)

photomultiplier. For many scintillators, the light output, and hence the amplitude of the electrical output signal, is nearly proportional to the absorbed energy. Therefore, scintillators are suitable as devices for energy measurements, although their energy resolution and linearity is far inferior compared to semiconductor detectors (Figure 4.19). On the other hand, scintillators have certain advantages over semiconductors. First, they have fast response and recovery times and hence are frequently used if the measurement of the time differences between two events is of interest. Second, scintillators can be produced in a variety of sizes and shapes.

For any scintillator, a significant fraction of the light emitted from the track of the ionizing radiation must be collected. However, many light photons are reflected one or more times at the scintillator surface before reaching the photomultiplier tube. If the angle of incidence of the light is less than a certain value (called the *critical angle*), then only partial reflection takes place and some light will escape from the surface. For a given scintillator shape, the fraction of light lost will in general depend on the location of the radiation track with respect to the photomultiplier tube. The uniformity of the light collection determines the variation in signal pulse amplitude and thus the energy resolution of the scintillator. Therefore, scintillator crystals are usually surrounded by a reflecting surface (e.g., paint, powder, or foil) to recapture some of the escaping light. In certain instances, light collection may also be improved by viewing the scintillator with more than one photomultiplier tube. On the other hand, any internal reflection

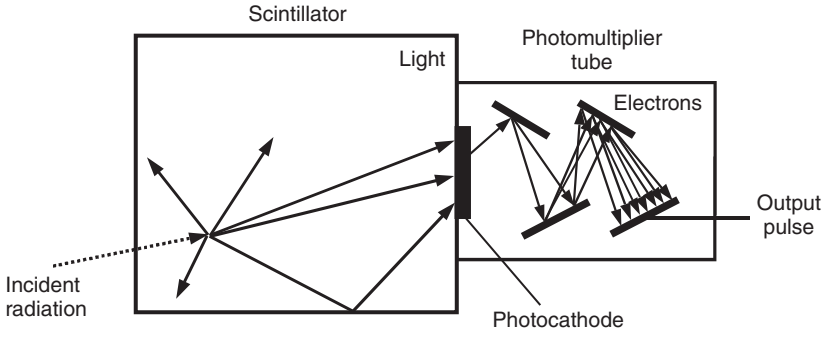

Figure 4.21 Schematic diagram of a scintillation detector. Incident radiation produces light in the scintillator material. The light strikes the photocathode and the few emitted secondary electrons are multiplied in the photomultiplier tube by a series of dynodes. The output pulse is extracted from the anode.

must be minimized at the interface between scintillator and the glass end window of the photomultiplier tube. This is usually achieved by using silicon oil of high viscosity as an optical coupling fluid. Furthermore, scintillation detectors must be shielded from room light.

Many different types of scintillators in solid, liquid, or gaseous form are used in radiation detection studies. Here, we will focus on inorganic scintillators for photon detection and organic scintillators for counting charged particles and fast neutrons.

4.4.3.1 Inorganic Scintillator Photon Detectors

The most common inorganic scintillators are single crystals of alkali halides, such a NaI. A polycrystalline scintillator would cause light reflections and absorptions at crystal surfaces and thus a single crystal is needed to achieve light transparency. To increase the probability for light emission and to reduce self-absorption of light, small amounts of impurities, called *activators*, are added to the crystal, with thallium being a common choice. For NaI(Tl), the high atomic number of thallium ($Z_{Tl} = 53$) results in a larger γ-ray efficiency compared to germanium detectors ($Z_{Ge} = 32$). Therefore, inorganic scintillators are preferred in certain types of experiments, even though they have an inferior energy resolution (Figure 4.19b). A disadvantage of NaI(Tl) is the fast crystal degradation in the presence of moisture (hygroscopy). Consequently, these scintillators must be contained in air tight protective closures.

The energy resolution of NaI(Tl) detectors is customarily quoted at an energy of 662 keV (as provided by a ^{137}Cs source). For smaller cylindrical detectors, resolutions of 6–7% can be achieved, while for more complicated crystal shapes the light collection is less uniform and the energy resolution becomes worse.

Two pure inorganic scintillators, neither of which require the presence of an activator element to promote the scintillation process, are bismuth germanate ($Bi_4Ge_3O_{12}$ or BGO) and barium fluoride (BaF_2). The very high atomic number of

bismuth ($Z_{Bi} = 83$) in the BGO material has major advantages for the detection of γ-rays above 10 MeV energy compared to other detector types, although the energy and time resolution of BGO detectors is inferior compared to NaI(Tl). The scintillation light of barium fluoride contains a very fast component with a decay time of less than 1 ns, which is smaller than decay times achieved even by the fastest organic scintillators. Therefore, BaF_2 detectors are attractive for applications where large efficiencies and fast timing are required, for example, for the time-of-flight technique in neutron-capture studies (Section 4.6.3).

4.4.3.2 Organic Scintillator Charged-Particle and Neutron Detectors

Organic scintillators consist of aromatic hydrocarbon compounds that contain benzene-ring structures. Their most outstanding feature is a very rapid signal pulse decay time of about 1–2 ns. They can be used in many physical forms, such as liquid or solid solutions, without loss of their scintillating properties. The most widely used organic radiation detectors are organic scintillators in a solid plastic solvent, called *plastic scintillators*. These are easily shaped and fabricated to desired forms. Plastic scintillators are produced as sheets, blocks, cylinders, and thin films of a few micrograms per centimeter square thickness. They are rugged and resistant to lower alcohols, but not to acetone and body acids and, therefore, must be handled with care. Liquid solutions of organic scintillators in an organic solvent, called *liquid scintillators*, are also widely used. They have the advantage that they can be loaded easily with certain materials to increase their efficiency for specific applications. Liquid scintillators are, however, very sensitive to impurities in the solvent.

It is sometimes of advantage if the scintillator is not directly coupled to the photomultiplier tube. This may be, for example, because of geometrical considerations or an unusual shape of the scintillator. The coupling can then be achieved using a transparent solid with a high refractive index, such as lucite, which acts as a guide for the scintillation light and hence is called a *light guide*. In principle, a light guide should transmit all the light that enters at its input but in practice some light loss will occur. Alternatively, optical fibers may be used as light guides, allowing for a flexible connection between scintillator and photomultiplier tube (Longland *et al.*, 2006).

Organic scintillators are not suitable as high-resolution γ-ray spectrometers because their small atomic number results in greatly reduced γ-ray interaction probabilities for photoelectric effect and pair production. Recall, that either of these processes has to occur besides Compton scattering to contribute to the full-energy peak count rate. Gamma-ray pulse height spectra of organic scintillators show pronounced Compton edges, but virtually no full-energy peaks. Organic scintillators are very useful for the detection of γ-rays when fast timing rather than pulse height resolution is of primary interest, such as in time-of-flight measurements of neutron-capture reactions (Section 4.6.3).

Figure 4.22 shows a room background spectrum measured with a plastic scintillator detector. The counter is viewed by a single photomultiplier tube. The surfaces of plastic scintillators are highly polished to increase internal

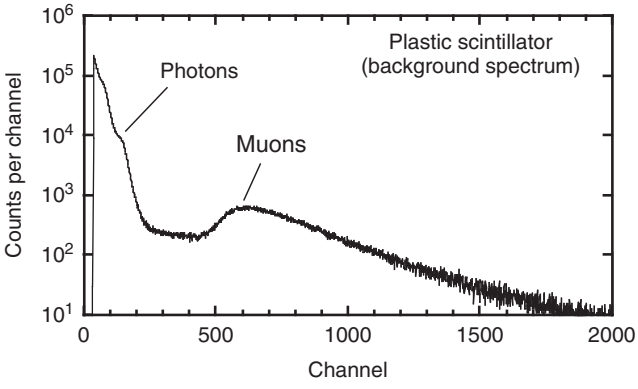

Figure 4.22 Room background spectrum measured with a plastic scintillator detector over a period of 14 h at sea level. The detector dimensions for the length, width, and thickness are 30 cm, 20 cm, and 5 cm, respectively. Compton edges of photons dominate the spectrum at low pulse heights, while the broad peak at larger pulse heights is caused by cosmic-ray muons that deposit a small fraction of their energy traversing the scintillator. From Longland *et al.* (2006).

reflection. The scintillator was wrapped first with aluminum foil to increase external reflection and then with black tape to provide a light-tight layer. A thin layer of air, having a small refractive index, between scintillator and aluminum foil also increases internal reflection. The spectrum shown was measured over a period of 14 h. The structures at low pulse heights represent the Compton edges of various room background γ-ray lines, while the broad peak at large pulse heights is caused by cosmic-ray muons that deposit a small fraction of their energy traversing the scintillator. Plastic scintillators are frequently used as muon anticoincidence shields around a primary detector (e.g., a germanium crystal). In such an arrangement, the output of the primary detector is accepted only if, during a certain time window, no coincident pulse is present at the output of the plastic scintillator. With this method, the background induced by cosmic rays in the primary detector can be reduced significantly (Section 4.7).

Liquid organic scintillator detectors are frequently employed for the detection of fast neutrons. Incident neutrons elastically scatter on the hydrogen contained in the active detector volume. In each scattering process, a neutron transfers energy to a recoil proton. The latter particle, in turn, is detected in the scintillator like any other energetic proton as it slows down in the active volume. Depending on the scattering angle, the transferred energy can range between zero and the total incident neutron energy. Furthermore, for incident neutron energies below 10 MeV, the elastic scattering from hydrogen is nearly isotropic. As a result, the energy distribution of the recoil protons, and hence the detector response function, should have a rectangular shape. In reality, several factors distort this simple rectangular distribution (Knoll, 1989). Some organic scintillators consist of special liquids that have the characteristic of producing different pulse shapes in response to different types of incident radiation. For example, a scintillator loaded with NE213 will

give rise to different pulse shapes for neutrons and γ-rays (Lynch, 1975). Based on the measured pulse shape differences, events from various radiation types can be distinguished electronically. This procedure is referred to as *pulse shape discrimination*. It allows for a substantial reduction of an unwanted γ-ray background in the detection of fast neutrons. The efficiency of liquid scintillator detectors for MeV neutrons can be as high as 50%.

4.4.4 Proportional Counters

A proportional counter consists of a vessel with conducting walls, acting as a cathode, and an anode (e.g., a metal wire) located inside the vessel. The vessel is filled with a suitable gas and a large positive voltage is applied to the anode. Incident radiation deposits energy in the counter gas and thereby creates a certain number of electron–ion pairs. For most gases, on average about one electron–ion pair is created per 30 eV of energy lost. The mean number of ion pairs created depends then on the energy deposited by the incident radiation quantum in the gas. The electrons and ions are accelerated toward the anode and cathode, respectively. If the electric field strength is sufficiently large, the primary electrons are accelerated toward the anode to energies at which they are also capable of ionizing gas molecules in the detector. The created secondary electrons, in turn, are also accelerated and give rise to still more ionization and so on. The result is an ionization avalanche, with a total number of electron–ion pairs that is directly proportional to the number of primary electron–ion pairs.

A frequently used counter gas is a mixture of 90% Ar and 10% CH_4 (methane). The excited Ar ions in the avalanche de-excite by emission of visible or ultraviolet photons capable of ionizing the cathode and causing further avalanches. This effect is undesirable since it leads to a loss of proportionality. The methane molecules act as a quencher by absorbing the emitted photons and then by dissipating this energy through dissociation or elastic collisions. With such a gas mixture, the factor of proportionality, or multiplication factor, can be as high as 10^6. The gas is usually at atmospheric pressure, but higher pressures are sometimes used to increase the detection efficiency. A potential problem is the relatively large number of quencher molecules depleted in each detected event, causing changes in the operational characteristics after a certain total number of events has been observed. This problem can be avoided by using a continuous gas flow instead of a sealed vessel.

Proportional counters are used for detecting charged particles and low-energy X-rays. They are less useful for detecting γ-rays since the probability of interaction between a photon and the detector gas is very small. Proportional counters can also be used for neutron detection by choosing a fill gas with a large cross section for a neutron-induced reaction. The most frequently used fill gases for converting incident neutrons to directly detectable charged particles are $^{10}BF_3$ and ^3He. These take advantage of the reactions $^{10}B(n,\alpha)^7Li$ and $^3He(n,p)^3H$, respectively. If slow neutrons are incident on such a detector, the neutron energy is negligible

compared to the energy release per reaction. Therefore, the total energy imparted to the charged reaction products (^{7}Li $+\alpha$ or ^{3}H + p) for each event is equal to the Q-value, while any information about the incident neutron energy is lost.

4.4.5 Microchannel Plate Detectors

Microchannel plates consist of a lead glass plate with a large number ($\approx 10^7$) of microscopic channels, typically 10–50 μm in diameter, oriented parallel to each other (Wiza, 1979). The inner surfaces of the channels are treated so as to act as secondary electron emitters. The front and rear surfaces of the plate are coated with a metallic alloy, such as nichrome ($Ni_7Cr_2Fe_3$), and act as electrodes so that a voltage can be applied along the length of the channels. This device has a direct sensitivity for detecting charged particles (electrons, ions) and energetic photons. A radiation quantum incident on the front face enters one of the microchannels and produces secondary electrons upon impact with the channel wall. The secondary electrons are accelerated along the channel until they eventually strike the wall again, releasing further electrons, and so on. Typical electron multiplication factors amount to $\approx 10^4$ for a single microchannel plate. This avalanche of secondary electrons is collected at the anode and results in a large output pulse. Each microchannel acts as an independent electron multiplier. Several plates may be used together to provide a higher overall gain. In this case, the microchannels are oriented at an angle with respect to the plate surface and to each other in order to reduce troublesome feedback effects from positive ions that occasionally form in the channels and that drift back to the plate front face. In this "chevron" geometry, the ions are made to strike the channel wall before their energy is high enough to create secondary electrons.

Microchannel plate detectors are not useful for energy measurements because relatively few secondary electrons are emitted upon impact of the incident radiation. Their main advantage is an excellent timing property. The total transit time of the secondary electrons through a channel is only a few nanoseconds. The timing performance depends on the spread in transit time and amounts to only $\approx$ 100 ps, a value that is considerably smaller compared to the fastest plastic scintillators. Microchannel plate detectors are very robust and have been used in experiments with count rates of up to $\approx 10^7$ s^{-1} (Mosher *et al.*, 2001). Their intrinsic efficiency varies according to the energy and type of the incident radiation (Wiza, 1979). For ions with masses of $A = 3$–16 and energies of $E = 0.3$–10 MeV, measured intrinsic efficiencies are 65–90% (Mosher *et al.*, 2001).

4.5 Nuclear Spectroscopy

The science and study of spectra is called *spectroscopy*. We will be mainly concerned with detector pulse height spectra induced by nuclear radiation. Most

important is the analysis of relatively sharp peaks in the spectrum. The energy of a discrete line corresponds frequently to the energy difference between the initial and final nuclear states involved in the transition and thus reflects the origin of the measured radiation. The intensity of a discrete line is proportional to the number of decaying nuclear states and hence allows for the determination of nuclear cross sections. The quantitative interpretation of pulse height spectra requires the knowledge of certain detector properties. First, the signal pulse height (or channel number) has to be calibrated and expressed in terms of the radiation energy. Second, the measured peak intensity needs to be corrected for the detector efficiency. These procedures are referred to as *energy and efficiency calibrations*. In the following, we will discuss some typical experimental situations encountered in charged particle, γ-ray, and neutron spectroscopy.

4.5.1 Charged-Particle Spectroscopy

4.5.1.1 Energy Calibrations

Consider first a radioactive source that emits charged particles. The most common radioactive charged-particle sources emit α-particles since long-lived proton emitting sources do not exist. Suppose further that an α-particle source is placed at some distance from a charged-particle detector, such as a silicon counter. The α-particles from the nuclear source are emitted with discrete energies. If the thickness of the active detector volume is larger than the α-particle range ($R < 100$ μm for $E_\alpha < 10$ MeV; Figure 4.7) and since processes that backscatter the incident particle or otherwise result in partial energy deposition are usually negligible, the incident radiation will deposit its entire energy in the silicon detector. As a result, discrete peaks of nearly Gaussian shape appear in the pulse height spectrum, each corresponding to an α-particle group of discrete energy (Figure 4.23). If the energies of the α-particles are well known from previous measurements, the horizontal axis of the pulse height spectrum can be calibrated by relating channel numbers C_i to energies E_i. As already pointed out, semiconductor detectors respond nearly linearly to the energy of the incident radiation and, therefore, a useful expression for the calibration is

$$E_i = aC_i + b \tag{4.45}$$

where a and b are empirical constants. Properties of some α-particle calibration sources are listed in Table 4.5. For precise energy calibrations, the α-particle energy loss in the detector dead layer may need to be taken into account. The thickness of the dead layer can be determined by measuring the energy of a monoenergetic charged-particle group at several different angles of incidence (Knoll, 1989). The energy loss in the source itself may also need to be considered. Most α-particle calibration sources are prepared by depositing a thin layer of the isotope on the surface of a backing to minimize energy losses and α-particle absorption. These sources are also protected with a very thin layer of foil.

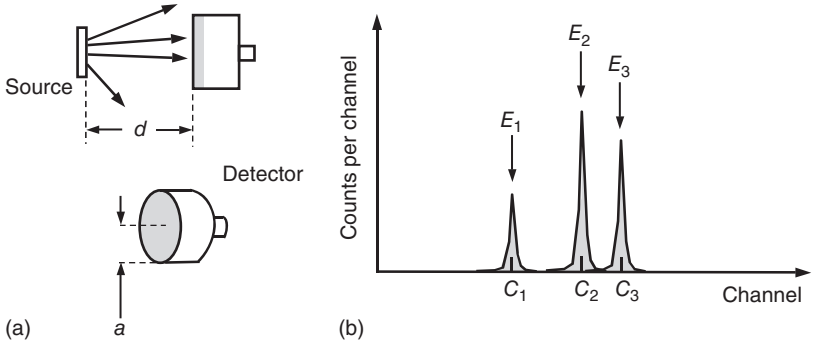

Figure 4.23 Measurement of charged particles emitted by an α-particle source. (a) Setup showing the source and the charged-particle detector; *d* and *a* are the source–detector distance and the radius of the active detector area, respectively. (b) Typical pulse height spectrum showing peaks at discrete channel numbers. An energy calibration of the spectrum is performed by relating the discrete channel numbers to known energies of the α-particle groups emitted by the source.

It must be emphasized that small differences in pulse heights from different incident light charged particles (e.g., protons and α-particles) of the same energy have been observed in semiconductor detectors (Knoll, 1989). These differences are on the order of 1% (≈30 keV for 3 MeV total deposited energy). Therefore, the pulse height spectrum should be calibrated, if possible, using the same species of particles as is emitted in the actual reaction measurement. For heavy ions, the pulse height differences are considerably larger. The effect is referred to as the *pulse height defect*.

4.5.1.2 **Efficiencies**

The intrinsic efficiency of silicon counters for detecting charged particles is close to unity and, therefore, the peak efficiency is given by the solid angle Ω subtended by the detector. The efficiency can be measured using a calibration source of well-known activity. Assuming that the source emits radiation isotropically and that no attenuation takes place between source and detector, we obtain for the peak efficiency (see Eqs. (4.43) and (4.44))

$$\eta_{\text{peak}} = \frac{\Omega}{4\pi} = \frac{\mathcal{N}_{\text{peak}}}{\mathcal{N}_0} = \frac{\mathcal{N}_{\text{peak}}}{AtB} \tag{4.46}$$

where the solid angle Ω is in units of steradians and $\mathcal{N}_{\text{peak}}$ is the net area of the full-energy peak; A, t, and B are the activity of the source at the time of the measurement, the measuring time, and the branching ratio of the radiation, respectively. Branching ratios, defined as the fraction of a specific transition per nuclear decay, for some common calibration sources are listed in Table 4.5. As a test of consistency, it is often useful to estimate the efficiency without relying on the activity of radioactive sources. For the common case of a point-like source and a circular detector positioned with its face normal to the source–detector axis,

Table 4.5 Properties of some α-particle calibration sources.

Isotope	Half-life[a]	Energies (keV)	Branching (%)
^{148}Gd	70.9(10) y	3182.68(2)[b]	100.0[b]
^{230}Th	75.4(3) ky	4620.5(15)[b]	23.4(1)[b]
		4687.0(15)[b]	76.3(3)[b]
^{241}Am	432.6(6) y	5442.86(12)[c]	13.23(10)[c]
		5485.56(12)[c]	84.45(10)[c]
^{242}Cm	162.86(8)[c] d	6069.37(9)[c]	25.94(7)[c]
		6112.72(8)[c]	74.06(7)[c]

The error is given in parenthesis and refers to the last significant digit(s).
Sources: [a] Wang *et al.* (2012). [b] Nichols (1996). [c] Bé *et al.* (2013).

the peak efficiency is given by (Knoll, 1989)

$$\eta_{\text{peak}} = \frac{1}{2}\left(1 - \frac{d}{\sqrt{d^2 + a^2}}\right) \tag{4.47}$$

where d and a are the distance between source and detector and the detector radius, respectively. If the distance d is large compared to the radius, $d \gg a$, the peak efficiency reduces to

$$\eta_{\text{peak}} \approx \frac{\pi a^2}{4\pi d^2} = \frac{a^2}{4d^2} \tag{4.48}$$

4.5.1.3 Elastic Scattering Studies

An example of a setup for the study of elastic scattering is shown in Figure 4.24a. A proton beam of energy $E_{\text{p}} = 440$ keV is incident on a transmission target consisting of a thin MgO layer evaporated onto a thin carbon foil. A silicon detector with a resolution of ≈ 10 keV, positioned at an angle of $\theta = 155°$ with respect to the beam direction, is used for detecting elastically scattered protons. The measured pulse height spectrum is shown in Figure 4.24b. Three peaks are observed in the spectrum, corresponding to elastic scattering from Mg, O, and C, the three elements present in the target.

The observed peak centroids can be used for calibrating the proton energy in the spectrum if the target is relatively thin so that energy loss effects are negligible. In this case, the widths of the peaks resulting from proton scattering on Mg and O are given by the detector resolution. The peak centroids correspond to the energy $E_{\text{p}'}$ of the elastically scattered protons which, for a given bombarding energy E_{p} and detector angle θ, are determined by the kinematics of the scattering process (Appendix C.1).

In general, however, the target thickness has to be taken into account and the widths and centroids of the measured peaks are influenced both by the proton energy loss in the target and the detector resolution. The energy calculated from kinematics only applies to those protons that are elastically scattered from the first target layers. For protons scattered from Mg or O deeper inside the target, not only

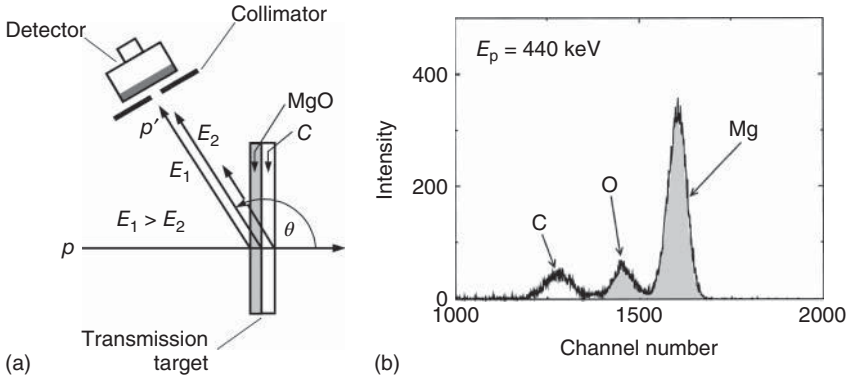

Figure 4.24 Typical elastic scattering study. (a) Setup showing a proton beam, a MgO transmission target evaporated on a thin carbon backing, and a particle detector mounted at a back-angle. Detected protons scattered from the backside of the target have a smaller energy (E_2) than those scattered from the front side (E_1) because of energy loss effects. (b) Measured spectrum of elastically scattered protons at an incident proton energy of $E_p = 440$ keV. The peaks correspond to protons scattered from the target (Mg and O) and the backing (C). Data adopted from Powell *et al.* (1999).

the energy loss of the projectiles has to be considered, but that of the scattered protons on their path through the target as well. The location of the carbon elastic scattering peak is also influenced by energy loss. To reach the carbon layer, the projectiles have to traverse the MgO target, while the scattered protons also lose a fraction of their energy moving through the target on their way to the detector.

The measured peak areas may be used to calculate the differential cross sections of elastic scattering if the number of target nuclei (or the target thickness) and the detector efficiency are known. Expressions relating measured yields to cross sections are given in Section 4.8. At sufficiently low bombarding energies, the cross section will be dominated by Coulomb scattering. This circumstance is frequently utilized to determine the number of target nuclei from the measured peak intensity and the calculated Rutherford cross section (see Eq. (4.138)). At higher energies, resonances may contribute to the elastic scattering process. In this case, the measured elastic scattering cross section provides information on the resonance parameters, such as resonance energies, partial widths, and quantum numbers (Section 2.5).

4.5.1.4 Nuclear Reaction Studies

Figure 4.25a shows an experimental arrangement for measuring the reaction $^{31}P(p,\alpha)^{28}Si$ at a bombarding energy of $E_p = 390$ keV. Cross sections of astrophysical interest at low energies are usually small. The charged-particle detector for measuring the reaction α-particles has to cover as large a solid angle as possible in order to maximize the count rate. The active area of the silicon detector and the distance between detector and target are 450 mm^2 and 5 cm, respectively. The energy resolution of the detector amounts to ≈ 20 keV. A directly water-cooled

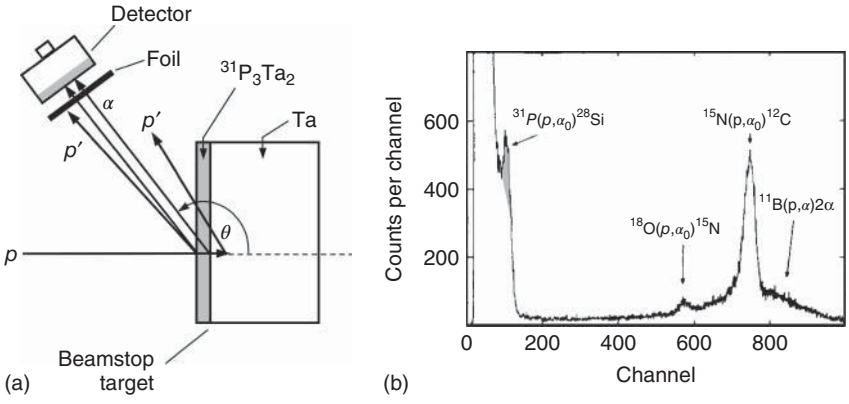

Figure 4.25 Study of the ^{31}P(p,α)^{28}Si reaction. (a) Setup showing the proton beam, the beamstop target consisting of ^{31}P implanted into Ta, and the particle detector covered by a foil to reduce the large number of elastically scattered protons reaching the detector. (b) Measured pulse height spectrum at a bombarding energy of E_p = 390 keV. The α-particle peak of interest, arising from a resonance in ^{31}P(p,α)^{28}Si, occurs at relatively small pulse heights in a region dominated by protons leaking through the foil (caused by foil thickness inhomogeneities). Alpha-particles originating from (p,α) reactions on the contaminants ^{11}B, ^{15}N, and ^{18}O are visible at higher energies. Data adopted from Iliadis *et al.* (1991).

beamstop target is used to allow for high proton beam currents of several 100 μA. The target is produced by implanting ^{31}P ions into a tantalum sheet and consists of a ^{31}P–Ta layer with a stoichiometry of 3 : 2 (Table 4.3). For a given beam energy (E_p = 390 keV) and detector angle (θ = 145°), the energy of the emitted α-particles is determined by the kinematics of the nuclear reaction (Appendix C.1) and amounts to ≈ 2 MeV.

Since the beamstop target consists of a high-Z material (tantalum), the number of elastically scattered protons becomes very large (> 10^6 s^{-1}). The protons are scattered both from the relatively thin ^{31}P–Ta target layer as well as the thick tantalum backing. Hence, their energies range from a maximum of ≈ 350 keV (protons scattered by the first target layers without energy loss) down to zero (protons scattered inside the tantalum backing and losing energy on the path to the detector). As a result, the detector count rate in the region of the expected reaction α-particles would be overwhelmed by the pileup of signals caused by the unwanted scattered protons. Therefore, a foil is placed in front of the charged-particle detector sufficiently thick to stop the elastically scattered protons, but at the same time thin enough to transmit the reaction α-particles.

The measured pulse height spectrum is shown in Figure 4.25b. The α-particles from the ^{31}P(p,α)^{28}Si reaction have lost a significant fraction of their energy in the foil and are observed in the first part of the spectrum (E_α ≈ 0.5 MeV). Furthermore, the α-particle peak is significantly broadened because of energy straggling in the foil (ΔE ≈ 100 keV). The steep background at low energies is mainly caused by elastically scattered protons leaking through the foil. At higher energies, the

spectrum displays contributions from the (p,α) reactions on ^{11}B, ^{15}N, and ^{18}O contaminants in the target and backing (Section 4.3.3). These contaminants give rise to discrete peaks, except in the case of the ^{11}B(p,α)2α reaction, which emits three particles in the exit channel and thus produces a continuous background.

The total number of induced reactions, $\mathcal{N}_R$, can be calculated from the measured peak intensity using an expression similar to Eq. (4.46). In general, the intensity of the reaction products is not isotropic (Appendix D) and, therefore, the angular correlation W has to be taken into account. One finds

$$\mathcal{N}_R = \frac{\mathcal{N}_{\text{peak}}}{\eta_{\text{peak}} BW} \tag{4.49}$$

The quantities η_{peak} and W are usually obtained at a laboratory detection angle of θ and have to be expressed in the center-of-mass system (Appendix C.2). The branching ratio, B, is now defined as the fraction of a specific transition per nuclear reaction.

4.5.2 γ-Ray Spectroscopy

4.5.2.1 Response Function

The response of γ-ray detectors to incident radiation is more complicated compared to charged-particle detectors. As already noted, γ-rays interact with matter via the photoelectric effect, Compton scattering and pair production (Section 4.2.2). The influence of these effects on the measured pulse height distribution is shown in Figure 4.26. In the following, we will assume that monoenergetic photons of energy E_γ are incident on the detector.

In case (a), an incident photon undergoes photoelectric absorption. The emitted photoelectron travels typically a distance of at most a few millimeters and loses

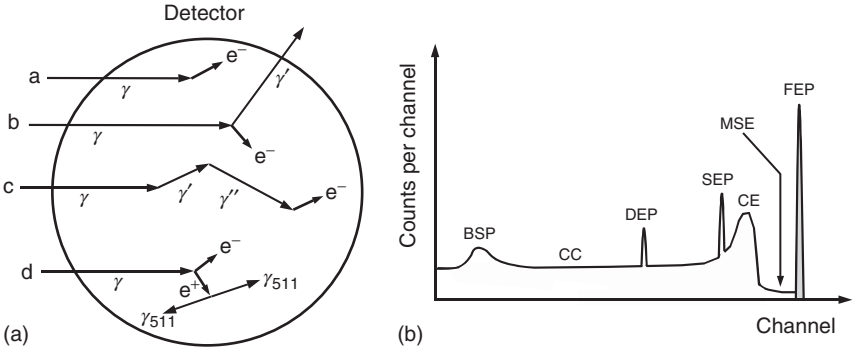

Figure 4.26 Response of a γ-ray detector to monoenergetic incident radiation. (a) Representation of different photon histories. (b) Pulse height spectrum; the meanings of the labels are: full-energy peak (FEP), multiple-site events (MSE), Compton edge (CE), single-escape peak (SEP), double escape peak (DEP), Compton continuum (CC) and back-scattering peak (BSP).

its energy through ionization and excitation of atoms in the active detector volume and through the emission of bremsstrahlung. For a sufficiently large active volume, the entire energy of the photoelectron is absorbed in the detector and, therefore, the resulting pulse height appears in the region of the full-energy peak (FEP), corresponding to a photon energy of E_γ.

In case (b), the incident photon undergoes Compton scattering. The scattered photon escapes from the active volume and thus only a fraction of the incident photon energy is deposited in the detector. The precise energy transferred to the recoil electron depends on the scattering angle. All scattering angles are possible and, therefore, the energy distribution of the recoil electrons gives rise to the Compton continuum (CC). The maximum possible value of $K_e^{\max}$, that is, the Compton edge (CE), corresponds to a photon-scattering angle of $\theta = 180^\circ$ (Section 4.2.2). The continuous Compton background is an unwanted contribution to the pulse height spectrum. It reduces the signal-to-noise ratio for the detection of weak discrete peaks and it also makes the interpretation of complex γ-ray spectra that result from incident photons of different energies more difficult.

In case (c), the incident photon is Compton scattered several times at different locations in the active volume until eventually photoabsorption occurs. The duration of this more complex history amounts to < 1 ns, a value that is smaller than the inherent response time of present day γ-ray detectors. Consequently, the different Compton scattering events and the final photoabsorption occur essentially in time coincidence and exactly the same total energy is deposited in the detector as if the incident photon had undergone a single photoelectric absorption. Such events appear then in the region of the full-energy peak. For incident photon energies above a few 100 keV, most events in the full-energy peak are caused by such multiple scattering histories (Figure 4.20). It has been pointed out in Section 4.2.2 (see also Figure 4.11) that there is an energy gap between the full-energy peak and the Compton edge. In measurements, this gap is partially filled in by multiple Compton scattering events (MSE) that are followed by photon escape.

In case (d), an incident photon with an energy of $E_\gamma > 2m_e c^2$ undergoes pair production. The created electron and positron lose all their kinetic energy in the active detector volume. Subsequently, the positron will annihilate with another electron and two photons, each of 511 keV energy, are produced. Again, the annihilation radiation appears virtually in time coincidence with the original pair production event. If both 511 keV photons are absorbed by the detector (e.g., via photoelectric effect), then the resulting pulse height will appear in the region of the full-energy peak at E_γ. If only one 511 keV photon is absorbed, while the other one escapes detection, then the resulting pulse height will give rise to a discrete peak at an energy of $E_\gamma - 511\,\text{keV}$ called the *single-escape peak* (SEP). If both 511 keV photons escape from the detector, a discrete peak appears at an energy of $E_\gamma - 1022\,\text{keV}$, called the *double-escape peak* (DEP). More complicated histories involving Compton scattering of the annihilation quanta occur as well. Such events contribute to a continuum in the pulse height spectrum between the double-escape and full-energy peaks.

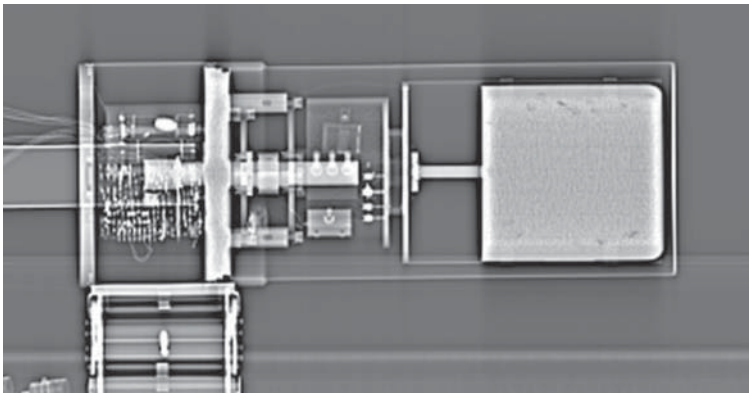

Figure 4.27 Computed-tomography (CT) image of a p-type closed end bulletized high-purity germanium detector, obtained using X-rays of 140 kVp and 350 mAs. Notice the slight misalignment of the crystal inside the end cap. (Reprinted from Carson *et al.* (2010). Copyright (2010), with permission from Elsevier.)

Finally, a broad peak is frequently observed in pulse height spectra at an energy of ≈ 200–250 keV. It is caused by photons that Compton scatter in material surrounding the active volume before detection. The peak is referred to as *backscattering peak* (BSP).

The response of a real γ-ray detector will depend on the size, shape, and composition of the active volume. It can be simulated theoretically using Monte Carlo calculations that track numerically the histories of many different events taking place in the detector. For accurate simulations, however, the exact geometry of the active volume must be known. For example, Figure 4.27 shows a computed-tomography (CT) image of a germanium detector. The precise crystal diameter, length, bulletization of the edges, and so on, can be extracted from such images and can be used in the simulations. For more images, see Carson *et al.* (2010).

4.5.2.2 Energy Calibrations

Full-energy peaks are of major interest in γ-ray spectroscopy studies. They correspond to the full-energy deposition of the incident photon energy and, therefore, their location in the spectrum is not influenced by any photon energy losses. The pulse heights in a γ-ray spectrum can be calibrated using absolute energy standards. Some useful γ-ray energy standards are provided in Table 4.6. The errors of the calibration energies are less than 0.001%. The listed radioactive sources are all commercially available and cover an energy range up to ≈ 3.5 MeV. Furthermore, the two γ-ray lines from ^{40}K and ^{208}Tl (1460.8 keV and 2614.5 keV, respectively) are the most prominent room background peaks in γ-ray spectra and thus provide a convenient internal calibration without using radioactive sources. The energy range may be extended up to ≈ 5 MeV using the radioisotope ^{66}Ga, although its half-life is rather short ($T_{1/2} = 9.5$ h). Therefore, the region above 3.5 MeV is frequently calibrated using γ-rays emitted in nuclear reactions. These energies can be

Table 4.6 Properties of common γ-ray calibration sources.

Source	Half-life	Energy (keV)	Branching ratio[a] (%)
^{152}Eu	13.522(16) y	121.7817(3)	28.41(13)
		244.6974(8)	7.55(4)
		344.2785(12)	26.59(12)
		411.1165(12)	2.238(10)
		778.9045(24)	12.97(6)
		867.380(3)	4.243(23)
		1085.837(10)	10.13(6)
		1089.737(5)	1.73(1)
		1112.076(3)	13.41(6)
		1212.948(11)	1.416(9)
		1299.142(8)	1.633(9)
		1408.013(3)	20.85(8)
^{56}Co	77.236(26) d	846.7638(19)	99.9399(23)
		1037.8333(24)	14.03(5)
		1175.0878(22)	2.249(9)
		1238.2736(22)	66.41(16)
		1360.196(4)	4.280(13)
		1771.327(3)	15.45(4)
		2015.176(5)	3.017(14)
		2034.752(5)	7.741(13)
		2598.438(4)	16.96(4)
		3201.930(11)	3.203(13)
		3253.402(5)	7.87(3)
		3272.978(6)	1.855(9)
		3451.119(4)	0.942(6)
^{57}Co	271.80(5) d	122.06065(12)	85.51(6)
		136.47356(29)	10.71(15)
^{198}Au	2.6943(3) d	411.80205(17)	95.62(6)
^{137}Cs	30.05(8) y	661.657(3)	84.99(20)
^{54}Mn	312.13(3) d	834.838(5)	99.9746(11)
^{88}Y	106.626(21) d	898.036(4)	93.90(23)
		1836.052(13)	99.32(3)
^{60}Co	5.2711(8) y	1173.228(3)	99.85(3)
		1332.492(4)	99.9826(6)
^{22}Na	2.6029(8) y	1274.537(7)	99.94(13)
^{40}K		1460.822(6)	10.55(11)
^{208}Tl		2614.511(10)	99.755(4)

[a] γ-Ray yield (%) per disintegration. The error is given in parenthesis and refers to the last significant digit(s).
Source: Bé *et al.* (2013).

calculated precisely from the kinematics of the reaction (Appendix C.1) if certain quantities (such as the bombarding energy, the masses of projectile and target, and the detector angle) are well known. The resulting calibration energies are not as precisely determined as those from radioisotopes. One also has to be careful since

many γ-rays emitted in nuclear reactions are Doppler shifted (see Eq. (C.12)). If capture reactions (e.g., (p,γ) or (α,γ) reactions) are used for the energy calibration, it is of advantage to position the detector at an angle of $\theta = 90°$, where the Doppler shift is zero to first order. Sometimes it may be possible to use the single- and double-escape peaks for calibrations since their energies relative to the location E_γ of the corresponding full-energy peak are well known ($E_\gamma - m_e c^2$ and $E_\gamma - 2m_e c^2$, respectively). However, small systematic shifts in the location of the escape peaks have been observed. The deviations can amount to several 100 eV and seem to depend on the type and geometry of the detector (Endt *et al.*, 1990). This effect has to be considered if γ-ray energies of high precision are of interest.

When several energy calibration points have been established over the region of interest, a calibration curve relating energies to channel numbers can be derived from a least-squares fit. With germanium detectors it is frequently sufficient to represent the energy as a linear function of the channel. Deviations from linearity depend primarily on nonlinearities of the electronic amplifier–analyzer system and may amount to several hundred electron volts. It is sometimes even appropriate to use for a linear energy calibration only two well-known peaks with energies E_1 and E_2 and channel centroids C_1 and C_2,

$$E_i = aC_i + b = E_1 + \frac{E_2 - E_1}{C_2 - C_1}(C_i - C_1) \tag{4.50}$$

If higher precision is desired, the energy calibration can be obtained from a cubic least-squares fit. Higher order polynomials may be necessary if NaI(Tl) detectors are used since their response is far less linear compared to germanium detectors.

4.5.2.3 Efficiency Calibrations

Measurements of cross sections require knowledge of detection efficiencies. Furthermore, the accuracy of the derived cross sections depends directly on the uncertainty of the efficiencies. Full-energy peak efficiencies may be calculated with Monte Carlo procedures if the crystal dimensions and the geometry of the setup are precisely known. However, for germanium detectors this is rarely the case. Crystals are not standardized to any degree and, furthermore, crystal dimensions supplied by manufacturers have been found to be inaccurate by several millimeters (Helmer *et al.*, 2003). Also, long-term changes in the charge collection process can cause the detector efficiency to vary with time. Consequently, it is recommended that users perform their own efficiency measurements. The measurements of the efficiency and of the cross section should be carried out in the same geometry, that is, the same distance and orientation of the detector with respect to the source or target. The same argument applies to any γ-ray absorbing material between source or target and detector (e.g., the target holder). Such effects are expected to be most important at relatively low γ-ray energies (<1 MeV; Section 4.2.2).

Typically, detector efficiencies are needed for an energy range between $\approx$ 100 keV and $\approx$ 15 MeV. Since no single process covers this entire energy region,

γ-rays from several different processes have to be used. The peak efficiency is related to the full-energy peak intensity by Eq. (4.46). A reliable determination of detector efficiencies requires accurate knowledge of the γ-ray branching ratios, B, defined as the fraction of a specific γ-ray transition per nuclear decay. Several radioactive sources for which very precise branching ratios are known (with relative errors of < 1% for most transitions) are listed in Table 4.6. Especially useful are the radioisotopes ^{152}Eu and ^{56}Co, which cover the energy ranges of 0.1–1.4 and 0.8–3.5 MeV, respectively. For higher energies, efficiencies have to be obtained using γ-rays from nuclear reactions. If charged-particle beams are available, frequently used calibration standards are provided by the 655 and 992 keV resonances in ^{27}Al(p,γ)^{28}Si, covering the energy range of 1–11 MeV. The errors in the reported branching ratios are < 3% (Endt, 1990). At lower bombarding energies, the 293 and 327 keV resonances in the same reaction may be used, although the reported branching ratio errors are larger (< 10%; Iliadis *et al.*, 1990). The relevant data are summarized in Table 4.7. The 278 keV resonance in the ^{14}N(p,γ)^{15}O reaction is also useful in this respect. This particular resonance emits photons in the range of 0.8–7 MeV and has a simple γ-ray decay scheme, with almost all decays proceeding via cascades that consist of two γ-rays only. Since the number of photons for each transition in a given cascade is the same, the measured intensity ratio of the two γ-rays is equal to the ratio of the corresponding efficiencies. The branching ratio data and the relevant decay scheme are shown in Table 4.8 and Figure 4.28, respectively. Furthermore, the γ-ray emission from this resonance is isotropic ($J = 1/2$) and hence angular correlation effects are negligible (Appendix D). If thermal neutrons are available, precise γ-ray efficiencies can be obtained from the ^{14}N(n,γ)^{15}N capture reaction. The prompt γ-ray emission probabilities per neutron-capture event from this reaction are listed in Table 4.9.

The following strategy is frequently employed to determine a composite γ-ray efficiency curve. The data from radioactive calibration sources are analyzed and plotted first. Their well-known activity also provides a normalization of the absolute efficiency scale. In a subsequent step, the reaction data are analyzed. The resulting efficiencies from each reaction measurement are vertically adjusted until they agree with the radioactive source values in the overlap region. An efficiency curve obtained in this manner is shown in Figure 4.29a. In this case, a HPGe detector of 582 cm^3 volume is positioned at a distance of 1.6 cm between source or target and detector. It can be seen that the peak efficiency drops drastically with increasing energy, because both photoelectric absorption and Compton scattering become less likely at higher energies (Section 4.2.2).

Once the efficiency of a detector has been measured at several energies, a fit to the data can be performed to determine efficiency values between measured points by interpolation. Frequently used analytical fitting functions are polynomials, but more complicated functions are also in use (Debertin and Helmer, 1988).

The full-energy peak efficiency cannot be calculated analytically since it depends on the γ-ray energy in a complicated way. We already mentioned that Monte Carlo

Table 4.7 γ-Ray branching ratios (fraction of a specific transition per proton capture event) of low-energy resonances in $^{27}Al(p,\gamma)^{28}Si$.

E_r[a]:	293[d]	327[d]	655[e]	992[e]
E_{xf}[b]: E_{xi}[c]:	11867	11900	12216	12541
0				
1779			42.1(10)	76.4(4)
4618	60.4(14)	72.2(8)		4.09(12)
6276			4.5(2)	2.15(7)
6879			1.63(9)	0.70(2)
6889	12.4(8)	12.1(5)		0.294(9)
7381				0.187(6)
7416			1.82(10)	0.297(9)
7799				8.5(3)
7933			6.4(2)	3.96(12)
8259			1.60(9)	
8328			1.27(7)	
8413	5.9(4)			
8589		5.3(5)	3.36(13)	0.173(6)
9165	5.1(3)			0.147(5)
9316			2.09(9)	0.047(2)
9382			29.1(9)	
9417		2.8(2)		0.79(3)
9479				1.11(4)
9765	3.2(3)			0.195(7)
10182				0.085(3)
10209				0.146(5)
10311				0.061(3)
10376			0.52(3)	
10540	2.3(2)			
10596			1.39(7)	
10668				0.288(9)
10900			0.63(4)	
11195				0.089(3)
11265				0.082(3)

Branching ratios are given in percent. The error is given in parenthesis and refers to the last significant digit(s). [a] Resonance energy in keV. [b] Excitation energy of final state in keV. [c] Excitation energy of initial state in keV.
Sources: [d] Iliadis *et al.* (1990). [e] Endt *et al.* (1990).

techniques may be used to calculate individual photon histories. Although in the end peak efficiencies should be measured directly for the reasons given above, the Monte Carlo calculations are useful for estimating *relative* peak efficiencies. Uncertainties in crystal dimensions or interaction parameters (i.e., cross sections for photoelectric absorption, Compton scattering and pair production) have a comparatively small effect on these relative values. Therefore, Monte Carlo calculations can provide the shape of the peak efficiency curve and aid in the interpolation between calibration points. An interesting application of the Monte Carlo

Table 4.8 Branching ratios (%) of ^{15}O levels.

E_{xf}:	E_{xi}:	5183	5241	6176	6793	6859	7276	7556
0		100	100	100	100	<10	3.8(12)	1.52(3)
5183				<2.5	<3	<4	<4	17.44(10)
5241				<2.5	<3	100	96.2(12)	0.16(3)
6176					<7	<0.4	<2	58.13(20)
6793								22.75(20)

E_{xi} and E_{xf} denote the excitation energies (in keV) of the initial and final states, respectively, involved in the transition. See also Figure 4.28a. The error is given in parenthesis and refers to the last significant digit(s).
Sources: From Ajzenberg-Selove (1991), unless noted otherwise. Branching ratios for the level at $E_{xi} = 7556$ keV, corresponding to a resonance at $E_r^{lab} = 278$ keV in ^{14}N(p,γ)^{15}O, are from Runkle *et al.* (2005), Imbriani *et al.* (2005), Marta *et al.* (2011), and Art Champagne, private communication.

method to obtain very precise germanium detector efficiencies can be found in Helmer *et al.* (2003).

So far, we have only discussed the determination of full-energy peak efficiencies. There are situations where the precise knowledge of *total* efficiencies becomes also important. For example, total efficiencies are typically needed for estimating coincidence summing corrections for germanium detectors (see below) or coincidence efficiencies for $\gamma\gamma$-detection techniques (Section 4.7.3). In contrast to peak efficiencies, the calculation of total efficiencies is in principle straightforward. The probability that an incident photon traversing a path length x in the active volume is *not* detected, that is, does not undergo any interaction in the crystal, is given by $\overline{P} = \mathcal{N}/\mathcal{N}_0 = e^{-\mu x}$ (see Eq. (4.30)), where $\mathcal{N}$ and $\mathcal{N}_0$ denote the total number of transmitted and incident quanta, respectively. Equivalently, we may calculate the probability that this incident photon will undergo any interaction and deposit any energy in the crystal from $P = 1 - \overline{P} = 1 - e^{-\mu x}$. In general, the path length x will depend on the angle of photon emission with respect to the crystal. Therefore, the total efficiency can be found by integrating over the solid angle Ω subtended by the detector,

$$\eta_{\text{tot}} = \frac{1}{4\pi} \int (1 - e^{-\mu x})\, d\Omega \tag{4.51}$$

For the case of a cylindrical detector of radius R and length t, and a point source located on the detector axis at a distance d (Figure 4.30) we obtain (Debertin and Helmer, 1988)

$$\begin{aligned} \eta_{\text{tot}} = {} & \frac{1}{2} \int_0^{\theta_1} \left[1 - e^{-(\mu t/\cos\theta)}\right] \sin\theta\, d\theta \\ & + \frac{1}{2} \int_{\theta_1}^{\theta_2} \left[1 - e^{-(\mu R/\sin\theta) + (\mu d/\cos\theta)}\right] \sin\theta\, d\theta \end{aligned} \tag{4.52}$$

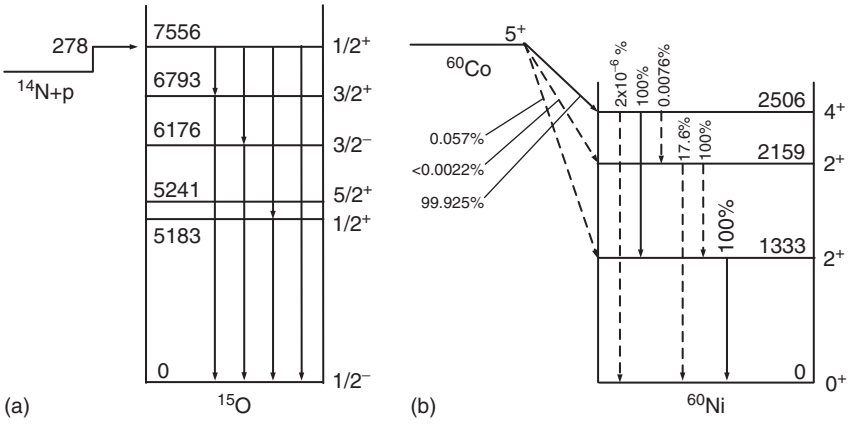

Figure 4.28 Energy level diagrams of (a) ^{15}O, and (b) ^{60}Ni. The γ-ray branching ratios of ^{15}O levels are presented in Table 4.8. The β-decay and γ-ray branching ratios for the ^{60}Co → ^{60}Ni decay are adopted from Firestone and Shirley (1996).

with $\theta_1 = \arctan[R/(d+t)]$ and $\theta_2 = \arctan(R/d)$. An unscattered photon emitted at an angle of θ_1 (as measured from the detector axis) passes through the detector backside, while an unscattered photon emitted at angles between θ_1 to θ_2 passes through the detector sides. The above integrals can be solved numerically.

Frequently, the detector crystal geometry is not a simple cylinder. For example, coaxial germanium detectors have an insensitive cylindrical core that reduces the calculated total efficiency. Or, sources may be placed inside annular NaI(Tl) detectors (Section 4.7.3) to maximize counting rates. In these cases, total efficiencies can be calculated by using more complicated analytical expressions (Longland *et al.*, 2006). Interactions in any absorbing material located between source or target and detector can additionally be taken into account by calculating the γ-ray attenuation. The total efficiency of a HPGe detector estimated in this manner is displayed in Figure 4.29b. The detector crystal has a length and diameter of 93 and 90 mm, respectively, and the insensitive core a length and diameter of 79 and 9 mm, respectively. The detector–source distance is 16 mm. The solid line is obtained from an analytical expression, while the diamonds represent the results of a Monte Carlo simulation. It can be seen that η_{tot} varies smoothly beyond a γ-ray energy of ≈ 3 MeV. The results from the analytical expression agree with those from the Monte Carlo calculation within 3% (Longland *et al.*, 2006).

The above considerations apply only to an ideal measuring geometry with no photon scattering in the surroundings of the detector. Photons that are originally emitted in a direction outside the solid angle of the detector could be scattered in the surrounding material and may thus reach the active detector volume. These photons will then contribute to the total efficiency (but not to the full-energy peak efficiency; see also Figure 4.14b). Although calculated values of η_{tot} are useful for estimates of *relative* total efficiencies, it is preferable to measure absolute

Table 4.9 γ-Ray emission probabilities per neutron-capture event from the $^{14}N(n,\gamma)^{15}N$ reaction induced by thermal neutrons.

E_γ (keV)	B (%)	E_γ (keV)	B (%)
1678	7.96(9)	5269	29.94(20)
1885	18.72(20)	5298	21.27(18)
2000	4.05(5)	5533	19.66(21)
2520	5.68(7)	5562	10.66(12)
2831	1.72(3)	6322	18.45(14)
3532	9.09(9)	7299	9.56(9)
3678	14.70(15)	8310	4.17(5)
4509	16.63(17)	10829	14.0(3)

The error is given in parenthesis and refers to the last significant digit(s).
Source: Raman *et al.* (2000).

total efficiencies in a geometry identical to that used for the cross section measurement. Experimental η_{tot} values can be obtained using single-line γ-ray emitters, such as ^{137}Cs or ^{54}Mn. In the data analysis, the background intensity (without source) needs to be subtracted appropriately and, in addition, the spectrum has to be extrapolated beyond the discriminator threshold to zero pulse height (Figure 4.17b). Alternatively, two-line γ-ray emitters, such as ^{60}Co, can be used to measure total efficiencies (see below). Multiple-line γ-ray emitters are not as useful for this purpose because of coincidence summing effects, which will be described below.

4.5.2.4 Coincidence Summing

In many cases of practical interest, nuclear levels de-excite to the ground state via the sequential emission of two or more photons, rather than by emitting only a single γ-ray. Suppose that two coincident photons, belonging to the same γ-ray cascade, interact simultaneously with the detector. The resulting summed pulse will appear in the spectrum in a region that is different from the full-energy peak of either photon. Furthermore, the coincident photons that give rise to the summed signal are missing from the full-energy peaks of the individual photons. The effect is referred to as *coincidence summing* and has to be properly accounted for to avoid errors when efficiencies and cross sections are measured. It is particularly severe for a nuclear level with a complicated decay scheme, that is, if the level can decay through a large number of lower lying states.

Notice that coincidence summing is not related to the phenomenon of pulse pileup. The latter effect is also referred to as *random summing* and occurs when photons belonging to different cascades sum their energies randomly because of relatively high pulse rates (Knoll, 1989). Coincidence summing, on the other hand, is independent of the pulse rate, but depends on the distance between detector and source. In principle, coincidence summing effects can always be reduced to insignificant levels by increasing the detector–source distance. This procedure, however, may decrease the counting efficiency to intolerable levels, especially in

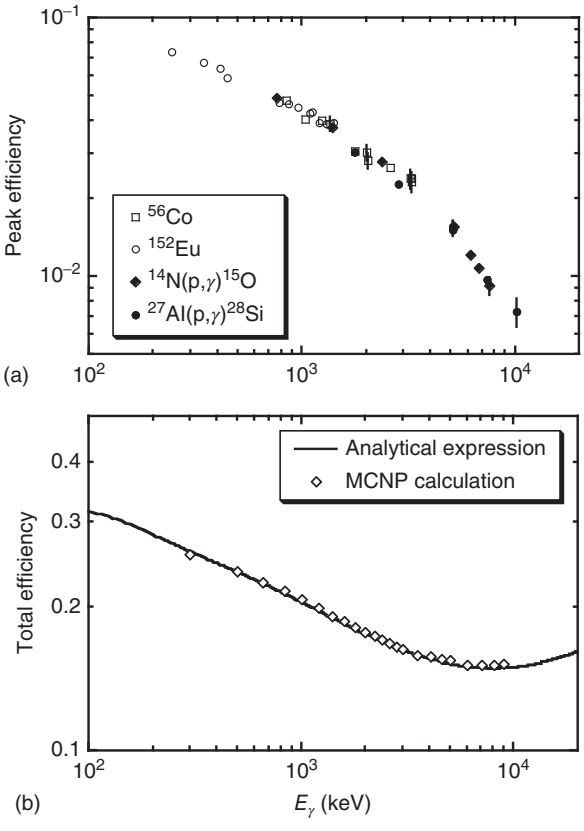

Figure 4.29 Efficiencies for a HPGe detector of 582 cm^3 volume, positioned at a distance of 1.6 cm between source (or target) and detector. (a) Experimental peak efficiencies; the curve is constructed by using calibration sources (^{56}Co and ^{152}Eu) and calibration resonances [^{14}N(p,γ)^{15}O and ^{27}Al(p,γ)^{28}Si]. The displayed efficiencies are corrected for coincidence summing. (Courtesy of Robert Runkle.) (b) Calculated total efficiencies; the solid line is obtained from an expression similar to Eq. (4.52), but additionally taking into account the insensitive detector core. The results agree with those from Monte Carlo simulations (shown as diamonds) using the computer code MCNP (Briesmeister, 1993). (Courtesy of Chris Fox and Richard Longland.)

measurements of very weak cross sections. The experimentalist has frequently little choice but to maximize the counting efficiency by minimizing the detector–source distance and, at the same time, to properly account for coincidence summing effects.

As a simple example, consider Figure 4.31 showing a decay scheme involving three levels in nucleus Y. Level 2 is populated, say, by a capture reaction. It may either decay directly to the ground state ($2 \rightarrow 0$) via emission of photon γ_{20} with a branching ratio of B_{20}, or to level 1 ($2 \rightarrow 1$) via emission of photon γ_{21} with a branching ratio of B_{21}. Subsequently, level 1 decays to the ground state ($1 \rightarrow 0$)

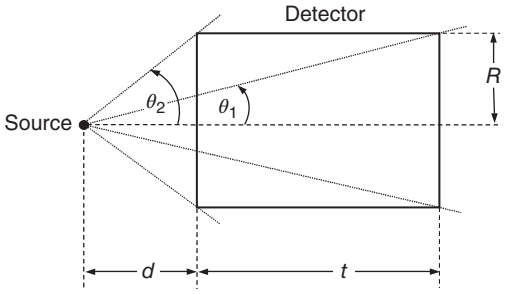

Figure 4.30 Geometry for the calculation of the total γ-ray efficiency of a cylindrical detector according to Eq. (4.52); *d* is the distance between source and detector front face, *t* is the length of the detector crystal, and *R* is the crystal radius.

via emission of photon γ_{10} with a branching ratio of 100% ($B_{10} = 1$). Note that $B_{20} + B_{21} = 1$. Angular correlations between γ-rays will be neglected in the following. With the total number of nuclei in the second excited state given by $\mathcal{N}$, the number of detected photons γ_{21} in the full-energy peak is equal to

$$\mathcal{N}_{21} = \mathcal{N} B_{21} \eta_{21}^P - \mathcal{N} B_{21} \eta_{21}^P \eta_{10}^T = \mathcal{N} B_{21} \eta_{21}^P (1 - \eta_{10}^T) \tag{4.53}$$

with η_{21}^P and η_{10}^T the (full-energy) peak and total efficiency of photon γ_{21} and γ_{10}, respectively. The intensity of the full energy peak is *reduced* by the amount $\mathcal{N} B_{21} \eta_{21}^P \eta_{10}^T$, which corresponds to the probability that photon γ_{21} is fully detected and, at the same time, the coincident photon γ_{10} leaves any measurable amount of energy in the detector (e.g., through Compton scattering). Equivalently, the term $\mathcal{N} B_{21} \eta_{21}^P (1 - \eta_{10}^T)$ corresponds to the probability that photon γ_{21} is fully detected and, at the same time, photon γ_{10} escapes detection. If both photons γ_{21} and γ_{10} are detected simultaneously, then counts are removed from the full energy peak of photon γ_{21}. This effect, which depends on both the peak and total detector efficiency, is referred to as *summing-out*. Similarly, we obtain for the number of detected photons γ_{10} in the full-energy peak

$$\mathcal{N}_{10} = \mathcal{N} B_{21} \eta_{10}^P - \mathcal{N} B_{21} \eta_{10}^P \eta_{21}^T = \mathcal{N} B_{21} \eta_{10}^P (1 - \eta_{21}^T) \tag{4.54}$$

On the other hand, the number of detected photons γ_{20} in the full energy peak is

$$\mathcal{N}_{20} = \mathcal{N} B_{20} \eta_{20}^P + \mathcal{N} B_{21} \eta_{21}^P \eta_{10}^P \tag{4.55}$$

The intensity of the full energy peak is *increased* by the amount $\mathcal{N} B_{21} \eta_{21}^P \eta_{10}^P$, which corresponds to the probability that both photons γ_{21} and γ_{10} are fully absorbed in the detector. This effect, which depends only on the peak efficiency of the detector, is referred to as *summing-in*.

Coincidence summing effects become significant for large efficiency values or, equivalently, for close detector–source geometries. For example, if the ground-state transition via emission of photon γ_{20}, is weak ($B_{20} \approx 0$), the measured intensity $\mathcal{N}_{20}$ may arise entirely from summing-in. Consequently, neglecting

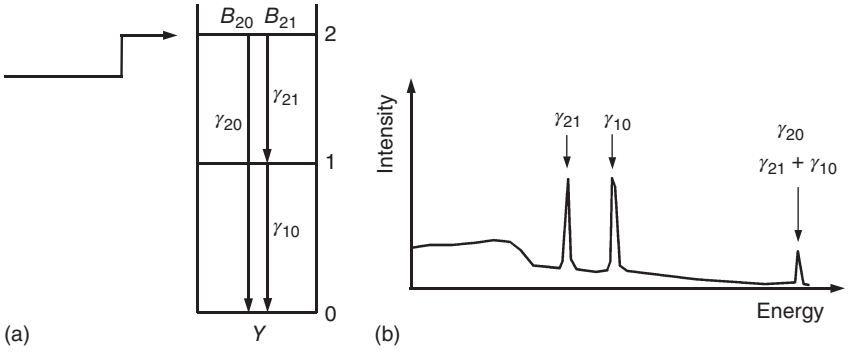

Figure 4.31 Coincidence summing of γ-rays. (a) Scheme of three levels (0, 1, 2). Level 2 is populated either in a capture reaction or by β-decay. It can γ-decay either to level 1 or to the ground state 0. The intermediate level 1 can only decay to the ground state. (b) Corresponding pulse height spectrum. The peaks labeled "γ_{21}" and "γ_{10}" are affected by summing-out, while the peak labeled "$\gamma_{20}, \gamma_{21} + \gamma_{10}$" is influenced by summing-in.

coincidence summing corrections may cause large systematic errors in the interpretation of the γ-ray decay scheme. If the decay shown in Figure 4.31 is used for determining the peak efficiencies of photons γ_{21} and γ_{10}, then we obtain from Eqs. (4.53) and (4.54)

$$\eta_{21}^P = \frac{\mathcal{N}_{21}}{\mathcal{N} B_{21}(1-\eta_{10}^T)}, \qquad \eta_{10}^P = \frac{\mathcal{N}_{10}}{\mathcal{N} B_{21}(1-\eta_{21}^T)} \tag{4.56}$$

A comparison of Eqs. (4.43) and (4.56) shows that, in the presence of coincidence summing, the efficiency expression has to be modified by the total detection efficiency factor $(1-\eta_{ij}^T)$. Similar arguments hold if this decay is used for determining the number $\mathcal{N}$ of decaying levels 2 (proportional to the source activity or the cross section) from the measured peak intensities of γ_{21} or γ_{10}. A proper account for summing corrections gives (see Eqs. (4.53) and (4.54))

$$\mathcal{N} = \frac{\mathcal{N}_{21}}{B_{21}\eta_{21}^P(1-\eta_{10}^T)} = \frac{\mathcal{N}_{10}}{B_{21}\eta_{10}^P(1-\eta_{21}^T)} \tag{4.57}$$

In more complicated cases involving different multiple-γ-ray cascades, β-decays to intermediate levels, internal conversion transitions, angular correlations and so on, summing corrections can no longer be calculated analytically. Positron decays to excited levels in the daughter nucleus give rise to annihilation quanta that are coincident with γ-rays from the de-excitation of those levels and thus have to be considered carefully as well (even for single-line γ-ray sources). General numerical methods have been developed for such cases (Debertin and Helmer, 1988; Semkow *et al.*, 1990).

Coincidence summing effects are frequently apparent from a visual inspection of the (uncorrected) full-energy peak efficiency curve if data are taken in close geometry. Some efficiency values will lie on a smooth curve, corresponding

to noncoincident photons, while other data points that are affected by coincidence summing will lie away from the curve. Based on this information, the experimentalist can decide if corrections need to be applied to achieve the desired precision. Coincidence summing not only influences peak intensities in the pulse height spectrum, but also impacts the total intensities since two (or more) photons are registered by the detector as one pulse.

4.5.2.5 Sum Peak Method

The importance of absolute normalization of the peak and total efficiency curves has been stressed in previous sections. For some commercially available γ-ray sources, absolute activities can be quoted to about 1% precision. In many cases, however, a set of absolutely calibrated sources may not be available to the experimentalist. Here we will describe a method that not only provides simultaneously absolute peak and total efficiencies without knowledge of the source activity, but the derived results will also be automatically corrected for coincidence summing effects. The technique is referred to as the *sum peak method* and utilizes the coincidence summing of photons that belong to a two-γ-ray cascade.

Consider again the decay scheme in Figure 4.31. Level 2 is populated by some process (e.g., β-decay of a parent nucleus), but assume now that it decays exclusively to the intermediate level 1 ($B_{21} = 1$, $B_{20} = 0$) and, subsequently, to the ground state 0 ($B_{10} = 1$). The measured intensities of the full-energy peaks ($\mathcal{N}_{21}$, $\mathcal{N}_{10}$), the sum peak ($\mathcal{N}_{20}$), and the total intensity in the spectrum ($\mathcal{N}_t$) are given by

$$\mathcal{N}_{21} = \mathcal{N}\eta_{21}^{P}\left(1 - W\eta_{10}^{T}\right) \tag{4.58}$$

$$\mathcal{N}_{10} = \mathcal{N}\eta_{10}^{P}\left(1 - W\eta_{21}^{T}\right) \tag{4.59}$$

$$\mathcal{N}_{20} = \mathcal{N}\eta_{21}^{P}\eta_{10}^{P}W \tag{4.60}$$

$$\mathcal{N}_t = \mathcal{N}\left(\eta_{21}^{T} + \eta_{10}^{T} - \eta_{21}^{T}\eta_{10}^{T}W\right) \tag{4.61}$$

These relationships take explicitly the angular correlation W of photons γ_{21} and γ_{10} into account, but otherwise the first three expressions are identical to Eqs. (4.53)–(4.55). The term $\eta_{21}^{T}\eta_{10}^{T}W$ in the last expression corresponds to the probability that each of the coincident photons deposits some amount of energy in the detector. In this case, the two photons are registered in the detector as one pulse and, consequently, the total intensity in the spectrum is reduced. As already pointed out, it is assumed that the intensity $\mathcal{N}_t$ has been corrected for the background (without source) and is extrapolated to zero pulse height.

The above equations can be solved iteratively until convergence in the solutions is achieved. However, in certain important cases (e.g., ^{60}Co; see below) the energies of the two emitted photons are very similar. Hence, we can replace in the above expressions the total efficiencies η_{21}^{T} and η_{10}^{T} by their average value $\eta^{T} \approx (\eta_{21}^{T} + \eta_{10}^{T})/2$. With this approximation, one obtains after some algebra

$$\mathcal{N} = \left(\frac{\mathcal{N}_{21}\mathcal{N}_{10}}{\mathcal{N}_{20}} + \mathcal{N}_t\right) W \tag{4.62}$$

$$\eta_{21}^{P} = \frac{1}{W}\sqrt{\frac{\mathcal{N}_{21}\mathcal{N}_{20}^{2}}{\mathcal{N}_{10}\mathcal{N}_{20}\mathcal{N}_{t} + \mathcal{N}_{21}\mathcal{N}_{10}^{2}}} \tag{4.63}$$

$$\eta_{10}^{P} = \frac{1}{W}\sqrt{\frac{\mathcal{N}_{10}\mathcal{N}_{20}^{2}}{\mathcal{N}_{21}\mathcal{N}_{20}\mathcal{N}_{t} + \mathcal{N}_{10}\mathcal{N}_{21}^{2}}} \tag{4.64}$$

$$\eta^{T} = \frac{1}{W} - \frac{1}{W}\sqrt{\frac{\mathcal{N}_{21}\mathcal{N}_{10}}{\mathcal{N}_{20}\mathcal{N}_{t} + \mathcal{N}_{21}\mathcal{N}_{10}}} \tag{4.65}$$

These expressions for the total number of decaying nuclei ($\mathcal{N}$) and the absolute peak and total efficiencies (η_{21}^{P}, η_{10}^{P}, η^{T}) depend, apart from the factor W, only on the measured intensities $\mathcal{N}_{21}$, $\mathcal{N}_{10}$, $\mathcal{N}_{20}$, and $\mathcal{N}_{t}$.

As a specific example, consider the decay scheme of the radioisotope ^{60}Co (Figure 4.28b). The β-decay populates the 2506 keV level in the daughter nucleus ^{60}Ni. This level, in turn, γ-decays to the first excited state at 1333 keV by emission of a 2506–1333 keV = 1173 keV photon. Subsequently, this state de-excites to the ground state by emission of a 1333 keV photon. Other β- and γ-decays are very weak and, therefore, this decay represents an almost ideal realization of the schematic case discussed above. The angular correlation for the two coincident photons from the decay of ^{60}Co is given by (Example D.1)

$$W(\theta) = 1 + \frac{5}{49}Q_{2}^{21}Q_{2}^{10}P_{2}(\cos\theta) + \frac{4}{441}Q_{4}^{21}Q_{4}^{10}P_{4}(\cos\theta) \tag{4.66}$$

where $P_{n}(\cos\theta)$ denotes a Legendre polynomial of order n and Q_{n}^{ab} is the solid angle attenuation factor for photon γ_{ab}; θ is the angle between the directions of the two photons. In this case, $\theta = 0°$ and hence $P_{2}(\cos\theta) = P_{4}(\cos\theta) = 1$ (see Eqs. (A.12) and (A.14)). The factors Q_{n}^{ab} can be estimated from the efficiency and the detector crystal geometry using, for example, Monte Carlo simulations (Appendix D.5). Strictly speaking, the factors Q_{n}^{ab} also depend on the type of event (*full-energy peak efficiency* solid angle attenuation factor versus *total efficiency* solid angle attenuation factor). For example, Eq. (4.58) must in principle be replaced by

$$\mathcal{N}_{21} = \mathcal{N}\eta_{21}^{P}\left[1 - \left(1 + \frac{5}{49}Q_{2}^{21,P}Q_{2}^{10,T} + \frac{4}{441}Q_{4}^{21,P}Q_{4}^{10,T}\right)\eta_{10}^{T}\right] \tag{4.67}$$

In practice, the distinction between the factors $Q_{n}^{ab,P}$ and $Q_{n}^{ab,T}$ is found to have a negligible effect on the final results if the distance between detector and source is small (< 1% change in the derived efficiencies for distances < 1 cm). However, at larger distances this distinction may need to be taken into account (Kim, Park, and Choi, 2003; Longland *et al.*, 2006).

4.5.2.6 γ-Ray Branching Ratios

The γ-ray decay probability for a transition from a given initial state to a specific lower lying final state, normalized to the total γ-ray decay probability of the initial

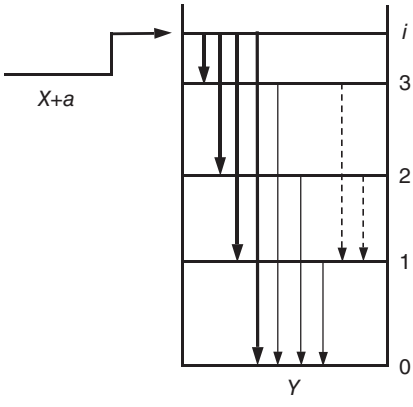

Figure 4.32 Level scheme showing primary (thick solid arrows) and secondary (thin solid and dashed arrows) γ-ray transitions. The thick solid arrows originate from level *i* that is directly populated in the capture reaction X + a → Y. The thin solid arrows correspond to those secondary transitions that proceed to the ground state of nucleus Y.

level, is called the γ-*ray branching ratio*. It is defined by the ratio of the γ-ray partial width for a specific transition and the total γ-ray partial width of the initial state (see Eq. (1.30)). Branching ratios contain important information regarding the nuclear structure of the initial and final nuclear states. They are also needed to calculate from the measured intensities of specific transitions the total number of populated compound levels. This number is equal to the total number of reactions that occurred and thus determines the reaction cross section (Sections 4.8 and 4.9).

Consider the schematic level diagram shown in Figure 4.32. An initial level *i* in nucleus Y is populated by some fusion reaction X + a. The initial state can directly decay either to the ground state (0) or to three lower lying excited states (1, 2, 3). These transitions (thick solid arrows) are referred to as *primary* γ-ray decay branches. The corresponding primary γ-ray branching ratios are experimentally given by

$$B_{ij} \equiv \frac{\mathcal{N}_{ij}/(\eta_{ij}^{P} W_{ij})}{\sum_{j} \mathcal{N}_{ij}/(\eta_{ij}^{P} W_{ij})} \tag{4.68}$$

with $\mathcal{N}_{ij}$, η_{ij}^{P}, and W_{ij} the measured full-energy peak intensity, peak efficiency, and angular correlation, respectively, for the transition leading from the initial level *i* to a specific final state *j*. It is assumed that $\mathcal{N}_{ij}$ and η_{ij}^{P} have been corrected for coincidence summing effects. There are further decay possibilities involving levels other than the initial state *i*. These transitions (indicated by thin solid and dashed arrows) are referred to as *secondary* γ-ray decay branches.

The total number of compound nuclei created in the fusion reaction, that is, the total number of initially populated levels *i*, can be obtained either from the primary branching ratios (thick solid arrows),

$$\mathcal{N}_i = \sum_{j=0,1,2,3} \frac{\mathcal{N}_{ij}}{\eta_{ij}^{P} W_{ij}} = \frac{\mathcal{N}_{ij}}{B_{ij}\eta_{ij}^{P} W_{ij}} \tag{4.69}$$

or from all transitions leading to the ground state (thin solid arrows plus the primary ground-state branch),

$$\mathcal{N}_i = \sum_{j=1,2,3,i} \frac{\mathcal{N}_{j0}}{\eta_{j0}^{P} W_{j0}} \tag{4.70}$$

The proper interpretation of a γ-ray spectrum can be challenging if the decay scheme is complex. Sometimes it is found that peaks originating from the reaction of interest overlap with escape peaks, room background lines, or peaks from reactions involving target or beam contaminants. For the analysis of reaction data, it is frequently of advantage to compare spectra obtained with beam on target with those measured without beam (room background) or with beam on a blank backing.

It is sometimes possible to determine ratios of partial widths from the observed intensity balance of primary and secondary γ-ray transitions. For example, consider Figure 4.33 showing a level scheme of ^{25}Al and a germanium γ-ray spectrum measured in the ^{24}Mg(p,γ)^{25}Al reaction. The reaction populates a resonance located at $E_r = 1616$ keV, corresponding to a level at $E_x = 3823$ keV in the compound nucleus. This level decays via several primary γ-ray transitions. One of

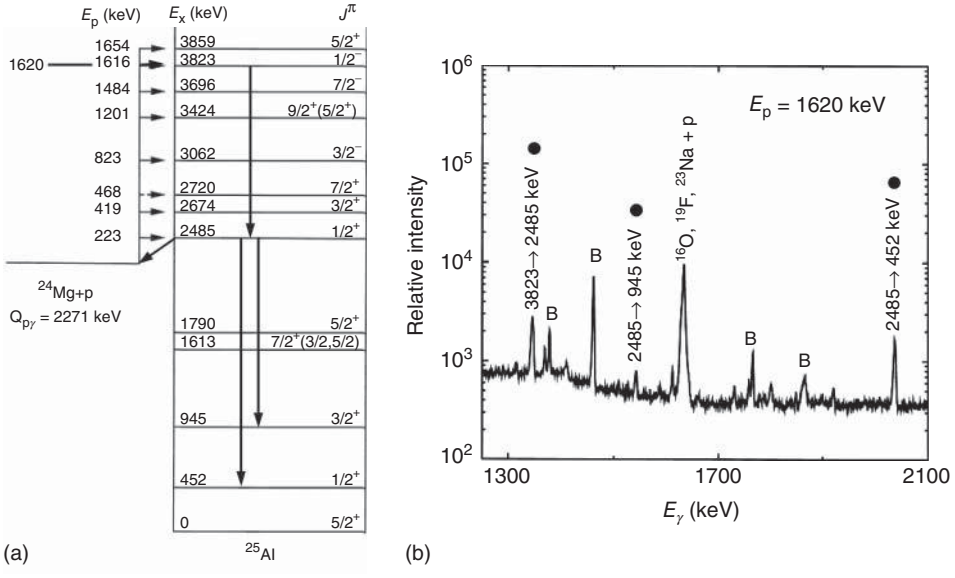

Figure 4.33 Study of the ^{24}Mg(p,γ)^{25}Al reaction at a proton bombarding energy of $E_p = 1620$ keV. (a) Level scheme of ^{25}Al. The capture reaction populates a level at $E_x = 3823$ keV, which γ-ray decays to a state at $E_x = 2485$ keV. The latter state decays either via proton emission or via γ-ray transitions to lower-lying levels ($E_x = 452$ or 945 keV). (b) Measured pulse height spectrum. The γ-ray transitions populating or decaying from the $E_x = 2485$ keV state are indicated by solid circles. See discussion in the text. Data adopted from Powell *et al.* (1999).

these primary transitions proceeds to the proton unbound $E_x = 2485$ keV level. This state, in turn, has three possibilities of decay: (i) a γ-ray transition to the $E_x = 452$ keV state; (ii) a γ-ray transition to the $E_x = 945$ keV state, and (iii) a transition to the ^{24}Mg ground state via emission of a proton. The partial width ratio Γ_γ/Γ of the $E_x = 2485$ keV state is then given by the ratio of the total number of γ-ray transitions decaying from this level (2485 → 452, 2485 → 945) and the number of γ-ray transitions feeding this level (3823 → 2485),

$$\frac{\Gamma_\gamma}{\Gamma} = \frac{\Gamma_\gamma}{\Gamma_p + \Gamma_\gamma} = \frac{(\mathcal{N}_{2485\to452}/\eta^P_{2485\to452}) + (\mathcal{N}_{2485\to945}/\eta^P_{2485\to945})}{(\mathcal{N}_{3823\to2485}/\eta^P_{3823\to2485})} = 0.91 \pm 0.04 \tag{4.71}$$

Angular correlation effects are negligible in this case. The measured value provides important input information for the extrapolation of the ^{24}Mg(p,γ)^{25}Al cross section to low energies (Powell *et al.*, 1999).

4.5.2.7 4π Detection of γ-Rays

The interpretation of a complex γ-ray spectrum to determine the branching ratios of individual γ-ray transitions, and eventually cross sections, can be a very time-consuming task. Such investigations are especially tedious if a large number of resonances has to be measured in a specific reaction. Furthermore, if the Q-value of the capture reaction is large and if the target nucleus is heavy, then incident charged-particles or neutrons may excite a number of overlapping resonances simultaneously, giving rise to a multitude of capture γ-rays lines in the pulse height spectrum. The experimental information on individual γ-ray transitions is not necessarily required to determine the number of nuclear reactions that took place during the experiment. All that is needed from the astrophysical point of view is the total number of γ-ray cascades initiated by the reaction of interest.

Consider, for example, the setup shown in Figure 4.34. The target or sample is located at the center of a large detector crystal covering a solid angle of nearly 4π. If every single γ-ray of a specific cascade emitted by the target is fully absorbed by the detector, then each radiative capture would result in a single pulse. The system would have a detection efficiency of unity for each radiative capture, independent of the cascade structure. The pulse height spectrum will show a peak at an energy equal to the sum of the Q-value and the center-of-mass bombarding energy, $E_\gamma^{\text{sum}} = Q + E_{\text{cm}}$. Not only does such a technique greatly simplify the data analysis, but it has the additional advantage that angular correlation effects are negligible. Furthermore, contaminant reactions will give rise to sum peaks at different locations in the spectrum since their Q-values are likely to differ from the Q-value of the reaction of interest. This technique takes advantage of coincidence summing.

The 4π detection method has been successfully applied in a number of investigations, including charged-particle and neutron-capture reactions (Lyons, Toevs, and Sargood, 1969; Wisshak *et al.*, 1990; Harissopulos, 2004). Complications arise

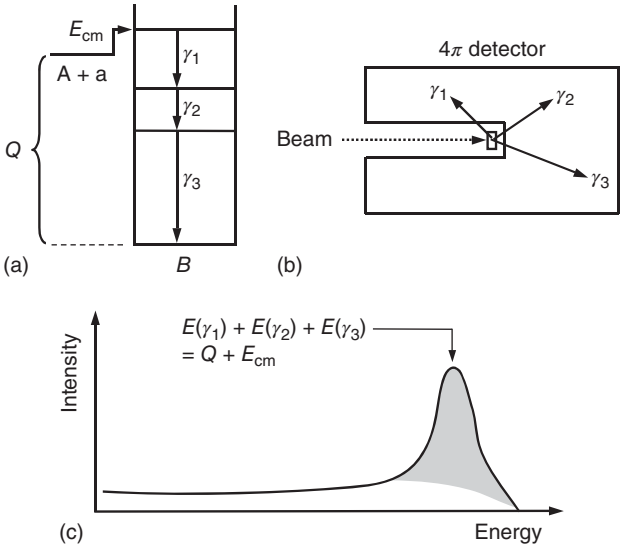

Figure 4.34 4π detection of cascading γ-rays. (a) Level scheme showing a cascade consisting of three photons (γ_1, γ_2, and γ_3). (b) Summing crystal covering a solid angle close to 4π. The target is located at the center of the detector. Photons emitted in the direction of the beam pipe escape detection. (c) Schematic pulse height spectrum showing a sum peak corresponding to an energy of $E(\gamma_1) + E(\gamma_2) + E(\gamma_3)$.

since any crystal of finite dimensions has a total detection efficiency of less than unity for any given photon. Some photons may escape through openings of the detector (e.g., the beam pipe). Others may be absorbed by the target chamber or may simply traverse the detector without interaction. Such effects cause incomplete summing and give rise to a continuum of pulses below the sum peak. Also, the efficiency for detecting a cascade (*summing efficiency*) is no longer constant and will depend on the γ-ray decay scheme. In practice, it is found, with sufficiently large detector crystals, that the summing efficiency depends only slightly on the cascade structure and that this dependence can be modeled using Monte Carlo transport codes (Tsagari *et al.*, 2004).

4.5.3
Neutron Spectroscopy

Neutrons must be observed through nuclear interactions (reactions or scattering) in the detection medium that result in energetic charged-particles (Section 4.2.3). The cross section for these processes depends in most cases strongly on neutron energy. Consequently, very different devices are in use for detecting neutrons in different energy regions. A detailed discussion of the various types of neutron detectors can be found in Knoll (1989). It has already been pointed out that astrophysically important reactions frequently have very small cross sections

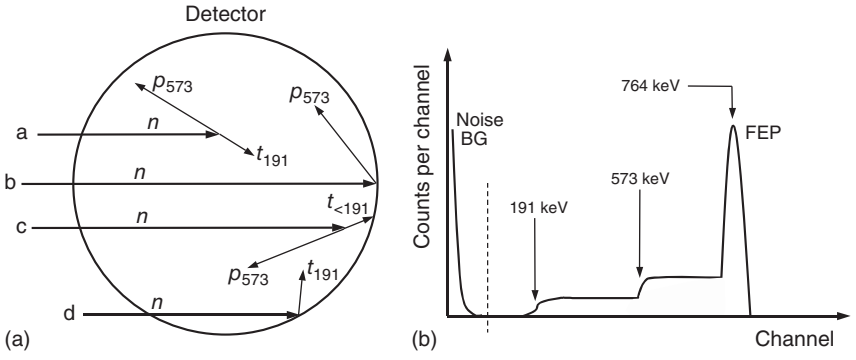

Figure 4.35 Measurement of thermal neutrons ($E_n = 0.025$ eV) with a ^{3}He gas proportional counter. (a) Histories of neutron interactions in the detector. (b) Pulse height spectrum. The full-energy peak occurs at the Q-value of the ^{3}He(n,p)^{3}H reaction ($Q = 764$ keV). The steps at 191 keV and 573 keV are caused by the wall effect. The discriminator threshold is indicated by the vertical dashed line.

and thus detectors with high efficiencies are required for these measurements. Most neutron measurements in nuclear astrophysics have been performed using moderated proportional counters. In the following, we will focus on this detector type. Scintillators also have high efficiencies for neutron detection (Section 4.4.3) but are also sensitive to beam-induced and room-background γ-rays. Although it is possible with scintillators to suppress unwanted γ-ray signals via pulse shape discrimination techniques, the remaining γ-ray background is not negligible. For this reason, moderated proportional counters achieve usually higher sensitivities than scintillators in measurements of weak cross sections.

4.5.3.1 Response Function

We start with a discussion of the response function of proportional counters. As a specific example, a detector filled with ^{3}He gas is chosen. Similar arguments will hold for $^{10}BF_3$ proportional counters. Suppose that thermal neutrons ($E_n = 0.025$ eV) are incident on such a detector, as shown in Figure 4.35a. The Q-value of the ^{3}He(n,p)^{3}H reaction amounts to 764 keV. Since the incoming neutron momentum is very small, the reaction products (protons and tritons) are emitted in opposite directions and the total reaction energy is imparted to the fragments as kinetic energy according to the ratio of their masses ($E_p = 573$ keV, $E_t = 191$ keV). If both particles are stopped in the counter gas (case a), then the magnitude of the current output pulse corresponds to 764 keV. These events appear in the full-energy peak (FEP) of the pulse height spectrum (Figure 4.35b). However, if one of the particles strikes the counter wall, then a smaller pulse is produced. This phenomenon is referred to as the *wall effect*. For example, case (b) shows a reaction occurring close to the counter wall. The proton is completely stopped in the gas, while the entire energy of the triton is absorbed by the wall. The corresponding event then appears in the pulse height spectrum at an energy of 573 keV. If the reaction occurs

at some distance from the wall (case c), so that the triton can deposit at least a fraction of its energy in the gas, then a larger pulse is produced. Similar arguments hold for the opposite case (case d), that is, when the energy of the triton is fully absorbed in the gas while only partial proton energy deposition occurs. The wall effect gives rise to steps at 191 keV and 573 keV in the pulse height spectrum, corresponding to the individual energies of the proton and triton fragments. It also depends on the geometry and size of the counter and is less pronounced for larger detectors and for higher gas pressures. The wall effect can be reduced by adding a small amount of a heavier gas (e.g., Kr) to the ^{3}He since then the ranges of the charged particles become smaller.

The resolution of the full-energy peak measured with ^{3}He or $^{10}BF_3$ proportional counters amounts typically to several percent for thermal neutrons. It should be clear from the above considerations that for incident thermal neutrons, the pulse height spectrum measured with proportional counters provides no information regarding the neutron energy.

An important property of proportional counters is their ability to discriminate neutrons from room or beam-induced background γ-rays. Photons interact mainly with the counter walls by creating secondary electrons. These electrons have relatively large ranges in gases and thus will deposit only a small fraction of their energy in the active volume before reaching the counter wall. As a result, most γ-rays will produce pulses of considerably smaller amplitude than those induced by neutrons. In practice, a discriminator threshold level (dashed line in Figure 4.35b) is set just below the structure caused by the wall effect. By accepting only events located above the threshold, all the neutrons are counted, while low amplitude events caused by electronic noise, γ-rays and so on, are rejected.

4.5.3.2 Moderated Proportional Counters

In analogy to the case of γ-rays (Section 4.5.2), the detection probability for an incident neutron traversing a path length of x in the active detector volume is given by $P = 1 - e^{-N\sigma x}$, with σ being the cross section of the reaction that converts the incoming neutron to charged particles, and N being the number density of active detector nuclei (^{10}B or ^{3}He). For example, for a 30 cm long cylindrical $^{10}BF_3$ proportional counter of 600 Torr gas pressure we obtain a total efficiency of about 90% for thermal neutrons incident along the detector axis (Example 4.2). However, in astrophysically important reactions the neutrons are typically emitted with energies in the kilo electron volts to mega electron volt range rather than with thermal energies. The cross sections of the reactions ^{3}He(n,p)^{3}H and ^{10}B(n,α)^{7}Li decrease rapidly for increasing neutron energies, as can be seen from Figure 4.15a. Consequently, the efficiency of proportional counters for directly detecting fast neutrons is small, making such detectors unsuitable for measuring weak cross sections of astrophysical interest. The detection efficiency of proportional counters for fast neutrons can be substantially improved by surrounding the detector with a suitable moderator, such as polyethylene or paraffin. The incident fast neutrons slow down in the moderating medium before reaching the counter and are detected with a significantly higher efficiency.

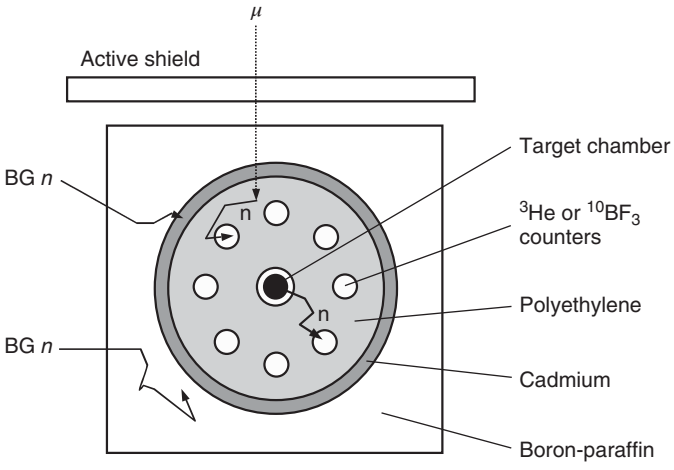

Figure 4.36 Moderated proportional counter. Several ^{3}He or $^{10}BF_3$ proportional detectors (open circles) are arranged in a concentric ring around the target chamber (shown as full circle). The detectors are embedded in polyethylene, which acts as a moderator for beam-induced fast neutrons. After moderation, these neutrons are more efficiently detected. The inner detector core is surrounded by layers of cadmium and boron–paraffin. These act as shields for unwanted contributions from background neutrons. The entire assembly may be surrounded by plastic scintillator veto shields (Section 4.4.3) to reduce the background induced by cosmic-ray muons.

Figure 4.36 shows a typical setup of a system with a high efficiency for detecting fast neutrons. It consists of several ^{3}He- or $^{10}BF_3$-filled proportional counters, arranged in a concentric ring around the target chamber. The counters are embedded in a cylindrical polyethylene moderator and are surrounded by layers of boron–paraffin and cadmium. The latter materials act as shields by moderating room background neutrons in the paraffin and by absorbing the moderated neutrons in the boron or cadmium layer before they can reach the active detector volume. The (beam-induced) reactions of interest take place in the target chamber, located close to the center of the entire detector. The total efficiency of such devices can amount to ≈ 20–30% for neutron energies between 0.5 and 10 MeV (Section 4.7.4). The choice between ^{3}He and $^{10}BF_3$ as filler gas is usually governed by considerations of efficiency and γ-ray sensitivity (East and Walton, 1969). When the largest detection efficiency is required, ^{3}He counters are preferable to $^{10}BF_3$ tubes since the former can be operated at higher pressures. On the other hand, the latter are less sensitive to γ-ray background because the $^{10}B(n,\alpha)^7Li$ reaction has a higher Q-value than the $^3He(n,p)^3H$ reaction.

4.5.3.3 Efficiency Calibrations

Most efficiency calibrations of neutron detectors are performed with calibrated neutron sources. Radioisotopes that emit neutrons with discrete energies are practically not available as sources and thus laboratory neutron sources are based either on spontaneous fission or on nuclear reactions.

Many transuranium elements decay by spontaneous fission and thereby release fast neutrons, fission fragments, β- and γ-radiation. The material is usually encapsulated in a relatively thick container so that only neutrons and γ-rays emerge from the source. The most common type of this source is ^{252}Cf ($T_{1/2} = 2.65$ y). The energy spectrum of the neutrons is continuous up to about 10 MeV with a maximum at ≈ 0.6 MeV. The neutron yield amounts to about 2.3×10^6 s^{-1}μg^{-1} (Knoll, 1989). Compared to other neutron sources, ^{252}Cf can be made in relatively small sizes.

Neutron sources can also be produced by mixing an α-emitting isotope with a substance such as ^{9}Be, which exhibits a relatively large (α,n) reaction cross section. One of the most common sources of this type consists of a ^{239}Pu–Be mixture in which α-particles of 5.14 MeV energy from the decay of ^{239}Pu initiate the reaction ^{9}Be$(\alpha,n)^{12}$C. The neutron transitions occur either to the ground state or to various excited states in ^{12}C. The α-particles lose some of their initial energy in the source before reacting with the ^{9}Be nuclei and, therefore, the neutron energy spectrum is continuous up to about 11 MeV. Similar arguments hold for other (α,n) neutron sources. A ^{239}Pu–Be source yields about 60 neutrons per 10^6 primary α-particles. The neutron yield of these sources should decay according to the half-life of the α-emitting nuclei. However, this assumption does not necessarily hold if the source contains contaminants that either emit directly α-particles or decay to α-emitting daughter nuclei. Such contaminants can even cause the neutron yield to increase with time (Knoll, 1989).

Similarly, γ-ray emitters are sometimes used to produce neutrons via the photoneutron reactions ^{9}Be$(\gamma,n)^8$Be ($Q = -1.66$ MeV) or ^{2}H(γ,n)p ($Q = -2.23$ MeV). Suitable γ-ray emitters must provide photons of relatively large energies to initiate (γ,n) reactions. An example for such a neutron source is a mixture of ^{88}Y–Be. Since the γ-rays are emitted with discrete energies and are not slowed down in the source, the emitted neutrons will also be monoenergetic, apart from a small kinematic energy spread. The disadvantage of (γ,n) neutron sources is that high γ-ray activities are required to achieve reasonable neutron intensities. As a result, the neutrons are accompanied by a large γ-ray background.

Specific examples for the types of sources discussed above, together with their neutron energy regions, are listed in Table 4.10. Neutrons can also be produced directly at accelerators in reactions such as d(d,n)^{3}He ($Q = 3.27$ MeV) and ^{7}Li(p,n)^{7}Be ($Q = -1.64$ MeV). In addition, theoretical calculations of neutron detector efficiencies are routinely performed using Monte Carlo simulations (Briesmeister, 1993).

4.6 Miscellaneous Experimental Techniques

A number of experimental techniques are used in direct measurements of astrophysically important reactions that require special equipment and procedures. In this section, we will focus on three particularly important examples:

Table 4.10 Properties of neutron calibration sources.

Source	Type	Half-life[a]	E_n[b] (MeV)
^{252}Cf	spon. fission	2.645(8) y	< 10[c]
^{239}Pu–Be	(α,n)	24110(30) y	< 11
^{241}Am–Be	(α,n)	432.6(6) y	< 10[c]
^{88}Y–Be	(γ,n)	106.626(21) d	0.152
			0.949
^{124}Sb–Be	(γ,n)	60.20(3) d	0.023

Sources: [a] Wang *et al.* (2012). [b] Knoll (1989), unless mentioned otherwise. [c] Lorch (1973).

(i) radioactive ion beams, (ii) the activation method, and (iii) the time-of-flight technique. The last two are used both in charged-particle and neutron-induced reaction studies, but in nuclear astrophysics their main (although not exclusive) application is in the field of neutron-induced reactions. For other interesting techniques, such as accelerator mass spectrometry (Wallner *et al.*, 2006) or the use of etched track detectors (Somorjai *et al.*, 1998), the reader is referred to the literature.

4.6.1 Radioactive Ion Beams

Proton- and α-particle-induced reactions in a stellar plasma at elevated temperatures do not only involve stable nuclides, as will become apparent in the next chapter, but unstable nuclides also participate in the nucleosynthesis. The instability of one of the interacting nuclei represents a significant challenge for the experimentalist. If the half-life exceeds a few days, then it may be possible to fabricate a radioactive target and to measure directly the reaction of interest by bombarding the target with protons or α-particles using the experimental techniques and procedures described so far. Examples for such studies are the measurements of proton capture reactions on the radioactive species ^{22}Na (Seuthe *et al.*, 1990; Stegmüller *et al.*, 1996) and ^{26}Al^{g} (Buchmann *et al.*, 1984; Vogelaar, 1989) with half-lives of $T_{1/2} = 2.6$ y and 7.2×10^5 y, respectively. However, if the half-life of a species amounts to a few minutes or less, the fabrication of a radioactive target is not feasible. A direct measurement of such reactions is nevertheless possible if the role of target and projectile are interchanged. Consider a reaction between a light particle x (proton or α-particle) and a short-lived heavy nucleus X. The bombardment of target X with projectiles x may not be feasible. However, it may be possible to produce a beam of radioactive nuclei X that is directed onto a stationary target consisting of the light nuclei x. Such measurements are referred to as *inverse kinematics* studies. For example, suppose one would like to measure the proton capture cross section of the p + X reaction at a center-of-mass energy of $E_{cm} = 0.5$ MeV, where the short-lived nucleus X has a mass

number of $A = 20$. The laboratory beam energy of X must then be $E_{\rm lab}(^{20}X) = E_{\rm cm}(m_{\rm p} + m_X)/m_{\rm p} = 10.5$ MeV (see Eq. (C.24)). The time of flight of X over a distance of ≈ 100 m amounts only to ≈ 10 μs and, therefore, a measurement of the reaction $p + X$ is in principle feasible if the half-life of X is not too short (say, in this example, $T_{1/2} > 10$ μs).

The production, transport, and acceleration of radioactive ion beams suitable for nuclear astrophysics measurements requires substantial resources and efforts. Several different techniques have been developed that are complementary in their capabilities. In the simplest case, the radioactive material of interest is produced offline at a nuclear reactor or accelerator and is then converted into a suitable chemical form before installation in an ion source of a second accelerator capable of accelerating the radioactive heavy ions. This method, called the *batch mode technique*, is suitable only for beams of relatively long-lived nuclei. It has been applied, for example, in studies of the ^{7}Be(p,γ)^{8}B and ^{44}Ti(α,p)^{47}V reactions (Gialanella *et al.*, 2000; Sonzogni *et al.*, 2000). The most direct approach, however, is the online production of radioactive nuclei, their ionization and extraction from an ion source, and their subsequent acceleration. This method, referred to as the *isotope separator online (ISOL) technique*, has been used extensively in nuclear astrophysics measurements. In the following we will briefly describe this method. More specific information can be found in Smith and Rehm (2001) and Blackmon, Angulo, and Shotter (2006). Other techniques involving measurements with (low-energy) unaccelerated radioactive ion beams or with high-energy radioactive beams produced via projectile fragmentation are mainly used in indirect studies of important nuclear structure properties. Since they are usually not suitable for direct measurements of low-energy nuclear reactions, they will not be discussed here. The reader can find more information on the latter topics in Mueller and Sherrill (1993).

The isotope separator online (ISOL) technique is shown schematically in Figure 4.37. A beam of stable nuclei from a production accelerator bombards a thick target and produces radioactive nuclei. These diffuse out of the target, through a transfer tube, and into an ion source where they are ionized and continuously extracted. The radioactive ions are then mass separated from other, undesired, isotopes. At this stage they represent a beam of unaccelerated, low-energy radioactive ions. Subsequently, they are accelerated by a post accelerator, which allows a tuning of the beam energy to the desired value. This accelerated radioactive ion beam is finally incident on a hydrogen or helium target. The radiation emitted in the reaction of interest is then observed using suitable detectors. Beams from ISOL facilities have excellent beam qualities (resolution and spread). The success of an experiment depends on the radioactive ion beam intensity, which is limited by the primary production cross section, the diffusion velocity of the radioactive ions in the production target, the effusion of radioactive ions out of the target, and the ionization efficiency in the ion source. Unfortunately, no single combination of production beam, thick target, and ion source can produce all radioactive species of astrophysical interest. More typically, each radioactive ion beam experiment requires an extensive

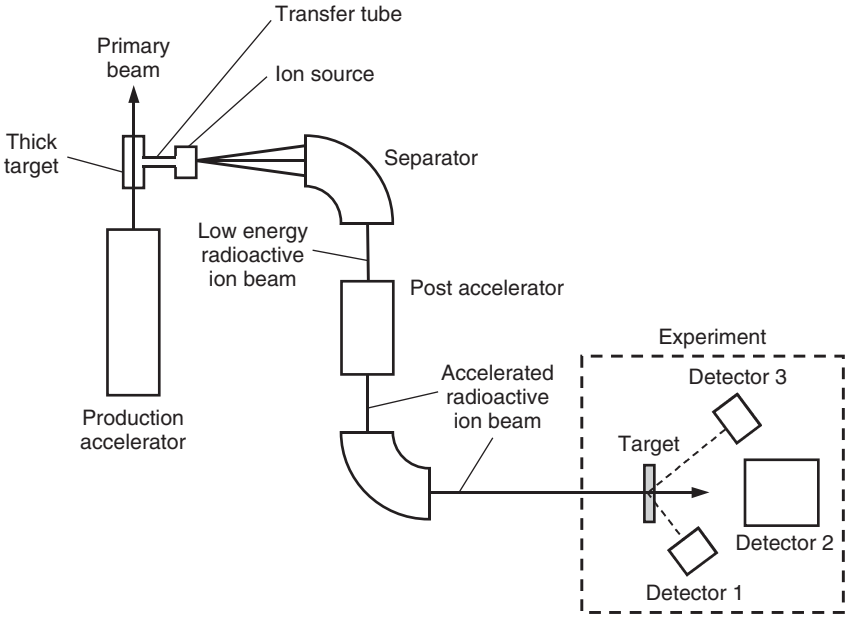

Figure 4.37 Basic components of an isotope separator online (ISOL) facility for the production of accelerated radioactive ion beams. The dashed square marks the location of the reaction measurement of astrophysical interest. In a reaction of type $X(a,b)Y$, detectors 1 or 3 detect the emitted light particle *b*. Alternatively, the light particle *b* and the corresponding heavy residual nucleus *Y* may be detected in coincidence. In a capture reaction, $X(a,\gamma)Y$, the heavy residual nucleus *Y* may be detected in a recoil separator (detector 2). Alternatively, the residual nuclei may be detected by detector 2 in coincidence with the corresponding prompt γ-rays in detectors 1 or 3.

and time-consuming effort of beam development where the composition and chemistry of the production target is varied until the intensity of the radioactive species of interest is maximized. Beams of some elements, for example, noble gases or alkali metals, can be produced with relatively high intensities, while beams of refractory elements are difficult to extract from the production target and are thus available only with considerably lower intensities. Some of the issues related to the production of radioactive beams at ISOL facilities are discussed in Dombsky, Bricault, and Hanemaayer (2004). At present, even under favorable circumstances, the radioactive beam intensities delivered to an experiment amount to at most $\approx 10^{10}$ ions/s. Comparison to a value of 6×10^{14} particles/s for a 100 μA proton beam in a typical normal kinematics experiment reveals that a radioactive ion beam facility must be carefully designed and optimized to avoid any intensity losses of the precious radioactive beam. In addition, it is imperative that the detection system has a large detection efficiency and large discriminating power against unwanted beam-induced background contributions.

We will first briefly discuss some important components of ISOL facilities before describing a specific experiment in more detail. In a star, most charged-particle reactions involving radioactive ions are induced by protons or α-particles. Therefore, hydrogen and helium are the most important target materials in direct radioactive ion beam measurements. The target requirements differ somewhat from those appropriate for normal kinematics experiments (Section 4.3). In the case of hydrogen, thin polyethylene $[(CH_2)_n]$ foils have been employed successfully in several measurements. They are mechanically stable, even if stretched to thicknesses of 20–1000 μg/cm^2, and they have been used with beam intensities of up to 10^9 particles/s without significant degradation. However, the carbon content may give rise to an intense beam-induced background dominated by elastic scattering. Gas targets are a choice for helium, and are also advantageous for hydrogen. Gas cells with thin entrance and exit windows are easy to handle but the window foils degrade the beam energy resolution and induce background reactions. Windowless gas targets are the preferred choice (Section 4.3.2) although they are bulky and expensive since they require many pumping stations to reduce the pressure to the 10^{-7} Torr range.

Radioactive beam experiments are performed in inverse kinematics. For the reaction products, this has the interesting consequence that the solid angle in the center-of-mass system is compressed into a significantly smaller solid angle in the laboratory reference frame (Appendix C.2). Detection systems used in radioactive ion beam experiments take advantage of this circumstance to increase the efficiency and sensitivity. Light charged particles from (p,α) or (α,p) reactions have been measured using arrays of silicon strip detectors, arranged to cover a large solid angle around the target. These are highly segmented, with well over 100 elements, and provide excellent energy and angle resolution. Thicknesses for these counters amount to 50–1000 μm and arrays can be stacked to allow for particle identification by measuring both energy loss (ΔE) and total energy (E). In some cases, the heavy reaction products Y have been detected in coincidence using additional detectors placed downstream of the target. Such experiments require typically radioactive ion beam intensities in excess of 10^5 particles/s to achieve sufficient counting statistics.

Radiative capture reactions of type (p,γ) or (α,γ) can in principle be studied by the in-beam measurement of γ-rays (Section 4.5.2) or by the activation method (Section 4.6.2). Both of these techniques have drawbacks. The direct detection of γ-rays alone is especially difficult for proton-rich radioactive beams that give rise, after scattering and positron decay in and near the target chamber, to a high background from 511 keV photons. The activation measurement is useful only if the observed decay is a signature of the reaction of astrophysical interest. The best method of studying capture reactions is by directly detecting the recoil nuclei Y. This technique is particularly well suited to radioactive ion beam measurements in inverse kinematics. The outgoing γ-ray transfers a very small momentum to the compound nucleus, which is therefore typically emitted within an angle of $\phi_{\mathrm{lab}} \approx 1^\circ$ with respect to the beam direction (Problem 4.9). This allows for an efficient detection of the heavy reaction products, provided that they can be separated

from the incident radioactive beam moving into the same direction. The incident projectiles and the heavy reaction products have the same linear momentum and differ in mass and velocity by only a few percent. In addition, the cross sections of interest are usually small and thus the number of beam projectiles exceeds the number of reaction products by very large factors (10^{10}–10^{15}). Recoil separators are sophisticated devices that facilitate the detection of reaction products in the presence of an overwhelming background of beam particles. Mass separation and beam rejection are accomplished using an arrangement of dipole magnets, electrostatic deflectors, and Wien filters. The reaction products are collected at the focal plane of the device and are dispersed according to their mass-to-charge ratio. A variety of detection schemes may be employed, for example, time-of-flight, Z identification or delayed activity detection. The detection sensitivity may be significantly improved by measuring the heavy recoils at the focal plane of the separator in coincidence with prompt γ-rays detected near the target. Typically, radioactive ion beam intensities in excess of $\approx 10^7$ particles/s are required for such experiments to accumulate sufficient counting statistics.

The first nuclear astrophysics experiment with an accelerated radioactive ion beam was the measurement of the ^{13}N(p,γ)^{14}O reaction at Louvain-la-Neuve (Delbar *et al.*, 1993). Since this pioneering study, several astrophysically important reactions have been measured directly or indirectly at a number of different radioactive ion beam facilities worldwide. A discussion of some of these experiments is given in Smith and Rehm (2001) and Blackmon, Angulo, and Shotter (2006) and will not be repeated here. Radioactive ion beam facilities have opened a window of previously unavailable capabilities in nuclear astrophysics. The results obtained from these measurements have a crucial impact on predictions of explosive nucleosynthesis. Therefore, it is worthwhile to discuss as an example one particular experiment in more detail.

The ^{21}Na(p,γ)^{22}Mg reaction is important for the production of the long-lived γ-ray emitter ^{22}Na in classical novae (Section 5.5.2). The reaction was directly measured (D'Auria *et al.*, 2004) at the TRIUMF-ISAC facility, located in Vancouver, Canada, in the energy range of the nova Gamow peak ($E_0 \pm \Delta/2 = 270 \pm 100$ keV at $T = 0.3$ GK). A 500 MeV proton beam of ≤ 30 μA intensity from the TRIUMF cyclotron bombarded a thick SiC production target. Spallation reactions on Si produced ^{21}Na, which diffused from the hot target through a transfer tube and was ionized in a surface ionization source. After mass separation, the low-energy ^{21}Na beam was accelerated to energies variable between 0.15 MeV/u and 1.5 MeV/u using a radiofrequency quadrupole (RFQ) accelerator and a drift-tube linac. The intensity of the ^{21}Na beam delivered to the experiment was up to 10^9 ^{21}Na ions per second. The radioactive ^{21}Na beam was then incident on a windowless hydrogen gas target. Prompt γ-rays were detected in an array of 30 BGO scintillator detectors, packed tightly around the gas target, with an almost 4π solid angle coverage. The ^{22}Mg nuclei were separated from the intense beam using the DRAGON recoil separator (Engel *et al.*, 2005) and were detected in the focal plane by a double-sided silicon strip detector. A coincidence requirement between the ^{22}Mg nuclei detected at the focal plane and the corresponding γ-rays measured

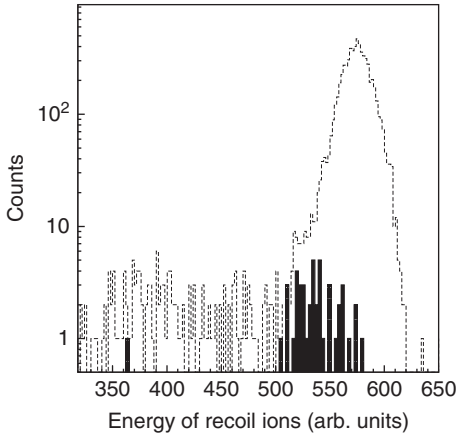

Figure 4.38 Pulse height spectrum of heavy ions detected at the focal plane of a recoil separator in the study of the $E_r^{cm} = 207$ keV resonance in ^{21}Na(p,γ)^{22}Mg. The dashed histogram shows the singles spectrum and is dominated by ^{21}Na beam particles leaking through the separator. The shaded spectrum displays those heavy ions that are in coincidence with prompt γ-rays detected in a BGO array surrounding the hydrogen gas target. These correspond to the reaction products ^{22}Mg, since ^{21}Na beam particles are not in coincidence with prompt γ-rays. (Reprinted with permission from D'Auria *et al.* (2004). Copyright (2004) by the American Physical Society.)

near the target by the BGO array allowed for a very high detection sensitivity, even though the ^{22}Mg nuclei had low energies. A pulse height spectrum of heavy ions detected at the focal plane of the recoil separator at a bombarding energy in the region of the lowest lying resonance ($E_r^{cm} = 207$ keV) in ^{21}Na(p,γ)^{22}Mg is shown in Figure 4.38. The dashed histogram displays the singles spectrum and is dominated by unwanted ^{21}Na beam particles leaking through the separator. The shaded histogram shows only those heavy ions that are in coincidence with γ-rays ($E_\gamma \geq 3$ MeV) detected in the BGO array. These correspond to ^{22}Mg ions since the ^{21}Na beam particles are not expected to be in coincidence with prompt γ-rays. The clean identification of ^{22}Mg recoils allowed for a precise measurement of the energy and strength of this resonance, which dominates the total ^{21}Na(p,γ)^{22}Mg reaction rates at typical nova temperatures.

4.6.2 Activation Method

We already discussed the prompt detection of reaction products, that is, the direct detection of the emitted particles or γ-rays in reactions of type $X(a,b)Y$ or $X(a,\gamma)Y$, respectively. From their measured intensity, we can infer the total number of reactions that took place. This information is used to calculate cross sections or resonance strengths (Sections 4.8 and 4.9). There are instances where such a reaction will produce a radioactive nucleus Y in its ground state

(or a long-lived isomeric state). Instead of detecting the prompt radiation b, one could count the number of nuclei Y by observing the delayed residual radioactivity after the bombardment of the target or sample with projectiles has stopped. This technique is referred to as the *activation method*. In nuclear astrophysics measurements, it is mainly used for studies of neutron-capture reactions (Käppeler, 1999). For applications to charged-particle-induced reaction studies see, for example, Sauter and Käppeler (1997) or Gyuerky *et al.* (2003).

The activation method has certain advantages. For example, consider a capture reaction that gives rise to a complicated γ-ray decay scheme. The determination of prompt γ-ray intensities and branching ratios to infer the number of nuclear reactions that took place may become very challenging in this case (Section 4.5.2). However, all these γ-ray cascades will eventually make transitions to the ground state (or a long-lived isomeric state) of nucleus Y. Counting the number of radioactive nuclei Y via the activity provides directly the information of astrophysical interest, independent of the details of decay branchings or angular correlation effects. Furthermore, since the activity is measured after the irradiation took place, there is no prompt beam-induced background and the counting setup can be optimized more easily for efficiency since geometrical complications, such as target chambers and beam pipes, are absent in the offline measurement. Finally, the activation method is selective for specific reactions, that is, by measuring the energies of the radioactive decay products or the time evolution of the radioactive decay, one can infer the identity of the radioactive nuclei Y. It is sometimes even possible to determine cross sections for several different reactions in a single measurement. The activation method is suitable for radioactive reaction products with half-lives between several years and fractions of a second (Beer *et al.*, 1994).

The rate of change in the number of radioactive nuclei Y is given by the difference of production and decay rates,

$$\frac{d\mathcal{N}_Y(t)}{dt} = P(t) - \lambda_Y \mathcal{N}_Y(t) \tag{4.72}$$

with $\mathcal{N}_Y$ and $\lambda_Y = \ln 2/T_{1/2}$ the number and decay constant of nuclei Y, respectively. The production rate is given by

$$P(t) = \mathcal{N}_X \int \sigma(E)\phi(E,t)\,dE = \mathcal{N}_X \hat{\sigma} \int \phi(E,t)\,dE = \mathcal{N}_X \hat{\sigma}\phi(t) \tag{4.73}$$

with $\mathcal{N}_X$ the number of target nuclei X, σ the cross section for the $X(a,b)Y$ reaction, and $\phi(t)$ the incident particle flux (in particles per area per time). A number of assumptions have been made in the above expression: (i) the number of target or sample nuclei X does not change during the irradiation (i.e., the target does not deteriorate and the fraction of target nuclei destroyed is negligible), and (ii) the target or sample is sufficiently thin so that the energy loss of incident charged particles in the target, or the attenuation of incident neutrons in the sample, is small. The quantity $\hat{\sigma}$ represents a cross section averaged over the energy distribution of incident projectiles (and over the target thickness for charged

particles). For the general case of a varying incident particle flux, Eq. (4.72) has to be integrated numerically. For the special case of a constant flux, $\phi(t) = \text{const}$, we can solve Eq. (4.72) analytically. For the initial condition $\mathcal{N}_Y(t = 0) = 0$, the solution is

$$\mathcal{N}_Y(t) = \frac{\mathcal{N}_X \hat{\sigma} \phi}{\lambda_Y} \left(1 - e^{-\lambda_Y t}\right) \tag{4.74}$$

If $\lambda_Y t \ll 1$, we find $\mathcal{N}_Y(t) \approx \mathcal{N}_X \hat{\sigma} \phi [1 - (1 - \lambda_Y t)]/\lambda_Y = \mathcal{N}_X \hat{\sigma} \phi t$, that is, $\mathcal{N}_Y(t)$ increases linearly for small irradiation times. For $\lambda_Y t \gg 1$, we obtain $\mathcal{N}_Y(t) \approx \mathcal{N}_X \hat{\sigma} \phi / \lambda_Y = \mathcal{N}_X \hat{\sigma} \phi T_{1/2} / \ln 2 = \mathcal{N}_Y^S$ and $\mathcal{N}_Y(t)$ reaches a saturation value, $\mathcal{N}_Y^S$, where the production rate becomes equal to the destruction rate. At the end of the irradiation period, $t = t_0$, the number of nuclei $\mathcal{N}_Y$ is $\mathcal{N}_Y(t_0) = \mathcal{N}_X \hat{\sigma} \phi (1 - e^{-\lambda_Y t_0})/\lambda_Y$. Since nuclei Y are no longer produced for $t > t_0$, the production rate is zero and the time evolution of $\mathcal{N}_Y(t)$ is given by

$$\begin{aligned} \mathcal{N}_Y(t) &= \mathcal{N}_Y(t_0) e^{-\lambda_Y (t - t_0)} \\ &= \frac{\mathcal{N}_X \hat{\sigma} \phi}{\lambda_Y} \left(1 - e^{-\lambda_Y t_0}\right) e^{-\lambda_Y (t - t_0)} \qquad \text{for } t > t_0 \end{aligned} \tag{4.75}$$

If the sample is counted between t_1 and t_2, the number of disintegrations in that period is given by the integral over the activity $A_Y(t) = \mathcal{N}_Y(t) \lambda_Y$,

$$\begin{aligned} D(t_1, t_2) &= \int_{t_1}^{t_2} \lambda_Y \mathcal{N}_Y(t)\, dt = \mathcal{N}_X \hat{\sigma} \phi \left(1 - e^{-\lambda_Y t_0}\right) \int_{t_1}^{t_2} e^{-\lambda_Y (t - t_0)}\, dt \\ &= \frac{\mathcal{N}_X \hat{\sigma} \phi}{\lambda_Y} \left(e^{\lambda_Y t_0} - 1\right) \left(e^{-\lambda_Y t_1} - e^{-\lambda_Y t_2}\right) \end{aligned} \tag{4.76}$$

Hence, the cross section $\hat{\sigma}$ can be determined from the number of disintegrations, the number of target nuclei, and the total flux of incident particles. Equation (4.76) can also be used to determine an unknown neutron flux from a well-known cross section.

Figure 4.39 shows schematically the time evolution of the number of radioactive nuclei Y. In this example, the incident particle flux is constant, $\phi(t) = \text{const}$. The irradiation of the target starts at $t = 0$ and stops at $t_0 = 6T_{1/2}$, where $\mathcal{N}_Y(t)$ is close to the saturation value $[\mathcal{N}_Y(t)/\mathcal{N}_Y^S = 0.984]$. After some waiting period between t_0 and t_1, the activity is counted between t_1 and t_2, when $\mathcal{N}_Y(t)$ decays exponentially. The relationship between the number of disintegrations (or the measured number of counts) and the cross section is discussed in Sections 4.8 and 4.9.

Targets or samples must be sufficiently thick to achieve reasonable counting statistics. But they should not be too thick or otherwise: (i) incident neutrons may be attenuated significantly or undergo multiple scattering and the effects may be difficult to correct for; (ii) the cross section for incident charged particles will be integrated over too large an energy range and cannot be determined with a reasonable energy resolution; and (iii) the self-absorption of the emitted delayed radiation (e.g., electrons or photons) may become significant. The loss of radioactive nuclei Y caused by sputtering or backscattering is another problem when targets

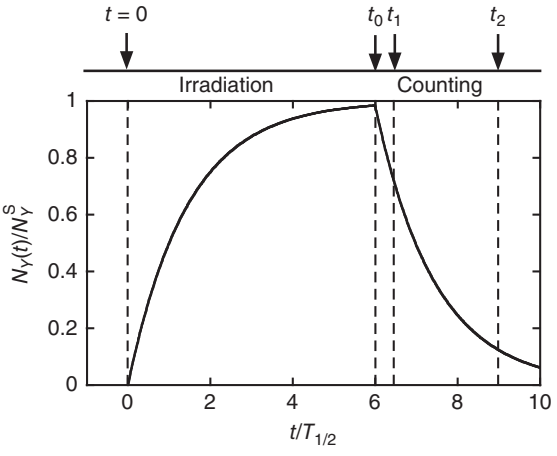

Figure 4.39 Evolution of the number of radioactive nuclei Y (in units of the saturation value $\mathcal{N}_Y^S$) versus time (in units of the half-life $T_{1/2}$). Here, the incident particle flux is assumed to be constant. The irradiation of the target starts at time $t = 0$ and stops at $t_0 = 6T_{1/2}$, when the ratio $\mathcal{N}_Y(t)/\mathcal{N}_Y^S$ is close to unity. After some waiting period, $t_1 - t_0$, the activity is counted between t_1 and t_2 when $\mathcal{N}_Y(t)$ decays exponentially.

are bombarded with intense charged-particle beams. Such losses can be measured and accounted for by surrounding the target with a catcher foil. Furthermore, one must ensure that the radioactive nuclei Y of interest are not produced during the irradiation via some other nuclear reaction, $Z(c,d)Y$, involving contaminants in the beam or the target. For example, a measurement of the ^{27}Al(n,γ)^{28}Al reaction may be complicated by the presence of a ^{28}Si contamination in the aluminum sample since the ^{28}Si(n,p)^{28}Al reaction also produces ^{28}Al and hence interferes with the measurement.

4.6.3 Time-of-Flight Technique

The time-of-flight method provides neutron beams with a resolution that is far superior compared to most other techniques. Consider Figure 4.40 showing a pulsed proton or electron beam incident on a neutron production target, as described in Section 4.1.2. With each pulse, a group of neutrons with a broad energy distribution is produced. The neutrons travel to the irradiation sample located at a distance of L from the neutron-producing target. Neutron-induced reactions take place in the sample and the prompt radiation produced in the interaction is detected using a suitable counter. For example, detector 1 in Figure 4.40 is a γ-ray detector for the study of (n,γ) reactions. The neutron velocity is determined by the measured length of the flight path and the time difference, $t = t_{\text{stop}} - t_{\text{start}}$, between the arrival time of the primary electron or proton pulse at the neutron-producing target and the time of detection of the prompt reaction products (provided that the latter time is practically simultaneous with the arrival

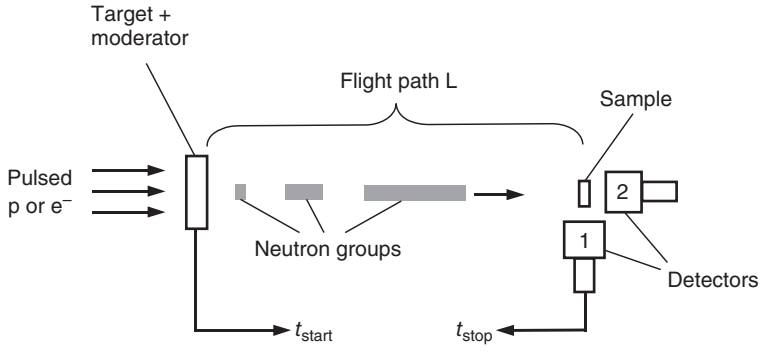

Figure 4.40 Neutron time-of-flight technique. A pulsed proton or electron beam is incident on a neutron production target. With each pulse, a neutron group with a broad energy distribution is produced. The neutrons travel a distance of L to the irradiation sample. Prompt radiation, for example, γ-rays from an (n,γ) reaction induced in the sample, is detected by counter 1, while counter 2 represents a neutron detector for measuring the transmission (Section 4.2.3). The incident neutron energy is given by the flight path length L and the time difference, $t = t_{stop} - t_{start}$, between the primary electron or proton pulse arrival time at the neutron-producing target and the detection time of the prompt reaction products in counter 1 (or of the transmitted neutrons in counter 2).

of the neutrons at the sample). The neutron energy is given by

$$E = \frac{1}{2} m_n v^2 = \frac{1}{2} m_n \left(\frac{L}{t}\right)^2 \tag{4.77}$$

with m_n the neutron mass. The use of this nonrelativistic expression introduces an error of less than 0.2% at $E = 1$ MeV. In practice, the events are sorted electronically into a histogram displaying the flight time on the horizontal axis (i.e., a particular channel corresponds to flight times between t_i and t_{i+1}). Subsequently, the flight time scale is converted to a neutron energy scale. From Eq. (4.77) we find numerically

$$\frac{t}{L} = \frac{72.3}{\sqrt{E}} \tag{4.78}$$

with t, L, and E in units of microsecond, meter, and electron volt, respectively. For example, for a flight path of 10 m and neutrons of 1 keV energy the flight time amounts to ≈ 23 μs. For a broad energy distribution of incident neutrons, the time-of-flight technique allows a measurement of the intensity of reaction products as a function of the incident neutron energy in a single experiment.

According to Eq. (4.77), the energy resolution of the neutron beam is given by

$$\frac{\Delta E}{E} = 2\sqrt{\left(\frac{\Delta L}{L}\right)^2 + \left(\frac{\Delta t}{t}\right)^2} \tag{4.79}$$

The uncertainty in the flight path (e.g., because of the finite sizes of the neutron-producing target and the detector) can be reduced by increasing L, although the intensity of the neutron beam at the sample position will simultaneously decrease.

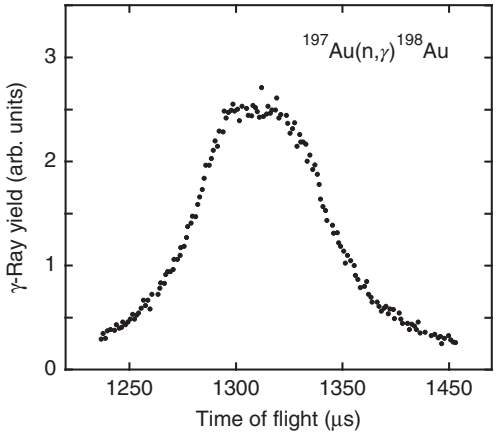

Figure 4.41 Measured count rate versus time of flight in the vicinity of the 4.9 eV resonance in the ^{197}Au(n,γ)^{198}Au reaction. Data adopted from Macklin, Halperin, and Winters (1979).

In most cases, the uncertainty in flight time will dominate the energy resolution. One finds numerically

$$\Delta E = 0.028 \frac{\Delta t}{L} E^{3/2} \tag{4.80}$$

The uncertainty Δt is influenced by a number of factors, including the time width of a neutron group after a particular proton or electron burst (< 100 ns), the pulse rise time of the detector (< 5 ns), and the uncertainty in the neutron slowing down time if the neutron-producing target is surrounded by a moderator. The primary requirements for the detector are fast timing properties, relatively high efficiency and low sensitivity to neutron-induced background radiation. For neutron-capture studies, organic scintillators or BaF_2 detectors are frequently used, while ionization chambers or solid-state counters are the detectors of choice for (n,p) or (n,α) type experiments. With time-of-flight techniques, energy resolutions of better than 1 eV have been obtained for neutron energies up to a few kilo electron volts (i.e., $\Delta E/E \approx 0.001$). For example, Figure 4.41 shows the measured count rate versus time of flight in the vicinity of the 4.9 eV resonance in the ^{197}Au(n,γ)^{198}Au reaction. Other examples of transmission and neutron-capture yield curves obtained with the time-of-flight technique are shown in Figure 4.61.

4.7 Background Radiation

All radiation detectors used in fusion reaction measurements will record a certain number of pulses that are caused by natural radioactivity in the environment or by cosmic radiation. For relatively large reaction cross sections, the background

count rate may be negligible compared to the signal count rate. However, astrophysically important reactions have frequently very small cross sections at the energies of interest. In such cases, the experiment has to be designed carefully so that the signal is not obscured by the background. It has to be kept in mind that in nuclear counting experiments the sensitivity for detecting a signal above background is approximately directly proportional to the signal count rate, but inversely proportional to the *square root* of the background count rate (Knoll, 1989). For example, a background reduction by a factor of 100 corresponds to an improvement in sensitivity by only a factor of 10. Thus, a substantial effort of reducing the background is required in order to observe very weak cross sections or resonance strengths. For developing detection techniques that reduce the background, it is first necessary to understand the nature of the background in more detail. A comprehensive review of these issues can be found in Knoll (1989) and Heusser (1995). Here, we will discuss the influence of natural radioactivity and cosmic rays on detectors that are used in nuclear astrophysics measurements. We are especially interested in methods of background suppression. Other important sources of background, for example, from electronic noise or from beam-induced processes (Section 4.3.3 and Table 4.4), are not discussed in this section.

4.7.1 General Aspects

Figure 4.42 shows a typical experimental setup consisting of accelerator, target chamber, detector, and shielding. The most important sources of background radiation are indicated. Terrestrial radiation near the Earth's surface and in ordinary construction materials (walls, detector, shielding materials, air, and so on) is caused by naturally occurring radioisotopes. In particular, Th, U, and Ra are members of radioactive decay series and lead to a large number of daughter nuclei that emit α-, β-, and γ-radiation. Among these daughter products are the short-lived radioactive gases ^{220}Rn and ^{222}Rn that are present in the ambient air. The background from radon and progenitors may be reduced by replacing the air surrounding the detection setup with a radon-free gas (e.g., nitrogen). Furthermore, spontaneous fission (in particular of ^{238}U) contributes to the γ-ray and neutron background. Another important source of terrestrial β- and γ-radiation originates from the decay of ^{40}K ($T_{1/2} = 1.3 \times 10^9$ y). The activity of certain fission products that originate from past nuclear weapons testing also contributes to the background (e.g., ^{137}Cs).

The activity levels in common materials vary substantially (Knoll, 1989). In demanding low-background applications, the construction and shielding materials have to be selected carefully. One may ordinarily expect that the background count rate is inversely proportional to the thickness of the detector shield. However, beyond a certain optimum thickness the background will not decrease any further because a more massive shield represents a larger target for cosmic-ray-induced background (see below).

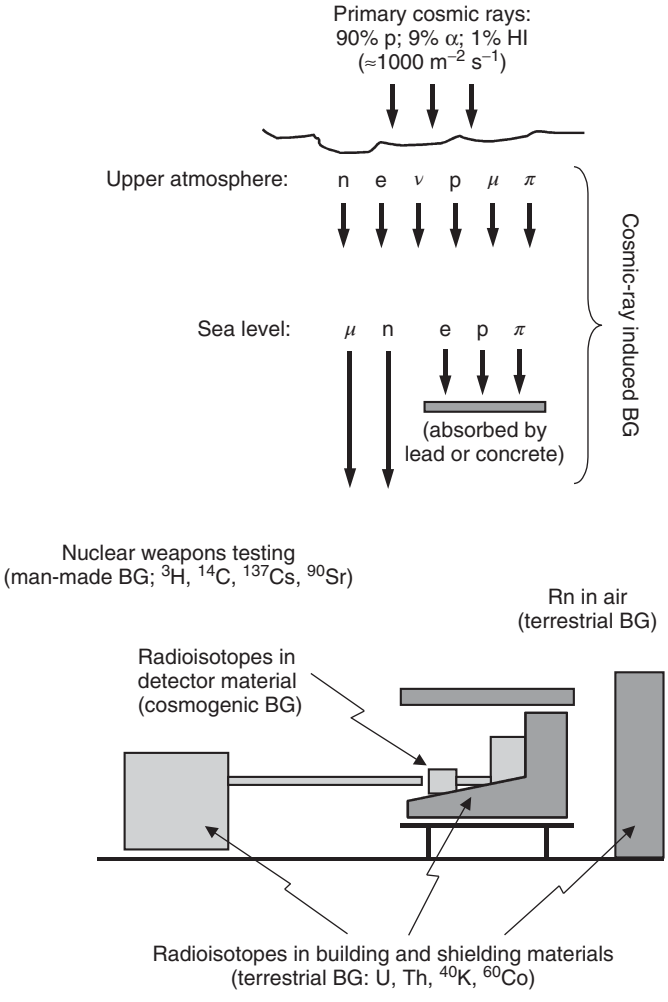

Figure 4.42 Sources of environmental background in a typical nuclear physics counting experiment. Other sources, such as electronic noise or beam-induced background radiation, are not shown. See discussion in the text.

Primary cosmic radiation consists mainly of protons and α-particles with extremely high kinetic energies. They hit the upper atmosphere with an intensity of about $10^3\ m^{-2}s^{-1}$. Through interactions with air molecules, a large number of different (secondary) elementary particles with energies extending into the 100 MeV range are produced. Among the secondary radiation, protons, electrons, and pions are easily absorbed by the concrete floors of a building. The most relevant components for low level background measurements are muons and neutrons.

The muon-induced background arises from direct ionization events in the detector volume, radioisotope production via interactions with nuclei

(e.g., spallation), muon bremsstrahlung, production of δ electrons, muon decay ($\mu^{\pm} \rightarrow e^{\pm} + \nu + \overline{\nu}$), and electron–positron pair production. The latter three processes also give rise to bremsstrahlung. Secondary neutrons originate from primary cosmic radiation, while tertiary neutrons are produced by slow muons via the capture reaction p(μ^-,ν_μ)n and by fast muons via (γ,n) reactions and photofission. Neutron background originates not only from cosmic-ray interactions but also from terrestrial radioisotopes via (α,n) reactions and spontaneous fission of ^{238}U. Fast neutrons react with nuclei via (n,n'γ) reactions, while thermal neutrons interact via (n,γ) reactions.

Muons are very penetrating particles and large shielding depths (e.g., several 100 m of earth) are required to attenuate their intensity substantially. For this reason, low-level detection systems are sometimes operated deep underground. Such a laboratory, dedicated to nuclear astrophysics experiments, is described in Bemmerer *et al.* (2005). Alternatively, in measurements near sea level, it is usually possible to surround the primary detector (e.g., germanium) with a secondary (guard) counter (e.g., plastic scintillator). If both detectors are operated in anticoincidence mode, that is, if events are rejected when both counters respond at the same time, then the background is significantly reduced.

The magnitude of some background components can change with time. Such fluctuations may arise from variations in cosmic-ray intensity or in airborne radioactivity depending on the meteorological conditions. For the analysis of pulse height spectra obtained with beam on target, it is therefore helpful to carry out background measurements (without beam) before and after the experiment.

4.7.2
Background in Charged-Particle Detector Spectra

We will focus in this section on semiconductor charged-particle detectors. The extreme degree of purity required of semiconductor crystals results in relatively low levels of inherent radioactivity. However, radioactive impurities in the construction materials of the setup (detector holder, target chamber, shielding, and so on) will contribute to the measured background. This background will extend to several mega electron volts, corresponding to typical energies of α-particles from terrestrial radioisotopes. For example, commercial aluminum shows a low-level α-activity of ≈ 0.3 α-particles $h^{-1}cm^{-2}$ above 250 keV energy (Knoll, 1989). The α-particle emission rate of stainless steel is about an order of magnitude lower. For low-level background measurements, it is thus important to select the construction materials carefully.

Terrestrial γ-radiation and cosmic-ray-induced γ-rays, charged particles, and neutrons will also contribute to the background in charged-particle detector spectra. These components can effectively be reduced through the use of appropriate shielding such as low-activity lead or mercury. Cosmic-ray muons, on the other hand, are only weakly absorbed in the shield. The muons are minimum ionizing

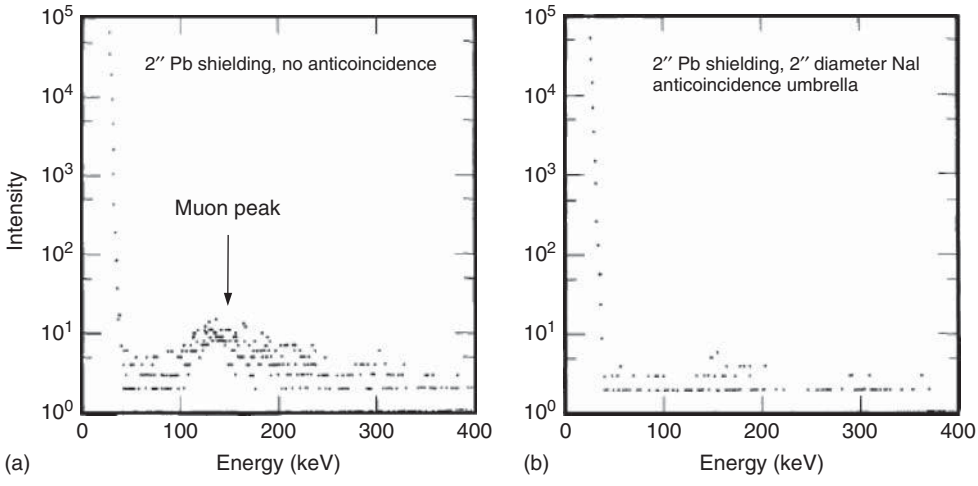

Figure 4.43 (a) Background spectrum measured with a silicon charged-particle detector of 300 μm thickness. The active detector surface is positioned parallel to the surface of the Earth. The muon peak, which has the same origin as the one shown in Figure 4.22, occurs at about 120 keV. (b) Same as part (a), but with rejection of all events corresponding to simultaneous signals from the silicon detector and a NaI(Tl) active shield counter that was positioned above the silicon detector. The substantial reduction of the muon background is evident. (Reprinted from Walter and Boshart (1966). Copyright (1966), with permission from Elsevier.)

(Section 4.2.1) and lose energy in silicon at a rate of $dE/dx \approx -400$ keV/mm. The spatial distribution of the muons is at maximum in a direction perpendicular to the Earth's surface. Therefore, the energy deposited by the muons in the detector is approximately equal to the product of dE/dx and the effective thickness of the active detector volume. Since some muons will pass at oblique angles through the sensitive region, the background peak in the pulse height spectrum will exhibit a high-energy tail. This general behavior is displayed in Figure 4.43a, showing a background spectrum measured with a silicon detector of 300 μm thickness, with its active surface positioned parallel to the surface of the Earth. In order to reduce the terrestrial background, the detector was mounted in a high-purity aluminum oxide insulator and the detector container was made from low-contamination copper. The muon peak in the spectrum is expected to occur at about (400 keV/mm)(0.3 mm) = 120 keV, consistent with observation. The spectrum in Figure 4.43b was obtained by rejecting all events corresponding to simultaneous signals from the silicon detector and a NaI(Tl) active shield counter that was positioned above the silicon detector. The muon background is substantially reduced using anticoincidence techniques.

Figure 4.44 shows the measured background of a 300 μm thick silicon detector in the energy range of 50–400 keV versus mode of operation. The results are given in units of counts per minute (cpm) and per square centimeter of the active detector surface that is oriented parallel to the Earth's surface. The background

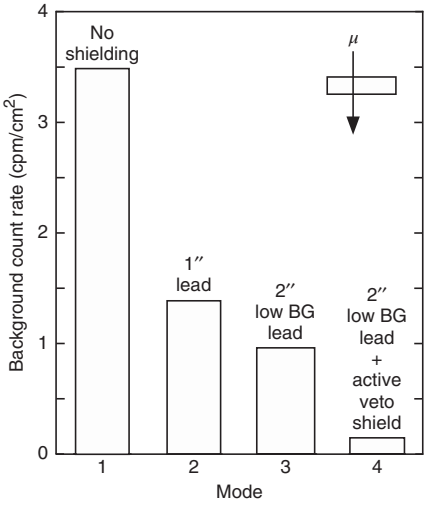

Figure 4.44 Measured background (in counts per minute and per square centimeter) of a 300 μm thick silicon detector in the energy range of 50–400 keV versus mode of operation: (1) no passive or active shielding; (2) Passive shield of 2.5 cm thick lead; (3) Passive shield of 5.1 cm thick low-activity lead; (4) Additional use of an (active) anticoincidence shield. The muon-induced background rate, given by the difference of histogram heights in mode 3 and 4, amounts to ≈ 0.8 cpm/cm^2 in the energy range of 50–400 keV at sea level. Data from Walter and Boshart (1966).

count rate amounts to ≈ 3.5 cpm/cm^2 without passive or active shielding. Surrounding the setup with lead of 2.5 cm thickness shields the detector from terrestrial and cosmic-ray-induced γ-radiation and reduces the background count rate to ≈ 1.4 cpm/cm^2. A further improvement is achieved using 5.1 cm of low-background lead for a passive shield (≈ 0.97 cpm/cm^2). Finally, the additional use of an anticoincidence shield reduces the background count rate to ≈ 0.16 cpm/cm^2. We can infer from these results that the muon-induced background rate at sea level amounts to (0.97–0.16) cpm/cm^2 ≈ 0.8 cpm/cm^2 in the energy range of 50–400 keV.

In certain reactions with relatively large Q-values, it is sometimes of advantage to use two instead of one silicon detector. The nuclear reaction products of interest deposit a fraction of their energy in a thin front ("ΔE") detector and are completely stopped in a thick rear ("E") counter. By requiring a coincidence between the two detector signals, events that are caused by terrestrial α-, β-, and γ-radiation and that deposit energy in only one of the detectors are rejected. The muon-induced background can then be suppressed either by locating the setup deep underground (Junker *et al.*, 1998) or by surrounding the setup with a suitable active veto counter. This technique is not applicable to the study of reactions with Q-values of less than several mega electron volts since in this case the emitted nuclear reaction products will have insufficient energies to penetrate even the thinnest commercially available ΔE detectors.

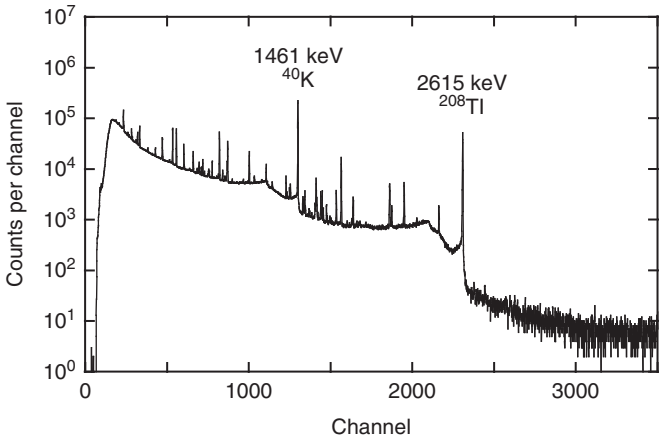

Figure 4.45 Room background γ-ray spectrum, recorded for 15 h without beam on target using a HPGe detector of 582 cm^3 volume. Two prominent peaks occur at 1461 keV and 2615 keV. They originate from the decays of the radioisotopes ^{40}K and ^{208}Tl, respectively. All the other peaks originate from the sources shown in Figure 4.42. The γ-ray background beyond $E_\gamma \approx 2.6$ MeV is continuous and shows no discrete peaks.

4.7.3 Background in γ-Ray Detector Spectra

The background in γ-ray spectra is usually higher compared to charged-particle spectra for two reasons. First, γ-ray detectors have a larger volume and second, the nature of the γ-ray background is rather complex. A typical background γ-ray spectrum, recorded without beam on target with a HPGe detector of 582 cm^3 volume for 15 h, is shown in Figure 4.45. A large number of discrete peaks can be observed. Most of these originate from radionuclides that occur naturally in the material of the detector and the surroundings. The two most intense room background γ-ray peaks occur at 1461 keV and 2615 keV and originate from the decays of the radioisotopes ^{40}K and ^{208}Tl, respectively (Table 4.6 and Figure 4.46). The nucleus ^{40}K β-decays to the 1461 keV level in ^{40}Ar which, in turn, decays to the ground state by emission of a single photon. The nucleus ^{208}Tl β-decays to several ^{208}Pb levels with excitation energies between 3 MeV and 4 MeV. Subsequently, these states decay through the first excited state at 2615 keV to the ground state via γ-ray cascades (i.e., by emission of two or more coincident photons). Compilations of other background peaks can be found in Debertin and Helmer (1988) and Knoll (1989). The analysis of a spectrum obtained with beam on target requires a careful identification of room background peaks. Furthermore, the peaks are superimposed on a continuous background, caused by Compton scattering of room background photons and by cosmic-ray-induced processes. In nuclear astrophysics measurements, the cross sections are frequently very small and, therefore, it is ultimately this continuous background

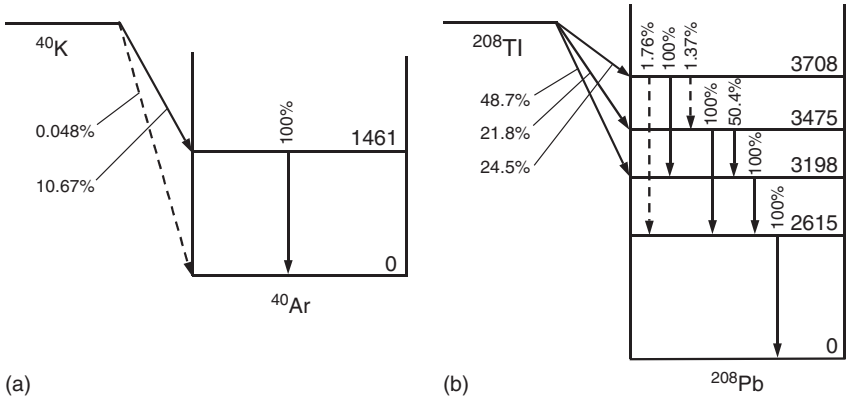

Figure 4.46 Level schemes of (a) ^{40}Ar and (b) ^{208}Pb. The decay of ^{40}K produces a single photon (1461 keV), while the decay of ^{208}Tl gives rise to the emission of two or more coincident photons. Data from Firestone and Shirley (1996).

that is the major obstacle in observing the peaks from the nuclear reactions of interest.

Similar to the case of silicon detectors, the inherent activity of high-purity germanium is very small. However, radioimpurities in construction materials including the aluminum crystal housing, stainless steel and copper cooling rod, electrical solder in the preamplifier, and so on, may contribute to the γ-ray background. In scintillation counters, the glass envelope of the photomultiplier tube and the tube base are a potential source of background. In low-background detectors, the contribution from these sources is substantially reduced by a careful selection of the construction materials.

The vast majority of γ-rays from terrestrial or cosmogenic background sources have energies of less than 3.0 MeV, although some γ-rays with energies of up to 7 MeV are produced in the spontaneous fission of ^{238}U. Contributions from these sources can be reduced by surrounding the detector with metal shields of high purity. Because of its high density and large atomic number, specially refined lead with a low concentration of the radioisotope ^{210}Pb ($T_{1/2} = 22.3$ y) is the best choice for a γ-ray shield. Iron and copper are also used but have higher cross sections for the cosmogenic production of radionuclides compared to lead. Beyond a certain optimum shielding thickness (≈ 10–15 cm for lead), the background is not reduced any further because of an increase in secondary radiation caused by cosmic-ray interactions in the shield. Most γ-rays from neutron inelastic scattering and radiative neutron capture on the detector material have energies of less than about 3 MeV, although neutron capture on iron can produce γ-rays with energies of about 10 MeV. The neutron-induced component is sometimes reduced by an additional neutron absorber in the shield (e.g., borated polyethylene). When the detector shield contains hydrogen (e.g., concrete), neutron capture sometimes gives rise to a discrete γ-ray of 2.2 MeV energy in the spectrum.

The continuous γ-ray background caused by cosmic-ray muons arises from several different types of interactions and it is not apparent which of the processes discussed in Section 4.7.1 dominates. Monte Carlo simulations have been performed to investigate this issue. It is found (Vojtyla, 1995) that bremsstrahlung from δ electron production dominates the background at energies below $E \approx 5$ MeV. At higher energies, the background is dominated by direct ionization events that give rise to a broad peak between 10 and 40 MeV, with the exact location depending on the crystal size. The observed broad peaks in Figures 4.22 and 4.43a are caused by the same process.

Gamma-ray background count rates, measured by specially designed low-background germanium detector systems, are compared in Figure 4.47. The horizontal axis displays the location (shielding depth) of the apparatus in units of meter water equivalent (m w.e.) and the vertical axis shows the measured total count rate in the energy region below 3 MeV in units of counts per hour per 100 cm^3 detector volume. The construction materials for all of these detection systems were carefully selected to reduce radioimpurities. Passive shields consisted of several layers of different low-activity materials (Pb, Cu, Fe, and so on). In some cases (shown as triangles), plastic scintillators or multiwire proportional

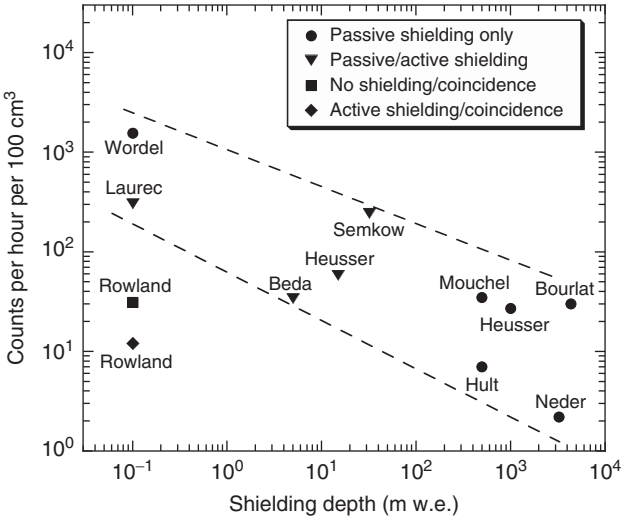

Figure 4.47 Comparison of γ-ray background count rates in the energy region below $E_\gamma = 3$ MeV (in units of counts per hour per 100 cm^3 detector volume) versus shielding depth (in units of meter water equivalent). The data indicated by the circles (passive shielding only) and triangles (passive and active shielding) are adopted from Semkow *et al.* (2002). All these spectrometers are specially designed for ultralow background measurements. The two dashed lines are to guide the eye. The γ-ray (singles) background in this energy range can be reduced by at least two orders of magnitude by placing the apparatus deep underground. Results from γγ-coincidence measurements using conventional detectors (Rowland *et al.*, 2002b) are shown as square (no shielding) and diamond (active shielding).

chambers have been used for active cosmic-ray background discrimination. It can be seen that in laboratories located at sea level (shielding depths < 1 m w.e.) the lowest achieved background count rates are ≈ 1000 counts/h. This represents already an improvement by orders of magnitude compared to the background shown in Figure 4.45, which was obtained using a conventional detector and setup. At moderate shielding depths of 10–15 m w.e., background count rates of ≈ 100 counts/h have been measured. Another order of magnitude can be gained by locating the apparatus deep underground (shielding depths of several 1000 m w.e.), where measured background count rates amount to ≈ 10 counts/h.

4.7.3.1 $\gamma\gamma$-Coincidence Techniques

In many nuclear reactions of astrophysical interest, two or more photons are emitted in a cascade. In such cases, the background can be reduced substantially through the use of coincidence techniques. Consider a simple setup consisting of two γ-ray detectors. Most background events will occur only in one detector at a time and, therefore, are eliminated by demanding a coincidence between the signal outputs of both detectors.

An example for a setup is shown in Figure 4.48a. A HPGe detector is positioned in very close geometry to the target to maximize the peak efficiency and a NaI(Tl) annulus surrounds both the target and the germanium crystal. Figure 4.48b shows for coincidence events the energy deposited in the HPGe detector versus the energy deposited in the NaI(Tl) detector. We will first discuss the simple case

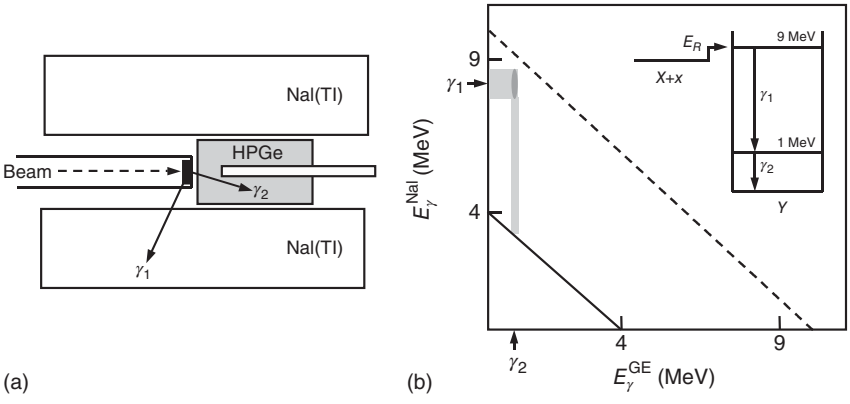

Figure 4.48 γγ-Coincidence technique. (a) Setup consisting of a HPGe detector and a NaI(Tl) annulus surrounding the target chamber. (b) Two-dimensional histogram displaying the energy deposited in the HPGe detector (horizontal axis) and the NaI(Tl) detector (vertical axis). The inset shows a simple decay scheme consisting of a two-photon cascade (E_{γ_1} = 9 MeV −1 MeV = 8 MeV; E_{γ_2} = 1 MeV). If two photons are detected in coincidence, and only if those events located between the solid and dashed lines are accepted, then the environmental background is substantially reduced. The events located below the solid line are mainly caused by room background (E_γ < 4 MeV), while those located above the dashed line originate from cosmic-ray interactions.

of a two-γ-ray cascade. Assume that a capture reaction populates an initial state of 9 MeV excitation energy and that this state decays through an intermediate level at 1 MeV to the ground state. The two diagonal lines correspond to a total energy deposition (in both the HPGe and NaI(Tl) detector) of 4 MeV and 9.5 MeV. Events located above the dashed line ($E_\gamma^{\mathrm{Ge}} + E_\gamma^{\mathrm{NaI}} > 9.5$ MeV) can immediately be excluded from the analysis since any event that originates from the capture reaction of interest can at most have a total energy of 9 MeV (apart from a small energy spread caused by the finite detector resolutions). Such high-energy events originate, for example, from cosmic-ray muons that traverse and deposit energy in both detectors. Most room background coincidence events appear in the region below the solid line ($E_\gamma^{\mathrm{Ge}} + E_\gamma^{\mathrm{NaI}} < 4$ MeV). These include 1461 keV photons from ^{40}K decay that deposit energy in both detectors via Compton scattering, as well as coincident γ-rays (including 2615 keV photons) from ^{208}Tl decay (Figure 4.46). By accepting only events located in the region between the solid and the dashed lines, the background is significantly reduced.

Suppose now that the primary 8 MeV γ-ray is observed in the NaI(Tl) detector, while the secondary 1 MeV photon is counted in the HPGe detector. Events corresponding to the full-energy peaks of both incident photons are located in the dark-shaded oval region of the two-dimensional energy spectrum. The oval shape is caused by the far better energy resolution of the HPGe detector. If only these events are accepted in the data analysis, the background is drastically reduced. However, at the same time the efficiency of the coincidence apparatus, given by the product of HPGe and NaI(Tl) peak efficiencies, is significantly reduced compared to the peak efficiency of a single detector. This result is undesirable in view of the very weak cross sections of astrophysical interest. The problem is solved by accepting all events located between the two diagonal lines, including those caused by Compton scattering and pair production in the NaI(Tl) detector. In this particular mode, the HPGe detector provides the spectroscopic information of interest (peak energies and intensities), while the main function of the NaI(Tl) annulus is to provide a large coincidence efficiency.

The power of the coincidence method is demonstrated in Figure 4.49. It shows three HPGe pulse height spectra in the energy range between 0.8 MeV and 2.5 MeV, measured at the weak $E_r = 227$ keV resonance in the ^{26}Mg(p,γ)^{27}Al reaction. Each spectrum was recorded with a proton beam intensity of only 1.5 μA for a measuring time of 10 h. The vertical dashed lines indicate the locations of expected secondary γ-ray transitions in ^{27}Al at 1014 keV and 2211 keV. The spectrum shown in part (a) was obtained without detector shielding. All observed γ-ray peaks are caused by environmental background contributions. The middle spectrum (part b) was measured by shielding the detector with 5 cm thick lead. The background is reduced by about one order of magnitude, but still no peaks originating from the ^{26}Mg(p,γ)^{27}Al reaction can be identified. The spectrum in part (c) was measured in coincidence with γ-rays observed in a NaI(Tl) annulus. The coincidence requirement was $4\ \mathrm{MeV} < E_\gamma^{\mathrm{Ge}} + E_\gamma^{\mathrm{NaI}} < 9\ \mathrm{MeV}$. No shielding was used in this case. Compared to the unshielded singles HPGe spectrum

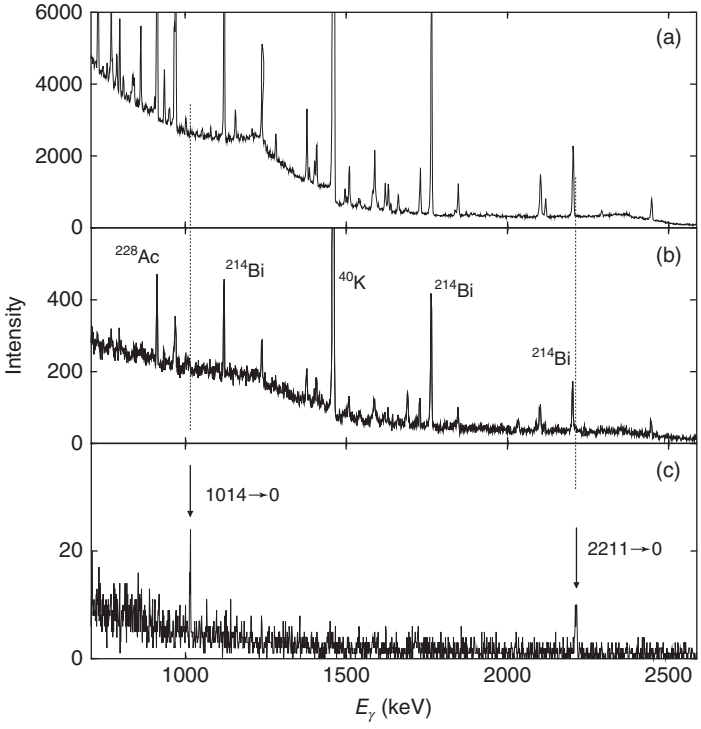

Figure 4.49 HPGe γ-ray spectra in the energy range between 0.8 MeV and 2.5 MeV, measured at the weak E_r = 227 keV resonance in the ^{26}Mg(p,γ)^{27}Al reaction (Q = 8271 keV). Each spectrum was recorded with a proton beam intensity of 1.5 μA for a running time of 10 h. The vertical dashed lines indicate the location of expected secondary γ-ray transitions in ^{27}Al at 1014 keV and 2211 keV. (a) No detector shielding; (b) passive 5 cm thick lead shielding; (c) coincidence requirement of 4 MeV $< E_\gamma^{\mathrm{Ge}} + E_\gamma^{\mathrm{NaI}} <$ 9 MeV (without shielding). The background is reduced by more than three orders of magnitude and the expected secondary transitions induced by the weak ^{26}Mg(p,γ)^{27}Al resonance are clearly observed. The peak close to a γ-ray energy of 2211 keV shown in parts (a) and (b) originates from room background (^{214}Bi) and not from decays in ^{27}Al. (Reprinted from Rowland *et al.* (2002b). Copyright (2002), with permission from Elsevier.)

(part a), the γ-ray background is reduced by more than three orders of magnitude and all the discrete peaks originating from environmental radioactivity have disappeared. The resonant γ-rays from the decays of the 1014 keV and 2211 keV levels in ^{27}Al are now clearly observed.

The remaining continuous background in the coincidence spectrum is caused by cosmic-ray-induced bremsstrahlung and by muons that directly ionize both detectors. The measured *coincidence* background count rate, shown as a square in Figure 4.47, compares favorably with *singles* background count rates measured with specially designed low-level detection systems that are located deep underground. The coincidence background count rate can be further reduced using a

muon veto shield (e.g., plastic scintillators; see Rowland *et al.*, 2002b), as indicated by the diamond in Figure 4.47. Notice that coincidence techniques will not improve the detection sensitivity significantly if the background is mainly induced by contaminant reactions that produce two or more photons of sufficient energy in coincidence (as is the case for the troublesome $^{11}B(p,\gamma)^{12}C$ reaction; Table 4.4). The need for targets and backings that are almost free of contaminants has already been pointed out in Section 4.3.3.

The total number $\mathcal{N}$ of compound nuclei created in a fusion reaction can be calculated from the peak intensity measured in a coincidence spectrum using an expression similar to Eq. (4.69). The factor $B\eta W$ has to be replaced by the quantity $f(B, \eta, W)$, which is a function of branching ratios, detection efficiencies, and angular correlations. Consider, for example, the level diagram displayed in Figure 4.50a, showing the decay of a compound nucleus to the ground state via several different γ-ray cascades. First, suppose that photon γ_{10} is fully absorbed in a HPGe detector and that other photons belonging to the same cascade are detected in coincidence in a NaI(Tl) annulus. Neglecting angular correlation effects (i.e., assuming $W = 1$), the contribution of the two-γ-ray cascade (a) to the peak intensity of γ_{10} in the HPGe coincidence spectrum is given by

$$\mathcal{N}_{10}^{\mathrm{Ge},C,a} = \mathcal{N} B_{31} B_{10} \eta_{10}^{\mathrm{Ge},P} \eta_{31}^{\mathrm{NaI},T} = \mathcal{N} B_{31} B_{10} \eta_{10}^{\mathrm{Ge},P} \left[1 - \left(1 - \eta_{31}^{\mathrm{NaI},T}\right)\right] \quad (4.81)$$

where the product of branching ratios $B_{31}B_{10}$ represents the probability that the compound nucleus decays via the cascade $3 \rightarrow 1 \rightarrow 0$; $\eta_{31}^{\mathrm{NaI},T}$ is the *total* NaI(Tl)

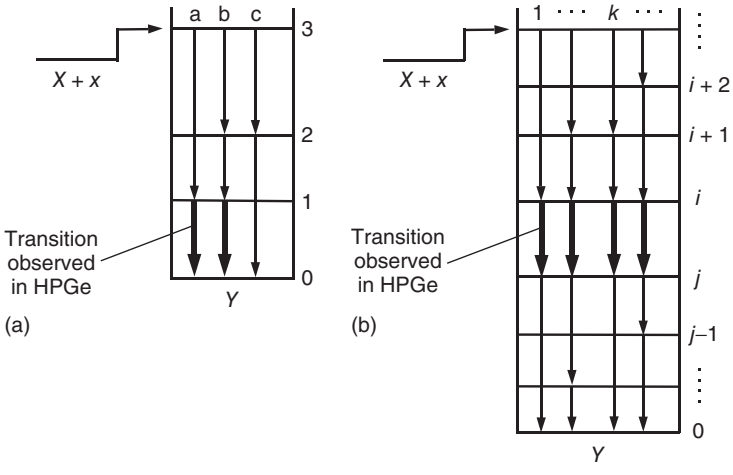

Figure 4.50 (a) Level scheme showing three different γ-ray decays from excited level 3 to the ground state 0. It is assumed that the transition $1 \rightarrow 0$ is observed in a HPGe detector and that other photons of the same cascade are detected in coincidence in a NaI(Tl) annulus. (b) General case; the transition $i \rightarrow j$ is observed in a HPGe detector, while coincident photons are detected in a NaI(Tl) detector.

efficiency. Similarly, we obtain for the contribution of the three-γ-ray cascade (b)

$$\begin{aligned}\mathcal{N}_{10}^{\mathrm{Ge},C,b} &= \mathcal{N}B_{32}B_{21}B_{10}\eta_{10}^{\mathrm{Ge},P}\left[\eta_{32}^{\mathrm{NaI},T}\left(1-\eta_{21}^{\mathrm{NaI},T}\right)+\eta_{21}^{\mathrm{NaI},T}\left(1-\eta_{32}^{\mathrm{NaI},T}\right)\right.\\ &\quad\left.+\eta_{32}^{\mathrm{NaI},T}\eta_{21}^{\mathrm{NaI},T}\right]\\ &= \mathcal{N}B_{32}B_{21}B_{10}\eta_{10}^{\mathrm{Ge},P}\left[1-\left(1-\eta_{32}^{\mathrm{NaI},T}\right)\left(1-\eta_{21}^{\mathrm{NaI},T}\right)\right] \end{aligned} \tag{4.82}$$

The term $\eta_{32}^{\mathrm{NaI},T}(1-\eta_{21}^{\mathrm{NaI},T})$ corresponds to the probability that photon γ_{32} is observed in the NaI(Tl) annulus and, at the same time, photon γ_{21} escapes detection in the NaI(Tl) annulus. The term $(1-\eta_{32}^{\mathrm{NaI},T})(1-\eta_{21}^{\mathrm{NaI},T})$ is equal to the probability that neither photon γ_{32} nor γ_{21} is detected in the NaI(Tl) annulus. Equivalently, the term $1-(1-\eta_{32}^{\mathrm{NaI},T})(1-\eta_{21}^{\mathrm{NaI},T})$ corresponds to the total probability of detecting photon γ_{32} or γ_{21}. Cascade (c) does not contribute to the peak intensity of γ_{10}.

The above expressions can be generalized (Figure 4.50b) to find the total full-energy peak intensity of photon γ_{ij} in the HPGe coincidence spectrum,

$$\mathcal{N}_{ij}^{\mathrm{Ge},C} = \mathcal{N}\eta_{ij}^{\mathrm{Ge},P}\sum_{k}\left\{\left[\prod_{i'>j'}B_{i'j',k}\right]\left[1-\prod_{\substack{i'>j'\\ i\neq j}}\left(1-\eta_{i'j',k}^{\mathrm{NaI},T}\right)\right]\right\} \tag{4.83}$$

where the sum is over all cascades k containing the transition $i \to j$. The first product is over the branching ratios of all transitions in cascade k and represents the probability that the initial level will decay via this particular cascade. The second product is over the total NaI(Tl) detector efficiencies for all transitions in cascade k, except the branch $i \to j$ that is observed in the HPGe detector. Hence, we obtain for the total number $\mathcal{N}$ of compound nuclei created in the fusion reaction

$$\mathcal{N} = \frac{\mathcal{N}_{ij}^{\mathrm{Ge},C}}{\eta_{ij}^{\mathrm{Ge},P}f(B_{i'j',k},\eta_{i'j',k}^{\mathrm{NaI},T})} = \frac{\mathcal{N}_{ij}^{\mathrm{Ge},C}}{\eta_{ij}^{\mathrm{Ge},P}\sum_{k}\left\{\left[\prod_{i'>j'}B_{i'j',k}\right]\left[1-\prod_{\substack{i'>j'\\ i\neq j}}\left(1-\eta_{i'j',k}^{\mathrm{NaI},T}\right)\right]\right\}} \tag{4.84}$$

Equations (4.82)–(4.84) need to be modified if the total NaI(Tl) efficiency has been obtained using an energy gate (Problem 4.7).

The total NaI(Tl) efficiency for a particular energy range selected by a gate in the two-dimensional spectrum of E_γ^{Ge} versus E_γ^{NaI}, $\eta_{i'j',k}^{\mathrm{NaI},T}$, can be obtained in the following way. For example, consider again a two-γ-ray cascade $3 \to 1 \to 0$ (Figure 4.50a). The intensities of photons γ_{10} and γ_{31} observed in the singles and coincidence HPGe spectrum are given by expressions similar to Eqs. (4.53) and (4.81). Neglecting coincidence summing corrections, we find

$$\begin{aligned}\mathcal{N}_{10}^{\mathrm{Ge}} &= \mathcal{N}B_{31}B_{10}\eta_{10}^{\mathrm{Ge},P} & \mathcal{N}_{31}^{\mathrm{Ge}} &= \mathcal{N}B_{31}\eta_{31}^{\mathrm{Ge},P}\\ \mathcal{N}_{10}^{\mathrm{Ge},C} &= \mathcal{N}B_{31}B_{10}\eta_{10}^{\mathrm{Ge},P}\eta_{31}^{\mathrm{NaI},T} & \mathcal{N}_{31}^{\mathrm{Ge},C} &= \mathcal{N}B_{31}B_{10}\eta_{31}^{\mathrm{Ge},P}\eta_{10}^{\mathrm{NaI},T}\end{aligned} \tag{4.85}$$

and thus

$$\eta_{31}^{\mathrm{NaI},T} = \frac{\mathcal{N}_{10}^{\mathrm{Ge},C}}{\mathcal{N}_{10}^{\mathrm{Ge}}} \qquad \text{and} \qquad \eta_{10}^{\mathrm{NaI},T} = \frac{\mathcal{N}_{31}^{\mathrm{Ge},C}}{\mathcal{N}_{31}^{\mathrm{Ge}}} \tag{4.86}$$

In the derivation of Eq. (4.86), we explicitly assumed that cascades consisting of three or more γ-rays do not contribute to the measured intensities in the HPGe coincidence spectrum (i.e., $B_{31} = 1$ and $B_{10} = 1$). It can be seen that the above relations provide absolute *total* NaI(Tl) detector efficiencies without using the activity of calibrated radioactive sources or the cross section of capture reactions. If the γ-ray source or the target is located very close to both detectors, then Eq. (4.86) becomes inaccurate because of coincidence summing (Section 4.5.2). In this case, a Monte Carlo simulation of the detection setup must be performed (Longland *et al.*, 2006).

4.7.4
Background in Neutron Detector Spectra

The neutron background originates from (α,n) reactions induced by terrestrial α-particle emitters, spontaneous fission of ^{238}U, and cosmic-ray-induced processes. Different principles apply to the shielding of neutrons compared to the shielding of charged particles or γ-rays. Neutrons need to be quickly moderated and absorbed in a medium of a high absorption cross section. The most effective moderators consist of light nuclei and contain preferably hydrogen (Section 4.2.3). Frequently used materials include paraffin, polyethylene, or water. Mean free paths of fast neutrons amount typically to several tens of centimeters and, therefore, thicknesses of about 1 m are required to moderate fast neutrons effectively. After moderation, the neutrons have to be captured. Since the capture cross section of hydrogen is relatively small, another component with a large neutron absorption cross section (e.g., ^{10}B, ^{6}Li, or Cd) is added, either as a homogeneous mixture with the moderator or as an absorbing layer between moderator and detector. The (n,α) reaction on ^{10}B and the (n,γ) reaction on Cd produce secondary γ-rays, while the (n,α) reaction on ^{6}Li proceeds directly to the ground state. Thus, ^{6}Li is preferred as neutron absorber material in applications that are sensitive to γ-ray background. The importance of other background sources depends on the type and the constructional details of the neutron detector. For example, for $^{10}BF_3$ or ^{3}He proportional counters (Section 4.5.3) the intrinsic α-radioactivity of the detector itself may cause a significant background count rate if the construction materials have not been selected carefully.

Figure 4.51 shows the neutron flux (number of neutrons per second per square centimeter) from various sources, together with the muon flux, versus shielding depth in meter water equivalent. Without any shielding, the contribution from secondary neutrons dominates the background. This intensity decreases rapidly with increasing shielding depth and becomes smaller than the neutron intensity from (α,n) reactions and spontaneous fission beyond a moderate shielding depth of $\approx$ 10 m w.e. The figure also shows for comparison the intensity of

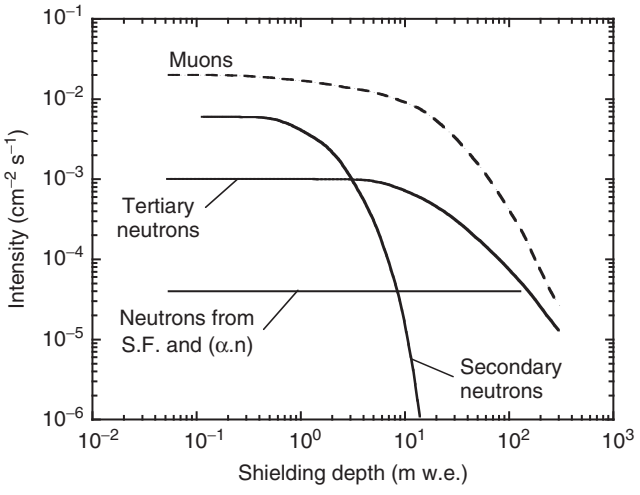

Figure 4.51 Neutron fluxes (number of neutrons per second per square centimeter) from various sources (solid lines) versus shielding depth (in units of meter water equivalent). The muon flux is shown as a dashed line. Secondary neutrons are produced by primary cosmic rays. The solid line labeled "Tertiary neutrons" represents the flux of neutrons produced by muons in a typical lead shield; the label "S.F." refers to neutrons from spontaneous fission. Data from Heusser (1995).

tertiary neutrons produced by muons in a typical lead shield. This background contribution dominates the neutron flux at shielding depths of 2–100 m w.e. Consequently, the use of massive shields should be avoided in this shielding depth region, if possible.

The background count rate measured by a neutron detector depends strongly on the location, measuring geometry, and constructional details. Thus, one has to be very careful when comparing experimental background rates measured by different detectors. Nevertheless, such a comparison is interesting since relatively little information on this subject is given in the literature. Table 4.11 compares background count rates measured in four different studies. Other parameters, such as efficiency, location, and the type of shielding, are also given. In each case, the setup consisted of ^{3}He proportional counters moderated by either polyethylene or paraffin. At sea level and without active shielding, the measured background count rate is $\approx$ 10 cpm. With active shielding, the background is substantially suppressed and amounts to $\approx$ 2 cpm. It is likely that a further reduction can be achieved by locating the setup underground, although the results listed in the table are inconclusive if adjusted for differences in total efficiencies or the size of the analyzed region in the pulse-height spectrum.

Finally, a word may be added regarding the suppression of muon-induced neutrons via anticoincidence techniques. With polyethylene or paraffin as moderator, it takes on average $\approx$ 200 μs for a fast neutron to be thermalized and captured in the neutron detector. Thus, if the anticoincidence counter indicates a muon

Table 4.11 Comparison of low-background neutron spectrometers.

Reference	Giesen *et al.* (1993)	Wang, Vogelaar, and Kavanagh (1991)	Stella *et al.* (1995)	Mayer *et al.* (1993)
Detector	^{3}He	^{3}He	^{3}He	^{3}He
Moderator	Polyethylene	Polyethylene	Polyethylene	Paraffin
Number of counters	31	12	2[a]	18
Efficiency (%)	20	22	6[a]	22
Calibration source	Am-Li	^{252}Cf	M.C.[b]	^{nat}UO
Location (m w.e.)	Sea level	Sea level	3950[c]	50[d]
Passive shield	Yes	Yes	Yes	Yes
Active shield	No	Yes[e]	No	No
Background (cpm)	11[f]	2[f]	0.6[f] (0.06[g])	0.06[h]

[a] Full detector consists of seven $^{10}BF_3$ and two ^{3}He counters; the $^{10}BF_3$ counters are not listed here for comparison because of their higher background count rate. [b] Result of Monte Carlo simulation. [c] At Gran Sasso underground laboratory. [d] On a conventionally powered submarine. [e] Plastic scintillator. [f] Total counts above discriminator threshold. [g] Counts in a region of the spectrum representing 95% of thermal neutron peak intensity. [h] Counts in a region of the spectrum representing 70% of thermal neutron peak intensity.

hit, the signals from the neutron detector have to be vetoed for several 100 μs to suppress such events effectively.

4.8 Yields and Cross Sections for Charged-Particle-Induced Reactions

The calculation of thermonuclear reaction rates requires knowledge of the nuclear reaction cross section. However, what is usually determined experimentally is the total number of nuclear reactions that occurred and the total number of incident beam particles. The ratio of these two quantities,

$$Y \equiv \frac{\text{total number of nuclear reactions}}{\text{total number of incident beam particles}} = \frac{\mathcal{N}_R}{\mathcal{N}_b} \tag{4.87}$$

is called the *yield* of the reaction. Comparison to Eq. (2.1) shows that the yield is related, but not equal, to the cross section σ. In this section, we will derive relationships for these two quantities. We will also discuss how to derive resonance strengths (i.e., integrated cross sections) from measured yields. A function of yield versus bombarding energy is referred to as *yield curve* or *excitation function*.

The following, definitions will be used for the stopping power (in units of eV cm^2/atom),

$$\varepsilon(E) \equiv S_A(E) = -\frac{1}{N}\frac{dE}{dx} \tag{4.88}$$

and for the concentration of target nuclei,

$$n \equiv Nd = \frac{\mathcal{N}_t}{A} \tag{4.89}$$

The quantities $\mathcal{N}_t$ and N denote the total number of target nuclei and the number density of target nuclei (atoms per unit volume), respectively (Section 4.2.1); d is the target thickness (in units of length). Hence, n is the number of target nuclei per unit area. All quantities in this section will be expressed in the center-of-mass system, unless mentioned otherwise.

4.8.1 Nonresonant and Resonant Yields

Suppose that a beam of energy E_0 is incident on a target. The target can be divided into a number of slices of thickness Δx_i, and it can be assumed that the energy lost by the beam in each slice, ΔE_i, is small. In other words, both the cross section, σ_i, and the stopping power, ε_i, are constant over Δx_i. With Eqs. (2.1), (4.87), and (4.89) we obtain for the yield from a particular slice in the target

$$\Delta Y_i = \frac{\mathcal{N}_{R,i}}{\mathcal{N}_b} = \sigma_i \frac{\mathcal{N}_{t,i}}{A} = \sigma_i N_i \Delta x_i \tag{4.90}$$

The total yield is given by integrating over all target slices,

$$\begin{aligned} Y(E_0) &= \int \sigma(x) N(x)\, dx = \int \sigma(x) N(x)\, dx \frac{dE(x)}{dx} \frac{dx}{dE(x)} \\ &= \int_{E_0-\Delta E}^{E_0} \frac{\sigma(E)}{\varepsilon(E)}\, dE \end{aligned} \tag{4.91}$$

The quantity ΔE is the total energy lost by the beam in the target, that is, the target thickness in energy units. The above expression applies either to total cross sections and total yields or to differential cross sections and differential yields (yield per steradian). The expression neglects the effects of beam resolution and straggling that will be discussed later. The cross section $\sigma = \sigma(E)$ can be found from the measured yield by solving Eq. (4.91) numerically. In special cases, which occur frequently in practice, the above integral can be evaluated analytically. Such cases will be addressed below.

4.8.1.1 Constant σ and ε Over Target Thickness

Suppose that the cross section is approximately constant over the target thickness. This may be the case, for example, if the reaction proceeds via a nonresonant mechanism or a broad resonance. Furthermore, we assume that the energy lost by the beam in the target is small so that the stopping power is nearly constant as well. The situation is displayed as case (a) in Figure 4.52. The yield follows directly from Eqs. (4.14) and (4.91),

$$Y(E_0) = \frac{\sigma(E_{\text{eff}})}{\varepsilon(E_0)} \int_{E_0-\Delta E}^{E_0} dE = \frac{\Delta E(E_0)}{\varepsilon(E_0)} \sigma(E_{\text{eff}}) = n\sigma(E_{\text{eff}}) \tag{4.92}$$

The effective or average energy in the target is $E_{\text{eff}} = E_0 - \Delta E/2$ and, therefore, we can assign this energy to the cross section obtained from Eq. (4.92). The above assumption of a constant cross section implies that reactions will occur over the

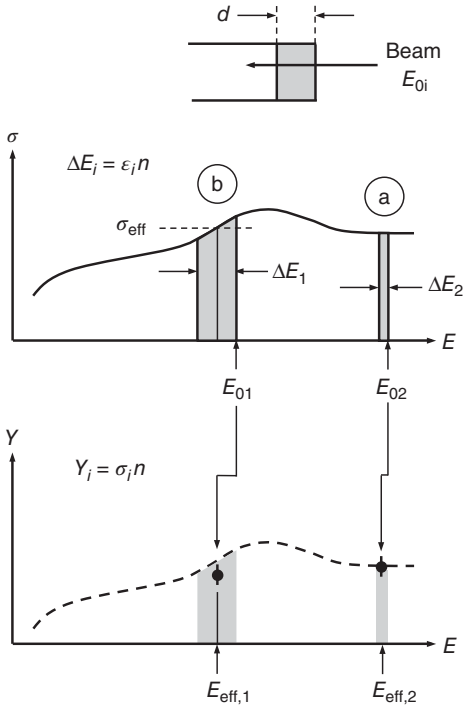

Figure 4.52 Yield for (a) constant cross section, and (b) moderately energy-dependent cross section. The yield is given by the area under the cross section curve (shaded areas in the top part). The integration is performed from the bombarding energy E_0 to an energy of $E_0 - \Delta E$, with ΔE the target thickness in energy units. In situation (a), the shape of the yield and cross section curves are identical. In situation (b), the cross section depends approximately linearly on energy and the effective energy is given by $E_{\text{eff}} = E_0 - \Delta E/2$.

entire thickness of the target. Furthermore, the shapes of the measured yield curve and the cross section will be similar. The situation is schematically shown as case (a) in Figure 4.52. Similarly, for differential cross sections, $(d\sigma/d\Omega)_\theta$, and differential yields, $(dY/d\Omega)_\theta$, one finds

$$\left[\frac{dY(E_0)}{d\Omega}\right]_\theta = \frac{\Delta E(E_0)}{\varepsilon(E_0)}\left[\frac{d\sigma(E_{\text{eff}})}{d\Omega}\right]_\theta = n\left[\frac{d\sigma(E_{\text{eff}})}{d\Omega}\right]_\theta \tag{4.93}$$

We assumed so far that the target consists of a pure element. If instead the target consists of a compound X_aY_b with n_X active nuclei per square centimeter (the target nuclei of interest) and n_Y inactive nuclei per square centimeter (nuclei that do not participate in the reaction of interest), then we obtain from Eqs. (4.17), (4.88), and (4.89)

$$\frac{\Delta E_c}{n_X} = \frac{\varepsilon_X n_X + \varepsilon_Y n_Y}{n_X} = \varepsilon_X + \frac{n_Y}{n_X}\varepsilon_Y \equiv \varepsilon_{\text{eff}} \tag{4.94}$$

where $n_Y/n_X = b/a$. The quantity ε_{eff}, which is different from the total stopping power for a compound (see Eq. (4.15)), is referred to as the *effective stopping power*. The total and differential yields are given by Eqs. (4.92)–(4.94) as

$$Y(E_0) = n_X \sigma(E_{\text{eff}}) = \frac{\Delta E_c(E_0)}{\varepsilon_{\text{eff}}(E_0)} \sigma(E_{\text{eff}}) \tag{4.95}$$

$$\left[\frac{dY(E_0)}{d\Omega}\right]_\theta = n_X \left[\frac{d\sigma(E_{\text{eff}})}{d\Omega}\right]_\theta = \frac{\Delta E_c(E_0)}{\varepsilon_{\text{eff}}(E_0)} \left[\frac{d\sigma(E_{\text{eff}})}{d\Omega}\right]_\theta \tag{4.96}$$

As long as the stopping power is constant over the target thickness, it follows that the yield is calculated in the same way as for a pure target (see Eqs. (4.92) and (4.93)), except that the stopping power is replaced by ε_{eff}. Similar arguments apply to yield expressions obtained for other assumptions (e.g., resonances) as will be seen below.

Example 4.3

Suppose that a beam of singly charged protons with a laboratory energy of 200 keV and 1 μA intensity is incident on a 5 keV thick (in the laboratory system) natural carbon target for a period of one hour. Calculate the total number of photons originating from the ^{13}C(p,γ)^{14}N capture reaction, assuming that one photon is emitted per reaction. Assume further that both the cross section and the stopping power are approximately constant over the target thickness. The cross section amounts to $\sigma_{^{13}\text{C(p,}\gamma)}(E_{\text{lab}} = 200\,\text{keV}) = 10^{-7}$ b and the stopping power of protons in carbon, calculated using the computer code SRIM (Ziegler, 2003), is given by $\varepsilon_{\text{p}\to\text{C}}(E_{\text{lab}} = 200\,\text{keV}) = 11.8 \times 10^{-15}\,\text{eV cm}^2/\text{atom}$.

The target consists of active ^{13}C (1.1%) and inactive ^{12}C (98.9%) nuclei. If we assume that the stopping power of hydrogen in ^{12}C and ^{13}C is the same, we obtain for the effective stopping power (see Eq. (4.94))

$$\begin{aligned}\varepsilon_{\text{eff}} &= \varepsilon_{\text{p}\to^{13}\text{C}} + \frac{98.9}{1.1}\varepsilon_{\text{p}\to^{12}\text{C}} = \varepsilon_{\text{p}\to\text{C}}\left(1 + \frac{98.9}{1.1}\right) \\ &= (11.8 \times 10^{-15}\,\text{eV cm}^2/\text{atom})\left(1 + \frac{98.9}{1.1}\right) = 1.0 \times 10^{-12}\,\text{eV cm}^2/\text{atom}\end{aligned}$$

The yield is then given by

$$\begin{aligned}Y = \frac{\Delta E_c}{\varepsilon_{\text{eff}}}\sigma &= \frac{5 \times 10^3\,\text{eV}}{1.0 \times 10^{-12}\,\text{eV cm}^2/\text{atom}}(10^{-7} \cdot 10^{-24}\,\text{cm}^2) \\ &= 5.0 \times 10^{-16} = \frac{\mathcal{N}_\gamma}{\mathcal{N}_\text{p}}\end{aligned}$$

The total number of incident protons can be calculated from the total accumulated charge Q and the elementary charge e (Section 4.3.4). The value of Q is given by the beam intensity and the measuring time,

$$\mathcal{N}_\text{p} = \frac{Q}{e} = \frac{It}{e} = \frac{(1 \times 10^{-6}\,\text{A})(3600\,\text{s})}{1.6 \times 10^{-19}\,\text{C}} = 2.25 \times 10^{16}$$

Thus, for a measuring time of one hour, we obtain for the number of emitted photons at a laboratory bombarding energy of $E_{\text{lab}} = 200\,\text{keV}$

$$\mathcal{N}_\gamma = Y\mathcal{N}_\text{p} = (5.0 \times 10^{-16})(2.25 \times 10^{16}) \approx 11$$

In this example, the yield is obtained from the ratio of the two quantities ΔE_c and ε_{eff} that are both given in the laboratory system. The ratio $\Delta E_c/\varepsilon_{\text{eff}} = n_X$ is independent of the reference frame. Multiplication of the numerator and denominator by the center of mass to the laboratory frame conversion factor $M_X/(M_X + M_p)$ (see Eq. (C.24); M_X and M_p are the relative atomic masses of the active target nuclei and the projectiles, respectively) shows that the tabulated effective stopping power has to be multiplied by this factor if the yield is calculated from the target thickness in the center-of-mass system.

4.8.1.2 Moderately Varying σ and Constant ε Over Target Thickness

If the stopping power is constant, but the cross section varies over the target thickness, then the yield is given by (see Eq. (4.91))

$$Y(E_0) = \frac{1}{\varepsilon(E_0)} \int_{E_0-\Delta E}^{E_0} \sigma(E)\, dE \tag{4.97}$$

We will assume that the cross section does not vary drastically, that is, we exclude narrow-resonance cross sections, which will be discussed later. The situation is shown as case (b) in Figure 4.52. If the above integral is replaced by the product $\sigma(E_{\text{eff}})\Delta E(E_0)$, we obtain again the expression (see Eq. (4.92))

$$Y(E_0) = \frac{\Delta E(E_0)}{\varepsilon(E_0)} \sigma(E_{\text{eff}}) \tag{4.98}$$

With this substitution, the effective energy, E_{eff}, is defined as the energy at which the cross section, evaluated at this energy, equals the cross section averaged over the target thickness. As was the case before, reactions occur over the entire thickness of the target, but the number of reaction products emitted from different target depths is no longer constant.

In general, the effective beam energy must be obtained numerically, but in special cases analytical approximations may be used. Following Brune and Sayre (2013), we assume again that the stopping power is constant over the target thickness and that the energy dependence of the cross section is at most quadratic. Expansion around an energy at the center of the target, $E_h = E_0 - \Delta E/2$, yields

$$\sigma(E) = \sigma(E_h) + \left(\frac{d\sigma}{dE}\right)_{E_h} (E - E_h) + \left(\frac{d^2\sigma}{dE^2}\right)_{E_h} (E - E_h)^2 \tag{4.99}$$

With the definitions,

$$R_1 \equiv \frac{1}{\sigma(E_h)} \left(\frac{d\sigma}{dE}\right)_{E_h} \quad \text{and} \quad R_2 \equiv \frac{(d^2\sigma/dE^2)_{E_h}}{(d\sigma/dE)_{E_h}} \tag{4.100}$$

the right-hand sides of Eqs. (4.97) and (4.98) can be set equal to solve for the effective energy. The result is

$$E_{\text{eff}} = E_0 - \frac{\Delta E}{2} + \frac{\sqrt{1 + R_2^2(\Delta E)^2/12} - 1}{R_2} \tag{4.101}$$

If the cross section depends linearly on energy, then $R_2 = 0$, and the effective energy becomes $E_{\text{eff}} = E_0 - \Delta E/2$.

Sometimes it may be of advantage to adopt an energy that differs from the effective energy introduced above. Alternative formulations involve the mean (or cross section weighted) energy, or the median energy (i.e., the energy at which half of the total yield is obtained). In such cases, the yield must be divided by a correction factor before the cross section can be extracted from Eq. (4.98). For more information, see Wrean, Brune, and Kavanagh (1994), Lemut (2008), and Brune and Sayre (2013).

4.8.1.3 Breit–Wigner Resonance σ and Constant ε Over Resonance Width

Suppose that a resonant cross section is given by the Breit–Wigner formula (see Eq. (2.185)). It is also assumed that the stopping power ε, the de Broglie wavelength λ, and the partial widths Γ_i of the resonance are independent of energy over the resonance width. Hence, these quantities can be evaluated at the resonance energy E_r. With the substitutions $\omega \equiv (2J+1)(1+\delta_{01})/[(2j_0+1)(2j_1+1)]$ and $\omega\gamma \equiv \omega\Gamma_a\Gamma_b/\Gamma$ (Section 3.2.4), we obtain from Eqs. (3.113) and (4.91) (Fowler, Lauritsen, and Lauritsen, 1948)

$$\begin{aligned} Y(E_0) &= \int_{E_0-\Delta E}^{E_0} \frac{1}{\varepsilon(E)} \frac{\lambda^2}{4\pi} \omega \frac{\Gamma_a\Gamma_b}{(E_r - E)^2 + \Gamma^2/4}\, dE \\ &= \frac{\lambda_r^2}{2\pi} \frac{\omega\gamma}{\varepsilon_r} \frac{\Gamma}{2} \int_{E_0-\Delta E}^{E_0} \frac{dE}{(E_r - E)^2 + (\Gamma/2)^2} \\ &= \frac{\lambda_r^2}{2\pi} \frac{\omega\gamma}{\varepsilon_r} \left[\arctan\left(\frac{E_0 - E_r}{\Gamma/2}\right) - \arctan\left(\frac{E_0 - E_r - \Delta E}{\Gamma/2}\right) \right] \end{aligned} \tag{4.102}$$

where λ_r and ε_r denote the de Broglie wavelength and the stopping power at the resonance energy E_r, respectively. With the expressions $\tan(x-y) = [\tan(x) - \tan(y)]/[1 + \tan(x)\tan(y)]$ and $d(\arctan x)/dx = 1/(1+x^2)$, one finds after some algebra

$$E_{0,\max} = E_r + \frac{\Delta E}{2} \tag{4.103}$$

$$Y_{\max} = Y(E_{0,\max}) = \frac{\lambda_r^2}{\pi} \frac{\omega\gamma}{\varepsilon_r} \arctan\left(\frac{\Delta E}{\Gamma}\right) \tag{4.104}$$

$$E_{0,50\%} = E_r + \frac{\Delta E}{2} \pm \frac{1}{2}\sqrt{\Gamma^2 + \Delta E^2} \tag{4.105}$$

$$\text{FWHM} = \sqrt{\Gamma^2 + \Delta E^2} \tag{4.106}$$

with $E_{0,\max}$, $Y_{\max}$, $E_{0,50\%}$, and FWHM the location of the maximum, the maximum yield, the energies corresponding to one half of the maximum yield, and the FWHM of the resonance yield curve, respectively. For the de Broglie wavelength (in the center-of-mass system), we find numerically

$$\frac{\lambda_r^2}{2} = 2\pi^2 \frac{\hbar^2}{2m_{01}E_r} = \left(\frac{M_0 + M_1}{M_1}\right)^2 \frac{4.125 \times 10^{-18}}{M_0 E_r^{\text{lab}}} \qquad (\text{cm}^2) \qquad (4.107)$$

with m_{01}, M_0, and M_1 the reduced mass of the projectile–target system, the projectile mass (u), and the target mass (u), respectively; E_r^{lab} is the laboratory resonance energy in units of electron volts.

These results are illustrated in Figure 4.53, showing a Breit–Wigner cross section (Figure 4.53a) and the corresponding yield (Figure 4.53b) of a resonance at $E_r = 500$ keV with a total width of $\Gamma = 15$ keV for different values of the target

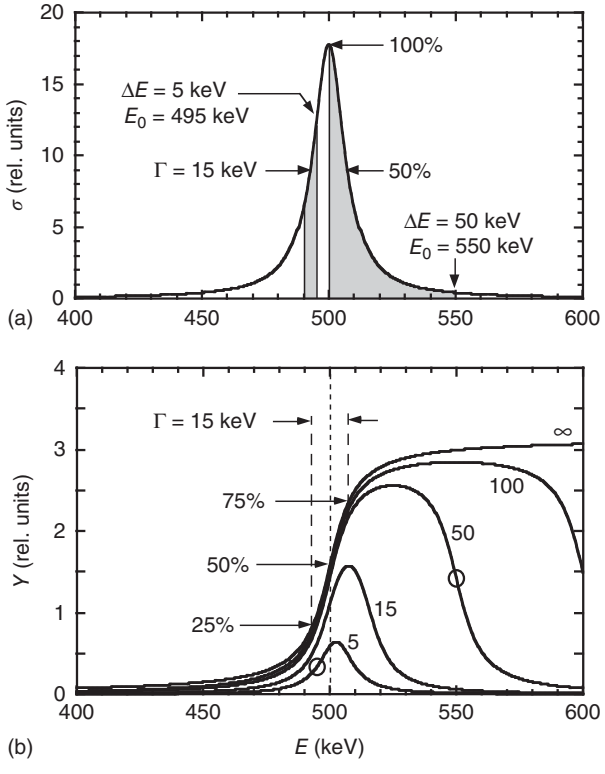

Figure 4.53 (a) Cross section and (b) yield curve for a Breit–Wigner resonance with energy-independent partial widths. The resonance is located at $E = 500$ keV and has a width of $\Gamma = 15$ keV. The yield depends strongly on the bombarding energy and the target thickness. The shaded areas (part a) and corresponding open circles (part b) depict the situation for two different sets of conditions ($E_0 = 495$ keV, $\Delta E = 5$ keV on the left-hand side, and $E_0 = 550$ keV, $\Delta E = 50$ keV on the right-hand side). The symbol ∞ in part (b) labels the resonant yield for an infinitely thick target.

thickness ΔE. If the target thickness is considerably smaller than the resonance width, $\Delta E \ll \Gamma$, the shape of the yield curve corresponds to the shape of the cross section (i.e., a Lorentzian shape). The maximum yield is located close to the resonance energy, $E_{0,\max} \approx E_r$, and the width of the yield curve is given by the resonance width, FWHM $\approx \Gamma$. For example, at a bombarding energy of $E_0 = 495$ keV and a target thickness of $\Delta E = 5$ keV (shaded area on the left-hand side in Figure 4.53a) the target integrates only over a small region of the cross section (i.e., between 490 and 495 keV). The resulting yield is shown as the open circle at 495 keV in Figure 4.53b. In this case, reactions occur over the entire thickness of the target. On the other hand, if the target thickness is considerably larger than the total resonance width, $\Delta E \gg \Gamma$, the shape of the yield curve is determined by the arctan function. The yield curve shows a flat plateau with a maximum located at $E_{0,\max} = E_r + \Delta E/2$ and the width is FWHM $\approx \Delta E$. For example, at $E_0 = 550$ keV and $\Delta E = 50$ keV (shaded region on right-hand side in Figure 4.53a) the target integrates over almost half of the entire cross section curve (i.e., between 500 and 550 keV). The resulting yield, shown as the open circle at 550 keV in Figure 4.53b, represents about 50% of the maximum yield at the plateau height. In this case, the number of reactions varies strongly over the thickness of the target.

For an increasing target thickness ΔE, both the maximum yield $Y_{\max}$ and the width of the yield curve will increase since the target integrates the cross section over a larger energy region. In the limit of an infinitely thick target, $\Delta E \to \infty$, the yield in Eq. (4.102) becomes

$$Y_{\Delta E\to\infty}(E_0) = \frac{\lambda_r^2}{2\pi}\frac{\omega\gamma}{\varepsilon_r}\left[\arctan\left(\frac{E_0 - E_r}{\Gamma/2}\right) + \frac{\pi}{2}\right] \tag{4.108}$$

and Eqs. (4.104) and (4.105) give

$$Y_{\max,\Delta E\to\infty} = \frac{\lambda_r^2}{2}\frac{\omega\gamma}{\varepsilon_r} \tag{4.109}$$

$$E_{0,50\%,\Delta E\to\infty} = E_r \tag{4.110}$$

The yield $Y_{\Delta E\to\infty}$ for a resonance at $E_0 = 500$ keV with a total width of $\Gamma = 15$ keV is also shown in Figure 4.53b. The difference between the energies at which the yield for an infinitely thick target is at 75% and 25% of its maximum value is equal to the total resonance width, that is,

$$E_{0,75\%,\Delta E\to\infty} - E_{0,25\%,\Delta E\to\infty} = \Gamma \tag{4.111}$$

It is interesting to investigate the ratios $Y_{\max}/Y_{\max,\Delta E\to\infty}$, FWHM$/\Delta E$, and $(E_r - E_{0,50\%})/\Gamma$ as a function of $\Delta E/\Gamma$. The results are shown in Figure 4.54. The thicker the target, the closer the yield resembles that of an infinitely thick target. For example, suppose that the target thickness is 10 times larger than the total resonance width ($\Delta E/\Gamma = 10$). The maximum yield at the plateau is then 94% of the yield for an infinitely thick target and the FWHM is equal to the target thickness within 0.5%. Furthermore, the difference of energies at which the yield is at 50% of its maximum and the resonance energy amounts to 0.025Γ (see Eq. (4.105)). This deviation is only 0.37 keV for a total resonance width of $\Gamma = 15$ keV.

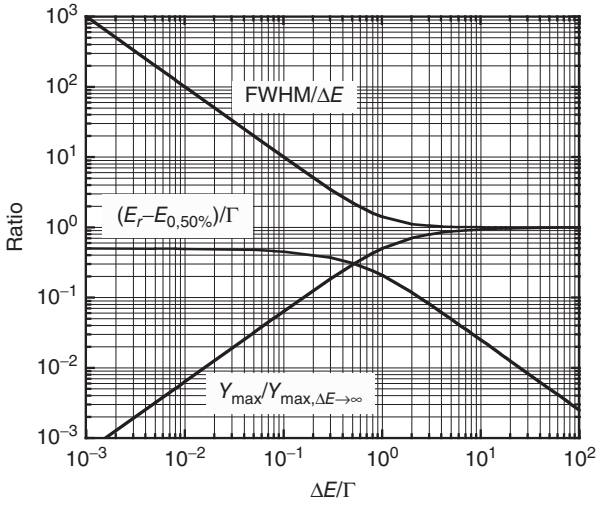

Figure 4.54 Ratios $Y_{max}/Y_{max,\Delta E\to\infty}$, FWHM/$\Delta E$, and $(E_r - E_{0,50\%})/\Gamma$ as a function of $\Delta E/\Gamma$ for a Breit–Wigner resonance with energy-independent partial widths.

4.8.2 General Treatment of Yield Curves

We neglected so far the influence of certain experimental factors on the measured yield. These include the finite beam energy resolution, beam straggling in the target, target nonuniformities, and the thermal motion of target atoms. To account for such effects, we have to replace Eq. (4.91) by the general expression (Gove, 1959)

$$Y(E_0) = \int_{E_0-\Delta E}^{E_0} dE' \int_{E_i=0}^{\infty} dE_i \int_{E=0}^{E_i} \frac{\sigma(E)}{\varepsilon(E)} g(E_0, E_i) f(E_i, E, E')\, dE \qquad (4.112)$$

where $g(E_0, E_i)\, dE_i$ is the probability that a particle in the incident beam of mean energy E_0 has an energy between E_i and $E_i + dE_i$; $f(E_i, E, E')\, dE$ is the probability that a particle incident on the target at an energy E_i has an energy between E and $E + dE$ at a depth inside the target corresponding to the energy E' (i.e., $E_0 - \Delta E < E' < E_0$). The functions $g(E_0, E_i)$ and $f(E_i, E, E')$ are assumed to be normalized. The cross section $\sigma(E)$ can be found numerically from the measured yield $Y(E_0)$ using deconvolution procedures (see, e.g., McGlone and Johnson, 1991).

For a constant cross section and stopping power, the triple integral reduces to our earlier result (see Eq. (4.92)), as can be seen using the normalizations of g and f, and by carrying out the integrations in the order E, E_i, and E'. It follows that the yield for nonresonant cross sections ($\sigma \approx$ const) and thin targets ($\varepsilon \approx$ const) is not affected by the beam resolution and beam straggling. In other words, all projectiles in the beam can in principle contribute to the yield.

In the following, resonance yield curves will be discussed in more detail. We will make a few assumptions that apply frequently in practice: (i) the energy distribution of particles in the beam is a function of $E_0 - E_i$ only, $g(E_0, E_i) = g(E_0 - E_i)$, that is, the beam spread is independent of the mean energy E_0; (ii) the distribution describing energy loss and straggling is a function of $E_i - E$ and E' only, $f(E_i, E, E') = f(E_i - E, E')$, that is, the spread in f is independent of the energy E_i; (iii) the functions g, f, and σ vanish on both sides of their maximum values; and (iv) the stopping power is constant over the total width of the resonance and the total width of the target, $\varepsilon(E) = \varepsilon_r$. The latter condition implies that the target is uniform. Otherwise, if the target consists of a compound with changing stoichiometry, the energy and depth dependence of the effective stopping power, $\varepsilon_{\text{eff}}(E)$, has to be taken explicitly into account. With the above assumptions, Eq. (4.112) becomes

$$Y(E_0) = \frac{1}{\varepsilon_r} \int_{E_0-\Delta E}^{E_0} dE' \int_{E_i=0}^{\infty} dE_i \int_{E=0}^{E_i} \sigma(E) g(E_0 - E_i) f(E_i - E, E')\, dE \quad (4.113)$$

A typical situation is represented in Figure 4.55. A beam of initial mean energy E_0, with an energy distribution given by $g(E_0 - E_i)$, traverses a target of thickness ΔE. The energies E and E' represent the projectile energy at a fixed depth x in the target and the mean energy of the beam, respectively. The vertical thick line indicates the position of a narrow resonance with $E_r < E_0$. At position (a) near the target surface, all projectile energies are too large to excite the resonance and the yield will be negligible. At position (b) inside the target, the beam has slowed down so that the maximum of the projectile energy distribution coincides with the resonance

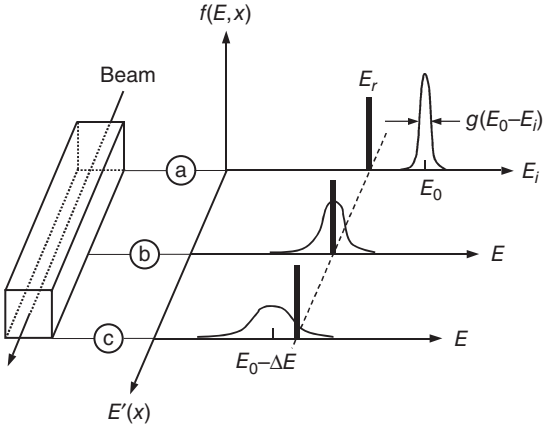

Figure 4.55 Slowing down process of a beam with initial mean energy E_0 and an energy distribution given by $g(E_0 - E_i)$, traversing a target of thickness ΔE. The energies E and E' represent the projectile energy at a fixed depth x in the target and the mean energy of the beam, respectively; E' decreases as the target is traversed. The z-axis represents the magnitude of the probability distribution f. The vertical thick line indicates the position of a narrow resonance with $E_r < E_0$. Positions (a), (b), and (c) indicate different depths within the target. The largest contribution to the resonance yield arises from position (b).

energy and, consequently, the largest contribution to the yield arises from this depth in the target. At position (c) near the back side of the target, most projectiles have slowed to energies below E_r. Only a few projectiles on the high-energy tail of the distribution f can excite the resonance. The contribution of this target depth to the yield is larger than for position (a), but less than for position (b).

4.8.2.1 Target of Infinite Thickness

For an infinitely thick target, $\Delta E \to \infty$, the lower integration limit of E' in Eq. (4.113) is zero. The shape of the yield curve can be obtained using the normalization of the function f, since the probability of finding a projectile that experienced a specific energy loss of $E_i - E$ anywhere in the target is unity. Thus,

$$\begin{aligned} Y_{\Delta E\to\infty}(E_0) &= \frac{1}{\varepsilon_r}\int_{E'=0}^{E_0} f(E_i - E, E')\,dE' \int_{E_i=0}^{\infty} dE_i \int_{E=0}^{E_i} \sigma(E) g(E_0 - E_i)\,dE \\ &= \frac{1}{\varepsilon_r}\int_{E_i=0}^{\infty} g(E_0 - E_i)\,dE_i \int_{E=0}^{E_i} \sigma(E)\,dE \end{aligned} \tag{4.114}$$

The yield depends on both the cross section (e.g., the total resonance width) and the beam spread, but is independent of beam straggling. The maximum yield for an infinitely thick target can be obtained in the limit $E_0 \to \infty$. In this case, the only contribution from the integration over E_i results from $E_i \to \infty$. Using the normalization of the distribution g we find

$$Y_{\max,\Delta E\to\infty} = \frac{1}{\varepsilon_r}\int_{E=0}^{\infty} \sigma(E)\,dE \tag{4.115}$$

It follows that the maximum yield for an infinitely thick target is not affected by the beam resolution, beam straggling, or the total resonance width. The value of $Y_{\max,\Delta E\to\infty}$ depends only on the stopping power and the integrated cross section. If the target consists of a compound, ε_r has to be replaced by $\varepsilon_{\mathrm{eff},r}$ (see Eq. (4.94)) and, consequently, $Y_{\max,\Delta E\to\infty}$ depends on the stoichiometry of the target compound. If the cross section is given by the Breit–Wigner formula with constant partial widths and de Broglie wavelength over the width of the resonance, the integration over σ yields

$$Y_{\max,\Delta E\to\infty} = \frac{1}{\varepsilon_r}\frac{\lambda_r^2}{2}\omega\gamma \tag{4.116}$$

which is identical to our earlier result (see Eq. (4.109)).

4.8.2.2 Target of Finite Thickness

For a target of finite thickness, the area under the resonance yield curve is obtained by evaluating the expression

$$\begin{aligned} A_Y &= \int_{E_0=0}^{\infty} Y(E_0)\,dE_0 \\ &= \frac{1}{\varepsilon_r}\int_{E_0=0}^{\infty} dE_0 \int_{E_0-\Delta E}^{E_0} dE' \int_{E_i=0}^{\infty} dE_i \int_{E=0}^{E_i} \sigma(E) g(E_0 - E_i) f(E_i - E, E')\,dE \end{aligned} \tag{4.117}$$

The multiple integral can be solved using the normalizations of g and f, and by carrying out the integrations in the order E_0, E_i, and E'. The integral over E can be taken with an upper limit of infinity since the beam energy varies between zero and infinity. Thus,

$$\begin{aligned} A_Y &= \frac{1}{\varepsilon_r} \int_{E_0=0}^{\infty} g(E_0 - E_i)\, dE_0 \int_{E_0-\Delta E}^{E_0} dE' \int_{E_i=0}^{\infty} dE_i \int_{E=0}^{E_i} \sigma(E) f(E_i - E, E')\, dE \\ &= \frac{1}{\varepsilon_r} \int_{E_i=0}^{\infty} f(E_i - E, E')\, dE_i \int_{E_0-\Delta E}^{E_0} dE' \int_{E=0}^{\infty} \sigma(E)\, dE \end{aligned} \tag{4.118}$$

The probability that, at a target depth corresponding to E', a projectile of energy E has an initial energy of E_i anywhere between zero and infinity is unity and, therefore,

$$\begin{aligned} A_Y &= \frac{1}{\varepsilon_r} \int_{E_0-\Delta E}^{E_0} dE' \int_{E=0}^{\infty} \sigma(E)\, dE \\ &= \frac{\Delta E}{\varepsilon_r} \int_{E=0}^{\infty} \sigma(E)\, dE = n \int_{E=0}^{\infty} \sigma(E)\, dE \end{aligned} \tag{4.119}$$

We obtain the important result that the area under a resonance yield curve for a target of finite thickness is independent of beam resolution, straggling, target thickness, stopping power, and total resonance width. The value of A_Y depends only on the total number of target nuclei per square centimeter and the integrated cross section. If the target consists of a compound, then n has to be replaced by the number of active target nuclei, $n_X = \Delta E_c / \varepsilon_{\text{eff}}$ (see Eq. (4.94)). It has been shown (Palmer *et al.*, 1963) that the above expression also holds for nonuniform targets (e.g., targets of varying stoichiometry). From Eqs. (4.115) and (4.119), we find that the area under the resonance yield curve is equal to the product of maximum yield for an infinitely thick target and the target thickness,

$$A_Y = Y_{\max,\Delta E \to \infty} \Delta E \tag{4.120}$$

For example, for a Breit–Wigner cross section with constant partial widths and de Broglie wavelength over the width of the resonance, one obtains with Eq. (4.116)

$$A_Y = \frac{\Delta E}{\varepsilon_r} \frac{\lambda_r^2}{2} \omega\gamma = n \frac{\lambda_r^2}{2} \omega\gamma \tag{4.121}$$

We will now discuss the influence of beam resolution and straggling on the shape of resonance yield curves for targets of finite thickness. We are specifically interested to investigate the changes of the quantities $Y_{\max}$, $E_{0,50\%}$, and FWHM (see Eqs. (4.104)–(4.106)) caused by these effects. In the following, results will be discussed that are obtained by solving Eq. (4.113) numerically, assuming specific distributions for σ, g, and f. For these calculations, the following assumptions will be made: (i) the cross section is given by the Breit–Wigner formula with constant partial widths and de Broglie wavelength over the total resonance width; the resonance is located at an energy of $E_r = 500$ keV and the area under the resonance cross section (i.e., the resonance strength) is fixed; (ii) the beam profile is approximated by a Gaussian with a full width at half maximum of Δ_{beam}; and (iii) the

distribution f is also approximated by a Gaussian, which is an appropriate assumption if the number of collisions is large. The full width at half maximum of f can be approximated by Eq. (4.19), which is applicable for relatively thin absorbers. Assuming a constant stopping power over the total resonance width, one finds from Eqs. (4.14) and (4.19)

$$\begin{aligned}\Delta_{\text{stragg}} &= 1.20 \times 10^{-9} \sqrt{Z_p^2 Z_t (E_0 - E')/\varepsilon} \qquad \text{(keV)} \\ &= \text{const} \sqrt{E_0 - E'} \qquad \text{(keV)} \end{aligned} \tag{4.122}$$

We adopt here arbitrary values of $Z_p = 1$, $Z_t = 10$, and $\varepsilon = 10 \times 10^{-15}$ eV cm^2/atom, yielding const = 1.2. The resulting calculated yield curves are shown in Figure 4.56.

Figure 4.56a shows the effect of varying the beam energy spread Δ_{beam}. For the target thickness, total resonance width, and beam straggling, values of $\Delta E = 10$ keV, $\Gamma = 0$, and $\Delta_{\text{stragg}} = 0$, respectively, are adopted. The curves are obtained for values of $\Delta_{\text{beam}} = 0$, 1, 3, 5, and 8 keV. The rectangular yield curve corresponds to the case of $\Gamma = 0$, $\Delta_{\text{stragg}} = 0$, and $\Delta_{\text{beam}} = 0$. It can be seen that the beam spread causes a decrease in the slope of both the low-energy and the high-energy edge of the yield curve. If the beam spread is small compared to the target thickness, $\Delta_{\text{beam}}/\Delta E < 0.5$, then the beam resolution is equal to the difference of energies at which the yield reaches 12% and 88% of its maximum value (assuming $\Delta_{\text{beam}} \gg \Gamma$), which is appropriate for a Gaussian distribution. For ratios in excess of $\Delta_{\text{beam}}/\Delta E \approx 0.5$, the quantities $Y_{\max}$, $E_{0,50\%}$, and FWHM are all influenced by the beam resolution. The maximum yield decreases, the energy at which the yield reaches 50% of its maximum value shifts below the resonance energy E_r, and the value of FWHM becomes larger than the target thickness. For example, for $\Delta_{\text{beam}} = 8$ keV the energy difference $E_r - E_{0,50\%}$ is ≈ 0.5 keV. The influence of the beam spread on the shape of the yield curve has to be taken into account if the resonance strength $\omega\gamma$ is derived from the observed value of $Y_{\max}$ using Eq. (4.104).

Figure 4.56b demonstrates the influence of beam straggling. For the total resonance width, beam energy resolution, and straggling constant, values of $\Gamma = 0$, $\Delta_{\text{beam}} = 0$, and const = 1.2, respectively, are adopted. The curves are obtained for target thicknesses of $\Delta E = 1$, 3, 5, and 10 keV. The rectangular yield curve corresponds again to the case of $\Gamma = 0$, $\Delta_{\text{beam}} = 0$, and $\Delta_{\text{stragg}} = 0$. It can be seen that straggling has no effect on the low-energy edge of the yield curve and, therefore, the energy difference $E_r - E_{0,50\%}$ is negligible (assuming $\Gamma = 0$). However, straggling causes a decrease in the slope of the high-energy edge of the yield curve. The value of Δ_{stragg} (at $E_0 - E' = \Delta E$) is approximately equal to the difference of energies at which the yield reaches 12% and 88% of its maximum value (assuming $\Delta_{\text{stragg}} \gg \Gamma$ and $\Delta_{\text{stragg}} \gg \Delta_{\text{beam}}$). Straggling will reduce the maximum yield if the target becomes too thin ($\Delta E < 3$ keV in our specific case). As was the case for the beam spread, the effects of straggling have to be taken into account if $\omega\gamma$ is derived from the observed value of $Y_{\max}$. The value of FWHM is relatively insensitive to straggling.

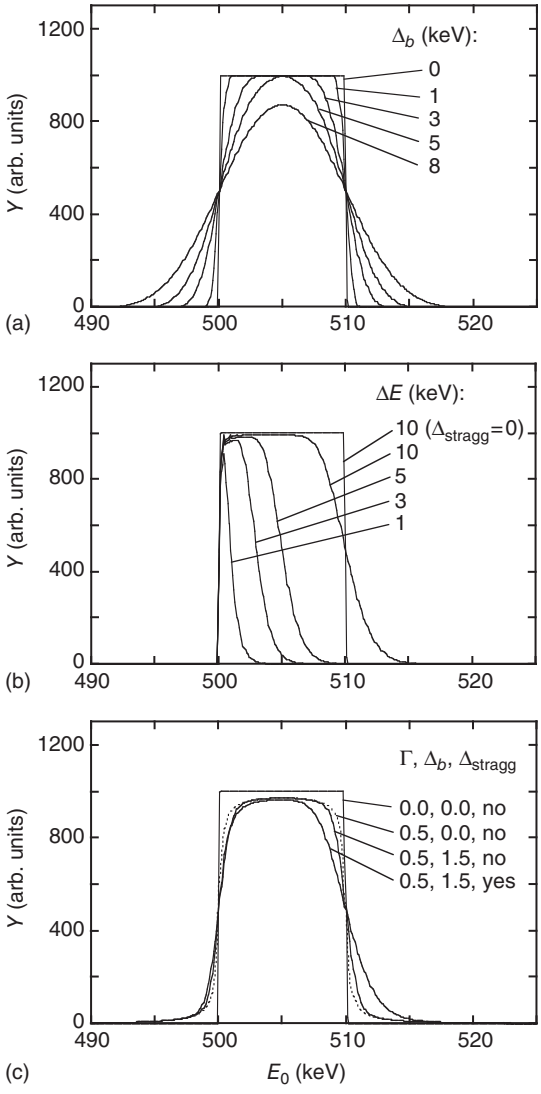

Figure 4.56 General shape of resonance yield curves, obtained by solving Eq. (4.113) numerically. See the text for specific assumptions. The curves are obtained for the following conditions of target thickness ΔE, total resonance width Γ, beam straggling Δ_{stragg}, and beam energy spread Δ_{beam}: (a) ΔE= 10 keV, $\Gamma = 0$, $\Delta_{\text{stragg}} = 0$, $\Delta_{\text{beam}} = 0$, 1, 3, 5, 8 keV; (b) $\Gamma = 0$, $\Delta_{\text{beam}} = 0$, const = 1.2, $\Delta E = 1$, 3, 5, 10 keV; (c) the target thickness amounts to $\Delta E = 10$ keV for each curve; $\Gamma = 0$, $\Delta_{\text{beam}} = 0$, $\Delta_{\text{stragg}} = 0$; $\Gamma = 0.5$ keV, $\Delta_{\text{beam}} = 0$, $\Delta_{\text{stragg}} = 0$; $\Gamma = 0.5$ keV, $\Delta_{\text{beam}} =$ 1.5 keV, $\Delta_{\text{stragg}} = 0$; $\Gamma = 0.5$ keV, $\Delta_{\text{beam}} =$ 1.5 keV, const = 1.2. The areas under all curves shown in part (c) are identical.

Figure 4.56c shows the combined effects of the total resonance width, beam resolution, and beam straggling on the shape of a resonance yield curve for specific sets of parameters. For the target thickness, a value of $\Delta E = 10$ keV is adopted. The rectangular profile is obtained with the values $\Gamma = 0$, $\Delta_{\text{beam}} = 0$, and $\Delta_{\text{stragg}} = 0$. Since $\Delta E/\Gamma \to \infty$, the plateau height corresponds to the maximum yield for an infinitely thick target (see Eq. (4.109)). The dotted line is calculated by using the values $\Gamma = 0.5$ keV, $\Delta_{\text{beam}} = 0$, and $\Delta_{\text{stragg}} = 0$. Since $\Delta E/\Gamma = 20$, the plateau height decreases to $0.97 Y_{\text{max},\Delta E\to\infty}$, consistent with the results shown in Figure 4.54. In addition, the slopes of the high- and low-energy edges of the yield curve decrease. The solid line obtained with the values of $\Gamma = 0.5$ keV, $\Delta_{\text{beam}} = 1.5$ keV, and $\Delta_{\text{stragg}} = 0$ includes the effects of a finite beam energy resolution. Since we have $\Delta_{\text{beam}} \ll \Delta E$, the maximum yield Y_{max} is only slightly affected by the beam spread, but the low- and high-energy edges become less steep. Finally, the solid line calculated with $\Gamma = 0.5$ keV, $\Delta_{\text{beam}} = 1.5$ keV, and const = 1.2 for the straggling constant shows the effects of straggling. It causes the high-energy edge of the yield curve to become less steep. Since we have $\Delta_{\text{stragg}} \ll \Delta E$, the value of Y_{max} is little affected by beam straggling. The values of $E_{0,50\%}$ and FWHM are very close to E_r and ΔE, respectively. The areas under all curves shown in Figure 4.56c have the same value according to Eq. (4.121).

4.8.3 Measured Yield Curves and Excitation Functions

We will now discuss what kind of information may be extracted from the properties of a measured yield curve, that is, its observed width (FWHM), the slope of the low-energy edge, the maximum yield (Y_{max}), the energy at which the yield reaches 50% of its maximum value ($E_{0,50\%}$), and the area under the yield curve (A_Y). To properly interpret the data, some information must be known *a priori*. We will assume in the following that the data represent the yield curve of an isolated, well-resolved resonance and that the total resonance width Γ is known from independent sources.

Consider a first example, Figure 4.57a, showing a yield curve for the 151 keV resonance in the ^{18}O(p,γ)^{19}F reaction. The yield is obtained from the measured intensity of a specific primary transition. This resonance has a total width of $\Gamma = 130 \pm 10$ eV (Table 4.1). The target was produced by anodizing a tantalum backing in ^{18}O-enriched water. Such targets are known to consist of a ^{18}O–Ta compound (Vermilyea, 1953).

The yield curve shows a structure with an observed width of FWHM = 34 keV. The beam spread influences the slopes of the low-energy and high-energy edges of the yield curve, while straggling contributes only to the slope of the high-energy edge. Both edges extend over energy regions that are smaller than the observed width of the yield curve. In addition, the flat plateau indicates that the plateau height is not influenced by the beam resolution or by straggling. Otherwise, the yield maximum would show a round shape (Figure 4.56). From these arguments, it follows that FWHM $\gg \Delta_{\text{beam}}$ and FWHM $\gg \Delta_{\text{stragg}}$. Furthermore, we have

FWHM $\gg \Gamma$, and thus we conclude that the observed width is equal to the target thickness, FWHM $= \Delta E = 34$ keV.

The low-energy edge extends over an energy range of several kilo electron volts. Since Γ is very small, the slope reflects the resolution of the beam. From the difference of energies at which the yield reaches 12% and 88% of its maximum value, we find $\Delta_{\text{beam}} = 4.0$ keV. The Doppler effect caused by the thermal motion of the target atoms also contributes to the slopes of yield curve edges (Rolfs and Rodney, 1988). The beam spread together with the Doppler broadening can be described by a Gaussian with a full width at half maximum of $\Delta_{\text{beam+Dopp}} = (\Delta^2_{\text{beam}} + \Delta^2_{\text{Dopp}})^{1/2}$. In practice, one finds $\Delta_{\text{Dopp}} \leq 100$ eV and, unless beams of very high resolution are used, we have $\Delta_{\text{beam+Dopp}} \approx \Delta_{\text{beam}}$. The energy at which the yield reaches 50% of its maximum value is in this case neither influenced by the total resonance width (since $\Delta E \gg \Gamma$; see Eq. (4.105)), nor by the beam spread (since the ratio $\Delta_{\text{beam}}/\Delta E = 4.0$ keV/34 keV $= 0.11$ is small; see Figure 4.56). Thus, we find $E_{0,50\%} = E_r = 150.5$ keV.

We concluded that the plateau height is not influenced by beam spread and straggling effects. From the ratio $\Delta E/\Gamma = 34$ keV/130 eV ≈ 260, we find with Eqs. (4.104) and (4.109) that the maximum yield $Y_{\max}$ is equal to $0.998 Y_{\max,\Delta E\to\infty}$ and, therefore, represents the yield of an infinitely thick target to within 0.2%. Furthermore, the area A_Y under the yield curve depends only on the number of active target nuclei (^{18}O) and on the resonance strength $\omega\gamma$ (see Eq. (4.121)).

Similar arguments apply to the data displayed in Figure 4.57b, showing a yield curve of the 918 keV resonance in ^{36}Ar(p,γ)^{37}K. The yield is obtained from the intensity of the primary transition to the ^{37}K ground state. This resonance has a total width of $\Gamma = 300 \pm 50$ meV (Endt, 1998). The target was prepared by implanting ^{36}Ar ions into a tantalum sheet. Consequently, the target consists of an ^{36}Ar–Ta compound (Table 4.3). The width of the structure (FWHM = 6.5 keV) is cosiderably larger than the total resonance width. The energy region of the leading edge is small compared to the value of FWHM and, therefore, the beam spread neither reduces the maximum yield nor contributes to the observed width of the yield curve. Furthermore, straggling does not influence the leading edge or the observed value of FWHM. Thus, we extract from the yield curve values of $\Delta E = 6.5$ keV, $\Delta_{\text{beam}} = 1.0$ keV, and $E_r = 917.5$ keV.

There is an important difference between the two yield curves shown in Figure 4.57. In Figure 4.57b, a flat plateau is not observed and the high-energy edge displays a pronounced tail. This effect is partly caused by proton beam straggling, but also reflects the range straggling of the implanted ^{36}Ar ions in the tantalum backing. Although these straggling effects will not influence the deduced values of ΔE, Δ_{beam}, and E_r, we can no longer conclude that the influence of straggling on the maximum yield height $Y_{\max}$ is negligible.

Narrow resonance yield curves also provide information on the number of active target nuclei and on the stoichiometry of the target compound if the resonance strength is well known. According to Eq. (4.121), the number of active target nuclei per square centimeter for pure targets or compounds is given by $n_X = 2A_Y/(\lambda_r^2 \omega\gamma)$. For a target compound $X_a Y_b$, the effective stopping power can

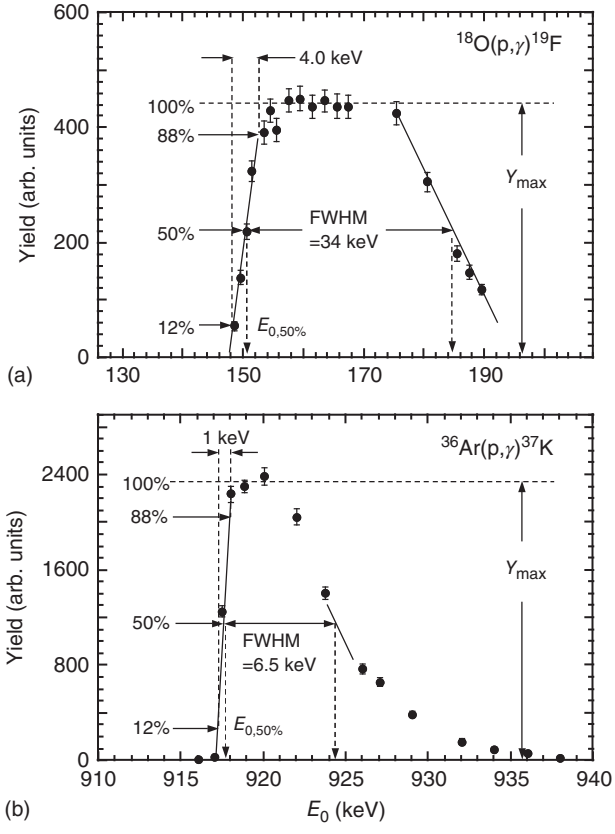

Figure 4.57 (a) Measured yield curve of the $E_r^{lab} = 151$ keV resonance in the $^{18}O(p,\gamma)^{19}F$ reaction, obtained from the intensity of the primary transition to the $E_x = 3908$ keV state. The total resonance width is $\Gamma = 130 \pm 10$ eV (Table 4.1). The target was produced by anodizing a tantalum backing in ^{18}O-enriched water (Vermilyea, 1953). (b) Measured yield curve of the $E_r^{lab} = 918$ keV resonance in $^{36}Ar(p,\gamma)^{37}K$, obtained from the intensity of the primary transition to the ^{37}K ground state. The total resonance width is $\Gamma = 300 \pm 50$ meV (Endt, 1998). The target was prepared by implanting ^{36}Ar ions into a tantalum sheet (Table 4.3).

be found from the measured target thickness by using Eq. (4.94). This procedure does not rely on the maximum yield Y_{max}, which may be influenced by straggling effects. The stoichiometry n_Y/n_X can then be derived from the effective stopping power (see Eq. (4.94)).

A yield curve over a narrow resonance provides a wealth of information, including the resonance energy, beam energy resolution, target thickness, number of active target nuclei per square centimeter, and the target stoichiometry. Alternatively, if the beam energy spread is small compared to the total resonance width ($\Delta_{beam} \ll \Gamma$) and if $\Gamma \ll \Delta E$, then the difference in energies at which the yield reaches 25% and 75% of its maximum value will be equal to Γ (see Eq. (4.111)).

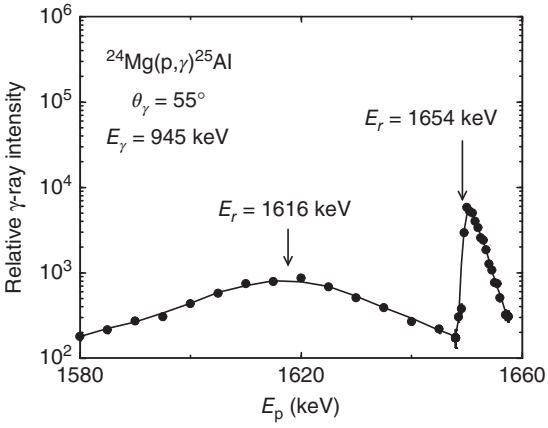

Figure 4.58 Measured yield versus laboratory bombarding energy for the ^{24}Mg(p,γ)^{25}Al reaction at energies near 1.6 MeV. The yield is obtained from the intensity of the secondary 945 keV → 0 transition in ^{25}Al. The target was produced by evaporating ^{24}Mg onto a tantalum backing. The narrow structure at ≈ 1.65 MeV shows the yield curve over a narrow resonance (E_r^{lab} = 1654 keV, Γ = 0.1 keV), while the broad structure at ≈ 1.62 MeV corresponds to the yield curve of a broad resonance (E_r^{lab} = 1616 keV, Γ = 36 keV). (Reprinted from Powell *et al.* (1999). Copyright (1999), with permission from Elsevier.)

Such techniques are frequently applied for measuring the quantities E_r, Δ_{beam}, ΔE, n_X, n_Y/n_X, and Γ.

As a final example, consider the yield curve displayed in Figure 4.58, which was measured in the ^{24}Mg(p,γ)^{25}Al reaction at bombarding energies near 1.6 MeV. The yield was obtained from the intensity of a secondary transition. The measurement was performed using an evaporated, enriched ^{24}Mg target. The narrow structure at ≈ 1.65 MeV shows the yield curve over a narrow resonance (E_r = 1654 keV, Γ = 0.1 keV), similar to the examples discussed above. The full width at half maximum of about 3 keV, as measured with respect to the underlying continuum, reflects the target thickness, since $\Delta E \gg \Gamma$. The broad structure at ≈ 1.62 MeV corresponds to the yield curve of a broad resonance (E_r = 1616 keV, Γ = 36 keV). Since in this case we have $\Delta E \ll \Gamma$, the yield curve reflects the shape of the cross section curve, as discussed in Section 4.8.1.

4.8.4 Determination of Absolute Resonance Strengths and Cross Sections

The importance of absolute cross sections and resonance strengths for the calculation of thermonuclear reaction rates has been stressed in Chapter 3. What is directly measured in experiments are yields rather than cross sections or resonance strengths, as we have seen in previous sections. We will now discuss methods of deriving absolute values of σ and $\omega\gamma$ from measured yields. It is again assumed that the stopping power is approximately constant over the width of the

target. The assumption is justified if the target thickness is less than a few tens of kilo electron volts. In this case, the target thickness and stopping power are related by Eqs. (4.14) or (4.17).

4.8.4.1 Experimental Yields

Yields of nuclear reactions are usually measured with detectors located at a certain detection angle θ with respect to the incident beam direction and cover a solid angle Ω. The total yield is experimentally given by Eqs. (4.49), (4.69), and (4.87),

$$Y = \frac{\mathcal{N}_R}{\mathcal{N}_b} = \frac{\mathcal{N}}{\mathcal{N}_b B \eta W} \tag{4.123}$$

with $\mathcal{N}_R$ the total number of reactions that occurred, $\mathcal{N}_b$ the total number of incident projectiles, and B, $\mathcal{N}$, η, and W the branching ratio (probability of emission per reaction), the total number of detected particles or photons, the detector efficiency, and the angular correlation, respectively, for a specific nuclear transition. The latter three quantities depend, in general, on the detection angle θ. If the reaction proceeds to only one final state, or if the yield is presented for a specific transition rather than for the total number of reactions, then $B = 1$.

The differential yield for a nonresonant cross section is usually given for a specific transition ($B = 1$). With Eqs. (4.44) and (4.123) we write

$$\left(\frac{dY}{d\Omega}\right)_\theta = \frac{\mathcal{N}}{\mathcal{N}_b \eta_{\text{int}} \Omega} \tag{4.124}$$

where η_{int} denotes the intrinsic detection efficiency (e.g., $\eta_{\text{int}} = 1$ for silicon charged-particle detectors; Section 4.5.1) and Ω is the detector solid angle in steradians.

4.8.4.2 Absolute Resonance Strengths and Cross Sections

With few exceptions, most experimental resonance strengths have been determined using the plateau height of thick target yields (see Eq. (4.109)),

$$\omega\gamma = \frac{2\varepsilon_r}{\lambda_r^2} Y_{\max,\Delta E\to\infty} = \frac{2\varepsilon_r}{\lambda_r^2} \frac{\mathcal{N}_{\max,\Delta E\to\infty}}{\mathcal{N}_b B \eta W} \tag{4.125}$$

where the subscript r indicates that the corresponding quantities relate to the resonance energy E_r. The quantities B, η, and W are usually constant over a given resonance yield curve. Notice that the resonance strength in the above expression does not depend on the absolute number of target nuclei, but only on the stopping power, and the stoichiometry if the target consists of a compound. When using Eq. (4.125), one has to verify carefully that the maximum observed yield is not affected by the beam spread, straggling, or the total resonance width. Since the area under the yield curve is independent of such effects (see Eq. (4.119)), it is usually more reliable to deduce the resonance strength from Eq. (4.121) instead of Eq. (4.125). From Eqs. (4.121) and (4.123), one finds

$$\omega\gamma = 2\frac{A_Y}{n\lambda_r^2} = \frac{2}{\lambda_r^2}\frac{\varepsilon_r}{\Delta E}\int_0^\infty Y(E_0)\,dE_0 = \frac{2}{\lambda_r^2}\frac{\varepsilon_r}{\Delta E}\frac{1}{B\eta W}\int_0^\infty \frac{\mathcal{N}(E_0)}{\mathcal{N}_b(E_0)}\,dE_0 \tag{4.126}$$

The subscript r is omitted for the target thickness ΔE, although this quantity also refers to an energy near E_r. Similarly, we may use Eqs. (4.92) and (4.123) for determining slowly varying absolute cross sections,

$$\sigma(E_{\text{eff}}) = \frac{Y(E_0)}{n} = Y(E_0)\frac{\varepsilon(E_0)}{\Delta E(E_0)} = \frac{\varepsilon(E_0)}{\Delta E(E_0)}\frac{\mathcal{N}(E_0)}{\mathcal{N}_b(E_0)B(E_0)\eta(E_0)W(E_0)} \tag{4.127}$$

Determinations of absolute $\omega\gamma$ and σ values by using Eqs. (4.126) and (4.127) are difficult. These procedures require knowledge of the absolute number of incident particles, absolute detector efficiencies, absolute branching ratios, and so on. In particular, absolute stopping powers carry relatively large errors (Section 4.2.1). Furthermore, if the target consists of a compound, then the effective stopping power ε_{eff} has to be used in the above expressions and, consequently, the target stoichiometry has to be accurately known (see Eq. (4.94)).

Uncertainties of measured $\omega\gamma$ and σ values are typically in the 10–20% range, where the effective stopping power contributes frequently the major fraction of the error. In some cases, the $\omega\gamma$ values for a given resonance, measured by different research groups, deviate from each other by factors of 2–4. Similar arguments apply to some cross sections. These deviations reflect the difficulties in measuring the absolute magnitudes of quantities entering into the resonance strength or cross section calculations. For example, the absolute beam intensity is usually determined from the total charge deposited by the beam on a Faraday cup, but systematic errors are likely if secondary electron emission is not properly accounted for (Section 4.3.4).

A major problem for the determination of absolute $\omega\gamma$ and σ values is the incomplete knowledge of the target stoichiometry. If evaporated targets are used (Section 4.3.2) it is frequently assumed that the composition of the target during the nuclear reaction measurement is the same as the composition of the raw material used before the evaporation took place. This assumption is rarely valid since the target composition can change either during evaporation or later during ion beam bombardment. For example, Mg targets are frequently prepared by reductive evaporation of MgO (Takayanagi *et al.*, 1966) and, therefore, such targets are expected to consist of a pure layer of Mg. However, measurements have shown (Iliadis *et al.*, 1990) that these targets consist of a compound Mg_5O, indicating either incomplete oxygen reduction during target preparation or oxidization in air before the experiment. Another striking example is NaCl targets. It was shown (Paine, Kennett, and Sargood, 1978) that such targets change their stoichiometry during proton bombardment from NaCl to $Na_{17}Cl_{10}$ after an accumulated charge of only $\approx 1 \times 10^{-4}$ C.

4.8.4.3 Relative Resonance Strengths and Cross Sections

It is considerably simpler and more reliable to obtain resonance strengths and cross sections relative to some absolute, carefully measured, standard resonance strength or cross section. Using the expression for the maximum yield of an infinitely thick target (see Eq. (4.125)) we obtain

$$\frac{\omega\gamma_1}{\omega\gamma_2} = \frac{\varepsilon_{r,1}}{\varepsilon_{r,2}} \frac{\lambda_{r,2}^2}{\lambda_{r,1}^2} \frac{Y_{\max,\Delta E\to\infty,1}}{Y_{\max,\Delta E\to\infty,2}} = \frac{\varepsilon_{r,1}}{\varepsilon_{r,2}} \frac{\lambda_{r,2}^2}{\lambda_{r,1}^2} \frac{\mathcal{N}_{\max,\Delta E\to\infty,1}}{\mathcal{N}_{\max,\Delta E\to\infty,2}} \frac{\mathcal{N}_{b,2}}{\mathcal{N}_{b,1}} \frac{B_2}{B_1} \frac{\eta_2}{\eta_1} \frac{W_2}{W_1} \quad (4.128)$$

where the subscripts 1 and 2 correspond to the resonance of interest and the standard resonance, respectively. The error of the resonance strength $\omega\gamma_1$ depends on the accuracy of the $\omega\gamma_2$ value of the standard resonance. Otherwise, only ratios of stopping powers, efficiencies, numbers of incident particles, and so on, enter in Eq. (4.128), thus minimizing the influence of potential sources of error. If we use instead the respective areas under the yield curves (see Eq. (4.126)), then

$$\begin{aligned}\frac{\omega\gamma_1}{\omega\gamma_2} &= \frac{A_{Y,1}}{A_{Y,2}} \frac{\lambda_{r,2}^2}{\lambda_{r,1}^2} \frac{\varepsilon_{r,1}}{\varepsilon_{r,2}} \frac{\Delta E_2}{\Delta E_1} = \frac{\lambda_{r,2}^2}{\lambda_{r,1}^2} \frac{\varepsilon_{r,1}}{\varepsilon_{r,2}} \frac{\Delta E_2}{\Delta E_1} \frac{\int_0^\infty Y_1(E_{0,1})\, dE_{0,1}}{\int_0^\infty Y_2(E_{0,2})\, dE_{0,2}} \\ &= \frac{\lambda_{r,2}^2}{\lambda_{r,1}^2} \frac{\varepsilon_{r,1}}{\varepsilon_{r,2}} \frac{\Delta E_2}{\Delta E_1} \frac{B_2\eta_2 W_2}{B_1\eta_1 W_1} \frac{\int_0^\infty \frac{\mathcal{N}_1(E_{0,1})}{\mathcal{N}_{b,1}(E_{0,1})} dE_{0,1}}{\int_0^\infty \frac{\mathcal{N}_2(E_{0,2})}{\mathcal{N}_{b,2}(E_{0,2})} dE_{0,2}}\end{aligned} \quad (4.129)$$

The above expression does not depend on the stopping power or the target thickness if $\omega\gamma_1$ is determined relative to a standard resonance in the same reaction when using the same target, since then $\varepsilon_{r,1}/\Delta E_1 = \varepsilon_{r,2}/\Delta E_2 = n$.

Similarly, we find from Eq. (4.127) for slowly varying cross sections

$$\begin{aligned}\frac{\sigma_1(E_{\mathrm{eff},1})}{\sigma_2(E_{\mathrm{eff},2})} &= \frac{\varepsilon_1(E_{0,1})}{\varepsilon_2(E_{0,2})} \frac{\Delta E_2(E_{0,2})}{\Delta E_1(E_{0,1})} \frac{Y_1(E_{0,1})}{Y_2(E_{0,2})} \\ &= \frac{\varepsilon_1(E_{0,1})}{\varepsilon_2(E_{0,2})} \frac{\Delta E_2(E_{0,2})}{\Delta E_1(E_{0,1})} \frac{\mathcal{N}_1(E_{0,1})}{\mathcal{N}_2(E_{0,2})} \frac{\mathcal{N}_{b,2}(E_{0,2})}{\mathcal{N}_{b,1}(E_{0,1})} \frac{B_2(E_{0,2})}{B_1(E_{0,1})} \frac{\eta_2(E_{0,2})}{\eta_1(E_{0,1})} \frac{W_2(E_{0,2})}{W_1(E_{0,1})}\end{aligned} \quad (4.130)$$

where the subscripts 1 and 2 refer to the nonresonant cross section of interest and the standard cross section, respectively. Again, the stopping powers and target thicknesses cancel if both cross sections are measured in the same reaction using the same target.

A nonresonant cross section σ can also be determined relative to a well-known resonance strength $\omega\gamma$ (or vice versa). We obtain, for example, from Eqs. (4.125) and (4.127)

$$\begin{aligned}\frac{\sigma_1(E_{\mathrm{eff},1})}{\omega\gamma_2} &= \frac{\lambda_{r,2}^2}{2\Delta E_1(E_{0,1})} \frac{\varepsilon_1(E_{0,1})}{\varepsilon_{r,2}} \frac{\mathcal{N}_1(E_{0,1})}{\mathcal{N}_{\max,\Delta E\to\infty,2}} \\ &\quad \times \frac{\mathcal{N}_{b,2}}{\mathcal{N}_{b,1}(E_{0,1})} \frac{B_2}{B_1(E_{0,1})} \frac{\eta_2}{\eta_1(E_{0,1})} \frac{W_2}{W_1(E_{0,1})}\end{aligned} \quad (4.131)$$

or from Eqs. (4.126) and (4.127)

$$\begin{aligned}\frac{\sigma_1(E_{\mathrm{eff},1})}{\omega\gamma_2} &= \frac{\lambda_{r,2}^2}{2} \frac{\varepsilon_1(E_{0,1})}{\varepsilon_{r,2}} \frac{\Delta E_2}{\Delta E_1(E_{0,1})} \frac{B_2}{B_1(E_{0,1})} \frac{\eta_2}{\eta_1(E_{0,1})} \frac{W_2}{W_1(E_{0,1})} \\ &\quad \times \frac{\mathcal{N}_1(E_{0,1})}{\mathcal{N}_{b,1}(E_{0,1}) \int_0^\infty \frac{\mathcal{N}_2(E_{0,2})}{\mathcal{N}_{b,2}(E_{0,2})}\, dE_{0,2}}\end{aligned} \quad (4.132)$$

where in the last two expressions the subscripts 1 and 2 refer to the nonresonant cross section and the resonance, respectively.

Example 4.4

For the narrow $E_r^{\text{lab}} = 317$ keV resonance in the ^{25}Mg(p,γ)^{26}Al reaction ($\Gamma < 40$ eV), a yield curve is measured using the intensity of the primary γ-ray transition to the 417 keV state in ^{26}Al ($R \rightarrow 417$ keV). An evaporated $^{25}Mg_5O$ target has a thickness of $\Delta E = 15$ keV. The beam spread amounts to $\Delta_{\text{beam}} = 0.5$ keV. Calculate the resonance strength from the measured values given below. Neglect angular correlation effects ($W_{R\rightarrow 417} = 1$).

$\mathcal{N}_{\text{max},R\rightarrow 417} = 3480 \pm 63$	γ-ray intensity on the yield curve plateau
$Q = (0.090 \pm 0.005)\ C$	accumulated ion beam charge on target
$\eta_{R\rightarrow 417} = (7.34 \pm 0.30) \times 10^{-4}$	peak efficiency for $R \rightarrow 417$ keV
$B_{R\rightarrow 417} = (33 \pm 1)\%$	branching ratio of $R \rightarrow 417$ keV

Assume that the stopping power is constant over the thickness of the target. Use the following values (with 10% errors) for protons in Mg and O, as obtained from the computer code SRIM (Ziegler, 2003): $\varepsilon_{\text{p}\rightarrow Mg}(E_r^{\text{lab}} = 317\,\text{keV}) = 12.8 \times 10^{-15}$ eV cm^2/atom, $\varepsilon_{\text{p}\rightarrow O}(E_r^{\text{lab}} = 317\,\text{keV}) = 10.6 \times 10^{-15}$ eV cm^2/atom.

With a stoichiometry of $n_{\text{Mg}} : n_{\text{O}} = 5 : 1$, we obtain for the effective stopping power (see Eq. (4.94))

$$\begin{aligned}\varepsilon_{\text{eff}} &= \frac{M_{^{25}\text{Mg}}}{M_{^{25}\text{Mg}} + M_{\text{H}}} \left[\varepsilon_{^{25}\text{Mg}} + \frac{n_{\text{O}}}{n_{\text{Mg}}}\varepsilon_{\text{O}}\right] \\ &= \frac{24.985}{24.985 + 1.008} \left[(12.8 \times 10^{-15}\,\text{eV cm}^2/\text{atom}) \right. \\ &\qquad \left. + \frac{1}{5}(10.6 \times 10^{-15}\,\text{eV cm}^2/\text{atom})\right] \\ &= 1.43 \times 10^{-14}\,\text{eV cm}^2/\text{atom}\,(\pm 10\%)\end{aligned}$$

The de Broglie wavelength is given by (see Eq. (4.107))

$$\begin{aligned}\frac{\lambda_r^2}{2} &= \left(\frac{M_p + M_t}{M_t}\right)^2 \frac{4.125 \times 10^{-18}}{M_p E_r^{\text{lab}}} \qquad (\text{cm}^2) \\ &= \left(\frac{1.008 + 24.985}{24.985}\right)^2 \frac{4.125 \times 10^{-18}}{(1.008)(317000)}\,\text{cm}^2 = 1.40 \times 10^{-23}\,\text{cm}^2\end{aligned}$$

The total number of incident protons (assuming a positively charged proton beam, q=1) amounts to

$$\mathcal{N}_{\text{p}} = \frac{Q}{qe} = \frac{(0.090 \pm 0.005)\,\text{C}}{1 \cdot (1.6 \times 10^{-19}\,\text{C})} = 5.63 \times 10^{17}\,(\pm 6\%)$$

If we neglect the influence of the beam spread (which is small compared to the target thickness), straggling, and total resonance width ($\Gamma \ll \Delta E$) on the maximum yield, then the observed plateau height corresponds to the maximum yield of an infinitely thick target, $Y_{\max,\Delta E\to\infty}$. With Eq. (4.125) one finds

$$\begin{aligned}\omega\gamma &= \frac{2\varepsilon_{\mathrm{eff},r}}{\lambda_r^2}\frac{\mathcal{N}_{\max,\Delta E\to\infty}}{\mathcal{N}_b B\eta W}\\ &= \frac{1.43\times10^{-14}\,\mathrm{eV\,cm^2}}{1.40\times10^{-23}\,\mathrm{cm^2}}\frac{3480}{(5.63\times10^{17})(0.33)(7.34\times10^{-4})}\\ &= 2.61\times10^{-2}\,\mathrm{eV}\,(\pm13\%)\end{aligned}$$

All energies in the general yield expression of Eq. (4.91) are given in the center-of-mass system. The quantity $dx = dE/(dE/dx)$ is independent of the reference frame. Multiplication of numerator and denominator by the center of mass to laboratory frame conversion factor $M_t/(M_t + M_p)$ (see Eq. (C.24); M_t and M_p are the relative atomic masses of the active target nuclei and the projectiles, respectively) shows that the effective stopping power measured in the laboratory or calculated with SRIM must be multiplied by this factor before it can be used in yield calculations.

4.8.4.4 Determination of Resonance Strengths and Cross Sections Relative to Rutherford Scattering

It is apparent from the above discussion that measurements of absolute resonance strengths and cross sections are difficult to perform since a variety of experimental artifacts, such as beam spread, straggling, stoichiometries, stopping powers, integrated beam charge, and so on, may lead to substantial systematic errors. Nevertheless, for a number of resonances, careful measurements of their absolute strengths have been performed. The results are given in Table 4.12. This set of recommended $\omega\gamma$ values can be used as an absolute standard for the determination of other resonance strengths or nonresonant cross sections according to Eqs. (4.128)–(4.132).

Almost all the $\omega\gamma$ values listed in the table have been determined relative to the intensity of Rutherford-scattered projectiles. The experimental details vary from study to study, but such techniques essentially eliminate the influence of at least some experimental artifacts on the $\omega\gamma$ values. Consequently, we expect that these results are more reliable than those obtained from Eqs. (4.125)–(4.127). In the following, a method will be discussed that eliminates almost all experimental artifacts. This technique provides absolute resonance strengths and cross sections that depend almost exclusively on measured intensities and, in particular, does not require knowledge of beam or target properties. The method is based on certain quantities cancelling in the determination of $\omega\gamma$ if the nuclear reaction products and Rutherford-scattered beam particles are measured simultaneously.

Table 4.12 Recommended resonance strengths.

Reaction	E_r^{lab} (keV)	J^π	$\omega\gamma_{cm}$ (eV)	Error (%)
$^{14}N(p,\gamma)^{15}O$	278	$1/2^+$	$1.287(38)\times10^{-2}$ [a]	3.0
$^{18}O(p,\gamma)^{19}F$	151	$1/2^+$	$9.7(5)\times10^{-4}$ [b]	5.2
$^{22}Ne(p,\gamma)^{23}Na$	479	$1/2^+$	$5.24(51)\times10^{-1}$ [c]	9.7
$^{23}Na(p,\alpha)^{20}Ne$	338	1^-	$7.16(29)\times10^{-2}$ [d]	4.0
$^{23}Na(p,\gamma)^{24}Mg$	512	$(1,2^+)$	$9.13(125)\times10^{-2}$ [e]	13.7
$^{24}Mg(p,\gamma)^{25}Al$	223	$1/2^+$	$1.27(9)\times10^{-2}$ [f]	7.1
	419	$3/2^+$	$4.16(26)\times10^{-2}$ [g]	6.2
$^{25}Mg(p,\gamma)^{26}Al$	435	4^-	$9.42(65)\times10^{-2}$ [g]	6.9
	591	1^+	$2.28(17)\times10^{-1}$ [h]	7.4
$^{26}Mg(p,\gamma)^{27}Al$	338	$3/2^-$	$2.73(16)\times10^{-1}$ [g]	5.9
	454	$1/2^+$	$7.15(41)\times10^{-1}$ [g]	5.7
	1966	$5/2^+$	5.15(45) [e]	8.7
$^{27}Al(p,\gamma)^{28}Si$	406	4^+	$8.63(52)\times10^{-3}$ [g]	6.0
	632	3^-	$2.64(16)\times10^{-1}$ [e]	6.1
	992	3^+	1.91(11) [e]	5.7
$^{30}Si(p,\gamma)^{31}P$	620	$1/2^-$	1.95(10) [e]	5.1
$^{31}P(p,\gamma)^{32}S$	642	1^-	$5.75(50)\times10^{-2}$ [e]	8.7
	811	2^+	$2.50(20)\times10^{-1}$ [e]	8.0
$^{34}S(p,\gamma)^{35}Cl$	1211	$7/2^-$	4.50(50) [e]	11.1
$^{35}Cl(p,\gamma)^{36}Ar$	860	3^-	$7.00(100)\times10^{-1}$ [e]	14.3
$^{36}Ar(p,\gamma)^{37}K$	918	$5/2^+$	$2.38(19)\times10^{-1}$ [i]	8.0
$^{37}Cl(p,\gamma)^{38}Ar$	846	1^-	$1.25(16)\times10^{-1}$ [e]	12.8
$^{39}K(p,\gamma)^{40}Ca$	2042	1^+	1.79(19) [e]	10.6
$^{40}Ca(p,\gamma)^{41}Sc$	1842	$7/2^+$	$1.40(15)\times10^{-1}$ [e]	10.7

The absolute error is given in parenthesis and refers to the last significant digit(s).
Sources: [a] Weighted average of Becker *et al.* (1982), Imbriani *et al.* (2005), Bemmerer *et al.* (2006), and Art Champagne, private communication; [b] Weighted average of Wiescher *et al.* (1980), Becker *et al.* (1982), and Vogelaar *et al.* (1990); [c] Longland *et al.* (2010); [d] Rowland *et al.* (2002a); [e] Paine and Sargood (1979); [f] Powell *et al.* (1999); [g] Powell *et al.* (1998); [h] Anderson *et al.* (1980); [i] Weighted average of Goosman and Kavanagh (1967), and Mohr *et al.* (1999).

We start with Eq. (4.126), which relates the resonance strength to the area under the resonance yield curve,

$$\omega\gamma_1 = 2\frac{A_{Y,1}}{n\lambda_{r,1}^2} = \frac{2}{n\lambda_{r,1}^2}\frac{1}{B_1\eta_1 W_1}\int_0^\infty \frac{\mathcal{N}_1(E_{0,1})}{\mathcal{N}_{b,1}(E_{0,1})}\,dE_{0,1} \tag{4.133}$$

where the subscript 1 is used for all quantities related to the measurement of the resonance. As already noted, the above expression is independent of the beam spread, straggling, and the total resonance width. For the derivation of this result, we used the assumptions that the resonant cross section is given by the Breit–Wigner formula with constant partial widths and de Broglie wavelength over the total resonance width, and that the stopping power is approximately constant over the width of the target (Section 4.8.2).

Suppose the projectiles that are Rutherford-scattered by the active target nuclei are measured in a second detector located at an angle of θ_2 with respect to the incident beam direction. If the target is sufficiently thin (say, <10 keV), so that the variation of the Rutherford-scattering cross section over the target thickness is small, we obtain from Eq. (4.93)

$$\left[\frac{dY_2(E_{0,2})}{d\Omega}\right]_{\theta_2}^{\text{Ruth}} = n\left[\frac{d\sigma_2(E_{\text{eff},2})}{d\Omega}\right]_{\theta_2}^{\text{Ruth}} \tag{4.134}$$

where the subscript 2 refers to all quantities related to the measurement of the Rutherford-scattered beam particles by the second detector. Solving for n, one finds with Eq. (4.124) (assuming $\eta_{\text{int},2} = 1$ for silicon charged-particle detectors)

$$n = \frac{\left[\frac{dY_2(E_{0,2})}{d\Omega}\right]_{\theta_2}^{\text{Ruth}}}{\left[\frac{d\sigma_2(E_{\text{eff},2})}{d\Omega}\right]_{\theta_2}^{\text{Ruth}}} = \frac{\frac{\mathcal{N}_2(E_{0,2})}{\mathcal{N}_{b,2}(E_{0,2})\Omega_2}}{\left[\frac{d\sigma_2(E_{\text{eff},2})}{d\Omega}\right]_{\theta_2}^{\text{Ruth}}} \tag{4.135}$$

It follows that the ratio of differential yield and differential cross section for Rutherford scattering is constant (i.e., equal to n) and thus may be measured at any bombarding energy. If the resonant reaction products are measured *simultaneously* with the Rutherford-scattered particles, so that $E_{0,1} = E_{0,2} \equiv E_0$ and $\mathcal{N}_{b,2}(E_{0,2}) = \mathcal{N}_{b,1}(E_{0,1})$, we obtain from Eqs. (4.133) and (4.135)

$$\omega\gamma_1 = \frac{2}{\lambda_{r,1}^2}\frac{1}{B_1 W_1}\frac{\Omega_2}{\eta_1}\int_0^\infty \frac{\mathcal{N}_1(E_0)}{\mathcal{N}_2(E_0)}\left[\frac{d\sigma_2(E_{\text{eff},2})}{d\Omega}\right]_{\theta_2}^{\text{Ruth}} dE_0 \tag{4.136}$$

The resonance strength in this expression is independent of the properties of the target (stoichiometry, stopping power, uniformity) and the beam (current integration, straggling). It depends on (i) the observed number of resonant reaction products (particles or photons) and Rutherford-scattered particles, $\mathcal{N}_1(E_0)$ and $\mathcal{N}_2(E_0)$; (ii) the calculated Rutherford scattering cross section, $[d\sigma_2(E_{\text{eff},2})/d\Omega]_{\theta_2}^{\text{Ruth}}$; and (iii) the de Broglie wavelength, branching ratio, and angular correlation of the resonant reaction products ($\lambda_{r,1}^2$, B_1, W_1). Also, $\omega\gamma_1$ depends on the ratio Ω_2/η_1 and, consequently, is independent of the knowledge of absolute detection properties.

If a nonresonant reaction cross section is measured relative to Rutherford scattering, we find similarly

$$\sigma_1(E_{\text{eff},1}) = \frac{1}{B_1(E_0)W_1(E_0)}\frac{\Omega_2}{\eta_1}\frac{\mathcal{N}_1(E_0)}{\mathcal{N}_2(E_0)}\left[\frac{d\sigma_2(E_{\text{eff},2})}{d\Omega}\right]_{\theta_2}^{\text{Ruth}} \tag{4.137}$$

For (p,α) or (α,p) type reactions, we can substitute in Eqs. (4.136) and (4.137) $\eta_1 = \Omega_1/(4\pi)$, assuming that the intrinsic efficiency for detecting the resonant particles is unity ($\eta_{\text{int},1} = 1$). In general, we have $E_{\text{eff},1} \neq E_{\text{eff},2}$ as can be seen, for example, from Eq. (4.101).

The theoretical Rutherford scattering cross section is given by (Evans, 1955)

$$\left[\frac{d\sigma(E)}{d\Omega}\right]_{\theta}^{\text{Ruth}} = \left(\frac{Z_p Z_t e^2}{4E}\right)^2 \frac{1}{\sin^4(\theta/2)}$$
$$= 1.296 \left(\frac{Z_p Z_t}{E}\right)^2 \frac{1}{\sin^4(\theta/2)} \qquad \text{(mb/sr)} \qquad (4.138)$$

with Z_p and Z_t the atomic numbers of projectile and target, respectively. In the numerical expression, the energy E is in units of mega electron volts.

The method of measuring absolute resonance strengths and cross sections described above depends on the assumption that the intensity of elastically scattered beam particles at the energy of the resonance, or in the region of the nonresonant cross section, is well described by the Rutherford formula. However, at higher bombarding energies ($E > 0.5$ MeV) and for relatively broad resonances ($\Gamma > 1$ keV) the elastic scattering cross section generally deviates from Rutherford scattering since it is influenced by resonant scattering (Section 2.5.3). The above technique is most useful at low bombarding energies and for relatively narrow resonances, a situation that is frequently of interest for thermonuclear reactions. In any case, one has to verify experimentally through careful measurements that the elastic scattering cross section is indeed described by the Rutherford formula.

For example, consider the measurement of the $E_r^{\text{lab}} = 338$ keV resonance ($\Gamma = 0.7$ keV) in the ^{23}Na(p,α)^{20}Ne reaction. The setup is shown in Figure 4.59a. It consists of two silicon charged-particle detectors ($\eta_{\text{int}} = 1$). The first detector, positioned at 140°, covers a relatively large solid angle and is used for measuring the resonant α-particles. A thin metal foil is placed in front of this counter to prevent the large number of elastically scattered protons from interfering with the detection of the α-particles (Section 4.5.1). The second detector, placed at 155°, covers a very small solid angle and is used for measuring the elastically scattered protons. A proton beam of a few 100 nA intensity is incident on a transmission target that was prepared by evaporating NaCl on a thin carbon foil.

Typical α-particle and proton spectra, measured at $E_{\text{p}}^{\text{lab}} = 341$ keV and 400 keV, respectively, are shown in Figure 4.59b,c. In the proton spectrum, only the intensity of the peak corresponding to protons elastically scattered from (the active) ^{23}Na nuclei is of interest here. The resonant α-particle yield curve is displayed in Figure 4.60a. It can be seen that the target is about 6 keV thick. Figure 4.60b shows the measured yields of elastically scattered protons from ^{23}Na at a fixed detector angle as a function of bombarding energy over the region of the $E_r^{\text{lab}} = 338$ keV resonance. The solid line represents the calculated Rutherford yield, normalized to the data. It is apparent that the data are well described by the Rutherford formula.

The value of the resonance strength measured with this technique and derived from Eq. (4.136) is listed in Table 4.12. It is significantly smaller compared to previous $\omega\gamma$ values that have been determined by using the maximum yield of thick targets (see Eq. (4.125)). The disagreement is caused by previous studies

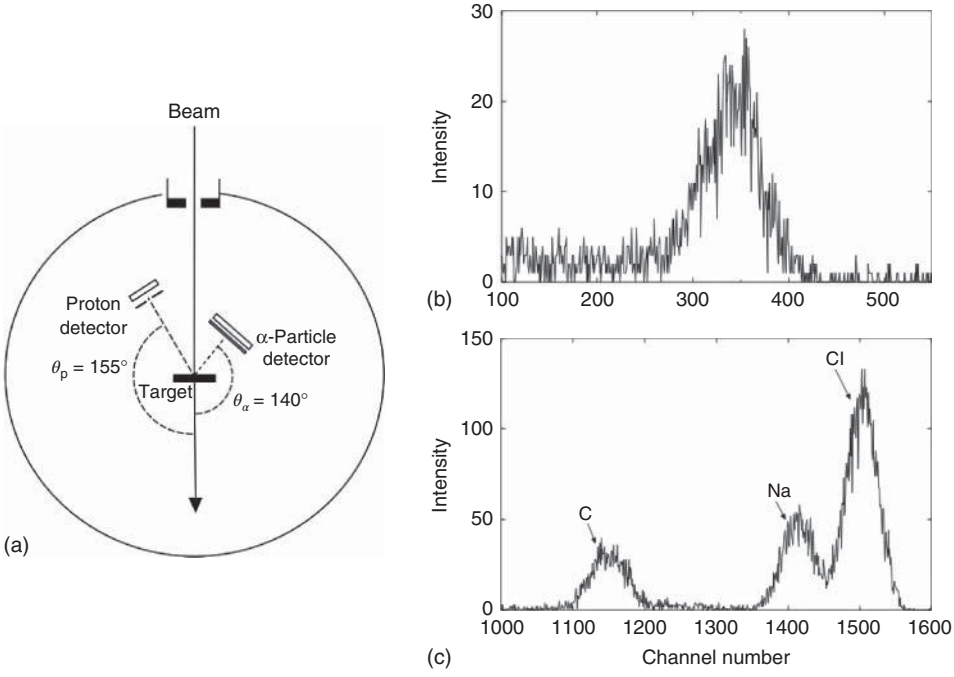

Figure 4.59 Measurement of the E_r^{lab} = 338 keV resonance (Γ = 0.7 keV) in the ^{23}Na(p,α)^{20}Ne reaction. (a) Setup showing the proton beam ($\approx$ 100 nA), the transmission target prepared by evaporating NaCl (6 keV thick) on a thin carbon foil, and two silicon charged-particle detectors. The first detector is used for measuring resonant α-particles and is covered by a thin metal foil. The second detector is used for measuring elastically scattered protons. (b) α-Particle spectrum measured in the region of the resonance at a laboratory proton energy of 341 keV. (c) Spectrum of elastically scattered protons, measured at a laboratory proton energy of 400 keV. (Reprinted with permission from Rowland *et al.* (2002a). Copyright (2002) by the American Physical Society.)

erroneously assuming a target stoichiometry of Na_1Cl_1, whereas the technique described above is independent of the target stoichiometry (Rowland *et al.*, 2002a).

4.9
Transmissions, Yields, and Cross Sections for Neutron-Induced Reactions

In this section, the relationships between directly measured quantities (yields and transmissions) and cross sections or resonance strengths are given for neutron-induced reactions. Examples for measured transmission and yield curves will be presented, and the determination of absolute cross sections is briefly discussed.

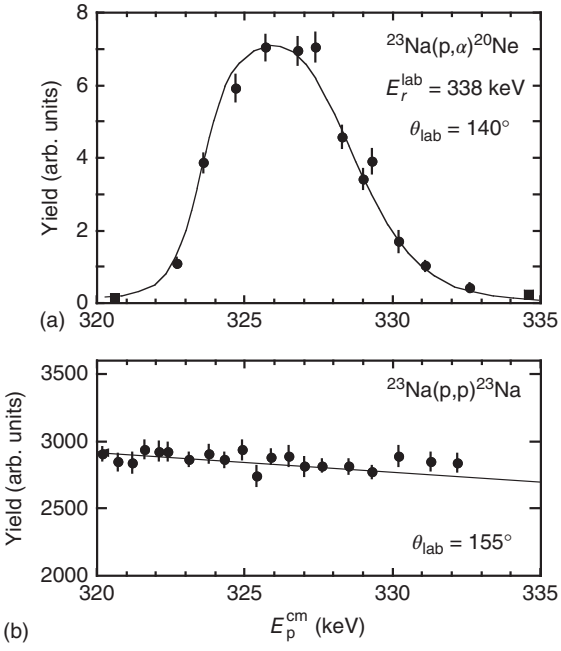

Figure 4.60 (a) Resonant α-particle yield versus proton energy for the $E_r^{lab} = 338$ keV resonance in ^{23}Na(p,α)^{20}Ne; (b) yield of elastically scattered protons from ^{23}Na versus energy; the solid line represents the calculated Rutherford yield, normalized to the data. Both yield curves were measured with the setup shown in Figure 4.59.

4.9.1 Resonance Transmission

Of particular interest are transmission measurements of resolved resonances. The shape of the measured transmission curve depends not only on the total cross section, but also on other factors, such as the Doppler effect or the resolution of the neutron detector (Beckurts and Wirtz, 1964). The quantity of interest, however, is usually not the energy dependence of the total resonance cross section, but the determination of the resonance properties that enter in the expression for the resonant reaction rate (Section 3.2.4).

Consider the simplest case of an isolated resonance. Suppose that (i) the resonance cross section is given by the Breit–Wigner formula, (ii) only the neutron and γ-ray channels are open, and (iii) the energy dependence of the partial widths over the total resonance width can be neglected. In the vicinity of an isolated resonance, the *total* neutron-induced cross section can be written as (Section 2.5.5)

$$\sigma_{T,\mathrm{BW}}(E) = \frac{\lambda^2}{4\pi}\omega\frac{\Gamma_n\Gamma}{(E_r - E)^2 + \Gamma^2/4} = \sigma_{T,\max}\frac{\Gamma}{2}\frac{\Gamma/2}{(E_r - E)^2 + \Gamma^2/4} \tag{4.139}$$

with $\sigma_{T,\max} = \sigma_{T,\mathrm{BW}}(E = E_r) = (\lambda_r^2/\pi)\omega\Gamma_\mathrm{n}/\Gamma$ denoting the maximum total cross section. For an incident beam of monoenergetic neutrons, the transmission is (see Eq. (4.37))

$$T(E) = \exp\left[-n\sigma_{T,\max}\frac{\Gamma}{2}\frac{\Gamma/2}{(E_r - E)^2 + \Gamma^2/4}\right] \tag{4.140}$$

with n the number of sample nuclei per unit area. For the area *above* the transmission curve, one finds

$$A_T = \int_0^\infty \left\{1 - \exp\left[-n\sigma_{T,\max}\frac{\Gamma}{2}\frac{\Gamma/2}{(E_r - E)^2 + \Gamma^2/4}\right]\right\} dE \tag{4.141}$$

which reduces for the limiting case of a thin sample ($n\sigma_{T,\max} \ll 1$) to

$$\begin{aligned} A_T^{n\sigma_{T,\max}\ll 1} &= \int_0^\infty n\sigma_{T,\max}\frac{\Gamma}{2}\frac{\Gamma/2}{(E_r - E)^2 + \Gamma^2/4}dE \\ &= \frac{\pi}{2}n\sigma_{T,\max}\Gamma = \frac{\lambda_r^2}{2}n\omega\Gamma_\mathrm{n} \end{aligned} \tag{4.142}$$

Hence, a measurement of the transmission curve provides an estimate of the neutron partial width Γ_n. This expression also holds if the instrumental resolution and the Doppler effect change the shape of the transmission curve. For thin samples, the area above the transmission curve is independent of these effects. More information on transmission curves can be found in Lynn (1968).

4.9.2 Resonant and Nonresonant Yields

The general expression for the yield of a neutron-induced reaction can be derived from the expression for the transmission (see Eq. (4.37))

$$Y = \int_0^\infty f(E)\left[1 - e^{-n\sigma_T(E)}\right]\frac{\sigma(E)}{\sigma_T(E)}\,dE \tag{4.143}$$

with $\sigma(E)$ and $\sigma_T(E)$ the cross section for the reaction of interest and the total cross section (see Eq. (4.34)), respectively, and $f(E)$ the fraction of incident neutrons having energies between E and $E + dE$ per unit energy interval. For either a monoenergetic incident neutron beam or for constant cross sections $\sigma_T(E)$ and $\sigma(E)$, one finds

$$Y = (1 - e^{-n\sigma_T})\frac{\sigma}{\sigma_T}\int_0^\infty f(E)\,dE = (1 - e^{-n\sigma_T})\frac{\sigma}{\sigma_T} \tag{4.144}$$

If the cross sections $\sigma_T(E)$ and $\sigma(E)$ are not constant, but if the sample is very thin ($n\sigma_T \ll 1$), Eq. (4.143) becomes

$$Y_{n\sigma_T\ll 1} = \int_0^\infty f(E)\left[1 - \left(1 - n\sigma_T(E)\right)\right]\frac{\sigma(E)}{\sigma_T(E)}\,dE = n\int_0^\infty f(E)\sigma(E)\,dE = n\overline{\sigma} \tag{4.145}$$

where we defined an average reaction cross section by $\overline{\sigma} \equiv \int f(E)\sigma(E)\,dE$. A few specialized expressions for the *thin-sample* yield are given below.

4.9.2.1 Constant σ Over Neutron Energy Distribution

This situation occurs, for example, for a smoothly varying cross section and a nearly monoenergetic neutron beam. The yield is given by

$$Y_{n\sigma_T \ll 1} = n\sigma \int_0^\infty f(E)\, dE = n\sigma \tag{4.146}$$

This expression also applies to an isolated resonance when the total width is large compared to the neutron beam resolution ($\Gamma \gg \Delta E_{\mathrm{n}}$). The yield is then directly proportional to the cross section and the resulting excitation function has a resonance shape. In the latter case, we may describe the resonance by the Breit–Wigner formula. Suppose that only the neutron and γ-ray channels are open, as is frequently the case, and that the partial widths are energy independent. The area under the resonance neutron-capture yield curve for a thin sample follows from Eq. (4.146),

$$\begin{aligned} A_Y^{n\sigma_T \ll 1} &= n \int_0^\infty \sigma_{\mathrm{BW}}(E)\, dE = n \int_0^\infty \frac{\lambda^2}{4\pi} \omega \frac{\Gamma_{\mathrm{n}}\Gamma_\gamma}{(E_r - E)^2 + \Gamma^2/4}\, dE \\ &= \frac{\lambda_r^2}{2\pi} n\omega\gamma \int_0^\infty \frac{\Gamma/2}{(E_r - E)^2 + \Gamma^2/4}\, dE = n\frac{\lambda_r^2}{2}\omega\gamma \end{aligned} \tag{4.147}$$

Exactly the same result was obtained for the area under a resonance yield curve in charged-particle-induced reactions (see Eq. (4.121)).

4.9.2.2 Narrow Resonance with $\Gamma \ll \Delta E_{\mathrm{n}}$

If a narrow resonance located at E_r has a small total width compared to the neutron beam resolution, one finds from the Breit–Wigner formula

$$\begin{aligned} Y_{n\sigma_T \ll 1} &= n \int_0^\infty f(E)\sigma_{\mathrm{BW}}(E)\, dE = nf(E_r) \int_0^\infty \sigma_{\mathrm{BW}}(E)\, dE \\ &= \frac{\lambda_r^2}{2\pi} nf(E_r)\omega\gamma \int_0^\infty \frac{\Gamma/2}{(E_r - E)^2 + \Gamma^2/4}\, dE = n\frac{\lambda_r^2}{2} f(E_r)\omega\gamma \end{aligned} \tag{4.148}$$

with $f(E_r)$ the fraction of neutrons per unit energy interval at the resonance energy. In contrast to charged-particle reaction studies (see Eq. (4.116)), the narrow resonance yield for neutron-induced reactions depends on the absolute number of sample nuclei per unit area.

4.9.3 Effective Cross Section

If the incident neutrons are not monoenergetic, an effective cross section is sometimes introduced that is defined in terms of the neutron current density, or neutron flux, instead of the number density of neutrons. If we divide the neutron energy distribution into thin slices, then the number of reactions per volume and per time from each slice is given by Eq. (3.1),

$$\frac{(\mathcal{N}_{R,i}/V)}{t} = \frac{\mathcal{N}_t}{V}\sigma_i v_i \frac{\mathcal{N}_{v,i}}{V} \tag{4.149}$$

with $\mathcal{N}_t/V$ and $\mathcal{N}_{v,i}/V$ the target density and neutron density, respectively. Integrating over all energies, we find

$$\frac{(\mathcal{N}_R/V)}{t} = \frac{\mathcal{N}_t}{V}\int_0^\infty \sigma(E)v\frac{\mathcal{N}_v(E)}{V}\,dE = \frac{\mathcal{N}_t}{V}\int_0^\infty \sigma(E)\phi(E)\,dE \tag{4.150}$$

The neutron flux is defined by $\phi(E) \equiv v\mathcal{N}_v(E)/V$ and the total flux for all neutron energies is $\phi = \int \phi(E)\,dE$ (in units of neutrons per area per time). Alternatively, we may express the total number of reactions per volume and per time in terms of an effective reaction cross section $\hat{\sigma}$ by

$$\frac{(\mathcal{N}_R/V)}{t} = \frac{\mathcal{N}_t}{V}\hat{\sigma}\int_0^\infty v\frac{\mathcal{N}_v(E)}{V}\,dE = \frac{\mathcal{N}_t}{V}\hat{\sigma}\int_0^\infty \phi(E)\,dE = \frac{\mathcal{N}_t}{V}\hat{\sigma}\phi \tag{4.151}$$

Equating the above two expressions, we obtain for the effective cross section

$$\hat{\sigma} = \frac{\int_0^\infty \sigma(E)v\frac{\mathcal{N}_v(E)}{V}\,dE}{\int_0^\infty v\frac{\mathcal{N}_v(E)}{V}\,dE} = \frac{\int_0^\infty \sigma(E)\phi(E)\,dE}{\int_0^\infty \phi(E)\,dE} = \frac{N_\mathrm{n}\int_0^\infty \sigma(E)vf(E)\,dE}{N_\mathrm{n}\int_0^\infty vf(E)\,dE} \tag{4.152}$$

where we used $\mathcal{N}_v(E)/V = f(E)N_\mathrm{n}$, with N_n the total number density of neutrons.

If the energies of the incident neutrons are given by a Maxwell–Boltzmann distribution (Section 4.1.2 and Figure 4.2), one finds with Eq. (3.8) for the flux

$$\begin{aligned}\phi &= \int_0^\infty \phi(E)\,dE = N_\mathrm{n}\int_0^\infty vf(E)\,dE \\ &= N_\mathrm{n}\int_0^\infty \sqrt{\frac{2E}{m_{01}}}\frac{2}{\sqrt{\pi}}\frac{1}{(kT)^{3/2}}\sqrt{E}e^{-E/kT}\,dE = N_\mathrm{n}\frac{2}{\sqrt{\pi}}\sqrt{\frac{2kT}{m_{01}}} = \frac{2}{\sqrt{\pi}}N_\mathrm{n}v_T\end{aligned} \tag{4.153}$$

The effective cross section is given by Eqs. (3.8), (3.70), (4.152), and (4.153),

$$\begin{aligned}\hat{\sigma} &= \frac{N_\mathrm{n}\int_0^\infty \sigma(E)vf(E)\,dE}{N_\mathrm{n}\frac{2}{\sqrt{\pi}}v_T} = \int_0^\infty \sigma(E)\sqrt{\frac{2E}{m_{01}}}\frac{1}{v_T(kT)^{3/2}}\sqrt{E}e^{-E/kT}\,dE \\ &= \frac{1}{(kT)^2}\int_0^\infty \sigma(E)Ee^{-E/kT}\,dE = \frac{\sqrt{\pi}}{2}\frac{\langle\sigma v\rangle}{v_T}\end{aligned} \tag{4.154}$$

Hence, the measured effective reaction cross section gives directly the reaction rate (Section 4.1.2).

4.9.4 Measured Yields and Transmissions

The transmission can be expressed either in terms of intensities (see Eq. (4.35)) or in terms of count rates,

$$T \equiv \frac{I}{I_0} = \frac{dC/dt}{dC_0/dt} \tag{4.155}$$

where dC/dt and dC_0/dt are the measured count rates with and without sample, respectively, between incident neutron beam and detector. The transmission is independent of absolute detection efficiencies. The expressions for T given above is strictly valid only if neutrons that undergo an interaction in the sample are *not* counted by the detector. However, for any sample and detector of finite size, neutrons scattered forward in the sample toward the detector will be counted as if no interaction had occurred. Corrections for this *in-scattering effect* (Miller, 1963) can be obtained most reliably from Monte Carlo simulations.

In terms of experimental quantities, the yield can be expressed by

$$Y = \frac{\mathcal{N}_R}{\mathcal{N}_\nu} = \frac{C}{\eta B f \mathcal{N}_\nu} = \frac{C}{\eta B f \Phi A} \tag{4.156}$$

where $\mathcal{N}_\nu$ and C are the total number of incident neutrons and the measured total number of counts induced by the nuclear reaction of interest, respectively; $\Phi = \int \phi(t)\, dt$ is the time-integrated neutron flux (in units of particles per area); A is the area of the sample exposed to the beam; η is the detection efficiency; B is the branching ratio (probability of emission per nuclear reaction); and the factor f takes any necessary corrections into account (e.g., for multiple neutron scattering in the sample, self-absorption of reaction products, and so forth). Depending on the experimental procedure, the yield may also need to be corrected for angular correlation effects (Appendix D). Multiple elastic scattering of neutrons may become a serious problem for thicker samples. Scattered neutrons have a higher chance of undergoing a reaction than the incident neutrons because of an increase in the average path length in the sample. The situation becomes even more complex when the total and the reaction cross section exhibit a narrow resonance structure. In this case, incident neutrons with energies somewhat higher than the location of the narrow resonance are scattered and thereby lose a fraction of their energy. These scattered neutrons may then undergo reactions in the region of the resonance. Consequently, the measured reaction yield can become larger than the true reaction yield caused by the incident (unscattered) neutrons. Such effects can be corrected by using Monte Carlo procedures (Poenitz, 1984).

Examples of a yield curve and a transmission curve, both measured in the $^{144}\mathrm{Sm} + \mathrm{n}$ reaction, are shown in Figure 4.61. The data have been obtained with the time-of-flight technique (Section 4.6.3) using the Oak Ridge Electron Accelerator (ORELA). The neutron-capture data are fitted with Breit–Wigner expressions, while the transmission data are analyzed using the R-matrix method to account for the additional complication of potential scattering (Section 2.5). Necessary corrections caused by Doppler broadening, multiple scattering, and instrumental resolution were applied to both data sets. The shapes of the narrow resonance at the lowest energy are dominated by the instrumental resolution and by Doppler broadening, while the shapes of the broad resonances at higher energies are dominated by their total widths.

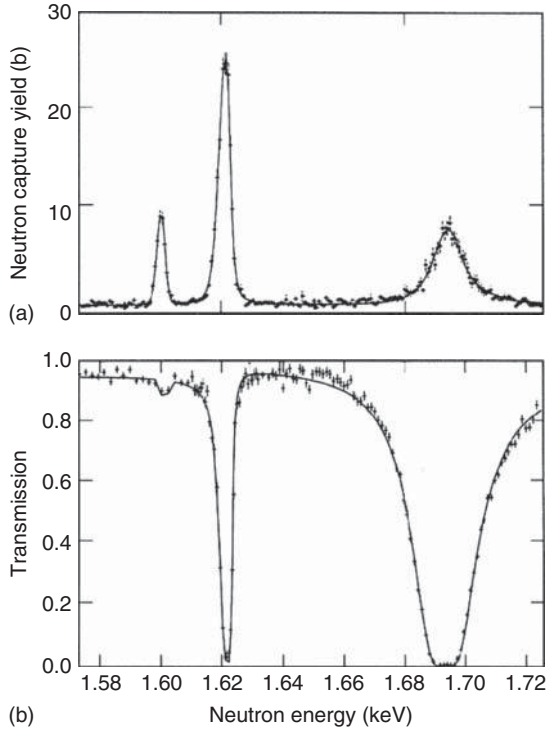

Figure 4.61 (a) Yield curve for the ^{144}Sm(n,γ)^{145}Sm reaction; (b) Transmission curve for ^{144}Sm + n. The data have been obtained with the time-of-flight technique (Section 4.6.3) using the Oak Ridge Electron Accelerator (ORELA). The neutron-capture data (top) are fitted with Breit–Wigner expressions, while the transmission data (bottom) are analyzed using the *R*-matrix method. (Reprinted with permission from R. L. Macklin et al., Phys. Rev. C, Vol. 48, p. 1120 (1993). Copyright (1993) by the American Physical Society.)

4.9.5
Relative and Absolute Cross Sections

We will first discuss the determination of an unknown cross section relative to a standard value. The activation method (Section 4.6.2) will be chosen as an example. The situation is shown in Figure 4.62a. A proton beam is incident on a Li target that is mounted on a water-cooled Cu backing. The irradiation sample is mounted close to a foil consisting of a material relative to which the neutron cross section is being measured (e.g., a gold foil). For the sake of simplicity, we will assume that the incident neutron flux is constant, $\phi(t) = \text{const}$ (see Beer and Käppeler (1980) for a time-dependent flux). After the irradiation period is over, at $t = t_0$, the samples are moved to an off-line detection system for counting the delayed activity between t_1 and t_2 (Figure 4.62b).

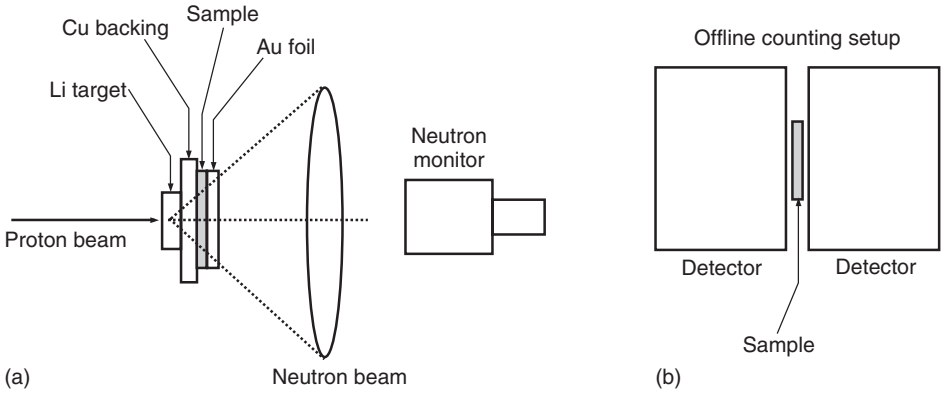

Figure 4.62 Example for the measurement of a neutron cross section using the activation technique (Section 4.6.2). (a) A proton beam is incident on a Li target that is mounted on a water-cooled Cu backing. The irradiation sample is mounted close to a foil consisting of a material (gold foil) relative to which the neutron cross section is measured. (b) After the irradiation period, the samples are moved to an offline detector system for counting the delayed activity.

The number of disintegrations between t_1 and t_2, $D(t_1, t_2)$, is related to the net number of counts, C, in the region of interest in the offline pulse height spectrum by

$$D(t_1, t_2) = \frac{C}{\eta B f} \tag{4.157}$$

with η and B the detection efficiency and the branching ratio of a particular transition, respectively; the factor f takes any necessary corrections into account (self-absorption of γ-rays in the sample, multiple elastic scattering of neutrons, and so on). Using Eqs. (4.76) and (4.157) and solving for the effective cross section gives

$$\hat{\sigma} = \frac{C\lambda}{\eta B f \phi \mathcal{N} \left(e^{\lambda t_0} - 1\right)\left(e^{-\lambda t_1} - e^{-\lambda t_2}\right)} \tag{4.158}$$

where λ denotes the decay constant of the residual radioactive nuclei and $\mathcal{N}$ is the number of sample nuclei. The ratio of effective cross sections for the sample of interest, i, and the standard material, s, is then

$$\frac{\hat{\sigma}_i}{\hat{\sigma}_s} = \frac{C_i \lambda_i \eta_s B_s f_s \mathcal{N}_s \left(e^{\lambda_s t_0} - 1\right)\left(e^{-\lambda_s t_1} - e^{-\lambda_s t_2}\right)}{C_s \lambda_s \eta_i B_i f_i \mathcal{N}_i \left(e^{\lambda_i t_0} - 1\right)\left(e^{-\lambda_i t_1} - e^{-\lambda_i t_2}\right)} \tag{4.159}$$

The relative determination of an effective cross section according to Eq. (4.159) has the advantage that the total neutron flux, $\phi(t) = \Phi/t_0 = \text{const}$, cancels if the sample of interest and the standard sample are irradiated simultaneously (corrections are necessary for a time-dependent flux). Furthermore, only *relative* detection efficiencies are required if the sample of interest and the standard sample are measured with the same experimental setup. However, the number of nuclei in the

two samples, $\mathcal{N}_i$ and $\mathcal{N}_s$, have to be determined carefully. The number of sample nuclei is given by (see Eq. (1.14))

$$\mathcal{N} = \frac{m_{\text{sample}} N_A}{M} X \tag{4.160}$$

with m_{sample} and M the mass and relative mass of the sample, respectively. If the sample consists of a compound, then m_{sample}, M, and the mass fraction X refer to the active sample nuclei, that is, the nuclei participating in the reaction of interest. Masses of self-supporting samples are frequently determined by weighing, whereas masses of deposited samples can be found from the weight difference between the backing and the combined sample-plus-backing. For compounds or samples consisting of more than one isotope, a chemical or isotopic analysis is required to obtain the number of nuclei $\mathcal{N}$ (Wagemans, 1989).

The ^{197}Au(n,γ)^{198}Au capture reaction provides one of the most widely used absolute cross section standards in the kilo electron volt neutron energy range, that is, the region of astrophysical interest. We will describe in the following a method for determining this cross section standard by using the activation method. For more information, see Ratynski and Käppeler (1988). Suppose that in Figure 4.62 a proton beam of $E_{\text{p}} = 1912$ keV energy is incident on a thick Li target that is mounted on a water-cooled Cu backing. As pointed out previously (Section 4.1.2), under such circumstances the neutron energy distribution closely resembles a Maxwell–Boltzmann distribution at $kT = 25$ keV (Figure 4.2) and all the neutrons are kinematically focused in the forward direction into a cone with an opening angle of 120°. A gold sample covers the entire solid angle of the neutron emission cone. It consists of a homogeneous spherical segment instead of a flat foil, so that the sample appears equally thick for all neutrons passing through it. The number of Au nuclei is determined by carefully measuring the weight and the thickness of the sample. The half-life of ^{198}Au amounts to $T_{1/2} = 2.6$ d and the decay produces a γ-ray of 412 keV energy. We will again assume for simplicity that the neutron flux is constant, that is, $\phi(t) = \text{const}$. According to Eqs. (4.76) and (4.157), we find for the total number of disintegrations during the measuring interval between t_1 and t_2

$$\begin{aligned} D_{\text{Au}}(t_1, t_2) &= \frac{C_{\text{Au}}}{(\eta B f)_{\text{Au}}} \\ &= \frac{(\mathcal{N}_{\text{Au}}/A)\hat{\sigma}_{\text{Au}} \mathcal{N}_\nu(t_0)}{\lambda_{\text{Au}} t_0} \left(e^{\lambda_{\text{Au}} t_0} - 1\right) \left(e^{-\lambda_{\text{Au}} t_1^{\text{Au}}} - e^{-\lambda_{\text{Au}} t_2^{\text{Au}}}\right) \end{aligned} \tag{4.161}$$

where we used $\phi = \Phi/t_0 = \mathcal{N}_\nu(t_0)/(A t_0)$. The quantity $\mathcal{N}_\nu(t_0)$ is the total number of incident neutrons after irradiation time t_0 and A denotes the area covered by the sample.

Since the ^{7}Li(p,n)^{7}Be reaction is used as a source of neutrons, one ^{7}Be nucleus ($T_{1/2} = 53$ d) is produced for each emitted neutron. Hence, the total number of neutrons emitted from the Li target, and that are incident on the Au foil, can be deduced by measuring the 478 keV γ-rays emitted by the radioactive decay of ^{7}Be in the Li target. The proton energy loss in the Li production target amounts to

about 100 keV. Therefore, the production rate of ^{7}Be is given by Eq. (4.112) rather than Eq. (4.73). We will simply assume that the incident proton current, and hence the production rate of ^{7}Be, is constant. The total number of neutrons, or the total number of ^{7}Be nuclei, produced after a time t_0 is then given by $\mathcal{N}_{\rm Be}(t_0) = \mathcal{N}_\nu(t_0) = P_{\rm Be} t_0$. For the number of disintegrations during a measuring interval between t_1 and t_2, we obtain from Eqs. (4.76) and (4.157)

$$D_{\rm Be}(t_1, t_2) = \frac{C_{\rm Be}}{(\eta B f)_{\rm Be}} = \frac{P_{\rm Be}}{\lambda_{\rm Be}} \left(e^{\lambda_{\rm Be} t_0} - 1\right) \left(e^{-\lambda_{\rm Be} t_1^{\rm Be}} - e^{-\lambda_{\rm Be} t_2^{\rm Be}}\right)$$
$$= \frac{\mathcal{N}_\nu(t_0)}{\lambda_{\rm Be} t_0} \left(e^{\lambda_{\rm Be} t_0} - 1\right) \left(e^{-\lambda_{\rm Be} t_1^{\rm Be}} - e^{-\lambda_{\rm Be} t_2^{\rm Be}}\right) \tag{4.162}$$

From Eqs. (4.161) and (4.162), one finds for the ^{197}Au(n,γ)^{198}Au cross section

$$\hat{\sigma}_{\rm Au} = \frac{1}{(\mathcal{N}_{\rm Au}/A)} \frac{C_{\rm Au}(\eta B f)_{\rm Be} \lambda_{\rm Au}}{C_{\rm Be}(\eta B f)_{\rm Au} \lambda_{\rm Be}} \frac{\left(e^{\lambda_{\rm Be} t_0} - 1\right) \left(e^{-\lambda_{\rm Be} t_1^{\rm Be}} - e^{-\lambda_{\rm Be} t_2^{\rm Be}}\right)}{\left(e^{\lambda_{\rm Au} t_0} - 1\right) \left(e^{-\lambda_{\rm Au} t_1^{\rm Au}} - e^{-\lambda_{\rm Au} t_2^{\rm Au}}\right)} \tag{4.163}$$

In this expression, the number of neutrons cancels and only relative detection efficiencies are needed if the same setup is used for counting the delayed activities of ^{198}Au and ^{7}Be. The measured average cross section amounts to $\hat{\sigma}_{^{197}{\rm Au(n,\gamma)}^{198}{\rm Au}} = 586 \pm 8$ mb (Ratynski and Käppeler, 1988) and corresponds to a (quasi-)Maxwellian neutron energy distribution at $kT = 25$ keV. The error represents an uncertainty of only 1.4%. This standard has been used for the determination of a large number of astrophysically important neutron-capture cross sections. Other standard cross sections are provided by the ^{6}Li(n,α)^{3}H, ^{10}B(n,α)^{7}Li, and ^{10}B(n,$\alpha\gamma$)^{7}Li reactions. More information can be found in Bao *et al.* (2000).

Problems

4.1 The energy loss of charged particles is calculated in Example 4.1 using the *thin-absorber approximation*, that is, by assuming that the stopping power is approximately constant over the absorber thickness. If the stopping power is not constant, the energy loss can always be obtained from a numerical integration of Eq. (4.12). If a graph of range versus energy is available, however, a simpler method can be used by expressing Eq. (4.12) in terms of ranges. Explain this method and use it to estimate from Figure 4.7 the energy loss of a 10 MeV cosmic-ray proton incident on a 400 μm thick silicon detector.

4.2 Derive Eq. (4.18) from the expressions for energy and linear momentum conservation (see Eqs. (C.1)–(C.3)) in the elastic scattering of an incident particle on an electron at rest. Assume a head-on collision for maximum energy transfer.

4.3 Calculate the attenuation of 0.5 MeV and 5 MeV γ-rays in (i) a tantalum absorber ($\rho_{\rm Ta} = 16.7$ g/cm^3) of 0.5 mm thickness, and (ii) a lead

absorber ($\rho_{Pb} = 11.4\,g/cm^3$) of 1.3 cm thickness. Assume the following numerical values for the mass attenuation coefficients: $(\mu/\rho)_{Ta,0.5\,MeV} = 0.13\,cm^2/g$, $(\mu/\rho)_{Ta,5.0\,MeV} = 0.041\,cm^2/g$, $(\mu/\rho)_{Pb,0.5\,MeV} = 0.16\,cm^2/g$, $(\mu/\rho)_{Pb,5.0\,MeV} = 0.041\,cm^2/g$.

4.4 Estimate the thickness of water ($\rho = 1.0\,g/cm^3$) necessary to reduce the intensity of incident neutrons with an energy of 300 keV by a factor of 10^{10}. Assume for the total neutron cross section at this energy a value of 60 b.

4.5 Solve the equations for the total energy and linear momentum conservation in α-decay when the decaying nucleus is at rest. Apply the expressions to the α-decay of ^{241}Am and calculate the total energy release (or the *Q*-value) using the information given in the α-particle spectrum shown in Figure 4.18. Assume that the α-particle group with the largest kinetic energy populates the ground state of the daughter nucleus ^{237}Np and consider only this particular transition. What is the kinetic energy of the daughter nucleus?

4.6 Suppose that an excited nuclear level (2) decays to the ground state (0) via a two-γ-ray cascade through an intermediate state (1), that is, $B_{21} = B_{10} = 1$ and $B_{20} = 0$ (Figure 4.31). The energies of the photons are $E_{21} = 1$ MeV and $E_{10} = 2$ MeV. Their measured peak intensities are $\mathcal{N}_{21} = 357$ and $\mathcal{N}_{10} = 237$. The values for the peak and total efficiencies amount to $\eta_{21}^P = 0.043$, $\eta_{21}^T = 0.21$, $\eta_{10}^P = 0.030$, $\eta_{10}^T = 0.17$. (i) Calculate the total number $\mathcal{N}$ of decaying levels 2 with and without coincidence summing corrections. (ii) What do you expect for the intensity of the sum peak at 3 MeV?

4.7 Consider again Figure 4.50 and Eq. (4.82), which apply to the *total* NaI(Tl) efficiency. However, as explained in Section 4.7.3, the environmental background can be significantly reduced by gating on the energy in the NaI(Tl) pulse height spectrum. By introducing the quantity $f_{ij} \equiv \eta_{ij}^{NaI,G}/\eta_{ij}^{NaI,T}$, that is, the ratio of the *gated* to the *total* NaI(Tl) detection efficiencies, find the term by which Eq. (4.82) has to be corrected when a particular energy gate is selected in the two-dimensional histogram of E_γ^{Ge} versus E_γ^{NaI}.

4.8 A gold sample with a mass of 10 g is irradiated with a thermal neutron flux of $10^{14}\,cm^{-2}\,s^{-1}$. The cross section for the ^{197}Au(n,γ)^{198}Au reaction amounts to 99 b and the half-life of ^{198}Au is $T_{1/2} = 2.7$ d. (i) Calculate the saturation value for the number of radioactive ^{198}Au nuclei. (ii) What is the irradiation time necessary until the number of ^{198}Au nuclei achieves 90% of the saturation value?

4.9 Consider a measurement of the ^{21}Na + p → ^{22}Mg + γ radiative capture reaction in inverse kinematics, that is, by bombarding a stationary hydrogen target with radioactive ^{21}Na nuclei. The *Q*-value amounts to $Q = 5504.2$ keV. Suppose that the reaction excites the astrophysically important resonance at $E_r^{cm} = 206.8$ keV. Calculate for the γ-ray transition to the ground state (branching ratio of 14%): (i) the laboratory bombarding energy, disregarding any energy losses in the target; (ii) the energy of the photon emitted at a laboratory angle of $\theta = 0°$. What are the magnitudes of the full Doppler and recoil energy shifts? Neglect any energy losses of the

^{22}Mg recoil nuclei in the target; (iii) the maximum laboratory angle ϕ_{max} of the ^{22}Mg recoil emission direction. Use the following values for the masses: $M(^{1}\mathrm{H}) = 1.0078250$ u, $M(^{21}\mathrm{Na}) = 20.9976546$ u, $M(^{22}\mathrm{Mg}) = 21.9995706$ u (Mukherjee *et al.*, 2004).

4.10 Calculate the number of p(p,e$^{+}\nu$)d reactions that occur if a pure hydrogen target with a thickness of 10^{20} protons/cm^2 is bombarded with a proton beam of 1 MeV laboratory energy and 1 A intensity. The S-factor is given by Eq. (5.4).

4.11 An α-particle beam of 15 MeV bombarding energy and 1 μA intensity is incident on a 1 μm thick, pure ^{12}C target ($\rho = 1.9$ g/cm^3) for a duration of one hour. Each incident α-particle has a charge of 2+ ($^{4}\mathrm{He}^{2+}$). Neutrons are produced via the $^{12}\mathrm{C}(\alpha,\mathrm{n})^{15}\mathrm{O}$ reaction. The cross section at this bombarding energy amounts to 25 mb. A neutron detector has an efficiency of 1%. Assume that both the cross section and the stopping power are constant over the target thickness. How many neutrons are detected?

5
Nuclear Burning Stages and Processes

In the previous sections, we considered the thermonuclear rate of individual nuclear reactions and the relationship of forward and reverse reactions. In general, however, different nuclear processes take place simultaneously in the stellar plasma. Nuclides that are created by some fusion reactions are destroyed by other reactions. Thus, when discussing stellar nucleosynthesis, it is more appropriate to consider a network of nuclides linked by different, and frequently competing, nuclear processes. In this chapter, we will discuss the interplay of nuclear processes in the stellar plasma.

It was pointed out in Section 1.4.3 that nuclear reactions give rise to the necessary internal pressure preventing stars from collapsing gravitationally. All stable stars maintain a hydrostatic equilibrium between the internal pressure and the force of gravity. We showed earlier (Figure 3.15) that, for a given temperature and composition of the stellar plasma, those reactions with the smallest Coulomb barriers will proceed most rapidly and will account for most of the nuclear energy generation. Consequently, we expect nuclear reactions involving hydrogen and helium to be the main energy sources in most stars. It is tempting to consider the simplest processes among these nuclides, for example, $p + p \rightarrow {}^{2}He$, $p + {}^{4}He \rightarrow {}^{5}Li$, and ${}^{4}He + {}^{4}He \rightarrow {}^{8}Be$, as the most likely nuclear reactions. However, the newly created ${}^{2}He$, ${}^{5}Li$, and ${}^{8}Be$ nuclei are unstable and decay back into the entrance channel after very short time periods. Therefore, we have to consider more complicated processes.

Thermonuclear reactions change the composition of the stellar gas. When the nuclei with the smallest nuclear charges have been consumed, a star will contract under the influence of gravity. The temperature steadily increases until nuclei with the next lowest Coulomb barriers, which were previously inactive, are consumed. The nuclear energy produced by the burning of the new fuel stabilizes the star against further contraction. Depending on its total mass, a star may experience several of these nuclear burning stages, referred to as *hydrogen burning, helium burning, carbon burning, neon burning, oxygen burning*, and *silicon burning* (Section 1.4.3). When the ignition of the new fuel gives rise to an advanced burning stage in the stellar core, the previous burning stage does not completely disappear, but continues in a shell surrounding the core. We will discuss the nuclear physics aspects of these stages in detail in the next sections.

Nuclear Physics of Stars, Second Edition. Christian Iliadis.

The advanced burning stages, carbon through silicon burning, will be described with the aid of reaction network calculations performed at constant temperature–density conditions representative of the hydrostatic core burning stages for a solar-metallicity star with an initial mass of $M = 25\,M_{\odot}$. Stars of this mass have been shown to produce elemental abundances similar to observed solar system abundances.

The different nuclear burning stages have a profound influence on the structure and evolution of the star. The temperature–density evolution for the center of a star with solar initial composition and an initial mass of $M = 25\,M_{\odot}$ is shown in Figure 5.1a. The circles indicate the T–ρ conditions representative of a particular burning stage in the core. Most of the burning occurs near the location of the circles, where the star spends most of its time during a particular burning stage. It can be seen that the temperature and density vary by about two and eight orders of magnitude, respectively, between hydrogen and silicon burning.

Hydrogen burning releases far more energy per unit fuel consumed ($\approx 6 \times 10^{24}$ MeV/g or $\approx 10^{19}$ erg/g) compared to helium burning ($\approx 6 \times 10^{23}$ MeV/g or $\approx 10^{18}$ erg/g) or more advanced burning stages ($\approx 3 \times 10^{23}$ MeV/g or $\approx 5 \times 10^{17}$ erg/g for carbon and oxygen burning). Thus, a star will consume its hydrogen fuel more slowly than other fuel to balance both gravity and the energy radiated from its surface. There is also a fundamental difference in how the nuclear energy generated in the stellar interior is transformed and radiated from the surface. For hydrogen and helium burning, nuclear energy is almost exclusively converted to light. When the temperature exceeds $T = 0.5$ GK during later burning stages, the thermonuclear energy released is almost entirely radiated as neutrino–antineutrino pairs, produced via electron–positron pair annihilation ($e^- + e^+ \rightarrow \nu + \overline{\nu}$) or the photo-neutrino process ($e^- + \gamma \rightarrow e^- + \nu + \overline{\nu}$), and the light radiated from the star's surface represents only a very small fraction of the total energy release. Neutrino energy losses rise strongly with temperature (Clayton, 1983). Since the temperature increases from one advanced burning stage to the next (Figure 5.1a), the fuel consumption rapidly accelerates during carbon, neon, oxygen, and silicon burning. This can be seen in Figure 5.1b, showing the duration of various burning stages in the stellar core versus initial stellar mass for solar metallicity models. For example, silicon burning in the core of a $25\,M_{\odot}$ star lasts only for one day. The advanced burning stages in the stellar core proceed so quickly that the stellar surface cannot keep pace with the evolution of the interior. Frequently, the appearance of the massive star – luminosity and effective emission temperature – does not change until the end of hydrostatic silicon burning. It also follows from these considerations that hydrogen burning lasts longer than helium burning or any of the advanced burning stages. Thus, perhaps as many as 90% of the observed stars are burning hydrogen. In other words, the probability of observing stars in their advanced stages of evolution is very small. Although most of a star's life is spent in the hydrogen burning stage, it is the later burning stages that account for the synthesis of the majority of heavy elements in the $A = 16$–64 mass range.

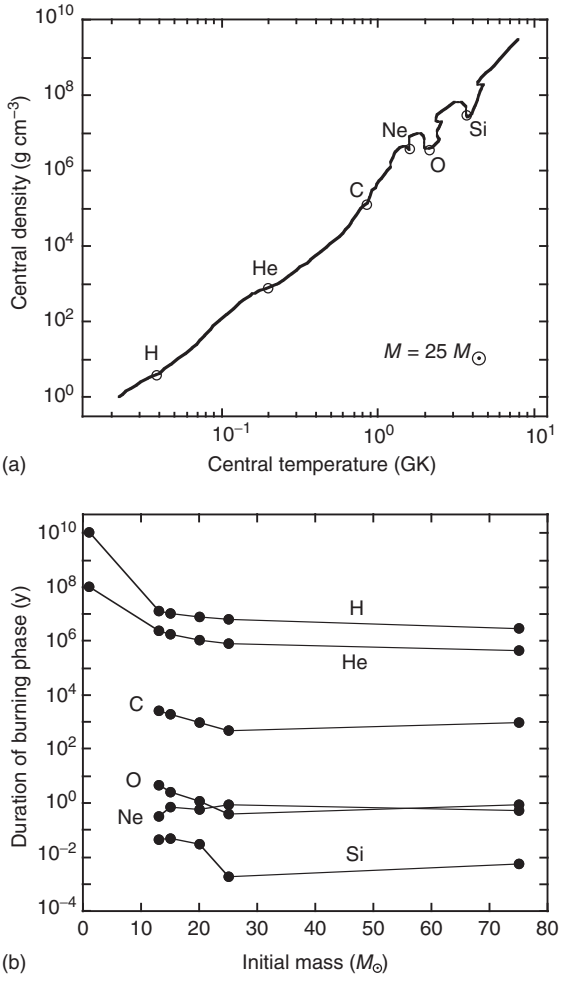

Figure 5.1 (a) Central temperature–density evolution of a $M = 25\ M_{\odot}$ star with solar initial composition. The circles indicate conditions that are representative of a particular hydrostatic burning stage in the stellar core. (b) Durations of various hydrostatic burning stages in the stellar core versus initial stellar mass for solar metallicity models. Data adopted from Woosley, Heger, and Weaver (2002).

The synthesis of the heavier nuclides ($A > 60$) requires a drastically different mechanism. Their observed abundances cannot be explained by charged-particle fusion reactions, since the transmission probability through the Coulomb barrier becomes negligibly small at these higher nuclear charges. Such nuclides are synthesized instead, unhindered by the Coulomb repulsion, via the capture of neutrons. Two distinct neutron capture processes, the s-process and the r-process, will also be discussed. A subsequent section describes the synthesis of

those heavy nuclides (p-nuclides) that cannot be accounted for by neutron capture processes.

Toward the end of this chapter, two non-stellar nucleosynthesis processes will be discussed. The first covers the nucleosynthesis in the early universe, and the second addresses cosmic-ray nucleosynthesis. The last section summarizes information on the origin of the solar system nuclides.

Many of the reaction rates used here are adopted from published evaluations (Angulo *et al.*, 1999; Iliadis *et al.*, 2001; Sallaska *et al.*, 2013). They are based on currently available experimental information (cross sections, resonance energies and strengths, excitation energies, spectroscopic factors). These evaluations do not only present reaction rates versus stellar temperature, but also report *uncertainties* for each individual rate. Reaction rate uncertainties may strongly influence stellar model predictions and, therefore, significant experimental efforts are underway to improve the accuracy of many important reaction rates. An investigation of how reaction rate uncertainties influence predictions of isotopic abundances or energy generation is beyond the scope of this book (see, e.g., Bahcall *et al.*, 1982; The *et al.*, 1998; Hoffman, Woosley, and Weaver, 2001; Iliadis *et al.*, 2002; Jordan, Gupta, and Meyer, 2003). Unless noted otherwise, we are not concerned here with reaction rate uncertainties, but will use the latest published *recommended* reaction rates to illustrate how the different burning stages influence the nucleosynthesis and the nuclear energy generation. Values for masses, Q-values, and particle separation energies used in this chapter are adopted from Wang *et al.* (2012). Reaction rates, stellar enhancement factors, and normalized partition functions derived from the Hauser–Feshbach statistical model are adopted from Rauscher and Thielemann (2000), unless noted otherwise.

Many different nuclear processes take part in the nucleosynthesis, especially during the advanced and explosive burning stages. In those situations, we will visualize the nucleosynthesis paths by introducing the *time-integrated net abundance flow* between two specific nuclides i and j,

$$F_{ij} = \int f_{ij}\, dt = \int \left[\left(\frac{dN_i}{dt} \right)_{i \to j} - \left(\frac{dN_j}{dt} \right)_{j \to i} \right] dt \tag{5.1}$$

where $(dN_i/dt)_{i \to j}$ is the partial rate of change of the number density N_i induced by all processes converting nucleus i to j (Section 3.1.3). For example, if we are interested in the nuclear activity caused by transformations between ^{24}Mg and ^{25}Al (Figure 3.4), then we only need to take into account the ^{24}Mg(p,γ)^{25}Al capture reaction and the (reverse) ^{25}Al(γ,p)^{24}Mg photodisintegration. Hence, the time-integrated net abundance flow is

$$F_{^{24}Mg^{25}Al} = \int \left[\left(\frac{d^{24}\mathrm{Mg}}{dt} \right)_{^{24}\mathrm{Mg(p,}\gamma\mathrm{)}} - \left(\frac{d^{25}\mathrm{Al}}{dt} \right)_{^{25}\mathrm{Al}(\gamma\mathrm{,p})} \right] dt \tag{5.2}$$

Large values of F_{ij} indicate an enhanced nuclear activity between two species, thereby helping to identify important links. It is advantageous to express Eqs. (5.1) and (5.2) in terms of mole fractions, $Y_i = N_i/(\rho N_A)$, rather than number densities, N_i, if the density ρ changes during the nucleosynthesis. Variations in Y_i (or X_i) are independent of density and reflect only nuclear transformations, as pointed out in Section 1.5.4. We will mostly consider net abundance flows that are integrated over the entire duration of the network calculation. Such flows represent gross properties of the nucleosynthesis, but do not reveal details at any particular instant of time. Nevertheless, they are very useful for providing an overview of the nucleosynthesis.

5.1 Hydrostatic Hydrogen Burning

Hydrogen is the most abundant isotope in the universe. The fusion of four ^{1}H nuclei to the tightly bound ^{4}He nucleus is called *hydrogen burning*. Independent of the details of this transformation, the process releases an energy (Section 1.5.3) of

$$\begin{aligned} Q &= 4(\text{M.E.})_{\text{H}} - (\text{M.E.})_{^4\text{He}} = 4 \cdot (7288.97\,\text{keV}) - (2424.92\,\text{keV}) \\ &= 26.731\,\text{MeV} \end{aligned} \tag{5.3}$$

But precisely how does this fusion process takes place? Early estimates showed that the probability for the simultaneous interaction of four protons in the stellar plasma is far too small to account for the observed luminosity of stars. Instead, sequences of interactions involving two particles in the entrance channel are considerably more likely to occur. The two principal mechanisms whereby hydrogen is converted to helium in hydrostatic hydrogen burning are called the *proton–proton chains* and the *CNO cycles*. These processes were first suggested more than 70 years ago (Atkinson, 1936; Bethe and Critchfield, 1938; von Weizsäcker, 1938; Bethe, 1939) and will be described in this section. It is useful for the following discussion to keep in mind that, depending on the stellar mass and metallicity, typical temperatures in core hydrogen burning are in the range of $T \approx 8$–55 MK, while the hydrogen burning shells in AGB stars achieve temperatures of $T \approx 45$–100 MK. The central temperature of the Sun, for example, is $T = 15.6$ MK (Bahcall, 1989). On the other hand, far higher temperatures are attained in explosive hydrogen burning, which will be discussed in later sections. As we shall see, the details of the nuclear processes depend sensitively on the stellar temperature.

5.1.1 pp Chains

The following three sequences of nuclear processes are referred to as *proton–proton (*or *pp) chains*:

pp1 chain	pp2 chain	pp3 chain
$p(p,e^+\nu)d$	$p(p,e^+\nu)d$	$p(p,e^+\nu)d$
$d(p,\gamma)^3He$	$d(p,\gamma)^3He$	$d(p,\gamma)^3He$
$^3He(^3He,2p)\alpha$	$^3He(\alpha,\gamma)^7Be$	$^3He(\alpha,\gamma)^7Be$
	$^7Be(e^-,\nu)^7Li$	$^7Be(p,\gamma)^8B$
	$^7Li(p,\alpha)\alpha$	$^8B(\beta^+\nu)^8Be$
		$^8Be(\alpha)\alpha$

$T_{1/2}$: ^{8}B (770 ms)

The different pp chains are also displayed in Figure 5.2. Each of these chains starts with hydrogen and converts four protons to one ^{4}He nucleus (or α-particle). The first two reactions are the same for each chain. Other nuclear reactions involving the light nuclides ^{1}H, ^{2}H, ^{3}He, and so on, are less likely to occur in stars (Parker, Bahcall, and Fowler, 1964).

The p(p,$e^+\nu$)d reaction

The first reaction of each pp chain, $^1H + {}^1H \rightarrow {}^2H + e^+ + \nu$, fuses two protons to one deuterium nucleus. The reaction releases an energy of $Q = 1.442$ MeV, including the annihilation energy of the positron with another electron from the environment (Example 1.3). The $p(p,e^+\nu)d$ reaction represents a special case since it converts a proton into a neutron, a process that closely resembles a β-decay. Thus, unlike almost all other stellar fusion reactions that are governed exclusively by the strong nuclear force and the Coulomb force, the $p(p,e^+\nu)d$ reaction is influenced by the weak nuclear force as well. Since this process involves two charged particles in the entrance channel, the overall energy dependence of the cross section is mainly determined by the transmission through the Coulomb barrier. The absolute magnitude of the cross section, however, is relatively small because of the influence of the weak nuclear force. A calculation of the $p(p,e^+\nu)d$ cross section is presented, for example, in Bahcall and May (1969) and is not repeated here. The theoretical *S*-factor varies smoothly with energy and is given by (Angulo *et al.*, 1999)

$$S(E) = 3.94 \times 10^{-25} + 4.61 \times 10^{-24} E + 2.96 \times 10^{-23} E^2 \qquad \text{(MeV b)} \qquad (5.4)$$

For example, at a center-of-mass energy of 0.5 MeV (corresponding to a laboratory proton bombarding energy of 1 MeV) the above *S*-factor translates into a cross section of about $\sigma_{pp} = 8 \times 10^{-48}$ cm^2. With this cross section, a 1 MeV proton beam of 1 A intensity (6.3×10^{18} protons/s) incident on a dense proton target (10^{20} protons/cm^2) will produce a single p + p reaction in about 6 years (Problem 4.10). Such a small event rate seems immeasurably small in the forseeable future and, therefore, the *S*-factor is based entirely on theory. Nevertheless, the different factors that determine the *S*-factor can be calculated with confidence. The quoted reaction rate errors (Angulo *et al.*, 1999) amount to only a few percent

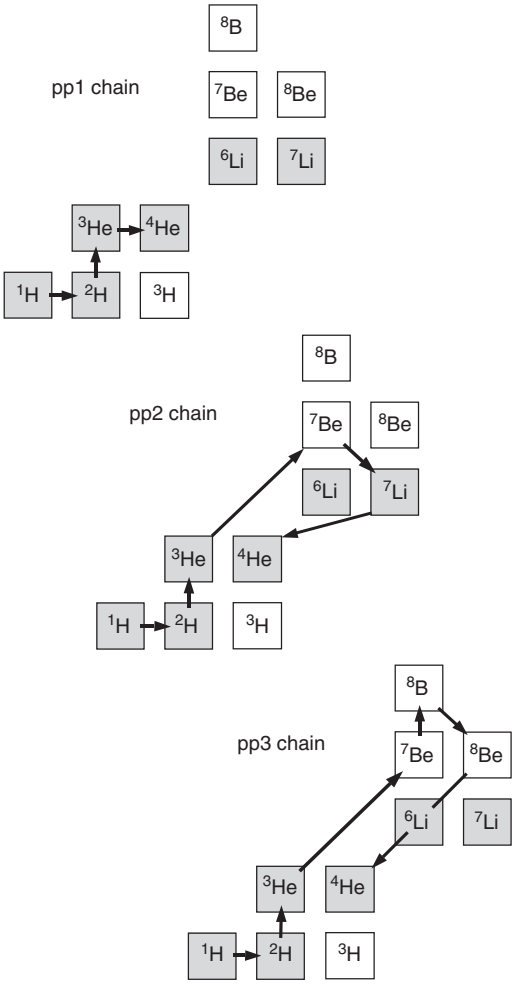

Figure 5.2 Representation of the pp chains in the chart of the nuclides. Each arrow represents a specific nuclear interaction connecting the initial with the final nucleus. For example, the reaction ^{3}He(α,γ)^{7}Be is represented by an arrow extending from ^{3}He to ^{7}Be (middle and bottom panel). Each of the pp chains effectively fuses four protons to one ^{4}He nucleus. Stable nuclides are shown as shaded squares.

and are significantly smaller than the rate errors of most measured stellar fusion reactions.

The energy of 1.442 MeV released in the p + p reaction is shared among the reaction products. The neutrino, however, has a large probability for escaping from the star and, hence, its energy is carried away and is not converted into heat. From the detailed shape of the neutrino energy spectrum, one obtains an average neutrino energy of about 265 keV (Bahcall, 1989). The nuclear energy available from this reaction for conversion into heat is then $1442\,\mathrm{keV} - 265\,\mathrm{keV} = 1177\,\mathrm{keV}$.

Alternative processes to the p(p,$e^+\nu$)d reaction have been proposed. For example, the reaction $^1H + {}^1H + e^- \rightarrow {}^2H + \nu$, referred to as the *pep reaction*, also fuses two hydrogen nuclei to one deuterium nucleus. Calculations have shown that this process can compete with p(p,$e^+\nu$)d only at stellar densities in excess of 10^4 g/cm^3 (Bahcall and May, 1969). Therefore, the pep reaction plays no significant role in hydrostatic hydrogen burning. However, it may contribute to the energy production in the early stages of explosive hydrogen burning (Section 5.5.2).

The d(p,γ)^{3}He Reaction

The deuterium produced in the p(p,$e^+\nu$)d reaction can, in principle, be destroyed by a number of different interactions. The d(p,γ)^{3}He reaction is by far the most important among these. Other reactions, such as d + d → p + t or d + d → n + ^{3}He, may have higher cross sections. However, recall that the reaction rate does not only depend on the cross section, but also on the abundances of the interacting nuclei (see Eq. (3.6)). Since there are far more protons available compared to the few deuterium nuclei produced by the very slow p + p reaction, the d + p interaction is far more likely to occur compared to the d + d interaction.

The d(p,γ)^{3}He reaction ($Q = 5.493$ MeV) has been measured at center-of-mass energies above $E_{cm} \approx 10$ keV. For the calculation of the reaction rates at all temperatures of practical interest, the data can be extrapolated to zero energy by using, for example, the direct capture model of nuclear reactions. The S-factor is given by (Angulo *et al.*, 1999)

$$S(E) = 0.20 \times 10^{-6} + 5.60 \times 10^{-6} E + 3.10 \times 10^{-6} E^2 \qquad \text{(MeV b)} \qquad (5.5)$$

This reaction depends only on the electromagnetic and the strong nuclear force. As a result, the S-factor and the reaction rate are many orders of magnitude larger compared to the p + p reaction. Reaction rate uncertainties amount to about 30–40%. Such errors are typical for many stellar fusion reactions.

pp1 Chain

The ^{3}He nuclei created by the two processes discussed above can, in principle, fuse with the abundant protons to form ^{4}He via the process $^3He + p \rightarrow \gamma + {}^4Li \rightarrow \gamma + {}^4He + e^+ + \nu$. However, the ^{4}Li nucleus is unstable, with a proton separation energy of about −2.5 MeV, and decays back to ^{3}He after a very short time period. It turns out that the ^{3}He(^{3}He,2p)^{4}He reaction is the most likely ^{3}He destroying process, and it completes the conversion of four protons to one ^{4}He nucleus in the pp1 chain. It is not so obvious to see why the ^{3}He(^{3}He,2p)^{4}He reaction is more important compared to another ^{3}He destroying reaction, ^{3}He(d,p)^{4}He, especially considering that both of these reactions have similar cross sections. This question will be addressed, among other issues, in this section. The S-factor of the ^{3}He(^{3}He,2p)^{4}He reaction is given by (Angulo *et al.*, 1999)

$$S(E) = 5.18 - 2.22\,E + 0.80\,E^2 \qquad \text{(MeV b)} \qquad (5.6)$$

Although this S-factor is larger compared to that of the d(p,γ)^{3}He reaction (see Eq. (5.5)), the ^{3}He(^{3}He,2p)^{4}He reaction rate per particle pair is actually smaller because of the larger value of the product Z_pZ_t, resulting in a considerably reduced transmission through the Coulomb barrier. This circumstance has an important consequence for the mean lifetimes of deuterium and ^{3}He in the stellar plasma, as will be shown below.

In the following, we will investigate how the ^{2}H and ^{3}He abundances evolve in the pp1 chain. The isotope ^{2}H is created by the p + p reaction and is destroyed via the d + p reaction, while ^{3}He is created by the d + p reaction and destroyed via the ^{3}He + ^{3}He reaction. Disregarding at first other reactions, we find by using Eqs. (3.20) and (3.26) for the time dependence of the ^{2}H and ^{3}He abundances the differential equations

$$\begin{aligned}\frac{dD}{dt} &= r_{\mathrm{pp}} - (1+\delta_{\mathrm{dp}})r_{\mathrm{dp}} = \frac{H^2\langle\sigma v\rangle_{\mathrm{pp}}}{(1+\delta_{\mathrm{pp}})} - (1+\delta_{\mathrm{dp}})\frac{HD\langle\sigma v\rangle_{\mathrm{dp}}}{(1+\delta_{\mathrm{dp}})} \\ &= \frac{H^2}{2}\langle\sigma v\rangle_{\mathrm{pp}} - HD\langle\sigma v\rangle_{\mathrm{dp}} \qquad (5.7)\\ \frac{d(^3He)}{dt} &= r_{\mathrm{dp}} - (1+\delta_{^3\mathrm{He}^3\mathrm{He}})r_{^3\mathrm{He}^3\mathrm{He}} \\ &= DH\langle\sigma v\rangle_{\mathrm{dp}} - (^3He)^2\langle\sigma v\rangle_{^3\mathrm{He}^3\mathrm{He}} \qquad (5.8)\end{aligned}$$

To avoid confusion, we use italic symbols H, D, and ^3He for the number densities of the isotopes ^{1}H (or p), ^{2}H (or d), and ^{3}He, respectively. Also, no Kronecker symbol occurs in front of the first term on the right-hand side of the above equations since a single p + p reaction or a single d + p reaction creates only one ^{2}H or ^{3}He nucleus, respectively.

We start with the abundance of ^{2}H. If no deuterium is initially present in the stellar plasma, the second term on the right-hand side of Eq. (5.7) is zero. With increasing time, the deuterium abundance builds up because of the p + p reaction. The more deuterium is created, the larger the second term describing the destruction of deuterium via the d + p reaction will become. Eventually, an equilibrium, $dD/dt = 0$, is established. Alternatively, if for some reason the initial deuterium abundance is very large, then the second term on the right-hand side of Eq. (5.7) will dominate the first term. With progressing time, the deuterium abundance will decrease and hence, the second term will become smaller. This continues until an equilibrium, $dD/dt = 0$, is established. The above equation has been called *self-regulating* (Clayton, 1983) since the deuterium abundance always seeks an equilibrium value. The equilibrium ratio $(D/H)_e$, obtained for the condition $dD/dt = 0$, is given by

$$\left(\frac{D}{H}\right)_e = \frac{\langle\sigma v\rangle_{\mathrm{pp}}}{2\langle\sigma v\rangle_{\mathrm{dp}}} = \frac{N_A\langle\sigma v\rangle_{\mathrm{pp}}}{2N_A\langle\sigma v\rangle_{\mathrm{dp}}} = \frac{\tau_{\mathrm{p}}(\mathrm{d})}{2\tau_{\mathrm{p}}(\mathrm{p})} \qquad (5.9)$$

The quantity $(D/H)_e$ is determined by the ratio of the p + p and d + p reaction rates and is shown in Figure 5.3a versus stellar temperature. It can be seen that the

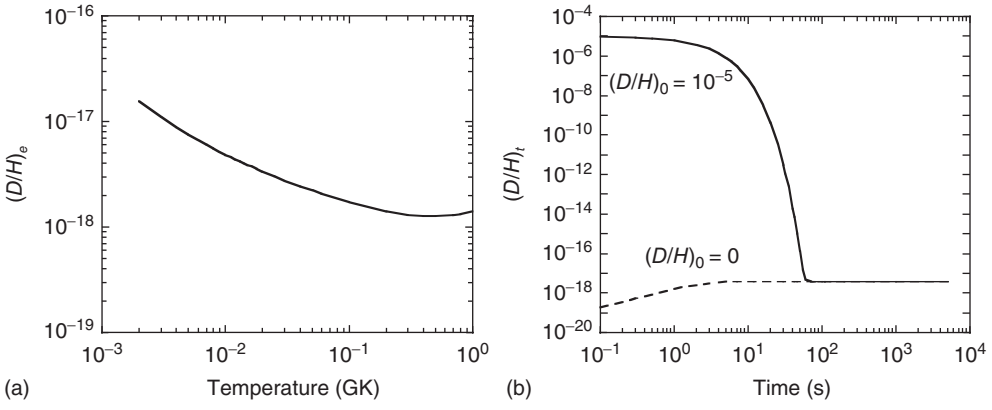

Figure 5.3 (a) Equilibrium abundance ratio $(D/H)_e$ versus stellar temperature. (b) Time evolution of the abundance ratio (D/H) for the conditions $T = 15$ MK, $\rho = 100$ g/cm^3, and $X_H = 0.5$. The dashed and solid lines are obtained for initial deuterium abundances of $(D/H)_0 = 0$ and $(D/H)_0 = 10^{-5}$, respectively. In either case, the deuterium abundance reaches equilibrium in a time negligible compared to the lifetime of stars.

$(D/H)_e$ value amounts to about $(D/H)_e \approx 10^{-18}$–10^{-17} over most of the relevant temperature range.

We can be more specific and ask how long it takes for the deuterium abundance to achieve equilibrium. It was shown above that the deuterium lifetime against destruction via the d + p reaction is very short compared to the hydrogen lifetime against destruction via that p + p reaction. Thus, the deuterium abundance will change more quickly compared to the hydrogen abundance. The difference in the respective lifetimes is so large that it is safe to assume that the deuterium abundance achieves equilibrium in a time too short for the hydrogen abundance to change significantly. With this approximation of a constant hydrogen abundance, Eq. (5.7) can be solved, and we obtain

$$\frac{d(D/H)}{dt} = \frac{H}{2}\langle\sigma v\rangle_{\rm pp} - H\left(\frac{D}{H}\right)\langle\sigma v\rangle_{\rm dp} \tag{5.10}$$

With the substitutions $x = (D/H)$, $a = (H/2)\langle\sigma v\rangle_{\rm pp}$, and $b = H\langle\sigma v\rangle_{\rm dp}$, we write

$$\frac{dx}{dt} = a - bx \tag{5.11}$$

With $y = a - bx$ and $dy/dx = -b$, we obtain, assuming $y = y_0$ at $t = 0$,

$$\frac{dy}{y} = -b\,dt \qquad \text{and} \qquad y = y_0 e^{-bt} \tag{5.12}$$

Thus, with Eqs. (3.23) and (5.9) one finds

$$H\langle\sigma v\rangle_{\rm dp}\left(\frac{D}{H}\right)_t = \frac{H}{2}\langle\sigma v\rangle_{\rm pp} - \left[\frac{H}{2}\langle\sigma v\rangle_{\rm pp} - H\langle\sigma v\rangle_{\rm dp}\left(\frac{D}{H}\right)_0\right] e^{-H\langle\sigma v\rangle_{\rm dp}t}$$

$$\left(\frac{D}{H}\right)_t = \left(\frac{D}{H}\right)_e - \left[\left(\frac{D}{H}\right)_e - \left(\frac{D}{H}\right)_0\right] e^{-t/\tau_{\rm p}({\rm d})} \tag{5.13}$$

The deuterium abundance approaches its equilibrium value exponentially with a $1/e$ time of τ_p(d). The time evolution of the quantity (D/H) for the conditions $T = 15$ MK, $\rho = 100$ g/cm^3, and $X_H = 0.5$ is shown in Figure 5.3b. The two lines are obtained for (i) a zero initial deuterium abundance, $(D/H)_0 = 0$, and (ii) a value of $(D/H)_0 = 10^{-5}$. The deuterium abundance reaches equilibrium in a time negligible compared to the lifetime of stars.

The very small deuterium-to-hydrogen ratio of $(D/H)_e = 10^{-18}$–10^{-17} that is established in the hydrogen burning cores of stars has interesting astrophysical implications. Any significant deuterium abundance that might be present when a star forms will be quickly depleted during the hydrogen burning stage. Since there are no other stellar sites that produce deuterium in significant amounts, deuterium is destroyed as the universe evolves and interstellar gas is cycled through generations of stars. Observations of the deuterium abundance in the universe will thus provide lower limits on the primordial deuterium abundance that was established before stellar formation took place. Observations indicate a primordial deuterium abundance of about $(D/H)_{prim} \approx 3 \times 10^{-5}$. It is commonly assumed that primordial deuterium was produced during the nucleosynthesis in the early universe and, therefore, the observed $(D/H)_{prim}$ value provides an important test of standard big bang nucleosynthesis (Section 5.7.1). Furthermore, if stars are born from interstellar matter with a (D/H) ratio on the order of 10^{-5}, then the deuterium abundance is sufficiently large for initiating the d(p,γ)^{3}He reaction already at relatively low temperatures during the stellar contraction phase, that is, before the hydrogen burning stage. Therefore, the d(p,γ)^{3}He reaction is the first thermonuclear energy source in some stars. This process is referred to as *deuterium burning* and will not only slow the contraction of the newly forming star, but may also provide an important source of ^{3}He in the young star.

We will next discuss the evolution of the ^{3}He abundance. Since the deuterium abundance achieves equilibrium in a negligible amount of time, Eq. (5.8) can be simplified using Eq. (5.9),

$$\frac{d(^3He)}{dt} = \frac{H^2}{2}\langle\sigma v\rangle_{pp} - (^3He)^2\langle\sigma v\rangle_{^3He^3He} \tag{5.14}$$

This expression is also self-regulating in the sense that the ^{3}He abundance will seek an equilibrium value. The equilibrium ratio $(^3He/H)_e$ is again obtained for the condition $d(^3He)/dt = 0$, with the result

$$\left(\frac{^3He}{H}\right)_e = \sqrt{\frac{\langle\sigma v\rangle_{pp}}{2\langle\sigma v\rangle_{^3He^3He}}} = \sqrt{\frac{N_A\langle\sigma v\rangle_{pp}}{2N_A\langle\sigma v\rangle_{^3He^3He}}} \tag{5.15}$$

The quantity $(^3He/H)_e$ is determined by the ratio of the p + p and ^{3}He + ^{3}He reaction rates and is shown in Figure 5.4a versus stellar temperature. Since the ^{3}He(^{3}He,2p)^{4}He reaction rate is smaller compared to the d(p,γ)^{3}He reaction rate, the ^{3}He abundance builds up to a larger value compared to the deuterium abundance to achieve equilibrium.

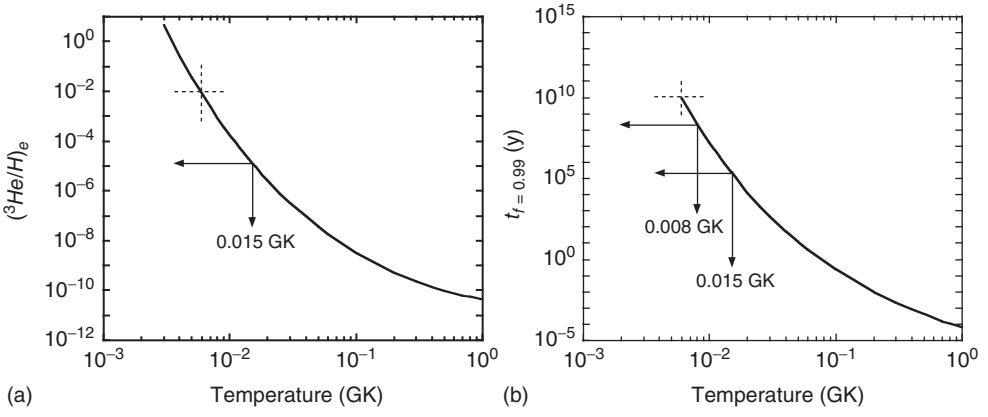

Figure 5.4 (a) Equilibrium abundance ratio $(^3He/H)_e$ versus stellar temperature. (b) Time required for ^{3}He to reach 99% of its equilibrium abundance versus temperature. The curve is calculated for the conditions $\rho = 100$ g/cm^3 and $X_H = 0.5$.

The time it takes for the ^{3}He abundance to achieve equilibrium can be calculated assuming that the hydrogen abundance stays nearly constant. It can be seen from Figure 5.4a that this is a reasonable assumption for temperatures above $T = 6$ MK where $(^3He/H)_e < 0.01$. With the approximation of a constant hydrogen abundance, Eq. (5.14) can be solved, and we obtain

$$\frac{d(^3He/H)}{dt} = \frac{H}{2}\langle\sigma v\rangle_{\rm pp} - H\left(\frac{^3He}{H}\right)^2 \langle\sigma v\rangle_{^3\rm He^3He} \tag{5.16}$$

Using the substitutions $x = (^3He/H)$, $a = (H/2)\langle\sigma v\rangle_{\rm pp}$, and $b = H\langle\sigma v\rangle_{^3\rm He^3He}$ we write

$$\frac{dx}{dt} = a - bx^2 \qquad \text{or} \qquad \frac{1}{a}\frac{dx}{dt} = 1 - \frac{b}{a}x^2 \tag{5.17}$$

From $y = x\sqrt{b/a}$ and $dy/dx = \sqrt{b/a}$, we obtain

$$\frac{dy}{1-y^2} = a\sqrt{\frac{b}{a}}\,dt \qquad \text{or} \qquad y = \tanh(t\sqrt{ab}) \tag{5.18}$$

assuming $y = 0$ at $t = 0$. From Eqs. (3.23) and (5.15), we find

$$\left(\frac{^3He}{H}\right)_t = \sqrt{\frac{\langle\sigma v\rangle_{\rm pp}}{2\langle\sigma v\rangle_{^3\rm He^3He}}}\tanh\left(t\sqrt{\frac{H}{2}\langle\sigma v\rangle_{\rm pp}H\langle\sigma v\rangle_{^3\rm He^3He}}\right)$$
$$= \left(\frac{^3He}{H}\right)_e \tanh\left(\frac{t}{[\tau_{^3\rm He}(^3He)]_e}\right) \tag{5.19}$$

We have explicitly assumed that the initial ^{3}He abundance is zero ($y = 0$ at $t = 0$). The quantity $[\tau_{^3\rm He}(^3He)]_e$ denotes the mean lifetime of ^{3}He against destruction via

the ^{3}He(^{3}He,2p)^{4}He reaction after ^{3}He has reached its equilibrium value. The time required for the ^{3}He abundance to achieve a fraction $f = (^3He/H)_t/(^3He/H)_e$ of its equilibrium abundance is obtained from

$$t_f = [\tau_{^3\mathrm{He}}(^3He)]_e \,\mathrm{arctanh}(f) = \frac{\mathrm{arctanh}(f)}{\rho \frac{X_\mathrm{H}}{M_\mathrm{H}} N_A \langle \sigma v \rangle_{^3\mathrm{He}^3\mathrm{He}} \left(\frac{^3He}{H}\right)_e} \tag{5.20}$$

This time is shown in Figure 5.4b at temperatures above $T = 6$ MK (where the hydrogen abundance is approximately constant) for the conditions $f = 0.99$, $\rho = 100$ g/cm^3, and $X_\mathrm{H} = 0.5$. It can be seen that the value of t_f exceeds 10^9 years below $T \approx 8$ MK and becomes comparable to the lifetime of some stars. For sufficiently small temperatures, the ^{3}He abundance will never reach equilibrium. For a temperature of $T = 15$ MK, on the other hand, the ^{3}He abundance increases gradually and reaches an equilibrium value of $(^3He/H)_e = 10^{-5}$ after about 10^6 years.

It is interesting to compare the mean lifetimes τ_p(p), τ_p(d), $\tau_\alpha(^3He)$, $[\tau_\mathrm{d}(\mathrm{d})]_e$, $[\tau_\mathrm{d}(^3He)]_e$, $[\tau_{^3\mathrm{He}}(\mathrm{d})]_e$, and $[\tau_{^3\mathrm{He}}(^3He)]_e$. The first three quantities are given by the usual relation (see Eq. (3.22)), while, for example, the fifth quantity denotes the mean lifetime of ^{3}He against destruction via the ^{3}He(d,p)^{4}He reaction *after the deuterium abundance has reached an equilibrium value*. From Eqs. (3.22), (5.9), and (5.15), we find

$$[\tau_\mathrm{d}(\mathrm{d})]_e = \left(\frac{N_A \langle \sigma v \rangle_\mathrm{pp}}{2 N_A \langle \sigma v \rangle_\mathrm{dp}} \rho \frac{X_\mathrm{H}}{M_\mathrm{H}} N_A \langle \sigma v \rangle_\mathrm{dd} \right)^{-1} \tag{5.21}$$

$$[\tau_\mathrm{d}(^3He)]_e = \left(\frac{N_A \langle \sigma v \rangle_\mathrm{pp}}{2 N_A \langle \sigma v \rangle_\mathrm{dp}} \rho \frac{X_\mathrm{H}}{M_\mathrm{H}} N_A \langle \sigma v \rangle_{^3\mathrm{He}\,\mathrm{d}} \right)^{-1} \tag{5.22}$$

$$[\tau_{^3\mathrm{He}}(\mathrm{d})]_e = \left(\sqrt{\frac{N_A \langle \sigma v \rangle_\mathrm{pp}}{2 N_A \langle \sigma v \rangle_{^3\mathrm{He}^3\mathrm{He}}}} \rho \frac{X_\mathrm{H}}{M_\mathrm{H}} N_A \langle \sigma v \rangle_{^3\mathrm{He}\,\mathrm{d}} \right)^{-1} \tag{5.23}$$

$$[\tau_{^3\mathrm{He}}(^3He)]_e = \left(\sqrt{\frac{N_A \langle \sigma v \rangle_\mathrm{pp}}{2 N_A \langle \sigma v \rangle_{^3\mathrm{He}^3\mathrm{He}}}} \rho \frac{X_\mathrm{H}}{M_\mathrm{H}} N_A \langle \sigma v \rangle_{^3\mathrm{He}^3\mathrm{He}} \right)^{-1} \tag{5.24}$$

The subscripts pp, dp, dd, ^{3}Hed, and ^{3}He^{3}He denote the reactions p(p,e$^+\nu$)d, d(p,γ)^{3}He, d(d,n)^{3}He, ^{3}He(d,p)^{4}He, and ^{3}He(^{3}He,2p)^{4}He, respectively. The mean lifetimes are calculated for the conditions $\rho = 100$ g/cm^3, $X_\mathrm{H} = X_\mathrm{He} = 0.5$, and are shown in Figure 5.5a. Several important points can be made. First, it can be seen that $\tau_\mathrm{p}(\mathrm{d}) \ll [\tau_{^3\mathrm{He}}(\mathrm{d})]_e \ll [\tau_\mathrm{d}(\mathrm{d})]_e$, and hence the assumption of Eq. (5.7), that deuterium is predominantly destroyed via the d(p,γ)^{3}He reaction, is justified. Second, we have $[\tau_{^3\mathrm{He}}(^3He)]_e \ll [\tau_d(^3He)]_e$ and thus ^{3}He is predominantly destroyed via the ^{3}He(^{3}He,2p)^{4}He reaction, while the ^{3}He(d,p)^{4}He reaction plays no significant role after ^{3}He has reached its equilibrium value. We suspect that the ^{3}He(d,p)^{4}He reaction is more likely to occur than the ^{3}He(^{3}He,2p)^{4}He reaction only before ^{3}He reaches equilibrium, when its abundance is still very small. Under such conditions, however, the production rate of ^{3}He via the two reactions p(p,e$^+\nu$)d and d(p,γ)^{3}He is far larger compared to the destruction rate

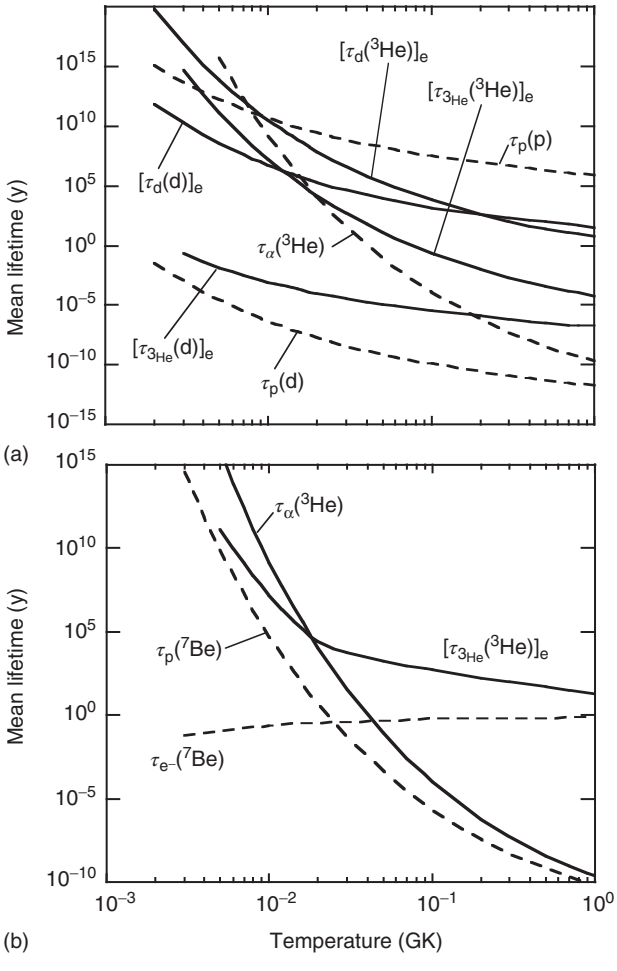

Figure 5.5 Mean lifetimes versus stellar temperature, calculated for the conditions $\rho = 100$ g/cm^3 and $X_H = X_{He} = 0.5$. In (a) the operation of only the pp1 chain is considered, while in (b) all three pp chains are assumed to operate simultaneously. For hydrostatic hydrogen burning, only temperatures below $T = 0.1$ GK are of interest.

and the latter can be neglected. Therefore, the assumption of Eq. (5.8) that ^{3}He is predominantly destroyed in the pp1 chain via the ^{3}He(^{3}He,2p)^{4}He reaction is justified.

The energy production rate in the pp1 chain can be expressed as a sum of two parts. The first step involves the p(p,e$^+\nu$)d and d(p,γ)^{3}He reactions. Their cumulative effect is to convert three protons to one ^{3}He nucleus at a rate that is given by the very slow p(p,e$^+\nu$)d reaction. The produced energy is calculated according to Eq. (1.11) from the atomic mass excesses and amounts to 6.936 MeV. Subtracting an average neutrino energy of 0.265 MeV (see above) yields an

energy of 6.671 MeV available to the star. In the second step, the ^{3}He(^{3}He,2p)^{4}He reaction releases an energy of 12.861 MeV. The total energy production rate in the pp1 chain is then given by (see Eq. (3.64))

$$\begin{aligned}\varepsilon_{\rm pp1} &= \frac{6.671\ {\rm MeV}}{\rho} r_{\rm pp} + \frac{12.861\ {\rm MeV}}{\rho} r_{^3{\rm He}^3{\rm He}} \\ &= \frac{6.671\ {\rm MeV}}{2\rho} H^2 \langle \sigma v \rangle_{\rm pp} + \frac{12.861\ {\rm MeV}}{2\rho} H^2 \left(\frac{^3He}{H}\right)^2 \langle \sigma v \rangle_{^3{\rm He}^3{\rm He}} \end{aligned} \quad (5.25)$$

The energy generation rate depends on whether the ^{3}He abundance has achieved equilibrium or not. In the general case, when equilibrium has not been reached yet, the ^{3}He abundance and the corresponding energy generation rate are changing with time and both quantities have to be computed numerically. Alternatively, for the conditions of a constant temperature, for $(^3He/H)_e < 0.01$ (i.e., a constant hydrogen abundance) and a zero initial ^{3}He abundance, the ratio $(^3He/H)$ can be approximated by Eq. (5.19). The expression for the energy generation rate simplifies considerably after the ^{3}He abundance has achieved equilibrium. From Eqs. (5.15) and (5.25), we find

$$\begin{aligned}\varepsilon^e_{\rm pp1} &= \frac{6.671\ {\rm MeV}}{2\rho} H^2 \langle \sigma v \rangle_{\rm pp} + \frac{12.861\ {\rm MeV}}{2\rho} \frac{H^2}{2} \frac{N_A \langle \sigma v \rangle_{\rm pp}}{N_A \langle \sigma v \rangle_{^3{\rm He}^3{\rm He}}} \langle \sigma v \rangle_{^3{\rm He}^3{\rm He}} \\ &= 6.551\, N_A \langle \sigma v \rangle_{\rm pp} \left(\frac{X_{\rm H}}{M_{\rm H}}\right)^2 \rho N_A \qquad ({\rm MeV g^{-1} s^{-1}}) \end{aligned} \quad (5.26)$$

The energy generation rate in the pp1 chain at ^{3}He equilibrium is determined by the p + p reaction rate. The temperature dependence of $\varepsilon^e_{\rm pp1}$ is thus given by Eq. (3.90). For example, near $T_0 = 15$ MK we obtain $\tau = 13.6$ for the p(p,e$^+\nu$)d reaction, implying

$$\varepsilon^e_{\rm pp1}(T) = \varepsilon^e_{\rm pp1}(T_0) \left(T/T_0\right)^{(\tau-2)/3} = \varepsilon^e_{\rm pp1}(T_0) \left(T/T_0\right)^{3.9} \quad (5.27)$$

The quantity $\varepsilon^e_{\rm pp1}$ will be presented versus temperature in Section 5.1.2 and will be compared to the energy generation rate from the CNO cycles.

pp2 and pp3 Chains

So far we have disregarded reactions other than ^{3}He(^{3}He,2p)^{4}He that destroy ^{3}He. Figure 5.5a also compares the quantity $[\tau_{^3{\rm He}}(^3He)]_e$ with the lifetime of ^{3}He against destruction via the ^{3}He(α,γ)^{7}Be reaction, $\tau_\alpha(^3He)$. It can be seen that the ^{3}He(α,γ)^{7}Be reaction becomes the dominant destruction mechanism for ^{3}He if the temperature and the ^{4}He abundance are sufficiently large. The ^{4}He may either be produced during hydrogen burning or may be of primordial origin. Following the ^{3}He(α,γ)^{7}Be reaction, the ^{7}Be nucleus can β-decay to ^{7}Li and the subsequent ^{7}Li(p,α)^{4}He reaction completes the conversion of four protons to one ^{4}He nucleus. This reaction sequence is referred to as the pp2 chain (Figure 5.2). The β-decay of ^{7}Be has interesting properties. In the laboratory, ^{7}Be has a half-life of $T_{1/2} = 53$ d and decays by capture of an atomic electron, $^7{\rm Be} + {\rm e}^- \rightarrow {}^7{\rm Li} + \nu$. In the stellar plasma, on the other hand, ^{7}Be is partially ionized and the decay

can occur either by capture of one of the remaining atomic electrons or of a free electron from the surrounding continuum (Section 1.8.4). A calculation of the electron capture rate of ^{7}Be in the stellar environment can be found in Bahcall and Moeller (1969). To calculate the decay constant, the tabulated values for the rate have to be multiplied by n_{e^-}/N_A, where n_{e^-} denotes the electron density (see Eq. (1.68)). It will be shown below that this decay rate depends only weakly on temperature, in contrast to the strong temperature dependence of charged-particle reactions. In particular, at sufficiently high temperatures, the ^{7}Be(p,γ)^{8}B reaction instead of ^{7}Be(e$^-$,ν)^{7}Li becomes the dominant ^{7}Be destruction mechanism. The β^+-decay of ^{8}B to ^{8}Be and the subsequent breakup of the particle-unstable ^{8}Be nucleus, $^{8}\mathrm{Be} \rightarrow \alpha + \alpha$, complete the pp3 chain (Figure 5.2).

The pp2 and pp3 chains have an output of two α-particles, but require an input of one α-particle. The net effect is the formation of one ^{4}He nucleus per reaction sequence and, hence, one of the α-particles acts only as a catalyst allowing the ^{3}He(α,γ)^{7}Be reaction to take place. The total energy released in any of the chains is the same (26.731 MeV), but the amount of energy carried away by the neutrinos will be different in each case. The nuclear energy available to the star for conversion to thermal energy for each chain is given by

$$Q_{\mathrm{pp1}} = 26.73\,\mathrm{MeV} - 2\overline{E}_{\nu}^{\mathrm{pp}} = 26.19\,\mathrm{MeV} \tag{5.28}$$

$$Q_{\mathrm{pp2}} = 26.73\,\mathrm{MeV} - \overline{E}_{\nu}^{\mathrm{pp}} - \overline{E}_{\nu}^{^{7}\mathrm{Be}} = 25.65\,\mathrm{MeV} \tag{5.29}$$

$$Q_{\mathrm{pp3}} = 26.73\,\mathrm{MeV} - \overline{E}_{\nu}^{\mathrm{pp}} - \overline{E}_{\nu}^{^{8}\mathrm{B}} = 19.75\,\mathrm{MeV} \tag{5.30}$$

The average neutrino energies $\overline{E}_{\nu}^{i}$ are adopted from Bahcall (1989). The neutrino losses in the pp1, pp2, and pp3 chains amount to 2%, 4%, and 26%, respectively.

In a hydrogen-burning star that contains a significant ^{4}He abundance, all three pp chains will operate simultaneously. The contributions of the different chains to the energy production and the nucleosynthesis depend on the conditions of temperature, density, and composition. If we consider a situation where convection, expansion, and mixing in the stellar plasma can be disregarded, then nuclear transformations are the only source of abundance changes. In this case, one obtains the following set of nonlinear coupled differential equations

$$\frac{dH}{dt} = 2\frac{(^{3}He)^{2}\langle\sigma v\rangle_{^{3}\mathrm{He}^{3}\mathrm{He}}}{2} - 2\frac{H^{2}\langle\sigma v\rangle_{\mathrm{pp}}}{2} - HD\langle\sigma v\rangle_{\mathrm{pd}} - H(^{7}Be)\langle\sigma v\rangle_{\mathrm{p}^{7}\mathrm{Be}} - H(^{7}Li)\langle\sigma v\rangle_{\mathrm{p}^{7}\mathrm{Li}} \tag{5.31}$$

$$\frac{dD}{dt} = \frac{H^{2}}{2}\langle\sigma v\rangle_{\mathrm{pp}} - HD\langle\sigma v\rangle_{\mathrm{pd}} \tag{5.32}$$

$$\frac{d(^{3}He)}{dt} = HD\langle\sigma v\rangle_{\mathrm{pd}} - 2\frac{(^{3}He)^{2}\langle\sigma v\rangle_{^{3}\mathrm{He}^{3}\mathrm{He}}}{2} - (^{3}He)(^{4}He)\langle\sigma v\rangle_{\alpha^{3}\mathrm{He}} \tag{5.33}$$

$$\frac{d(^{4}He)}{dt} = \frac{(^{3}He)^{2}\langle\sigma v\rangle_{^{3}\mathrm{He}^{3}\mathrm{He}}}{2} + 2H(^{7}Be)\langle\sigma v\rangle_{\mathrm{p}^{7}\mathrm{Be}} + 2H(^{7}Li)\langle\sigma v\rangle_{\mathrm{p}^{7}\mathrm{Li}} - (^{3}He)(^{4}He)\langle\sigma v\rangle_{\alpha^{3}\mathrm{He}} \tag{5.34}$$

$$\frac{d(^7Be)}{dt} = (^3He)(^4He)\langle\sigma v\rangle_{\alpha^3\mathrm{He}} - (^7Be)\lambda_{e^7\mathrm{Be}} - H(^7Be)\langle\sigma v\rangle_{p^7\mathrm{Be}} \tag{5.35}$$

$$\frac{d(^7Li)}{dt} = (^7Be)\lambda_{e^7\mathrm{Be}} - H(^7Li)\langle\sigma v\rangle_{p^7\mathrm{Li}} \tag{5.36}$$

The factor of two, for example, in the numerator of the first term on the right-hand side of Eq. (5.31) appears because *two* protons are created in *one* ^{3}He(^{3}He,2p)^{4}He reaction. The term λ_{e^7Be} denotes the decay constant for ^{7}Be electron capture. The ^{8}B and ^{8}Be abundances have been eliminated because both decays have very short mean lifetimes (1.1 s and 4×10^{-22} s, respectively). Therefore, the sequence ^{7}Be(p,γ)^{8}B($\beta^+\nu$)^{8}Be(α)α can be considered a single step, $^7\mathrm{Be} + \mathrm{p} \rightarrow 2\alpha + \nu$. This set of equations can be solved numerically. It is instructive, however, to calculate analytical solutions using certain approximations. We have seen in the discussion of the pp1 chain that several important results can be expressed in terms of the ^{3}He equilibrium abundance. Therefore, we will first focus on this quantity and will then estimate the overall energy generation in the pp chains.

It is again safe to assume that the deuterium abundance will achieve equilibrium in a negligible amount of time (seconds to hours) compared to the evolutionary timescale of the star. Hence, $dD/dt = 0$ in Eq. (5.32), and $HD\langle\sigma v\rangle_{\mathrm{pd}}$ can be replaced in Eq. (5.33) by $H^2\langle\sigma v\rangle_{\mathrm{pp}}/2$, with the result

$$\frac{d(^3He)}{dt} = \frac{H^2}{2}\langle\sigma v\rangle_{\mathrm{pp}} - 2\frac{(^3He)^2\langle\sigma v\rangle_{^3\mathrm{He}^3\mathrm{He}}}{2} - (^3He)(^4He)\langle\sigma v\rangle_{\alpha^3\mathrm{He}} \tag{5.37}$$

We will also assume that the ^{3}He abundance has reached equilibrium. The $(^3He)_e$ abundance will be smaller compared to what it was during the operation of the pp1 chain alone because of an additional ^{3}He destroying reaction. With $d(^3He)/dt = 0$ we find

$$(^3He)_e^2\langle\sigma v\rangle_{^3\mathrm{He}^3\mathrm{He}} = \frac{H^2}{2}\langle\sigma v\rangle_{\mathrm{pp}} - (^3He)_e(^4He)\langle\sigma v\rangle_{\alpha^3\mathrm{He}} \tag{5.38}$$

Solving for $(^3He)_e$ yields the expression

$$(^3He)_e = \frac{-(^4He)\langle\sigma v\rangle_{\alpha^3\mathrm{He}} + \sqrt{(^4He)^2\langle\sigma v\rangle_{\alpha^3\mathrm{He}}^2 + 2H^2\langle\sigma v\rangle_{\mathrm{pp}}\langle\sigma v\rangle_{^3\mathrm{He}^3\mathrm{He}}}}{2\langle\sigma v\rangle_{^3\mathrm{He}^3\mathrm{He}}} \tag{5.39}$$

It is apparent that for a zero hydrogen abundance ($H \rightarrow 0$), the $(^3He)_e$ abundance also vanishes. Furthermore, for a zero ^{4}He abundance, implying no destruction of ^{3}He via the ^{3}He(α,γ)^{7}Be reaction, the above expression reduces to Eq. (5.15). The ratio of $(^3He)_e$ values obtained from Eq. (5.39) to that resulting from the operation of the pp1 chain alone (see Eq. (5.15)) is shown in Figure 5.6 for a composition of $X_{\mathrm{H}} = X_\alpha = 0.5$. The ratio amounts to unity for temperatures below $T = 10$ MK and decreases rapidly for increasing temperature because of the operation of the pp2 and pp3 chains (see below).

We are now in a position to investigate the competition between the pp1, pp2, and pp3 chains. The pp2 and pp3 chains will dominate over the pp1 chain when the ^{3}He(α,γ)^{7}Be reaction becomes more likely than the ^{3}He(^{3}He,2p)^{4}He reaction.

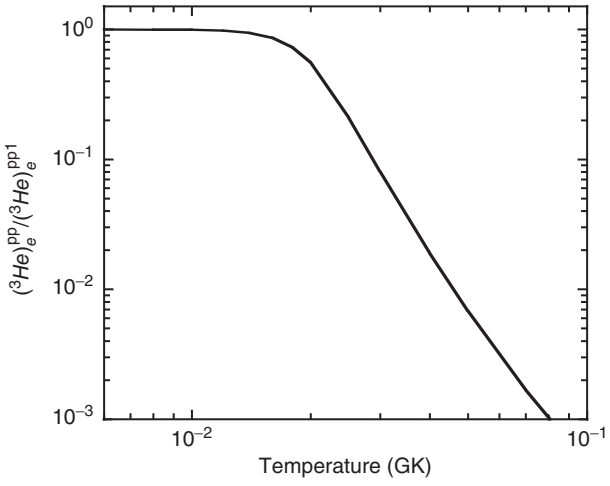

Figure 5.6 Values of $(^3He)_e$ obtained from the operation of all three pp chains, divided by $(^3He)_e$ values derived from the operation of the pp1 chain only. The curve is obtained for a composition of $X_H = X_\alpha = 0.5$. The ratio of $(^3He)_e$ values shown is unity below $T = 10$ MK and decreases rapidly for increasing temperatures because of the operation of the pp2 and pp3 chains.

Similarly, the pp3 chain will dominate over the pp2 chain when the ^{7}Be(p,γ)^{8}B reaction becomes more likely than the competing electron capture ^{7}Be(e$^-$,ν)^{7}Li. According to Eqs. (3.22) and (5.39), the corresponding mean lifetimes are

$$\tau_\alpha(^3He) = \left(\rho \frac{X_\alpha}{M_\alpha} N_A \langle \sigma v \rangle_{\alpha^3\mathrm{He}}\right)^{-1} \tag{5.40}$$

$$[\tau_{^3\mathrm{He}}(^3He)]_e = \left(-\frac{\rho}{2}\frac{X_\alpha}{M_\alpha} N_A \langle \sigma v \rangle_{\alpha^3\mathrm{He}} + \frac{\rho}{2}\sqrt{\frac{X_\alpha^2}{M_\alpha^2}(N_A\langle \sigma v \rangle_{\alpha^3\mathrm{He}})^2 + 2\frac{X_\mathrm{H}^2}{M_\mathrm{H}^2} N_A \langle \sigma v \rangle_{\mathrm{pp}} N_A \langle \sigma v \rangle_{^3\mathrm{He}^3\mathrm{He}}}\right)^{-1} \tag{5.41}$$

$$\tau_\mathrm{p}(^7Be) = \left(\rho \frac{X_\mathrm{H}}{M_\mathrm{H}} N_A \langle \sigma v \rangle_{\mathrm{p}^7\mathrm{Be}}\right)^{-1} \tag{5.42}$$

$$\tau_{\mathrm{e}^-}(^7Be) = \left(\lambda_{\mathrm{e}^7\mathrm{Be}}\right)^{-1} \tag{5.43}$$

The mean lifetimes are calculated from the above expressions for the conditions $\rho = 100$ g/cm^3 and $X_\mathrm{H} = X_\mathrm{He} = 0.5$. To calculate $\lambda_{e^7\mathrm{Be}}$, the approximation $n_{\mathrm{e}^-}/N_A \approx \rho(1 + X_\mathrm{H})/2$ is used (Fowler, Caughlan, and Zimmerman, 1975), which is applicable for a fully ionized gas. The results are shown in Figure 5.5b. We find that, for the conditions assumed, $\tau_\alpha(^3He) \approx [\tau_{^3\mathrm{He}}(^3He)]_e$ at $T \approx 18$ MK. Above this temperature, the pp2 and pp3 chains will dominate over the pp1 chain. Furthermore, we obtain $\tau_\mathrm{p}(^7Be) \approx \tau_{\mathrm{e}^-}(^7Be)$ at $T \approx 25$ MK, implying that the pp3 chain will dominate over the pp2 chain at temperatures in excess of this value.

These two temperature values are independent of density, as can be seen from Eqs. (5.40)–(5.43).

Finally, the nuclear energy generated by all the pp chains operating together is estimated under the assumption that ^{3}He has achieved an equilibrium abundance. Remember that the neutrino losses are different in each chain. The energy generation rate, corrected for neutrino losses, can be written as the product

$$\varepsilon_{\rm pp} = \frac{Q_{\rm 4H\rightarrow{}^4He}}{\rho}\frac{d(^4He)}{dt}\left(f_{\rm pp1}F_{\rm pp1} + f_{\rm pp2}F_{\rm pp2} + f_{\rm pp3}F_{\rm pp3}\right) \quad ({\rm MeV g^{-1}s^{-1}}) \tag{5.44}$$

with $Q_{\rm 4H\rightarrow{}^4He} = 26.73$ MeV the energy release per ^{4}He nucleus produced and $d(^4He)/dt$ the production rate of ^{4}He. The factor $f_{{\rm pp}i}$ is the fraction of the total energy $Q_{\rm 4H\rightarrow{}^4He}$ retained in the star if the ^{4}He nucleus is produced in the pp$i$ chain ($f_{\rm pp1} = 0.98$, $f_{\rm pp2} = 0.96$, $f_{\rm pp3} = 0.74$; see above). The quantity $F_{{\rm pp}i}$ denotes the fraction of ^{4}He nuclei produced by the pp$i$ chain (with $F_{\rm pp1} + F_{\rm pp2} + F_{\rm pp3} = 1$). The production rate of ^{4}He is given by Eq. (5.34). The mean lifetimes of ^{7}Be and ^{7}Li are less than a year at most temperatures and densities of interest. Thereafter, both abundances will follow the buildup of ^{3}He. With $d(^7Be + {}^7Li)/dt \approx 0$ one finds from Eqs. (5.35) and (5.36)

$$H(^7Be)\langle\sigma v\rangle_{\rm p^7Be} + H(^7Li)\langle\sigma v\rangle_{\rm p^7Li} = (^3He)(^4He)\langle\sigma v\rangle_{\alpha^3{\rm He}} \tag{5.45}$$

This expression is satisfied long before ^{3}He achieves equilibrium. Substitution of Eq. (5.45) into Eq. (5.34) yields a simplified expression for the ^{4}He production rate,

$$\frac{d(^4He)}{dt} = \frac{(^3He)^2\langle\sigma v\rangle_{^3{\rm He}^3{\rm He}}}{2} + (^3He)(^4He)\langle\sigma v\rangle_{\alpha^3{\rm He}} \tag{5.46}$$

When ^{3}He achieves equilibrium, we obtain with Eq. (5.38)

$$\frac{d(^4He)}{dt} = \frac{H^2}{4}\langle\sigma v\rangle_{\rm pp} + \frac{1}{2}(^3He)_e(^4He)\langle\sigma v\rangle_{\alpha^3{\rm He}} \tag{5.47}$$

The fraction of ^{4}He nuclei produced by the pp1 chain can be written as the ratio of reaction rates (see Eq. (3.6)),

$$F_{\rm pp1} = \frac{r_{^3{\rm He}^3{\rm He}}}{r_{^3{\rm He}^3{\rm He}} + r_{\alpha^3{\rm He}}} = \frac{(^3He)_e\langle\sigma v\rangle_{^3{\rm He}^3{\rm He}}}{(^3He)_e\langle\sigma v\rangle_{^3{\rm He}^3{\rm He}} + 2(^4He)\langle\sigma v\rangle_{\alpha^3{\rm He}}} \tag{5.48}$$

Similarly, one finds for the fraction of ^{4}He nuclei produced in the pp2 chain

$$F_{\rm pp2} = (1 - F_{\rm pp1})\frac{r_{\rm e^7Be}}{r_{\rm e^7Be} + r_{\rm p^7Be}} = (1 - F_{\rm pp1})\frac{\lambda_{\rm e^7Be}}{\lambda_{\rm e^7Be} + H\langle\sigma v\rangle_{\rm p^7Be}} \tag{5.49}$$

with $(1 - F_{\rm pp1})$ the probability that the ^{4}He nucleus is *not* produced in the pp1 chain. Furthermore, the fraction of ^{4}He nuclei produced by the pp3 chain is given by $F_{\rm pp3} = 1 - F_{\rm pp1} - F_{\rm pp2}$. The fractions $F_{{\rm pp}i}$, which are independent of density, are shown in Figure 5.7a assuming a composition of $X_{\rm H} = X_\alpha = 0.5$ and a fully ionized gas. It is again apparent that for temperatures below $T = 18$ MK the ^{4}He nuclei are mainly produced via the pp1 chain. The pp2 chain takes over above this temperature value, while for $T > 25$ MK the pp3 chain is the main producer of ^{4}He.

The energy production rate of the pp chains, after ^{3}He has achieved an equilibrium abundance, $\varepsilon^e_{\rm pp}$, can now be calculated from Eqs. (5.44) and (5.47)–(5.49) as a

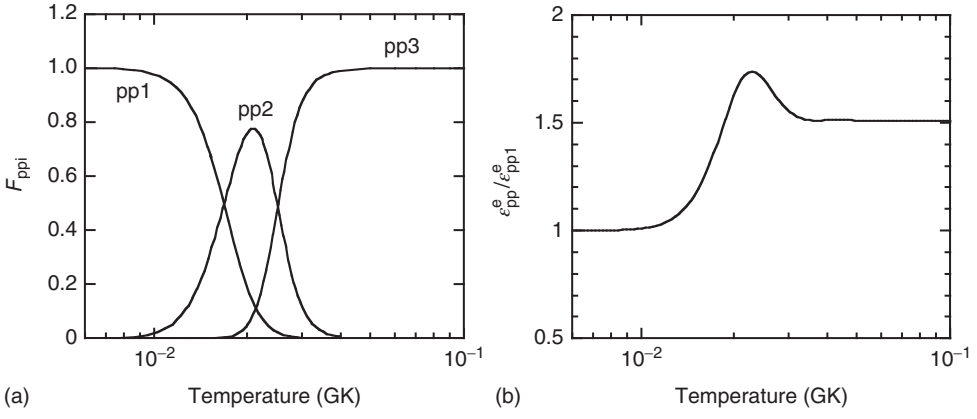

Figure 5.7 (a) Fraction of ^{4}He nuclei produced by the pp1, pp2, and pp3 chains, which are the main producers of ^{4}He at temperatures of $T < 18$ MK, $T = 18$–25 MK, and $T > 25$ MK, respectively. (b) Ratio of the energy generation rate by all three pp chains to that by the pp1 chain alone versus temperature. The ratio is unity for $T < 10$ MK, where the pp1 chain dominates. The maximum at $T \approx 23$ MK is caused by the dominant operation of the pp2 chain. About 90% of the Sun's energy is produced by the pp1 chain. All curves shown are independent of density and are calculated for a composition of $X_H = X_\alpha = 0.5$ and a fully ionized gas.

function of temperature and composition. The ratio of the energy generation rate by the pp chains to the pp1 chain alone, $\varepsilon^e_{pp}/\varepsilon^e_{pp1}$, is displayed in Figure 5.7b for a composition of $X_H = X_\alpha = 0.5$ and a fully ionized gas. The ratio is independent of density and amounts to unity at temperatures below $T = 10$ MK where the pp1 chain is the dominant process. Recall that in the pp1 chain two p + p reactions are necessary for the production of one ^{4}He nucleus. On the other hand, in the pp2 and pp3 chains, the creation of one ^{4}He nucleus requires only one p + p reaction, causing an increase in $d(^4He)/dt$ (by a factor of two) and in ε^e_{pp} (by a factor of two minus neutrino losses) compared to the operation of the pp1 chain alone. This can be seen at temperatures above $T = 40$ MK, where the pp3 chain dominates, yielding a ratio of $\varepsilon^e_{pp}/\varepsilon^e_{pp1} = 2(f_{pp3}/f_{pp1}) = 2(0.74/0.98) = 1.51$. The maximum at $T \approx 23$ MK is caused by the dominant operation of the pp2 chain, for which the neutrino losses are considerably smaller less compared to those of the pp3 chain. In the center of the Sun, the temperature amounts to $T = 15.6$ MK. Averaged over the entire hydrogen burning region, it turns out that about 90% of the Sun's energy is produced in the pp1 chain. The remainder is mostly provided by the pp2 chain, while the energy contributions from other processes (e.g., the pp3 chain, pep reaction, and CNO cycle) are very small. This result agrees with the direct detection of solar neutrinos from the p+p reaction in the Borexino experiment (Bellini *et al.*, 2014).

We conclude the discussion of the pp chains with a few final remarks. The evolution of the ^{3}He abundance is more complicated compared to the deuterium abundance. We already discussed that any initial deuterium nuclei are quickly converted inside stars to ^{3}He, thus increasing the ^{3}He abundance. Compared

to the deuterium destroying d(p,γ)^{3}He reaction, the ^{3}He consuming reactions ^{3}He(^{3}He,2p)^{4}He and ^{3}He(α,γ)^{7}Be involve higher Coulomb barriers and, therefore, have smaller cross sections. In the cooler outer layers of most stars and throughout most of the volume of cooler low-mass stars, ^{3}He will thus survive. However, in the hotter stellar regions, ^{3}He is converted to ^{4}He via the pp chains. The situation becomes more complex because the outer cooler layers of a star may be mixed to the hotter interior regions, a process that will contribute to the destruction of ^{3}He. There is a delicate balance between stellar ^{3}He production and destruction. Whether or not this ^{3}He will survive and, after ejection, enrich the interstellar medium is controversial (see the review by Tosi, 2000).

The isotope ^{7}Li is produced in the pp2 chain. However, the cross section of the ^{7}Li(p,α)α reaction is very large, and hence, the ^{7}Li abundance at any time during the operation of the pp chains becomes very small [$(^7Li/H)_{pp} \approx 2 \times 10^{-9}$; Parker, Bahcall, and Fowler, 1964]. There is strong evidence that a large fraction of the ^{7}Li abundance observed in the solar system [$(^7Li/H)_{\odot} \approx 2 \times 10^{-9}$] is not produced in stars, but originates from high-energy spallation reactions involving cosmic rays and the interstellar medium, and from primordial nucleosynthesis (Section 5.7). Nevertheless, models of Galactic chemical evolution require a stellar source that produces the remaining, unexplained fraction of the ^{7}Li abundance (Romano *et al.*, 2001). In these sources, ^{7}Be is produced by the ^{3}He(α,γ)^{7}Be reaction and is transported via convection from the hot burning zone to the outer, cooler layers where it decays by electron capture to ^{7}Li. This beryllium transport process is referred to as the *Cameron–Fowler mechanism* (Cameron and Fowler, 1971) and explains the lithium enrichments observed in certain red giants and AGB stars.

Finally, we comment on the cross sections of the reactions that are part of the pp chains. All these reactions exhibit nonresonant cross sections in the energy range important to hydrostatic hydrogen burning. Direct cross section measurements for d(p,γ)^{3}He, ^{3}He(^{3}He,2p)^{4}He, ^{3}He(α,γ)^{7}Be, ^{7}Be(p,γ)^{8}B, and ^{7}Li(p,α)α have been performed down to center-of-mass energies of 10 keV, 15 keV, 100 keV, 70 keV, and 10 keV, respectively (Angulo *et al.*, 1999). In comparison, the centers of the solar Gamow peaks ($T_{\odot} = 15.6$ MK; see Eq. (3.77)) for these reactions are located at 7 keV, 22 keV, 23 keV, 18 keV, and 15 keV, respectively. Thus, measurements of the d(p,γ)^{3}He, ^{3}He(^{3}He,2p)^{4}He, and ^{7}Li(p,α)α reactions cover the energy range important to hydrogen burning in stars with masses of $M \geq M_{\odot}$. In other cases (e.g., for ^{3}He(α,γ)^{7}Be and ^{7}Be(p,γ)^{8}B at solar temperature, or for all of the above reactions at lower temperatures that are typical of stars with $M < M_{\odot}$), the astrophysical S-factor has to be extrapolated down to the energy range of interest, either by a polynomial expansion or by using a suitable nuclear reaction model (Section 3.2.1).

5.1.2 CNO Cycles

If a star consists exclusively of hydrogen and helium, then significant amounts of energy can only be generated during the hydrogen burning stage via the operation

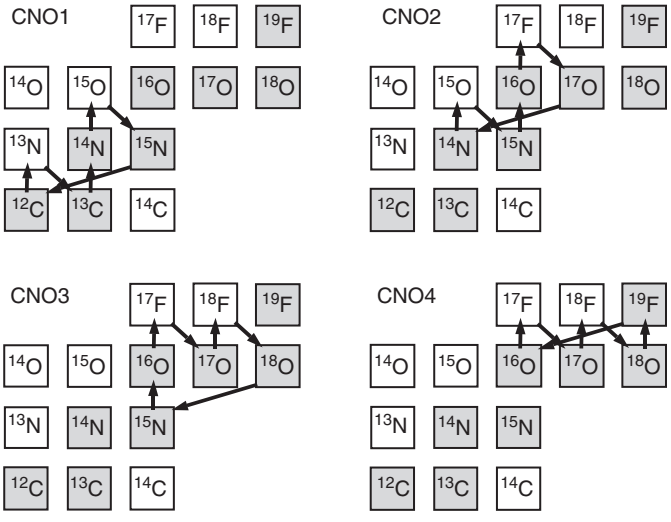

Figure 5.8 Representation of the four CNO cycles in the chart of the nuclides. Stable nuclides are shown as shaded squares. Each reaction cycle fuses effectively four protons to one ^{4}He nucleus.

of the pp chains. Most stars, however contain heavier nuclides, particularly those in the C, N, and O mass region. Hence, these nuclides can participate in hydrogen burning. The resulting four sets of reactions that convert hydrogen to helium are referred to as the *CNO cycles*. They are listed below (together with the β-decay half-lives) and are shown in Figure 5.8.

CNO1	CNO2	CNO3	CNO4
^{12}C(p,γ)^{13}N	^{14}N(p,γ)^{15}O	^{15}N(p,γ)^{16}O	^{16}O(p,γ)^{17}F
^{13}N($\beta^+\nu$)^{13}C	^{15}O($\beta^+\nu$)^{15}N	^{16}O(p,γ)^{17}F	^{17}F($\beta^+\nu$)^{17}O
^{13}C(p,γ)^{14}N	^{15}N(p,γ)^{16}O	^{17}F($\beta^+\nu$)^{17}O	^{17}O(p,γ)^{18}F
^{14}N(p,γ)^{15}O	^{16}O(p,γ)^{17}F	^{17}O(p,γ)^{18}F	^{18}F($\beta^+\nu$)^{18}O
^{15}O($\beta^+\nu$)^{15}N	^{17}F($\beta^+\nu$)^{17}O	^{18}F($\beta^+\nu$)^{18}O	^{18}O(p,γ)^{19}F
^{15}N(p,α)^{12}C	^{17}O(p,α)^{14}N	^{18}O(p,α)^{15}N	^{19}F(p,α)^{16}O

$T_{1/2}$: ^{13}N (9.965 min); ^{15}O (122.24 s); ^{17}F (64.49 s); ^{18}F (109.77 min)

These cycles have interesting properties. The result of each process is the same as for the pp chains, that is, $4\mathrm{H} \rightarrow {}^4\mathrm{He} + 2\mathrm{e}^+ + 2\nu$. In each cycle, C, N, O, or F nuclei act only as catalysts, in the sense that the total abundance of the heavy nuclei is not altered while only hydrogen is consumed. Therefore, a substantial amount of nuclear energy can be generated even if the total abundance of the heavy nuclei is relatively low. The operation of a particular cycle will change the abundance of the individual heavy nuclei. Consider the CNO1 cycle as an example. If there are initially only ^{12}C nuclei present in the stellar gas, then some of these

will be converted to other CNO nuclei, and the individual abundances will evolve depending on the magnitude of the reaction rates involved. The energy generation rate depends on the abundance of the catalysts and the time it takes to complete the cycle.

The various CNO cycles exist because for the proton-induced reactions involving the nuclei ^{15}N, ^{17}O, ^{18}O, and ^{19}F, both the (p,γ) and (p,α) channels are energetically allowed. In contrast, the proton-induced reactions on the nuclei ^{12}C, ^{13}C, ^{14}N, and ^{16}O can only proceed via the (p,γ) reaction. A (p,α) reaction will convert a heavier nucleus to a lighter one, thereby giving rise to a cycle of nuclear processes. At each of the branch point nuclides ^{15}N, ^{17}O, ^{18}O, and ^{19}F, the (p,α) reaction will compete with the (p,γ) reaction. The branching ratio, or the ratio of probabilities for the occurrence of the (p,α) and (p,γ) reaction, is then given by the ratio of the corresponding reaction rates, $B_{\mathrm{p}\alpha/\mathrm{p}\gamma} = N_A\langle\sigma v\rangle_{(\mathrm{p},\alpha)}/N_A\langle\sigma v\rangle_{(\mathrm{p},\gamma)}$. The branching ratios versus temperature are displayed in Figure 5.9. The solid lines show the upper and lower limits of $B_{\mathrm{p}\alpha/\mathrm{p}\gamma}$, caused by presently unknown contributions to the reaction rates (e.g., unobserved resonances). Despite the rate uncertainties, it can be seen that for the target nuclei ^{15}N, ^{17}O, ^{18}O, and ^{19}F the (p,α) reaction is faster than the (p,γ) reaction over the entire temperature range (except perhaps for ^{17}O and ^{18}O at very low temperatures of $T < 20$ MK). An impression regarding the relative likelihood of the various CNO reactions can be obtained from Figure 5.10, showing the reaction rates normalized to the rate of the slowest reaction, ^{16}O(p,γ)^{17}F.

A few important points need to be stressed before continuing the discussion. First, at relatively low temperatures characteristic of hydrostatic hydrogen burning ($T \leq 55$ MK), β^+-decays of unstable nuclei in the CNO mass range proceed on considerably faster time scales compared to the competing proton-induced reactions. Thus, reactions involving unstable nuclei are unimportant under such conditions. At temperatures above $T = 100$ MK, additional reactions not listed above (those involving unstable target nuclei) take place in the CNOF mass region and the properties of the cycles change substantially. In this section, we will concentrate on the temperature range $T < 100$ MK, while the hydrogen burning in the CNOF mass region at higher temperatures is discussed in Section 5.5.2. Second, the relative initial abundance of the various CNOF isotopes is important for describing the detailed operation of the CNO cycles. These seed nuclei are produced at the helium burning stage in a previous generation of stars. The most abundant nuclides produced during helium burning (see Section 5.2.2) are ^{12}C, ^{16}O, and, to a lesser extent, ^{14}N. For example, the solar ratio of these isotopes is ^{12}C:^{14}N:^{16}O = 10:3:24. Hence, the CNO cycles will most likely operate with ^{12}C and ^{16}O as seed nuclei. Third, consider now the different fate of these two nuclides. The ^{12}C nuclei will initiate the CNO1 cycle. At ^{15}N, there is a small chance of about 1 : 1000, according to Figure 5.9, that catalytic material leaks into the CNO2 cycle via the ^{15}N(p,γ)^{16}O reaction. However, most of the catalytic material will be transformed back to ^{12}C via the dominant (p,α) reaction. On the other hand, ^{16}O is transformed to ^{17}O, but the subsequent processing is more complicated. A large fraction of ^{17}O nuclei will be

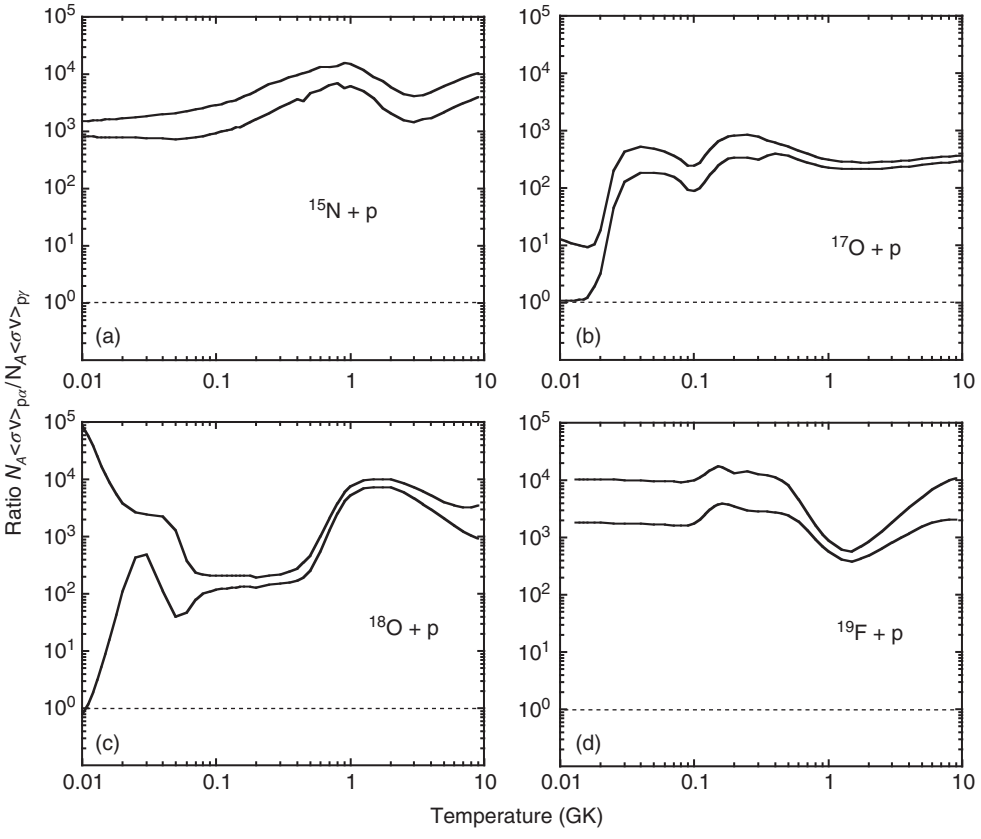

Figure 5.9 Branching ratio $B_{p\alpha/p\gamma} = N_A\langle\sigma v\rangle_{(p,\alpha)}/N_A\langle\sigma v\rangle_{(p,\gamma)}$ versus temperature for the reactions (a) ^{15}N + p, (b) ^{17}O + p, (c) ^{18}O + p, and (d) ^{19}F + p. The two solid lines in each panel represent the upper and lower boundaries of $B_{p\alpha/p\gamma}$. The area between the solid lines indicates the uncertainty in $B_{p\alpha/p\gamma}$ that is caused by unknown contributions to the (p,γ) and (p,α) reaction rates.

destroyed by the (p,α) reaction, leading to the formation of ^{14}N and the further operation of the CNO1 and CNO2 cycles. But another fraction, depending on the stellar temperature, will be converted to ^{18}F, thus initiating the CNO3 and CNO4 cycles.

To gain insight into the operation of the CNO cycles, we will proceed as follows. It is first assumed that only ^{12}C, ^{13}C, ^{14}N, or ^{15}N seed nuclei are present in the stellar plasma and that the CNO1 cycle is closed, that is, the (p,γ) reaction on ^{15}N is negligible compared to the competing (p,α) reaction. The corresponding set of differential equations describing the evolution of isotopic abundances will then be solved for the equilibrium operation of the CNO1 cycle. In a second step, the interplay of all CNO cycles is considered for different assumptions of initial

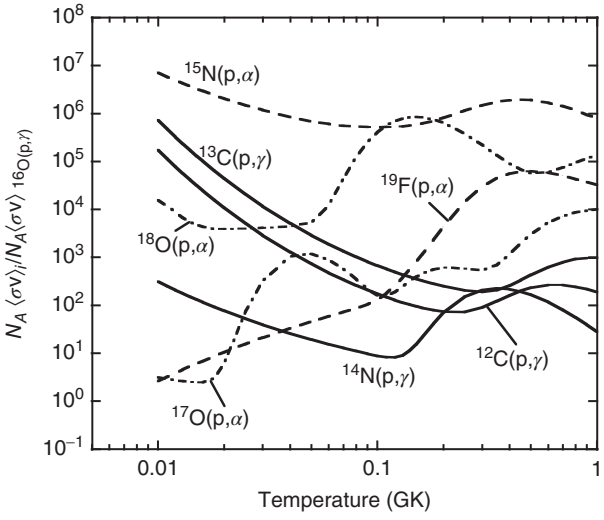

Figure 5.10 Reaction rates in the CNO cycles versus temperature. For a better comparison, the values of $N_A\langle\sigma v\rangle$ are normalized to the rate of the slowest reaction, $^{16}O(p,\gamma)^{17}F$.

seed abundances by solving the equations describing the abundance changes numerically.

Steady-State Operation of the CNO1 Cycle

Assuming that nuclear transformations are the only source of abundance changes, the following set of coupled differential equations can be obtained for a closed CNO1 cycle (also called *CN cycle*):

$$\frac{d(^{12}C)}{dt} = H(^{15}N)\langle\sigma v\rangle_{^{15}N(p,\alpha)} - H(^{12}C)\langle\sigma v\rangle_{^{12}C(p,\gamma)} \tag{5.50}$$

$$\frac{d(^{13}N)}{dt} = H(^{12}C)\langle\sigma v\rangle_{^{12}C(p,\gamma)} - (^{13}N)\lambda_{^{13}N(\beta^+\nu)} \tag{5.51}$$

$$\frac{d(^{13}C)}{dt} = (^{13}N)\lambda_{^{13}N(\beta^+\nu)} - H(^{13}C)\langle\sigma v\rangle_{^{13}C(p,\gamma)} \tag{5.52}$$

$$\frac{d(^{14}N)}{dt} = H(^{13}C)\langle\sigma v\rangle_{^{13}C(p,\gamma)} - H(^{14}N)\langle\sigma v\rangle_{^{14}N(p,\gamma)} \tag{5.53}$$

$$\frac{d(^{15}O)}{dt} = H(^{14}N)\langle\sigma v\rangle_{^{14}N(p,\gamma)} - (^{15}O)\lambda_{^{15}O(\beta^+\nu)} \tag{5.54}$$

$$\frac{d(^{15}N)}{dt} = (^{15}O)\lambda_{^{15}O(\beta^+\nu)} - H(^{15}N)\langle\sigma v\rangle_{^{15}N(p,\alpha)} \tag{5.55}$$

At the temperatures of interest here ($T < 0.1$ GK), the β-decay lifetime of ^{13}N is considerably shorter compared to the lifetime of ^{12}C versus destruction by the (p,γ) reaction (i.e., the preceding step). For all practical purposes, the abundances of H and ^{12}C will be constant over the short time it takes ^{13}N to reach steady state.

Hence, Eq. (5.51) can be solved with the same method used to derive Eq. (5.10). With $(^{13}N)_{t=0} = 0$ we obtain

$$(^{13}N)_t = \frac{H\langle\sigma v\rangle_{^{12}\mathrm{C(p,\gamma)}}}{\lambda_{^{13}\mathrm{N}(\beta^+\nu)}}(^{12}C) - \left[\frac{H\langle\sigma v\rangle_{^{12}\mathrm{C(p,\gamma)}}}{\lambda_{^{13}\mathrm{N}(\beta^+\nu)}}(^{12}C)\right] e^{-\lambda_{^{13}\mathrm{N}(\beta^+\nu)}t}$$
$$= \frac{\tau_\beta(^{13}N)}{\tau_\mathrm{p}(^{12}C)}(^{12}C)\left[1 - e^{-t/\tau_\beta(^{13}N)}\right] \tag{5.56}$$

The result shows that the ^{13}N abundance approaches its steady-state value $(^{13}N/^{12}C)_e = \tau_\beta(^{13}N)/\tau_\mathrm{p}(^{12}C)$ in times on the order of $\tau_\beta(^{13}N)$, that is, in a few minutes. The same arguments hold for the ^{15}O abundance. Therefore, we can set the time derivaties in Eqs. (5.51) and (5.54) equal to zero and eliminate ^{13}N and ^{15}O from the system of equations. After a few minutes, the nuclear burning in the CNO1 cycle is described by the system of equations

$$\frac{d(^{12}C)}{dt} = H(^{15}N)\langle\sigma v\rangle_{^{15}\mathrm{N(p,\alpha)}} - H(^{12}C)\langle\sigma v\rangle_{^{12}\mathrm{C(p,\gamma)}} \tag{5.57}$$
$$\frac{d(^{13}C)}{dt} = H(^{12}C)\langle\sigma v\rangle_{^{12}\mathrm{C(p,\gamma)}} - H(^{13}C)\langle\sigma v\rangle_{^{13}\mathrm{C(p,\gamma)}} \tag{5.58}$$
$$\frac{d(^{14}N)}{dt} = H(^{13}C)\langle\sigma v\rangle_{^{13}\mathrm{C(p,\gamma)}} - H(^{14}N)\langle\sigma v\rangle_{^{14}\mathrm{N(p,\gamma)}} \tag{5.59}$$
$$\frac{d(^{15}N)}{dt} = H(^{14}N)\langle\sigma v\rangle_{^{14}\mathrm{N(p,\gamma)}} - H(^{15}N)\langle\sigma v\rangle_{^{15}\mathrm{N(p,\alpha)}} \tag{5.60}$$

Several observations are immediately apparent. First, since $d(^{12}C)/dt + d(^{13}C)/dt + d(^{14}N)/dt + d(^{15}N)/dt = 0$, the sum of CNO1 abundances is constant, $\sum\mathrm{CNO1} = \mathrm{const}$. Second, after the CNO1 cycle has reached steady state, all time derivatives in the above expressions are zero. As a result, the rates of all CNO1 reactions become equal, while the ratio of any two nuclidic abundances is given by the inverse ratio of their reaction rates (or the ratio of mean lifetimes). For example,

$$\left(\frac{^{14}N}{^{12}C}\right)_e = \frac{\langle\sigma v\rangle_{^{12}\mathrm{C(p,\gamma)}}}{\langle\sigma v\rangle_{^{14}\mathrm{N(p,\gamma)}}} = \frac{\tau_\mathrm{p}(^{14}N)}{\tau_\mathrm{p}(^{12}C)} \tag{5.61}$$

The fractional abundance, for example, of ^{12}C is

$$\frac{(^{12}C)_e}{\sum\mathrm{CNO1}} = \frac{(^{12}C)_e}{(^{12}C)_e + (^{13}C)_e + (^{14}N)_e + (^{15}N)_e}$$
$$= \left(1 + \frac{\langle\sigma v\rangle_{^{12}\mathrm{C(p,\gamma)}}}{\langle\sigma v\rangle_{^{13}\mathrm{C(p,\gamma)}}} + \frac{\langle\sigma v\rangle_{^{12}\mathrm{C(p,\gamma)}}}{\langle\sigma v\rangle_{^{14}\mathrm{N(p,\gamma)}}} + \frac{\langle\sigma v\rangle_{^{12}\mathrm{C(p,\gamma)}}}{\langle\sigma v\rangle_{^{15}\mathrm{N(p,\alpha)}}}\right)^{-1}$$
$$= \frac{\tau_\mathrm{p}(^{12}C)}{\tau_\mathrm{p}(^{12}C) + \tau_\mathrm{p}(^{13}C) + \tau_\mathrm{p}(^{14}N) + \tau_\mathrm{p}(^{15}N)} \tag{5.62}$$

The CNO1 abundance ratios and fractional abundances are shown in Figure 5.11 versus temperature.

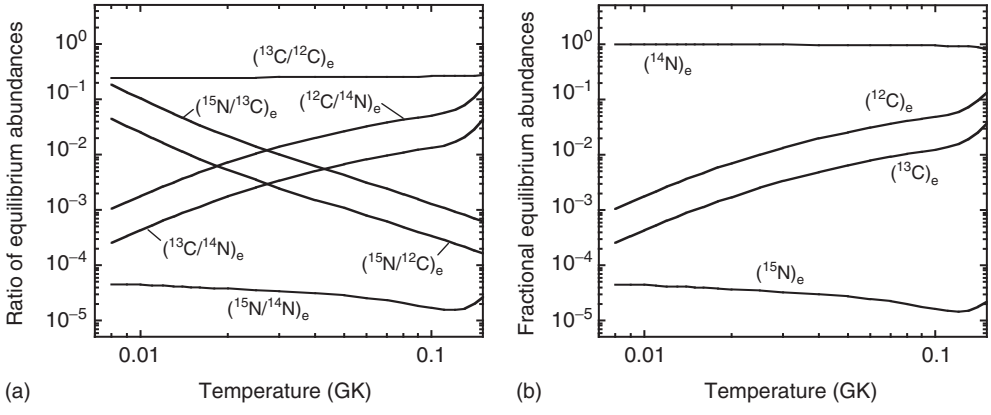

Figure 5.11 (a) Abundance ratios and (b) fractional abundances versus temperature. The curves are calculated by assuming steady-state operation of a closed CNO1 cycle.

The net effect of the CNO1 cycle operation is the conversion of carbon and nitrogen seed nuclei to ^{14}N, which becomes by far the most abundant heavy nuclide when steady state is reached. This result is a consequence of the fact that the ^{14}N destroying reaction, ^{14}N(p,γ)^{15}O, is the slowest process in the CNO1 cycle for temperatures of $T < 0.1$ GK, as can be seen from Figure 5.10. Also, not all abundances are constant with time, even under steady-state conditions, since hydrogen is continuously converted to helium [$dH/dt < 0$ and $d(^4He)/dt > 0$].

The energy generation rate from the operation of the CNO1 cycle at constant temperature and density can be expressed as (see Eq. (3.64))

$$\varepsilon_{\mathrm{CNO1}} = \sum_{i\to j} \varepsilon_{i\to j} = \frac{1}{\rho} \sum_{i\to j} (Q_{i\to j} - \overline{E}_\nu^{\,i\to j}) r_{i\to j} \tag{5.63}$$

where the sum is over all relevant processes $i \to j$, and $\overline{E}_\nu$ denotes the average energy of the neutrinos released in the β-decays. Since the β$^+$-decays of ^{13}N and ^{15}O occur on negligibly small time scales, we can consider them together with the preceding reactions ^{12}C(p,γ)^{13}N and ^{14}N(p,γ)^{15}O, respectively. The reaction and decay energies available to the star are given by

$$\begin{aligned} Q_{^{12}\mathrm{C(p,}\gamma)^{13}\mathrm{N}(\beta^+\nu)} - \overline{E}_\nu^{\,^{13}\mathrm{N}(\beta^+\nu)} &= (1.944 + 2.220 - 0.706)\,\mathrm{MeV} \\ &= 3.458\,\mathrm{MeV} \qquad (5.64) \\ Q_{^{13}\mathrm{C(p,}\gamma)} &= 7.551\,\mathrm{MeV} \qquad (5.65) \\ Q_{^{14}\mathrm{N(p,}\gamma)^{15}\mathrm{O}(\beta^+\nu)} - \overline{E}_\nu^{\,^{15}\mathrm{O}(\beta^+\nu)} &= (7.297 + 2.754 - 0.996)\,\mathrm{MeV} \\ &= 9.055\,\mathrm{MeV} \qquad (5.66) \\ Q_{^{15}\mathrm{N(p,}\alpha)} &= 4.966\,\mathrm{MeV} \qquad (5.67) \end{aligned}$$

The average neutrino energies $\overline{E}_\nu^{\,i}$ are adopted from Bahcall (1989) (see also Eq. (1.48) and Problem 1.9). For the equilibrium operation of the CNO1 cycle,

we obtain from Eq. (5.63)

$$\begin{aligned}\rho\varepsilon^{e}_{\mathrm{CNO1}} &= (3.458\,\mathrm{MeV})H(^{12}C)_e\langle\sigma v\rangle_{^{12}\mathrm{C(p,\gamma)}} + (7.551\,\mathrm{MeV})H(^{13}C)_e\langle\sigma v\rangle_{^{13}\mathrm{C(p,\gamma)}} \\ &+ (9.055\,\mathrm{MeV})H(^{14}N)_e\langle\sigma v\rangle_{^{14}\mathrm{N(p,\gamma)}} + (4.966\,\mathrm{MeV})H(^{15}N)_e\langle\sigma v\rangle_{^{15}\mathrm{N(p,\alpha)}} \\ &= (3.458\,\mathrm{MeV})\frac{(^{12}C)_e}{\tau_{\mathrm{p}}(^{12}C)} + (7.551\,\mathrm{MeV})\frac{(^{13}C)_e}{\tau_{\mathrm{p}}(^{13}C)} \\ &+ (9.055\,\mathrm{MeV})\frac{(^{14}N)_e}{\tau_{\mathrm{p}}(^{14}N)} + (4.966\,\mathrm{MeV})\frac{(^{15}N)_e}{\tau_{\mathrm{p}}(^{15}N)} \end{aligned} \tag{5.68}$$

From Eq. (5.62), we find

$$\begin{aligned}\frac{(^{12}C)_e}{\tau_{\mathrm{p}}(^{12}C)} &= \frac{(^{13}C)_e}{\tau_{\mathrm{p}}(^{13}C)} = \frac{(^{14}N)_e}{\tau_{\mathrm{p}}(^{14}N)} = \frac{(^{15}N)_e}{\tau_{\mathrm{p}}(^{15}N)} \\ &= \frac{\sum \mathrm{CNO1}}{\tau_{\mathrm{p}}(^{12}C) + \tau_{\mathrm{p}}(^{13}C) + \tau_{\mathrm{p}}(^{14}N) + \tau_{\mathrm{p}}(^{15}N)}\end{aligned} \tag{5.69}$$

Hence, the energy generation rate at equilibrium can be written as

$$\varepsilon^{e}_{\mathrm{CNO1}} = \frac{25.030\,\mathrm{MeV}}{\rho}\,\frac{\sum \mathrm{CNO1}}{\tau_{\mathrm{p}}(^{12}C) + \tau_{\mathrm{p}}(^{13}C) + \tau_{\mathrm{p}}(^{14}N) + \tau_{\mathrm{p}}(^{15}N)} \tag{5.70}$$

The sum of the lifetimes in the denominator is called the *cycle time*, and is almost entirely dominated by the long ^{14}N lifetime. Hence,

$$\begin{aligned}\varepsilon^{e}_{\mathrm{CNO1}} &\approx \frac{25.030\,\mathrm{MeV}}{\rho}\,\frac{\sum \mathrm{CNO1}}{\tau_{\mathrm{p}}(^{14}N)} = \frac{25.030\,\mathrm{MeV}}{\rho}\Big(\sum \mathrm{CNO1}\Big)H\langle\sigma v\rangle_{^{14}\mathrm{N(p,\gamma)}} \\ &= 25.030\,N_A\langle\sigma v\rangle_{^{14}\mathrm{N(p,\gamma)}}\left(\sum_i \frac{X_i}{M_i}\right)\frac{X_{\mathrm{H}}}{M_{\mathrm{H}}}\,\rho N_A \quad (\mathrm{MeV\,g^{-1}s^{-1}})\end{aligned} \tag{5.71}$$

where the sum is over all CNO1 nuclides. The energy generation rate in the CNO1 cycle at steady state is determined by the ^{14}N(p,γ)^{15}O reaction rate. This reaction is nonresonant for temperatures below $T = 0.1$ GK and, therefore, the temperature dependence of the energy generation rate is obtained from Eq. (3.90). For example, at $T = 25$ MK, characteristic of CNO burning on the upper main sequence, we obtain $\tau = 51.96$ and hence,

$$\varepsilon^{e}_{\mathrm{CNO1}}(T) = \varepsilon^{e}_{\mathrm{CNO1}}(T_0)\left(T/T_0\right)^{(\tau-2)/3} = \varepsilon^{e}_{\mathrm{CNO1}}(T_0)\left(T/T_0\right)^{16.7} \tag{5.72}$$

We are now in a position to compare the equilibrium energy generation rates of the pp1 chain and the CNO1 cycle. These processes will compete with each other in hydrogen-burning stars that contain initial CN seed nuclei. In Figure 5.12, the quantities $\varepsilon^{e}_{\mathrm{pp1}}/(\rho X^2_{\mathrm{H}})$ from Eq. (5.26) and $\varepsilon^{e}_{\mathrm{CNO1}}/(\rho X^2_{\mathrm{H}})$ from Eq. (5.71) are displayed versus temperature. The former expression is a function of temperature only (through the p(p,e$^+\nu$)d reaction rate), while the latter depends both on temperature (through the ^{14}N(p,γ)^{15}O reaction rate) and on the mass fractions of the CNO1 isotopes relative to the hydrogen mass fraction. For illustration purposes, values of $X_{\mathrm{H}} = 0.711$, $X_{^{12}\mathrm{C}} = 2.46 \times 10^{-3}$, $X_{^{14}\mathrm{N}} = 7.96 \times 10^{-4}$, and $X_{^{13}\mathrm{C}} = 2.98 \times 10^{-5}$ are chosen, which are representative of the solar system and

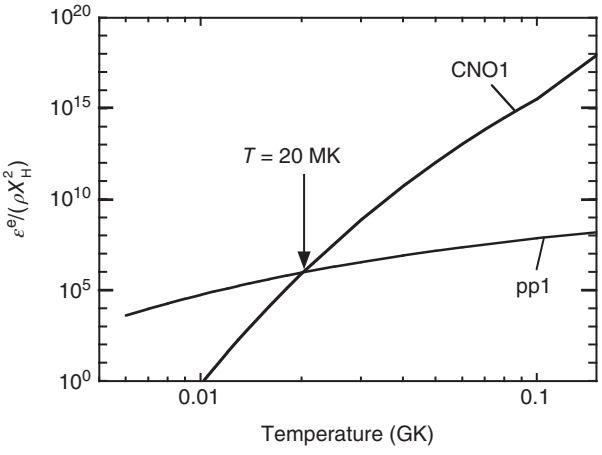

Figure 5.12 Equilibrium energy generation rates of the pp1 chain and the CNO1 cycle. The curve for the CNO1 cycle is calculated for a solar system composition (Lodders, 2003). For a different composition, the CNO1 curve shifts vertically. The rate of the $^{14}N(p,\gamma)^{15}O$ reaction is adopted from Runkle *et al.* (2005). The pp1 chain and the CNO1 cycle dominate for temperatures below and above $T = 20$ MK, respectively. The pp1 chain is the primary energy source in the Sun.

population I stars (Lodders, 2003). These initial seed abundances can be used in Eq. (5.71) since we assumed a closed CNO1 cycle [$\sum(X/M)$ = const]. For other values of X_i/M_i, the CNO1 curve shown in Figure 5.12 will shift vertically. For these conditions, the pp1 chain generates most of the nuclear energy for temperatures below $T = 20$ MK. At higher temperatures, most of the energy is produced in the CNO1 cycle. The temperature in the stellar interior depends on the stellar mass. We conclude that the pp chains dominate the energy production in all hydrogen burning stars with insignificant CNO seed abundances. In stars with significant CNO seed abundances, the pp chains will dominate in the cores of low-mass stars, while in stars of higher mass (slightly more massive than the Sun; Section 1.4.3) the CNO cycles are the dominant source of energy in the stellar core.

The different temperature dependence for the energy generation rate of the pp chains compared to the CNO cycles has a profound influence on the internal structure of a star. For example, if helium is mainly synthesized by the pp chains, then energy is transported through the central regions by radiation. In contrast, the rate of the CNO cycles is so sensitive to temperature that, when it is the dominant process, the energy-generating regions are unstable to convection, which becomes the main energy transport mechanism to the outer regions of the star.

Approach to Steady State in the CNO Cycles

We have so far considered only the steady state operation of the CNO1 cycle and will now investigate nonequilibrium situations. Two aspects are of special interest: (i) the approach to steady state in the CNO1 cycle, and (ii) the simultaneous

operation of all CNO cycles. The system of coupled differential equations describing the abundance changes of all CNO nuclides is similar in structure to Eqs. (5.50)–(5.55), but it is more complex because of the inclusion of oxygen and fluorine isotopes. Such a system of equations represents an example of a nuclear reaction network (Section 3.1.3). It can only be solved analytically if a number of simplifying assumptions are made (Clayton, 1983). With one exception, we will not make such assumptions but will instead compute the time evolution of CNO abundances numerically. For the numerical calculations described in this section, the assumption of constant temperature and density conditions is made. It must be emphasized that the internal temperature of a real star is changing during its evolution on the main sequence. However, in hydrostatic burning environments these changes occur slowly over long time periods. Therefore, the assumption of constant T and ρ, although not correct for a real star, is useful for obtaining physical insight into the nucleosynthesis and energy production.

We first consider the approach to steady state in the CNO1 cycle. The temperature and density are assumed to be $T = 25$ MK and $\rho = 100$ g/cm^3, respectively. Such values are typical of CNO burning on the upper main sequence. For the initial composition, we assume $X_H^0 = 0.70$, $X_{^4\mathrm{He}}^0 = 0.28$, and $X_{^{12}\mathrm{C}}^0 = 0.02$, that is, only ^{12}C is initially present as a CNO seed. The reaction network, including all four CNO cycles, is solved until the hydrogen concentration falls below $X_\mathrm{H} = 0.001$. The time evolution of abundances is shown in Figure 5.13a. As expected from the operation of the CNO cycles, the hydrogen abundance declines from its initial value, while the helium abundance increases. Hydrogen is exhausted after 30 million years. The initial carbon abundance is steadily depleted and converted to other nuclides. It can be seen that, for the chosen temperature and density conditions, steady state in the CNO1 cycle is reached after only 4000 years. The abundances of ^{12}C, ^{13}C, ^{14}N, and ^{15}N remain then constant until the end of the calculation. The most abundant CNO nuclide in equilibrium is ^{14}N, while the least abundant one is ^{15}N because of its small lifetime versus destruction by the (p,α) reaction. For example, from the numerical results shown in Figure 5.13a one obtains $(X_{^{12}\mathrm{C}}/X_{^{14}\mathrm{N}})_e = 0.008$, and thus the ratio of number abundances is $(^{12}C/^{14}N)_e = 0.008(M_{^{14}\mathrm{N}}/M_{^{12}\mathrm{C}}) \approx 0.01$, in agreement with the results obtained analytically (Figure 5.11a).

The conversion of initial ^{12}C seed nuclei to ^{14}N proceeds at a rate determined by the ^{12}C lifetime, which, for the chosen conditions, amounts to $\tau_\mathrm{p}(^{12}\mathrm{C}) = 350$ y. It is apparent from Figure 5.13a that the ^{12}C abundance decays with a $1/e$ time approximately equal to $\tau_\mathrm{p}(^{12}\mathrm{C})$, while the CNO1 cycle reaches steady state after several ^{12}C half-lives. There is a small leakage of material from the CNO1 to the CNO2 cycle, as can be seen from the increasing ^{16}O abundance. However, it remains insignificant compared to the ^{14}N abundance. The time evolution of the nuclear energy generation rate is shown in Figure 5.13b. The energy generation rate falls by more than an order of magnitude until equilibrium is reached after about 4000 years. For example, at $t = 10^4$ y, we obtain from the numerical results presented in Figure 5.13b a value of $\varepsilon_\mathrm{CNO} \approx 2.2 \times 10^{10}$ MeV g^{-1}s^{-1}, in agreement with the

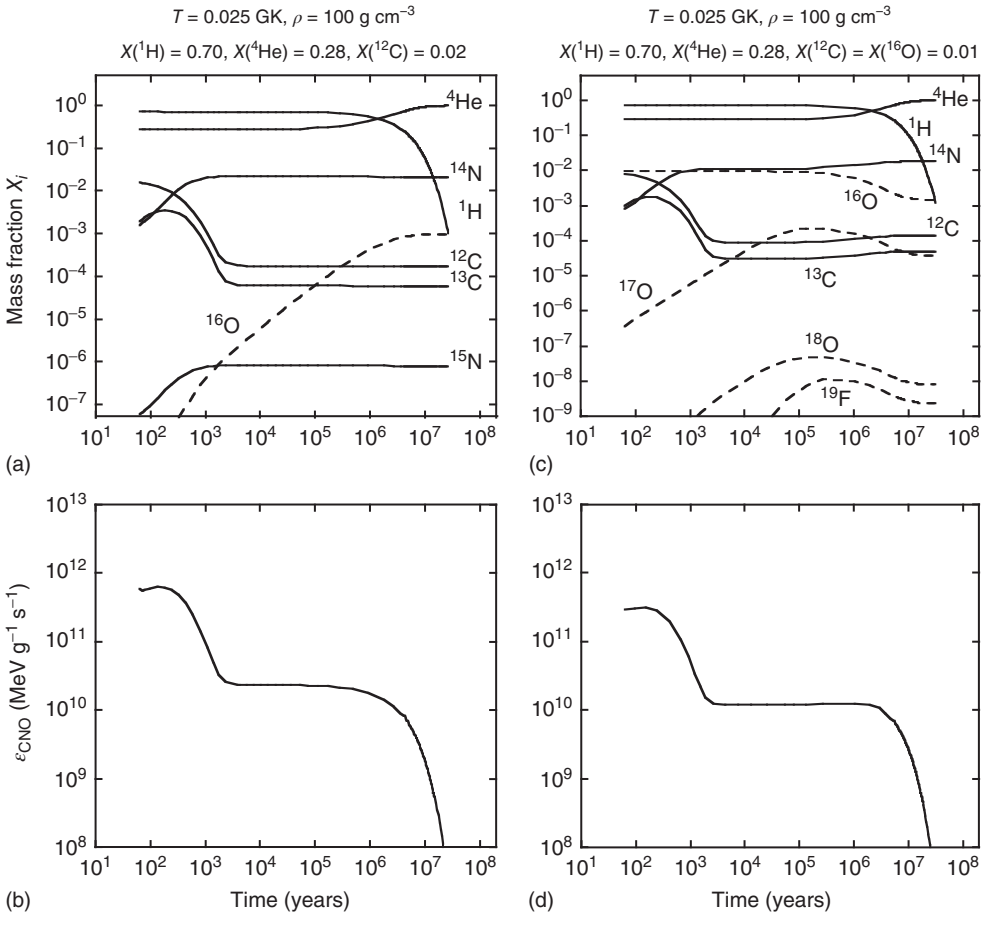

Figure 5.13 Time evolution of abundances and nuclear energy generation rate for two different compositions: (a), (b) $X^0_{\rm H} = 0.70$, $X^0_{^4{\rm He}} = 0.28$, $X^0_{^{12}{\rm C}} = 0.02$, and (c), (d) $X^0_{\rm H} = 0.70$, $X^0_{^4{\rm He}} = 0.28$, $X^0_{^{12}{\rm C}} = X^0_{^{16}{\rm O}} = 0.01$. For the temperature and density, constant values of $T = 25$ MK and $\rho = 100$ g/cm^3 are assumed in both cases. All curves shown are obtained by solving the reaction network numerically. The calculations are terminated when the hydrogen mass fraction falls below $X_{\rm H} = 0.001$.

steady state value calculated analytically from Eq. (5.71). For times beyond $t = 3 \times 10^5$ y, the energy production rate falls because the abundance of the hydrogen fuel decreases.

We consider next the effects caused by a change in composition. The temperature and density are the same as before ($T = 25$ MK, $\rho = 100$ g/cm^3). For the initial composition, we assume $X^0_{\rm H} = 0.70$, $X^0_{^4{\rm He}} = 0.28$, $X^0_{^{12}{\rm C}} = 0.01$, and $X^0_{^{16}{\rm O}} = 0.01$, that is, both ^{12}C and ^{16}O are now present with equal concentrations as seed nuclei. The reaction network is again solved until hydrogen is exhausted ($X_{\rm H} < 0.001$).

The results are displayed in Figure 5.13c. The hydrogen and helium abundance evolves similar as before. The abundances of ^{12}C, ^{13}C, and ^{14}N again reach steady state after about 4000 years, with ^{14}N by far the most abundant species. The ^{15}N abundance is omitted in Figure 5.13c since it is very small. At $t = 10^4$ y, the ratio of ^{12}C to ^{14}N mass fractions is the same as in the previous network calculation $[(X_{^{12}\mathrm{C}}/X_{^{14}\mathrm{N}})_e = 0.008]$. At this point, only vanishingly small amounts of ^{16}O have been consumed and little else has changed because of the presence of ^{16}O as seed nucleus. Recall that the ^{16}O(p,γ)^{17}F reaction is one of the slowest processes in the CNO cycles (Figure 5.10). Therefore, it takes a significant time for ^{16}O to be depleted. Small, but noticeable, changes occur after $t = 10^4$ y. The ^{16}O abundance starts to decline, while at the same time the ^{17}O, ^{18}O, and ^{19}F abundances start to increase. After $t = 10^5$ y, the ^{12}C, ^{13}C, and ^{14}N abundances increase, indicating a transfer of catalytic material from the CNO2 cycle to the CNO1 cycle by means of the strong ^{15}N(p,α)^{12}C reaction. After $t = 10^7$ y, individual CNO abundances stay constant and steady state has been achieved in all CNO cycles. At this point, the abundance ratios obtained from Figure 5.13c agree with those calculated analytically from the ratio of lifetimes (see Eq. (5.61)). For example, one finds $(^{17}O/^{16}O)_e = \langle\sigma v\rangle_{^{16}\mathrm{O(p,}\gamma)}/[\langle\sigma v\rangle_{^{17}\mathrm{O(p,}\gamma)} + \langle\sigma v\rangle_{^{17}\mathrm{O(p,}\alpha)}] = 0.025$, consistent with the value derived from Figure 5.13c. The ^{18}O and ^{19}F abundances are very small, indicating a small leakage from the CNO2 cycle to the CNO3 and CNO4 cycles at $T = 0.025$ GK. The presence of ^{16}O seed nuclei has changed the final ^{12}C, ^{13}C, and ^{14}N abundances by less than 20% compared to the earlier network calculation with only ^{12}C as seed nucleus (Figure 5.13a). These results show that, despite the simultaneous operation of all CNO cycles, the initial ^{12}C and ^{16}O seed nuclei are transformed to ^{14}N if the time is sufficient for achieving steady state.

The time evolution of the energy generation rate is shown in Figure 5.13d. Only about half of the energy per unit time is produced compared to the results shown in Figure 5.13b since only half of the initial ^{12}C seed nuclei are present. At times of $t = 10^5$ y, 10^6 y, and 10^7 y, the energy generation rate displayed in Figure 5.13d amounts to $\varepsilon_{\mathrm{CNO}} = 1.2 \times 10^{10}$ MeV g^{-1}s^{-1}, 1.3×10^{10} MeV g^{-1}s^{-1}, and 2.7×10^9 MeV g^{-1}s^{-1}, respectively. Interestingly, these values are very close (within 10%) to those calculated analytically from Eq. (5.71) assuming a closed CNO1 cycle in steady state, with only ^{12}C as initial seed nuclei. Hence, after the CNO1 cycle reaches steady state, the energy generation rate of the simultaneous operation of all CNO cycles is approximately equal to that of the CNO1 cycle alone, that is, $\varepsilon_{\mathrm{CNO}} \approx \varepsilon^e_{\mathrm{CNO1}}$. This circumstance is explained by several factors. First, the (p,α) reactions on the branching point nuclides ^{15}N, ^{17}O, ^{18}O, and ^{19}F are considerably faster compared to the competing (p,γ) reactions (Figure 5.9), which tends to increase the CNO1 abundances, and specifically that of ^{14}N, at the expense of the abundances in the other cycles. Second, the CNO1 cycle reactions involve lower Coulomb barriers and, therefore, are generally faster compared to the reactions of the other cycles (Figure 5.10). Third, the Q-values in the CNO1 cycle are larger compared to the energy released by processes that complete the CNO2 cycle ($Q_{^{16}\mathrm{O(p,}\gamma)} = 0.600$ MeV; $Q_{^{17}\mathrm{F}(\beta^+\nu)} = 2.761$ MeV; $Q_{^{17}\mathrm{O(p,}\alpha)} = 1.192$ MeV). Only in special cases, when the initial oxygen abundance is overwhelmingly larger than

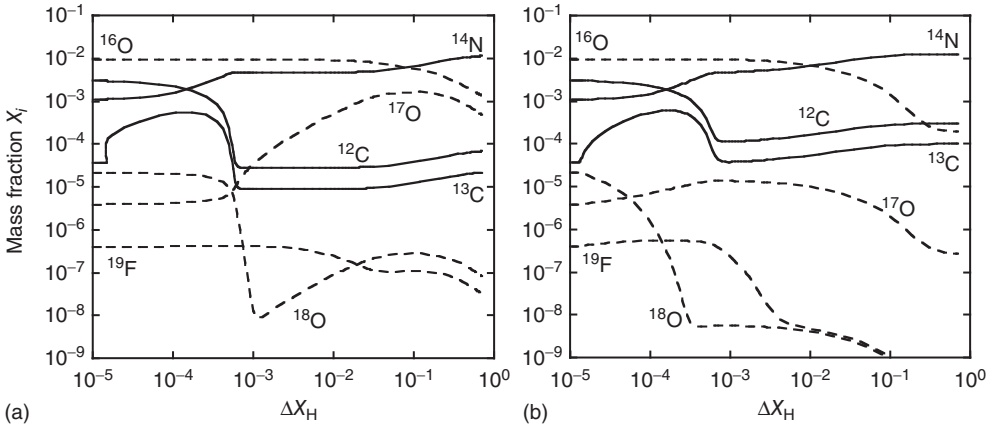

Figure 5.14 Abundance evolutions versus the amount of hydrogen consumed for two different constant temperatures: (a) $T = 20$ MK, and (b) $T = 55$ MK. The density ($\rho = 100$ g/cm^3) and the initial composition (solar) is the same for both cases. All curves shown are obtained by solving the reaction network numerically. The calculations are terminated when the hydrogen mass fraction falls below $X_H = 0.001$.

the initial carbon or nitrogen abundance, and if oxygen has not yet reached steady state, will the assumption of $\varepsilon_{CNO} \approx \varepsilon^e_{CNO1}$ be invalid.

The results of two network calculations, performed for different constant temperatures of $T = 20$ and 55 MK, a constant density of $\rho = 100$ g/cm^3 and a solar initial composition ($X^0_H = 0.706$; $\sum X^0_{CNO} = 0.0137$; $^{12}C{:}^{14}N{:}^{16}O = 10:3:24$), are displayed in Figure 5.14. The abundance evolutions are shown versus the amount of hydrogen consumed, $\Delta X_H = X^0_H - X_H(t)$, with time increasing from left to right. Some similarities between the two calculations can be noticed. All CNO abundances reach steady state at the end of the calculations (when $X_H < 10^{-3}$), although this is not readily apparent in Figure 5.14a if the ^{16}O, ^{17}O, ^{18}O, and ^{19}F abundances are plotted versus ΔX_H. The ^{14}N abundance increases steadily, first as a result of ^{12}C to ^{14}N conversion in the CNO1 cycle, and at a later time because of ^{16}O to ^{14}N conversion in the CNO2 cycle. Thus, ^{14}N is enhanced while ^{12}C and ^{16}O are depleted at the end of the calculation. The abundances of ^{18}O and ^{19}F are also depleted during the nuclear burning, while the final ^{13}C abundance changes by less than a factor of two compared to its initial abundance. The evolution of ^{17}O is interesting. At $T = 20$ MK, the nuclear burning strongly enhances the ^{17}O abundance by the time hydrogen is exhausted, while at $T = 55$ MK its abundance is depleted. The two calculations predict final ^{17}O abundances that differ by more than three orders of magnitude. In other words, the ^{17}O abundance is very sensitive to the hydrogen burning temperature. The higher the temperature, the larger the reaction rates and, hence, the time it takes to reach hydrogen exhaustion is conaiderably shorter at $T = 55$ MK compared to $T = 20$ MK.

There is significant observational evidence for the operation of the CNO cycles during hydrogen burning. In many stars, the products of the nucleosynthesis

have been carried by turbulent convection from the stellar interior to the surface. Consider, for example, the isotopes of carbon. Stars that form from matter with a solar composition will initially exhibit an abundance ratio of $(^{13}C/^{12}C)_{\odot} = 0.011$ at their surface. Once CNO steady state has been achieved, we expect, according to Figure 5.11a, an abundance ratio of $(^{13}C/^{12}C)_{e} = 0.25$ in the hydrogen burning region. Note that the latter value is insensitive to temperature below $T < 0.1$ GK. Many stars show (^{13}C/^{12}C) surface abundance ratios between these two values, indicating that a fraction of the hydrogen burning matter has been transported to the stellar surface. Some stars even display $(^{13}C/^{12}C)$ surface abundance ratios close to the steady state value (Sneden, Pilachowski, and Vandenberg, 1986). Such observations not only provide evidence for CNO burning, but also demonstrate that most of the matter at the stellar surface must have been cycled through the hydrogen burning region in the stellar interior. The operation of the CNO cycles in AGB stars is believed to be a major source of ^{13}C and ^{14}N in the universe (see Table 5.2).

We will now briefly summarize the experimental situation regarding measurements of CNO-cycle reactions. At the upper temperature range characteristic of hydrostatic hydrogen burning ($T \approx 55$ MK), the Gamow peaks for the ^{12}C + p and ^{19}F + p reactions are located at $E_0 \pm \Delta/2 = 60 \pm 20$ keV and 80 ± 24 keV, respectively. From the experimental point of view, the CNO reactions can be divided into two groups, depending on whether measured cross sections exist in the Gamow peak or not. For example, the reactions ^{13}C(p,γ)^{14}N, ^{14}N(p,γ)^{15}O, ^{15}N(p,γ)^{16}O, and ^{16}O(p,γ)^{17}F have been measured down to center-of-mass energies of 100 keV, 93 keV, 130 keV, and 130 keV, respectively (Angulo *et al.*, 1999). In these cases, no data exist in the Gamow peak for hydrostatic hydrogen burning ($T \leq 55$ MK) and, hence, the S-factor has to be extrapolated down to the energy range of interest, either by a polynomial expansion or by using a suitable nuclear reaction model (Section 3.2.1). The S-factors for the above reactions are determined by nonresonant contributions (tails of broad resonances or direct capture) at $E < 100$ keV. Measurements of the important ^{14}N(p,γ)^{15}O reaction are reported in Formicola *et al.* (2004) and Runkle *et al.* (2005). The ^{17}O(p,γ)^{18}F, ^{18}O(p,γ)^{19}F, and ^{19}F(p,γ)^{20}Ne reactions have also not been measured down to the relevant Gamow-peak region. In these cases, the reaction rates at $T \leq 55$ MK are expected to be dominated by unobserved (low-lying) narrow resonances. These contributions have been estimated using all the available nuclear structure information for the corresponding states in the compound nuclei. On the other hand, the ^{12}C(p,γ)^{13}N, ^{15}N(p,α)^{12}C, and ^{18}O(p,α)^{15}N reactions have all been measured down to energies of about 70 keV, covering at least part of the Gamow peak for the higher temperatures near $T \approx 55$ MK. The first two reactions are nonresonant, while the latter process is influenced both by resonant and nonresonant contributions to the reaction mechanism. The ^{17}O(p,α)^{14}N reaction represents an exceptional case. At temperatures of $T = 18$–55 MK, the most important contribution to the reaction rates originates from a narrow resonance located at $E_r^{\mathrm{cm}} = 65$ keV. This particular resonance has been observed and represents one of the weakest resonances measured in the laboratory (with $\omega\gamma_{\mathrm{p}\alpha} = (4.7 \pm 0.8) \times 10^{-9}$ eV;

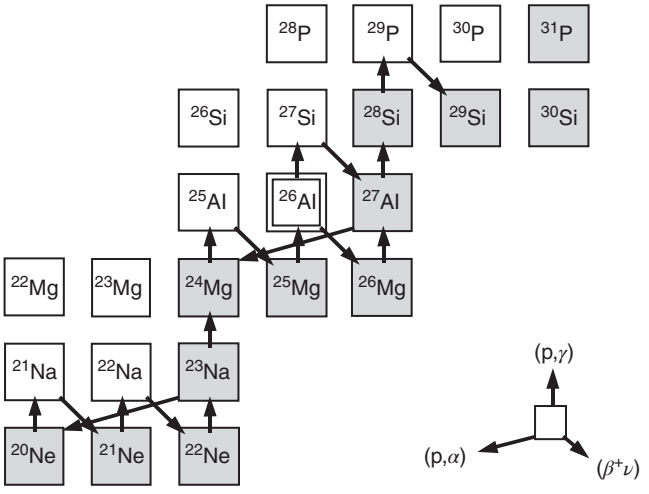

Figure 5.15 Nuclear interactions in the mass $A \geq 20$ region during hydrostatic hydrogen burning. Stable nuclides are shown as shaded squares. The key relates an arrow to a specific interaction (proton capture, (p,α) reaction, or β^+-decay). The nuclide ^{26}Al can be formed either in its ground state or in its isomeric state ($E_x = 228$ keV).

Blackmon *et al.*, 1995). For uncertainties in CNO reaction rates, the reader is referred to Angulo *et al.* (1999) and Sallaska *et al.* (2013). A discussion of the influence of reaction rate uncertainties on the evolution of CNO abundances is presented in Arnould, Goriely, and Jorissen (1999).

5.1.3
Hydrostatic Hydrogen Burning Beyond the CNO Mass Region

The nucleosynthesis in hydrostatic hydrogen burning not only involves nuclides in the CNO mass range, but heavier nuclides as well. The most likely reactions to occur in the mass region above $A = 20$ are shown in Figure 5.15. In the following, we will discuss some general properties of hydrostatic hydrogen burning involving heavier nuclides and will explain why some processes are more likely to occur than others. It must be stressed that the CNO and $A \geq 20$ mass ranges are disconnected. In other words, preexisting CNO seed nuclei will be transformed to other nuclei in the CNO mass range only. In principle, the ^{19}F(p,γ)^{20}Ne reaction could provide a link between the CNO and $A \geq 20$ mass ranges. However, its reaction rate is at least three orders of magnitude smaller compared to the competing ^{19}F(p,α)^{16}O reaction (Figure 5.9). Consequently, hydrostatic hydrogen burning beyond the CNO mass range must start from preexisting seed nuclei with masses of $A \geq 20$.

These nuclides are transformed by β-decays, (p,γ), and (p,α) reactions, and the competition between these processes defines the resulting nucleosynthesis paths in the nuclidic chart. As was the case in the previous section, proton-induced

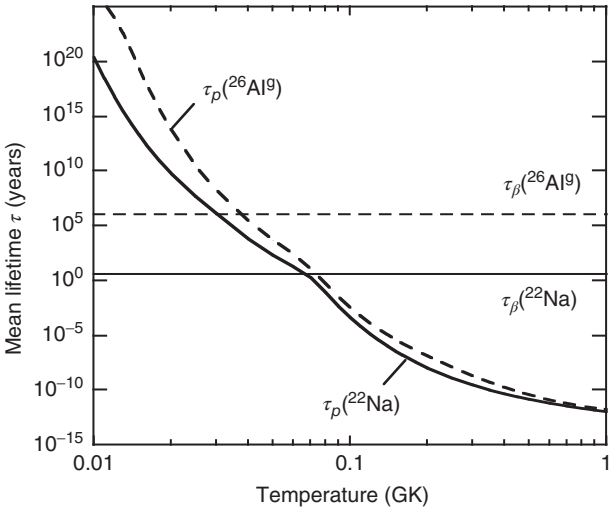

Figure 5.16 Mean lifetimes of ^{22}Na (solid lines) and ^{26}Al^{g} (dashed lines) versus temperature. The curves are calculated for the conditions $\rho = 100$ g/cm^3 and $X_{\rm H}/M_{\rm H} = 1$. The mean lifetimes for the β^+-decays, $\tau_\beta(^{22}{\rm Na})$ and $\tau_\beta(^{26}{\rm Al}^g)$, are independent of temperature and density for the conditions of hydrostatic hydrogen burning.

reactions involving unstable target nuclei play no significant role in hydrostatic hydrogen burning since the competing β-decays are considerably faster (with τ_β of seconds to minutes in most cases). This conclusion applies even to long-lived nuclides, such as ^{22}Na with a half-life of $T_{1/2} = 2.6$ y. The mean lifetime of ^{22}Na versus destruction by the (p,γ) reaction is compared in Figure 5.16 with the mean lifetime of the ^{22}Na β^+-decay (Example 3.1). A density of $\rho = 100$ g/cm^3 and $X_{\rm H}/M_{\rm H} = 1$ are assumed. The quantity $\tau_\beta(^{22}{\rm Na})$ is independent of temperature and density for the conditions considered here (Section 1.8.4), while $\tau_{\rm p}(^{22}{\rm Na})$ decreases with increasing T and ρ (see Eq. (3.22)). The ^{22}Na(p,γ)^{23}Mg reaction dominates over the competing β^+-decay only at $T > 0.065$ GK, which is well above the temperature range characteristic of most hydrostatic hydrogen burning environments. The nucleus ^{26}Al represents an important exception. The half-life of the ground state is $T_{1/2} = 7.2 \times 10^5$ y, which is sufficiently long for proton capture to compete with the β^+-decay. The mean lifetimes $\tau_\beta(^{26}{\rm Al}^g)$ and $\tau_{\rm p}(^{26}{\rm Al}^g)$ are shown in Figure 5.16 (the superscript g labels the ground state). It is apparent that below $T = 37$ MK the ^{26}Al^g nucleus is mainly destroyed by β^+-decay, while the (p,γ) reaction dominates at higher temperatures. In other words, both processes will be important in hydrostatic hydrogen burning. An additional complication arises because of the existence of an isomeric state in ^{26}Al at $E_x = 228$ keV (Figure 1.15). This level, with a half-life of $T_{1/2} = 6.3$ s, is also produced in hydrogen burning. As explained in Section 1.7.5, the ground state, ^{26}Al^g, and the isomeric state, ^{26}Al^m, do not come into equilibrium at temperatures below $T = 0.4$ GK and hence, have to be treated as two separate species in the reaction network describing hydrostatic hydrogen burning.

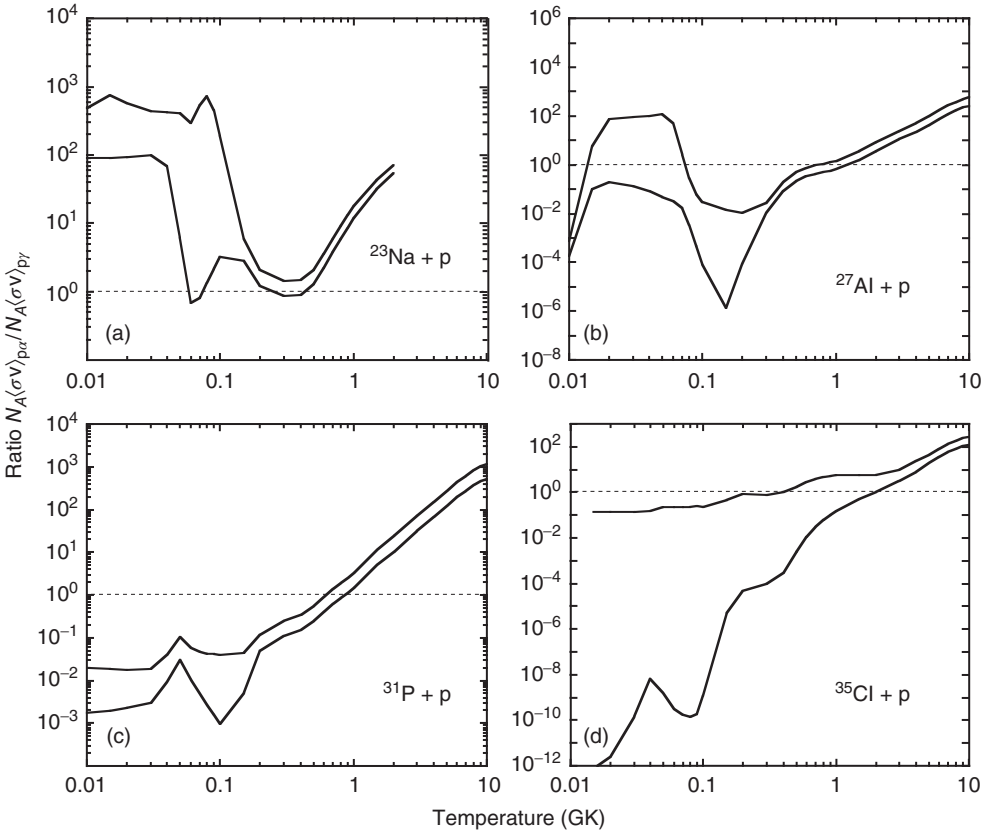

Figure 5.17 Branching ratio $B_{p\alpha/p\gamma} = N_A\langle\sigma v\rangle_{(p,\alpha)}/N_A\langle\sigma v\rangle_{(p,\gamma)}$ versus temperature for the reactions (a) ^{23}Na + p, (b) ^{27}Al + p, (c) ^{31}P + p, and (d) ^{35}Cl + p. The two solid lines in each panel represent the upper and lower boundaries of $B_{p\alpha/p\gamma}$. The area between the solid lines indicates the uncertainty in $B_{p\alpha/p\gamma}$ that is caused by unknown contributions to the (p,γ) and (p,α) reaction rates.

For a number of nuclides in the mass $A = 20$–40 range, most notably ^{23}Na, ^{27}Al, ^{31}P, and ^{35}Cl, the (p,α) reaction channel is energetically allowed and the (p,γ) and (p,α) reactions will compete. If the reaction rate branching ratio $B_{p\alpha/p\gamma} = N_A\langle\sigma v\rangle_{(p,\alpha)}/N_A\langle\sigma v\rangle_{(p,\gamma)}$ is sufficiently large, reaction cycles similar to the CNO cycles may develop. These processes are sometimes referred to as NeNa, MgAl, SiP, and SCl cycles. However, the current (p,γ) and (p,α) reaction rate uncertainties have to be considered carefully before drawing such conclusions. The quantity $B_{p\alpha/p\gamma}$ is displayed in Figure 5.17 for the branching point nuclides ^{23}Na, ^{27}Al, ^{31}P, and ^{35}Cl. The solid lines in each panel indicate the upper and lower limits of $B_{p\alpha/p\gamma}$ caused by unobserved narrow resonances in the (p,γ) and (p,α) reactions. Below $T = 55$ MK, the (p,α) reaction on ^{23}Na dominates over the competing (p,γ) reaction and hence, a NeNa cycle may

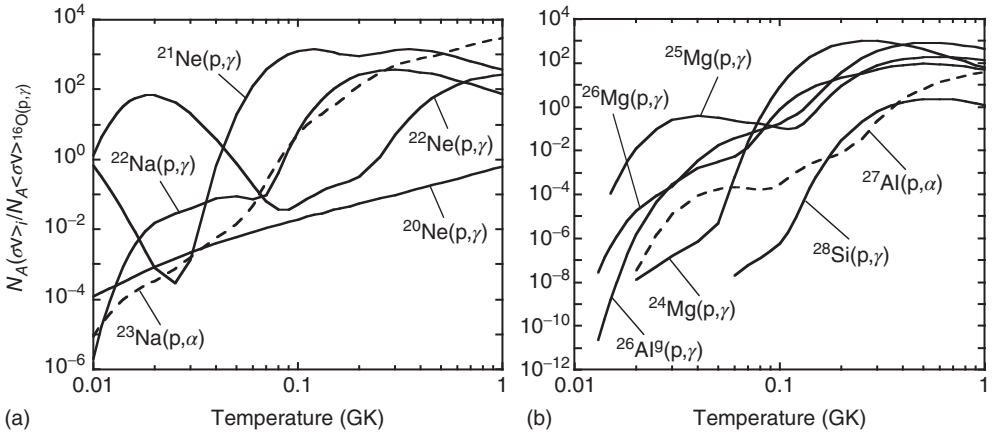

Figure 5.18 Rates of proton-induced reactions versus temperature in two mass regions: (a) NeNa, and (b) MgAlSi. For a better comparison, the values of $N_A\langle\sigma v\rangle$ are normalized to the rate of the $^{16}O(p,\gamma)^{17}F$ reaction.

develop (but only if the cycling time is shorter than the duration of hydrogen burning). The situation is not as clear for the other branching point nuclides. For ^{27}Al, the quantity $B_{p\alpha/p\gamma}$ ranges from about 0.04 to 100 below $T = 55$ MK and, therefore, current reaction rate uncertainties do not permit an unambiguous conclusion regarding the existence of a MgAl cycle. For the nuclides ^{31}P and ^{35}Cl, on the other hand, we obtain $B_{p\alpha/p\gamma} < 1$ at temperatures characteristic of hydrostatic hydrogen burning and hence, closed SiP and SCl cycles do not exist.

The rates of various reactions in the $A \geq 20$ mass range are compared in Figure 5.18 to the $^{16}O(p,\gamma)^{17}F$ reaction rate. Recall that the latter process represents the slowest reaction in the CNO mass region (Figure 5.10). It can be seen that below $T = 55$ MK, as a result of the increasing Coulomb barrier, most reactions involving heavier target nuclei are considerably slower than the $^{16}O(p,\gamma)^{17}F$ reaction. The only two exceptions are the proton captures on ^{21}Ne and ^{22}Ne. Therefore, we expect reactions in the $A \geq 20$ mass range to be insignificant contributors to the overall nuclear energy generation rate in hydrostatic hydrogen burning. Nevertheless, an understanding of the nucleosynthesis is important for the interpretation of certain abundance observations that are discussed below.

The evolution of abundances in the mass range $A \geq 20$ versus the amount of hydrogen consumed is displayed in Figure 5.19. The results are obtained from two network calculations that are performed for constant temperatures of $T = 25$ and 55 MK, a constant density of $\rho = 100$ g/cm^3, and a solar initial composition ($X^0_H = 0.706$; $\sum X^0_{A=20-40} = 0.00375$). The most abundant seed nuclei in the $A = 20$–40 mass range are ^{20}Ne, ^{28}Si, ^{24}Mg, ^{32}S, and ^{22}Ne. We will first discuss the situation at $T = 25$ MK. At this temperature, hydrogen is exhausted

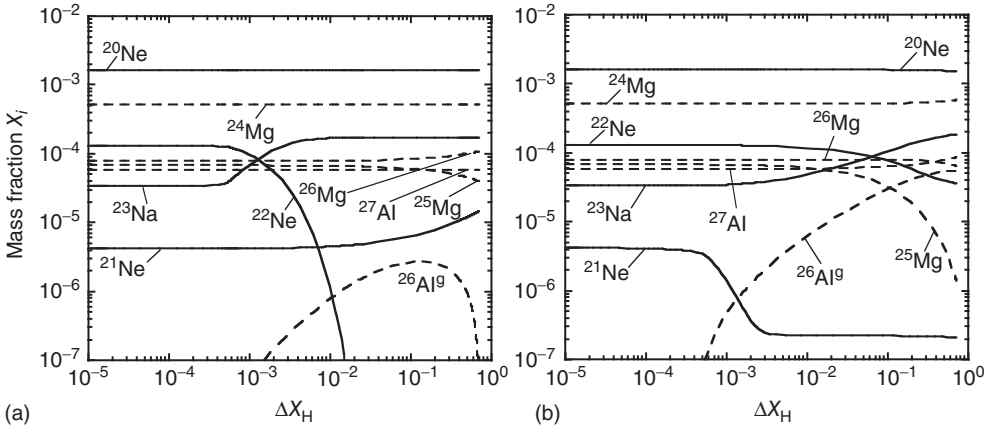

Figure 5.19 Abundance evolutions in the $A \geq 20$ mass region versus the amount of hydrogen consumed for two different constant temperatures: (a) $T = 25$ MK, and (b) $T = 55$ MK. The density ($\rho = 100$ g/cm^3) and the initial composition (solar) is the same for both cases. All curves shown are obtained by solving the reaction network numerically. The calculations are terminated when the hydrogen mass fraction falls below $X_H = 0.001$.

($X_H < 10^{-3}$) after $t \approx 5 \times 10^7$ y. According to Figure 5.18, the fastest reactions in the $A \geq 20$ mass range are ^{22}Ne(p,γ)^{23}Na and ^{25}Mg(p,γ)^{26}Al. Therefore, the abundances of ^{22}Ne and ^{25}Mg are depleted, while those of ^{23}Na and ^{26}Al^g increase with time. At this temperature, the nuclide ^{26}Al^g is mainly destroyed via β^+-decay (Figure 5.16). Thus, its abundance, after reaching a maximum, starts to decline. As a result, the abundance of the daughter nucleus ^{26}Mg increases. The ^{20}Ne abundance stays almost constant during the calculation since the ^{20}Ne(p,γ)^{21}Na reaction is slow. Nevertheless, a small amount of ^{20}Ne is depleted, giving rise to a noticeable increase in the abundance of the rare isotope ^{21}Ne, which is produced via ^{21}Na($\beta^+\nu$)^{21}Ne. Other reactions, including ^{24}Mg + p and ^{27}Al + p, are too slow to cause any abundance changes. The same applies to the ^{23}Na + p reactions. At $T = 25$ MK, the mean lifetime of ^{23}Na versus destruction by the (p,α) reaction is $\tau_p(^{23}\text{Na}) \approx 2 \times 10^9$ y. This lifetime far exceeds the time for hydrogen exhaustion. Hence, ^{20}Ne is not produced and, in particular, no NeNa cycle develops, even though the ^{23}Na(p,α)^{20}Ne reaction is faster than the ^{23}Na(p,γ)^{24}Mg reaction (Figure 5.17). Also, for the assumed conditions, no significant nuclear transformations occur in the $A \geq 28$ mass range. At the end of the network calculation, ^{21}Ne, ^{23}Na, and ^{26}Mg are overproduced, while ^{22}Ne and ^{25}Mg have been depleted.

We will now discuss the situation at $T = 55$ MK. At this temperature, hydrogen is exhausted after only $t \approx 510$ y. The temperature is sufficiently high for more nuclear reactions to take part in the nucleosynthesis. As was the case before, ^{22}Ne is converted to ^{23}Na. It can be seen that, contrary to the results obtained at $T = 25$ MK, the ^{22}Ne abundance is not entirely destroyed. This occurs because the ^{20}Ne(p,γ)^{21}Na reaction, although still the slowest process

in the NeNa region (Figure 5.18), is now fast enough to initiate the chain ^{20}Ne(p,γ)^{21}Na($\beta^+\nu$)^{21}Ne(p,γ)^{22}Na($\beta^+\nu$)^{22}Ne. Indeed, the ^{20}Ne abundance is slightly depleted, as can be seen in Figure 5.19b. The mean lifetime of ^{23}Na versus destruction by protons is $\tau_p(^{23}\text{Na}) \approx 100$ y. A fraction of ^{23}Na nuclei is transformed to ^{20}Ne, although the total ^{20}Ne abundance declines because of the destruction via ^{20}Ne(p,γ)^{21}Na. Nevertheless, a closed NeNa cycle does not develop since the mean lifetime of ^{20}Ne is $\tau_p(^{20}\text{Ne}) \approx 600$ y, which is close to the time for hydrogen exhaustion. The leakage out of the NeNa mass region via ^{23}Na(p,γ)^{24}Mg is seen in Figure 5.19b as an increase in the ^{24}Mg abundance. The isotope ^{24}Mg is not destroyed, because the ^{24}Mg(p,γ)^{25}Al reaction is the slowest process in the $A \leq 27$ range, with a mean lifetime of $\tau_p(^{24}\text{Mg}) \approx 75\,000$ y. On the other hand, ^{25}Mg is converted to ^{26}Al^g via the ^{25}Mg(p,γ)^{26}Al reaction. At this temperature, ^{26}Al^g is mainly destroyed by the ^{26}Al^g(p,γ)^{27}Si reaction. However, the mean lifetime of ^{26}Al^g amounts to $\tau_p(^{26}\text{Al}^g) \approx 1000$ y and, therefore, it has little time to decay to ^{26}Mg. The ^{26}Mg(p,γ)^{27}Al reaction is now fast enough to cause the depletion of ^{26}Mg and the production of ^{27}Al, as can be seen in Figure 5.19b. The ^{27}Al + p reactions play only a minor role [$\tau_p(^{27}\text{Al}) \approx 10\,000$ y]. As was the case at $T = 25$ MK, nuclear transformations in the $A \geq 28$ mass range are unimportant. In summary, ^{23}Na, ^{26}Al^g, and ^{27}Al are enhanced, while ^{21}Ne, ^{22}Ne, ^{25}Mg, and ^{26}Mg are depleted at the end of the network calculation.

Hydrostatic hydrogen burning in the mass $A \geq 20$ range is important for the interpretation of Ne, Na, Mg, and Al abundance observations in stars. The relative isotopic and elemental abundances depend, as shown above, on the conditions of temperature and density in the hydrogen burning region. For these species to be observed, either in stellar atmospheres or in presolar grains, they have to be transported from the hydrogen burning region to the stellar surface. Hence, such abundance observations provide important clues regarding stellar evolution and stellar mixing processes. Accurate thermonuclear reaction rates are required when comparing abundances from stellar models with those from observations. Hydrostatic hydrogen burning in the mass $A \geq 20$ range is also of interest for the Galactic origin of the radioisotope ^{26}Al. It seems likely that a fraction of the observed ^{26}Al originates from Wolf–Rayet stars, where it is synthesized during hydrostatic core hydrogen burning at temperatures of $T = 35$–45 MK (Section 1.7.5).

Finally, we will summarize the experimental situation regarding measurements of reactions in the NeNa and MgAl region. At the upper temperature range characteristic of hydrostatic hydrogen burning ($T \approx 55$ MK), the Gamow peaks for the ^{20}Ne + p and ^{27}Al + p reactions are located at $E_0 \pm \Delta/2 = 80 \pm 23$ keV and 95 ± 25 keV, respectively. None of the NeNa or MgAl reactions have been measured down to such low energies. To estimate the total reaction rates at low temperatures, it becomes therefore important to measure directly, at higher energies, as many different resonant and nonresonant reaction components as possible (narrow resonances, broad resonances, and direct processes). In addition, indirect reaction studies populating compound levels located between

the proton threshold and the lowest lying observed resonance are of crucial importance. Despite these time-consuming experimental efforts, it must be realized that the rates of certain reactions in the mass $A = 20$–40 range still have appreciable uncertainties. The ^{20}Ne(p,γ)^{21}Na reaction rate is determined by the tail of a subthreshold state (Example 2.1) and by direct radiative capture. The present reaction rate uncertainties range from 40% to a factor of two below $T = 55$ MK. The ^{24}Mg(p,γ)^{25}Al reaction proceeds mainly through an observed narrow resonance at $E_r^{\rm cm} = 214$ keV (Example 3.7 and Figure 3.29) and via direct radiative capture. With an uncertainty of $\leq$ 20% below $T = 55$ MK, the rate of this reaction is among the most precisely known in the $A = 20$–40 region (Powell *et al.*, 1999). All other reaction rates in the NeNa and MgAl region are strongly influenced by unobserved narrow resonances, with rate uncertainties amounting in some cases to orders of magnitude. Significant efforts are at present underway to detect the most important of these unobserved resonances. Their resonance strengths are expected to be far smaller compared to the strength of the $E_r^{\rm cm} = 149$ keV resonance in ^{26}Mg(p,γ)^{27}Al, which represents one of the weakest measured (p,γ) resonances [$\omega\gamma_{\rm p\gamma} = (8 \pm 3) \times 10^{-8}$ eV; Iliadis *et al.*, 1990]. Such experiments are a challenge to the nuclear experimentalist (Chapter 4). A discussion of the influence of reaction rate uncertainties on the evolution of abundances in the NeNa and MgAl regions is given in Arnould, Goriely, and Jorissen (1999).

5.2 Hydrostatic Helium Burning

The second most abundant nuclide in the universe is ^{4}He. In Section 5.1 we discussed how ^{4}He is synthesized during the hydrogen burning phase. When all the hydrogen is consumed in the core, the star will contract and the central temperature will increase. At some point, the helium in the core is ignited and undergoes nuclear transformations. The end products of these processes are ^{12}C and ^{16}O, which represent the fourth and third most abundant nuclides, respectively, in the universe. Helium burning is the last core burning stage for stars in the mass range of $0.4\,M_\odot \lesssim M \lesssim 9\,M_\odot$ (Section 1.4.3 and Figure 1.4).

How exactly the transformation from ^{4}He to ^{12}C and ^{16}O comes about has not been understood for some time. The observation that no stable nuclides with mass numbers of $A = 5$ and $A = 8$ exist represented a major hurdle in this regard (Section 1.1). For example, we have seen in Section 5.1.1 that the ^{3}He(α,γ)^{7}Li reaction can bridge the $A = 5$ instability in the pp2 and pp3 chains, giving rise to the synthesis of small amounts of ^{7}Be, ^{7}Li, and ^{8}B. But at typical hydrogen burning temperatures none of these nuclides survive since they are all transformed back into ^{4}He (Figure 5.2). Other ideas involved the formation of ^{12}C as a result of the simultaneous fusion of three α-particles. However, it was shown that such a many-particle collision has a very small probability and cannot account for the fusion of

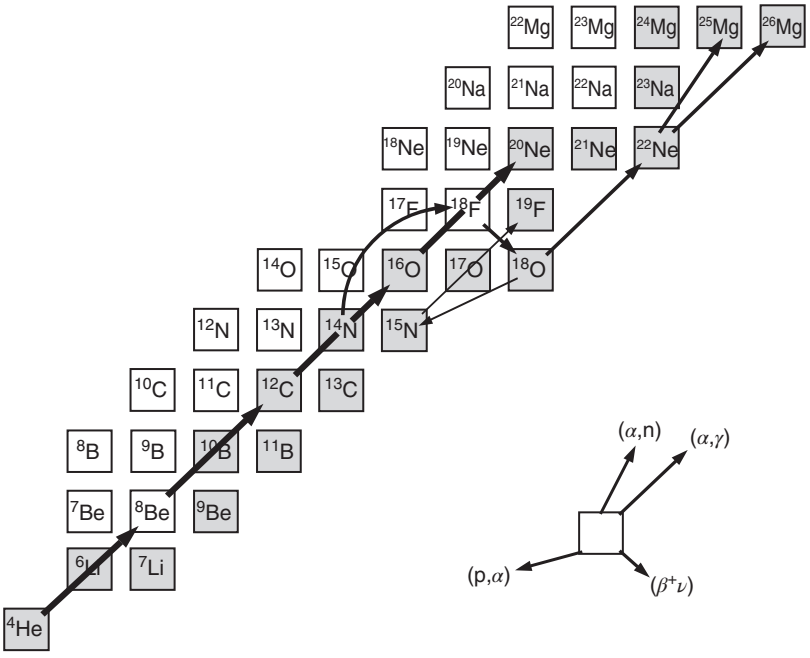

Figure 5.20 Representation of helium-burning reactions in the chart of the nuclides. Stable nuclides are shown as shaded squares. The key relates an arrow to a specific interaction. The 3α reaction and the (α,γ) reactions on ^{12}C and ^{16}O are displayed as thick arrows. Other helium-burning reactions are shown as thinner arrows. The reaction ^{14}N(α,γ)^{18}F is represented by an arc for reasons of clarity.

^{4}He to ^{12}C and ^{16}O. The problem was solved by taking into account some curious nuclear properties, as will be seen in this section.

The following reactions take place during helium burning:

$$^4\mathrm{He}(\alpha\alpha,\gamma)^{12}\mathrm{C} \qquad (Q = 7274.7\,\mathrm{keV}) \tag{5.73}$$

$$^{12}\mathrm{C}(\alpha,\gamma)^{16}\mathrm{O} \qquad (Q = 7161.9\,\mathrm{keV}) \tag{5.74}$$

$$^{16}\mathrm{O}(\alpha,\gamma)^{20}\mathrm{Ne} \qquad (Q = 4729.8\,\mathrm{keV}) \tag{5.75}$$

$$^{20}\mathrm{Ne}(\alpha,\gamma)^{24}\mathrm{Mg} \qquad (Q = 9316.6\,\mathrm{keV}) \tag{5.76}$$

These processes are shown schematically in Figure 5.20 and will be discussed in more detail in the following. It is worth keeping in mind that, depending on the stellar mass and metallicity, the ranges of temperature and density during hydrostatic helium burning in massive stars amount to $T = 0.1$–0.4 GK and $\rho = 10^2$–10^5 g/cm^3, respectively. The last reaction listed above only plays a role at the higher temperatures. Helium burning in massive stars is believed to be the main source of ^{16}O and ^{18}O in the universe, while helium burning in massive stars and AGB stars contributes similar amounts to the cosmic ^{12}C abundance (see Table 5.2).

5.2.1 Helium-Burning Reactions

The Triple-α Reaction

Helium burning starts with the 3α reaction which we already encountered in the discussion of reaction rate equilibria (Example 3.4). The 3α reaction represents a (sequential) two-step process (Salpeter, 1952). In the first step, two α-particles interact to form ^{8}Be in its ground state. This nucleus is unstable by an energy of only 92 keV and disintegrates back into two α-particles with a half-life of $T_{1/2} = 8.2 \times 10^{-17}$ s (Audi *et al.*, 2012). Over time, a small concentration of ^{8}Be builds up until the rate of ^{8}Be formation becomes equal to its decay rate,

$$^4\text{He} + {}^4\text{He} \leftrightarrow {}^8\text{Be} \tag{5.77}$$

In the second step, a third α-particle interacts with the ^{8}Be nucleus to form ^{12}C via

$$^8\text{Be}(\alpha,\gamma)^{12}\text{C} \tag{5.78}$$

It was pointed out by Fred Hoyle (Hoyle *et al.*, 1953) that the overall conversion of three α-particles to one ^{12}C nucleus during helium burning would be too slow unless the second step proceeds via an excited state in ^{12}C near 7.7 MeV excitation energy. This level was experimentally verified by Dunbar *et al.* (1953) and its properties were determined by Cook *et al.* (1957), who showed that the spin-parity is 0^+, corresponding to an s-wave resonance. The 3α reaction bypasses the stable nuclides in the mass $A = 6$–11 region. Therefore, these nuclides are not synthesized in stars through thermonuclear reactions. Their extremely low observed abundances are the result of other processes, such as the big bang nucleosynthesis and cosmic-ray spallation (Section 5.7).

The energy level diagram for this reaction sequence is shown in Figure 5.21. The Q-value for the $\alpha + \alpha \rightarrow {}^8$Be reaction is -91.84 ± 0.04 keV and, therefore, ^{8}Be is unstable to α-particle emission. The Q-value of the ^{8}Be$(\alpha,\gamma)^{12}$C reaction amounts to 7366.59 ± 0.04 keV. With a value of $E_x = 7654.20 \pm 0.15$ keV (Ajzenberg-Selove, 1990) for the excitation energy of the astrophysically important ^{12}C level, we obtain a center-of-mass energy of $E_r = E_x - Q = 287.6 \pm 0.2$ keV for the corresponding resonance in ^{8}Be$(\alpha,\gamma)^{12}$C. The resonance is formed by α-particle capture and decays to the ^{12}C ground state either by emission of γ-rays or by internal pair formation (Section 1.7.1 and Example B.4). The partial widths for these processes are given by $\Gamma_\alpha = 8.3 \pm 1.0$ eV and $\Gamma_{\text{rad}} = \Gamma_\gamma + \Gamma_{\text{pair}} = (3.7 \pm 0.5) \times 10^{-3}$ eV (Ajzenberg-Selove, 1990). With $J(^{12}\text{C}) = j_0(\alpha) = j_1(^8Be) = 0$, we obtain for the resonance strength (Section 3.2.4)

$$\omega\gamma_{^8\text{Be}(\alpha,\gamma)} \equiv \frac{(2J+1)}{(2j_0+1)(2j_1+1)} \frac{\Gamma_\alpha \Gamma_{\text{rad}}}{\Gamma} \approx \Gamma_{\text{rad}} = (3.7 \pm 0.5) \times 10^{-3}\,\text{eV} \tag{5.79}$$

To derive the decay constant for the 3α reaction, we start by using the expression from Example 3.4,

$$\lambda_{\alpha+\alpha+\alpha\rightarrow{}^{12}\text{C}} = \lambda_{3\alpha} = 3N_\alpha \left(\frac{h^2}{2\pi}\right)^{3/2} \frac{1}{(m_{\alpha\alpha}kT)^{3/2}} e^{Q_{\alpha+\alpha\rightarrow{}^8\text{Be}}/kT}\, \lambda_{^8\text{Be}(\alpha,\gamma)} \tag{5.80}$$

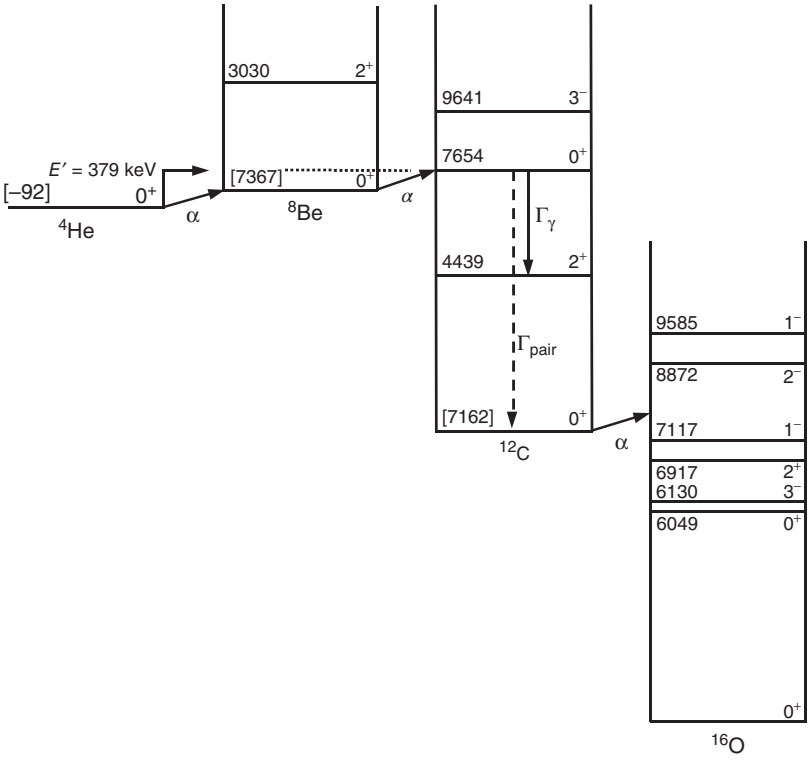

Figure 5.21 Energy level diagrams for the most important nuclides participating in helium burning. The numbers in square brackets represent the energy of the ground state of the system ${}^{A}_{Z}X_{N} + {}^{4}_{2}He_{2}$ with respect to the ground state of the nucleus ${}^{A+4}_{Z+2}Y_{N+2}$ (i.e., the Q-value of the (α,γ) reaction on ${}^{A}_{Z}X_{N}$, or the α-particle separation energy of ${}^{A+4}_{Z+2}Y_{N+2}$). All information is adopted from Ajzenberg-Selove (1990) and Wang *et al.* (2012).

The decay constant for the second step, $\lambda_{^8\mathrm{Be}(\alpha,\gamma)}$, can be expressed by using Eq. (3.23),

$$\lambda_{^8\mathrm{Be}(\alpha,\gamma)} = \lambda_{\alpha}(^8Be) = N_{\alpha}\langle\sigma v\rangle_{^8\mathrm{Be}(\alpha,\gamma)} \tag{5.81}$$

where $\langle\sigma v\rangle_{^8\mathrm{Be}(\alpha,\gamma)}$ is given by the expression for the reaction rate of a narrow resonance (see Eq. (3.115))

$$\langle\sigma v\rangle_{^8\mathrm{Be}(\alpha,\gamma)} = \left(\frac{2\pi}{m_{\alpha^8\mathrm{Be}}kT}\right)^{3/2}\hbar^2 e^{-E_r/kT}\omega\gamma_{^8\mathrm{Be}(\alpha,\gamma)} \tag{5.82}$$

From Eqs. (5.80)–(5.82), it follows

$$\begin{aligned}\lambda_{3\alpha} &= 3N_{\alpha}\left(\frac{h^2}{2\pi}\right)^{3/2}\frac{e^{Q_{\alpha+\alpha\to^8\mathrm{Be}}/kT}}{\left(m_{\alpha\alpha}kT\right)^{3/2}}N_{\alpha}\left(\frac{2\pi}{m_{\alpha^8\mathrm{Be}}kT}\right)^{3/2}\hbar^2 e^{-E_r/kT}\omega\gamma_{^8\mathrm{Be}(\alpha,\gamma)} \\ &= 3N_{\alpha}^2\,3^{3/2}\left(\frac{2\pi}{m_{\alpha}kT}\right)^{3}\hbar^5 e^{-E'/kT}\omega\gamma_{^8\mathrm{Be}(\alpha,\gamma)}\end{aligned} \tag{5.83}$$

where we defined $E' \equiv E_r - Q_{\alpha+\alpha\rightarrow{}^8\mathrm{Be}}$. Numerically, one finds

$$\begin{aligned}\lambda_{3\alpha} &= 0.23673\frac{(\rho X_\alpha)^2}{T_9^3}e^{-11.6048E'/T_9}\omega\gamma_{{}^8\mathrm{Be}(\alpha,\gamma)} \qquad (\mathrm{s}^{-1}) \\ &= 8.7590\times10^{-10}\frac{(\rho X_\alpha)^2}{T_9^3}e^{-4.4040/T_9} \qquad (\mathrm{s}^{-1})\end{aligned} \tag{5.84}$$

where we used $E' = 287.6\,\mathrm{keV} - (-91.84\,\mathrm{keV}) = 379.4\,\mathrm{keV}$ and $\omega\gamma_{{}^8\mathrm{Be}(\alpha,\gamma)} = \Gamma_{\mathrm{rad}} = 3.7\times10^{-3}$ eV. This expression is valid only for temperatures of $0.1 \leq T_9 \leq 2$. For lower and higher temperatures, additional contributions to the reaction rates have to be taken into account (Angulo *et al.*, 1999).

The temperature dependence of the decay constant for the 3α reaction can be found from a calculation similar to the one described in Section 3.2.1. One obtains (see Problem 5.2)

$$(\lambda_{3\alpha})_T = (\lambda_{3\alpha})_{T_0}(T/T_0)^{(4.4040/T_9)-3} \tag{5.85}$$

The energy generation rate of the 3α process is given, according to Eq. (3.64), by the product of the reaction rate (the number of reactions per second and per cubic centimeter) and the energy released per reaction, $Q_{3\alpha} = (3m_{{}^4\mathrm{He}} - m_{{}^{12}\mathrm{C}})c^2 = 7.275$ MeV. Each 3α reaction consumes three α-particles and, therefore, the decay constant (the number of α-particles disappearing each second) is related to the reaction rate by $r_{3\alpha} = N_\alpha\lambda_{3\alpha}/3$. It follows

$$\begin{aligned}\varepsilon_{3\alpha} &= \frac{Q_{3\alpha}}{\rho}r_{3\alpha} = \frac{Q_{3\alpha}}{\rho}\frac{N_\alpha\lambda_{3\alpha}}{3} \\ &= \frac{7.275\,\mathrm{MeV}}{\rho}\frac{1}{3}8.7590\times10^{-10}\left(\rho N_A\frac{X_\alpha}{M_\alpha}\right)\frac{(\rho X_\alpha)^2}{T_9^3}e^{-4.4040/T_9} \\ &= 3.1771\times10^{14}\frac{\rho^2X_\alpha^3}{T_9^3}e^{-4.4040/T_9} \qquad (\mathrm{MeV\,g^{-1}s^{-1}})\end{aligned} \tag{5.86}$$

The 3α reaction has a remarkable temperature dependence. For example, near $T_0 = 0.1$ GK, we obtain for the energy generation rate

$$\varepsilon_{3\alpha}(T) = \varepsilon_{3\alpha}(T_0)\left(T/T_0\right)^{(4.4040/T_9)-3} = \varepsilon_{3\alpha}(T_0)\left(T/T_0\right)^{41.0} \tag{5.87}$$

Therefore, energy generation via the 3α reaction in a helium-burning star occurs predominantly in the regions of highest temperature. Furthermore, if the helium gas is electron degenerate, then a small rise in temperature will cause a large release of energy. As a result, the temperature rises faster, producing even more energy. The cycle continues until the degeneracy is lifted in a thermonuclear explosion. This *helium flash* is believed to occur at the onset of hydrostatic helium burning in some stars (Section 1.4.3).

We will briefly comment on the experimental situation. The 3α reaction represents a two-step sequential process and has not been measured yet directly in the laboratory. Even the second step, the ${}^8\mathrm{Be}(\alpha,\gamma){}^{12}\mathrm{C}$ reaction, has not been measured directly since the ^{8}Be half-life is very short ($T_{1/2} \approx 10^{-16}$ s). Furthermore, the reverse reaction, ${}^{12}\mathrm{C}(\gamma,\alpha){}^8\mathrm{Be}$, cannot be measured either because

the direct γ-ray transition from the ^{12}C ground state ($J^\pi = 0^+$) to the level at $E_x = 7654$ keV ($J^\pi = 0^+$) is forbidden (Figure 5.21 and Example B.4). However, the quantities E' and $\omega\gamma_{^8\mathrm{Be}(\alpha,\gamma)} = \Gamma_{\mathrm{rad}}$ entering the expression for the 3α reaction decay rate (see Eq. (5.83)) have been measured by indirect studies (see, e.g., Rolfs and Rodney, 1988). In the temperature range important for hydrostatic helium burning, $0.1 \leq T_9 \leq 0.4$, the total reaction rate of the 3α reaction (or, equivalently, the decay constant) has an uncertainty of only 15% (Angulo *et al.*, 1999). This accuracy is remarkable for a process that cannot be measured directly in the laboratory. The error is mainly caused by the present uncertainty in the partial width $\Gamma_{\mathrm{rad}} = \Gamma_\gamma + \Gamma_{\mathrm{pair}} = (3.7 \pm 0.5) \times 10^{-3}$ eV. Although the quantity $E' = [E_x(^{12}\mathrm{C}) - Q_{^8Be(\alpha,\gamma)}] - Q_{\alpha+\alpha\rightarrow{}^8\mathrm{Be}} = 379.4 \pm 0.2$ keV enters exponentially in Eq. (5.83), its uncertainty has a negligible effect on the total decay constant.

The ^{12}C(α,γ)^{16}O and ^{16}O(α,γ)^{20}Ne Reactions

If the subsequent ^{12}C(α,γ)^{16}O reaction would be sufficiently rapid, most α-particles would be converted to ^{16}O or perhaps heavier nuclei, with no ^{12}C left at the end of helium burning. However, the ratio of number abundances of ^{12}C and ^{16}O in the universe amounts to about $N(^{12}\mathrm{C})/N(^{16}\mathrm{O}) \approx 0.4$, suggesting that the ^{12}C(α,γ)^{16}O reaction is rather slow and that, as a result, some ^{12}C remains after helium is exhausted. The presence of comparable amounts of ^{12}C and ^{16}O also implies that the ^{12}C(α,γ)^{16}O reaction gives rise to a sensitive balance of these two species. In other words, the precise magnitude of the ^{12}C(α,γ)^{16}O reaction rate will strongly influence the relative production of ^{12}C and ^{16}O.

At a typical temperature of $T = 0.2$ GK, the location and width of the Gamow peak for the ^{12}C(α,γ)^{16}O reaction are $E_0 = 315$ keV and $\Delta = 170$ keV, respectively. The lowest lying resonance occurs at $E_r^{\mathrm{cm}} \approx 2.4$ MeV and corresponds to the broad $E_x = 9585$ keV ($J^\pi = 1^-$) level in ^{16}O (Figure 5.21). Although a lower lying level exists in ^{16}O at $E_x = 8872$ keV ($J^\pi = 2^-$), it cannot be excited as a resonance in the ^{12}C $+\alpha$ reaction because it has unnatural parity (Example B.1). Thus, no narrow resonance is located in the Gamow peak and the ^{12}C(α,γ)^{16}O reaction must proceed through other reaction mechanisms that will be necessarily slower. These mechanisms include the capture into the low-energy wing of the $E_r^{\mathrm{cm}} \approx 2.42$ MeV resonance and the capture into the high-energy wings of the subthreshold resonances (Example 2.1) at $E_r^{\mathrm{cm}} = -45$ keV and $E_r^{\mathrm{cm}} = -245$ keV, corresponding to ^{16}O levels at $E_x = 7117$ keV ($J^\pi = 1^-$) and 6917 keV ($J^\pi = 2^+$), respectively (Figure 5.21). Another contribution arises from direct radiative capture.

The ^{12}C(α,γ)^{16}O reaction has been measured down to a center-of-mass energy of ≈ 1 MeV. The Gamow peak for most situations of astrophysical interest is located far below this energy (e.g., $E_0 \approx 0.3$ MeV for $T = 0.2$ GK). It has been estimated (Kunz *et al.*, 2002) that the cross section of the ^{12}C(α,γ)^{16}O reaction at energies important for helium burning is of order $\sigma \approx 10^{-17}$ b, that is, orders of magnitude below present experimental observation thresholds. Therefore, the cross section measured at higher energies needs to be extrapolated down

to the astrophysically important energy range using a suitable nuclear reaction model (usually an R-matrix description; Section 2.5.5). This extrapolation is not straightforward because several different amplitudes contribute to the reaction mechanism, as pointed out already. These amplitudes can interfere with each other, further complicating the picture. More reliable cross section extrapolations are obtained if the directly measured data are supplemented with other information for the $^{12}C + \alpha$ system. This includes, for example, α-particle reduced widths (or α-particle spectroscopic factors; Section 1.6.2) of the important ^{16}O levels that are populated in α-particle transfer studies, or phase shifts measured in $^{12}C(\alpha,\alpha)^{12}C$ elastic scattering. An overview of some of the techniques can be found in Rolfs and Rodney (1988), and Wallerstein *et al.* (1997). At present, different rates of the $^{12}C(\alpha,\gamma)^{16}O$ reaction are in use by stellar modelers. Current reaction rate uncertainties amount typically to about ±35% (Kunz *et al.*, 2002) at temperatures of $T = 0.12$–0.35 GK. The magnitude of the $^{12}C(\alpha,\gamma)^{16}O$ reaction rate determines the relative amounts of ^{12}C and ^{16}O at the end of helium burning, as will be shown below. Subsequent advanced burning stages rely on ^{12}C and ^{16}O fuel. Consequently, the $^{12}C(\alpha,\gamma)^{16}O$ reaction has a profound influence on the abundances of many elements up to iron and on the evolution of massive stars that explode as supernovae (Weaver and Woosley, 1993). Therefore, a more reliable rate for this reaction is highly desirable.

If the subsequent $^{16}O(\alpha,\gamma)^{20}Ne$ reaction would be fast, then ^{16}O is converted to ^{20}Ne or heavier nuclei and little ^{16}O would survive during hydrostatic helium burning. Since ^{16}O is relatively abundant in the universe, however, we suspect that this reaction must be rather slow. For example, the Gamow peak for a temperature of $T = 0.2$ GK is located at $E_0 \pm \Delta/2 = 390 \pm 90$ keV. The Q-value of $^{16}O(\alpha,\gamma)^{20}Ne$ is $Q = 4.73$ MeV. The lowest lying resonance, located at $E_r^{cm} = 893$ keV (Tilley *et al.*, 1998), is formed via incoming f-waves ($\ell = 3$) and corresponds to the ^{20}Ne level at $E_x = 5621$ keV ($J^\pi = 3^-$). A lower lying compound level exists at $E_x = 4967$ keV ($J^\pi = 2^-$), but this state cannot be excited as a $^{16}O + \alpha$ resonance because it has unnatural parity (Example B.1). The subthreshold resonance located closest to the α-particle threshold occurs at $E_r^{cm} = -482$ keV, and is formed via incoming g-waves ($\ell = 4$). These resonances are not only located far away from the Gamow peak at $T = 0.2$ GK, but their formation is also inhibited by the centripetal barrier. The cross section contributions arising from the wings of these resonances are so small that the direct-capture process, although inherently slow for (α,γ) reactions on even–even, $N = Z$ target nuclei, dominates the $^{16}O(\alpha,\gamma)^{20}Ne$ reaction rates for temperatures of $T < 0.25$ GK. At higher temperatures, resonances with $E_r^{cm} \geq 893$ keV move into the Gamow peak and dominate the total reaction rates.

The lowest lying resonance in the $^{16}O(\alpha,\gamma)^{20}Ne$ reaction has been observed at $E_r^{cm} = 893$ keV. As already mentioned above, the reaction rates at $T < 0.25$ GK are determined by direct capture. However, this process has not been measured yet in the $^{16}O(\alpha,\gamma)^{20}Ne$ reaction, neither at energies below $E_\alpha^{cm} = 1$ MeV, nor at higher energies. Therefore, the reaction rates at these temperatures are largely based on theoretical model calculations. At temperatures below $T = 0.2$ GK, the

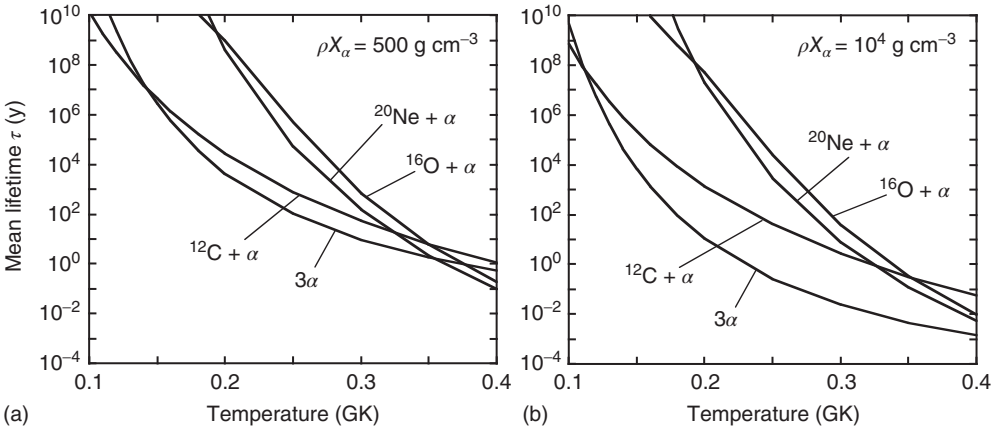

Figure 5.22 Mean lifetimes of ^{4}He, ^{12}C, ^{16}O, and ^{20}Ne versus destruction by α-particles as a function of temperature for (a) ρX_α = 500 g/cm^3, and (b) $\rho X_\alpha = 10^4$ g/cm^3. The mean lifetime $\tau_{3\alpha}(^4\text{He})$ depends on $(\rho X_\alpha)^{-2}$ while the mean lifetimes of ^{12}C, ^{16}O, and ^{20}Ne depend on $(\rho X_\alpha)^{-1}$.

present ratio of upper and lower reaction rate limits amounts to about an order of magnitude (Angulo *et al.*, 1999). Above this temperature, the reaction rate uncertainties are less than 30%.

Comparison of Mean Lifetimes

The mean lifetimes of ^{4}He, ^{12}C, and ^{16}O versus destruction by α-particles as a function of temperature are displayed in Figure 5.22 for values of $\rho X_\alpha = 500$ g/cm^3 and $\rho X_\alpha = 10^4$ g/cm^3. Although we have not explicitly discussed the next α-particle capture reaction, ^{20}Ne$(\alpha,\gamma)^{24}$Mg, the corresponding mean lifetime $\tau_\alpha(^{20}\text{Ne})$ is also included in Figure 5.22. The curves are obtained from the expressions

$$\tau_{3\alpha}(^4He) = 1/\lambda_{3\alpha}(^4He) = \left[8.7590\times10^{-10}\frac{(\rho X_\alpha)^2}{T_9^3}e^{-4.4040/T_9}\right]^{-1} \tag{5.88}$$

$$\tau_\alpha(^{12}C) = \left[\frac{(\rho X_\alpha)}{M_\alpha}N_A\langle\sigma v\rangle_{^{12}\text{C}(\alpha,\gamma)}\right]^{-1} \tag{5.89}$$

$$\tau_\alpha(^{16}O) = \left[\frac{(\rho X_\alpha)}{M_\alpha}N_A\langle\sigma v\rangle_{^{16}\text{O}(\alpha,\gamma)}\right]^{-1} \tag{5.90}$$

$$\tau_\alpha(^{20}Ne) = \left[\frac{(\rho X_\alpha)}{M_\alpha}N_A\langle\sigma v\rangle_{^{20}\text{Ne}(\alpha,\gamma)}\right]^{-1} \tag{5.91}$$

The mean lifetime $\tau_{3\alpha}(^4\text{He})$ depends on $(\rho X_\alpha)^{-2}$, while the mean lifetimes of ^{12}C, ^{16}O, and ^{20}Ne depend on $(\rho X_\alpha)^{-1}$. Hence, carbon production via the 3α reaction is favored by higher density or, equivalently, by lower stellar mass, as will be shown later. It can be seen in Figure 5.22 that the mean lifetime $\tau_{3\alpha}(^4\text{He})$ is the shortest for a wide range of temperatures. Only at very low temperatures

($T < 0.14$ GK for $\rho X_\alpha = 500$ g/cm^3, or $T < 0.12$ GK for $\rho X_\alpha = 10^4$ g/cm^3) is the mean lifetime $\tau_\alpha(^{12}\mathrm{C})$ shorter than $\tau_{3\alpha}(^4\mathrm{He})$. It is also apparent that $\tau_{3\alpha}(^4\mathrm{He})$ and $\tau_\alpha(^{12}\mathrm{C})$ are considerably smaller than $\tau_\alpha(^{16}\mathrm{O})$ and $\tau_\alpha(^{20}\mathrm{Ne})$ at temperatures of $T < 0.3$ GK. Consequently, the destruction of ^{16}O is very slow and most ^{16}O nuclei will survive under these conditions. At relatively high temperatures of $T > 0.3$ GK, all four mean lifetimes become comparable in magnitude.

5.2.2 Nucleosynthesis During Hydrostatic He Burning

In this section, we discuss the evolution of abundances at hydrostatic helium burning conditions. Early in the burning, helium will be consumed by the 3α process. As the helium abundance decreases, and since the mean lifetime $\tau_{3\alpha}(^4\mathrm{He})$ depends on $(\rho X_\alpha)^{-2}$, α-particle captures on ^{12}C and beyond will become increasingly important. The differential equations for the abundances are

$$\frac{d(^4He)}{dt} = -3r_{3\alpha} - (^4He)(^{12}C)\langle\sigma v\rangle_{^{12}\mathrm{C}(\alpha,\gamma)} - (^4He)(^{16}O)\langle\sigma v\rangle_{^{16}\mathrm{O}(\alpha,\gamma)} \tag{5.92}$$

$$\frac{d(^{12}C)}{dt} = r_{3\alpha} - (^4He)(^{12}C)\langle\sigma v\rangle_{^{12}\mathrm{C}(\alpha,\gamma)} \tag{5.93}$$

$$\frac{d(^{16}O)}{dt} = (^4He)(^{12}C)\langle\sigma v\rangle_{^{12}\mathrm{C}(\alpha,\gamma)} - (^4He)(^{16}O)\langle\sigma v\rangle_{^{16}\mathrm{O}(\alpha,\gamma)} \tag{5.94}$$

$$\frac{d(^{20}Ne)}{dt} = (^4He)(^{16}O)\langle\sigma v\rangle_{^{16}\mathrm{O}(\alpha,\gamma)} - (^4He)(^{20}Ne)\langle\sigma v\rangle_{^{20}\mathrm{Ne}(\alpha,\gamma)} \tag{5.95}$$

$$\frac{d(^{24}Mg)}{dt} = (^4He)(^{20}Ne)\langle\sigma v\rangle_{^{20}Ne(\alpha,\gamma)} \tag{5.96}$$

The factors of 3 and 1 in the first term on the right-hand sides of the first two equations appear because each 3α reaction consumes three ^{4}He nuclei and creates one ^{12}C nucleus. The reaction rate $r_{3\alpha}$ (in units of reactions per second and per cubic centimeter) is related to the decay constant and the mean lifetime by $3r_{3\alpha} = (^4He)\lambda_{3\alpha} = (^4He)/\tau_{3\alpha}$. We included the $^{20}\mathrm{Ne}(\alpha,\gamma)^{24}\mathrm{Mg}$ reaction to account for the destruction of ^{20}Ne. As will be seen below, this reaction plays a minor role in most hydrostatic helium burning environments.

The above network is numerically solved for constant temperatures and densities of: (i) $T = 0.15$ GK, $\rho = 5000$ g/cm^3, and (ii) $T = 0.2$ GK, $\rho = 800$ g/cm^3. Such conditions occur typically in core helium burning of stars with initial masses of $5\,M_\odot$ and $20\,M_\odot$, respectively, and are nearly independent of the initial metallicity of the star (Schaller *et al.*, 1992). It must be emphasized that our calculations do not represent the situation in real stars. As the helium fuel is consumed, the energy production rate would also decrease with time if the burning would take place under constant temperature and density conditions. To maintain a certain luminosity, the stellar core contracts gravitationally and, consequently, the temperature and density must increase from the start to the end of helium burning in a realistic stellar model. Nevertheless, a reasonable qualitative estimate of helium burning nucleosynthesis can be obtained by reducing

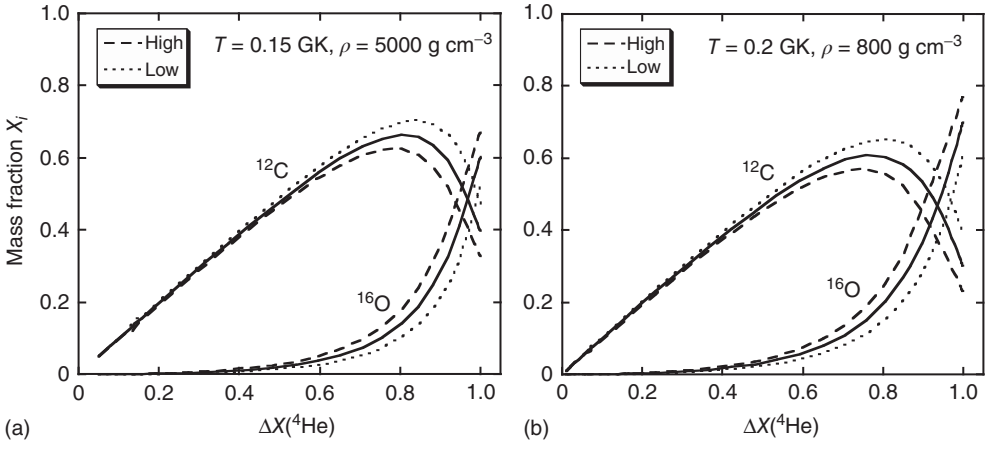

Figure 5.23 Evolution of ^{12}C and ^{16}O versus the amount of helium consumed during hydrostatic helium burning for constant temperatures and densities of (a) $T = 0.15$ GK and $\rho = 5000$ g/cm^3, and (b) $T = 0.2$ GK and $\rho = 800$ g/cm^3. The results are obtained by solving the reaction network numerically, assuming a pure ^{4}He gas at the beginning of helium burning. The calculation is terminated when the helium mass fraction falls below $X_{^4\text{He}} = 0.001$. The solid lines are obtained by adopting recommended $^{12}\text{C}(\alpha,\gamma)^{16}\text{O}$ reaction rates, while the dotted and dashed lines result from using the lower and upper limit of the $^{12}\text{C}(\alpha,\gamma)^{16}\text{O}$ reaction rates, respectively.

a complex situation to its simplest form by assuming constant temperatures and densities. Furthermore, we will assume a pure ^{4}He gas ($X^0_{^4\text{He}} = 1$) at the beginning of helium burning. The reaction network is solved until helium exhaustion ($X_{^4\text{He}} < 0.001$).

The abundance evolutions of ^{12}C and ^{16}O at $T = 0.15$ GK and $\rho = 5000$ g/cm^3 versus the amount of helium consumed, $\Delta X_{^4\text{He}} = X^0_{^4\text{He}} - X_{^4\text{He}}(t)$, are shown in Figure 5.23a as solid lines (time is increasing from left to right). Initially, as ^{4}He is depleted by the 3α reaction, the ^{12}C abundance increases linearly. Eventually, the ^{12}C abundance reaches a maximum and then declines because of the increasing importance of α-particle captures on ^{12}C. At the same time, the ^{16}O abundance increases toward the end of the calculation. The end products are ^{12}C and ^{16}O, with a number abundance ratio of $(^{12}C/^{16}O) = (X_{^{12}C}/X_{^{16}O})(M_{^{16}O}/M_{^{12}C}) \approx 0.89$. The final mass fractions of heavier nuclides, such as ^{20}Ne and ^{24}Mg, amount to $\approx 10^{-6}$ and $\approx 10^{-14}$, respectively, emphasizing the very slow destruction of ^{16}O via α-particle capture. The total nuclear energy generated amounts to 4.8×10^{23} MeV/g (or 7.6×10^{17} erg/g). The relative contributions of the 3α reaction and the $^{12}\text{C}(\alpha,\gamma)^{16}\text{O}$ reaction to the total nuclear energy production are 66% and 34%, respectively. It is interesting to consider how the abundances change when the current reaction rate uncertainties of the $^{12}\text{C}(\alpha,\gamma)^{16}\text{O}$ reaction (±35%; Kunz *et al.*, 2002) are taken into account. The results are indicated by the dotted and dashed lines, obtained by using the lower and upper limit for the $^{12}\text{C}(\alpha,\gamma)^{16}\text{O}$ reaction rate, respectively. At helium exhaustion, the number abundance ratio

($^{12}C/^{16}O$) varies significantly, between 0.65 and 1.23. The current uncertainties in the rates of the 3α reaction (±15%; Angulo *et al.*, 1999) have a smaller influence on the $^{12}C/^{16}O$ ratio.

The abundance evolutions of ^{12}C and ^{16}O at $T = 0.2$ GK and $\rho = 800$ g/cm^3 versus the amount of helium consumed, $\Delta X_{^4\mathrm{He}}$, are shown in Figure 5.23b as solid lines. Again, the ^{12}C abundance increases, reaches a maximum, and then starts to decline, while at the same time the ^{16}O abundance grows steadily. However, at this higher burning temperature and lower density, more ^{16}O and less ^{12}C is produced compared to the previous case. By the end of the calculation, we obtain a value of ($^{12}C/^{16}O$) = 0.57. The 3α reaction and the ^{12}C(α,γ)^{16}O reaction provide again all the nuclear energy, with relative contributions of 62% and 38%, respectively. The influence of the ^{16}O(α,γ)^{20}Ne and ^{20}Ne(α,γ)^{24}Mg reactions is small. The final mass fractions of ^{20}Ne and ^{24}Mg amount only to $\approx 10^{-5}$ and $\approx 10^{-11}$, respectively. The dotted and dashed lines display the abundance evolutions when the ^{12}C(α,γ)^{16}O reaction rate uncertainties are taken into account. At helium exhaustion, the abundance ratio ($^{12}C/^{16}O$) varies between 0.39 and 0.85. Smaller variations are caused by current uncertainties in the 3α reaction rate.

5.2.3 Other Helium-Burning Reactions

The previous sections showed that the end products of helium burning are mainly ^{12}C and ^{16}O. The precise abundance ratio depends on the helium-burning conditions (e.g., temperature and density) which, in turn, are determined by the stellar mass. The more massive the star, the more ^{16}O is produced relative to ^{12}C. The precise abundance ratio ($^{12}C/^{16}O$) is influenced by the rate of the ^{12}C(α,γ)^{16}O reaction. We assumed so far that helium burning starts exclusively with ^{4}He as fuel in the stellar core. However, at the end of hydrogen burning most stars contain a small, but significant, fraction of ^{14}N as a result of CNO-cycle operation (Section 5.1.2). During helium burning, ^{14}N will be consumed via the reaction sequence (Cameron, 1960)

$$^{14}\mathrm{N}(\alpha,\gamma)^{18}\mathrm{F}(\beta^+\nu)^{18}\mathrm{O}(\alpha,\gamma)^{22}\mathrm{Ne} \tag{5.97}$$

as shown in Figure 5.20. Subsequently, some of the ^{22}Ne nuclei will be converted by the competing reactions ^{22}Ne(α,γ)^{26}Mg ($Q = 10.62$ MeV) and ^{22}Ne(α,n)^{25}Mg ($Q = -0.48$ MeV). The latter reaction has a negative Q-value and is rather slow in the lower temperature region of $T \approx 0.1$–0.2 GK. However, toward the end of helium burning, when the temperature exceeds $T \approx 0.25$ GK, the ^{22}Ne(α,n)^{25}Mg reaction provides a crucial source of neutrons. These neutrons undergo reactions and sensitively influence the synthesis of neutron-rich nuclides in the mass $A = 60$–90 range. The resulting network of neutron-induced reactions and β-decays will be discussed in Section 5.6. The above reaction sequence is also important because it significantly increases the neutron excess parameter η during core helium burning (Section 1.8). Helium burning in massive stars and in AGB stars is the main source of ^{22}Ne production in the universe. It is

also an important contributor to the cosmic production of ^{25}Mg and ^{26}Mg (see Table 5.2).

During shell helium burning in massive stars, the sequence of Eq. (5.97) does not go to completion. The surviving ^{18}O is the main source of ^{18}O in the universe. Helium burning also contributes to the synthesis of fluorine via the sequence (Figure 5.20)

$$^{18}\mathrm{O}(\mathrm{p},\alpha)^{15}\mathrm{N}(\alpha,\gamma)^{19}\mathrm{F} \tag{5.98}$$

with the protons supplied by the ^{14}N(n,p)^{14}C reaction (Meynet and Arnould, 2000).

5.3 Advanced Burning Stages

5.3.1 Carbon Burning

When the helium is consumed in the center of the star, the core contracts gravitationally and the central temperature simultaneously rises until the next nuclear fuel begins to burn. The ashes of helium burning consist overwhelmingly of ^{12}C and ^{16}O (Section 5.2.2). Of all the possible fusion reaction involving these two nuclei, $^{12}C + {}^{12}C$, $^{12}C + {}^{16}O$, and $^{16}O + {}^{16}O$, the first process has the smallest Coulomb barrier and, therefore, initiates the next burning stage. We mentioned already in Section 5.2.1 that the precise abundance ratio of ^{12}C to ^{16}O obtained at the end of core helium burning sensitively influences the future evolution of the star.

The $^{12}C + {}^{12}C$ fusion reaction is the first process we encounter that involves two heavy nuclei in the entrance channel. The ^{24}Mg compound nucleus formed in the fusion of two ^{12}C nuclei is highly excited, with the mass difference between $^{12}C + {}^{12}C$ and ^{24}Mg amounting to ≈ 14 MeV. At such high excitation energies, the reaction will proceed through a large number of overlapping ^{24}Mg states, and we expect that for these levels the particle partial widths (for proton, neutron, and α-particle emission) dominate over the γ-ray partial width. In other words, the excess energy of the highly excited $^{12}C + {}^{12}C$ system is most effectively removed by emission of light particles. The most likely *primary* reactions are (Salpeter, 1952; Hoyle, 1954)

$$^{12}\mathrm{C}(^{12}\mathrm{C},\mathrm{p})^{23}\mathrm{Na} \qquad (Q = 2241\,\mathrm{keV}) \tag{5.99}$$

$$^{12}\mathrm{C}(^{12}\mathrm{C},\alpha)^{20}\mathrm{Ne} \qquad (Q = 4617\,\mathrm{keV}) \tag{5.100}$$

$$^{12}\mathrm{C}(^{12}\mathrm{C},\mathrm{n})^{23}\mathrm{Mg} \qquad (Q = -2599\,\mathrm{keV}) \tag{5.101}$$

while other processes, such as ^{12}C(^{12}C,γ)^{24}Mg or ^{12}C(^{12}C,^{8}Be)^{16}O, are considerably less important at energies of astrophysical interest (see, e.g., Patterson, Winkler, and Zaidins, 1969). The ^{12}C(^{12}C,n)^{23}Mg reaction is endothermic, that is, it

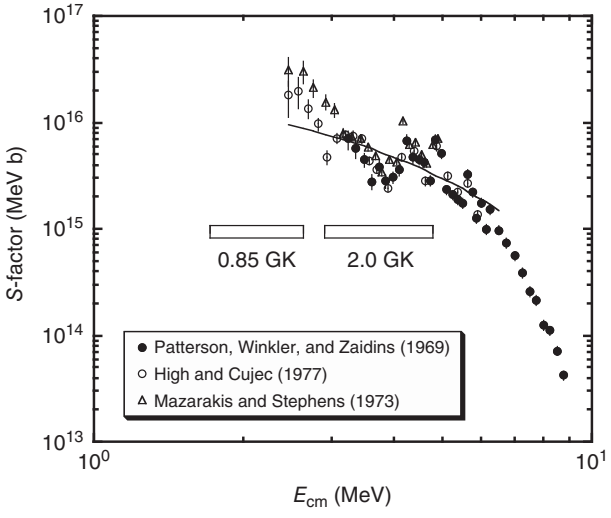

Figure 5.24 Total *S*-factor for the $^{12}C + {}^{12}C$ reaction. The data are adopted from Patterson, Winkler, and Zaidins (1969), Mazarakis and Stephens (1973), and High and Cujec (1977). The data of Becker *et al.* (1981) are not shown. The open bars indicate the location of the Gamow peaks for $T \approx 0.85$ GK (core carbon burning) and $T \approx 2.0$ GK (explosive carbon burning). The origin of the strong fluctuation in the *S*-factor (or cross section) remains obscure. The solid line shows the fitted total *S*-factor adopted by Caughlan and Fowler (1988).

can only occur above a threshold energy of $E_{cm} \approx 2.6$ MeV. The liberated protons, α-particles, and neutrons will be quickly consumed at elevated temperatures by initiating *secondary* reactions involving, for example, the ashes of helium burning (^{12}C and ^{16}O) and the heavy product nuclei of the primary reactions (^{23}Na and ^{20}Ne). This network of primary and secondary reactions is referred to as *carbon burning*. Typical temperatures in core carbon burning amount to $T = 0.6$–1.0 GK, depending on the mass of the star, while slightly higher temperatures are achieved in hydrostatic shell carbon burning. Carbon burning is the last core burning stage for stars in the mass range of $9\,M_\odot \lesssim M \lesssim 11\,M_\odot$ (Section 1.4.3 and Figure 1.4).

The total *S*-factor for $^{12}C + {}^{12}C$ is shown in Figure 5.24. The reaction has been measured down to a center-of-mass energy of $E_{cm} \approx 2.5$ MeV. The height of the Coulomb barrier is ≈ 8 MeV (Section 2.4.3). Since the measured energies are *not* far below the Coulomb barrier, the Gamow factor (see Eq. (2.125)) will not remove entirely the energy dependence of the cross section and, consequently, the *S*-factor shown in Figure 5.24 varies strongly (see also Eq. (2.124)). The open bar on the left indicates the location of the Gamow peak for $T \approx 0.85$ GK, a temperature typical of core carbon burning ($E_0 \pm \Delta/2 = 2169 \pm 460$ keV). It can be seen that data for the $^{12}C + {}^{12}C$ reaction barely touch the Gamow peak region. However, for explosive carbon burning ($T \approx 2.0$ GK), data exist throughout the Gamow peak. The cross section at the lowest measured energy amounts only to a few nanobarn

and, hence, measurements at even lower energies represent a serious experimental challenge. It was already mentioned that the $^{12}C + {}^{12}C$ reaction will most likely proceed through many overlapping levels of the highly excited ^{24}Mg compound nucleus. It is reasonable to expect that the cross section or S-factor should vary smoothly with energy. However, this behavior is not at all reflected in the data, which show a strongly fluctuating cross section up to an energy of $E_{cm} \approx 6$ MeV. The origin of this structure remains obscure, although many suggestions have been made (see the summary given in Rolfs and Rodney, 1988). It must also be pointed out that the various measurements are in poor agreement at the lowest energies. The average trend of the data, disregarding the fluctuations, has been described by a variety of methods to extrapolate the cross section to energies important for core carbon burning. The fitted total S-factor adopted by Caughlan and Fowler (1988) is shown in Figure 5.24 as a solid line.

The $^{12}C + {}^{12}C$ reactions populate not only the ground states of the residual ^{23}Na, ^{20}Ne, and ^{23}Mg nuclei, but several excited states as well. Hence, the various reaction channels can be studied by applying several different experimental techniques, including the direct measurement of the emitted light particles (Patterson, Winkler, and Zaidins, 1969; Mazarakis and Stephens, 1973; Becker *et al.*, 1981), the detection of γ-rays emitted from excited levels in the residual nuclei (High and Cujec, 1977; Kettner, Lorenz-Wirzba, and Rolfs, 1980), and the activation method (Dayras, Switkowski, and Woosley, 1977). The data reveal that the $^{12}C(^{12}C,p)^{23}Na$ and $^{12}C(^{12}C,\alpha)^{20}Ne$ reactions dominate the total $^{12}C + {}^{12}C$ fusion cross section, with about equal probabilities for the proton and α-particle channels to occur. The branching ratios amount to $B_p \approx B_\alpha \approx (1 - B_n)/2$, where B_n is a small number. The measured neutron branching ratios, B_n, amount to 2–10% at energies of $E_{cm} = 3.5$–5.0 MeV. For lower energies, the B_n values decrease, as predicted by an extrapolation of the data using the Hauser–Feshbach model (Dayras, Switkowski, and Woosley, 1977).

The thermonuclear reaction rates for the various $^{12}C + {}^{12}C$ reaction channels (Caughlan and Fowler, 1988; Dayras, Switkowski, and Woosley, 1977) are displayed in Figure 5.25 where, for better comparison, the results are normalized to the $^{12}C(^{12}C,\alpha)^{20}Ne$ reaction rate. The $^{12}C(^{12}C,\alpha)^{20}Ne$ and $^{12}C(^{12}C,p)^{23}Na$ rates are approximately equal, while the $^{12}C(^{12}C,n)^{23}Mg$ reaction rate is far smaller and declines rapidly for decreasing temperatures. The latter behavior is expected since the lower integration limit of zero in Eq. (3.70) must be replaced by the threshold energy for endothermic reactions ($E_t = 2.6$ MeV in this case). The reaction rates displayed in Figure 5.25 disregard corrections for electron screening (Section 3.2.6). Such corrections can be significant at temperature and density conditions of advanced burning stages. The present uncertainties in the rates of the primary carbon burning reactions near $T \approx 0.85$ GK are difficult to quantify. A crude estimate is a factor of ≈ 3. The rates per particle pair, $N_A\langle\sigma v\rangle$, of most (secondary) proton-, neutron-, or α-particle-induced reactions exceed the rates of all the primary carbon burning reactions by many orders of magnitude. For comparison, the rates for the various $^{12}C + {}^{16}O$ reaction channels are also shown in Figure 5.25. Because of the larger Coulomb barrier, these are

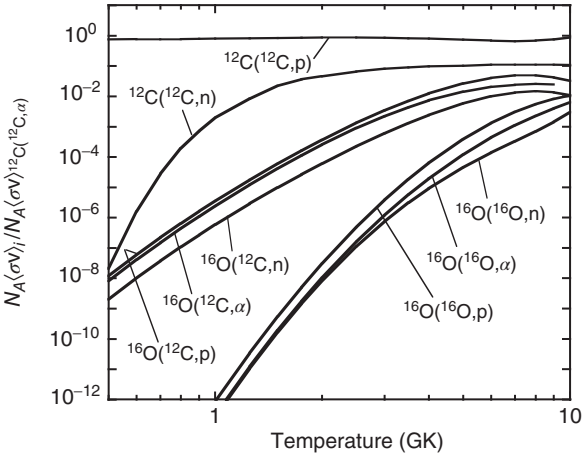

Figure 5.25 Reaction rates for various $^{12}C + {}^{12}C$, $^{12}C + {}^{16}O$, and $^{16}O + {}^{16}O$ reaction channels. From Caughlan and Fowler (1988); Dayras, Switkowski, and Woosley (1977). For better comparison, the $N_A\langle\sigma v\rangle$ values are given relative to the $^{12}C(^{12}C,\alpha)^{20}Ne$ reaction rate. The displayed results disregard electron screening corrections.

considerably smaller compared to those of the primary carbon burning reactions and are thus of interest only in special situations (Arnett, 1996).

The secondary reactions contribute significantly to the nuclear energy released by the primary carbon burning reactions. It can be estimated that each $^{12}C + {}^{12}C$ reaction liberates on average an energy of $\overline{Q}_C \approx 10$ MeV (see later). The energy generation rate during hydrostatic carbon burning is then given by Eq. (3.64),

$$\varepsilon_C = \frac{\overline{Q}_C}{\rho} r_{^{12}C+^{12}C} = \frac{\overline{Q}_C}{\rho} \frac{(N_{^{12}C})^2 \langle\sigma v\rangle_{^{12}C+^{12}C}}{2} = \frac{N_A \overline{Q}_C}{288} X_{^{12}C}^2 \rho N_A \langle\sigma v\rangle_{^{12}C+^{12}C}$$
$$= 2.09 \times 10^{22} X_{^{12}C}^2 \rho N_A \langle\sigma v\rangle_{^{12}C+^{12}C} \qquad (\mathrm{MeV\,g^{-1}s^{-1}}) \tag{5.102}$$

where $N_A\langle\sigma v\rangle_{^{12}C+^{12}C}$ is the total $^{12}C + {}^{12}C$ reaction rate. The temperature dependence of the $^{12}C + {}^{12}C$ reaction rate and the energy generation rate during carbon burning is obtained by using the expression for nonresonant reactions (see Eq. (3.90)). From Eq. (3.91), we find near a typical temperature of $T_0 = 0.9$ GK a value of $\tau = 87$ and thus, neglecting electron screening,

$$\varepsilon_C(T) = \varepsilon_C(T_0) \left(T/T_0\right)^{(87-2)/3} = \varepsilon_C(T_0) \left(T/T_0\right)^{28} \tag{5.103}$$

The total energy released during carbon burning can be found from Eq. (3.69),

$$\int \varepsilon_C(t)\, dt = \frac{N_A \overline{Q}_C}{2M_{^{12}C}} \Delta X_{^{12}C} = 2.51 \times 10^{23} \Delta X_{^{12}C} \qquad (\mathrm{MeV/g}) \tag{5.104}$$

where $\Delta X_{^{12}C}$ is the mass fraction of the consumed carbon fuel.

We will discuss in the following the results obtained by solving an appropriate reaction network for constant temperature and density. In a given star, carbon

burning will take place over a range of temperatures and densities, but during most of the carbon consumption the variations in temperature and density are relatively small (Figure 5.1a). This simplification will provide a reasonable estimate of the nucleosynthesis (see also Arnett and Truran, 1969). Values of $T = 0.9$ GK and $\rho = 10^5$ g/cm^3 are chosen for the temperature and density, respectively. These are close to the results obtained by stellar model calculations for core carbon burning in stars with an initial mass of $M = 25\,M_\odot$ and with initial solar metallicity (Woosley, Heger, and Weaver, 2002). The initial abundances at the beginning of carbon burning are given by the composition of the ashes of the preceding core helium helium-burning stage (Section 5.2). We expect mainly ^{12}C and ^{16}O, with smaller amounts of ^{20}Ne (Section 5.2.2) and ^{22}Ne (Section 5.2.3). Small traces of other elements may also be present, but will be neglected in the following for the sake of simplicity. We assume values of $X^0_{^{12}\mathrm{C}} = 0.25$, $X^0_{^{16}\mathrm{O}} = 0.73$, $X^0_{^{20}\mathrm{Ne}} = 0.01$, and $X^0_{^{22}\mathrm{Ne}} = 0.01$, which are similar to those reported in Arnett (1996). The network is solved until the carbon fuel is exhausted ($X_{^{12}\mathrm{C}} < 10^{-3}$). The electron screening correction factor for the $^{12}\mathrm{C} + {}^{12}\mathrm{C}$ reaction amounts to ≈ 1.2 for the T–ρ conditions adopted here (Problem 3.10).

Net abundance flows and the abundance evolutions of selected nuclides are shown in Figure 5.26. The dominant abundance flows are caused by the primary $^{12}\mathrm{C}(^{12}\mathrm{C},\mathrm{p})^{23}\mathrm{Na}$ and $^{12}\mathrm{C}(^{12}\mathrm{C},\alpha)^{20}\mathrm{Ne}$ reactions, and a large fraction of the liberated protons and α-particles is consumed by the secondary $^{23}\mathrm{Na}(\mathrm{p},\alpha)^{20}\mathrm{Ne}$ and $^{16}\mathrm{O}(\alpha,\gamma)^{20}\mathrm{Ne}$ reactions. Weaker, but still substantial, flows are caused by the (p,γ) reactions on ^{21}Ne, ^{22}Ne, ^{23}Na, ^{25}Mg, ^{26}Mg, the (α,γ) reaction on ^{20}Ne, the (α,n) reactions on ^{13}C, ^{21}Ne, ^{22}Ne, the (n,p) reaction on ^{22}Na, and the β^+-decay of $^{26}\mathrm{Al}^m$. The primary $^{12}\mathrm{C}(^{12}\mathrm{C},\mathrm{n})^{23}\mathrm{Mg}$ reaction is also visible as a weak flow. Removing this link from the network has only minor effects on the abundances of the *major* isotopes. However, this reaction may become more important at higher temperatures typical of *shell* carbon burning. The most important source of neutrons is the $^{22}\mathrm{Ne}(\alpha,\mathrm{n})^{25}\mathrm{Mg}$ reaction, with a smaller contribution coming from $^{21}\mathrm{Ne}(\alpha,\mathrm{n})^{24}\mathrm{Mg}$. The liberated neutrons initiate a number of neutron-induced processes, including (n,γ) reactions on ^{12}C, ^{20}Ne, ^{23}Na, ^{24}Mg, and ^{25}Mg. On the other hand, the $^{13}\mathrm{C}(\alpha,\mathrm{n})^{16}\mathrm{O}$ reaction is not a net producer of neutrons, since the species ^{13}C is mainly produced via $^{12}\mathrm{C}(\mathrm{n},\gamma)^{13}\mathrm{C}$ and, hence, one neutron is consumed for each neutron liberated by the (α,n) reaction on ^{13}C. Neutron-induced nucleosynthesis will be discussed in Section 5.6. The neutron excess parameter η (Section 1.8) increases slightly because of the sequence $^{20}\mathrm{Ne}(\mathrm{n},\gamma)^{21}\mathrm{Ne}(\mathrm{p},\gamma)^{22}\mathrm{Na}(\mathrm{n},\mathrm{p})^{22}\mathrm{Ne}(\alpha,\mathrm{n})^{25}\mathrm{Mg}(\mathrm{p},\gamma)^{26}\mathrm{Al}(\beta^+\nu)^{26}\mathrm{Mg}$. Even in a star with zero initial metallicity, the neutron excess will increase during core carbon burning because of the sequence $^{12}\mathrm{C}(^{12}\mathrm{C},\mathrm{n})^{23}\mathrm{Mg}(\beta^+\nu)^{23}\mathrm{Na}$.

The number of free protons, α-particles, and neutrons is very small during carbon burning. At maximum, their mass fractions are only $X_\mathrm{H} = 7 \times 10^{-16}$, $X_{^4\mathrm{He}} = 2 \times 10^{-11}$, and $X_\mathrm{n} = 2 \times 10^{-19}$, respectively. This circumstance has important implications. First, nuclear reactions involving radioactive target nuclei are unimportant during the nucleosynthesis (Figure 5.26) even though the temperature is relatively high and the rates $N_A\langle\sigma v\rangle$ for many proton

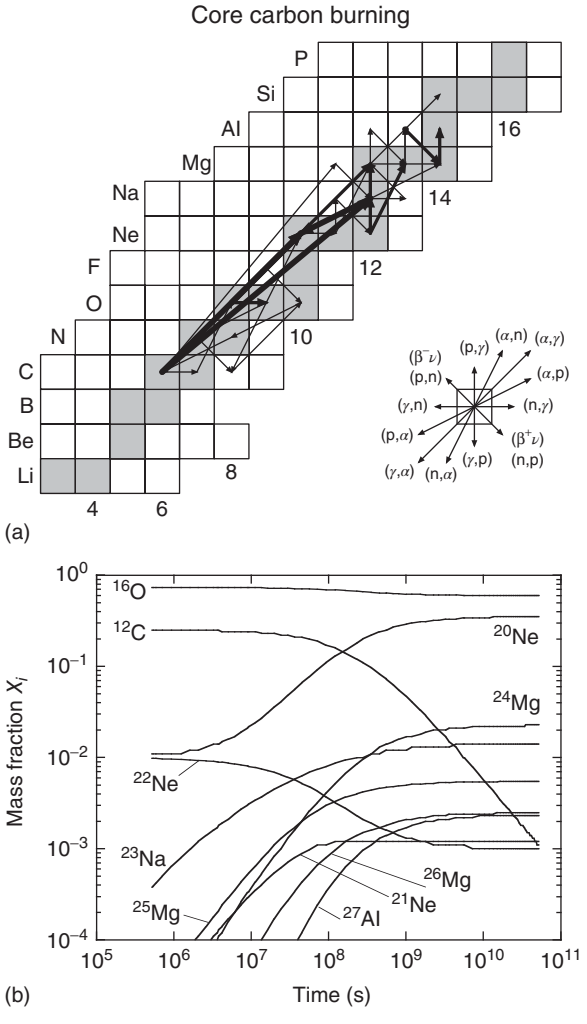

Figure 5.26 (a) Time-integrated net abundance flows, and (b) abundance evolutions for a constant temperature and density of $T = 0.9$ GK and $\rho = 10^5$ g/cm^3, respectively. Such conditions are typical of core carbon burning in stars with an initial mass of $M = 25\ M_\odot$ and with initial solar metallicity. The reaction network is solved numerically until the carbon fuel is exhausted ($X_{^{12}C} < 10^{-3}$ after ≈ 1600 y). Arrows represent net (forward minus reverse) abundance flows, integrated over the entire computation time. The magnitude of the abundance flows is represented by arrows of three different thicknesses: $F^{max} \geq F_{ij} > 0.1F^{max}$ (thick arrows), $0.1F^{max} \geq F_{ij} > 0.01F^{max}$ (intermediate arrows), and $0.01F^{max} \geq F_{ij} > 0.001F^{max}$ (thin arrows), where F^{max} corresponds to the reaction with the maximum net flow. Shaded squares indicate stable isotopes. A particular nuclide can be identified from the element symbol (vertical axis) and neutron number (horizontal axis). The key (middle right) indicates the correspondence between abundance flow arrow direction and reaction type. The $^{16}O(\alpha,\gamma)^{20}Ne$ reaction is obscured by $^{12}C(^{12}C,\alpha)^{20}Ne$ in part (a).

and α-particle-induced reactions are rather large. The decay constant for the destruction of nucleus 0 by a reaction with light particle 1 depends on the mass fraction X_1 (see Eq. (3.23)). Since X_1 is a very small number, a radioactive nucleus will β-decay rather than undergo a reaction, that is, $\lambda_\beta(0) \gg \lambda_1(0)$. Second, for the $T-\rho$ conditions adopted here, the photodisintegration of ^{13}N prevents ^{13}C production via the sequence ^{12}C(p,γ)^{13}N($\beta^+\nu$)^{13}C ($Q_{^{12}C+p} = 1944$ keV). The decay constants for the β^+-decay and the photodisintegration of ^{13}N amount to $\lambda_\beta(^{13}\text{N}) = 1.2 \times 10^{-3}$ s^{-1} and $\lambda_\gamma(^{13}\text{N}) = 5.2 \times 10^{1}$ s^{-1}, respectively. Hence, an equilibrium between ^{12}C and ^{13}N is quickly established. The equilibrium abundance ratio and the decay constant $\lambda_{^{12}C\rightarrow{}^{13}N\rightarrow{}^{13}C}$ are directly proportional to the mass fraction of protons (see Eqs. (3.50) and (3.63)). Since the proton mass fraction is very small at all times during the nucleosynthesis, the flow through ^{12}C(p,γ)^{13}N($\beta^+\nu$)^{13}C becomes negligible. For lower core carbon burning temperatures typical of stars with smaller masses, however, the photodisintegration of ^{13}N is less important and the sequence ^{12}C(p,γ)^{13}N($\beta^+\nu$)^{13}C(α,n) may become the dominant neutron source and give rise to a significant increase in the neutron excess parameter η (Arnett and Thielemann, 1985).

While the ^{12}C fuel is consumed, most of the initially present ^{16}O nuclei survive until the end of the calculation. The ^{22}Ne abundance also declines, but the abundances of many other isotopes increase steadily (Figure 5.26). With progressing time, the number of liberated protons and α-particles available for capture by various nuclides decreases and the nucleosynthesis slows down. Beyond $t = 10^{10}$ s, the abundances of the major nuclides change little. The ^{12}C fuel is exhausted ($X_{^{12}\text{C}} < 0.001$) after ≈ 1600 y ($t = 5 \times 10^{10}$ s). The total nuclear energy generated amounts to 6.3×10^{22} MeV/g, consistent with the value obtained from Eq. (5.104), where we assumed an average energy release of ≈ 10 MeV per primary $^{12}C + {}^{12}C$ reaction. The most abundant nuclides at the end of the calculation are ^{16}O ($X_f = 0.60$), ^{20}Ne ($X_f = 0.35$), ^{24}Mg ($X_f = 0.025$), and ^{23}Na ($X_f = 0.014$). Many other isotopes with $A < 20$ and $A \geq 28$ are produced with mass fractions less than $X = 5 \times 10^{-4}$, and their abundance evolutions are not displayed in Figure 5.26.

We already commented on the experimental situation for the primary $^{12}C + {}^{12}C$ reactions. Some information regarding important secondary reactions is summarized below. The important neutron sources ^{13}C(α,n)^{16}O and ^{22}Ne(α,n)^{25}Mg will be discussed Section 5.6.1. We need to consider first the location of the Gamow peaks. At a temperature of $T = 0.9$ GK one obtains, for example, $E_0 \pm \Delta/2 = 555 \pm 240$ keV and $E_0 \pm \Delta/2 = 1250 \pm 360$ keV for the ^{23}Na + p and ^{20}Ne +α reactions, respectively. Similar values are found for other proton or α-particle-induced reactions. The rates for the proton-induced reactions on ^{21}Ne, ^{22}Ne, ^{23}Na, ^{25}Mg, and ^{26}Mg are displayed in Figure 5.18. The branching ratio $B_{p\alpha/p\gamma}$ for ^{23}Na is shown in Figure 5.17. The lowest lying observed resonances in the ^{21}Ne(p,γ)^{22}Na, ^{23}Na(p,γ)^{24}Mg, ^{23}Na(p,α)^{20}Ne, ^{25}Mg(p,γ)^{26}Al, and ^{26}Mg(p,γ)^{27}Al reactions are located at $E_r^{cm} = 120$ keV, 241 keV, 170 keV, 190 keV, and 149 keV, Hence, direct measurements entirely cover the region of the Gamow peak at $T \approx 0.9$ GK. See also the information given at the end of Section 5.1.3.

The ^{22}Ne(p,γ)^{23}Na reaction has only been measured down to a resonance energy of $E_r^{cm} = 417$ keV, but the expected lower lying resonances do not influence the reaction rates at $T = 0.9$ GK (Hale *et al.*, 2001). The lowest lying resonances in the ^{16}O(α,γ)^{20}Ne, and ^{20}Ne(α,γ)^{24}Mg reactions are located at $E_r^{cm} = 893$ keV and 799 keV, respectively (Section 5.1.3 and Angulo *et al.*, 1999), and the region of the Gamow peak has been covered by direct measurements. At $T = 0.9$ GK, typical uncertainties for the rates of the above proton- and α-particle-induced reactions amount to ≈ 10–30%, in contrast to the situation at lower temperatures, where reaction rate uncertainties can amount to several orders of magnitude (Section 5.1.3).

5.3.2 Neon Burning

The core burning stages discussed below occur in stars with initial masses in excess of $M \lesssim 11\,M_\odot$ (Section 1.4.3 and Figure 1.4). At the end of core carbon burning, when most of the ^{12}C nuclei have been consumed, the core consists mainly of ^{16}O, ^{20}Ne, ^{23}Na, and ^{24}Mg. Other nuclides will be present as well, but with considerably smaller abundances ($X_i < 5 \times 10^{-3}$; see Figure 5.26). The core contracts gravitationally and the temperature and density both increase (Figure 5.1a). It is reasonable to assume that the next nuclear fuel to ignite is oxygen via the $^{16}O + {}^{16}O$ fusion reaction. However, before this happens the temperature has risen to values where photodisintegration reactions will become important ($T > 1$ GK). The proton, neutron, and α-particle separation energies of the above nuclei are in the range of ≈ 7–17 MeV and, therefore, they are rather inert against photodisintegration even at high temperatures. The exception is ^{20}Ne, which has a relatively small α-particle separation energy of 4.73 MeV. For a typical temperature of $T = 1.5$ GK, the photodisintegration decay constant of ^{20}Ne can be calculated from Eq. (3.46) using the rate of the (forward) ^{16}O(α,γ)^{20}Ne reaction (Angulo *et al.*, 1999). The result is $\lambda_\gamma(^{20}\text{Ne}) = 1.5 \times 10^{-6}$ s^{-1} and thus the ^{20}Ne nuclei will photodisintegrate. The liberated α-particles, in turn, induce secondary reactions involving any of the more abundant nuclei. The rates for the most important α-particle-consuming reactions are shown in Figure 5.27. Recall that the decay constant of α-particles for destruction by a reaction with nucleus 1 is given by $\lambda_1(\alpha) = \rho(X_1/M_1)N_A\langle\sigma v\rangle_{\alpha 1}$ (see Eq. (3.23)). For typical values of temperature and density ($T = 1.5$ GK and $\rho = 5 \times 10^6$ g/cm^3; see below) and assuming an isotopic composition obtained at the end of carbon burning (Figure 5.26), one finds decay constants of $\lambda_{^{16}\text{O}(\alpha,\gamma)}(\alpha) = 2.3 \times 10^4$ s^{-1}, $\lambda_{^{20}\text{Ne}(\alpha,\gamma)}(\alpha) = 1.6 \times 10^4$ s^{-1}, $\lambda_{^{23}\text{Na}(\alpha,\text{p})}(\alpha) = 5.7 \times 10^3$ s^{-1}, and $\lambda_{^{24}\text{Mg}(\alpha,\gamma)}(\alpha) = 4.1 \times 10^2$ s^{-1}. Hence, some of the α-particles will be captured by ^{16}O, again synthesizing ^{20}Ne. But there is also a good chance that the liberated α-particles will be consumed by reactions such as ^{20}Ne(α,γ)^{24}Mg, ^{23}Na(α,p)^{26}Mg, or ^{24}Mg(α,γ)^{28}Si. A number of other α-particle-induced reactions will occur that release protons and neutrons, and these light particles will also participate in the nucleosynthesis. Details will be discussed below.

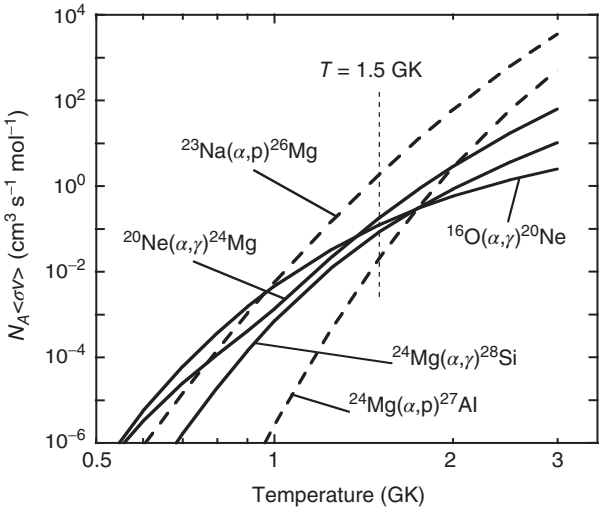

Figure 5.27 Rates for α-particle-induced reactions on ^{16}O, ^{20}Ne, ^{23}Na, and ^{24}Mg versus temperature. The vertical dashed line indicates a temperature of $T = 1.5$ GK typical for core neon burning in massive stars.

To summarize, the network of reactions consisting of the primary reaction

$$^{20}\mathrm{Ne}(\gamma,\alpha)^{16}\mathrm{O} \qquad (Q = -4730\,\mathrm{keV}) \tag{5.105}$$

and subsequent secondary reactions

$$^{20}\mathrm{Ne}(\alpha,\gamma)^{24}\mathrm{Mg}(\alpha,\gamma)^{28}\mathrm{Si} \qquad (Q_{^{20}\mathrm{Ne}(\alpha,\gamma)} = 9316\,\mathrm{keV})$$
$$(Q_{^{24}\mathrm{Mg}(\alpha,\gamma)} = 9984\,\mathrm{keV}) \tag{5.106}$$

$$^{23}\mathrm{Na}(\alpha,\mathrm{p})^{26}\mathrm{Mg}(\alpha,\mathrm{n})^{29}\mathrm{Si} \qquad (Q_{^{23}\mathrm{Na}(\alpha,\mathrm{p})} = 1821\,\mathrm{keV})$$
$$(Q_{^{26}\mathrm{Mg}(\alpha,\mathrm{n})} = 34\,\mathrm{keV}) \tag{5.107}$$

is referred to as *neon burning*. The primary reaction is endothermic since it consumes energy. In combination with the subsequent secondary reactions, however, there is a net production of energy for each ^{20}Ne nucleus destroyed by photodisintegration, as we shall see. Typical temperatures during core neon burning are in the range of $T = 1.2$–1.8 GK, with somewhat higher values during hydrostatic shell neon burning.

The two most important reactions for the nuclear energy generation are ^{20}Ne(γ,α)^{16}O and ^{20}Ne(α,γ)^{24}Mg. An energy level diagram is displayed in Figure 5.28. At $T = 1.5$ GK, the ^{20}Ne(γ,α)^{16}O reaction proceeds mainly through ^{20}Ne levels at $E_x = 5621$ keV and 5788 keV (see Problem 3.8), while the most important ^{24}Mg levels for the ^{20}Ne(α,γ)^{24}Mg reaction are located at $E_x = 10\,680$ keV, 10 917 keV, and 11 016 keV (Endt, 1990). The rearrangement effectively converts two ^{20}Ne nuclei to ^{16}O and ^{24}Mg. Thus, we have

$$^{20}\mathrm{Ne} + {}^{20}\mathrm{Ne} \rightarrow {}^{16}\mathrm{O} + {}^{24}\mathrm{Mg} + 4586\,\mathrm{keV} \tag{5.108}$$

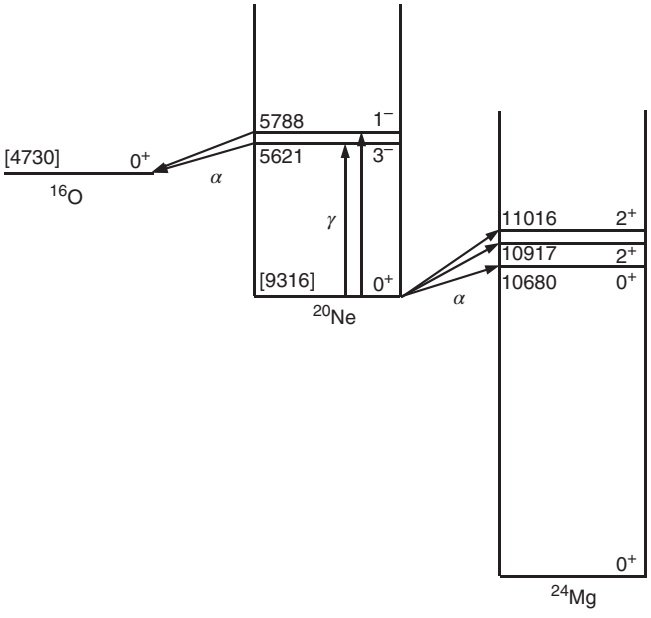

Figure 5.28 Energy level diagrams for the most important nuclides participating in neon burning. Numbers in square brackets represent reaction *Q*-values (Wang *et al.* 2012; see also caption to Figure 5.21). Excitation energies and quantum numbers are from Tilley *et al.* (1998) and Endt (1990). Levels that are not important for neon burning are omitted.

where the value for the energy release is obtained either from Eq. (1.11) or from $Q_{^{20}\mathrm{Ne}(\gamma,\alpha)} + Q_{^{20}\mathrm{Ne}(\alpha,\gamma)}$. Other secondary reactions contribute to the energy production as well. It can be estimated from network calculations that each $^{20}\mathrm{Ne} + {}^{20}\mathrm{Ne}$ conversion liberates on average an energy of $\overline{Q}_{\mathrm{Ne}} \approx 6.2$ MeV near $T \approx 1.5$ GK (see below). For the total energy release during neon burning, one finds from Eq. (3.69)

$$\int \varepsilon_{\mathrm{Ne}}(t)\, dt = \frac{N_A \overline{Q}_{\mathrm{Ne}}}{2M_{^{20}\mathrm{Ne}}} \Delta X_{^{20}\mathrm{Ne}} = 9.32 \times 10^{22} \Delta X_{^{20}\mathrm{Ne}} \qquad (\mathrm{MeV/g}) \qquad (5.109)$$

where $\Delta X_{^{20}\mathrm{Ne}}$ is the mass fraction of the consumed ^{20}Ne fuel. Compared to carbon burning, the total energy release is a factor of ≈ 3 smaller for the same mass of consumed fuel.

An approximate analytical expression for the energy generation rate during hydrostatic neon burning can be found by assuming an $^{16}\mathrm{O} + \alpha \leftrightarrow {}^{20}\mathrm{Ne} + \gamma$ equilibrium. The values of $\lambda_{^{16}\mathrm{O}(\alpha,\gamma)}(\alpha)$, $\lambda_{^{20}\mathrm{Ne}(\alpha,\gamma)}(\alpha)$, and $\lambda_{^{23}\mathrm{Na}(\alpha,\mathrm{p})}(\alpha)$ quoted above were obtained with $X_{^{16}\mathrm{O}} = 0.60$, $X_{^{20}\mathrm{Ne}} = 0.35$, and $X_{^{23}\mathrm{Na}} = 0.014$, respectively. The ^{20}Ne and ^{23}Na abundances, however, decline during neon burning while the ^{16}O abundance increases. Hence, $^{16}\mathrm{O}(\alpha,\gamma)^{20}\mathrm{Ne}$ will be the dominant α-particle consuming reaction and the assumption of an $^{16}\mathrm{O} + \alpha \leftrightarrow {}^{20}\mathrm{Ne} + \gamma$ equilibrium is

justified. The energy generation rate is then given by (see Problem 5.5)

$$\varepsilon_{\mathrm{Ne}} \approx 6.24 \times 10^{33} \frac{(X_{^{20}\mathrm{Ne}})^2}{X_{^{16}\mathrm{O}}} T_9^{3/2} e^{-54.89/T_9} N_A \langle \sigma v \rangle_{^{20}Ne(\alpha,\gamma)} \qquad (\mathrm{MeV\,g^{-1}s^{-1}}) \quad (5.110)$$

and is independent of the density. The reaction rate for $^{20}\mathrm{Ne}(\alpha,\gamma)^{24}\mathrm{Mg}$ above $T = 1$ GK can be described by the analytical expression $N_A\langle\sigma v\rangle_{^{20}\mathrm{Ne}(\alpha,\gamma)} = 3.74 \times 10^2 T_9^{2.229} \exp(-12.681/T_9)$ (Angulo *et al.*, 1999). For the temperature dependence of the energy generation rate during neon burning, one finds from Eq. (5.110)

$$\varepsilon_{\mathrm{Ne}} \sim T_9^{1.5} T_9^{2.229} e^{-54.89/T_9} e^{-12.681/T_9} \sim T_9^{3.729} T_9^{67.57/T_9} \quad (5.111)$$

where the term $\exp(-67.57/T_9)$ is derived according to the method described by Eqs. (3.85)–(3.90). Near $T_0 \approx 1.5$ GK we find

$$\varepsilon_{\mathrm{Ne}}(T) = \varepsilon_{\mathrm{Ne}}(T_0) \left(T/T_0\right)^{49} \quad (5.112)$$

and thus neon burning is very temperature sensitive.

Network calculations for neon burning are performed for a constant temperature of $T = 1.5$ GK and density of $\rho = 5 \times 10^6$ g/cm^3. These values are close to those obtained from stellar model calculations for core neon burning in stars with an initial mass of $M = 25\,M_\odot$ and with initial solar metallicity (Woosley, Heger, and Weaver, 2002). For the initial abundances at the beginning of core neon burning, we adopt the final abundances obtained at the end of core carbon burning, that is, mainly ^{16}O ($X_i = 0.60$) and ^{20}Ne ($X_i = 0.35$), with smaller contributions from nuclides in the ^{21}Ne–^{28}Si range (Figure 5.26). The network is solved until the neon fuel is exhausted ($X_{^{20}\mathrm{Ne}} < 0.0015$).

Net abundance flows are shown in Figure 5.29. The dominant flows are caused by the reactions $^{20}\mathrm{Ne}(\gamma,\alpha)^{16}\mathrm{O}$ and $^{20}\mathrm{Ne}(\alpha,\gamma)^{24}\mathrm{Mg}(\alpha,\gamma)^{28}\mathrm{Si}$, consistent with our earlier discussion. Smaller, but substantial, flows are caused by $^{24}\mathrm{Mg}(\alpha,\mathrm{p})^{27}\mathrm{Al}(\alpha,\mathrm{p})^{30}\mathrm{Si}$ and $^{23}\mathrm{Na}(\alpha,\mathrm{p})^{26}\mathrm{Mg}$. The released protons initiate a number of different reactions, most notably $^{26}\mathrm{Mg}(\mathrm{p},\gamma)^{27}\mathrm{Al}$, $^{23}\mathrm{Na}(\mathrm{p},\alpha)^{20}\mathrm{Ne}$, and $^{25}\mathrm{Mg}(\mathrm{p},\gamma)^{26}\mathrm{Al}(\beta^+\nu)^{26}\mathrm{Mg}$. Neutrons are produced by the $^{21}\mathrm{Ne}(\alpha,\mathrm{n})^{24}\mathrm{Mg}$, $^{25}\mathrm{Mg}(\alpha,\mathrm{n})^{28}\mathrm{Si}$, and $^{26}\mathrm{Mg}(\alpha,\mathrm{n})^{29}\mathrm{Si}$ reactions. The liberated neutrons undergo (n,γ) reactions involving mainly ^{20}Ne, ^{24}Mg, and ^{28}Si. At maximum, the mass fractions of the light particles amount to $X_{\mathrm{H}} = 2 \times 10^{-17}$, $X_{^4\mathrm{He}} = 1 \times 10^{-12}$, and $X_{\mathrm{n}} = 1 \times 10^{-21}$. Changes in the neutron excess parameter η are relatively small during neon burning (Thielemann and Arnett, 1985). For the adopted temperature and density conditions, the stellar decay constants for some β-decays differ significantly from their terrestrial values (Section 1.8.4). For example, the laboratory half-life for $^{24}\mathrm{Na}(\beta^-\nu)^{24}\mathrm{Mg}$ amounts to $T_{1/2} = 15$ h compared to $T_{1/2} = 0.52$ h at neon-burning conditions (Fuller, Fowler, and Newman, 1982).

The evolution of the most abundant nuclides, except for ^{21}Ne, ^{22}Ne, and ^{23}Na, is also displayed in Figure 5.29. The latter three nuclides are quickly depleted from their initial abundance values. While the ^{20}Ne fuel is gradually consumed,

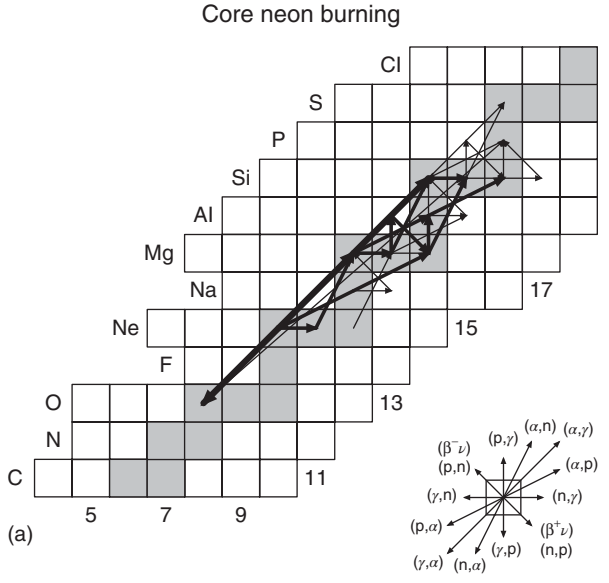

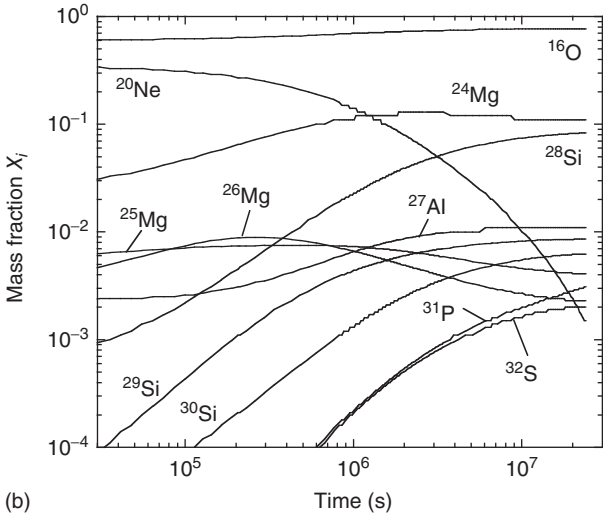

Figure 5.29 (a) Time-integrated net abundance flows, and (b) abundance evolutions for a constant temperature and density of $T = 1.5$ GK and $\rho = 5 \times 10^6$ g/cm^3, respectively. Such conditions are typical of core neon burning in stars with an initial mass of $M = 25\ M_\odot$ and with initial solar metallicity. The reaction network is solved numerically until the neon fuel is exhausted ($X_{^{20}\mathrm{Ne}} < 0.0015$ after ≈ 280 d). The arrows, shaded squares, and key in the top part have the same meaning as in Figure 5.26.

the ^{16}O abundance increases with time. Most of the other nuclides displayed in Figure 5.29 also increase in abundance, except ^{25}Mg and ^{26}Mg, whose abundances change little during the nucleosynthesis. After $t = 2 \times 10^6$ s, the number of liberated protons, α-particles, and neutrons that are available for capture by various nuclides decreases and the nucleosynthesis slows down. Beyond $t = 1.8 \times 10^7$ s the abundances of the major nuclides change little. The ^{20}Ne fuel is exhausted ($X_{^{20}\mathrm{Ne}} < 0.0015$) after 280 d ($t = 2.4 \times 10^7$ s). The total nuclear energy generated amounts to 3.3×10^{22} MeV/g. The most abundant nuclides at the end of the calculation are ^{16}O ($X_f = 0.77$), ^{24}Mg ($X_f = 0.11$), and ^{28}Si ($X_f = 0.083$), while nuclides in the ^{25}Mg–^{32}S region have final mass fractions in the range of $X_f = 0.002$–0.01. All other nuclides that are not shown in the figure have mass fractions of $X \leq 10^{-4}$ throughout the calculation. Similar results are obtained from a more involved stellar model simulation (Arnett, 1996).

At a temperature of $T = 1.5$ GK, the Gamow peaks for the reactions ^{20}Ne(α,γ)^{24}Mg, ^{24}Mg(α,γ)^{28}Si, ^{23}Na(p,α)^{20}Ne, and ^{25,26}Mg(p,γ)^{26,27}Al are located at $E_0 \pm \Delta/2 = 1760 \pm 550$ keV, 2010 ± 590 keV, 780 ± 370 keV, and 830 ± 380 keV, respectively. For the ^{16}O(α,γ)^{20}Ne reaction (i.e., the reverse of ^{20}Ne(γ,α)^{16}O; see Problem 5.5), we obtain $E_0 \pm \Delta/2 = 1500 \pm 510$ keV at $T = 1.5$ GK. All of these reactions have been measured directly over the Gamow peak region. Near this temperature, the reaction rates for ^{16}O(α,γ)^{20}Ne, ^{23}Na(p,α)^{20}Ne, ^{25}Mg(p,γ)^{26}Al, and ^{26}Mg(p,γ)^{27}Al have uncertainties of $< 20\%$ (Angulo *et al.*, 1999; Iliadis *et al.*, 2001). The important ^{20}Ne(α,γ)^{24}Mg and ^{24}Mg(α,γ)^{28}Si reaction rates, however, may be subject to systematic errors on the order of a factor of two as can be seen from the different results reported by Caughlan and Fowler (1988), Angulo *et al.* (1999), and Rauscher *et al.* (2000).

5.3.3 Oxygen Burning

After the neon fuel has been consumed, the most abundant nuclides in the stellar core are ^{16}O, ^{24}Mg, and ^{28}Si (Figure 5.29). The core contracts and the temperature increases until the burning of the next fuel starts to generate energy. Among the reactions induced by combinations of the above nuclides, the ^{16}O + ^{16}O fusion reaction is the most likely process to occur since it has the lowest Coulomb barrier (Hoyle, 1954; Cameron, 1959). The situation resembles carbon burning, in the sense that a reaction induced by two heavy nuclei in the incoming reaction channel (^{16}O + ^{16}O) is the primary process sustaining the nuclear burning. The ^{32}S compound nucleus formed in the fusion of two ^{16}O nuclei is highly excited, with a mass difference between ^{16}O + ^{16}O and ^{32}S of ≈ 16.5 MeV. The fusion reaction will then involve many overlapping ^{32}S compound levels. Excess energy is most effectively removed by emission of light particles (as opposed to the emission of γ-rays). In contrast to the ^{12}C + ^{12}C reaction, there are many more exit channels possible for the ^{16}O + ^{16}O reaction since the ^{32}S compound nucleus achieves much higher excitation energies (Spinka and Winkler, 1974). The most likely *primary* reactions are

$$^{16}\mathrm{O}(^{16}\mathrm{O},\mathrm{p})^{31}\mathrm{P} \qquad (Q = 7678\,\mathrm{keV}) \tag{5.113}$$

$$^{16}\mathrm{O}(^{16}\mathrm{O},2\mathrm{p})^{30}\mathrm{Si} \qquad (Q = 381\,\mathrm{keV}) \tag{5.114}$$

$$^{16}\mathrm{O}(^{16}\mathrm{O},\alpha)^{28}\mathrm{Si} \qquad (Q = 9594\,\mathrm{keV}) \tag{5.115}$$

$$^{16}\mathrm{O}(^{16}\mathrm{O},2\alpha)^{24}\mathrm{Mg} \qquad (Q = -390\,\mathrm{keV}) \tag{5.116}$$

$$^{16}\mathrm{O}(^{16}\mathrm{O},\mathrm{d})^{30}\mathrm{P} \qquad (Q = -2409\,\mathrm{keV}) \tag{5.117}$$

$$^{16}\mathrm{O}(^{16}\mathrm{O},\mathrm{n})^{31}\mathrm{S} \qquad (Q = 1499\,\mathrm{keV}) \tag{5.118}$$

The ^{16}O(^{16}O,d)^{30}P and ^{16}O(^{16}O,2α)^{24}Mg reactions are endothermic, that is, they can only occur above a threshold energy of $E_{\mathrm{cm}} = -Q$. Also, the deuterons released in the ^{16}O(^{16}O,d)^{30}P reaction will be immediately photodisintegrated ($\mathrm{d} + \gamma \rightarrow \mathrm{p} + \mathrm{n}$) at the elevated stellar temperatures. The liberated light particles are quickly consumed by *secondary* reactions involving, for example, the ashes of neon burning and the heavy product nuclei of the primary reactions. This network of primary and secondary reactions is referred to as *oxygen burning*. Typical temperatures during core oxygen burning are in the range of $T = 1.5$–2.7 GK, depending on the stellar mass, with somewhat higher values during shell oxygen burning.

It should be pointed out that the photodisintegrations of the nuclides ^{16}O, ^{24}Mg, and ^{28}Si do not contribute significantly to the nuclear energy generation during hydrostatic oxygen burning. Their proton, neutron, and α-particle separation energies exceed ≈ 9 MeV, except the α-particle separation energy of ^{16}O, which amounts to 7.2 MeV. Hence, the ^{16}O(γ,α)^{12}C reaction is the most likely process to occur among these photodisintegrations. The decay constants $\lambda_i(^{16}\mathrm{O})$ for the reactions $^{16}\mathrm{O} + {}^{16}\mathrm{O}$ and ^{16}O(γ,α)^{12}C are shown versus temperature in Figure 5.30.

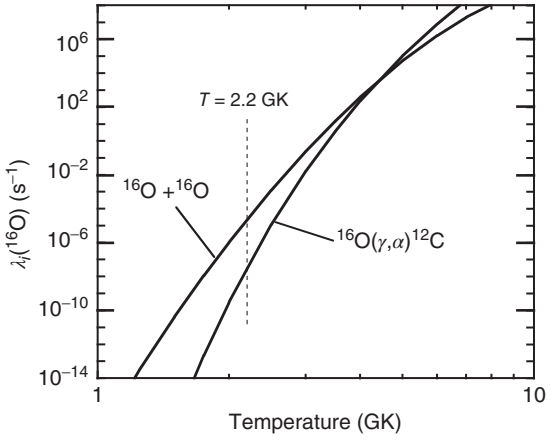

Figure 5.30 Decay constants $\lambda_i(^{16}\mathrm{O})$ for the ^{16}O + ^{16}O and ^{16}O(γ,α)^{12}C reactions versus temperature. The curve for ^{16}O + ^{16}O is calculated assuming $\rho = 3 \times 10^6$ g/cm^3 and $X_{^{16}\mathrm{O}} = 0.5$, while the one for ^{16}O(γ,α)^{12}C is derived from the ^{12}C(α,γ)^{16}O reaction rate and is independent of ρ and $X_{^{16}\mathrm{O}}$. The dashed vertical line indicates a temperature of $T = 2.2$ GK typical for core oxygen burning in massive stars.

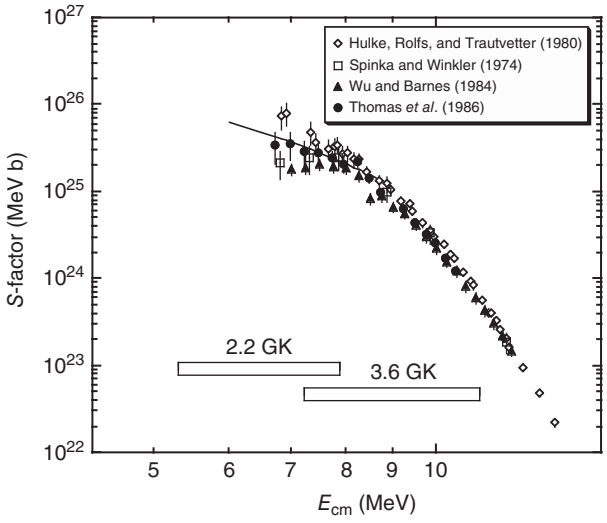

Figure 5.31 Total *S*-factor for the $^{16}O + ^{16}O$ reaction. The data are adopted from Spinka and Winkler (1974), Hulke, Rolfs, and Trautvetter (1980), Wu and Barnes (1984), and Thomas *et al.* (1986). The data from Thomas *et al.* (1986) are extracted from their Figures 9 and 10. The open bars indicate the location of the Gamow peaks for $T \approx 2.2$ GK (core oxygen burning) and $T \approx 3.6$ GK (explosive oxygen burning). The solid line shows the fitted total *S*-factor adopted by Caughlan and Fowler (1988).

The decay constant for $^{16}O + ^{16}O$ is obtained from $\lambda_{^{16}O}(^{16}O) = \rho(X_{^{16}O}/M_{^{16}O})$ $N_A\langle\sigma v\rangle$ (see Eq. (3.23)), assuming values of $\rho = 3 \times 10^6$ g/cm^3 and $X_{^{16}O} = 0.5$, whereas $\lambda_\gamma(^{16}O)$ is calculated from the forward $^{12}C(\alpha,\gamma)^{16}O$ reaction rate and is independent of ρ and $X_{^{16}O}$ (see Eq. (3.46)). Under these conditions, the $^{16}O + ^{16}O$ fusion is more likely to occur at temperatures below $T = 4$ GK and thus will be the dominant ^{16}O depleting process during hydrostatic oxygen burning.

The total $^{16}O + ^{16}O$ *S*-factor is shown in Figure 5.31. The reaction has been measured down to a bombarding energy of $E_{cm} \approx 6.8$ MeV. The height of the Coulomb barrier is ≈ 13 MeV and, similar to the case discussed in Section 5.3.1, the total *S*-factor varies strongly with energy because the Gamow factor does not remove entirely the energy dependence of the cross section at the measured energies (see Eq. (2.124)). The two shaded bars indicate the locations of the Gamow peaks at temperatures typical for core oxygen burning ($T \approx 2.2$ GK; $E_0 \pm \Delta/2 = 6600 \pm 1290$ keV) and explosive oxygen burning ($T = 3.6$ GK; $E_0 \pm \Delta/2 = 9170 \pm 1950$ keV). It can be seen that the data reach down to the center of the Gamow peak ($E_{cm} \approx E_0$) for $T = 2.2$ GK, whereas the data cover entirely the Gamow peak region for $T = 3.6$ GK. As expected, the total *S*-factor varies smoothly with energy since the $^{16}O + ^{16}O$ reaction proceeds through many overlapping resonances at each bombarding energy. In particular, the unexplained cross-section fluctuations observed in the total *S*-factor of $^{12}C + ^{12}C$ (Figure 5.24) are absent in the $^{16}O + ^{16}O$ data. However, the various

measurements are in poor agreement at the lower energies ($E_{cm} < 8$ MeV). The data have been fitted by a number of methods (see, e.g., Wu and Barnes, 1984). The fitted total *S*-factor adopted by Caughlan and Fowler (1988) at the lower energies is shown in Figure 5.31 as a solid line.

The $^{16}O + {}^{16}O$ reaction populates many levels in the residual nuclei. The different reaction channels have been investigated using a variety of techniques, including the direct detection of emitted light particles (Spinka and Winkler, 1974), detection of γ-rays emitted from excited levels in the residual nuclei (Spinka and Winkler, 1974; Wu and Barnes, 1984; Thomas *et al.*, 1986), and the activation method (Spinka and Winkler, 1974; Wu and Barnes, 1984). The cross-section data suggest significant contributions from reactions involving three particles in the exit channel, such as $^{16}O(^{16}O,2p)^{30}Si$ or $^{16}O(^{16}O,2\alpha)^{24}Mg$. These three-particle exit channel contributions may account for ≈ 20% of the total cross section at the lowest measured energy of $E_{cm} \approx 6.8$ MeV (Spinka and Winkler, 1974). The available data on the *partial* cross sections are also in poor agreement. Furthermore, little information is available on the competition between two- and three-particle exit channels that produce the same kind of particles, for example, between $^{16}O(^{16}O,p)^{31}P$ and $^{16}O(^{16}O,2p)^{30}Si$, or between $^{16}O(^{16}O,\alpha)^{28}Si$ and $^{16}O(^{16}O,2\alpha)^{24}Mg$. The average values of the reported branching ratios at $E_{cm} \approx 6.8$ MeV amount to ≈ 60% for $^{16}O(^{16}O,p)^{31}P$ and $^{16}O(^{16}O,2p)^{30}Si$, ≈ 25% for $^{16}O(^{16}O,\alpha)^{28}Si$ and $^{16}O(^{16}O,2\alpha)^{24}Mg$, ≈ 10% for $^{16}O(^{16}O,d)^{30}P$, and ≈ 5% for $^{16}O(^{16}O,n)^{31}S$.

The thermonuclear reaction rates for different $^{16}O + {}^{16}O$ exit channels are shown in Figure 5.25 (Caughlan and Fowler, 1988). The individual rates are normalized to the yields of the respective emitted light particles (p,α, n) rather than the number of reactions. For example, the curve labeled "$^{16}O(^{16}O,\alpha)$" represents the reaction rate for the production of as many α-particles as are produced by the reactions $^{16}O(^{16}O,\alpha)^{28}Si$ and $^{16}O(^{16}O,2\alpha)^{24}Mg$ combined. Similar arguments hold for the proton- and neutron-producing reaction channels. In particular, the curve labeled "$^{16}O(^{16}O,n)$" represents the reaction rate for neutron production from both $^{16}O(^{16}O,n)^{31}S$ and from deuteron breakup after $^{16}O(^{16}O,d)^{30}P$. It can be seen in Figure 5.25 that the proton exit channel dominates at all temperatures. At $T = 2.2$ GK, the reaction rate contributions for the emission of protons, α-particles, and neutrons are ≈ 62%, ≈ 21%, and ≈ 17%, respectively (Caughlan and Fowler, 1988). The present uncertainties in the rates of the primary oxygen burning reactions are difficult to quantify. Considering the poor agreement in the reported total $^{16}O + {}^{16}O$ cross section below $E_{cm} = 8$ MeV and our incomplete knowledge of the branching ratios for the different exit channels, one can conclude that the rates of the primary oxygen burning reactions at temperatures below $T = 3$ GK are uncertain by at least a factor of ≈ 3.

Similar to the case of carbon burning (Section 5.5.1), the secondary reactions contribute significantly to the nuclear energy released by the primary oxygen burning reactions. The result of a reaction network calculation near $T = 2.2$ GK (see below) yields an average energy release of $\overline{Q}_O \approx 17.2$ MeV for each $^{16}O + {}^{16}O$ reaction (see also Woosley, Heger, and Weaver, 2002). The energy generation rate

in hydrostatic oxygen burning is then given by Eq. (3.64),

$$\varepsilon_O = \frac{\overline{Q}_{\rm O}}{\rho} r_{^{16}{\rm O}+^{16}{\rm O}} = \frac{\overline{Q}_{\rm O}}{\rho} \frac{(N_{^{16}{\rm O}})^2 \langle \sigma v \rangle_{^{16}{\rm O}+^{16}{\rm O}}}{2} = \frac{N_A \overline{Q}_{\rm O}}{512} X^2_{^{16}{\rm O}} \rho N_A \langle \sigma v \rangle_{^{16}{\rm O}+^{16}{\rm O}}$$
$$= 2.03 \times 10^{22} X^2_{^{16}{\rm O}} \rho N_A \langle \sigma v \rangle_{^{16}{\rm O}+^{16}{\rm O}} \qquad ({\rm MeV\ g^{-1} s^{-1}}) \tag{5.119}$$

with $N_A \langle \sigma v \rangle_{^{16}{\rm O}+^{16}{\rm O}}$ the total $^{16}{\rm O} + {}^{16}{\rm O}$ reaction rate. The temperature dependence of the $^{16}{\rm O} + {}^{16}{\rm O}$ rate and of the energy generation rate during oxygen burning can be found from the expression for nonresonant reactions (see Eq. (3.90)). Near a typical temperature of $T_0 = 2.2$ GK, one finds a value of $\tau = 104.5$ (see Eq. (3.91)) and, thus, neglecting electron screening,

$$\varepsilon_{\rm O}(T) = \varepsilon_{\rm O}(T_0) \left(T/T_0\right)^{(104.5-2)/3} = \varepsilon_{\rm O}(T_0) \left(T/T_0\right)^{34} \tag{5.120}$$

The total energy released during oxygen burning can be found from Eq. (3.69),

$$\int \varepsilon_{\rm O}(t)\, dt = \frac{N_A \overline{Q}_O}{2 M_{^{16}{\rm O}}} \Delta X_{^{16}{\rm O}} = 3.24 \times 10^{23} \Delta X_{^{16}{\rm O}} \qquad ({\rm MeV/g}) \tag{5.121}$$

where $\Delta X_{^{16}{\rm O}}$ is the mass fraction of the consumed oxygen fuel. This value exceeds the total amount of energy released during either carbon or neon burning (see Eqs. (5.104) and (5.109)).

The results of a network calculation for a constant temperature $T = 2.2$ GK and density $\rho = 3 \times 10^6$ g/cm^3 are shown in Figure 5.32. These values are similar to those obtained from stellar model calculations for core oxygen burning in stars with an initial mass of $M = 25\, M_\odot$ and initial solar metallicity (Woosley, Heger, and Weaver, 2002). For the initial abundances at the start of core oxygen burning, we adopt the final abundances obtained at the end of core neon burning: ^{16}O ($X_i = 0.77$), ^{24}Mg ($X_i = 0.11$), and ^{28}Si ($X_i = 0.083$), with smaller contributions from nuclides in the ^{25}Mg–^{32}S range (Figure 5.29). The network is solved until oxygen exhaustion ($X_{^{16}{\rm O}} < 0.001$). The electron screening correction factor for the primary $^{16}{\rm O} + {}^{16}{\rm O}$ reaction amounts to ≈ 1.3 for the T–ρ conditions adopted here.

It can be seen from Figure 5.32 that many different nuclear processes occur during oxygen burning. Those links with the largest net abundance flows (represented by the thickest arrows) will be described first. The primary $^{16}{\rm O} + {}^{16}{\rm O}$ reactions produce ^{28}Si and ^{32}S via different sequences: (i) $^{16}{\rm O}(^{16}{\rm O},{\rm p})^{31}{\rm P}({\rm p},\gamma)^{32}{\rm S}$, (ii) $^{16}{\rm O}(^{16}{\rm O},{\rm p})^{31}{\rm P}({\rm p},\alpha)^{28}{\rm Si}$, (iii) $^{16}{\rm O}(^{16}{\rm O},\alpha)^{28}{\rm Si}$, and (iv) $^{16}{\rm O}(^{16}{\rm O},{\rm n})^{31}{\rm S}(\gamma,{\rm p})^{30}{\rm P}(\gamma,{\rm p})^{29}{\rm Si}(\alpha,{\rm n})^{32}{\rm S}$. The two $(\gamma,{\rm p})$ reactions occur because the proton separation energies of ^{31}S and ^{30}P are relatively small ($S_{\rm p} = 6133$ and 5595 keV, respectively) and, consequently, the photodisintegrations dominate over the competing β^+-decays. The decay $^{31}{\rm S}(\beta^+\nu)^{31}{\rm P}$, although weaker than $^{31}{\rm S}(\gamma,{\rm p})^{30}{\rm P}$, is nevertheless significant, as will be seen below. Some of the ^{28}Si nuclei are converted to ^{32}S via $^{28}{\rm Si}(\alpha,\gamma)^{32}{\rm S}$. A fraction of the ^{32}S nuclei is either transformed back to ^{31}P via $^{32}{\rm S}({\rm n},\gamma)^{33}{\rm S}({\rm n},\alpha)^{30}{\rm Si}({\rm p},\gamma)^{31}{\rm P}$, or is converted to heavier nuclei via $^{32}{\rm S}(\alpha,{\rm p})^{35}{\rm Cl}({\rm p},\gamma)^{36}{\rm Ar}$, and so on. Some of the liberated α-particles deplete the initially abundant ^{24}Mg nuclei via the processes $^{24}{\rm Mg}(\alpha,\gamma)^{28}{\rm Si}$

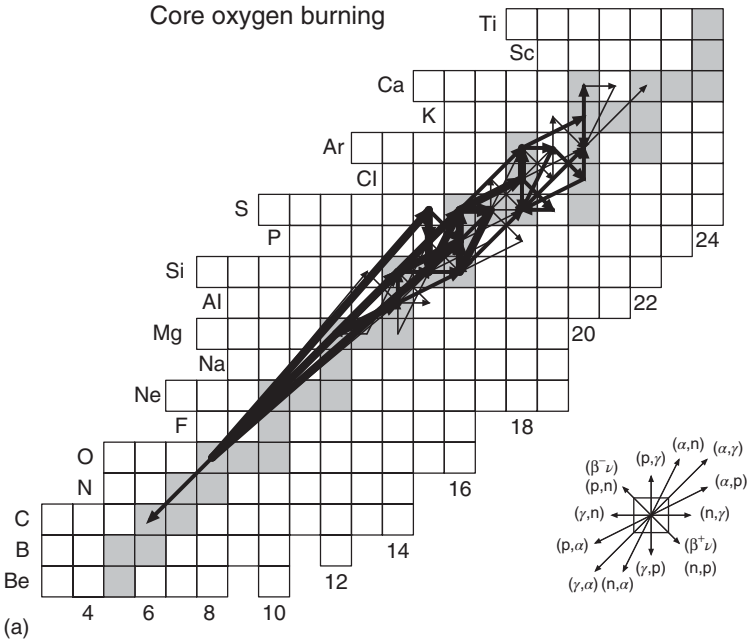

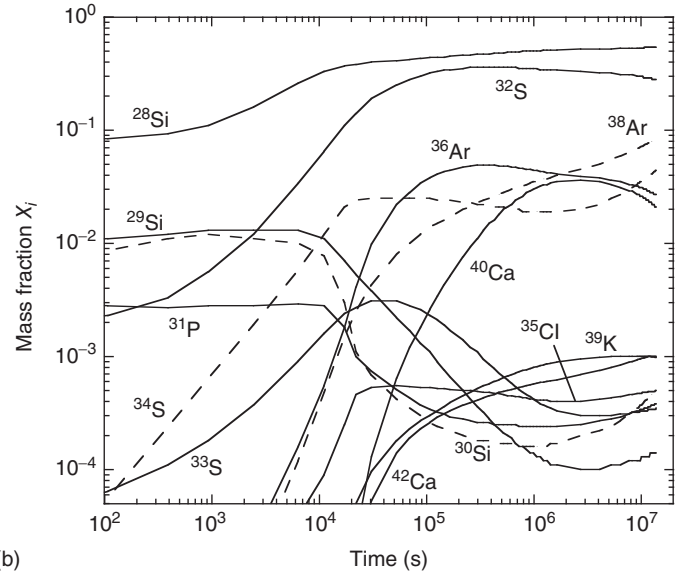

Figure 5.32 (a) Time-integrated net abundance flows, and (b) abundance evolutions for a constant temperature and density of $T = 2.2$ GK and $\rho = 3 \times 10^6$ g/cm^3, respectively. Such conditions are typical of core oxygen burning in stars with an initial mass of $M = 25\ M_\odot$ and with initial solar metallicity. The reaction network is solved numerically until the oxygen fuel is exhausted ($X_{^{16}\mathrm{O}} < 0.001$ after ≈ 162 d). The arrows, shaded squares, and key in the top part have the same meaning as in Figure 5.26. The ^{24}Mg$(\alpha,\gamma)^{28}$Si reaction is obscured by ^{16}O$(^{16}$O,$\alpha)^{28}$Si in part (a).

and ^{24}Mg(α,p)^{27}Al. Reactions such as ^{16}O(p,γ)^{17}F, ^{16}O(α,γ)^{20}Ne, ^{28}Si(p,γ)^{29}P, ^{32}S(p,γ)^{33}Cl, and ^{36}Ar(p,γ)^{37}K do not give rise to significant net flows. Their Q-values are so small (Q = 600 keV, 4730 keV, 2749 keV, 2277 keV, and 1858 keV, respectively) that in each case the forward rate is considerably smaller than the reverse photodisintegration rate.

The evolution of the most abundant nuclides is also shown in Figure 5.32. For reasons of clarity, the nuclides ^{16}O, ^{24,25,26}Mg, and ^{27}Al are not displayed in the figure. They are quickly depleted with progressing time. While the oxygen fuel is being consumed, the abundances of ^{28}Si and ^{32}S increase with time. The abundances of ^{34}S, ^{35}Cl, ^{36}Ar, ^{38}Ar, ^{39}K, ^{40}Ca, and ^{42}Ca also increase, while those of ^{29,30}Si and ^{31}P decrease from their initial values. The ^{16}O fuel is exhausted after about 162 days ($t = 1.4 \times 10^7$ s). The total nuclear energy generated is 2.5×10^{23} MeV/g. The most abundant nuclides at the end of the calculation are ^{28}Si ($X_f = 0.54$), ^{32}S ($X_f = 0.28$), ^{38}Ar ($X_f = 0.084$), ^{34}S ($X_f = 0.044$), ^{36}Ar ($X_f = 0.027$), and ^{40}Ca ($X_f = 0.021$), while nuclides in the ^{29}Si–^{42}Ca region have final mass fractions in the range of $X_f = 10^{-4}$–10^{-3} (see also Arnett, 1996; Chieffi, Limongi, and Straniero, 1998). All other nuclides not shown in the figure have mass fractions of $X < 6 \times 10^{-5}$ throughout the calculation.

The neutron excess increases significantly (by a factor of five in the above calculation) during core oxygen burning. The most important weak interactions that influence η are the positron decays ^{31}S(e$^+\nu$)^{31}P and ^{30}P(e$^+\nu$)^{30}Si, and the electron captures ^{33}S(e$^-$,ν)^{33}P, ^{35}Cl(e$^-$,ν)^{35}S, and ^{37}Ar(e$^-$,ν)^{37}Cl. The neutron excess becomes so large ($\eta \approx 0.007$) that the composition of the core matter deviates dramatically from a solar system abundance distribution. The products of hydrostatic oxygen burning are completely reprocessed in the subsequent explosive oxygen (and explosive silicon) burning phase before being ejected into the interstellar medium at the end of the massive star evolution.

It is also interesting that some of the weak interactions compete with nuclear reactions that link the same pair of nuclei. For instance, the *net* abundance flow between ^{33}S and ^{33}P is determined by the individual flows from ^{33}S(e$^-$,ν)^{33}P, ^{33}S(n,p)^{33}P, and ^{33}P(p,n)^{33}S. In the above network calculation, the latter reaction gives rise to the largest *individual* flow among these processes, but the first two processes have a larger *combined* flow. Hence, the arrow in Figure 5.32 points from ^{33}S to ^{33}P.

At temperatures typical of core oxygen burning, the influence of thermally excited levels on the rates of most reactions is relatively small. Almost all reactions involve stable (or long-lived) target nuclei (Figure 5.32) for the reasons given in Section 5.3.1 and, with few exceptions, their stellar enhancement factors and normalized partition functions are close to unity at $T \approx 2$ GK (see also Section 3.1.5). The situation is very different for the weak interactions. At $T = 2.2$ GK and $\rho = 3 \times 10^6$ g/cm^3, the half-life, for example, of ^{30}P(e$^+\nu$)^{30}Si is reduced from a laboratory value of $T_{1/2} = 150$ s to a stellar value of $T_{1/2} = 84$ s. As expected, even more drastic changes occur for electron captures. The stellar half-lives for ^{33}S(e$^-$,ν)^{33}P, ^{35}Cl(e$^-$,ν)^{35}S, and ^{37}Ar(e$^-$,ν)^{37}Cl at the assumed conditions are

$T_{1/2} = 4 \times 10^5$ s, 2×10^5 s, and 2×10^4 s, respectively, while in the laboratory ^{33}S and ^{35}Cl are stable and ^{37}Ar is long-lived ($T_{1/2} = 3.0 \times 10^6$ s; see Figure 1.18).

We already pointed out that oxygen burning resembles carbon burning in the sense that the nucleosynthesis is mainly driven by the fusion of two heavy nuclei. However, these two hydrostatic burning stages differ fundamentally because of the significantly higher temperature achieved in oxygen burning. In carbon burning, the number of protons, neutrons, and α-particles that can be captured by various nuclei decreases toward the end as the ^{12}C fuel is consumed and, consequently, the nucleosynthesis ceases. In hydrostatic oxygen burning, on the other hand, the temperature is sufficiently high that photodisintegrations of nuclei with the smallest particle separation energies provide another source of light particles, even when the ^{16}O fuel has been consumed. In the above network calculation, the proton and α-particle abundances are approximately constant ($X_{\rm H} \approx 10^{-13}$, $X_{^4{\rm He}} \approx 10^{-11}$) throughout the nucleosynthesis. A steady supply of light particles takes part in reactions, with the result that less tightly bound nuclides are transformed to more stable species, as discussed in Section 3.1.4. This aspect is reflected in Figure 5.32, where, toward the end of the calculation, the abundances of most nuclides do not stay constant, but change as a result of the nuclear rearrangement. As oxygen burning proceeds, many pairs of nuclides achieve an equilibrium between forward and reverse (photodisintegration) rate. Several such pairs eventually come into mutual equilibrium, giving rise to a *quasi-equilibrium cluster* (Section 3.1.6). Stellar model calculations demonstrated that, for progressing time and increasing temperature, more species join this group of nuclides (Woosley, Arnett, and Clayton, 1973; Chieffi, Limongi, and Straniero, 1998). After oxygen exhaustion and before the ignition of the next nuclear fuel, the nuclides in the $A = 24$–46 range form one large quasi-equilibrium cluster. A second cluster consisting of iron peak nuclides also starts to form at the end of oxygen burning. It originates from heavier nuclides initially present in the star that were so far disregarded in our discussion. Most of these nuclides take part in neutron-induced reactions, especially during core helium burning, but also during carbon and neon burning (Section 5.6.1). At the temperatures attained in core oxygen burning, all of these heavy nuclides are destroyed by (γ,p), (γ,α), and (γ,n) reactions and are transformed to the most tightly bound nuclides, that is, the iron peak species (Sections 1.5.1). The physics of quasi-equilibrium clusters will be described in more detail in the next section. See also Woosley, Arnett, and Clayton (1972).

The experimental information for the primary ^{16}O + ^{16}O reaction has already been presented. The secondary reactions are too numerous to be discussed in detail here. We will focus on a few secondary reactions that give rise to the largest net abundance flows (Figure 5.32). The following discussion will provide an impression on the sources and the reliability of the nuclear physics information entering oxygen burning calculations. The rates of reactions such as ^{31}P(p,γ)^{32}S, ^{31}P(p,α)^{28}Si, ^{35}Cl(p,γ)^{36}Ar, ^{30}Si(p,γ)^{31}P, ^{32}S(α,p)^{35}Cl, ^{24}Mg(α,p)^{27}Al, and ^{30}P(γ,p)^{29}Si near $T = 2.2$ GK are based on directly measured resonance energies and strengths (see Iliadis *et al.*, 2010). The rates of the latter three reverse

reactions are calculated from the corresponding forward rates. Branching ratios for ^{31}P + p and ^{35}Cl + p are displayed in Figure 5.17. Typical uncertainties of the above reaction rates at $T = 2.2$ GK amount to ±25%, except for the ^{32}S(α,p)^{35}Cl reaction where the rates are uncertain by a factor of two. The rates for the α-capture reactions ^{24}Mg(α,γ)^{28}Si, ^{28}Si(α,γ)^{32}S, and ^{32}S(α,γ)^{36}Ar are also based on direct experimental information, but may be subject to systematic errors on the order of factors of ≈ 2–3, as can be seen from the differences in the results reported by Caughlan and Fowler (1988) and Rauscher *et al.* (2000). Somewhat larger uncertainties are expected for the rates of reactions such as ^{31}S(γ,p)^{30}P, ^{33}S(n,α)^{30}Si, and ^{29}Si(α,n)^{32}S, which are based on Hauser–Feshbach statistical model calculations (Goriely, 1998; Rauscher and Thielemann, 2000).

5.3.4 Silicon Burning

Near the conclusion of core oxygen burning, when the ^{16}O fuel is depleted, the most abundant nuclides are ^{28}Si and ^{32}S (Figure 5.32). The stellar core contracts and the temperature increases. Fusion reactions, such as ^{28}Si + ^{28}Si or ^{28}Si + ^{32}S, are unlikely to occur because of Coulomb barrier considerations, even at the elevated temperatures achieved at the end of the massive star evolution. Instead, the nucleosynthesis proceeds via photodisintegrations of less tightly bound nuclei and the capture of the liberated light particles (protons, neutrons, and α-particles) to create gradually heavier and more tightly bound species, as described in Section 3.1.4. In this process, many forward and reverse reactions achieve equilibrium, and with increasing temperature and progressing time several pairs of nuclides link together to form quasi-equilibrium clusters. The overall result is another *photodisintegration rearrangement* process, similar to neon burning, but on a more extensive scale. We will describe below how ^{28}Si, ^{32}S, and other nuclides in the $A = 24$–46 region are gradually transformed to the most tightly bound species, that is, the iron peak nuclides (Section 1.5.1 and Figure 1.9). This process provides the star with another source of energy and is referred to as *silicon burning*. Temperatures during core silicon burning are in the range of $T = 2.8$–4.1 GK, depending on the stellar mass, with somewhat higher values during hydrostatic shell silicon burning.

Some of the fundamental concepts of silicon burning will now be discussed. For more information, the reader is referred to the pioneering work of Bodansky, Clayton, and Fowler (1968) and Woosley, Arnett, and Clayton (1973). Suppose first that ^{28}Si and ^{32}S are the only nuclear species present near the conclusion of oxygen burning. The decay constants for the photodisintegrations of both nuclides are displayed in Figure 5.33. The curves are calculated from Eq. (3.46) using the rates of the corresponding forward reactions. The photodisintegration decay constant depends strongly on the particle separation energy (or the Q-value of the forward reaction), as explained in Section 3.1.4 (see also Figure 3.6). The proton, neutron, and α-particle separation energies of ^{32}S and ^{28}Si amount to $S_p = 8.90$ MeV, $S_n = 15.00$ MeV, $S_\alpha = 6.95$ MeV, and

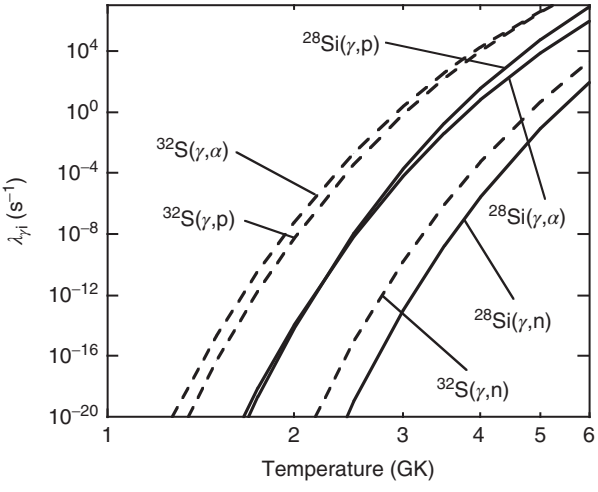

Figure 5.33 Decay constants for the photodisintegrations of ^{28}Si (solid lines) and ^{32}S (dashed lines) versus temperature. The curves are calculated from the rates of the corresponding forward reactions.

$S_p = 11.60$ MeV, $S_n = 17.20$ MeV, $S_\alpha = 9.98$ MeV, respectively. Hence, ^{32}S is the more fragile nucleus and is destroyed first. As the core temperature increases above $T \approx 2$ GK, ^{32}S will be consumed via ^{32}S(γ,α)^{28}Si and ^{32}S(γ,p)^{31}P. The last reaction is quickly followed by sequences, such as ^{31}P(γ,p)^{30}Si(γ,n)^{29}Si(γ,n)^{28}Si, converting effectively ^{32}S to ^{28}Si. The destruction of ^{32}S already starts near the end of oxygen burning, as can be seen from Figure 5.32.

The temperature increases further until the photodisintegration of ^{28}Si becomes substantial. The separation energy is not the only factor determining the photodisintegration rate, as can be seen in Figure 5.33. The decay constants for ^{28}Si(γ,p)^{27}Al and ^{28}Si(γ,α)^{24}Mg have comparable magnitudes although the separation energy for the (γ,α) reaction is considerably smaller than for the competing (γ,p) reaction. Other factors that sensitively influence the photodisintegration rate are the transmission probabilities of the photoejected charged particles through the Coulomb barrier and the reduced particle widths of the resonances through which the photodisintegration process proceeds.

The resulting nucleosynthesis that transforms Si and other intermediate mass nuclides to iron peak species is complex. To obtain a first impression, the results of a reaction network calculation, performed at constant temperature and density, will now be discussed. Subsequently, several analytical expressions are derived to gain a deeper understanding of silicon burning. For the network calculation, we chose a temperature and density of $T = 3.6$ GK and $\rho = 3 \times 10^7$ g/cm^3, respectively. These values are similar to those obtained from stellar evolution calculations for core silicon burning in stars with an initial mass of $M = 25\,M_\odot$ and with initial solar composition (Chieffi, Limongi, and Straniero, 1998; Woosley, Heger, and Weaver, 2002). The stellar evolution models also predict significant

abundance variations at elevated temperatures ($T > 2.2$ GK) between the termination of oxygen burning and the ignition of silicon burning in the stellar core (Chieffi, Limongi, and Straniero, 1998). In particular, the ^{32}S abundance decreases, while the abundances of ^{30}Si and ^{34}S, and hence the neutron excess parameter η, increase. As we shall see below, the initial value of η at the beginning of silicon burning sensitively influences silicon burning nucleosynthesis. For the network calculation, initial abundances of $X_i(^{28}\text{Si}) = 0.70$ and $X_i(^{30}\text{Si}) = 0.30$ are chosen. These translate into a value of $\eta_i = 0.02$ for the initial neutron excess parameter, in approximate agreement with the results presented by Thielemann and Arnett (1985) and Chieffi, Limongi, and Straniero (1998). Thermally excited levels have a profound effect at these elevated temperatures, not only on weak interaction decay constants, as already mentioned in Section 5.3.3, but also on the rates of many forward and reverse reactions through stellar enhancement factors and normalized partition functions that differ significantly from unity (Section 3.1.5). The network is solved until silicon exhaustion ($X_{^{28}\text{Si}} < 0.001$). The results are shown in Figure 5.34.

The time-integrated net abundance flows, F_{ij}, show an interesting pattern. Recall that the flows F_{ij} are integrated over the entire time until silicon exhaustion and thus present only the gross properties of the nucleosynthesis. Nevertheless, some of the most outstanding features of silicon burning are reflected in the global flow pattern. The fuel consists initially only of ^{28}Si and ^{30}Si. These nuclides are photodisintegrated, producing a net downward flow from ^{24}Mg to ^{4}He. The recapture of the liberated protons, α-particles, and neutrons gives rise to a net upward flow via a multitude of secondary reactions. A dense flow pattern in the $A = 25$–40 mass range, consisting of reactions such as (p,γ), (α,γ), (n,γ), (α,p), (α,n), (n,p), and their reverses, is apparent. Nuclides in the region $A = 46$–64 are also linked by numerous processes, giving rise to another dense flow pattern. There is considerably less nuclear activity between these two groups of nuclides in the $A = 40$–46 region. The reader may already suspect that the two groups of nuclides referred to above ($A = 25$–40 and $A = 46$–64) represent quasi-equilibrium clusters that are linked by reactions involving nuclides in the $A = 40$–46 region.

The evolution of the most abundant nuclides is shown in Figure 5.34. It is apparent how the abundances of nuclides in the $A < 40$ range gradually decrease (dashed lines), while at the same time the abundances of nuclides in the iron peak region increase (solid lines). Heavier and more tightly bound nuclides (Figure 1.9) build up as a result of a relatively small leakage of abundance flows from the intermediate mass region toward the iron peak. The silicon fuel is exhausted after $t = 4000$ s ($X_{^{28}\text{Si}} < 0.001$). At the end of the calculation, most of the matter ($\approx 94\%$ by mass) has been converted to ^{56}Fe ($X_f = 0.56$), ^{52}Cr ($X_f = 0.19$), ^{54}Fe ($X_f = 0.11$), ^{55}Fe ($X_f = 0.050$), and ^{53}Mn ($X_f = 0.034$). Recall, that ^{56}Fe is one of the most tightly bound nuclides (Section 1.5.1 and Figure 1.9). Similar values of final abundances have been obtained in stellar evolution calculations (Chieffi, Limongi, and Straniero, 1998). The abundances of free protons, α-particles, and neutrons amount to $X_\text{p} \approx 10^{-7}$, $X_\alpha \approx 10^{-6}$, and $X_\text{n} \approx 10^{-11}$, respectively, during most of the burning.

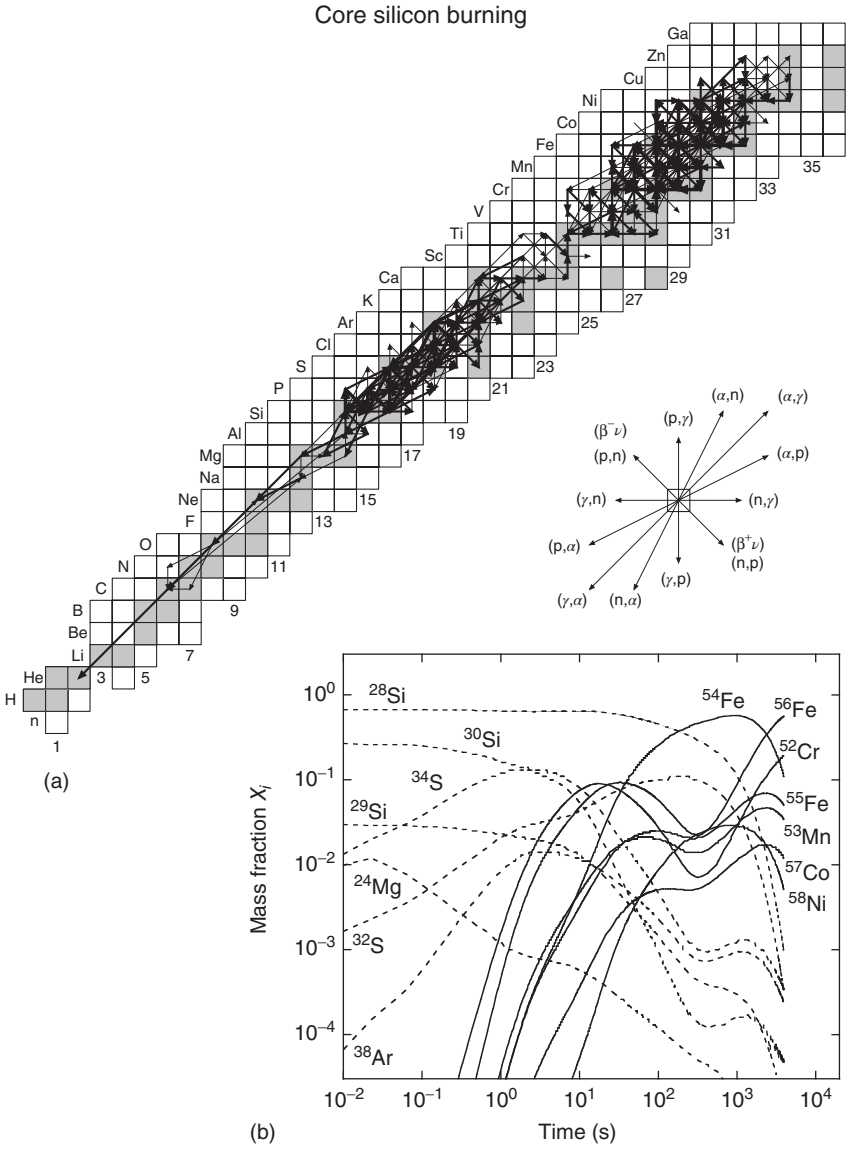

Figure 5.34 (a) Time-integrated net abundance flows, and (b) abundance evolutions for a constant temperature and density of $T = 3.6$ GK and $\rho = 3 \times 10^7$ g/cm^3, respectively. Such conditions are typical of core silicon burning in stars with an initial mass of $M = 25\ M_\odot$ and with initial solar metallicity. The reaction network is solved numerically until the silicon fuel is exhausted ($X_{^{28}\mathrm{Si}} < 0.001$ after ≈ 4000 s). Abundance flows are represented by arrows of three thicknesses: thick, intermediate and thin arrows show flows of $F^{\max} \geq F_{ij} > 10^{-2}F^{\max}$, $10^{-2}F^{\max} \geq F_{ij} > 10^{-4}F^{\max}$ and $10^{-4}F^{\max} \geq F_{ij} > 10^{-5}F^{\max}$, respectively, where $F^{\max}$ corresponds to the reaction with the maximum flow. The abundance flows in part (a) show the existence of two quasi-equilibrium clusters in the $A = 25$–40 and $A = 46$–64 mass ranges.

The neutron excess (Section 1.8) remains initially constant (until $t \approx 200$ s), but increases significantly afterward, as can be seen in Figure 5.34 from the transition of ^{54}Fe to ^{56}Fe as the most abundant species. The behavior of η is influenced by the slowness of the weak interactions. They become mainly important when the iron peak nuclides are reached by the flow. The electron captures ^{53}Mn(e$^-$,ν)^{53}Cr, ^{54}Fe(e$^-$,ν)^{54}Mn, ^{55}Fe(e$^-$,ν)^{55}Mn, ^{55}Co(e$^-$,ν)^{55}Fe, and ^{56}Co(e$^-$,ν)^{56}Fe have the largest impact on the evolution of η. The final neutron excess amounts to $\eta_f = 0.067$. Exactly the same values of X_f are obtained if the initial abundances are placed in sulfur or argon instead of silicon isotopes, as long as η_i is kept constant. On the other hand, a variation of η_i strongly influences the resulting composition of the iron peak species. In any case, the neutron excess becomes so large that the composition of the core matter deviates strongly from a solar abundance distribution. The products of hydrostatic silicon burning are completely reprocessed by the subsequent explosive burning phase before being (partially) ejected into the interstellar medium at the end of the massive star evolution. The core collapse and the subsequent supernova explosion depend critically on the composition, and hence, the neutron excess, of the matter resulting from core silicon burning. Furthermore, we already pointed out in the discussion of the previous advanced burning stages that the released thermonuclear energy is almost entirely radiated as neutrino–antineutrino pairs that are produced by thermal processes. During silicon burning, however, weak interactions contribute significantly to the neutrino losses.

The net abundance flows F_{ij} shown in Figure 5.34 are integrated over the entire running time of the network calculation. Figure 5.34 provides us neither with information regarding abundance flows at a particular instant in time, nor does it tell us which pairs (or groups) of nuclides are in equilibrium. Instead of showing the time-integrated net abundance flows, we can gain further insight into the nucleosynthesis by displaying the quantity $\phi_{ij} \equiv |r_{i\to j} - r_{j\to i}| / \max(r_{i\to j}, r_{j\to i})$ (see Eq. (3.55)). Recall, that a value of $\phi_{ij} \approx 0$ characterizes an equilibrium between a pair of nuclides i and j. On the other hand, for a pair of nuclides that is far from equilibrium we obtain $\phi_{ij} \approx 1$. Figure 5.35 shows the flows ϕ_{ij} at different instants in time ($t = 0.01$ s, 1 s, and 100 s) for the same reaction network calculation displayed in Figure 5.34. In each panel, the thickest lines show flows with $\phi_{ij} \leq 0.01$ (approximate equilibrium), those of intermediate thickness represent flows with $0.01 < \phi_{ij} \leq 0.1$, and the thinnest lines correspond to flows with $0.1 < \phi_{ij} \leq 1$ (no equilibrium). At early times ($t = 0.01$ s), we see a dense pattern of the thickest lines in the $A = 28$–44 range. For each of these pairs of nuclides, the forward reaction is partially balanced by the reverse reaction. The *net* abundance flow is considerably smaller compared to the corresponding *total* flows. In other words, the net abundance flow represents a very small difference between two large and nearly equal opposing reaction rates (hence, $\phi_{ij} \approx 0$). These pairs of nuclides in the $A = 28$–44 range are linked. They are in mutual equilibrium and form a quasi-equilibrium cluster (Section 3.1.6). The upper mass boundary of the cluster can be explained by the doubly-magic nature of ^{40}Ca, since a captured α-particle, for example, is easily removed by photodisintegration. At later times ($t = 1$ s), the

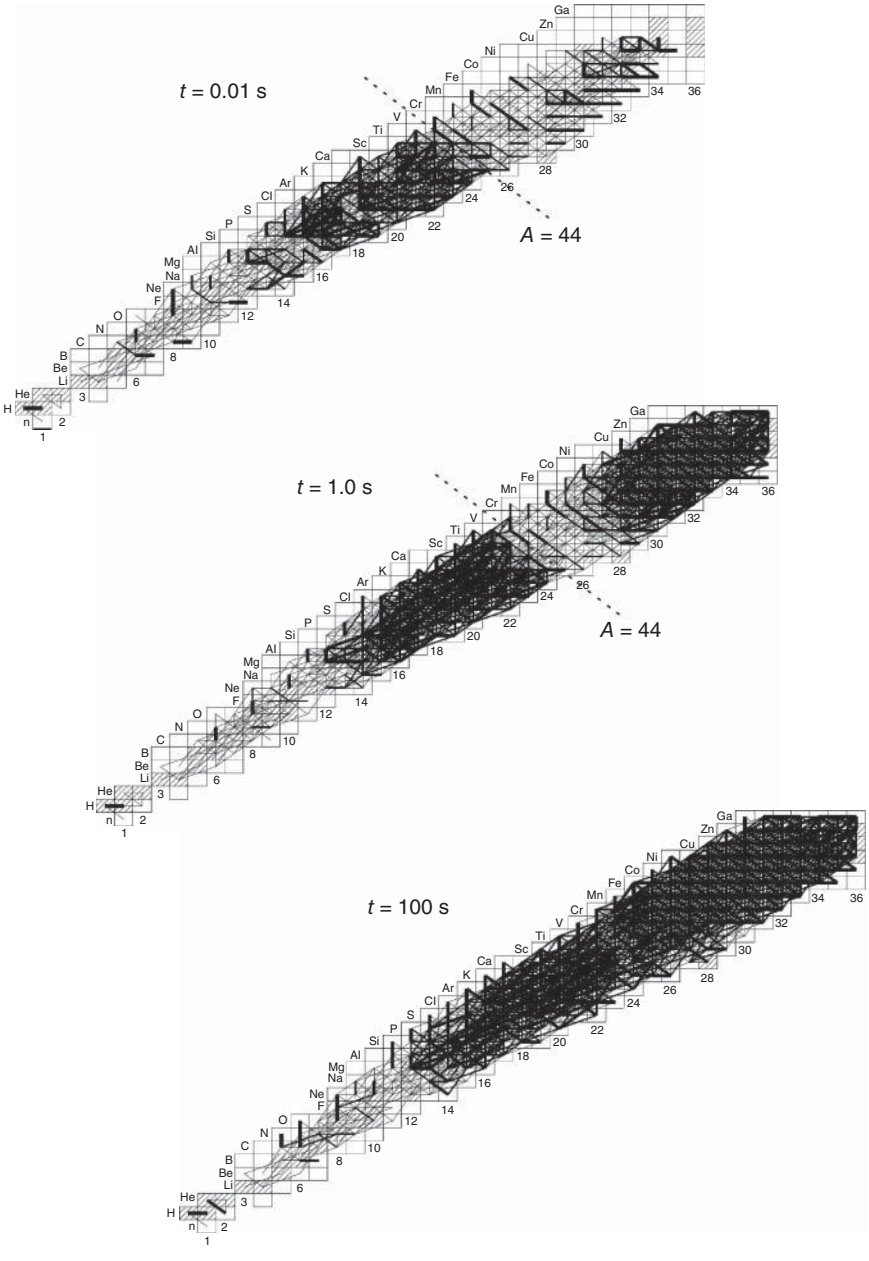

Figure 5.35 Normalized net abundance flows, $\phi_{ij} \equiv |r_{i\to j} - r_{j\to i}| / \max(r_{i\to j}, r_{j\to i})$, at three different times ($t = 0.01$ s, 1 s, 100 s) for the same reaction network calculation that is shown in Figure 5.34. In each panel, the thick lines show flows with $\phi_{ij} \leq 0.01$ (approximate equilibrium), those of intermediate thickness represent flows with $0.01 < \phi_{ij} \leq 0.1$, and the thin lines correspond to flows with $0.1 < \phi_{ij} \leq 1$ (no equilibrium). The flows ϕ_{ij} are not integrated over time, but provide instead a snapshot for the evolution of quasi-equilibrium clusters during the nuclear burning.

first cluster has grown in size ($A = 24$–44), while a second cluster appears in the iron peak region ($A = 50$–67). These two quasi-equilibrium clusters are not in mutual equilibrium, that is, they are not linked by the thickest lines. Closer to the end of the calculation ($t = 100$ s), the two groups have merged forming one large quasi-equilibrium cluster in the $A = 24$–67 region. A discussion of reactions linking the two clusters, for a range of temperature and density conditions or in stellar evolution models, can be found in Hix and Thielemann (1996) or Chieffi, Limongi, and Straniero (1998), respectively.

Reaction network calculations similar to those just discussed provide a reliable description of silicon burning nucleosynthesis. To gain further insight, we will now derive a number of analytical expressions, for constant temperature and density conditions, by focussing our attention mainly on the reaction links between the even–even $N = Z$ nuclides (or *α-nuclides*), such as ^{12}C, ^{16}O, ^{20}Ne, ^{24}Mg, and so on. Although the following considerations are very helpful, the reader should be aware that any truncation of the complex problem of silicon burning (i.e., the restriction to certain nuclides and reactions) will inevitably give rise to oversimplifications.

Suppose first, that the fuel consists only of ^{28}Si and that (α,γ) and (γ,α) reactions are the only interactions in the ensuing nuclear rearrangement. The reaction links between ^{12}C and ^{40}Ca are shown in Figure 5.36b. The numbers next to the arrows indicate the decay constants λ_α or λ_γ (in units of s^{-1}) at $T = 3.6$ GK for (α,γ) or (γ,α) reactions, respectively. The quantity λ_α is calculated from the reaction rates $N_A\langle\sigma v\rangle$ assuming $\rho = 3 \times 10^7$ g/cm^3 and $X_\alpha = 10^{-6}$ (see Eq. (3.23)). The latter value is adopted from the network calculation shown in Figure 5.34. Also, λ_α and λ_γ for a pair of forward and reverse reactions are related by Eq. (3.46). An interesting point becomes apparent here. The decay constant for ^{28}Si(γ,α)^{24}Mg is considerably smaller than the λ_γ values for all other α-nuclides shown. Some of the liberated α-particles will be captured by ^{24}Mg, a process that is more likely to occur than the competing photodisintegration of ^{24}Mg [$\lambda_\alpha(^{24}\text{Mg}) \gg \lambda_\gamma(^{24}\text{Mg})$]. Hence, the ^{24}Mg and ^{28}Si abundances will quickly seek an equilibrium. Another fraction of the liberated α-particles is captured by ^{28}Si. The subsequent photodisintegration of ^{32}S is more likely to occur than the competing ^{32}S(α,γ)^{36}Ar reaction [$\lambda_\alpha(^{32}\text{S}) \ll \lambda_\gamma(^{32}\text{S})$]. As a result, the ^{28}Si and ^{32}S abundances will also seek quickly an equilibrium. The number densities of ^{24}Mg and ^{28}Si, or of ^{28}Si and ^{32}S, are related by the Saha equation (see Eq. (3.50)),

$$\frac{N_3}{N_0 N_1} = \frac{1}{N_1}\frac{\lambda_1(0)}{\lambda_\gamma(3)} = \frac{1}{\theta}\left(\frac{M_0 + M_1}{M_0 M_1}\right)^{3/2} \frac{g_3}{g_0 g_1}\frac{G_3^{\text{norm}}}{G_0^{\text{norm}} G_1^{\text{norm}}} e^{Q_{01\to\gamma 3}/kT} \qquad (5.122)$$

with $\theta \equiv (2\pi m_u kT/h^2)^{3/2} = 5.943 \times 10^{33} T_9^{3/2}$ cm^{-3}; g_i denotes the statistical weights, m_u is the atomic mass unit, and the index 1 refers to α-particles for the pairs of nuclides quoted above (see Problem 5.6).

Similar equilibria are established between pairs of heavier α-nuclides since in each case the (γ,α) reaction is more likely to occur than the competing (α,γ) reaction (Figure 5.36b). Hence, the number densities of ^{24}Mg, ^{32}S, ^{36}Ar, and so on,

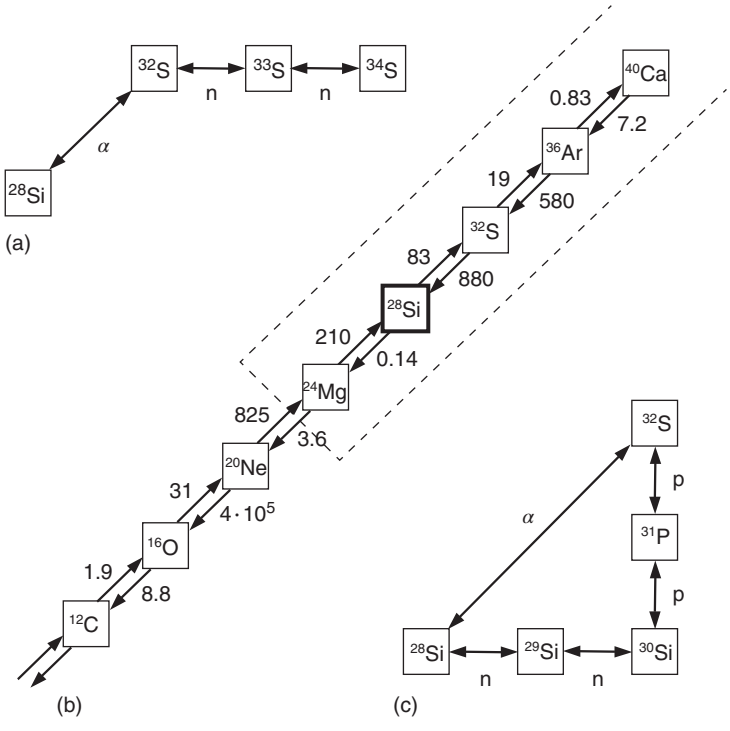

Figure 5.36 Reaction chains in silicon burning. (a) The reaction chain $^{28}Si \leftrightarrow {}^{32}S \leftrightarrow {}^{33}S \leftrightarrow {}^{34}S$ in equilibrium. (b) $(\alpha,\gamma)\leftrightarrow(\gamma,\alpha)$ reaction links between ^{12}C and ^{40}Ca. The numbers next to the arrows indicate values of the decay constants λ_α and λ_γ (in units of s^{-1}) for (α,γ) and (γ,α) reactions, respectively, assuming a temperature of $T = 3.6$ GK. The quantity λ_α is calculated using $\rho = 3 \times 10^7$ g/cm^3 and $X_\alpha = 10^{-6}$. The latter value is adopted from the network calculation displayed in Figure 5.34. Nuclides located within the region demarked by the dashed lines are in quasi-equilibrium. (c) The closed reaction chain $^{28}Si \leftrightarrow {}^{32}S \leftrightarrow {}^{31}P \leftrightarrow {}^{30}Si \leftrightarrow {}^{29}Si \leftrightarrow {}^{28}Si$ in equilibrium.

are all in quasi-equilibrium with ^{28}Si and the free α-particles. Photodisintegration reactions of the type (γ,p) and (γ,n) do also occur and give rise to the synthesis of non-α-nuclides that also come into equilibrium with the α-nuclides (and with ^{28}Si in particular) and the free nucleons. As a result, a quasi-equilibrium group of nuclides comes into existence, which is built around the tightly bound ^{28}Si. This conclusion remains unchanged if we take the $^{28}Si(\gamma,p)^{27}Al$ reaction into account, which has been disregarded so far. According to Figure 5.33, the $^{28}Si(\gamma,p)^{27}Al$ reaction is even more likely to occur above $T = 2.2$ GK than the $^{28}Si(\gamma,\alpha)^{24}Mg$ reaction. Nevertheless, ^{28}Si has by far the smallest *total* decay constant, $\lambda = \lambda_{\gamma\alpha} + \lambda_{\gamma p} + \lambda_{\gamma n}$, among all nuclides in the $A = 24$–67 range. Furthermore, ^{24}Mg comes into equilibrium with ^{28}Si, thereby greatly slowing the disintegration of ^{28}Si (see below). In summary, the quasi-equilibrium with respect to the residual ^{28}Si can be maintained because the intermediate-mass nuclei capture and emit α-particles, protons, or neutrons at rates considerably larger than the small net rate of ^{28}Si

disintegration. The time scale of the process is thus determined by the rate at which ^{28}Si can be decomposed.

The quasi-equilibrium abundance of a nuclide ${}^{A}_{Z}\mathrm{Y}_{N}$ relative to ^{28}Si is given by (Bodansky, Clayton, and Fowler, 1968, ; see also Problem 5.7)

$$\frac{N_Y}{N_{^{28}\mathrm{Si}}} = N_\alpha^{\delta_\alpha} N_\mathrm{p}^{\delta_\mathrm{p}} N_\mathrm{n}^{\delta_\mathrm{n}} \left(\frac{M_Y}{M_{^{28}\mathrm{Si}} M_\alpha^{\delta_\alpha} M_\mathrm{p}^{\delta_\mathrm{p}} M_\mathrm{n}^{\delta_\mathrm{n}}} \right)^{3/2} \frac{G_Y^{\mathrm{norm}}}{G_{^{28}\mathrm{Si}}^{\mathrm{norm}}} \frac{g_Y}{2^{\delta_\mathrm{p}+\delta_\mathrm{n}}} \frac{1}{\theta^{\delta_\alpha+\delta_\mathrm{p}+\delta_\mathrm{n}}} \times e^{[B(Y)-B(^{28}\mathrm{Si})-\delta_\alpha B(\alpha)]/kT} \tag{5.123}$$

where $A = Z + N$; N_α, N_p, and N_n are the number abundances of α-particles, protons, and neutrons, respectively; δ_α, δ_p, and δ_n specify the number of α-particles and nucleons of nuclide ${}^{A}_{Z}\mathrm{Y}_{N}$ in excess of their number in ^{28}Si. They are computed relative to the heaviest α-nucleus contained within ${}^{A}_{Z}\mathrm{Y}_{N}$. If this heaviest α-nucleus contains $N' = Z'$ protons and neutrons, then the integers δ_i are given by $\delta_\alpha = (N' + Z' - 28)/4$, $\delta_\mathrm{p} = Z - Z'$, and $\delta_n = N - N'$. For example, ^{34}S may be considered being composed of ^{32}S plus two neutrons, hence, $\delta_\alpha = (16 + 16 - 28)/4 = 1$, $\delta_\mathrm{p} = 16 - 16 = 0$, and $\delta_\mathrm{n} = 18 - 16 = 2$. The exponent $B(Y) - B(^{28}\mathrm{Si}) - \delta_\alpha B(\alpha)$ is the energy required to decompose ${}^{A}_{Z}\mathrm{Y}_{N}$ into ^{28}Si $+\delta_\alpha\,^4$He + nucleons, with $B(Y)$ the binding energy of ${}^{A}_{Z}\mathrm{Y}_{N}$. For example, for the ratio $N_{^{56}\mathrm{Ni}}/N_{^{28}\mathrm{Si}}$ we obtain from Eq. (5.123)

$$\frac{N_{^{56}\mathrm{Ni}}}{N_{^{28}\mathrm{Si}}} = N_\alpha^7 \left(\frac{2}{4^7} \right)^{3/2} \frac{1}{\theta^7} e^{[B(^{56}\mathrm{Ni})-B(^{28}\mathrm{Si})-7B(\alpha)]/kT} \tag{5.124}$$

where $B(^{56}\mathrm{Ni}) - B(^{28}\mathrm{Si}) - 7B(\alpha) = 49.385$ MeV. This result will be used later in the discussion of the energy generation rate. The free α-particles, protons, and neutrons maintain an equilibrium via many different closed reaction chains, such as $^{28}\mathrm{Si}\leftrightarrow{}^{32}\mathrm{S}\leftrightarrow{}^{31}\mathrm{P}\leftrightarrow{}^{30}\mathrm{Si}\leftrightarrow{}^{29}\mathrm{Si}\leftrightarrow{}^{28}\mathrm{Si}$ (Figure 5.36c). The light-particle abundances are related by (Problem 5.8)

$$N_\alpha = \frac{1}{16} N_\mathrm{n}^2 N_\mathrm{p}^2 \frac{1}{\theta^3} \left(\frac{M_\alpha}{M_\mathrm{p}^2 M_\mathrm{n}^2} \right)^{3/2} e^{B(\alpha)/kT} \tag{5.125}$$

where $B(\alpha) = 28.295$ MeV is the binding energy of the α-particle. From Eqs. (5.123) and (5.125), one can see that the equilibrium abundance of each nucleus relative to ^{28}Si is determined by the abundances of any two light particles. We also conclude that the quasi-equilibrium abundance of nucleus ${}^{A}_{Z}\mathrm{Y}_{N}$ is uniquely specified by the four parameters $N_{^{28}\mathrm{Si}}$, N_α, N_p, and T.

The net downward flow from ^{24}Mg to ^{4}He will be considered next (Figure 5.34). According to Figure 5.35, the lower bound of the silicon quasi-equilibrium cluster is ^{24}Mg. Nuclides lighter than ^{24}Mg are generally *not* in equilibrium with ^{28}Si. This can also be seen from the decay constants given in Figure 5.36b. The α-captures on ^{20}Ne and ^{12}C are *less* likely to occur than the competing (γ,α) reactions $[\lambda_{\alpha\gamma}(^{20}\mathrm{Ne}) \ll \lambda_{\gamma\alpha}(^{20}\mathrm{Ne})$ and $\lambda_{\alpha\gamma}(^{12}\mathrm{C}) \ll \lambda_{\gamma 3\alpha}(^{12}\mathrm{C})]$ and, hence, the abundances of the pairs ^{20}Ne–^{24}Mg and ^{12}C–^{16}O will not quickly seek an equilibrium. The effective rate of ^{28}Si destruction is then determined by the photodisintegration of

^{24}Mg. Net flows f_i between pairs of the light α-nuclides are given by Eqs. (3.23) and (3.53),

$$f_{^{24}\mathrm{Mg}\to^{20}\mathrm{Ne}} = N_{^{24}\mathrm{Mg}}\lambda_{\gamma\alpha}(^{24}\mathrm{Mg}) - N_{^{20}\mathrm{Ne}}\lambda_{\alpha\gamma}(^{20}\mathrm{Ne}) \tag{5.126}$$

$$f_{^{20}\mathrm{Ne}\to^{16}\mathrm{O}} = N_{^{20}\mathrm{Ne}}\lambda_{\gamma\alpha}(^{20}\mathrm{Ne}) - N_{^{16}\mathrm{O}}\lambda_{\alpha\gamma}(^{16}\mathrm{O}) \tag{5.127}$$

$$f_{^{16}\mathrm{O}\to^{12}\mathrm{C}} = N_{^{16}\mathrm{O}}\lambda_{\gamma\alpha}(^{16}\mathrm{O}) - N_{^{12}\mathrm{C}}\lambda_{\alpha\gamma}(^{12}\mathrm{C}) \tag{5.128}$$

$$f_{^{12}\mathrm{C}\to^{4}\mathrm{He}} = N_{^{12}\mathrm{C}}\lambda_{\gamma 3\alpha}(^{12}\mathrm{C}) - r_{3\alpha} \tag{5.129}$$

where $r_{3\alpha} = N_\alpha\lambda_{3\alpha}/3$ is the rate of the 3α reaction, which depends on N_α^3 (see Eq. (5.83)); $\lambda_{\gamma 3\alpha}(^{12}\mathrm{C})$ is the decay constant for the disintegration $^{12}\mathrm{C} \to \alpha + \alpha + \alpha$. Since the decomposition of ^{28}Si is so slow, and thus determines the overall time scale of the process, we conclude that the abundances of the light α-nuclides are small compared to the ^{28}Si abundance. This also means that the abundances of the light α-nuclides achieve a steady state, that is, the abundance flow into each of the nuclides ^{20}Ne, ^{16}O, and ^{12}C is balanced by the flow out. Therefore, the net flows f_i are equal, $f_{^{24}\mathrm{Mg}\to^{20}\mathrm{Ne}} = f_{^{20}\mathrm{Ne}\to^{16}\mathrm{O}} = f_{^{16}\mathrm{O}\to^{12}\mathrm{C}} = f_{^{12}\mathrm{C}\to^{4}\mathrm{He}} \equiv f_{\mathrm{an}}$. With this assumption, the above system of equations can be solved for f_{an}, with the result (Problem 5.9)

$$f_{\mathrm{an}} = \frac{N_{^{24}\mathrm{Mg}}\lambda_{\gamma\alpha}(^{24}\mathrm{Mg}) - \frac{\lambda_{\alpha\gamma}(^{20}\mathrm{Ne})}{\lambda_{\gamma\alpha}(^{20}\mathrm{Ne})}\frac{\lambda_{\alpha\gamma}(^{16}\mathrm{O})}{\lambda_{\gamma\alpha}(^{16}\mathrm{O})}\frac{\lambda_{\alpha\gamma}(^{12}\mathrm{C})}{\lambda_{\gamma 3\alpha}(^{12}\mathrm{C})}r_{3\alpha}}{1 + \frac{\lambda_{\alpha\gamma}(^{20}\mathrm{Ne})}{\lambda_{\gamma\alpha}(^{20}\mathrm{Ne})}\left[1 + \frac{\lambda_{\alpha\gamma}(^{16}\mathrm{O})}{\lambda_{\gamma\alpha}(^{16}\mathrm{O})}\left(1 + \frac{\lambda_{\alpha\gamma}(^{12}\mathrm{C})}{\lambda_{\gamma 3\alpha}(^{12}\mathrm{C})}\right)\right]} \tag{5.130}$$

The above analytical expression gives the effective photodisintegration rate of ^{24}Mg and, hence, the effective rate for the conversion of ^{28}Si into heavier nuclides as a function of temperature and α-particle abundance. The ^{24}Mg abundance, $N_{^{24}\mathrm{Mg}}$, can be obtained from Eq. (5.122).

Figure 5.37 compares the total ^{28}Si photodisintegration rate, $r_{^{28}\mathrm{Si}+\gamma} = N_{^{28}\mathrm{Si}}[\lambda_{\gamma\alpha}(^{28}\mathrm{Si}) + \lambda_{\gamma\mathrm{p}}(^{28}\mathrm{Si})]$, where $\lambda_{\gamma\mathrm{n}}(^{28}\mathrm{Si})$ is negligible, with the effective rate f_{an} of ^{28}Si consumption. The curves are computed for the conditions $T = 3.6$ GK and $\rho = 3 \times 10^7$ g/cm^3 as a function of the remaining ^{28}Si abundance. The α-particle abundance is adopted from the numerical results of a network calculation (Figure 5.34). A few interesting points are apparent. First, it can be seen that the effective rate of ^{28}Si consumption is two to three orders of magnitude smaller than the total photodisintegration rate of ^{28}Si. This is caused by the ^{28}Si photodisintegration flow being almost exactly balanced by the flow upward from ^{24}Mg (so that the *net* flow is small) and supports the above arguments regarding the very slow conversion of ^{28}Si. Second, it is apparent that the downward flow, f_{an}, from ^{28}Si decreases with time as ^{28}Si burns. Since the liberated light particles are used to build up iron peak nuclides, the upward flow from ^{28}Si also decreases with time as ^{28}Si burns. Third, the long-dashed line shows the flow $f_{\mathrm{num}} = f_{^{24}Mg\to^{20}\mathrm{Ne}}$, which is directly obtained from a network calculation according to Eq. (5.126). The curves for f_{an} and f_{num} are in good agreement. Hence, Eq. (5.130) provides a reliable approximation for the effective rate of ^{28}Si consumption. This also means that only (γ,α) or (α,γ) reactions between pairs of α-nuclides are important for the downward flow from ^{28}Si to ^{4}He. However,

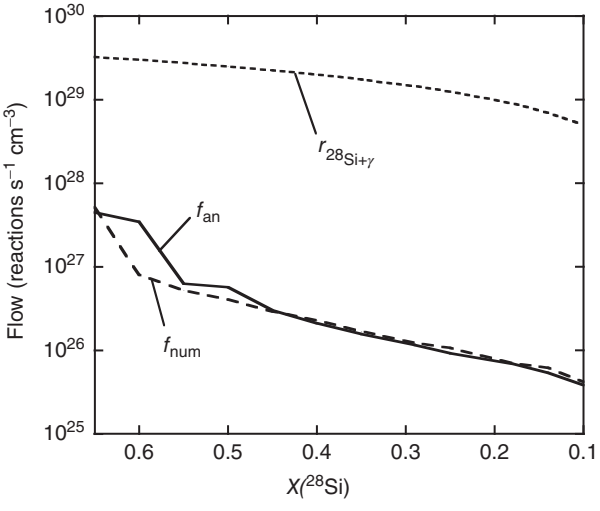

Figure 5.37 Comparison of total ^{28}Si photodisintegration rate ($r_{^{28}Si+\gamma}$; short-dashed line) with the effective rate of ^{28}Si consumption (f_{an}; solid line). The curves are computed as a function of the remaining ^{28}Si abundance for the conditions $T =$ 3.6 GK and $\rho = 3 \times 10^7$ g/cm^3. The α-particle abundance is adopted from the numerical results of the network calculation displayed in Figure 5.34. The long-dashed line shows the flow $f_{^{24}Mg\rightarrow^{20}\mathrm{Ne}} = f_{\mathrm{num}}$ that is directly obtained from the network calculation.

for different temperature and density conditions, a number of other reactions play an important role as well (Hix and Thielemann, 1996). Finally, for the temperature adopted here, the curve for f_{an} is almost indistinguishable from the values obtained with the approximation $f \approx N_{^{24}\mathrm{Mg}}\lambda_{\gamma\alpha}(^{24}\mathrm{Mg})$. For increasing temperature, the α-particle capture on ^{20}Ne becomes important (see Eq. (5.130)) and, consequently, the above approximation deviates from f_{an}.

The total energy release during hydrostatic silicon burning can be estimated approximately from Eq. (3.69), if we assume that for each two ^{28}Si nuclei that are destroyed, one ^{56}Fe nucleus is produced (see also Figure 5.34). The photodisintegration of the first ^{28}Si nucleus provides a free α-particle that is then captured by the second ^{28}Si nucleus. With $\overline{Q}_{\mathrm{Si}} \approx Q_{2^{28}\mathrm{Si}\rightarrow^{56}\mathrm{Fe}} = 17.62$ MeV, we find

$$\int \varepsilon_{\mathrm{Si}}(t)\,dt = \frac{N_A \overline{Q}_{\mathrm{Si}}}{2M_{^{28}\mathrm{Si}}}\Delta X_{^{28}\mathrm{Si}} = 1.90 \times 10^{23}\Delta X_{^{28}\mathrm{Si}} \qquad (\mathrm{MeV/g}) \qquad (5.131)$$

where $\Delta X_{^{28}\mathrm{Si}}$ is the mass fraction of the consumed silicon fuel. This value is smaller than what is expected from either carbon or oxygen burning, but exceeds the total energy released during neon burning (see Eqs. (5.104), (5.109), and (5.121)).

The nuclear energy generation *rate* cannot be described precisely by an analytical expression since the nuclear transformations during silicon burning are very complex. Reaction network calculations show that the energy generation rate is sensitive to the temperature and density conditions, but also to the neutron

excess (Hix and Thielemann, 1996). In the simplest case, an order-of-magnitude estimate can be found if one assumes that the initial neutron excess is very small ($\eta \approx 0$), that weak interactions are negligible, and that for each two ^{28}Si nuclei that are destroyed one ^{56}Ni nucleus is produced (Bodansky, Clayton, and Fowler, 1968). Recall from Figure 1.9 that ^{56}Ni is the most tightly bound $N = Z$ nuclide. As explained above, the rate of ^{28}Si consumption is mainly determined by the ^{24}Mg(γ,α)^{20}Ne reaction. Starting from Eq. (3.64), one finds

$$\begin{aligned}\varepsilon_{\mathrm{Si}} &= \frac{Q_{2^{28}Si\rightarrow^{56}\mathrm{Ni}}}{\rho} r_{2^{28}\mathrm{Si}\rightarrow^{56}\mathrm{Ni}} \approx \frac{Q_{2^{28}\mathrm{Si}\rightarrow^{56}\mathrm{Ni}}}{\rho} r_{^{24}\mathrm{Mg}(\gamma,\alpha)^{20}\mathrm{Ne}} \\ &= \frac{Q_{2^{28}\mathrm{Si}\rightarrow^{56}\mathrm{Ni}}}{\rho} N_{^{24}\mathrm{Mg}} \lambda_{\gamma\alpha}(^{24}\mathrm{Mg}) \end{aligned} \tag{5.132}$$

The quantity $N_{^{24}\mathrm{Mg}}$ can be replaced by the ^{28}Si abundance using Eq. (5.122) (see also Problem 5.6). The decay constant $\lambda_{\gamma\alpha}(^{24}\mathrm{Mg})$ can be expressed in terms of the corresponding forward reaction rate using Eq. (3.46). The normalized partition functions for ^{20}Ne, ^{24}Mg, and ^{28}Si in these two expressions are close to unity for $T \leq 5$ GK. Equation (5.122) contains the α-particle abundance, which is derived from Eq. (5.124). Substitution of these three expressions into Eq. (5.132) gives

$$\begin{aligned}\varepsilon_{\mathrm{Si}} = 9.8685 \times 10^9 \frac{2^{3/14}}{8} \frac{Q_{2^{28}\mathrm{Si}\rightarrow^{56}\mathrm{Ni}}}{\rho} \left(\frac{M_{^{20}\mathrm{Ne}} M_\alpha^2}{M_{^{28}\mathrm{Si}}}\right)^{3/2} N_{^{28}\mathrm{Si}} \left(\frac{N_{^{28}\mathrm{Si}}}{N_{^{56}\mathrm{Ni}}}\right)^{1/7} \\ \times e^{11.605[B(^{56}\mathrm{Ni})-B(^{28}\mathrm{Si})-7B(\alpha)]/(7T_9)} e^{-11.605[Q_{^{20}\mathrm{Ne}(\alpha,\gamma)}+Q_{^{24}\mathrm{Mg}(\alpha,\gamma)}]/T_9} \\ \times T_9^{3/2} N_A \langle \sigma v \rangle_{^{20}\mathrm{Ne}(\alpha,\gamma)} \qquad (\mathrm{MeV\,g^{-1}s^{-1}}) \end{aligned} \tag{5.133}$$

If one assumes in addition that most of the matter resides in either ^{28}Si or ^{56}Ni, then $X_{^{28}\mathrm{Si}} + X_{^{56}\mathrm{Ni}} = 1$. Inserting the numerical values of $Q_{2^{28}\mathrm{Si}\rightarrow^{56}\mathrm{Ni}} = 10.918$ MeV, $Q_{^{20}\mathrm{Ne}(\alpha,\gamma)} = 9.317$ MeV, $Q_{^{24}\mathrm{Mg}(\alpha,\gamma)} = 9.984$ MeV, and $[B(^{56}\mathrm{Ni}) - B(^{28}\mathrm{Si}) - 7B(\alpha)] = 49.385$ MeV, and replacing the number abundances by mass fractions (see Eq. (1.14)) yields

$$\begin{aligned}\varepsilon_{\mathrm{Si}} = 1.2985 \times 10^{34} X_{^{28}\mathrm{Si}} \left(\frac{2X_{^{28}\mathrm{Si}}}{1 - X_{^{28}\mathrm{Si}}}\right)^{1/7} e^{-142.12/T_9} T_9^{3/2} N_A \langle \sigma v \rangle_{^{20}Ne(\alpha,\gamma)} \\ (\mathrm{MeV\,g^{-1}s^{-1}}) \end{aligned} \tag{5.134}$$

where $[2X_{^{28}\mathrm{Si}}/(1 - X_{^{28}\mathrm{Si}})]^{1/7} \approx 1$ within a factor of two between $X_{^{28}\mathrm{Si}} = 0.01 - 0.99$. Equation (5.134) is independent of the density. An analytical expression for the ^{20}Ne(α,γ)^{24}Mg reaction rate is given in Section 5.3.2. The temperature dependence of the energy generation rate during silicon burning is then

$$\varepsilon_{\mathrm{Si}} \sim T_9^{2.229} e^{-12.681/T_9} e^{-142.12/T_9} T_9^{1.5} \sim T_9^{3.729} T_9^{154.80/T_9} \tag{5.135}$$

where the term $\exp(-154.80/T_9)$ is derived according to the method described by Eqs. (3.85)–(3.90). For example, near $T_0 = 3.6$ GK we find

$$\varepsilon_{\mathrm{Si}}(T) = \varepsilon_{\mathrm{Si}}(T_0) \left(T/T_0\right)^{47} \tag{5.136}$$

Since so many nuclides achieve quasi-equilibrium, the thermonuclear rates of most reactions are not important for the nucleosynthesis and energy production during silicon burning. What is mainly needed in terms of nuclear physics input are binding energies (or Q-values), nuclear masses, spins (see Eqs. (5.122) and (5.123)), and stellar weak interaction rates. Binding energies and masses of nuclides close to stability are well known. The thermonuclear rates are important, however, for those reactions that are not in quasi-equilibrium for a significant amount of time during the burning. This applies to reactions that determine the net downward flow from ^{24}Mg, and to those that mediate between the two quasi-equilibrium clusters built around ^{28}Si and the iron-peak nuclides. For the reaction network calculation discussed above, the downward flow from ^{24}Mg is governed by ^{24}Mg(γ,α)^{20}Ne, while ^{42}Ca(α,γ)^{46}Ti and ^{45}Sc(p,γ)^{46}Ti are among the reactions which link the two clusters. Detailed lists of reactions are given in Hix and Thielemann (1996) and Chieffi, Limongi, and Straniero (1998). The reverse ^{24}Mg(γ,α)^{20}Ne reaction rate can be calculated from the forward ^{20}Ne(α,γ)^{24}Mg rate, which has already been discussed in connection with carbon and neon burning (Sections 5.3.1 and 5.3.2). Near $T \approx 3.6$ GK, the ^{20}Ne(α,γ)^{24}Mg reaction rate may be subject to systematic errors of about a factor of two, as can be seen from the different results reported by Caughlan and Fowler (1988), Angulo *et al.* (1999), and Rauscher *et al.* (2000). Several, but not all, of the reactions linking the two quasi-equilibrium clusters have been measured directly in the Gamow peaks appropriate for hydrostatic and explosive silicon burning. Among the measured reactions are ^{42}Ca(α,γ)^{46}Ti, ^{42}Ca(α,p)^{45}Sc (Mitchell *et al.*, 1985), ^{42}Ca(α,n)^{45}Ti (Cheng and King, 1979), ^{41}K(α,p)^{44}Ca (Scott *et al.*, 1991) and ^{45}Sc(p,γ)^{46}Ti (Solomon and Sargood, 1978). Typical reaction rate uncertainties are about $\pm$20% where direct data exist. Other mediating reactions, some of which involve radioactive target nuclei, such as ^{41}Ca, ^{44}Sc, and ^{44}Ti, have not been measured yet. In these cases, the Hauser–Feshbach statistical model is used to estimate the reaction rates theoretically (Goriely, 1998; Rauscher and Thielemann, 2000).

5.3.5
Nuclear Statistical Equilibrium

As the ^{28}Si disappears at the end of silicon burning, the temperature in the stellar core increases steadily (Section 1.4.3 and Figure 5.1). At some point, the previously nonequilibrated reactions in the $A < 24$ region come into equilibrium as well (Figures 5.35 and 5.36). The last link to achieve equilibrium is $3\alpha \leftrightarrow ^{12}$C. Every nuclide in the network is now in equilibrium via strong and electromagnetic interactions and one large quasi-equilibrium group stretches from p, n, α to the iron peak nuclides. This situation is referred to as *nuclear statistical equilibrium* (NSE). For a distinction between nuclear statistical equilibrium and the related e-process (Burbidge *et al.*, 1957), see Wallerstein *et al.* (1997).

Weak interactions do not participate in the equilibrium. For example, the reverse link of electron capture on some parent nucleus is neutrino capture on

the corresponding daughter nucleus. Neutrinos normally escape from the star without interaction since their mean free path exceeds the stellar radius. Hence, a true equilibrium involving weak interactions is not achieved. In nuclear statistical equilibrium, the abundance of any nuclide ${}^{A}_{\pi}\mathrm{Y}_{\nu}$ can be determined by repeated application of the Saha equation (see Eq. (5.122)). The result is (Clifford and Tayler, 1965, see also Problem 5.10)

$$N_Y = N_{\mathrm{p}}^{\pi} N_{\mathrm{n}}^{\nu} \frac{1}{\theta^{A-1}} \left(\frac{M_Y}{M_{\mathrm{p}}^{\pi} M_{\mathrm{n}}^{\nu}} \right)^{3/2} \frac{g_Y}{2^A} G_Y^{\mathrm{norm}} e^{B(Y)/kT} \tag{5.137}$$

with θ defined as in Eq. (5.122), $B(Y)$ the binding energy of ${}^{A}_{\pi}\mathrm{Y}_{\nu}$ and $A = \pi + \nu$. The symbols π and ν are used instead of Z and N for the number of protons and neutrons, respectively, to avoid confusion with the number density N_i. The abundance of any isotope is hence given in terms of its nuclear properties (binding energy, mass, spin, and so on) and the free nucleon abundances, N_{p} and N_{n}. The above equation is by itself inadequate to yield the equilibrium abundance N_Y since N_{p} and N_{n} are not given. But two additional constraints can be applied. One unknown quantity (say N_{p}) can be eliminated using conservation of mass (see Eq. (1.13))

$$\sum_i X_i = \frac{\sum_i N_i M_i}{\rho N_A} = 1 \tag{5.138}$$

where the sum i is over all nuclides in the network, including free protons, neutrons, and α-particles. Recall that the strong and electromagnetic interactions occur considerably more rapidly than weak interactions. Thus, nuclei and photons come into equilibrium in a relatively short time, while the total numbers of free and bound protons and neutrons are essentially constant. Conservation of total charge is frequently expressed by the requirement that the total number densities of (free and bound) protons and neutrons must preserve the neutron excess (see Eq. (1.36))

$$\sum_i \frac{(\nu_i - \pi_i)}{M_i} X_i = \frac{\sum_i N_i (\nu_i - \pi_i)}{\rho N_A} \equiv \eta \tag{5.139}$$

It follows immediately from Eqs. (5.137)–(5.139) that the abundance of any nuclide in nuclear statistical equilibrium is specified by only three independent parameters: temperature, density, and neutron excess. Weak interactions may also occur. They are assumed to be sufficiently slow so that nuclear statistical equilibrium at a specific value of η is established in a considerably shorter time than the time required for a significant change in the value of η to occur. Weak interactions must be monitored carefully because the composition of the iron peak depends sensitively on η, as will be shown below.

In the following, some interesting properties of Eq. (5.137) will be explored. First, consider the simplest case with $\eta \approx 0$. Assume that weak interactions are negligible, and that the decomposition of ^{28}Si during the preceding silicon burning stage has mainly produced ^{56}Ni, which is the most tightly bound species with

$N = Z$ (Figure 1.9). By combining two equations of the form of Eq. (5.137), one for ^{4}He and the other for ^{56}Ni, one finds

$$\frac{N_{^4\mathrm{He}}^{14}}{N_{^{56}\mathrm{Ni}}} = \theta^{13}\frac{2^{42}}{56^{3/2}}e^{[14B(^4\mathrm{He})-B(^{56}\mathrm{Ni})]/kT} \tag{5.140}$$

where $g_{^4\mathrm{He}} = g_{^{56}\mathrm{Ni}} = 1$ and $G_{^4\mathrm{He}}^{\mathrm{norm}} = G_{^{56}\mathrm{Ni}}^{\mathrm{norm}} = 1$. The latter equality holds within 10% up to $T = 5$ GK. Furthermore, $14B(^4\mathrm{He}) - B(^{56}\mathrm{Ni}) = -87.853$ MeV is the energy required to separate ^{56}Ni into 14 α-particles. Now, assume that the stellar plasma consists entirely of ^{4}He and ^{56}Ni. We would like to know the T–ρ conditions for which the mass fractions of these two nuclides are equal ($X_{^4\mathrm{He}} = X_{^{56}\mathrm{Ni}} = 0.5$). This boundary can be calculated by rewriting Eq. (5.140) in terms of mass fractions and by solving for the density ρ. The numerical result is

$$\rho = 3.80 \times 10^{11} T_9^{3/2} e^{-78.42/T_9} \qquad (\mathrm{g/cm^3}) \tag{5.141}$$

Similarly, another boundary can be obtained assuming instead that the matter consists entirely of α-particles and (free) nucleons to equal amounts (see Problem 5.11). These two boundaries are displayed in Figure 5.38. They reflect the competition between ^{56}Ni, ^{4}He, and nucleons in a plasma at nuclear statistical equilibrium for $\eta \approx 0$. In the lower temperature region (to the left of the solid line), ^{56}Ni dominates the composition. At intermediate temperatures (between the solid and the dotted lines), ^{4}He is the dominant nucleus. At higher temperatures (to the right of the dotted line), the composition consists mainly of protons and neutrons. It is apparent that, with rising temperatures and given density, an increasing fraction of the composition resides in light particles (α, n, p). This circumstance is important, both for triggering the collapse of the core of an evolved massive star and for causing energy losses to the shock wave generated by the core bounce (Section 1.4.3). Also, for decreasing densities at a given temperature, an increasing fraction of the composition resides in light particles.

Consider now temperature–density conditions where most of the matter resides in iron peak nuclides (the region to the left of the solid line in Figure 5.38). We would like to find the dominant constituents favored by nuclear statistical equilibrium for a non-zero neutron excess parameter. A value of $\eta > 0$ will allow the dominant nucleus to be one with a neutron excess. If the plasma would consist of only one species, then η must be equal to the individual neutron excess, $(N - Z)/A$, of the nuclide in question. It is then reasonable to assume that the abundance of each nuclide will be at maximum close to its individual neutron excess. The most abundant nuclide in a composition of given neutron excess η is then, in general, the one with an individual neutron excess of $(N - Z)/A \approx \eta$ and the largest binding energy (see Eq. (5.137)).

The abundances of the dominant nuclides versus neutron excess parameter η in a nuclear statistical equilibrium composition at $T = 3.5$ GK and $\rho = 10^7$ g/cm^3 are shown in Figure 5.39. The results are calculated from Eqs. (5.137)–(5.139) by taking into account individual binding energies, spins, and normalized partition functions for a large set of nuclides (from H to Zr). As expected, for $\eta = 0$ the dominant nucleus is ^{56}Ni [$(N - Z)/A = (28 - 28)/56 = 0$], which has the largest

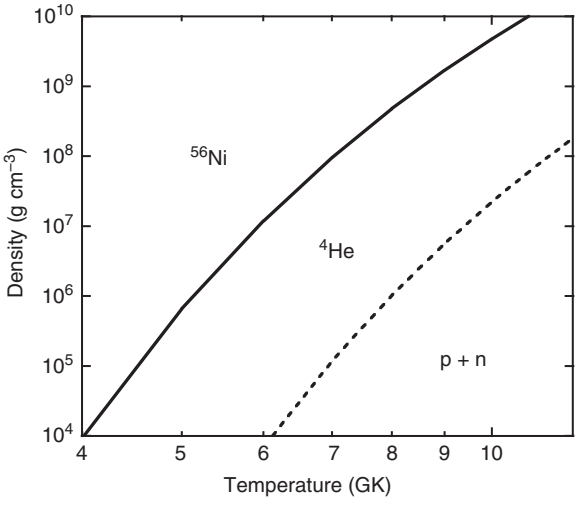

Figure 5.38 Temperature–density conditions in a plasma at nuclear statistical equilibrium with $\eta \approx 0$ for $X_{^{56}\mathrm{Ni}} = X_{^4\mathrm{He}} = 0.5$ (solid line) and $X_{^4\mathrm{He}} = 0.5$, $X_\mathrm{p} = X_\mathrm{n} = 0.25$ (dotted line). The lines define regions of the dominant nuclear constituents. The two boundaries are not sharp since a distribution of nuclei and nucleons exists at all T–ρ conditions. The above assumptions are schematic because a region exists above the solid line where nuclear statistical equilibrium favors ^{54}Fe + 2p over ^{56}Ni as the dominant constituent (Clayton, 1983). The point here is that, with rising temperatures at a given density, or with decreasing densities at a given temperature, an increasing fraction of the composition resides in light particles (α, p, n) and that this transformation absorbs a large amount of energy. The boundaries at the higher temperatures are only approximate since the normalized partition functions have been set equal to unity.

binding energy per nucleon among all $N = Z$ species (Figure 1.9). Near $\eta = 0.04$, ^{54}Fe dominates [$(28 - 26)/54 = 0.037$], while ^{56}Fe is the most abundant nucleus for $\eta \approx 0.07$ [$(30 - 26)/56 = 0.071$]. For larger values of η, the equilibrium composition shifts to still heavier and more neutron-rich nucildes. Interestingly, the most tightly bound nuclide with $(N - Z)/A \approx \eta$ is not always the most abundant one. For example, consider the species ^{54}Fe and ^{58}Ni, which have similar values of $(N - Z)/A$. The binding energies per nucleon, B/A, are almost identical. This means that the binding energy, B, is larger for ^{58}Ni. Nevertheless, at $\eta \approx 0.04$ the mass fraction of ^{54}Fe exceeds the ^{58}Ni mass fraction by more than a factor of two in Figure 5.39. Hence, the binding energy is not the only factor influencing the abundance. In the above example, the A dependences of both θ and ρ also play an important role (see Eq. (5.137)).

Interestingly, for the temperature and density conditions shown in Figure 5.39, the abundance distributions on either side of $\eta = 0$ display a very different behavior. It can be seen that on the proton-rich side ($\eta < 0$) the nuclide ^{56}Ni remains the most abundant species. The main reason is the steeper drop of the binding energy per nucleon from the peak at ^{56}Ni toward lighter nuclides compared to heavier

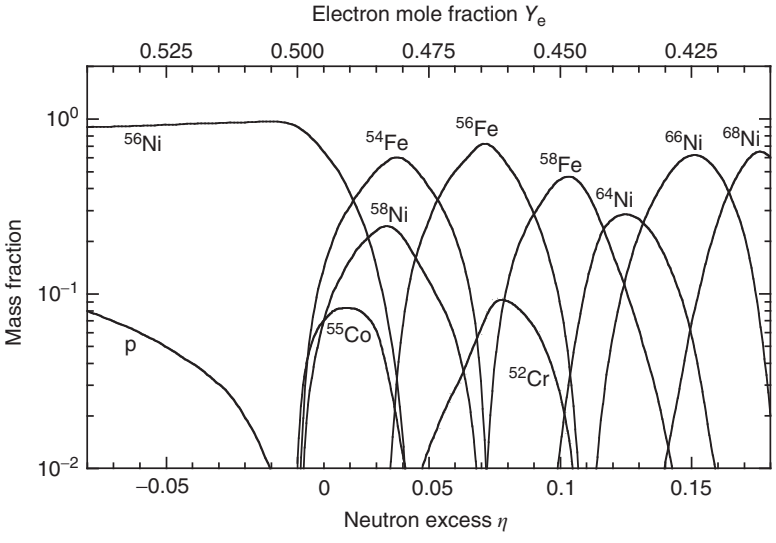

Figure 5.39 Abundances of the dominant species versus neutron excess parameter η (or electron mole fraction Y_e) in a nuclear statistical equilibrium composition at $T = 3.5$ GK and $\rho = 10^7$ g/cm^3. The abundances on either side of $\eta = 0$ ($Y_e = 0.5$) show a different behavior. (Courtesy of Ivo Seitenzahl.)

nuclides. For nuclear statistical equilibrium compositions at different temperatures, see Seitenzahl *et al.* (2008).

An extensive discussion of nuclear statistical equilibrium is given in Clifford and Tayler (1965). It is found that abundances vary rapidly with η, fairly rapidly with temperature T, and very slowly with density ρ. Furthermore, at lower temperatures there are fewer nuclides with relatively large abundances, whereas the abundances are spread more evenly at higher temperatures, which is also apparent from the exponential factor $e^{B(Y)/kT}$ in Eq. (5.137).

A system at any temperature and density will come into equilibrium, provided it is maintained long enough. When we say that, at a particular temperature of T, the nuclear reactions are in equilibrium, we mean that this temperature exists long enough for a good approximation to equilibrium to occur. The nuclear gas requires a finite amount of time to adjust to equilibrium. The approximate time (in seconds) to reach nuclear statistical equilibrium for given values of T and ρ can be estimated from the numerical expression (Khokhlov, 1991)

$$\tau_{\mathrm{NSE}} = \rho^{0.2} e^{179.7/T_9 - 40.5} \quad \text{(s)} \tag{5.142}$$

where ρ is in units of gram per cubic centimeter. This time is displayed in Figure 5.40 versus temperature for two values of the density ($\rho = 10^4$ g/cm^3 and $\rho = 10^{10}$ g/cm^3). At $T = 4$ GK, for example, nuclear statistical equilibrium is established in about 1 h, while at $T = 6$ GK the time is only $\approx 10^{-3}$ s. Therefore, at these higher temperatures, nuclear statistical equilibrium is also achieved in explosive events (see below). At lower temperatures, however, if thermodynamic

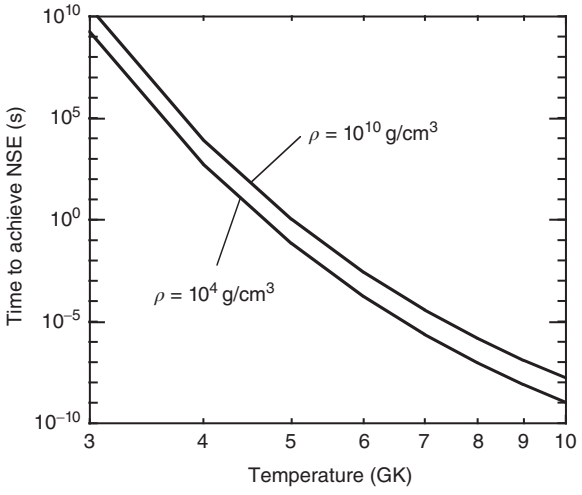

Figure 5.40 Approximate time to reach nuclear statistical equilibrium versus temperature. The solid lines are computed for two different densities ($\rho = 10^4$ g/cm^3 and $\rho = 10^{10}$ g/cm^3) using Eq. (5.142).

conditions vary sufficiently rapidly, nuclear statistical equilibrium may provide a poor approximation for the abundances.

As already pointed out in Section 5.3.4, the neutron excess at the end of silicon burning amounts to $\eta_f = 0.067$ for the stellar model considered here. As the temperature and density increase steadily in the core (Figure 5.1a), weak interactions give rise to a continuous change of the neutron excess parameter and nuclear statistical equilibrium adjusts the composition accordingly. For the last pre-supernova model computed by Chieffi, Limongi, and Straniero (1998), the core temperature and density amount to $T = 5.5$ GK and $\rho = 1.6 \times 10^9$ g/cm^3, respectively, with a neutron excess of $\eta = 0.13$. Consequently, the most abundant nuclides at this stage in the core are ^{60}Fe, ^{64}Ni, and ^{54}Cr, with individual neutron excesses of $(N - Z)/A = 0.133$, 0.125, and 0.110, respectively.

The structure of a $25M_\odot$ star of solar metallicity at this stage of its evolution is schematically shown in Figure 1.7 (left side). It displays the most abundant nuclides in each layer and, at the bottom, the nuclear burning stage that produced those particular ashes. The subscripts "C" and "S" stand for core and shell burning, respectively. The label "Fe" in the core denotes the most abundant iron peak nuclides at a given value of the neutron excess. In the next layer, on top of the core, the species ^{28}Si is the most abundant nuclide, which is the product of oxygen shell burning. The nuclear transformation of ^{28}Si to iron peak nuclides (silicon shell burning) continues at the intersection of the silicon layer and the iron core; the transformation of ^{16}O to ^{28}Si (oxygen shell burning) takes place at the intersection of the oxygen and silicon layers; and so on. The dramatic processes that take place next in the innermost region of the massive star will be discussed below.

5.4
Explosive Burning in Core-Collapse Supernovae (Type II, Ib, Ic)

5.4.1
Core Collapse and the Role of Neutrinos

Core-collapse supernovae are powered by the release of gravitational energy in the collapse of a massive star's core to a proto-neutron star. We will now consider the core collapse in more detail. Before the onset of the collapse ($t = 0$), temperatures and densities at the center of the iron core amount to $T \approx 10$ GK and $\rho \approx 10^{10}$ g/cm^3, respectively. Under these conditions, nuclear statistical equilibrium is established. The silicon burning shell has continuously increased the mass of the core, which is supported by electron degeneracy pressure. When the core reaches the Chandrasekhar mass ($\approx 1.4\,M_\odot$), it has no other thermonuclear energy source available to support the pressure and it becomes unstable to gravitational collapse.

The collapse and the infall dynamics depend sensitively on two parameters, the electron mole fraction, Y_e (see Eq. (1.37)), and the entropy per baryon, s. For a radiation dominated environment, the entropy per baryon is related to the photon-to-baryon ratio, ϕ, via

$$s \sim 10\,\phi \sim \frac{T^3}{\rho} \tag{5.143}$$

where T and ρ denote the temperature and density, respectively. In simple terms, for a small value of the entropy per baryon, nuclear statistical equilibrium favors a composition of iron peak nuclides that are tightly bound. On the other hand, a large value of s implies that many photons are available per baryon, which favors the photodisintegration of heavier nuclei into free nucleons.

During the early stages, the core collapse is accelerated by two effects. First, as the (electron) density increases, electrons capture onto nuclei, (e^-, ν_e), hence removing electrons that were contributing to the pressure. As Y_e decreases, the neutron excess increases in the core and, in addition, a burst of electron neutrinos is produced. Second, at the very high temperatures the thermal radiation becomes sufficiently energetic and intense that iron peak nuclides are photodisintegrated into lighter and less stable species, thus removing energy that could have provided pressure. Within a fraction of a second, the core with a size of several thousand kilometers collapses to a proto-neutron star of several tens of kilometer radius.

The most important neutrino interactions during the collapse are (Bruenn and Haxton, 1991): (neutral current) elastic scattering on nuclei, (ν_e, ν_e); electron-neutrino scattering, $e^-(\nu_e, \nu_e)\,e^-$; inverse β-decay, (ν_e, e^-); and inelastic scattering on nuclei, (ν_e, ν_e'). At $t \approx 0.1$ s, when the density reaches a value near $\approx 10^{12}$ g/cm^3, the neutrino diffusion time becomes longer than the collapse time and, consequently, the neutrinos become trapped (Bethe, 1990). Inside this region, called *neutrino sphere*, the neutrinos are coupled via interactions with matter and are in thermal equilibrium. Outside, the neutrinos escape almost

freely, with an average energy that is determined at the radius of the neutrino sphere, R_ν. The location of the neutrino sphere depends both on the neutrino type and flavor (Section 1.8), and on the neutrino energy. At $t \approx 0.11$ s, the inner core ($M \approx 0.5\,M_\odot$) reaches nuclear densities ($\approx 10^{14}$ g/cm^3), bounces, and drives a shock wave into the infalling matter. At the time of the bounce, the electron mole fraction in the inner core is relatively small ($Y_e \approx 0.3$ for $M \lesssim 0.5\,M_\odot$) and increases gradually in the outer core ($Y_e \approx 0.45$ near $M \approx 1.0\,M_\odot$). At $t \approx 0.12$ s, the prompt shock propagates outward, but loses severely energy by dissociating iron peak nuclei into free nucleons (≈ 9 MeV per nucleon). When the shock reaches the neutrino sphere, additional electron captures on free protons also remove energy from the shock, giving rise to a strong burst of electron neutrinos (prompt ν_e burst, corresponding to $\approx 10^{46}$ J/s for a duration of $\approx$ 10–20 ms). At $t \approx 0.2$ s, the shock stalls at a radius of $\approx$ 100–200 km in the outer core.

During core collapse, a gravitational binding energy of several 10^{46} J, representing a staggering $\approx 10\%$ of the iron core's rest mass, is released in form of neutrino radiation. Therefore, the stalled shock is thought to be revived by neutrinos and antineutrinos that emerge from the hot and dense proto-neutron star (Bethe and Wilson, 1985). At the very high temperatures prevailing in the core, neutrinos and antineutrinos of all flavors (electron, muon, and tau) are produced, mainly by electron-positron pair annihilation, $e^- + e^+ \rightarrow \nu_e + \overline{\nu}_e$, neutrino-antineutrino pair annihilation, $\nu_e + \overline{\nu}_e \rightarrow \nu_{\mu,\tau} + \overline{\nu}_{\mu,\tau}$, and nucleon bremsstrahlung, $N + N \rightarrow N + N + \nu_{\mu,\tau} + \overline{\nu}_{\mu,\tau}$ (Buras *et al.*, 2003). While the neutrinos diffuse out of the core, the luminosities and average energies for each of the different neutrino types evolve with time. First, muon and tau neutrinos have smaller opacities compared to electron neutrinos since their energies are too low for charged-current interactions, such as $\overline{\nu}_\mu + p \rightarrow n + \mu^+$ (because of the large masses of the μ and τ leptons). Thus, the muon and tau neutrinos decouple at smaller radii, R_ν, that is, at higher density and temperature, and hence, emerge with higher average energies from the proto-neutron star compared to the electron neutrinos. Second, there are fewer protons than neutrons in the outer layers of the proto-neutron star and thus the charged-current interaction $n + \nu_e \leftrightarrow p + e^-$ occurs more frequently compared to $p + \overline{\nu}_e \leftrightarrow n + e^+$. Hence, electron neutrinos have a higher opacity than electron antineutrinos and thus decouple at larger radii with smaller average energies.

The situation at this stage is represented in Figure 5.41a. The matter between the neutrino sphere and the stalling shock front consists mainly of free neutrons and protons. The *gain radius* divides this region into two parts: the first is located closer to the neutrino sphere and is characterized by the dominance of $p + e^- \rightarrow n + \nu_e$ and $n + e^+ \rightarrow p + \overline{\nu}_e$ over their reverse interactions, thus giving rise to effective neutrino cooling by neutrino emission; the second is located closer to the shock, where $n + \nu_e \rightarrow p + e^-$ and $p + \overline{\nu}_e \rightarrow n + e^+$ dominate over their reverse interactions, hence giving rise to effective heating via neutrino absorption. The continuous neutrino energy deposition in the latter region keeps the pressure high, may rejuvenate the shock, and thereby cause the supernova explosion (*delayed shock model*; Wilson and Mayle, 1993). Only a fraction ($\approx 1\%$)

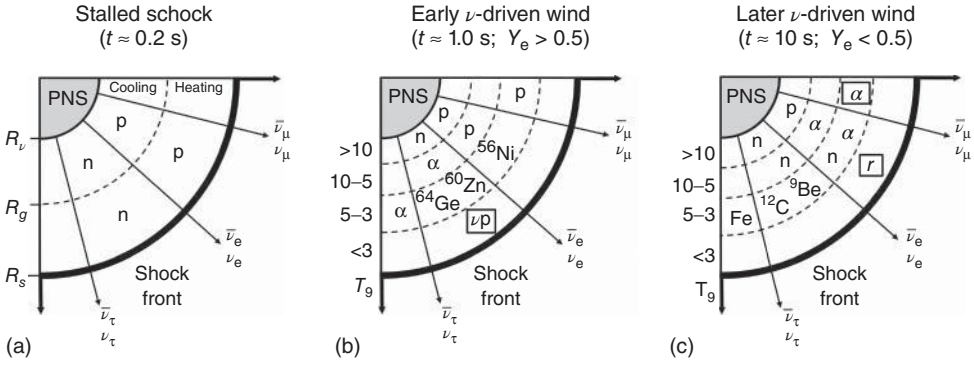

Figure 5.41 Evolution of the region near the proto-neutron star (PNS) surface, as a result of neutrino-induced processes, expansion and cooling. The proto-neutron star surface can be defined by the radius of the energy-integrated electron neutrino sphere. The radii of the various zones differ from panel to panel and are not to scale. Approximate temperature ranges (GK) are indicated. Only the main constituents are given in each zone. Symbols in open rectangles indicate nucleosynthesis processes: νp-process (νp); α-process (α); r-process (r). (a) Region between proto-neutron star surface and stalled shock, $t \approx 0.2$ s after core collapse. The main constituents are free protons and neutrons. Inside the gain radius neutrino cooling prevails, while outside matter is effectively heated by neutrinos; radii: R_ν (neutrino sphere); R_g (gain radius); R_s (shock radius). (b) The early neutrino-driven wind, $t \approx 1.0$ s, is proton-rich, $Y_e > 0.5$, giving rise to the νp-process (Section 5.4.2). (c) The later neutrino-driven wind, $t \approx 10$ s, may become neutron-rich, $Y_e < 0.5$, giving rise to the α- and r-processes (Section 5.6.2). Note that the abundances of ^{9}Be and ^{12}C are very small since these species are destroyed almost as quickly as they are produced. The label "Fe" denotes a distribution of seed nuclei in the $A \approx 50$–100 mass range.

of the total gravitational binding energy, deposited by neutrinos as thermal energy of nucleons, leptons, and photons in this region, would be required to initiate a powerful shock propagating through the stellar mantle and giving rise to an explosion. The success of this model depends crucially, among other things, on the product of neutrino luminosity and neutrino interaction cross sections (i.e., the square of the average neutrino energy). However, almost none of the most advanced, self-consistent core-collapse stellar models have produced an explosion and the exact mechanisms by which neutrinos cause the explosion remain elusive. Instead, many models artificially change the neutrino properties, such as the charged-current interaction rates, to increase the neutrino energy deposition behind the shock. The problem is highly complex, involving energy-dependent neutrino transport in three dimensions, a convectively unstable region near a compact hot and dense object, possible diffusive instabilities, and magneto-rotational effects.

Below, we will consider nucleosynthesis processes that effect the deepest layers to be ejected in a core-collapse supernova. After the rejuvenated shock has been launched, the strong electron neutrino and antineutrino fluxes drive a continuous flow of protons and neutrons from the region near the proto-neutron

star surface. This outflow of matter is called the *neutrino-driven wind* (Duncan, Shapiro, and Wasserman, 1986). Matter in this region expands and cools at high (possibly supersonic) velocity and eventually collides with the slower earlier supernova ejecta, resulting in a wind termination (or reverse) shock (Burrows, Hayer, and Fryxell, 1995). The nucleosynthesis in the early ejecta depends strongly on the entropy (or photon-to-baryon ratio; Eq. (5.143)), expansion time scale, and electron mole fraction (or electron-to-baryon ratio; Eq. (1.37)). The first two quantities depend on the average neutrino energies and total luminosities, and the properties of the proto-neutron star, given by the equation of state. The electron mole fraction, Y_e, depends on the complicated interplay of the four (charged-current) electron neutrino and antineutrino interactions with free nucleons, $n + \nu_e \leftrightarrow p + e^-$ and $p + \overline{\nu}_e \leftrightarrow n + e^+$, in the wind region. If the neutrino-driven wind is proton-rich, then conditions are favorable for the synthesis of neutron-deficient nuclides (Section 5.4.2), while a neutron-rich wind may give rise to the production of neutron-rich species (Section 5.6.2). The outcome of the nucleosynthesis is highly sensitive to the uncertain physical conditions of the neutrino-driven wind.

5.4.2
ν- and νp-Processes

The large energy release during the core collapse in form of neutrinos gives likely rise to the neutrino-induced synthesis of certain nuclides in the expanding mantle of the exploding star. Specifically, neutrinos can interact with nuclei via inelastic (neutral-current) neutrino scattering, (ν,ν'). Since μ and τ neutrinos emerging from the proto-neutron star have larger predicted average energies compared to electron neutrinos, and since the neutrino cross sections scale with the square of their energy, the interactions of the former neutrino species with nuclei predominate. On the other hand, electron neutrinos may interact with nuclei via charged-current interactions, (ν_e, e^-) or $(\overline{\nu}_e, e^+)$. All of the neutrino interactions can populate excited nuclear levels that subsequently decay via emission of light particles (p, n, α). The released light particles, in turn, undergo reactions with nuclei in the high-temperature environment and thus contribute to the synthesis of certain nuclides. In any given layer of the star, neutrino-induced nucleosynthesis may occur before the arrival of the shock, during explosive burning (Section 5.4.3), or after shock passage when the material expands and cools. This mechanism is referred to as the *ν-process* (Woosley *et al.*, 1990). Simulations have shown (Heger *et al.*, 2005) that it may contribute appreciably to the solar abundance of the rare species ^{11}B (made in the carbon–oxygen layer; see right side of Figure 1.7), ^{19}F and ^{138}La (both made in the oxygen–neon layer). Yield predictions from ν-process calculations are sensitively influenced by current uncertainties in neutrino interaction cross sections, average neutrino energies of each flavor, total neutrino luminosity, as well as by the details of the adopted stellar evolution and explosion models.

Some core-collapse simulations that include energy-dependent neutrino transport have obtained a *proton-rich* ($Y_e > 0.5$) neutrino-driven wind, either at very early times (Buras *et al.*, 2006) or for an extended time period of up to 20 s (Fischer *et al.*, 2009). The situation is schematically displayed in Figure 5.41b. The wind is ejected at temperatures above 10 GK and consists of free neutrons and protons in nuclear statistical equilibrium. Four distinct phases can be identified during the ensuing nucleosynthesis: (i) expansion and cooling through the temperature range of $T \approx 10$–5 GK causes all neutrons to combine with protons, leaving a composition consisting of α-particles and an excess of protons; (ii) further cooling through temperatures of $T \approx 5$–3 GK allows the α-particles to combine to heavier nuclei, giving mainly rise to the production of the nuclides ^{56}Ni, ^{60}Zn, and ^{64}Ge that consist of an equal number of neutrons and protons ($N = Z$). Since the slowest link in this sequence is the triple-α reaction, the number of synthesized heavy seed nuclei is equal to the number of produced ^{12}C nuclei. Abundance flows beyond ^{64}Ge are inhibited by strong reverse flows and by its long half-life ($T_{1/2} = 64$ s in the laboratory); (iii) in the temperature range of $T \approx 3$–1.5 GK the (charged-current) interaction $p + \overline{\nu}_e \rightarrow n + e^+$ on the abundant protons produces free neutrons ($\approx 10^{14}$ cm^{-3} for several seconds) that participate in the nucleosynthesis. This aspect is important, because fast (n,p) reactions on waiting point nuclides, such as ^{56}Ni, ^{60}Zn, and ^{64}Ge, together with subsequent (p,γ) reactions allow for a continuation of the abundance flow toward heavier nuclides on the neutron-deficient side of the valley of stability. Note that a (n,p) reaction connects the same pair of nuclides as a corresponding β^+-decay; (iv) when the temperature falls below $T \approx 1.5$ GK, the (p,γ) reactions freeze out and (n,p) reactions and β^+-decays convert the heavy nuclides to stable, neutron-deficient, daughters. This nucleosynthesis mechanism is called the *νp-process* (Fröhlich *et al.*, 2006).

The *νp*-process is not terminated by the exhaustion of free protons, but by the cooling of matter to temperatures below $T \approx 1$ GK. A few studies (e.g., Wanajo, Janka, and Kubono, 2011) have shown that the *νp*-process may account for the solar abundances of the light p-nuclides up to ^{108}Cd, including ^{92}Mo, ^{94}Mo, ^{96}Ru, and ^{98}Ru, that are underproduced by the p-process (Section 5.6.3). However, other studies (Pruet *et al.*, 2006; Fisker, Hoffman, and Pruet, 2009) could not reproduce the solar abundances of the light p-nuclides and thus the issue remains controversial. It is also important to stress that, although several model simulations have predicted an early proton-rich neutrino-driven wind, the *νp*-process is highly sensitive to the details of the explosion mechanism, the mass, and possibly the rotation rate of the proto-neutron star. Thus, it is expected that the nucleosynthesis varies considerably from event to event. Currently, the key uncertainties originate from the neutrino luminosities and average energies, which determine the electron mole fraction, Y_e, in the neutrino-driven wind. A larger value of Y_e will generally give rise to the synthesis of heavier p-nuclides. For example, models with $Y_e \approx 0.6$ (i.e., at the onset of the *νp*-process, when $T \approx 3$ GK) produce p-nuclides up to $A = 152$. For even larger values of Y_e, the density of free neutrons increases as a result of the charged-current interaction between electron antineutrinos and the large proton abundance. Consequently, the (n,p) reactions

would not only carry the abundance flow to the valley of β stability, but (n,γ) reactions will carry the flow to the neutron-rich side. The protons do not participate directly in the nucleosynthesis, but mainly act as a source of free neutrons (Pruet *et al.*, 2006).

The νp-process is sensitive to nuclear physics uncertainties. For example, the slow triple-α-reaction (Section 5.2.1) represents a bottleneck for the synthesis of the heavy seed nuclei, near $T = 3$ GK, before the start of the νp-process. Varying this rate will impact the production of the p-nuclides in the $A = 100$–110 mass region. Changing the rates of the (n,p) reactions on the waiting point nuclides that control the abundance flow to heavier nuclides, especially ^{56}Ni(n,p)^{56}Co and ^{60}Zn(n,p)^{60}Cu, strongly influences the production of the p-nuclides in the $A > 100$ mass region. These (n,p) rates are based on theory (Hauser-Feshbach model; see Wanajo, Janka, and Kubono, 2011), since experimental data are lacking at present. A study of the modest impact of nuclear mass uncertainties on the νp-process path can be found in Weber *et al.* (2008).

5.4.3 Explosive Nucleosynthesis

In Section 5.3, we discussed the nucleosynthesis processes that occur in the core of a massive star at different evolutionary stages, with each stage attaining a higher temperature and density compared to the previous one. We will now address the processes that occur when the outward moving shock wave compresses and heats layers of different compositions for short periods of time. An overview of the nucleosynthesis outcome is shown in Figure 1.7 (right side).

It will be helpful for the following discussion to adopt a simple analytical parametrization for the temperature-density evolution of the shock. The passing shock heats a layer of nuclear fuel to a peak temperature, $T_{\rm peak}$, and compresses the material to a peak density, $\rho_{\rm peak}$. If it is assumed that the subsequent expansion is adiabatic, the time dependence of the temperature and density of this radiation dominated gas can be approximated by

$$T(t) = T_{\rm peak} e^{-t/(3\tau)} \quad \text{and} \quad \rho(t) = \rho_{\rm peak} e^{-t/\tau} \tag{5.144}$$

where the factor of three in the first expression derives from Eq. (5.143). The expansion time scale, defined as the time at which the density has fallen to $1/e$ of the peak value, is frequently approximated by the hydrodynamic free-fall time scale, given by (Fowler and Hoyle, 1964)

$$\tau_{hd} \approx \frac{446}{\sqrt{\rho_{\rm peak}}} \quad \text{(s)} \tag{5.145}$$

where the density is in units of grams per cubic centimeter. For example, peak densities of $\rho_{\rm peak} = 10^6$ g/cm^3 and 10^7 g/cm^3 yield free-fall expansion times of $\tau_{hd} = 0.45$ s and 0.14 s, respectively. In this simple model, the thermodynamic evolution of the zone is specified once values for $T_{\rm peak}$ and $\rho_{\rm peak}$ are adopted.

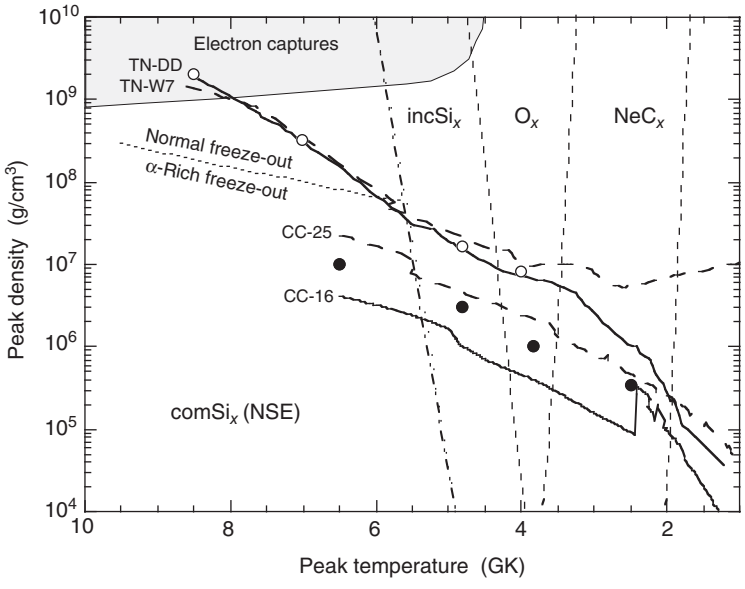

Figure 5.42 Peak temperatures and peak densities attained in different mass zones during the outward propagation of burning fronts in supernova explosion models. The two lower tracks are from core-collapse (type II, Ib, Ic) supernova models (CC-16: Young *et al.*, 2006; CC-25: Limongi and Chieffi, 2003), while the two upper tracks are from thermonuclear (type Ia) supernova models (TN-W7: Nomoto, Thielemann, and Yokoi, 1984; TN-DD: Bravo and Martínez-Pinedo, 2012). Regions of predominant nucleosynthesis processes are indicated: complete silicon burning ("comSi$_x$ (NSE)", entire region to the left of dashed-dotted line); normal freeze-out (above dotted line); α-rich freeze-out (below dotted line); incomplete silicon burning ("incSi$_x$"), explosive oxygen burning ("O$_x$"), and explosive neon-carbon burning ("NeC$_x$"). The boundaries between the different regions depend on the explosion time scale and are only approximate. The gray shaded area at the top left indicates the region where electron captures change the neutron excess significantly during the explosion (Section 5.5.1). The full and open circles mark peak temperature and density conditions adopted for the reaction network calculations discussed in the text.

More involved analytical expressions can be found in Nadyozhin and Deputovich (2002). Because of the strong temperature dependence of the reaction rates, we expect that the temperature evolution will have a considerably stronger impact on the nucleosynthesis compared to the density evolution. It is implicitly assumed that the rise of temperature and density to their peak values is instantaneous. As will become apparent, the neutron excess is crucial for the nucleosynthesis. In the shells of silicon, oxygen, and neon that will experience explosive burning and be ejected (Figure 1.7), the neutron excess is on the order of $\eta \approx 0.003$ for solar metallicity stars. We will adopt this initial value in the following reaction network calculations.

A first impression regarding the explosive nucleosynthesis is given in Figure 5.42, displaying peak temperatures and peak densities attained in different

mass zones during the outward propagation of burning fronts in some supernova models. Each point on a displayed track corresponds to a given mass layer in the ejecta that is heated and compressed to the given peak temperature and density, and then cools and expands as a result of the passage of the shock. The lower two tracks correspond to core-collapse supernovae (CC-16: $16\,M_\odot$ model of Young *et al.*, 2006; CC-25: $25\,M_\odot$ model of Limongi and Chieffi, 2003). The tracks start, on the left, in a mass zone comprised of the innermost ejecta. The nearly horizontal or vertical dashed and dotted lines divide the parameter space into regions dominated by different nucleosynthesis processes. We will focus here on core-collapse supernovae. Thermonuclear supernovae are discussed in Section 5.5.1. The peak temperature and peak density conditions adopted for the network calculations that will be discussed below are marked by the solid circles.

The first zone encountered by the shock, consisting mainly of ^{28}Si, is heated to peak temperatures in excess of $T_{\rm peak} \approx 5$ GK. At these high temperatures, the rates of all forward and reverse strong or electromagnetic interactions achieve nuclear statistical equilibrium. Recall from Section 5.3.5 that, for known nuclear properties, the abundance of any nuclide is then determined by the temperature, density, and the neutron excess. The initial silicon will be entirely destroyed and transformed into iron peak species. Hence, this stage is referred to as *complete explosive silicon burning*. The region of parameter space dominated by this regime (labeled "comSi$_x$ (NSE)") is located on the left-hand side of the dashed-dotted line in Figure 5.42. For our assumption of a small neutron excess ($\eta \approx 0.003$), nuclear statistical equilibrium will favor $^{56}_{28}\mathrm{Ni}_{28}$ as the main constituent, since it is the most tightly bound nuclide with $N = Z$ (Figures 1.9 and 5.39).

The fate of matter in nuclear statistical equilibrium depends on the expansion time scale as the gas quickly cools, and on the density of free light particles (α, n, p) when nuclear reactions start to fall out of equilibrium at a certain freeze-out temperature (Woosley, Arnett, and Clayton, 1973). If the density is high and the expansion time slow, nuclear statistical equilibrium predicts only very small light particle abundances. As the temperature falls below the freeze-out temperature, there is not enough time to produce the light particles necessary to maintain nuclear statistical equilibrium and hence the equilibrium will be terminated by a lack of light particles. The first reaction to drop out of equilibrium is the triple-α reaction. There are so few light particles that their subsequent capture during this *normal freeze-out* does not alter the nuclear statistical equilibrium composition, consisting mainly of ^{56}Ni and other iron peak nuclides. On the other hand, if the density is low and the expansion time fast, nuclear statistical equilibrium predicts a significant light particle abundance, especially of α-particles. When the temperature falls below the freeze-out temperature, the α-particles cannot be converted fast enough to iron peak nuclides to maintain nuclear statistical equilibrium. The equilibrium is thus terminated by an excess of α-particles and their capture by nuclei during freeze-out will alter the nuclear statistical equilibrium composition. For a small neutron excess, the main product of this α*-rich freeze-out* is again ^{56}Ni, as will be shown below, but additional species

are produced, for example, the important γ-ray emitter ^{44}Ti. No significant production of nuclides occurs beyond the iron peak in either normal or α-rich freeze-out.

The two regions just discussed are separated by the dotted line in Figure 5.42. This boundary is obtained from network calculations (see below) and corresponds to $T_{\rm peak}$–$\rho_{\rm peak}$ conditions for which the final α-particle mass fraction amounts to $X_\alpha = 0.001$. Above this line, X_α falls fast, while below this line X_α increases. The inner ejecta for both core collapse supernova models displayed in Figure 5.42 undergo α-rich freeze-out and never reach the higher densities required for normal freeze-out. This applies to most models of core collapse supernovae.

Time-integrated net abundance flows and abundance evolutions, obtained with an exponential T–ρ profile (see Eqs. (5.145) and (5.144)) and a peak temperature and peak density of 6.5 GK and 10^7 g/cm^3, respectively, are shown in Figures 5.43a and 5.44a. These conditions, indicated by the first solid circle in Figure 5.42, fall between the two core collapse supernova model trajectories in the region labeled "comSi$_x$ (NSE)". In an actual explosion, the shock gives rise to a continuous distribution of $T_{\rm peak}$ and $\rho_{\rm peak}$ values while it moves through different mass layers. Therefore, the results presented in the figures correspond to the nucleosynthesis in a single homogeneous region. The initial composition of the zone is assumed to consist mainly of ^{28}Si, with a small contribution of ^{30}Si to set the neutron excess equal to $\eta = 0.003$. The destruction of ^{28}Si and the transformation of matter to iron peak nuclides is apparent in Figure 5.43. The reactions mediating between the silicon and iron peak regions have abundance flows that are smaller by three orders of magnitude compared to the maximum flow and hence do not appear in the figure. The displayed abundance flows are integrated over the entire duration of the network calculation. The abundance flows at an instant when the matter is in nuclear statistical equilibrium, that is, before freeze-out occurs, would look very similar to the pattern shown in the lower panel of Figure 5.35. The most abundant species at the end of the calculation is ^{56}Ni ($X_f = 0.80$), with smaller contributions from other iron peak nuclides (^{57}Ni and ^{58}Ni). Notice the large final α-particle abundance ($X_f = 0.06$), demonstrating that the freeze-out was of the α-rich variety. Furthermore, a significant amount of ^{44}Ti is produced, with a final mass fraction of $X_f = 5 \times 10^{-5}$.

The next zone encountered by the shock, still composed mainly of ^{28}Si, is heated to peak temperatures of $T_{\rm peak} \approx 4$–5 GK. Instead of nuclear statistical equilibrium, quasi-equilibrium is established. Recall from Sections 5.3.3 and 5.3.4 that the abundance of any nuclide in quasi-equilibrium with, for example, ^{28}Si, is specified by four parameters (apart from nuclear binding energies, masses, and spins): temperature, density, neutron excess, and the abundance of ^{28}Si. When the shock encounters this zone, it starts to dissociate silicon and neighboring species, quickly forming a cluster in quasi-equilibrium with the dominant species ^{28}Si, which has the largest binding energy of all nuclides in this mass region. Soon thereafter, another quasi-equilibrium cluster forms in the iron peak region, which consists of nuclides of even higher binding energies, mediated by reactions in the $A = 40$–44 mass range linking the two clusters. The situation is reminiscent

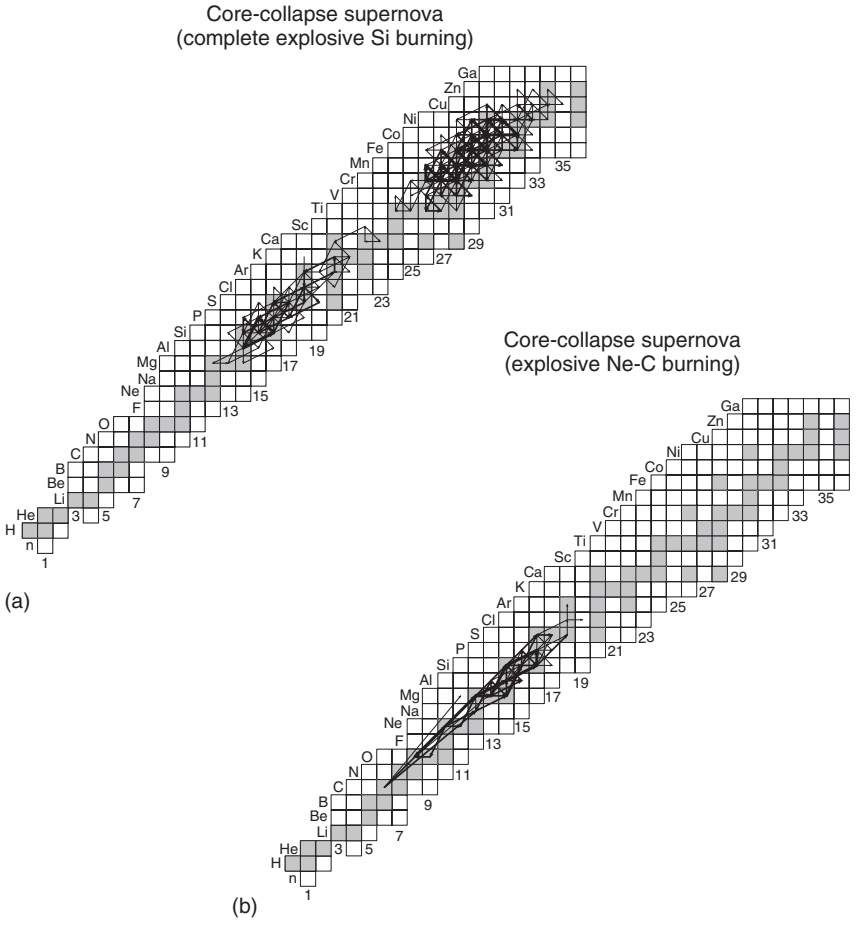

Figure 5.43 Time-integrated net abundance flows during core-collapse supernova nucleosynthesis. The network calculations are performed using exponential T–ρ evolutions (see Eq. (5.144)) and a free-fall expansion time scale (see Eq. (5.145)); (a) complete explosive silicon burning with $T_{\mathrm{peak}} = 6.5$ GK and $\rho_{\mathrm{peak}} = 10^7$ g/cm^3; (b) explosive neon-carbon burning with $T_{\mathrm{peak}} = 2.5$ GK and $\rho_{\mathrm{peak}} = 3.2 \times 10^5$ g/cm^3. See the text for the initial composition. The abundance evolutions for the two flow diagrams are shown in Figure 5.44a,d. The arrows have the same meaning as in Figure 5.26: $F^{\mathrm{max}} \geq F_{ij} > 0.1F^{\mathrm{max}}$ (thick arrows), $0.1F^{\mathrm{max}} \geq F_{ij} > 0.01F^{\mathrm{max}}$ (intermediate arrows), and $0.01F^{\mathrm{max}} \geq F_{ij} > 0.001F^{\mathrm{max}}$ (thin arrows), where F^{max} corresponds to the reaction with the maximum net flow. The abundance flows are defined here in terms of mole fractions rather than number densities since the mass density varies.

of hydrostatic silicon burning (Section 5.3.4). If sufficient temperatures and time would be available, all of the silicon group species would be transformed to the iron peak and nuclear statistical equilibrium would be established. However, the expansion causes the freeze-out to occur before this can happen. Since a significant amount of ^{28}Si remains, the process is called *incomplete silicon burning*.

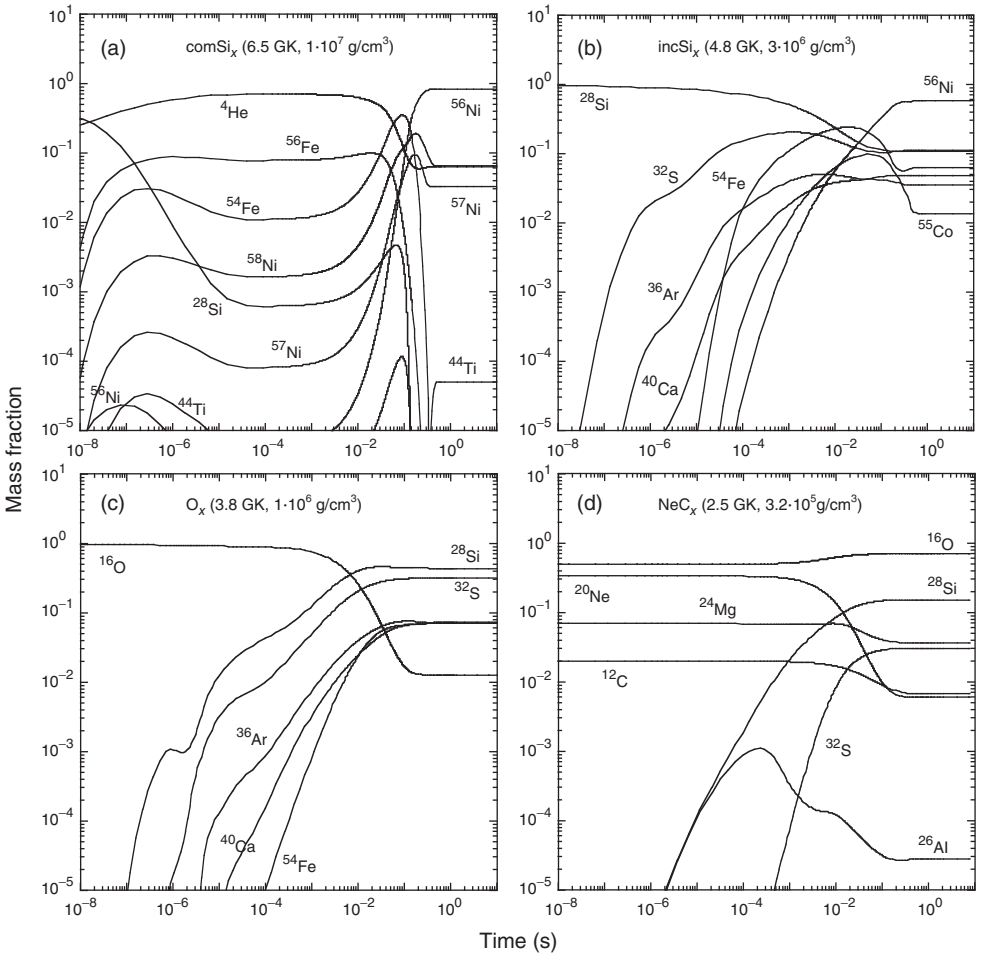

Figure 5.44 Abundance evolutions for explosive nucleosynthesis in core collapse supernovae (type II, Ib, Ic). Results are obtained using exponential T-ρ trajectories (see Eqs. (5.145) and (5.144)) that approximate the conditions in the outward moving shock. Adopted values of $T_{\rm peak}$, $\rho_{\rm peak}$, τ_{hd} are: (a) 6.5 GK, 10^7 g/cm^3, 0.14 s; (b) 4.8 GK, 3×10^6 g/cm^3, 0.26 s; (c) 3.8 GK, 10^6 g/cm^3, 0.45 s; (d) 2.5 GK, 3.2×10^5 g/cm^3, 0.79 s. These conditions correspond to complete explosive silicon burning, incomplete explosive silicon burning, explosive oxygen burning, and explosive neon-carbon burning, respectively, and are marked by solid circles in Figure 5.42. All results shown are obtained with an initial neutron excess of $\eta = 0.003$.

The time evolutions of the most abundant species for representative peak temperature and peak density conditions (4.8 GK and 3×10^6 g/cm^3) are displayed in Figure 5.44b. For the initial composition, we assume again mainly ^{28}Si, with a small contribution of ^{30}Si. It is apparent that the ^{28}Si abundance declines and iron peak species are produced. The most abundant nuclide at the end of the calculation is

again ^{56}Ni ($X_f = 0.60$), as was the case in complete explosive silicon burning, but now a significant amount of ^{28}Si remains at the end ($X_f = 0.10$). Other abundant species are ^{32}S ($X_f = 0.10$), ^{54}Fe ($X_f = 0.06$), ^{40}Ca ($X_f = 0.05$), ^{36}Ar ($X_f = 0.035$), and ^{55}Co ($X_f = 0.012$). The complete and incomplete silicon burning regions are separated by the dashed-dotted line in Figure 5.42. It corresponds to T_{peak}–ρ_{peak} conditions for which a significant ^{28}Si abundance remains after the passage of the shock.

Subsequently, the shock reaches a zone composed mainly of ^{16}O (Figure 1.7). *Explosive oxygen burning* occurs at peak temperatures near $T_{\text{peak}} \approx 3.5$–4 GK. The process is similar to incomplete silicon burning, in the sense that the fuel (^{16}O) is dissociated, giving rise to two quasi-equilibrium clusters in the mass regions of silicon and the iron peak. However, since the peak temperature is lower, less matter is converted to the iron peak and more material remains locked in the silicon region. The results of a network calculation for a peak temperature and peak density of 3.8 GK and 10^6 g/cm^3, respectively, are shown in Figure 5.44c. For the initial composition, we assumed mainly ^{16}O, with a small contribution of ^{18}O to set the neutron excess equal to $\eta = 0.003$. The species ^{16}O is quickly depleted, and the most abundant nuclides at the end of the calculation are ^{28}Si ($X_f = 0.40$), ^{32}S ($X_f = 0.30$), ^{36}Ar ($X_f = 0.07$), ^{40}Ca ($X_f = 0.07$), and ^{54}Fe ($X_f = 0.07$). The first dashed line in Figure 5.42 separates the regions of incomplete explosive silicon burning and explosive oxygen burning. It corresponds to T_{peak}–ρ_{peak} conditions for which ^{56}Ni is significantly depleted ($X_f = 10^{-4}$) after the passage of the shock.

In the above discussion, the explosive burning regimes have been associated with the shock wave moving through a particular nuclear fuel. For example, we described how explosive silicon burning occurs in a zone consisting of silicon, which is the product of hydrostatic oxygen (shell) burning before the core collapse (see Figure 1.7). Similarly, explosive oxygen burning takes place in a layer consisting of oxygen, which was synthesized in hydrostatic neon burning. However, it must be emphasized that these explosive burning regimes mainly depend on the peak temperature and the freeze-out conditions in a particular layer rather than on the composition of the fuel (Woosley, Arnett, and Clayton, 1973). The reason is that nuclear statistical equilibrium or quasi-equilibrium will seek the energetically most favorable configuration for the nuclear composition. For example, exactly the same nucleosynthesis products would result in complete explosive silicon burning if the explosively burning nuclear fuel in this temperature regime would not consist of ^{28}Si, but instead of any other species, as long as the initial neutron excess is kept near $\eta \approx 0.003$. We will return to this issue in Section 5.5.1.

Finally, the shock encounters a zone mainly composed of ^{16}O, ^{20}Ne, and ^{12}C, and heats it to peak temperatures of $T_{\text{peak}} \approx 2$–3.5 GK. As a result, ^{20}Ne, and to a lesser extend ^{12}C, burns explosively. The process is referred to as *explosive neon-carbon burning*. In this case, the temperature and expansion time scale are too small for establishing quasi-equilibrium and the forward and reverse nuclear reactions operate far from equilibrium. Hence, the abundance of a given species does not only depend on a few parameters, such as temperature and density, but in addition

is sensitively influenced by the initial composition and the magnitude of the thermonuclear reaction rates. Time-integrated net abundance flows and abundance evolutions for a representative peak temperature and peak density of 2.5 GK and 3.2×10^5 g/cm^3, respectively, are shown in Figure 5.43b and Figure 5.44d. For the initial composition, we adopt values of ^{12}C ($X_i = 0.02$), ^{16}O ($X_i = 0.50$), ^{20}Ne ($X_i = 0.34$), ^{24}Mg ($X_i = 0.07$), and ^{25}Mg ($X_i = 0.07$). These are similar to the results obtained in a hydrodynamic simulation of a $20\,M_\odot$ star (Limongi and Chieffi, 2006). It is apparent that the abundances of both ^{20}Ne and ^{12}C are depleted by the shock while the composition is rearranged. At the end of the calculation, the most abundant species are ^{16}O ($X_f = 0.70$) and ^{28}Si ($X_f = 0.15$). Interestingly, a significant amount of ^{26}Al ($X_f = 3 \times 10^{-5}$) is produced via the sequence

$$^{24}\mathrm{Mg(n,}\gamma)^{25}\mathrm{Mg(p,}\gamma)^{26}\mathrm{Al} \tag{5.146}$$

The required neutrons are released by the ^{25}Mg(α,n)^{28}Si and ^{26}Mg(α,n)^{29}Si reactions (Iliadis *et al.*, 2011). Some ^{26}Al nuclei are destroyed via ^{26}Al(n,p)^{26}Mg and, to a lesser degree, ^{26}Al(n,α)^{23}Na. Hydrodynamic models (Limongi and Chieffi, 2006) predict that explosive neon-carbon burning in core-collapse supernovae is the most prolific site of ^{26}Al synthesis in the Galaxy (Sections 1.7.5 and 5.4.4). The second dashed line in Figure 5.42 separates the regions of explosive oxygen burning and explosive neon-carbon burning. It corresponds to T_{peak}–ρ_{peak} conditions for which equal mass fractions of ^{16}O and ^{28}Si are obtained after the passage of the shock.

The time scale is too short at the peak densities typically achieved in the explosive burning of core collapse supernovae for electron captures to change the neutron excess significantly. Unlike the situation in hydrostatic oxygen and silicon burning, the final neutron excess remains close to its initial value in all of the network calculations displayed in Figures 5.43 and 5.44.

The outer zones of the star are heated to peak temperatures of less than $T \approx 2$ GK (the region to the right of the third dashed line in Figure 5.42) for very short periods of time and, as a result, do not experience significant nucleosynthesis in most stellar explosion models. These layers are ejected with a composition resulting from various hydrostatic burning stages prior to the explosion. About one hour after core collapse, the shock, traveling at an average speed of several thousand kilometer per second, reaches the stellar surface.

The sequence of events sketched above depends sensitively on all factors that influence the mass-radius relation (or the density profile) of the pre-supernova star, since it determines the amount of matter exposed to the four main explosive burning episodes. For example, the treatment of convection is important in this regard, because it impacts the size of the convective regions and the mixing efficiency in those zones. Also, as already mentioned in Section 5.2.1, the ^{12}C(α,γ)^{16}O reaction rate determines the ^{12}C/^{16}O abundance ratio at the end of core helium burning and hence impacts the amount of fuel available for the subsequent advanced hydrostatic shell burnings and the location of those shells. Furthermore, the magnitude of the time delay between core collapse and the

revival of the shock impacts the amount of matter located in each compositional layer. Besides the mass-radius relation, the neutron excess (or Y_e) profile of the pre-supernova star is crucial to the outcome of those explosive burning episodes that take place under the conditions of nuclear statistical equilibrium and quasi-equilibrium. The neutron excess profile, in turn, is influenced by the treatment of convection, the time delay between core collapse and shock revival, and the previous hydrostatic evolution of the star.

5.4.4 Observations

Direct evidence for the nucleosynthesis predicted by current core-collapse supernova models can be obtained from observations of Galactic radioactivity and neutrinos. For example, among the radioisotopes predicted to be synthesized by massive stars are ^{26}Al (during explosive neon–carbon burning) and ^{60}Fe (during carbon and helium convective shell burning, before the core collapse). Their half-lives ($T_{1/2} = 7.17 \times 10^5$ y and $T_{1/2} = 2.62 \times 10^6$ y, respectively) are very long compared to a typical frequency of about two Galactic core-collapse supernovae per century. Therefore, these nuclides accumulate in the interstellar medium after ejection from thousands of supernovae. The diffuse γ-ray emission from the decay of both species has been observed by detectors onboard satellites (Sections 1.7.5 and 5.6.1; color Figure 12 on page624). The ^{60}Fe/^{26}Al γ-ray line flux ratios measured by both the RHESSI instrument (Smith, 2004) and the SPI spectrometer onboard INTEGRAL (Wang *et al.*, 2007) are near ≈ 0.15. Stellar model predictions (Limongi and Chieffi, 2006) are consistent with observation when the theoretical yields from stars of different initial masses are folded with a standard distribution of stellar masses (i.e., the initial mass function).

The best-studied supernova to date, supernova 1987A, most likely resulted from the core collapse of a progenitor star with a mass near $20\,M_\odot$ (see color Figure 6 on page 618). A few months after the explosion, the evolution of its brightness (light curve) closely followed the radioactive decay of ^{56}Co ($T_{1/2} = 77.2$ d), the daughter nuclide of radioactive ^{56}Ni ($T_{1/2} = 6.1$ d) that is the main product of explosive silicon burning. Gamma-rays from ^{56}Co decay were also directly detected with the SMM satellite (Matz *et al.*, 1988). Together, both observations imply a total ^{56}Co mass of $\approx 0.07\,M_\odot$ in the ejecta (Leising and Share, 1993). Furthermore, a few hours before the light from supernova 1987A reached Earth, 11 electron antineutrinos were recorded by the KamiokaNDE-II detector (Hirata *et al.*, 1987) and 8 electron antineutrinos by the Irvine–Michigan–Brookhaven (IMB) detector (Bionta *et al.*, 1987). The number of detected neutrinos, their energies, and the measured burst duration are in agreement with theoretical predictions of the processes deep inside an exploding massive star.

The radioisotope ^{44}Ti has a half-life ($T_{1/2} = 60$ y) comparable to the Galactic supernova rate and thus can be used to probe individual supernovae. Gamma-rays from the decay of ^{44}Ti, with energies of 68 keV and 78 keV, have been detected

both in the 350-year old supernova remnant Cassiopeia A and in supernova 1987A (Renaud *et al.*, 2006; Grebenev *et al.*, 2012; Grefenstette *et al.*, 2014), confirming the theoretical prediction that this nuclide is synthesized in the α-rich freeze-out during complete explosive silicon burning in core-collapse supernovae. The spatial distribution of ^{44}Ti in Cassiopeia A is shown in color Figure 8 on page 620. Based on observations of Cassiopeia A and supernova 1987A, the ejected masses of ^{44}Ti amount to $\approx 1.6 \times 10^{-4}\, M_\odot$ and $\approx 3.1 \times 10^{-4}\, M_\odot$, respectively, in agreement with stellar model predictions. The radioactive decay of ^{44}Ti is also predicted to power the infrared, optical, and ultraviolet emission of supernova remnants about 3–4 years after the explosion, when the luminosity from the radioactive decays of ^{56}Co and ^{57}Co fades away.

5.5
Explosive Burning Involving Binary Stars

5.5.1
Explosive Burning in Thermonuclear Supernovae (Type Ia)

The two favored progenitor scenarios for the majority of type Ia supernovae are the single-degenerate and the double-degenerate model (Section 1.4.4). Although both models explain key features of the explosion, they also have major drawbacks.

In the single-degenerate model, a carbon-oxygen white dwarf accretes hydrogen- or helium-rich matter from a non-degenerate companion (main sequence star, red giant, or helium star). The mass of the white dwarf increases until it approaches the Chandrasekhar limit, triggering an explosion by compressional heating near the center of the white dwarf. The model explains why the majority of type Ia supernovae have similar peak luminosities and early-time spectra, since the Chandrasekhar limit provides a natural limit for the amount of fuel that can be burnt to ^{56}Ni. The main problem with the model is that stellar evolution theory predicts a maximum carbon–oxygen white dwarf mass of $\approx 1.1\, M_\odot$ (Althaus *et al.*, 2010). Therefore, the white dwarf must accrete about $0.3\, M_\odot$ before a type Ia supernova can occur. Whether or not the white dwarf grows in mass depends crucially on the mass-transfer rate: it must be relatively large to avoid mass loss through a nova-like event (Section 5.5.2), but not too large since then the system will enter into a common envelope phase. Only for a narrow range of mass-transfer rates will the accreted matter burn steadily and increase the white dwarf mass toward the Chandrasekhar limit (Kahabka and van den Heuvel, 1997).

In the double-degenerate model, two close carbon–oxygen white dwarfs with a combined mass near or in excess of the Chandrasekhar limit merge as a result of gravitational wave radiation, and thereby initiate a thermonuclear explosion. The model naturally explains the absence of hydrogen or helium emission lines in the spectra of type Ia supernovae. However, it does not easily explain the homogeneity

in peak luminosity and spectra of the majority of type Ia supernovae, since the merger mass, and thus the nuclear fuel that can be burnt to ^{56}Ni, has a wide range (1.1–2.0 $M_\odot$; Wang and Han, 2010). Furthermore, when the less massive white dwarf (companion) in the binary system fills its Roche lobe, it may be rapidly accreted by the more massive white dwarf (primary). As a consequence, the companion transforms into a disk-like structure around the more massive white dwarf. The maximum temperature in this configuration occurs at the interface of the disk and the primary, and hence this is the location where the carbon fuel is ignited first. The burning front propagates inward, transforming the carbon–oxygen white dwarf into an oxygen–neon white dwarf, which, as a consequence of electron captures on ^{24}Mg, could collapse and form a neutron star instead of producing a type Ia supernova explosion (*accretion-induced collapse*; Nomoto and Iben, 1985).

Modeling type Ia supernova explosions is a task of enormous complexity. Among the ingredients that need to be considered are the stellar evolution, rotation and mass loss of the progenitor, the accretion process, the ignition mechanism, and the propagation of the nuclear flames. Despite advances in these areas, we are still not in a position to explain these titanic explosions from first principles. In the framework of simplified one-dimensional models, the free parameters both for the single-degenerate and double-degenerate scenarios are the chemical structure of the exploding white dwarf, the initial metallicity of the progenitor on the main sequence, and the accretion rate onto the white dwarf that determines the central density at the time of ignition. In addition, for the double-degenerate model, the mass and composition of the companion white dwarf needs to be added to this list, while for the single-degenerate scenario the description of the initial deflagration and the magnitude of nuclear burning before the transition to detonation have to be included as well.

In the following, we will focus on one class of progenitors, the single-degenerate model, and discuss the nucleosynthesis during the thermonuclear explosion in more detail. Our goal is not to derive realistic abundances for type Ia explosions, but to shed some light on the different burning stages that ensue when the flame moves through different mass layers of the white dwarf. For this purpose, we will adopt some schematic and simplifying assumptions.

Consider a white dwarf consisting of ^{12}C, ^{16}O, and ^{22}Ne (Domínguez, Höflich, and Straniero, 2001). The composition of the inner core formed during the prior convective core helium burning phase (Section 5.2), while the outer layers formed during the prior shell burning on the asymptotic giant branch (Section 1.4.3). Suppose that the white dwarf accretes matter at a rate of $\approx 10^{-7}\,M_\odot$ for millions of years, thereby increasing the mass until it approaches the Chandrasekhar limit. The central temperature increases steadily because of compressional heating and nuclear energy generated by the fusion of carbon (Section 5.3.1). At the high densities in the core, electron screening becomes important for the ^{12}C+^{12}C reaction rate (Section 3.2.6 and Problem 3.10). When the central temperature and density reach values of ≈ 300 MK and $\approx 2 \times 10^9$ g/cm^3, respectively, the energy generation rate from the highly temperature-dependent

$^{12}C+^{12}C$ reaction (see Eq. (5.103)) starts to exceeds the neutrino cooling rate and the point of *ignition* is reached. As the temperature rises, matter near the core becomes convectively unstable. The convective core grows until it encompasses the entire star. Several hundred years after ignition, the nuclear energy generation becomes so vigorous that it cannot be quenched anymore by convective motion. When the temperature reaches a value of ≈ 700 MK, the time scales for nuclear burning and convection are of similar magnitude (≈ 10 s), and a thermonuclear runaway ensues. By the time any fluid element reaches a temperature near 10^9 K, the nuclear burning becomes faster than the time it takes a sound wave to cross a pressure scale height. The surface of such a fluid element becomes a *flame* with a well-determined laminar speed. For a detailed discussion of our incomplete knowledge about this early phase, see Arnett (1996).

Recall from Section 1.4.4 that a pure (supersonic) detonation flame will most likely produce iron-peak nuclides only and thus cannot account for the observation of intermediate mass elements in the spectra of type Ia supernovae. On the other hand, a pure (subsonic) deflagration flame, resulting in an expansion of the white dwarf, does not produce enough ^{56}Ni to explain the majority of type Ia events and leaves too much residual carbon and oxygen at low expansion velocities behind, contrary to observation. The favored single-degenerate scenario involves an initial deflagration, allowing the star to expand, followed by a detonation, when the density is on the order of 10^7 g/cm^3 (Khokhlov, 1991). As already mentioned in Section 1.4.4, the mechanism of the deflagration-detonation transition is not yet understood. The nuclear energy release takes about one second and rapidly incinerates the expanded white dwarf.

The explosive nuclear burning near the flame proceeds in different regimes and thus the chemical structure of the ejecta will reflect the thermodynamic conditions during the explosion. As an illustration, Figure 5.42 shows the peak temperature and peak density conditions for two thermonuclear supernova models (upper solid and dashed tracks) when the flame reaches different mass zones of the white dwarf (TN-DD: delayed detonation model of Bravo and Martínez-Pinedo, 2012; TN-W7: deflagration model of Nomoto, Thielemann, and Yokoi, 1984). The models evolve from the upper left (near the center of the white dwarf) to the lower right (the outer white dwarf layers). It is apparent that models of thermonuclear supernovae achieve considerably higher peak temperatures and densities compared to core-collapse supernova models.

Similar to the discussion in Section 5.4.3, we will describe the nucleosynthesis with the aid of numerical network calculations, performed for an exponential T-ρ time evolution (see Eq. (5.144)). For the initial composition, we assume ^{12}C ($X_i = 0.475$), ^{16}O ($X_i = 0.50$), with a small concentration of ^{22}Ne ($X_i = 0.025$). The latter species is produced during the prior helium burning stage (see Eq. (5.97)). Since the production of ^{22}Ne during helium burning depends on the initial concentration of C, N, and O, the neutron excess is related to the metallicity of the supernova progenitor (Timmes, Brown, and Truran, 2003). The initial neutron excess amounts to $\eta = 0.0023$ for our choice of composition. Recall that

we approximated the expansion time scale, τ, by the free-fall time scale, τ_{hd}, in the core-collapse supernova nucleosynthesis calculations (Section 5.4.3). For the thermonuclear supernova calculations discussed below, we will use the same value of $\tau = 0.3$ s for the expansion time scale. This value agrees approximately with hydrodynamic model results reported in the literature (Travaglio *et al.*, 2004a; Meakin *et al.*, 2009; Chamulak *et al.*, 2012).

The flame starts in the central region of the white dwarf at a peak temperature and density near 8.5 GK and 2×10^9 g/cm^3, respectively. For such conditions, nuclear statistical equilibrium (Section 5.3.5) is quickly established and the nuclear fuel (^{12}C, ^{16}O, ^{22}Ne) is converted to iron peak nuclides, with no intermediate-mass nuclides (such as ^{28}Si) left behind. The matter in this region will experience complete explosive silicon burning (labeled "comSi$_x$ (NSE)" in Figure 5.42). We already encountered this burning phase in our discussion of core-collapse supernovae (Section 5.4.3). However, the central densities in thermonuclear supernovae are considerably higher than in core-collapse supernovae. This has two interesting consequences. First, while most core-collapse supernova models experience α-*rich* freeze-out in the innermost ejecta, models of thermonuclear supernovae experience mostly *normal* freeze-out in the inner layers. The dotted line in Figure 5.42 separates the region of complete explosive silicon burning (to the left of the dashed-dotted line) into these two freeze-out regimes. Second, the densities predicted by thermonuclear supernova models are so high that the large Fermi energy of the electrons leads to electron captures (Section 1.8.4) on (i) free protons, $p + e^- \rightarrow n + \nu_e$, which exist copiously in nuclear statistical equilibrium under these conditions, and (ii) iron peak nuclei, even on the short explosive time scales. The electron captures move the nuclear statistical equilibrium concentrations away from the $N = Z$ line (^{56}Ni), toward neutron-rich species, that is, they increase the neutron excess, η, significantly. The dominant species produced under such conditions depends sensitively on the value of η attained in a given layer, as discussed in Section 5.3.5. The shaded area at the upper left in Figure 5.42 marks the region where electron captures are important. Its boundary corresponds to conditions for which the neutron excess increases by one order of magnitude, starting from $\eta_i = 0.0023$, when an exponential T–ρ evolution with an expansion time scale of $\tau = 0.3$ s is adopted. Only the innermost zones of the white dwarf, with an enclosed mass of less than $\approx 0.1\, M_\odot$, are expected to experience a significant neutronization caused by electron captures.

Results of a network calculation, obtained using Eq. (5.144) with a peak temperature and peak density of 8.5 GK and 2×10^9 g/cm^3, respectively, are shown in Figure 5.45a. These conditions, indicated by the first open circle in Figure 5.42, fall on the tracks of the two thermonuclear supernova models in the region labeled "comSi$_x$ (NSE)". In an explosion, the flame gives rise to a continuous distribution of $T_{\rm peak}$ and $\rho_{\rm peak}$ values while it moves through different mass layers. Hence, the results presented in Figure 5.45 correspond to the nucleosynthesis in a single homogeneous region. At the end of the calculation, electron captures have increased the neutron excess by more than an order of magnitude, from

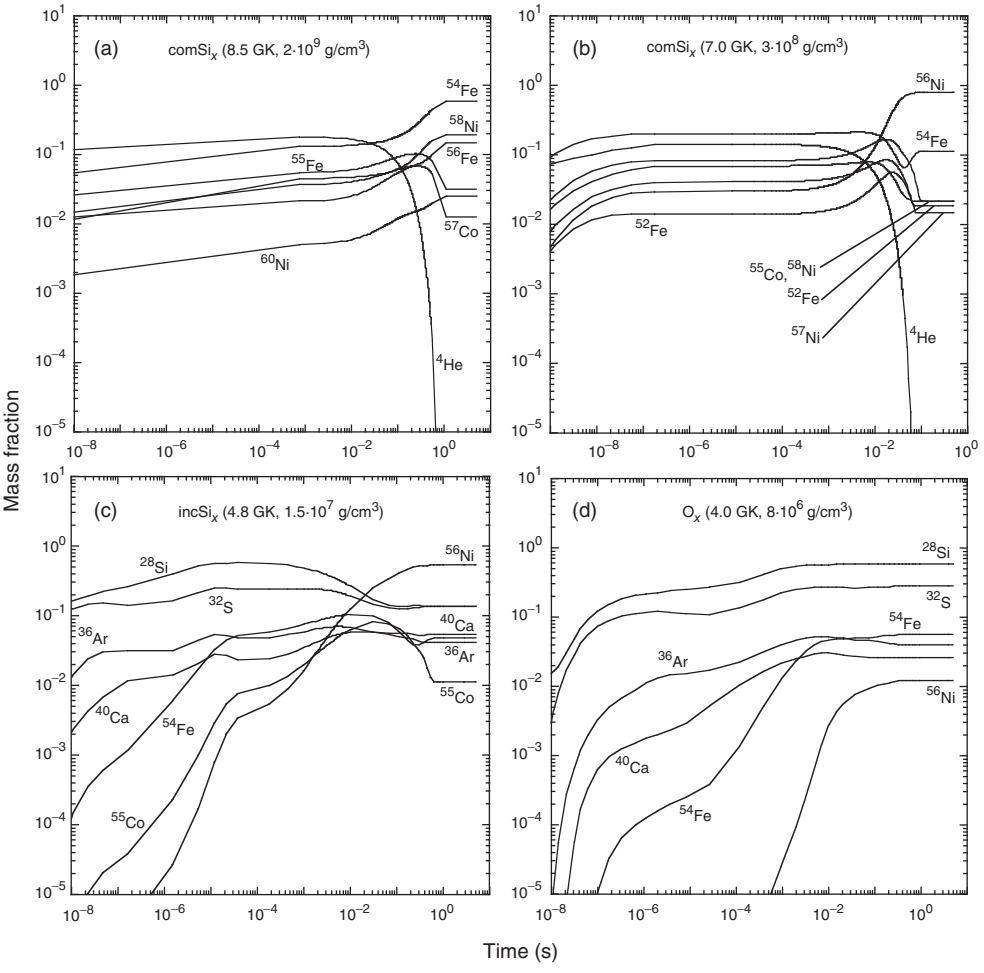

Figure 5.45 Abundance evolutions for explosive nucleosynthesis in thermonuclear supernovae (type Ia). Results are obtained using exponential T–ρ trajectories (see Eq. (5.144)) that approximate the conditions in the outward moving flame. Adopted values of $T_{\rm peak}$, $\rho_{\rm peak}$ are: (a) 8.5 GK, 2×10^9 g/cm^3; (b) 7.0 GK, 3×10^8 g/cm^3; (c) 4.8 GK, 1.5×10^7 g/cm^3; (d) 4.0 GK, 8×10^6 g/cm^3. These conditions correspond to complete explosive silicon burning (upper two panels), incomplete explosive silicon burning, and explosive oxygen burning, respectively, and are marked by open circles in Figure 5.42. The same value of $\tau = 0.3$ s is used for the expansion time scale. The adopted initial composition is: ^{12}C (X_i = 0.475); ^{16}O (X_i = 0.500); ^{22}Ne (X_i = 0.025), corresponding to an initial neutron excess of $\eta = 0.0023$.

an initial value of $\eta_i = 0.0023$ to a final value of $\eta_f = 0.043$ (corresponding to $Y_{\rm e} = 0.4784$). The most abundant species at the end of the calculation are ^{54}Fe ($X_f = 0.58$), ^{58}Ni ($X_f = 0.19$), and ^{56}Fe ($X_f = 0.15$), in agreement with expectation since these nuclides have the highest binding energies at individual neutron

excess parameters of $(N - Z)/A = 0.037$, 0.035, and 0.071, respectively. Also, notice in Figure 5.45a the negligible final α-particle abundance, indicating that the freeze-out was of the normal variety.

Outside the shaded area in Figure 5.42, but still in the complete explosive silicon burning (with normal freeze-out) regime, the densities have dropped to values where the impact of electron captures has lessened considerably. Since the fuel consists mainly of ^{12}C and ^{16}O, with equal numbers of protons and neutrons, nuclear statistical equilibrium will favor ^{56}Ni in these layers, which represents the most tightly bound nuclide with $N = Z$ (Figures 1.9 and 5.39). The time evolutions of the most abundant species for a peak temperature and peak density of 7.0 GK and 3×10^8 g/cm^3, respectively, are displayed in Figure 5.45b. These conditions are marked by the second open circle in Figure 5.42. The final neutron excess amounts to $\eta_f = 0.0057$, representing an increase by almost a factor of three over the initial value, but still small enough to favor a nuclide with $N = Z$ as the most abundant species. It is apparent in the figure that at the end of the calculation the most abundant species by far is ^{56}Ni ($N = Z = 28$), with a final mass fraction of $X_f = 0.79$. The next abundant nuclide, ^{54}Fe, has a final mass fraction that is lower by about an order of magnitude. Intermediate-mass elements (Si, S, Ar, Ca) are not significantly produced.

The next layers encountered by the flame, with a range of enclosed white dwarf masses of ≈ 0.3–$1.0\,M_\odot$, are heated to peak temperatures of $T \approx 4.5$–5.5 GK and experience incomplete explosive silicon burning (labeled "incSi$_x$" in Figure 5.42). As already discussed in Section 5.4.3, for these conditions quasi-equilibrium, not nuclear statistical equilibrium, is established. The time-integrated net abundance flows for a representative peak temperature and peak density of 4.8 GK and 1.5×10^7 g/cm^3, respectively, are shown in Figure 5.46a. These conditions are indicated by the third open circle in Figure 5.42. A cluster in quasi-equilibrium with ^{28}Si is quickly formed, followed by the formation of a quasi-equilibrium cluster in the iron-peak region. The expansion causes the freeze-out to occur before all of the intermediate mass elements can be transformed to iron-peak species. We expect that the relative abundances of the intermediate-mass elements and of ^{56}Ni will depend sensitively on the adopted values for the initial neutron excess and the expansion time scale. The corresponding time evolutions of the most abundant species are displayed in Figure 5.45c. The most abundant nuclide at the end of the calculation is again ^{56}Ni ($X_f = 0.53$), but this time significant amounts of ^{28}Si ($X_f = 0.14$), ^{32}S ($X_f = 0.14$), ^{36}Ar ($X_f = 0.041$), and ^{40}Ca ($X_f = 0.053$) remain. The complete and incomplete explosive silicon burning regions are separated by the dash-dotted line in Figure 5.42. For the adopted conditions, the neutron excess does not change noticeably over the course of the calculation.

The layers further out with a range of enclosed white dwarf masses of ≈ 1.0–$1.2\,M_\odot$, when the peak temperature in the flame has declined to $T \approx 3.5$–4.5 GK, experience explosive oxygen burning (labeled "O$_x$" in Figure 5.42). The time-integrated net abundance flows for a representative peak temperature and peak density of 4.0 GK and 8×10^6 g/cm^3, respectively, are shown in Figure 5.46b.

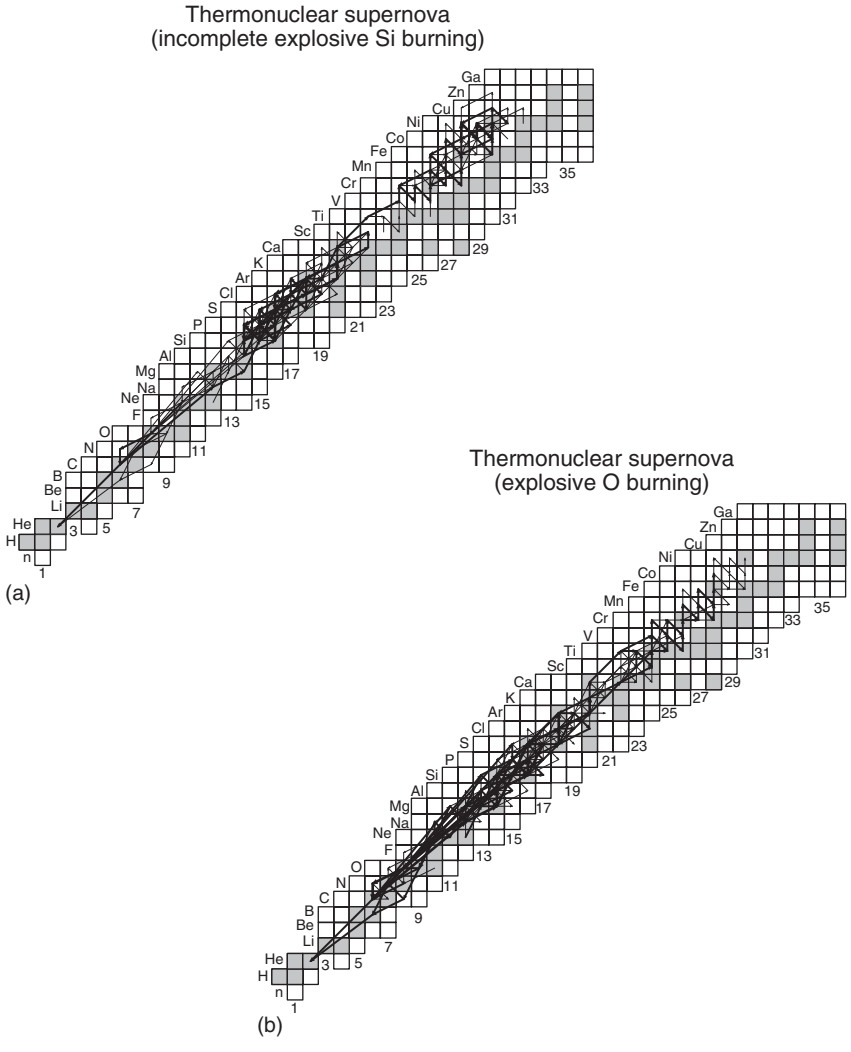

Figure 5.46 Time-integrated net abundance flows during thermonuclear supernova nucleosynthesis. The network calculations are performed using exponential T–ρ evolutions (see Eq. (5.144)) and an expansion time scale of $\tau = 0.3$ s; (a) incomplete explosive silicon burning with $T_{\rm peak} = 4.8$ GK and $\rho_{\rm peak} = 1.5 \times 10^7$ g/cm^3; (b) explosive oxygen burning with $T_{\rm peak} = 4.0$ GK and $\rho_{\rm peak} = 8 \times 10^6$ g/cm^3. The initial composition is: ^{12}C ($X_i = 0.475$); ^{16}O ($X_i = 0.500$); ^{22}Ne ($X_i = 0.025$). The two flow diagrams correspond to the abundance evolutions shown in Figure 5.45c,d. The arrows have the same meaning as in Figure 5.26: $F^{\rm max} \geq F_{ij} > 0.1F^{\rm max}$ (thick arrows), $0.1F^{\rm max} \geq F_{ij} > 0.01F^{\rm max}$ (intermediate arrows), and $0.01F^{\rm max} \geq F_{ij} > 0.001F^{\rm max}$ (thin arrows), where $F^{\rm max}$ corresponds to the reaction with the maximum net flow. The abundance flows are defined here in terms of mole fractions rather than number densities since the mass density varies.

These conditions are marked by the fourth open circle in Figure 5.42. Again, two quasi-equilibrium clusters form in the mass regions of silicon and the iron peak, but because of the lower peak temperature far less matter is converted to the iron peak region and most of the material remains locked in the silicon region. The corresponding abundance evolutions are displayed in Figure 5.45d. The most abundant species at the end of the calculation are by far ^{28}Si ($X_f = 0.58$) and ^{32}S ($X_f = 0.28$). The neutron excess remains unchanged for these conditions.

We already discussed in Section 5.4.3 that the nucleosynthesis during explosive burning is mainly determined by the peak temperature and the freeze-out conditions in a particular layer rather than by the composition of the fuel. The reason is that nuclear statistical equilibrium or quasi-equilibrium will seek the energetically most favorable configuration for the nuclear composition. Although the matter in the layers discussed so far undergoes explosive *silicon* and *oxygen* burning, it must be kept in mind that we assumed for the nuclear fuel a uniform distribution of mainly ^{12}C and ^{16}O, with a small contribution of ^{22}Ne. Since the neutron excess of the fuel is very small, the main nucleosynthesis products outside the central region, where electron captures play an important role, are $N = Z$ nuclides of large binding energy per nucleon, that is, ^{56}Ni, ^{28}Si, and so on (Figure 1.9). The production of minor nuclides will depend sensitively on the value of the adopted initial neutron excess.

The outer layers of the white dwarf, with an enclosed mass of ≈ 1.2–$1.3\,M_\odot$, are heated by the flame to peak temperatures of $T \approx 2$–3.5 GK and experience explosive neon-carbon burning (see also Section 5.4.3). Further out, at still lower peak temperatures, the hydrodynamic time scale is too short for thermonuclear reactions to take place and the nucleosynthesis ceases.

A few seconds after the explosion the ejecta expand freely. The matter density decreases with time and the ejecta become increasingly transparent for emitted photons, allowing for the observation of deeper layers as time progresses. The observations indicate a layered chemical structure reflecting the different burning regimes of the flame. Near the center of the ejecta there is a region depleted in ^{56}Ni and occupied by neutron-rich iron-peak elements (Höflich *et al.*, 2004), consistent with their production in the *complete explosive silicon burning with electron capture* regime. Above this region, there is a volume filled mainly with ^{56}Ni produced during complete and incomplete explosive silicon burning. Farther out, intermediate mass elements (Si, S, Ar, Ca) and other iron peak species are the main constituents, which are synthesized during incomplete explosive silicon burning and explosive oxygen burning.

Most Chandrasekhar mass single-degenerate models produce ^{56}Ni, which powers the light curves of type Ia supernovae, in a region of mass shells with ≈ 0.2–$0.8\,M_\odot$. The inferred amount of ^{56}Ni synthesized per event is about $0.6\,M_\odot$. The similarity in peak brightness between different observed type Ia supernovae (Section 1.4.4) can be understood by assuming that the amount of fuel, consisting mainly of carbon and oxygen, is similar from event to event (given by the Chandrasekhar limit) and that most of the fuel burns to iron-peak and intermediate-mass elements, with little remaining unburned fuel.

Finally, we briefly address the situation regarding the nuclear physics input. The high temperatures and densities achieved in the explosion imply that most nuclear reactions will take part in either nuclear statistical equilibrium or quasi-equilibrium. Therefore, the nucleosynthesis and nuclear energy generation will in general not be sensitive to individual reaction rates, but will depend on reaction Q-values, nuclear spins, and partition functions. The masses of the nuclides taking part in the nucleosynthesis are well known. We expect current reaction rate uncertainties to play a role only during the ignition phase (mainly for $^{12}C+^{12}C$) or during freeze-out. However, sensitivity studies (Bravo and Martínez-Pinedo, 2012; Parikh *et al.*, 2013b) have identified a handful of nuclear reactions, $^{12}C+^{12}C$, $^{12}C(\alpha,\gamma)^{16}O$, $^{20}Ne(\alpha,\gamma)^{24}Mg$, $^{24}Mg(\alpha,p)^{27}Al$, and $^{30}Si(p,\gamma)^{31}P$, that impact the nucleosynthesis in type Ia models in the temperature range of $T \approx 2$–4 GK, although their influence is modest. The importance of stellar weak interaction rates (Section 1.8.4) for the nucleosynthesis in the inner region of the exploding white dwarf has already been discussed above. Estimations of the uncertainties associated with stellar weak rates exist for a handful of interactions only (Cole *et al.*, 2012) and more work is needed. At the high densities occurring in type Ia explosions, electron screening corrections (Section 3.2.6) are also crucial and have to be taken into account for precise predictions (Calder *et al.*, 2007).

5.5.2
Explosive Hydrogen Burning and Classical Novae

In Section 5.1, we discussed hydrogen burning in the stellar temperature range of $T < 0.06$ GK. If, under such conditions, the stellar gas consists of pure hydrogen, then hydrogen burning must proceed via the pp chains (with perhaps a contribution from the pep reaction; Section 5.1.1). On the other hand, if a significant fraction of CNO nuclei is present in the stellar gas, then the CNO cycles will generate most of the energy above a certain temperature (e.g., above 20 MK for a solar mass fraction of CNO nuclei; see Figure 5.12). There are two important points that need to be kept in mind regarding hydrogen burning at temperatures below 0.06 GK. First, a specific radioactive nucleus that is produced during the burning will be destroyed by its relatively fast β-decay rather than by the considerably slower competing proton-induced reaction (with the exceptions of ^{7}Be in the pp3 chain and ^{26}Al in the region of $A \geq 20$; see Figure 5.2 and Section 5.1.3). Second, in the reaction network of the pp chains or the CNO cycles, all the radioactive decays are faster compared to the slowest proton-induced reaction and, consequently, the energy generation rate does not depend on the half-lives of the radioactive decays. At elevated temperatures typical of explosive hydrogen burning, the situation described above changes dramatically.

In the following, we will discuss the explosive nucleosynthesis in the $A < 20$ and $A \geq 20$ mass regions at temperatures of $T = 0.1$–0.4 GK. Another important point needs to be stressed. So far, we explored the nucleosynthesis in hydrostatic

burning environments analytically by considering equilibrium burning conditions or numerically by performing reaction network calculations assuming a constant temperature and density. These considerations provide a qualitative picture of the interplay between different nuclear processes. However, the above assumptions are not valid for explosive events. First, the time to approach equilibrium conditions is often comparable to the macroscopic hydrogen burning time scale. Second, temperatures and densities in an explosive event change dramatically with time. The time evolution of T and ρ depends strongly on the properties of the exploding star. In this section, the reaction networks for explosive hydrogen burning are solved numerically, first with the assumption of constant T–ρ conditions, and then by using temperature and density evolutions adopted from simulations of classical novae.

Hot CNO Cycles

If a star consists of a gas containing a significant fraction of CNO nuclei, then at elevated temperatures ($T = 0.1$–0.4 GK) most of the nuclear energy is generated by the *hot CNO cycles* (or HCNO cycles). The reactions of the HCNO cycles are listed below and are shown in Figure 5.47.

Hot CNO1	Hot CNO2	Hot CNO3
$^{12}C(p,\gamma)^{13}N$	$^{15}O(\beta^+\nu)^{15}N$	$^{15}O(\beta^+\nu)^{15}N$
$^{13}N(p,\gamma)^{14}O$	$^{15}N(p,\gamma)^{16}O$	$^{15}N(p,\gamma)^{16}O$
$^{14}O(\beta^+\nu)^{14}N$	$^{16}O(p,\gamma)^{17}F$	$^{16}O(p,\gamma)^{17}F$
$^{14}N(p,\gamma)^{15}O$	$^{17}F(\beta^+\nu)^{17}O$	$^{17}F(p,\gamma)^{18}Ne$
$^{15}O(\beta^+\nu)^{15}N$	$^{17}O(p,\gamma)^{18}F$	$^{18}Ne(\beta^+\nu)^{18}F$
$^{15}N(p,\alpha)^{12}C$	$^{18}F(p,\alpha)^{15}O$	$^{18}F(p,\alpha)^{15}O$

$T_{1/2}$: ^{14}O (70.62 s); ^{15}O (122.24 s); ^{17}F (64.49 s)

The hot CNO cycles have a number of important properties in common with the CNO cycles discussed in Section 5.1.2: (i) each of the hot CNO cycles converts four hydrogen nuclei to one helium nucleus; (ii) the CNOF nuclei involved in the hot CNO cycles act as catalysts and their total number is nearly constant; and (iii) the energy generation rate of the hot CNO cycles depends on the abundances of the catalysts. It will be shown in Section 5.5.3 that, above a certain temperature ($T \geq 0.4$ GK), catalytic material will be lost from the hot CNO cycles by various breakout reactions. In this section, we will discuss the operation of the hot CNO cycles in the temperature region of $T = 0.1$–0.4 GK.

We will start our discussion by considering the CNO1 cycle (Figure 5.8) and how this cycle is modified when the temperature gradually increases. The ^{13}N nucleus has the longest half-life ($T_{1/2} = 9.96$ min) among all the β^+-decays in the CNO1 cycle. For an increasing temperature, a point will be reached where the destruction of ^{13}N by proton-capture competes favorably with the β^+-decay of ^{13}N. Hence,

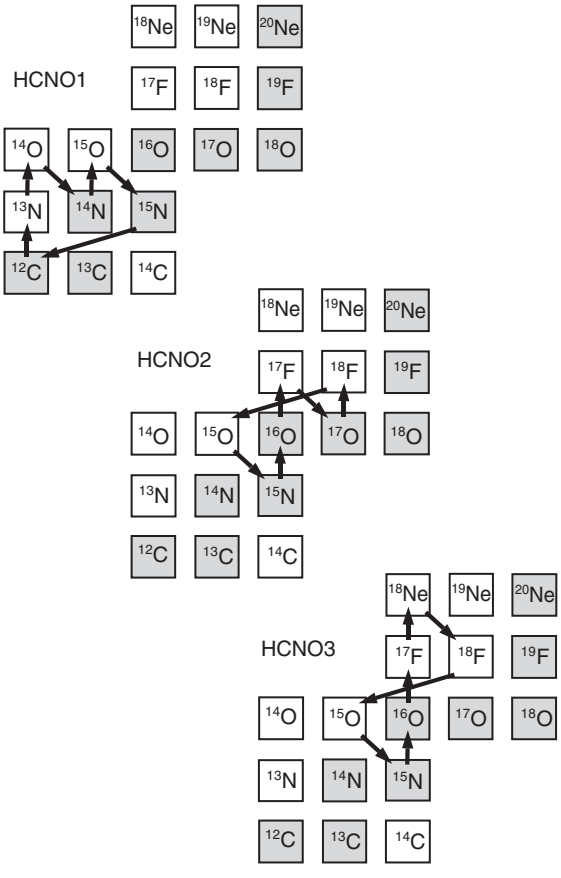

Figure 5.47 Representation of the three hot CNO cycles in the chart of the nuclides. Stable nuclides are shown as shaded squares. Each reaction cycle fuses effectively four protons to one ^{4}He nucleus. In explosive hydrogen burning, the CNO2 cycle (Figure 5.8) is more likely to occur than the HCNO2 cycle since the ^{17}O(p,α)^{14}N reaction rate dominates over the ^{17}O(p,γ)^{18}F rate (Figure 5.9).

instead of the sequence that occurs in the CNO1 cycle,

$$^{13}\mathrm{N}(\beta^+\nu)^{13}\mathrm{C}(\mathrm{p},\gamma)^{14}\mathrm{N} \tag{5.147}$$

the alternative path

$$^{13}\mathrm{N}(\mathrm{p},\gamma)^{14}\mathrm{O}(\beta^+\,\nu)^{14}\mathrm{N} \tag{5.148}$$

becomes more likely. The half-life of ^{14}O ($T_{1/2} = 70.6$ s) is less than that of ^{13}N. Thus, ^{13}N is converted to ^{14}N on a faster time scale for the latter path. Furthermore, it was shown in Section 5.1.2 that the ^{14}N(p,γ)^{15}O reaction is the slowest process in the CNO1 cycle and, therefore, determines the energy generation rate. For an increasing temperature, all the rates for proton-induced reactions will

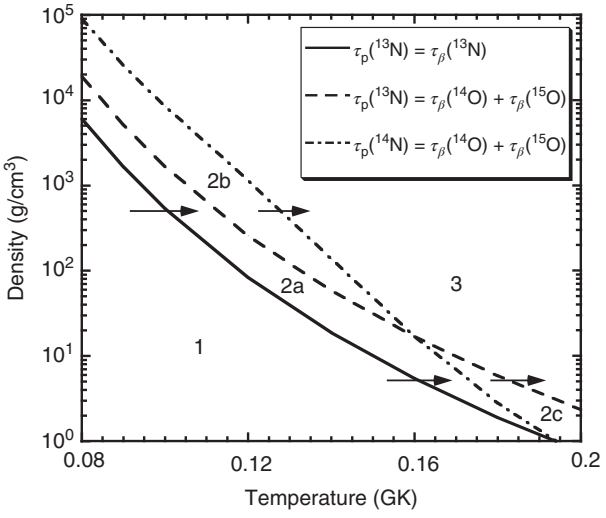

Figure 5.48 Temperature–density diagram showing the transition from the CNO1 cycle (region 1) to the HCNO1 cycle (region 3). The solid curve represents the T–ρ conditions at which the ^{13}N β^+-decay lifetime is equal to the lifetime of ^{13}N destruction via proton capture. The dashed (dashed-dotted) curve is obtained for the condition that the ^{13}N (^{14}N) lifetime versus destruction by proton capture is equal to the sum of the ^{14}O and ^{15}O β^+-decay lifetimes. All curves are calculated for the solar value $X_H/M_H = 0.70$. On the left-hand side of each curve, the β^+-decay is more likely to occur than the proton-induced reaction, while the opposite applies on the right-hand side.

increase strongly. Eventually a point is reached where all (p,γ) and (p,α) reactions, including the ^{14}N(p,γ)^{15}O reaction, are faster compared to the β^+-decays of ^{14}O and ^{15}O. As a result of these two modifications, the CNO1 cycle transforms at higher temperatures into the hot CNO1 cycle (Figure 5.47). It was mentioned earlier that the energy generation rate of the CNO1 cycle is highly sensitive to the temperature (see Eq. (5.71)). The HCNO1 cycle, on the other hand, has the interesting property that the energy generation rate depends on the β^+-decays of ^{14}O and ^{15}O (i.e., the slowest links in the cycle) and hence is independent of temperature. For this reason, the HCNO1 cycle is also referred to as β-*limited CNO cycle*. The time around one HCNO1 cycle is then at least $\tau_\beta(^{14}O) + \tau_\beta(^{15}O) = T_{1/2}(^{14}O)/\ln 2 + T_{1/2}(^{15}O)/\ln 2 \approx 278$ s. It follows that a significant fraction of the CNO nuclei will be transformed into ^{14}O and ^{15}O. Proton captures on ^{14}O and ^{15}O are unlikely to occur since the corresponding compound nuclei ^{15}F and ^{16}F are unstable by proton emission.

The transition from the CNO1 cycle to the HCNO1 cycle can be represented in a temperature-density diagram (Figure 5.48). The lifetimes of the ^{13}N, ^{14}O, and ^{15}O β^+-decays are given by $\tau_\beta = T_{1/2}/\ln 2$, while the lifetimes of ^{13}N and ^{14}N versus destruction by protons are $\tau_p = [\rho(X_H/M_H)N_A\langle\sigma v\rangle]^{-1}$. The solid curve represents the T–ρ conditions for which the ^{13}N β^+-decay lifetime is equal to the lifetime of

^{13}N destruction via proton capture, that is

$$\frac{1}{\rho(X_{\rm H}/M_{\rm H})N_A\langle\sigma v\rangle_{^{13}N({\rm p},\gamma)}} = \frac{T_{1/2}(^{13}{\rm N})}{\ln 2} \tag{5.149}$$

The dashed (or dashed-dotted) curve is obtained for the condition that the ^{13}N (or ^{14}N) lifetime versus destruction by proton capture is equal to the sum of ^{14}O and ^{15}O lifetimes,

$$\frac{1}{\rho(X_{\rm H}/M_{\rm H})N_A\langle\sigma v\rangle_{^{x}N({\rm p},\gamma)}} = \frac{T_{1/2}(^{14}O)}{\ln 2} + \frac{T_{1/2}(^{15}O)}{\ln 2} \tag{5.150}$$

All curves are calculated for a solar value of $X_{\rm H}/M_{\rm H} = 0.70$. On the left-hand side of each curve, the β^+-decays are more likely to occur than the proton-induced reaction, while the opposite situation prevails on the right-hand side. The CNO1 cycle operates in region 1 where ^{13}N β^+-decays $[\tau_\beta(^{13}N) < \tau_{\rm p}(^{13}N)]$ and where ^{14}N(p,γ)^{15}O is the slowest link in the cycle $[\tau_\beta(^{14}O) + \tau_\beta(^{15}O) < \tau_{\rm p}(^{14}N)]$. Suppose we start out in region 1 and slowly increase the temperature by keeping the density constant, for example, at $\rho = 500$ g/cm^3. When the solid curve is crossed at $T \approx 0.100$ GK, we have $\tau_\beta(^{13}N) > \tau_{\rm p}(^{13}N)$, and the slow ^{13}N β^+-decay is bypassed by the sequence ^{13}N(p,γ)^{14}O($\beta^+\nu$)^{14}N (region 2a). When the dashed curve is crossed at $T \approx 0.113$ GK, the ^{13}N proton-capture reaction becomes faster than the ^{14}O and ^{15}O β^+-decays $[\tau_\beta(^{14}O) + \tau_\beta(^{15}O) > \tau_{\rm p}(^{13}N)]$. At this stage (region 2b), the ^{14}N(p,γ)^{15}O reaction is still the slowest link in the cycle and determines the energy generation rate. Finally, when the dashed-dotted curve is crossed at $T \approx 0.128$ GK, the proton capture on ^{14}N becomes faster than the ^{14}O and ^{15}O β^+-decays $[\tau_\beta(^{14}O) + \tau_\beta(^{15}O) > \tau_{\rm p}(^{14}N)]$. We have now reached region 3, where the β-limited HCNO1 cycle operates.

For other densities, the situation is similar when increasing the temperature, although the curves may be crossed in different order. For example, at a lower density of $\rho = 5$ g/cm^3 the solid curve is crossed at $T \approx 0.161$ GK (region 2a), while the dashed-dotted curve is crossed at $T \approx 0.174$ GK. At this stage (region 2c), the sequence ^{13}N(p,γ)^{14}O($\beta^+\nu$)^{14}N dominates over the ^{13}N β^+-decay and the proton capture reaction on ^{14}N is faster than the ^{14}O and ^{15}O β^+-decays. However, the dashed curve has not been crossed yet, that is, the ^{13}N(p,γ)^{14}O reaction is slower than the ^{14}O and ^{15}O β^+-decays. The proton-capture reaction on ^{13}N is now the slowest link in the cycle and determines the energy generation rate. Finally, the dashed curve is crossed at $T \approx 0.185$ GK and the CNO cycle becomes again β-limited (region 3).

The HCNO1 cycle discussed above represents a nearly closed reaction sequence, in the sense that very little catalytic material is lost. This occurs because the branching ratio $B_{{\rm p}\alpha/{\rm p}\gamma}$ at ^{15}N exceeds a factor of 1000 (Figure 5.9). Hence, if ^{12}C seed nuclei are present in the gas, they will be converted mostly to ^{14}O and ^{15}O, assuming that hydrogen is not near exhaustion (see later). We already pointed out in Section 5.1.2 that in addition to ^{12}C, other seed nuclei, such as ^{16}O, may be present in the stellar gas. The ^{16}O nuclei are processed in a

number of different, competing reaction cycles. One possibility of processing is the CNO2 cycle, which was introduced in Section 5.1.2,

$$^{16}\mathrm{O}(\mathrm{p},\gamma)^{17}\mathrm{F}(\beta^{+}\nu)^{17}\mathrm{O}(\mathrm{p},\alpha)^{14}\mathrm{N}(\mathrm{p},\gamma)^{15}\mathrm{O}(\beta^{+}\nu)^{15}\mathrm{N}(\mathrm{p},\gamma)^{16}\mathrm{O} \tag{5.151}$$

Inspection of Figure 5.9 reveals that the ^{17}O(p,α)^{14}N reaction dominates over the competing ^{17}O(p,γ)^{18}F reaction at temperatures of $T = 0.1$–0.4 GK by a factor of ≈ 200. A small fraction of the ^{16}O seed nuclei will be processed via the ^{17}O(p,γ)^{18}F reaction, giving rise to the HCNO2 cycle,

$$^{16}\mathrm{O}(\mathrm{p},\gamma)^{17}\mathrm{F}(\beta^{+}\nu)^{17}\mathrm{O}(\mathrm{p},\gamma)^{18}\mathrm{F}(\mathrm{p},\alpha)^{15}\mathrm{O}(\beta^{+}\nu)^{15}\mathrm{N}(\mathrm{p},\gamma)^{16}\mathrm{O} \tag{5.152}$$

The branching ratio $B_{\mathrm{p}\alpha/\mathrm{p}\gamma}$ at ^{18}F is shown in Figure 5.49a. In the temperature range of $T = 0.1$–0.4 GK, the ^{18}F(p,α)^{15}O reaction is faster than the competing ^{18}F(p,γ)^{19}Ne reaction by more than a factor of 1000. Under conditions of explosive hydrogen burning, the ^{18}F(p,α)^{15}O reaction is also faster than the ^{18}F β^{+}-decay. This is demonstrated in Figure 5.49b. The dashed line shows the T–ρ conditions (for $X_{\mathrm{H}}/M_{\mathrm{H}} = 0.70$) at which the ^{18}F β^{+}-decay lifetime is equal to the lifetime of ^{18}F destruction via the (p,α) reaction [$\tau_{\mathrm{p}\alpha}(^{18}\mathrm{F}) = \tau_{\beta}(^{18}\mathrm{F})$]. For example, at a density of $\rho = 500$ g/cm^3 the ^{18}F(p,α)^{15}O reaction dominates over the competing β^{+}-decay for temperatures of $T > 0.058$ GK. Consequently, once the nucleosynthesis path in explosive hydrogen burning reaches ^{18}F, the (p,α) reaction is the dominant destruction mode. The solid line in Figure 5.49b shows the T–ρ conditions at which the ^{17}F β^{+}-decay lifetime is equal to the lifetime of ^{17}F destruction via

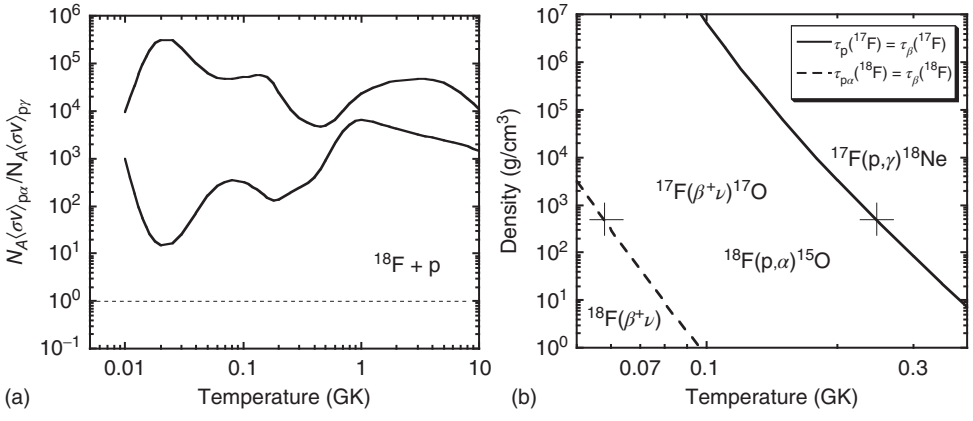

Figure 5.49 (a) Branching ratio $B_{\mathrm{p}\alpha/\mathrm{p}\gamma} = N_A\langle\sigma v\rangle_{(\mathrm{p},\alpha)}/N_A\langle\sigma v\rangle_{(\mathrm{p},\gamma)}$ versus temperature for the ^{18}F + p reactions. The two solid lines represent the upper and lower boundaries of $B_{\mathrm{p}\alpha/\mathrm{p}\gamma}$ (de Séréville, Berthoumieux, and Coc, 2005). The area between the solid lines indicates the uncertainty in $B_{\mathrm{p}\alpha/\mathrm{p}\gamma}$ caused by unknown contributions to the (p,γ) and (p,α) reaction rates. (b) Temperature–density conditions showing the competing destruction modes of ^{17}F and ^{18}F. The dashed line represents the conditions at which the ^{18}F β^{+}-decay lifetime is equal to the lifetime of ^{18}F destruction via the (p,α) reaction. The solid line corresponds to the conditions at which the ^{17}F β^{+}-decay lifetime is equal to the lifetime of ^{17}F destruction via the (p,γ) reaction. The curves in part (b) are calculated assuming $X_{\mathrm{H}}/M_{\mathrm{H}} = 0.70$.

the (p,γ) reaction [$\tau_p(^{17}F) = \tau_\beta(^{17}F)$]. Considering again, for example, a density of $\rho = 500$ g/cm^3, it can be seen that the ^{17}F(p,γ)^{18}Ne reaction dominates over the competing β^+-decay at temperatures of $T > 0.23$ GK. Hence, the HCNO3 cycle develops,

$$^{16}\mathrm{O}(\mathrm{p},\gamma)^{17}\mathrm{F}(\mathrm{p},\gamma)^{18}\mathrm{Ne}(\beta^+\nu)^{18}\mathrm{F}(\mathrm{p},\alpha)^{15}\mathrm{O}(\beta^+\nu)^{15}\mathrm{N}(\mathrm{p},\gamma)^{16}\mathrm{O} \tag{5.153}$$

which bypasses the isotope ^{17}O.

Network Calculations at Constant Temperature and Density

To gain a better understanding of the nucleosynthesis, we will first solve the reaction network of the HCNO cycles numerically for constant temperature and density conditions. The extra complications that arise from the more realistic assumptions of time-dependent temperatures and densities will be dealt with later. We assume for the initial abundances values of $X^0_{\mathrm{H}} = 0.60$, $X^0_{^4\mathrm{He}} = 0.20$, and $X^0_{^{12}\mathrm{C}} = 0.20$, that is, only ^{12}C is initially present as seed for the hot CNO cycles. The reaction network is solved until hydrogen exhaustion ($X_{\mathrm{H}} < 0.001$). The time evolution of ^{1}H and the HCNO1 abundances (^{12}C, ^{13}N, ^{14}O, ^{14}N, ^{15}O) is shown in Figure 5.50 for temperatures of $T = 0.15$ GK and $T = 0.3$ GK. For both calculations, a density of $\rho = 200$ g/cm^3 has been chosen. Although all reactions of the HCNO cycles have been included in the network, the graphs represent mainly the operation of the HCNO1 cycle, since the leakage to the other cycles via the ^{15}N(p,γ)^{16}O reaction is very small. For the initial conditions chosen, the abundances of ^{16}O, ^{17}O, ^{17}F, and ^{18}F never exceed a value of $X_i = 10^{-4}$. Also, the abundance of ^{15}N is very small because of its strong destruction via the (p,α) reaction and is not displayed in Figure 5.50.

For a temperature of $T = 0.15$ GK (Figure 5.50a), ^{12}C is initially converted to ^{13}N via the ^{12}C(p,γ)^{13}N reaction. The ^{13}N abundance reaches a maximum after $t = 20$ s. The subsequent ^{13}N(p,γ)^{14}O reaction causes the ^{14}O abundance to peak after about $t = 80$ s. The slow ^{14}O β^+-decay increases the ^{14}N abundance, while the subsequent ^{14}N(p,γ)^{15}O reaction is responsible for the growing abundance of ^{15}O. At a time around $t = 500$ s, the hydrogen abundance has dropped to $X_{\mathrm{H}} = 0.5$ and all CNO abundances achieve equilibrium. The ratio of any two number abundances is then given by Eq. (5.61),

$$\left(\frac{A}{B}\right)_e = \left(\frac{X_A}{X_B}\right)_e \left(\frac{M_B}{M_A}\right) = \frac{\tau_A}{\tau_B} \tag{5.154}$$

At this stage, the sum of mean lifetimes in the HCNO1 cycle amounts to

$$\begin{aligned}\sum \tau_{\mathrm{CNO1}} &\equiv \tau_p(^{12}C) + \tau_p(^{13}N) + \tau_\beta(^{14}O) + \tau_p(^{14}N) + \tau_\beta(^{15}O) \\ &= (13 + 63 + 102 + 91 + 176)\,\mathrm{s} = 445\,\mathrm{s}\end{aligned} \tag{5.155}$$

The nuclide ^{15}O is the most abundant species in the CNO mass range because its mean lifetime has the largest value. Although the ^{14}O and ^{15}O β^+-decays represent the slowest links in the HCNO1 cycle, the contribution from proton-induced reactions to the sum of mean lifetimes is significant. Further processing of matter is influenced by the substantially decreasing hydrogen abundance until exhaustion.

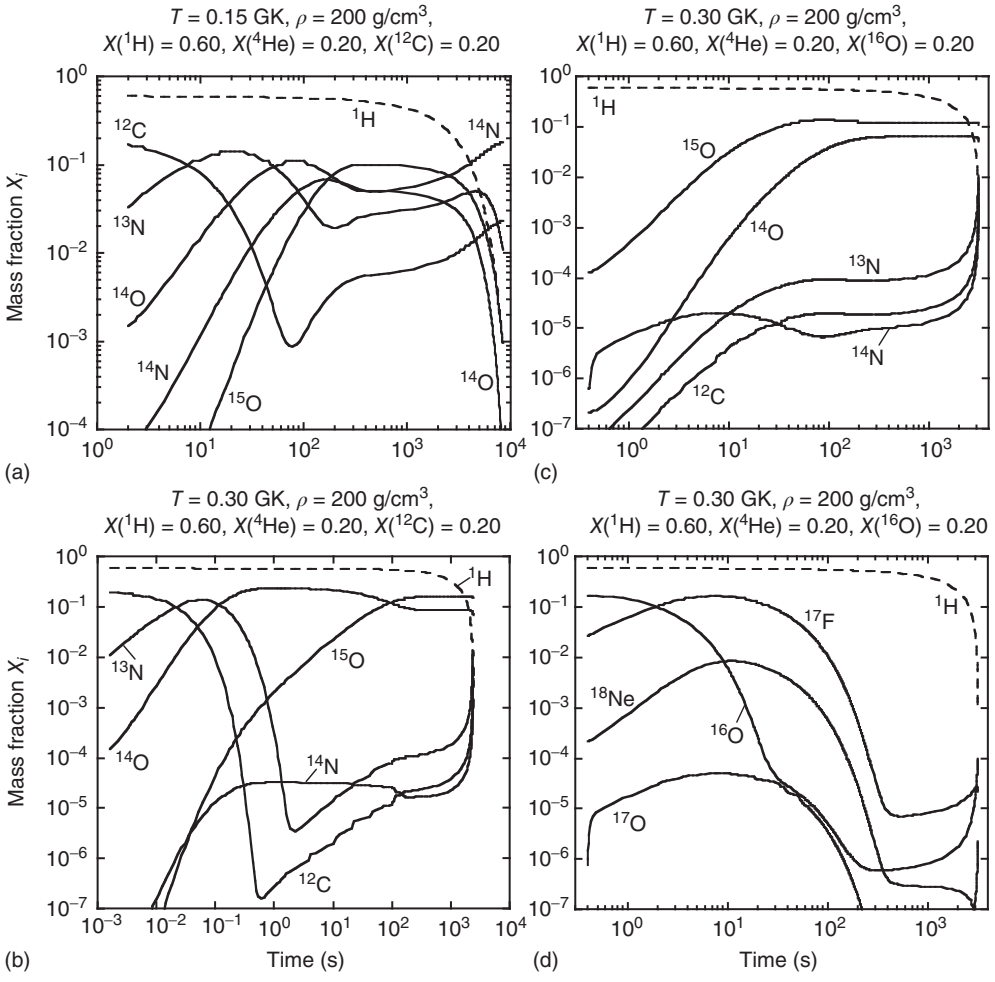

Figure 5.50 Time evolution of abundances during the operation of the hot CNO cycles for different conditions: (a) $T = 0.15$ GK, $X_{\mathrm{H}}^0 = 0.60$, $X_{^4\mathrm{He}}^0 = 0.20$, and $X_{^{12}\mathrm{C}}^0 = 0.20$; (b) $T = 0.30$ GK, $X_{\mathrm{H}}^0 = 0.60$, $X_{^4\mathrm{He}}^0 = 0.20$, and $X_{^{12}\mathrm{C}}^0 = 0.20$; (c), (d) $T = 0.30$ GK, $X_{\mathrm{H}}^0 = 0.60$, $X_{^4\mathrm{He}}^0 = 0.20$, and $X_{^{16}\mathrm{O}}^0 = 0.20$. For the density, a constant value of $\rho = 200$ g/cm^3 is assumed. All curves shown are obtained by solving the reaction network numerically. The calculations are terminated when the hydrogen mass fraction falls below $X_{\mathrm{H}} = 0.001$.

As a result, all the lifetimes for proton-induced reactions increase (see Eq. (3.22)). For example, at a time of $t = 3000$ s, the hydrogen abundance has dropped to a value of $X_{\mathrm{H}} = 0.18$ and we obtain

$$\sum \tau_{\mathrm{CNO1}} = (34 + 168 + 102 + 252 + 176)\,\mathrm{s} = 732\,\mathrm{s} \tag{5.156}$$

with $^{14}\mathrm{N}(\mathrm{p},\gamma)^{15}\mathrm{O}$ representing the slowest link in the cycle. With decreasing hydrogen abundance, the ^{14}O and ^{15}O abundances also decline since their

β^+-decays are now faster than their production via ^{13}N(p,γ)^{14}O and ^{14}N(p,γ)^{15}O. The nuclide ^{14}N becomes the most abundant species and its abundance increases further until the end of the calculation is reached. It is remarkable that hydrogen is exhausted after only $t = 8400$ s, a time period that is significantly shorter compared to the situation prevailing in hydrostatic hydrogen burning environments. This result is a direct consequence of the strong temperature sensitivity of charged-particle reaction rates.

At a higher temperature of $T = 0.3$ GK (Figure 5.50b), the abundances evolve initially similar to the previous case. The nuclide ^{12}C is first converted to ^{13}N and then further processed to ^{14}O. The β^+-decay of the latter nucleus feeds the increasing ^{15}O abundance via the sequence $^{14}O(\beta^+\nu)^{14}N(p,\gamma)^{15}O$. Equilibrium CNO abundances are reached after $t = 300$ s. At that stage, the hydrogen abundance has dropped to $X_H = 0.5$ and the sum of all mean lifetimes in the HCNO1 cycle amounts to

$$\begin{aligned}\sum \tau_{CNO1} &= (0.035 + 0.15 + 102 + 0.016 + 176)\,\mathrm{s} \\ &\approx \tau_\beta(^{14}O) + \tau_\beta(^{15}O) = 278\,\mathrm{s}\end{aligned} \tag{5.157}$$

with a negligible contribution from proton-capture reactions. The reaction cycle is β-limited, and the most abundant species are ^{15}O and ^{14}O. For their number abundance ratio, we obtain

$$\left(\frac{^{15}O}{^{14}O}\right)_e = \left(\frac{X_{^{15}O}}{X_{^{14}O}}\right)_e \left(\frac{M_{^{14}O}}{M_{^{15}O}}\right) = \frac{\tau_\beta(^{15}O)}{\tau_\beta(^{14}O)} = \frac{176\,\mathrm{s}}{102\,\mathrm{s}} = 1.7 \tag{5.158}$$

in agreement with the numerical results displayed in Figure 5.50b. This situation prevails almost until the end of the calculation. Only at times very close to hydrogen exhaustion do the mean proton-capture lifetimes sufficiently increase to cause a slight drop in the ^{14}O and ^{15}O abundances, with a corresponding rise of the ^{12}C, ^{13}N, and ^{14}N abundances. Nevertheless, even at hydrogen exhaustion ($X_H = 0.001$) we have

$$\sum \tau_{CNO1} = (18 + 77 + 102 + 8 + 176)\,\mathrm{s} = 381\,\mathrm{s} \tag{5.159}$$

and the ^{14}O and ^{15}O β^+-decays are still the slowest links in the HCNO1 cycle. Hydrogen is exhausted after a time of $t = 2400$ s. This value is significantly shorter compared to the result obtained in the previous network calculation since the proton-capture reactions become faster with increasing temperature.

We will now consider the nucleosynthesis resulting from a change in initial composition. We assume values of $X^0_H = 0.60$, $X^0_{^4He} = 0.20$, and $X^0_{^{16}O} = 0.20$, that is, only ^{16}O instead of ^{12}C is initially present as seed for the hot CNO cycles. For the temperature and density, we have again assumed values of $T = 0.3$ GK and $\rho = 200$ g/cm^3, respectively. The results of a network calculation are displayed in Figure 5.50c,d. The ^{16}O(p,γ)^{17}F reaction quickly destroys the ^{16}O seed nuclei and converts them to ^{17}F, whose abundance peaks after $t = 8$ s. For the chosen T–ρ conditions, the ^{17}F(p,γ)^{18}Ne reaction dominates over the competing ^{17}F β-decay (see Figure 5.49b). Hence, the HCNO3 cycle operates, as can be seen from the

rising ^{18}Ne abundance. Subsequent to $^{18}\text{Ne}(\beta^+\nu)^{18}\text{F}$, the fast $^{18}\text{F(p,}\alpha)^{15}\text{O}$ reaction feeds the abundance of ^{15}O that increases steadily. A small abundance flow also proceeds through the CNO2 and HCNO2 cycles, as indicated by the evolution of the ^{17}O abundance. Further processing of matter is similar to the previous case of $T = 0.3$ GK and only ^{12}C present as seed (see Figure 5.50b). All HCNO1 abundances achieve equilibrium after $t \approx 300$ s, with ^{15}O and ^{14}O being the most abundant species. In effect, the HCNO3 cycle feeds the HCNO1 cycle and most of the ^{16}O seed nuclei are transformed to ^{14}O and ^{15}O. Hydrogen is exhausted after $t = 3170$ s, which is longer than the time obtained in the previous calculation. The delay is caused by the additional initial processing of matter through the HCNO3 cycle. Finally, it can be seen that the ^{16}O, ^{17}F, and ^{17}O abundances increase toward the end of the calculation, indicating that a small fraction of matter leaks out of the HCNO1 cycle via the $^{15}\text{N(p,}\gamma)^{16}\text{O}$ reaction.

The total energy generated per HCNO1 cycle that is available to the star is

$$Q_{4\text{H}\rightarrow{}^4\text{He}} - \overline{E}_\nu^{\,{}^{14}\text{O}(\beta^+\nu)} - \overline{E}_\nu^{\,{}^{15}\text{O}(\beta^+\nu)} = 24.827\,\text{MeV} \tag{5.160}$$

with $Q_{4\text{H}\rightarrow{}^4\text{He}} = 26.731$ MeV and $\overline{E}_\nu^{\,i}$ the average neutrino energies released in the β^+-decays (see Eq. (1.48) and Problem 1.9). Since four hydrogen atoms have a mass of $4\,M_\text{H}/N_A$ gram, the total energy generated per gram of consumed hydrogen is

$$\begin{aligned}\frac{Q_{4\text{H}\rightarrow{}^4\text{He}} - \overline{E}_\nu^{\,{}^{14}\text{O}(\beta^+\nu)} - \overline{E}_\nu^{\,{}^{15}\text{O}(\beta^+\nu)}}{4M_\text{H}/N_A\,\text{g}} &= \frac{24.827\,\text{MeV}}{4\cdot 1.0078/6.022\times 10^{23}\,\text{g}} \\ &= 3.71\times 10^{24}\,\text{MeV/g}\end{aligned} \tag{5.161}$$

For the previously discussed network calculations, we assumed $X_\text{H}^0 = 0.60$ and, therefore, the total energy generated until hydrogen exhaustion is $0.60\cdot(3.71\times 10^{24}\,\text{MeV/g}) = 2.2\times 10^{24}$ MeV/g (or 3.5×10^{18} erg/g). The same value is directly obtained from Eq. (3.69). This result does not depend on the values assumed for the density, ρ, or the initial CNO mass fraction, as long as most of the hydrogen is converted to helium via the HCNO1 cycle. The latter quantities do, however, influence the time it takes until hydrogen is exhausted. This time is displayed in Figure 5.51 as a function of temperature, with the density held constant at a value of $\rho = 200\,\text{g/cm}^3$. The curves correspond to different assumptions for the initial CNO abundances. In each case, the time until hydrogen exhaustion increases with decreasing temperature since the contribution of proton-induced reactions to the sum of mean lifetimes in the HCNO1 cycle becomes increasingly important, as explained in the previous examples. All curves are approximately constant at temperatures in excess of $T = 0.25$ GK, where the β^+-decays of ^{14}O and ^{15}O alone determine the time scale for the HCNO1 cycle. Consider now a fixed value of temperature, say, $T = 0.3$ GK. The longest time until hydrogen exhaustion ($t = 3170$ s) is obtained when only ^{16}O is initially present ($X_{^{12}\text{C}}^0 = 0.00$, $X_{^{16}\text{O}}^0 = 0.20$). The reason is that it takes some additional time until ^{16}O is consumed and its abundance can feed the HCNO1 cycle. Adding even a small amount of ^{12}C ($X_{^{12}\text{C}}^0 = 0.01$, $X_{^{16}\text{O}}^0 = 0.20$) noticeably decreases the time until hydrogen exhaustion ($t = 2965$ s). The rate

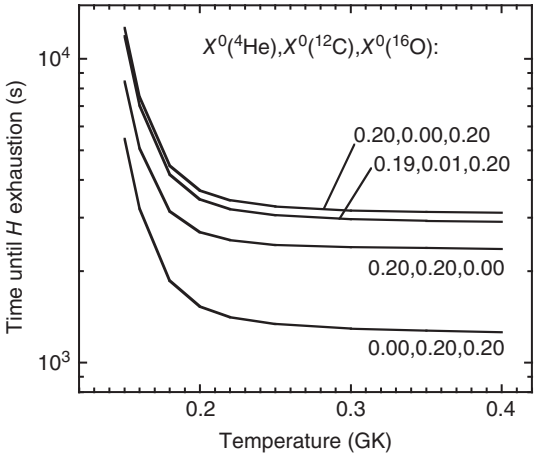

Figure 5.51 Time until hydrogen exhaustion ($X_H < 0.001$) during the operation of the HCNO cycles. The solid lines correspond to different assumptions for the initial CNO abundances. For the initial hydrogen abundance and the density, values of $X_H^0 = 0.60$ and $\rho = 200$ g/cm^3 are adopted. The curves are obtained by performing a series of numerical reaction network calculations, with T and ρ held constant in each calculation.

of hydrogen consumption increases substantially ($t = 2398$ s) when only ^{12}C instead of ^{16}O is initially present ($X^0_{^{12}C} = 0.20$, $X^0_{^{16}O} = 0.00$). Finally, hydrogen is consumed even faster ($t = 1294$ s) if equal amounts of ^{12}C and ^{16}O are initially present ($X^0_{^{12}C} = X^0_{^{16}O} = 0.20$).

Network Calculations for a Classical Nova: Accreting CO White Dwarf

We will now discuss the more realistic situation of changing temperature and density during the nucleosynthesis. Classical novae (Section 1.4.4) represent an example of explosive hydrogen burning in the temperature region of $T = 0.1$–0.4 GK. Figure 5.52a shows a temperature and density profile adopted from hydrodynamic studies (José and Hernanz, 1998) of a thermonuclear runaway caused by the accretion of solar-like matter onto the surface of a $1.0\,M_\odot$ white dwarf of CO composition. The curves represent the temperature and density evolution of the hottest hydrogen-burning zone, that is, the region in which most of the nucleosynthesis takes place. This particular nova model achieves a maximum temperature of $T = 0.17$ GK after a time of $t \approx 360$ s. At $t = 1700$ s, the temperature has fallen to a value of $T \approx 0.12$ GK. The density evolves from $\rho = 870$ g/cm^3 before the outburst to a value of $\rho = 21$ g/cm^3 at $t = 1700$ s. The reaction network of the HCNO cycles will be solved numerically using this T–ρ profile. For the initial composition, values of $X^0_H = 0.35$, $X^0_{^4He} = 0.15$, and $X^0_{^{12}C} = X^0_{^{16}O} = 0.25$ are assumed. These are similar to those used for the calculation of the T–ρ profile displayed in Figure 5.52a. The network calculation is terminated after $t = 1700$ s.

Time-integrated net abundance flows are shown in Figure 5.53a. The corresponding abundance evolutions are displayed in Figure 5.54a,b. The results are

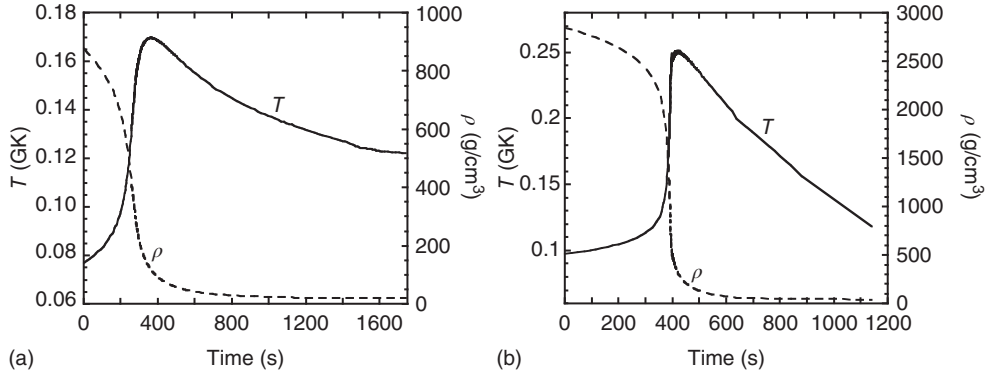

Figure 5.52 Temperature and density evolution of the hottest hydrogen-burning zone during the thermonuclear runaway on the surface of a white dwarf with (a) $M = 1.0\ M_\odot$ and CO composition, and (b) $M = 1.25\ M_\odot$ and ONe composition. The curves are adopted from hydrodynamic simulations of classical nova explosions (José and Hernanz, 1998). Abundance flows computed using these profiles are shown in Figure 5.53.

more complicated compared to the earlier calculations since the rapidly changing temperature and density keep the CNO abundances far from equilibrium. Nevertheless, the operation of the HCNO1 cycle is apparent. The isotope ^{12}C is first transformed into ^{13}N and further processed to ^{14}O, ^{14}N, and ^{15}O. In contrast to the previous calculations for constant T–ρ conditions, a ^{13}C abundance builds up since for $t > 1000$ s the temperature and density evolve in a region in which the decay $^{13}N(\beta^+\nu)^{13}C$ is more likely to occur than the $^{13}N(p,\gamma)^{14}O$ reaction (Figures 5.48 and 5.52a). For the peak temperature achieved in this nova model, the $^{16}O(p,\gamma)^{17}F$ reaction is rather slow and, therefore, only a small fraction of ^{16}O is converted, first to ^{17}F, and then to ^{17}O. For the adopted T–ρ profile the HCNO3 cycle never operates since the decay $^{17}F(\beta^+\nu)^{17}O$ is always faster than the $^{17}F(p,\gamma)^{18}Ne$ reaction (Figures 5.49b and 5.52a). At the end of the calculation, the hydrogen abundance has fallen to $X_H = 0.24$ and the most abundant CNO nuclides are ^{14}N, ^{16}O, ^{13}N, ^{12}C, ^{17}O, and ^{13}C with mass fractions of 0.21, 0.20, 0.046, 0.030, 0.026, and 0.017, respectively. The results agree qualitatively with observations of large nitrogen and oxygen abundances in the shells of several classical novae (Warner, 1995).

The final CNO abundances differ substantially from the steady state values achieved in hydrostatic hydrogen burning. If we assume that short-lived nuclides present at the end of the network calculation decay to their stable daughter nuclides (^{13}N to ^{13}C, ^{14}O to ^{14}N, and so on), then we obtain, for example,

$$\left(\frac{^{13}C}{^{12}C}\right) = \frac{X_{^{13}C} + X_{^{13}N}}{X_{^{12}C}}\frac{12}{13} = \frac{0.017 + 0.046}{0.030}\frac{12}{13} = 1.9 \tag{5.162}$$

$$\left(\frac{^{15}N}{^{14}N}\right) = \frac{X_{^{15}N} + X_{^{15}O}}{X_{^{14}N} + X_{^{14}O}}\frac{14}{15} = \frac{4.6 \times 10^{-6} + 0.0019}{0.21 + 0.00076}\frac{14}{15} = 0.0085 \tag{5.163}$$

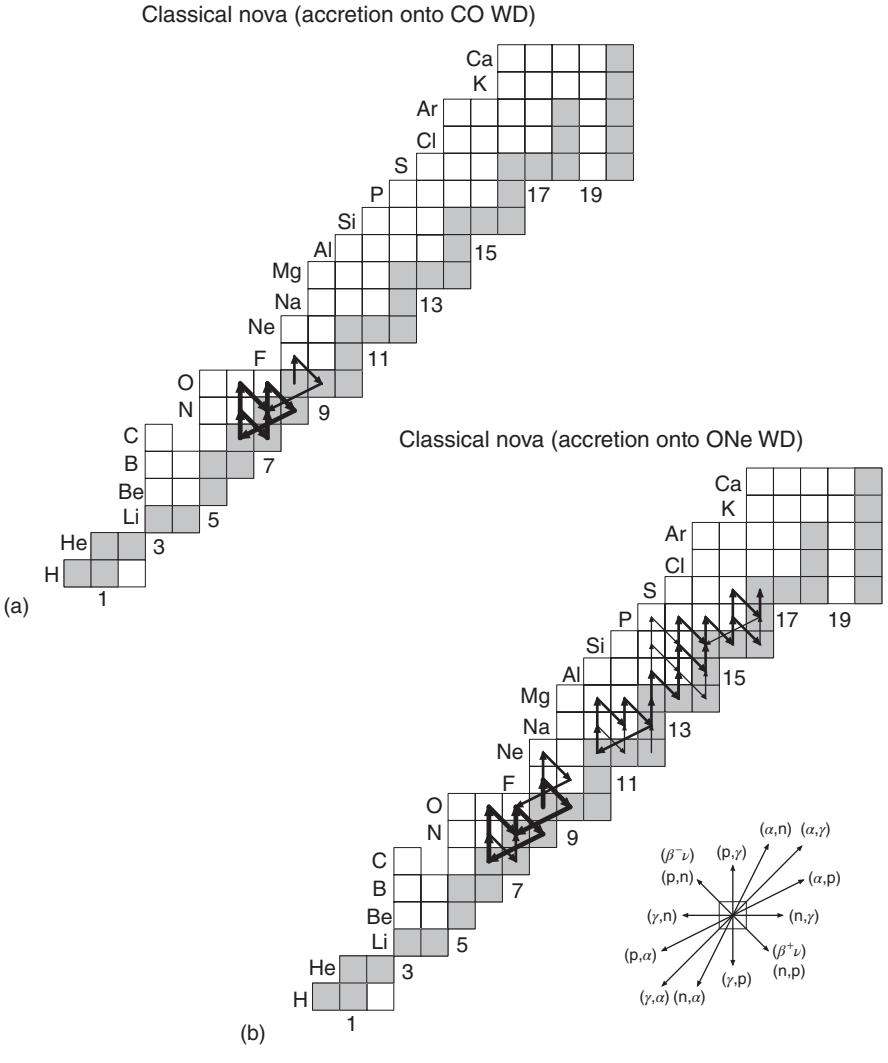

Figure 5.53 Time-integrated net abundance flows during classical nova nucleosynthesis: (a) accretion onto a CO white dwarf; (b) accretion onto a ONe white dwarf. For each model, the network calculation is performed for the hottest zone only, with the T–ρ evolution displayed in Figure 5.52. The arrows have the same meaning as in Figure 5.26: $F^{\max} \geq F_{ij} > 0.1F^{\max}$ (thick arrows), $0.1F^{\max} \geq F_{ij} > 0.01F^{\max}$ (intermediate arrows), and $0.01F^{\max} \geq F_{ij} > 0.001F^{\max}$ (thin arrows), where $F^{\max}$ corresponds to the reaction with the maximum net flow. The abundance flows are defined here in terms of mole fractions rather than number densities since the mass density varies.

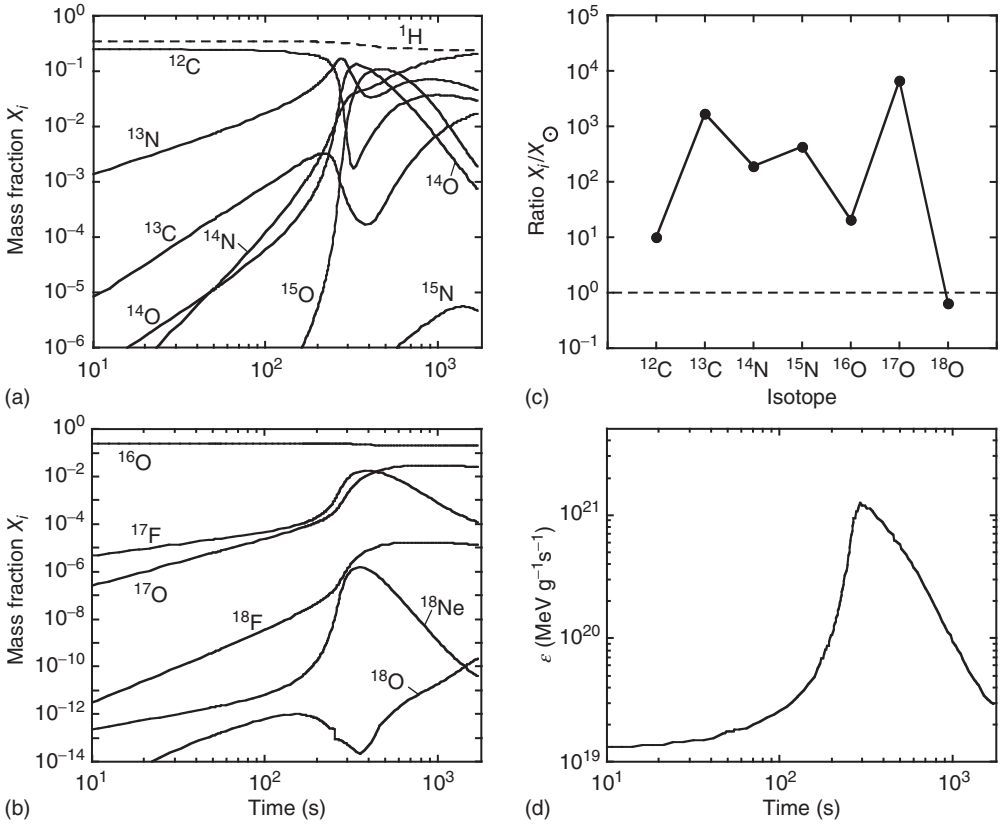

Figure 5.54 Explosive hydrogen burning during the thermonuclear runaway on the surface of a CO white dwarf. The results show the operation of the HCNO cycles and are obtained by performing a numerical reaction network calculation using the temperature and density evolution for the hottest zone displayed in Figure 5.52a. Corresponding abundance flows are shown in Figure 5.53a. (a), (b) Abundance evolutions in the $A < 20$ mass region; (c) ratios of final mass fractions (after all β^+-decays have been completed), and the corresponding solar system mass fractions; (d) time evolution of the energy generation rate.

compared to $(^{13}C/^{12}C)_e \approx 0.25$ and $(^{15}N/^{14}N)_e \approx (1\text{–}5) \times 10^{-5}$ for the equilibrium values in hydrostatic hydrogen burning at temperatures of $T < 0.1$ GK (Figure 5.11a). It is also interesting to point out that certain nuclides are strongly overproduced compared to their solar values. Ratios of final mass fractions, after all β^+-decays have been completed, and the corresponding solar mass fractions, $(X/X_\odot)$, are shown in Figure 5.54c. The three most overproduced nuclides are ^{13}C, ^{15}N, and ^{17}O, with overproduction factors in the range of $(X/X_\odot) \approx 500$–6000. It has been suggested (Kovetz and Prialnik, 1997) that classical novae are the predominant source of the latter two nuclides in the universe (see Table 5.2). Significant amounts of ^{18}F ($X_{^{18}\mathrm{F}} = 1.4 \times 10^{-5}$) are produced as well. The decay of

^{18}F ($T_{1/2}$ = 110 min) produces photons of 511 keV energy when the expanding nova shell becomes transparent to γ-rays (Hernanz *et al.*, 1999). This signature from nearby classical novae could be detectable in the future with detectors onboard satellites.

The time evolution of the energy generation rate is shown in Figure 5.54d. It is characterized by a continuous increase, a maximum of $\epsilon = 1.3 \times 10^{21}$ MeV g^{-1}s^{-1} close to the time of peak temperature ($t \approx 360$ s), and afterward a steady decline as the temperature drops.

The experimental situation regarding reactions involving CNOF nuclei is summarized below. We already pointed out in Section 5.1.2 that the reactions ^{13}C(p,γ)^{14}N, ^{14}N(p,γ)^{15}O, ^{15}N(p,γ)^{16}O, and ^{16}O(p,γ)^{17}F have been measured down to center-of-mass energies of 100, 93, 130, and 130 keV, respectively. Compared to the situation in hydrostatic hydrogen burning, the Gamow peaks in explosive hydrogen burning are located at higher energies. For example, for the ^{14}N + p reaction we obtain $E_0 \pm \Delta/2 = 149 \pm 59$ keV near $T \approx 0.2$ GK. Hence, for reactions involving stable CNO nuclei, data do generally exist in the Gamow peak and, as a consequence, the reaction rates at $T = 0.1$–0.4 GK have relatively small uncertainties (typically < 30%; Iliadis *et al.*, 2010). The situation is different for reactions involving unstable nuclei. We have seen that the HCNO cycles are initiated by the reactions ^{13}N(p,γ)^{14}O, ^{18}F(p,α)^{15}O, and ^{17}F(p,γ)^{18}Ne. Our knowledge of the corresponding reaction rates has improved substantially as a result of experiments with radioactive ion beams (Section 4.6.1). The proton capture on ^{13}N was the first astrophysically important reaction that was directly measured with a radioactive ion beam (Delbar *et al.*, 1993). In that study, the strength of the broad $E_r^{\rm cm} = 528$ keV resonance was obtained. However, the ^{13}N + p Gamow peak for temperatures of $T \leq 0.4$ GK is located far below this resonance. Hence, the S-factor has to be extrapolated to astrophysically important energies. Current reaction rate uncertainties in the range of $T = 0.1$–0.4 GK amount to a factor of ≈ 2. For the ^{18}F(p,α)^{15}O reaction, at least some data exist in the Gamow peak at $T = 0.3$–0.4 GK since the strength of a low-lying resonance at $E_r^{\rm cm} = 330$ keV has been measured directly (Graulich *et al.*, 1997; Bardayan *et al.*, 2002). These studies represent the first direct measurements in the nova Gamow peak using radioactive ion beams. Nevertheless, the current reaction rate uncertainties are relatively large and amount to factors of 6–30 at temperatures of $T = 0.1$–0.4 GK because of additional contributions from unobserved resonances (Figure 5.49a). The ^{17}F(p,γ)^{18}Ne reaction, on the other hand, has not been directly measured yet. In this case, experiments have been performed (some involving radioactive beams) that measure nuclear quantities, such as excitation energies, level widths, and J^π-values, from which the reaction rates are partially inferred. The current reaction rate uncertainties in the range of $T = 0.1$–0.4 GK amount to at least a factor of two.

Network Calculations for a Classical Nova: Accreting ONe White Dwarf

Hydrogen burning at elevated temperatures also involves nuclides in the $A \geq 20$ mass range. As was the case in hydrostatic hydrogen burning environments

(Section 5.1.3), almost no leakage of material occurs from the CNO region to the $A \geq 20$ mass range at temperatures of $T = 0.1$–0.4 GK. Reactions that could provide a link between both regions at $T \geq 0.4$ GK will be discussed in Section 5.5.3. Therefore, the nucleosynthesis must start from preexisting seed nuclei with masses of $A \geq 20$. The character of the burning, however, changes drastically since proton-induced reactions on short-lived nuclei can compete with their β^+-decays. Reactions that occur in the mass region $A \geq 20$ are displayed in Figure 5.53. Comparison to Figure 5.15 shows that more proton-capture reactions and β^+-decays have to be taken into account at elevated temperatures. The most likely nucleosynthesis paths will depend on the temperature–density history of the explosion.

At temperatures of $T = 0.1$–0.4 GK, reaction cycles play a less prominent role in the $A \geq 20$ range compared to their outstanding importance in the CNO mass region. From Figure 5.17 it is apparent that the branching ratios $B_{p\alpha/p\gamma}$ for ^{27}Al, ^{31}P, and ^{35}Cl are less than unity and hence, closed MgAl, SiP, and SCl cycles do not exist for this temperature range. For ^{23}Na, the branching ratio amounts to $B_{p\alpha/p\gamma} \approx 30$ at $T \approx 0.1$ GK, but is only $B_{p\alpha/p\gamma} \approx 1$ in the range of $T \approx 0.2$–0.4 GK. Thus, a closed NeNa cycle develops only at the lower temperature end. It will be shown in the following that reactions in the mass $A \geq 20$ range can also contribute substantially to the energy generation rate. This energy is generated by building up heavier nuclei from lighter seed nuclei via proton-captures and β^+-decays, rather than by the conversion of four protons to one ^{4}He nucleus, which takes place in the HCNO cycles.

The nucleosynthesis in the $A \geq 20$ mass range will be explored by considering again classical novae (Section 1.4.4). Heavier white dwarfs will likely consist of oxygen and $A \geq 20$ nuclides, while the carbon abundance is relatively small since it was consumed in the progenitor star during core carbon burning (Section 1.4.3 and Figure 1.4). Thermonuclear runaways involving such ONe white dwarfs achieve higher peak temperatures compared to those involving CO white dwarfs because the strength of the explosion scales with the surface gravity and the amount of accreted material. Heavier nuclides, mainly Ne, Na, and Mg, will participate in hydrogen burning. Figure 5.52b shows temperature and density profiles adopted from hydrodynamic studies (José and Hernanz, 1998) of a classical nova explosion caused by the accretion of solar-like matter onto the surface of a $1.25\,M_\odot$ white dwarf of ONe composition. The curves represent again the temperature and density evolution in the hottest hydrogen-burning zone. This nova model achieves a maximum temperature of $T = 0.25$ GK after a time of $t \approx 420$ s. Temperature and density evolve from $T = 0.10$ GK and $\rho = 2800$ g/cm^3 before the outburst to values of $T = 0.12$ GK and $\rho = 38$ g/cm^3 at $t = 1140$ s. The network is solved numerically for the temperature–density evolution shown in Figure 5.52b and is terminated after $t = 1140$ s. For the initial composition, values of $X^0_{\rm H} = 0.35$, $X^0_{^4{\rm He}} = 0.15$, $X^0_{^{16}{\rm O}} = 0.26$, $X^0_{^{20}{\rm Ne}} = 0.16$, $X^0_{^{23}{\rm Na}} = 0.04$, $X^0_{^{24}{\rm Mg}} = 0.03$, and $X^0_{^{25}{\rm Mg}} = 0.01$ are assumed. These are similar to those adopted in hydrodynamic studies (José and Hernanz, 1998).

Time-integrated net abundance flows are shown in the bottom part of Figure 5.53. We will briefly summarize the nucleosynthesis in the CNO region and then discuss in more detail the hydrogen burning in the $A \geq 20$ region. Since there are no ^{12}C seed nuclei, hydrogen burning in the $A < 20$ mass range has to start with ^{16}O. The temperatures achieved in this nova model are sufficiently high for ^{16}O to be destroyed by the ^{16}O(p,γ)^{17}F reaction. Further processing via ^{17}F($\beta^+\nu$)^{17}O(p,α)^{14}N and ^{17}F(p,γ)^{18}Ne($\beta^+\nu$)^{18}F(p,α)^{15}O quickly initiates the HCNO1 cycle. Although there are quantitative differences in the evolution of $A < 20$ nuclides compared to the CO nova model, the final results are qualitatively similar. At the end of the calculation, the hydrogen abundance has fallen to $X_{\rm H} = 0.19$, and the most abundant CNO nuclides are ^{14}N, ^{13}N, ^{12}C, ^{15}O, and ^{17}O with mass fractions of 0.081, 0.052, 0.041, 0.020, and 0.014, respectively. For the carbon and nitrogen isotopic ratios, we obtain values of $(^{13}C/^{12}C) = 1.3$ and $(^{15}N/^{14}N) = 0.22$. The most overproduced isotopes are ^{13}C, ^{15}N, and ^{17}O, with overproduction factors of $(X/X_\odot) \approx 1600$, 4500, and 3600, respectively.

The abundance evolutions in the $A \geq 20$ range are displayed in Figure 5.55a,b. For the following discussion, it is useful to keep in mind that a peak temperature of $T \approx 0.25$ GK is maintained for about 50 s before the temperature starts to decrease again (Figure 5.52b). During this time, the hydrogen abundance is about $X_{\rm H} \approx 0.30$, while the density amounts to $\rho \approx 300$ g/cm^3. It can be seen in Figure 5.55 that ^{23}Na seed nuclei are quickly destroyed. Proton-induced reactions start to deplete ^{23}Na noticeably at $t = 200$ s when the temperature amounts to $T \approx 0.1$ GK, that is, long before peak temperature is reached. At $T \approx 0.1$ GK, the ^{23}Na(p,α)^{20}Ne reaction dominates over the competing ^{23}Na(p,γ)^{24}Mg reaction (Figure 5.17). Therefore, the largest fraction of the ^{23}Na seed nuclei is converted to ^{20}Ne. Its abundance increases from an initial value of $X^0_{^{20}\rm Ne} = 0.16$ to 0.19, giving rise to the small bump seen at $t = 400$ s in Figure 5.55a. Around peak temperature, a fraction of the ^{20}Ne abundance is destroyed by the ^{20}Ne(p,γ)^{21}Na reaction and the flow reaches again ^{23}Na. At $T = 0.25$ GK, the branching ratio for ^{23}Na is near $B_{\rm p\alpha/p\gamma} \approx 1$ (Figure 5.17) and, hence, about one half of the ^{23}Na nuclei are transformed to ^{24}Mg. Very little material is processed via ^{23}Mg(p,γ)^{24}Al($\beta^+\nu$)^{24}Mg since the ^{23}Mg β^+-decay is far more likely to occur at $T \approx 0.25$ GK than the competing (p,γ) reaction $[\tau_\beta(^{23}Mg) = T_{1/2}/\ln 2 = 16$ s versus $\tau_{\rm p}(^{23}Mg) = [\rho(X_{\rm H}/M_{\rm H})N_A\langle\sigma v\rangle]^{-1} \approx 1370$ s]. Once ^{24}Mg is reached, no process can feed this material back to the NeNa mass region. At the end of the calculation, most of the ^{23}Na seed nuclei have been transformed to $A \geq 24$ nuclei, while the ^{20}Ne abundance has not changed from its initial value. This is caused by the slow ^{20}Ne(p,γ)^{21}Na reaction $[\tau_{\rm p}(^{20}Ne) \approx 200$ s at $T = 0.25$ GK]. The other seed nuclei, ^{24}Mg and ^{25}Mg, are rapidly transformed, via proton captures and β^+-decays, to heavier nuclides. We can estimate the nucleosynthesis path by considering the competition between β^+-decays and proton captures of certain key nuclides. For ^{25}Al and ^{27}Si, the mean lifetimes versus β^+-decay are $\tau_\beta \approx 10$ s and 6 s, respectively. The mean lifetimes versus proton capture at $T = 0.25$ GK are $\tau_{\rm p} = 60$ s and 24 s, respectively. Thus, both ^{25}Al and ^{27}Si will preferentially β^+-decay rather than undergo proton captures. As a result, around

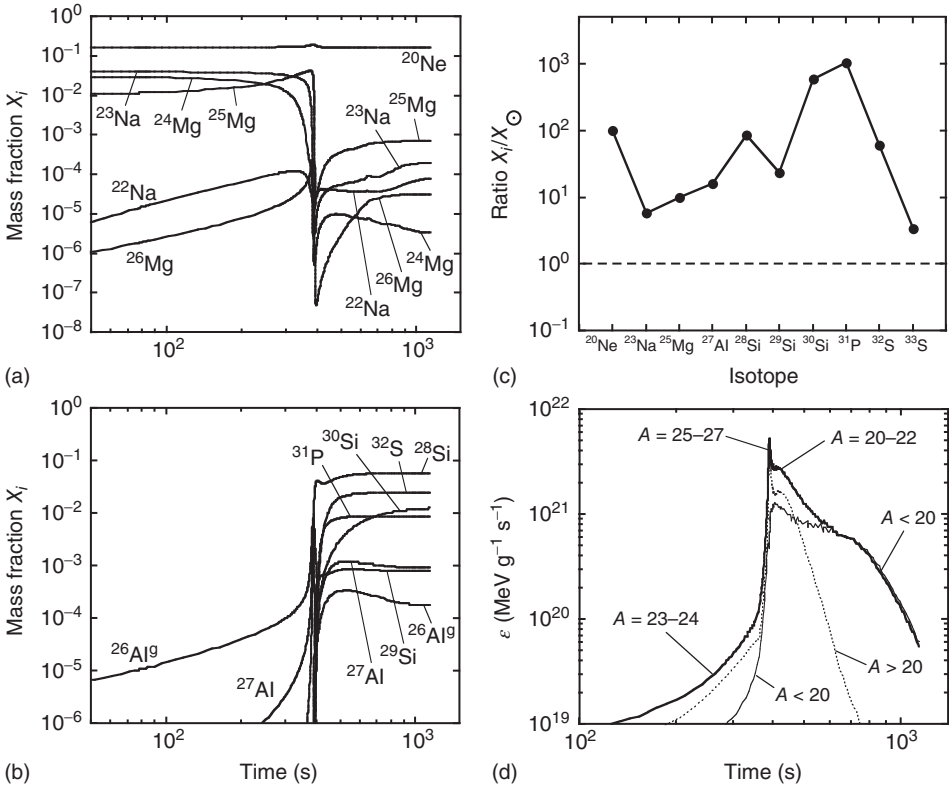

Figure 5.55 Explosive hydrogen burning during the thermonuclear runaway on the surface of a ONe white dwarf. The results show the operation of nuclear processes in the $A \geq 20$ region and are obtained from a numerical reaction network calculation using the temperature and density evolution for the hottest zone displayed in Figure 5.52b. Corresponding abundance flows are shown in Figure 5.53b. (a), (b) Abundance evolutions in the $A \geq 20$ mass region; (c) ratios of final mass fractions (after all β^+-decays have been completed), and the corresponding solar system mass fractions; (d) time evolution of the energy generation rate.

peak temperature, the most likely nucleosynthesis path is

$$^{24}\mathrm{Mg(p,\gamma)}^{25}\mathrm{Al}(\beta^+\nu)^{25}\mathrm{Mg(p,\gamma)}^{26}\mathrm{Al(p,\gamma)}^{27}\mathrm{Si}(\beta^+\nu)^{27}\mathrm{Al(p,\gamma)}^{28}\mathrm{Si} \qquad (5.164)$$

The sum of mean lifetimes for this sequence is

$$\begin{aligned}\tau_{\mathrm{p}}(^{24}Mg) + \tau_{\beta}(^{25}Al) + \tau_{\mathrm{p}}(^{25}Mg) + \tau_{\mathrm{p}}(^{26}Al^g) + \tau_{\beta}(^{27}Si) + \tau_{\mathrm{p}}(^{27}Al) \\ = (0.014 + 10.4 + 0.39 + 0.43 + 6.0 + 1.2)\,\mathrm{s} = 18.4\,\mathrm{s}\end{aligned} \qquad (5.165)$$

and is dominated by the β^+-decays of ^{25}Al and ^{27}Si. The sequence does not delay the transformation from ^{24}Mg to ^{28}Si significantly since the sum of mean lifetimes is considerably smaller than the duration for which hydrogen burning takes place at peak temperature (50 s). The mean lifetime of ^{28}Si versus proton

capture at $T = 0.25$ GK, however, amounts to $\tau_p(^{28}Si) = 69$ s and represents a significant delay. Nevertheless, a substantial abundance flow occurs beyond ^{28}Si. The flow effectively ends at ^{32}S since the proton capture on ^{32}S is very process [$\tau_p(^{32}S) = 11\,100$ s at $T = 0.25$ GK]. At the end of the calculation, most of the ^{23}Na, ^{24}Mg, and ^{25}Mg seed nuclei have been converted to ^{28}Si, ^{32}S, ^{30}Si, and ^{31}P with final mass fractions of 0.056, 0.024, 0.013, and 0.0084, respectively. The large ^{20}Ne, ^{28}Si, and ^{32}S final abundances appear because the ^{20}Ne(p,γ)^{21}Na, ^{28}Si(p,γ)^{29}P, and ^{32}S(p,γ)^{33}Cl reactions are the slowest proton captures involving stable target nuclei in the $A = 20$–32 mass range. These results agree qualitatively with observations of large neon, silicon, and sulfur abundances in the shells of several classical novae (Warner, 1995). Ratios of final mass fractions, after all β^+-decays have been completed, and the corresponding solar mass fractions are shown in Figure 5.55c for $A = 20$–33 nuclides. The two most overproduced isotopes in this mass range are ^{31}P and ^{30}Si, with overproduction factors of $(X/X_\odot) \approx 1000$ and 590, respectively. The explosive burning of hydrogen also produces interesting amounts of the radioisotopes ^{22}Na ($T_{1/2} = 2.6$ y) and ^{26}Al^g ($T_{1/2} = 7.4 \times 10^5$ y), with mass fractions of $X_{^{22}Na} = 8 \times 10^{-5}$ and $X_{^{26}Al^g} = 2 \times 10^{-4}$. The decay of ^{22}Na produces γ-rays with an energy of $E_\gamma = 1275$ keV and this signature from nearby classical novae may be observed in the future with detectors onboard satellites. Novae could also contribute to the abundance of Galactic ^{26}Al^g.

We will next discuss the nuclear energy generation. The total energy produced amounts to 5.4×10^{23} MeV/g. About 70% of the total energy is generated via reactions and decays involving CNOF nuclei, while the $A \geq 20$ mass range contributes $\approx 30\%$. The evolution of the energy generation rate is shown in Figure 5.55d. Its shape is more complex compared to the case of accretion onto a CO white dwarf (Figure 5.54d). The heavy solid line represents the total energy generation rate, while the thinner solid and dotted lines correspond to the energy generated per time by processes in the CNOF and $A \geq 20$ mass regions, respectively. Although the CNOF mass range generates the largest fraction of the total energy, the $A \geq 20$ mass region gives rise to a larger energy generation rate before and near peak temperature. Before peak temperature is achieved ($t < 360$ s), most of the energy is produced by the reactions ^{23}Na(p,α)^{20}Ne, ^{23}Na(p,γ)^{24}Mg, and ^{24}Mg(p,γ)^{25}Al. These processes are rather fast and, in particular, their reaction rates at $T = 0.1$–0.4 GK are larger than the rate for ^{16}O(p,γ)^{17}F, as shown in Figure 5.18. At later times, two maxima are visible near peak temperature ($t = 360$–430 s). The first one is narrow and high, indicating a rapid release of energy within a short period of time. It is caused by the sequence ^{25}Mg(p,γ)^{26}Al^g(p,γ)^{27}Si($\beta^+\nu$)^{27}Al(p,γ)^{28}Si, which consists of relatively fast processes. The second one, at later times, is broader and lower in magnitude. It is caused by reactions and decays in the NeNa mass region. These are significantly delayed by the slow ^{20}Ne(p,γ)^{21}Na reaction. Around $t \approx 460$ s, similar amounts of energy are produced in the CNOF and $A \geq 20$ mass regions. At later times, reactions and decays in the CNOF mass range generate most of the energy. The half-lives of ^{14}O and ^{15}O sensitively influence the evolution of the energy generation rate in the CNOF mass region. If both half-lives were

shorter, the shape of the energy generation rate curve would become narrower and higher.

The nova model discussed above achieves a peak temperature of $T_{\rm peak} = 0.25$ GK. In this case, the β^+-decays of ^{23}Mg, ^{25}Al, and ^{27}Si are faster than the competing proton-capture reactions and, therefore, the nucleosynthesis path runs close to the line of stable nuclides. Some models of classical novae involve white dwarfs of higher masses and achieve larger peak temperatures. For example, at $T_{\rm peak} = 0.35$ GK, $\rho = 300$ g/cm^3, and $X_H = 0.3$, we obtain for the ^{23}Mg(p,γ)^{24}Al, ^{25}Al(p,γ)^{26}Si, and ^{27}Si(p,γ)^{28}P reactions mean lifetimes of $\tau_{\rm p}(^{23}Mg) = 4.3$ s, $\tau_{\rm p}(^{25}Al) = 0.35$ s, and $\tau_{\rm p}(^{27}Si) = 0.44$ s. Consequently, the nucleosynthesis path will run closer to the proton dripline. The exact path depends on the temperature history during the explosion.

We will now comment on the experimental situation. For a representative peak temperature of 0.25 GK, the Gamow peaks for the ^{20}Ne + p and ^{32}S + p reactions are located at $E_0 \pm \Delta/2 = 220 \pm 80$ keV and 304 ± 94 keV, respectively. The ^{20}Ne(p,γ)^{21}Na reaction has already been discussed in Section 5.1.3. It was measured down to an energy of about $E^{\rm cm} = 350$ keV and, hence, the data do not reach the Gamow peak. The reaction rates are determined by the tail of a subthreshold state and by direct capture. The reaction rate uncertainty at $T = 0.25$ GK is about $\pm$20% (Iliadis *et al.*, 2010). The lowest lying resonance in the ^{28}Si(p,γ)^{29}P reaction occurs at $E_r^{\rm cm} = 358$ keV. It is located in the Gamow peak and determines the reaction rates at classical nova temperatures. Reaction rate uncertainties are about $\pm$10% at $T = 0.25$ GK (Iliadis *et al.*, 2010). No resonances are expected to occur in the nova Gamow peak of the ^{32}S(p,γ)^{33}Cl reaction and, therefore, this reaction is very slow. The three lowest lying resonances, located at $E_r^{\rm cm} = 409$ keV, 563 keV, and 570 keV, dominate the reaction rates at classical nova temperatures. Reaction rate uncertainties amount to $\pm$10% at $T = 0.25$ GK (Iliadis *et al.*, 2010). With one exception, none of the reactions involving unstable target nuclei in the $A = 20$–40 range have been measured directly. Their reaction rates are estimated indirectly from nuclear structure information. Hence, rate uncertainties for reactions such as ^{23}Mg(p,γ)^{24}Al, ^{25}Al(p,γ)^{26}Si, and ^{27}Si(p,γ)^{29}P can amount to an order of magnitude or more. The exception is the ^{21}Na(p,γ)^{22}Mg reaction, which influences the production of ^{22}Na in classical novae. It is the first radiative capture reaction that has been measured directly in the nova Gamow peak using radioactive ion beams (see Section 4.6.1). All the important resonances in the energy range $E_r^{\rm cm} \geq 206$ keV have been observed and the reaction rate uncertainties are about $\pm$20% at $T = 0.25$ GK.

5.5.3
Explosive Hydrogen-Helium Burning and Type I X-Ray Bursts

We argued in Section 3.2.1 that, if a mixture of different nuclides is present in the stellar plasma, usually those reactions involving the nuclear fuel with the smallest Coulomb barrier will account for most of the nuclear energy generation and nucleosynthesis. Therefore, we considered in the previous sections burning stages

that were mostly characterized by the consumption of one particular type of fuel. Interesting situations arise, however, if the stellar temperature is sufficiently large for two different types of fuels, for example, hydrogen and helium, to burn at the same location. In this section, we will discuss the burning of a mixture of hydrogen and helium fuel at temperatures of $T > 0.4$ GK. At such high temperatures, several effects will influence the nucleosynthesis. Foremost among these are photodisintegration reactions and the precise location of the proton dripline, that is, the line that separates proton-bound ($S_p \geq 0$) from proton-unbound ($S_p < 0$) nuclides.

The nucleosynthesis in hydrogen–helium burning at elevated temperatures involves many nuclear processes and is complex. First, we will discuss how, with increasing temperature, certain reaction sequences (*breakout sequences*) convert nuclides from the HCNO cycle region to the $A = 20$–21 mass range. Second, by performing reaction network calculations for a number of different constant temperatures, we will investigate the location of the nucleosynthesis paths between the group of stable nuclides and the proton dripline. Of interest are the nucleosynthesis time scales, the heaviest nuclides synthesized (*endpoints of nucleosynthesis*) and the dependence of the nuclear energy generation rate on the assumed initial composition. Finally, as an example for a more realistic situation, we will discuss the nucleosynthesis occurring during a type I X-ray burst (Section 1.4.4).

Breakout from the HCNO Cycles

For stellar temperatures of $T \leq 0.4$ GK, very little material is lost from the operation of either the cold or the hot CNO cycles (Sections 5.1.2 and 5.5.2, respectively). The reason is that the heaviest nuclides synthesized in the CNO and the HCNO cycles are ^{19}F and ^{18}F, respectively. As can be seen from Figures 5.9d and 5.49a, the branching ratios $B_{p\alpha/p\gamma}$ for these two nuclides amount to factors of 10^3–10^4 in the temperature ranges of the CNO and HCNO cycles ($T < 0.1$ GK and $T = 0.1$–0.4 GK, respectively). Thus, both ^{19}F and ^{18}F are predominantly converted to lighter nuclides via (p,α) reactions. Since α-particle-induced reactions are unlikely to occur at temperatures of $T \leq 0.4$ GK in the presence of hydrogen fuel, the above reaction cycles are closed.

The situation changes at higher temperatures. For $T > 0.5$ GK, a number of reaction sequences involving α-particle-induced reactions will convert ^{14}O or ^{15}O to nuclides in the mass range of $A = 20$–21. These nuclei are permanently lost as catalysts for the HCNO cycles since there are no nuclear processes that can transform them back to the CNO mass range. The three main breakout sequences (BOSs) are listed below and are displayed in Figure 5.56.

Sequence 1	Sequence 2	Sequence 3
^{15}O(α,γ)^{19}Ne	^{14}O(α,p)^{17}F	^{14}O(α,p)^{17}F
^{19}Ne(p,γ)^{20}Na	^{17}F(p,γ)^{18}Ne	^{17}F(γ,p)^{16}O
	^{18}Ne(α,p)^{21}Na	^{16}O(α,γ)^{20}Ne

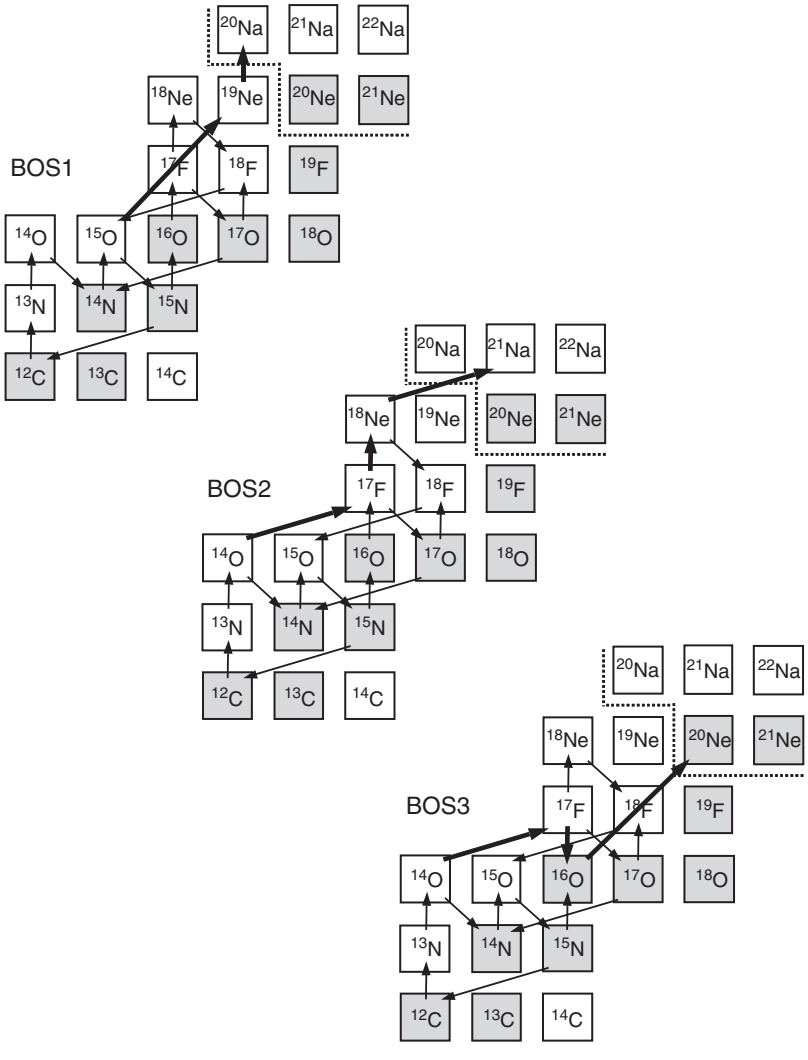

Figure 5.56 Representation of the three breakout sequences (BOS) from the $A < 20$ mass region (thick arrows) during hydrogen–helium burning. Nuclear interactions that are part of the HCNO cycles are displayed as thin arrows. Stable nuclides are shown as shaded squares. Once a nucleus has been transformed to a species beyond the dotted line ($A = 20$) it is permanently lost for the HCNO cycles since there are no processes that can transform the species back to the $A < 20$ region.

To obtain a first impression, consider Figure 5.57a showing the rates of these reactions, normalized to the $^{16}O(p,\gamma)^{17}F$ rates. It is apparent that the $^{19}Ne(p,\gamma)^{20}Na$ rates exceed the rates of the preceding $^{15}O(\alpha,\gamma)^{19}Ne$ reaction by orders of magnitude. Hence, we suspect that the time scale for breakout sequence 1 is determined by the slower $^{15}O(\alpha,\gamma)^{19}Ne$ reaction. Furthermore,

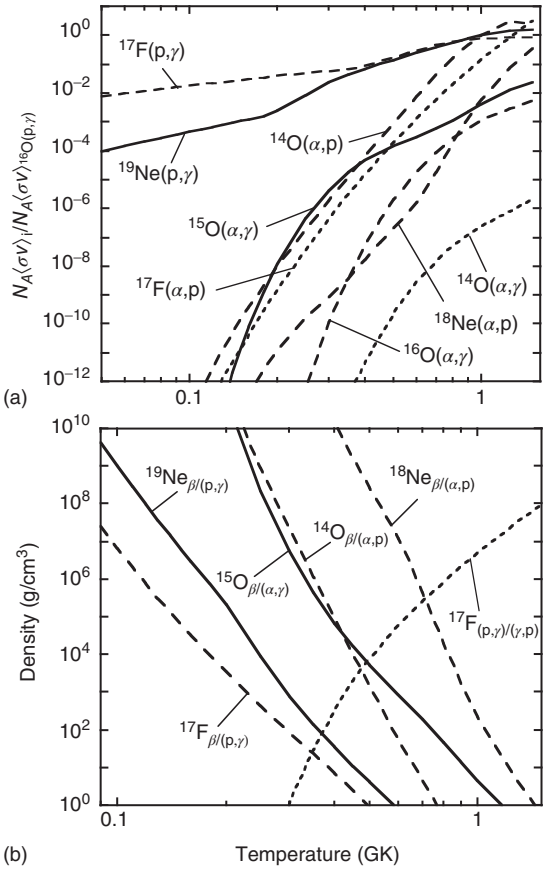

Figure 5.57 (a) Rates that are part of the three breakout sequences versus temperature. For a better comparison, the values $N_A\langle\sigma v\rangle$ are normalized to the rate of the $^{16}O(p,\gamma)^{17}F$ reaction. Rates for the $^{14}O(\alpha,\gamma)^{18}Ne$ and $^{17}F(\alpha,p)^{20}Ne$ reactions are also shown for comparison, but are negligible in the present context. (b) Temperature–density conditions for the competition between β^+-decay and nuclear reaction for unstable nuclides that participate in the three breakout sequences (solid and dashed lines). The β^+-decay dominates in the region to the left of a solid or dashed line, while on the right-hand side the competing proton- or α-particle-induced reaction is more likely to occur. The dotted line shows the conditions at which the decay constants for the competing $^{17}F(p,\gamma)^{18}Ne$ and $^{17}F(\gamma,p)^{16}O$ reactions are of equal magnitude. The $^{17}F(p,\gamma)^{18}Ne$ reaction dominates on the left-hand side of the dotted curve, while on the right-hand side, the $^{17}F(\gamma,p)^{16}O$ reaction is more likely to occur. All curves are calculated assuming $X_H = 0.7$ and $X_{^4He} = 0.3$.

both the $^{18}Ne(\alpha,p)^{21}Na$ and $^{16}O(\alpha,\gamma)^{20}Ne$ rates are smaller than the rates of the preceding $^{14}O(\alpha,p)^{17}F$ reaction. Thus, the former reactions will be more important compared to the latter reaction for setting the time scale of breakout sequence 2 or 3. Figure 5.57a also displays reaction rates of some alternative breakout sequences. It can be seen that the $^{14}O(\alpha,\gamma)^{18}Ne$ reaction rate is negligible

compared to the rate of the competing $^{14}O(\alpha,p)^{17}F$ reaction. Similarly, the rates of the $^{17}F(\alpha,p)^{20}Ne$ reaction are far smaller compared to those of the competing $^{17}F(p,\gamma)^{18}Ne$ reaction, except at high temperatures ($T > 1.2$ GK) where both rates become comparable. However, even at $T > 1.2$ GK, the $^{17}F(\alpha,p)^{20}Ne$ reaction will play a role only in the extreme case when the helium mass fraction substantially exceeds the hydrogen mass fraction ($X_{^4He}/M_{^4He} > X_H/M_H$). For the present discussion, none of these alternative breakout sequences are important.

Next, consider Figure 5.57b showing the temperature–density conditions for the competition between β^+-decay and nuclear reaction for those nuclides that participate in the three breakout sequences. The solid and dashed curves represent $T-\rho$ conditions for which the decay constants (or mean lifetimes) of the two competing processes are of equal magnitude, $\lambda_1(0) = \lambda_\beta(0)$. They are calculated from the expression (see Eq. (5.149))

$$\rho = \frac{\ln 2}{T_{1/2}(0)(X_1/M_1)N_A\langle\sigma v\rangle_{01}} \tag{5.166}$$

with 0 the nuclide of interest and 1 denoting either hydrogen or helium, depending on the type of reaction. The relevant β^+-decay half-lives are given by $T_{1/2}(^{14}O) = 70.62$ s, $T_{1/2}(^{15}O) = 122.24$ s, $T_{1/2}(^{17}F) = 64.49$ s, $T_{1/2}(^{18}Ne) = 1.67$ s, and $T_{1/2}(^{19}Ne) = 17.26$ s (Audi *et al.*, 2012). The β^+-decay dominates in the region to the left of a solid or dashed line, while on the right-hand side the competing proton- or α-particle-induced reaction is more likely to occur. Furthermore, the dotted line in Figure 5.57b shows the $T-\rho$ conditions at which the decay constants for the competing $^{17}F(p,\gamma)^{18}Ne$ and $^{17}F(\gamma,p)^{16}O$ reactions are of equal magnitude, $\lambda_p(^{17}F) = \lambda_\gamma(^{17}F)$. The dotted line is obtained from the expression (see Eqs. (3.23) and (3.46))

$$\rho = 9.8685\times10^9 T_9^{3/2}\frac{(2j_{^{16}O}+1)(2j_p+1)}{(2j_{^{17}F}+1)}\left(\frac{G^{norm}_{^{16}O}G^{norm}_{p}}{G^{norm}_{^{17}F}}\right)\left(\frac{M_{^{16}O}M_H}{M_{^{17}F}}\right)^{3/2}$$
$$\times\left(\frac{X_H}{M_H}\right)^{-1} e^{-11.605Q_{^{16}O(p,\gamma)}/T_9}\frac{N_A\langle\sigma v\rangle_{^{16}O(p,\gamma)}}{N_A\langle\sigma v\rangle_{^{17}F(p,\gamma)}} \tag{5.167}$$

with $Q_{^{16}O(p,\gamma)} = 0.600$ MeV. The $^{17}F(p,\gamma)^{18}Ne$ reaction dominates on the left-hand side of the dotted curve, while on the right-hand side the competing $^{17}F(\gamma,p)^{16}O$ reaction is faster. All the curves in Figure 5.57b are calculated using the values of $X_H = 0.7$ and $X_{^4He} = 0.3$. For the following considerations, it is assumed that ^{14}O and ^{15}O are the most abundant CNO nuclei as a result of prior HCNO cycle operation (Section 5.5.2). A density of $\rho = 10^4$ g/cm^3 is chosen as a representative value and we are particularly interested in the fate of ^{14}O and ^{15}O when the temperature is slowly increased.

First, consider only breakout sequence 1 (the two solid curves in Figure 5.57b). We start at $T \approx 0.1$ GK, where the HCNO cycles operate (Figure 5.48), and slowly increase the temperature. The line corresponding to the condition $\tau_p(^{19}Ne) = \tau_\beta(^{19}Ne)$ is crossed at $T = 0.23$ GK. Beyond this temperature, the $^{19}Ne(p,\gamma)^{20}Na$ reaction becomes more likely than the competing ^{19}Ne β^+-decay. However, no breakout from the hot CNO cycles occurs yet because

the ^{15}O β^+-decay still dominates over the competing $^{15}O(\alpha,\gamma)^{19}Ne$ reaction [$\tau_\alpha(^{15}O) > \tau_\beta(^{15}O)$]. Further increasing the temperature, the line corresponding to the condition $\tau_\alpha(^{15}O) = \tau_\beta(^{15}O)$ is crossed at $T \approx 0.46$ GK. Beyond this temperature, ^{15}O nuclei are lost from the HCNO cycles as a result of the operation of the breakout sequence 1.

Next, the breakout sequences 2 and 3 (dashed and dotted lines in Figure 5.57b) will be discussed. For $T > 0.18$ GK, the nuclide ^{17}F is preferentially destroyed by the (p,γ) reaction rather than by β^+-decay (i.e., the HCNO3 cycle starts to operate beyond $T \approx 0.18$ GK; see Figure 5.49b). Increasing the temperature, we cross the line corresponding to the condition $\tau_\alpha(^{14}O) = \tau_\beta(^{14}O)$ at $T \approx 0.43$ GK. Beyond this point, the $^{14}O(\alpha,p)^{17}F$ reaction dominates over the competing ^{14}O β^+-decay. Although breakout sequences 2 and 3 do not operate yet, the $^{14}O(\alpha,p)^{17}F$ reaction is already important at this stage because it provides an additional link between the HCNO1 and HCNO3 cycles (Figure 5.47). In other words, ^{14}O is converted to ^{15}O via the sequence $^{14}O(\alpha,p)^{17}F(p,\gamma)^{18}Ne(\beta^+\nu)^{18}F(p,\alpha)^{15}O$. Accordingly, at $T > 0.46$ GK, the $^{14}O(\alpha,p)^{17}F$ reaction increases the fraction of CNO nuclei that is lost through breakout sequence 1. Further increasing the temperature, we next cross the dotted line, defined by the condition $\tau_p(^{17}F) = \tau_\gamma(^{17}F)$, at $T \approx 0.5$ GK. For $T > 0.5$ GK, ^{17}F is preferentially destroyed by the (γ,p) reaction, and one is tempted to assume that the breakout sequence 3 starts to operate at this point. This is not the case, however, since the subsequent breakout reaction $^{16}O(\alpha,\gamma)^{20}Ne$ is considerably slower than the competing $^{16}O(p,\gamma)^{17}F$ reaction (Figure 5.57a). The low Q-value of the $^{16}O(p,\gamma)^{17}F$ reaction ($Q = 0.600$ MeV) ensures that an equilibrium is quickly established between the abundances of ^{17}F and ^{16}O. The breakout sequences 2 and 3 must then proceed from these equilibrium abundances. For example, the rate at which ^{14}O nuclei are lost from the HCNO cycles through breakout sequence 3 depends on the equilibrium number of ^{16}O nuclei, given by the temperature (see Eq. (3.50)), and the magnitude of the rate for the subsequent $^{16}O(\alpha,\gamma)^{20}Ne$ reaction. Therefore, breakout sequence 3 will become increasingly important for higher temperatures. We will see in the next subsection that breakout sequence 3 operates at $T > 1.0$ GK (for $\rho = 10^4$ g/cm^3).

Finally, the line corresponding to the condition $\tau_\alpha(^{18}Ne) = \tau_\beta(^{18}Ne)$ is crossed at $T \approx 0.81$ GK. Beyond this point, the $^{18}Ne(\alpha,p)^{21}Na$ reaction dominates over the competing ^{18}Ne β^+-decay. Thus, ^{14}O nuclei are lost from the HCNO cycles as a result of the operation of the breakout sequence 2. Qualitatively similar results are obtained for other values of the density, although the various lines are crossed at different temperature values.

Network Calculations at Constant Temperature and Density

We will now turn our attention to the nucleosynthesis that results after breakout from the HCNO cycles has occurred. A representative value of $\rho = 10^4$ g/cm^3 is again chosen for the density. Numerical network calculations are performed for three different temperatures ($T = 0.5$ GK, 1.0 GK, and 1.5 GK) and the results

will be discussed below. To properly account for the nuclear activity at such high temperatures, the network has to be expanded dramatically in size compared to our earlier hydrogen- or helium burning calculations. It now consists of ≈ 520 nuclides, including all stable and proton-rich β^+-unstable (but proton-stable) nuclides up to the element palladium. Some proton-unstable nuclides are also included to account for sequential two-proton captures involving nuclides at and beyond the proton dripline (Section 3.1.6). Neutron-rich β^--unstable nuclides are not included in the network since they cannot be synthesized via hydrogen or helium-induced reactions on stable or proton-rich β^+-unstable nuclei. The different nuclides in the network are linked by ≈ 5500 nuclear processes, including β^+-decays, (p,γ), (p,α), (α,γ) reactions, inverse processes such as photodisintegrations, (α,p) reactions, and so on. For the initial composition, values of $X^0_{\rm H} = 0.73$, $X^0_{^4{\rm He}} = 0.25$, $X^0_{^{14}{\rm O}} = 0.01$, and $X^0_{^{15}{\rm O}} = 0.01$ are assumed. This assumption is consistent with the earlier result that during the rise to temperatures of $T \geq 0.5$ GK, ^{14}O and ^{15}O are the most abundant products as a result of HCNO cycle operation (Section 5.5.2). The network is solved numerically until a time of $t = 100$ s is reached. This is considerably shorter compared to our previous hydrogen- or helium burning network calculations, but is consistent with the assumption that stellar explosions at elevated temperatures have short durations.

In the $A \leq 40$ mass range, we adopt for the majority of reactions the experimental rates of Angulo *et al.* (1999) and Iliadis *et al.* (2001). Above $A = 40$, however, very few nuclear reactions have been measured directly or indirectly. For most reactions in the latter mass region, the reaction rates must be estimated theoretically. The ^{56}Ni(p,γ)^{57}Cu reaction represents an exception (see below). In the $A > 40$ range, we will adopt theoretical rates that are calculated using the Hauser–Feshbach statistical model of nuclear reactions (Section 2.7). It must be emphasized that, except in special cases such as p(p,e$^+\nu$)d, reaction rates based on theory carry larger uncertainties compared to rates based on experimental input.

Before discussing the results of reaction network calculations, it is instructive to consider Figure 5.58, showing the chart of the nuclides from Sc ($Z = 21$) to Sr ($Z = 38$). The heavy solid line represents the proton dripline. Nuclides that are shaded gray are β^+-unstable and have half-lives in excess of $T_{1/2} \approx 10$ s. All other nuclides shown have half-lives of less than $T_{1/2} \approx 3$ s. In general, we expect the nucleosynthesis paths to be located somewhere between the dripline and the group of gray shaded nuclides, with the exact locations determined by the relative probability of various processes, such as (p,γ) reactions, photodisintegrations, β^+-decays, and so on. If, for some reason, the abundance flow reaches one of the gray shaded nuclides and can only proceed via a slow β^+-decay, presumably because proton capture is inhibited, then the nucleosynthesis will be significantly delayed, or in extreme cases, may halt altogether. The most obvious reason for an inhibited proton capture is a small $Q_{\rm p\gamma}$-value since the reverse photodisintegration process will then quickly remove the proton that was just added to the target

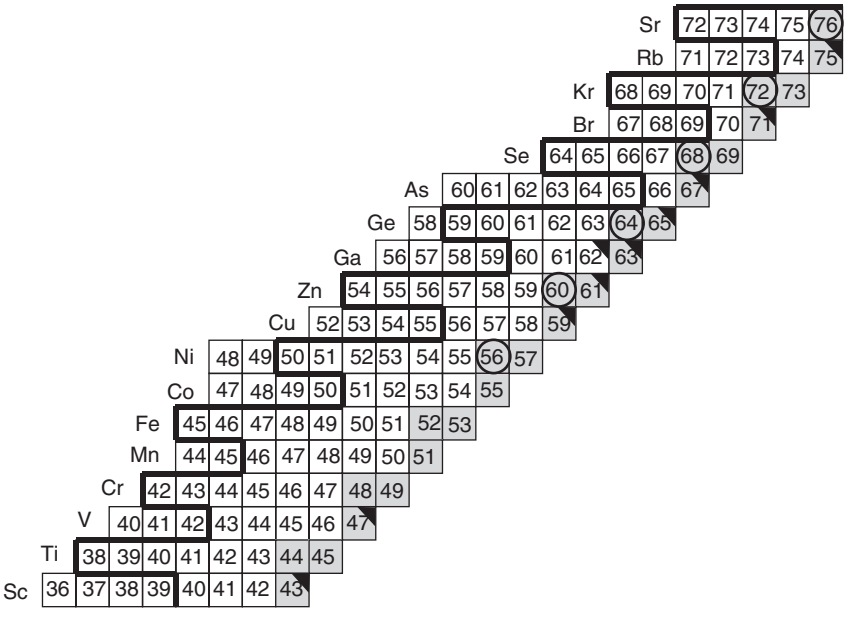

Figure 5.58 Section of the chart of the nuclides between Sc ($Z = 21$) and Sr ($Z = 38$) on the proton-rich side of the stability valley. The proton dripline according to Audi, Wapstra, and Thibault (2003) is marked by a thick solid line. All displayed nuclides are unstable. Those represented by shaded squares have half-lives in excess of $T_{1/2} \approx 10$ s, while all other nuclides have half-lives of less than $T_{1/2} \approx 3$ s. Nuclides with negative or small positive $Q_{p\gamma}$-values and relatively long β^+-decay half-lives are marked by circles (waiting point nuclides). The solid triangles indicate nuclides for which both the (p,γ) and (p,α) reaction channels are open.

nucleus. Nuclides with negative or small positive $Q_{p\gamma}$-values and relatively long β^+-decay half-lives are referred to as *waiting point nuclides* and are marked by circles in Figure 5.58.

Interestingly, the proton dripline runs very close to the group of gray shaded nuclides in the Ge–Rb mass region. In particular, the abundance flow must pass through the potential waiting point nuclides ^{64}Ge, ^{68}Se, ^{72}Kr, and ^{76}Sr ($T_{1/2} = 64$ s, 36 s, 17 s, and 9 s, respectively). Their slow β^+-decays may, however, be bypassed via sequential two-proton captures. For example, the negative Q-value for ^{64}Ge(p,γ)^{65}As ensures that an equilibrium is quickly established between ^{64}Ge and ^{65}As. The relative probability of the two alternative paths, ^{64}Ge($\beta^+\nu$)^{64}Ga and ^{64}Ge(p,γ)^{65}As(p,γ)^{66}Se, will then depend on the magnitude of the quantities $T_{1/2}(^{64}\mathrm{Ge})$, $\rho \exp[Q_{^{64}\mathrm{Ge(p,\gamma)}}/kT]$, and $N_A\langle\sigma v\rangle_{^{65}\mathrm{As(p,\gamma)}}$, as explained in Section 3.1.6. For the following reaction network calculations, all reverse (γ,p) reaction rates are calculated from experimental or theoretical forward (p,γ) rates using $Q_{p\gamma}$-values from Audi, Wapstra, and Thibault (2003).

For nuclides marked with a solid triangle in Figure 5.58, both the (p,γ) and the (p,α) reaction channels are open ($Q_{p\gamma} > 0$ and $Q_{p\alpha} > 0$). At elevated temperatures,

(p,α) reactions play a much smaller role because of the increasing Coulomb barrier in the $A > 40$ mass region compared to the CNO range where they give rise to reaction cycles. Consider the ^{71}Br(p,α)^{68}Se reaction ($Q_{p\alpha} = 2020$ keV) as an example. At $T = 1.5$ GK, the Gamow peak is located at $E_0 = 1700$ keV. Furthermore, suppose that a fictitious resonance is located in the middle of the Gamow peak, $E_r \approx E_0$. Reaction α-particles from the decay of this resonance have energies of $E_\alpha = E_r + Q_{p\alpha} \approx 3720$ keV. For an orbital angular momentum of $\ell_\alpha = 0$, the single-particle α-width amounts to $\Gamma^{^{68}\mathrm{Se}+\alpha}_{\ell_\alpha=0}(E_\alpha = 3720\,\mathrm{keV}) \approx 10^{-5}$ eV. This is smaller than typical γ-ray partial widths and, hence, we find $\Gamma_\gamma \gg \Gamma_\alpha$ or $B_{p\alpha/p\gamma} \ll 1$. On the other hand, at very high temperatures, $T \geq 2$ GK, the α-particle widths, Γ_α, increase and may become comparable to, or even exceed, typical values of Γ_γ.

Nucleosynthesis at $T = 0.5$ GK, $\rho = 10^4$ g/cm^3, and $t = 100$ s

Net abundance flows, integrated over a time of $t = 100$ s, are displayed in Figure 5.59. Major flows (those with $F^{max} \geq F_{ij} > 0.1F^{max}$) are shown as thick solid arrows, while minor flows ($0.1F^{max} \geq F_{ij} > 0.01F^{max}$) are indicated as thin solid arrows. The direction of the arrows corresponds to the direction of the abundance flows. The heavy solid line represents the proton dripline, while stable nuclides are shown as shaded squares. Under these conditions, the breakout from the HCNO cycles proceeds via ^{15}O(α,γ)^{19}Ne(p,γ)^{20}Na (sequence 1; Figure 5.56). After the initiation of breakout, sequences of (p,γ) reactions and β^+-decays transform CNO nuclei within $t = 100$ s to the Fe–Co region. The resulting network is referred to as the *r(apid)p(roton capture)-process* (Wallace and Woosley, 1981). Recall that the amount of energy generated by the HCNO cycles is independent of temperature since it is limited by the slow ^{14}O and ^{15}O β^+-decays (beyond a certain value of temperature and for a given composition; see Figure 5.51). The rp-process is important since it circumvents these slow β^+-decays. It will be shown below that the processing of CNO seeds to heavier nuclei can lead to a significantly larger energy generation rate than given by the HCNO cycles alone.

The most likely nucleosynthesis path in the rp-process is defined by the competition between β^+-decays, (p,γ), and (γ,p) reactions. During explosive burning, a specific nucleus will add progressively more protons. With each proton addition, a nucleus is synthesized that is located closer to the proton dripline. Eventually a nuclide is reached that β^+-decays instead of undergoing another proton capture. The process of proton addition and β^+-decay repeats itself until the end of the network calculation. Why does the probability of β^+-decay increase compared to proton capture when the proton dripline is approached? First, by approaching the proton dripline for a fixed neutron number, one moves away from the valley of stability and, therefore, the β^+-decay half-lives become progressively shorter. Eventually, a β^+-decay becomes more likely than another proton capture, that is, $\lambda_\beta > \lambda_{p\gamma}$. Second, nuclides right at the proton dripline have, per definition, negative Q-values, while some (but not the majority of) nuclides close to the dripline have small positive Q-values. In either

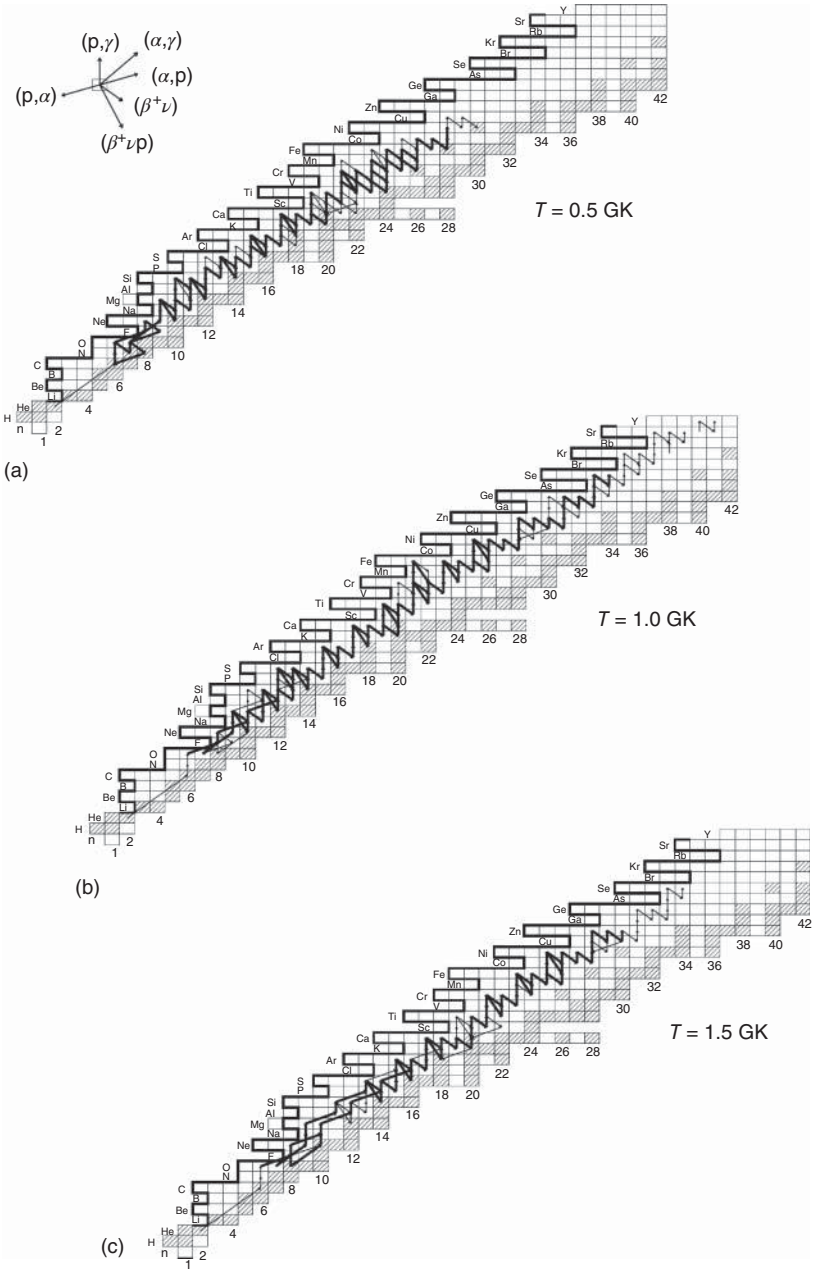

Figure 5.59 Results of numerical reaction network calculations for hydrogen–helium burning at a constant temperature of (a) 0.5 GK, (b) 1.0 GK, and (c) 1.5 GK. The same constant density ($\rho = 10^4$ g/cm^3) and initial composition is used. Arrows represent net abundance flows, integrated over the entire computation time of $t = 100$ s. Thick arrows show the strongest time-integrated net flows ($F^{\max} \geq F_{ij} > 0.1F^{\max}$). Thin arrows represent flows that are weaker by an order of magnitude ($0.1F^{\max} \geq F_{ij} > 0.01F^{\max}$). The heavy solid line marks the proton dripline (Audi, Wapstra, and Thibault, 2003).

case, photodisintegration will inhibit the addition of another proton. The nucleosynthesis must then proceed with a β^+-decay, even if the condition $\lambda_\beta < \lambda_{p\gamma}$ applies.

It can also be seen that below Ti the nucleosynthesis path reaches a number of nuclides that are located right at the proton dripline (^{24}Si, ^{29}S, ^{33}Ar, ^{37}Ca, ^{38}Ca, ^{41}Ti, and so on). Above Ti, however, the major abundance flows do not reach the dripline. This is a consequence of decreasing proton capture rates as the Coulomb barrier increases. The interplay of β^+-decays, (p,γ), and (γ,p) reactions near ^{30}S is addressed in Problem 5.4. See also Example 3.3.

The evolution of the most abundant nuclides is shown in Figure 5.60a. Only a small amount of hydrogen is consumed over a period of $t = 100$ s. The protons are used to produce heavier nuclides via capture reactions, while the fusion of protons to helium via reaction cycles plays only a minor role under these burning conditions. Hence, the helium abundance stays constant. The ^{15}O abundance increases until about $t = 20$ s because of the sequence $^{14}\mathrm{O}(\alpha,\mathrm{p})^{17}\mathrm{F}(\mathrm{p},\gamma)^{18}\mathrm{Ne}(\beta^+\nu)^{18}\mathrm{F}(\mathrm{p},\alpha)^{15}\mathrm{O}$. Around this time, a significant fraction of material breaks out of the CNO region via the $^{15}\mathrm{O}(\alpha,\gamma)^{19}\mathrm{Ne}(\mathrm{p},\gamma)^{20}\mathrm{Na}$ sequence. The abundance flow quickly reaches the $A \approx 50$ region. The most abundant nuclides at the end of the calculation in the $A > 20$ region are ^{52}Fe, ^{56}Ni, and ^{55}Co. These nuclides have long laboratory β^+-decay half-lives ($T_{1/2} = 8.3$ h, 6.1 d and 17.5 h, respectively), although their *stellar* β^+-decay half-lives are expected to be somewhat smaller (Section 1.8.4). At the same time, their proton-capture rates are relatively small, yielding mean lifetimes of $\tau_{p\gamma} = 120$ s, 24 s, and 14 s, respectively, for the burning conditions adopted here. The latter values are significant in magnitude compared to the total burning time and, therefore, these three nuclides represent endpoints for the nucleosynthesis.

Nucleosynthesis at $T = 1.0$ GK, $\rho = 10^4$ g/cm^3, and $t = 100$ s

Flows and time evolutions of the most abundant species are displayed in Figures 5.59 and 5.60b. The hydrogen abundance declines slightly with progressing time, whereas the ^{4}He abundance stays almost constant. The breakout from the CNO mass region proceeds through both sequence 1 and sequence 2 (Figure 5.56). The tranformation of ^{14}O and ^{15}O to ^{21}Na and ^{20}Na, respectively, is so fast (within a fraction of a second) that the operation of the HCNO cycles is not discernible in Figure 5.59. At this higher temperature, the proton capture rates become considerably faster and, consequently, nuclides up to the $A \approx 80$ region are synthesized via the rp-process. Compared to the previous case, the abundance flow reaches the dripline at a number of locations over the entire mass region shown. All the material initially in the form of ^{14}O and ^{15}O is converted to heavier nuclides, with ^{60}Zn, ^{64}Ge, and ^{68}Se being the most abundant species in the $A > 20$ region at the end of the calculation.

It is apparent from Figure 5.59 that the network of nuclear processes is complex. However, it should be pointed out that the time scale of the nucleosynthesis is mainly determined by processes involving only a handful of waiting point

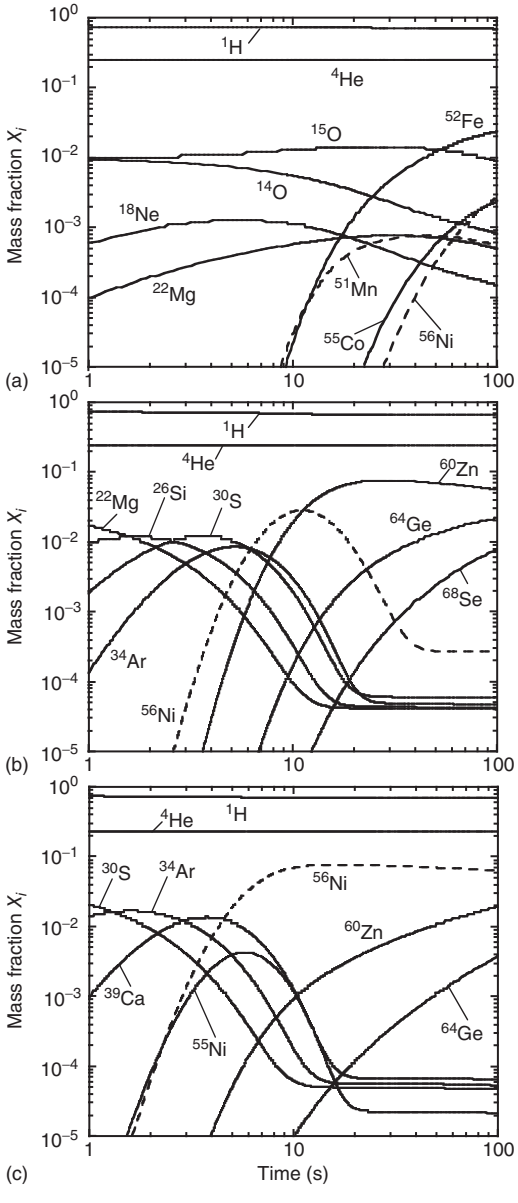

Figure 5.60 Abundance evolutions during hydrogen–helium burning at a constant temperature of (a) $T = 0.5$ GK, (b) $T = 1.0$ GK, and (c) $T = 1.5$ GK. The same constant density ($\rho = 10^4$ g/cm^3) and initial composition is used. The results are extracted from the same numerical reaction network calculations that are displayed in Figure 5.59.

nuclides: ^{22}Mg, ^{26}Si, ^{30}S, ^{34}Ar, ^{56}Ni, ^{60}Zn, ^{64}Ge, and ^{68}Se. What these nuclides have in common are relatively long β^+-decay half-lives and small $Q_{p\gamma}$-values (between −450 keV for ^{68}Se and 861 keV for ^{26}Si). Their $Q_{p\gamma}$-values are so small that the proton-capture rate is significantly smaller than the reverse photodisintegration rate. Hence, photodisintegration will inhibit the proton capture reaction, and the abundance flow is significantly delayed. The abundance of each waiting point nuclide increases until some maximum is reached. Eventually the abundance flow continues via a β^+-decay (although the competing (α,p) and (p,γ) reactions are also important for ^{22}Mg and ^{26}Si, respectively) until the next waiting point nuclide is reached. The species ^{60}Zn has the largest abundance, apart from hydrogen and helium, at the end of the calculation because it possesses the longest half-life ($T_{1/2} = 2.4$ min) among the heaviest waiting point nuclides (Figure 5.58). The species ^{56}Ni represents an exception. Since its half-life is so long compared to the burning time, the flow must continue exclusively via the (p,γ) reaction. This case is discussed in detail below. It can be seen in Figure 5.60b that it takes about 10 s until ^{60}Zn becomes the most abundant nuclide. This time is approximately equal to the sum of the mean lifetimes of the waiting point nuclides below ^{60}Zn. For $t \geq 40$ s, the abundances of ^{22}Mg, ^{26}Si, ^{30}S, ^{34}Ar, and ^{56}Ni stay constant. This is caused by the operation of the 3α reaction as the abundance flows between ^{4}He and ^{56}Ni attain equilibrium.

Nucleosynthesis at $T = 1.5$ GK, $\rho = 10^4$ g/cm^3, and $t = 100$ s

Results of a network calculation at this higher temperature are shown in Figures 5.59 and 5.60c. The hydrogen and helium abundances are almost constant over the duration of the burning. It can be seen that all three breakout sequences operate under these conditions (Figure 5.56). Once breakout from the $A \leq 20$ region is initiated, the abundance flow initially follows two sequences of (α,p) and (p,γ) reactions,

$$^{20}\mathrm{Na}(\mathrm{p},\gamma)^{21}\mathrm{Mg}(\alpha,\mathrm{p})^{24}\mathrm{Al}(\mathrm{p},\gamma)^{25}\mathrm{Si}(\alpha,\mathrm{p})^{28}\mathrm{P} \tag{5.168}$$

$$^{21}\mathrm{Na}(\mathrm{p},\gamma)^{22}\mathrm{Mg}(\alpha,\mathrm{p})^{25}\mathrm{Al}(\mathrm{p},\gamma)^{26}\mathrm{Si}(\alpha,\mathrm{p})^{29}\mathrm{P}(\mathrm{p},\gamma)^{30}\mathrm{S}(\alpha,\mathrm{p})^{33}\mathrm{Cl} \tag{5.169}$$

This part of the network is referred to as the *αp-process* (Wallace and Woosley, 1981). In the previously discussed network calculation, the abundance flow in the $A \leq 30$ region had to wait for slow β^+-decays of waiting point nuclides since photodisintegration impeded further proton captures. Therefore, the mean lifetime of the waiting point nuclides, and hence, the overall time scale of the nucleosynthesis in this mass region, was independent of temperature and density. The αp-process is important because it bypasses the slow β^+-decays. The nucleosynthesis in the $A \leq 33$ region becomes now sensitive to temperature and, therefore, the burning of hydrogen and helium proceeds at an accelerated pace and larger energy generation rates can be achieved. For the burning conditions adopted here, the αp-process switches to the rp-process above mass $A = 33$, where the Coulomb barrier impedes reactions induced by α-particles.

The most important waiting point nuclides are ^{34}Ar, ^{39}Ca, ^{56}Ni, and ^{60}Zn. In each case, with the exception of ^{56}Ni, the reverse photodisintegration rate dominates over the forward rate and the abundance flow must proceed via a slow β^+-decay. At the end of the calculation, the most abundant nuclides, besides hydrogen and helium, are ^{56}Ni, ^{60}Zn, and ^{64}Ge. The large final abundance of ^{56}Ni is striking, especially when compared to the previous calculation, where only a small ^{56}Ni abundance was left over at $t = 100$ s. Here, the main abundance flow extends only to ^{60}Zn, whereas in the previous calculation, at $T = 1.0$ GK, the main flow reached considerably farther (to ^{68}Se; see Figure 5.59). This issue will be discussed in detail below. It is also apparent that for $t \geq 20$ s the abundances of ^{30}S, ^{34}Ar, ^{39}Ca, and ^{56}Ni stay constant because of the operation of the 3α reaction (see discussion at $T = 1.0$ GK).

The nucleosynthesis in the $A \geq 20$ region depends neither on the precise values of the rates, nor the identity of the breakout reactions. If we would entirely remove the reactions ^{19}N(p,γ)^{20}Na, ^{18}Ne(α,p)^{21}Na, and ^{16}O(α,γ)^{20}Ne from the network, that is, those reactions which complete the breakout sequences shown in Figure 5.56, then the $A < 20$ and $A \geq 20$ regions would be bridged by slower reactions, such as ^{19}Ne(α,p)^{22}Na, ^{19}Ne(α,γ)^{23}Mg, ^{18}Ne(α,γ)^{22}Mg, and ^{17}F(α,p)^{20}Ne, and the abundance evolutions in the $A \geq 20$ region would closely resemble the results shown in Figure 5.60b,c.

The ^{56}Ni Bottleneck

To understand why the abundance flow is significantly delayed at ^{56}Ni, we need to consider the properties of this waiting point nuclide. It has a relatively long half-life of $T_{1/2} = 6.1$ d in the laboratory and decays with 100% probability by electron capture. At elevated temperatures and densities, the β-decay half-life will change somewhat (Section 1.8.4; see also Fuller, Fowler, and Newman, 1982). Values of $Q_{p\gamma}$ and $T_{1/2}$ for nuclides in the vicinity of ^{56}Ni are given in Figure 5.61a. The Q-value for the ^{56}Ni(p,γ)^{57}Cu reaction amounts to only $Q_{p\gamma} = 695$ keV. The subsequent ^{57}Cu(p,γ)^{58}Zn reaction has a Q-value of $Q_{p\gamma} = 2280$ keV. At a density of $\rho = 10^4$ g/cm^3, the abundance flows will pass through the ^{56}Ni(p,γ)^{57}Cu reaction (Figure 5.59). We are interested in the effective mean lifetime (or decay constant) of ^{56}Ni. For temperatures below $T = 0.77$ GK, the photodisintegration of ^{57}Cu is less likely to occur than the competing β^+-decay of ^{57}Cu, that is, $\lambda_{^{57}\mathrm{Cu}(\gamma,\mathrm{p})} < \lambda_{^{57}\mathrm{Cu}(\beta^+\nu)}$, as can be calculated from the numerical values of $N_A\langle\sigma v\rangle_{^{56}\mathrm{Ni}(\mathrm{p},\gamma)}$ and $T_{1/2}(^{57}\mathrm{Cu})$ (Fig 5.61a). Since photodisintegration plays only a minor role in this temperature range, we obtain the effective mean lifetime of ^{56}Ni, $\tau_{\mathrm{eff}} = 1/\lambda_{\mathrm{eff}}$, from (see Eq. (3.23))

$$\lambda_{\mathrm{eff}}(^{56}\mathrm{Ni}) = \rho\frac{X_{\mathrm{H}}}{M_{\mathrm{H}}}N_A\langle\sigma v\rangle_{^{56}\mathrm{Ni}(\mathrm{p},\gamma)} \tag{5.170}$$

Values of the effective mean lifetime are plotted in Figure 5.61b versus temperature for $\rho = 10^4$ g/cm^3 and $X_{\mathrm{H}} = 0.73$. At $T = 0.4$ GK, we obtain $\tau_{\mathrm{eff}}(^{56}\mathrm{Ni}) = 185$ s. This value is considerably shorter than the laboratory lifetime of ^{56}Ni, but is large compared to typical macroscopic explosion time scales ($t \leq 100$ s). The

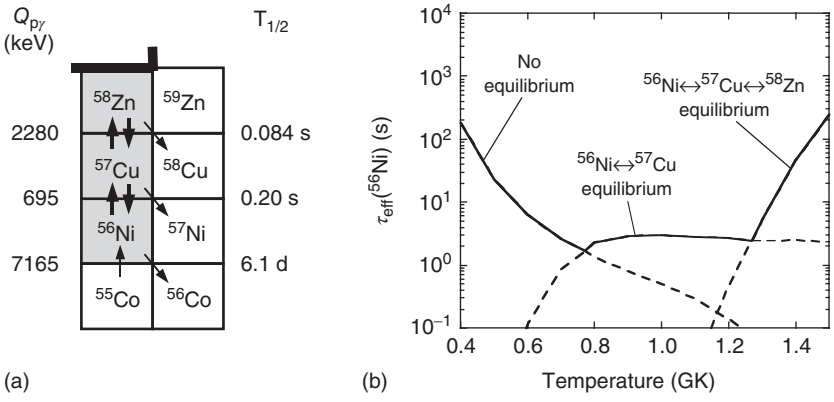

Figure 5.61 (a) Section of the chart of nuclides in the vicinity of the bottleneck ^{56}Ni. Nuclides that eventually reach equilibrium are shown as shaded squares. Values of $Q_{p\gamma}$ (left-hand side) and $T_{1/2}$ (right-hand side) are adopted from Audi, Wapstra, and Thibault (2003) and Audi *et al.* (2003), respectively. (b) Effective mean lifetime of ^{56}Ni versus temperature for the conditions $\rho = 10^4$ g/cm^3 and $X_H = 0.73$. There is a window at intermediate temperatures ($T = 0.77$–1.27 GK), where ^{56}Ni does not represent a major waiting point for the abundance flow.

^{56}Ni(p,γ)^{57}Cu reaction rate increases for higher temperatures and thus the effective mean lifetime decreases. For example, at $T = 0.77$ GK, one obtains a value of $\tau_{eff}(^{56}\text{Ni}) = 1.7$ s. At temperatures of $T = 0.77$–1.27 GK, the photodisintegration of ^{57}Cu cannot be disregarded anymore. The ^{57}Cu(γ,p)^{56}Ni reaction is now faster than the competing processes ^{57}Cu(p,γ)^{58}Zn and ^{57}Cu($\beta^+\nu$)^{57}Ni [$\lambda_{^{57}\text{Cu}(\gamma,\text{p})} > \lambda_{^{57}\text{Cu}(\text{p},\gamma)} + \lambda_{^{57}\text{Cu}(\beta^+\nu)}$]. The conditions of Eqs. (3.56) and (3.57) are fulfilled and, as a result, the abundances of ^{56}Ni and ^{57}Cu quickly achieve equilibrium. The effective mean lifetime of ^{56}Ni is then given by Eq. (3.62),

$$\lambda_{\text{eff}}(^{56}\text{Ni}) = \frac{\lambda_{^{56}\text{Ni}(\text{p},\gamma)}}{\lambda_{^{57}\text{Cu}(\gamma,\text{p})}}[\lambda_{^{57}\text{Cu}(\text{p},\gamma)} + \lambda_{^{57}\text{Cu}(\beta^+\nu)}] \tag{5.171}$$

As the temperature increases from 0.77 to 1.27 GK, the ratio of decay constants in Eq. (5.171) becomes smaller (see Eq. (3.62)). Simultaneously, the ^{57}Cu(p,γ)^{58}Zn reaction rate increases and, as a result, the effective mean lifetime is approximately constant, $\tau_{\text{eff}}(^{56}\text{Ni}) \approx 3.0$ s (Figure 5.61b). The use of Eq. (5.171) implies that the photodisintegration of ^{58}Zn plays a minor role compared to the decay ^{58}Zn($\beta^+\nu$)^{58}Cu (see condition $\lambda_{C\to C'} > \lambda_{C\to B}$; Section 3.1.6). At temperatures in excess of $T = 1.27$ GK, however, the ^{58}Zn(γ,p)^{57}Cu reaction becomes faster than the competing β^+-decay of ^{58}Zn. Furthermore, the ^{57}Cu(p,γ)^{58}Zn reaction is faster than the competing β^+-decay ^{57}Cu($\beta^+\nu$)^{57}Ni. For these conditions, the abundances of ^{56}Ni, ^{57}Cu, and ^{58}Zn quickly achieve equilibrium. The effective mean lifetime of ^{56}Ni is then obtained from (see Problem 3.1)

$$\lambda_{\text{eff}}(^{56}\text{Ni}) = \frac{\lambda_{^{56}\text{Ni}(\text{p},\gamma)}}{\lambda_{^{57}\text{Cu}(\gamma,\text{p})}}\left(\frac{\lambda_{^{57}\text{Cu}(\text{p},\gamma)}}{\lambda_{^{58}\text{Zn}(\gamma,\text{p})}}\lambda_{^{58}\text{Zn}(\beta^+\nu)} + \lambda_{^{57}\text{Cu}(\beta^+\nu)}\right) \tag{5.172}$$

The decay constants for the two β^+-decays are constant with temperature, but both ratios of decay constants for the forward and reverse reaction are proportional to $e^{Q_i/kT}$ and decrease rapidly for increasing temperature. Therefore, the effective mean lifetime of ^{56}Ni increases steeply beyond $T = 1.27$ GK, as can be seen in Figure 5.61b. For example, one obtains $\tau_{\text{eff}}(^{56}\text{Ni}) \approx 246$ s at $T = 1.5$ GK. It is interesting that a window exists at intermediate temperatures ($T = 0.77$–1.27 GK), where ^{56}Ni does not represent a major waiting point. Consequently, the abundance flow reaches far beyond the Ni region in Figure 5.59b. At lower and higher temperatures, the Coulomb barrier of ^{56}Ni + p and two sequential photodisintegration reactions, respectively, are responsible for a substantial increase in the value of $\tau_{\text{eff}}(^{56}\text{Ni})$. Therefore, the abundance flow does not reach as far (Figure 5.59a,c).

Energy Generation

The rp- and αp-processes generate energy in a different manner compared to the HCNO cycles. The former processes consist of *sequences* of capture reactions and β^+-decays. An (α,p) reaction followed by a (p,γ) reaction yields the same product as a single (α,γ) reaction. Reaction cycles play only a minor role, and, therefore, none of the nuclides involved in the nucleosynthesis will act as catalysts. Energy is generated not by the fusion of four protons to one ^{4}He nucleus, but by using protons and α-particles to build up heavier nuclides starting from CNO seed nuclei. Also, at these higher temperatures, the 3α reaction operates and supplies a fraction of the CNO seeds. The energy generation rate is sensitive to the total mass fraction of CNO seed nuclei and to the initial hydrogen-to-helium abundance ratio ($X^0_{\text{H}}/X^0_{^4\text{He}}$), but it is relatively insensitive to the exact initial CNO composition or the manner by which breakout from the CNO region proceeds.

Energy generation rates for the previously discussed network calculations at $T = 0.5$ GK, 1.0 GK, and 1.5 GK are shown in Figure 5.62. The density ($\rho = 10^4$ g/cm^3) and initial composition are the same for each calculation. The solid lines are obtained with the full reaction network. The final hydrogen abundances amount to $X_{\text{H}} = 0.70$, 0.67, and 0.69 at $T = 0.5$ GK, 1.0 GK, and 1.5 GK, respectively. The main abundance flow eventually reaches the waiting point nuclide ^{52}Fe ($T = 0.5$ GK), ^{60}Zn ($T = 1.0$ GK), or ^{56}Ni ($T = 1.5$ GK). The flow slows down significantly and material accumulates at the waiting point nuclide (Figure 5.60). As a result, the energy generation rate drops, giving rise to the broad maxima displayed in Figure 5.62. Furthermore, the higher the temperature, the faster the CNO seed nuclei are transformed to the final, most abundant waiting point nuclide. As a result, the maximum in the energy generation rate occurs at earlier times ($t_{\text{peak}} = 33$ s, 7.0 s, and 4.3 s at $T = 0.5$ GK, 1.0 GK, and 1.5 GK, respectively). The dashed lines in Figure 5.62 correspond to the energy generation rate if the reaction rates of all possible breakout processes are set equal to zero so that the HCNO cycles and the 3α reaction are the sole sources of nuclear energy. It is apparent that the rp- and αp-processes enhance the energy

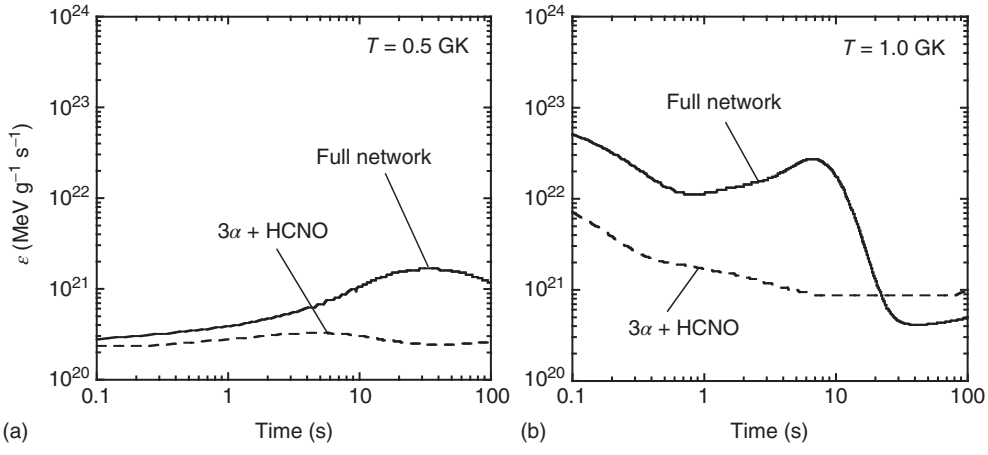

Figure 5.62 Evolution of the energy generation rate during hydrogen–helium burning at a constant temperature of (a) $T = 0.5$ GK and (b) $T = 1.0$ GK. The same constant density ($\rho = 10^4$ g/cm^3) and initial composition is used. The results are extracted from the same numerical reaction network calculations that are displayed in Figure 5.59. Results for $T = 1.5$ GK are very similar to those shown in part (b) and are not displayed in the figure. The solid lines are obtained with the full reaction network. The dashed lines correspond to the energy generation rate if the reaction rates of all possible breakout processes are set equal to zero so that the HCNO cycles and the 3α reaction are the sole sources of nuclear energy generation.

generation rate significantly. For $T = 0.5$ GK, 1.0 GK, and 1.5 GK, the maximum enhancement amounts to a factor of 6, 33, and 25, respectively.

If one would repeat the above calculations at $T = 1.0$ GK or 1.5 GK by setting all initial CNO abundances equal to zero, then the nucleosynthesis must start with the 3α reaction. The newly created CNO nuclei are the seeds for the subsequent rp- and αp-processes, and the resulting abundance flow patterns in the $A \geq 20$ region would closely resemble those shown in Figure 5.59b,c. Eventually, the energy generation rate will stay constant with time as the abundance flows between ^{4}He, ^{56}Ni, and heavier nuclides attain equilibrium. Also, the energy generation rate would be considerably smaller compared to the results shown as solid lines in Figure 5.62.

For more information on the rp- or αp-processes at constant temperature and density conditions, see, e.g., Schatz *et al.* (1998).

Network Calculations for a Type I X-Ray Burst: Accreting Neutron Star

We will now consider the more realistic situation of a changing temperature and density during the nucleosynthesis. Type I X-ray bursts (Section 1.4.4) represent examples of explosive (thermally unstable) hydrogen–helium burning at temperatures in excess of $T = 0.5$ GK. Figure 5.63 shows a temperature and density profile that is similar to those obtained in stellar model studies of a thermonuclear runaway caused by the accretion of hydrogen and helium

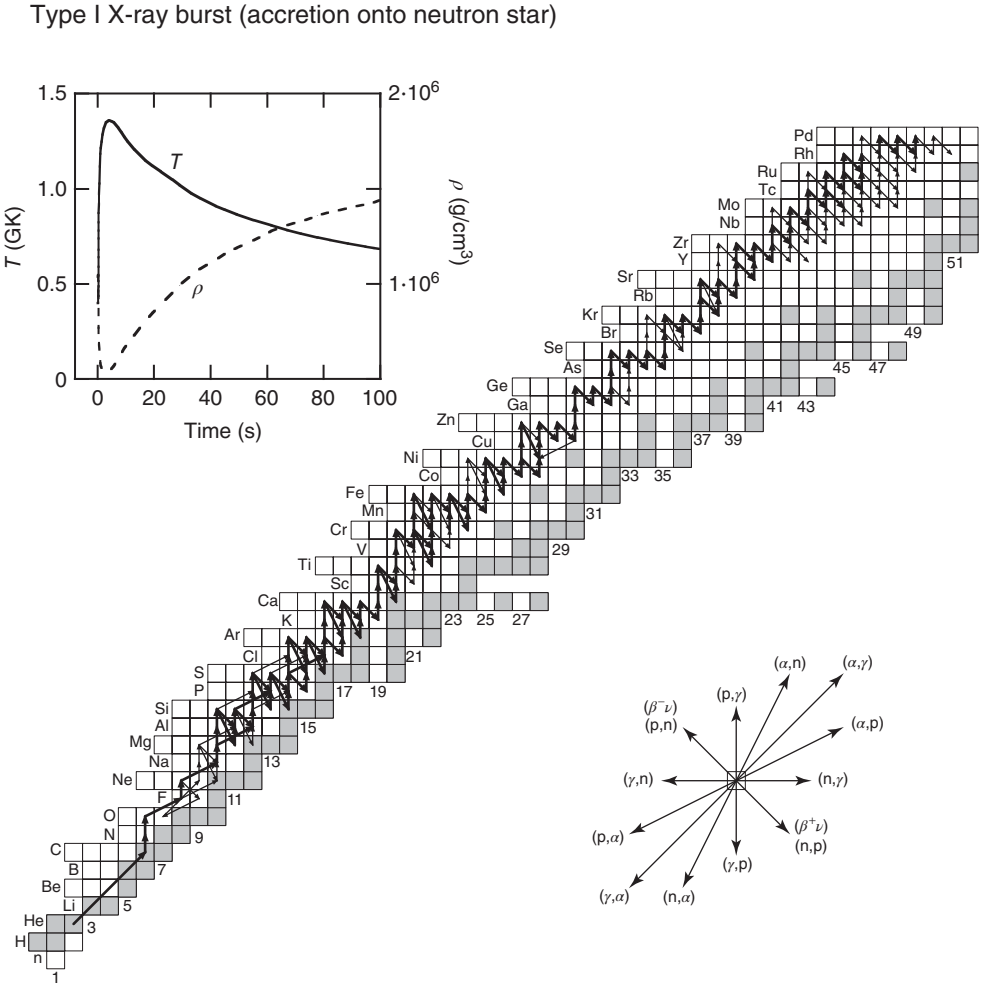

Figure 5.63 Time-integrated net abundance flows during a thermonuclear runaway caused by the accretion of hydrogen and helium onto the surface of a 1.3 $M_\odot$ neutron star with a radius of 8 km. The evolution of temperature and density in the nuclear burning zone during explosive hydrogen–helium burning, shown in the inset, is similar to the result obtained from hydrodynamic simulations of type I X-ray bursts (Koike *et al.*, 2004). The reaction network calculation is terminated after $t = 100$ s. The arrows and shaded squares have the same meaning as in Figure 5.59. The abundance flows are defined here in terms of mole fractions rather than number densities since the mass density varies.

onto the surface of a $1.3\,M_\odot$ neutron star with a radius of 8 km (Koike *et al.*, 2004). The curves represent the temperature and density evolutions in the hottest nuclear burning zone. In this particular example, the nuclear burning starts with temperature and density values of $T = 0.4$ GK and $\rho = 10^6$ g/cm^3.

At $t = 4$ s, a maximum temperature of $T_{\rm peak} = 1.36$ GK and a minimum density of $\rho_{\rm peak} = 5 \times 10^5$ g/cm^3 are achieved. After $t = 100$ s, the temperature has fallen to $T = 0.7$ GK and the density increased to $\rho = 1.4 \times 10^6$ g/cm^3. The density is about two orders of magnitude larger compared to the constant value assumed in the previous section. Recall that the forward reaction rates depend on the density, but the photodisintegration rates are independent of ρ (see Eqs. (3.23) and (3.46)). The reaction network is solved numerically using this T–ρ profile. For the initial composition, values of $X^0_{\rm H} = 0.73$, $X^0_{^4{\rm He}} = 0.25$, and $X^0_{^{14}{\rm O}} = X^0_{^{15}{\rm O}} = 0.01$ are assumed. The network calculation is terminated after $t = 100$ s.

The major abundance flows extend from helium all the way up to the end of the network (palladium), as can be seen from Figure 5.63. Breakout from the CNO mass region proceeds via sequences 1 and 2 (Figure 5.56). The latter sequence is more important since the ^{14}O abundance is fed by $\alpha(2\alpha)^{12}{\rm C}({\rm p},\gamma)^{13}{\rm N}({\rm p},\gamma)^{14}{\rm O}$. After breakout, matter is processed via the αp-process (below the chlorine region) and the rp-process. The abundance flow reaches the dripline at many locations over the entire mass region shown. The major flow then has to wait in most cases for a β^+-decay before continuing. The waiting point nuclides ^{64}Ge, ^{68}Se, ^{72}Kr, and ^{76}Sr represent interesting cases. Their $Q_{\rm p\gamma}$-values are predicted to be negative (Audi *et al.*, 2012), while their half-lives amount to $T_{1/2} = 64$ s, 36 s, 17 s, and 8 s, respectively. It can be seen that at ^{64}Ge, the major flow continues via sequential two-proton capture instead of the very slow β^+-decay, which would otherwise terminate the nucleosynthesis. For the other three waiting point nuclides, the β^+-decay is more likely to occur, for the conditions assumed here, than the competing sequential two-proton capture. Hence, the abundance flow will be delayed significantly, and we expect an accumulation of material, especially at ^{68}Se and ^{72}Kr, toward the end of the calculation.

A significant fraction of ^{1}H and ^{4}He nuclei is consumed during the thermonuclear explosion. Their abundances decrease gradually with time until they reach values of $X_{\rm H} = 0.16$ and $X_{^4{\rm He}} = 0.02$ at the end of the calculation. Figure 5.64a shows the abundance evolution of the most important waiting point nuclides, that is, for those nuclides that are most abundant at any given time. It is evident how the flow reaches the nuclides ^{18}Ne, ^{24}Si, ^{25}Si, and so on, in sequence. In each case, the abundance flow is delayed by a slow process that consumes the waiting point nucleus (e.g., the (α,p) reaction on ^{18}Ne; β^+-decays of ^{24}Si, ^{25}Si; sequential two-proton captures on ^{64}Ge). As a result, the abundance of a particular waiting point nucleus increases until a maximum is reached and then decreases with time. At $t = 4$ s, when the peak temperature is attained, the most abundant nuclides (besides ^{1}H and ^{4}He) are ^{60}Zn, ^{55}Ni, ^{38}Ca, ^{59}Zn, and ^{64}Ge, with similar mass fractions of $X \approx 0.03$. Notice that ^{56}Ni is not a major waiting point nucleus. For the densities adopted here, one finds from Eq. (5.172) a mean lifetime of only $\tau_{\rm eff}(^{56}{\rm Ni}) = 0.02$ s. Therefore, the ^{56}Ni abundance stays relatively small throughout the calculation. Also, ^{56}Ni cannot be bypassed via the sequence $^{55}{\rm Ni}({\rm p},\gamma)^{56}{\rm Cu}({\rm p},\gamma)^{57}$Zn, as is sometimes erroneously assumed (Forstner *et al.*, 2001), since ^{57}Zn decays preferentially (Audi *et al.*, 2012) by β-delayed proton

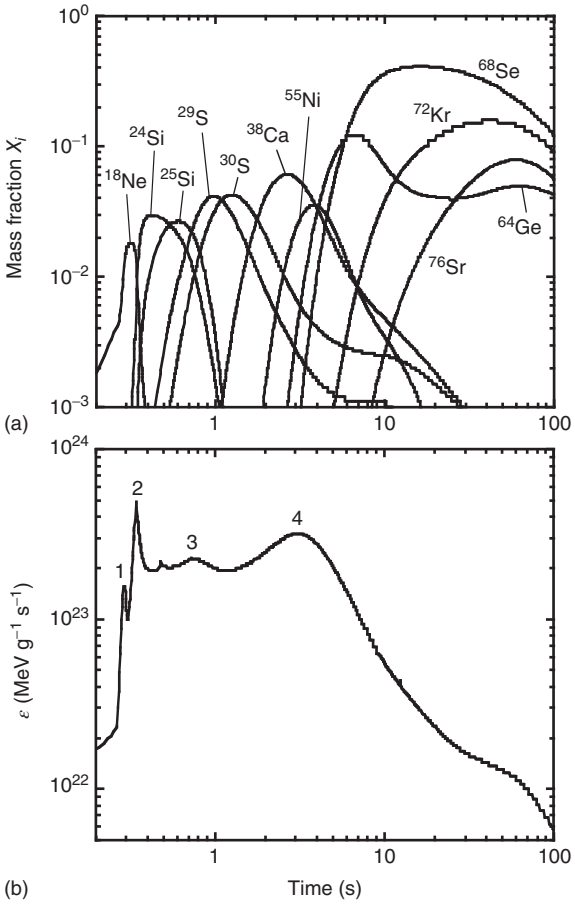

Figure 5.64 (a) Abundance evolutions of the most important waiting point nuclides, and (b) time evolution of the energy generation rate during explosive hydrogen–helium burning. The results are extracted from the same numerical reaction network calculation that is displayed in Figure 5.63. The narrow and broad maxima of the energy generation rate shown in part (b) are correlated with the abundance evolution of the waiting point nuclides displayed in part (a).

emission [^{57}Zn($\beta^+\nu$p)^{56}Ni] rather than by β^+-decay [^{57}Zn($\beta^+\nu$)^{57}Cu]. At $t = 10$ s, ^{68}Se has by far the largest abundance ($X_{^{68}\mathrm{Se}} = 0.35$) among all nuclides except ^{1}H since the abundance flow must wait for its slow β^+-decay, as noted earlier. With progressing time, ^{68}Se is slowly depleted and the abundances of some nuclides in the $A > 68$ region are building up. At $t = 100$ s, the most abundant nuclides (besides ^{1}H) are ^{68}Se, ^{72}Kr, ^{76}Sr, and ^{64}Ge. These species will quickly decay to ^{68}Ge ($T_{1/2} = 271$ d), ^{72}Se ($T_{1/2} = 8.4$ d), ^{76}Kr ($T_{1/2} = 14.8$ h), and ^{64}Zn (stable), respectively, after the thermonuclear explosion has ceased. A significant fraction of matter ($\Sigma X_i = 0.20$) has been converted to nuclides in the Zr–Ru mass region.

The total mass fraction of nuclides located at the end of the network (Rh and Pd) amounts to $\Sigma X_i = 0.16$. This material would be converted to even heavier nuclides if we would not have truncated the network artificially. For a discussion of abundance evolutions in the mass range above Pd, see Schatz *et al.* (2001) or Koike *et al.* (2004).

It must be emphasized that the nucleosynthesis in the mass range $A \geq 64$ depends sensitively on the Q-values for the (p,γ) reactions on ^{64}Ge, ^{68}Se, and ^{72}Kr, and on the reaction rates for the (p,γ) reactions on ^{65}As, ^{69}Br, and ^{73}Rb. Consider the waiting point ^{64}Ge as an example. We adopted a value of $Q_{p\gamma} = -80 \pm 300$ keV (Audi, Wapstra, and Thibault, 2003) for ^{64}Ge(p,γ)^{65}As and the ^{65}As(p,γ)^{66}Se reaction rate from Goriely (1998). With these values, the mean lifetime of ^{64}Ge versus destruction by sequential two-proton capture at $T = 1.34$ GK and $\rho = 5.9 \times 10^5$ g/cm^3 (when the ^{64}Ge abundance reaches a maximum; Figure 5.64a) amounts to $\tau_{2p}(^{64}\text{Ge}) = 1.5$ s. Two-proton capture is more likely to occur than the competing β^+-decay [$\tau_\beta(^{64}\text{Ge}) = T_{1/2}(^{64}\text{Ge})/\ln 2 = 92$ s], and the relatively short effective lifetime of ^{64}Ge allows for a significant production of nuclides in the $A > 64$ range, as discussed above. Repeating the calculation using a value of $Q_{p\gamma} = -380$ keV instead yields $\tau_{2p}(^{64}\text{Ge}) = 21$ s, and ^{64}Ge, rather than ^{68}Se, would be the most abundant nuclide at the end of the network calculation, with a considerably reduced total abundance of nuclides in the $A > 80$ range. See also Problem 5.12.

The time evolution of the energy generation rate is displayed in Figure 5.64b. Two narrow and two broad maxima are visible. They are correlated with the abundance evolution of waiting point nuclides. The first narrow maximum ($t \approx 0.29$ s) is caused by the evolution of ^{18}Ne. Shortly after the ^{18}Ne abundance increases most rapidly, the flow is temporarily delayed, and the ^{18}Ne abundance peaks. Consequently, the energy generation rate decreases, giving rise to the first maximum. The second ($t \approx 0.33$ s) and third ($t \approx 0.74$ s) maxima are similarly caused by the abundance evolutions of ^{24}Si and ^{29}S, respectively. The transformation of the bulk material from ^{29}S to ^{38}Ca via the rp-process takes only ≈ 1.6 s, while the major abundance flow reaches the isotope ^{55}Ni after an additional ≈ 1.3 s. Subsequently, matter starts to accumulate at the major waiting point nuclides ^{64}Ge and ^{68}Se. The energy generation rate decreases and, as a result, the fourth maximum ($t \approx 3.0$ s) is produced.

For an extensive investigation of type I X-ray burst nucleosynthesis, see Parikh *et al.* (2013a). A discussion of thermally stable hydrogen–helium burning on accreting neutron stars can be found in Schatz *et al.* (1999).

Experimental Nuclear Physics Information

Among the processes that are part of the breakout sequences (Section 5.4.1 and Figure 5.56), the ^{19}Ne(p,γ)^{20}Na and ^{18}Ne(α,p)^{21}Na reactions have been measured directly using radioactive ion beams (Groombridge *et al.*, 2002; Couder *et al.*, 2004). These difficult experiments provided only partial information, however, and thus the present uncertianties in the reaction rates amount to 1–2 orders of magnitude at $T = 0.5$–1.0 GK (with the larger error at the lower temperature

value). The $^{14}O(\alpha,p)^{17}F$ reaction rate has been estimated by measuring the reverse $^{17}F(p,\alpha)^{14}O$ reaction (Harss *et al.*, 2002; Blackmon *et al.*, 2003), but the rate uncertainties still amount to orders of magnitude. The $^{15}O(\alpha,\gamma)^{19}Ne$ reaction rate was obtained indirectly using experimental nuclear structure information (Iliadis *et al.*, 2010). The current reaction rate uncertainties at $T = 0.5$ and 1.0 GK amount to a factors of 3 and 2, respectively. The experimental situations for the $^{17}F(p,\gamma)^{18}Ne$ and $^{16}O(\alpha,\gamma)^{20}Ne$ reactions have already been described in Sections 5.5.2 and 5.2.1, respectively.

After breakout from the HCNO cycles has been achieved, several thousand nuclear processes take part in the nucleosynthesis (rp- and αp-processes). The nuclear physics information necessary to quantitatively describe the nuclear burning consists of: (i) reaction Q-values, (ii) thermonuclear reaction rates, and (iii) β-decay half-lives. Precise Q-values are especially necessary for pairs of nuclides that achieve an equilibrium between forward and backward reaction at elevated stellar temperatures. For example, the Q-value for $^{56}Ni(p,\gamma)^{57}Cu$ is known to reasonable precision ($Q_{p\gamma} = 695 \pm 19$ keV), but the Q-values for the (p,γ) reactions on the waiting point nuclides ^{64}Ge, ^{68}Se, ^{72}Kr, and ^{76}Sr carry large uncertainties. We have adopted the values of $Q_{p\gamma} = -80 \pm 300$ keV, -450 ± 100 keV, -600 ± 150 keV, and -50 ± 50 keV, respectively. The present uncertainties are substantial, especially since these Q-values enter exponentially in Eq. (3.63). It should also be pointed out that the errors quoted above do not represent experimental uncertainties, but have been derived from systematic trends of measured masses (see Wang *et al.*, 2012, for details). Hence, the true uncertainties are expected to be somewhat larger than the quoted values. With the exception of the $^{21}Na(p,\gamma)^{22}Mg$ reaction (D'Auria *et al.*, 2004), none of the thermonuclear rates for reactions along the rp- or αp-process paths have been measured directly. Some of the rates have been estimated using experimental nuclear structure information (see, e.g., Iliadis *et al.*, 2010 or Forstner *et al.*, 2001), but the vast majority of reaction rates are based on the Hauser–Feshbach statistical model (Rauscher and Thielemann, 2000; Goriely, 1998). It must be pointed out that not all the reactions that are part of the network have an influence on the nucleosynthesis (Iliadis *et al.*, 1999). Of particular importance are (α,p) reactions on waiting point nuclides, for example, $^{22}Mg(\alpha,p)^{25}Al$, $^{25}Si(\alpha,p)^{28}P$, $^{30}S(\alpha,p)^{33}Cl$, and second-step (p,γ) reactions in sequential two-proton capture, for example, $^{57}Cu(p,\gamma)^{58}Zn$, $^{65}As(p,\gamma)^{66}Se$, $^{69}Br(p,\gamma)^{70}Kr$, and $^{73}Rb(p,\gamma)^{74}Sr$. The half-lives of the (most-likely proton-unbound) nuclides ^{65}As, ^{69}Br, and ^{73}Rb are predicted to be very short (170 ms, < 24 ns, < 30 ns, respectively; Audi *et al.*, 2012) and, therefore, direct measurements of the proton-capture reactions on these target nuclei are not feasible yet. All of these reaction rates carry large uncertainties at present.

For an investigation of the impact of current reaction rate and Q-value uncertainties on the nucleosynthesis during type I X-ray bursts, see Parikh *et al.* (2008) and Parikh *et al.* (2009), respectively.

5.6
Nucleosynthesis Beyond the Iron Peak

The transmission through the Coulomb barrier decreases drastically with increasing nuclear charges. For this reason, charged-particle cross sections are far too small at moderate stellar temperatures to explain the observed solar system abundances of nuclides with masses beyond $A \approx 60$. At very high temperatures, on the other hand, charged-particle reactions will give rise to abundances that are described by nuclear statistical equilibrium, either favoring nuclides of the iron peak group or lighter species (see Figure 5.38). The situation is different when considering neutron-induced reactions as the mechanism for the synthesis of the heavy nuclides. There is no Coulomb barrier for neutrons and thus the neutron capture cross sections, even at moderate stellar energies, are frequently large. The cross sections for most neutron-induced reactions even increase with decreasing incident neutron energies (Figure 3.31). It is therefore reasonable to assume that heavy nuclides can be synthesized by exposing lighter seed nuclei to a source of neutrons. There is unambiguous evidence for such a mechanism. As will be seen, it provides a natural explanation for the solar system abundance peaks near the mass numbers $A \approx 84$, 138, and 208 (Figure 5.65), corresponding to the neutron magic numbers of $N = 50$, 82, and 126, respectively (Section 1.6.1). It should be remembered that neutrons are unstable, with a half-life of $T_{1/2} = 614$ s.

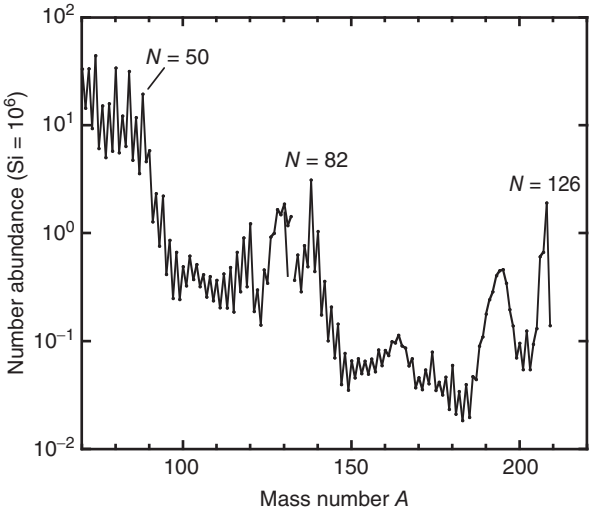

Figure 5.65 Solar system abundances (relative to 10^6 Si atoms) of the heavy nuclides. Adopted from Lodders (2003). Abundances of different isobars are added together. Narrow peaks occur at mass numbers of $A \approx 84$, 138, and 208, corresponding to the neutron magic numbers of $N = 50$, 82, and 126, respectively. Broader peaks are located approximately 10 mass units below the narrow peaks.

The interstellar medium does not contain a significant concentration of free neutrons. They must be produced in stars. We have already encountered some neutron-producing reactions in helium burning (Section 5.2.3) and carbon burning (Section 5.3.1). We will first concentrate on the properties of neutron capture nucleosynthesis and afterward discuss the sources of neutrons in various stellar environments. Unlike previously discussed processes, the neutron capture processes do not generate any significant amount of energy, as can be seen from the decline of the binding energy per nucleon beyond the iron peak (Figure 1.9).

Consider the nuclear transformations that can occur if a stable nucleus, for example ^{156}Gd, is exposed to a flux of neutrons (Figure 5.66). Successive stable isotopes of the same element (Gd) will capture neutrons, initiating the sequence $^{156}\mathrm{Gd}(\mathrm{n},\gamma)^{157}\mathrm{Gd}(\mathrm{n},\gamma)^{158}\mathrm{Gd}(\mathrm{n},\gamma)^{159}\mathrm{Gd}$. The last nuclide, ^{159}Gd, is radioactive ($T_{1/2} = 18.5$ h). Further suppose that the neutron flux is sufficiently small so that the β-decay constant of any unstable nucleus created after neutron capture is large compared to the decay constant of the competing (n,γ) reaction ($\lambda_\beta \gg \lambda_{\mathrm{n}\gamma}$). The path will then continue via $^{159}\mathrm{Gd}(\beta^-\nu)^{159}\mathrm{Tb}(\mathrm{n},\gamma)^{160}\mathrm{Tb}$. The last nuclide, ^{160}Tb, is radioactive ($T_{1/2} = 72.3$ d). The process repeats itself, giving rise to the sequence $^{160}\mathrm{Tb}(\beta^-\nu)^{160}\mathrm{Dy}(\mathrm{n},\gamma)^{161}\mathrm{Dy}(\mathrm{n},\gamma)^{162}\mathrm{Dy}$, and so on. In summary, successive neutron captures by a chain of isotopes occur until a radioactive isotope is reached, at which point a β^--decay takes place and another successive chain of neutron captures is initiated. The resulting path is shown as the solid line

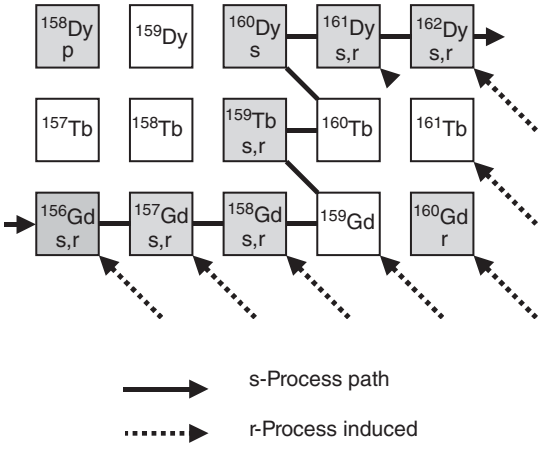

Figure 5.66 The s-process path through the elements Gd, Tb and Dy (solid line). Shaded squares indicate stable nuclides. Nuclides reached by the s-process are labeled "s." Stable nuclides that are reached via the r-process (dotted arrows) through β^--decay chains along A = const after termination of the neutron flux are labeled "r." Neither process can explain the synthesis of the stable nuclide labeled "p." Some stable nuclides can be synthesized only in the s-process or the r-process, but not by both processes. These are referred to as *s-only or r-only nuclides*. The s-process branchings in this mass region are weak and have been omitted in the figure.

in Figure 5.66. This mechanism is referred to as *s(low neutron capture)-process* (Burbidge *et al.*, 1957). The s-process path must run close to the group of stable nuclides. More specifically, it will reach only those stable nuclides that are labeled "s" in Figure 5.66. It will neither reach very neutron-deficient stable nuclides (such as ^{158}Dy), nor very neutron-rich stable nuclides (such as ^{160}Gd). The abundances synthesized by the s-process will depend on the magnitude of the neutron-capture cross sections involved in the chain. Nuclides with very small neutron-capture cross sections are expected to pile up in abundance, while those with large cross sections will be quickly destroyed and achieve only small abundances. Maxwellian-averaged neutron-capture cross sections on stable and long-lived nuclides at a thermal energy of $kT = 30$ keV versus mass number A are shown in Figure 5.67. Recall that nuclides with a magic neutron number ($N = 50$, 82, and 126) have energetically favorable configurations (Section 1.6.1). The capture of another neutron produces a product nucleus with a relatively small neutron separation energy and, therefore, the compound nucleus is formed at a relatively small excitation energy in a region with a small level density. The reaction must then proceed through a reduced number of compound levels, and the cross section becomes relatively small, as can be seen from the location of the minima in Figure 5.67. In other words, we expect that the s-process will produce these very same nuclides with increased abundances. This is precisely the reason for the narrow peaks at the neutron magic numbers $N = 50$, 82, and 126 in the solar system abundance curve (Figure 5.65).

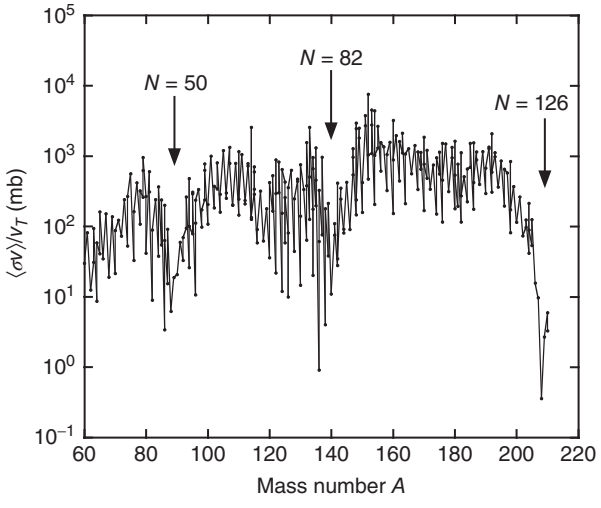

Figure 5.67 Maxwellian-averaged neutron-capture cross sections on stable and long-lived nuclides at a thermal energy of $kT = 30$ keV versus mass number A. From Bao *et al.* (2000). Nuclides with a magic neutron number ($N = 50$, 82, and 126) have energetically favorable configurations and give rise to relatively small neutron capture cross sections.

Consider now the other extreme, that is, a neutron flux so large that the β-decay constant of an unstable nucleus created after neutron capture is small compared to the decay constant of the competing (n,γ) reaction ($\lambda_\beta \ll \lambda_{n\gamma}$). In this case, the nucleosynthesis path will run close to the neutron dripline. When the neutron flux terminates, all neutron-rich radioactive nuclei will undergo successive β^--decays (dashed arrows in Figure 5.66) along isobaric chains until the most neutron-rich, stable (or very long-lived) isobar is reached. This nucleosynthesis process is called the *r(apid neutron capture)-process* and will be discussed in more detail in Section 5.6.2. In the example of Figure 5.66, the r-process synthesizes all nuclides labeled "r." It is interesting that certain nuclides (e.g., ^{156}Gd, ^{157}Gd) can be produced by both the s- and the r-process. Other nuclides, such as ^{160}Gd, are never reached in the s-process and are referred to as *r-only* nuclides. The latter nuclide does not undergo a β^--decay since it is stable. Hence, ^{160}Dy, which is less neutron-rich than ^{160}Gd, cannot be reached in the r-process. It is called an *s-only* nuclide because it is shielded from the r-process.

Some of the most neutron-deficient stable nuclides, such as ^{158}Dy in Figure 5.66, cannot be synthesized by either the s-process or the r-process. They are shielded from both neutron-capture processes and are referred to as *p-nuclides*. The mechanism responsible for their synthesis is called the *p-process* and will be discussed in Section 5.6.3. It is sufficient to remark here that the abundances of almost all p-nuclides are considerably smaller compared to those of the s- and r-nuclides of the same mass number.

Crude estimates for the number densities of neutrons in the s- and r-process can be obtained by considering typical cross sections for neutron capture. According to Figure 5.67, the mean value for the Maxwellian-averaged neutron-capture cross section of nuclides in the $A = 60$–210 region at a thermal energy of $kT = 30$ keV is $\langle\sigma\rangle_T = \langle\sigma v\rangle/v_T \approx 100$ mb. Since average neutron capture cross sections do not vary drastically with thermal energy (Figure 3.32), this value will be adopted as an order-of-magnitude estimate. For the s-process, typical β^--decay lifetimes of radioactive nuclides near the valley of stability range from minutes to years. Since $\tau_\beta \ll \tau_{n\gamma}$, the mean lifetime for neutron capture must then typically be $\tau_{n\gamma} \approx 10$ y or more. With $v_T = (2kT/m_{01})^{1/2} \approx [2 \cdot 30\,\text{keV} \cdot c^2/(m_n c^2)]^{1/2} \approx 2.4 \times 10^8$ cm/s, we find from Eq. (3.22) a value of $N_n = (\tau_{n\gamma}\langle\sigma v\rangle_{n\gamma})^{-1} \approx 10^8$ cm^{-3} for the neutron number density in the s-process. In the r-process, β^--decay lifetimes for radioactive nuclides far from the valley of stability range from milliseconds to seconds. Since $\tau_\beta \gg \tau_{n\gamma}$, the mean lifetime for neutron capture must then typically be $\tau_{n\gamma} \approx 10^{-4}$ s or less. For these conditions, a value of $N_n \approx 10^{21}$ cm^{-3} or more is obtained as an order-of-magnitude estimate for the neutron number density in the r-process. It is interesting that the gross properties of the solar system abundances in the $A > 60$ range can be accounted for in terms of two extreme pictures, that is, by relatively low neutron densities achieved in the s-process and by very high neutron exposures characteristic of the r-process. Intermediate exposures between these two extremes seem to play only a minor role for the solar system abundance distribution.

5.6.1 The s-Process

Starting from some seed nuclei, the s-process path runs close to the group of stable nuclides. The majority of neutron captures involves stable target nuclei and all of these reactions are accessible in the laboratory (Chapter 4). The heaviest nuclides synthesized by charged-particle reactions are those of the iron peak. Hence, these nuclei will most likely form the seeds for the s-process. Since ^{56}Fe is by far the most abundant nuclide in the iron peak (Figure 1.2), we will assume for the sake of simplicity that it is the sole seed for the neutron captures. The s-process will eventually reach ^{209}Bi, which is the most massive stable nuclide. Further neutron captures produce radioactive species that decay by α-particle emission. Thus, heavier nuclides cannot be synthesized by the s-process, and ^{209}Bi represents the termination point.

Consider Figure 5.68, showing the basic building blocks of the s-process path. In Figure 5.68a, the stable nucleus with mass number A, shown as shaded square, is destroyed by neutron capture. The same nucleus is produced by neutron capture on nucleus $A-1$. The same holds true if nucleus A is radioactive, but has such a long half-life that it can be regarded as being stable for all practical purposes concerning the s-process (i.e., if $\lambda_\beta \ll \lambda_{n\gamma}$). In Figure 5.68b, nucleus A is again destroyed by neutron capture, but it is also produced by neutron capture on nucleus $A-1$ and the subsequent β^--decay. We will initially assume that the β^--decay is so fast that the abundance of the radioactive species can be neglected since it decays immediately to the stable (or very long-lived) nucleus A. Under these assumptions, the abundance at each value of the mass number A resides in precisely one particular nuclide and thus the s-process path is uniquely defined by the mass number. The abundance evolution of any stable (or very long-lived) nuclide with mass number A is then given by

$$\frac{dN_s(A)}{dt} = -N_n N_s(A)\langle\sigma v\rangle_A + N_n N_s(A-1)\langle\sigma v\rangle_{A-1} \tag{5.173}$$

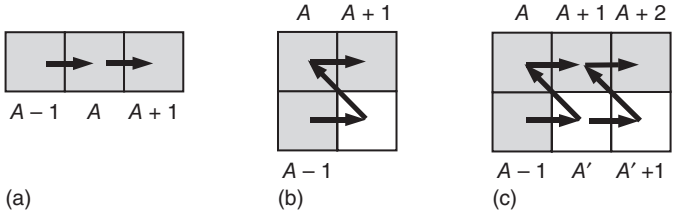

Figure 5.68 Basic building blocks of the s-process path. Stable (or very long-lived) nuclides are shown as shaded squares, short-lived nuclides as open squares. In part (a), the nucleus with mass number A is destroyed by neutron capture and is produced by neutron capture on nucleus $A-1$. In part (b), nucleus A is again destroyed by neutron capture, but is produced by neutron capture on nucleus $A-1$ and the subsequent β^--decay. In the s-process, it is generally assumed that the β^--decay is fast compared to neutron capture. Part (c) shows a simple example for an s-process branching.

where $N_s(A)$ and N_n are the number densities of nucleus A and of free neutrons, respectively; $\langle \sigma v \rangle_A$ is the neutron-capture reaction rate per particle pair of nucleus A. The free neutron density may vary with time, $N_n = N_n(t)$, depending on the details of the stellar model. The reaction rate depends on the time only through variations of the stellar temperature T. As a further simplification, we will assume that the temperature is constant during a given neutron irradiation episode, so that $\langle \sigma v \rangle_i = \text{const}$, until the neutron source turns off.

The reaction rate per particle pair can be substituted by the Maxwellian-averaged cross section, $\langle \sigma v \rangle_A = \langle \sigma \rangle_A v_T$ (see Eq. (3.11)). For the heavy target nuclei participating in the s-process, the reduced mass is nearly equal to the neutron mass ($m_{01} \approx m_n$). Therefore, the thermal velocity, $v_T = (2kT/m_{01})^{1/2}$, is almost independent of the target mass. Hence,

$$\begin{aligned} \frac{dN_s(A)}{dt} &= -N_n(t) N_s(A) \langle \sigma \rangle_A v_T + N_n(t) N_s(A-1) \langle \sigma \rangle_{A-1} v_T \\ &= v_T N_n(t) [-N_s(A) \langle \sigma \rangle_A + N_s(A-1) \langle \sigma \rangle_{A-1}] \end{aligned} \tag{5.174}$$

In Section 4.9.3 it was found that for a Maxwell–Boltzmann distribution of neutron energies, the flux is given by the product of neutron number density and thermal velocity, $\phi = (2/\sqrt{\pi}) N_n v_T$. We introduce the *neutron exposure* (with units of neutrons per area),

$$\tau = v_T \int N_n(t)\, dt \qquad \text{or} \qquad d\tau = v_T N_n(t)\, dt \tag{5.175}$$

which, apart from a factor $2/\sqrt{\pi}$, is equal to the time-integrated neutron flux $\Phi = \int \phi(t)\, dt$ (Section 4.9.4). Rewriting Eq. (5.174) by replacing the variable t with τ yields

$$\begin{aligned} \frac{dN_s(A,\tau)}{d\tau} N_n(t) v_T &= v_T N_n(t) \left[-N_s(A,\tau) \langle \sigma \rangle_A + N_s(A-1,\tau) \langle \sigma \rangle_{A-1} \right] \\ \frac{dN_s(A,\tau)}{d\tau} &= -N_s(A,\tau) \langle \sigma \rangle_A + N_s(A-1,\tau) \langle \sigma \rangle_{A-1} \end{aligned} \tag{5.176}$$

with the boundary conditions $N_s(56,0) = f N_s^{\text{seed}}(56)$ and $N_s(A > 56, 0) = 0$. The quantity f is the fraction of the number of ^{56}Fe seed nuclei, $N_s^{\text{seed}}(56)$, that are subjected to an exposure of neutrons. It is clear that $N_s(A,\tau)$ decreases if it becomes too large with respect to $N_s(A-1,\tau)$, and vice versa,

$$\begin{aligned} dN_s/d\tau < 0 \quad &\text{for} \quad N_s(A,\tau) > [\langle \sigma \rangle_{A-1} / \langle \sigma \rangle_A] N_s(A-1,\tau) \\ dN_s/d\tau > 0 \quad &\text{for} \quad N_s(A,\tau) < [\langle \sigma \rangle_{A-1} / \langle \sigma \rangle_A] N_s(A-1,\tau) \end{aligned} \tag{5.177}$$

The coupled equations (see Eq. (5.176)) are self-regulating in the sense that they attempt to minimize the difference $N_s(A-1,\tau)\langle \sigma \rangle_{A-1} - N_s(A,\tau)\langle \sigma \rangle_A$. In the mass regions between the magic neutron numbers, the Maxwellian-averaged cross sections are relatively large (Figure 5.67) so that the difference

$N_s(A-1,\tau)\langle\sigma\rangle_{A-1} - N_s(A,\tau)\langle\sigma\rangle_A$ becomes considerably smaller than the magnitude of either product $N_s(A,\tau)\langle\sigma\rangle_A$ or $N_s(A-1,\tau)\langle\sigma\rangle_{A-1}$. In other words, for any nucleus with a mass number removed from closed neutron shells, the abundance builds up until the destruction rate approximately equals the production rate. In these mass regions, a steady flow is achieved along the s-process path, $dN_s/d\tau \approx 0$, and we find

$$N_s(A,\tau)\langle\sigma\rangle_A \approx N_s(A-1,\tau)\langle\sigma\rangle_{A-1} \qquad \text{or} \qquad N_s(A,\tau)\langle\sigma\rangle_A \approx \text{const} \quad (5.178)$$

This result is called the *local (equilibrium) approximation* since it is only satisfied locally in regions between magic neutron numbers.

The prediction of Eq. (5.178) can be tested by considering isotopes of the element tellurium ($Z = 52$). Of eight stable isotopes, three belong to the s-only category (^{122}Te, ^{123}Te, ^{124}Te). Two can be synthesized by both the s- and r-process (^{125}Te, ^{126}Te), two are r-only isotopes (^{128}Te, ^{130}Te), and ^{120}Te is a p-nuclide. The product of solar system abundance, $N_\odot(A)$ (Lodders, Palme, and Gail, 2009), and Maxwellian-averaged cross section at $kT = 30$ keV, $\langle\sigma\rangle_A$ (Bao *et al.*, 2000), is shown in Figure 5.69 versus mass number A. It is apparent that for the s-only nuclides

$$N_\odot(122)\langle\sigma\rangle_{122} \approx N_\odot(123)\langle\sigma\rangle_{123} \approx N_\odot(124)\langle\sigma\rangle_{124} \quad (5.179)$$

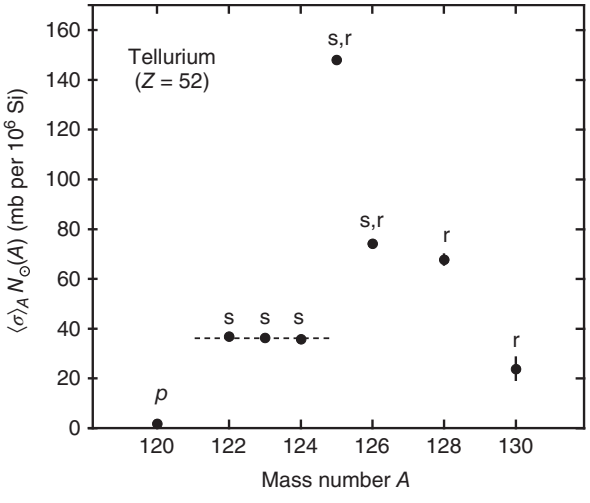

Figure 5.69 The product $N_\odot(A)\langle\sigma\rangle_A$ (in units of millibarn per 10^6 Si atoms) versus mass number A for nuclides of the element tellurium ($Z = 52$); ^{122}Te, ^{123}Te, ^{124}Te are s-only nuclides; ^{125}Te, ^{126}Te are s,r-nuclides; and ^{128}Te, ^{130}Te are r-only nuclides. ^{120}Te is not synthesized via neutron capture (p-nucleus). The Maxwellian-averaged cross sections $\langle\sigma\rangle_A$ (in units of millibarn and appropriate for a thermal energy of $kT = 30$ keV) are adopted from Bao *et al.* (2000) and the solar system abundances $N_\odot(A)$ are from Lodders (2003) (these are relative to 10^6 Si atoms). Most of the error bars are smaller than the size of the symbols. It is apparent that $N_s(A)\langle\sigma\rangle_A \approx$ const for the s-only nuclides (dashed line).

thus confirming the local approximation for the s-process. It is also clear that the product $\langle\sigma\rangle_A N_\odot(A)$ is not constant for ^{128}Te and ^{130}Te, which are both synthesized by the r-process only. Furthermore, ^{125}Te and ^{126}Te are overabundant since both the s- and the r-process contribute to their synthesis, that is, $N_\odot(A) = N_s(A) + N_r(A)$. If the averaged neutron capture cross sections are known, one can use the local approximation to estimate the separate contributions of the s- and r-process to the total observed solar system abundances (see Problem 5.13).

The local approximation is most useful for nuclides with adjacent mass numbers in regions between closed neutron shells, but does not hold over the entire $A =$ 56–209 mass range. This is seen in Figure 5.70, where the symbols show the product $N_\odot(A)\langle\sigma\rangle_A$ versus mass number A for the s-only isotopes. The $N_\odot(A)\langle\sigma\rangle_A$ values vary by a factor of ≈ 100. They decrease monotonically with increasing mass number, with particularly large variations occurring at $A \approx 84$, 138, and 208, corresponding to closed neutron shells. In the following, an expression for $N_s(A)\langle\sigma\rangle_A$ will be derived as a function of neutron exposure. We will again assume a constant temperature. It was found (Clayton *et al.*, 1961) that a single neutron exposure τ would not suffice to explain the observed $N_\odot(A)\langle\sigma\rangle_A$ values. Seeger, Fowler, and

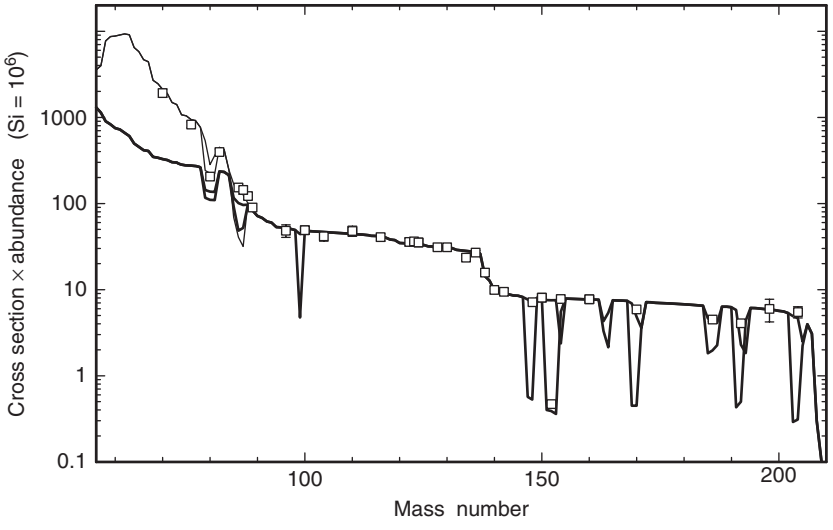

Figure 5.70 The product $N_\odot(A)\langle\sigma\rangle_A$ (in units of millibarn per 10^6 Si atoms) of solar system s-process abundance and Maxwellian-averaged neutron-capture cross section (at a thermal energy of $kT = 30$ keV) versus mass number A. The symbols correspond to s-only nuclides. The solid curves are obtained by fitting the data to an expression similar to Eq. (5.187) but which includes the effects of significant s-process branchings. The thick solid line is calculated using a single exponential distribution of neutron exposures (main s-process component). For $A \leq 90$, the main component falls below the data points and a second distribution (weak s-process component) must be included in the fit (thin solid line). The sharp structures result from s-process branchings. At these mass numbers the solid lines split into two parts, one corresponding to the more neutron-rich nuclide and the other one to the less neutron-rich nuclide. (Courtesy of Franz Käppeler.)

Clayton (1965) showed that better agreement could be obtained by adopting an exponential distribution of neutron exposures. Such a distribution reflects the physically reasonable assumption of decreased probabilities for increasing neutron exposures, that is, the total exposure experienced by some fraction of material relates to the number of times that material had been processed through successive generations of stars (Clayton, 1983) or through successive burning episodes in a specific star (Ulrich, 1973).

Suppose that f is the fraction of the number of ^{56}Fe seed nuclei, $N_s^{\text{seed}}(56)$, that has been subjected to an exponential distribution of neutron exposures, given by

$$p(\tau) = \frac{fN_s^{\text{seed}}(56)}{\tau_0} e^{-\tau/\tau_0} \tag{5.180}$$

where $p(\tau)\,d\tau$ is the fraction of ^{56}Fe seed nuclei having received an exposure in the range between τ and $\tau + d\tau$. The parameter τ_0 is the mean neutron exposure and determines how rapidly the exposure distribution falls off. The total number of irradiated seed nuclei is

$$\int_0^\infty p(\tau)\,d\tau = fN_s^{\text{seed}}(56)[-e^{-\tau/\tau_0}]_0^\infty = fN_s^{\text{seed}}(56) \tag{5.181}$$

The resulting abundances are

$$\overline{N_s(A,\tau_0)} = \frac{\int_0^\infty N_s(A,\tau)p(\tau)\,d\tau}{\int_0^\infty p(\tau)\,d\tau} = \int_0^\infty \frac{N_s(A,\tau)}{\tau_0} e^{-\tau/\tau_0}\,d\tau \tag{5.182}$$

For the first two nuclides on the s-process path, ^{56}Fe and ^{57}Fe, the abundance evolutions are given by (see Eq. (5.176))

$$\frac{dN_s(56,\tau)}{d\tau} = -N_s(56,\tau)\langle\sigma\rangle_{56} \tag{5.183}$$

$$\frac{dN_s(57,\tau)}{d\tau} = -N_s(57,\tau)\langle\sigma\rangle_{57} + N_s(56,\tau)\langle\sigma\rangle_{56} \tag{5.184}$$

For an exponential exposure distribution (see Eq. (5.180)), the solutions can be found analytically. The results are (see Problem 5.14)

$$\langle\sigma\rangle_{56}\overline{N_s(56,\tau_0)} = \frac{fN_s^{\text{seed}}(56)}{\tau_0} \frac{1}{\left[1 + \frac{1}{\tau_0\langle\sigma\rangle_{56}}\right]} \tag{5.185}$$

$$\langle\sigma\rangle_{57}\overline{N_s(57,\tau_0)} = \frac{fN_s^{\text{seed}}(56)}{\tau_0} \frac{1}{\left[1 + \frac{1}{\tau_0\langle\sigma\rangle_{56}}\right]} \frac{1}{\left[1 + \frac{1}{\tau_0\langle\sigma\rangle_{57}}\right]} \tag{5.186}$$

and so on. The general solution of Eq. (5.176) is easily deduced from these results. We find (see also Clayton and Ward, 1974)

$$\langle\sigma\rangle_A\overline{N_s(A,\tau_0)} = \frac{fN_s^{\rm seed}(56)}{\tau_0}\prod_{i=56}^{A}\frac{1}{\left[1+\frac{1}{\tau_0\langle\sigma\rangle_i}\right]} \tag{5.187}$$

Once the capture cross sections $\langle\sigma\rangle_A$ are known, a fit of this expression to the observed solar system values of $N_\odot(A)\langle\sigma\rangle_A$ for the s-only nuclides yields the parameters f and τ_0. The magnitude of these parameters, in turn, is important for identifying the sites and the history of s-process nucleosynthesis. It is interesting that, according to Eq. (5.187), the relative $\langle\sigma\rangle_A\overline{N_s(A,\tau_0)}$ values for any two nuclides (beyond the last seed nucleus) on the s-process path are independent of the true distribution of seed nuclei (Clayton and Ward, 1974). Hence, the particular choice of pure ^{56}Fe as seed material is as good as any other distribution of iron peak nuclides. On the other hand, this also means that the observed solar system $N_\odot(A)\langle\sigma\rangle_A$ values for the s-only nuclides are not a sensitive probe of the initial seed distribution. A useful quantity is the average number of neutrons captured per ^{56}Fe seed nucleus,

$$\mathrm{n}_c = \frac{\sum_{A=56}^{209}(A-56)\overline{N_s(A,\tau_0)}}{fN_s^{\rm seed}(56)} = \frac{1}{\tau_0}\sum_{A=56}^{209}\frac{(A-56)}{\langle\sigma\rangle_A}\prod_{i=56}^{A}\frac{1}{\left[1+\frac{1}{\tau_0\langle\sigma\rangle_i}\right]} \tag{5.188}$$

Its magnitude provides another constraint on the physical environment. For two nuclides of adjacent mass numbers, one finds from Eq. (5.187)

$$\langle\sigma\rangle_A\overline{N_s(A,\tau_0)} = \frac{\langle\sigma\rangle_{A-1}\overline{N_s(A-1,\tau_0)}}{\left[1+\frac{1}{\tau_0\langle\sigma\rangle_A}\right]} \tag{5.189}$$

Between closed neutron shells, the capture cross section $\langle\sigma\rangle_A$, and thus the product $\tau_0\langle\sigma\rangle_A$, is large. Therefore, we find from Eq. (5.189) $\langle\sigma\rangle_A\overline{N_s(A,\tau_0)} \approx \langle\sigma\rangle_{A-1}\overline{N_s(A-1,\tau_0)}$, consistent with the local approximation discussed above. Near closed neutron shells the cross section $\langle\sigma\rangle_A$, and thus $\tau_0\langle\sigma\rangle_A$, is relatively small. Consequently, the denominator in the above expression becomes relatively large, producing a step in the distribution of $\langle\sigma\rangle_A\overline{N_s(A,\tau_0)}$ values. In other words, the small capture cross sections of the neutron magic nuclides represent bottlenecks for a continuous abundance flow. The resulting steps are seen in Figure 5.70 at mass numbers of $A \approx 84$, 138, and 208, corresponding to closed neutron shells. The height and shape of the steps are sensitive to the magnitude of the mean neutron exposure τ_0, while the fraction f acts as an overall scaling factor.

The solid curves in Figure 5.70 are obtained by fitting the data for $N_\odot(A)\langle\sigma\rangle_A$ to an expression similar to Eq. (5.187). The sharp structures result from s-process branchings that will be discussed later. The thick solid line is calculated using a single exponential distribution of neutron exposures. It describes all the observed $N_\odot(A)\langle\sigma\rangle_A$ values for s-only nuclides in a wide range from $A = 90$ to $A = 205$ and is called the *main s-process component*. The mean square deviation between the thick solid line and the data points in Figure 5.70 is only 3% (Käppeler *et al.*, 1990).

This excellent agreement is remarkable considering that the main component is represented by a single exponential distribution of neutron exposures with only the scaling factor and the mean neutron exposure as fitting parameters. The fit gives values of $f \approx 0.06\%$, where it is assumed that the number of seed nuclei is equal to the solar system abundance of ^{56}Fe, $\tau_0 \approx 0.3$ mb^{-1} (for cross sections $\langle\sigma\rangle_A$ at $kT = 30$ keV), and $n_c \approx 10$ (Käppeler *et al.*, 1990). These results imply that the main s-process component was produced by irradiating only 0.06% of the solar system ^{56}Fe nuclei with neutrons, while each ^{56}Fe seed nucleus captured on average about 10 neutrons. For mass numbers of $A < 90$, the thick solid line falls below the data points. Therefore, a second component is required to explain the synthesis of the s-process nuclides in this lower mass range. It is called the *weak s-process component* and is shown as the thin solid line in Figure 5.70. Käppeler *et al.* (1990) find for this component values of $f \approx 1.6\%$, $\tau_0 \approx 0.07$ mb^{-1}, and $n_c \approx 3$, that is, a lower mean neutron exposure and a higher fraction of irradiated seed nuclei compared to the main component. Only in the Pb–Bi mass region, close to the termination point of the s-process, does the two-component model give an unsatisfactory description. In particular, more than 50% of the solar system ^{208}Pb abundance cannot be accounted for in this way. Therefore, a third component has been postulated (Clayton and Rassbach, 1967). It is called the *strong s-process component*, for which parameters of $f \approx 10^{-4}\%$, $\tau_0 \approx 7$ mb^{-1}, and $n_c \approx 140$ have been reported in Käppeler *et al.* (1990). In this case, the mean neutron exposure is so large that on average about 140 neutrons are captured per seed nucleus to convert a very small fraction of ^{56}Fe nuclei to nuclides in the mass region between ^{206}Pb and ^{209}Bi. As will be seen below, it is unlikely that these three vastly different neutron exposures can be obtained in a single astrophysical site. It is more reasonable to assume that different sites are required to explain each of the observed s-process components.

Both the observed $N_\odot(A)\langle\sigma\rangle_A$ values and the calculated solid lines in Figure 5.70 are obtained for a constant s-process temperature of $kT = 30$ keV (or $T = 0.35$ GK). This particular value is traditionally used in discussions of the phenomenological s-process model described here. However, a precise value for the s-process temperature cannot be deduced easily by matching observed $N_\odot(A)\langle\sigma\rangle_A$ values with calculated $\langle\sigma\rangle_A \overline{N_s(A,\tau_0)}$ curves (except when analyzing branching ratios; see later) because most of the neutron-capture cross sections vary in a similar manner with temperature (Section 3.2.2 and Figure 3.32). Instead, the shape of the $\langle\sigma\rangle_A \overline{N_s}(A,\tau_0)$ curve will provide information about the mean neutron exposure τ_0 when the temperature has been selected by other means (see also Seeger, Fowler, and Clayton, 1965).

In the derivation of Eq. (5.187), it was explicitly assumed that all neutron capture rates on unstable nuclides are either considerably faster ($\lambda_\beta \ll \lambda_{n\gamma}$) or considerably slower ($\lambda_\beta \gg \lambda_{n\gamma}$) than the competing β^--decay rates so that the s-process path is uniquely defined at each mass number A. At certain locations along the s-process path, however, the abundance flow encounters unstable nuclides with decay constants (or half-lives) that are comparable in magnitude to the competing neutron capture rates, $\lambda_\beta \approx \lambda_{n\gamma}$. At these locations the s-process path splits

into two branches. These s-process *branchings* can also be incorporated into the phenomenological s-process model described above if one assumes that the neutron density, $N_n(t)$, in addition to the temperature, is constant with time. In this case, the s-process branchings can be described analytically (Ward, Newman, and Clayton, 1976). Otherwise, the abundance evolutions must be solved by numerical integration.

Consider a simple example of the situation shown in Figure 5.68c. At the unstable nucleus of mass number A', the abundance flow splits into two parts because its β^--decay rate is comparable in magnitude to the rate of the competing neutron capture. The unstable nucleus A' becomes a branch point for the s-process path. Only a fraction of the flow passes through stable nucleus A. But the entire flow passes through *stable* nucleus $A+1$ since we assume that the β^--decay of *unstable* nucleus $A'+1$ is considerably faster than the competing neutron capture. If the branch point is located in a mass region between closed neutron shells, then Eq. (5.178) has to be replaced by

$$N_s(A,\tau)\langle\sigma\rangle_A + N_s(A',\tau)\langle\sigma\rangle_{A'} \approx N_s(A+1,\tau)\langle\sigma\rangle_{A+1} \tag{5.190}$$

The ratio $N_s(A,\tau)\langle\sigma\rangle_A / N_s(A+1,\tau)\langle\sigma\rangle_{A+1}$ defines a branching ratio, B, which can also be expressed in terms of the decay constants of nucleus A' as

$$\begin{aligned} B &\equiv \frac{N_s(A,\tau)\langle\sigma\rangle_A}{N_s(A+1,\tau)\langle\sigma\rangle_{A+1}} = \frac{\lambda_\beta(A')}{\lambda_\beta(A') + \lambda_{n\gamma}(A')} \\ &= \frac{\ln 2/T_{1/2}(A')}{\ln 2/T_{1/2}(A') + N_n\langle\sigma\rangle_{A'} v_T} \end{aligned} \tag{5.191}$$

With $N_n\langle\sigma v\rangle_{A'} = N_n\langle\sigma\rangle_{A'} v_T$, we obtain

$$\begin{aligned} N_n &= \left[\frac{N_s(A+1,\tau)\langle\sigma\rangle_{A+1}}{N_s(A,\tau)\langle\sigma\rangle_A} - 1\right] \frac{1}{\langle\sigma\rangle_{A'} v_T} \frac{\ln 2}{T_{1/2}(A')} \\ &= \left(\frac{1-B}{B}\right) \frac{1}{\langle\sigma\rangle_{A'} v_T} \frac{\ln 2}{T_{1/2}(A')} \end{aligned} \tag{5.192}$$

Hence, the analysis of branchings yields the neutron density, which is an important parameter for determining the physical conditions during the s-process. A precise value of N_n provides a strong constraint for stellar models of s-process sites.

Equation (5.192) describes the simplest case of an s-process branching. In reality, more extensive expressions are required for most branchings since each one has its own complications, for example, the interplay of several branchings, or isomeric states. Nevertheless, Eq. (5.192) contains the important physics and, in particular, emphasizes the input data needed for a reliable extraction of the physical conditions from branching analyses. The first term, $(1-B)/B$, depends on the ratio of abundances for the stable nuclides A and $A+1$ and on the ratio of their neutron-capture cross sections. Depending on the value of B, these input values have to be known to about $\pm 1\%$ for many branchings so that the neutron density can be extracted with an uncertainty of, say, $\pm 10\%$. It is of advantage if A and $A+1$ are s-only nuclides, since in this case their abundances do not have

to be corrected for r-process contributions. Also, since they are isotopes of the same element their relative abundances are accurately known (Lodders, Palme, and Gail, 2009). Very precise capture cross section measurements involving these stable target nuclei are crucial as well (Sections 4.6.2 and 4.6.3; see also Käppeler, 1999). The second term in Eq. (5.192) contains the Maxwellian-averaged capture cross section for the radioactive branching point nucleus A'. In the past, no data existed for these reactions, and the cross sections had to be estimated using the Hauser–Feshbach theory. However, a number of cross section measurements involving radioactive branching point nuclides have been performed (see, e.g., Jaag and Käppeler, 1995; Reifarth *et al.*, 2003; Abbondanno *et al.*, 2004). Also, measured capture cross sections have to be corrected for (theoretical) stellar enhancement factors since the quantity $\langle\sigma\rangle_{A'}$ in Eq. (5.191) refers to the *stellar* cross section (Section 3.1.5). The third term in Eq. (5.192) represents the *stellar* half-life of the branching point nucleus A' and the corresponding stellar enhancement factors are based on nuclear theory (Takahashi and Yokoi, 1987). In some cases, no difference exists between the terrestrial and the stellar half-life value. For other branching point nuclides, however, the stellar half-life is very sensitive to the precise temperature or density conditions in the plasma (Section 1.8.4).

There are about 15–20 significant branchings on the s-process path. The following strategy is then employed to derive estimates for the physical conditions of the s-process. First, the mean neutron density is deduced by analyzing those branchings that are nearly independent of temperature and density. With this information, the stellar β-decay half-lives are determined from other branchings that depend sensitively on temperature (or density). Finally, the known temperature (or density) dependence of these half-lives yields estimates for the mean s-process temperature (or electron density). By considering several different branchings together, one can then attempt to derive a set of parameters that characterizes the average physical conditions during the s-process. The results thus obtained from the study of s-process branchings (N_n, T, ρ) and from the global fit to the observed $N_\odot(A)\langle\sigma\rangle_A$ distribution for s-only nuclides (f, τ_0 or n_c) represent important constraints for stellar models and the identification of the astrophysical sites of the s-process. For more information, see Käppeler (1999).

The empirical s-process described above is called the *classical s-process model*. It is very simple since it disregards the time dependence of s-process parameters, such as neutron density and stellar temperature. It provides a satisfactory description of most observed $N_\odot(A)\langle\sigma\rangle_A$ values for s-only nuclides over the entire mass region of interest, requiring only a relatively small number of adjustable parameters. The classical s-process model makes no assumption on the stellar site or the specific reactions that act as neutron sources. In view of these restrictions, the classical model offers remarkable insight into the s-process.

We already pointed out that the shape of the $N_\odot(A)\langle\sigma\rangle_A$ distribution for s-only nuclides is a measure for the total number of neutron captures to which seed nuclei have been subjected and, therefore, it contains the global history of the s-process. However, the composition of the interstellar gas out of which the solar

system formed reflects a mixture of the ejecta of countless stars. The composition has been homogenized by interstellar mixing to the degree where it represents the average rate of nucleosynthesis up to the time of solar system formation. The stars that provided the sites for the s-process had certainly a range of masses and metallicities. It is clear from these arguments that a single set of average parameters (f, τ_0, N_n, T, ρ) derived from the $N_\odot(A)\langle\sigma\rangle_A$ distribution does not correspond directly to the properties of any single model star. For this reason, one must be careful when using such average parameters to constrain stellar s-process models.

The limitations of the classical s-process model became apparent with the availability of precisely measured neutron-capture cross sections (Käppeler, 1999; Bao *et al.*, 2000). It was shown, for example, that the classical model significantly overproduces ^{142}Nd (Arlandini *et al.*, 1999). Such results imply that the distribution of neutron exposures during the s-process differs from a simple exponential function (see Eq. (5.180)). Further evidence came from s-process branchings. Analyses of the branching point nuclides ^{147}Pm, ^{185}W, and ^{192}Ir with the classical model gave for the neutron density values of $N_n = (4.94^{+0.60}_{-0.50}) \times 10^8$ cm^{-3} (Reifarth *et al.*, 2003), $(4.7^{+1.4}_{-1.1}) \times 10^8$ cm^{-3} (Mohr *et al.*, 2004), and $(7.0^{+0.5}_{-0.2}) \times 10^7$ cm^{-3} (Koehler *et al.*, 2002), respectively. Similarly, classical analyses of the temperature-sensitive branching point nuclides ^{176}Lu, ^{151}Sm, and ^{128}I yielded values of $T = 0.30 \pm 0.05$ GK (Doll *et al.*, 1999), ≈ 0.4 GK (Abbondanno *et al.*, 2004), and ≈ 0.093 GK (Reifarth, 2002), respectively. The classical s-process model provides neither a consistent solution for the neutron density nor for the temperature. A more sophisticated approach, based on realistic stellar models, is required to reproduce all the observed s-process abundances.

We now turn to a discussion of stellar models that currently best reproduce the observed s-process abundance pattern. The main s-process component is thought to originate from thermally pulsing, low-mass ($1.5–3\,M_\odot$) AGB stars (Section 1.4.3; see also Busso, Gallino, and Wasserburg, 1999). After a thermal pulse and third dredge up event, some protons from the convective envelope mix into the radiative intershell (see Figure 1.6), which consists mainly of ^{4}He ($\approx 75\%$ by mass) and ^{12}C ($\approx 25\%$ by mass). The nature of this mixing mechanism is not understood at present, and its magnitude is usually described by a free parameter in stellar models. The protons that are mixed downward initiate the sequence

$$^{12}\mathrm{C}(\mathrm{p},\gamma)^{13}\mathrm{N}(\beta^+\nu)^{13}\mathrm{C}(\mathrm{p},\gamma)^{14}\mathrm{N} \tag{5.193}$$

giving rise to two separate thin regions near the top of the intershell that are rich in ^{13}C and ^{14}N and are referred to as the ^{13}C *pocket* and the ^{14}N *pocket*, respectively. When the temperature reaches $T \approx 0.09$ GK (or $kT \approx 8$ keV), the mean lifetime of ^{13}C versus destruction by the ^{13}C(α,n)^{16}O reaction becomes smaller than the time between the two thermal pulses. Hence, neutrons are released during the inter pulse period within the ^{13}C pocket under radiative conditions and are captured by preexisting seed nuclei (mainly Fe and s-process material from the previous pulse) to produce most of the nuclides in the main component of

the s-process. The neutron flux lasts typically ≈ 20 000 y and produces locally high neutron exposures (≈ 0.1 mb^{-1}). Since the time scale is long, however, the neutron density remains low ($N_n \approx 10^7$ cm^{-3}). Only a small number of reaction branchings occur since the β^--decay constant exceeds the neutron-capture decay constant in most cases. During this time, ^{13}C is entirely consumed in the thin ^{13}C pocket. The temperature achieved at this evolutionary stage is not sufficient for initiating the $^{14}N(\alpha,\gamma)^{18}O$ reaction. During hydrogen-shell burning, the mass of the intershell increases steadily (and so do temperature and density), up to a point where the He at the bottom of the intershell ignites. This *thermal He pulse* (labeled "TP" in Figure 1.6) grows outward until it almost reaches the H-burning shell. The large energy release also causes the stellar envelope to expand and extinguishes the H-burning shell. The thermal pulse engulfs the ashes of H-shell burning. It gives rise to higher temperatures ($T \approx 0.27$ GK or $kT \approx 23$ keV), initiating the sequence

$$^{14}N(\alpha,\gamma)^{18}F(\beta^+\nu)^{18}O(\alpha,\gamma)^{22}Ne \tag{5.194}$$

As a consequence, the $^{22}Ne(\alpha,n)^{25}Mg$ neutron source is (marginally) activated and a second neutron burst occurs. Here, the time scale amounts to a few years, with neutron exposures of ≈ 0.01 mb^{-1} and a peak neutron density of $N_n \approx 10^{10}$ cm^{-3}. This second neutron burst does not contribute considerably to the overall production of the s-process nuclides. It does, however, significantly influence the s-process branchings that are operating more efficiently at the higher temperatures. After the thermal pulse, the He shell becomes inactive, the envelope contracts, and the H shell ignites again. The cycle can repeat tens to hundreds of times. For more information, see Busso, Gallino, and Wasserburg (1999) or Habing and Olofsson (2004).

Figure 5.71 demonstrates how well current stellar models of thermally pulsing AGB stars reproduce the solar system abundance distribution of s-process nuclides. The results were obtained for a model star with a mass of $1.5\,M_\odot$ and a metallicity of $Z = 0.01$ (Arlandini *et al.*, 1999). Abundances are shown as overproduction factors, that is, as ratios of predicted abundances and the corresponding solar system values. The solid circles represent s-only nuclides. The agreement is remarkable, especially since the solar system s-process abundances of the main component are most likely the products of countless low-mass AGB stars with a range of masses and metallicities. It is also evident that these stars cannot account for the weak s-process component ($A < 90$).

Stellar model studies of thermally pulsing, low-mass AGB stars (Gallino *et al.*, 1998) revealed that variations in stellar metallicity have a strong effect on the resulting total neutron exposure. In this scenario, the $^{13}C(\alpha,n)^{16}O$ or $^{22}Ne(\alpha,n)^{25}Mg$ reactions are referred to as *primary* neutron sources, because the ^{13}C or ^{14}N (and hence, ^{22}Ne) are produced in the star itself from the available hydrogen and ^{12}C. For decreasing metallicity, more neutrons per iron seed nuclei are available from these sources and, consequently, heavier nuclides can be synthesized. The increased neutron exposure during s-processing in early generation, metal-poor AGB stars causes an accumulation of material at the end of the

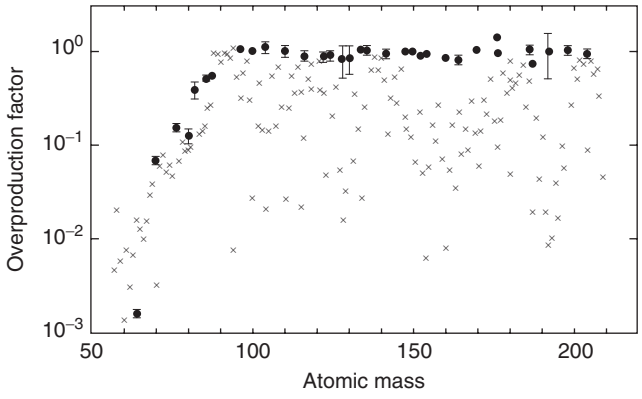

Figure 5.71 Abundance distribution resulting from s-process studies of a thermally pulsing AGB star of mass 1.5 $M_\odot$ and metallicity $Z = 0.01$. Abundances are shown as overproduction factors, that is, as ratios of predicted abundances and the corresponding solar system values, normalized to ^{150}Sm. It is evident that the stellar model reproduces the solar system abundances for the s-only nuclides (solid circles) of the main s-process component ($A > 90$). Even the abundances of those s-only nuclides are reproduced that are partially bypassed by the flow because of nearby branchings. Crosses represent all the other heavy nuclides produced in the s-process. Their overproduction factors are less than unity since they are also synthesized by the r-process. (From Arlandini *et al.* (1999). © IOP Publishing. Reproduced by permission of IOP Publishing. All rights reserved.)

s-process path (^{208}Pb and ^{209}Bi). These objects provide a natural explanation for the strong s-process component (Gallino *et al.*, 1998; Travaglio *et al.*, 2001).

A major fraction of the weak s-process component is believed to originate from the core helium burning stage in massive stars with $M \geq 13\,M_\odot$ (Sections 1.4.3 and 5.2.3; see also Peters, 1968). The ^{14}N nuclei produced by the CNO cycles during the preceding hydrogen burning stage are rapidly transformed to ^{22}Ne via $^{14}\mathrm{N}(\alpha,\gamma)^{18}\mathrm{F}(\beta^+\nu)^{18}\mathrm{O}(\alpha,\gamma)^{22}\mathrm{Ne}$ at the beginning of the helium burning stage. But only near helium exhaustion in the core has the temperature risen sufficiently ($T \geq 0.25$ GK or $kT \geq 22$ keV) to ignite the $^{22}\mathrm{Ne}(\alpha,\mathrm{n})^{25}\mathrm{Mg}$ neutron source. More massive stars burn at higher core temperature and thus consume a larger quantity of ^{22}Ne. Therefore, they give rise to a more efficient s-process compared to less massive stars. Total consumption of ^{22}Ne occurs only in very massive stars. If some of the ^{22}Ne survives at the end of core helium burning, the $^{22}\mathrm{Ne}(\alpha,\mathrm{n})^{25}\mathrm{Mg}$ neutron source is reactivated during carbon burning by α-particles that are released by the primary $^{12}\mathrm{C} + {}^{12}\mathrm{C}$ reaction (Section 5.3.1). Core carbon burning is not a promising s-process site since, first, the core matter will not be ejected in the subsequent supernova explosion and, second, any s-process nuclides will be destroyed later via photodisintegration reactions during core oxygen burning (Section 5.3.3). However, the situation is different for convective shell carbon burning, where stellar models predict s-processing with a neutron exposure comparable to that achieved during the previous core helium burning stage. The situation is schematically depicted on the left-hand side of Figure 1.7, showing

the pre-supernova structure of a massive star. Any s-process nuclides present in the innermost regions outside the iron core will be destroyed during the subsequent explosive burning stages caused by the passage of the shock. The next layer, which experienced shell carbon burning including s-processing (labeled "C_S"), will be ejected with a composition almost unchanged by the explosion. The layer labeled "He_C", on top of the convective carbon shell, is a remnant of core helium burning, with a composition unchanged by other hydrostatic burning stages. These two layers carry the bulk of the weak s-process component. The layer further out experiences convective shell helium burning (labeled "He_S") and may also contribute to the s-process abundances, depending on the temperature achieved at the bottom of the shell, although stellar models differ in their predictions. Finally, this shell could also be affected by the passing supernova shock, since any ^{22}Ne nuclei present would activate the ^{22}Ne(α,n)^{25}Mg neutron source, and thereby modify the pre-explosion s-process yields.

Three aspects are especially important when discussing the *neutron economy* during weak s-process nucleosynthesis: (i) the abundance of the neutron source nuclei (^{22}Ne), (ii) the abundance of the seed nuclei (^{56}Fe and other iron-peak species), and (iii) the abundances of any *neutron poisons*. The latter expression refers to nuclides which capture neutrons that would otherwise contribute to the s-process. For example, the neutron source ^{22}Ne(α,n)^{25}Mg is sometimes called *self-poisoning* because the product nucleus ^{25}Mg has a relatively high cross section for neutron capture. A significant fraction of the produced neutrons is removed in this way without synthesizing nuclides in the $A = 65$–90 region, thus constraining the s-process efficiency. In this scenario, the ^{22}Ne(α,n)^{25}Mg reaction is also referred to as a *secondary* neutron source since ^{14}N (i.e., the progenitor of ^{22}Ne) is not produced in the star itself. Both the number of neutrons released by ^{22}Ne(α,n)^{25}Mg and the amount of iron-peak seed nuclei (mainly ^{56}Fe) scale with stellar metallicity, while the neutron-to-seed ratio is metallicity independent. On the other hand, ^{12}C and ^{16}O are *primary* nuclides since they are produced within the star itself. Their neutron capture cross sections are relatively small, but their abundances become large during helium burning. Therefore, the ^{12}C(n,γ)^{13}C and ^{16}O(n,γ)^{17}O reactions could represent important sinks of neutrons, especially if the stellar metallicity is small. Detailed calculations have shown that, independent of metallicity, ^{12}C does not represent an important neutron poison because the lost neutrons are recycled, and thus recovered, by the sequence ^{12}C(n,γ)^{13}C(α,n)^{16}O. The situation is different for ^{16}O, where the sequence ^{16}O(n,γ)^{17}O(α,n)^{20}Ne competes with ^{16}O(n,γ)^{17}O(α,γ)^{21}Ne. The neutrons are recovered in the former case, but are lost for the s-process in the latter case. Hence, ^{16}O most likely represents an important neutron poison in low metallicity massive stars (Rayet and Hashimoto, 2000). The strong metallicity dependence of the weak s-process component is important because it may be used to study the role of massive stars in the early phase of galactic chemical evolution.

Some important aspects of the weak s-process component derived from massive stars will be illustrated in the following. The evolution of central

temperature and density from the end of core hydrogen burning to the end of core helium burning for a $25\,M_\odot$ star with initial solar system composition is shown in Figure 5.72. At the end of core hydrogen burning, the most abundant nuclides are ^{4}He ($X_\alpha = 0.982$), ^{14}N ($X_{^{14}\mathrm{N}} = 0.0122$), ^{20}Ne ($X_{^{20}\mathrm{Ne}} = 0.0016$), and ^{56}Fe ($X_{^{56}\mathrm{Fe}} = 0.00117$). The other abundances are given by their respective solar system values. Using this temperature–density profile and the initial abundances, we will perform a core helium burning (postprocessing) reaction network calculation. The results are presented in Figure 5.72. The neutron capture rates are adopted from the compilation of Bao *et al.* (2000), while temperature- and density-dependent weak interaction rates are taken from Raiteri *et al.* (1993). Energy is produced via the helium burning sequence $\alpha(2\alpha)^{12}\mathrm{C}(\alpha,\gamma)^{16}\mathrm{O}$ (Section 5.2.2). At the end of the calculation, the mass fractions of ^{12}C and ^{16}O amount to 0.22 and 0.75, respectively. We will now discuss processes related to the production and consumption of neutrons. As already noted, the nuclide ^{14}N is converted via the sequence $^{14}\mathrm{N}(\alpha,\gamma)^{18}\mathrm{F}(\beta^+\nu)^{18}\mathrm{O}(\alpha,\gamma)^{22}\mathrm{Ne}$ (Section 5.2.3) while, subsequently, the $^{22}\mathrm{Ne}(\alpha,\mathrm{n})^{25}\mathrm{Mg}$ neutron source competes with the $^{22}\mathrm{Ne}(\alpha,\gamma)^{26}\mathrm{Mg}$ reaction. The most important neutron poison reaction is $^{25}\mathrm{Mg}(\mathrm{n},\gamma)^{26}\mathrm{Mg}$, followed by $^{22}\mathrm{Ne}(\mathrm{n},\gamma)^{23}\mathrm{Ne}$. The sequence $^{12}\mathrm{C}(\mathrm{n},\gamma)^{13}\mathrm{C}(\alpha,\mathrm{n})^{16}\mathrm{O}$ shows a significant abundance flow but, in terms of the neutron economy, it is neither a net producer nor a net destroyer of neutrons (see also Section 5.3.1). Moving up in mass, a network of (n,γ), (n,α), (n,p) reactions and β^--decays stretches from Al to the iron-peak group. Although the s-process in massive stars is usually interpreted as a way to produce the weak component, a number of lighter nuclides in the $A = 35$–45 mass range is also synthesized. The s-process in massive stars has been suggested to be a major source of ^{36}S, ^{37}Cl, ^{40}Ar, and ^{40}K in the universe (see Table 5.2). An increased nuclear activity is seen in the iron peak region. Starting mainly from ^{56}Fe seed nuclei, sequences of neutron captures and β^--decays give rise to a typical s-process flow pattern and synthesize nuclides in the $A = 60$–90 region, that is, the weak component of the s-process. Smaller abundance flows extend beyond $A = 90$ and are not shown in Figure 5.72. The neutron exposure and peak neutron density typically amount to ≈ 0.2 mb^{-1} and $N_\mathrm{n} \approx 10^7$ cm^{-3}, respectively. Most of the ^{22}Ne consumption occurs at the end of the burning, with less than 10% of helium remaining in the core, when the temperature increases from $T \approx 0.27$ GK to 0.30 GK, and the density climbs from $\rho = 1800$ g/cm^3 to 2600 g/cm^3 (The, El Eid, and Meyer, 2000). This temperature–density range is labeled "S" in Figure 5.72.

For stars with masses of $M < 30\,M_\odot$, the partial survival of ^{22}Ne at the end of core helium burning offers the opportunity for another episode of s-processing during carbon shell burning, as discussed above. The higher temperatures achieved here ($kT \approx 90$) give rise to high peak neutron densities ($N_\mathrm{n} \approx 10^{11}$ cm^{-3}), which significantly alter the weak s-process abundance pattern established during core helium burning. Figure 5.73 shows overabundances of nuclides relative to their solar system values. The results are obtained from a stellar model calculation of a $25\,M_\odot$ star with solar initial metallicity after the completion of core helium and shell carbon burning. The diamonds indicate

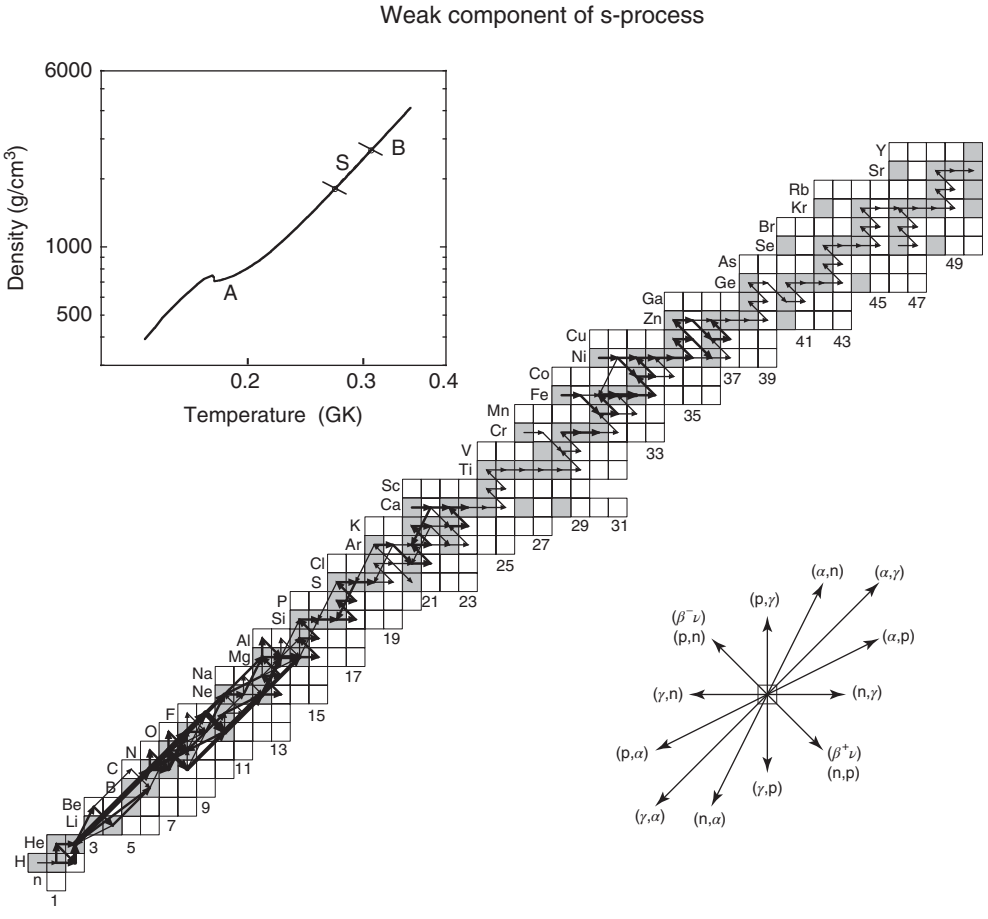

Figure 5.72 Time-integrated net abundance flows during core helium burning. The evolution of central temperature and density, shown in the inset, from the end of core H burning (A) to the end of core He burning (B) is adopted from stellar model studies of a 25 $M_\odot$ star with initial solar system composition (The, El Eid, and Meyer, 2000). The numerical network calculation is terminated after $t = 6 \times 10^{12}$ s (the time it takes the star to evolve from A to B). The arrows have the same meaning as in Figure 5.26, except that four different thicknesses are used, with each thickness representing a flow range of two orders of magnitude. The abundance flows are defined here in terms of mole fractions rather than number densities since the mass density varies. The flow pattern in the $A =$ 60–90 region reflects the weak component of the s-process. Most of the s-processing occurs toward the end of He burning for T–ρ conditions that are marked by "S" in the inset.

s-only nuclides. The large overproduction values in the $A = 60$–90 mass range are evident. Some lighter nuclides ($A < 50$) are also overproduced. The efficiency of the s-process in massive stars declines rapidly beyond $A = 90$. The two locations of the weak s-process component, in the carbon–oxygen layer (labeled "He_C";

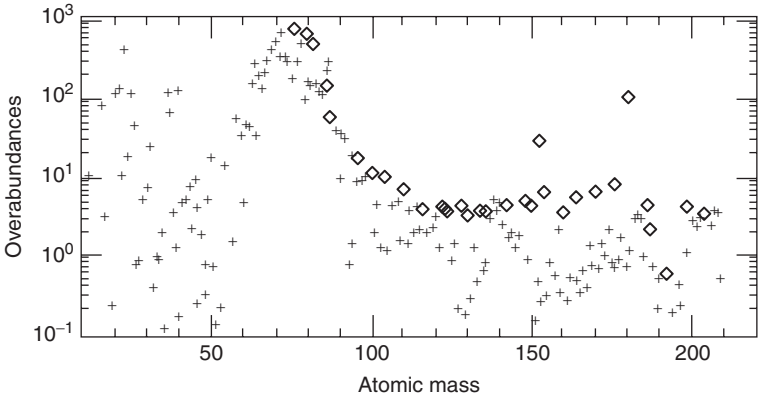

Figure 5.73 Overabundances of heavy nuclides relative to their solar system values after the completion of core helium and shell carbon burning. The results are obtained from a stellar model calculation of a 25 $M_\odot$ star with solar initial metallicity. The diamonds indicate s-only nuclides. The large overproduction values in the $A = 60$–90 mass range are evident. The efficiency of the s-process in massive stars declines rapidly beyond $A = 90$. (From Raiteri *et al.* (1991). © IOP Publishing. Reproduced by permission of IOP Publishing. All rights reserved.)

a remnant of core helium burning) and the oxygen–neon layer (resulting from shell carbon burning), are schematically shown in Figure 1.7 (left side). The latter layer has been predicted to be a major source of the important γ-ray emitter ^{60}Fe (Limongi and Chieffi, 2006).

The experimental information for reactions important to s-process nucleosynthesis is briefly described below. The ^{13}C(α,n)^{16}O reaction ($Q = 2216$ keV), responsible for the synthesis of the main s-process component in low-mass AGB stars, has been measured down to a center-of-mass energy of $E_\alpha^{\rm cm} = 280$ keV (Drotleff *et al.*, 1993). The Gamow peak for $T \approx 0.09$ GK is located at $E_0 \pm \Delta/2 = 190 \pm 40$ keV. The reaction rates in the astrophysically important temperature range are found by extrapolating the existing low-energy data, including the high-energy wing of a subthreshold resonance ($E_r^{\rm cm} = -3$ keV). The present uncertainty of this rate is a factor of ≈ 4 at $T = 0.09$ GK (Angulo *et al.*, 1999). This uncertainty seems to have a negligible influence on models of low-mass AGB stars (Cristallo, Straniero, and Gallino, 2005). The situation is different for the ^{22}Ne(α,n)^{26}Mg neutron source ($Q = -478$ keV). Here, the Gamow peak near $T \approx 0.25$ GK (the lower temperature limit where this neutron source becomes operational) is located at $E_0 \pm \Delta/2 = 540 \pm 120$ keV, while the lowest lying measured resonance occurs at $E_r^{\rm cm} = 704$ keV. Several studies have focused on the possible contribution from an undetected natural-parity resonance near $E_r^{\rm cm} = 538$ keV. However, it could be unambiguously shown that this resonance has unnatural parity and, consequently, does not contribute to the ^{22}Ne(α,n)^{26}Mg neutron source (Longland *et al.*, 2009). The rates for this reaction are controversial at present since several other natural-parity states

exist in ^{26}Mg between the α-particle threshold and the lowest lying measured resonance. Jaeger *et al.* (2001) and Karakas *et al.* (2006) estimate a factor of ≈ 2 uncertainty for the rate near $T \approx 0.25$ GK. Even a factor of two uncertainty in the rate has a strong influence on the nucleosynthesis, both in low-mass AGB stars (Pignatari *et al.*, 2005) and massive stars (The, El Eid, and Meyer, 2000). The ^{22}Ne(α,γ)^{26}Mg reaction is also important in this respect since it competes with the (α,n) reaction in the destruction of ^{22}Ne without producing neutrons. The *recommended* rates for the ^{22}Ne(α,n)^{25}Mg and ^{22}Ne(α,γ)^{26}Mg reactions are of similar magnitude at $T \approx 0.25$ GK (Longland, Iliadis, and Karakas, 2012), but the present errors are too large to determine which reaction channel dominates near this temperature value. The ratio of rates for ^{17}O(α,n)^{20}Ne and ^{17}O(α,γ)^{21}Ne is also poorly known at present. These reactions are important for defining the role of ^{16}O as a neutron poison in massive stars (Rayet and Hashimoto, 2000).

For neutron-induced reactions in various s-process scenarios, Maxwellian-averaged cross sections have to be known at energies ranging from $kT \approx 8$ keV in low-mass AGB stars to $kT \approx 90$ keV during shell carbon burning in massive stars. The averaged (n,γ) cross reactions for the neutron poisons ^{12}C, ^{16}O, ^{22}Ne, and ^{25}Mg are experimentally known to better than ±10% (Bao *et al.*, 2000). The most important neutron poison reaction in low-mass AGB stars is ^{14}N(n,p)^{14}C (Lugaro *et al.*, 2003). In this case, the present uncertainties in the averaged cross sections are somewhat larger (see Wagemans *et al.*, 2000, and references therein), and more accurate values are desirable.

For a large number of nuclides in the mass region $A \leq 210$, Maxwellian-averaged neutron-capture cross sections are compiled in Bao *et al.* (2000) for s-process conditions. The required data accuracy is different for charged-particle-induced reaction rates compared to neutron-capture reaction rates. In the former case, few reaction rates have been determined experimentally with uncertainties of less than 10%. In the latter case, however, cross sections with uncertainties of $\leq 5\%$ are essential for modeling s-process scenarios. Recall that nuclides near the neutron magic numbers $N = 50$, 82, and 126 act as bottlenecks for the abundance flow. In this case, the desired accuracy in the neutron capture cross section is $\leq 3\%$. Even more accurate capture cross sections ($\leq 1\%$) are required for s-only isotopes. These nuclides represent crucial normalization points for the s-process abundance distribution and are also important for the analysis of s-process branchings. For many of the important neutron-capture reactions the required level in cross section accuracy has been reached, and the reliability of current cross section data sets for modeling s-process scenarios is impressive (Bao *et al.*, 2000). Nevertheless, additional and more accurately measured cross sections are needed for a number of reactions, including (n,γ) reactions on short-lived branching point nuclides (Jaag and Käppeler, 1995; Reifarth *et al.*, 2003; Abbondanno *et al.*, 2004). Theoretical reaction rates are also indispensable for s-process calculations. The (n,γ) rates for many short-lived branching point nuclides are currently based on the Hauser–Feshbach theory (Section 2.7). These rates can be calculated using *local* nuclear model parameters that are obtained via

interpolation from neighboring nuclides. Such results are more reliable compared to neutron capture rates for nuclides far from the stability valley, where *global* parameter sets must be employed. Furthermore, stellar enhancement factors (Section 3.1.5) must be estimated using theoretical nuclear models. Calculations indicate that (n,γ) reactions on 25% of all nuclides involved in the s-process have stellar enhancement factors in the range of 2–40% at $kT = 30$ keV (Bao *et al.*, 2000). Corrections at this level are significant for stellar models of the s-process. For more information on the s-process, see Käppeler *et al.* (2011).

5.6.2 The r-Process

In the previous section, it was shown how well s-process models reproduce the solar system abundances of s-only nuclides (Figures 5.71 and 5.73). For the majority of the heavy nuclides, both the s-process and the r-process contribute to the observed abundance. Therefore, one can subtract the well-known s-process contribution from the total solar system abundance of a given nuclide ${}^{A}_{Z}\mathrm{X}$ to find the corresponding solar system r-process abundance,

$$N_r(A,Z) = N_\odot(A,Z) - N_s(A,Z) = N_\odot(A,Z) - \frac{\langle\sigma\rangle_{A,Z} N_s(A,Z)}{\langle\sigma\rangle_{A,Z}} \qquad (5.195)$$

The resulting N_r values versus mass number A are displayed in Figure 5.74a. The s-process contributions are calculated using the classical model according to Eq. (5.187) (see also Problem 5.13). It is apparent that the distribution of solar system r-process abundances is smooth and that it is also consistent with the abundances of the r-only nuclides shown as solid circles. Interestingly, a very similar solar system r-process abundance distribution is obtained if the s-process abundances are calculated using stellar models instead of the classical approach (Arlandini *et al.*, 1999). The most outstanding features in Figure 5.74a are the two pronounced peaks at mass numbers $A = 130$ and 195, which are about 10 mass units removed from the s-process peaks near $A = 138$ and 208. The existence of the r-process abundance peaks and of the long-lived radioisotopes ${}^{232}\mathrm{Th}$ ($T_{1/2} = 1.4 \times 10^{10}$ y), ${}^{235}\mathrm{U}$ ($T_{1/2} = 7.0 \times 10^{8}$ y), and ${}^{238}\mathrm{U}$ ($T_{1/2} = 4.5 \times 10^{9}$ y), located beyond the endpoint of the s-process, provide the strongest evidence for the occurrence of a neutron-induced process that is different from the s-process. The solar system r-process abundance distribution represents a strong constraint for models of the r-process. Elemental solar system r-process abundances can be obtained by summing over isotopic values. These are most useful for comparison to results from stellar spectroscopy which, in most cases, only provide information on elemental abundances. The resulting elemental solar system s- and r-process abundances are displayed in Figure 5.74b. It is remarkable that two processes so vastly different as the s- and r-process provide abundances of similar magnitude.

The most straightforward explanation of the r-process abundance peaks in Figure 5.74a is that they are caused, like the s-process abundance maxima

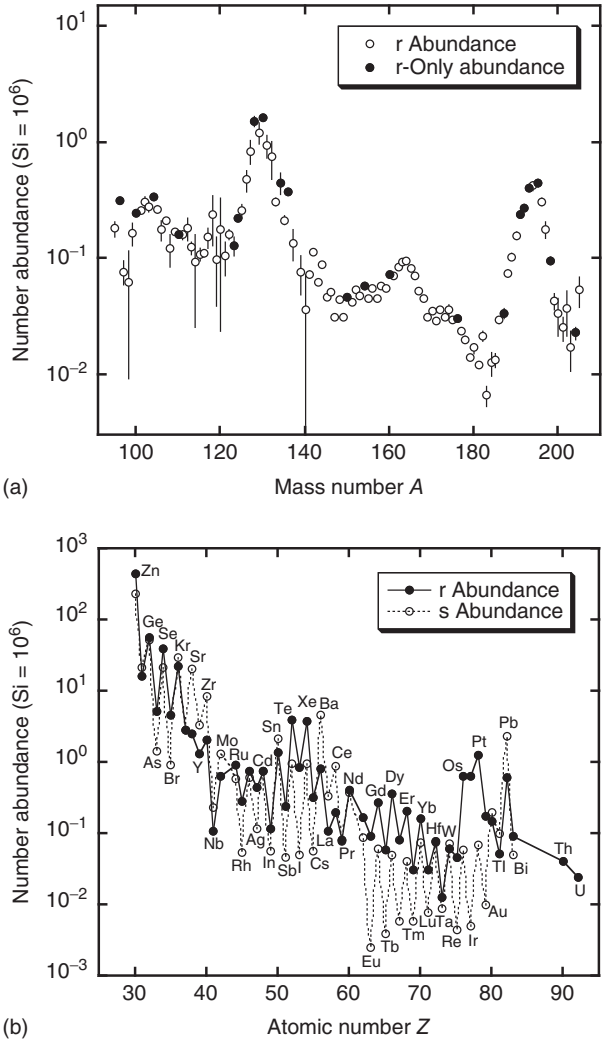

Figure 5.74 (a) Solar system r-process abundances for $A > 90$, obtained by subtracting the s-process contribution from the total solar system abundance. The s-process abundance is calculated by using the classical s-process model (Arlandini *et al.*, 1999). The full circles show abundances of r-only nuclides, defined here as those species for which the s-process contribution amounts to $\leq 3\%$. The influence of the p-process on the displayed abundances is negligible and has been disregarded. The error bars are largest in those regions where the s-process contribution dominates. (b) Elemental solar system s- and r-process abundances. Data from Burris *et al.* (2000).

(Figure 5.65), by the neutron magic numbers $N = 50$, 82, and 126 (Section 1.6.1). The large neutron flux drives the matter to the neutron-rich side, far away from the stability valley, where, for reasons to be discussed later, the abundances of the neutron magic nuclides accumulate. These neutron magic nuclides are proton

deficient compared to their counterparts produced in the s-process that are located close to the valley of stability. After termination of the neutron flux in the r-process, these neutron magic nuclides undergo sequences of β^--decays along isobaric chains (A = const) until the most neutron-rich stable (or very long-lived) isobar is reached (Figure 5.66). Consequently, the r-process produces abundance maxima in mass regions located *below* the corresponding s-process abundance peaks. It must be emphasized that the observed abundances of the r-process nuclides are not correlated with their neutron-capture cross sections, contrary to the case for the s-process abundances (Figure 5.69). Instead, the observed r-process abundances reflect the nuclear properties of radioactive progenitors on the neutron-rich side, far away from the stability valley.

We will now discuss a simple model for the r-process. Consider seed nuclei, say iron, that are exposed to a constant temperature of $T \geq 1$ GK and a constant neutron density of $N_\mathrm{n} \geq 10^{21}$ cm^{-3}. In such a hot and neutron-rich environment, both (n,γ) and (γ,n) reactions are considerably faster than β^--decays. The abundance evolution of species ${}^A_Z\mathrm{X}$ is then given by

$$\frac{dN(Z,A)}{dt} = -N_\mathrm{n} N(Z,A)\langle\sigma v\rangle_{Z,A} + N(Z,A+1)\lambda_\gamma(Z,A+1) \tag{5.196}$$

where $N(Z,A)$ is the number density of nuclide ${}^A_Z\mathrm{X}$, $\langle\sigma v\rangle_{Z,A}$ is the neutron-capture reaction rate per particle pair for ${}^A_Z\mathrm{X}$, and $\lambda_\gamma(Z,A+1)$ is the photodisintegration decay constant of ${}^{A+1}_{\ Z}\mathrm{X}$. For sufficiently large values of N_n and T, the rates of neutron capture and reverse photodisintegration are large enough to ensure thermal equilibrium along the isotopic chain [$dN(Z,A)/dt \approx 0$ for Z = const]. Under such conditions, the abundance ratios for two adjacent isotopes, ${}^{A+1}_{\ Z}\mathrm{X}$ and ${}^A_Z\mathrm{X}$, are given by the Saha equation (see Eq. (3.50))

$$\frac{N(Z,A+1)}{N(Z,A)} = N_\mathrm{n}\left(\frac{\hbar^2}{2\pi m_{A\mathrm{n}} kT}\right)^{3/2} \frac{(2j_{Z,A+1}+1)}{(2j_{Z,A}+1)(2j_\mathrm{n}+1)} \frac{G^\mathrm{norm}_{Z,A+1}}{G^\mathrm{norm}_{Z,A}}\, e^{Q_{\mathrm{n}\gamma}/kT} \tag{5.197}$$

where $Q_{\mathrm{n}\gamma}$ is the reaction Q-value for the (forward) ${}^A_Z\mathrm{X}(\mathrm{n},\gamma){}^{A+1}_{\ Z}\mathrm{X}$ reaction or, equivalently, the neutron separation energy of ${}^{A+1}_{\ Z}\mathrm{X}$.

It follows from Eq. (5.197) that the abundance ratio $N(Z,A+1)/N(Z,A)$ depends mainly on the Q-value (or neutron separation energy) and is a function only of the temperature T and the neutron density N_n during the r-process. The situation is shown in Figure 5.75a. Within a given isotopic chain, (n,γ)↔(γ,n) equilibria are established. The number abundance of any isotope in the chain can be found by successive application of the Saha equation, similar to the methods described in Section 5.3.4. If N_{x_m} is the number density of isotope x_m produced after m neutron captures on (an arbitrary) species N_{x_0}, then (Problem 5.15)

$$\begin{aligned} N_{x_m} &= N_{x_0}\frac{N_\mathrm{n}^m}{\theta^m}\left(\frac{M_{x_m}}{M_{x_0}M_\mathrm{n}^m}\right)^{3/2} \frac{g_{x_m}}{g_{x_0}g_\mathrm{n}^m}\frac{G^\mathrm{norm}_{x_m}}{G^\mathrm{norm}_{x_0}} \exp\left[\frac{1}{kT}\sum_{j=0}^{m-1} Q_{x_j(\mathrm{n},\gamma)}\right] \\ &\approx N_{x_0}\left(\frac{N_\mathrm{n}}{1.188\times 10^{34} T_9^{3/2}}\right)^m \exp\left[\frac{11.605}{T_9}\sum_{j=0}^{m-1} Q_{x_j(\mathrm{n},\gamma)}\right] \end{aligned} \tag{5.198}$$

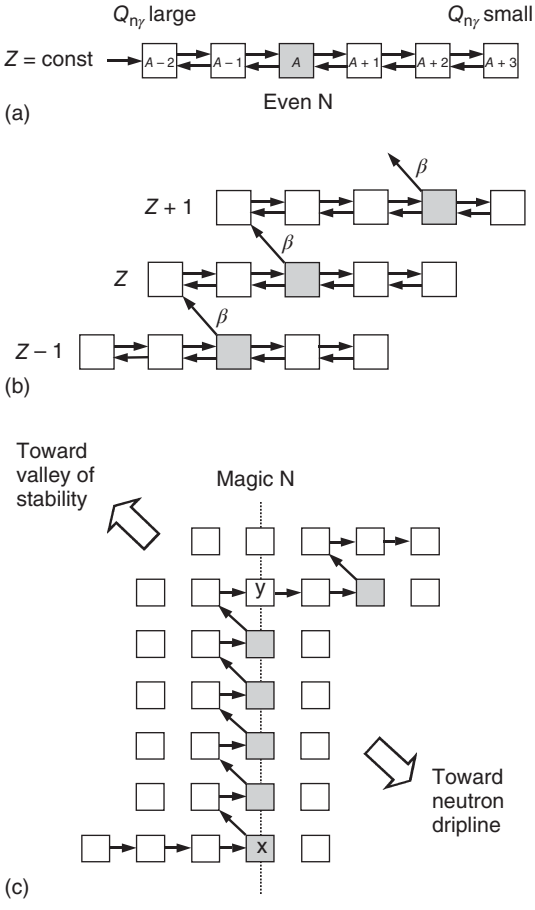

Figure 5.75 Basic building blocks of the r-process path. Part (a) shows an isotopic chain in (n,γ)↔(γ,n) equilibrium (waiting point approximation). For reasons of clarity, it is assumed that most of the abundance resides in a single isotope (shaded square). Part (b) shows how β^--decays of the waiting point nuclides transfer matter from one isotopic chain to the next. The steady flow approximation assumes that the abundance of each element Z is inversely proportional to the total β-decay constant of the chain. Part (c) shows the special case when the r-process path encounters a neutron magic number.

where the symbols have the same meanings as in Section 5.3.4. In the above numerical expression, the number densities and Q-values are in units of cm^{-3} and MeV, respectively, while the normalized partition functions and the spins of the heavy nuclei are set equal to unity. Suppose first that all values of $Q_{n\gamma}$ in a given isotopic chain are the same. For a specific temperature and neutron density, we can then solve Eq. (5.197) for the value of $Q_{n\gamma}$ that gives rise to the same abundances throughout the chain, $N(Z, A+1) \approx N(Z, A)$. For example, with $T = 1.25\,\mathrm{GK}$ and $N_n = 10^{22}\,\mathrm{cm}^{-3}$, and again neglecting spins and normalized

partition functions, we find a value of $Q_{n\gamma} \approx 3.0$ MeV. Of course, the neutron capture Q-values are not all equal but decrease on average when moving away from the stability valley toward the neutron dripline. In other words, closer to the stability valley, where $Q_{n\gamma} > 3$ MeV, we have $N(Z, A+1) > N(Z, A)$, while closer to the neutron dripline, where $Q_{n\gamma} < 3$ MeV, we obtain $N(Z, A+1) < N(Z, A)$. Consequently, the equilibrium abundances are not all the same but will show a maximum close to that isotope for which the $Q_{n\gamma}$-value amounts to about ≈ 3 MeV. For a given temperature and neutron density, the abundance maxima in all chains will occur at the *same* neutron capture Q-value ($Q_{n\gamma} \approx 3$ MeV for the conditions chosen above). According to Eq. (5.197), an increase in N_n shifts the abundance maxima in all isotopic chains toward the neutron-rich side (to smaller $Q_{n\gamma}$-values), while a higher temperature moves the abundance maxima toward the less neutron-rich side (to larger $Q_{n\gamma}$-values). The quantities T and N_n are correlated in the sense that a variation in temperature can always be compensated for by a corresponding adjustment in neutron density to keep the location of the abundance maxima unchanged.

The situation just discussed represents an oversimplification because even–odd effects in nuclear binding energies caused by the pairing effect (Section 1.6.2) have been disregarded so far. Nuclides with an even number of neutrons have relatively small values of $Q_{n\gamma}$, and those with an odd number of neutrons have relatively large $Q_{n\gamma}$-values. Thus, according to Eq. (5.198), the abundance maximum in each isotopic chain is identified with nuclides of even neutron number. A specific example is in order. Equation (5.198) is used to calculate the abundance distribution for neutron-rich selenium isotopes ($A = 92$–99) with the conditions $T = 1.25$ GK and $N_n = 10^{22}$ cm^{-3}. The results are shown in Figure 5.76a. The horizontal line represents a constant Q-value of 3 MeV. The $Q_{n\gamma}$ values (from Möller, Nix, and Kratz, 1997) are shown as a dashed line and display a pronounced odd–even structure because of the pairing effect. The abundance distribution (solid line) peaks at that even-N isotope where the average $Q_{n\gamma}$-curve falls below 3 MeV, in this case ${}^{96}_{34}\mathrm{Se}_{62}$ and, to a lesser degree, ${}^{94}_{34}\mathrm{Se}_{60}$. A more quantitative criterion will be derived in Problem 5.16. In practice, it is found that the abundance distributions are relatively sharp for given values of T and N_n. Only one or two even-N isotopes exist in any significant amount. On the other hand, if the r-process is characterized by some spread in temperature and neutron density, then the abundance distributions will be broadened to include more values of A. Equilibrium may not be achieved throughout the entire isotopic chain. In particular, closer to the valley of stability the Q-values are large and, therefore, the photodisintegration rates become smaller. The reverse (γ,n) reactions cannot balance the forward (n,γ) reactions and these lighter isotopes are rapidly destroyed. This does not represent a problem for the above model since it is found that the (n,γ)↔(γ,n) equilibrium condition holds for all isotopes with any significant abundance at equilibrium (Seeger, Fowler, and Clayton, 1965). Hence, the next step is clear. The even-N isotopes with significant abundances in each isotopic chain represent waiting points for the abundance flow. At these locations, the r-process path can only continue via β^--decays that are sufficiently slow as to not affect the equilibrium distribution

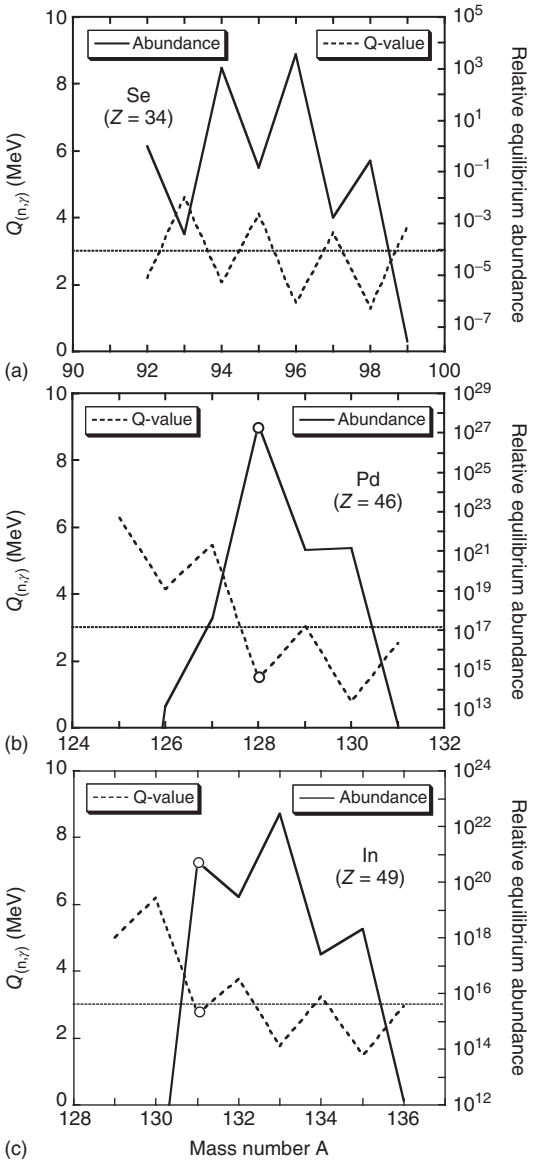

Figure 5.76 Neutron capture Q-values (dashed lines) and abundance distributions (solid lines) for neutron-rich isotopes of (a) selenium, (b) palladium, and (c) indium. The $Q_{n\gamma}$-values are adopted from Möller, Nix, and Kratz (1997) and display a pronounced odd–even structure caused by the pairing effect. (For some of the isotopes shown, experimental values exist; see Wang *et al.*, 2012). The horizontal lines represent a constant Q-value of 3 MeV. The abundance distributions are calculated using Eq. (5.198) assuming conditions of $T = 1.25$ GK and $N_n = 10^{22}$ cm^{-3}. They peak at those even-N isotopes where the average $Q_{n\gamma}$-curve falls below 3 MeV. Circles mark isotopes with neutron magic numbers.

in the isotopic chains (Figure 5.75b). For this reason, the (n,γ)↔(γ,n) equilibrium condition is also referred to as the *waiting point approximation*.

The β^--decays transfer matter from one isotopic chain to the next, where again an independent equilibrium within the chain is established (Figure 5.75b). This repetitive sequence of events gives rise to the r-process path. The total β^--decay probability of an isotopic chain with a given value of Z can be defined by

$$\lambda_Z \equiv \sum_A p(Z,A)\lambda_\beta(Z,A) \tag{5.199}$$

where $p(Z,A) = N(Z,A)/N_Z$ is the abundance distribution in the chain for given values of T and N_n, normalized to the total abundance, $N_Z \equiv \sum_A N(Z,A)$, of element Z. The quantity λ_Z depends explicitly on T and N_n through the equilibrium abundances $p(Z,A)$. The time evolution of the total abundance N_Z is given by

$$\frac{dN_Z}{dt} = -\lambda_Z N_Z + \lambda_{Z-1} N_{Z-1} \tag{5.200}$$

where the first term describes the destruction of element Z via β^--decay to element $Z+1$, while the second term represents the creation of element Z via β^--decay from element $Z-1$. The above expressions (see Eqs. (5.199) and (5.200)) determine the *elemental* abundance of each isotopic chain, while Eq. (5.198) determines the *isotopic* equilibrium abundances within each isotopic chain. For the boundary conditions of Eq. (5.200), one can assume that initially all nuclei are in a specific isotopic chain Z_0: $N_Z(t=0) = N_0$ for $Z = Z_0$ and $N_Z(t=0) = 0$ for $Z \neq Z_0$. The general solution of the above set of differential equations is given by (Bateman, 1910)

$$N_{Z_0}(t) = N_0 e^{-\lambda_{Z_0} t} \tag{5.201}$$

$$N_Z(t) = N_0 \sum_{i=Z_0}^{Z} e^{-\lambda_i t} \frac{\lambda_i}{\lambda_Z} \prod_{\substack{j=Z_0 \\ j\neq i}} \frac{\lambda_j}{\lambda_j - \lambda_i} \qquad \text{for } Z \neq Z_0 \tag{5.202}$$

provided that all values of λ_i are different, which is a good assumption if these values are computed precisely. One sees from Eq. (5.202) that the abundance N_Z varies inversely with the corresponding total β-decay constant λ_Z. As was the case with Eq. (5.176) in the discussion of the s-process, the above coupled equations (see Eq. (5.200)) are self-regulating, in the sense that they attempt to achieve a constant β^--decay flow from one isotopic chain to the next, $dN_Z/dt \approx 0$. Hence, after a sufficient time has passed, we obtain

$$\lambda_Z N_Z \approx \lambda_{Z-1} N_{Z-1} \qquad \text{or} \qquad \lambda_Z N_Z \approx \text{const} \tag{5.203}$$

This condition is referred to as the *steady flow approximation*.

The importance of nuclides with neutron magic numbers $N = 50$, 82, and 126 for the r-process path will now be addressed. The situation is sketched in Figures 5.75c and 5.77. Suppose the abundance flow reaches the isotopic chain with the neutron magic nucleus x as a member. This nucleus has an energetically favorable neutron shell configuration. As a result, the Q-value for

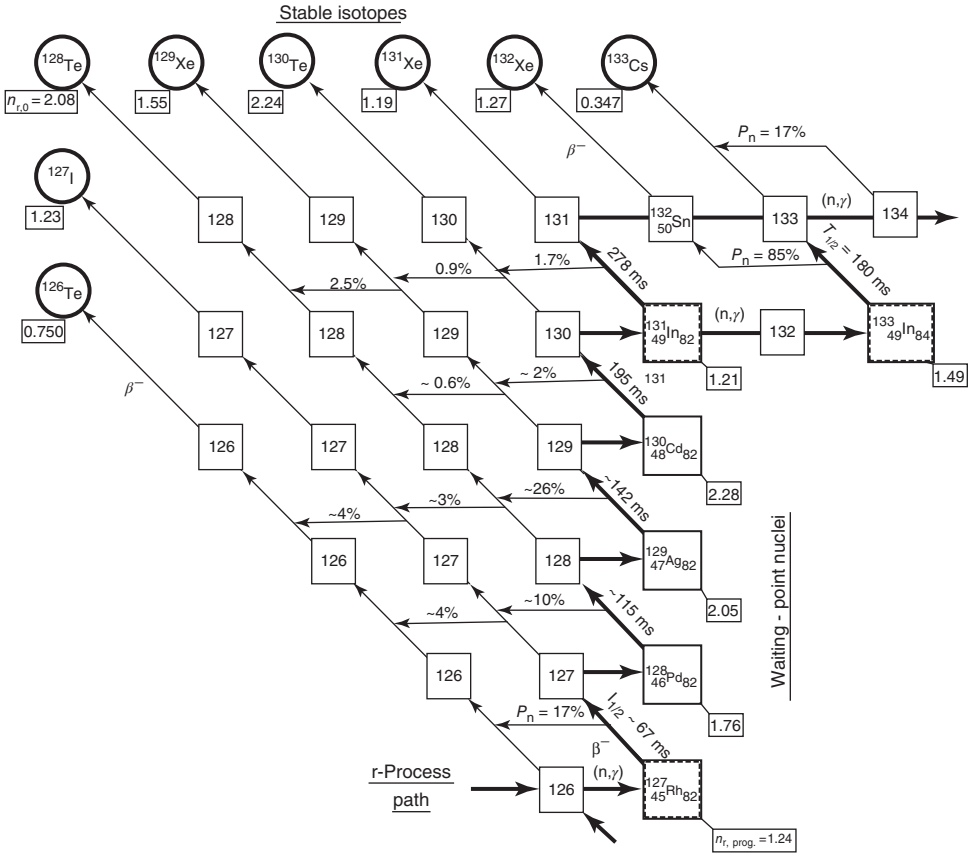

Figure 5.77 Schematic r-process path near $A \approx 130$ and $N \approx 82$. Numbers near diagonal arrows represent β^--decay half-lives (in seconds) and those near horizontal arrows show branching ratios (in percent) for β-delayed neutron decay. The quoted values are adopted from experiment or, when preceded by "~", from nuclear model calculations. Stable end products of the r-process (after freeze-out) are shown in circles and their observed solar system r-abundances are given in square boxes. More information on nuclear properties and abundances can be found in Audi *et al.* (2012), Möller, Nix, and Kratz (1997), and Lodders, Palme, and Gail (2009). Note that ^{130}Cd is the neutron magic waiting point nucleus with $N = 82$ that is located closest to stability. At the next element (indium), the r-process path branches off horizontally toward heavier nuclides. The nuclide ^{130}Cd is the progenitor of the stable isobar ^{130}Te situated at the maximum of the $A = 130$ peak in the solar system r-process abundance distribution. (From Kratz *et al.* (1988). © IOP Publishing. Reproduced by permission of IOP Publishing. All rights reserved.)

the $x(\mathrm{n},\gamma)$ reaction is relatively small, while the Q-value for the preceding $(\mathrm{n},\gamma)x$ reaction is relatively large. The element palladium ($Z = 46$) is an example for this situation. The neutron capture Q-values in the $A = 125$–131 region are shown in Figure 5.76b. It is apparent that the neutron magic nucleus $^{128}_{46}\mathrm{Pd}_{82}$ coincides with the location at which the average $Q_{\mathrm{n}\gamma}$-curve falls below the 3-MeV line.

Consequently, $^{128}_{46}Pd_{82}$ is by far the most abundant species in the chain and represents a waiting point. After the subsequent β^--decay the process repeats itself in the next isotopic chain: the average $Q_{n\gamma}$-value curve crosses the 3-MeV line at the location of the neutron magic nucleus (in this specific case, $^{129}_{47}Ag_{82}$) that becomes another waiting point. Therefore, a sequence of waiting points is encountered at the same magic neutron number N. The r-process path has no choice but to move vertically upward in Z toward the stability valley (Figure 5.75c). Moreover, the closer the path approaches the group of stable nuclides, the longer the β^--decay half-lives of the neutron magic nuclides. Typical half-lives along the r-process path amount to $T_{1/2} \approx 0.01–0.05$ s, but near neutron magic waiting point nuclides close to the stability valley (e.g., $^{130}_{48}Cd_{82}$), they are considerably longer. Hence, the abundance flow is significantly delayed and these isotopes will build up to relatively large abundances. An interesting situation occurs when the neutron magic nucleus y is reached (Figure 5.75c). A specific example is the element indium, and the corresponding $Q_{n\gamma}$-values are shown in Figure 5.76c. As was the case before, the neutron-capture Q-values drop significantly at the location of the neutron magic nucleus ($^{131}_{49}In_{82}$). However, this isotope is located closer to the stability line than the lighter neutron magic nuclides. The extra stability is reflected in the larger overall neutron-capture Q-values. The average $Q_{n\gamma}$-curve now falls below the 3-MeV line at a location beyond the neutron magic nucleus $^{131}_{49}In_{82}$ (in this case, at $^{133}_{49}In_{84}$). In other words, the r-process path overcomes the group of isotones with neutron magic number N at a location sufficiently close to the region of the stable nuclides (Figure 5.75c).

At the cessation of the neutron flux, the neutron-rich nuclides β^--decay along lines of constant A to their stable isobars. Thus, the r-process produces one stable (or long-lived) isotope for each value of A. In the simplest case, we may assume that the neutron flux and temperature fall instantly to zero after some time τ. Then, knowing the isotopic abundances for each Z at a time τ when the r-process is halted, one can find the final r-process abundance at each A by summing

$$N_{r,A} = \sum_Z N_Z(\tau) p(Z, A) \tag{5.204}$$

To summarize, for given values of N_n, T, and τ, the r-process path (and, hence, the abundances $N_{r,A}$) can be calculated precisely if the nuclear properties are known. The neutron-capture Q-values determine the isotopic equilibrium abundances for each element (see Eq. (5.198)), while the relative amount of material at a given element Z depends only on the total β^--decay probabilities of the isotopic chains (see Eq. (5.202)). Cross sections for neutron captures or photodisintegrations are unimportant since we adopted the waiting point approximation. Furthermore, the time it takes to establish an $(n,\gamma)\leftrightarrow(\gamma,n)$ equilibrium is negligible compared to the β^--decay half-lives, which determine the time delay of the r-process flow toward heavier nuclides. The closer the r-process path is located to the neutron dripline, the shorter the β^--decay half-lives become, resulting in a faster r-process flow. The longest delays for the abundance flow are expected near the neutron magic waiting point nuclides located closest to stability: $^{80}_{30}Zn_{50}$, $^{130}_{48}Cd_{82}$, and $^{195}_{69}Tm_{126}$. The

abundances near these locations accumulate and, after termination of the neutron flux, give rise to the abundance peaks at $A = 80$, 130, and 195 in the distribution of observed $N_{r,A}$ values (see Figure 5.74a).

We assumed in Eq. (5.204) that β^--decays are the only processes responsible for the decay of nuclides from the r-process path back to the stability valley after freeze-out of the neutron exposure. There are a number of other processes, however, that also need to be taken into account. First, β^--decays may not always populate neutron bound states in the daughter nucleus. If neutron unbound states are populated, then β-delayed neutron emission may occur (Section 1.8.2). This process has the tendency to smooth out the strong odd–even signatures in the equilibrium abundances, caused by the dependence of $Q_{n\gamma}$ on the neutron number, that would otherwise be present in the final r-process distribution. Second, in the higher mass range ($Z > 80$), spontaneous and β-delayed fission could become faster than β^--decay and will thus influence the final abundances. Third, beyond mass $A = 210$ the decay toward the stability valley reaches (β-stable) radioactive α-particle emitters. The transmutation of these nuclides along α-decay chains gives rise to the production of the very long-lived species ^{232}Th, ^{235,238}U, and ^{244}Pu, which are important for nucleochronology (see, e.g., Truran *et al.*, 2002).

The termination of the r-process depends, among other things, on the duration of the neutron exposure and thus on the astrophysical environment. For relatively short neutron exposures, the r-process terminates because of a lack of free neutrons before the mass region $A \approx 260$ is reached. For longer neutron exposures, the successive addition of neutrons will continue until the Coulomb barrier, which is proportional to Z^2, becomes so large that the heavy nuclides decay via neutron-induced or β-delayed fission. Calculations indicate that this happens near $A_{max} \approx 260$ and $Z_{max} \approx 94$. The precise location depends sensitively on (yet unmeasured) fission barriers for nuclides far from stability (Panov *et al.*, 2005). After the fission of a heavy nucleus with mass A_{max}, two fragments with masses of roughly $A_{max}/2$ are produced, thereby feeding two seed nuclei back into the neutron-capture chain and giving rise to a *fission cycle*. The number of r-process nuclei is doubled with each cycle. The cycle time, τ_{cycle}, required to build an average fission fragment back up to A_{max} may only take a few seconds or less. If the neutron supply lasts sufficiently long, $\tau \gg \tau_{cycle}$, the abundances will grow exponentially as nuclei pass around the fission cycle and large abundances of heavy nuclides can be build up in this way. Fission can also be incorporated into the phenomenological r-process model described above by adding a term to Eq. (5.200). Analytical solutions are given in Seeger, Fowler, and Clayton (1965).

The nuclear properties required to describe the r-process include neutron capture Q-values (or neutron separation energies), β^--decay half-lives, branching ratios for β-delayed neutron emission, normalized partition functions, fission probabilities, and α-decay half-lives. Nuclear masses play a central role for the r-process since they determine directly or indirectly most of the properties listed above. Also, recall that the $Q_{n\gamma}$-values (which are given by mass differences; see

Eq. (1.6)) enter exponentially in the determination of the equilibrium abundances (see Eq. (5.197)) and, therefore, must be known accurately. The nuclear properties are needed for nuclides that are located far away from the valley of stability. The available experimental information will be summarized later in this section. At this point, it is sufficient to mention that, with few exceptions, the required information is not known from experiments since most of the nuclides on the r-process path cannot be produced yet in the laboratory. The required nuclear properties must be estimated using nuclear models. The various models will not be discussed here (see, e.g., Cowan, Thielemann, and Truran, 1991). In practice, one attempts to derive semiempirical formulas from the known properties of nuclides close to stability that can be extrapolated into the region covered by the r-process path. Such extrapolation procedures are subject to significant uncertainties even for the most sophisticated models. For example, Möller, Pfeiffer, and Kratz (2003) estimate an uncertainty of ± 0.5 MeV for calculated values of $Q_{n\gamma}$ and Q_β, while half-lives and branching ratios for β-delayed neutron emission can only be predicted within a factor of 2–3 for nuclides far from stability. It remains to be seen if new *global* mass models can be developed that are not subject to these limitations. Any deficiencies in current nuclear models will have a direct impact on r-process predictions. The associated nuclear physics uncertainties affect most discussions of the r-process.

The phenomenological model discussed above is referred to as the *classical r-process model*. It is simple because it assumes: (i) a constant temperature and neutron density, (ii) an instantaneous termination of the neutron flux after a duration τ, and (iii) the waiting point and steady flow approximations. The waiting point approximation will only hold for sufficiently large values of T and N_n (Goriely and Arnould, 1996; Rauscher, 2004). Otherwise, the abundance flow in each isotopic chain of given element Z is steadily depleted by β^--decays before the waiting point in the chain is reached. The steady flow approximation is only valid if the duration of the neutron exposure exceeds the β^--decay half-lives of nuclides on the r-process path. Finally, the assumption of a sudden termination of the neutron density disregards that (n,γ) and (γ,n) reactions will fall out of equilibrium if N_n decreases over a short, but finite, time.

How the classical model can provide insight into the astrophysical conditions of the r-process is discussed below. Consider, for example, Figure 5.77 showing the r-process path near the neutron magic number $N = 82$. If the waiting point approximation holds, then the path moves vertically upward through ${}^{127}_{45}\mathrm{Rh}_{82}$, ${}^{128}_{46}\mathrm{Pd}_{82}$, ${}^{129}_{47}\mathrm{Ag}_{82}$, and ${}^{130}_{48}\mathrm{Cd}_{82}$ before it branches off horizontally toward heavier nuclides. As discussed earlier, these nuclides are by far the most abundant species in their respective isotopic chains because of the sudden drop of the $Q_{n\gamma}$-value near neutron magic numbers. For the $Z = 49$ chain, however, most of the abundance resides in ${}^{131}_{49}\mathrm{In}_{82}$ and ${}^{133}_{49}\mathrm{In}_{84}$ (Figure 5.76c). After termination of the neutron flux, the decays of the nuclides near $N = 82$ give rise to the observed $A = 130$ solar r-abundance peak. The nuclides ^{130}Cd and ^{131}In will β^--decay to the stable isobars ^{130}Te and ^{131}Xe, respectively. The isotope ^{133}In, on the other hand, has a large probability for β-delayed neutron decay and thus decays mainly

to the stable nuclide ^{132}Xe. Assuming in addition a steady flow approximation (see Eq. (5.203)) for the $Z = 48$ (cadmium) and 49 (indium) isotopic chains, we can calculate a value of the ^{130}Cd half-life from the observed solar system r-abundances of ^{130}Te, ^{131}Xe, and ^{132}Xe and the measured half-lives of ^{131}In and ^{133}In (Problem 5.17). The result is $T_{1/2}^{\mathrm{calc}}(^{130}\mathrm{Cd}) \approx 187$ ms, which is close to the experimental value of $T_{1/2}^{\mathrm{exp}} = 162 \pm 7$ ms (Dillmann *et al.*, 2003). Hence, it appears that the solar system r-process peak at $A = 130$ was formed under the conditions of an (n,γ)↔(γ,n) equilibrium and a steady flow equilibrium. Similar arguments can be applied to the $A = 80$ r-process peak. We can also estimate the conditions of temperature and neutron density that gave rise to the observed r-abundances. Earlier we calculated equilibrium abundances from given $Q_{\mathrm{n}\gamma}$-values *assuming* values for T and N_{n} (Figure 5.76). The argument can be turned around to derive constraints on T and N_{n} from known equilibrium abundances in a specific isotopic chain. For example, consider again the pair ^{131}In and ^{133}In. From the observed solar system r-abundances of ^{131}Xe and ^{132}Xe (Arlandini *et al.*, 1999), one may derive, after correcting for β-delayed neutron decays (see Problem 5.17), the equilibrium abundances of the precursors ^{131}In and ^{133}In on the r-process path. These determine, according to Eq. (5.198), the temperature and neutron density if the $Q_{\mathrm{n}\gamma}$-values are known either from experiment or theory. Results of such a procedure for isotopes near $N = 82$ (^{131,133}In) are shown as the dashed lines in Figure 5.78. For example, one finds that a neutron density of $N_{\mathrm{n}} \approx 10^{22}$ cm^{-3} corresponds to a temperature near $T \approx 1.35$ GK. As already noted, T and N_{n} are correlated and thus the possible solutions are located anywhere on the dashed lines.

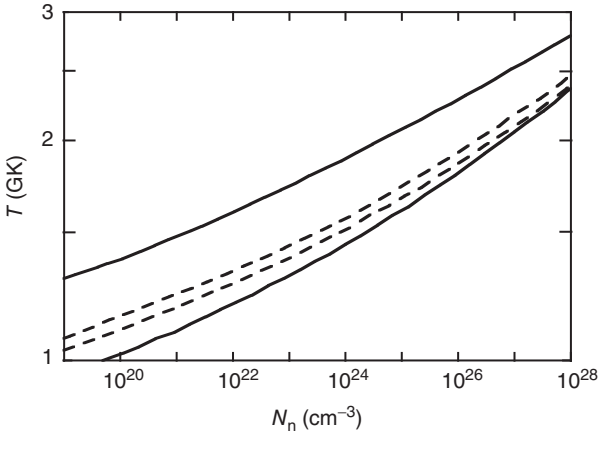

Figure 5.78 Conditions for temperature and neutron density in the r-process. The dashed lines are derived from the equilibrium abundance ratio of ^{133}In–^{131}In. The abundance ratio of these isotopes, which are located on the r-process path, is deduced from the observed solar system r-abundances of ^{132}Xe and ^{131}Xe. The two dashed lines are obtained from two different mass formulas. The region between the two solid lines shows the conditions at which all $N = 82$ species between ^{127}Rh and ^{130}Cd represent waiting points. Data adopted from Kratz *et al.* (1988).

Attempts to describe the entire observed distribution of solar system r-abundances using the classical r-process model and a single set of T–N_n–τ conditions were unsuccessful (Kratz *et al.*, 1993). Such *global* descriptions reproduce three r-abundance peaks, but neither at the correct mass number location, nor with the correct magnitude. It is also found that at least three different sets of T–N_n–τ conditions, each corresponding to a specific r-process path, are required in different mass ranges to reproduce the observed solar-system abundance distribution. Furthermore, the steady flow approximation applies *locally* in each of these mass ranges, but not globally over the entire mass region. Each of the components proceeds up to one of the r-abundance peaks ($A = 80$, 130, or 195) and achieves a local steady flow equilibrium. However, the steady flow equilibrium breaks down beyond the maximum of each peak, where the half-lives of the r-process progenitors are relatively long ($\approx$ seconds). This could indicate that the duration of the neutron exposure is large compared to most of the relatively short β^--decay half-lives on the r-process path, but is comparable to the longer half-lives of the neutron magic nuclides that come closest to stability. The overall implication is that the solar system r-abundance distribution results from a superposition of components representing different r-process conditions. This could be caused by several different astrophysical r-process sites or by a single site with varying conditions in different zones. An example for the comparison of observed solar system r-abundances and the results of the classical r-process model is shown in Figure 5.79. The model predictions are obtained from a superposition of three different r-process components: (i) $T = 1.35$ GK, $N_n = 3 \times 10^{20}$ cm^{-3}, $\tau = 1.5$ s for $A \approx 80$; (ii) $T = 1.2$ GK, $N_n = 1 \times 10^{21}$ cm^{-3}, $\tau = 1.7$ s for $A = 90$–130; and (iii) $T = 1.2$ GK, $N_n = 3 \times 10^{22}$ cm^{-3}, $\tau = 2.5$ s for $A = 135$–195. The weights of the components are 10 : 2.6 : 1. The T–N_n values of each component do not represent a unique set, but similar r-abundances are obtained for all values that are located on an extended boundary in the T–N_n diagram (see Figure 5.78 and Figure 12 of Kratz *et al.*, 1993). Some of the deviations between observed and calculated abundances (lower part of Figure 5.79) originate from systematic defects of the mass model used to compute the nuclear properties (Freiburghaus *et al.*, 1999).

There is no obvious reason why the observed solar system r-abundance distribution should be the result of a superposition of only three components. If a number of astrophysical sites, or different zones representing different conditions in the same site, contribute to the observed r-abundances, then it would be reasonable to assume a superposition of many different components. Following this line of thought, some researchers have employed many components, each with its associated fitting parameters, and thereby achieve an almost perfect agreement between predicted and observed r-abundances (see, e.g., Goriely and Arnould, 1996). However, such results mask deficiencies in calculated nuclear properties and, at the same time, could compromise the predictive power of the model beyond the mass range of fitted abundances. Other researchers have employed a continuous superposition of r-process components, assuming constant temperature and power-law distributions for component weights and exposure times as

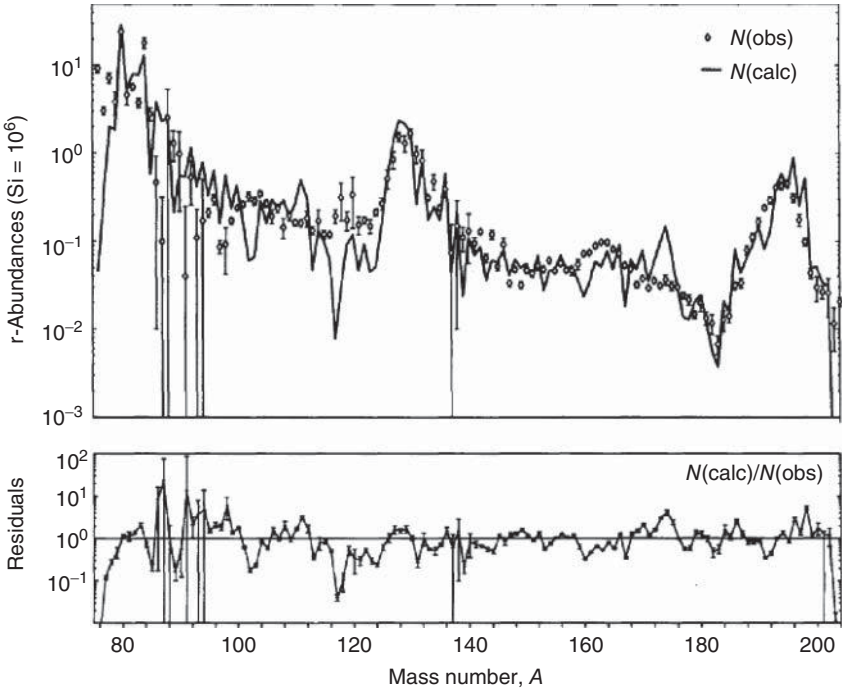

Figure 5.79 Distribution of observed solar system r-abundances (data points) compared to predictions of the classical r-process model (solid line). The solid line is calculated from Eqs. (5.198) and (5.202) and depends only on neutron separation energies, β^--decay half-lives, β-delayed neutron decay probabilities, and so on, but not on cross sections for neutron capture or photodisintegration. The model prediction is obtained from a superposition of three different r-process components. (From Kratz *et al.* (1993). © IOP Publishing. Reproduced by permission of IOP Publishing. All rights reserved.)

a function of neutron density. This procedure requires only a small number of fitting parameters and yields a slight improvement in the predicted r-abundances compared to the results shown in Figure 5.79 (Freiburghaus *et al.*, 1999). However, neither method seems to directly reflect the physical properties of a realistic r-process site.

Figure 5.80 shows some results obtained with the second procedure, that is, by assuming a continuous superposition of r-process components. Each component is characterized by constant values of T, N_n, and τ. The component weights and neutron exposure time scales are given by $\omega(N_n) = a_1 N_n^{a_2}$ and $\tau(N_n) = a_3 N_n^{a_4}$, respectively, where the a_i are fitting parameters. The temperature remains constant at $T = 1.35$ GK. Since different T–N_n conditions correspond to different r-process paths, the overall distribution of waiting point nuclides (large open or solid squares) in each isotopic chain is broadened compared to the use of a single component. The resulting r-process abundance flow pattern represents more appropriately a *boulevard* rather than a narrow path (Kratz, 2006). Nevertheless,

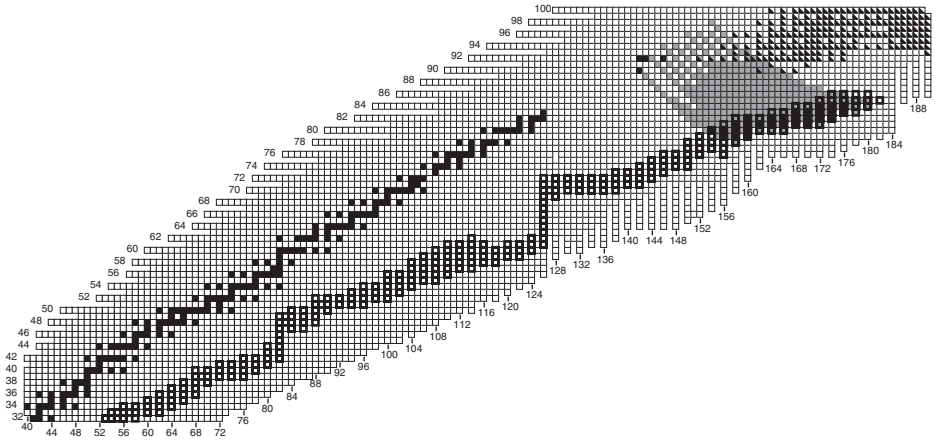

Figure 5.80 Results of a classical r-process calculation assuming a continuous superposition of many components. The components are determined by power-law distributions of component weights and exposure durations as functions of neutron density. The large open and solid squares show all waiting point nuclides that, after instant freeze-out of the neutron exposure, contribute more than 1% to the abundance of any stable or long-lived nuclide (small solid squares). The large solid squares are a subset of waiting point nuclides that decay along the path marked with gray squares and contribute to the production of the long-lived chronometers ^{238}U and ^{232}Th. Nuclides that fission after production via β^--decay are shown as triangles. The calculation is based on the ETFSI-Q mass model (Pearson, Nayak, and Goriely, 1996). (From Schatz *et al.* (2002). © IOP Publishing. Reproduced by permission of IOP Publishing. All rights reserved.)

it can be seen that the abundance flow for all components is funneled through the isotones with neutron magic numbers ($N = 82$ and 126) before reaching the $A \approx 260$ region. At the cessation of the neutron flux, the short-lived nuclides on the r-process path decay via β^--decay, β-delayed neutron emission, α-decay, and fission (the latter two decays occur only in the region $A > 210$), and transmute into stable or long-lived isotopes (small solid squares).

The phenomenological model described above makes no assumption regarding the site of the r-process. It is nevertheless useful and provides insight into several aspects. As we have seen, the classical r-process model describes the gross behavior of the solar system r-abundance distribution. It has also been applied for reproducing or predicting abundance ratios of neighboring nuclides, for example, for chronometers (Kratz *et al.*, 2004) or isotopic anomalies in primitive meteorites (Kratz *et al.*, 2001). Such abundance ratios are most likely influenced by nuclear properties rather than by the details of the astrophysical r-process site. The classical r-process model also provides a simple framework for studying the impact of nuclear physics uncertainties on predicted r-abundances. But it is also clear from the preceding discussion that the classical model does not account for the observations in terms of a realistic astrophysical site.

It is worthwhile at this point to visualize the results of a dynamic r-process calculation as opposed to the static models described up to now. In reality, the

temperature and neutron density will evolve with time. Early during the r-process, T and N_n will be sufficiently large to ensure that a (n,γ)↔(γ,n) equilibrium holds in all isotopic chains. Now suppose that the temperature and neutron density decrease with time. The abundance flow will continuously adjust to the new conditions according to the waiting point approximation. This means that the r-process path, which is defined by T and N_n, must continuously move, starting from a location closer to the neutron dripline to one that is located closer to stability. For each location of the path, the β^--decay half-lives are different. Just before termination of the neutron exposure, when the r-process path is still about 15–35 mass units away from stability, the waiting point nuclides have neutron capture Q-values of $Q_{n\gamma} \approx 2$–4 MeV. When the neutron flux disappears, the r-process nuclides decay toward stability. But it is apparent that only the r-process path just before freeze-out, and in particular the sections near neutron magic nuclides, matters for the observed final distribution of r-abundances. In other words, at freeze-out the r-process has mostly forgotten its earlier history.

Before discussing possible locations of the r-process, we will briefly mention some of the observational evidence. Up to now, we have only focused on reproducing the observed solar system r-abundance distribution using the classical r-process model. In addition, important conclusions can be drawn from stellar spectroscopy. Figure 5.81 displays the total heavy element abundances (data points) for an extremely metal-poor Galactic halo giant star. For comparision, the solar system r-abundances are shown as a solid line. This star is among the oldest in the Galaxy. The remarkable agreement between the two abundance distributions for elements above barium ($A \geq 135$) provides strong evidence that most of the heavy elements observed in this star were synthesized by the r-process early in the evolution of the Galaxy, with no apparent contribution from the s-process. Similar results have been found for other ultra-metal poor halo giants (Truran *et al.*, 2002). The r-process elements were not synthesized in the halo stars themselves. They must have been produced by progenitors that evolved very rapidly and ejected the matter into the interstellar medium before the formation of the currently observed halo giants. The ultra-metal poor halo giants formed so early in the history of the Galaxy that they may have received contributions from only one, or at most a few, r-process events. The most likely r-process sites seem to be associated with massive stars since low-mass stars or intermediate-mass stars evolve on considerably longer time scales. The agreement with the solar system r-abundances above mass $Z \approx 56$ supports the conclusion that the r-process mechanism is robust in the sense that a similar abundance pattern is produced in each r-process event. Interestingly, the agreement between stellar and solar system r-abundances does not extend to the lighter elements below barium ($Z < 56$). There have been many suggestions to explain their synthesis, including a *weak r-process* (Kratz, 2007), a *light element primary process* (Travaglio *et al.*, 2004b), and the α-*process* (Qian and Wasserburg, 2007; see also below). More observations and studies will be needed to understand the synthesis of these elements.

A major goal of r-process studies is the identification of the astrophysical sites and, by using r-abundances observed in the solar system and in stars, to draw

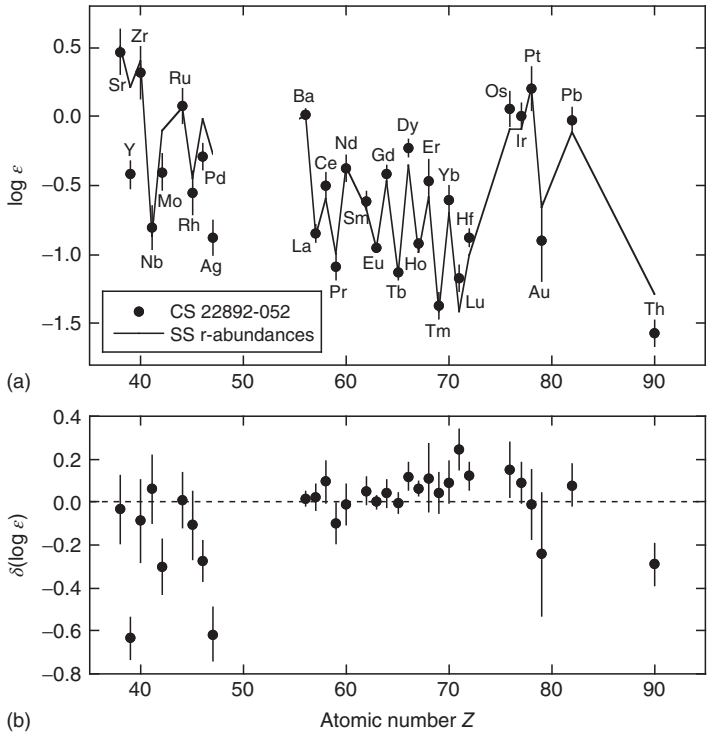

Figure 5.81 (a) Heavy-element abundances of the low-metallicity halo giant star CS 22892-052 (solid circles) compared to the solar system r-process abundances (solid line). The abundances are given in standard spectroscopic notation, where $\log \varepsilon(x) \equiv \log(N_x/N_{\rm H}) + 12.0$, and N_x denotes the number abundance. The stellar data are from Sneden, Cowan, and Gallino (2008). The solar system r-abundances (total solar system abundance minus s-abundance) are from Simmerer *et al.* (2004) and have been normalized to the stellar Eu abundance. The graph does not include the uncertainties introduced by the deconvolution of s- and r-abundances. (b) Difference between total stellar and scaled r-process solar system abundances. The remarkable agreement between the two abundance distributions for elements heavier than barium ($Z \geq 56$) provides strong evidence that most of the heavy elements observed in this star were synthesized by the r-process early during the evolution of the Galaxy.

conclusions regarding their detailed properties. This procedure has been very successful in the case of the s-process. However, the site of the r-process remains a mystery. Many different objects have been suggested (see the summary in Cowan, Thielemann, and Truran, 1991) but only a few of these seem promising. We already mentioned that observations place the beginning of r-processing very early in the evolution of the Galaxy and, therefore, the r-process site is most likely related to massive stars. It is also clear that the site must provide very high neutron densities ($N_{\rm n} \geq 10^{21}$ cm^{-3}) over short time scales ($\approx$ seconds). On the other hand, the temperature should not be too high. Otherwise, the heavy nuclides will either be destroyed by photodisintegration (see Sections 5.3.4 and 5.3.5) or the waiting

point abundances shift too close to the stability valley (see Eq. (5.197)) where the β^--decay half-lives are too slow to allow for efficient r-processing.

One possible site is the merger of two neutron stars (Rosswog *et al.*, 1999). Calculations show that the matter ejected in such events has a solar system composition in the mass range of $A \geq 140$. A problem with this source is that the event rate is perhaps too low and, hence, the required mass of r-process matter ejected per event would be too large to be consistent with observations (Qian, 2000). A second possibility is the ejection of neutronized material in magnetized jets from asymmetric massive star explosions (Cameron, 2003). Unfortunately, the thermodynamic conditions for this model are at present poorly determined. The third proposed site involves the neutrino-driven wind from a neutron star resulting from a core-collapse supernova (Section 5.4.1).

Although the nature of these sites varies significantly, the basic nuclear rearrangements are similar. We already pointed out that any successful r-process site requires very large neutron densities, sufficiently high temperatures, and rapid expansion time scales. It is worthwhile to briefly discuss the nucleosynthesis in the last scenario to better understand the origin of the neutron flux that could give rise to an r-process. Suppose that the neutrino-driven wind at late times has a significant neutron excess. Four different phases can be identified, as shown schematically in Figure 5.41c.

First, above a temperature of $T \approx 10$ GK, the wind consists of free neutrons and protons in nuclear statistical equilibrium (Figure 5.38). Second, as the wind expands and cools below $T \approx 10$ GK, nucleons start to combine to α-particles. Near $T \approx 7$ GK, α-particles become the dominant constituent, leaving behind an excess of neutrons. Furthermore, some α-particles begin to assemble into nuclei via the strongly density-dependent sequence

$$\alpha + \alpha + \mathrm{n} \rightarrow {}^{9}\mathrm{Be} \quad \text{and} \quad {}^{9}\mathrm{Be}(\alpha, \mathrm{n})^{12}\mathrm{C} \tag{5.205}$$

Third, near $T \approx 5$ GK, nuclear statistical equilibrium breaks down because the expansion time scale becomes shorter than the time required to maintain nuclear statistical equilibrium under conditions of high temperature, low density, and large α-particle abundance. The slow process $\alpha + \alpha + \mathrm{n} \rightarrow {}^{9}\mathrm{Be}$ is the first reaction to fall out of equilibrium. The situation is similar to the α-rich freeze-out discussed in Section 5.4.3. There is again an excess of α-particles, which cannot be consumed fast enough by the slow helium-induced reactions in the time available. The important difference, however, is the presence of a neutron excess. Both the abundant α-particles and the neutrons will participate in the buildup of heavier nuclides, starting with the sequence

$$^{12}\mathrm{C}(\mathrm{n}, \gamma)^{13}\mathrm{C}(\alpha, \mathrm{n})^{16}O(\alpha, \gamma)^{20}\mathrm{Ne} \ldots \tag{5.206}$$

Recall from the discussion in Section 5.4.3 that without the presence of neutrons, the α-rich freeze-out mainly produces the $N = Z$ isotope ^{56}Ni, while the abundance flows beyond the iron peak are negligible. This occurs because the Q-values for (α,γ) reactions beyond ^{56}Ni along the $N = Z$ line are relatively small. These

nuclides are located on the proton-rich side of the stability valley, and little binding energy is gained by adding another α-particle. As a consequence of the relatively small Q-values, photodisintegration prevents the synthesis of species beyond the iron peak. The capture of neutrons has the important effect of shifting the abundance flow toward the stability valley, where the nuclides are more neutron rich and the α-particle separation energies are larger. Hence, photodisintegrations do not terminate the nucleosynthesis beyond the iron peak. The most important processes in the buildup of these heavy nuclides are (α,n) and (n,γ) reactions. This *neutron rich,* α*-rich freeze-out* is sometimes referred to as the *α-process*. (The same name was originally given by Burbidge *et al.* (1957) to a process that in modern terminology is referred to as neon burning (Section 5.3.2)). Fourth, at a temperature near $T \approx 3$ GK, the α-induced reactions become too slow to change the composition of the matter, and the α-process ceases. At this time, the composition resides in α-particles, neutrons, and seed nuclei in the $A \approx 50$–110 mass range. If the neutron-to-seed ratio is sufficiently large, an r-process can be launched while the matter further expands and cools.

The r-process model described above has a number of interesting aspects. First, the properties of the neutrino-driven wind are determined by the proto-neutron star, not by the pre-supernova evolution. Thus, r-processing in this site may produce similar abundances for events involving neutron stars of the same mass. Second, the r-process may be sensitive to the proto-neutron star evolution and the neutrino interactions, and thus could become an important diagnostic of the event. Third, starting from seeds with $A \approx 100$ implies that the r-process does not need to overcome the waiting point nuclides near the closed neutron shell at $N = 50$ and, therefore, the overall time scale for r-processing shortens. Furthermore, the presence of these heavier seed nuclei reduces the neutron-to-seed ratio that is necessary to reproduce the solar system r-abundance distribution. For example, to explain the abundance peaks at $A = 130$, 195, and the synthesis of the elements Th, U, one requires about 30, 100, and 140 neutrons per seed nucleus, respectively. Fourth, the physical properties of the neutrino-driven wind result in an ejected amount of r-process material per supernova that is about consistent with the total mass of r-processed material presently existing in the Galaxy ($\approx 10^4 M_\odot$). It is crucial for a successful r-process that the preceding α-process is not too efficient. Otherwise, too many heavy seed nuclei are produced and too many neutrons are consumed, resulting in insufficient neutron-to-seed ratios for synthesizing nuclides up to $A \approx 200$ during the subsequent r-process. This requirement translates into relatively high entropies (or low densities) in the neutrino-driven wind so that the $\alpha + \alpha + \mathrm{n} \rightarrow {}^9\mathrm{Be}$ reaction is less efficient in converting α-particles to heavy nuclei. A fast expansion time scale limits the duration over which the freeze-out operates and is also helpful for reaching a high neutron-to-seed ratio. To summarize, an appropriate combination of a large neutron excess (or low electron mole fraction), a high entropy (i.e., high temperatures and low densities), and a fast expansion time is a necessary condition for a successful r-process in the neutrino-driven wind model.

Some studies have attempted to reproduce the solar system r-process abundance distribution by assuming a superposition of many individual contributions in the neutrino-driven wind, each representing an appropriate combination of electron mole fraction, entropy, and expansion time (Farouqi *et al.*, 2010). It was found that the heavier r-abundances ($A > 120$), including Th and U, could be reproduced with electron mole fractions of $Y_e < 0.48$ and modest entropies of $s < 300$. Furthermore, the dynamic simulations confirmed that the waiting point and steady flow approximations of the classical r-process apply locally, but not globally, over certain mass regions. Interestingly, studies (Farouqi, Kratz, and Pfeiffer, 2009) have found that many, although not all, nuclides between zinc ($Z = 30$, $A \approx 65$) and ruthenium ($Z = 44$, $A \approx 100$) could be synthesized in the neutrino-driven wind under suitable *low-entropy* conditions, via the α-process, when the free neutron abundance at charged-particle freeze-out is negligible (i.e., no subsequent r-process occurs). This scenario *co-produces*, via a charged-particle process, a fraction of the $A \approx 65$–100 nuclides, which were commonly thought to originate from other processes (s-, r-, and p-process). More observations and studies are needed.

Calculations of r-process nucleosynthesis require a very large set of nuclear physics quantities, including nuclear masses, β^--decay half-lives, branching ratios for β-delayed neutron decay, fission properties, partition functions, and so on. If the freeze-out from equilibrium is to be followed explicitly, that is, if the waiting point and steady flow approximations are not applied and the network is solved numerically, then reaction rates for neutron captures and photodisintegrations are required as well. All of this information is needed for neutron-rich isotopes that are located far away from stability. If the α-process is to be followed explicitly, then another large data set consisting of rates for charged-particle reactions and neutron-induced processes, such as (n,α) and (n,p), is required. The process $\alpha + \alpha + n \rightarrow {}^{9}\mathrm{Be}$ is key among the reactions involving light nuclides. Its impact on the r-abundances is discussed in Sasaqui *et al.* (2005). Almost all of the information needed for r-process simulations must be obtained from global, semi-empirical, models for nuclear masses and β^--decays, and from Hauser–Feshbach calculations. Information on directly measured properties, mainly lifetimes and β-delayed neutron emission probabilities, of nuclides located near or on the r-process path has been obtained in some cases. For example, pioneering experiments leading to the identification of the neutron magic waiting point nuclides ^{80}Zn (Lund *et al.*, 1986; Gill *et al.*, 1985) and ^{130}Cd (Kratz *et al.*, 1986) provided the first evidence for the existence of a local steady flow equilibrium in the r-process. Results from experiments on unstable nuclides off the r-process path are also important since the information gathered can be used to test current nuclear models from which properties of nuclides on the r-process path are derived. Many experimental r-process studies have focussed on three mass regions: (i) the neutron-rich Fe, Co, and Ni isotopes up to the double-magic nuclide ^{78}Ni, since these species represent the seed nuclei for the classical r-process model; (ii) isotopes of Zr and Pd near $A \approx 115$, where most r-process calculations underpredict the observed solar system r-abundances

(see Figure 5.79), an effect that is possibly caused by deficiencies in present nuclear models; and (iii) the region near the $N = 82$ neutron magic number (Figure 5.77), which gives rise to the second r-process abundance peak near $A \approx 130$.

Although the neutrino-driven wind represents a popular r-process site, simulations of core-collapse supernovae predict unfavorable conditions for an r-process (Fischer *et al.*, 2009; Hüdepohl *et al.*, 2010). In particular, these studies obtained, for an extended time period of up to 20 s, neutrino-driven winds that are proton rich ($Y_e > 0.5$) instead of neutron rich. This represents a serious difficulty for r-process scenarios in core-collapse supernovae. Thus, the sites of the r-process remain an unsolved puzzle. For additional information on the r-process, see Arnould, Goriely, and Takahashi (2007) and Farouqi *et al.* (2010).

5.6.3 The p-Process

The neutron-deficient, stable nuclides with mass numbers of $A \geq 74$ (between ^{74}Se and ^{196}Hg) are bypassed by the s- and r-process. These species are referred to as *p-nuclides*, where the letter *p* designates that they contain more protons relative to other stable isotopes of the same element. (Recall that all stable nuclides above ^{40}Ca consist of more neutrons than protons.) The mechanism responsible for the synthesis of the p-nuclides is called the *p-process*. A list of the p-nuclides and their associated abundances is given in Table 5.1. The solar system abundances of the p-nuclides are displayed in Figure 5.82, where they are compared to the abundances that originate from the s- and r-processes. It is apparent that as a group the p-nuclides are the rarest among the stable species. Their abundances are typically a factor of ≈ 100 smaller compared to those of adjacent s- and r-nuclides. No single element has a p-process isotope as a dominant component. This implies that all knowledge of abundance systematics of these species is based on measurements of solar system material. It is generally accepted that the more abundant s- and r-nuclides serve as seeds for the p-process.

Important clues regarding the mechanism of the p-process can be obtained from the nuclear structure of the p-nuclides. Almost all of these have even numbers of protons and neutrons (Table 5.1). The only exceptions are $^{113}_{49}\mathrm{In}_{64}$, $^{115}_{50}\mathrm{Sn}_{65}$, $^{138}_{57}\mathrm{La}_{81}$, and $^{180}_{73}\mathrm{Ta}_{107}$, but their abundances are, except for ^{115}Sn, considerably smaller compared to those of the adjacent p-nuclides. It is also apparent from Figure 5.82 that the p-abundance distribution has maxima at $^{92}_{42}\mathrm{Mo}_{50}$, $^{112}_{50}\mathrm{Sn}_{62}$, and $^{144}_{62}\mathrm{Sm}_{82}$. The first and third of these have closed neutron shells, while the second has a closed proton shell. Therefore, the p-process seems to favor the production of more strongly bound nuclides, that is, those that have paired protons and neutrons.

There are two kinds of reactions that allow for the production of neutron-deficient nuclides starting from s- or r-process seeds: (p,γ) reactions and (γ,n) photodisintegrations. Note that (p,n) reactions also produce neutron deficient nuclides, but their Q-values on the proton-rich side of the stability valley are

Table 5.1 Nuclides that are mainly produced by the p-process.

Nuclide	Z	N	Abundance[a]	Contribution[b] (%)
^{74}Se	34	40	0.60	0.89
^{78}Kr	36	42	0.20	0.362
^{84}Sr	38	46	0.13	0.5580
^{92}Mo	42	50	0.370	14.525
^{94}Mo	42	52	0.233	9.151
^{96}Ru	44	52	0.099	5.542
^{98}Ru	44	54	0.033	1.869
^{102}Pd	46	56	0.0139	1.02
^{106}Cd	48	58	0.020	1.25
^{108}Cd	48	60	0.014	0.89
^{113}In	49	64	0.008	4.288
^{112}Sn	50	62	0.035	0.971
^{114}Sn	50	64	0.024	0.659
^{115}Sn	50	65	0.012	0.339
^{120}Te	52	68	0.005	0.096
^{124}Xe	54	70	0.007	0.129
^{126}Xe	54	72	0.006	0.112
^{130}Ba	56	74	0.005	0.106
^{132}Ba	56	76	0.005	0.101
^{138}La	57	81	0.0004	0.091
^{136}Ce	58	78	0.002	0.186
^{138}Ce	58	80	0.003	0.250
^{144}Sm	62	82	0.008	3.073
^{156}Dy	66	90	0.0002	0.056
^{158}Dy	66	92	0.0004	0.095
^{162}Er	68	94	0.0004	0.139
^{168}Yb	70	98	0.0003	0.12
^{174}Hf	72	102	0.0003	0.162
^{180}Ta	73	107	0.0000026	0.0123
^{180}W	74	106	0.0002	0.120
^{184}Os	76	108	0.0001	0.020
^{190}Pt	78	112	0.0002	0.014
^{196}Hg	80	116	0.001	0.15

^{180}Ta and ^{180}W may also be synthesized by the s-process; see, for example, Arlandini *et al.* (1999) for s-process contributions to the solar system abundances.
[a] Solar system nuclidic abundance relative to 10^6 silicon atoms. [b] Contribution (in %) of isotope to element abundance.
Source: Lodders, Palme, and Gail (2009).

negative and thus their reaction rates are considerably smaller compared to the competing (p,γ) reactions. Early models placed the p-process in the *hydrogen-rich* layers of core-collapse supernovae. During the passage of the supernova shock, a combination of (p,γ) and (γ,n) reactions would produce nuclides that are shielded from the neutron-capture processes at temperatures and densities of $T \approx 2.5$ GK and $\rho \approx 100$ g/cm^3 over an explosive expansion time scale of

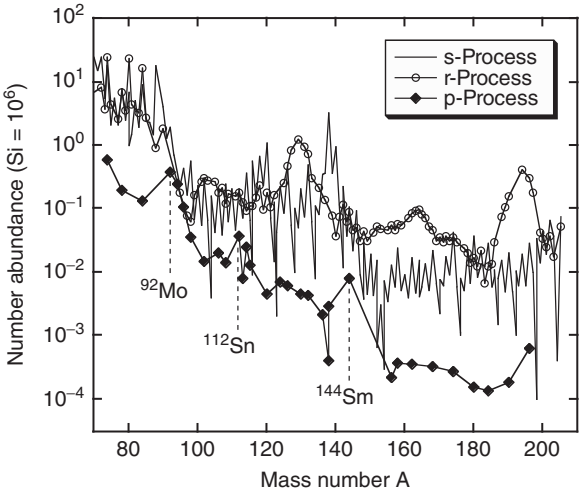

Figure 5.82 Decomposition of the observed solar system abundances of the heavy nuclides into components that are synthesized by the s-, r- and p-processes. The contributions from the s- and r-processes are adopted from Arlandini *et al.* (1999), while the p-process abundances are from Anders and Grevesse (1989). The abundance of the rare species ^{180}Ta is off scale and is omitted.

10–100 s (Burbidge *et al.*, 1957). However, it was pointed out by Woosley and Howard (1978) that the required high densities, temperatures, and relatively long time scales are unlikely to exist in hydrogen-rich zones of common stars. An exception are type I X-ray bursts (Section 1.4.4). These objects have been proposed (Schatz *et al.*, 1998) to produce some of the lighter p-nuclides via proton captures during the rp-process (Section 5.5.3). A major obstacle with this scenario is the unlikely escape of any significant amount of accreted and processed matter from the large gravitational potential of the neutron star.

Before describing specific sites for the production of the p-nuclides, it is instructive to discuss the generally accepted mechanism of the p-process. Instead of a hydrogen-rich zone it involves a *hot photon* environment with temperatures in the range of $T \approx 2$–3 GK. Starting from some seed nuclei, the most likely interactions to occur at elevated temperatures in *hydrogen-exhausted* stellar zones are photodisintegrations. The decay constants for the photoejection of neutrons, protons, or α-particles can be calculated from Eq. (3.46). At a given temperature, the decay constants depend strongly on the Q-value of the forward reaction, $0 + 1 \rightarrow \gamma + 3$, or equivalently, on the particle separation energy of nucleus 3 (see also the discussion in Section 5.3.4).

For example, consider the chain of tellurium isotopes at a temperature of $T = 2.5$ GK, shown in Figure 5.83a. Their photodisintegration decay constants are displayed in Figure 5.83b. The seed isotope ^{122}Te, which is synthesized by the s-process (Figure 5.69), is most likely destroyed by the (γ,n) reaction. The next isotope, ^{121}Te, will also most likely undergo a (γ,n) reaction. As we move along the

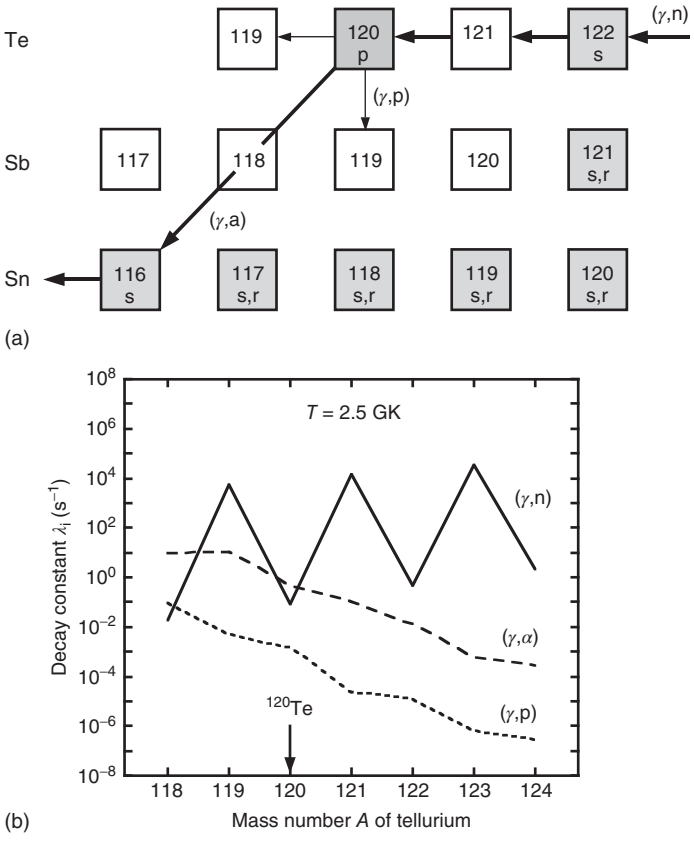

Figure 5.83 (a) Section of the chart of the nuclides in the region of neutron-deficient Sn, Sb, and Te isotopes. Stable nuclides are shown as shaded squares. The letters s, r, or p refer to their productions in the s-, r-, or p-process, respectively. (b) Decay constants of neutron-deficient tellurium isotopes, calculated for a temperature of $T = 2.5$ GK. From Rauscher and Thielemann (2000). At ^{120}Te, the (γ,α) reaction dominates over the competing (γ,n) reaction. As a consequence, the abundance flow branches off to an isotope of a different element (here ^{116}Sn).

isotopic chain toward more neutron-deficient nuclides, the (γ,n) decay constants fluctuate greatly. The photoejection of a neutron is far more likely for an odd-N isotope compared to an even-N one. This behavior is mainly caused by the pairing effect (Section 1.6.2), which leads to pronounced odd–even fluctuations in the corresponding neutron separation energies (see also Figure 5.76). The (γ,n) decay constants also decrease on average because more energy is required to remove a neutron from increasingly neutron-deficient nuclei. At the same time, the proton and α-particle separation energies decrease when moving along the isotopic chain from the stability valley toward the proton dripline. In other words, the proton-richer an isotope, the less energy is required to remove a proton or α-particle, and the larger the (γ,p) and (γ,α) decay constants become

(Figure 5.83b). At some even-N nucleus along the isotopic chain, either the (γ,p) or the (γ,α) reaction will dominate over the competing (γ,n) reaction. When this first occurs (at ^{120}Te in Figure 5.83), the abundance flow branches off to an isotope of a different element (here ^{116}Sn), and the sequence of events repeats itself in the chain of Sn isotopes.

In each isotopic chain of proton number Z, the branch point is defined by the condition

$$\lambda_{\gamma \mathrm{p}} + \lambda_{\gamma \alpha} > \lambda_{\gamma \mathrm{n}} \tag{5.207}$$

From the arguments presented above, it is also clear that in each isotopic chain the longest photodisintegration lifetimes on the flow path tend to occur near the branch point. These even-N nuclides become waiting points and material accumulates at their location. This applies especially to nuclides with closed neutron or proton shells since they have unusually large separation energies (Section 1.6.2). On the other hand, little accumulation of material is expected at odd-N nuclides since their neutron separation energies are relatively small and, consequently, their (γ,n) decay constants are large. In the above example, the branch (and waiting) point occurs at a stable nuclide (^{120}Te), which becomes a p-nuclide (Table 5.1). Ultimately, the original seed nuclide (here ^{122}Te) is photodisintegrated into several lighter waiting point nuclides until the iron peak is reached, where further photodisintegrations become energetically unfavorable. In any realistic situation there will be a distribution of s- and r-process seed nuclei extending up to Pb, all subject to the same hot photon environment. The abundance flow then reaches from lead down to iron and, along the way, is fed by the destruction of many seed nuclei. The mean lifetimes for photodisintegration reactions, $\tau_{\gamma i} \equiv 1/\lambda_{\gamma i}$, along the p-process path are < 100 s and thus β-decays, which are significantly slower, are negligible for the nucleosynthesis as long as high temperatures of $T \approx 2-3$ GK are maintained. In the above discussion, proton- or α-particle-induced reactions (e.g., (p,γ) or (α,γ)) play no role. Because of the dominance of photodisintegrations, the above mechanism of the p-process is sometimes referred to as the γ-*process* (Woosley and Howard, 1978). Some of the neutrons released during the p-process may also contribute to the nucleosynthesis. It was shown that at higher temperatures these impede the reverse (γ,n) reactions, especially in the region of the lighter p-nuclides (Rayet, Prantzos, and Arnould, 1990).

A few points must be clarified. First, if the hot photon environment is maintained for too long a period of time, then all seed nuclei would be photodissociated into iron peak nuclei, free protons, neutrons, and α-particles, as dictated by nuclear statistical equilibrium (Section 5.3.5). Thus, for any realistic site responsible for the synthesis of the p-nuclides, the values of temperature and time scales must guarantee the occurrence of some nuclear transformations, yet not reduce all nuclides to iron. These arguments support the conclusion that the p-process occurs during stellar explosions with an associated rapid expansion and cooling of material. Thus, the nucleosynthesis during the p-process will depend sensitively on the distribution of temperatures and expansion time scales, the abundances

of seed nuclei, and the hydrodynamic conditions of the explosion. Second, in the above example (Figure 5.83), the waiting point coincides with a p-nuclide. This is generally the case for lighter species. In the region of heavier nuclides, however, the waiting points correspond to proton-rich progenitors that subsequently transmute to p-nuclides via β^+-decays after cooling, expansion, and ejection of the material. For example, the stable p-nuclide ^{196}Hg is produced by the decay of the unstable waiting point nucleus ^{196}Pb, that is, via $^{196}\text{Pb}(\beta^+\nu)^{196}\text{Tl}(\beta^+\nu)^{196}\text{Hg}$. Third, the abundance flow at the waiting point nucleus ^{120}Te (Figure 5.83) continues via a (γ,α) reaction. This is the preferred path in the region of the heavier nuclides. On the other hand, most (but not all) decays of waiting point nuclides in the lighter mass range proceed via the (γ,p) reaction (Rauscher, 2005). Fourth, since the photodisintegration rates are highly temperature dependent, the location of the branch point in a given isotopic chain depends on the value of the temperature. A branch point has the tendency to shift toward more proton-rich nuclides for increasing temperatures (Problem 5.18). The question of why almost all p-nuclides exhibit an even number of protons is explored in Problem 5.19.

It is interesting to consider the total photodisintegration decay constant, $\Lambda = \lambda_{\gamma\alpha} + \lambda_{\gamma\text{p}} + \lambda_{\gamma\text{n}}$, of the p-nuclides or, if appropriate, of their proton-rich progenitors. The results are shown in Figure 5.84 as a function of mass number for temperatures of $T = 2.0$ GK, 2.5 GK, and 3.0 GK. The decay constants $\lambda_{\gamma i}$ are obtained from Hauser–Feshbach reaction rates. The structure seen in the curves is influenced by nuclear shell effects but will not concern us here. The outstanding feature shown in Figure 5.84 is the large variation of Λ, at each temperature, by several orders of magnitude over the displayed mass range. Suppose that all the p-nuclides were synthesized at the same single and constant value of temperature. If that were the case, then any photon exposure sufficient to produce the lighter p-nuclides in the $A = 70-100$ range would destroy all the heavy p-nuclides in the $A = 160-200$ region. Thus, the strong variation of Λ shown in Figure 5.84 supports the conclusion that stellar regions of different temperature are responsible for the synthesis of the p-nuclides. The heavy p-nuclides are produced at relatively low temperature, while the light p-nuclides are created at relatively high values of T. Also, Λ is an *increasing* function of mass number. If the opposite were the case, then any photon exposure sufficient to destroy the heavy seed nuclei (e.g., lead) would also destroy the photodisintegration products of lead, and so on, until the iron region is reached. The nucleosynthesis of intermediate-mass nuclides could not occur, and the p-process model described above would fail.

Most investigations to date have assumed that the p-process occurs in core-collapse supernovae when the shock wave passes through the oxygen–neon-rich layer of a massive star (Section 1.4.3). For a short period of time (≈ 1 s), the shock wave compresses and heats this stellar region. During the explosion, different zones in the oxygen–neon-rich layer will undergo different thermodynamic histories and thus will achieve different peak temperatures. Calculations show that during the p-process the range of peak temperatures in these zones amounts

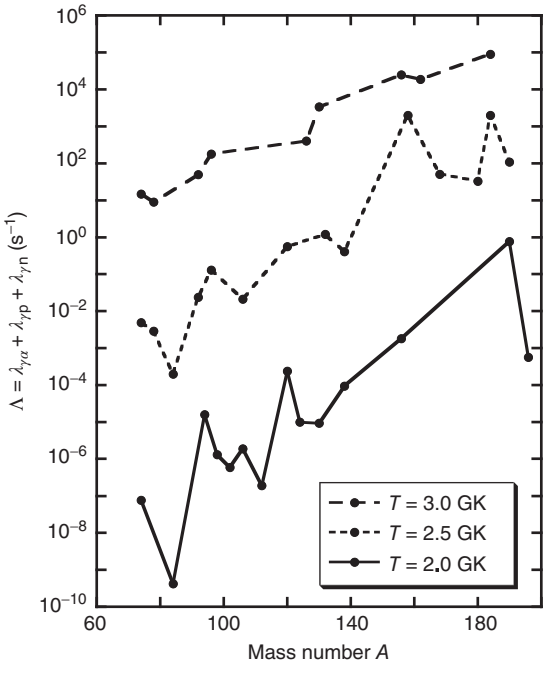

Figure 5.84 Total photodisintegration rates Λ for the p-nuclides, or their proton-rich progenitors, at stellar temperatures of T = 2.0 GK, 2.5 GK, and 3.0 GK, as a function of mass number. The photodisintegration rates are calculated using the Hauser–Feshbach model (Rauscher and Thielemann, 2000).

to $T_{\text{peak}} \approx 1.8$–$3.3$ GK. The weak s-process component, operating mainly during the preceding core helium burning stage in the pre-supernova star, strongly enhances the p-process seed abundances in the $A \approx 60$–90 region (Section 5.6.1). It has been demonstrated that p-nuclides with masses of $A \leq 92$, $A \approx 92$–144, and $A \geq 144$ are mainly produced in stellar zones with peak temperatures of $T_{\text{peak}} \geq 3$ GK, $T_{\text{peak}} \approx 2.7$–$3.0$ GK, and $T_{\text{peak}} \leq 2.5$ GK, respectively. Each p-nuclide is synthesized in a relatively narrow temperature range only (Rayet, Prantzos, and Arnould, 1990). The abundances obtained from such calculations have been weighted and averaged over a range of stars with different masses. As a result, the abundances of about 60% of the p-nuclides can be reproduced within a factor of three of their solar system values. This is a remarkable success in view of the complexities of the nuclear physics input (see below) and of the stellar models. However, a number of discrepancies persist. Most notable is the underproduction of the light p-nuclides ^{92}Mo, ^{94}Mo, ^{96}Ru, and ^{98}Ru. The odd-A nuclides ^{113}In, ^{115}Sn, and the odd–odd species ^{138}La are also underproduced in most calculations. On the other hand, the rarest species occurring naturally in the solar system, the odd–odd nuclide ^{180}Ta, seems to be a product of the p-process, although the s-process during thermal pulses in

certain AGB stars may also contribute to its observed solar system abundance (Gallino *et al.*, 1998).

Several other sites have also been considered for the production of p-nuclides, including supernovae of type Ia and Ib/Ic (Section 1.4.3). Interestingly, although the stellar models for all these scenarios are very different, similar p-abundance distributions are obtained in each case. Most of the p-abundances are reproduced within a factor of three of their solar system values, while certain species (^{92}Mo, ^{94}Mo, ^{96}Ru, ^{98}Ru, ^{113}In, ^{115}Sn, ^{138}La) are significantly underproduced. Hence, it appears likely that the p-process occurs in a number of different sites. The underproduction of some nuclides is perhaps caused by nuclear physics uncertainties or by an unreliable estimate of the s-nuclide seed distribution for the p-process. Alternatively, some of the underproduced species could be synthesized in a different site, such as sub-Chandrasekhar white dwarf explosions. For more information on sites and other issues related to the p-process, see Arnould and Goriely (2003) and Rauscher *et al.* (2013).

We now move from a qualitative discussion to a numerical treatment. The oxygen–neon layer during a core-collapse supernova is chosen as an example for a p-process site (Section 5.4.3, and left side of Figure 1.7). It was already pointed out that the p-nuclides, depending on their mass number, are synthesized in different zones that achieve different peak temperatures. We will discuss below the results of a network calculation performed for the explosive evolution of a single zone in a oxygen-neon layer of a $25\,M_\odot$ star. The temperature–density profile of the selected zone is shown in Figure 5.85. The profile starts at point A ($T = 1.4$ GK, $\rho = 1.4 \times 10^5$ g/cm^3), evolves to point B at the peak of the explosion ($T = 3.0$ GK, $\rho = 6 \times 10^5$ g/cm^3), and then settles at point C ($T = 1.4$ GK, $\rho = 7.0 \times 10^4$ g/cm^3). The entire evolution from A to C lasts for about $t = 1.1$ s. The network consists of 1100 nuclides, stretching from ^{1}H to ^{209}Bi, and includes about 11 000 reactions induced by neutrons, protons, α-particles, and their reverse reactions. The 3α reaction and the ^{12}C + ^{12}C and ^{16}O + ^{16}O reactions are also included. Above calcium, all reaction rates are adopted from Hauser–Feshbach statistical model calculations. For (n,γ) reaction rates involving stable target nuclei, which are required for calculating the corresponding reverse (γ,n) reaction rates, the statistical model results are normalized to experimental values (Bao *et al.*, 2000). Beta-decays are also included, but are expected to have a negligible influence, as discussed above, except after the termination of the explosion, when some radioactive progenitors decay to stable p-nuclides. It must be stressed that, contrary to the s-process or the r-process, the concepts of steady flows or reaction rate equilibria cannot be used here to simplify this complex situation. The p-process operates far from equilibrium and, as a result, the entire network must be followed by an explicit calculation. The initial abundances are adopted from the pre-supernova evolution models of Rayet *et al.* (1995). The most abundant species are ^{16}O ($X_i = 0.73$), ^{20}Ne ($X_i = 0.17$), and ^{24}Mg ($X_i = 0.05$), while the seed abundances in the mass $A = 60$–90 region are significantly increased compared to a solar system composition because of the operation of the weak s-process component during the preceding core helium burning stage (Section 5.6.1).

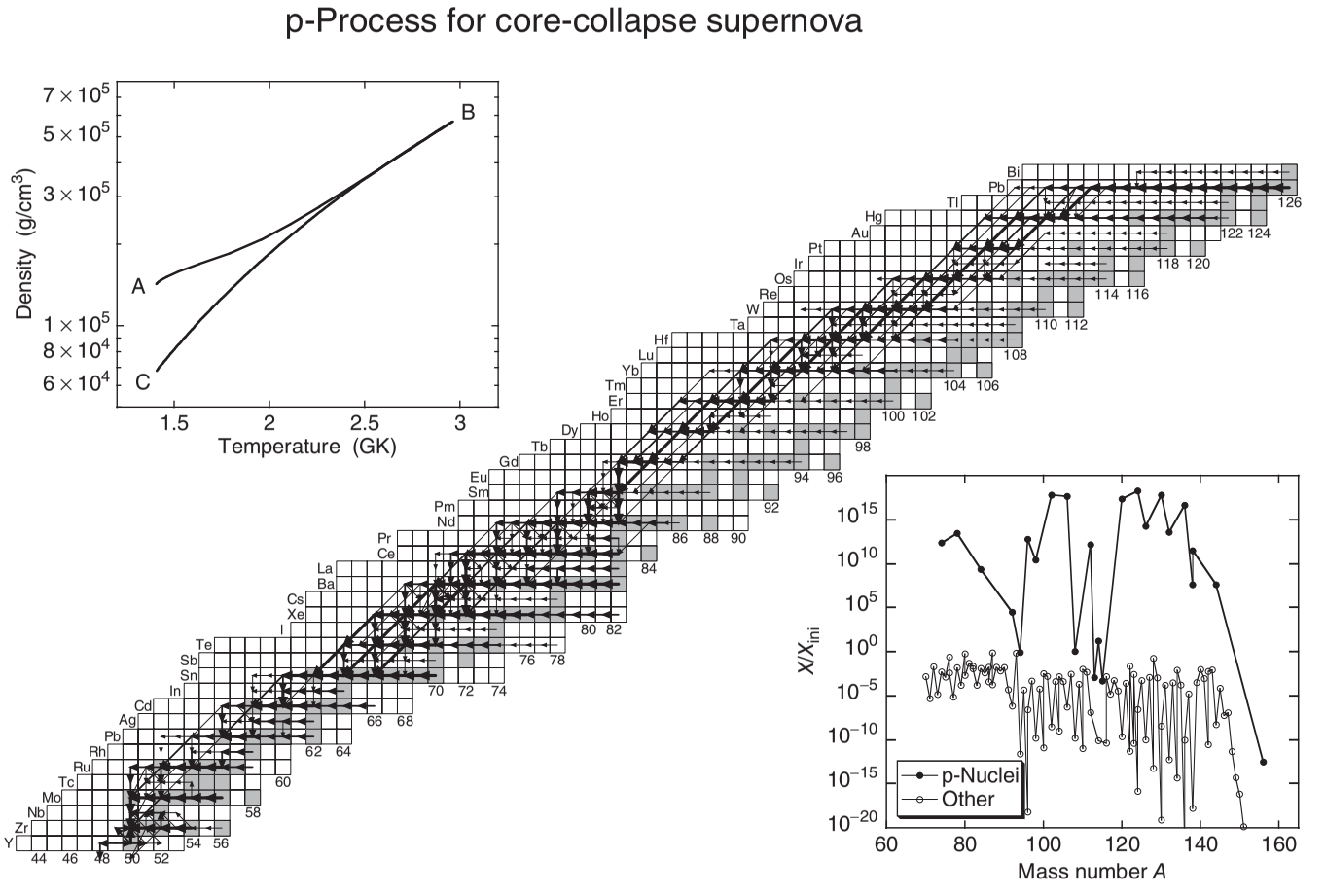
p-Process for core-collapse supernova
Density (g/cm3)
7 × 10^5
5 × 10^5
3 × 10^5
1 × 10^5
8 × 10^4
6 × 10^4
A
B
C
1.5
2
2.5
3
Temperature (GK)
Bi
Pb
Tl
Hg
Au
Pt
Ir
Os
Re
W
Ta
Hf
Lu
Yb
Tm
Er
Ho
Dy
Tb
Gd
Eu
Sm
Pm
Nd
Pr
Ce
La
Ba
Cs
Xe
I
Te
Sb
Sn
In
Cd
Ag
Pb
Rh
Ru
Tc
Mo
Nb
Zr
Y
126
122 124
118 120
114 116
110 112
108
104 106
100 102
98
94 96
92
86 88 90
84
80 82
76 78
70 72 74
66 68
62 64
60
58
54 56
44 46 48 50 52
X/X_ini
10^15
10^10
10^5
10^0
10^−5
10^−10
10^−15
10^−20
p-Nuclei
Other
60 80 100 120 140 160
Mass number A

Figure 5.85 Time-integrated net abundance flows in the region above yttrium for the p-process during explosive burning in a core-collapse supernova. The calculation represents the results from a single zone of the oxygen–neon layer for which the T–ρ profile is shown in the inset (Rapp *et al.*, 2006). The peak temperature achieved during the explosion in this particular zone is $T_{\rm peak} = 3.0$ GK. The reaction network calculation is terminated after $t = 1.1$ s (the time it takes for the zone to evolve from point A to B to C during the explosion). Abundance flows are represented by arrows of three thicknesses: thick, intermediate and thin arrows show flows of $F_{ij} > 10^{-8} F^{\rm max}$, $10^{-8} F^{\rm max} \geq F_{ij} > 10^{-9} F^{\rm max}$, and $10^{-9} F^{\rm max} \geq F_{ij} > 10^{-10} F^{\rm max}$, respectively, where $F^{\rm max}$ corresponds to the maximum flow of a link in the mass $A < 60$ region, which is not shown in the figure. Notice the overall flow pattern from heavier to lighter nuclides, unlike all other abundance flow patterns displayed in previous sections. The lower right part shows the ratio of final abundances obtained at the end of the p-process calculation and the initial (seed) abundances. For a peak temperature of $T = 3.0$ GK, most p-nuclides (solid dots) in the $A = 96$–144 region are strongly overproduced, while other nuclides (open circles) are underproduced. The underproduction of the p-nuclides ^{92}Mo, ^{94}Mo, ^{113}In, and ^{115}Sn remains unexplained.

Abundance flows integrated over the duration of the network calculation are presented in Figure 5.85. We are interested here only in the nucleosynthesis that takes place in the mass region above germanium. The obtained flow pattern reflects the qualitative arguments presented above. The p-process has the remarkable property that the abundance flow proceeds from heavy nuclides at the top of the network down toward lighter nuclides. In other words, a particular p-nuclide is synthesized exclusively from those seed isotopes that are heavier than the p-nuclide itself. The seed nuclei are converted via (γ,n) reactions until, in each isotopic chain, a branching point nuclide is reached. For the chosen conditions, the branching point nuclides above europium are almost exclusively destroyed via (γ,α) reactions. Also, the p-process path in this region is located on average 2–4 mass units away from the neutron-deficient side of the stability valley and, therefore, the branching point nuclides are all radioactive. In the region below europium, the branching point nuclides are destroyed either via (γ,α) or (γ,p) reactions and they frequently coincide with p-nuclides. Apart from these three photodisintegration reactions and certain (n,γ) reactions, no other processes are important for the nucleosynthesis. As already mentioned above, for lower peak temperatures the branching point nuclides have the tendency to shift to a location closer to the stability valley.

The ratio of final abundances obtained at the end of the calculation ($t = 1.1$ s) and the initial (seed) abundances is shown in the lower right of Figure 5.85. It can be seen that, for a peak temperature of $T_{\rm peak} = 3.0$ GK achieved in this particular zone, most p-nuclides (solid dots) in the $A = 96$–144 region are strongly overproduced, while other nuclides (open circles) are underproduced. The net effect of the nucleosynthesis is the conversion of s- and r-process seeds to p-nuclides. At this high peak temperature, all species beyond $A = 150$ (p-nuclides and others) are destroyed and converted via photodisintegrations to p-nuclides in the $A = 96$–144 region. A proper analysis of overproduction factors requires an averaging over all stellar zones (peak temperatures) in the oxygen–neon layer

of the pre-supernova star. Nevertheless, it is interesting that even this one-zone calculation hints at an unsolved problem of current p-process simulations, that is, the relative underproduction of species such as ^{92}Mo, ^{94}Mo, ^{113}In, and ^{115}Sn.

Finally, we will address issues related to the nuclear physics input required for p-process calculations. A number of charged-particle reactions in the mass $A \leq 25$ range could play an important role. For example, the $^{12}C(\alpha,\gamma)^{16}O$ rate (Section 5.2.1) influences the pre-supernova evolution of the massive star and, hence, the composition of the O–Ne layer prior to core collapse (Rayet *et al.*, 1995). The $^{22}Ne(\alpha,n)^{25}Mg$ reaction is crucial since it is responsible for the weak s-process component (Section 5.6.1) during core helium burning in massive stars. An increase in this rate will enhance the s-nuclide seed abundances for the p-process and would reduce the underproduction of Mo and Ru p-nuclides in current core-collapse supernova models (Arnould and Goriely, 2003).

With relatively few exceptions, almost all rates for a very large number of reactions (> 10 000) in the region of the p-process ($A > 60$) have to be calculated using the Hauser–Feshbach model. As we have seen, the most important interactions are (γ,n), (γ,α), and (γ,p) photodisintegrations. Their decay constants are usually calculated from Eq. (3.46) using the rates of the corresponding forward reactions. The p-process path involves neutron-deficient nuclides that are located close to the stability valley. This is a fortunate circumstance since the reaction Q-values (and separation energies) in this region are experimentally well known. It has been demonstrated that different prescriptions of the Hauser–Feshbach model sensitively influence the final p-nuclide abundances obtained from type II supernovae. The predicted abundances of the heavier p-nuclides are most sensitive to the α-nucleus optical potential, while the lighter species are mainly affected by uncertainties in nuclear level densities and nucleon–nucleus optical potentials (Arnould and Goriely, 2003).

Experimental (n,γ), (α,γ), and (p,γ) rates on stable target nuclei in the $A > 60$ mass range (Bao *et al.*, 2000; Arnould and Goriely, 2003) play an important role for p-process studies for two reasons. First, they are used for adjusting statistical model parameters and, as a result, Hauser–Feshbach rate predictions for a multitude of unmeasured reactions become more reliable. Second, the decay constants for the corresponding reverse photodisintegration reactions can be calculated from Eq. (3.46). A number of (γ,n) reactions have also been measured directly using real photons. We argued in Section 3.2.3 that the astrophysically most important energy range for a reaction $A(\gamma,n)B$ is located at a γ-ray energy of $E_\gamma^{\rm eff} \approx S_n + kT/2$ (for $\ell = 0$ neutrons). The quantity S_n is the neutron separation energy of nucleus A (or the reaction Q-value of $B(n,\gamma)A$). Consequently, direct (γ,n) measurements relevant to p-process studies ($T < 3$ GK or $kT/2 < 0.15$ MeV) have to be performed in a relatively narrow photon energy window close to the reaction threshold. This method was applied, for example, in the study of the reaction $^{181}Ta(\gamma,n)^{180}Ta$ (Utsunomiya *et al.*, 2003). The laboratory photodisintegration rates need to be corrected for the contributions of thermally excited target states using the Hauser-Feshbach model. It was already pointed out

in Section 3.1.5 that under p-process conditions the stellar enhancement factors for heavy target nuclei are typically in the range of ≈ 100–10 000. For reaction rate sensitivity studies of the p-process, see Arnould and Goriely (2003) and Rapp *et al.* (2006).

5.7
Non-stellar Processes

5.7.1
Big Bang Nucleosynthesis

Initial ideas for the big bang model were proposed by Gamow, Alpher, Herman, and collaborators in the 1940s to explain the origin of the chemical elements. They proposed that the universe was initially very dense and hot, and expanded and cooled to its present state. The elements would then be synthesized during an early time, when the temperature and density conditions were appropriate for nuclear reactions to occur (Gamow, 1946; Alpher, Bethe, and Gamow, 1948). Such a model would also predict a relic background radiation of photons with a present temperature of a few kelvin (Alpher and Hermann, 1949). While the bulk of the elements is produced in stars rather than the early universe, the idea proved correct for the origin of the light species ^{2}H, ^{3}He, ^{4}He, and part of ^{7}Li. In addition, the observation of the cosmic microwave background radiation (Penzias and Wilson, 1965), corresponding to a blackbody spectrum with a temperature of ≈ 3 K, was of paramount importance in this regard. It singled out the big bang theory as the prime candidate for the model of our universe.

Modern theories of cosmology are based on the assumption of a homogeneous and isotropic universe, as implied by the *cosmological principle*. The geometry and evolution of the universe can then be predicted by the theory of general relativity, with a number of cosmological parameters describing the spatial curvature, energy content, and overall expansion of the universe. The Hubble parameter, H, provides a measure for the expansion rate and its present-day value is called *Hubble's constant*, H_0. The mass density of baryons (more precisely, of nucleons), ρ_b, can be expressed relative to the present-day critical density, $\rho_{0,c}$, by introducing the cosmological baryon density parameter, $\Omega_b \equiv \rho_b/\rho_{0,c}$. The critical density describes the borderline between a closed and an open universe, that is, the total density at which the universe is spatially flat. It is defined by the Friedmann equation as $\rho_{0,c} \equiv 3H_0^2/(8\pi G)$, with G the gravitational constant. The number ratio of baryons to photons, $\eta \equiv N_b/N_\gamma$, stayed constant since the epoch of electron–positron annihilation, which occurred between a time of ≈ 4 s and ≈ 200 s after expansion began. The photon number density after that epoch can be found from the precise value for the present-day temperature of the cosmic microwave background radiation, $T = 2.7255 \pm 0.0006$ K (Fixsen, 2009), and is given by $N_\gamma = 410.73\ \mathrm{cm}^{-3}$. Using the definition $H_0 = 100\,h\ \mathrm{km\,s^{-1}\ Mpc^{-1}}$, one finds for the relationship of the parameters introduced above the expression $\Omega_b\, h^2 = 3.6528 \times 10^7 \eta$.

The microwave background radiation carries a record of the conditions in the early universe at a time of last scattering, when hydrogen and helium nuclei recombined with electrons to form neutral atoms. As a result, photons decoupled from baryons and the universe became transparent to radiation. Oscillations in the photon-baryon fluid around that time, about 400 000 years after the beginning of expansion, gave rise to tiny variations of temperature (at the 10^{-5} level) in different parts of the present microwave sky. These anisotropies have been observed to unprecedented precision and accuracy by NASA's Wilkinson Microwave Anisotropy Probe (WMAP) (Hinshaw *et al.*, 2013) and by ESA's Planck mission (Ade *et al.*, 2014). Color Figure 13 on page 625 shows the all-sky image from the Planck mission. The observed anisotropies can be decomposed in terms of spherical harmonics, where each term describes the magnitude of the anisotropy on a particular angular scale. The observed features in the resulting angular power spectrum are closely related to specific cosmological parameters. The analysis of the Planck Collaboration data yields values of $\Omega_b h^2 = 0.02207 \pm 0.00033$ for the present-day physical baryon density and $\Omega_c h^2 = 0.1196 \pm 0.0031$ for the present-day cold dark matter density. From the results, a number of other parameters can be derived: $t_0 = 13.813 \pm 0.058$ Gy for the age of the universe, $\eta = (6.04 \pm 0.09) \times 10^{-10}$ for the baryon-to-photon ratio, $\Omega_m h^2 = 0.1423 \pm 0.0029$ for the present-day total matter density, $\Omega_\Lambda = 0.686 \pm 0.020$ for the dark energy density, and $h = 0.674 \pm 0.014$ for the dimensionless Hubble parameter. These results imply that ordinary (baryonic) matter makes up only $\approx 16\%$ of all matter and that the expansion of the universe is presently accelerating.

Besides the cosmic microwave background, the other relic of the big bang is the abundance distribution of the light nuclides ^{2}H, ^{3}He, ^{4}He, and ^{7}Li. When the universe was less than 0.5 s old, at temperatures of $T \gtrsim 15$ GK, the energy density was dominated by radiation (photons and neutrinos) and all weak, strong, and electromagnetic interaction processes established a thermal equilibrium. The process $e^- + e^+ \leftrightarrow \nu + \overline{\nu}$ equilibrated the electron and neutrino gases, while the weak interactions $e^- + p \leftrightarrow \nu + n$, $e^+ + n \leftrightarrow \overline{\nu} + p$, and $n \leftrightarrow p + e^- + \overline{\nu}$ coupled the electron and neutrino gases to the baryon gas. In thermal equilibrium, the neutron-to-proton number ratio is determined by a Boltzmann distribution, $N_n/N_p = e^{-Q/kT}$ (see Eq. (1.35)), where $Q = 1293.3$ keV is the neutron-to-proton mass difference. During expansion and cooling, a temperature is eventually reached where the neutrino (weak) interaction processes become too slow to maintain the equilibrium. This freeze-out of the weak interactions depends on their cross sections and occurs near $T \approx 15$ GK, at a time of ≈ 0.5 s, when the neutron-to-proton number ratio is near 2/5. As the temperature declines below 15 GK, the matter is in nuclear statistical equilibrium (Section 5.3.5) until charged-particle freeze-out occurs. Beyond a time of ≈ 10 s, when $T \approx 3$ GK, the decay of free neutrons to protons, with a mean lifetime of $\tau = 880.1 \pm 1.1$ s, or a half-life of $T_{1/2} = 610.0 \pm 0.8$ s (Beringer *et al.*, 2012), becomes the dominant weak interaction. As will be seen below, further expansion and cooling gave rise to the onset of primordial nucleosynthesis. This stage is reached at a temperature

and density of $T \approx 0.9$ GK and $\rho_b \approx 2 \times 10^{-5}$ g/cm^3, respectively, near a time of ≈ 200 s, when nuclear reactions can compete with the destruction of nuclei by photons from the high-energy tail of the Planck distribution. By this time, the decay of free neutrons gave rise to a neutron-to-proton number ratio of about 1/7.

The subsequent nuclear reactions are relatively fast and, for reasons given below, nearly all neutrons are incorporated into the tightly bound species ^{4}He, while only very small amounts of other nuclides are synthesized. Under such conditions, the primordial ^{4}He abundance can be estimated using a simple counting argument: for a ratio of $N_\mathrm{n}/N_\mathrm{p} = 1/7 = 2/14$, one ^{4}He nucleus can form, while 12 protons remain free. Consequently, we find for the predicted primordial helium mass fraction a value of $X_{\alpha,\mathrm{pred}} \approx 4/(4+12) = 0.25$. From the above arguments, it is apparent that the primordial ^{4}He abundance is determined by the weak interaction cross sections (which are normalized by the neutron half-life), the neutron-proton mass difference, and the expansion rate, but it is rather insensitive to either the baryon density or to any nuclear reaction cross sections. Observations of ^{4}He in metal-poor clouds of ionized hydrogen (H II) in dwarf galaxies reveal a small contribution from stellar nucleosynthesis that is correlated with metallicity. Extrapolation to zero metal abundance yields an observed primordial ^{4}He mass fraction of $X_{\alpha,\mathrm{obs}} = 0.2465 \pm 0.0097$ (Aver *et al.*, 2013). The agreement with the predicted value provides a key piece of evidence for the standard cosmological model.

For a time window of ≈ 200–1000 s after expansion began, corresponding to temperatures and densities of $T \approx 0.9$–0.4 GK and $\rho_b \approx 2 \times 10^{-5}$–$2 \times 10^{-6}$ g/cm^3, respectively, the early universe passed through an epoch of nucleosynthesis. Note that the cosmic microwave background radiation and primordial nucleosynthesis probe different eras of the cosmic expansion. Initially, at the higher temperature end, the strong and electromagnetic interactions are sufficiently fast to ensure quasi-equilibrium (Section 5.3.3) among the abundances of the light nuclides ^{2}H, ^{3}H, ^{3}He, ^{4}He, ^{7}Li, and ^{7}Be. As the universe expands and cools, the nuclear reactions slow down, both because there is a decrease in the density and because the Coulomb barriers become harder to overcome. As a result, individual reactions freeze out of equilibrium at characteristic values of temperature. The final abundance of a particular nuclide in primordial nucleosynthesis is then mainly given by the ratio of the largest production and destruction reaction rates at the freeze-out temperature (Esmailzadeh, Starkman, and Dimopoulos, 1991; Smith, Kawano, and Malaney, 1993). Nuclear reactions cease once the temperature and density are sufficiently low. Among the synthesized light species, ^{4}He becomes by far the most abundant, since it has a higher binding energy per nucleon ($B/A = 7.074$ MeV) compared to all other nuclides in this mass region.

We will now briefly discuss the results of a numerical reaction network calculation, incorporating all important production and destruction reactions. The nuclear reaction rates depend on the baryon-to-photon ratio, η, which is the only free parameter for big bang nucleosynthesis in the standard cosmological model. If one adopts in the nucleosynthesis calculation the value of the baryon-to-photon

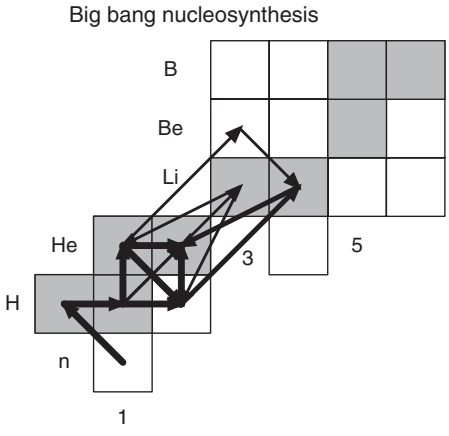

Figure 5.86 Time-integrated net abundance flows for standard big bang nucleosynthesis. The temperature-density evolution used in the network calculation is shown in Figure 5.87b. The reaction network is solved numerically for a total time of $t = 15\,000$ s. The magnitude of the abundance flows is represented by arrows of three different thicknesses: thick, intermediate, and thin arrows show flows of $F^{\max} \geq F_{ij} > 10^{-4}F^{\max}$, $10^{-4}F^{\max} \geq F_{ij} > 10^{-6}F^{\max}$, and $10^{-6}F^{\max} \geq F_{ij} > 10^{-8}F^{\max}$, respectively, where $F^{\max}$ corresponds to the reaction with the maximum net flow. Stable nuclides are shown as shaded squares.

ratio quoted above that was obtained from observations of the cosmic microwave background radiation, $\eta = 6.04 \times 10^{-10}$, then standard primordial nucleosynthesis becomes a parameter-free model. In other words, the temperature and density evolution in the early universe is determined by the value of η. The comparison of computed final abundances to observed values can then be used to investigate the galactic chemical evolution of the light species or to search for possible extensions of the standard cosmological model.

The resulting net abundance flows, integrated over a time of 15 000 s, are displayed in Figure 5.86. The corresponding abundance evolutions of the most important species (except hydrogen) are shown in Figure 5.87a, together with the temperature and density evolution in Figure 5.87b. It is apparent that significant nucleosynthesis starts at $t \approx 200$ s, when $T \approx 0.9$ GK and $\rho \approx 2 \times 10^{-5}$ g/cm^3, and ends a few thousand seconds later. The most important nuclear reactions that occur during big bang nucleosynthesis are listed below:

p(n,γ)d	t(d,n)^{4}He	^{7}Li(p,α)^{4}He
d(p,γ)^{3}He	t(α,γ)^{7}Li	^{7}Be(n,p)^{7}Li
d(d,n)^{3}He	^{3}He(n,p)t	
d(d,p)t	^{3}He(d,p)^{4}He	
	^{3}He(α,γ)^{7}Be	

Primordial nucleosynthesis starts with the p(n,γ)d reaction, resulting in a rapid increase of the deuterium abundance, followed by destruction via d(d,n)^{3}He,

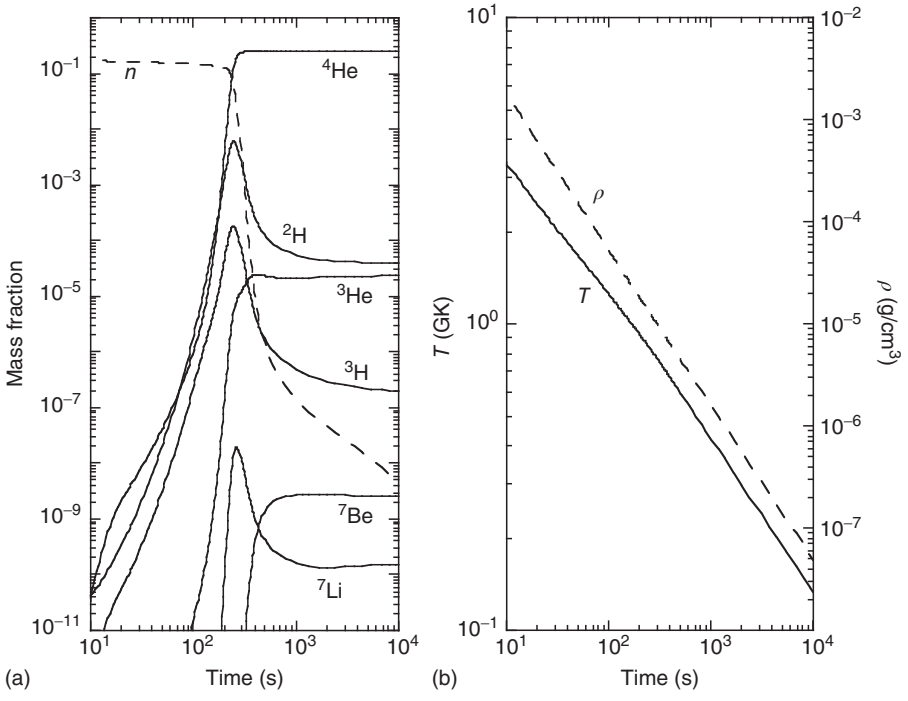

Figure 5.87 Big bang nucleosynthesis computed using a baryon-to-photon ratio of $\eta = 6.04 \times 10^{-10}$, obtained from observations of the cosmic microwave background radiation (Ade *et al.*, 2014). (a) Mass fractions of the most important light species versus time. The hydrogen abundance is almost constant on this scale and is not displayed. The neutron abundance (dashed line) declines even at late times because of radioactive decay. The species ^{7}Li is mainly produced as radioactive ^{7}Be. (b) Evolution of temperature and density. Significant nucleosynthesis starts at $t \approx 200$ s, when $T \approx 0.9$ GK and $\rho \approx 2 \times 10^{-5}$ g/cm^3. For comparison, the density of air at room temperature amounts to $\rho_{air} \approx 1.2 \times 10^{-3}$ g/cm^3. (Data in part (b) are courtesy of Alain Coc.)

d(d,p)t, d(p,γ)^{3}He, and t(d,n)^{4}He. Tritium is produced by the d(d,p)t and ^{3}He(n,p)t reactions and is mainly destroyed via t(d,n)^{4}He. The species ^{3}He is synthesized via d(d,n)^{3}He and d(p,γ)^{3}He, and is destroyed by the ^{3}He(n,p)t and ^{3}He(d,p)^{4}He reactions. The species ^{7}Li is mainly produced as ^{7}Be via ^{3}He(α,γ)^{7}Be, with ^{7}Be(n,p)^{7}Li and ^{7}Li(p,α)^{4}He as the most important destruction mechanisms. Notice that the abundance flow through ^{4}He(t,γ)^{7}Li is considerably larger compared to the flow through ^{3}He(α,γ)^{7}Be. However, the ^{7}Li nuclei produced by the former process are quickly destroyed by the strong ^{7}Li(p,α)^{4}He reaction. Other light-particle reactions that are not listed above do also occur, but their abundance flows are significantly weaker. At the end of primordial nucleosynthesis, ^{4}He is the most abundant species by orders of magnitude, followed by deuterium, ^{3}He, and tritium. The neutron abundance (dashed line) declines even at late times because of radioactive decay. For most of the reactions, direct cross

section measurements have been performed at relevant energies corresponding to the individual freeze-out temperatures (Descouvemont *et al.*, 2004). Only for the p(n,γ)d reaction are the rates largely based on theory (Ando *et al.*, 2006), although the rate uncertainty has been estimated to be on the order of only $\approx 1\%$.

We will now compare computed values with observed abundances. The predicted primordial ^{4}He abundance amounts to $X_{\alpha,\mathrm{pred}} = 0.24725 \pm 0.00032$ (Ade *et al.*, 2014). The result agrees with the observational value quoted above. For the number abundance ratio of deuterium to hydrogen, the predicted value amounts to $(D/H)_{\mathrm{pred}} = (2.656 \pm 0.067) \times 10^{-5}$ (Ade *et al.*, 2014). Deuterium is a very fragile nuclide and is easily destroyed in stars. Its primordial abundance can be determined by observing isotope-shifted (Lyman-α) absorption lines arising from low-metallicity gas clouds that fall on the line of sight between the observer and a high-redshift quasar. The low metallicity implies that the processing of deuterium by the previous-generation stars, which always deplete deuterium during hydrogen burning (Section 5.1), is negligible. Observations of very metal-poor, damped Lyman-α systems yield a value of $(D/H)_{\mathrm{obs}} = (2.53 \pm 0.04) \times 10^{-5}$ (Cooke *et al.*, 2014). Considering that the computed deuterium abundance depends rather strongly on the value of η, the agreement between predicted and observed values of D/H can be regarded as another key piece of evidence in favor of the standard cosmological model. Finally, the predicted number abundance ratio of ^{7}Li to hydrogen amounts to $(^7Li/H)_{\mathrm{pred}} = (4.9 \pm 0.4) \times 10^{-10}$ (Coc, Uzan, and Vangioni, 2014). It has been known for some time that unevolved metal-poor dwarf stars exhibit a remarkably constant lithium abundance (Spite and Spite, 1982), independent of metallicity. The *Spite plateau* has been interpreted as being representative for the primordial lithium abundance. This assumes that the lithium observed in the atmospheres of these stars has not been depleted. Observations have shown that, at the lowest observed metallicities, there is a scatter in lithium abundance and that the lithium abundance is correlated with metallicity (Bonifacio *et al.*, 2007), although the effect is small. The measurement of the primordial ^{7}Li abundance remains a challenging problem. One source of systematic uncertainty is the determination of the effective temperature of the stellar atmosphere in which the lithium absorption line is formed. Another problem is the possible depletion of lithium, either before the currently observed stars were formed, or within the stars we currently observe. Studies of metal-poor field and globular cluster stars yield for the primordial ^{7}Li abundance a value of $(^7Li/H)_{\mathrm{obs}} = (1.6 \pm 0.3) \times 10^{-10}$ (Sbordone *et al.*, 2010). Despite the observational difficulties, the predicted and observed values are in disagreement (at the 4–5σ level). This *lithium problem* represents the central unresolved issue for primordial nucleosynthesis.

At present, it seems unlikely that this problem is caused by either erroneous reaction cross sections (see also Hammache *et al.*, 2013) or by wrong effective stellar temperatures. Studies have focused on two possibilities: (i) depletion of ^{7}Li in stellar interiors, and (ii) physics beyond the standard cosmological model. The

first possibility has been discussed in the literature for a long time and many different mechanisms have been proposed, such as atomic and turbulent diffusion processes, meridional circulation, gravity waves, or rotational mixing (Michaud and Charbonneau, 1991). The second possibility is more intriguing, and could involve a time variation of the fundamental coupling constants, modifications of the expansion rate during big bang nucleosynthesis, neutrino degeneracy, or negatively charged relic particles. For a review, see Fields (2011). More work is needed to resolve the lithium problem.

5.7.2 Cosmic-Ray Nucleosynthesis

So far, we have addressed the origin of most nuclides, except of the light species ^{6}Li, ^{9}Be, ^{10}B, and ^{11}B. Their solar abundances are smaller by about six orders of magnitude compared to other light nuclides, although their abundances are larger compared to almost all s-, r-, or p-nuclides. Similar to the case for ^{2}H and ^{7}Li, their cross sections for proton-induced reactions are so large, because of the small Coulomb barriers, that they are already destroyed at temperatures below a few million kelvin during the hydrogen burning phase in stellar interiors. Under such conditions, their mean lifetimes amount to less than a few billion years. On the other hand, standard big bang nucleosynthesis (Section 5.7.1) produces only negligible amounts of ^{6}Li, ^{9}Be, ^{10}B, and ^{11}B, with predicted number abundances that are four orders of magnitude smaller compared to ^{7}Li. Their origin seemed so obscure that it was attributed to some unknown *x process* in the seminal work of Burbidge *et al.* (1957). Among the suggestions made in that work was the production, via spallation reactions, involving high-energy protons, neutrons, or α-particles of energies in excess of 100 MeV per nucleon incident on abundant CNO nuclei in stellar atmospheres. While it was convincingly demonstrated that the energy available during the T Tauri phase of young stars is insufficient to produce the light nuclides in stellar atmospheres (Ryter *et al.*, 1970), the association of lithium, beryllium, and boron synthesis with spallation reactions proved correct.

An important piece of evidence was uncovered around 1970, when it was pointed out that in the solar system the ratio of number abundances of Li, Be, and B compared to C, N, and O amounts to $\approx 10^{-6}$, while the value in Galactic cosmic rays is near ≈ 0.2 (Figure 5.88a). Thus, the idea was born that spallation reactions between Galactic cosmic rays and nuclei in the interstellar medium are responsible for the production of Li, Be, and B. This conjecture is supported by the observation that the spallation cross sections of protons and α-particles on C, N, and O nuclei at energies in excess of 100 MeV per nucleon favor the production, in decreasing order, of B, Li, and Be (Figure 5.88b). The observed Galactic cosmic-ray abundances of these light species exhibit the exact same ordering. Early quantitative models (Meneguzzi, Auduze, and Reeves, 1971), based on measured spallation cross sections, showed that this scenario could

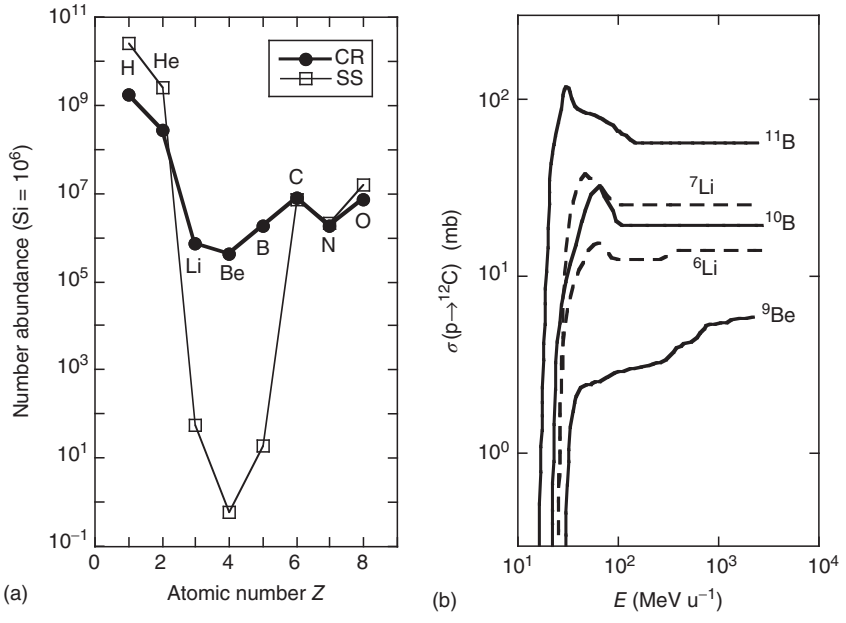

Figure 5.88 (a) Number abundances of light elements in Galactic cosmic rays (solid circles) and the solar system (open squares), normalized to silicon. The cosmic-ray values for H and He are adopted from measurements by the balloon-borne BESS instrument and the GSFC instrument on the IMP-8 spacecraft, while those for the other elements shown are from CRIS measurements. The cosmic-ray abundances were measured during solar minimum at 170 MeV per nucleon. Solar system abundances are from Lodders, Palme, and Gail (2009). In cosmic rays, B is more abundant than Li, which in turn is more abundant than Be. However, in the solar system, Li is more abundant than B, which is more abundant than Be, supporting the conjecture that a significant fraction of the solar system ^{7}Li must have been produced by some stellar source (perhaps classical novae or AGB stars). (b) Cross sections for the production of Li, Be, and B via spallation of protons incident on ^{12}C as a function of energy. Note the decreasing sequence of B, Li, and Be. (Data are from Ramaty *et al.* (1997).)

reasonably account for the abundances of ^{6}Li, ^{9}Be, and ^{10}B observed in the solar system and in stars after 10 Gy of Galactic chemical evolution.

On the other hand, ^{7}Li and ^{11}B are underproduced in the standard cosmic-ray spallation scenario, and it is believed that additional mechanisms contributed to their synthesis. During the first billion years, most of the existing ^{7}Li nuclei derived from big bang nucleosynthesis (Section 5.7.1), while later a stellar source, perhaps classical novae or AGB stars, must have contributed significantly to the production (Figure 5.88). Therefore, ^{7}Li is exceptional among all naturally occurring nuclides in that its origin can be attributed to three distinct sites: the big bang, Galactic cosmic rays, and stars. In the case of ^{11}B, it was found that neutrino-induced interactions with ^{12}C during core-collapse supernovae may also produce significant amounts of this species (Section 5.4). However, the presently predicted

yields both for the stellar production of ^{7}Li and for the neutrino-induced synthesis of ^{11}B have large associated uncertainties.

Galactic cosmic rays consist predominantly of energetic protons, α-particles, and heavier nuclides, with kinetic energies up to several hundred tera electron volt per nucleon and beyond. Their energy density amounts to about 2 eV cm^{-3} (Webber, 1997) and thus exceeds the energy density of star light in the solar neighborhood ($\approx$ 0.3 eV cm^{-3}). Near an energy of 10 GeV per nucleon, for example, the number fractions of hydrogen, helium, CNO, and LiBeB nuclei amount to 95%, 4.5%, 0.4%, and 0.07%, respectively (Sanuki *et al.*, 2000). An energetic, cosmic-ray particle propagating through the Galaxy faces a number of possibilities. First, it may undergo a high-energy nuclear collision (spallation) with interstellar nuclei. Second, an energetic cosmic-ray particle may slow down significantly because of many collisions with interstellar electrons. Such ionization losses are responsible for the eventual deposition of cosmic-ray matter into the interstellar medium. Third, the cosmic-ray particle may escape into intergalactic space, depending on the value of the escape length, that is, the amount of matter the cosmic-ray particle traverses between its source and the Galactic boundary. The escape length, which can be inferred from the abundance ratio of spallation products (e.g., Li, Be, and B) and target nuclei (mostly C, N, and O), amounts to $\approx$ 10 g/cm^2 for Galactic cosmic rays near an energy of 1 GeV per nucleon (Strong, Moskalenko, and Ptuskin, 2007). During propagation an energetic charged particle is strongly deflected by Galactic magnetic fields. Therefore, the information regarding its original direction of motion is lost.

Spallation may involve a proton or α-particle with energies in excess of several mega electron volts per nucleon impinging on a heavy nucleus in the interstellar medium, of which C, N, and O are most abundant. Alternatively, an energetic heavy nucleus, again mainly C, N, or O, may interact with interstellar H and He. A third possibility, thought to be especially important for the production of the lithium isotopes in the early Galaxy when the CNO abundance was small, is the spallation of α-particles with energies in the range of tens of mega electron volts per nucleon with other ^{4}He nuclei of the interstellar medium. The production rate of a given LiBeB species, i, expressed in terms of the number abundance ratio with respect to hydrogen, $R_i = N_i/N_{\rm H}$, is given by an expression of the form

$$\frac{dR_i}{dt} = \sum_{j,k} F_j \, \sigma(i; j \rightarrow k) \, R_k \, P_i \tag{5.208}$$

with F_j the average cosmic-ray flux (number of particles per cm^2 and s), $\sigma(i; j \rightarrow k)$ the average spallation cross section (cm^2) for the production of species i assuming projectiles j impinging on target nuclei k, and P_i the probability that species i will be thermalized and retained in the interstellar medium after production; the indices j and k denote protons, α-particles, or CNO nuclei.

Consider the following simple example. With a typical cosmic-ray proton flux of $F_{\rm p} \approx 10\,{\rm cm}^{-2}\,{\rm s}^{-1}$, an average spallation cross section of $\sigma({\rm Be}; {\rm p} \rightarrow {\rm CO}) \approx 5 \times 10^{-27}$ cm^2 for the production of ^{9}Be assuming energetic protons impinging

on C or O nuclei near an energy of 200 MeV per nucleon (Ramaty *et al.*, 1997), a CNO abundance of $R_{\rm CNO} \approx 10^{-3}$ in the interstellar medium, a probability of $P_{\rm Be} \approx 1$, and integrating over a time period of $\approx 10^{10}$ y, we find an estimated ^{9}Be abundance of $R^{\rm est}_{\rm Be} \approx 1.6 \times 10^{-11}$. The observed solar system ^{9}Be abundance from solar photospheric and meteoritic data amounts to $R^{\rm obs}_{\rm Be} = (2.1 \pm 0.1) \times 10^{-11}$ (Lodders, Palme, and Gail, 2009), in overall agreement with the calculated result. This simple estimate does not account for the change of the ^{9}Be abundance over time.

The study of the Li, Be, and B abundances, and in particular their evolution over the past several billion years, yields important clues for testing ideas regarding stellar nucleosynthesis, the physics of outer stellar layers, and models of the early Galaxy. Moreover, the Li, Be, and B abundance evolutions may hint at the origin of Galactic cosmic rays. Although it can be safely assumed that the sources of the cosmic-ray particles, except perhaps those of the very highest energies, are located within the Galaxy, their origin and acceleration mechanism have not found a satisfactory explanation yet. The mystery of cosmic-ray origin represents a long-standing problem of foremost importance. Energy arguments severely constrain the kind of candidate sources: for an assumed energy density of $\epsilon = 2$ eV cm^{-3}, maintained on average over the volume of our Galaxy, $V \approx 7 \times 10^{66}$ cm^3, and a cosmic-ray lifetime of $\tau \approx 20$ My near 1 GeV per nucleon, as derived from the cosmic-ray abundances of the radioactive *clock* isotopes ^{10}Be, ^{26}Al, ^{36}Cl, and ^{54}Mn (Mewaldt *et al.*, 2001), one finds a total cosmic-ray power of $P_{\rm CR} = \epsilon V/\tau \approx 4 \times 10^{33}$ J/s (or 4×10^{40} erg/s). Thus, Galactic cosmic rays are expected to be associated with the most energetic phenomena in the Galaxy. For example, a typical core-collapse supernova releases a kinetic energy of $(1-2) \times 10^{44}$ J (Section 5.4). Assuming a frequency of about two such events per century gives a power of $P_{\rm SN} \approx 10^{35}$ J/s, that is, significantly larger than what is needed for accelerating Galactic cosmic rays. Observational evidence indeed relates the origin of Galactic cosmic rays to supernova remnants (Acciari *et al.*, 2009; Tavani *et al.*, 2010).

Consider now the abundance evolution of ^{9}Be and suppose that supernovae are the source of Galactic cosmic rays. One possibility for producing this species is via energetic protons or α-particles colliding with interstellar C, N, and O nuclei. The production rate of ^{9}Be will then depend on the cosmic-ray flux and the CNO abundance. The former quantity is proportional to the supernova rate, $dn_{\rm SN}/dt$, while the latter is proportional to the total number of supernovae up to that time, $n_{\rm SN}$. Consequently, the observed ^{8}Be abundance at any given instant should be proportional to $n^2_{\rm SN}$ or, in other words, proportional to the *square* of the metallicity (as measured, e.g., by the Fe abundance). On the other hand, ^{9}Be may be produced by energetic CNO nuclei colliding with interstellar protons or α-particles. In this case, assuming a constant abundance of CNO nuclei in Galactic cosmic rays, the cosmic-ray flux is again proportional to the supernova rate, but the H or He abundance in the interstellar medium is independent of $n_{\rm SN}$. Thus, one would expect that the ^{9}Be abundance at any given time is *directly* proportional to the metallicity (Vangioni-Flam, Cassé, and Audouze, 2000). Alternatively, a linear relationship

between the ^{9}Be abundance and the metallicity could naturally arise if supernova-produced protons or α-particles undergo spallation reactions with CNO nuclei in the ejecta of the same supernova (Gilmore *et al.*, 1992). Similar arguments hold for the boron abundance evolution.

Observations in the 1990s of beryllium and boron in metal-poor stars were of paramount importance in this regard (Duncan, Lambert, and Lemke, 1992; Ryan *et al.*, 1992; Boesgaard and King, 1993). Unlike lithium, which exhibits the Spite plateau at low metallicities (Section 5.7.1), the beryllium and boron abundances showed no such plateau and, furthermore, revealed a linear dependence on metallicity. Therefore, it is unlikely that Galactic cosmic rays originate from supernova-induced energetic protons or α-particles colliding with CNO nuclei of the interstellar medium (which would give rise to a beryllium or boron abundance proportional to the metallicity *squared*). The observations can neither be explained by a CNO abundance in Galactic cosmic rays that, similar to the CNO abundance in the interstellar medium, would increase with time (because then the relationship between the beryllium or boron abundance and metallicity could not be *linear*). In addition, the CRIS instrument onboard the Advanced Composition Explorer (ACE) detected significant amounts of ^{59}Co in Galactic cosmic rays, but only very small amounts of the radioactive precursor ^{59}Ni (Mewaldt *et al.*, 2001). The latter isotope decays by electron capture, with a half-life of $T_{1/2} = 7.6 \times 10^4$ y in the laboratory, but is stable once fully stripped of its electrons and accelerated to high energies. From the observed abundance ratio of ^{59}Ni and ^{59}Co, it can be estimated that the time delay between explosive nucleosynthesis and acceleration of radioactive ^{59}Ni must exceed $\approx 10^5$ y. At that time, the ejecta of a particular supernova are presumably diluted and mixed into the interstellar medium. Consequently, it seems unlikely that individual supernovae accelerate their own ejecta and thereby contribute directly to the Galactic cosmic ray flux.

Several ideas have been proposed. A popular model refers to the production of Galactic cosmic rays in superbubbles, which result from the evolution of massive star clusters (Higdon, Lingenfelter, and Ramaty, 1998; Alibés, Labay, and Canal, 2002). The massive stars create cavities of hot, low-density, gas in the interstellar medium through their strong winds. The cavities increase in size with each supernova explosion and eventually merge to create superbubbles. Assuming that, in the simplest case, the composition of the metal-rich, low-density material within the superbubble does not change with time, Galactic cosmic rays could be launched from this reservoir by subsequent supernova shocks. The superbubble origin has been criticized (Prantzos, 2012a) since it does not account for the high ^{22}Ne/^{20}Ne abundance ratio observed in Galactic cosmic rays (about five times solar). Instead, it has been suggested that the only site compatible with all direct observational requirements concerning the present-day Galactic cosmic-ray composition involves the propagation of the supernova shock wave through stellar wind material that was previously ejected during the pre-supernova evolution of the massive star (Prantzos, 2012b).

5.8 Origin of the Nuclides

We will close this chapter by summarizing briefly the origin of the nuclides in nature. In principle, it seems possible to predict the main astrophysical sources for a given nuclide by considering the fraction of the yield contributed to the interstellar medium by each of the astrophysical sites mentioned in this book. We would need to know: (i) the number of stars, as a function of time since the formation of the Milky Way, of a given mass and metallicity (since stellar evolution depends on both parameters), (ii) the efficiency of various nucleosynthesis processes in each star, (iii) the fraction of the matter expelled via explosions or stellar winds, and so on. A large number of nuclides originates from massive stars. In this case, many of the predicted abundances depend strongly on the mass cut dividing the material that is ejected in the core-collapse supernova explosion from material that falls back onto the remnant neutron star or black hole. There are major uncertainties also associated with the other astrophysical sites. Nevertheless, the overall picture regarding the origin of the nuclides in the solar system seems well established and this achievement certainly represents a triumph for the theory of nucleosynthesis.

The origin of the light nuclides with masses of $A \leq 70$ is presented in Table 5.2. Only the dominant sources are listed. Radioactive nuclides are denoted by an asterisk. Hydrogen (^{1}H, ^{2}H) and helium (^{3}He, ^{4}He) are made in the big bang (BB). Cosmic-ray spallation (CR) accounts for the abundances of ^{6}Li, ^{9}Be, ^{10}Be, and ^{10}B. The nuclide ^{7}Li is likely synthesized in four distinct sites: big bang, Galactic cosmic rays, AGB stars, and the ν-process (ν). Galactic cosmic rays and the ν-process likely contribute to the synthesis of ^{11}B.

Classical novae (CN) produce large amounts of ^{13}C, ^{15}N, and ^{17}O, while AGB stars are prolific sources of ^{12}C, ^{13}C, ^{14}N, ^{22}Ne, ^{25}Mg, and ^{26}Mg (including the main component of the s-process, which is not listed in the table). Normal type Ia supernovae (Ia) synthesize a major fraction of the iron peak, for example, ^{51}V, ^{55}Mn, ^{54}Fe, ^{56}Fe, ^{57}Fe, and ^{56}Ni. A number of species, such as ^{48}Ca and ^{54}Cr, are likely synthesized by rare varieties of type Ia supernovae because they are underproduced in other sites. These peculiar events include the freeze-out from nuclear statistical equilibrium in type Ia explosions of white dwarfs that accrete matter very near the Chandrasekhar limit (IaVnCh) and type Ia supernovae caused by helium detonations (IaHeDet).

All other nuclides listed in the table are synthesized in massive stars, during hydrostatic hydrogen burning (H), hydrostatic helium burning (He), hydrostatic shell burning (C, Ne, O), explosive burning (xC, xNe, xO), incomplete explosive silicon burning (xSi), α-rich freeze-out (αRF), and the weak component of the s-process (s) that is produced both during core helium burning and hydrostatic carbon shell burning. Notice that some stable nuclides are mainly synthesized in stars as their radioactive progenitors. For example, ^{44}Ca is produced as ^{44}Ti in the α-rich freeze-out, and ^{56}Fe is produced as ^{56}Ni in both type II and type Ia supernova explosions.

Table 5.2 Origin of the nuclides with $A \leq 70$.

Nuclide	Origin	Nuclide	Origin	Nuclide	Origin
^{1}H	BB	^{30}Si	C, Ne	^{51}V	Ia, xSi, xO
^{2}H	BB	^{31}P	C, Ne	^{50}Cr	xO, xSi
^{3}He	BB	^{32}S	xO, O	^{52}Cr	Ia, xSi
^{4}He	BB	^{33}S	xO, O	^{53}Cr	xSi, xO
^{6}Li	CR	^{34}S	xO, O	^{54}Cr	IaVnCh
^{7}Li	BB, CR, AGB, ν	^{36}S	[s, Ne]	^{53}Mn*	Ia, xSi
^{9}Be	CR	^{35}Cl	xO	^{55}Mn	Ia, xSi
^{10}Be*	CR	^{36}Cl*	[xO, s]	^{54}Fe	Ia, xSi
^{10}B	CR	^{37}Cl	[xO, s]	^{56}Fe	Ia, xSi, αRF
^{11}B	CR, ν	^{36}Ar	xO	^{57}Fe	Ia, xSi, αRF
^{12}C	He, AGB	^{38}Ar	xO, O	^{58}Fe	s, IaVnCh
^{13}C	CN, AGB, H	^{40}Ar	[s, Ne]	^{60}Fe*	s
^{14}N	AGB, H	^{39}K	xO, O	^{56}Co*	Ia, xSi, αRF
^{15}N	CN, ν	^{40}K*	s, C, xO	^{57}Co*	Ia, xSi, αRF
^{16}O	He	^{41}K	xO	^{59}Co	s, αRF, Ia
^{17}O	CN	^{40}Ca	xO, xSi,O	^{60}Co*	s
^{18}O	He	^{41}Ca*	s, xO	^{56}Ni*	Ia, xSi, αRF
^{19}F	[ν, He, AGB]	^{42}Ca	xO, O	^{58}Ni	αRF, xSi, Ia
^{20}Ne	C	^{43}Ca	[C, Ne, αRF, xO, O]	^{60}Ni	αRF, xSi, Ia, s
^{21}Ne	C	^{44}Ca	αRF	^{61}Ni	s, αRF
^{22}Ne	He, AGB	^{46}Ca	[s, C, Ne]	^{62}Ni	s, αRF, Ia
^{22}Na*	[CN]	^{48}Ca	IaVnCh	^{64}Ni	s, IaVnCh
^{23}Na	C	^{45}Sc	αRF, C, xO, O	^{63}Cu	s, αRF, Ia
^{24}Mg	C	^{44}Ti*	αRF	^{65}Cu	s, αRF, xSi
^{25}Mg	C, AGB	^{46}Ti	xO, O	^{64}Zn	αRF, s, xSi
^{26}Mg	C, AGB	^{47}Ti	[IaHeDet, xO, xSi]	^{66}Zn	s, αRF, IaVnCh
^{26}Al*	xNe, xC, C	^{48}Ti	xSi	^{67}Zn	s
^{27}Al	C	^{49}Ti	xSi	^{68}Zn	s
^{28}Si	xO, O, Ia	^{50}Ti	[IaVnCh, s]	^{70}Zn	s
^{29}Si	C, Ne	^{50}V	[Ia, xO, xNe]		

The labels denote: big bang (BB); cosmic-ray spallation (CR); asymptotic giant branch stars (AGB); ν-process (ν); classical novae (CN); normal type Ia supernovae (Ia); peculiar type Ia supernovae (IaVnCh, IaHeDet). All other labels refer to sites in massive stars: hydrostatic hydrogen burning (H); hydrostatic helium burning (He); hydrostatic carbon shell burning (C); hydrostatic neon shell burning (Ne); hydrostatic oxygen shell burning (O); explosive carbon burning (xC); explosive neon burning (xNe); explosive oxygen burning (xO); incomplete explosive silicon burning (xSi); α-rich freeze-out in complete explosive silicon burning (αRF); s-process during hydrostatic helium core burning and hydrostatic carbon shell burning. Information from Arnett (1996), Woosley, Heger, and Weaver (2002), Clayton (2003), José, Lattanzio and Limongi (private communication). Uncertain assignments are given in square parenthesis. The asterisk denotes radioactive nuclides.

The sources for a number of species listed in the table, notably ^{19}F, ^{22}Na, ^{36}S, ^{37}Cl, ^{40}Ar, ^{43}Ca, ^{46}Ca, ^{47}Ti, ^{50}Ti, and ^{50}V, have been placed in square parentheses since the assignments are uncertain. These nuclides may be produced in a number of sites, although the relative contributions are controversial at present.

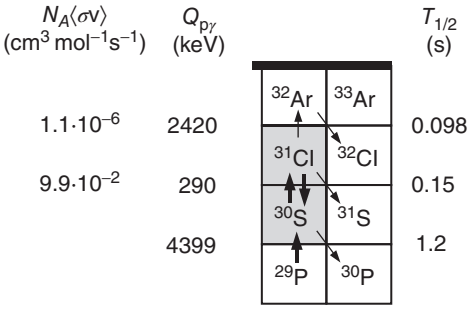

Figure 5.89 Section of the chart of the nuclides in the vicinity of ^{30}S. Nuclides that eventually reach equilibrium are shown as shaded squares. Values of $Q_{p\gamma}$ (left-hand side) and $T_{1/2}$ (right-hand side; they correspond to the diagonal arrows), are adopted from Audi, Wapstra, and Thibault (2003) and Audi *et al.* (2003), respectively. The values given for $N_A\langle\sigma v\rangle$ apply to a temperature of $T = 0.5$ GK (Iliadis *et al.*, 2001). See Problem 5.4.

Above mass $A = 70$ the situation is clearer since for most of these nuclides the relative contributions of the s-, r-, and p-process can be estimated in a straightforward manner (Section 5.6 and Figure 5.82). For more information on the origin of the nuclides in nature, see Arnett (1996), Woosley, Heger, and Weaver (2002), and Clayton (2003).

Problems

5.1 Calculate the lifetime of: (i) a proton against destruction via the p(p,e$^+\nu$)d reaction, and (ii) a deuteron against destruction via the d(p,γ)^{3}He reaction for a temperature of $T = 15$ MK, a density of $\rho = 100$ g/cm^3, and a hydrogen mass fraction of $X_{\rm H} = 0.5$. Use the following numerical values for the reaction rates: $N_A\langle\sigma v\rangle_{\rm pp} = 7.90 \times 10^{-20}$ cm^3 mol^{-1}s^{-1}, $N_A\langle\sigma v\rangle_{\rm dp} = 1.01 \times 10^{-2}$ cm^3 mol^{-1}s^{-1} (Angulo *et al.*, 1999).

5.2 Derive an expression for the temperature dependence of the decay constant for the 3α reaction (see Eq. (5.85)).

5.3 Calculate the decay constant for the reverse process of the 3α reaction, that is, the photodisintegration of ^{12}C into three α-particles. Assume that the photodisintegration will most likely proceed through the ^{12}C level at $E_x = 7.654$ MeV (Figure 5.21), and that the state at $E_x = 4.439$ MeV is in thermal equilibrium with the ground state.

5.4 Consider the nucleus ^{30}S for the conditions $T = 0.5$ GK, $\rho = 10^4$ g/cm^3 and $X_{\rm H} = 0.73$ (Figure 5.89). Explain why, according to Figure 5.59a, the net abundance flow prefers to follow the link ^{30}S($\beta^+\nu$)^{30}P instead of the competing ^{30}S(p,γ)^{31}Cl reaction. Use the values of $T_{1/2}$, Q, and $N_A\langle\sigma v\rangle$ given in Figure 5.89.

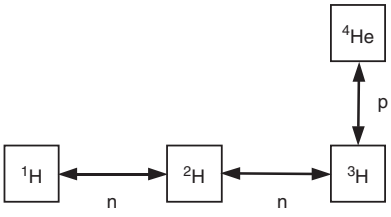

Figure 5.90 The reaction chain $^{1}H \leftrightarrow {}^{2}H \leftrightarrow {}^{3}H \leftrightarrow {}^{4}He$ in equilibrium. See Problem 5.10.

5.5 Derive an approximate analytical expression for the energy generation rate during neon burning. Assume an $^{16}O + \alpha \leftrightarrow {}^{20}Ne + \gamma$ equilibrium and that the subsequent $^{20}Ne(\alpha,\gamma)^{24}Mg$ reaction involves the equilibrium α-particle abundance. The spins of ^{4}He, ^{16}O, and ^{20}Ne are all $j_i = 0$. The normalized partition functions of these nuclides for typical neon burning temperatures are equal to unity (Rauscher and Thielemann, 2000). Disregard all contributions to the energy generation rate from other (secondary) reactions.

5.6 According to Figure 5.34, the mass fractions of ^{28}Si and ^{24}Mg at $t = 100$ s amount to $X_{^{28}Si} = 0.45$ and $X_{^{24}Mg} = 0.00011$, respectively. Calculate the equilibrium α-particle mass fraction at $t = 100$ s for the conditions $T = 3.6$ GK and $\rho = 3 \times 10^7$ g/cm^3.

5.7 Derive the quasi-equilibrium abundance ratio $N_{^{34}S}/N_{^{28}Si}$ explicitly by successive application of the Saha equation (see Figure 5.36a). Compare your result to the one obtained directly from Eq. (5.123).

5.8 Prove the relationship for the light particle abundances during silicon burning (see Eq. (5.125)).

5.9 Derive the expression for the effective photodisintegration rate of ^{24}Mg, f_{an}, during silicon burning (see Eq. (5.130)).

5.10 The reaction sequence $^{1}H \leftrightarrow {}^{2}H \leftrightarrow {}^{3}H \leftrightarrow {}^{4}He$ is shown in Figure 5.90. Calculate the number abundance of ^{4}He in nuclear statistical equilibrium by repeated application of the Saha equation. Compare your result to Eq. (5.125). Generalization of your result will yield directly Eq. (5.137).

5.11 Consider nuclear statistical equilibrium at $\eta = 0$. Assume that all the matter consists only of α-particles, protons, and neutrons. Find the temperature–density conditions at which the α-particle abundance (by mass) is equal to the total nucleon abundance, that is, $X_\alpha = 0.5$, $X_p = 0.25$, and $X_n = 0.25$ (see dotted line in Figure 5.38).

5.12 Consider the $^{64}Ge(p,\gamma)^{65}As$ reaction at $T = 1.34$ GK and $\rho = 5.9 \times 10^5$ g/cm^3. Calculate the mean lifetime of ^{64}Ge versus destruction by sequential two-proton capture for a value of $Q_{^{64}Ge(p,\gamma)} = -0.38$ MeV. Furthermore, assume that the reaction rate for $^{65}As(p,\gamma)^{66}Se$ is $N_A\langle\sigma v\rangle = 1.0 \times 10^{-2}$ cm^3 mol^{-1}s^{-1}, that is, a factor of 10 smaller than the value predicted by a Hauser–Feshbach calculation (Goriely, 1998). Assume a hydrogen mass fraction of $X_H = 0.47$. The half-lives of ^{65}As and ^{66}Se are $T_{1/2} = 0.170$ s and $T_{1/2} = 0.033$ s, respectively (Audi *et al.*, 2012). The reaction rate and decay constant for $^{64}Ge(p,\gamma)^{65}As$ and $^{66}Se(\gamma,p)^{65}As$

are given by $N_A\langle\sigma v\rangle = 0.011\ \mathrm{cm^3\ mol^{-1}s^{-1}}$ and $\lambda = 0.29\ \mathrm{s^{-1}}$, respectively (Goriely, 1998). The spins and normalized partition functions are $j_{^{64}Ge} = 0$, $j_{^{65}\mathrm{As}} = 3/2$, $j_{\mathrm{p}} = 1/2$ and $G^{\mathrm{norm}}_{^{64}\mathrm{Ge}} = 1.005$, $G^{\mathrm{norm}}_{^{65}\mathrm{As}} = 1.306$ and $G^{\mathrm{norm}}_{\mathrm{p}} = 1$ (Rauscher and Thielemann, 2000).

5.13 Estimate the r-process contribution to the solar system abundance of the s,r-isotope ^{125}Te. Use values of $N_\odot(124) = 0.2319$ and $N_\odot(125) = 0.3437$ for the number abundances of ^{124}Te and ^{125}Te per 10^6 Si atoms, respectively (Lodders, 2003). The Maxwellian-averaged neutron-capture cross sections at $kT = 30$ keV for ^{124}Te and ^{125}Te are $\langle\sigma\rangle_{124} = 155 \pm 2$ mb and $\langle\sigma\rangle_{125} = 431 \pm 4$ mb, respectively (Bao *et al.*, 2000).

5.14 Solve the abundance evolution of ^{56}Fe in the s-process (see Eq. (5.183)) for an exponential distribution of neutron exposures (see Eq. (5.180)), that is, derive the solution given in Eq. (5.185).

5.15 Derive an expression (see Eq. (5.198)) for the number abundance of an isotope in the r-process by successive application of the Saha equation to an $(\mathrm{n},\gamma)\leftrightarrow(\gamma,\mathrm{n})$ equilibrium in an isotopic chain of a given element Z.

5.16 Find a quantitative criterion from Eq. (5.198) for predicting the location of the abundance maximum in an isotopic chain at $(\mathrm{n},\gamma)\leftrightarrow(\gamma,\mathrm{n})$ equilibrium in the r-process. Also, choose the conditions $T = 1.25$ GK and $N_{\mathrm{n}} = 10^{22}\ \mathrm{cm^{-3}}$ together with the $Q_{\mathrm{n}\gamma}$-values from Möller, Nix, and Kratz (1997) to reproduce the abundance maxima shown in Figure 5.76. Disregard partition functions and the spins of the heavy nuclides.

5.17 By using the waiting point and steady flow approximations of the r-process, calculate the half-life of ^{130}Cd from the measured half-lives (Audi *et al.*, 2012) of ^{131}In ($T_{1/2} = 280 \pm 30$ ms) and ^{133}In ($T_{1/2} = 165 \pm 3$ ms) and from the observed solar system r-abundances (Anders and Grevesse, 1989; Arlandini *et al.*, 1999) of ^{130}Te (1.634), ^{131}Xe (0.946), and ^{132}Xe (0.748). The latter values are given relative to Si ($N_{\mathrm{Si}} \equiv 10^6$). Also, the measured branching ratio for the β-delayed neutron decay of ^{133}In amounts to $P_{\mathrm{n}} = 85\%$ (Audi *et al.*, 2012). Disregard all other β-delayed neutron decays (see Figure 5.77).

5.18 Explain why, during the p-process, the branch point in a given isotopic chain has the tendency to shift to more proton-rich nuclides for increasing temperature.

5.19 The location of a branch point nuclide in a given isotopic chain is specified by the condition of Eq. (5.207). The decay constants for the (reverse) photodisintegrations can be calculated from Eq. (3.46) using Hauser–Feshbach rates for the (forward) particle-induced reactions. Branch point nuclides for all elements between selenium ($Z = 34$) and lead ($Z = 82$) during p-process nucleosynthesis, calculated with this method, can be found in Rauscher (2005). Use these results together with a nuclidic chart to explain qualitatively why almost all p-nuclides exhibit an even number of protons.

Appendix A
Solutions of the Schrödinger Equation in Three Dimensions

The three-dimensional time-independent Schrödinger equation in cartesian coordinates is given by

$$-\frac{\hbar^2}{2m}\left(\frac{\partial^2\psi}{\partial x^2}+\frac{\partial^2\psi}{\partial y^2}+\frac{\partial^2\psi}{\partial z^2}\right)+V(x,y,z)\psi=E\psi \tag{A.1}$$

with ψ the total wave function, V the potential, E the total energy, and m the particle mass. For many quantum mechanical problems, the potential V depends only on the distance but not on the direction, that is, $V(\vec{r})=V(r)$. We call this a *central potential*. For such potentials, we can take advantage of the symmetry and replace the cartesian coordinates x, y, and z by the spherical coordinates r, θ, and ϕ. The wave function ψ for a central potential is separable into three different functions,

$$\psi(r,\theta,\phi)=R(r)\Theta(\theta)\Phi(\phi) \tag{A.2}$$

The Schrödinger equation is then separable as well and one obtains three different equations, one for each of the variables r, θ, and ϕ. The differential equation for Φ is

$$\frac{d^2\Phi}{d\phi^2}+m_\ell^2\Phi=0 \tag{A.3}$$

where m_ℓ^2 is the separation constant. The solution is

$$\Phi_{m_\ell}(\phi)=\frac{1}{\sqrt{2\pi}}e^{im_\ell\phi} \tag{A.4}$$

with $m_\ell=0,\pm1,\pm2,\ldots$, and so on. The quantity m_ℓ is called the *magnetic quantum number*. The equation for Θ is

$$\frac{1}{\sin\theta}\frac{d}{d\theta}\left(\sin\theta\frac{d\Theta}{d\theta}\right)+\left[\ell(\ell+1)-\frac{m_\ell^2}{\sin^2\theta}\right]\Theta=0 \tag{A.5}$$

with $\ell=0,1,2,\ldots$, and so on, and $m_\ell=0,\pm1,\ldots,\pm\ell$. The quantity ℓ is referred to as the *orbital angular momentum quantum number*. The solutions can be expressed in terms of *associated Legendre polynomials* $P_\ell^{m_\ell}$,

$$\Theta_{\ell m_\ell}(\theta)=\sqrt{\frac{(2\ell+1)}{2}\frac{(\ell-m_\ell)!}{(\ell+m_\ell)!}}P_\ell^{m_\ell}(\theta) \tag{A.6}$$

Nuclear Physics of Stars, Second Edition. Christian Iliadis.

The product of the two angle-dependent functions gives the *spherical harmonics*

$$Y_{\ell m_\ell}(\theta, \phi) = \Theta_{\ell m_\ell}(\theta)\, \Phi_{m_\ell}(\phi) \tag{A.7}$$

which describe the angular part of a wave function for any central potential. The parity π of a function describes the behavior under the coordinate transformation $\vec{r} \to -\vec{r}$ (space reflection), or in polar coordinates $r \to r$, $\theta \to \pi - \theta$, $\phi \to \pi + \phi$. Since two such transformations must yield again the original function ($\pi^2 = 1$), the parity can possess only the values $\pi = +1$ (positive or *even* parity) or $\pi = -1$ (negative or *odd* parity). The spherical harmonics have the important property

$$Y_{\ell m_\ell}(\pi - \theta, \pi + \phi) = (-1)^\ell Y_{\ell m_\ell}(\theta, \phi) \tag{A.8}$$

and hence the parity is even or odd for ℓ even or odd, respectively. In general, the functions $Y_{\ell m_\ell}$ are complex valued. For the special case of $m_\ell = 0$ the spherical harmonics are real valued and we obtain

$$Y_{\ell 0}(\theta, \phi) = \sqrt{\frac{2\ell + 1}{4\pi}} P_\ell(\cos\theta) \tag{A.9}$$

where the functions $P_\ell(\cos\theta)$ are called *Legendre polynomials*. For the lowest values of ℓ they are given by

$$P_0(x) = 1 \tag{A.10}$$

$$P_1(x) = x \tag{A.11}$$

$$P_2(x) = \frac{1}{2}(3x^2 - 1) \tag{A.12}$$

$$P_3(x) = \frac{1}{2}(5x^3 - 3x) \tag{A.13}$$

$$P_4(x) = \frac{1}{8}(35x^4 - 30x^2 + 3) \tag{A.14}$$

The equation for the radial function R is

$$-\frac{\hbar^2}{2m}\left(\frac{d^2R}{dr^2} + \frac{2}{r}\frac{dR}{dr}\right) + \left[V(r) + \frac{\ell(\ell+1)\hbar^2}{2mr^2}\right] R = ER \tag{A.15}$$

Only the radial equation depends on the central potential. The $\ell(\ell + 1)$ term is called the *centripetal potential*. It keeps the particle away from the origin when $\ell > 0$. We can rewrite the radial equation by substituting $u(r) = rR(r)$,

$$\frac{d^2u}{dr^2} + \frac{2m}{\hbar^2}\left[E - V(r) - \frac{\ell(\ell+1)\hbar^2}{2mr^2}\right] u = 0 \tag{A.16}$$

Frequently, one writes with $E = p^2/(2m) = \hbar^2k^2/(2m)$

$$\frac{d^2u}{dr^2} + \left[k^2 - \frac{\ell(\ell+1)}{r^2} - \frac{2m}{\hbar^2}V(r)\right] u = 0 \tag{A.17}$$

where k is the wave number of the free particle. Applied to nuclear scattering, this equation is correct only for distances larger than the nuclear radius ($r > R$), since the motion inside the nucleus cannot be described by a wave function, which depends only on one coordinate. The two general, linearly independent, solutions

of Eq. (A.17) are denoted by $F_\ell(r)$ and $G_\ell(r)$. These satisfy the condition that the *Wronskian* combination is independent of r,

$$\left(\frac{dF_\ell}{dr}\right) G_\ell - F_\ell \left(\frac{dG_\ell}{dr}\right) = k \tag{A.18}$$

In the following, we will discuss three special cases.

A.1
Zero Orbital Angular Momentum and Constant Potential

For $\ell = 0$ and $V = 0$, the radial equation (see Eq. (A.17)) becomes

$$\frac{d^2u}{dr^2} + k^2 u = 0 \tag{A.19}$$

Two independent solutions that satisfy this equation are the spherical wave functions e^{ikr} and e^{-ikr}. The general solution is given in terms of the linear combination

$$u = \alpha e^{ikr} + \beta e^{-ikr}, \qquad k^2 = \frac{2m}{\hbar^2}E \tag{A.20}$$

If $V(r) = \text{const} \neq 0$, then the general solution is given by

$$u = \alpha e^{i\hat{k}r} + \beta e^{-i\hat{k}r}, \qquad \hat{k}^2 = \frac{2m}{\hbar^2}(E - V) \tag{A.21}$$

A.2
Arbitrary Orbital Angular Momentum and Zero Potential

For the special case of the free particle or for neutrons, the potential outside the nucleus is zero ($V = 0$). We write

$$\frac{d^2u_\ell}{dr^2} + \left[k^2 - \frac{\ell(\ell+1)}{r^2}\right] u_\ell = 0 \tag{A.22}$$

With the substitution $\rho = kr$, one finds

$$\frac{d^2u_\ell}{d\rho^2} + \left[1 - \frac{\ell(\ell+1)}{\rho^2}\right] u_\ell = 0 \tag{A.23}$$

The solutions to this radial equation depend on ρ. They are given by the *spherical Bessel functions* $j_\ell(kr)$ and *spherical Neumann functions* $n_\ell(kr)$ (Abramowitz and Stegun, 1965; note that other authors designate by n_ℓ the same function with the opposite sign)

$$F_\ell = (kr) j_\ell(kr) = (kr)\left(-\frac{r}{k}\right)^\ell \left(\frac{1}{r}\frac{d}{dr}\right)^\ell \frac{\sin(kr)}{kr} \tag{A.24}$$

$$G_\ell = (kr) n_\ell(kr) = (kr)\left(-\frac{r}{k}\right)^\ell \left(\frac{1}{r}\frac{d}{dr}\right)^\ell \frac{\cos(kr)}{kr} \tag{A.25}$$

Only the function j_ℓ is regular at the origin. For the special case of $\ell = 0$ (s-waves), we obtain

$$j_0(kr) = \frac{\sin(kr)}{kr} \qquad \text{and} \qquad n_0(kr) = \frac{\cos(kr)}{kr} \tag{A.26}$$

For the asymptotic values, one finds

$$j_\ell \xrightarrow[kr\to\infty]{} \frac{1}{kr}\sin(kr - \ell\pi/2) \qquad \text{and} \qquad n_\ell \xrightarrow[kr\to\infty]{} \frac{1}{kr}\cos(kr - \ell\pi/2) \tag{A.27}$$

A.3
Arbitrary Orbital Angular Momentum and Coulomb Potential

For the Coulomb potential, we have to consider the equation

$$\frac{d^2u_\ell}{dr^2} + \left[k^2 - \frac{\ell(\ell+1)}{r^2} - \frac{2m}{\hbar^2}V(r)\right]u_\ell = 0 \tag{A.28}$$

where

$$V(r) = \frac{Z_pZ_te^2}{r} \tag{A.29}$$

The quantities Z_p and Z_t are the charges of the projectile and target, respectively. With the substitutions $\eta = Z_pZ_te^2/(\hbar v) = mZ_pZ_te^2/(\hbar^2 k)$ and $\rho = kr$, we obtain

$$\frac{d^2u_\ell}{d\rho^2} + \left[1 - \frac{\ell(\ell+1)}{\rho^2} - \frac{2\eta}{\rho}\right]u_\ell = 0 \tag{A.30}$$

The solutions are called *regular* and *irregular Coulomb wave functions*, $F_\ell(\eta,\rho)$ and $G_\ell(\eta,\rho)$ (Abramowitz and Stegun, 1965), and cannot be written in terms of elementary functions. The functions $F_\ell(\eta,\rho)$ and $G_\ell(\eta,\rho)$, which depend both on energy (through k) and charge (through Z_pZ_t), are best calculated using available computer codes (see, for example, Barnett, 1982). Numerically, we find for the arguments

$$\rho = 0.218735 \cdot r\sqrt{\frac{M_pM_t}{M_p+M_t}E} \tag{A.31}$$

$$\eta = 0.1574854 \cdot Z_pZ_t\sqrt{\frac{M_pM_t}{M_p+M_t}\frac{1}{E}} \tag{A.32}$$

where M_i, E, and r are in units of u, MeV, and fm, respectively.

Appendix B
Quantum Mechanical Selection Rules

The quantum mechanical (selection) rules for the coupling of angular momenta and parities are explained in any quantum mechanics textbook (see, for example, Messiah, 1999). Here we give, without proof, the most important results.

Consider a system composed of two parts with angular momentum vectors of $\vec{j}_1$ and $\vec{j}_2$. The components have eigenfunctions $\phi_{j_1 m_1}$ and $\phi_{j_2 m_2}$ that are labeled according to their value of the total angular momentum quantum numbers j_1 and j_2. The z-components of their total angular momenta are labeled by the magnetic quantum numbers m_1 and m_2, where

$$m_i = -j_i, -j_i + 1, \ldots, j_i - 1, j_i \tag{B.1}$$

The composite system of angular momentum $\vec{J}$ has an eigenfunction Φ_{JM} labeled according to the total angular momentum quantum number J and the magnetic quantum number M. The eigenfunction of the composite system can be expanded according to

$$\Phi_{JM}(j_1, j_2) = \sum_{m_1, m_2} (j_1 m_1 j_2 m_2 | JM) \phi_{j_1 m_1} \phi_{j_2 m_2} \tag{B.2}$$

The amplitudes $(j_1 m_1 j_2 m_2 | JM)$ are called *Clebsch–Gordan coefficients*. Their squares represent the probability of finding the coupled state $\Phi_{JM}(j_1, j_2)$ in the product state $\phi_{j_1 m_1} \phi_{j_2 m_2}$. The Clebsch–Gordan coefficients have important symmetry properties. They vanish unless the coupling of angular momentum vectors, $\vec{J} = \vec{j}_1 + \vec{j}_2$, obeys the following rules:

$$|j_1 - j_2| \leq J \leq j_1 + j_2 \tag{B.3}$$

$$M = m_1 + m_2 = -J, -J + 1, \ldots, J - 1, J \tag{B.4}$$

Clebsch–Gordan coefficients are widely tabulated (Rotenberg *et al.*, 1959). They can also be calculated with readily available computer codes.

The total angular momentum $\vec{J}$ and total parity Π are conserved in a nuclear reaction. While $\vec{J}$ can be obtained from the above quantum mechanical rules of angular momentum coupling, the total parity of the composite system is given by the product of the parities for the individual parts (Appendix A). If a channel contains two nuclei 1 and 2 with spins $\vec{j}_1, \vec{j}_2$ and parities π_1, π_2, then $\vec{J}$ and Π are

Nuclear Physics of Stars, Second Edition. Christian Iliadis.

given by

$$\vec{J} = \vec{\ell} + \vec{j}_1 + \vec{j}_2 = \vec{\ell} + \vec{s} \tag{B.5}$$

$$\Pi = \pi_1 \pi_2 (-1)^{\ell} \tag{B.6}$$

where $\ell = 0, 1, 2, 3, \ldots$, and so on, is the relative orbital angular momentum of the pair of nuclei and the vector sum $\vec{s} = \vec{j}_1 + \vec{j}_2$ is called the *channel spin*. If a channel only contains nucleus 1 plus a photon, then one has

$$\vec{J} = \vec{L} + \vec{j}_1 \tag{B.7}$$

$$\Pi = \pi_1 (-1)^L \qquad \text{for electric (E) multipole radiation} \tag{B.8}$$

$$\Pi = \pi_1 (-1)^{L+1} \qquad \text{for magnetic (M) multipole radiation} \tag{B.9}$$

where $L = 1, 2, 3, \ldots$, and so on, is the multipolarity of the electromagnetic radiation. Electric and magnetic radiation of the same multipolarity have opposite parities and hence cannot be emitted together in a transition connecting two given nuclear levels. Also, γ-ray transitions to or from spin-0 states or those between spin-$\frac{1}{2}$-states are pure, that is, they can only proceed via a single value of L and unique character (either electric or magnetic). A few examples will be given in the following to illustrate angular momentum and parity conservation in nuclear reactions and decays.

Example B.1

Suppose that excited ^{32}S levels are populated via resonances in the $^{28}\mathrm{Si} + \alpha \rightarrow {}^{32}\mathrm{S}$ reaction. The spin and parity of both the α-particle and of ^{28}Si is 0^+. The spins and parities of the populated levels (or, equivalently, of the resonances) are given by the quantum numbers j_r and π_r. Conservation of angular momentum and parity demands (see Eqs. (B.5) and (B.6))

$$\begin{array}{llll} \vec{j}_\alpha + \vec{j}_{^{28}\mathrm{Si}} + \vec{\ell}_\alpha = \vec{j}_r & & \text{and} & \pi_\alpha \pi_{^{28}\mathrm{Si}} (-1)^{\ell_\alpha} = \pi_r \\ 0 \quad 0 \quad \ell_\alpha \rightarrow j_r & & & (+1)(+1)(-1)^{\ell_\alpha} = \pi_r \end{array}$$

The individual spins $\vec{j}_\alpha, \vec{j}_{^{28}Si}$ can only couple to a unique value of the channel spin,

$$s = |j_\alpha - j_{^{28}\mathrm{Si}}|, \ldots, j_\alpha + j_{^{28}\mathrm{Si}} = |0 - 0|, \ldots, 0 + 0 = 0$$

In this case, we simply find $j_r = \ell_\alpha$ and $\pi_r = (-1)^{\ell_\alpha}$. The allowed orbital angular momentum quantum numbers ℓ_α for particular values of j_r and π_r are thus

given by

α	+	^{28}Si		→	^{32}S
0^+		0^+	ℓ_α	→	$j_r^{\pi_r}$
			0		0^+
			1		1^-
			2		2^+
			3		3^-
			⋮		⋮

In other words, the resonance spin and parity are uniquely determined by the orbital angular momentum. For $\ell_\alpha = 0, 1, 2, \ldots$, and so on, the resonance quantum numbers are $j_r^{\pi_r} = 0^+, 1^-, 2^+, \ldots$, and so on. Levels with this combination of quantum numbers are referred to as *natural parity* states. In particular, levels of unnatural parity ($j_r^{\pi_r} = 0^-, 1^+, 2^-, \ldots$, and so on) cannot be populated in the $^{28}\text{Si} + \alpha \rightarrow {}^{32}\text{S}$ reaction (if the target and projectile are in their ground states). The spin and parities couple in exactly the same manner for the decay of excited ^{32}S levels into the channel $^{28}\text{Si} + \alpha$.

Example B.2

Suppose that excited ^{33}Cl levels are populated via resonances in the $^{32}\text{S} + \text{p} \rightarrow {}^{33}\text{Cl}$ reaction. The spin and parity of the proton and of ^{32}S are $1/2^+$ and 0^+, respectively. Conservation of angular momentum and parity demands

$$\vec{j}_\text{p} + \vec{j}_{^{32}S} + \vec{\ell}_\text{p} = \vec{j}_r \qquad \text{and} \qquad \pi_\text{p}\pi_{^{32}S}(-1)^{\ell_\text{p}} = \pi_r$$

$$\frac{1}{2} \quad 0 \quad \ell_\text{p} \rightarrow j_r \qquad\qquad (+1)(+1)(-1)^{\ell_\text{p}} = \pi_r$$

The individual spins $\vec{j}_\text{p}, \vec{j}_{^{32}S}$ can only couple to the channel spin value of

$$s = |j_\text{p} - j_{^{32}S}|, \ldots, j_\text{p} + j_{^{32}S} = \left|\frac{1}{2} - 0\right|, \ldots, \frac{1}{2} + 0 = \frac{1}{2}$$

Thus, we find in this case, $\vec{j}_r = \vec{s} + \vec{\ell}_\text{p}$ and $\pi_r = (-1)^{\ell_\text{p}}$. The allowed orbital angular momentum quantum numbers ℓ_p for particular values of $j_r^{\pi_r}$ are, according to

$|j_r - s| \le \ell_p \le j_r + s$ (see Eq. (B.3)) and $\pi_r = (-1)^{\ell_p}$, given by

p	+	^{32}S		→	^{33}Cl
$\frac{1}{2}^+$		0^+	ℓ_p	→	$j_r^{\pi_r}$
			0		$\frac{1}{2}^+$
			1		$\frac{1}{2}^-$
			2		$\frac{3}{2}^+$
			1		$\frac{3}{2}^-$
			⋮		⋮

As was the case in the previous example, a level (or resonance) of given spin and parity ($j_r^{\pi_r}$) can be populated only with a single value of the orbital angular momentum quantum number (ℓ_p).

Example B.3

Suppose that excited ^{32}S levels are populated via resonances in the $^{31}\mathrm{P} + \mathrm{p} \rightarrow {}^{32}\mathrm{S}$ reaction. The spin and parity of both the proton and of ^{31}P is $1/2^+$. Conservation of angular momentum and parity demands

$$\vec{j}_p + \vec{j}_{^{31}P} + \vec{\ell}_p = \vec{j}_r \qquad \text{and} \qquad \pi_p \pi_{^{31}P}(-1)^{\ell_p} = \pi_r$$
$$\frac{1}{2} \quad \frac{1}{2} \quad \ell_p \rightarrow j_r \qquad (+1)(+1)(-1)^{\ell_p} = \pi_r$$

The individual spins $\vec{j}_p, \vec{j}_{^{31}P}$ can couple to the channel spin values of

$$s = |j_p - j_{^{31}P}|, \ldots, j_p + j_{^{31}P} = \left|\frac{1}{2} - \frac{1}{2}\right|, \ldots, \frac{1}{2} + \frac{1}{2} = 0 \text{ or } 1$$

Thus, we find in this case $\vec{j}_r = \vec{s} + \vec{\ell}_p$ and $\pi_r = (-1)^{\ell_p}$. The allowed orbital angular momentum quantum numbers ℓ_p for particular values of $j_r^{\pi_r}$ are, according to

$|j_r - s| \leq \ell_p \leq j_r + s$ (see Eq. (B.3)) and $\pi_r = (-1)^{\ell_p}$, given by

p	+	^{31}P		→	^{32}S
$\frac{1}{2}^+$		$\frac{1}{2}^+$	ℓ_p	→	$j_r^{\pi_r}$
			$0\,(s=0)$		0^+
			$1\,(s=1)$		0^-
			$0,2\,(s=1)$		1^+
			$1\,(s=0,1)$		1^-
			$2\,(s=0,1)$		2^+
			$1,3\,(s=1)$		2^-
			⋮		⋮

In this example, some ^{32}S levels are formed with unique values of ℓ_p and s ($j_r = 0$), while other levels can be formed with two different values of either ℓ_p or s ($j_r = 1, 2$). The relative contribution of the two components to the total cross section is described by parameters referred to as orbital angular momentum and channel spin *mixing ratios* (Appendix D).

Example B.4

We will next discuss the situation when a photon is present in a particular channel. Suppose that an excited level in ^{32}S has been populated by some means, for example, in an (α,γ) or (p,γ) reaction. The level has a spin and parity of $j_r^{\pi_r}$. The angular momentum and parity coupling in the incoming channel is described in Examples B.1 and B.3. We will now focus on the γ-ray decay of this level to lower-lying states in ^{32}S with spins and parities of j_1 and π_1, respectively. Conservation of angular momentum and parity demands (see Eqs. (B.7)–(B.9))

$$\vec{j}_r = \vec{j}_1 + \vec{L} \quad \text{and} \quad \begin{aligned} \pi_r &= \pi_1(-1)^L && \text{for electric multipole radiation} \\ \pi_r &= \pi_1(-1)^{L+1} && \text{for magnetic multipole radiation} \end{aligned}$$

First suppose that the decaying ^{32}S level has a spin and parity of $j_r^{\pi_r} = 0^+$. The allowed values of the γ-ray multipolarity L for given values of $j_1^{\pi_1}$ for the lower lying

states are, according to $|j_r - j_1| \leq L \leq j_r + j_1$ (see Eqs. (B.3) and (B.7)), given by

$^{32}S^*$	$\rightarrow$	γ	+	^{32}S
0^+		L		$j_1^{\pi_1}$
		forbidden		0^+
		forbidden		0^-
		M1		1^+
		E1		1^-
		E2		2^+
		M2		2^-
		$\vdots$		$\vdots$

The $0 \rightarrow 0$ transitions are forbidden since monopole radiation ($L = 0$) does not exist. In other words, photons must carry at least an angular momentum of $\hbar$. Such transitions may still proceed (Section 1.7.1) by internal conversion (de-excitation of the nucleus via emission of an atomic electron) or internal pair formation (de-excitation of the nucleus via emission of an electron–positron pair if the excitation energy exceeds an amount of $2m_e c^2$). All other γ-ray transitions proceed with a unique value of the multipolarity L.

If, on the other hand, the decaying level has a spin and parity of $j_r^{\pi_r} = 1^-$, then the following values of L are allowed for given values of $j_1^{\pi_1}$ for the lower-lying states:

$^{32}S^*$	$\rightarrow$	γ	+	^{32}S
1^-		L		$j_1^{\pi_1}$
		E1		0^+
		M1		0^-
		E1, M2		1^+
		M1, E2		1^-
		E1, M2, E3		2^+
		M1, E2, M3		2^-
		$\vdots$		$\vdots$

The $1 \rightarrow 0$ transitions proceed either via electric or magnetic dipole radiation ($L = 1$). All other transitions can proceed via radiations of different multipolarities. The relative contribution of the individual components to the total transition probability is described by the γ-ray mixing ratio (see Eq. (1.32)). As already noted above, parity conservation implies that electric and magnetic radiation of the same multipolarity can never be emitted together in the same transition. The γ-ray transition probability decreases fast for increasing multipolarity and in practice one usually encounters the mixing of no more than the lowest two multipole radiations.

Appendix C
Kinematics

In the following, expressions are presented that describe the kinematics of a binary interaction $a + A \rightarrow b + B$, where species a, A, and B are particles with rest mass. For more detailed discussions of the kinematics in nuclear physics, the reader is referred to Marmier and Sheldon (1969) and references therein. Kinematics calculations can be conveniently performed using readily available computer codes.

The kinematics of a nuclear reaction or of elastic scattering is determined by the conservation of total energy and linear momentum. Consider Figure C.1a, showing a collision between a projectile a and a stationary target nucleus A in the laboratory. After the collision, the recoil nucleus B moves into a direction specified by the laboratory angle ϕ, while species b moves into a direction given by laboratory angle θ. If species b is a photon, then the collision represents a radiative capture process. If species a is identical to b, and species A is identical to B (including their state of excitation), then the collision represents elastic scattering. First, expressions that only relate quantities appropriate to the laboratory coordinate system are given. Afterward, formulas for the transformation of quantities between laboratory and center-of-mass coordinate systems are presented.

C.1
Relationship of Kinematic Quantities in the Laboratory Coordinate System

Consider first a collision involving only particles with rest mass. The target nucleus A is assumed to be stationary in the laboratory system. Conservation of energy and linear momentum yields the three equations

$$m_a c^2 + E_a + m_A c^2 = m_b c^2 + E_b + m_B c^2 + E_B \tag{C.1}$$

$$\sqrt{2m_a E_a} = \sqrt{2m_B E_B}\cos\phi + \sqrt{2m_b E_b}\cos\theta \tag{C.2}$$

$$0 = \sqrt{2m_B E_B}\sin\phi - \sqrt{2m_b E_b}\sin\theta \tag{C.3}$$

where E and m denote the kinetic energy and the rest mass, respectively. The linear momenta are given by $p = \sqrt{2mE}$. The second and third expressions describe the total linear momentum parallel and perpendicular, respectively, to the incident beam direction. It is usually difficult to detect species B if it represents a heavy recoil nucleus. By eliminating E_B and ϕ and using the definition of the reaction

Nuclear Physics of Stars, Second Edition. Christian Iliadis.

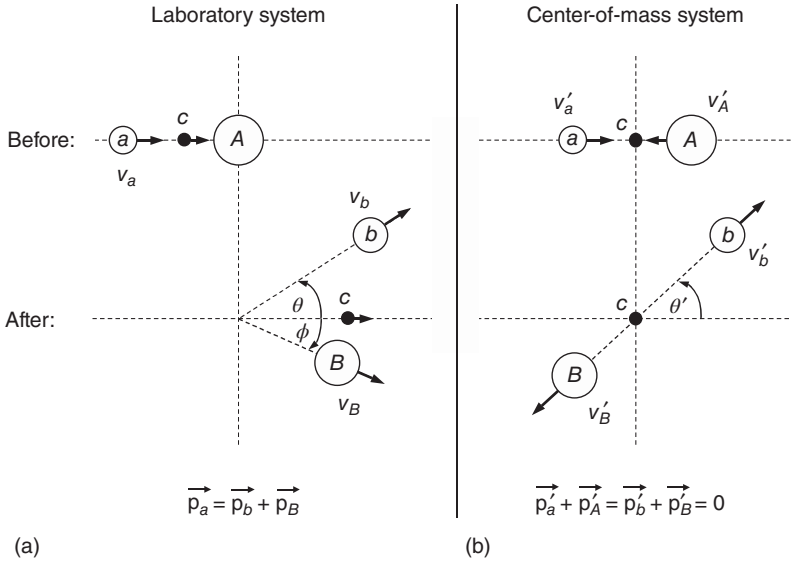

Figure C.1 Kinematic properties of a reaction $A(a,b)B$ in the (a) laboratory coordinate system, and (b) center-of-mass coordinate system. The target nucleus A is assumed to be stationary in the laboratory ($v_A = 0$). Unprimed and primed quantities are used in the laboratory and center-of-mass frame, respectively. The location of the center of mass is labeled "c."

Q-value, $Q = (m_a + m_A - m_b - m_B)c^2$ (see Eq. (1.4)), one finds

$$Q = E_b\left(1 + \frac{m_b}{m_B}\right) - E_a\left(1 - \frac{m_a}{m_B}\right) - \frac{2}{m_B}\sqrt{m_a m_b E_a E_b}\cos\theta \tag{C.4}$$

This expression is sometimes used to determine an unknown Q-value by measuring E_a, E_b, and θ if the masses m_a, m_b, and m_B are known. Frequently, one is interested in the energy E_b of the emitted particle as a function of the bombarding energy E_a and the angle θ. From Eq. (C.4) one obtains

$$\sqrt{E_b} = r \pm \sqrt{r^2 + s} \tag{C.5}$$

where

$$r = \frac{\sqrt{m_a m_b E_a}}{m_b + m_B}\cos\theta \qquad \text{and} \qquad s = \frac{E_a(m_B - m_a) + m_B Q}{m_b + m_B} \tag{C.6}$$

We assumed above that in low-energy nuclear reactions, the speeds of the particles are sufficiently small to disregard relativistic effects. For very accurate work, one can take the relativistic correction into account if each mass m in the above expressions is replaced by $m + E/(2c^2)$. Only real and positive solutions of E_b in Eqs. (C.5) and (C.6) are physically allowed. A number of different cases can be distinguished. If the reaction is exothermic ($Q > 0$) and if the projectile mass is smaller than the mass of the residual nucleus ($m_a < m_B$), then $s > 0$ and there will only be one positive solution for E_b. Because of the $\cos\theta$ dependence of r, E_b has a

minimum at $\theta = 180°$. For very small projectile energies, for example, in reactions involving thermal neutrons, we find $r \to 0$ and hence

$$E_b(E_a \approx 0) \approx s \approx Qm_B/(m_B + m_b) \tag{C.7}$$

This implies that the kinetic energy of the emitted particle b has the same value for all angles. The situation is more complex if the reaction is endothermic ($Q < 0$). For very small projectile energies, $E_a \approx 0$, one has again $r \to 0$, but s becomes negative so that no positive value of E_b exists. Hence, for each angle θ there will be a minimum energy below which the reaction cannot proceed. The value of this minimum energy is smallest at $\theta = 0°$ and is referred to as the *threshold energy*, given by

$$E_a^{\min}(\theta = 0°) = E_a^{\text{thresh}} = -Q\frac{m_b + m_B}{m_b + m_B - m_a} \tag{C.8}$$

At the threshold energy, the particles are emitted only in the direction $\theta = 0°$ with an energy of

$$E_b(E_a = E_a^{\text{thresh}}) = E_a^{\text{thresh}}\frac{m_a m_b}{(m_b + m_B)^2} \tag{C.9}$$

If one increases the bombarding energy beyond the threshold energy, then the particles b can be emitted at angles greater than $\theta = 0°$. It is also interesting that for endothermic reactions Eqs. (C.5) and (C.6) yield two positive solutions for $\theta < 90°$. In other words, two particle groups of different discrete energies are emitted in the forward direction. For bombarding energies exceeding

$$E_a = -Q\frac{m_B}{m_B - m_a} \tag{C.10}$$

there exists only a single positive solution for Eqs. (C.5) and (C.6).

Consider now a radiative capture process $a + A \to B + \gamma$. In this case, we have to replace in Eqs. (C.1)–(C.3) the total energy, $m_b c^2 + E_b$, and linear momentum, $\sqrt{2m_b E_b}$, of species b by E_γ and E_γ/c, respectively. Eliminating again E_B and ϕ and solving for the energy of the emitted photon yields

$$E_\gamma = Q + \frac{m_A}{m_B}E_a + E_\gamma\frac{v_B}{c}\cos\theta - \frac{E_\gamma^2}{2m_B c^2} = Q + \frac{m_A}{m_B}E_a + \Delta E_{\text{Dopp}} - \Delta E_{\text{rec}} \tag{C.11}$$

The photon energy is given by a sum of four terms: (i) the value of $Q = (m_a + m_A - m_B)c^2 = E_B + E_\gamma - E_a$; (ii) the bombarding energy in the center-of-mass system (see below); (iii) the *Doppler shift* since the photon is emitted by a recoil nucleus B moving at a speed of $v_B = v_a(m_a/m_B)$; and (iv) the *recoil shift* caused by the energy shift of the recoiling nucleus. The last two contributions represent relatively small corrections and are numerically given by

$$\Delta E_{\text{Dopp}} = 4.63367 \times 10^{-2}\frac{\sqrt{M_a E_a}}{M_B}E_\gamma\cos\theta \qquad \text{(MeV)} \tag{C.12}$$

$$\Delta E_{\text{rec}} = 5.36772 \times 10^{-4}\frac{E_\gamma^2}{M_B} \qquad \text{(MeV)} \tag{C.13}$$

where all energies are in units of MeV and the rest masses are in units of u. The calculation of the photon energy from Eq. (C.11) is not strictly valid since E_γ also occurs on the right-hand side. If an answer with a precision of a few kilo electron volts or so is sufficient, then one may replace the masses with (integer) mass numbers and use the approximation $E_\gamma \approx Q + E_a(m_A/m_B)$ for calculating ΔE_{Dopp} and ΔE_{rec}. For accurate work, however, the masses of a, A, and B in Eqs. (C.1)–(C.3) should be replaced by the factors $m_i + E_i/(2c^2)$. The exact relativistic expression for the photon energy is then given by

$$E_\gamma = \frac{Q(m_a c^2 + m_A c^2 + m_B c^2)/2 + m_A c^2 E_a}{m_a c^2 + m_A c^2 + E_a - \cos\theta\sqrt{E_a(2m_a c^2 + E_a)}} \tag{C.14}$$

The relationship between the photon emission angle θ and the recoil angle ϕ can be obtained from the ratio of Eqs. (C.2) and (C.3),

$$\phi = \arctan\left(\frac{\sin\theta}{E_\gamma^{-1}\sqrt{2m_a c^2 E_a} - \cos\theta}\right) \tag{C.15}$$

The maximum angle of ϕ is obtained when the photon is emitted perpendicular to the incident beam direction ($\theta = 90°$),

$$\phi_{\max} = \arctan\left(\frac{E_\gamma}{\sqrt{2m_a c^2 E_a}}\right) \tag{C.16}$$

Hence, the recoil nucleus B is emitted in the forward direction into a cone of half-angle $\phi_{\max}$.

A few comments are in order. If the reaction $A + a \rightarrow B + b$ or $A + a \rightarrow B + \gamma$ populates an excited state in nucleus B, then the Q-value in the above expressions must account for the energy of the excited state,

$$Q = Q_0 - E_x \tag{C.17}$$

where Q_0 is the Q-value for the ground state of B. Several excited levels may be populated in a given reaction. For a fixed angle θ, each of these states will give rise to a different value for the energy of the reaction products (e.g., E_b or E_γ), where the largest observed energy corresponds to the population of the ground state. From a measurement of E_b or E_γ, we can thus deduce an unknown excitation energy E_x by using Eqs. (C.5), (C.11), or (C.14). Also, for a radiative capture reaction the maximum emission angle $\phi_{\max}$ of B is given by Eq. (C.16), with E_γ denoting the photon energy for the ground state transition, even if the primary decay proceeds to an excited level (since subsequent de-excitation photons may also be emitted at $\theta = 90°$). The above expressions disregard the beam energy loss in the target and assume that the reaction is induced with a bombarding energy of E_a in the laboratory. If the reaction excites a narrow resonance, then the interaction is induced at the resonance energy E_r rather than at the incident beam energy. In this case, E_a in the above expressions represents E_r. Finally, for the case of radiative capture reactions it is assumed that the γ-ray emission occurs on a sufficiently short time scale for recoil energy losses in the target to be negligible, that is, the emitted

photon experiences the full Doppler energy shift. If the photon is emitted after the recoil nucleus experienced an energy loss in the target, then the Doppler shift is attenuated. It is sometimes possible to deduce the mean lifetime of a nuclear level by measuring the attenuated Doppler shift (see, for example, Bertone *et al.*, 2001).

C.2
Transformation Between Laboratory and Center-of-Mass Coordinate System

In experimental nuclear physics, all observations take place in a reference frame that is at rest in the laboratory. It is referred to as the *laboratory coordinate system*. From the theoretical point of view, however, the motion of the center of mass is of no consequence for the properties of a nuclear reaction. It is then often more convenient to use a moving coordinate frame in which the center of mass of the two colliding nuclei is at rest. It is called the *center-of-mass coordinate system*. Most kinematic quantities in Chapters 3 and 5 are given in the center-of-mass system. However, in Chapter 4 these quantities are frequently presented in the laboratory system, as is customary in the nuclear physics literature, since this is where the quantities are directly observed. We will only consider here the nonrelativistic transformation of kinematic quantities between these two reference frames. For the relativistic case, see Marmier and Sheldon (1969) and references therein.

The kinematic properties of a nuclear reaction $A(a,b)B$ in the laboratory and center-of-mass frames are shown in Figure C.1. Unprimed and primed quantities will be used in this section for the former and the latter coordinate system, respectively. It is assumed that the target nucleus is stationary in the laboratory ($v_A = 0$). In the center-of-mass frame, the total linear momentum is always equal to zero and, therefore, the nuclei b and B will recede in opposite directions. In other words, there is only one scattering angle θ'.

We will first consider the situation before the collision. The velocity $\vec{v}_c$ of the center-of-mass is given by the relations

$$(m_a + m_A)\vec{v}_c = m_a\vec{v}_a + m_A \cdot 0 \qquad \text{or} \qquad \vec{v}_c = \frac{m_a}{m_a + m_A}\vec{v}_a \tag{C.18}$$

and hence the projectile and target have velocities in the center-of-mass frame of

$$\vec{v}'_a = \vec{v}_a - \vec{v}_c = \left(1 - \frac{m_a}{m_a + m_A}\right)\vec{v}_a = \frac{m_A}{m_a + m_A}\vec{v}_a \tag{C.19}$$

$$\vec{v}'_A = \vec{v}_A - \vec{v}_c = -\vec{v}_c = -\frac{m_a}{m_a + m_A}\vec{v}_a \tag{C.20}$$

Since the total linear momentum of $a + A$ is zero in the center-of-mass frame, we find for the ratio of speeds

$$m_a\vec{v}'_a = m_A\vec{v}'_A \qquad \text{or} \qquad \frac{v'_a}{v'_A} = \frac{m_A}{m_a} \tag{C.21}$$

The kinetic energies of the two particles in the center-of-mass system are given by (see Eqs. (C.19) and (C.20))

$$E'_a = \frac{1}{2}m_a(v'_a)^2 = \frac{1}{2}m_a v_a^2\left(\frac{m_A}{m_a+m_A}\right)^2 = E_a\frac{m_A^2}{(m_a+m_A)^2} \tag{C.22}$$

$$E'_A = \frac{1}{2}m_A(v'_A)^2 = \frac{1}{2}m_A v_a^2\left(\frac{m_a}{m_a+m_A}\right)^2 = E_a\frac{m_A m_a}{(m_a+m_A)^2} \tag{C.23}$$

and the total kinetic energy in the center-of-mass system before the collision is related to the laboratory bombarding energy by

$$E'_i = E'_a + E'_A = E_a\frac{m_A^2 + m_A m_a}{(m_a+m_A)^2} = E_a\frac{m_A}{m_a+m_A} \tag{C.24}$$

The laboratory bombarding energy, E_a, can be expressed as the sum of total kinetic energy in the center-of-mass system before the collision, E'_i, and the kinetic energy of the center-of-mass motion, E_c, as can be seen from (see Eqs. (C.18) and (C.24))

$$\begin{aligned} E_a &= \frac{1}{2}m_a v_a^2 = \frac{1}{2}\frac{m_A m_a}{m_a+m_A}v_a^2 + \frac{1}{2}\frac{m_a^2}{m_a+m_A}\frac{m_a+m_A}{m_a+m_A}v_a^2 \\ &= E_a\frac{m_A}{m_a+m_A} + \frac{1}{2}(m_a+m_A)v_c^2 = E'_i + E_c \end{aligned} \tag{C.25}$$

Furthermore, we find from Eq. (C.24)

$$E'_i = \frac{1}{2}\frac{m_a m_A}{m_a+m_A}v_a^2 = \frac{1}{2}m_{aA}v_a^2 \tag{C.26}$$

and thus the total center-of-mass kinetic energy can be expressed in terms of the laboratory bombarding velocity, v_a, and the *reduced mass* of particles a and A, defined as $m_{aA} \equiv m_a m_A/(m_a+m_A)$. The above expressions apply equally to a radiative capture reaction, $A(a,\gamma)B$, or to elastic scattering, $A(a,a)A$.

We will now consider the situation after the collision. The total linear momentum in the center-of-mass system remains zero. For a reaction $A(a,b)B$, the two residual particles b and B separate in opposite directions with equal but opposite linear momenta,

$$m_b v'_b = m_B v'_B \tag{C.27}$$

The kinetic energies in the center-of-mass system are given by

$$E'_b = \frac{1}{2}m_b(v'_b)^2 \tag{C.28}$$

$$E'_B = \frac{1}{2}m_B(v'_B)^2 = \frac{1}{2}m_b(v'_b)^2 m_B\frac{m_b}{m_B^2} = \frac{m_b}{m_B}E'_b \tag{C.29}$$

The total kinetic energy in the center-of-mass system after the collision is then

$$E'_f = E'_b + E'_B = E'_b + \frac{m_b}{m_B}E'_b = E'_b\left(1+\frac{m_b}{m_B}\right) \tag{C.30}$$

The kinetic energies in the center-of-mass system after the collision can be expressed in terms of the laboratory bombarding energy using $E'_i + Q = E'_f$

(see Eq. (1.5)). The total kinetic energy is given by (see Eq. (C.24))

$$E'_f = E'_i + Q = E_a \frac{m_A}{m_a + m_A} + Q = Q + E_a \left(1 - \frac{m_a}{m_a + m_A}\right) \tag{C.31}$$

After some algebra, one obtains for the kinetic energies of the particles

$$E'_b = \frac{m_B}{m_b + m_B} \left[Q + E_a \left(1 - \frac{m_a}{m_a + m_A}\right)\right] \tag{C.32}$$

$$E'_B = \frac{m_b}{m_b + m_B} \left[Q + E_a \left(1 - \frac{m_a}{m_a + m_A}\right)\right] \tag{C.33}$$

Finally, we will present the transformation equations for the angles and solid angles in the laboratory and center-of-mass systems. After the collision, we have for a reaction $A(a, b)B$ (see Eq. (C.19))

$$\vec{v}'_b = \vec{v}_b - \vec{v}_c \tag{C.34}$$

or, in terms of the components parallel with and perpendicular to the beam direction

$$v'_b \cos\theta' = v_b \cos\theta - v_c \tag{C.35}$$

$$v'_b \sin\theta' = v_b \sin\theta - 0 \tag{C.36}$$

From these expressions, one can derive either of the following two relationships:

$$\tan\theta = \frac{v'_b \sin\theta'}{v'_b \cos\theta' + v_c} = \frac{\sin\theta'}{\cos\theta' + v_c/v'_b} = \frac{\sin\theta'}{\cos\theta' + \gamma} \tag{C.37}$$

$$\cos\theta = \frac{\gamma + \cos\theta'}{\sqrt{1 + \gamma^2 + 2\gamma\cos\theta'}} \tag{C.38}$$

The parameter γ is defined by the ratio of velocities of the center of mass and of particle b in the center-of-mass system,

$$\gamma \equiv \frac{v_c}{v'_b} = \sqrt{\frac{m_a m_b E_a}{m_B(m_b + m_B)Q + m_B(m_B + m_b - m_a)E_a}} \approx \sqrt{\frac{m_a m_b}{m_A m_B} \frac{E_a}{(1 + m_a/m_A)Q + E_a}} \tag{C.39}$$

where the approximation is obtained by setting $m_a + m_A \approx m_b + m_B$. For a very heavy target nucleus, one finds $\gamma \approx 0$ and hence the angle of the emitted particle b has about the same value in the laboratory and center-of-mass systems ($\theta \approx \theta'$). For elastic scattering, $m_a = m_b$, $m_A = m_B$, $Q = 0$, and thus one finds $\gamma = m_a/m_A$. For a radiative capture reaction, $A(a, \gamma)B$, the laboratory and center-of-mass angle of the emitted photon are related by (given here without proof)

$$\cos\theta = \frac{\cos\theta' + \beta}{1 + \beta\cos\theta'} \tag{C.40}$$

where the relativistic parameter β is defined as

$$\beta \equiv \frac{\sqrt{E_a(E_a + 2m_a c^2)}}{m_A c^2 + m_a c^2 + E_a} \tag{C.41}$$

The definition of the differential cross section implies that the same number of reaction products are emitted into the solid angle element $d\Omega$ in the direction θ (laboratory system) as are emitted into $d\Omega'$ in the corresponding direction θ' (center-of-mass system). Thus

$$\left(\frac{d\sigma}{d\Omega}\right)_\theta d\Omega = \left(\frac{d\sigma}{d\Omega}\right)'_{\theta'} d\Omega' \tag{C.42}$$

We assume that the cross section depends on θ or θ', but not on the azimuthal angle. Hence

$$\frac{(d\sigma/d\Omega)'_{\theta'}}{(d\sigma/d\Omega)_\theta} = \frac{d\Omega}{d\Omega'} = \frac{d(\cos\theta)}{d(\cos\theta')} \tag{C.43}$$

From Eq. (C.38), we find for a reaction $A(a, b)B$

$$\frac{d(\cos\theta)}{d(\cos\theta')} = \frac{1 + \gamma\cos\theta'}{(1 + \gamma^2 + 2\gamma\cos\theta')^{3/2}} = \frac{\sqrt{1 - \gamma^2\sin^2\theta}}{\left(\gamma\cos\theta + \sqrt{1 - \gamma^2\sin^2\theta}\right)^2} \tag{C.44}$$

For a radiative capture reaction, $A(a, \gamma)B$, one obtains from Eq. (C.40)

$$\frac{d(\cos\theta)}{d(\cos\theta')} = \frac{1 - \beta^2}{(1 + \beta\cos\theta')^2} \tag{C.45}$$

for the relationship of the solid angles of the emitted photon.

Appendix D
Angular Correlations

Traditionally, angular correlation measurements have been used in nuclear physics as a powerful tool to determine the angular momenta of states participating in nuclear transitions. It also turns out that angular correlations are sensitive to the ratios of nuclear matrix elements (i.e., mixing ratios; see later) that correspond to different possibilities of coupling angular momenta in a specific transition. We will not attempt here to summarize this vast field, but will focus on aspects that are of primary importance in low-energy nuclear astrophysics measurements.

Uncertainties in thermonuclear reaction rates are caused by contributions from resonances or nonresonant reaction processes that are as yet unobserved. The goal of the experimentalist is to measure such contributions. If the detection system covers the entire solid angle (4π sr), the measured intensities represent angle-integrated yields. These may then be converted to cross sections or resonance strengths (Sections 4.8 and 4.9). However, in most experimental Setups, the detector(s) will cover only a fraction of the full solid angle. What is measured in such cases are *differential* yields that may be influenced by angular correlation effects. It should be pointed out that the angular momenta for many levels participating in astrophysically important reactions are known or, at least, have been restricted to a certain range of values by previous nuclear structure studies. Hence, it becomes in principle possible to estimate angular correlation effects by making reasonable assumptions and, if necessary, to correct the measured differential yields appropriately.

A comprehensive theory of angular correlations is beyond the scope of the present work. The interested reader is referred to the specialized literature (see, for example, Devons and Goldfarb, 1957). The focus of this section is on angular correlations in astrophysically important reactions, that is, processes such as $A(a,b)B$ or $A(a,\gamma)B$, where a and b denote particles with rest mass. We will briefly explain the origin of angular correlations in such processes and examples of the application of angular correlations to specific cases will be given. In this section, all angles θ refer to the center-of-mass system.

Nuclear Physics of Stars, Second Edition. Christian Iliadis.

D.1 General Aspects

For the discussions in this section, we will make the following assumptions: (i) the beam is unpolarized and the target nuclei are randomly oriented; (ii) the nuclear levels involved in the transitions at each stage have unique spin and well-defined parity; (iii) the polarization of the detected radiations is not observed. These assumptions apply to most cases of interest here. The term *radiation* denotes bombarding (incident) particles or γ-rays as well as emitted (outgoing) particles or γ-rays. An angular correlation between two radiations (e.g., between the incident beam and an outgoing radiation, or between two successive outgoing radiations) is the result of the alignment of a particular nuclear level. An aligned level of spin J is prepared by some process that populates its $2J + 1$ magnetic substates *unequally* with the condition that the population of the $+m$ substate will be equal to the population of the $-m$ substate (since we assume unpolarized beam and target nuclei). Particles or γ-rays that are emitted from a specific substate m of the aligned level and that populate a substate m_f of a final level will then have a characteristic radiation pattern, or *angular correlation*, with respect to some (z-)axis of quantization, depending on the value of $\Delta m = m - m_f$. The total radiation pattern will consist of the superposition of all allowed transitions $m \to m_f$ between substates. The alignment in reactions of type $A(a, b)B$ or $A(a, \gamma)B$ is achieved since the orbital angular momentum carried by the incident radiation is perpendicular to its direction of motion. This simple circumstance, plus the additional fact that angular momentum is conserved, forms the foundation of the angular correlation theory for unpolarized radiations.

As a simple example, we will consider an excited level of spin and parity $J^\pi = 1^-$ that decays to a 0^+ ground state via emission of electric dipole (E1; $L = 1$) radiation (Figure D.1). The spatial distribution of the emitted photons will depend on the magnetic quantum numbers m and m_f of the decaying and the final level, respectively, where each allowed value of $\Delta m = m - m_f$ gives rise to a different radiation pattern. In our example, the decaying level consists of $(2 \cdot 1 + 1) = 3$ substates and the final level has only $(2 \cdot 0 + 1) = 1$ substate. The allowed transitions are then described by $m - m_f = 0 - 0 = 0$ and $m - m_f = \pm 1 - 0 = \pm 1$. The corresponding radiation patterns are given by $W_{\Delta m=0}(\theta) \sim \sin^2\theta$ and $W_{\Delta m=\pm 1}(\theta) \sim (1 + \cos^2\theta)/2$, respectively (Jackson, 1975). These are plotted as polar intensity diagrams in Figure D.1. Suppose first that the $J^\pi = 1^-$ level is populated by the β-decay of a parent state and that the β-particles are not detected. Under such conditions, the β-decay populates the magnetic substates *equally* that is, with a probability of $p(m) = 1/(2J + 1) = 1/3$. The total photon radiation pattern is thus given by

$$W(\theta) = \sum_m p(m) W_{m \to m_f}(\theta)$$
$$\sim \frac{1}{3} \cdot \frac{1}{2}(1 + \cos^2\theta) + \frac{1}{3}\sin^2\theta + \frac{1}{3} \cdot \frac{1}{2}(1 + \cos^2\theta) = \text{const} \qquad \text{(D.1)}$$

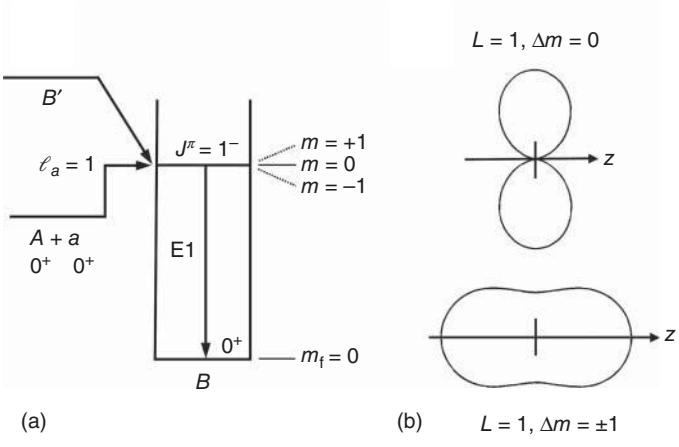

Figure D.1 (a) Level scheme for an excited state ($J^\pi = 1^-$), which can be populated either via β-decay from nucleus B' or via the capture reaction $A + a \rightarrow B + \gamma$. Both the target and the projectile have spins and parities of 0^+. The state decays via E1 emission to the ground state ($J^\pi = 0^+$). In the first case, the radiation pattern will be isotropic, while in the second case, the pattern is anisotropic because of a strong alignment. (b) Dipole radiation pattern for $\Delta m = 0$ (top) and $\Delta m = \pm 1$ (bottom).

and hence becomes isotropic. Now suppose that the $J^\pi = 1^-$ level is instead populated as a resonance in a capture reaction $A(a,\gamma)B$ involving target and projectile spins and parities of $j_A = 0^+$ and $j_a = 0^+$. The resonance can only be formed by absorption of particles a with an orbital angular momentum of $\ell_a = 1$ (Example B.1). Provided the incident particle beam is well collimated, the projection of the orbital angular momentum vector along the incident beam direction is zero (Figure 2.4). The allowed range of magnetic substates of the resonance that can be populated in this type of capture reaction is then given by $m_{\text{res}} \leq j_A + j_a$ (see Eqs. (B.3) and (B.4)). It follows that, among the three different magnetic substates of the resonance, only the $m = 0$ substate can be populated in the reaction. In other words, we obtain $p(0) = 1$ and $p(\pm 1) = 0$, and the γ-ray decay must proceed from $m = 0$ to $m_f = 0$. Consequently, the total radiation pattern is given by the $\Delta m = m - m_f = 0$ transition only

$$W(\theta) = \sum_m p(m) W_{m \rightarrow m_f}(\theta) \sim \sin^2 \theta \tag{D.2}$$

The alignment in this example is exceptionally strong and thus the variation of the γ-ray counting rate with angle is relatively large. If the beam or target nuclei have nonzero spin, then the alignment will be weaker, but angular correlation effects are in general nevertheless observed.

In certain situations involving nuclear reactions, all magnetic substates are populated equally, independent of the mode of formation. For example, the capture of unpolarized protons by spin-zero target nuclei leading to a $J = 1/2$ resonance will always populate the $m = \pm 1/2$ magnetic substates of the resonance uniformly. As a result, the total radiation pattern will be isotropic. Similar arguments apply to

a resonance of spin $J = 0$. In this case, only one magnetic substate exists and the transitions to the various substates in the final state proceed with equal probabilities. As a result, the total radiation pattern must necessarily be isotropic.

We considered so far only the angular correlation caused by the alignment of levels produced in nuclear reactions (also termed *angular distribution*). Another type of angular correlation occurs if an excited level de-excites to a final state through an intermediate level by emitting two successive radiations (e.g., two photons). In this case, measurement of the direction of the first radiation will produce an aligned intermediate state. The result is again a nonuniform intensity distribution of the second radiation with respect to the measured direction of the first radiation. We encountered this situation in the discussion of angular correlation effects for γ-ray detector summing corrections (Section 4.5.2). As we shall see, the angular correlation formalism is general and describes this situation as well.

The summation over magnetic quantum numbers is performed explicitly in Eq. (D.1). In more complicated situations involving a number of unobserved or coupled orientations, such a calculation becomes very tedious. More convenient, but equivalent, expressions have been developed where the magnetic substates are not explicitly introduced and where the sums over substates are automatically performed. A number of different formalisms and expressions can be found in the literature. Here, we will follow the work of Biedenharn (1960).

Any correlation where only two directions of motion are measured can be expressed as a Legendre polynomial series in the angle between those directions (see also Eqs. (A.9)–(A.14)). We write

$$\begin{aligned} W(\theta) &= \frac{1}{b_0} \sum_{n=0}^{n_{\max}} b_n P_n(\cos\theta) \\ &= 1 + \frac{b_2}{b_0} P_2(\cos\theta) + \frac{b_4}{b_0} P_4(\cos\theta) + \cdots + \frac{b_{n_{\max}}}{b_0} P_{n_{\max}}(\cos\theta) \end{aligned} \tag{D.3}$$

If the process under consideration is a nuclear reaction, then $W(\theta)$ is related to the differential and total cross section by

$$\left(\frac{d\sigma}{d\Omega}\right)_\theta = \frac{1}{4\pi}\,\sigma\, W(\theta) \tag{D.4}$$

An isotropic differential cross section implies $W(\theta) = 1$. The sum in Eq. (D.3) is restricted to even values of n because we are making the assumption that the reaction (or the successive decay) involves at each stage nuclear states of well-defined parity. The wave function describing the exit channel must then have the same parity as the resonance (or the intermediate state). The corresponding intensity of the emitted radiation (i.e., the square of the wave function) has even parity and is unchanged by the inversion $\vec{r} \to -\vec{r}$, or more specifically, by the substitution $\theta \to \pi - \theta$ (since for unpolarized beams and randomly oriented target nuclei the intensity does not depend on the azimuthal angle ϕ). The condition $W(\theta) = W(\pi - \theta)$ implies that $W(\theta)$ is symmetric about $\theta = 90°$ and, consequently, all odd Legendre polynomial terms in Eq. (D.3) must vanish.

The coefficients b_n in Eq. (D.3) depend on the angular momenta and nuclear matrix elements involved in the process. Theoretical expressions for b_n are given in the following. They can be factored into components referring separately to each transition. Each of these components, in turn, is expressed in terms of vector coupling (Clebsch–Gordan and Racah) coefficients. We will be using the coefficients F_n, defined by (Biedenharn, 1960)

$$F_n(LL'jJ) \equiv (-)^{j-J-1}\sqrt{(2L+1)(2L'+1)(2J+1)}\,(L1L'-1|n0)W(JJLL';nj) \quad \text{(D.5)}$$

where j and J are angular momenta (spins) of nuclear states and L and L' are orbital angular momenta (for particles) or multipolarities (for photons) of radiations; $(L1L'-1|n0)$ and $W(JJLL';nj)$ denotes a Clebsch–Gordan and a Racah coefficient, respectively. A tabulation of the functions $F_n(LjJ) \equiv F_n(LLjJ)$ is given in Biedenharn and Rose (1953). Numerical values of the mixed correlation coefficients $F_n(LL'jJ)$ for $L \neq L'$ can be found in Appel (1968). For $n = 0$, we obtain $F_0(LL'jJ) = 0$ and $F_0(LjJ) = 1$. To determine how many terms have to be taken into account in the sum of Eq. (D.3), it is useful to consider the symmetry properties of the functions $F_n(LL'jJ)$, which follow directly from those of the Clebsch–Gordan and Racah coefficients. For given values of L, L', and J, we obtain $F_n(LL'jJ) \neq 0$ only for $|L - L'| \leq n \leq \min(2J, L + L')$. It follows that $F_n(LjJ) \neq 0$ only for $0 \leq n \leq \min(2J, 2L)$.

D.2
Pure Radiations in a Two-Step Process

We start by considering a two-step process, where each step proceeds via a pure transition. An intermediate state of spin J is formed from an initial state of spin j_1 via absorption or emission of some radiation of angular momentum L_1. The intermediate state decays then to the final state of spin j_2 via emission of radiation with angular momentum L_2. We write symbolically $j_1(L_1)J(L_2)j_2$. The angular correlation function between the directions of the two radiations is then given in terms of the coefficients $A_n(i)$ and the particle parameters $a_n(i)$ by

$$W(\theta) = \sum_{n=0,2,\ldots} [a_n(1)A_n(1)][a_n(2)A_n(2)]P_n(\cos\theta) \quad \text{(D.6)}$$

for photons: $a_n(i) = 1$; $A_n(i) = F_n(L_i j_i J)$ (D.7)

for $s = 0$ particles: $a_n(i) = \dfrac{2L_i(L_i+1)}{2L_i(L_i+1) - n(n+1)}$; $A_n(i) = F_n(L_i j_i J)$ (D.8)

for $s \neq 0$ particles: $a_n(i) = \dfrac{2L_i(L_i+1)}{2L_i(L_i+1) - n(n+1)}$; $A_n(i) = F_n(L_i j_s J)$ (D.9)

For photons or particles, L_i denotes the γ-ray multipolarity or the orbital angular momentum, respectively. If a particle has a nonzero spin s, then the channel spin given by $\vec{j}_s = \vec{j}_i + \vec{s}$ and $|j_i - s| \leq j_s \leq j_i + s$ replaces the initial state spin j_i. The sum in Eq. (D.6) is restricted to $0 \leq n \leq \min(2L_1, 2L_2, 2J)$.

Example D.1

The β-decay of ^{60}Co populates a 4^+ level in the ^{60}Ni daughter nucleus. This level decays to an intermediate state of spin 2^+, which in turn decays to the ground state of spin 0^+ (Figure D.2a). Calculate the angular correlation between the two de-excitation γ-rays.

We encountered this case in Section 4.5.2 and Figure 4.28. The β-decay electron is emitted into a random direction and is not observed. Thus, the initial 4^+ level populated in the daughter nucleus is not aligned. The first γ-ray is also emitted into a random direction. If it is detected in a counter, then a line connecting the radioactive source with the detector represents a preferred direction relative to which the second γ-ray is emitted. Both transitions in this direction–direction correlation are γ-rays and θ represents the angle between their correlated emission directions. Both the first and the second γ-ray decay can only proceed via an E2 transition (Example B.4). Thus, we have to consider the angular momentum sequence $j_1(L_1)J(L_2)j_2 \rightarrow 4(2)2(2)0$. From Eqs. (D.6) and (D.7), we obtain

$$W(\theta) = \sum_{n=0,2,\ldots} F_n(L_1 j_1 J) F_n(L_2 j_2 J) P_n(\cos\theta) \qquad \text{with} \qquad 0 \leq n \leq \min(2L_1, 2L_2, 2J)$$

Hence,

$$\begin{aligned} W(\theta) &= \sum_{n=0,2,4} F_n(242) F_n(202) P_n(\cos\theta) \\ &= 1 + F_2(242)F_2(202)P_2(\cos\theta) + F_4(242)F_4(202)P_4(\cos\theta) \\ &= 1 + (-0.1707)(-0.5976)P_2(\cos\theta) + (-0.0085)(-1.069)P_4(\cos\theta) \\ &= 1 + 0.1020 P_2(\cos\theta) + 0.0091 P_4(\cos\theta) \end{aligned}$$

Example D.2

A resonance with spin and parity of $J^\pi = 2^+$ is populated in the ^{32}S(α,γ)^{36}Ar reaction. The resonance decays to a final state with $J^\pi = 0^+$ (Figure D.2b). Calculate the expected angular correlation between the incident beam (α-particles) and the emitted γ-radiation.

The ^{32}S target nuclei and the α-particles have both a spin and parity of 0^+. Therefore, the $J^\pi = 2^+$ resonance can be formed only from an α-particle orbital angular momentum of $\ell_\alpha = 2$ (Example B.1). Furthermore, the γ-ray transition can only

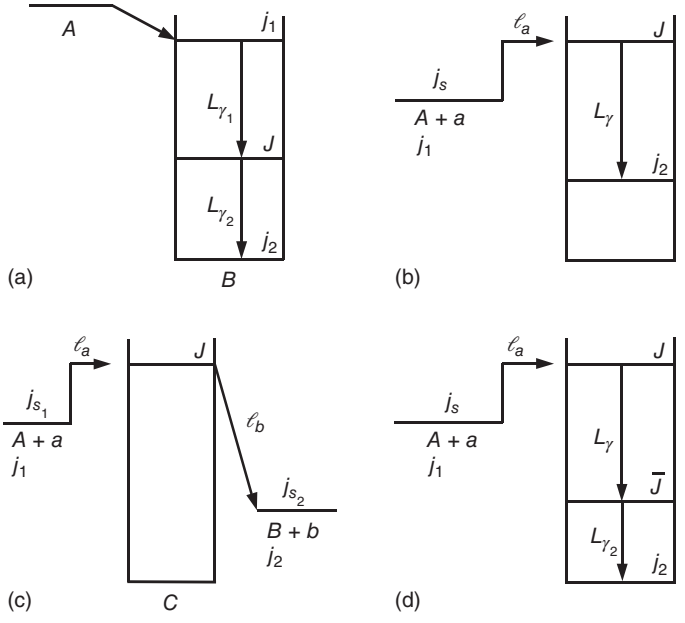

Figure D.2 Schematic level diagrams indicating the quantum numbers involved in various angular correlation schemes.

be of E2 character (Example B.4). The angular momentum sequence is therefore given by $j_1(L_1)J(L_2)j_2 \rightarrow j_{^{32}S}(\ell_\alpha)J(L_\gamma)j_{^{36}Ar} \rightarrow 0(2)2(2)0$. We obtain from Eqs. (D.6) and (D.8)

$$W(\theta) = \sum_{n=0,2,\ldots} \frac{2L_1(L_1+1)}{2L_1(L_1+1) - n(n+1)} F_n(L_1 j_1 J) F_n(L_2 j_2 J) P_n(\cos\theta)$$

From $0 \le n \le \min(2L_1, 2L_2, 2J)$ we find $n = 0$, 2, and 4. Hence

$$\begin{aligned} W(\theta) &= \sum_{n=0,2,4} \frac{2 \cdot 2(2+1)}{2 \cdot 2(2+1) - n(n+1)} F_n(202) F_n(202) P_n(\cos\theta) \\ &= 1 + \frac{12}{12-6} F_2(202) F_2(202) P_2(\cos\theta) + \frac{12}{12-20} F_4(202) F_4(202) P_4(\cos\theta) \\ &= 1 + 2(-0.5976)(-0.5976) P_2(\cos\theta) + (-1.5)(-1.069)(-1.069) P_4(\cos\theta) \\ &= 1 + 0.7143 P_2(\cos\theta) - 1.7143 P_4(\cos\theta) \end{aligned}$$

D.3
Mixed Radiations in a Two-Step Process

Sometimes, the angular momentum coupling in a sequential nuclear decay or in a nuclear reaction allows for different possibilities, each involving a unique

combination of angular momenta. In general, these pure transitions will interfere, that is, their contributions to the total angular correlation add either incoherently or coherently. In either case, new parameters have to be introduced that describe quantitatively the degree of mixing. These *mixing ratios* are usually determined experimentally by fitting the data and are eventually interpreted in terms of some nuclear model.

Incoherent interference applies, for example, to the channel spin j_s. Since we assumed that the beam and target nuclei are unpolarized, the channel spin is *randomly oriented*. As a consequence, the total angular correlation is given by the sum of the individual (pure) correlations, each weighted according to the probability for a particular channel spin value to occur. We write $W(\theta) = W_{j_s}(\theta) + \delta_c^2 W_{j_s'}(\theta)$, where the *channel spin mixing ratio* $\delta_c^2 \equiv P_{j_s'}/P_{j_s}$ is defined as the ratio of probabilities for forming (or of decay from) the intermediate state via the channel spins j_s' and j_s, where $j_s' > j_s$.

Coherent interference occurs when definite phase relationships are important. This is the case if several possible values of multipolarites are allowed for a specific γ-ray transition, or if the intermediate state can be formed (or decay) by several possible values of orbital angular momenta. In practice, only the smallest two allowed values of γ-ray multipolarities (L_i and $L_i + 1$) or orbital angular momenta (ℓ_i and $\ell_i + 2$) need to be considered (Example B.4). In such cases, we have to use in Eq. (D.6) the expression

$$a_n(i)A_n(i) = a_n(L_iL_i)F_n(L_ij_iJ) + 2\delta_i a_n(L_iL_i')F_n(L_iL_i'j_iJ) + \delta_i^2 a_n(L_i'L_i')F_n(L_i'j_iJ) \quad \text{(D.10)}$$

for photons: $$a_n(i) = 1 \quad \text{(D.11)}$$

for particles:
$$a_n(L_iL_i') = \cos(\xi_{L_i} - \xi_{L_i'})\frac{(L_i0L_i'0|n0)}{(L_i1L_i' - 1|n0)}$$
$$= \cos(\xi_{L_i} - \xi_{L_i'})\frac{2\sqrt{[L_i(L_i+1)][L_i'(L_i'+1)]}}{L_i(L_i+1) + L_i'(L_i'+1) - n(n+1)} \quad \text{(D.12)}$$

where the primed quantities refer to the higher value of angular momentum (particle orbital angular momentum or γ-ray multipolarity). For particles with spin, the channel spin j_s replaces again the initial state spin j_i in Eq. (D.10).

The *γ-ray multipolarity mixing ratio* δ_γ is defined by the relation $\delta_\gamma^2 \equiv \Gamma_{\gamma L+1}/\Gamma_{\gamma L}$, with $\Gamma_{\gamma L}$ the γ-ray partial width for the transition with multipolarity L (see Eq. (1.32)). The total angular correlation not only depends on the value but also on the phase (plus or minus) of δ_γ. Hence, the sign convention (i.e., the definition of δ_γ in terms of the nuclear matrix elements) becomes important when interpreting the data. We will adopt here the convention used by Biedenharn (1960). See Ferguson (1965) for a different sign convention.

For the mixing of particle orbital angular momenta, one introduces the *orbital angular momentum mixing ratio*, defined by $\delta_a^2 \equiv \Gamma_{L+2}/\Gamma_L$, with Γ_L the particle partial width for orbital angular momentum L. For charged particles, the phase

shifts ξ_L are given by (Ferguson, 1965)

$$\xi_L = -\arctan\left(\frac{F_L}{G_L}\right) + \sum_{n=1}^{L} \arctan\left(\frac{\eta}{n}\right) \tag{D.13}$$

where F_L and G_L are the regular and irregular Coulomb wave functions, respectively, and η is the Sommerfeld parameter (see Section 2.4.3 and Appendix A.3). The first term in the above expression is the hardsphere phase shift and the second term is the Coulomb phase shift, which is absent for neutral particles. The phase shift ξ_L is energy dependent.

If a transition is mixed with a mixing parameter of δ_i^2, then the total angular correlation is normalized to $(1 + \delta_i^2)$ instead of unity. If two or more different mixing processes are present with mixing parameters of δ_i^2, δ_{i+1}^2, δ_{i+2}^2,…, and so on, then $W(\theta)$ is normalized to the product $(1 + \delta_i^2)(1 + \delta_{i+1}^2)(1 + \delta_{i+2}^2)$ …, and so on.

Example D.3

A resonance with spin and parity of $J^\pi = 1^-$ is formed in the ^{31}P(p,α)^{28}Si reaction. The α-particle emission populates the ground state in the final ^{28}Si nucleus (Figure D.2c). Calculate the angular correlation between the incident proton beam and the emitted α-particles.

Both the ^{31}P target nucleus and the proton have a spin and parity of $J^\pi = 1/2^+$. Thus, the angular momentum coupling of the target and projectile can produce either one of two channel spin possibilities: $|1/2 - 1/2| \le j_s \le 1/2 + 1/2$, hence $j_s = 0$ or 1. The value of the orbital angular momentum is unique for the incoming and outgoing reaction channel ($\ell_p = 1$ and $\ell_\alpha = 1$). First, the angular correlations for the pure transitions will be calculated, that is, each channel spin case will be treated separately. We have to consider the angular momentum sequences $j_1(L_1)J(L_2)j_2 \to j_s(\ell_p)J(\ell_\alpha)j_{^{28}Si} \to 0(1)1(1)0 \quad (j_s = 0)$ and $\to 1(1)1(1)0 \quad (j_s = 1)$. For either channel, spin the sum in Eq. (D.6) is restricted to $0 \le n \le \min(2 \cdot 1, 2 \cdot 1)$, that is, $n = 0$ and 2. We obtain

$$\begin{aligned} W_{j_s=0}(\theta) &= \sum_{n=0,2} \frac{2L_1(L_1+1)}{2L_1(L_1+1) - n(n+1)} F_n(L_1 j_s J) \frac{2L_2(L_2+1)}{2L_2(L_2+1) - n(n+1)} \\ &\quad \times F_n(L_2 j_2 J) P_n(\cos\theta) \\ &= 1 + \frac{2\cdot 1\cdot 2}{2\cdot 1\cdot 2 - 2\cdot 3} F_2(101) \frac{2\cdot 1\cdot 2}{2\cdot 1\cdot 2 - 2\cdot 3} F_2(101) P_2(\cos\theta) \\ &= 1 + (-2)(0.7071)(-2)(0.7071) P_2(\cos\theta) = 1 + 2P_2(\cos\theta) \end{aligned}$$

Similarly

$$\begin{aligned} W_{j_s=1}(\theta) &= 1 + \frac{2\cdot 1\cdot 2}{2\cdot 1\cdot 2 - 2\cdot 3} F_2(111) \frac{2\cdot 1\cdot 2}{2\cdot 1\cdot 2 - 2\cdot 3} F_2(101) P_2(\cos\theta) \\ &= 1 + (-2)(-0.3536)(-2)(0.7071) P_2(\cos\theta) = 1 - P_2(\cos\theta) \end{aligned}$$

The total angular correlation is given by the sum of the correlations for the individual channel spins, each weighted according to the probability of the particular

j_s value. Thus

$$W(\theta) = W_{j_s=0}(\theta) + \delta_c^2 W_{j_s=1}(\theta) = [1 + 2P_2(\cos\theta)] + \delta_c^2[1 - P_2(\cos\theta)]$$
$$= 1 + \delta_c^2 + [2 - \delta_c^2]P_2(\cos\theta)$$

with $\delta_c^2 = P_{j_s=1}/P_{j_s=0}$ the ratio of the probabilities, or the ratio of the squares of the matrix elements, of forming the resonance via $j_s = 1$ relative to $j_s = 0$.

Example D.4

A resonance of spin and parity of $J^\pi = 1^-$ is populated in the ^{29}Si(p,γ)^{30}P reaction. The resonance decays via γ-ray emission to a final state in ^{30}P with spin and parity of $J^\pi = 1^-$ (Figure D.2b). Calculate the angular correlation of the emitted γ-rays with respect to the incident proton beam direction.

The spin and parity of both the ^{29}Si target nucleus and the proton is $1/2^+$. Thus, two values for the channel spin are allowed, j_s = 0 and 1. The only allowed value for the orbital angular momentum of the proton is ℓ_p = 1. The γ-ray decay may proceed either via a M1 or E2 transition. Hence, the angular correlation expression will contain two additional parameters, the channel spin mixing ratio δ_c and the γ-ray multipolarity mixing ratio δ_γ. We will first consider the two channel spins separately and write symbolically

$$j_1(L_1)J(L_2)j_2 \rightarrow j_s(\ell_p)J(L_\gamma)j_{30P} \rightarrow 0(1)1 \begin{pmatrix} 1 \\ 2 \end{pmatrix} 1 \qquad \text{and}$$
$$\rightarrow 1(1)1 \begin{pmatrix} 1 \\ 2 \end{pmatrix} 1$$

For either channel, spin the sum in Eq. (D.6) is restricted to $0 \le n \le 2J$, that is, n = 0 and 2. We obtain

$$W_{j_s=0}(\theta) = \sum_{n=0,2} \left[\frac{2L_1(L_1+1)}{2L_1(L_1+1) - n(n+1)} F_n(L_1 j_s J) \right]$$
$$\times [F_n(L_2 j_2 J) + 2\delta_\gamma F_n(L_2 L_2' j_2 J) + \delta_\gamma^2 F_n(L_2' j_2 J)] P_n(\cos\theta)$$
$$= (1 + \delta_\gamma^2) + \left[\frac{2 \cdot 1(1+1)}{2 \cdot 1(1+1) - 2(2+1)} F_2(101) \right]$$
$$\times [F_2(111) + 2\delta_\gamma F_2(1211) + \delta_\gamma^2 F_2(211)] P_2(\cos\theta)$$
$$= (1 + \delta_\gamma^2) + [(-2)0.7071]$$
$$\times [(-0.3536) + 2\delta_\gamma(-1.0607) + \delta_\gamma^2(-0.3535)] P_2(\cos\theta)$$
$$= (1 + \delta_\gamma^2) + (0.5 + 3\delta_\gamma + 0.5\delta_\gamma^2) P_2(\cos\theta)$$

Similarly

$$\begin{aligned}
W_{j_s=1}(\theta) &= (1+\delta_\gamma^2) + \left[\frac{2\cdot 1(1+1)}{2\cdot 1(1+1)-2(2+1)}F_2(111)\right] \\
&\quad \times [F_2(111) + 2\delta_\gamma F_2(1211) + \delta_\gamma^2 F_2(211)]P_2(\cos\theta) \\
&= (1+\delta_\gamma^2) + [(-2)(-0.3536)] \\
&\quad \times [(-0.3536) + 2\delta_\gamma(-1.0607) + \delta_\gamma^2(-0.3535)]P_2(\cos\theta) \\
&= (1+\delta_\gamma^2) + (-0.25 - 1.5\delta_\gamma - 0.25\delta_\gamma^2)P_2(\cos\theta)
\end{aligned}$$

The total angular correlation is given by the incoherent sum of the expressions for the individual channel spins,

$$\begin{aligned}
W(\theta) &= W_{j_s=0}(\theta) + \delta_c^2 W_{j_s=1}(\theta) \\
&= (1+\delta_\gamma^2) + (0.5 + 3\delta_\gamma + 0.5\delta_\gamma^2)P_2(\cos\theta) \\
&\quad + \delta_c^2[(1+\delta_\gamma^2) + (-0.25 - 1.5\delta_\gamma - 0.25\delta_\gamma^2)P_2(\cos\theta)] \\
&= (1+\delta_\gamma^2) + \delta_c^2(1+\delta_\gamma^2) \\
&\quad + (0.5 + 3\delta_\gamma + 0.5\delta_\gamma^2 - 0.25\delta_c^2 - \delta_c^2 1.5\delta_\gamma - \delta_c^2 0.25\delta_\gamma^2)P_2(\cos\theta) \\
&= (1+\delta_\gamma^2)(1+\delta_c^2) + 0.5(1 + 6\delta_\gamma + \delta_\gamma^2)(1 - 0.5\delta_c^2)P_2(\cos\theta)
\end{aligned}$$

The channel spin and γ-ray multipolarity mixing ratios are given by $\delta_c^2 = P_{j_s=1}/P_{j_s=0}$ and $\delta_\gamma^2 = \Gamma_{\gamma E2}/\Gamma_{\gamma M1}$, respectively.

Example D.5

Consider the ^{19}F(p,γ)^{20}Ne reaction, populating a resonance with a spin and parity of $J^\pi = 2^-$. The resonance decays to a lower lying state in ^{20}Ne with a spin and parity of $J^\pi = 1^+$ (Figure D.2b). Calculate the angular correlation of the emitted γ-rays with respect to the incident proton beam direction.

Both the ^{19}F target nucleus and the proton have a spin and parity of $1/2^+$. The channel spin has two allowed values, j_s = 0 and 1. However, the 2^- resonance cannot be formed from j_s = 0 since the total angular momentum and parity must be conserved simultaneously. Hence, only the channel spin j_s = 1 plays a role in this process. The resonance can be formed via orbital angular momenta of ℓ_p = 1 and 3 and thus this transition is mixed. For the sake of simplicity, we will assume that the γ-ray decay proceeds via an E1 transition only. We write symbolically

$$j_1(L_1)J(L_2)j_2 \rightarrow j_s(\ell_p)J(L_\gamma)j_{^{20}Ne} \rightarrow 1\begin{pmatrix}1\\3\end{pmatrix}2(1)1$$

The sum in Eq. (D.6) is restricted to $n \leq 2$ since we assumed $L_\gamma = 1$. It follows

$$
\begin{aligned}
W(\theta) = \sum_{n=0,2} \Bigg[& \cos(\xi_{L_1} - \xi_{L_1}) \frac{2L_1(L_1+1)}{2L_1(L_1+1) - n(n+1)} F_n(L_1 j_s J) \\
& + 2\delta_a \cos(\xi_{L_1} - \xi_{L_1'}) \frac{2\sqrt{[L_1(L_1+1)][L_1'(L_1'+1)]}}{L_1(L_1+1) + L_1'(L_1'+1) - n(n+1)} F_n(L_1 L_1' j_s J) \\
& + \delta_a^2 \cos(\xi_{L_1'} - \xi_{L_1'}) \frac{2L_1'(L_1'+1)}{2L_1'(L_1'+1) - n(n+1)} F_n(L_1' j_s J) \Bigg] \\
& \times F_n(L_2 j_2 J) P_n(\cos\theta) \\
= [1 \cdot 1 \cdot 1 + \delta_a^2 \cdot 1 \cdot 1 \cdot 1] \cdot 1 + \Bigg[& 1 \cdot \frac{2 \cdot 1 \cdot (1+1)}{2 \cdot 1 \cdot (1+1) - 2(2+1)} F_2(112) \\
& + 2\delta_a \cos(\xi_{\ell=1} - \xi_{\ell=3}) \frac{2\sqrt{[1(1+1)][3(3+1)]}}{1(1+1) + 3(3+1) - 2(2+1)} F_2(1312) \\
& + \delta_a^2 \cdot 1 \cdot \frac{2 \cdot 3(3+1)}{2 \cdot 3(3+1) - 2(2+1)} F_2(312) \Bigg] F_2(112) P_2(\cos\theta) \\
= 1 + \delta_a^2 + \Big[& 1 \cdot (-2)(0.4183) + 2\delta_a \cos(\xi_{\ell=1} - \xi_{\ell=3})(1.2247)(0.2390) \\
& + \delta_a^2 \cdot 1(1.333)(-0.7171) \Big] (0.4183) P_2(\cos\theta) \\
= 1 + \delta_a^2 + [& -0.35 + 0.25\delta_a \cos(\xi_{\ell=1} - \xi_{\ell=3}) - 0.4\delta_a^2] P_2(\cos\theta)
\end{aligned}
$$

The orbital angular momentum mixing ratio is given by $\delta_a^2 = \Gamma_{\ell=3}/\Gamma_{\ell=1}$.

D.4 Three-Step Process with Unobserved Intermediate Radiation

It is sometimes of interest in a particle capture reaction to determine the angular correlation of secondary γ-rays with respect to the incident beam direction. In this case, we have a three-step process, involving: (i) the formation of a resonance with spin J through the capture of an incident particle with orbital angular momentum L_1, (ii) the first (primary) γ-ray decay of multipolarity L to an intermediate level of spin $\bar{J}$, and (iii) finally the subsequent secondary γ-ray decay of multipolarity L_2 to the final state of spin j_2 (see Figure D.2d). Only the incident beam and the secondary γ-ray transition are observed, while the primary γ-ray transition is unobserved. We write symbolically

$$
j_1 \left(\begin{array}{c} L_1 \\ L_1' \end{array} \right) J \left(\begin{array}{c} L \\ L' \end{array} \right) \bar{J} \left(\begin{array}{c} L_2 \\ L_2' \end{array} \right) j_2 \tag{D.14}
$$

The angular correlation expression is then given by

$$
W(\theta) = \sum_{n=0,2,\ldots} [a_n(1) A_n(1)] C_n [a_n(2) A_n(2)] P_n(\cos\theta) \tag{D.15}
$$

$$C_n = \sqrt{(2J+1)(2\bar{J}+1)}\,W(JnL\bar{J};J\bar{J}) \tag{D.16}$$

The first link ($j_1 \to J$) and last link ($\bar{J} \to j_2$) are described by the terms $a_n(1)A_n(1)$ and $a_n(2)A_n(2)$, respectively, and are treated as before. The term C_n describes the unobserved primary radiation. Unobserved γ-rays of multipolarities L and L' mix incoherently, that is, the total correlation is given by $W(\theta) = W_L(\theta) + \delta^2_{\gamma LL'} W_{L'}(\theta)$. Furthermore, the sum over n is restricted by the condition $0 \le n \le \min(2L_1, 2L_2, 2J, 2\bar{J})$. In particular, the angular correlation becomes isotropic for either J or $\bar{J}$ equal to 0 or 1/2. Note that the multipolarity L of the unobserved primary radiation does not limit the sum over n.

Example D.6

Consider the ^{11}B(p,γ)^{12}C reaction leading to the formation of a resonance with spin and parity of $J^\pi = 2^+$ (Figure D.2d). The resonance γ-ray decays to an intermediate state ($J^\pi = 2^+$) which, in turn, decays to the ^{12}C ground state ($J^\pi = 0^+$). Calculate the angular correlation of the second γ-ray transition with respect to the incident beam direction.

The spin and parity of the ^{11}B ground state is $J^\pi = 3/2^-$. The two possible channel spins are j_s = 1 and 2. Of the two allowed proton orbital angular momenta (ℓ_p = 1 and 3), we will consider only the lower ℓ_p value. Similarly, of the two γ-ray multipolarities for the unobserved primary transition (M1 and E2), we will only consider the M1 case. Only one possibility is allowed for the multipolarity of the secondary γ-ray transition (E2). Symbolically we write

$$j_s \begin{pmatrix} L_1 \\ L_1' \end{pmatrix} J \begin{pmatrix} L \\ L' \end{pmatrix} \bar{J} \begin{pmatrix} L_2 \\ L_2' \end{pmatrix} j_2 \to 1(1)2(1)2(2)0 \quad \text{and} \quad \to 2(1)2(1)2(2)0$$

For either channel spin, the summation is restricted to $n \le 2$ (because of $\ell_p = 1$). The angular correlation is given by

$$\begin{aligned}
W_{j_s=1}(\theta) &= \sum_{n=0,2,\ldots} [a_n(1)A_n(1)]C_n[a_n(2)A_n(2)]P_n(\cos\theta) \\
&= \sum_{n=0,2} \frac{2L_1(L_1+1)}{2L_1(L_1+1)-n(n+1)} F_n(L_1 j_s J)\sqrt{(2J+1)(2\bar{J}+1)} \\
&\quad \times W(JnL\bar{J};J\bar{J}) F_n(L_2 j_2 J) P_n(\cos\theta) \\
&= 1\cdot 1\cdot \sqrt{(2\cdot 2+1)(2\cdot 2+1)}\,W(2012;22)\cdot 1 \\
&\quad + \frac{2\cdot 1\cdot 2}{2\cdot 1\cdot 2 - 2\cdot 3} F_2(112)\sqrt{(2\cdot 2+1)(2\cdot 2+1)} \\
&\quad \times W(2212;22) F_2(202) P_2(\cos\theta) \\
&= 1\cdot 5\cdot 0.2\cdot 1 + (-2)(0.4183)\cdot 5\cdot 0.1\cdot(-0.5976) P_2(\cos\theta) \\
&= 1 + 0.25 P_2(\cos\theta)
\end{aligned}$$

Similarly,

$$\begin{aligned} W_{j_s=2}(\theta) &= 1 \cdot 1 \cdot \sqrt{(2 \cdot 2 + 1)(2 \cdot 2 + 1)}\, W(2012; 22) \cdot 1 \\ &\quad + \frac{2 \cdot 1 \cdot 2}{2 \cdot 1 \cdot 2 - 2 \cdot 3} F_2(122) \sqrt{(2 \cdot 2 + 1)(2 \cdot 2 + 1)} \\ &\quad \times W(2212; 22) F_2(202) P_2(\cos\theta) \\ &= 1 \cdot 5 \cdot 0.2 \cdot 1 + (-2)(-0.4183) \cdot 5 \cdot 0.1 \cdot (-0.5976) P_2(\cos\theta) \\ &= 1 - 0.25 P_2(\cos\theta) \end{aligned}$$

The total angular correlation is given by the incoherent sum of the expressions for the individual channel spins,

$$\begin{aligned} W(\theta) &= W_{j_s=1}(\theta) + \delta_c^2 W_{j_s=2}(\theta) \\ &= [1 + 0.25 P_2(\cos\theta)] + \delta_c^2 [1 - 0.25 P_2(\cos\theta)] \\ &= 1 + \delta_c^2 + 0.25(1 - \delta_c^2) P_2(\cos\theta) \end{aligned}$$

D.5 Experimental Considerations

Experimental angular correlations and differential yields measured in the laboratory system must have both their intensities and angles converted to the center-of-mass system (Appendix C) before they can be compared to the theoretical expressions given above. Another important correction has to be performed since, strictly speaking, the theoretical angular correlation of Eq. (D.3) applies only to an ideal detector of negligible size. In an experiment, the measured intensities are obtained by integrating the theoretical angular correlation over the finite solid angle subtended by the detector. Hence, the effect of the finite solid angle is to reduce the anisotropy. For a detector of axial symmetry and for its symmetry axis pointing toward the source of the emitted radiation (Figure 4.30), it can be shown that the form of the angular correlation function remains unchanged, but each term in the series of Eq. (D.3) becomes multiplied by a correction factor. For example, if radiation originating from a nuclear reaction is detected, then the experimental angular correlation measured by a specific detector is given by

$$W_{\text{exp}}(\theta) = \frac{1}{b_0} \sum_{n=0}^{n_{\max}} b_n Q_n P_n(\cos\theta) \tag{D.17}$$

Similarly, the experimental angular correlation between two emitted radiations a and b measured with two different detectors (or with the same detector, as was the case for coincidence summing in Section 4.5.2) can be written as

$$W_{\text{exp}}(\theta) = \frac{1}{b_0} \sum_{n=0}^{n_{\max}} b_n Q_n^{(a)} Q_n^{(b)} P_n(\cos\theta) \tag{D.18}$$

The *attenuation factors* Q_n are given by (Rose, 1953)

$$Q_n = \frac{\int_0^{\beta_{\max}} P_n(\cos\beta)\eta(\beta, E)\sin\beta\, d\beta}{\int_0^{\beta_{\max}} \eta(\beta, E)\sin\beta\, d\beta} \tag{D.19}$$

with β the angle between the radiation incident on the detector and the detector symmetry axis, $\beta_{\max}$ the maximum angle subtended by the detector, and $\eta(\beta, E)$ the detector efficiency for the radiation of energy E at angle β. It is apparent that the factors Q_n depend on the detector geometry, the energy of the radiation, and the kind of event that takes place in the detection process (e.g., total versus partial energy deposition for γ-rays; see Section 4.5.2).

If the intrinsic detector efficiency is unity, as is generally the case for charged particle detectors, then the attenuation factor reduces to (Rose, 1953)

$$Q_n = \frac{P_{n-1}(\cos\beta_{\max}) - \cos\beta_{\max} P_n(\cos\beta_{\max})}{(n+1)(1-\cos\beta_{\max})} \tag{D.20}$$

Attenuation factors calculated from this expression are displayed in Figure D.3a for values of n = 1, 2, 3, and 4.

In the case of γ-ray detectors, where the efficiency for detecting an incident photon is smaller than unity, the attenuation factors will be larger than given by Eq. (D.20), that is, they will be closer to unity and, consequently, the difference between measured and theoretical angular correlation will be smaller. The *total efficiency* attenuation factors can be estimated with the same method used for calculating total efficiencies (Section 4.5.2). One simply substitutes $\eta^T(\beta, E) = 1 - e^{-\mu(E)x(\beta)}$ for the total efficiency in Eq. (D.19) and solves the integrals

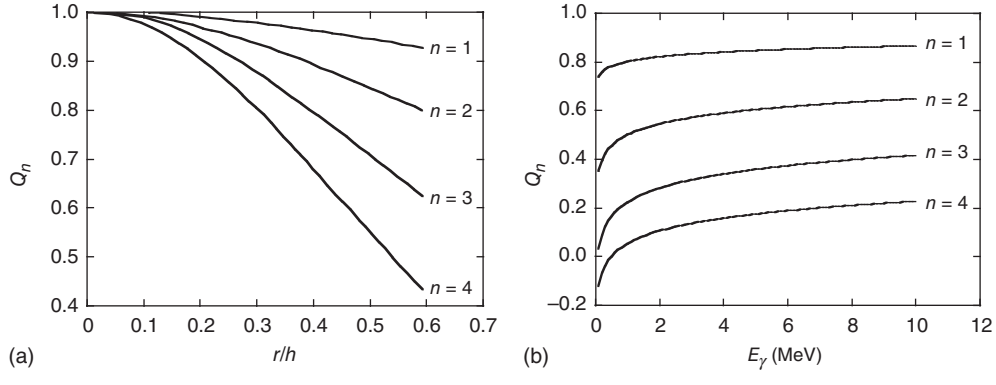

Figure D.3 (a) Attenuation factors for an intrinsic detector efficiency of unity (e.g., a silicon charged-particle counter). The horizontal axis displays the ratio r/h, with r and h the radius of the detector aperture and the source-detector distance, respectively. Note that $\tan\beta_{\max} = r/h$. The curves represent different values of n. After Gove (1959). (b) Attenuation factors for an HPGe detector versus γ-ray energy. The detector volume and source-detector distance amount to 582 cm^3 and 1.6 cm, respectively. The curves represent different values of n and are obtained by calculating peak efficiencies in Eq. (D.19) with the Monte Carlo code GEANT4. (Courtesy of Richard Longland.)

numerically. Similarly, the *peak efficiency* attenuation factors can be estimated if the peak efficiency $\eta^P(\beta, E)$ is first obtained from a Monte Carlo calculation. Peak efficiency attenuation factors estimated in this way for an HPGe detector are displayed in Figure D.3b. The curves show the values of Q_n versus γ-ray energy for a fixed source-detector distance of 1.6 cm. As expected, for decreasing photon energy the peak efficiency $\eta^P(\beta, E)$ increases and hence Q_n becomes smaller.

D.6 Concluding Remarks

We conclude this section with a few useful remarks. Since the angular momenta in low-energy nuclear reactions are rather small, the symmetry properties of the functions F_n restrict the series in Eq. (D.3) to a small number of terms. In practice, terms beyond $n = 4$ are rarely encountered. If for some reason the $n = 4$ term is zero or negligible, then we obtain $W(\theta = 55°) \approx 1$ or $W(\theta = 125°) \approx 1$, since the $P_2(\cos\theta)$ term is equal to zero at these angles (see Eq. (A.12)). Hence, the angle-integrated yield can be measured with a single detector located at a center-of-mass angle of $\theta = 55°$ or $\theta = 125°$. This circumstance has major practical advantages if very small yields need to be measured with a single detector in very close geometry to the target.

It is sometimes possible to simplify the theoretical angular correlation by making reasonable assumptions about the nuclear transition matrix elements. Mixtures of M1/E2 γ-ray multipolarites occur frequently, but E1/M2 mixtures are rarely important. In the latter case, it is often safe to assume that the E1 multipolarity dominates the γ-ray transition strength, hence $\delta_{\gamma M2/E1} \approx 0$. Similar arguments apply to the mixing of orbital angular momenta. Because of parity conservation (Appendix B), interfering orbital angular momenta must differ by two units, that is, ℓ_i and ℓ_{i+2}. The penetration factors decrease strongly for increasing values of orbital angular momentum, as can be seen from Figure 2.21. Therefore, unless the reduced width (or spectroscopic factor) of the ℓ_{i+2} component is considerably larger than that of the ℓ_i component, the degree of orbital angular momentum mixing will be small, that is, $\delta_{a\ell_{i+2}/\ell_i} \approx 0$. Both of these simplifying assumptions should be treated with caution if the purpose of an angular correlation measurement is the determination of unknown nuclear spins. However, they are useful in nuclear astrophysics measurements if the level spins are known and if one is mostly interested in estimating angular correlation corrections for measured differential yields.

Sometimes a single γ-ray detector is placed at $\theta = 0°$ in very close geometry to the target to maximize counting efficiency. Angular correlation effects may be significant for a specific primary γ-ray transition, but it may prove difficult to calculate the angular correlation if, for example, certain mixing ratios are unknown. In such cases, it could be of advantage to analyze instead the intensity of a corresponding secondary γ-ray decay for the calculation of the total yield. This is

especially useful if the secondary γ-ray transition proceeds from a level with a spin of 0 or 1/2 since then its angular correlation is isotropic.

We pointed out that the series of Eq. (D.3) will contain only terms with n = even if the correlation involves an intermediate state of well-defined parity. However, if a reaction proceeds through two or more overlapping resonances of opposite parity, then the resulting angular correlation will not be symmetric about 90° anymore and terms with n = odd will appear in the series of Eq. (D.3). We will not consider here the more involved angular correlation resulting from the interference of two overlapping resonances. The interested reader is referred to Biedenharn (1960). Expressions for the angular correlation in direct radiative capture, and for the interference between resonant and direct contributions, are given in Rolfs (1973).

Example D.7

A resonance at $E_r^{\text{lab}} = 519$ keV is excited in the $^{17}\text{O(p,}\gamma)^{18}\text{F}$ reaction. The strongest primary transition occurs to the ^{18}F level at $E_x = 1121$ keV ($E_\gamma \approx 5$ MeV, $B_\gamma = 0.55 \pm 0.03$). The theoretical angular correlation is given by

$$W_\gamma(\theta) = 1 - 0.10P_2(\cos\theta)$$

The γ-ray counter is located at $\theta = 0°$ with respect to the proton beam direction in very close geometry to the target. A (peak) attenuation factor of $Q_2 = 0.62 \pm 0.05$ is estimated from Eq. (D.19) for this geometry. The measured peak intensity is $\mathcal{N}_\gamma = 1530 \pm 47$ for a certain total number of incident protons. The peak efficiency at $E_\gamma \approx 5$ MeV amounts to $\eta_\gamma^P = 0.015$ (±5%). Calculate the total number of reactions that took place. Ignore coincidence summing effects.

The measured angular correlation is given by

$$W_{\text{exp},\gamma}(\theta) = 1 - 0.10Q_2P_2(\cos\theta) = 1 - 0.10(0.62 \pm 0.05)P_2(\cos\theta)$$

At $\theta = 0°$ we obtain $P_2(\cos\theta) = 1$ and hence

$$W_{\text{exp},\gamma}(0) = 1 - 0.10(0.62 \pm 0.05) \cdot 1 = 0.94(\pm 5\%)$$

From Eq. (4.69), we find

$$\mathcal{N}_R = \frac{\mathcal{N}_\gamma}{B_\gamma \eta_\gamma^P W_\gamma} = \frac{1530(\pm 3\%)}{[0.55(\pm 5\%)][0.015(\pm 5\%)][0.94(\pm 5\%)]} = 197292(\pm 9\%)$$

Appendix E
Constants, Data, Units, and Notation

Most of the physical constants used in this book are adopted from Mohr, Taylor, and Newell (2012) and are listed in Appendix E.1. The numbers in parenthesis denote the uncertainty. The mathematical symbols, units, and prefixes follow common usage and are given in Appendix E.2. Symbols for physical quantities are summarized in Appendix E.4. In several cases, the use of the same symbol for different physical quantities was unavoidable. Further help to the reader is provided by numbers given in parenthesis after a description of a symbol with multiple meanings. These refer to the chapter in which the specific meaning is used. For example, the symbol N denotes a normalization factor (in Chapters 2 or 3), the number *density* of particles or photons (in Chapters 3, 4, or 5), and the neutron number (in Chapters 1 or 5). The symbol $\mathcal{N}$ denotes the number (without unit) of particles, photons, disintegrations, or reactions throughout the text.

E.1
Physical Constants and Data

a_0	Bohr radius; $a_0 = 0.529\,177\,210\,92(17) \times 10^{-10}$ m
c	speed of light in a vacuum; $c = 299\,792\,458$ m s^{-1}
e	elementary charge; $e = 1.602\,176\,565(35) \times 10^{-19}$ C
h	Planck constant ($h \equiv 2\pi\hbar$);
	$h = 4.135\,667\,516(91) \times 10^{-15}$ eV s $= 6.626\,069\,57(29) \times 10^{-34}$ J s,
	$\hbar = 6.582\,119\,28(15) \times 10^{-16}$ eV s $= 1.054\,571\,726(47) \times 10^{-34}$ J s,
	$\hbar c = 197.326\,971\,8(44)$ MeV fm
k	Boltzmann constant; $k = 8.617\,332\,4(78) \times 10^{-5}$ eV K^{-1}
L	Loschmidt constant; $L = 2.686\,780\,5(24) \times 10^{25}$ m^{-3}
$L_\odot$	luminosity of the Sun (bolometric); $L_\odot = 3.826 \times 10^{26}$ W
m_e	electron mass; $m_\mathrm{e} = 9.109\,382\,91(40) \times 10^{-31}$ kg
	$= 0.000\,548\,579\,911\,1(12)$ u
m_u	atomic mass constant; $1\ m_u \equiv \frac{1}{12} m(^{12}\mathrm{C}) = 1.660\,538\,921(73) \times 10^{-27}$ kg
m_n	neutron mass; $m_\mathrm{n} = 1.008\,664\,916\,00(43)$ u
m_p	proton mass; $m_\mathrm{p} = 1.007\,276\,466\,812(90)$ u

Nuclear Physics of Stars, Second Edition. Christian Iliadis.

$m_u c^2$	energy equivalent of m_u; $m_u c^2 = 931.494\,061(21)$ MeV
$m_e c^2$	electron rest energy; $m_e c^2 = 0.510\,998\,928(11)$ MeV
$m_n c^2$	neutron rest energy; $m_n c^2 = 939.565\,379(21)$ MeV
$m_p c^2$	proton rest energy; $m_p c^2 = 938.272\,046(21)$ MeV
$M_\odot$	mass of the Sun; $M_\odot = 1.989 \times 10^{30}$ kg
N_A	Avogadro constant; $N_A = 6.022\,141\,29(27) \times 10^{23}$ mol^{-1}

E.2 Mathematical Expressions

$=$	equal to
$\sim$	proportional to
$\equiv$	defined as
$\approx$	approximately equal to
$>$	greater than
$<$	less than
$\gg$	considerably greater than
$\ll$	considerably less than
$\rightarrow$	limit toward
∞	infinity
∇^2	Laplace operator; in Cartesian coordinates $\nabla^2 \equiv \frac{\partial^2}{\partial x^2} + \frac{\partial^2}{\partial y^2} + \frac{\partial^2}{\partial z^2}$
*	complex conjugate; $z^* = \mathrm{Re}\, z - \mathrm{Im}\, z$
$\lvert z\rvert^2$	absolute magnitude of z; $\lvert z\rvert^2 = z^* z$
$\langle x \rangle$	expectation value of x; $\langle x \rangle = \int_x xP(x)\,dx$, where $P(x)$ is a normalized probability density function of x
δ_{ij}	Kronecker delta; $\delta_{ij} = 1$ if $i = j$, and 0 otherwise
e	base of natural logarithm; $e = 2.71828\ldots$
$\exp(x)$	exponential function; $\exp(x) \equiv e^x$
i	imaginary unit; $i \equiv \sqrt{-1}$
$\mathrm{Im}\, z$	imaginary part of z
$j_\ell(kr)$	spherical Bessel function
$\ln(x)$	natural logarithm; $\ln(x) = \log_e(x)$
$\log(x)$	common (base 10) logarithm; $\log(x) = \log_{10}(x)$
$n_\ell(kr)$	spherical Neumann function
π	ratio of a circle's circumference to its diameter; $\pi = 3.14159\ldots$
$P_\ell(x)$	Legendre polynomial
$\mathrm{Re}\, z$	real part of z
$Y_{\ell m_\ell}(\theta, \phi)$	spherical harmonic
Δa	difference; $\Delta a \equiv a_2 - a_1$
Ω	solid angle

E.3
Prefixes and Units

Prefixes

f- femto-; 10^{-15}
p- pico-; 10^{-12}
n- nano-; 10^{-9}
μ- micro-; 10^{-6}
m- milli-; 10^{-3}
c- centi-; 10^{-2}
k- kilo-; 10^{3}
M- mega-; 10^{6}
G- giga-; 10^{9}

Units

° degree of arc; $1° = \frac{\pi}{180}$ rad
A ampere; 1 A = 1 C/s
b barn; 1 b = 10^{-24} cm^2 = 10^{-28} m^2
Bq becquerel; 1 Bq = 1 s^{-1}
°C degree Celsius
C coulomb
Ci curie; 1 Ci = 3.7×10^{10} s^{-1}
erg cgs unit of energy; 1 erg = 10^{-7} J
eV electron volt; 1 eV = 1.602 176 565(35) $\times 10^{-19}$ J
g gram
Hz hertz; 1 Hz =1 s^{-1}
J joule
K kelvin
m meter
min minute
m w.e. meter water equivalent
rad radian; 1 rad = 57.29578°
s second
sr steradian; solid angle over entire sphere amounts to 4π sr; 1 sr = 3282.80635 deg^2
u (unified) atomic mass unit; 1 u = $m_u = \frac{1}{12} m(^{12}\mathrm{C})$
V volt
W.u. Weisskopf unit
y year; 1 sidereal year = 3.1558149984×10^7 s

E.4 Physical Quantities

A	activity (4); area (2, 3); mass number (1, 2, 3, 4, 5)
A_{pot}	hardsphere potential scattering amplitude
A_{res}	resonance scattering amplitude
a	diffuseness of Woods–Saxon potential
(a, b)	nuclear reaction involving incoming particle a and emitted particle b
B	branching ratio (1, 2, 3, 4, 5); binding energy (1, 5); magnetic field strength (4)
$B(\overline{\omega}L)$	reduced γ-ray transition probability
C	isospin Clebsch–Gordan coefficient (2); net number of counts (4); peak centroid in pulse height spectrum (4)
c	reaction channel
D	number density of deuterium or ^{2}H (5); number of disintegrations (4)
d	deuteron
d	target or absorber thickness (4), distance of point source to detector front face (4)
E	energy
E_0	energy location of Gamow peak maximum
E_r	observed resonance energy
e	electron, also e^-
e^+	positron
$e^{-2\pi\eta}$	Gamow factor
$(e^+\nu)$	nuclear emission of positron
(e^-, ν)	nuclear electron capture
F_{ij}	time-integrated net abundance flow between species i and j
$F_{\text{pp}i}$	fraction of ^{4}He nuclei produced in the pp$i$ chain
$F(Z, p)$	Fermi function
f	fraction of the number of ^{56}Fe seed nuclei that have been subjected to an exponential distribution of neutron exposures
f_{an}	effective rate of ^{28}Si consumption
f_ℓ	logarithmic derivative at the boundary for orbital angular momentum ℓ
f_{ij}	net abundance flow between species i and j
$f_{\text{pp}i}$	fraction of total energy retained in the star if ^{4}He nucleus is produced in pp$i$ chain
f_s	screening factor
$f(\theta)$	scattering amplitude

$f(E_i, E, E')$	probability that particle incident at energy E_i has energy E at a depth inside the target corresponding to E'
$f(Z, E_e^{max})$	Fermi integral
FWHM	full width at half maximum
G	partition function (1, 3, 5); gravitational constant (5)
G_A	axial-vector coupling constant
G_V	vector coupling constant
G^{norm}	normalized partition function
GSF	stellar rate ground state fraction
g_μ	statistical weight of nuclear state μ
$g(E_0, E_i)$	probability that particle in incident beam of mean energy E_0 has energy of E_i
H	Hamiltonian (2); number density of ^{1}H (5); pulse height (4); Hubble parameter (5)
H_0	Hubble's constant
H_{fi}	weak interaction matrix element
h	dimensionless Hubble parameter
I	current (4); particle spin (2)
J	nuclear spin (1); resonance spin (3); total particle spin (2)
j	current density (2); total particle spin (2, 3, 5)
K	kinetic energy (4); recoil energy of Compton electron (4); wave number (2)
k	wave number, also κ, $\hat{k}$, K
ℓ	orbital angular momentum quantum number
L	γ-ray multipolarity (1, 2, 3); length of flight path in time-of-flight experiment (4)
$\vec{L}$	angular momentum vector
M	relative atomic mass in units of u
M_F	Fermi matrix element
M_{GT}	Gamow–Teller matrix element
M.E.	atomic mass excess
M_W^2	γ-ray transition strength in Weisskopf units
m	atomic mass, nuclear mass (1, 2, 3, 4); magnetic quantum number (1, 2)
m_{ij}	reduced mass of particles i and j
N	harmonic oscillator quantum number (1); neutron number (1, 5); normalization factor (2, 3); number *density* of particles or photons (3, 4, 5)
$\mathcal{N}$	number (without units) of particles, photons, disintegrations, or reactions
$N_A\langle\sigma v\rangle$	reaction rate per particle pair in units of $cm^3\ mol^{-1}\ s^{-1}$

n	neutron
n	exponent in temperature dependence of reaction rate (3, 5); number of nodes in radial wave function (2); number of target or sample nuclei per unit area (4); radial quantum number (1)
n_c	average number of neutrons captured per ^{56}Fe seed nucleus
n_{e^-}	electron density
P	beam power (4); gas pressure (4); Maxwell–Boltzmann distribution (3); particle density (2); penetration factor (2, 3); population probability of excited levels (1, 3); probability (4); production rate of radioactive nuclei (4)
p	proton
p	linear momentum
$p(\tau)$	exponential probability distribution of neutron exposures
Q	angular correlation attenuation factor (4); Q-value (1, 2, 3, 4, 5); total accumulated charge (4)
q	ion charge state (4); neutrino linear momentum (1); parameter describing absorption in the nuclear interior (2)
R	nuclear radius (2, 3); radius of cylindrical detector (4)
R_0	radius of square-well potential (2, 3); radius of Woods–Saxon potential (1)
R_1	radius of outer boundary of square-barrier potential
R_c	classical turning point
R_D	Debye–Hückel radius
R_g	gain radius
R_s	shock radius
R_ν	radius of neutrino sphere
RUL	recommended upper limit
$\mathfrak{R}$	R-function or R-matrix
r	reaction rate in units of number of reactions per time per volume
$\vec{r}$	radius vector
r_0	radius parameter
S	astrophysical S-factor (2, 3, 4, 5); shift factor (2); spectroscopic factor (1, 2, 3); stopping power (4)
S_n, S_p, S_α	neutron, proton, and α-particle separation energy
SEF	stellar enhancement factor
s	channel spin
T	neutron transmission (4); temperature (3, 4, 5)
$\hat{T}$	transmission coefficient
$T_{1/2}$	half-life
T_9	temperature in units of GK, $T_9 \equiv T/10^9$ K
t	length of detector crystal (4); time (1, 2, 3, 4, 5)

U	electric potential
U_s	perturbing potential caused by electron shielding charge density
$u(r)$	radial wave function, $u(r) \equiv rR(r)$
V	potential (2); volume (3, 4)
V_C	Coulomb barrier
V_s	screening potential
v	velocity
v_T	location of the maximum of the Maxwell–Boltzmann velocity distribution
W	angular correlation
w	parameter $w = (Q_\beta + m_e c^2)/m_e c^2$
X	mass fraction
x	parameter for electron screening, $x(E) \equiv R_c/R_D$
Y	mole fraction (1, 3, 5); yield (4)
Z	atomic number (1, 4, 5); charge (2, 3, 4, 5)
α	alpha-particle
$\alpha(I_1 I_2)$	specific pair of nuclei 1 and 2 with spins of I_1 and I_2
β	nuclear emission or capture of electron or positron
β^+	nuclear emission of positron or electron capture
β^-	nuclear emission of electron
$(\beta\nu a)$	β-delayed emission of particle a
Γ	total width of resonance or compound nucleus level
Γ_a	partial width for emission or absorption of particle a
Γ_γ	partial width for emission or absorption of γ-ray
Γ_i^o	*observed* total or partial width
γ	γ-ray or photon
γ^2	reduced width
Δ	level shift (2); parameter $\Delta \equiv R_1 - R_0$ (2); systematic difference between tabulated and experimental stopping power (4); 1/e width of Gaussian approximation to Gamow peak (3, 5)
δ	mixing ratio (1, 3); scattering phase shift (2); δ electrons (4)
δ_α, δ_p, δ_n	number of α-particles, protons, and neutrons of nucleus ${}^A_Z\mathrm{Y}_N$ in excess of their number in ^{28}Si
ϵ	nuclear energy generation per unit time and per volume (3, 5); stopping power (4)
ϵ	dimensionless parameter, $\epsilon \equiv E/E_0$
ζ	parameter for electron screening
η	detector efficiency (4); neutron excess parameter (1, 5); Sommerfeld parameter (2, 3); baryon-to-photon number ratio (5)
θ	angle (2, 4); parameter $\theta \equiv (2\pi m_u kT/h^2)^{3/2}$ (5)

θ^2	dimensionless reduced width
θ^2_{pc}	dimensionless single-particle reduced width
θ_e	electron degeneracy factor
Λ	total photodisintegration decay constant
λ	de Broglie wavelength (2, 4); decay constant (1, 3, 4, 5); mean free path of photons or neutrons (4)
μ	linear absorption coefficient for photons (4); muon (4)
ν	frequency (3); neutrino (1, 3, 5); neutron number (5)
$\overline{\nu}$	antineutrino
π	parity (1, 2, 5); proton number (5)
ρ	mass density (1, 3, 4, 5); product $\rho \equiv kr$ (2)
ρ_b	baryon mass density
$\rho_{0,c}$	critical density
σ	cross section (2, 3, 4, 5); experimental stopping power error (4)
$\hat{\sigma}$	effective reaction cross section
$\overline{\sigma}$	average reaction cross section
$\langle\sigma\rangle_T$	Maxwellian-averaged cross section
σ_ℓ	Coulomb phase shift
$\langle\sigma v\rangle$	reaction rate per particle pair
τ	duration of r-process (5); mean lifetime (1, 2, 3, 5); neutron exposure in units of neutrons per area (5); parameter $\tau \equiv 3E_0/(kT)$ (3, 5)
τ_{cycle}	fission cycling time
τ_{NSE}	time to reach nuclear statistical equilibrium
Φ	time-integrated neutron flux in units of particles per area
ϕ	angle (2, 4); incident particle flux in units of particles per area and per time (4, 5); wave function (1)
ϕ_{ij}	parameter $\phi_{ij} \equiv \lvert r_{i\to j} - r_{j\to i}\rvert / \max(r_{i\to j}, r_{j\to i})$
Ψ, ψ	wave function
Ω_b	baryon density parameter
Ω_c	cold dark matter density parameter
Ω_m	total matter density parameter
Ω_Λ	dark energy density parameter
ω	angular frequency (2); spin factor $\omega \equiv (2J+1)(1+\delta_{01})/[(2j_0+1)(2j_1+1)]$ (3, 4, 5)
$\omega\gamma$	resonance strength

Color Plates

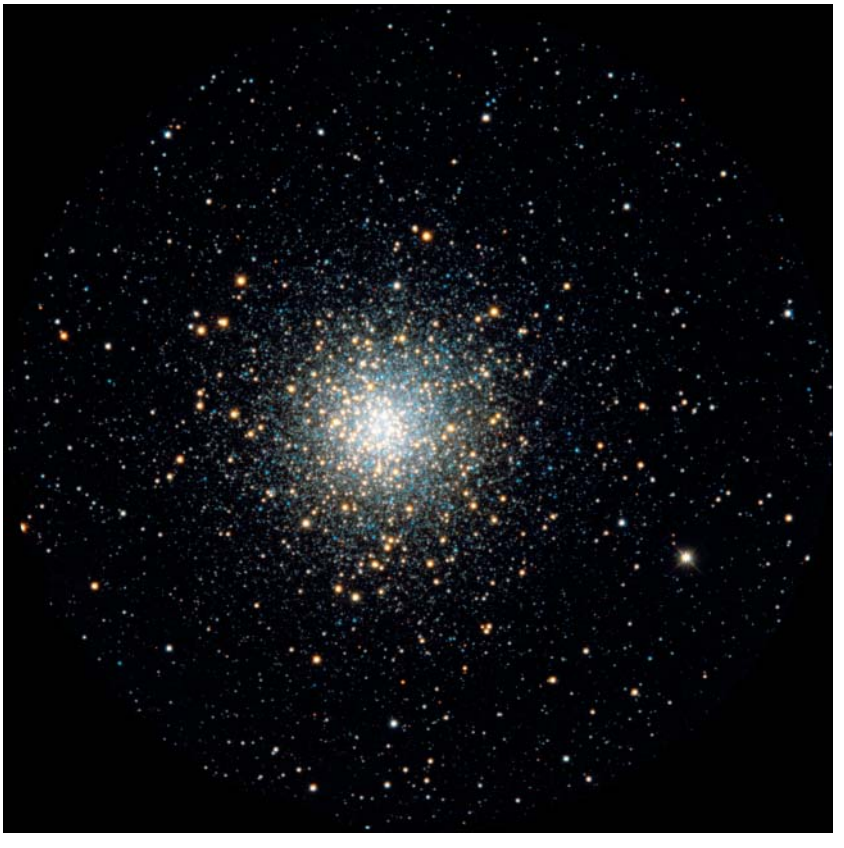

Figure 1 The bright globular cluster M 10. It is located at a distance of 14 000 light years from Earth and has an approximate diameter of 80 light years. The bright reddish-orange stars are red giants fusing hydrogen to helium via the CNO-cycles in a shell surrounding a helium core. The bright blue stars are horizontal branch stars that fuse helium to carbon and oxygen in the core and hydrogen to helium in a shell. Only the faint, gray-looking stars (i.e., those with the lowest mass) are most likely main sequence stars that fuse hydrogen to helium via the pp-chains in the core. The image is a two color composite. (Reprinted with permission. Credit and copyright: T. Credner and S. Kohle, Observatorium Hoher List, Sternwarte Bonn.)

Nuclear Physics of Stars, Second Edition. Christian Iliadis.

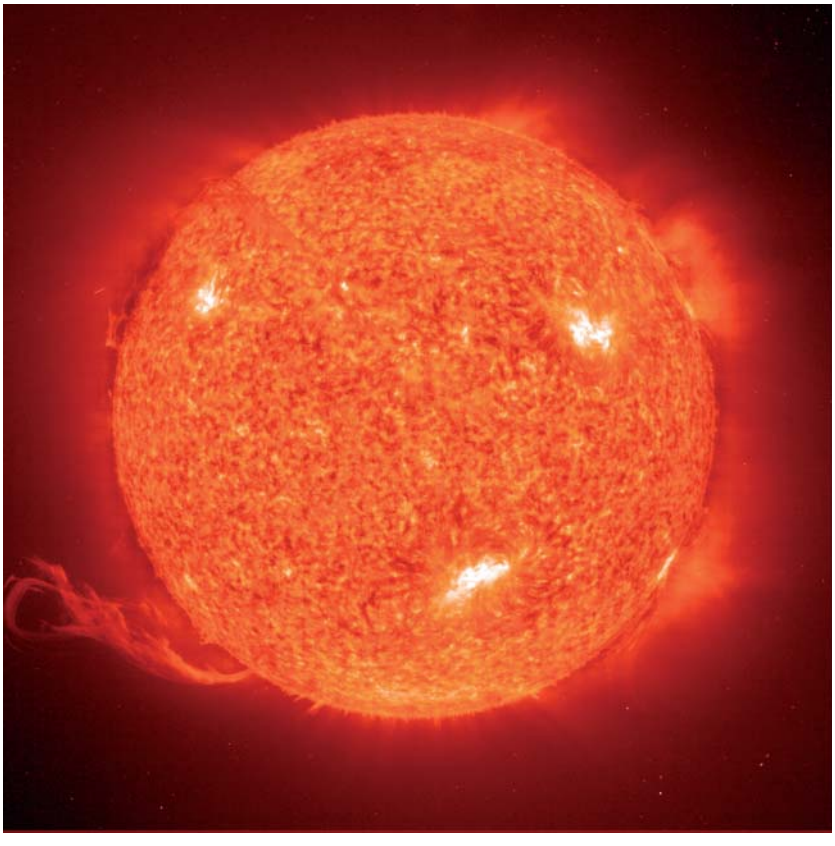

Figure 2 An average, but very special, main sequence star of spectral class G2 that fuses hydrogen to helium in its core via the pp chains. Its mean distance from the center of our Galaxy, which hosts more than 100 million similar stars, is 27 000 light years. The surface temperature amounts to 5800 K and its diameter is about 1.4 million kilometer. The Sun goes through an 11-year activity cycle caused by variations of its magnetic field. The above image was taken in 1997 in the ultraviolet light emitted by a specific type of ionized helium. Particularly hot areas appear in white, while cooler areas are displayed in red. The material in the eruptive prominence visible on the lower left side is at temperatures of 70 000 K and is considerably cooler than the surrounding corona, which has a temperature typically in excess of one million kelvin. Courtesy of SOHO/EIT consortium. SOHO (SOlar and Heliospheric Observatory) is a project of international cooperation between ESA and NASA.

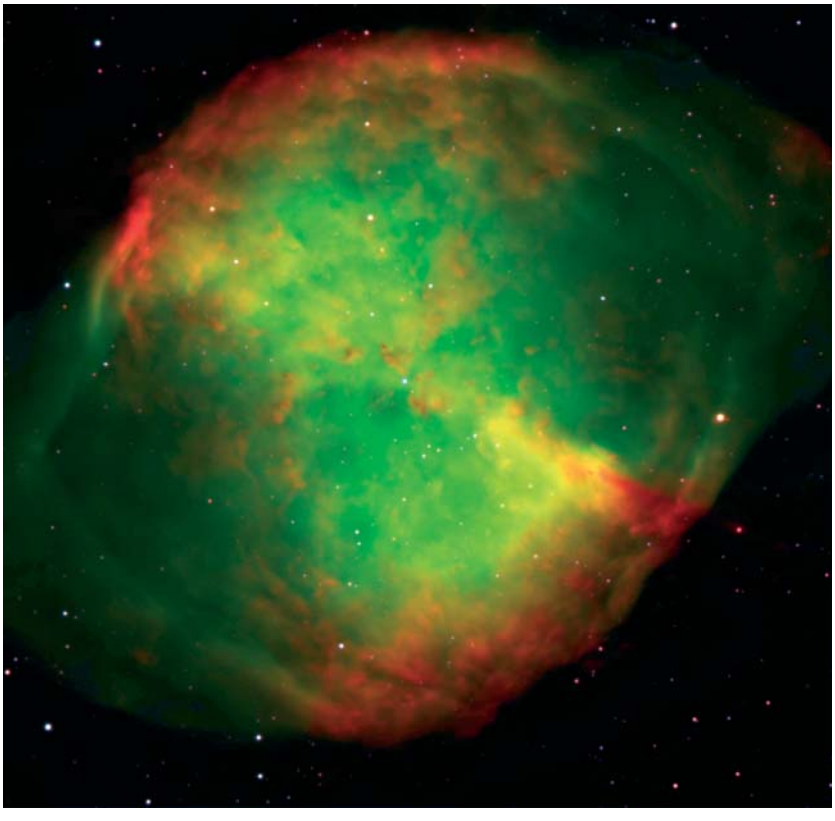

Figure 3 The Dumbbell Nebula (M 27). It was the first planetary nebula ever discovered. Its distance from Earth is 1200 light years. The red and green colors originate from the emission of hydrogen and oxygen, respectively. The gas is heated and excited by the ultraviolet radiation from a star that is located in the center of the nebula (visible at the middle of the image). The central star has a high surface temperature of about 85 000 K. Planetary nebulae are the result of a natural evolutionary stage of low mass stars. The Sun is expected to become the central star of a planetary nebula in several billion years. The image is a three color composite. (Reprinted with permission. Credit and copyright: European Southern Observatory.)

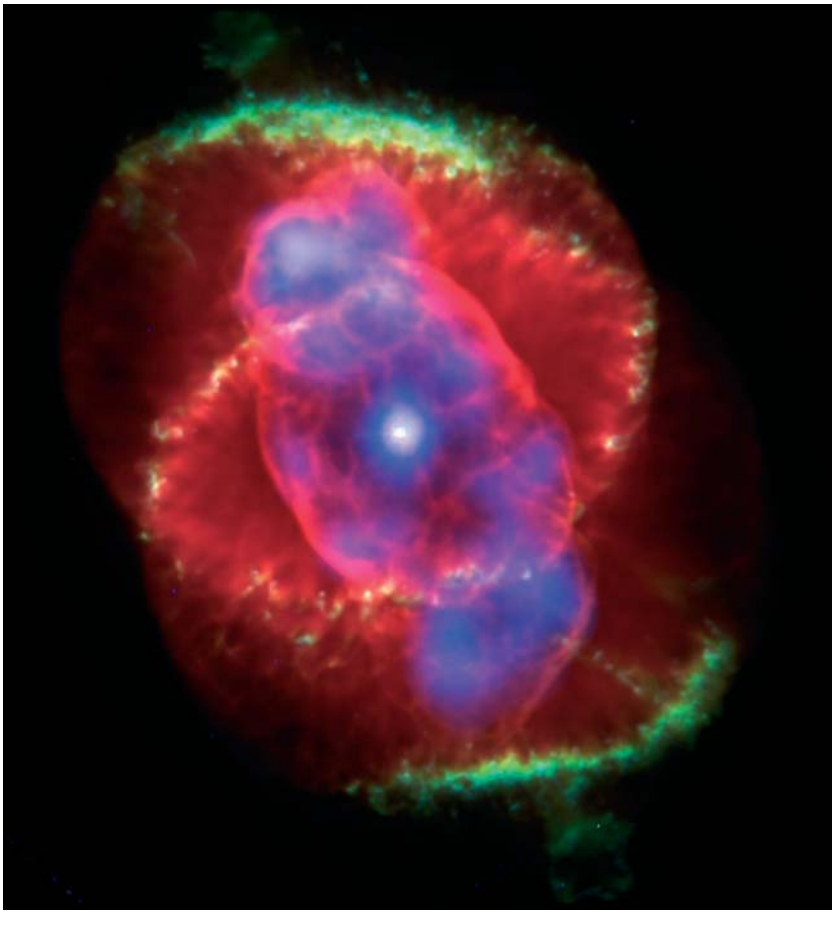

Figure 4 The planetary nebula NGC 6543, known as the Cat's Eye. It is located in the constellation Draco, at a distance of about 3000 light years from Earth. The image is a false-color composite of an X-ray part (shown in purple; obtained with the Chandra X-Ray Observatory) and an optical part (shown in red and green; obtained with the Hubble Space Telescope), and reveals where the hot, X-ray emitting gas appears in relation to the cooler material seen at optical wavelengths. The central star has a surface temperature of about 50 000 K and is expected to collapse to a white dwarf in a few million years. The fast stellar wind emitted from the central star shock-heats the gas that was previously expelled and gives rise to the X-ray emitting bubble (shown in purple). Pockets of hot gas seem to border on cooler gas emitting strongly at optical wavelengths, which may indicate that the expanding hot gas is sculpting the visible filaments and structures. The mechanisms that produced the complicated morphology of the planetary nebula are not well understood. (Credits: (X-ray) NASA/UIUC/Y, Chu et al.; (optical) NASA/J. P. Harrington, K. J Borkowski (UMD); (composite) Z. Levay (STScI).)

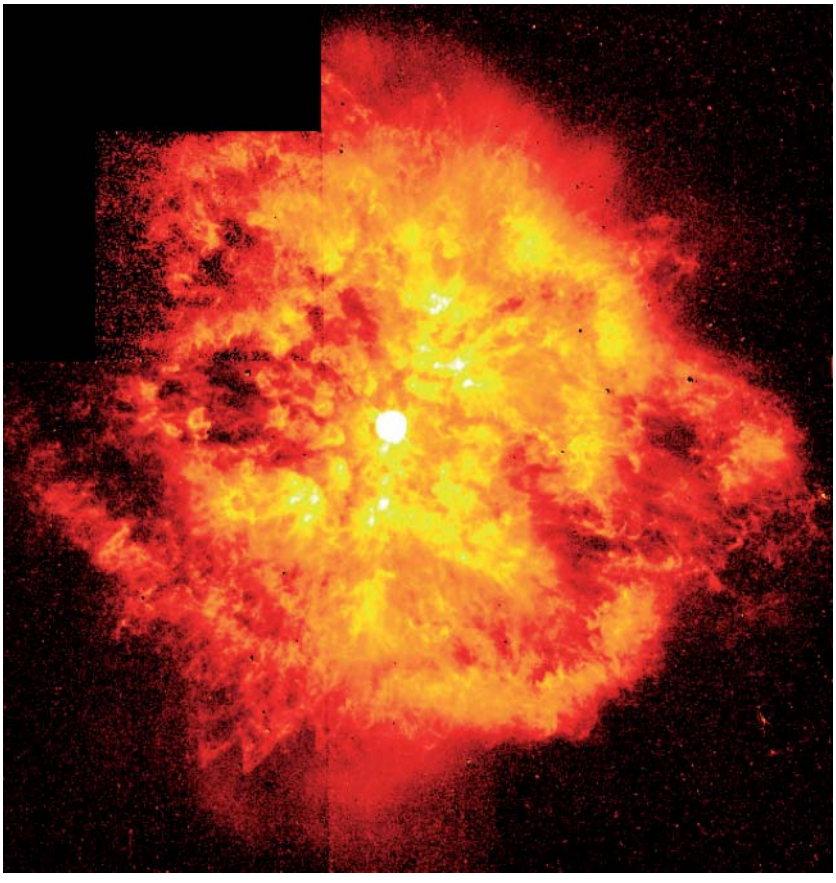

Figure 5 The nebula M1-67 surrounding the Wolf-Rayet star WR 124, located in the constellation Sagittarius. The distance of the nebula from Earth is 15 000 light years. The central Wolf-Rayet star is very hot (about 50 000 K). It is also massive and hence short-lived. Wolf–Rayet stars go through a phase of enormous mass loss via a strong stellar wind. The image reveals hot blobs of ejected gas, indicating that the stellar wind does not flow smoothly into space, but has instabilities that make the nebula appear clumpy. The age of the nebula is less than 10 000 years. The false color image was obtained with the Wide Field Planetary Camera 2 of the Hubble Space Telescope. (Credit: Yves Grosdidier (University of Montreal and Observatoire de Strasbourg), Anthony Moffat (Université de Montreal), Gilles Joncas (Université Laval), Agnes Acker (Observatoire de Strasbourg), and NASA.)

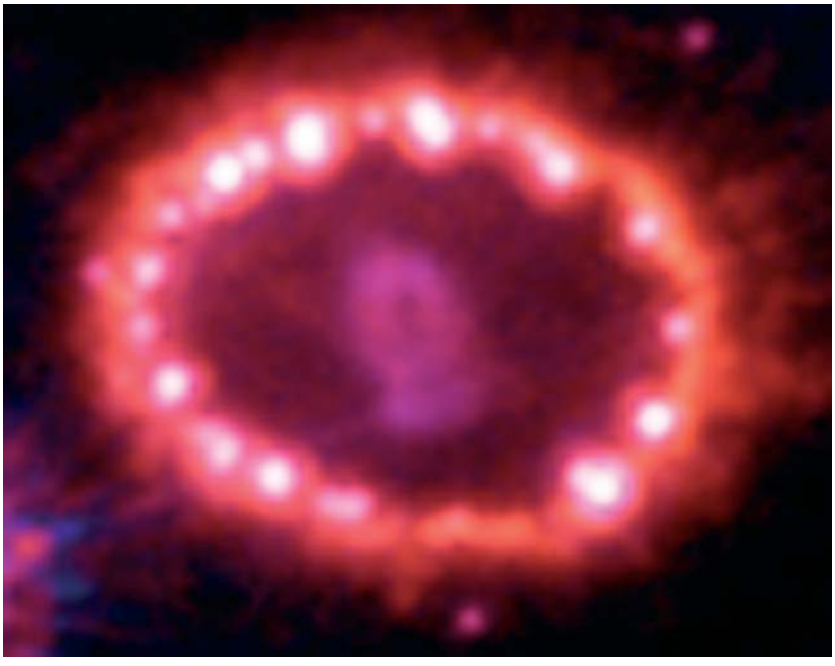

Figure 6 Supernova 1987A in the Large Magellanic Cloud (a nearby small galaxy that is a satellite of our Galaxy) was the brightest exploding star seen in 400 years. Its distance from Earth is 160 000 light years. The supernova was of type II and its progenitor was a massive star (a blue supergiant). The shock wave from the supernova has been moving toward a ring of matter, about two light years across, that was probably ejected by the central star about 20 000 years before the explosion. The image shows many hot spots that are created by the supernova shock compressing and heating the gas of the ring. (The brightest spot on the lower right side of the ring is a star that happens to lie along the Hubble Space Telescope's line of sight). The elongated and expanding object in the middle of the ring is the debris from the explosion. (Credit: NASA, P. Challis, R. Kirshner (Harvard-Smithsonian Center for Astrophysics) and B. Sugerman (STScI).)

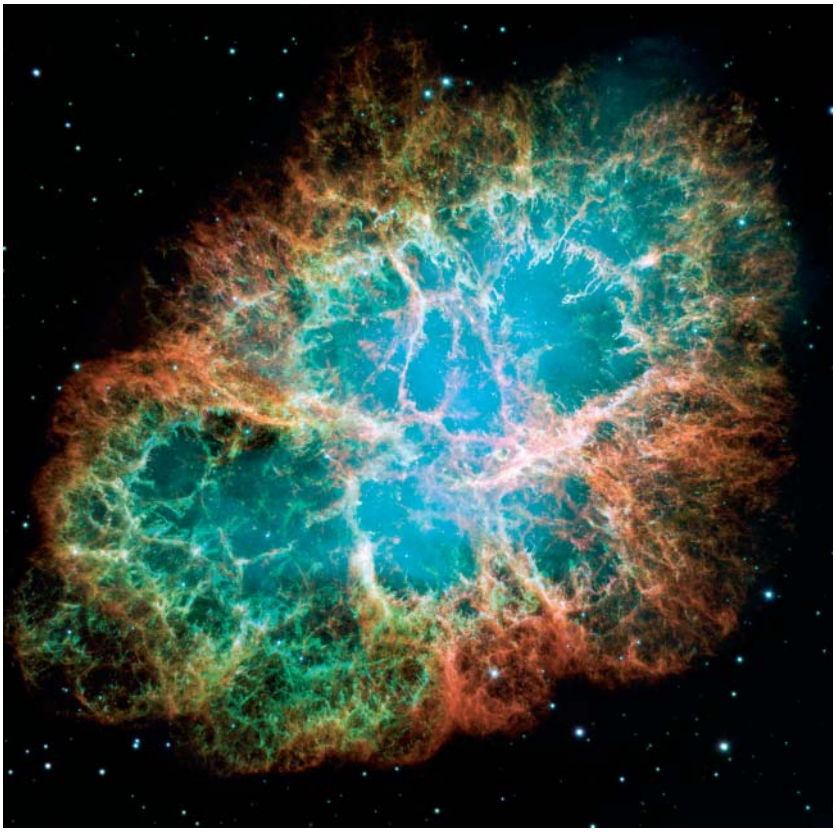

Figure 7 The Crab Nebula (M 1). The nebula consists of matter ejected in a supernova explosion. The material is spread over a volume of 10 light years in diameter and is still expanding at velocities of 1800 km/s. Its distance from Earth is about 6000 light years. The supernova explosion was detected on July 4, 1054, by Chinese astronomers. It is one of the very few historically observed supernovae in our Galaxy. The remnant of the supernova, located in the middle of the nebula, is a neutron star that spins with a period of 30 ms (pulsar). The presence of a remnant neutron star and of hydrogen in the ejecta supports the association of the Crab Nebula with a type II supernova. The image is a three color composite. The green light is predominantly produced by hydrogen emission from material that was ejected by the exploding star. The blue light arises mainly from relativistic electrons that spiral in a large-scale magnetic field (synchrotron radiation) and that are continuously ejected from the rapidly spinning neutron star. (Credit: NASA, ESA, and J. Hester (Arizona State University).)

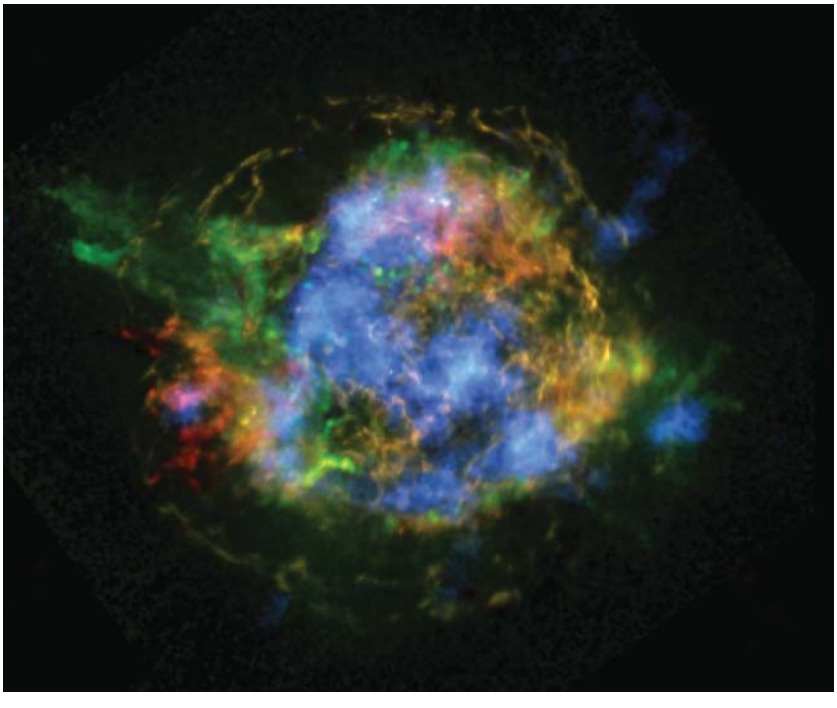

Figure 8 The supernova remnant Cassiopeia A in the constellation Cassiopeia, located at a distance of 11 000 light years from Earth, is one of the brightest extrasolar radio sources in the sky. The debris from the type IIb (core-collapse) supernova explosion is spread over a volume of 10 light years in diameter. Although first light of the supernova should have reached Earth about 350 years ago, there are no clear historical records of the event. The false color image was obtained using the Chandra X-Ray Observatory and the Nuclear Spectroscopic Telescope Array (NuSTAR). The colors represent different X-ray and γ-ray energy ranges that are emitted by different elements: iron (red); silicon and magnesium (green); radioactive ^{44}Ti (blue). The spatial distribution of iron does not match the distribution of ^{44}Ti, indicating that the explosion was not symmetric. (Credit: NASA/JPL-Caltech/CXC/SAO.)

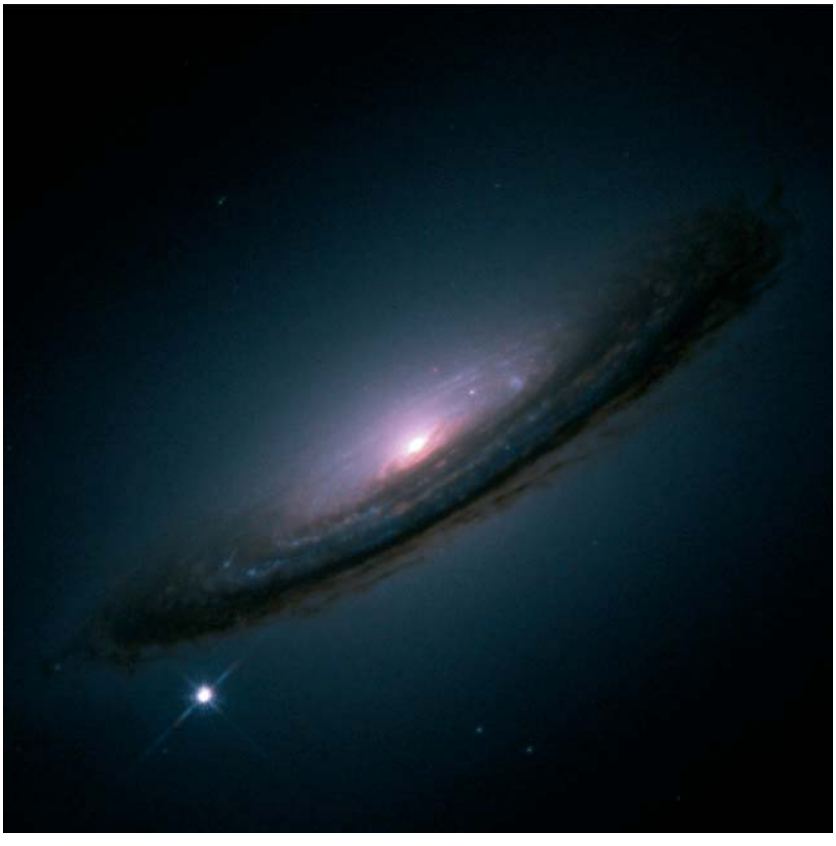

Figure 9 The spiral galaxy NGC 4526 in the constellation Virgo, about 100 million light years away from Earth. The bright spot at the lower left is Supernova 1994D. (The designation means that it was the fourth supernova discovered in 1994). The light emitted during the weeks after the stellar explosion showed that the supernova was of type Ia. (Credit: NASA, ESA, The Hubble Key Project Team, and The High-Z Supernova Search Team.)

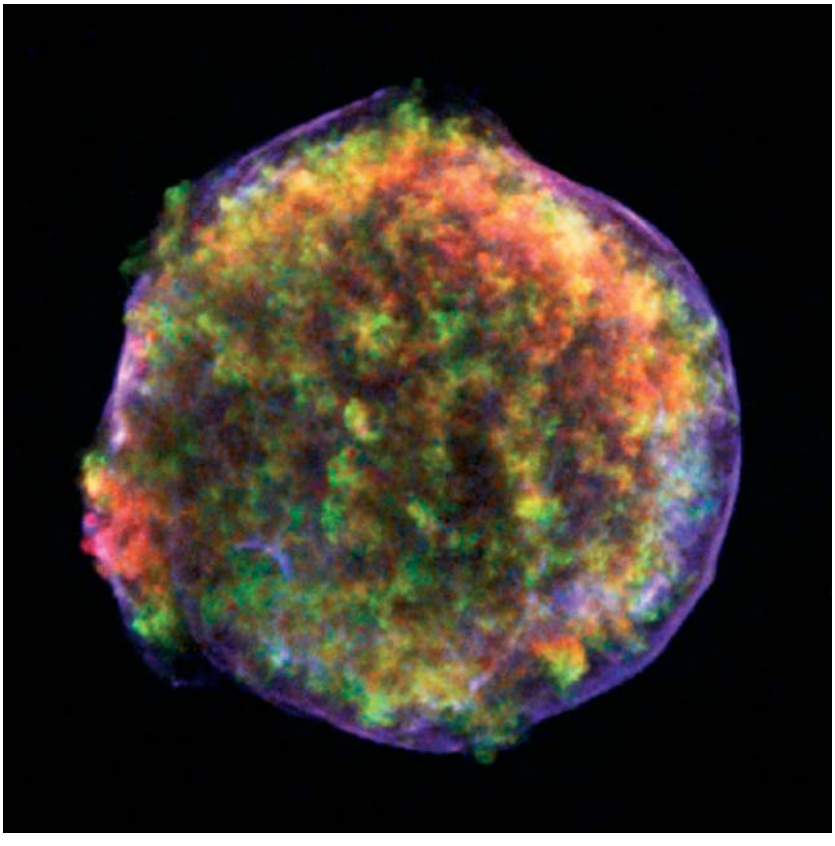

Figure 10 Tycho's supernova remnant in the constellation Cassiopeia, located at a distance of 7500 light years from Earth. The supernova was recorded by the Danish astronomer Tycho Brahe on November 11, 1572. The false color X-ray image was obtained with the Chandra X-Ray Observatory. The colors represent different X-ray energies (red: 0.95–1.26 keV; green: 1.63–2.26 keV; blue: 4.1–6.1 keV). The remnant glows at X-ray energies because of the strong interaction between the high-velocity expanding matter and the interstellar gas that was swept up by the explosion. No hot compact object has been found in the remnant, supporting the theory that the supernova was of type Ia. The cloud is nearly spherical with a diameter of about 20 light years, indicating both a spherical ejection of matter and a rather homogeneous environment in the explosion. (Credit: NASA/CXC/Rutgers/J. Warren and J. Hughes et al.)

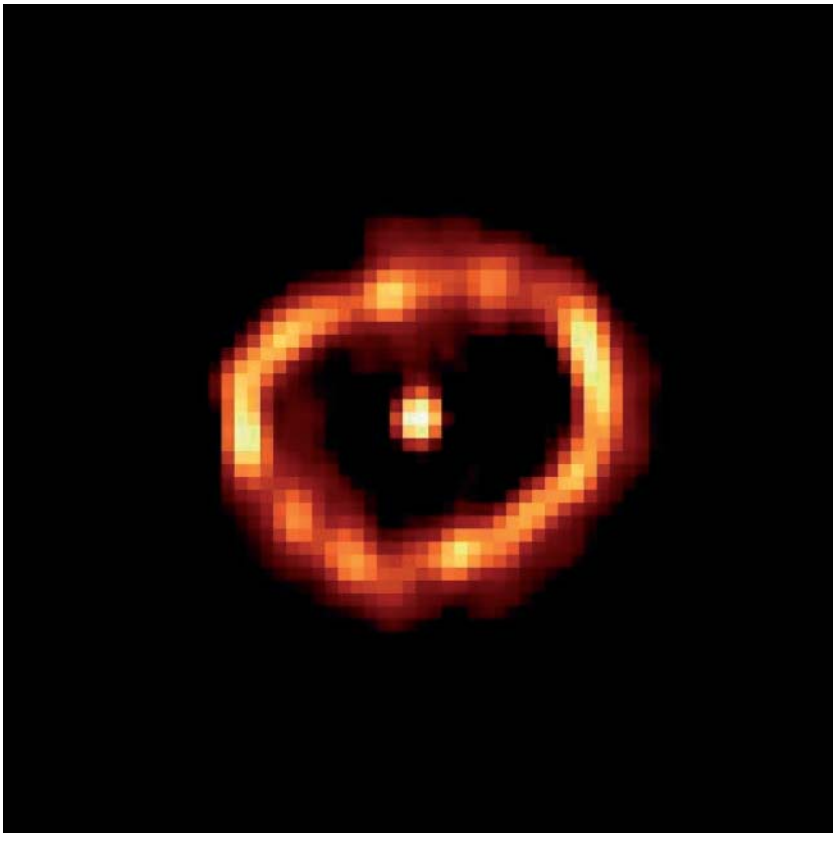

Figure 11 Nova V1974 Cygni 1992 erupted on February 19, 1992 and was one of the brightest classical novae in 20 years, reaching naked-eye visibility for a brief period of time. The distance of Nova Cygni from Earth is about 10 000 light years. The image reveals a nearly spherical and slightly lumpy ring-like structure, which represents the edge of a bubble of hot gas ejected into space by the outburst. The shell contains elements such as nitrogen, oxygen, neon, silicon, and sulfur, which are overabundant relative to their solar system values. This implies that the explosion occurred on the surface of an oxygen–neon white dwarf. These outbursts are also referred to as "neon novae." The white dwarf and the companion star in the center of the image are so close that they revolve around each other in about two hours. The image was taken by the Hubble Space Telescope in ultraviolet light 467 days after the explosion. (Credit: F. Paresce, R. Jedrzejewski (STScI), NASA/ESA.)

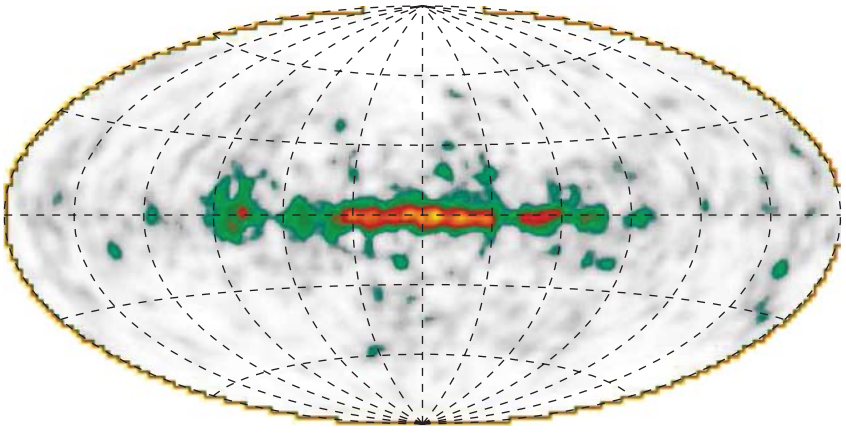

Figure 12 All-sky image of ^{26}Al γ-ray emission at 1809 keV, as derived from a 9-year survey of the COMPTEL instrument onboard the Compton Gamma Ray Observatory (CGRO). The entire sky is seen projected on a coordinate system that is centered on our Galaxy, with the galactic plane running horizontally across the middle of the image. Gamma-ray intensity is represented by a false color map - green (low) to yellow (high). It has been estimated that the Galaxy produces ^{26}Al at a rate of about two solar masses per million years. (Reprinted with permission from S. Plüschke, R. Diehl, V. Schönfelder, et al., ESA SP 459, 55 (2001).)

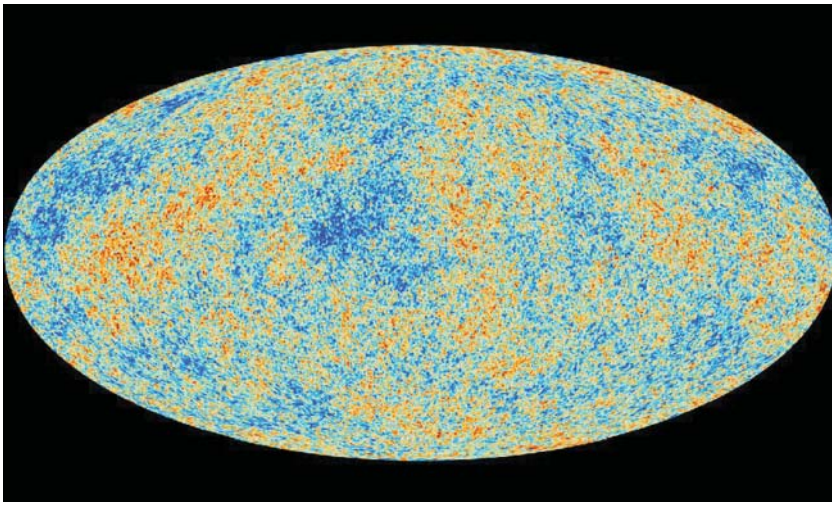

Figure 13 All-sky image from the Planck mission. It reveals temperature fluctuations over a range of only ± 30 μK, caused by oscillations in the photon-baryon fluid about 370 000 years after the big bang. The observed anisotropies can be decomposed in terms of spherical harmonics, with each term describing the magnitude of the anisotropy on a particular angular scale. The observed features in the resulting angular power spectrum are closely related to specific cosmological parameters. The analysis of the Planck mission data reveals that the universe is 13.8 Gy old, that ordinary (baryonic) matter makes up only about 16% of all matter, and that the expansion of the universe is currently accelerating. (Credit: ESA and the Planck Collaboration.)

References

Abbondanno, U. *et al.* (2004) *Phys. Rev. Lett.*, **93**, 161103.

Abramowitz, M. and Stegun, I.A. (1965) *Handbook of Mathematical Functions*, Dover Publications, New York.

Acciari, V.A. *et al.* (2009) *Nature*, **462**, 770.

Ade, P.A.R. *et al.* (2014) *Astron. Astrophys.*, **571**, A16.

Adelberger, E.G. *et al.* (1998) *Rev. Mod. Phys.*, **70**, 1265.

Ajzenberg-Selove, F. (1990) *Nucl. Phys.*, **A506**, 1.

Ajzenberg-Selove, F. (1991) *Nucl. Phys.*, **A523**, 1.

Alibés, A., Labay, J., and Canal, R. (2002) *Astrophys. J.*, **571**, 326.

Almen, O. and Bruce, G. (1961) *Nucl. Instrum. Methods*, **11**, 257.

Alpher, R.A., Bethe, H., and Gamow, G. (1948) *Phys. Rev.*, **73**, 803.

Alpher, R.A. and Hermann, R.C. (1949) *Phys. Rev.*, **75**, 1089.

Althaus, L.G. *et al.* (2010) *Astron. Astrophys. Rev.*, **18**, 471.

Anders, E. and Grevesse, N. (1989) *Geochim. Cosmochim. Acta*, **53**, 197.

Anderson, M.R. *et al.* (1980) *Nucl. Phys.*, **A349**, 154.

Ando, S. *et al.* (2006) *Phys. Rev.*, **C74**, 025809.

Angulo, C. *et al.* (1999) *Nucl. Phys.*, **A656**, 3.

Anttila, A., Keinonen, J., and Bister, M. (1977) *J. Phys.*, **G3**, 1241.

Appel, H. (1968) in *Numerical Tables for 3j-, 6j-, 9j-Symbols, F- and* Γ*-Coefficients* (ed. H. Schopper), Springer, Berlin.

Arlandini, C. *et al.* (1999) *Astrophys. J.*, **525**, 886.

Arnett, W.D. (1982) *Astrophys. J.*, **253**, 785.

Arnett, D. (1996) *Supernovae and Nucleosynthesis*, Princeton University Press, Princeton, NJ.

Arnett, W.D. and Thielemann, F.-K. (1985) *Astrophys. J.*, **295**, 589.

Arnett, W.D. and Truran, J.W. (1969) *Astrophys. J.*, **157**, 339.

Arnould, M. and Goriely, S. (2003) *Phys. Rep.*, **384**, 1.

Arnould, M., Goriely, S., and Jorissen, A. (1999) *Astron. Astrophys.*, **347**, 572.

Arnould, M., Goriely, S., and Takahashi, K. (2007) *Phys. Rep.*, **450**, 97.

Assenbaum, H.J., Langanke, K., and Rolfs, C. (1987) *Z. Phys.*, **A327**, 461.

Atkinson, R.d'E. (1936) *Astrophys. J.*, **84**, 73.

Atkinson, R.d'E. and Houtermans, F.G. (1929) *Z. Phys.*, **54**, 656.

Audi, G. *et al.* (2003a) *Nucl. Phys.*, **A729**, 3.

Audi, G., Wapstra, A.H., and Thibault, C. (2003b) *Nucl. Phys.*, **A729**, 337.

Audi, G. *et al.* (2012) *Chin. Phys.*, **C36**, 1157.

Aver, E. *et al.* (2013) *J. Cosmol. Astropart. Phys.*, **11**, 017.

Bahcall, J.N. (1964) *Astrophys. J.*, **139**, 318.

Bahcall, J.N. (1989) *Neutrino Astrophysics*, Cambridge University Press, Cambridge.

Bahcall, J.N. *et al.* (1982) *Rev. Mod. Phys.*, **54**, 767.

Bahcall, J.N., Chen, X., and Kamionkowski, M. (1998) *Phys. Rev.*, **C57**, 2756.

Bahcall, J.N. and May, R.M. (1969) *Astrophys. J.*, **155**, 501.

Bahcall, J.N. and Moeller, C.P. (1969) *Astrophys. J.*, **155**, 511.

Nuclear Physics of Stars, Second Edition. Christian Iliadis.

Bao, Z.Y. *et al.* (2000) *At. Data Nucl. Data Tables*, **76**, 70.
Bardayan, D.W. *et al.* (2000) *Phys. Rev.*, **C62**, 055804.
Bardayan, D.W. *et al.* (2002) *Phys. Rev. Lett.*, **89**, 262501.
Barker, F.C. (1998) *Nucl. Phys.*, **A637**, 576.
Barnett, A.R. (1982) *Comput. Phys. Commun.*, **27**, 147.
Bateman, H. (1910) *Proc. Cambridge Philos. Soc.*, **15**, 423.
Bé, M.-M. *et al.* (2013) *Table of Radionuclides*, Vol. 7 - *A* = 14 to 245, Bureau International des Poids et Mesures, Sèvres.
Becker, H.W. *et al.* (1981) *Z. Phys.*, **A303**, 305.
Becker, H.W. *et al.* (1982) *Z. Phys.*, **A305**, 319.
Becker, H.W. *et al.* (1995) *Z. Phys.*, **A351**, 453.
Beckurts, K.H. and Wirtz, K. (1964) *Neutron Physics*, Springer-Verlag, New York.
Beer, H. (1991) *Astrophys. J.*, **375**, 823.
Beer, H. *et al.* (1994) *Nucl. Instrum. Methods*, **A337**, 492.
Beer, H. and Käppeler, F. (1980) *Phys. Rev.*, **C21**, 534.
Beer, H., Voss, F., and Winters, R.R. (1992) *Astrophys. J. Suppl.*, **80**, 403.
Bellini, G. *et al.* (2014) *Nature*, **512**, 383.
Bemmerer, D. *et al.* (2005) *Eur. Phys. J.*, **A24**, 313.
Bemmerer, D. *et al.* (2006) *Nucl. Phys.*, **A779**, 297.
Beringer, J. *et al.* (2012) *Phys. Rev.*, **D86**, 010001.
Bertone, P.F. *et al.* (2001) *Phys. Rev. Lett.*, **87**, 152501.
Bethe, H.A. (1939) *Phys. Rev.*, **55**, 434.
Bethe, H.A. (1990) *Rev. Mod. Phys.*, **62**, 801.
Bethe, H.A. and Critchfield, C.L. (1938) *Phys. Rev.*, **54**, 248.
Bethe, H.A. and Wilson, J.R. (1985) *Astrophys. J.*, **295**, 14.
Biedenharn, L.C. (1960) in *Nuclear Spectroscopy* (ed. F. Ajzenberg-Selove), Academic Press, New York.
Biedenharn, L.C. and Rose, M.E. (1953) *Rev. Mod. Phys.*, **25**, 729.
Bindhaban, S.A. *et al.* (1994) *Nucl. Instrum. Methods*, **A340**, 436.
Binney, J. and Merrifield, M. (1998) *Galactic Astronomy*, Princeton University Press, Princeton, NJ.
Bionta, R.M. *et al.* (1987) *Phys. Rev. Lett.*, **58**, 1494.
Bittner, G., Kretschmer, W., and Schuster, W. (1979) *Nucl. Instrum. Methods*, **161**, 1.
Blackmon, J.C. *et al.* (1995) *Phys. Rev. Lett.*, **74**, 2642.
Blackmon, J.C. *et al.* (2003) *Nucl. Phys.*, **A718**, 127c.
Blackmon, J.C., Angulo, C., and Shotter, A.C. (2006) *Nucl. Phys.*, **A777**, 531.
Blanke, E. *et al.* (1983) *Phys. Rev. Lett.*, **51**, 355.
Blatt, J.M. and Weisskopf, V.F. (1952) *Theoretical Nuclear Physics*, John Wiley & Sons, Inc., New York.
Bloom, J.S. *et al.* (2012) *Astrophys. J. Lett.*, **744**, 17.
Bodansky, D., Clayton, D.D., and Fowler, W.A. (1968) *Astrophys. J. Suppl.*, **148**, 299.
Boesgaard, A.M. and King, J.R. (1993) *Astron. J.*, **106**, 2309.
Bohr, N. (1915) *Philos. Mag.*, **30**, 581.
Bohr, N. (1936) *Nature*, **137**, 344.
Bonifacio, P. *et al.* (2007) *Astron. Astrophys.*, **462**, 851.
Boone, J.M. and Chavez, A.E. (1996) *Med. Phys.*, **23**, 1997.
Bravo, E. and Martínez-Pinedo, G. (2012) *Phys. Rev. C*, **85**, 055805.
Breit, G. (1959) In *Handbuch der Physik, Nuclear Reactions II: Theory*, Vol. XLI (ed. S. Flugge), Springer, Berlin.
Briesmeister, J.F. (1993) MCNP - A General Monte Carlo N-Particle Transport Code, LA-12625-M, Los Alamos National Laboratory.
Bruenn, S.W. and Haxton, W.C. (1991) *Astrophys. J.*, **376**, 678.
Brune, C.R. and Sayre, D.B. (2013) *Nucl. Instrum. Methods*, **A698**, 49.
Brussaard, P.J. and Glaudemans, P.W.M. (1977) *Shell-Model Applications in Nuclear Spectroscopy*, North-Holland, Amsterdam.
Buchmann, L. *et al.* (1984) *Nucl. Phys.*, **A415**, 93.
Buras, R. *et al.* (2003) *Astrophys. J.*, **587**, 320.

Buras, R. *et al.* (2006) *Astron. Astrophys.*, **447**, 1049.
Burbidge, E.M., Burbidge, G.R., Fowler, W.A., and Hoyle, F. (1957) *Rev. Mod. Phys.*, **29**, 547.
Burris, D.L. *et al.* (2000) *Astrophys. J.*, **544**, 302.
Burrows, A., Hayer, J., and Fryxell, B.A. (1995) *Astrophys. J.*, **450**, 830.
Busso, M., Gallino, R., and Wasserburg, G.J. (1999) *Annu. Rev. Astron. Astrophys.*, **37**, 239.
Calder, A.C. *et al.* (2007) *Astrophys. J.*, **656**, 313.
Cameron, A.G.W. (1957) *Publ. Astron. Soc. Pac.*, **69**, 201.
Cameron, A.G.W. (1959) *Astrophys. J.*, **130**, 895.
Cameron, A.G.W. (1960) *Astron. J.*, **65**, 485.
Cameron, A.G.W. (2003) *Astrophys. J.*, **587**, 327.
Cameron, A.G.W. and Fowler, W.A. (1971) *Astrophys. J.*, **164**, 111.
Carson, S. *et al.* (2010) *Nucl. Instrum. Methods*, **A618**, 190.
Caughlan, G.R. and Fowler, W.A. (1988) *At. Data Nucl. Data Tables*, **40**, 284.
Chamulak, D.A. *et al.* (2012) *Astrophys. J.*, **744**, 27.
Cheng, C.W. and King, J.D. (1979) *J. Phys.*, **G5**, 1261.
Chieffi, A., Limongi, M., and Straniero, O. (1998) *Astrophys. J.*, **502**, 737.
Clayton, D.D. (1983) *Principles of Stellar Evolution and Nucleosynthesis*, University of Chicago Press, Chicago.
Clayton, D.D. (2003) *Handbook of Isotopes in the Cosmos*, Cambridge University Press, Cambridge.
Clayton, D.D., Fowler, W.A., Hull, T.E., and Zimmerman, B.A. (1961) *Ann. Phys.*, **12**, 331.
Clayton, D.D. and Rassbach, M. (1967) *Astrophys. J.*, **148**, 69.
Clayton, D.D. and Ward, R.A. (1974) *Astrophys. J.*, **193**, 397.
Clifford, F.E. and Tayler, R.J. (1965) *Mem. R. Astron. Soc.*, **69**, 21.
Coc, A., Porquet, M.-G., and Nowacki, F. (1999) *Phys. Rev.*, **C61**, 015801.
Coc, A., Uzan, J.-P., and Vangioni, E. (2014) *J. Cosmol. Astropart. Phys.*, **10**, 050.
Cockcroft, J.D. and Walton, E.T.S. (1932) *Nature*, **129**, 649.
Cole, W. and Grime, G.W. (1981) *World Conference of the International Nuclear Target Development Society*, Plenum Publishing Corporation, New York.
Cook, A.L. *et al.* (2012) *Phys. Rev.*, **C86**, 015809.
Condon, E.U. and Gourney, R.W. (1929) *Phys. Rev.*, **33**, 127.
Cook, C.W. *et al.* (1957) *Phys. Rev.*, **107**, 508.
Cooke, R.J. *et al.* (2014) *Astrophys. J.*, **781**, 31.
Corwin, T.M. and Carney, B.W. (2001) *Astron. J.*, **122**, 3183.
Couder, M. *et al.* (2004) *Phys. Rev.*, **C69**, 022801.
Cowan, J.J., Thielemann, F.-K., and Truran, J.W. (1991) *Phys. Rep.*, **208**, 267.
Cowley, C.R. (1995) *An Introduction to Cosmochemistry*, Cambridge University Press, Cambridge.
Cristallo, S., Straniero, O., and Gallino, R. (2005) *Nucl. Phys.*, **A758**, 509.
D'Auria, J.M. *et al.* (2004) *Phys. Rev.*, **C69**, 065803.
Davids, B. *et al.* (2003) *Phys. Rev.*, **C67**, 065808.
Davis, R. Jr., Harmer, D.S., and Hoffman, K.C. (1968) *Phys. Rev. Lett.*, **20**, 1205.
Dayras, R., Switkowski, Z.E., and Woosley, S.E. (1977) *Nucl. Phys.*, **A279**, 70.
Debertin, K. and Helmer, R.G. (1988) *Gamma- and X-Ray Spectrometry with Semiconductor Detectors*, Elsevier Science, Amsterdam.
Delbar, Th. *et al.* (1993) *Phys. Rev.*, **C48**, 3088.
Descouvemont, P. *et al.* (2004) *At. Data Nucl. Data Tables*, **88**, 203.
DeShalit, A. and Talmi, I. (1963) *Nuclear Shell Theory*, Academic Press, New York.
Devons, S. and Goldfarb, L.J.B. (1957) in *Handbuch der Physik*, Vol. XLII (ed. S. Flugge), Springer, Berlin.
DeWitt, H.E., Graboske, H.C., and Cooper, M.S. (1973) *Astrophys. J.*, **181**, 439.
Diehl, R. *et al.* (1993) *Astron. Astrophys.*, **97**, 181.
Diehl, R. *et al.* (2006) *Nature*, **439**, 45.
Dillmann, I. *et al.* (2003) *Phys. Rev. Lett.*, **91**, 162503.
Doll, C. *et al.* (1999) *Phys. Rev.*, **C59**, 492.

Dombsky, M., Bricault, P., and Hanemaayer, V. (2004) *Nucl. Phys.*, **A746**, 32c.
Domínguez, I., Höflich, P., and Straniero, O. (2001) *Astrophys. J.*, **557**, 279.
Drotleff, H.W. *et al.* (1993) *Astrophys. J.*, **414**, 735.
Dunbar, D.N.F. *et al.* (1953) *Phys. Rev.*, **92**, 649.
Duncan, D., Lambert, D., and Lemke, M. (1992) *Astrophys. J.*, **401**, 584.
Duncan, R.C., Shapiro, S.L., and Wasserman, I. (1986) *Astrophys. J.*, **309**, 141.
East, L.V. and Walton, R.B. (1969) *Nucl. Instrum. Methods*, **72**, 161.
Endt, P.M. (1990) *Nucl. Phys.*, **A521**, 1.
Endt, P.M. (1993) *At. Data Nucl. Data Tables*, **55**, 171.
Endt, P.M. (1998) *Nucl. Phys.*, **A633**, 1.
Endt, P.M. *et al.* (1990) *Nucl. Phys.*, **A510**, 209.
Engel, S. *et al.* (2005) *Nucl. Instrum. Methods*, **A553**, 491.
Esmailzadeh, R., Starkman, G.D., and Dimopoulos, S. (1991) *Astrophs. J.*, **378**, 504.
Evans, R.D. (1955) *The Atomic Nucleus*, McGraw-Hill, New York.
Farouqi, K., Kratz, K.-L., and Pfeiffer, B. (2009) *Publ. Astron. Soc. Aust.*, **26**, 194.
Farouqi, K. *et al.* (2010) *Astrophys. J.*, **712**, 1359.
Ferguson, A.J. (1965) *Angular Correlation Methods in Gamma-Ray Spectroscopy*, North-Holland, Amsterdam.
Fields, B. (2011) *Annu. Rev. Nucl. Part Sci.*, **61**, 47.
Fifield, L.K. and Orr, N.A. (1990) *Nucl. Instrum. Methods*, **A288**, 360.
Firestone, R.B. and Shirley, V.S. (1996) *Table of Isotopes*, John Wiley & Sons, Inc., New York.
Fischer, T. *et al.* (2009) *Astron. Astrophys.*, **499**, 1.
Fisker, J.L., Hoffman, R.D., and Pruet, J. (2009) *Astrophys. J. Lett.*, **690**, 135.
Fixsen, D.J. (2009) *Astrophys. J.*, **707**, 916.
Formicola, A. *et al.* (2004) *Phys. Lett.*, **B591**, 61.
Forstner, O. *et al.* (2001) *Phys. Rev.*, **C64**, 045801.
Fowler, W.A., Caughlan, G.R., and Zimmerman, B.A. (1967) *Annu. Rev. Astron. Astrophys.*, **5**, 525.
Fowler, W.A., Caughlan, G.R., and Zimmerman, B.A. (1975) *Annu. Rev. Astron. Astrophys.*, **13**, 69.
Fowler, W.A. and Hoyle, F. (1964) *Astrophys. J. Suppl.*, **9**, 201.
Fowler, W.A., Lauritsen, C.C., and Lauritsen, T. (1948) *Rev. Mod. Phys.*, **20**, 236.
Freiburghaus, C. *et al.* (1999) *Astrophys. J.*, **516**, 381.
Fröhlich, C. *et al.* (2006) *Phys. Rev. Lett.*, **96**, 142505.
Fuller, G.M., Fowler, W.A., and Newman, M.J. (1982) *Astrophys. J.*, **48**, 279.
Gallino, R. *et al.* (1998) *Astrophys. J.*, **497**, 388.
Gamow, G. (1928) *Z. Phys.*, **51**, 204.
Gamow, G. (1946) *Phys. Rev.*, **70**, 572.
Gamow, G. and Schoenberg, M. (1940) *Phys. Rev.*, **58**, 1117.
Geist, W.H. *et al.* (1996) *Nucl. Instrum. Methods*, **B111**, 176.
Gialanella, L. *et al.* (2000) *Eur. Phys. J.*, **A7**, 303.
Giesen, U. *et al.* (1993) *Nucl. Phys.*, **A561**, 95.
Gill, R.L. *et al.* (1986) *Phys. Rev. Lett.*, **56**, 1874.
Gilmore, G., Gustafsson, B., Edvardsson, B., and Nissen, P.E. (1992) *Nature*, **357**, 392.
Goldsmith, H.H., Ibser, H.W., and Feld, B.T. (1947) *Rev. Mod. Phys.*, **19**, 259.
Goosman, D.R. and Kavanagh, R.W. (1967) *Phys. Rev.*, **C161**, 1156.
Goriely, S. (1998) in *Nuclei in the Cosmos V* (eds N. Prantzos, S. Harissopulos), Edition Frontieres, Paris, p. 314.
Goriely, S. and Arnould, M. (1996) *Astron. Astrophys.*, **312**, 327.
Goriely, S., Hilaire, S., and Koning, A.J. (2008) *Phys. Rev.*, **C78**, 064307.
Gove, H.E. (1959) in *Nuclear Reactions*, Vol. I (eds P.M. Endt and M. Demeur), North-Holland, Amsterdam.
Gove, N.B. and Martin, M.J. (1971) *At. Data Nucl. Data Tables*, **10**, 205.
Graboske, H.C. *et al.* (1973) *Astrophys. J.*, **181**, 457.
Graulich, J.S. *et al.* (1997) *Nucl. Phys.*, **A626**, 751.

Grebenev, S.A. *et al.* (2012) *Nature*, **490**, 373.
Grefenstette, B.W. *et al.* (2014) *Nature*, **506**, 339.
Grevesse, N. and Sauval, A.J. (1998) *Space Sci. Rev.*, **85**, 161.
Grigorenko, L.V. and Zhukov, M.V. (2005) *Phys. Rev.*, **C72**, 015803.
Groombridge, D. *et al.* (2002) *Phys. Rev.*, **C66**, 055802.
Gyuerky, G. *et al.* (2003) *Phys. Rev.*, **C68**, 055803.
Habing, H.J. and Olofsson, H. (2004) *Asymptotic Giant Branch Stars*, Springer, Heidelberg.
Hale, S.E. *et al.* (2001) *Phys. Rev.*, **C65**, 015801.
Hammache, F. *et al.* (2013) *Phys. Rev.*, **C88**, 062802(R).
Hanson, A.O., Taschek, R.F., and Williams, J.H. (1949) *Rev. Mod. Phys.*, **21**, 635.
Harissopulos, S. (2004) *AIP Conf. Proc.*, **704**, 422.
Harss, B. *et al.* (2002) *Phys. Rev.*, **C65**, 035803.
Hauser, W. and Feshbach, H. (1952) *Phys. Rev.*, **15**, 366.
Heger, A. *et al.* (2005) *Phys. Lett.*, **B606**, 258.
Heil, M. *et al.* (2005) *Phys. Rev.*, **C71**, 025803.
Helmer, R.G. *et al.* (2003) *Nucl. Instrum. Methods*, **A511**, 360.
Hernanz, M. *et al.* (1999) *Astrophys. J. Lett.*, **526**, 97.
Heusser, G. (1995) *Annu. Rev. Nucl. Part. Sci.*, **45**, 543.
Higdon, J.C., Lingenfelter, R.E., and Ramaty, R. (1998) *Astrophys. J. Lett.*, **509**, 33.
High, M.D. and Cujec, B. (1977) *Nucl. Phys.*, **A282**, 181.
Hinshaw, G. *et al.* (2013) *Astrophys. J. Suppl.*, **208**, 19.
Hirata, K. *et al.* (1987) *Phys. Rev. Lett.*, **58**, 1490.
Hirata, K.S. *et al.* (1990) *Phys. Rev. Lett.*, **65**, 1297.
Hix, W.R. and Meyer, B.S. (2006) *Nucl. Phys.*, **A777**, 188.
Hix, W.R. and Thielemann, F.-K. (1996) *Astrophys. J.*, **460**, 869.
Höflich, P. *et al.* (2004) *Astrophys. J.*, **617**, 1258.
Höflich, P. *et al.* (2013) *Front. Phys.*, **8**, 144.
Hoffman, R.D., Woosley, S.E., and Weaver, T.A. (2001) *Astrophys. J.*, **549**, 1085.
Holland, L. (1956) *Vacuum Deposition of Thin Films*, Chapman and Hall, London.
Holstein, B.R. (1989) *Weak Interactions in Nuclei*, Princeton University Press, Princeton, NJ.
Hoyle, F. (1946) *Mon. Not. R. Astron. Soc.*, **106**, 343.
Hoyle, F. *et al.* (1953) *Phys. Rev.*, **92**, 1095.
Hoyle, F. (1954) *Astrophys. J. Suppl.*, **1**, 121.
Hoyle, F. and Fowler, W.A. (1960) *Astrophys. J.*, **132**, 565.
Hüdepohl, L. *et al.* (2010) *Phys. Rev. Lett.*, **104**, 251101.
Hulke, G., Rolfs, C., and Trautvetter, H.P. (1980) *Z. Phys.*, **A297**, 161.
Iben, I. Jr. (1985) *Q. J. R. Astron. Soc.*, **26**, 1.
Iben, I. Jr. (1991) *Astrophys. J. Suppl.*, **76**, 55.
Iliadis, C. (1996) Ph.D. thesis, University of Notre Dame.
Iliadis, C. (1997) *Nucl. Phys.*, **A618**, 166.
Iliadis, C. *et al.* (1990) *Nucl. Phys.*, **A512**, 509.
Iliadis, C. *et al.* (1991) *Nucl. Phys.*, **A533**, 153.
Iliadis, C. *et al.* (1999) *Astrophys. J.*, **524**, 434.
Iliadis, C. *et al.* (2001) *Astrophys. J. Suppl.*, **134**, 151.
Iliadis, C. *et al.* (2002) *Astrophys. J. Suppl.*, **142**, 105.
Iliadis, C. *et al.* (2010) *Nucl. Phys.*, **A841**, 31.
Iliadis, C. *et al.* (2011) *Astrophys. J. Suppl.*, **193**, 16.
Imbriani, G. *et al.* (2005) *Eur. Phys. J.*, **A25**, 455.
Jaag, S. and Käppeler, F. (1995) *Phys. Rev.*, **C51**, 3465.
Jackson, J.D. (1975) *Classical Electrodynamics*, 2nd edn, John Wiley & Sons, Inc., New York.
Jaeger, M. *et al.* (2001) *Phys. Rev. Lett.*, **87**, 202501.
Jordan, G.C., Gupta, S.S., and Meyer, B.S. (2003) *Phys. Rev.*, **C68**, 065801.
José, J. and Hernanz, M. (1998) *Astrophys. J.*, **494**, 680.
José, J., Hernanz, M., and Iliadis, C. (2006) *Nucl. Phys.*, **A777**, 550.

Junker, M. *et al.* (1998) *Phys. Rev.*, **C57**, 2700.
Kahabka, P. and van den Heuvel, E.P.J. (1997) *Annu. Rev. Astron. Astrophys.*, **35**, 69.
Käppeler, F. (1999) *Prog. Part. Nucl. Phys.*, **43**, 419.
Käppeler, F., Naqvi, A., and Al-Ohali, M. (1987) *Phys. Rev.*, **C35**, 936.
Käppeler, F. *et al.* (1990) *Astrophys. J.*, **354**, 630.
Käppeler, F. *et al.* (2011) *Rev. Mod. Phys.*, **83**, 157.
Karakas, A.I. *et al.* (2006) *Astrophys. J.*, **643**, 471.
Kettner, K.U., Lorenz-Wirzba, H., and Rolfs, C. (1980) *Z. Phys.*, **A298**, 65.
Khokhlov, A.M. (1991) *Astron. Astrophys.*, **245**, 114.
Kim, I.J., Park, C.S., and Choi, H.D. (2003) *Appl. Radiat. Isot.*, **58**, 227.
King, J.D. *et al.* (1994) *Nucl. Phys.*, **A567**, 354.
Kippenhahn, R. and Weigert, A. (1990) *Stellar Structure and Evolution*, Springer, Berlin.
Knoll, G.F. (1989) *Radiation Detection and Measurement*, 2nd edn, John Wiley & Sons, Inc., New York.
Koehler, P.E. (2001) *Nucl. Instrum. Methods*, **A460**, 352.
Koehler, P.E. *et al.* (2002) *Phys. Rev.*, **C66**, 055805.
Koike, O. *et al.* (2004) *Astrophys. J.*, **603**, 242.
Kovetz, A. and Prialnik, D. (1997) *Astrophys. J.*, **477**, 356.
Krane, K.S. (1988) *Introductory Nuclear Physics*, John Wiley & Sons, Inc., New York.
Kratz, K.-L. (2006) *AIP Conf. Proc.*, **819**, 409.
Kratz, K.-L. *et al.* (1986) *Z. Phys.*, **A325**, 489.
Kratz, K.-L. *et al.* (1988) *J. Phys.*, **G14**, S331.
Kratz, K.-L. *et al.* (1993) *Astrophys. J.*, **403**, 216.
Kratz, K.-L. *et al.* (2001) *Mem. Soc. Astron. Ital.*, **72**, 453.
Kratz, K.-L. *et al.* (2004) *New Astron. Rev.*, **48**, 105.
Kratz, K.-L. *et al.* (2007) *Astrophys. J.*, **662**, 39.
Krauss, L.M. and Chaboyer, B. (2003) *Science*, **299**, 65.
Kunz, R. *et al.* (2002) *Astrophys. J.*, **567**, 643.
Lane, A.M. and Thomas, R.G. (1958) *Rev. Mod. Phys.*, **30**, 257.
Lang, K.R. (1974) *Astrophysical Formulae*, Springer, Berlin.
Langanke, K. and Martínez-Pinedo, G. (2000) *Nucl. Phys.*, **A673**, 481.
Langanke, K. and Martínez-Pinedo, G. (2001) *At. Data Nucl. Data Tables*, **79**, 1.
Leising, M.D. and Share, G.H. (1990) *Astrophys. J.*, **357**, 638.
Lemut, A. (2008) *Eur. Phys. J.*, **A36**, 233.
Leo, W.R. (1987) *Techniques for Nuclear and Particle Physics Experiments*, Springer, Berlin.
Lewin, W.H.G., Paradijs, J., and Taam, R.E. (1993) *Space Sci. Rev.*, **62**, 233.
Li, W. *et al.* (2011a) *Mon. Not. R. Astron. Soc.*, **412**, 1441.
Li, W. *et al.* (2011b) *Mon. Not. R. Astron. Soc.*, **412**, 1473.
Limongi, M. and Chieffi, A. (2003) *Astrophys. J.*, **592**, 404.
Limongi, M. and Chieffi, A. (2006) *Astrophys. J.*, **647**, 483.
Limongi, M., Straniero, O., and Chieffi, A. (2000) *Astrophys. J. Suppl.*, **129**, 625.
Lindhard, J., Scharff, M., and Schiott, H.E. (1963) *Kgl. Danske Videnskab. Selskab, Mat.-Fys. Medd.*, **33**, 14.
Liolios, T.E. (2000) *Phys. Rev.*, **C61**, 055802.
Lodders, K. (2003) *Astrophys. J.*, **591**, 1220.
Lodders, K., Palme, H., and Gail, H.P. (2009) in *Landolt-Börnstein - Group VI Astronomy and Astrophysics Numerical Data and Functional Relationships in Science and Technology: Solar System*, Vol. 4B (ed. J.E. Trumper), Springer, Berlin.
Longland, R. *et al.* (2006) *Nucl. Instrum. Methods*, **A566**, 452.
Longland, R. *et al.* (2009) *Phys. Rev.*, **C80**, 055803.
Longland, R. *et al.* (2010) *Phys. Rev.*, **C81**, 055804.
Longland, R., Iliadis, C., and Karakas, A.I. (2012) *Phys. Rev.*, **C85**, 065809.
Lorch, E.A. (1973) *Int. J. Appl. Radiat. Isot.*, **24**, 585.
Lugaro, M. *et al.* (2003) *Astrophys. J.*, **586**, 1305.
Lund, E. *et al.* (1986) *Phys. Scr.*, **34**, 614.

Lunney, D., Pearson, J.M., and Thibault, C. (2003) *Rev. Mod. Phys.*, **75**, 1021.
Lynch, F.J. (1975) *IEEE Trans. Nucl. Sci.*, **NS-22**, 58.
Lynn, J.E. (1968) *The Theory of Neutron Resonance Reactions*, Clarendon Press, Oxford.
Lyons, P.B., Toevs, J.W., and Sargood, D.G. (1969) *Nucl. Phys.*, **A130**, 1.
Macklin, R.L., Halperin, J., and Winters, R.R. (1979) *Nucl. Instrum. Methods*, **169**, 213.
Mahoney, W.A. *et al.* (1982) *Astrophys. J.*, **262**, 742.
Mann, F.M. *et al.* (1975) *Phys. Lett.*, **B58**, 420.
Marion, J.B. (1966) *Rev. Mod. Phys.*, **38**, 660.
Marmier, P. and Sheldon, E. (1969) *Physics of Nuclei and Particles*, Academic Press, New York.
Marta, M. *et al.* (2011) *Phys. Rev.*, **C83**, 045804.
Matz, S. *et al.* (1988) *Nature*, **331**, 416.
Maxman, S.H. (1967) *Nucl. Instrum. Methods*, **50**, 53.
Mayer, R.E. *et al.* (1993) *Nucl. Instrum. Methods*, **A324**, 501.
Mazarakis, M.G. and Stephens, W.E. (1973) *Phys. Rev.*, **C7**, 1280.
McGlone, V.A. and Johnson, P.B. (1991) *Nucl. Instrum. Methods*, **B61**, 201.
Meakin, C.A. *et al.* (2009) *Astrophys. J.*, **693**, 1188.
Meneguzzi, M., Audouze, J., and Reeves, H. (1971) *Astron. Astrophys.*, **15**, 337.
Merrill, P.W. (1952) *Astrophys. J.*, **116**, 21.
Messiah, A. (1999) *Quantum Mechanics*, Dover Publications, New York.
Mewaldt, R.A. *et al.* (2001) *Space Sci. Rev.*, **99**, 27.
Meynet, G. and Arnould, M. (2000) *Astron. Astrophys.*, **355**, 176.
Michaud, G. and Charbonneau, P. (1991) *Space Sci. Rev.*, **57**, 1.
Miller, D.W. (1963) in *Fast Neutron Physics* (eds J.B. Marion and J.L Fowler), Interscience Publishers, New York.
Mitchell, L.W. *et al.* (1985) *Nucl. Phys.*, **A443**, 487.
Mitler, H.E. (1977) *Astrophys. J.*, **212**, 513.
Mizumoto, M. and Sugimoto, M. (1989) *Nucl. Instrum. Methods*, **A282**, 324.
Mohr, P. (1999) *Phys. Rev.*, **C59**, 1790.
Mohr, P. *et al.* (2004) *Phys. Rev.*, **C69**, 032801.
Mohr, P., Fülöp, Zs., and Utsunomiya, H. (2007) *Eur. Phys. J.*, **A32**, 357.
Mohr, P.J., Taylor, B.N., and Newell, D.B. (2012) *Rev. Mod. Phys.*, **84**, 1527.
Möller, P. (1995) *At. Data Nucl. Data Tables*, **59**, 185.
Möller, P., Nix, J.R., and Kratz, K.-L. (1997) *At. Data Nucl. Data Tables*, **66**, 131.
Möller, P., Pfeiffer, B., and Kratz, K.-L. (2003) *Phys. Rev.*, **C67**, 055802.
Moldauer, P.A. (1964) *Rev. Mod. Phys.*, **36**, 1079.
Mosher, J. *et al.* (2001) *Nucl. Instrum. Methods*, **A459**, 532.
Mueller, A.C. and Sherrill, B.M. (1993) *Annu. Rev. Nucl. Part. Sci.*, **43**, 529.
Mukherjee, M. *et al.* (2004) *Phys. Rev. Lett.*, **93**, 150801.
Nadyozhin, D.K. and Deputovich, A.Yu. (2002) *Astron. Astrophys.*, **386**, 711.
Newton, J.R. *et al.* (2007) *Phys. Rev.*, **C75**, 045801.
Nichols, A.L. (1996) in *Handbook of Nuclear Properties* (eds D. Poenaru and W. Greiner), Clarendon Press, Oxford.
Nomoto, K. and Iben, I. (1985) *Astrophys. J.*, **297**, 531.
Nomoto, K., Thielemann, F.-K., and Miyaji, S. (1985) *Astron. Astrophys.*, **149**, 239.
Nomoto, K., Thielemann, F.-K., and Yokoi, K. (1984) *Astrophys. J.*, **286**, 644.
Oda, T. *et al.* (1994) *At. Data Nucl. Data Tables*, **56**, 231.
Paine, B.M., Kennett, S.R., and Sargood, D.G. (1978) *Phys. Rev.*, **C17**, 1550.
Paine, P.M. and Sargood, D.G. (1979) *Nucl. Phys.*, **A331**, 389.
Palme, H. and Jones, A. (2003) *Treatise on Geochemistry*, Vol. 1, Elsevier Science, Amsterdam, p. 41.
Palmer, D.W. *et al.* (1963) *Phys. Rev.*, **130**, 1153.
Panov, I.V. *et al.* (2005) *Nucl. Phys.*, **A747**, 633.
Parikh, A., José, J., Moreno, F., and Iliadis, C. (2008) *Astrophys. J. Suppl.*, **178**, 110.
Parikh, A. *et al.* (2009) *Phys. Rev.*, **C79**, 045802.
Parikh, A., José, J., Sala, G., and Iliadis, C. (2013a) *Prog. Part. Nucl. Phys.*, **69**, 225.
Parikh, A. *et al.* (2013b) *Astron. Astrophys.*, **557**, A3.

Parker, P.D., Bahcall, J.N., and Fowler, W.A. (1964) *Astrophys. J.*, **139**, 602.
Patronis, N. *et al.* (2004) *Phys. Rev.*, **C69**, 025803.
Patterson, J.R., Winkler, H., and Zaidins, C.S. (1969) *Astrophys. J.*, **157**, 367.
Paul, H. and Schinner, A. (2002) *Nucl. Instrum. Methods*, **B195**, 166.
Paul, H. and Schinner, A. (2005) *Nucl. Instrum. Methods*, **B227**, 461.
Pearson, J.M., Nayak, R.C., and Goriely, S. (1996) *Phys. Lett.*, **B387**, 455.
Penzias, A.A. and Wilson, R.W. (1965) *Astrophys. J.*, **142**, 419.
Perlmutter, S. *et al.* (1999) *Astrophys. J.*, **517**, 565.
Peters, J.G. (1968) *Astrophys. J.*, **154**, 224.
Peterson, R.J. and Ristinen, R.A. (1975) *Nucl. Phys.*, **A246**, 402.
Phillips, M.M. (1993) *Astrophys. J. Lett.*, **413**, 105.
Pignatari, M. *et al.* (2005) *Nucl. Phys.*, **A758**, 541.
Poenitz, W.P. (1984) in *Neutron Radiative Capture* (ed. R.E. Chrien), Pergamon Press, Oxford.
Powell, D.C. *et al.* (1998) *Nucl. Phys.*, **A644**, 263.
Powell, D.C. *et al.* (1999) *Nucl. Phys.*, **A660**, 349.
Prantzos, N. (2012a) *Astron. Astrophys.*, **538**, A80.
Prantzos, N. (2012b) *Astron. Astrophys.*, **542**, A67.
Pruet, J. *et al.* (2006) *Astrophys. J.*, **644**, 1028.
Qian, Y.-Z. (2000) *Astrophys. J. Lett.*, **534**, 67.
Qian, Y.-Z., Wasserburg, G.J. *et al.* (2007) *Phys. Rep.*, **442**, 237.
Raiola, F. *et al.* (2002) *Eur. Phys. J.*, **A13**, 377.
Raiteri, C.M. *et al.* (1991) *Astrophys. J.*, **371**, 665.
Raiteri, C.M. *et al.* (1993) *Astrophys. J.*, **419**, 207.
Raman, S. *et al.* (2000) *Nucl. Instrum. Methods*, **A454**, 389.
Ramaty, R., Kozlovsky, B., Lingenfelter, R.E., and Reeves, H. (1997) *Astrophys. J.*, **488**, 730.
Rapp, W. *et al.* (2006) *Astrophys. J.*, **653**, 474.
Ratynski, W. and Käppeler, F. (1988) *Phys. Rev.*, **C37**, 595.
Rauscher, T. (2004) in *The R-Process: The Astrophysical Origin of the Heavy Elements and Related Rare Isotope Accelerator Physics* (eds Y.-Z. Qian, E. Rehm, H. Schatz, and F.-K. Thielemann), World Scientific, Singapore, p. 63.
Rauscher, T. (2005) *Nucl. Phys.*, **A758**, 549.
Rauscher, T. and Thielemann, F.-K. (2000) *At. Data Nucl. Data Tables*, **75**, 1; (2001) **79**, 47.
Rauscher, T., Thielemann, F.-K., and Kratz, K.-L. (1997) *Phys. Rev.*, **C56**, 1613.
Rauscher, T. *et al.* (2000) *Nucl. Phys.*, **A675**, 695.
Rauscher, T. *et al.* (2011) *Astrophys. J.*, **738**, 143.
Rauscher, T. *et al.* (2013) *Rep. Prog. Phys.*, **76**, 066201.
Rayet, M. *et al.* (1995) *Astron. Astrophys.*, **298**, 517.
Rayet, M. and Hashimoto, M. (2000) *Astron. Astrophys.*, **354**, 740.
Rayet, M., Prantzos, N., and Arnould, M. (1990) *Astron. Astrophys.*, **227**, 271.
Reifarth, R. (2002) *Wissenschaftliche Berichte, FZKA 6725*, Forschungszentrum Karlsruhe.
Reifarth, R. *et al.* (2003) *Astrophys. J.*, **582**, 1251.
Reines, F. and Cowan, C.L. (1959) *Phys. Rev.*, **113**, 273.
Renaud, M. *et al.* (2006) *Astrophys. J. Lett.*, **647**, 41.
Riess, A. *et al.* (1998) *Astron. J.*, **116**, 1009.
Ritossa, C., García-Berro, E., and Iben, I. Jr. (1996) *Astrophys. J.*, **460**, 489.
Rolfs, C. (1973) *Nucl. Phys.*, **A217**, 29.
Rolfs, C. and Rodney, W.S. (1975) *Nucl. Phys.*, **A241**, 460.
Rolfs, C.E. and Rodney, W.S. (1988) *Cauldrons in the Cosmos*, University of Chicago Press, Chicago.
Romano, D. *et al.* (2001) *Astron. Astrophys.*, **374**, 646.
Rose, M.E. (1953) *Phys. Rev.*, **91**, 610.
Rosman, K.J.R. and Taylor, P.D.P. (1998) *J. Phys. Chem. Ref. Data*, **27**, 1275.
Rosswog, S. *et al.* (1999) *Astron. Astrophys.*, **341**, 499.
Rotenberg, M. *et al.* (1959) *The 3-j and 6-j Symbols*, Technology Press MIT, Cambridge.

Rowland, C. *et al.* (2002a) *Phys. Rev.*, **C65**, 064609.
Rowland, C. *et al.* (2002b) *Nucl. Instrum. Methods*, **A480**, 610.
Ruiz-Lapuente, P. *et al.* (2004) *Nature*, **431**, 1069.
Runkle, R.C., Champagne, A.E., and Engel, J. (2001) *Astrophys. J.*, **556**, 970.
Runkle, R. *et al.* (2005) *Phys. Rev. Lett.*, **94**, 082503.
Ryan, S., Norris, J., Bessell, M., and Deliyannis, C. (1992) *Astrophys. J.*, **388**, 184.
Ryter, C., Reeves, H., Gradsztajn, E., and Audouze, J. (1970) *Astron. Astrophys.*, **8**, 389.
Sackmann, I.-J., Boothroyd, A.I., and Kraemer, K.E. (1993) *Astrophys. J.*, **418**, 457.
Sallaska, A.L. *et al.* (2013) *Astrophys. J. Suppl.*, **207**, 18.
Salpeter, E.E. (1952) *Astrophys. J.*, **115**, 326.
Salpeter, E.E. (1954) *Aust. J. Phys.*, **7**, 353.
Salpeter, E.E. and Van Horn, H.M. (1969) *Astrophys. J.*, **155**, 183.
Sanuki, T. *et al.* (2000) *Astrophys. J.*, **545**, 1135.
Sargood, D.G. (1982) *Phys. Rep.*, **93**, 61.
Sasaqui, T. *et al.* (2005) *Astrophys. J.*, **634**, 1173.
Satchler, G.R. (1990) *Introduction to Nuclear Reactions*, Oxford University Press, New York.
Sauter, T. and Käppeler, F. (1997) *Phys. Rev.*, **C55**, 3127.
Sbordone, L. *et al.* (2010) *Astron. Astrophys.*, **522**, 26.
Schaller, G. *et al.* (1992) *Astron. Astrophys. Suppl. Ser.*, **96**, 269.
Schatz, H. *et al.* (1995) *Phys. Rev.*, **C51**, 379.
Schatz, H. *et al.* (1998) *Phys. Rep.*, **294**, 167.
Schatz, H. *et al.* (1999) *Astrophys. J.*, **524**, 1029.
Schatz, H. *et al.* (2001) *Phys. Rev. Lett.*, **86**, 3471.
Schatz, H. *et al.* (2002) *Astrophys. J.*, **579**, 626.
Schatz, H. *et al.* (2005) *Phys. Rev.*, **C72**, 065804.
Schiffer, J.P. (1963) *Nucl. Phys.*, **46**, 246.
Schmidt, S. *et al.* (1995) *Nucl. Instrum. Methods*, **A364**, 70.
Schwarzschild, M. and Härm, R. (1965) *Astrophys. J.*, **142**, 855.
Scott, A.F. *et al.* (1991) *Nucl. Phys.*, **A523**, 373.
Seeger, P.A., Fowler, W.A., and Clayton, D.D. (1965) *Astrophys. J. Suppl.*, **11**, 121.
Seitenzahl, I.R. *et al.* (2008) *Astrophys. J. Lett.*, **685**, 129.
Selin, E., Arnell, S.E., and Almen, O. (1967) *Nucl. Instrum. Methods*, **56**, 218.
Semkow, T.M. *et al.* (1990) *Nucl. Instrum. Methods*, **A290**, 437.
Semkow, T.M. *et al.* (2002) *Appl. Radiat. Isot.*, **57**, 213.
de Séréville, N., Berthoumieux, E., and Coc, A. (2005) *Nucl. Phys.*, **A758**, 745.
Seuthe, S. *et al.* (1987) *Nucl. Instrum. Methods*, **A260**, 33.
Seuthe, S. *et al.* (1990) *Nucl. Phys.*, **A514**, 471.
Simmerer, J. *et al.* (2004) *Astrophys. J.*, **617**, 1091.
Skyrme, D.J. *et al.* (1967) *Nucl. Instrum. Methods*, **57**, 61.
Smith, D.M. (2004) *New Astron. Rev.*, **48**, 87.
Smith, M.S. *et al.* (1992) *Nucl. Phys.*, **A536**, 333.
Smith, M.S., Kawano, L.H., and Malaney, R.A. (1993) *Astrophys. J. Suppl.*, **85**, 219.
Smith, M.S. and Rehm, K.E. (2001) *Annu. Rev. Nucl. Part. Sci.*, **51**, 91.
Sneden, C., Cowan, J.J., and Gallino, R. (2008) *Annu. Rev. Astron. Astrophys.*, **46**, 241.
Sneden, C., Pilachowski, C.A., and Vandenberg, D. (1986) *Astrophys. J.*, **311**, 826.
Solomon, S.B. and Sargood, D.G. (1978) *Nucl. Phys.*, **A312**, 140.
Somorjai, E. *et al.* (1998) *Astron. Astrophys.*, **333**, 1112.
Sonzogni, A.A. *et al.* (2000) *Phys. Rev. Lett.*, **84**, 1651.
Spinka, H. and Winkler, H. (1974) *Nucl. Phys.*, **A233**, 456.
Spite, M. and Spite, F. (1982) *Nature*, **297**, 483.
Starrfield, S., Iliadis, C., and Hix, W.R. (2008) in *Classical Novae* (eds M.F. Bode and A. Evans), Cambridge University Press, Cambridge.
Stegmüller, F. *et al.* (1996) *Nucl. Phys.*, **A601**, 168.
Stella, B. *et al.* (1995) *Nucl. Instrum. Methods*, **A355**, 609.

Strong, A.W., Moskalenko, I.V., and Ptuskin, V.S. (2007) *Annu. Rev. Nucl. Part. Sci.*, **57**, 285.
Suess, H.E. and Urey, H.C. (1956) *Rev. Mod. Phys.*, **28**, 53.
Takahashi, K. and Yokoi, K. (1987) *At. Data Nucl. Data Tables*, **36**, 375.
Takayanagi, S. *et al.* (1966) *Nucl. Instrum. Methods*, **45**, 345.
Tavani, M. *et al.* (2010) *Astrophys. J. Lett.*, **710**, 151.
Terakawa, A. *et al.* (1993) *Phys. Rev.*, **C48**, 2775.
The, L.-S. *et al.* (1998) *Astrophys. J.*, **504**, 500.
The, L.-S., El Eid, M.F., and Meyer, B.S. (2000) *Astrophys. J.*, **533**, 998.
Thielemann, F.-K. and Arnett, W.D. (1985) *Astrophys. J.*, **295**, 604.
Thomas, R.G. (1951) *Phys. Rev.*, **81**, 148.
Thomas, J. *et al.* (1986) *Phys. Rev.*, **C33**, 1679.
Thompson, W.J. and Iliadis, C. (1999) *Nucl. Phys.*, **A647**, 259.
Tilley, D.R., Weller, H.R., and Cheves, C.M. (1993) *Nucl. Phys.*, **A564**, 1.
Tilley, D.R. *et al.* (1995) *Nucl. Phys.*, **A595**, 1.
Tilley, D.R. *et al.* (1998) *Nucl. Phys.*, **A636**, 249.
Timmes, F.X. (1999) *Astrophys. J. Suppl.*, **124**, 241.
Timmes, F.X., Brown, E.F., and Truran, J.W. (2003) *Astrophys. J. Lett.*, **590**, 83.
Tosi, M. (2000) *Proceedings of IAU Symposium 198* (eds L. da Silva, M. Spite, J.R. Medeiros), ASP Conference Series, p. 525.
Travaglio, C. *et al.* (2001) *Astrophys. J.*, **549**, 346.
Travaglio, C. *et al.* (2004a) *Astron. Astrophys.*, **425**, 1029.
Travaglio, C. *et al.* (2004b) *Astrophys. J.*, **601**, 864.
Truran, J.W. *et al.* (2002) *Publ. Astron. Soc. Pac.*, **114**, 1293.
Tsagari, P. *et al.* (2004) *Phys. Rev.*, **C70**, 015802.
Tueller, J. *et al.* (1990) *Astrophys. J. Lett.*, **351**, 41.
Ugalde, C. (2005) Ph.D. thesis, University of Notre Dame.
Uhrmacher, M. *et al.* (1985) *Nucl. Instrum. Methods*, **B9**, 234.
Ulrich, R.K. (1973) in *Explosive Nucleosynthesis* (eds D.N. Schramm and W.D. Arnett), University of Texas Press, Austin, TX.
Utsunomiya, H. *et al.* (2003) *Phys. Rev.*, **C67**, 015807.
Vancraeynest, G. *et al.* (1998) *Phys. Rev.*, **C57**, 2711.
Vangioni-Flam, E., Cassé, M., and Audouze, J. (2000) *Phys. Rep.*, **333**, 365.
Vermilyea, D.A. (1953) *Acta Metall.*, **1**, 282.
Vogelaar, R.B. (1989) Ph.D. thesis, California Institute of Technology.
Vogelaar, R.B. *et al.* (1990) *Phys. Rev.*, **C42**, 753.
Vogt, E. (1968) in *Advances in Nuclear Physics*, Vol. 1 (eds M. Baranger and E. Vogt), Plenum Press, New York.
Vojtyla, P. (1995) *Nucl. Instrum. Methods*, **B100**, 87.
Wagemans, C. (1989) *Nucl. Instrum. Methods*, **A282**, 4.
Wagemans, J. *et al.* (2000) *Phys. Rev.*, **C61**, 064601.
Walker, P. and Dracoulis, G. (1999) *Nature*, **399**, 35.
Wallace, R.K. and Woosley, S.E. *et al.* (1981) *Astrophys. J. Suppl.*, **45**, 389.
Wallerstein, G. *et al.* (1997) *Rev. Mod. Phys.*, **69**, 995.
Wallner, A. *et al.* (2006) *Eur. Phys. J. Suppl.*, **A27**, 337.
Walter, F.J. and Boshart, R.R. (1966) *Nucl. Instrum. Methods*, **42**, 1.
Wanajo, S., Janka, H.T., and Kubono, S. (2011) *Astrophys. J.*, **729**, 46.
Wang, B. and Han, Z. (2010) *Astron. Astrophys.*, **515**, A88.
Wang, B. and Han, Z. (2012) *New Astron. Rev.*, **56**, 122.
Wang, W. *et al.* (2007) *Astron. Astrophys.*, **469**, 1105.
Wang, T.R., Vogelaar, R.B., and Kavanagh, R.W. (1991) *Phys. Rev.*, **C43**, 883.
Wang, M. *et al.* (2012) *Chin. Phys.*, **C36**, 1603.
Ward, R.A. and Fowler, W.A. (1980) *Astrophys. J.*, **238**, 266.
Ward, R.A., Newman, M.J., and Clayton, D.D. (1976) *Astrophys. J. Suppl.*, **31**, 33.
Warner, B. (1995) *Cataclysmic Variable Stars*, Cambridge University Press, Cambridge.

Weaver, T.A. and Woosley, S.E. (1993) *Phys. Rep.*, **227**, 65.
Weber, C. *et al.* (2008) *Phys. Rev.*, **C78**, 054310.
Webber, W.R. (1997) *Space Sci. Rev.*, **81**, 107.
von Weizsäcker, C.F. (1938) *Phys. Z.*, **39**, 633.
Westin, G.D. and Adams, J.L. (1972) *Phys. Rev.*, **C4**, 363.
Wiescher, M. *et al.* (1980) *Nucl. Phys.*, **A349**, 165.
Wilkinson, D.H. (1994) *Z. Phys.*, **A348**, 129.
Wilson, J.R. and Mayle, W.R. (1993) *Phys. Rep.*, **227**, 97.
Wisshak, K. *et al.* (1990) *Nucl. Instrum. Methods*, **A292**, 595.
Wisshak, K. *et al.* (2001) *Phys. Rev. Lett.*, **87**, 251102.
Wiza, J.L. (1979) *Nucl. Instrum. Methods*, **162**, 587.
Wolf, R.A. (1965) *Phys. Rev.*, **137**, B1634.
Woosley, S.E., Arnett, W.D., and Clayton, D.D. (1972) *Astrophys.J.*, **175**, 731.
Woosley, S.E., Arnett, W.D., and Clayton, D.D. (1973) *Astrophys. J. Suppl.*, **26**, 231.
Woosley, S.E. *et al.* (1990) *Astrophys. J.*, **356**, 272.
Woosley, S.E., Heger, A., and Weaver, T.A. (2002) *Rev. Mod. Phys.*, **74**, 1015.
Woosley, S.E. and Howard, W.M. (1978) *Astrophys. J. Suppl.*, **36**, 285.
Wrean, P.R., Brune, C.R., and Kavanagh, R.W. (1994) *Phys. Rev.*, **C49**, 1205.
Wu, S.-C. and Barnes, C.A. (1984) *Nucl. Phys.*, **A422**, 373.
Young, P.A. *et al.* (2006) *Astrophys. J.*, **640**, 891.
Zhao, W.R. and Käppeler, F. (1991) *Phys. Rev.*, **C44**, 506.
Ziegler, J.F. and Biersack, J.P. (2003) program SRIM (unpublished).

Index

Nuclear Physics of Stars, Second Edition. Christian Iliadis.

WILEY END USER LICENSE AGREEMENT

Go to www.wiley.com/go/eula to access Wiley’s ebook EULA.